

AD 677103 AGARD CP No 30

AGARD CONFERENCE PROCEEDINGS No 30

AGARD

ADVISORY GROUP FOR AEROSPACE RESEARCH & DEVELOPMENT

Hypersonic Boundary Layers and Flow Fields

★

MAY 1968



NORTH ATLANTIC TREATY ORGANIZATION



Reproduced by the
CLEARINGHOUSE
for Federal Scientific & Technical
Information Springfield Va 22151

This document has been approved
for public release and its
distribution is unlimited.

NORTH ATLANTIC TREATY ORGANIZATION
ADVISORY GROUP FOR AEROSPACE RESEARCH AND DEVELOPMENT
(ORGANISATION DU TRAITE DE L'ATLANTIQUE NORD)

HYPERSONIC BOUNDARY LAYERS
AND FLOW FIELDS

Papers presented at a Specialists' Meeting of the Fluid Dynamics Panel of AGARD
held at the Royal Aeronautical Society, London, 1-3 May 1968.

The material in this publication has been produced
directly from copy supplied by each author.



*Printed by Technical Editing and Reproduction Ltd
Harford House, 7-9 Charlotte St, London, W.1.*

PREFACE

The possibility of steady state flight of hypersonic vehicles will be a reality in the near future. Some of the problems of the design of such aircraft were the subject of discussions by the Fluid Dynamics Panel of AGARD in the meeting in Delft, September 1966. One of the problems which was discussed was the prediction of the heat transfer and skin friction on such vehicles and the problems of the prediction of the general flow field around the rather complicated shapes of practical aircraft. In an attempt to summarize the current state of the art, as well as to focus attention on new results and new methods, it was decided to hold a meeting entitled "Hypersonic Boundary Layers and Flow Fields" with particular attention focusing on three-dimensional problems. The meeting, in a way, might be considered a continuation of the series of meetings on fundamental boundary layer problems which have been held by the Fluid Dynamics Panel over the past several years.

The call for papers resulted in many more submitted manuscripts than could be covered in the time allotted to the meeting. The final selection of the twenty-six papers presented was made on the basis of several general groupings and combined both theoretical and experimental studies. Many areas of interest and importance could not be covered. The program was broken down into three sessions which were boundary layer oriented with special emphasis on turbulent results, one session on inlet and wave riders, one session on specific problems of bodies at angle of attack, and a special session was introduced to cover some interesting problems of free flight and wind tunnel simulation which had not been recognized in previous work. A few papers on some special problems of controls, mass injection, and low density effects were included although the schedule did not permit any extensive review in these areas.

The meeting, held during the period of May 1-3, 1968, at the Royal Aeronautical Society in London, was organized by a Program Committee selected by the Fluid Dynamics Panel. The author, acting as Chairman, was most ably assisted by Dr D. Kuchemann, UK, Dr J. Lukasiewicz, USA, Dr J. Seddon, UK, and Professor J. Valensi, France. Dr Seddon, in addition, carried the burden of the full and excellent arrangements of the meeting at the Royal Aeronautical Society. Dr Barth, Executive Officer of the Fluid Dynamics Panel and the AGARD Secretariat were responsible for the administrative controls and the major burden of the paper publications.

Seymour M. Bogdonoff

532.526:533.6.011.55

AVANT PROPOS

La possibilité du vol en régime permanent des machines hypersoniques va se réaliser dans un proche avenir. Certains des problèmes que pose la conception de ces appareils ont fait l'objet de discussions au cours de la réunion de la Commission de la Dynamique des Fluides de l'AGARD tenue à Delft en septembre 1966. L'un de ces problèmes portait sur la possibilité de prédire le transfert de chaleur et le frottement de revêtement se produisant sur de tels avions. On a examiné aussi les questions de la prédiction du champ d'écoulement général autour des formes assez compliquées d'avions pratiques. Dans le but d'essayer de faire le point de l'état actuel des connaissances ainsi que de focaliser l'attention sur les nouveaux résultats obtenus et les nouvelles techniques utilisées il fut décidé d'organiser une réunion ayant pour thème "Les couches limitées et les champs d'écoulement hypersoniques", l'accent étant mis en particulier sur les problèmes tri-dimensionnels. Cette réunion pourrait peut-être être considérée comme la reprise de la série de réunions sur des problèmes fondamentaux de la couche limite qu'a organisée la commission de la Dynamique des Fluides au cours de ces dernières années.

Par suite de l'appel de communications lancé à cette occasion, un nombre de manuscrits beaucoup plus grand qu'il n'était possible de présenter dans la période consacrée à la réunion a été remis. Les vingt-six communications finalement présentées ont été choisies sur la base de plusieurs groupements de travaux de nature générale, et on portait sur des études tant théoriques qu'expérimentales. Bien des domaines qui présentent de l'intérêt et de l'importance n'ont pas pu être abordés. Le programme s'est déroulé au cours de trois séances ayant pour orientation principales les problèmes de la couche limite en attirant une attention particulière sur les résultats obtenus en ce qui concerne la turbulence, dont une séance consacrée aux prises d'air et les avions qui voguent sur des ondes de choc, une séance sur l'étude de problèmes particuliers concernant les corps à des angles d'incidence, et une séance spéciale prévue pour traiter de certains problèmes intéressants du vol libre et de la simulation en soufflerie des conditions de vol, problèmes dont il n'avait pas été tenu compte dans les travaux antérieurs. Quelques exposés relatifs à des problèmes particuliers soulevés par les commandes de vol, l'injection massive et les effets de faible densité ont été inscrits au programme, mais l'horaire prévu n'a permis qu'un aperçu sommaire de ces questions.

L'organisation de la réunion tenue du premier au 3 mai 1968 chez la Royal Aeronautical Society à Londres a été confiée à un comité créé pour établir le programme de communications, et dont les membres ont été choisis par la Commission de la Dynamique des Fluides. L'auteur, en sa qualité de Président de ce comité a reçu une aide précieuse de la part du Dr D. Kuchemann, R-U, du Dr J. Lukasiewicz, Etats-Unis, du Dr J. Seddon, R-U, et du Professeur J. Valensi, France. Le Dr Seddon a assumé, en outre, la responsabilité des dispositions, d'ailleurs excellentes, pour que la réunion puisse se tenir dans l'immenable de la Royal Aeronautical Society. Le Dr Barthe, Officier exécutif de la Commission de la Dynamique des Fluides, ainsi que le secrétariat de l'AGARD se sont chargés des aspects administratifs de la réunion et de la plus grande partie du travail en ce qui concerne la publication des exposés.

Seymour M. Bogdonoff

CONTENTS

	Page
PREFACE	iii
AVANT PROPOS	iv
	Reference
EXPERIMENTS WITH HYPERSONIC TURBULENT BOUNDARY LAYERS ON FLAT PLATES AND DELTA WINGS by M. H. Bertram, A. M. Carey, Jr and A. H. Whitehead, Jr	1
EXPERIMENTAL MEASUREMENTS OF COLD WALL TURBULENT HYPERSONIC BOUNDARY LAYERS by J. H. Perry and R. A. East	2
THEORY AND EXPERIMENT FOR THE STRUCTURE OF SOME HYPERSONIC BOUNDARY LAYERS by E. J. Softley and R. J. Sullivan	3
THE INTERACTION OF A TURBULENT BOUNDARY LAYER AND A SHOCK AT HYPERSONIC MACH NUMBERS by D. F. Myring	4
LAMINAR AND TURBULENT FLOW PAST AXISYMMETRIC CONVEX CORNERS AT HYPERSONIC MACH NUMBERS by K. J. Touryan and T. J. Tyson	5
ORDERLY THREE DIMENSIONAL PROCESSES IN TURBULENT BOUNDARY LAYERS ON ABLATING BODIES by T. N. Canning, M. E. Tauber, M. E. Wilkins and G. T. Chapman	6
This paper has been cancelled by mutual agreement	7
REYNOLDS AND MACH NUMBER SIMULATION OF APOLLO AND GEMINI RE-ENTRY AND COMPARISON WITH FLIGHT by B. J. Griffith and D. E. Boylan	8
MODULAR HYPERSONIC INLETS WITH CONICAL FLOWS by S. Mölder and J. M. Romekie	9
THE USE OF KNOWN FLOW FIELDS AS AN APPROACH TO THE DESIGN OF HIGH SPEED AIRCRAFT by J. Seddon and A. Spence	10

	Reference
CALCULATIONS OF THE PRESSURE DISTRIBUTION ON LIFTING CONICAL WINGS WITH APPLICATIONS TO THE OFF-DESIGN BEHAVIOR OF WAVE RIDERS by L.C.Squire	11
EXPERIMENTAL RESULTS FROM THREE CONE-FLOW WAVE RIDERS by J.Pike	12
EXPERIMENTAL INVESTIGATIONS OF WAVE RIDERS IN THE MACH NUMBER RANGE FROM 8 TO 15 by K.Kipke	13
HYPERSONIC VISCOUS - INVISCID INTERACTION BY A NEW TYPE OF ANALYSIS by S.G.Rubin, S.Rudman, T.C.Lin and M.Pierucci	14
This paper has been cancelled by mutual agreement	15
AN INVESTIGATION OF THREE-DIMENSIONAL JET CONTROL INTERACTION ON A CONICAL BODY by V.Zakkay, J.Erdos and W.Calarese	16
HYPERSONIC INTERACTIONS ABOUT A SLENDER CONE INDUCED BY A RADIAL MASS INJECTION by P.G.Simpkins	17
HYPERSONIC FLOW IN RECTANGULAR AND NON-RECTANGULAR CORNERS by R.J.Cresci, S.G.Rubin and C.T.Nardo	18
THE EXTERNAL FLOW FIELD ABOUT YAWED CIRCULAR CONES by W.J.Rainbird	19
ETUDE THEORIQUE ET EXPERIMENTALE DE LA COUCHE LIMITE AUTOUR D'UN CONE CIRCULAIRE PLACE EN INCIDENCE DANS UN COURANT HYPERSONIQUE par D.Guffroy, B.Roux, J.Marcillat, R.Brun et J.Valensi	20
DISPLACEMENT INTERACTION AND FLOW SEPARATION ON CONES AT INCIDENCE TO A HYPERSONIC STREAM by T.K.Fannelop and G.D.Wadman	21
ETUDE THEORIQUE ET EXPERIMENTALE DE L'ECOULEMENT HYPER- SONIQUE AUTOUR D'UN CORPS ENOUSSE EN INCIDENCE par R.Ceresuela, G.Kretzschmar et C.Rehbach	22
ETUDE DE L'ECOULEMENT SUPERSONIQUE ET HYPERSONIQUE AUTOUR D'UNE AILE ELANCEE EN INCIDENCE par B.Nonnerie et H.Werle	23

	Reference
HYPERSONIC LAMINAR BOUNDARY LAYER GROWTH IN AN ADVERSE PRESSURE GRADIENT by H. A. Fitzhugh	24
VISCOUS HYPERSONIC FLOW PAST A SLENDER CONE AT INCIDENCE by R. Vaglio-Laurin	25
VORTICAL LAYERS IN SUPERSONIC CONICAL FLOW by R. E. Melnik	26
ETUDE DE L'ECOULEMENT A UN NOMBRE DE MACH DE 18 AUTOUR D'UNE PLAQUE PLANE EN INCIDENCE ET A BORD D'ATTAQUE VARIABLE par J. Allegre et C. Bisch	27
STUDIES OF THREE-DIMENSIONAL COMPRESSIBLE BOUNDARY LAYERS ON BLUNT LIFTING ENTRY BODIES by S. W. Kang, W. J. Rae and M. G. Dunn	28

EXPERIMENTS WITH HYPERSONIC TURBULENT BOUNDARY LAYERS

ON FLAT PLATES AND DELTA WINGS

By Mitchel H. Bertram,* Aubrey M. Cary, Jr.,**
and Allen H. Whitehead, Jr.**
NASA Langley Research Center
Langley Station, Hampton, Va., U.S.A.

*Head, Hypersonic Fluid Mechanics Branch, Aero-Physics Division, NASA Langley Research Center.

**Aerospace Engineer, Aero-Physics Division, NASA Langley Research Center.

SUMMARY

Recent hypersonic turbulent-boundary-layer experiments and proposed prediction methods pertinent to the problems of the effect of wall temperature on skin friction and heat transfer, the transformation of the compressible boundary layer to the constant-density type, and the heat transfer to delta wings are considered. The level of the turbulent heat-transfer coefficient is found to be little affected by significant changes in wall-temperature level. Coles' transformation as modified by Baronti and Libby has been examined by utilizing turbulent-boundary-layer profiles covering a wide range of Mach number and wall-temperature ratio. Some success is found for the transformation up to the lower end of the hypersonic range and down to moderately low wall-temperature ratios. For delta wings at low angle of attack, in cases where the flow near the surface is essentially streamwise, strip application of successful flat-plate methods gives good predictions of the turbulent heat transfer if the pressures are known. On the lee side of delta wings where vortices are indicated, predictions by strip theory are surprisingly good in general; but predictions can be poor near the center line where the heat transfer is high. Ability to predict the heat transfer to delta wings appears to be contingent upon the ability to predict the flow field.

1. EXPERIMENTS WITH HYPERSONIC TURBULENT BOUNDARY LAYERS

ON FLAT PLATES AND DELTA WINGS

By Mitchel H. Bertram, Aubrey M. Cary, Jr.,
and Allen H. Whitehead, Jr.

INTRODUCTION

The study of the turbulent boundary layer still consists largely of qualitative theory combined with quantitative empiricism. In the present paper, emphasis will be on experimental results. Configurations are considered not for practicality in an engineering sense but to allow the assessment of the basic validity of various prediction methods for skin friction and heat transfer.

Data have been obtained on flat plates, cones, and nozzle walls, so that such a problem as the effect of wall temperature on skin friction and heat transfer can be evaluated. In 1961 Banner, Kuhl, and Quinn (ref. 1) reported heat-transfer experiments at low wall-temperature ratios from X-15 flights which were at variance with the results obtained by prediction methods in use at that time and provoked considerable controversy. Later results from wind tunnels reported by Bertram and Neal (ref. 2) have tended to confirm the trend indicated by the X-15 flight data. Recent experiments bearing on this problem are examined.

Allied to this problem but with the possibility of wider application is the prospect of a transformation for compressible turbulent boundary layers. This approach, which has appealed to investigators for a number of years, is to determine a transformation which, when applied to boundary-layer profiles or other characteristics, will precisely yield the incompressible result. After such a transformation has been obtained, the boundary-layer details are given in terms of the better known incompressible results. Coles has proposed one such transformation which has been modified by Baronti and Libby and examined by them in some detail (ref. 3). This transformation is intended to apply at arbitrary wall temperatures and pressure gradients and, if successful, would provide a tool for determining not only profiles but also skin friction and heat transfer over a wide range of high-speed flow conditions. Recently obtained boundary-layer profiles for extensive values of Mach number and wall temperature, combined with those previously available, allow the determination of the overall validity of the proposed transformation.

Finally, the heat transfer to the more practically shaped delta wing is considered for the case of low angles of attack. Although this wing shape has been dealt with extensively for the laminar case, there is a paucity of data for the turbulent case. Notable exceptions are the results reported in references 4 to 6. In references 4 and 5 the configuration is complicated by considerable leading-edge bluntness.

SYMBOLS

A	constant in law of the wall, taken here to be 2.43
b	constant in law of the wall (taken here to be 7.5) or wing semispan
C_f	local skin-friction coefficient
h	enthalpy
k	vertical height of roughness above plate
M	Mach number
N	exponent
N_{Pr}	Prandtl number
N_{St}	Stanton number
p	static pressure
r	body radius
R	Reynolds number
R_D	Reynolds number based on wing semispan
R_x	Reynolds number based on distance from leading edge or apex
$R_{x,k}$	Reynolds number based on distance to roughness location from leading edge

R_θ	Reynolds number based on boundary-layer-edge conditions and momentum thickness
R_p	Reynolds number based on distance to peak heating
R_v	Reynolds number based on local conditions and distance from peak shear or peak heating
T	absolute temperature
u	velocity
x	distance from leading edge in streamwise direction
x_c	distance from apex of delta wing along root chord
y	distance normal to root chord of delta wing or distance normal to surface for boundary-layer-profile measurements
α	angle of attack of instrumented surface
δ	boundary-layer thickness
δ_x	two-dimensional laminar boundary-layer thickness at roughness location
Λ	leading-edge sweep angle
ν	kinematic viscosity
ρ	density
θ	ray angle from apex of delta wing and root chord
μ	dynamic viscosity
τ	shearing stress
λ_n	leading-edge wedge angle

Subscripts:

aw	adiabatic wall
B-L	from Baronti-Libby method
i	incompressible
l	local conditions
meas	from direct measurement
S-C	from Spalding-Chi method
t	total
v	based on distance from virtual origin
w	conditions at wall
∞	conditions in undisturbed free stream

A bar over a symbol denotes that the variable is in transformed (constant density) flow.

ANALYSIS METHODS

In reducing the data and applying the various prediction methods, the approach was the same as that given in appendix A of reference 2. Although not explicitly mentioned in reference 2, the recovery factor used in reducing the heat-transfer data was as follows. When the recovery factor in the original data reduction was between 0.88 and 0.90, no correction for recovery factor was made. For data in which the recovery factor assumed in the original data reduction was outside these limits, the data were re-reduced by using a recovery factor of 0.89 and all new heat-transfer data were reduced by assuming this recovery factor.

Consistent with the previous paper (ref. 2) the virtual origin for the turbulent boundary layer was chosen as the place where the peak shear or peak heating occurred.

When the Spalding-Chi method (ref. 7) was applied, the values from this method and its modified form were generally taken from the charts given in reference 8. For this case, as well as for the various T' methods (refs. 9 to 11) and the method of Winkler-Cha (ref. 12), the Prandtl number was assumed to be 0.725 for use with the Karman-Reynolds analogy factor. This same Prandtl number was used with the laminar T' method of Monaghan (ref. 13) to obtain values of the laminar-boundary-layer thickness (δ) for defining values of k/δ_k .

In all cases where the ratios $C_f/C_{f,i}$ or $N_{St}/N_{St,i}$ are presented, whether for experiment or for a prediction method, the value of $C_{f,i}$ or $N_{St,i}$ used in the denominator is the Karman-Schoenherr value given in figures 2 and 3 of reference 8.

DISCUSSION

Effect of Wall-Temperature Ratio on Heat Transfer and Skin Friction

Since the time of the X-15 flight data, which was discussed in the "Introduction," a significant body of wind-tunnel results has been obtained. A comprehensive review of available results up to 1965 was presented by Bertram and Neal at a previous AGARD meeting (ref. 2). In results combined from a number of different facilities, general agreement was found with the trend from the X-15 experiments in which wall temperature was indicated to have little effect on the heat-transfer coefficient.

Recently, data have been obtained by A. M. Cary of the NASA Langley Research Center on a sharp flat plate cooled by interior circulation of liquid nitrogen. The plate was precooled outside the nozzle and upon attaining the desired temperature was suddenly plunged into the Mach number 6 airstream of the Langley 20-inch hypersonic tunnel at a preset angle of attack. The findings from this investigation, which are presented in the upper part of figure 1, show little effect of wall cooling on the Stanton number. The experimental trend agrees with that predicted by the Spalding-Chi method (ref. 7) as modified to heat transfer in appendix A of reference 2 and Hank's $\rho_r \mu_r$ method (appendix B of ref. 5). However, the level of the data favors the prediction by the Spalding-Chi method. Clearly the T' or reference temperature methods (refs. 9 to 11) significantly overestimate the heat transfer at the low wall temperatures, and the Winkler-Cha method (ref. 12) underestimates the heating. Examples of the data from which ratios were obtained are given in the lower part of figure 1, where the small scatter indicates the uniformity of the data for a given run and the repeatability of runs.

Further knowledge of the effect of low temperature ratios can be obtained from new work done by Wallace in a shock tunnel at the Cornell Aeronautical Laboratory (ref. 14). In this investigation shots were made at relatively low temperatures and at the lower end of the hypersonic Mach number range to obtain high Reynolds number. Wall temperature was essentially constant at room temperature. Pressure, skin friction, and heat-transfer data were obtained and the sharp flat-plate model was tested in the range of surface incidence from 0° to 20° . Only data from the sharp flat-plate model are considered here and these data were re-reduced from the original tabulation (ref. 15) as follows:

- Coefficients and Reynolds number were based on local conditions.
- Local conditions were determined from the average of measured wall pressures.
- The enthalpy recovery factor was corrected from a value of 1 to a value of 0.89.

The data of Wallace together with some presented by Softley, Graber, and Zempel (ref. 16) are summarized in figure 2, and details are given in figures 3, 4, and 5. For Wallace's data, local Reynolds numbers based on distance from the assumed virtual origin (peak heating) varied from about 10^6 to 2×10^8 . When peak heating occurred ahead of the first measuring station, a value was assumed for the Reynolds number at peak heating that was consistent with the data for which the location of peak heating was known, as shown in figure 6.

Median values of skin-friction and heat-transfer-coefficient ratios obtained by Wallace are shown in figure 2 compared with various prediction methods as in figure 1. The Mach numbers cover the range from 4.5 to 11.7 and the ratio of wall enthalpy to total enthalpy varied from 0.09 to 0.30. Except for the highest Mach number data, the best agreement with experiment is given by the Spalding-Chi theory. As for the Mach 6 results, the prediction of the Monaghan T' method is generally above the data and that of the $\rho_r \mu_r$ method is generally below the data. Whereas the experimental values of the skin-friction and heat-transfer-coefficient ratios are about equal, the $\rho_r \mu_r$ method predicts the values for the skin-friction-coefficient ratio to be significantly less than those for the heat-transfer-coefficient ratio. Examining these data in detail, one finds in figure 3 that the Spalding-Chi method is the only one of those shown that generally matches the level and trend of the shear and heating ratios with Reynolds number.

The highest Mach number data (fig. 2) were anomalous in that the best agreement is with the T' method which appreciably overpredicts all the other data. In this case, the measured wall pressures were 70 to 80 percent of the stream value with the quoted zero plate incidence, as shown in the upper part of figure 4. If the measured pressures are ignored and the pressure ratio is taken as unity, as was done by the authors themselves, there is good agreement of experiment and the Spalding-Chi prediction, as shown in the lower part of figure 4. The choice of these alternatives is unresolved.

There are shown in figure 2 more recent data obtained by Softley, Graber, and Zempel (ref. 16) in a shock tunnel at much the same conditions as the high Mach number results of Wallace (ref. 14). The results in reference 16 were obtained on a 5° half-angle cone and details are given in figure 5. Generally these data are below the Spalding-Chi prediction modified to account for the fact that transition takes place behind the cone apex (appendix B of ref. 2). These data, transformed to the flat-plate case, are presented in figure 2 and together with the Mach 11 Wallace data bracket the Spalding-Chi prediction.

Nerem and Hopkins (ref. 17) from tests in a shock tube have obtained heat-transfer data at h_w/h_{aw} in the range 0.01 to 0.04 at Mach numbers in the 2.5 to 3.5 range. Here, also, reasonable agreement was found between the prediction of Spalding-Chi and the experiments and poor agreement was found with predictions from the Eckert T' method.

The Transformation of Compressible-Boundary-Layer Profiles

One approach to the compressible turbulent-boundary-layer problem which has received considerable attention in recent years has been the effort to find a transformation which, when applied to the compressible turbulent-boundary-layer equations, will yield identically the better-known incompressible turbulent-boundary-layer equations. In this manner the more extensive knowledge for the incompressible turbulent boundary layer can, in theory, be extended to the compressible-flow case of interest. Typical investigations (refs. 18 to 23 and ref. 3) have achieved some measure of success in defining transformations for the turbulent boundary layer. Coles (ref. 23) has proposed an approach to the transformation of the compressible turbulent-boundary-layer equations in which the compressible and the constant-density flows are assumed to be related by three scaling parameters $\sigma(x)$, $\eta(x)$, and $\xi(x)$. The first parameter relates the stream functions of the two flows, the second is a multiplicative factor of the Dorodnitsyn-Howarth scaling of the normal coordinate, and the third relates the streamwise coordinates of the two flows. An additional assumption pertaining to the invariance of a Reynolds number characterizing the law-of-the-wall region of the boundary layer is necessary to complete the transformation. This assumption, which Coles has called the "substructure hypothesis," provides a substitute for a reference state utilized with many theoretical approaches. Coles' transformation has been extended by Crocco (ref. 22) and modified as well as applied to practical cases by Baronti and Libby (ref. 3). It is with the analysis of Baronti and Libby that the remainder of this section is concerned.

Baronti and Libby modified Coles' substructure hypothesis (they introduced a sublayer hypothesis) and applied the transformation technique by point-by-point mapping of supersonic velocity profiles into the incompressible plane. It should be noted that the transformation theory is applicable only for two-dimensional or axisymmetric ($r \gg \delta$) flow with and without heat transfer or streamwise pressure gradient. This analysis does not define completely the constant-density flow corresponding to the compressible case since the velocity profiles, once transformed, correspond to some unknown \bar{x} -station in the constant-density flow.

Baronti and Libby employed the conventional incompressible equations for the universal velocity profile such that the boundary-layer profile is composed of two distinct regions, a law-of-the-wall region near the wall and a wake or velocity defect region consisting of the major portion of the boundary layer. The equations governing each of these regions, respectively, are:

$$\text{Law of the wall, } \bar{u}/\bar{u}_\tau = f(\bar{\xi})$$

$$\text{Velocity defect law, } (\bar{u} - \bar{u}_1)/\bar{u}_\tau = F(\bar{y}/\bar{\delta}, \bar{x})$$

where

$$\bar{u}_\tau = (\bar{\tau}_w/\bar{\rho}_w)^{1/2}$$

and

$$\bar{\xi} = \bar{y}\bar{u}_\tau/\bar{v}$$

The law of the wall is conventionally expressed as:

$$\bar{u}/\bar{u}_\tau = \xi \quad (0 \leq \bar{\xi} \leq \bar{\xi}_f \text{ (sublayer)})$$

and

$$\bar{u}/\bar{u}_\tau = A \ln b\bar{\xi} \quad (\bar{\xi}_f \leq \bar{\xi} \leq \bar{\xi}_1)$$

where $\bar{\xi}_f$ and $\bar{\xi}_1$ are the values of $\bar{\xi}$ at the edge of the laminar sublayer and the outer limit of the region of application of the law of the wall, respectively. The coefficients A and b are 2.43 and 7.5, respectively, as taken from Clauser (ref. 24) so that $\bar{\xi}_f = 10.6$. The outer limit for the application of the law of the wall is taken as the end of the logarithmic portion of the boundary-layer profile on a scale of \bar{u}/\bar{u}_τ plotted against $\bar{\xi}$. Simplified equations for the direct application of the Baronti and Libby analysis to velocity profiles for compressible flow may be found in reference 25.

The process of applying the transformation theory through the law of the wall is actually an iterative one, since the value of the skin friction in the incompressible plane is necessary in order to transform the corresponding compressible velocity profile to the incompressible plane. In actual practice the procedure is to assume values of the wall skin friction in an incompressible plane until acceptable agreement of the velocity profile with the constant-density result is achieved. The success of the transformation may then be judged by observing how well the transformed velocity profile correlates with the incompressible results and comparing the resulting compressible-skin-friction estimate with that measured or predicted by a reliable theory. Once the incompressible skin friction has been determined from the law-of-the-wall analysis, a comparison with the velocity-defect law is directly obtainable.

Baronti and Libby applied the transformation to velocity profiles for compressible flows up to Mach 9 for adiabatic wall and moderate heat-transfer conditions. In general, their results indicated good correlation of the compressible velocity profiles for the law of the wall in the incompressible plane, and the values of skin friction resulting from the transformation compared well with those measured in most of the investigations cited. However, when a correlation was attempted with the velocity-defect law, the results indicated that a compressible velocity profile under a uniform flow would transform into the incompressible plane and show the characteristics of an incompressible velocity profile under the influence of a pressure gradient. Tennekes (ref. 26) has suggested that this discrepancy may be a result of a distortion of the velocity-defect region of the boundary layer by the Dorodnitsyn-Howarth density scaling of the normal coordinate.

Here the same procedures that were used by Baronti and Libby were used to reduce the compressible velocity profiles to the incompressible form, including the use of the Crocco relation to calculate the density integral through the boundary layer, but the range of Mach number and heat transfer is extended. Experimental velocity profiles were calculated by using measured temperature profiles where available; otherwise the Crocco relation was used. Illustrations of the correlation of the transformed compressible boundary-layer profiles according to the law of the wall with the classical incompressible results are shown in figure 7. Since C_f was not directly measured for most of the profiles presented, the skin-friction results obtained from the transformation for all the cases were normalized by the skin-friction coefficient predicted by the method of Spalding and Chi (ref. 7). In each case, the Spalding-Chi prediction was based on the measured R_0 and T_w/T_t .

The transformation of profiles obtained on tunnel walls in nominal zero-pressure-gradient flow as shown in figure 7(a) provides good correlation for Mach numbers from 2.5 to 8.¹ The skin-friction results from these profiles compare favorably with the Spalding-Chi predictions. For still higher Mach numbers, in the range from 15 to 20, the profiles shown in figure 7(b) appear to correlate well with the incompressible results, but the extent of the logarithmic part of the law-of-the-wall region of the profile is small in comparison with the lower Mach number profiles.² An inspection of the compressible velocity profiles indicates that, in general, as Mach number increases, the laminar sublayer thickness as well as the extent of the wake or velocity-defect region becomes larger. As a result, there appears to be a corresponding decrease in the extent of the logarithmic law-of-the-wall region. Since the wall shear obtained from the transformation is dependent upon a curve fit in the logarithmic law-of-the-wall region, a physical limit of the application of the transformation in the present form may thus exist. However, for profiles with thick laminar sublayers for which sublayer velocity measurements are accurate, the transformation could be applied directly in conjunction with the sublayer part of the law of the wall. The skin-friction results from the transformation of the high Mach number profiles show more deviation than those for the lower Mach number profiles. It should be remarked that the nitrogen profile presented in figure 7(b) is believed to be transitional by the experimenters (ref. 28). However, note that there is no particular difference between this transformed profile and the other presented at considerably higher values of R_0 .

Most of the profiles presented thus far are for moderate values of wall-temperature ratio. Transformed profiles for Mach numbers near 7 (ref. 14) and low values of wall-temperature ratio are given in figure 7(c). Correlation is as good as was found for the previous profiles in figure 7(a), but the resulting values of skin friction are significantly greater than Spalding-Chi predictions.

An illustration of the effect of previous history of the boundary layer on the results of the transformation is shown in figure 7(d). The transformed profiles correlate nicely, and the skin-friction results compare favorably with the predictions of Spalding and Chi, even though each of the boundary layers developed under different conditions.

A compilation of the skin-friction results obtained from the transformation technique is presented in figure 8(a). The skin-friction results from the transformation are referenced to the skin friction predicted by the Spalding-Chi method and presented as a function of the ratio of wall temperature to total temperature for each particular case. The data include all the experiments analyzed by Baronti and Libby, results cited in figure 7, and additional results from references 29 to 32. It has been shown in several investigations (for example, ref. 2 and in the first section of this

¹Mach 2.49 and 4.44 profiles from unpublished measurements by Stallings and Couch in the Langley Unitary wind tunnel; Mach 6.0 and 6.8 from reference 2; Mach 7.95 from unpublished measurements by W. V. Feller in Langley 18-inch variable-density wind tunnel, all with dp/dx essentially zero.

²Mach 15.6 profile from reference 27; Mach 20.2 profile from reference 25; Mach 18.4 profile from unpublished measurements by W. D. Harvey and F. L. Clark but a similar profile is found in reference 28.

paper) that the method of Spalding and Chi can be expected to give accurate skin-friction predictions on flat plates and cones at least up to Mach 9 and over the entire range of T_w/T_t for the data in figure 8.

In general, the skin-friction results from the transformation appear to be consistently higher than those predicted by the Spalding-Chi method. Although the overprediction is in the 10-percent range for adiabatic and moderately cooled walls, the error is large for extreme cooling conditions. Wallace (ref. 14) obtained direct skin-friction measurements on the nozzle wall at the same locations and the same flow conditions for which the profile data were taken. The measured skin-friction results shown in figure 8(b) are in good agreement with the Spalding-Chi predictions, as are the results from other investigations in which direct measurements of skin friction were made. It thus appears that the transformation as applied is not generally valid even for the logarithmic portion of the law of the wall.

Since in the application of the transformation theory it is necessary to define a temperature distribution through the boundary layer (the Crocco distribution for both this investigation and that of Baronti and Libby), it may be suspected that the particular distribution assumed would affect the skin friction obtained from the transformation. Thus, it is believed reasonable to examine some of the available temperature distributions in detail. A number of measured temperature profiles were presented in reference 2. Since that time some additional profiles have become available and these are shown in figure 9. The upper part of figure 9 is from reference 2, which presents data from references 29 and 33 to 36 with the addition of unpublished measurements obtained by R. L. Stallings and L. M. Couch in the Langley Unitary wind tunnel. These experimental profiles are compared with the suggested profiles of Crocco, Michel (ref. 37), and Walz (ref. 38). There is disagreement between the data of references 34 and 35 on one hand and the data of references 29, 36, and Stallings and Couch on the other. The former sets of data agree more closely with the Crocco and Michel prediction and the latter sets agree more closely with Walz' prediction.

Some relatively cold wall data are shown in the lower part of figure 9 from reference 39 and unpublished measurements obtained by W. V. Feller in the Langley 18-inch variable-density wind-tunnel. These data do not agree with any of the prediction methods previously shown and depart considerably from nonlinearity. This is also seen in the profiles presented in figures 18 and 19 of reference 2. A better fit to experiment, as shown in figure 9, would be a profile which had a quadratic form

$$\frac{T_t - T_w}{T_{t,\infty} - T_w} = \left(\frac{u}{u_\infty}\right)^2$$

This is equivalent to assuming that Walz' adiabatic wall-temperature distribution is independent of wall-temperature ratio.

Since the quadratic temperature profile represents experimental results better than the Crocco profile, at least at low wall-to-total-temperature ratios, the transformation was applied by using the quadratic temperature profile for several compressible profiles with low wall-to-total-temperature ratios. For each case the quadratic temperature law was applied in both the reduction of the pitot profile to velocity and in the transformation. The transformed results from one Wallace profile (Mach 7.61, fig. 7(c)) and one by Harvey and Clark (Mach 18.4, fig. 7(b)) exhibited poor correlation with the incompressible results, and the agreement of the resulting skin-friction coefficients with the Spalding-Chi predictions was no better than was found by using the Crocco relation. The Wallace profile at Mach 7.21 (fig. 7(c)) when transformed by use of the quadratic law did yield a skin-friction coefficient in good agreement with Spalding-Chi, but again poor correlation of the transformed profile was obtained with the incompressible results.

Thus, these limited results indicate that the quadratic profile offers little improvement over the approach of Baronti and Libby. The discrepancy in wall shear at low wall-to-total-temperature ratios does not appear to be a function of Mach number or Reynolds number and may result from a deficiency in the transformation theory itself. A true test of the validity of the theory in the low wall-to-total-temperature range will require more extensive data than that presented here.

Heat Transfer to Delta Wings at Low Angles of Attack

The delta planform is of interest as a practical shape wing for hypersonic flight purposes. For efficient flight, the angle of attack will be low and for the large air-breathing vehicles the leading-edge size necessary from aerothermodynamic considerations is small compared with wing chord. Here, the essentially idealized case of wings with sharp leading edges will be treated.

Consider the wing shown in figure 10(a), on which tests were made at zero angle of attack by Whitehead in the Mach 6 airstream of the Langley 20-inch hypersonic tunnel. (Part of this study was reported in ref. 40.) The cross section of the wing tested was actually half-diamond with the flat side instrumented and aligned with the flow. The shock was attached to the leading edge and the pressure ratio on the instrumented surface was essentially unity. Stanton number is shown as a function of Reynolds number and the boundary-layer flow is indicated to be transitional at the most forward measuring stations. If the virtual origin of the turbulent boundary layer is taken to be at the location of peak heating, the assumption of strip-like flow which is successful with laminar boundary layers is found to give a good prediction for turbulent flow over this delta wing. When this wing is inclined so that the instrumented surface faces 5° to the windward ($k/b_k \approx 2.2$), the shock remains

attached and the pressures are within 5 to 10 percent of the two-dimensional shock value as shown in conical coordinates in figure 10(b). As for the zero angle-of-attack case, the Stanton number is predicted within about 10 percent by strip theory, figure 10(b), using the predicted two-dimensional pressure.

Using two different wings at zero inclination to the flow, Murray and Stallings (ref. 6) were able to obtain data under conditions where the leading-edge shock was attached and detached. The attached-shock case occurs for a 60° swept delta wing at Mach 4.4 and is shown to the left in figure 11, and the detached-shock case occurs for a 70° swept delta wing at Mach 3 and is shown to the right in figure 11.³ In the upper part of figure 11, the heating and pressure data are shown as a function of streamwise Reynolds number and in the lower part of the figure in terms of ray angle. The heat-transfer parameter is chosen to correlate the heating data with the virtual origin of the Reynolds number (R_v) at the location of the boundary-layer trips. For simplicity, a power law for heat transfer was chosen which fitted the Spalding-Chi theory for the conditions of the test and the exponent from this fit was used in the heat-transfer correlation in figure 11.

Leading-edge shock detachment of the 70° swept wing is caused by a bevel on the under side. The pressures show a behavior typical of a subsonic cross flow where the stagnation point is on the beveled under side, and the pressure drops sharply as the flow expands around the sharp leading edge. Using the conical coordinate gives good correlation of the pressures measured on the wing surface, whereas using the linear coordinate gives poor correlation. The surface on which the pressures are measured is flat and aligned with the flow, but the pressures are as low as 50 percent of free-stream pressure at the most forward stations.

Oil flow in the same stream on a 70° swept wing with a smaller leading-edge bevel angle (also with a detached shock) indicated surface flow lines were essentially parallel to the root chord. This suggests using the modified Spalding-Chi method in stripwise fashion with local values of correlated experimental pressures. A good prediction of the heat transfer was obtained and is shown in the lower right side of figure 11. However, if the pressures had not been available and the surface pressure had been taken as equal to free-stream pressure, a significant error would have been incurred in heat-transfer predictions over much of the wing, as shown in figure 11.

At Mach 4.4, for the 60° swept wing there is a slight pressure gradient which may be due to warping of the model during the test. If the Spalding-Chi method is applied in the stripwise manner previously used, a good prediction of the heating is obtained when presented on a chordwise basis rather than conical as shown on the upper left side of figure 11.

The heat-transfer data at the most forward position show a trend which is different from the rest of the data. This behavior is believed caused by proximity to the oversize roughness. (A similar effect is shown on flat plates in ref. 41.)

Again consider the wing tested by Whitehead in the Mach 6 airstream. With the flat instrumented side of the wing facing leeward at the angle of 5° to the free stream, the shock is calculated to be attached. However, only a small deflection of the wing under load would suffice to cause leading-edge shock detachment. The pressures, shown in the right-hand side of figure 12, do not vary much over the span and appear to correlate well in conical coordinates with no particular difference in the pressure distribution between the case where the surface is smooth and the case where spherical boundary-layer trips ($k/b_k = 1.1$) are placed on the surface near the leading edge.

Without boundary-layer trips, the heat transfer to this surface was transitional only at the rearmost stations of the near root chord region. With spherical trips, the level of aerodynamic heating was increased to a general level expected with turbulent flow, as shown on the left-hand side of figure 12. In this case, Stanton number is shown as a function of Reynolds number based on free-stream conditions and distance from the leading edge parallel to the root chord. For reference purposes, the modified Spalding-Chi method was applied in stripwise fashion for a constant pressure on the wing equal to the two-dimensional value. (The virtual origin is taken as $R_{v,x} = 2 \times 10^6$, based on the indicated peak in heating along the root chord.) If the prediction method applied, then one would not expect more than about 20 percent difference, based on the variation in the pressures, between prediction and experiment. Clearly, there is no correlation of the data and there are large increases in heat transfer in the midportion of the wing where surface-oil-flow studies indicate a conical vortex system to be formed. (See ref. 40.) As in the previous presentation, the main body of the heat-transfer data appears to correlate in the conical coordinate as shown on the upper right-hand side of figure 12. The large increase in heating is seen to be confined to the central region of the wing influenced by the vortex system and referred to as the "feather" region in reference 40. Apparently, no increase in pressure is associated with this increase in heat transfer. However, there is a gap in the pressure data and such an increase in pressure may have occurred over a very narrow range of ray angle. If this pressure increase does exist at 5° angle of attack, the extent of the increase probably widens with angle of attack. (The pressure increase was seen on the lee side when the model was positioned at 10° angle of attack, as shown in fig. 13 of ref. 40.)

An analysis of the delta-wing data of reference 6 at Mach numbers from 3 to 4.4 and 5° angle of attack, windward and leeward, shows a similar behavior to the Mach 6 data previously presented in

³Test conditions: At $M_\infty = 4.44$, $T_t = 687^\circ \text{ R}$ and $k/b_k = 3.1$.

At $M_\infty = 2.98$, $T_t = 711^\circ \text{ R}$ and $k/b_k = 4.4$.

figures 10 and 12. These results are shown in figure 13 and indicate that the level of the heating on the lee side can approach that on the windward side near the center of the wing. Better coverage of the central region of the lee surface is needed to determine just how high the heating actually is.

CONCLUDING REMARKS

Recent hypersonic turbulent-boundary-layer experiments and proposed prediction methods pertinent to the problems of the effect of wall temperature, the transformation of the compressible boundary layer to a constant-density type, and heat transfer to the delta wing have been considered.

Up to a Mach number of at least 9, based on flat-plate experiments, the level of the turbulent heat-transfer coefficient is found to be little affected by significant changes in wall temperature, as was predicted by the Spalding-Chi method. The T' or reference-temperature method overpredicts skin friction and heat transfer at low wall-temperature ratios.

The Coles' transformation as modified by Baronti and Libby has been examined by utilizing turbulent-layer profiles covering a wide range of Mach number and wall-temperature ratio. Some success is found for the transformation up to the lower end of the hypersonic range and down to moderately low wall-temperature ratios. However, at the lowest wall-temperature ratios, the transformation gave high wall shears as compared with Spalding-Chi predictions and with shears that were actually measured. At high Mach numbers, very little of the logarithmic portion of the transformed profile remains because of an apparent thickening of the sublayer adjacent to the wall and the velocity-defect wake region comprising the outer part of the profile. It is the logarithmic portion of the profile from which the indicated shear is obtained.

Delta-wing turbulent heat transfer has been examined for several types of flow. At low angles of attack, in cases where the flow near the surface is essentially streamwise, strip application of successful flat-plate methods gives good predictions of the heat transfer if the pressures are known. This result applies whether the leading-edge shock is attached or detached. On the lee side of delta wings where vortices are indicated, predictions by strip theory are surprisingly good in general; but predictions can be poor near the center line where the heat transfer is high. Success in predicting the heat transfer to delta wings appears to be contingent upon the ability to predict the flow field.

REFERENCES

1. Banner, Richard D.; Kuhl, Albert E.; and Quinn, Robert D.: Preliminary Results of Aerodynamic Heating Studies on the X-15 Airplane. NASA TM X-638, 1962.
2. Bertram, Mitchel H.; and Neal, Luther, Jr.: Recent Experiments in Hypersonic Turbulent Boundary Layers. NASA TM X-56335. Presented at the AGARD Specialists' Meeting on Recent Developments in Boundary Layer Research Sponsored by the Fluid Dynamics Panel of AGARD, Naples, Italy, May 10-14, 1965.
3. Baronti, Paolo O.; and Libby, Paul A.: Velocity Profiles in Turbulent Compressible Boundary Layers. AIAA J., vol. 4, no. 2, Feb. 1966, pp. 193-202.
4. Paulsen, James J.; and Schadt, Gail H.: A Study of the Pressure and Heat Transfer Distribution on Highly Swept Slab Delta Wings in Supersonic Flow. AIAA Paper No. 66-130, Jan. 1966.
5. Nagel, A. L.; Fitzsimmons, H. D.; and Doyle, L. B.: Analysis of Hypersonic Pressure and Heat Transfer Tests on Delta Wings With Laminar and Turbulent Boundary Layers. NASA CR-535, 1966.
6. Murray, William M., Jr.; and Stallings, Robert L., Jr.: Heat-Transfer and Pressure Distributions on 60° and 70° Swept Delta Wings Having Turbulent Boundary Layers. NASA TN D-3644, 1966.
7. Spalding, D. B.; and Chi, S. W.: The Drag of a Compressible Turbulent Boundary Layer on a Smooth Flat Plate With and Without Heat Transfer. Jour. Fluid Mech., vol. 18, pt. 1, Jan. 1964, pp. 117-143.
8. Neal, Luther, Jr.; and Bertram, Mitchel H.: Turbulent-Skin-Friction and Heat-Transfer Charts Adapted From the Spalding and Chi Method. NASA TN D-3969, 1967.
9. Monaghan, R. J.: On the Behaviour of Boundary Layers at Supersonic Speeds. Fifth International Aeronautical Conference, Rita J. Turino and Caroline Taylor, eds., Inst. Aeron. Sci., Inc. 1955, pp. 277-315.
10. Eckert, E. R. G.: Engineering Relations for Friction and Heat Transfer to Surfaces in High Velocity Flow. J. Aero. Sci., vol. 22, no. 8, Aug. 1955, pp. 585-587.
11. Sommer, Simon C.; and Short, Barbara J.: Free-Flight Measurements of Turbulent-Boundary-Layer Skin Friction in the Presence of Severe Aerodynamic Heating at Mach Numbers From 2.8 to 7.0. NACA TN 3391, 1955.
12. Winkler, Eva M.; and Cha, Moon H.: Investigation of Flat Plate Hypersonic Turbulent Boundary Layers With Heat Transfer at a Mach Number of 5.2. NAVORD Rept. 6631, U.S. Naval Ord. Lab., Sept. 15, 1959.
13. Monaghan, R. J.: An Approximate Solution of the Compressible Laminar Boundary Layer on a Flat Plate. R & M No. 2760, British A.R.C., 1956.
14. Wallace, J. E.: Hypersonic Turbulent Boundary Layer Studies at Cold Wall Conditions. 1967 Heat Transfer and Fluid Mechanics Institute (San Diego, Calif.), June 19-21, 1967.
15. Heronimus, G. A.: Hypersonic Shock Tunnel Experiments on the W7 Flat Plate Model - Expansion Side, Turbulent Flow and Leading Edge Transpiration Data. CAL Rept. No. AA-1952-Y-2 Contract No. AF 33(615)-1847, Feb. 1966.
16. Softley, E. J.; Graber, B. C.; and Zempel, R. E.: Transition of the Hypersonic Boundary Layer on a Cone. Part 1 - Experiments at $M_\infty = 12$ and 15. General Electric Report R67DS39, November 1967. Part of this paper presented at the AIAA 6th Aerospace Sciences Meeting, Jan. 1968 as AIAA paper No. 68-39.
17. Nerem, Robert M.; and Hopkins, Richard A.: An Experimental Investigation of Heat Transfer From a Highly Cooled Turbulent Boundary Layer. Presented at the AIAA Sixth Aerospace Sciences Meeting, AIAA Paper 68-43, Jan. 22-24, 1968.
18. Burggraf, O. R.: The Compressibility Transformation and Turbulent-Boundary-Layer Equations. J. Aerospace Sci., vol. 29, no. 4, April 1962, pp. 434-439.
19. Mager, Artur: Transformation of the Compressible Turbulent Boundary Layer. J. Aeron. Sci., vol. 25, no. 5, May 1958, pp. 305-311.
20. Spence, D. A.: Velocity and Enthalpy Distributions in the Compressible Turbulent Boundary Layer on a Flat Plate. J. Fluid Mech., vol. 8, pt. 3, July 1960, pp. 368-387.
21. Coles, Donald E.: Measurements in the Boundary Layer on a Smooth Flat Plate in Supersonic Flow, III. Measurements in a Flat-Plate Boundary Layer at the Jet Propulsion Laboratory. Jet Propulsion Laboratory, Rept. No. 20-71 (Contract No. DA-04-495-Ord 18), Jet Propulsion Lab., California Inst. Technol., June 1, 1953.

22. Crocco, L.: Transformations of the Compressible Turbulent Boundary Layer With Heat Exchange. AIAA J., vol. 1, no. 12, Dec. 1963, pp. 2723-2731.
23. Coles, D. E.: The Turbulent Boundary Layer in a Compressible Fluid. U.S. Air Force Project RAND Rept. R-403-PR, The RAND Corp., Sept. 1962.
24. Clauser, F. H.: Turbulent Boundary Layers in Adverse Pressure Gradients. J. Aeron. Sci., vol. 21, no. 2, Feb. 1954, pp. 91-108.
25. Watson, Ralph D.; and Cary, A. M., Jr.: The Transformation of Hypersonic Turbulent Boundary Layers to Incompressible Form. AIAA J. (Tech. Notes), vol. 6, no. 6, June 1967, pp. 1202-1203.
26. Tennekes, H.: Law of the Wall for Turbulent Boundary Layers in Compressible Flow. AIAA J., vol. 5, no. 3, Mar. 1967, pp. 489-492.
27. Henderson, A., Jr.; Rogallo, R. S.; Woods, W. C.; and Spitzer, C. R.: Exploratory Hypersonic Boundary-Layer Transition Studies. AIAA J. (Tech. Notes), vol. 3, no. 7, July 1965, pp. 1363-1364.
28. Clark, Frank L.; Ellison, James C.; and Johnson, Charles B.: Recent Work in Flow Evaluation and Techniques of Operation for the Langley Hypersonic Nitrogen Facility. Fifth Hypervelocity Techniques Symposium, Denver Res. Inst. and Arnold Eng. Develop. Center, Mar. [16-17], 1967, vol. 1 - Advanced Experimental Techniques for Study of Hypervelocity Flight, pp. 347-373.
29. Lobb, Kenneth R.; Winkler, Eva M.; and Persh, Jerome: NOL Hypersonic Tunnel No. 4 Results VII: Experimental Investigation of Turbulent Boundary Layers in Hypersonic Flow. NAVORD Rept. 262, Mar. 1955.
30. Samuels, R. D.; Peterson, J. B., Jr.; and Adcock, J. B.: Experimental Investigation of the Turbulent Boundary Layer at a Mach Number of Six With Heat Transfer at High Reynolds Numbers. NASA TN D-3858, 1967.
31. Sterrett, J. R.; and Barber, J. B.: A Theoretical and Experimental Investigation of Secondary Jets in a Mach 6 Free Stream With Emphasis on the Structure of the Jet and Separation Ahead of the Jet. Presented at the Separated Flows Specialists' Meeting Fluid Dynamics Panel - AGARD, Brussels, Belgium, 1966.
32. Maddalon, D. V.; Rogallo, R. S.; and Henderson, A., Jr.: Transition Measurements at Hypersonic Mach Numbers. AIAA J. (Tech. Notes), vol. 5, no. 3, Mar. 1967, pp. 590-591.
33. Reynolds, W. C.; Kays, W. M.; and Kline, S. J.: Heat Transfer in the Turbulent Incompressible Boundary Layer. I - Constant Wall Temperature. NASA MEMO 12-1-58W, 1958.
34. Kistler, Alan L.: Fluctuation Measurements in Supersonic Turbulent Boundary Layers. BRL Report No. 1052, Aberdeen Proving Ground, Aug. 1958.
35. Nothwang, George J.: An Evaluation of Four Experimental Methods for Measuring Mean Properties of a Supersonic Turbulent Boundary Layer. NACA Rept. 1320, 1957. (Supersedes NACA TN 3721, 1956.)
36. Adcock, Jerry B.; Peterson, John B.; and McRee, Donald I.: Experimental Investigation of the Turbulent Boundary Layer at $M = 6$ and High Reynolds Numbers at Zero Heat Transfer. NASA TN D-2907, 1964.
37. Michel, R.; and Mentré, P.: Quelques Resultats sur les Caracteristiques Thermiques des Couches Limites Turbulentes a Temperature Elevee. AGARDograph 97, Recent Developments in Boundary Layer Research, Part 1, May 1965.
38. Walz, A.: Compressible Turbulent Boundary Layers. Int'l. Symp. on The Mechanics of Turbulence, Marseilles, France, Aug. 28-Sept. 2, 1961, Centre Nat'l de la Recherche Scientifique, N. Y., Gordon and Breach 1964, pp. 299-350.
39. Scaggs, Norman E.: Boundary Layer Profile Measurements in Hypersonic Nozzles. ARL 66-0141, U.S. Air Force, July 1966.
40. Whitehead, Allen H., Jr.; and Keyes, J. Wayne: Flow Phenomena and Separation Over Highly Swept Delta Wings With Trailing Edge Flaps at Mach 6. Presented at the AIAA Sixth Aerospace Sciences Meeting. AIAA Paper 68-97, Jan. 22-24, 1968.
41. Sterrett, J. R.; Morrisette, E. L.; Whitehead, A. H., Jr.; and Hicks, R. M.: Transition Fixing for Hypersonic Flow. NASA TN D-4129, 1967.

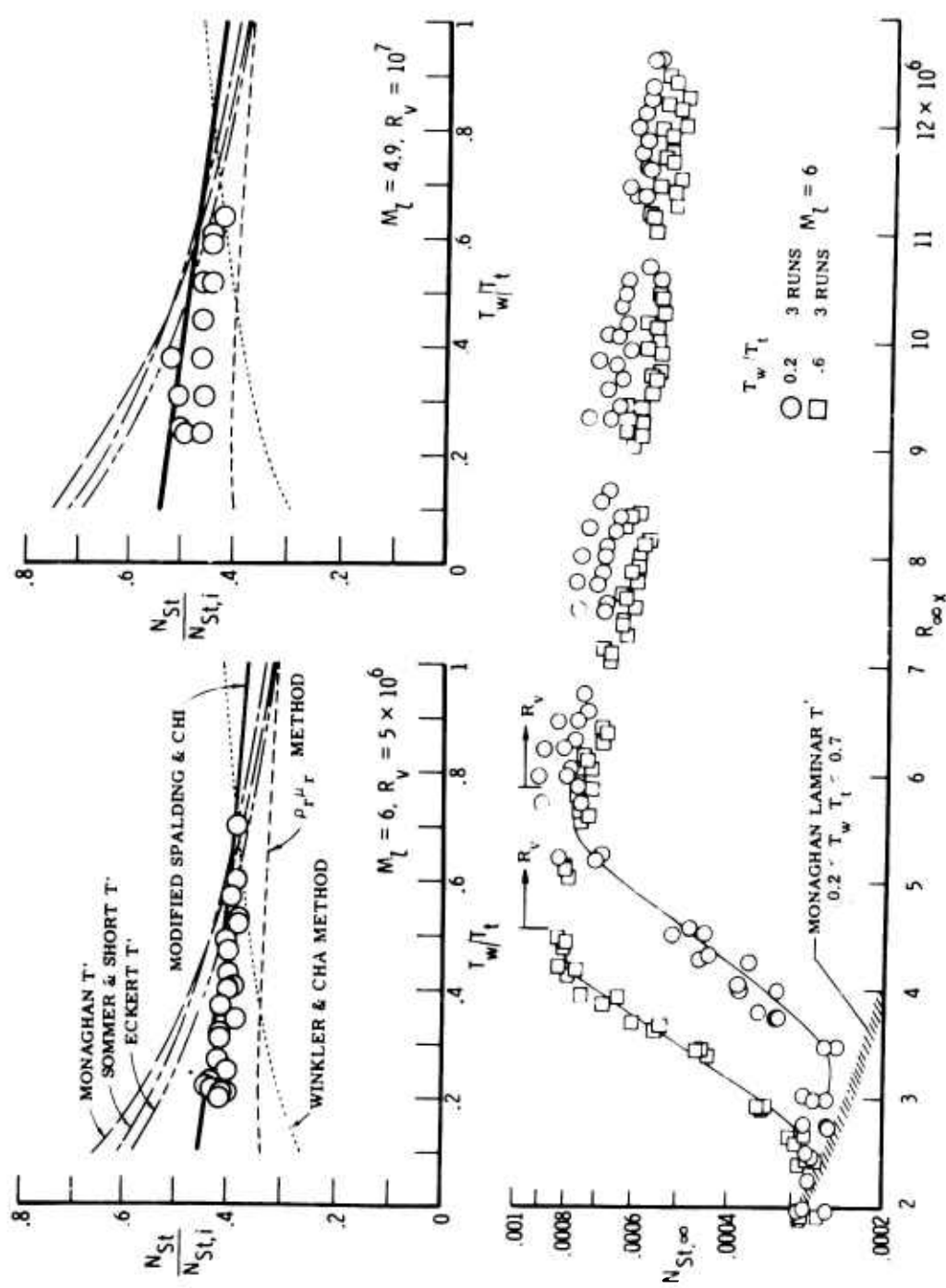


Figure 1.- Effect of wall temperature on turbulent heat transfer to a sharp flat plate at $M_\infty = 6$. $R_\infty/\text{in.} = 0.67 \times 10^6$; $T_t = 960^\circ R$.

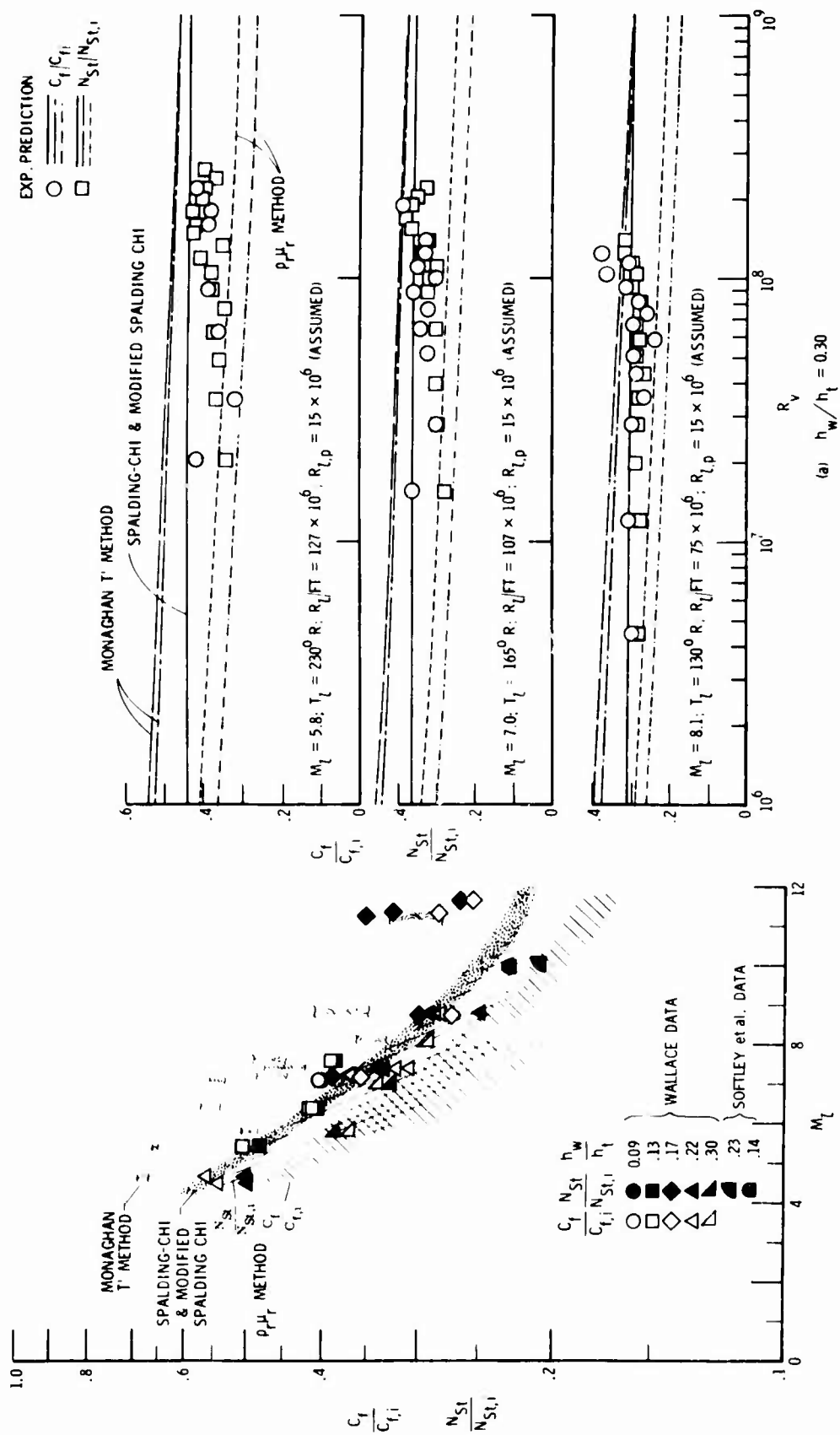


Figure 2.- Comparison of cold-wall turbulent skin-friction and heat-transfer results with prediction methods. $T_w \approx 530^\circ R$.

Figure 3.- Detailed comparison of Wallace's turbulent sharp flat-plate skin-friction and heat-transfer data with various prediction methods.

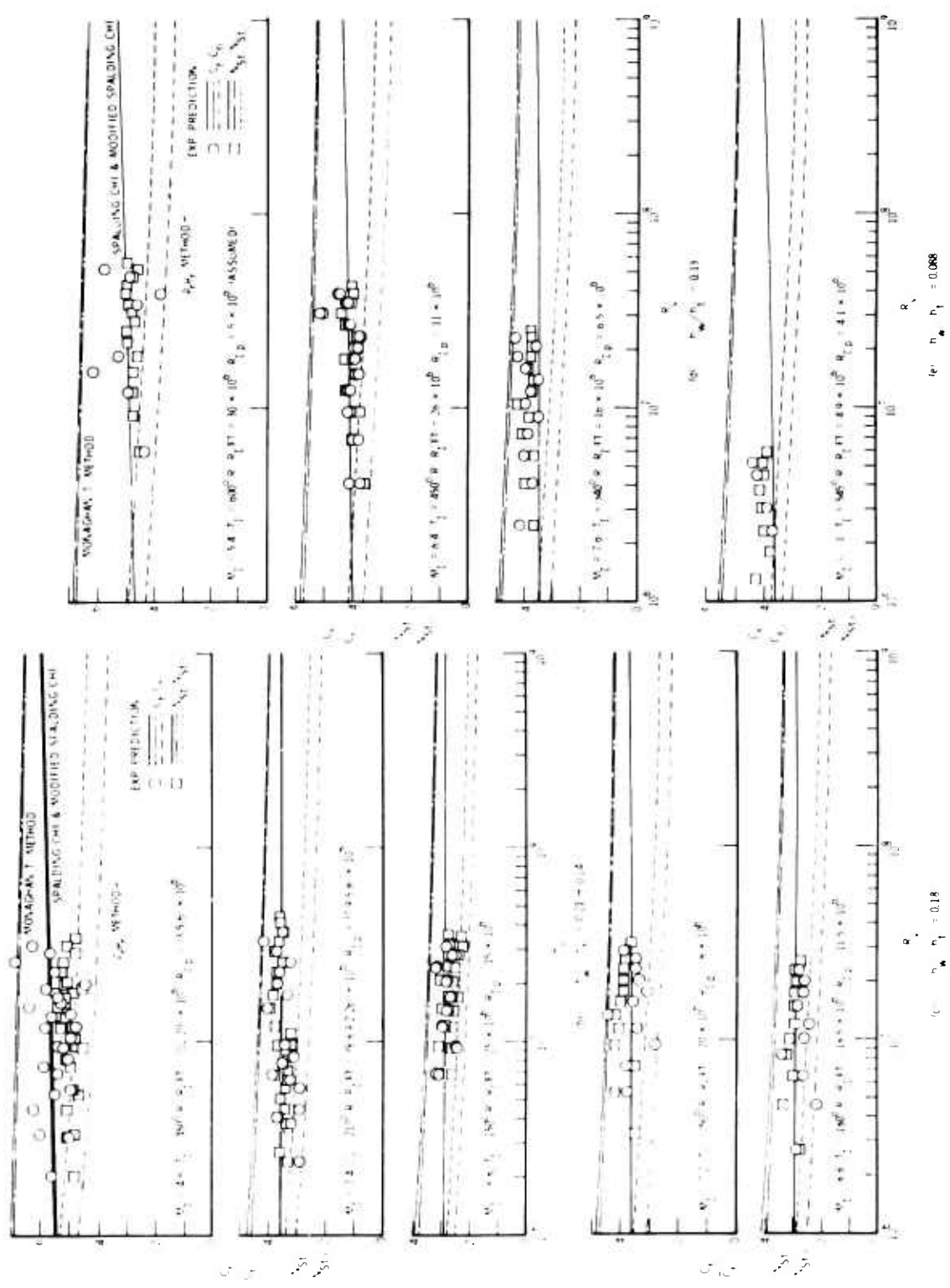


Figure 3.- Concluded.

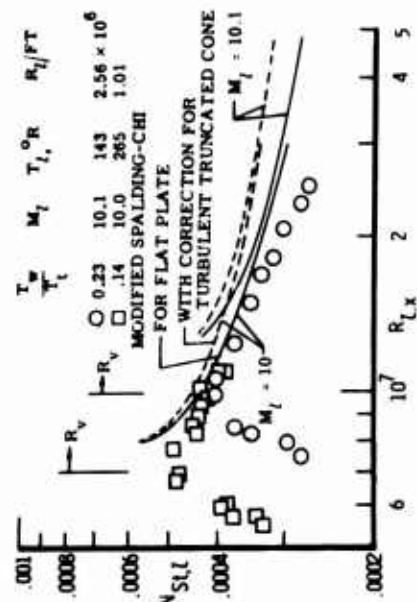


Figure 5.- Softley, Graber, and Zempel data from a cone. $\theta_c = 5^\circ$.

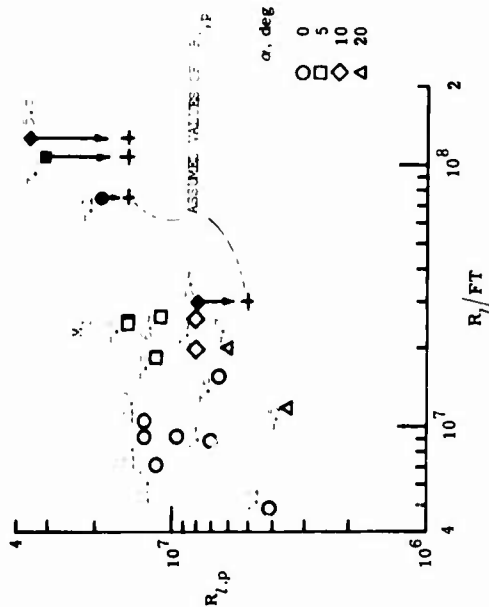


Figure 6.- Values of Reynolds number for peak heating used as virtual origin for Wallace's turbulent data.

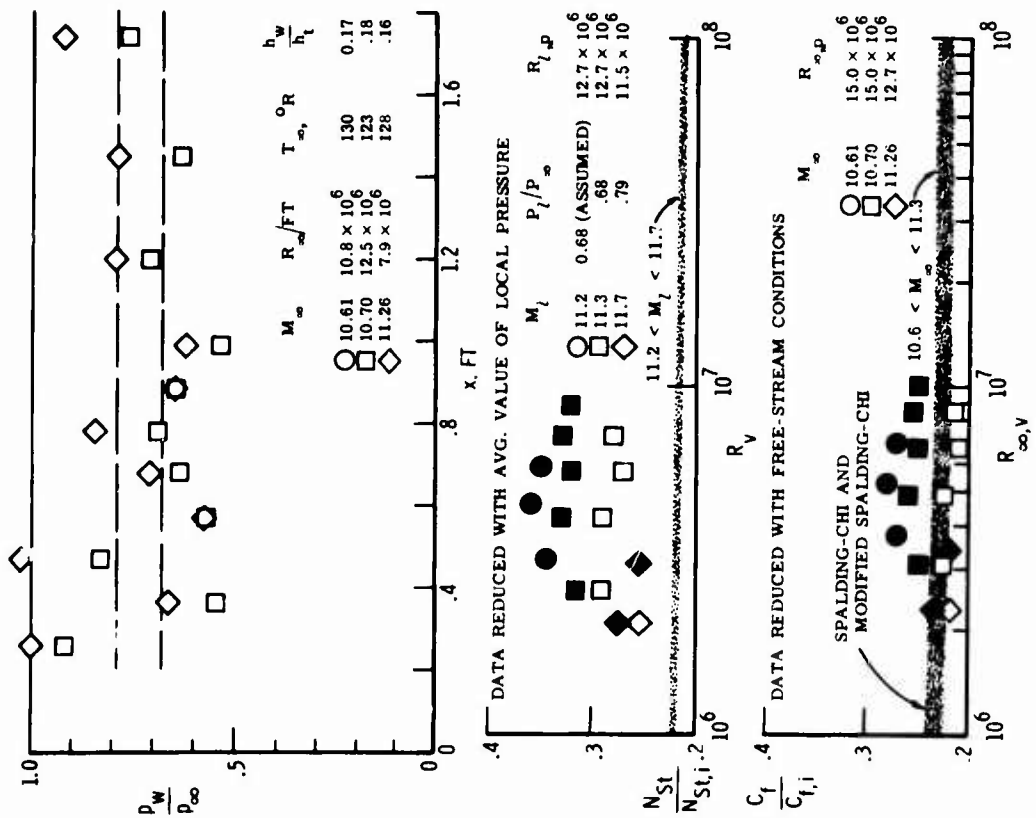


Figure 4.- Analysis of Wallace's highest Mach number turbulent data.

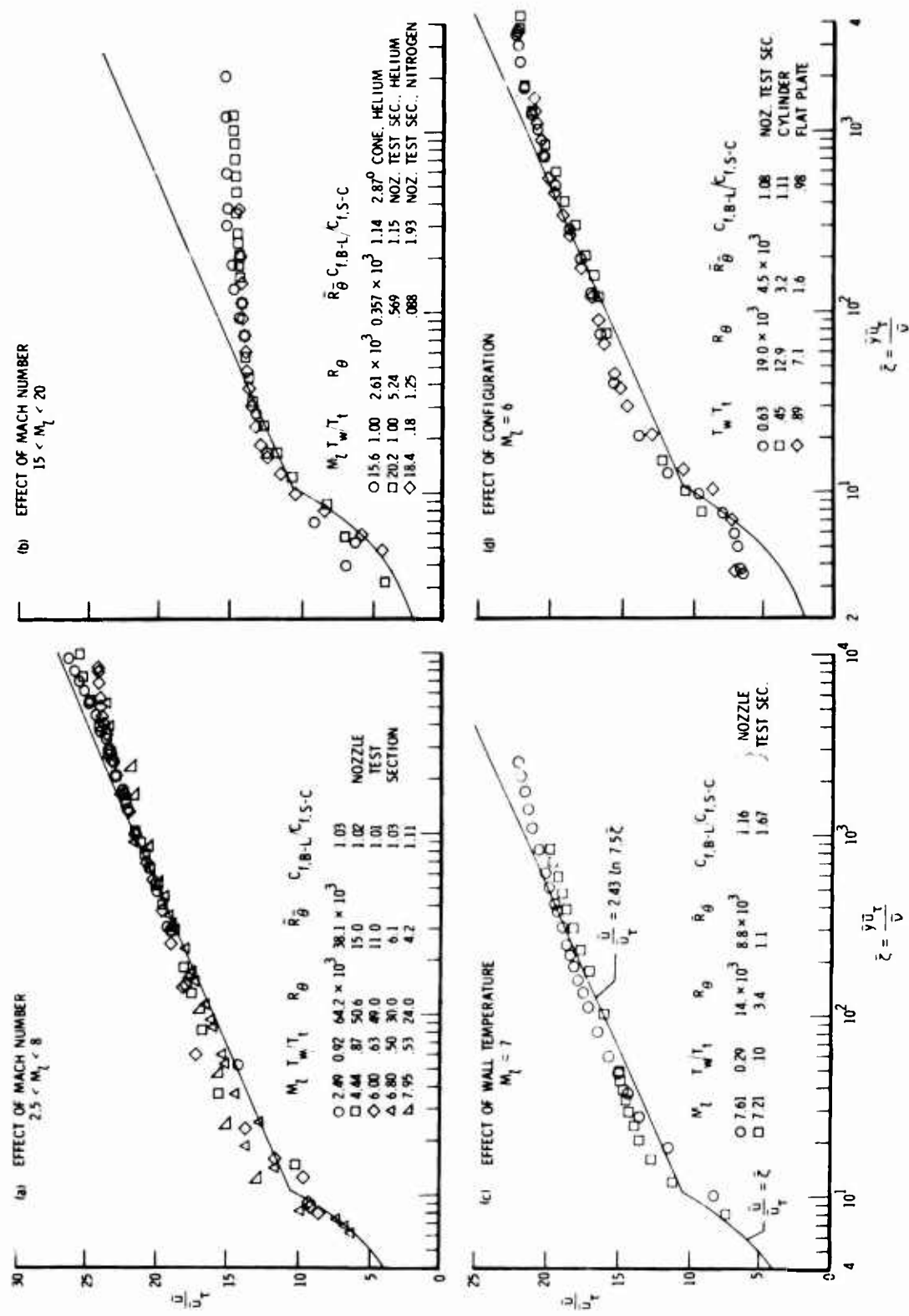


Figure 7.- Compressible turbulent velocity profiles in the incompressible plane according to the transformation of Coles and of Baronti and Libby.

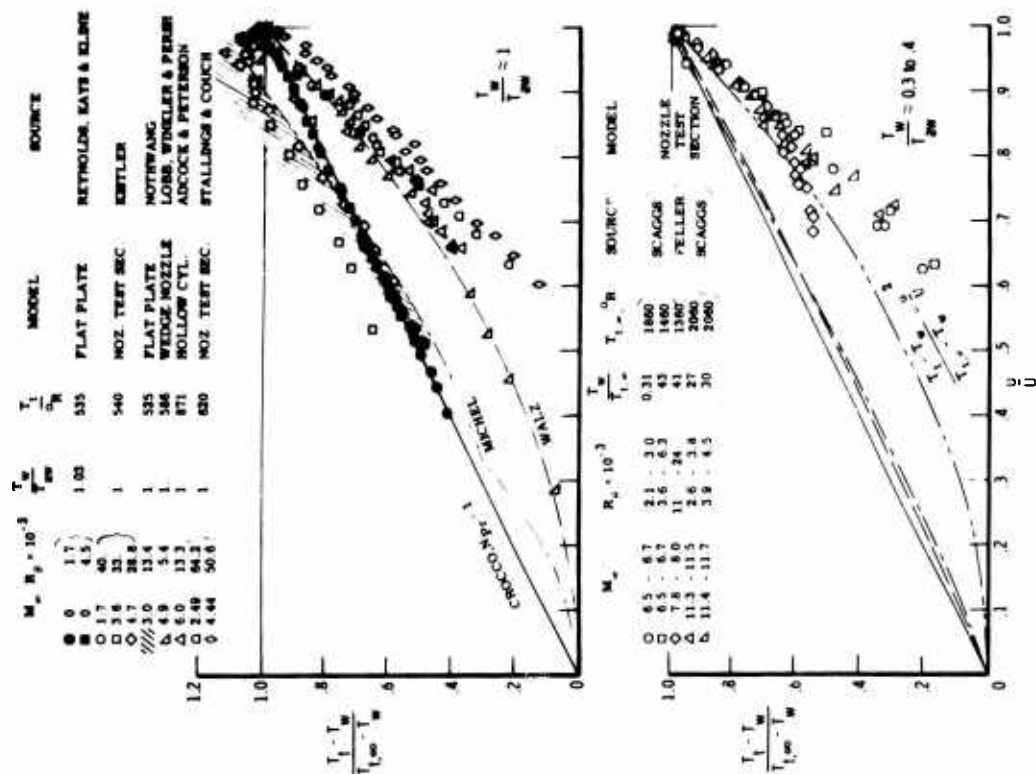


Figure 9.- Turbulent temperature-velocity profiles.

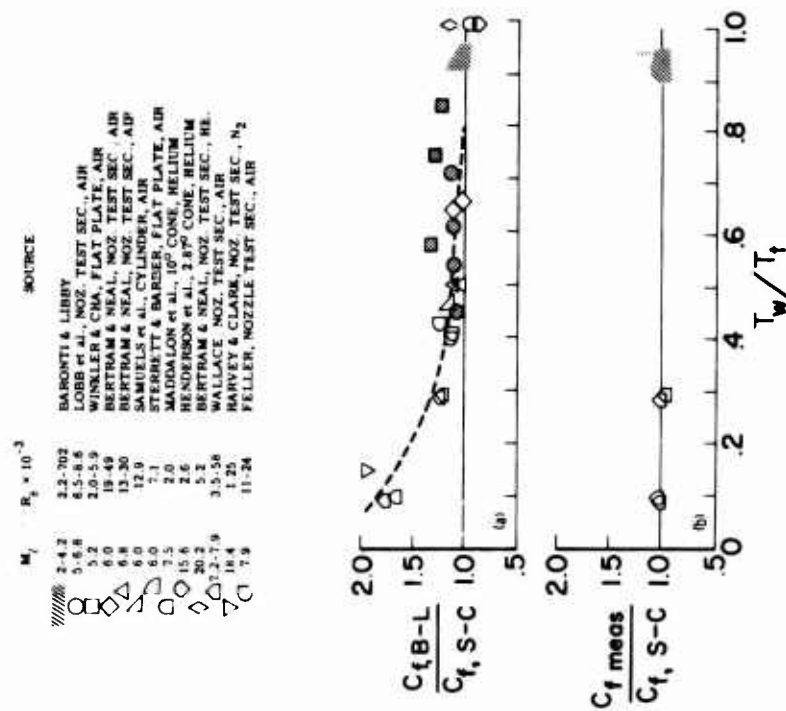


Figure 8.- Local skin friction from the Baronti-Libby transformation and from direct measurements at the same location.

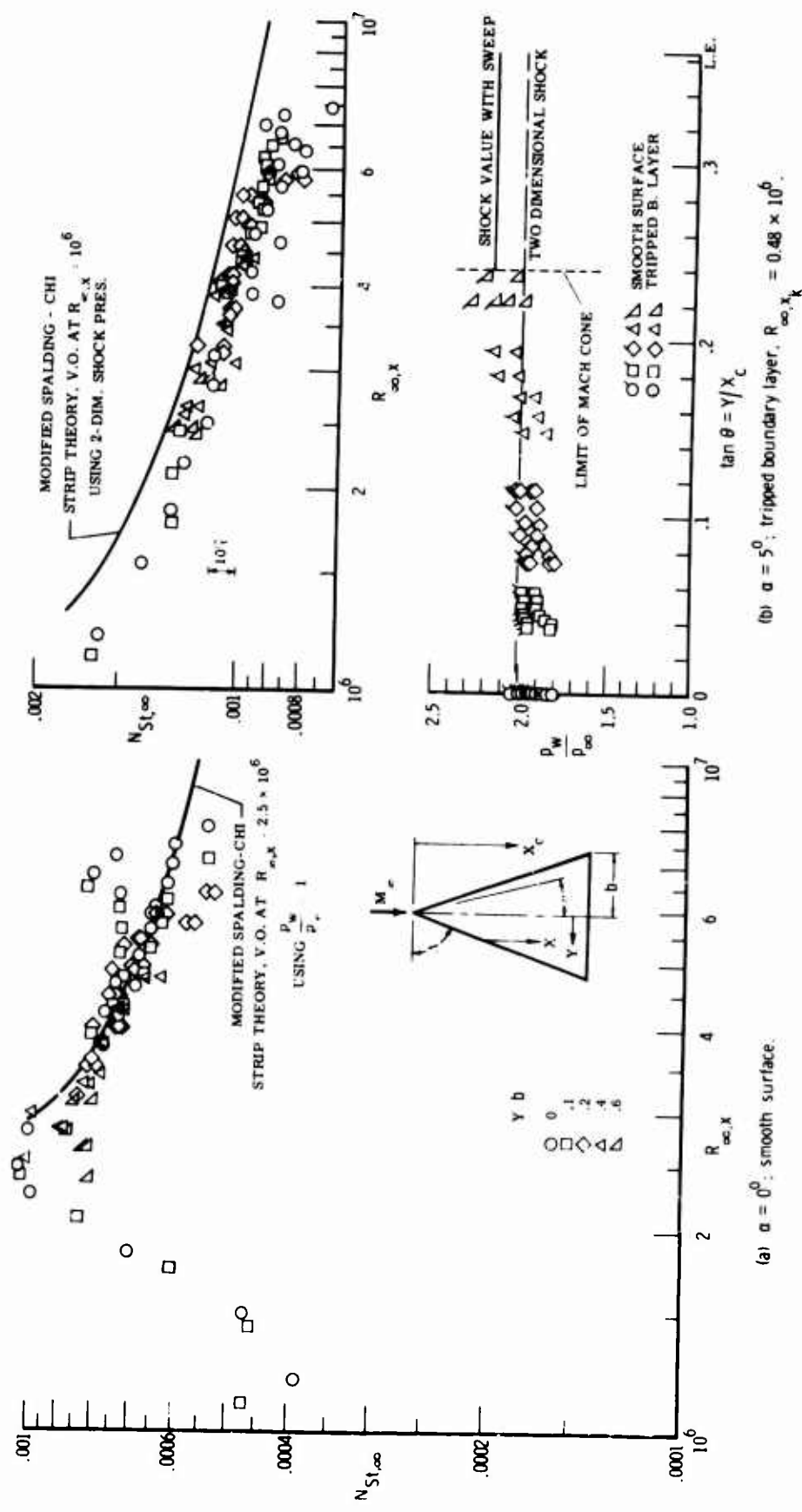


Figure 10.- Turbulent heat transfer to flat surface of a sharp delta wing at $M_\infty = 6$.
 $\Lambda = 70^\circ$; $T_t = 960^\circ R$; $T_w/T_t = 0.6$; $Re, b = 2.7 \times 10^6$; $b = 4.91$ in. Shock
 attached to leading edge; $\lambda_n = 9.25^\circ$.

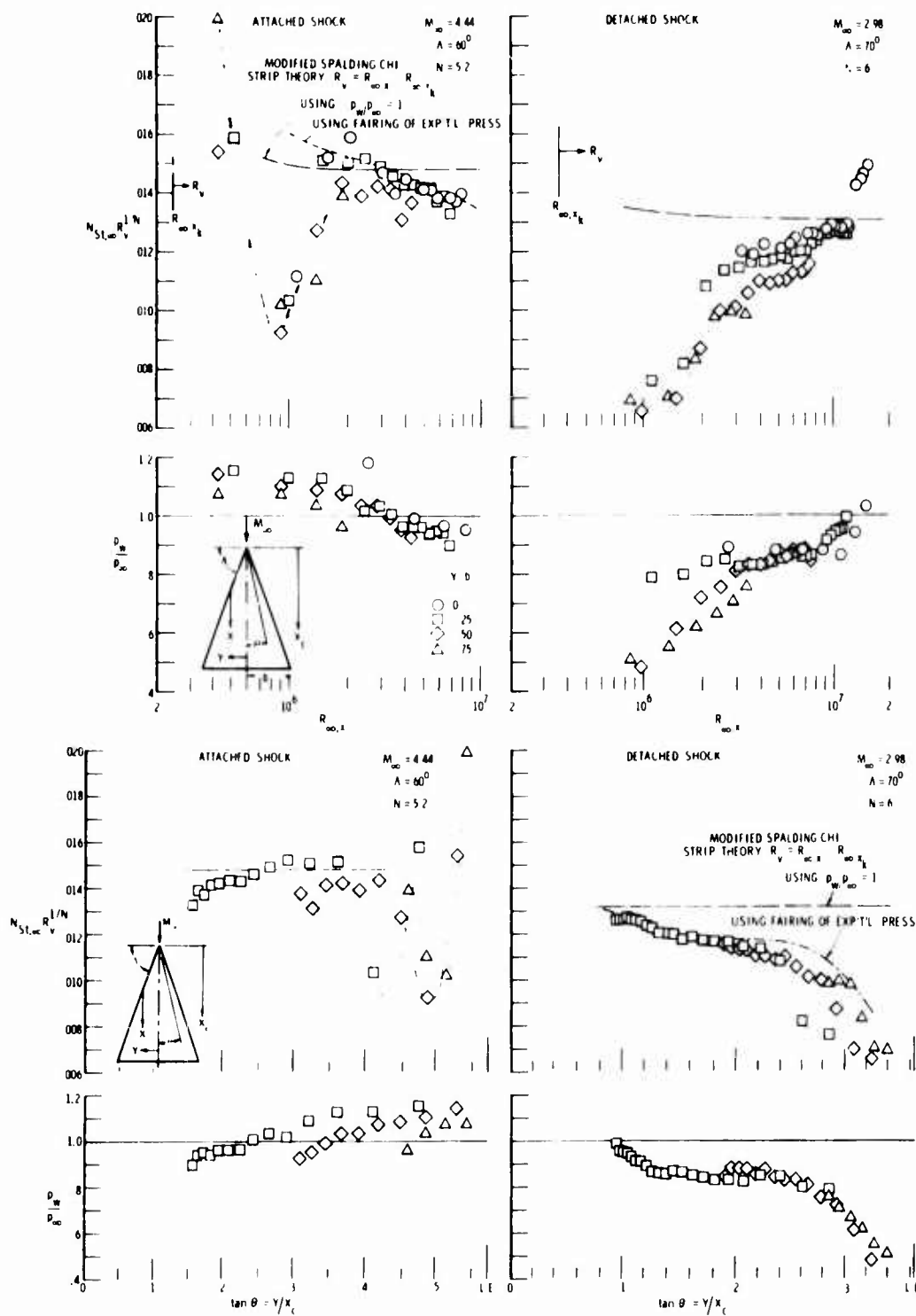


Figure 11.- Turbulent heat transfer and pressure distribution on sharp flat delta wings; $\alpha = 0^\circ$; $T_w/T_t = 0.83$; $b = 12$ in.; $\lambda_n = 15^\circ$. Data from NASA TN D-3644.

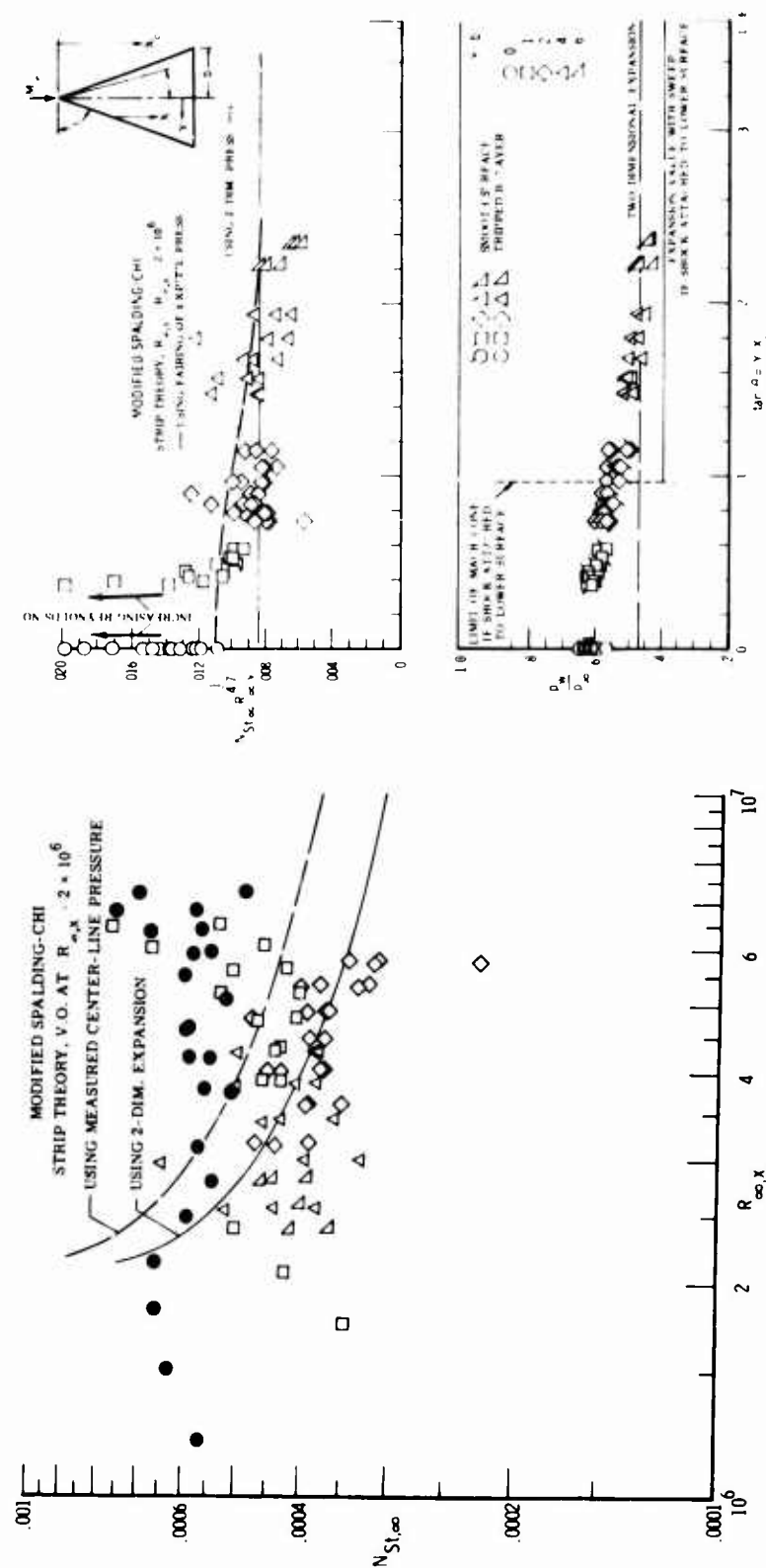


Figure 12.- Heat transfer and pressure distribution on leeward flat surface of sharp delta wing at $M_\infty = 6$. $\alpha = 5^\circ$; $\Lambda = 70^\circ$; $T_t = 960^\circ \text{ R}$; $T_w/T_t = 0.6$; $R_\infty, b = 2.7 \times 10^6$; $b = 4.91 \text{ in.}$; $R_\infty, x_k = 0.48 \times 10^6$.

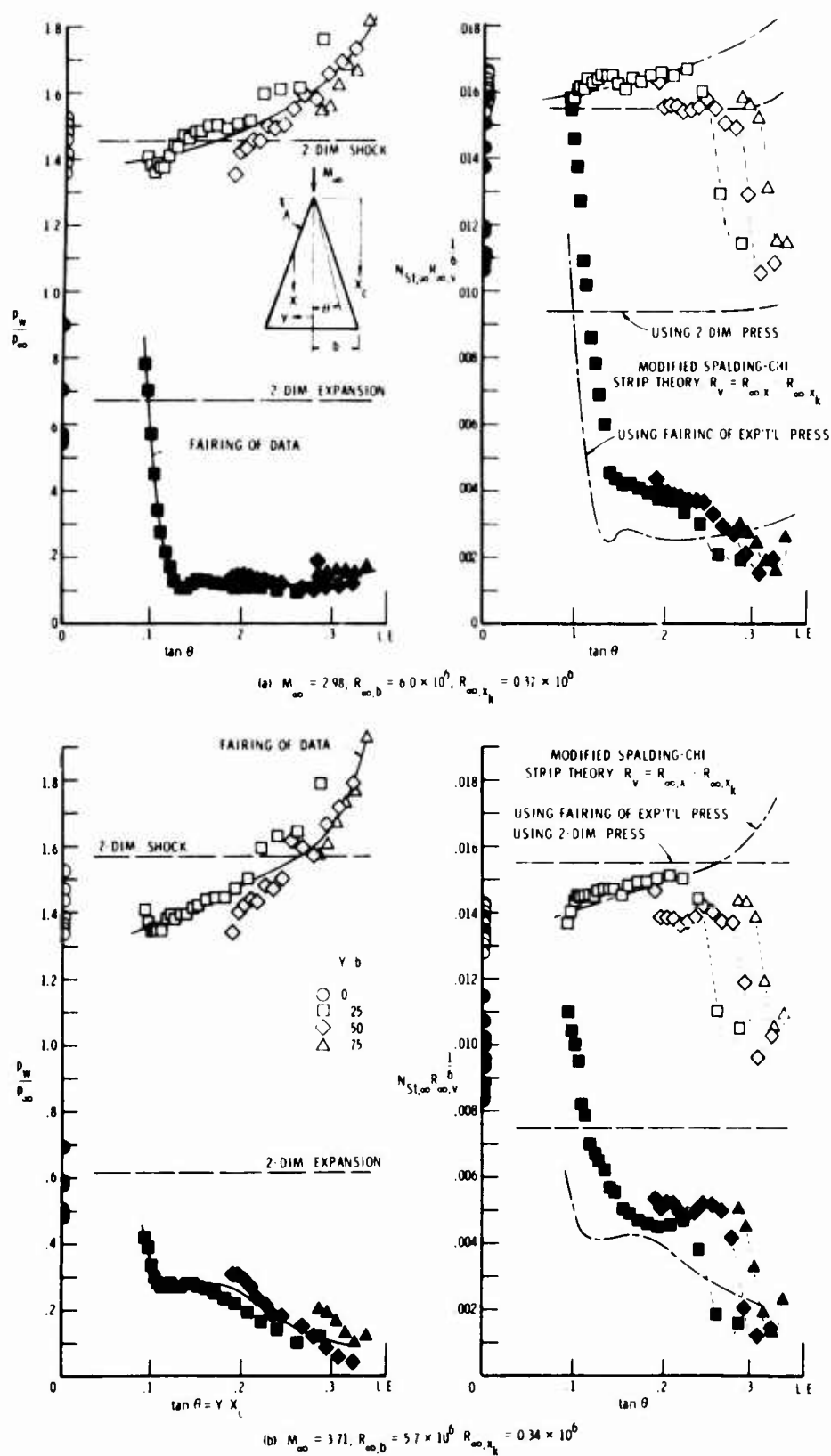
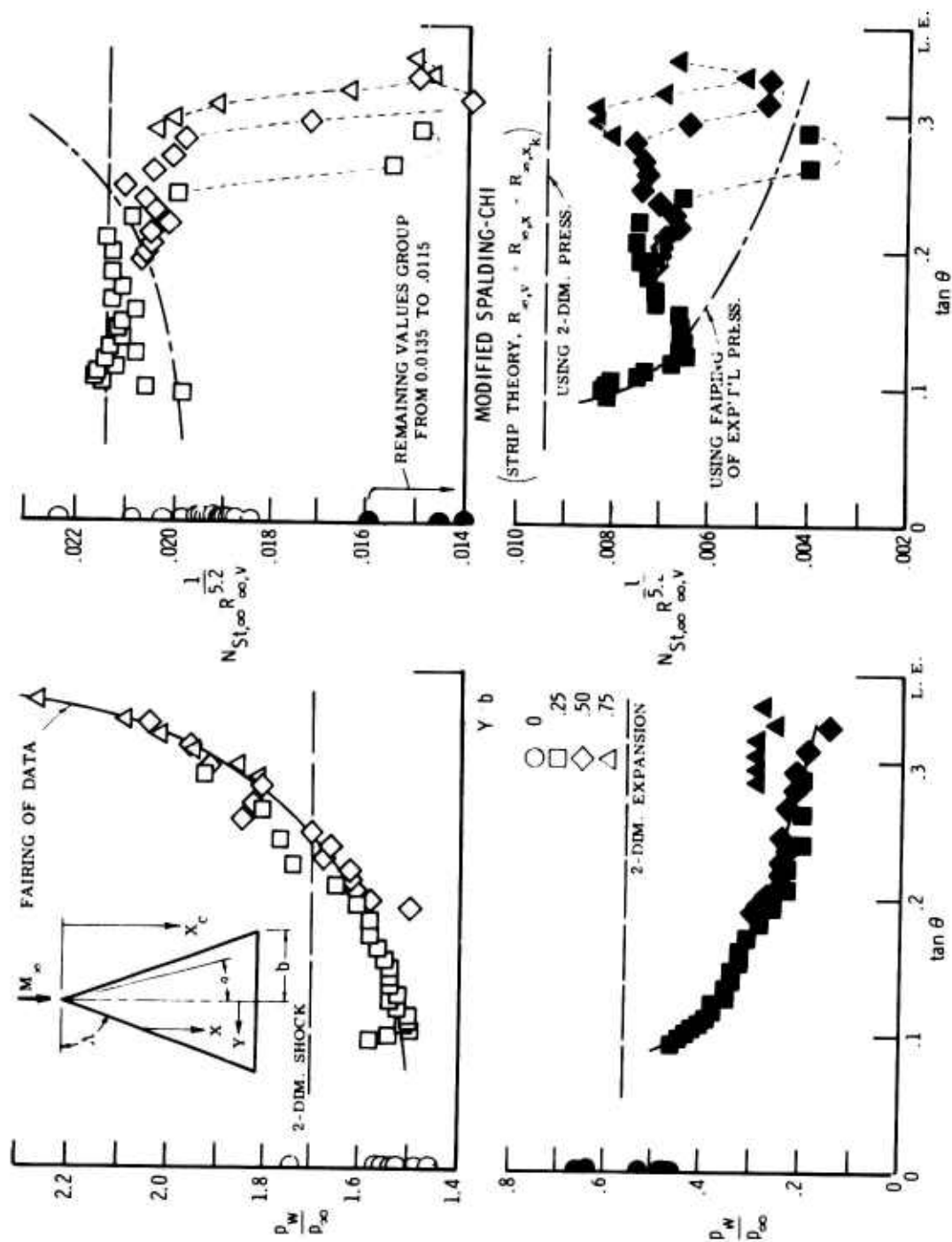


Figure 13.- Turbulent heat transfer on flat surface of sharp delta wing inclined windward and leeward. $\delta = 5^\circ$; leading-edge shock detached; $\Lambda = 70^\circ$; $T_w/T_t = 0.80 - .85$; $b = 12$ in.; $\lambda_n = 15^\circ$. Data from NASA TN D-3644.



(c) $M_\infty = 4.44$; $R_{\infty, b} = 5.8 \times 10^6$ $R_{\infty, x_k} = 0.35 \times 10^6$

Figure 13.- Concluded.

EXPERIMENTAL MEASUREMENTS OF GOLD WALL
TURBULENT HYPERSONIC BOUNDARY LAYERS

by

J.H. Perry* and R.A. East†

University of Southampton
Southampton
United Kingdom

*Research Assistant, Department of Aeronautics and Astronautics

†Lecturer, Department of Aeronautics and Astronautics

SUMMARY

Measurements of cold wall turbulent hypersonic boundary layer stagnation pressure and stagnation temperature profiles have been made on the wall of a conical nozzle in a hypersonic gun tunnel facility. A high speed traversing pitot tube and a short time response stagnation temperature probe were developed for the profile measurements.

The data was obtained for a freestream Mach number range of 8 to 11.5, a freestream Reynolds number range of 5×10^6 to 2.7×10^7 and wall to freestream stagnation temperature ratios of .26 to .36.

The measured temperature profiles compare unfavourably with available semi-empirical temperature/velocity functions.

Transformation of the velocity profile to the equivalent incompressible form, using the Baronti and Libby method, gave a successful transformation of the 'law of the wall' and fair transformation of the 'law of the wake'. Non-correspondence of the pressure gradient in the wake profile of the compressible flow to that in the related low speed flow was noted.

Two methods for determining the skin friction coefficient, Spalding and Chi and the Sommer and Short T' method, were compared to the experimental results. Neither method showed a satisfactory correlation with the Spalding and Chi method the better. The measured heat transfer rate, with the Reynolds analogy, compared favourably with the measured skin friction coefficients.

LIST OF SYMBOLS

A	constant in law of wall and equation 3.3 - taken to be equal to 2.43
C(x)	constant defined in equations 3.3 and 3.5
C _f	wall skin friction coefficient
St	wall Stanton number
F _c , F _{dx} , F _{Re}	function of Mach number and temperature ratio
k'	pressure gradient function defined in equation 3.4
M	Mach number
Pr	Prandtl number
r	nozzle radius less distance normal to wall
Re	Reynolds number
R	nozzle radius at x
T	temperature
u	velocity
u _τ	$(\tau_w/\rho)^{1/2}$
u ⁺	u/u _τ
W	parameter appearing in Coles 'wake' profile, equation 3.8
x	longitudinal distance
y	distance normal to the wall
y ⁺	y u _τ /ν
Π	'wake' parameter appearing in Coles 'wake' profile equation 3.8
δ	y at .95 u - defined as boundary layer velocity thickness
μ	dynamic viscosity
γ	ratio of specific heats
ν	kinematic viscosity
ρ	density
τ	skin friction
θ	momentum thickness $\int_0^\delta \frac{r}{R} \frac{\rho u}{\rho_\infty u_\infty} (1 - \frac{u}{u_\infty}) dy$

SUBSCRIPTS

S	stagnation conditions
∞	freestream conditions
w	wall conditions
f	edge of velocity profile sublayer
-	superimposed bar defines transformed flow
θ	momentum thickness

EXPERIMENTAL MEASUREMENTS OF COLD WALL

TURBULENT HYPERSONIC BOUNDARY LAYERS

J.H. PERRY and R.A. EAST

1. INTRODUCTION

Cold wall turbulent boundary layer flows at hypersonic speeds are of current interest in their application to hypersonic vehicle design. A theoretical treatment of the turbulent boundary layer, even in the incompressible case, is impossible at the present time due to the lack of an adequate theoretical model of the turbulence structure. In the hypersonic application the problem is further complicated by the presence of acoustic energy radiating from the layer, which may normally be ignored at lower speeds. The theoretical uncertainty necessitates a wide and varied range of experimental measurements to enable a comprehensive semi-empirical theory to be developed.

At present only a small amount of hypersonic turbulent boundary layer experimental data is generally available; for example, Adcock and Peterson (Ref.1), Banner and Williams (Ref.2), Burke (Ref.3), Danberg (Ref.4), Hill (Ref.5), Lobb et al (Ref.6), Matting et al (Ref.7), Neal (Ref.8), Samuels et al (Ref.9), Wallace (Ref.10) and Winkler and Cha (Ref.11). References 1 and 7 deal with measurements under adiabatic wall conditions. The experimental difficulties and expense entailed in making accurate boundary layer measurements in present hypersonic facilities has led to a greater emphasis on the development of transformation techniques (e.g. Coles (Ref.12)). These techniques set out to transform the hypersonic flow to a corresponding low speed flow where accurate experimental data already exist.

Although Coles and Crocco found the technique suitable at moderate supersonic Mach numbers with small ratios of heat transfer and pressure gradient further experiments in hypersonic boundary layers are required to assess the validity of the transformation methods under conditions of high wall cooling. An important aspect of experiments in this regime is the requirement to obtain accurate profiles of stagnation temperature through the boundary layer. Rotta (Ref.13) has examined the stagnation temperature profiles obtained in References 5 and 6 and has shown that in many cases inconsistencies exist between measured wall heat transfer and the slope of the temperature profile at the wall. Accurate temperature measurements under a variety of model configurations and wall and freestream conditions are required, together with measurements of skin friction and wall heat transfer rate. Such measurements are needed in order to provide confirmation on the use of existing semi-empirical methods to predict these quantities at high Mach numbers.

Considerable hypersonic aerodynamic testing has been performed in intermittent facilities and many of the techniques developed are applicable to the study of the properties of high Mach number and Reynolds number turbulent boundary layers. In particular, facilities of the shock/gun tunnel type may be operated with relatively high stagnation pressures and at Reynolds numbers appropriate to hypersonic flight in a realistic flight corridor, especially if the nozzle wall boundary layer is used for the experimental study. The disadvantages are that normally zero pressure gradient is difficult to achieve and the boundary layer characteristics are modified by the effects of transverse wall curvature. Of course the measurements are of great practical use in nozzle flow application.

The work reported here describes measurements of Mach number and temperature profiles in the boundary layer of up to one inch thickness on a conical nozzle in a hypersonic gun tunnel facility for a freestream Mach number range of 8 to 11.5. Related wall static pressure and heat transfer rate measurements have been made. Wall skin friction was inferred both from the slope of the velocity profile at the wall and from the velocity profile transformation method of Baronti and Libby (Ref.14).

The experimental results have been compared with previous data obtained at generally lower Mach numbers and lower wall heat transfer rates than for the present investigation. The measurements have provided further information concerning the use of velocity profile transformation methods at hypersonic speeds, the prediction of skin friction and heat transfer, together with new information regarding relationship between temperature and velocity in a highly cooled, hypersonic turbulent boundary layer.

2. EXPERIMENTAL PROGRAMME

The experimental data was obtained using the $7\frac{1}{2}^\circ$ total angle conical axisymmetric expansion nozzle of the University of Southampton hypersonic gun tunnel. Development of this tunnel has been reported by East (Ref.15) and East and Perry (Ref.16). The nozzle shown in Figure 1 was designed for boundary layer measurements at positions from the exit to approximately 6 inches downstream of the throat. Internal surface roughness is within 50 microinches. Two throat diameters were used giving a Mach number range, over the measuring positions, of 8 to 11.5. Variation of stagnation pressure and temperature resulted in a Reynolds number range, at the measuring stations, based upon distance from the nozzle throat, of 5×10^6 to 2.7×10^7 . The throat Reynolds numbers were within the range from 9.7×10^6 to 2.5×10^7 and should have been sufficiently high to ensure transition of the boundary layer at the nozzle throat. Boundary layer measurements were made during a running time of 10 to 20 ms., during which the nozzle wall could be assumed sensibly isothermal (except, perhaps, near the throat). Wall to stagnation temperature ratios ranged from .26 to .36 and the stagnation temperatures from 800°K to 1100°K. Table I shows the applicable experimental conditions and Figure 2 indicates the significance of the Mach number and Reynolds number parameters relative to a realistic flight envelope and previous hypersonic boundary layer measurements.

As a consequence of the short running time, special instrumentation was developed for stagnation pressure and stagnation temperature profile measurement. To reduce the number of runs necessary to obtain a complete boundary layer stagnation pressure profile and so reduce scatter resulting from the limited repeatability of flow conditions, a solenoid operated high speed traversing pitot assembly was developed capable of sweeping through approximately 0.5 in. of boundary layer in 17 ms. The accuracy of this approach has been investigated by comparing the Mach number profile measured by the traversing assembly with a profile determined from fixed impact tubes under comparable conditions. This check was made at each end of the freestream stagnation pressure range. Figure 3 shows the comparison for one set of flow conditions and the correspondence is good except close to the wall. To obtain acceptable accuracy in this region, mainly for skin friction determination, it was necessary to measure the pitot pressure for the inner 15% of the layer with fixed tubes. The remainder of the layer could be satisfactorily probed using the traversing technique. Further information on the traversing assembly is given in Reference 17.

Measurements of boundary layer stagnation temperature have usually presented greater difficulty than stagnation pressure measurements. A miniaturised version of a heated shield thermocouple probe, reported by East and Perry (Ref.18), was developed capable of measuring stagnation temperatures within a boundary layer in less than 10 ms. and up to a maximum temperature of 1500°K. The internal diameter of the probe nose was $1/32$ " and external dimensions were kept to a minimum to minimise flow interference. The design of the probe is shown in Figure 4 and follows normal practice for shielded thermocouple probes except for the heater windings on the shield. It operates as a 'null' measuring device. A minimum of two tunnel runs were necessary to specify a flow temperature; one with the initial shield temperature just above the expected flow temperature and the other with the initial shield temperature just below. Considerable development was necessary to obtain an understanding of the probe, especially as viscous effects within the small shield can influence the measurements in the low pressure and low density regions near the wall. Further constructional and operating details on this probe are presented in Reference 17. Stagnation temperature profiles have been obtained relatively easily from boundary layers of the order of 0.5 in. thick or greater; measuring within .05 in. from the wall.

Wall heat transfer rate was measured using platinum thin film gauges mounted flush with the wall. Standard probe calibration and data reduction techniques were adopted (note for example Ref.19).

Wall static pressure was measured using the cavity technique.

3. THEORETICAL CONSIDERATIONS AND DISCUSSION OF EXPERIMENTAL RESULTS

Temperature and pressure profiles and wall heat transfer rates have been measured for the range of conditions shown on Table I. A representative number of these measurements are given in this report and comparisons are made with the available semi-empirical methods. Full presentation of the experimental results can be found in Reference 17.

3.1 Mach number profiles

These profiles have been deduced from the measured stagnation pressure profiles, using the assumption of constant static pressure normal to the wall, with the local isentropic relations.

The assumption of locally constant static pressure has been confirmed by comparing the wall static pressure, measured using the cavity technique, with the freestream static pressure determined from the Rayleigh pitot formulae and local isentropic relations (Fig.5). The freestream pressure gradient is comparatively mild over the region of boundary layer profile measurements. For one representative flow condition (See Fig.5) the freestream pressure gradient varied from .0163 p.s.i./in., at the most downstream measuring station to .0471 p.s.i./in. four inches upstream. Fixed probe measurements have been used to specify the inner 15% of the layer as noted in Section 2.

Figure 6 shows three Mach number profiles compared with profiles drawn from other experimental sources. The profiles are typically turbulent and indicate the thick sublayers prevailing under these flow conditions. Sublayer thickness can be seen to vary with both Mach number and Reynolds number.

A typical measured Mach number profiles is shown in detail on Figure 3 to indicate the extent of experimental scatter resulting from the traversing technique and tunnel flow. The scatter is relatively small and to simplify the computation required for reducing the experimental data, faired profiles are used for reducing profile data.

Figure 7 contains six Mach number profiles, drawn from the experimental data, covering a representative range of freestream Mach number, pressure and temperature.

3.2 Stagnation temperature profiles

Stagnation temperature profiles have been measured using the heated shield thermocouple probe described earlier. Figure 9 contains six of these profiles for comparable conditions to those of the sample Mach number profiles of Figure 7. The experimental scatter of data points is of similar order as shown on Figure 3 for the Mach number profiles and, for similar reasons, faired data curves are used for data reduction. There are no experimental measurements of high wall heat transfer rate turbulent boundary layer stagnation temperature profiles, notably at high Mach numbers, known to these authors. Comparison with a few available stagnation temperature profiles (Fig.8), at lower wall heat transfer rate conditions and varying experimental environments, show that the general trend of the change in distribution with heat transfer is maintained in our results.

3.3 Temperature-velocity relationships

The experimentally determined temperature and Mach number profiles present an opportunity to test the available semi-empirical relationships between temperature and velocity under conditions of high Mach number and high wall heat transfer rate. Four expressions have been considered. Crocco (Ref.20) couples the momentum and energy equations with the assumptions of zero pressure gradient and unit Prandtl number, to obtain the function,

$$\frac{T_s}{T_{s_\infty}} = \frac{T_{s_\infty} - T_w}{T_{s_\infty}} \left(\frac{u}{u_\infty} \right) + \frac{T_w}{T_{s_\infty}} \quad \text{----- 3.1}$$

where subscripts s, w and ∞ refer to stagnation, wall and freestream conditions respectively.

Crocco (Ref.20) and Cohen (Ref.21), in an attempt to approximately account for pressure gradient and Prandtl number, produced a modified form of the above equation:

$$\frac{T_s}{T_{s_\infty}} = \frac{T_w}{T_{s_\infty}} + \left(1 - \frac{T_w}{T_{s_\infty}} - C(x) \right) \frac{u}{u_\infty} + C(x) \left(\frac{u}{u_\infty} \right)^2 \quad \text{----- 3.2}$$

where $C(x)$ is assumed independent of y . A solution for $C(x)$ has been obtained by Crocco (Ref.20) and is

$$C(x) = \left(1 - \frac{T_w}{T_{s_\infty}} \right) - \frac{1}{k'-1} \left((1 - Pr_w) \left(1 - \frac{T_\infty}{T_{s_\infty}} \right) - \left(1 - \frac{T_w}{T_{s_\infty}} \right) \right) \quad \text{----- 3.3}$$

with

$$k' = \frac{-2\mu_w}{\rho_\infty C_p 2u_\infty^2} \frac{du_\infty}{dx} \quad \text{----- 3.4}$$

Wallace (Ref.10) shows that the function, $C(x)$, can be determined from experimental wall heat transfer measurements and uses the Reynolds analog to obtain:

$$\frac{2C_H}{C_f} = \frac{1}{Pr_w} \left(1 - \frac{C(x)}{1 - T_w/T_\infty} \right) \quad \text{----- 3.5}$$

where C_H is the local Stanton number.

Spence (Ref.22) and Van Driest (Ref.23) introduced 'reasonable assumptions' for the shear stress profile $\tau_w \left(\frac{u}{u_\infty} \right)$ into the continuity, momentum and energy equations to obtain a solution, for Pr close to unity, of:

$$\frac{T}{T_\infty} = a + b \frac{u}{u_\infty} + c' \left(\frac{u}{u_\infty} \right)^2 \quad \text{----- 3.6}$$

where $a = 1 + r \frac{\gamma-1}{2} M_\infty^2 (1 - \Theta')$; $b = \Theta' r \frac{\gamma-1}{2} M_\infty^2$;

$$c' = -r \frac{\gamma-1}{2} M_\infty^2; \quad \Theta' = \frac{T_R - T_W}{T_R - T_\infty}; \quad r = \frac{T_R - T_\infty}{T_{s_\infty} - T_\infty};$$

$$\frac{T_R}{T_\infty} = 1 + r \frac{\gamma-1}{2} M_\infty^2$$

Figure 10 shows two experimentally determined profiles compared to the above semi-empirical expressions. The first profile shows the variations of $\left(\frac{T_R - T_W}{T_R - T_\infty} \right)$ with $\frac{u}{u_\infty}$ and the second, the variation of $\frac{T}{T_\infty}$ with y/δ using the experimentally determined velocity profile, in the semi-

empirical methods, to obtain the relation between u/u_∞ and y/δ . In both cases the correlation is poor, with the modified expression of Crocco/Cohen giving the closest approach to the experimental curve. This divergence between theory and experiment has been the subject of discussion by many authors (e.g. Walz (Ref.24) and Rotta (Ref.25)). With the aim of developing an improved semi-empirical method, an analysis based on the work of Rotta (Ref.13), is being investigated.

3.4 Velocity profiles

Boundary layer velocity profiles have been determined from the Mach number and stagnation temperature profiles using local isentropic relations and the assumption of constant static pressure normal to the wall. Four velocity profiles, covering a range of Mach number and Reynolds number, are shown on Figure 11. The outer part of the layer approximates to a $1/7$ power law.

3.5 Velocity profile transformation

The transformation technique mathematically transforms the compressible layer into an equivalent incompressible form which can be predicted with greater confidence. The latest and most promising contribution to transformation techniques has been made by Coles (Ref.12) and further developed by Crocco (Ref.20). This approach uses three stretching functions to relate the high speed case to the low speed flows and these relations are functions of the longitudinal distance in the high speed flow. The first relates the two stream functions, the second the density ratio and the third the differential of the longitudinal distances. The last two functions can generally be expressed as a function of the first in a general theory of the boundary layer (e.g. Crocco), but the first function requires some further relation to permit solution.

Baronti and Libby (Ref.14) have examined two sublayer assumptions for determining the first stretching function; the sublayer hypothesis of Donaldson (Ref.26) and the substructure hypothesis of Coles (Ref.12). The 'sublayer hypothesis' assumes that the Reynolds number associated with the laminar sublayer is invariant:

$$\text{i.e.} \quad \frac{\rho_f u_f^* y_f}{\mu_f} = \text{Const.} = \frac{\bar{\rho} u_f^* y_f}{\bar{\mu}} \quad \text{----- 3.7}$$

and the properties at the edge of the sublayer have been used in determining the Reynolds number. The 'substructure hypothesis' proposes that a substructure Reynolds number can be independent of compressibility when the density and viscosity are evaluated at a suitably defined mean temperature.

Baronti and Libby found that the sublayer hypothesis was more applicable to the wide range of experimental sublayer profiles which were considered than the substructure hypothesis. Contrary to the experimental evidence the methods available at present (Coles (Ref.12) and Rosenbaum (Ref.27)), for applying the transformation to the boundary layer, are both based upon Coles 'substructure hypothesis'.

An implication of the transformation is that the local pressure gradient of the compressible and transformed flows should correspond. Baronti and Libby (Ref.14) have investigated the general ability of the transformation to successfully transform the compressible velocity profiles to the transformed flow by applying the method to available reliable experimental measurements. Using the sublayer hypothesis, the 'law of the wall' (a portion of the velocity profile relatively insensitive to pressure gradient - note Ludwig and Tillman Ref.28), transformed successfully and the authors pointed out a useful method for determining the skin friction, from the transformed wall law profile, which is independent of measurements close to the wall. The 'wake' portion of the profile, when transformed to the incompressible flow indicated profiles of a more favourable pressure gradient (note Fig.14) and, from the experimental results, this divergence increases with increasing Mach number.

Figures 12 and 13 show sample transformations of the law of the wall and law of the wake profiles. Both have been transformed following the method outlined by Baronti and Libby (Ref.14), using the sublayer hypothesis to obtain the first stretching function and the experimentally derived temperature profile to determine the density integrals required for the remainder of the transformation.

In the transformation of the law of the wall the value of the stretching function has a large effect on the compressible skin friction coefficient determined from the law of the wall profile. If the experimentally derived temperature profile was used in determining this stretching function the resultant skin friction coefficient, determined from the linear log law portion of the profile, was some 60% above that obtained from experimental results (see below) and from the method of Spalding and Chi (Ref.29); whereas if the Crocco/Cohen relation was used (Equ.3.2) for the stretching function evaluation and the experimentally determined temperature profile for the remainder of the 'law of the wall' transformation, the skin friction determined from the transformed profile corresponded to the majority of the skin friction values determined from the velocity slope at the wall (note Fig.15) and correlated with the method of Spalding and Chi.

The difference between the two approaches is, in part, due to possible errors in the measured temperature profile near the wall (note Fig.9) but Figure 10 shows that the experimental profile and the Crocco/Cohen profile are basically different and wall errors are not the complete explanation. This result tends to indicate that, whereas the sublayer hypothesis is sufficiently accurate at zero heat transfer (note Baronti and Libby Ref.14) where the Crocco/Cohen function approaches the measured temperature profile (Rotta Ref.25), in the case of applied wall heat transfer, the errors introduced by applying the Crocco/Cohen function to determine the first stretching function are counterbalanced by applying the sublayer hypothesis.

Figure 12 shows the successful transformation of the velocity profile that applies to the 'law of the wall' region using the Crocco/Cohen function for determining the first stretching function and the experimentally derived temperature profile for the remainder of the profile transformation.

Coles (Ref.12) has given an explicit representation of the 'law of the wake' portion of the velocity profile in the form

$$\frac{\bar{u} - \bar{u}_\infty}{\bar{u}_\tau} = A \ln(\bar{y}/\delta) - A\pi(\bar{x}) (2 - W(\bar{y}/\delta)) \quad \text{--- 3.8}$$

Figure 13 shows the 'wake' transformation of the profiles in Figure 12. A constant π value can be applied approximately to the whole profile. Wall heat transfer rate and boundary layer upstream history are possible explanations for failure of the 'law of the wake' to transform as satisfactorily as the zero pressure gradient, zero heat transfer velocity profiles transformed by Baronti and Libby (Ref.14).

The wake parameter, $\Pi(\bar{x})$, is plotted against the transformed momentum thickness Reynolds number, Re_{θ}^* , on Figure 14. The results indicate that $\Pi(\bar{x})$ increases with increased stream to wall heat transfer rate and decreases with Mach number increase and Re_{θ}^* decrease. The figure confirms the conclusions drawn by Baronti and Libby concerning non-correspondence of the local pressure gradients between the high speed and transformed outer layer profiles.

3.6 Determination of wall skin friction

Two semi-empirical methods have been compared to the experimental results. The first has been proposed by Spalding and Chi (Ref.29). They postulate that a unique relationship exists between $C_f F_0$ and $R F_R$ where C_f is the skin friction coefficient, R the Reynolds number and F_0 and F_R are functions of Mach number and temperature ratio alone. The obvious lack of reliable experimental data has restricted calculation of F_0 and F_R from experiment and hence the authors determined F_0 by means of the mixing length theory and F_R semi-empirically. When compared with available experimental data, Spalding and Chi found that the predictions of the method give a root-mean square error of 9.9%.

The second is the Sommer and Short T' method (Ref.30). Peterson (Ref.31) examined available experimental results and compared them to a wide range of existing theories. The Sommer and Short method gave the best experimental correlation. In this method the fluid properties in the flow are evaluated at some intermediate or reference temperature in the boundary layer. This reference temperature is called T' and is a function of the freestream Mach number and the ratio of wall temperature to freestream temperature. These properties are then used in the von Karman-Schoenherr (Ref.32) incompressible turbulent skin friction formula to obtain the skin friction.

A survey has been made of other experimental data in the hypersonic region of $M_\infty = 5.0$ and upward. The skin friction data from these sources has been transformed by the Spalding and Chi method and are shown on Figure 15a, as a function of transformed position Reynolds number, and on Figure 15b, as a function of transformed momentum thickness Reynolds number. Peterson (Ref.31) indicated a method of transforming experimental data, through the Sommer and Short method, to equivalent incompressible co-ordinates for comparison. The experimental data is reduced using this method and compared on Figure 15c.

The skin friction data from the experimental programme in the present paper was determined by two methods; (i) from velocity slope at the wall and (ii) from the transformed law of the wall velocity profile following Baronti and Libby (Ref.14). Skin friction coefficients determined by the two methods compare favourably (note Fig.15) except in a few cases where the sublayer was very thin and accurate measurements in this region not possible. Figure 15 shows a comparison between the above semi-empirical methods and the experimental results of this report. Using the Spalding and Chi method and plotting against transformed position Reynolds number (Fig.15a) the correlation is fair, though a mean line through the data has a different slope to the Spalding and Chi line. Plotting against transformed momentum thickness Reynolds number (Fig.15b) indicates fair correlation for the lower Mach number range ($\sim 8-9$) but a poorer correlation for the higher Mach numbers (~ 9 to 11.5) where the freestream static pressures and densities are lower. Comparison with the Sommer and Short method (Fig.15c) is not as acceptable. A mean line through the data of this report falls somewhat below the Sommer and Short line.

Neither method shows good correlation of all of the available hypersonic data (Table II). The Spalding and Chi method is possibly the more acceptable.

3.7 Determination of wall heat transfer rate

The wall heat transfer rate was deduced from the platinum thin film gauge measurements by the normal method (note Ref.19). A skin friction coefficient was calculated from the heat transfer rate using various analogies and compared to the skin friction measurements obtained using the velocity gradient at the wall (Fig.15 and Table II). The un-modified Reynolds analogy, $C_f = 2 C_H$, resulted in the best comparison and confirms similar conclusions reached by Wallace (Ref.10) for axisymmetric nozzle measurements.

The temperature gradients at the wall, deduced from the heat transfer rate measurements, were compared, on Figure 9, to the wall temperature gradient obtained from stagnation temperature profiles, curve fitting from the last experimentally measured points to the wall. The comparison indicates that a small error occurs in the experimental points near the wall. This error is mainly within the expected range of experimental scatter, for this type of probe, of $\pm 3\frac{1}{2}\%$ (note Ref.15). The equivalence between the two wall temperature gradients, within experimental error, tend to confirm the accuracy of the measured stagnation temperature profiles.

4. CONCLUSIONS

- 1). Specialised instrumentation can be developed to measure turbulent boundary layer properties in short running time hypersonic facilities.
- 2). Measurements of stagnation pressure and stagnation temperature profiles compare favourably with extrapolated trends of previous experimental measurements.
- 3). The experimentally derived static temperature profile compares unfavourably with available semi-empirical temperature/velocity relationships.
- 4). Using the Baronti and Lioby velocity profile transformation method, successful transformation of the 'law of the wall' and fair transformation of the 'law of the wake' was achieved. The application of the 'sublayer hypothesis', used in the transformation, was found to be influenced by the high wall heat transfer rate. Non-correspondence of the pressure gradient in the wake profile of the compressible flow to that in the related low speed flow was noted.
- 5). The Spalding and Ori skin friction method indicated the more acceptable correlation with experiment.
- 6). The Reynolds analogy and the measured heat transfer rates indicated an acceptable correlation with the experimental skin friction coefficients.

REFERENCES

1. ADCOCK, J.B.
PETERSON, J.B. 'Experimental Investigation of a Turbulent Boundary Layer at Mach 6, High Reynolds Numbers and Zero Heat Transfer'. NASA TN D-2907 July, 1965
2. BANNER, L.T.
WILLIAMS, M.J. 'Boundary Layer Measurements in the A.R.L. Hypersonic Tunnel Conical Nozzle'. Australia - AdL/Aero 215 July, 1963
3. BURKE, A.F. 'Turbulent Boundary Layers on Highly Cooled Surfaces at High Mach Numbers'. Proceedings of Symposium on Aerothermoelasticity, Dayton, Ohio (1961) pp. 704 - 741
4. DANBERG, J.E. 'Characteristics of the Turbulent Boundary Layer with Heat and Mass Transfer: Data Tabulation'. N.O.L.T.R. 67-6 January, 1967
5. HILL, F.K. 'Turbulent Boundary Layer Measurements at Mach Numbers from 8-10'. Physics of Fluids 2 (1959) pp 668-680
6. LOBB, R.K.
WINKLER, S.M.
FERSH, J. 'Experimental Investigation of Turbulent Boundary Layers in Hypersonic Flow'. NAVAORD Report 3680 March, 1955
7. MATTING, F.W.
CHAPMAN, D.R.
NYHOLM, J.R.
THOMAS, A.S. 'Turbulent Skin Friction at High Mach Numbers and Reynolds Numbers in Air and Helium'. NASA TR E-82 (1960)
8. NEAL, L. 'A Study of the Pressure, Heat Transfer and Skin Friction on Sharp and Blunt Flat Plates at Mach 6.0'. NASA TN D-3312 1966
9. SAMUELS, R.D.
PETERSON, J.B.
ADCOCK, J.B. 'Experimental Investigation of the Turbulent Boundary Layer at a Mach number of 6 with Heat Transfer at High Reynolds Numbers'. NASA TN D-3858 March, 1967
10. WALLACE, J.E. 'Hypersonic Turbulent Boundary Layer Studies at Cold Wall Conditions'. Proc. (1967) Heat Transfer and Fluid Mechanics Institute.
11. WINKLER, S.M.
CHA, M.H. 'Experimental Investigations of the Effect of Heat Transfer on Hypersonic Turbulent Boundary Layer Skin Friction'. J. Aero/Space Sci. 26 123 1959
12. COLLES, D.E. 'The Turbulent Boundary Layer in a Compressible Fluid'. A.R.C. 24,497 February, 1963
13. ROTTA, J.C. 'Turbulent Boundary Layers with Heat Transfer in Compressible Flow'. AGARD Report 281 April, 1960
14. BARONET, P.O.
LISBY, P.A. 'Velocity Profiles in Turbulent Compressible Boundary Layers'. A.I.A.A. Journal, 4, 2 February, 1966
15. EAST, R.A. 'Performance and Operation of the University of Southampton Hypersonic Gun Tunnel'. A.A.S.U. Report 135 August, 1960
16. EAST, R.A.
PACIFY, J.H. 'A Study of the Characteristics of Gun Tunnel Operation at 10,000 p.s.i.'. A.A.S.U. Report 268 April, 1967

17. PERRY, J.H. 'An Experimental Study of the Turbulent Boundary Layer at High Mach Number and High Wall Heat Transfer'
Ph.D. Thesis, University of Southampton (to be submitted) 1968
18. EAST, R.A.
PERRY, J.H. 'A Short Time Response Stagnation Temperature Probe'
A.R.C. C.P. 909 1967
19. EDNEY, B.E. 'The Development of Thin Film Heat Transfer Gauges and Analogue Networks for Use in the F.F.A. Gun Tunnel'
F.F.A. (Sweden) Report AU-209:1 December, 1964
20. CROCCO, L. 'Transformation of the Compressible Turbulent Boundary Layer with Heat Transfer'
A.I.A.A. Journal 1, 1 December, 1963
21. COMET, H.B. 'A Method of Computing Turbulent Heat Transfer in the Presence of a Streamwise Pressure Gradient for Bodies in High-Speed Flow'
NASA Memo: 1-2-59 L (1959)
22. SPENCE, D.A. 'Some Applications of Crocco's Integral for the Turbulent Boundary Layer'
Proc. 1960 Heat Transf., Fluid Mech. Inst. Stanford University 62-76
23. VAN DRIEST, E.R. in C.C. Lin (1959) 'Turbulent Flows and Heat Transfer', Sect. F. 379-427 Princeton University, New Jersey.
24. WALZ, A. 'Compressible Turbulent Boundary Layers'
International Symp. of the Nat. Scientific Research Centre 'The Mechanics of Turbulence' Marseille 1961
25. KOTTA, J.C. 'A Review of Experimental Temperature Distributions in Supersonic and Hypersonic Turbulent Boundary Layers with Heat Transfer'
A.R.C. 26,485 December, 1964
26. DONALDSON, C. du P. 'On the Form of the Turbulent Skin-Friction Law and its Extension to Compressible Flows'
NACA TN 2692 (May, 1952)
27. ROSENBAUM, H. 'Turbulent Compressible Boundary Layer on a Flat Plate with Heat Transfer and Mass Diffusion'
A.I.A.A. Journal 4, 9, Sept. 1966
28. LUDWIG, H.
TILMAN, W. 'Investigations of the Wall-Shearing Stress in Turbulent Boundary Layers'
NACA TN 1285 1950
29. SPALDING, D.B.
CHI, S.W. 'The Drag of a Compressible Turbulent Boundary Layer on a Smooth Flat Plate with and without Heat Transfer'
J. Fluid Mech. 18 (1964) pp 117-143
30. SUMER, S.C.
SHORT, B.J. 'Free-Flight Measurements of Turbulent Boundary Layer Skin Friction in the Presence of Severe Aerodynamic Heating at Mach Numbers from 2.8 to 7.0'
NACA TN 3391 March, 1955
31. PETERSON, J.B. Jnr. 'A Comparison of Experimental and Theoretical Results for the Compressible Turbulent Boundary Layer Skin Friction with Zero Pressure Gradient'
NASA TN D-1795 March, 1963
32. SCHUEMIGER, K.E. 'Resistance of Flat Surfaces Moving Through a Fluid'
Soc. Nav. Arch. and Marine Eng. Trans.
Vol.40, 1932 pp 279-313
33. LEE
YANTA
LEONAS Private communication from NAVORD concerning unpublished data

TABLE I

Condition	Reservoir Temperature T_o °K	Reservoir Pressure lbf/in ²	Free Stream Temperature T °K	T_w/T_{a_∞}	Local Mach Number	Local Reynolds Number $\frac{\rho_\infty u_\infty x^*}{\mu_\infty} \times 10^6$	Distance From Nozzle Throat x^* Feet
1	823	1840	49.2	.352	8.87	13.72	2.47
2	823	1890	53.3	.352	8.50	14.37	2.14
3	823	1950	59.6	.352	8.00	14.07	1.80
4	916	1880	56.8	.317	8.70	12.98	2.47
5	916	1890	57.9	.317	8.61	11.36	2.14
6	916	1880	65.9	.317	8.03	11.58	1.80
7	930	4500	53.5	.312	9.05	27.4	2.47
8	930	4430	60.25	.312	8.50	26.7	2.14
9	930	4240	66.6	.312	8.05	25.7	1.80
10	1010	4450	58.7	.287	9.0	23.4	2.47
11	1010	4400	65.4	.287	8.50	24.2	2.14
12	1010	4210	72.2	.287	8.06	22.6	1.80
13	910	1980	34.5	.319	11.27	6.74	2.52
14	910	1990	38.8	.319	10.60	7.21	2.19
15	910	1965	43.7	.319	9.95	6.85	1.85
16	1020	1900	39.1	.284	11.20	5.24	2.52
17	1020	1900	44.4	.284	10.48	5.71	2.19
18	1020	1825	49.5	.284	9.90	5.42	1.85
19	1000	3140	36.9	.290	11.43	9.2	2.52
20	1020	4600	37.2	.284	11.50	12.8	2.52
21	1020	4520	41.4	.284	10.87	12.6	2.19
22	1020	4340	46.4	.284	10.25	12.2	1.85
23	1120	4500	40.2	.259	11.60	10.4	2.52
24	1120	4450	47.3	.259	10.65	11.2	2.19
25	1120	4280	51.4	.259	10.20	10.5	1.85

TABLE II
EXPERIMENTAL SKIN FRICTION TRANSFORMED WITH SPALDING AND CHI
AND SUMMER AND SHORT T⁺ METHODS FOR FIGURE 15

Author and Ref.	Mach No. Range	Position Reynolds No. Range	Momentum Thickness Reynolds No. Range	T_w/T_∞	Heat Transfer	Skin Friction Measuring Method	Symbol for Fig. 15
LOSEB et al Ref. 6	4.9 to 8.2	-	5,400 to 12,600	3.3 to 6.6	Yes	Velocity profile wall slope	O
WINKLER and CHA Ref. 11	5.0 to 5.4	2.7×10^6 to 6.0×10^6	1,000 to 4,300	3.5 to 5.6	Yes	Velocity profile wall slope	X
HILL Ref. 5	8.3 to 10.0	1.8×10^6 to 4.7×10^6	1,300 to 3,000	7.1 to 11.4	Yes	Velocity profile wall slope	Ø
MATTING et al Ref. 7	6.7 and 9.9	7.1×10^6 to 47.0×10^6	-	8.9 and 16.5	No	Skin friction balance	⊗
DAMBERG* Ref. 4	6.3 to 6.7	3.0×10^6 to 6.0×10^6	1,720 to 3,900	4.1 to 4.5	Yes	Velocity profile wall slope	⊠
NEAL Ref. 8	6.8	3.3×10^6 to 9.5×10^6	-	1.45 to 5.2	Yes	Skin friction balance	□
WALLACE Ref. 10	6.6 to 8.0	-	3,400 to 47,000	.92 to 4.0	Yes	Skin friction balance	+
THIS REPORT	8.0 to 11.6	5.2×10^6 to 27.4×10^6	6,300 to 34,900	4.0 to 7.9	Yes	Velocity gradient at the wall	Δ
						Transformed profile	▼
						Wall heat transfer rate & Reynolds analogy	⚡

*only the higher Reynolds number measurements seem to be in the fully turbulent regime.

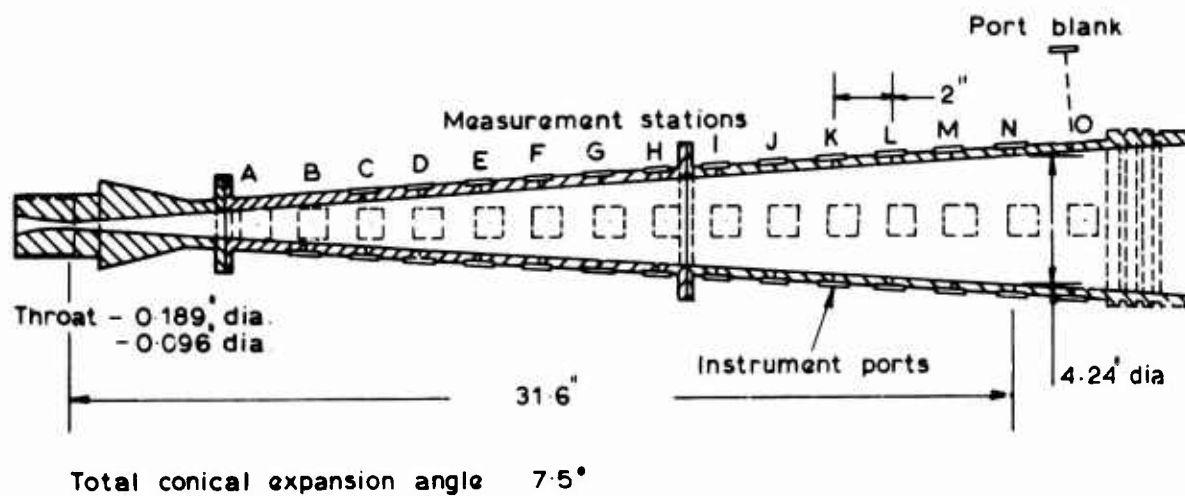


Fig.1 Boundary layer nozzle

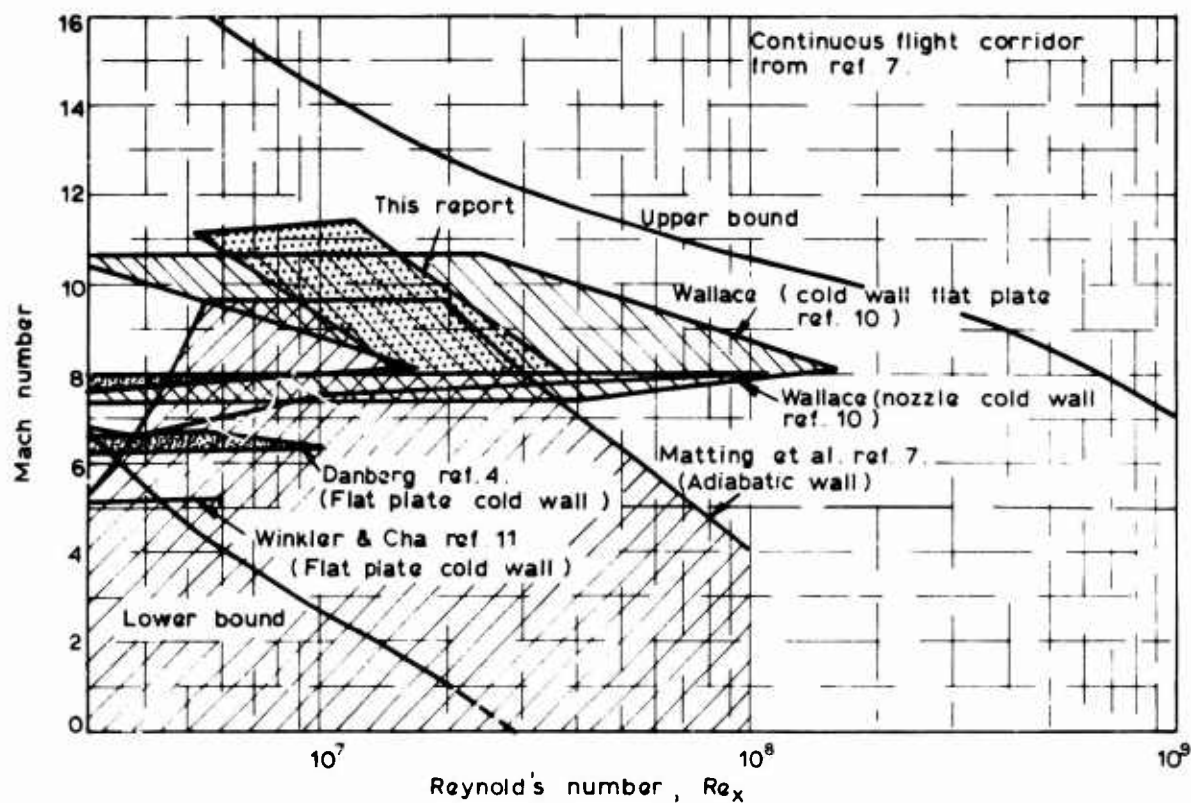


Fig.2 Significance of boundary layer measurements relative to continuous flight

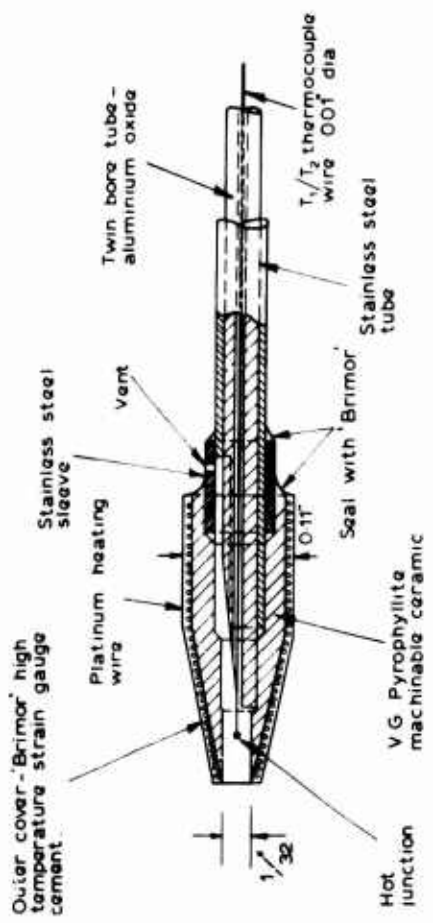


Fig.4 The short time response stagnation temperature probe design

o WALL STATIC PRESSURE - MEASURED BY CAVITY TECHNIQUE
x FREESTREAM STATIC PRESSURE - DERIVED FROM FREESTREAM IMPACT AND STAGNATION PRESSURES

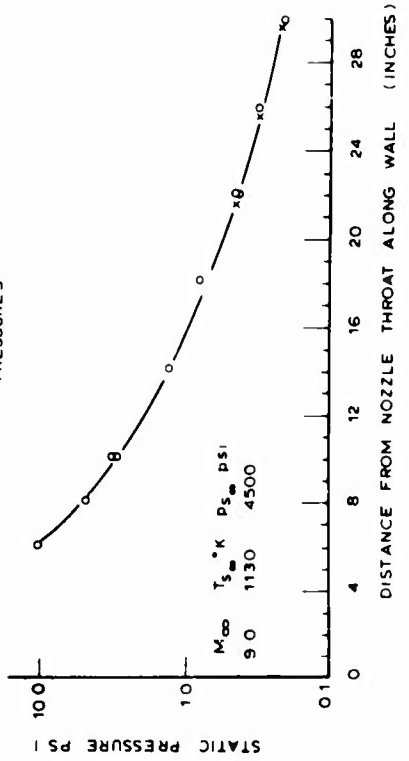


Fig.5 Comparison of freestream and wall static pressure measurements

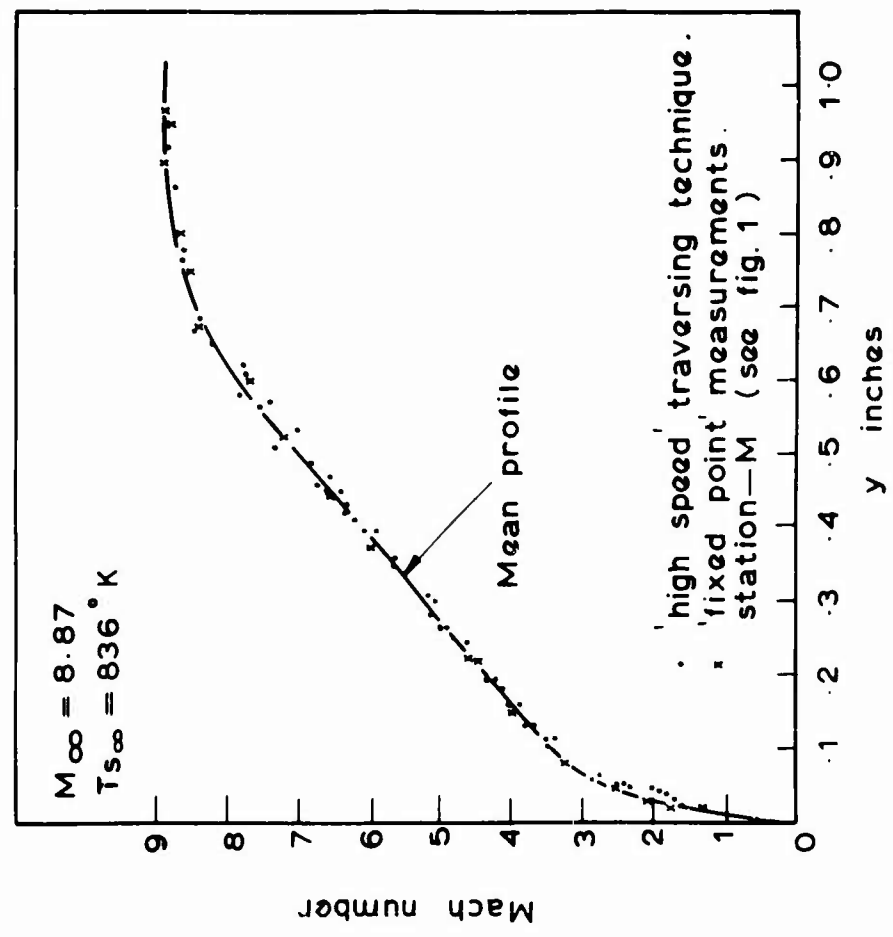


Fig.3 Comparison of traversed and 'fixed point' profile measurement

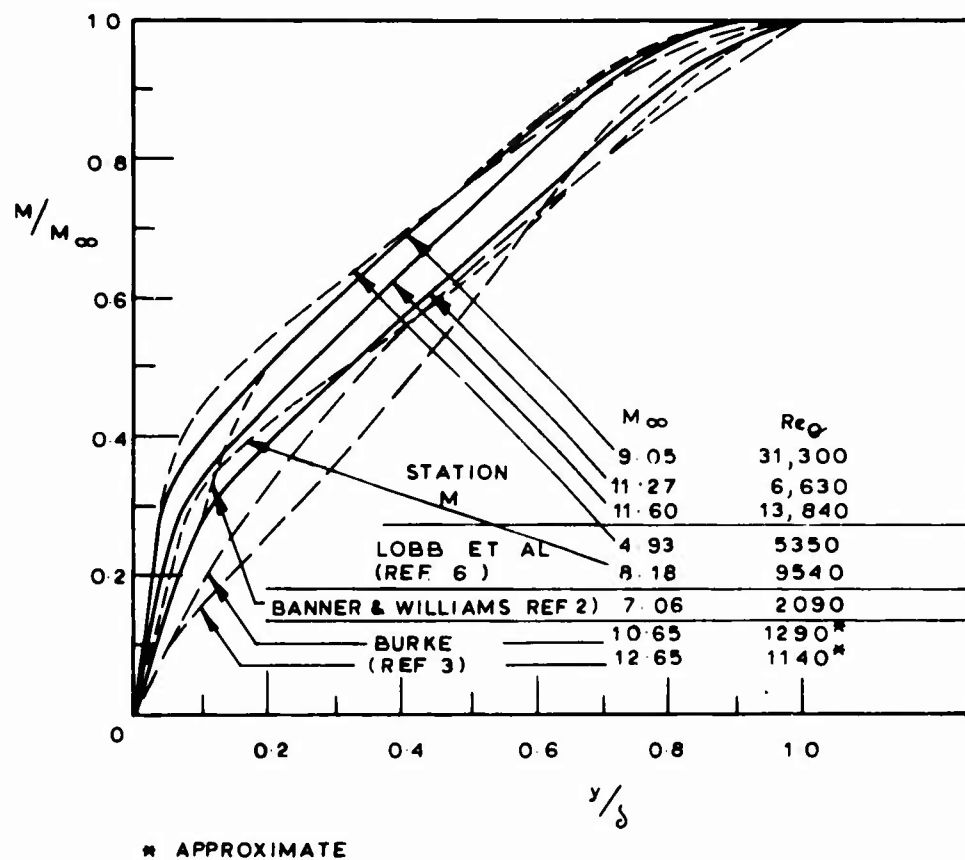


Fig.6 Comparison of Experimentally derived Mach number profiles

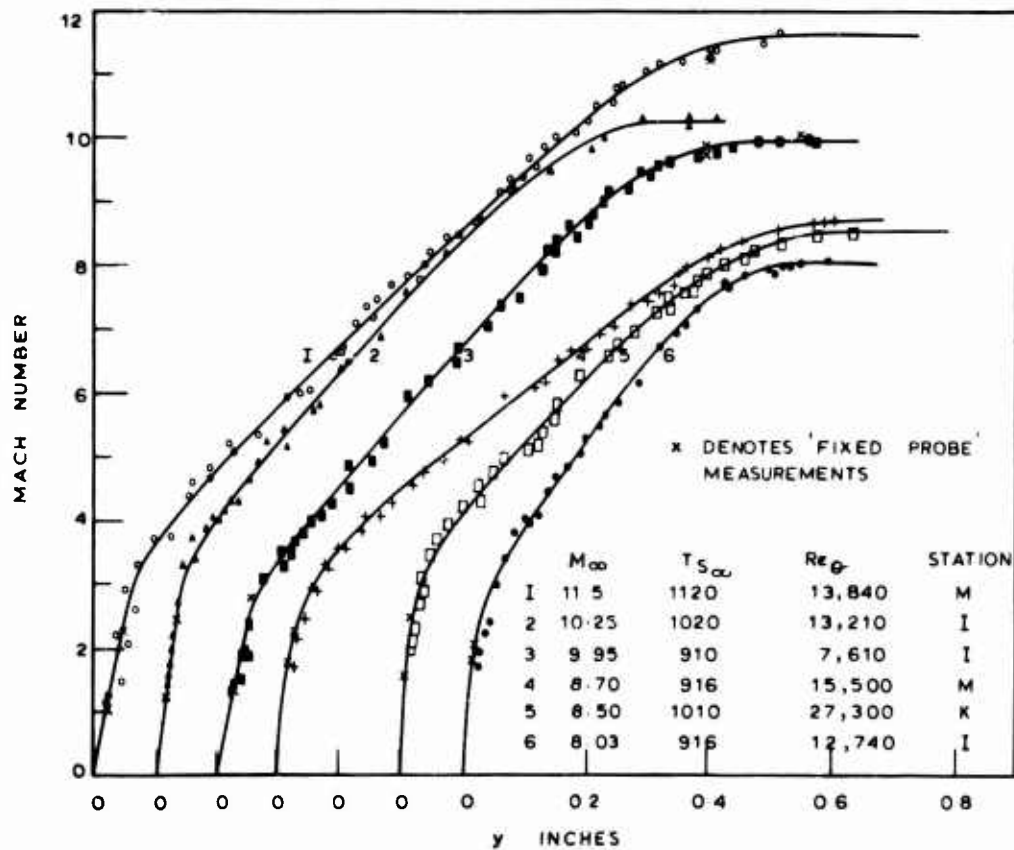


Fig.7 Sample Mach number profiles

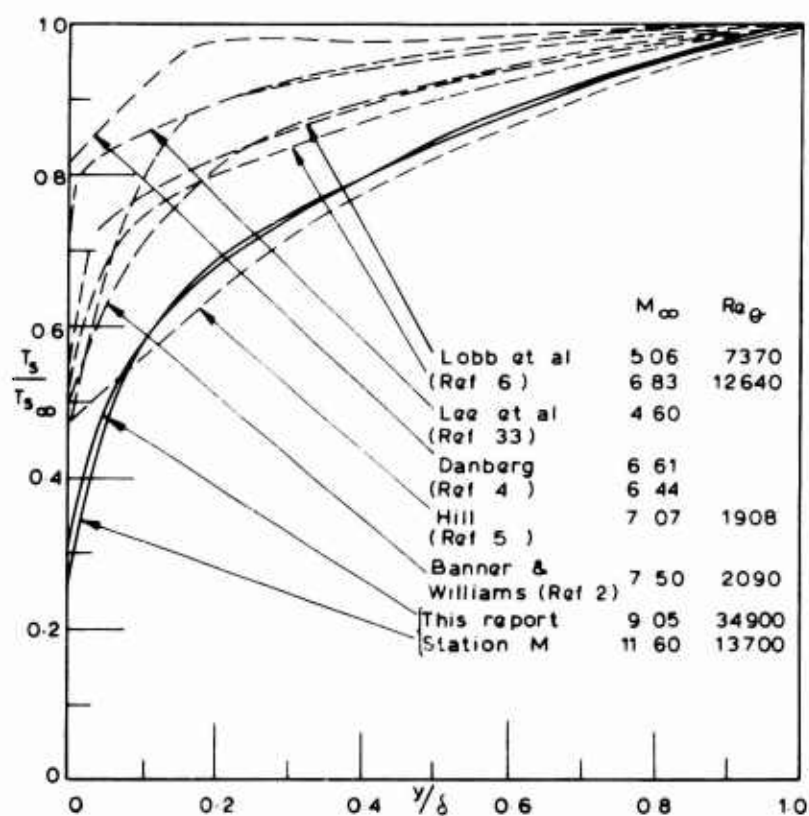


Fig.8 Comparison of experimentally measured stagnation temperature profiles

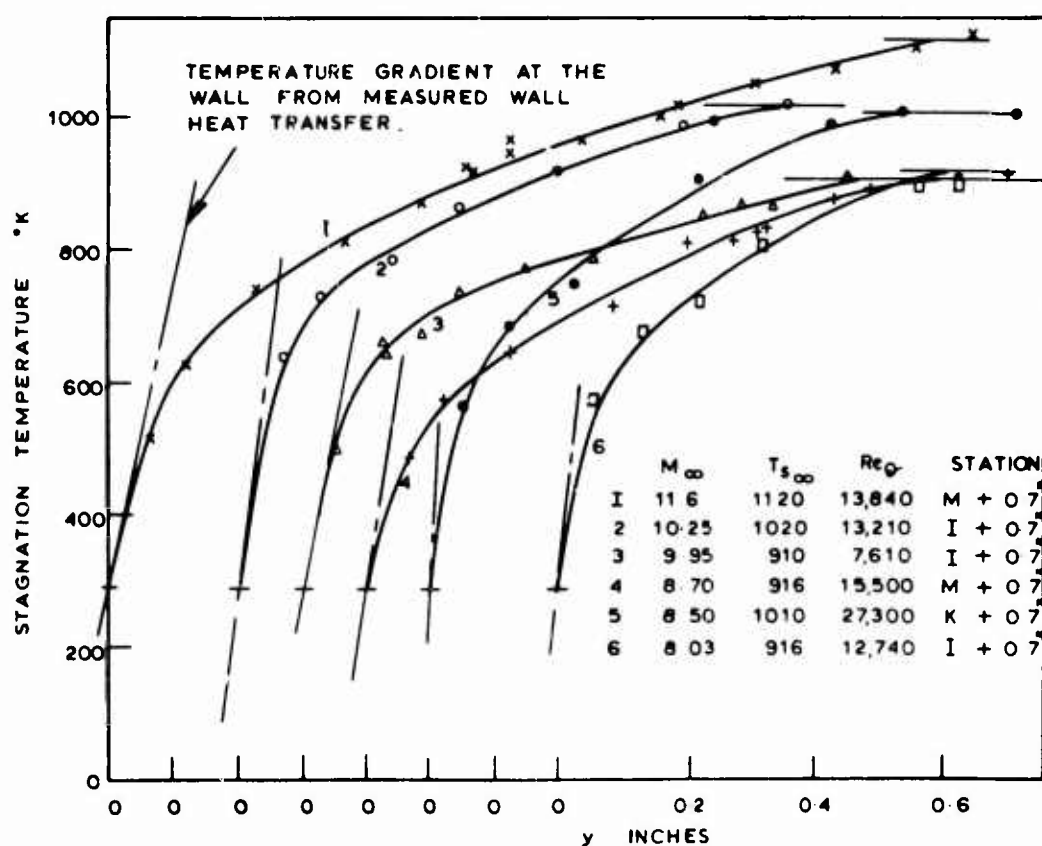


Fig.9 Sample stagnation temperature profiles

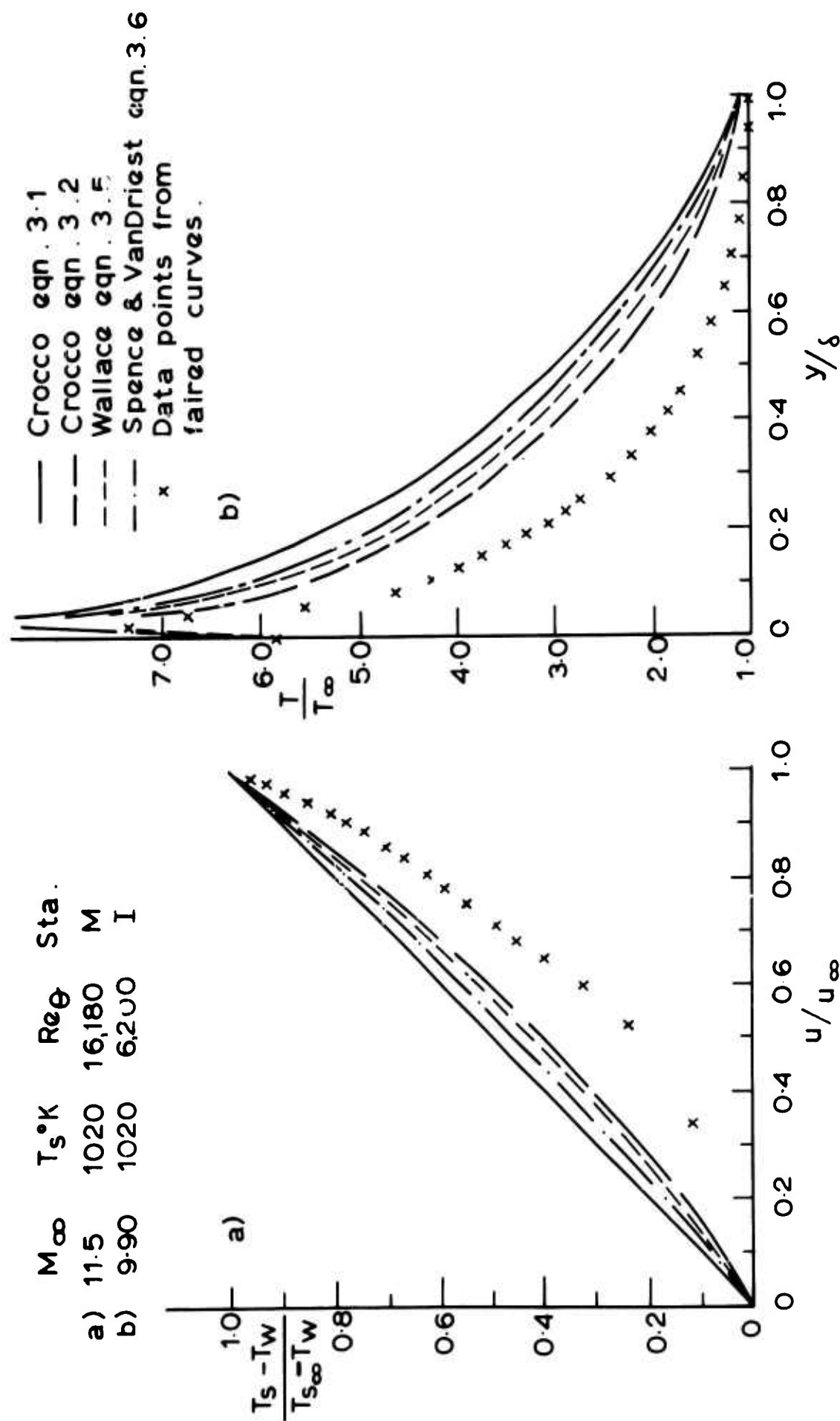


Fig. 10 Comparison of temperature-velocity functions with experiment

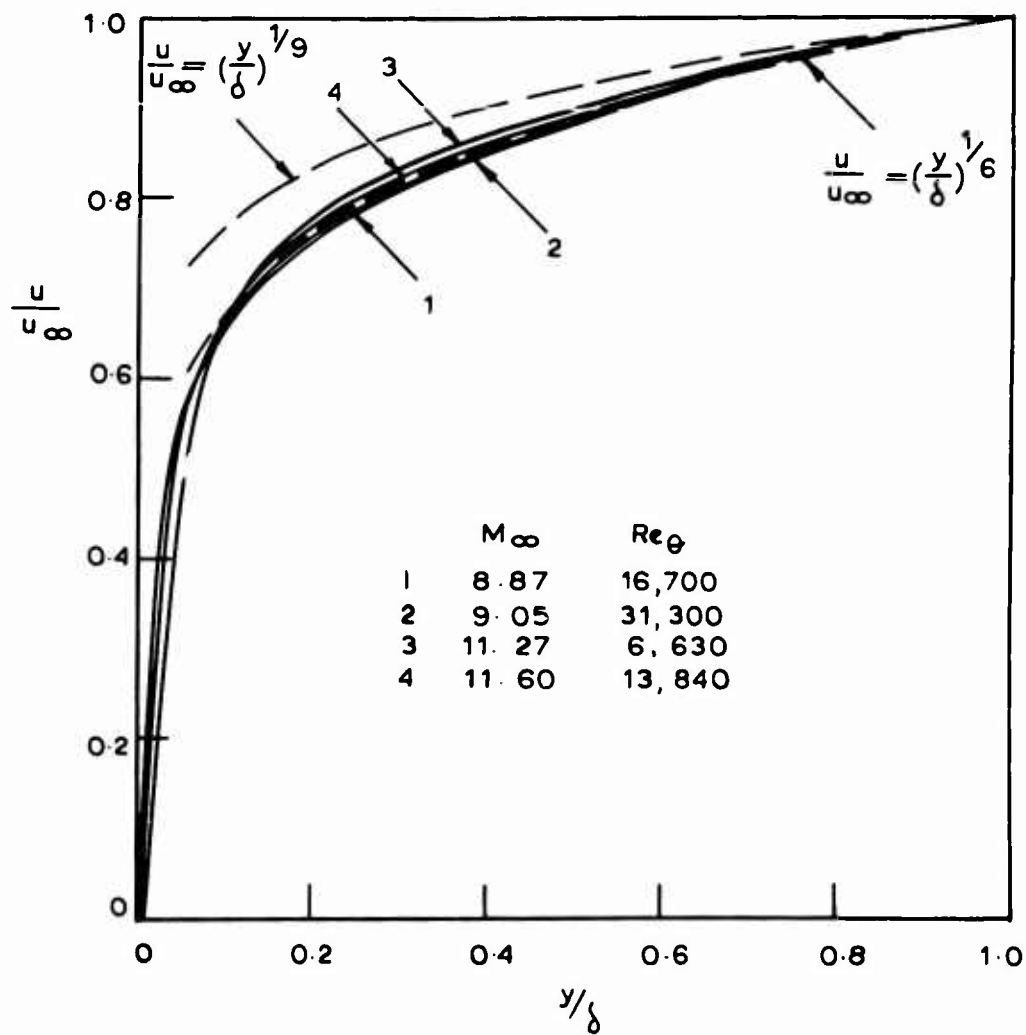


Fig.11 Typical velocity profiles

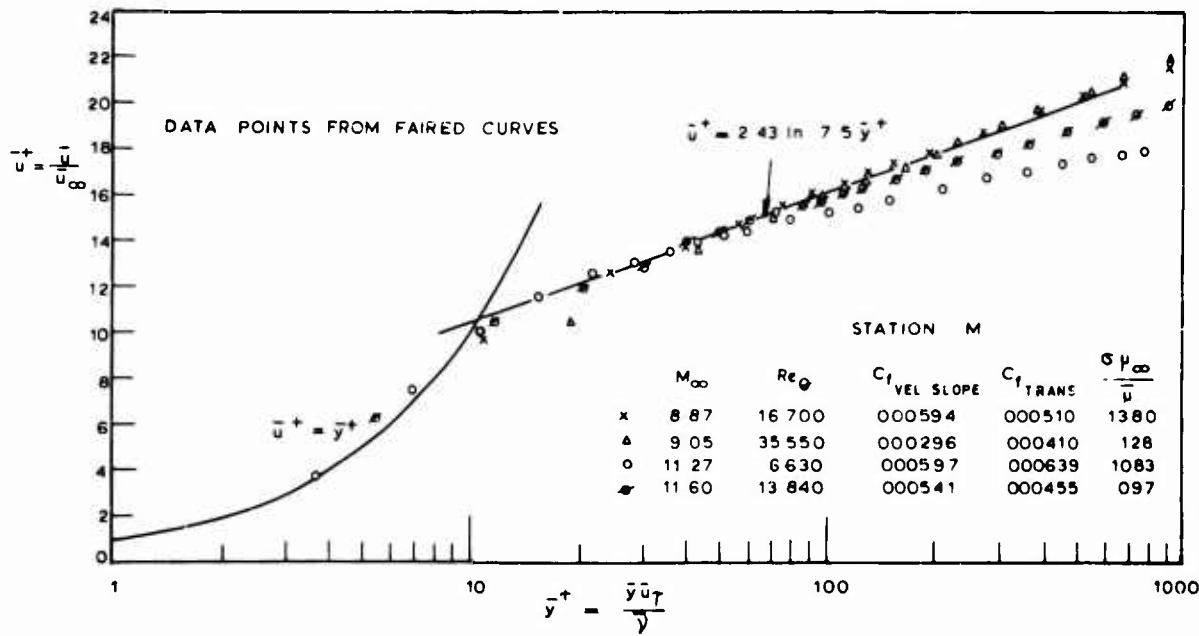


Fig.12 Transformed 'Law of the Wall'

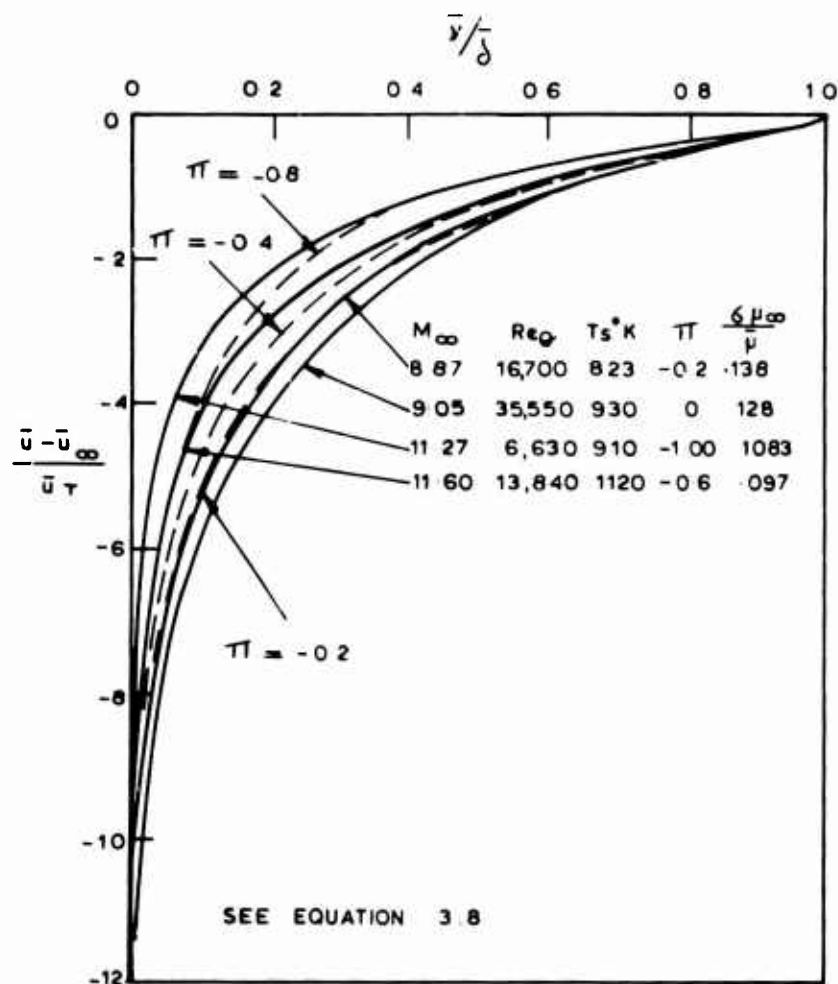
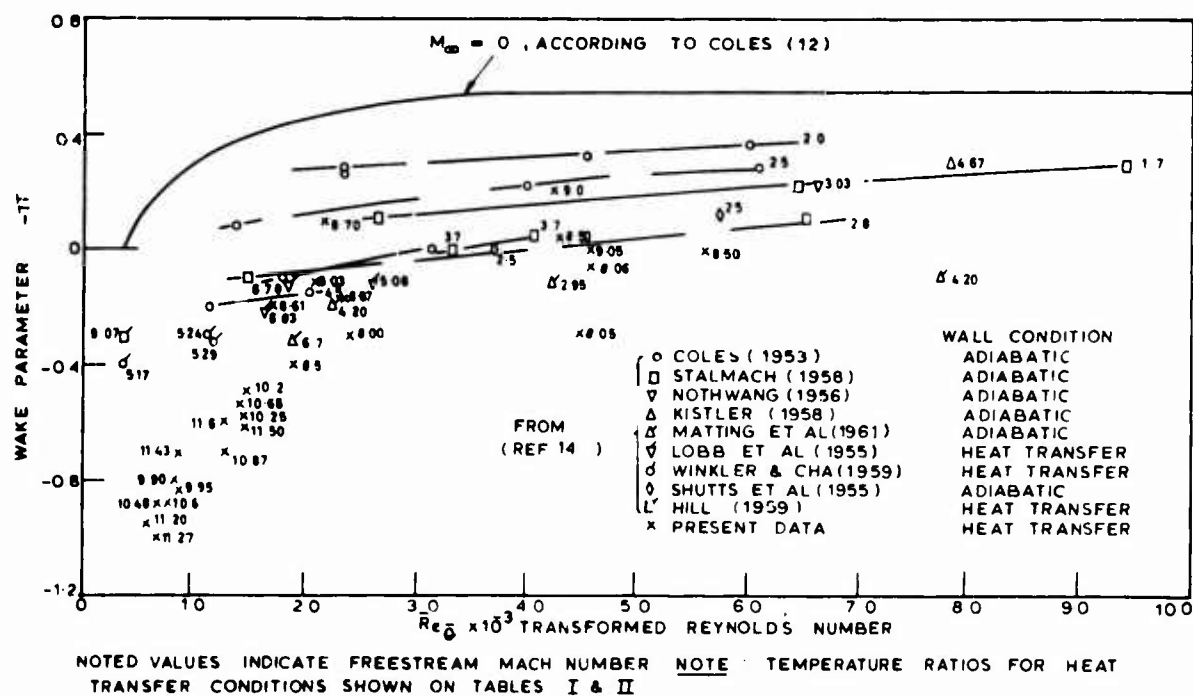


Fig.13 Transformed 'Law of the Wake'

Fig.14 Comparison of wake profile parameters, Π , from experimental correlation

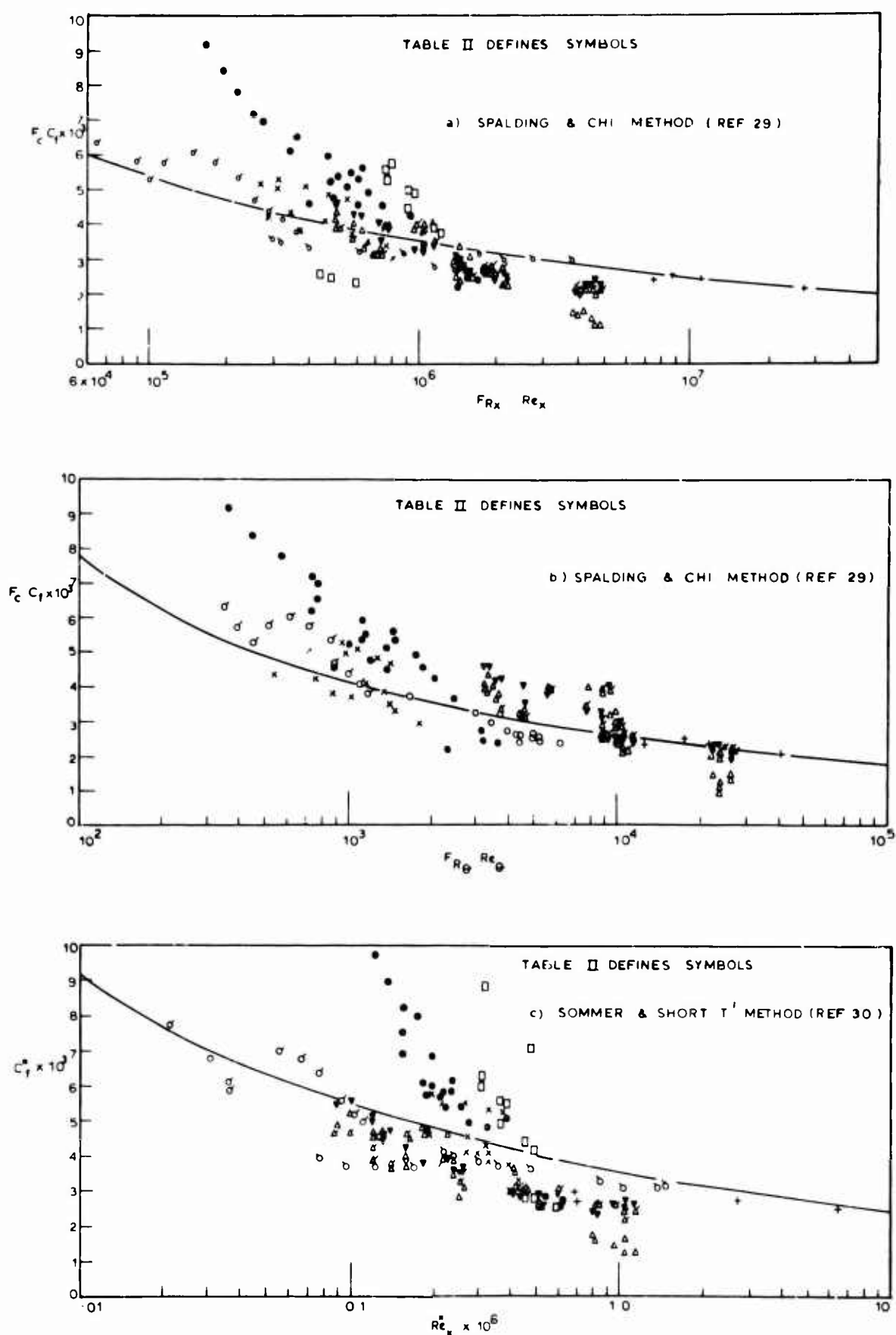


Fig. 15 Comparison of semi-empirical methods with experimentally derived skin friction coefficients

THEORY AND EXPERIMENT FOR THE
STRUCTURE OF SOME HYPERSONIC BOUNDARY LAYERS

by

Eric J. Softley, Robert J. Sullivan

General Electric Company
Missile & Space Division
King of Prussia, Pa.

SUMMARY

A recent study of hypersonic boundary layer transition on a 5° cone has given the opportunity to examine the structure of both laminar and turbulent boundary layers on sharp and blunt cones at edge Mach numbers of 10. From pitot probe and total temperature measurements, profiles of velocity and Mach number were obtained. The laminar boundary layer results are compared with a non-similar boundary layer theory calculated on a GE 635 computer. An interesting result for the turbulent boundary layer is that the total temperature is far removed from the Crocco relationship.

RESUME

Une étude récente de la transition de la couche limite hypersonique a donné occasion d'examiner la structure des couches limites, laminaires et turbulentes, sur des cônes tranchants et épointés au nombre de Mach de l'ordre de 10. Des profils de vitesse et de nombre de Mach ont été obtenus par les mesures de pression pitot et de la température totale. Les résultats de la couche limite laminaire sont comparés avec une théorie de couche limite non-similaire calculée sur une ordinateur GE 635. Un résultat intéressant pour la couche limite turbulente est que la température totale est très éloignée du rapport Crocco.

ACKNOWLEDGMENT

The authors wish to thank Mr Henry Rie for his efforts in providing a working computer program.

NOTATION

C_f skin friction coefficient

C_H heat transfer coefficient

f potential

ϵ enthalpy ratio

h enthalpy

M Mach number

p absolute pressure

Pr Prandtl number

q heat flux

r radius (body or shock)

S distance along surface

T absolute temperature

t time

u axial velocity component

v radial velocity component

x distance along axis of cone

y radial distance from cone surface

$$C_f = \frac{2\tau_w}{\rho_e u_e^2}, \quad C_H = \frac{\dot{q}}{\rho_e u_e (h_{0e} - h_w)}$$

γ ratio of specific heats

δ thickness (boundary or entropy layer)

η transformed y coordinate

μ viscosity

ξ transformed s coordinate

ρ density

τ shear force

Subscripts

e at boundary layer edge
ee at entropy layer edge
s at shock
w at wall
c total value
 ∞ ahead or outside shock

Superscripts

 behind local normal shock

THEORY AND EXPERIMENT FOR THE STRUCTURE OF SOME HYPERSONIC BOUNDARY LAYERS

Eric J. Softley, Robert J. Sullivan

1. INTRODUCTION

Recent studies of transition of a boundary layer on a cone at hypersonic conditions have been made in the GE-SSL large shock tunnel¹. The transition Reynolds number increases greatly with increasing Mach number and therefore a large model was needed. A 12 ft long 5° cone was selected. A feature of the large size and long boundary layer run was a thick boundary layer on the model. It was possible, therefore, to probe the boundary layer in some detail in both laminar and turbulent regions. The experiment was generally characterized by cold wall with uniform temperature and free stream Mach numbers from 10 to 15. Nose radii varied from sharp to a 1 inch radius.

It is apparent that, within these restrictions, there are four cases of interest. For the sharp cone both laminar and turbulent boundary layers exist. If a characteristic example of a blunted cone is that for which the boundary layer thickness is notably less than the entropy layer thickness then only the laminar case can be probed in this experiment. This was because an increase in nose Reynolds number delayed transition and made the existence of a turbulent boundary layer less likely.

For the three boundary layers, a study was made with pitot probes and total temperature probes. From the data obtained it is possible to calculate local velocities, densities, temperatures, etc. In addition, we have measured values of the surface heat transfer and pressure. The surface heat transfer was used to define the transition points (see Ref. 1) and the surface pressure was used in the definition of the flow field.

2. MODEL AND FLOW FIELDS

The model used for these tests was a 12 ft long 5° half angle cone. The location of the model in the shock tunnel nozzle is shown in Figure 1. This nozzle is a contoured nozzle designed to produce parallel flow at Mach 20 and has been operated satisfactorily down to Mach numbers of 10. For a description of the tunnel and nozzle see References 1, 2 and 3. The Mach numbers increase slightly along the length of the cone with corresponding variations in pressure, temperature, and velocity. The flow conditions were evaluated by using surface pressure measurements and plenum pressure measurements of the tunnel. An experimental pressure distribution along the cone is used to evaluate the edge Mach number and other parameters. The accuracy was checked using probe quantities outside the boundary layer and in the free stream at the axial location X (Figure 2).

For the blunt body flow fields an interesting problem exists in that the slightly divergent flow discussed earlier will interact with the blunted cone shock especially in the vicinity of the nose. The result is that the pressure on the rear of a slightly blunted cone is below that achieved by the sharp cone in the same flow. A non-uniform flow field calculation was made with the free stream conditions as an input and from this the pressure distribution on the blunted cone was calculated. The data obtained for the pressure measurements were then used as a check on this and are found to be quite satisfactory.

The edge Mach number for the blunt cone is dependent on the ability of the boundary layer to swallow the nose induced entropy layer. For purposes of the transition data shown in Reference 1, a GE VIZAAD computer program⁴ was used. The accuracy of this program of calculating edge Mach numbers is compared with the experimental values and with the non-similar boundary layer computation later in the paper. A summary of pertinent information is given in Table I.

3. EXPERIMENTAL TECHNIQUES

The surface pressure measurements described earlier were made with semi-conductor strain gage transducers. These were mounted in small cavities in the model such that response time was of order 100 microseconds. With flow durations typically 10 milliseconds this is ample for experimental measurements. The surface heat transfer measurements have been described in great detail in References 1, 6 and 7. These basically use thin film heat gages with a rapid response time. The boundary layer probe measurements were obtained using two five position probes. Measurements of stagnation pressure were made with the probe shown in Figure 3 and 4. Piezoelectric transducers approximately 1/8 inches diameter were located in the body of probes which were individually mounted on thin plates. Each probe was thus isolated to minimize any interference between probes. The tips were reduced in size to about 0.060 inches tip diameter to allow the best possible resolution for this experiment within the limitations of the instrumentation. The final response time of such a pitot probe is roughly half a millisecond. Note that because of the need to isolate the individual gages the profile is not made vertically out from the surface but is translated on the model in roughly half inch steps.

Total temperatures were measured using fine wire probes. These probes were usually pulsed to provide a two temperature technique. Figure 6 demonstrates the technique. An electrical pulse is used to increase the temperature of the wire from T_1 to T_2 . From measurements of the time derivatives of the wire temperature before and after the pulse plus knowledge of the end losses it is possible to calculate the recovery temperature T_R . This is then used with information on density and Mach number to calculate the total temperature. A more complete description is given in Reference 5. In the outer part of the boundary layer the density is sufficiently high that in some cases it was possible to reach recovery temperature during the test time of the tunnel and this technique was also used. The assembly shown for the pitot probe assembly was adapted to hold fine wires. Hence, the wire locations in the boundary layer were essentially that described for the pitot probe.

4. ANALYTICAL TECHNIQUES

Methods developed for the calculation of flow properties within the shock layer have been used to compare experiment and theory. These include the techniques used for calculation of the inviscid region and boundary layer region with the appropriate modifications to reflect the conditions that exist in the shock tunnel. These were taken as:

Equilibrium real gas nozzle expansion
Diverging free stream
Axial Mach number gradient

The problem involves the definition of the upstream flow conditions, the solution of the inviscid flow equations by the Method of Gravalos, et al.⁽¹⁰⁾, and use of these results as boundary conditions for the solution of the viscous region.

4.1 Non Uniform Flow Field Analysis

The analysis of the inviscid flow field departs from the technique in Reference 9. The method for the inviscid flow field was developed principally for conditions about a body

in flight, where the upstream conditions are uniform and the flow is parallel. These conditions are not satisfied in the shock tunnel experiment, and use of uniform conditions will not predict pressures measured on the cone during the experiment. The free stream input is modified to reflect the known divergence of the tunnel stream. The modification is then checked by comparing with the experimental pressure (Fig. 7). We then use this computed inviscid flow as the boundary conditions for the boundary layer computation.

For the blunt body the flow field is divided into three distinct regions. The subsonic region (near the axis of symmetry) is solved by relaxation. The transonic region is solved by direct numerical integration of the flow equations in physical space. The supersonic region is solved using the method of characteristics. The procedure assumes an initial shock shape and is iterated to the desired accuracy. Shock locations for this calculation are checked using total pressure traverse data taken from close to the body surface to beyond the bow shock.

The inclusion of the proper initial conditions results in surface pressure shown in Figure 7 for the non-uniform flow field analysis, and compares well with the measured test points. Shown for comparison is the uniform flow field computation, which gives an obvious incorrect answer.

4.2 Non Similar Boundary Layer Computations (N.S.B.L.)

The boundary layer equations are solved with a GE 635 digital computer using a finite difference scheme of the Crank-Nicolson¹² type. To specify the problem we require:

Conditions at the boundary layer edge
Thermal properties
Transport properties

The local surface pressure derived from the inviscid flow field is used as pressure at the boundary layer edge. A mass balance technique is then used to define the local velocity, enthalpy density and temperature, expressed as

$$\pi \rho_{\infty} u_{\infty} r_s^2 = 2\pi \left[r_w \int_0^{\delta} \rho u dy - \int_0^s m_w r_w ds \right]$$

which allows for the addition of ablating mass addition or boundary layer suction. The location on the shock, r_s defines the flow states behind the shock, and an isentropic expansion to local static pressure is used to find the conditions at the boundary layer edge.

The gas is assumed ideal within the inviscid flow field with a slight adjustment to γ at low temperatures. The transport properties required are Prandtl number and viscosity. The Prandtl number is assumed a function of temperature only. Viscosity follows Sutherland's law for $T > 100^\circ\text{K}$. For $T < 100^\circ\text{K}$ a linear function is used¹⁵.

The boundary layer equations used are written:

$$\begin{aligned} \frac{\partial}{\partial s}(\rho u r_w) + \frac{\partial}{\partial y}(\rho v r_w) &= 0 \\ \rho u \frac{\partial u}{\partial s} + \rho v \frac{\partial u}{\partial y} &= -\frac{\partial p}{\partial s} + \frac{\partial}{\partial y} \left(\mu \frac{\partial u}{\partial y} \right) \\ \rho u \frac{\partial h}{\partial s} + \rho v \frac{\partial h}{\partial y} &= u \frac{\partial p}{\partial s} + \frac{\partial}{\partial y} \left(\frac{\mu}{P_r} \frac{\partial h}{\partial y} \right) + \mu \left(\frac{\partial u}{\partial y} \right)^2 \end{aligned}$$

where s is the distance along the body surface and y is the local normal. The equations are transformed with the Levy-Lees transformation for numerical solution, where the independent variables are:

$$\xi = \int_0^s \rho_w \mu_w u_e r_w^2 ds$$

$$\eta = \frac{u_e r_w}{\sqrt{2\xi}} \int_0^y \rho dy$$

and the dependent variables are

$$v = \frac{2\xi}{d\xi/ds} \cdot \left[f' \frac{\partial \eta}{\partial s} + \frac{\rho v r_w}{\sqrt{2\xi}} \right]$$

$$f' = \frac{\partial f}{\partial \eta} = \frac{u}{u_e}, \quad g = \frac{h}{h_e}$$

The bluntness induced vorticity complicates the definitive of the boundary layer edge. The definition of δ in the present program is based upon the total temperature or total enthalpy. Mathematically

$$\frac{\partial}{\partial y} \left(\frac{h_0}{h_{0e}} \right) < \epsilon_1, \quad \left| \frac{h_0}{h_{0e}} \right| < 1 + \epsilon_2$$

and the net energy flux across streamlines tends to zero. Thus for the blunt cases the value of $\left(\frac{\partial u}{\partial y} \right)_{y=\delta} \neq 0$, since velocity gradients are induced by the entropy layer. Far downstream the conditions will approach the sharp cone.

The boundary layer is then computed, starting at the nose, for each chosen axial station. The boundary conditions are those of each streamline and reflect the pressure gradient and shock shape of the problem.

5. LAMINAR BOUNDARY LAYER COMPARISON

Comparison is made between theory and experiment in terms of the velocity, total temperature and Mach number profiles. The experiment yields pitot pressure and total temperature profiles. An average trend is drawn for each and values of Mach number, etc. computed by assuming constant pressure through the boundary layer.

5.1 Sharp Cone Boundary Layer

Data at three positions is combined as shown in Figure 8. To facilitate comparison, the data was originally plotted as y/δ , but since this depends upon the choice of δ to a great extent, the final comparison is made with experimental data as functions of y . ($\delta/3x$), and with a theoretical computation at $x = 3'$. Hence, only a ratio of thicknesses is needed. A computed ratio is used.

The sharp case provided the greatest difficulty in matching theory and experiment. The experimental data shows similarity in the pressure and temperature profiles of Figure 8. There is good agreement between theory and experiment in the inner boundary layer. However, both the measured pitot pressure and measured total temperature indicate a "tail" at the outer edge of the boundary layer which is not computed from the theory. Variations in

step size in the computation were found to be significant in this outer portion with the solution asymptotic to the final solution with increasing step size (until a practical upper limit is reached.) The deviation between theory and experiment occurs as Mach number increases and the static temperature decreases below 200°R. Figure 9 illustrates this deviation of M and u/u_e as we approach the boundary layer edge.

Since the temperature in the outer part of the boundary layer is low some attention must be given to the gas properties in the calculation. In particular the transport properties, in terms of viscosity and Prandtl number are needed. Some data on viscosity is given in Reference 15. Very little data is available on Prandtl number at low temperatures, however. Information given on hydrogen for conditions near the saturation line indicate an anomalous behavior of Pr . Some studies were made with the computer solution using a range of possible Prandtl number functions but none provided a solution similar to the experimental results. At the present time it is not known whether the "tail" is peculiar to the shock tunnel experiment or not.

Since the N.S.B.L. solutions agree with the experimental observations near the wall the calculated heat transfer also shows excellent agreement with that measured by surface heat gages (see Fig. 11).

Solutions are also given in Figures 8-10 with Prandtl number equal to unity. This gives increased heat transfer and decreased skin friction. It also gives the well known Crocco integral for total temperature as a function of velocity (Fig. 10). Departure from the linear solution is very slight for real Prandtl numbers.

5.2 Blunted Cone Boundary Layer

The laminar boundary layer on a blunted cone is shown in Figures 12-15. The N.S.B.L. computation of total temperature is shown in Figure 12 both with Prandtl number a function of temperature and also set equal to unity. Since the velocity is not constant external to the boundary layer the total temperature is used to define the boundary layer edge. The N.S.B.L. computation for total temperature seems to be a good average for the experimental values. The velocity profile also demonstrates excellent agreement between theory and experiment. The Mach number, however, indicates that the N.S.B.L. computation produces Mach numbers below those observed experimentally (at any y station). However, the experimental error is sufficient to cover the discrepancy.

For the boundary layer edge the computed Mach number of 6.4 compares with an experimental value of 6.8 ± 0.4 . Notice that because of the large value of $\frac{dM}{dy}$ at the edge, the choice of the exact boundary layer thickness becomes critical and the value of the comparison is limited. The VIZAAD calculation gives a value of 6.7.

This in fact demonstrates a problem for blunt body flows in general since the definitive of edge properties is used extensively in transition and heat transfer correlations.

Since the edge Mach number is not high the total temperature differs only slightly from Crocco's integral (see Fig. 14). Note the values of Prandtl numbers shown in Figure 15. Reynolds analogy is therefore a good approximation, as shown in Table I.

The computed heat transfer (from derivatives at the wall of the N.S.B.L. solution) are about 10-15% below those measured. A difference in the derivative of temperature of this magnitude would not be too evident in the profiles shown earlier.

A solution with Prandtl number unity was also computed. Viscosity is assumed unchanged and the increase in temperature derivative shown (at the wall) combines with a decrease in thermal conductivity to give only a slightly increased heat transfer.

6. TURBULENT BOUNDARY LAYER

The experimental profiles of the turbulent boundary layer are shown in Figure 17. The pitot profile shows a characteristic observed for the turbulent boundary layer namely a tendency for increasing scatter at and slightly beyond the edge of the boundary layer. The total temperature profile for this case is unfortunately incomplete since some data points were not obtained (due to program foreshortening). It seems reasonable, based on the experimental data available, to extrapolate down to T_w/T_{oe} as shown and further analysis uses the complete profile shown. Pitot profiles were also obtained at 9 ft on the cone for the same free stream condition and for a different condition at 4 1/2 ft location. The profiles were found to overlay so that the turbulent boundary layer would appear to be similar in the sense that the Mach number profile can be made independent of the X location by non-dimensionalizing the y coordinate.

The Mach number and velocity profiles obtained from the experimental data are shown in Figure 18. It is interesting to compare the velocity profile in this case with that obtained by using a Danberg or Crocco relationship together with the experimental pitot profile but we will return to this in a moment.

In Figure 19 the total temperature is considered a function of the non-dimensionalized velocity through the boundary layer. Comparison is made between the experimental values, the Crocco relation ($Pr = 1$) and the results of Danberg⁸. As can be seen the data is far removed from either of these two cases. Indeed this must be so since for most of the outer part of the boundary layer as observed in Figure 18 the Mach number is quite high. This means that the total temperature must be proportional to the square of the velocity, representing a gross departure from the Crocco integral where the total temperature is a linear function of velocity. Note that a Crocco relationship is often used in turbulent boundary layer analysis, e.g. Van Driest¹³. The hypersonic limit shown in Figure 19 is that obtained when the Mach number is infinite through the boundary layer which is a good approximation in the outer part of the boundary layer. It also represents a lower limit for the total temperature as a function of velocity. It is interesting to compare the experimental result with those shown earlier by Bertram and Neal¹⁴. At high Mach numbers there is a definite tendency for their data to demonstrate a velocity squared relationship for the outer half of the boundary layer.

It is possible to make a calculation of the velocity distribution through the boundary layer using the experimental pitot pressure and Crocco relationship. The resulting velocity profile is shown in Figure 18 and is quite different from that obtained from the experimental total temperature and pitot pressure in that it approximates a 1/7 power law rather than the 1/3 law shown. Hence, the skin friction coefficient for compressible boundary layer would be considerably less than for the incompressible one as is well known. Unfortunately it is difficult to obtain a numerical value for the skin friction from the velocity profile shown.

Returning to Figure 19 it is possible to find a value for $\frac{C_H}{C_f}$ and hence to examine Reynolds analogy. From the definitions

$$\frac{2C_H}{C_f} = \frac{1}{Pr_w} \frac{u_e}{T_{oe} - T_w} \left(\frac{\partial T_o}{\partial u} \right)_w \approx 0.44$$

from Figure 19. Hence for this hypersonic boundary layer Reynolds analogy no longer appears to be valid.

7. CONCLUSION

The structure of a hypersonic boundary layer on a cone has been studied for three cases. The laminar structure is predicted quite well by a non-similar boundary layer theory for

both a similar and non-similar laminar boundary layer. The outer edge of the sharp cone boundary layer computation is quite sensitive to the step size of the mathematical process and is more correct for larger steps. At edge Mach numbers of order 10 and $Pr \approx 0.7$, the total temperature/velocity function is slightly different from a Crocco relationship. In a hypersonic turbulent boundary layer the high Mach number in the outer half of the boundary layer requires the total temperature to be more like the square of the velocity and Crocco's relationship is no longer valid. In this turbulent boundary layer the velocity over most of the boundary layer approximates a $1/3$ power law relationship. For the two examples of laminar boundary layer Reynolds analogy is a good approximation. For the turbulent boundary layer, however, this is no longer true.

REFERENCES

1. Softley, E.J.
et al. *Experimental Observation of Transition of the Hypersonic Boundary Layer.* AIAA Report 68-39, January 1968.
2. Softley, E.J.
Graber, B.C. *Techniques for Low Level Pressure and Heat Transfer Measurements and Their Application to Base Flows.* GE TIS R67SD2.
3. Warren, W.R. *Design and Performance of the GE 6' Shock Tunnel Facility.* Proceedings of 1st Shock Tube Symposium, SWR-TM-57-2, February 1957.
4. Studerus, C.J.
Dienna, E.A. *Viscous Interaction Zero Angle of Attack (VIZAAD) Program.* GE-MSD TIS 64SD292, November 1964.
5. Softley, E.J. *Use of a Pulse Heated Fine Wire Probe for the Measurement of Total Temperature in Shock Driven Facilities.* GE TIS R68SD2, February 1968.
6. Graber, B.C.
et al. *Comparison of Laminar and Turbulent Cone Boundary Layer Flow With and Without Pressure Gradient.* GE TIS R67SD49.
7. GE TIS R67SD49A, Correction and Addition to above.
8. Danberg, J.E. *Characteristics of the Turbulent Boundary Layer with Heat and Mass Transfer at $M = 6.7$.* NOL TR64-99, Naval Ordnance Laboratory.
9. Walker, G.K. *The Growth of Laminar Boundary Layers with Zero Pressure Gradient.* GE RST Thermodynamics Fundamental Memo. TFM-8151-008, January 1963.
10. Gravalos, F.G.
et al. *The Supersonic Flow Field About a Blunt Body of Revolution for Gas at Chemical Equilibrium.* Proc. 9th Annual Congress IAF, August 1958.
11. Levine, J.N. *Finite Difference Solution of the Laminar Boundary Layer Equations Including the Effects of Transverse Curvature, Vorticity, and Displacement Thickness.* GE TIS R66SD349, December 15, 1966.

12. Crank, J.
Nicolson, P. *A Practical Method for Numerical Evaluation of Solutions of Partial Differential Equations of the Heat Conduction Type.* Proc. Comb. Phil. Soc. Vol. 43, p. 50, 1947.
13. Van Driest, E. R. *Turbulent Boundary Layer on a Cone in a Supersonic Flow at Zero Angle of Attack.* J. Aero Sciences, p. 55, January 1952.
14. Bertram, M. H.
Neal, L. N., Jr *Recent Experiments in Hypersonic Turbulent Boundary Layers.* AGARD Specialists Meeting on Boundary Layer Research, Naples, Italy, May 1965
15. Fiore, A. W. *Viscosity of Air.* Journal of Spacecraft, Vol. 3, p. 5, May 1966.

TABLE I

Air

Cone - 5° $1/2$ AngleWall Temperature - 300°K

Type	M_e	$\frac{T_w}{T_{oe}}$	$C_H^{(1)} \times 10^4$	$\frac{2 C_H^{(2)}}{C_f}$	$C_f^{(3)} \times 10^4$
Sharp - Laminar	$10.2 \pm 1^{(4)}$	0.21	2.6 (2.7)	1.09	4.8 (5.6)
Blunt - Laminar	$6.8^{(2)}$	0.21	6.1 (5.6)	1.15	10.6 (8.8)
Sharp - Turbulent	10.4	0.28	3.5	0.44	15.9

- Notes
- (1) Surface measurement or (NSBL calculation)
 - (2) From profile measurements
 - (3) From experimental C_H and $\frac{2 C_H}{C_f}$
 - (4) Data is composite for three locations

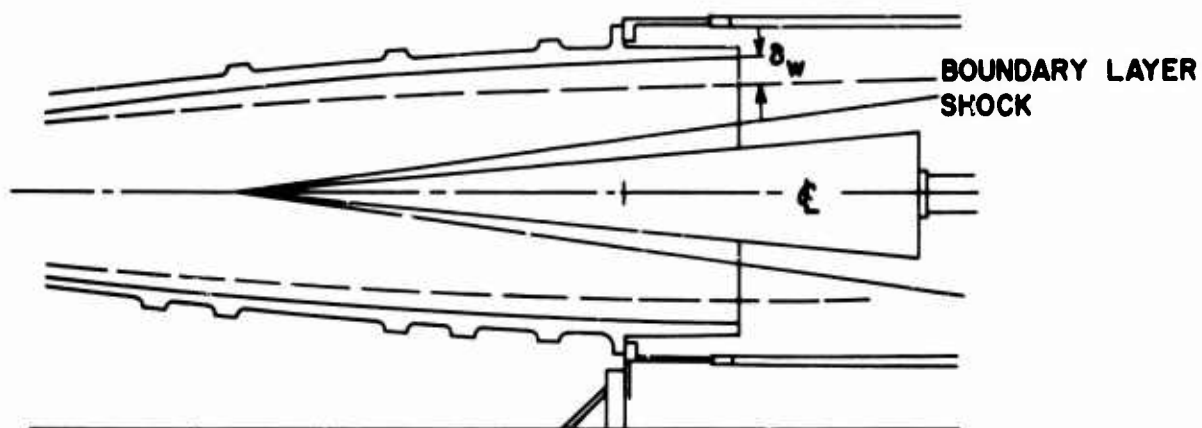


Fig. 1 Sketch of 12' cone model in nozzle

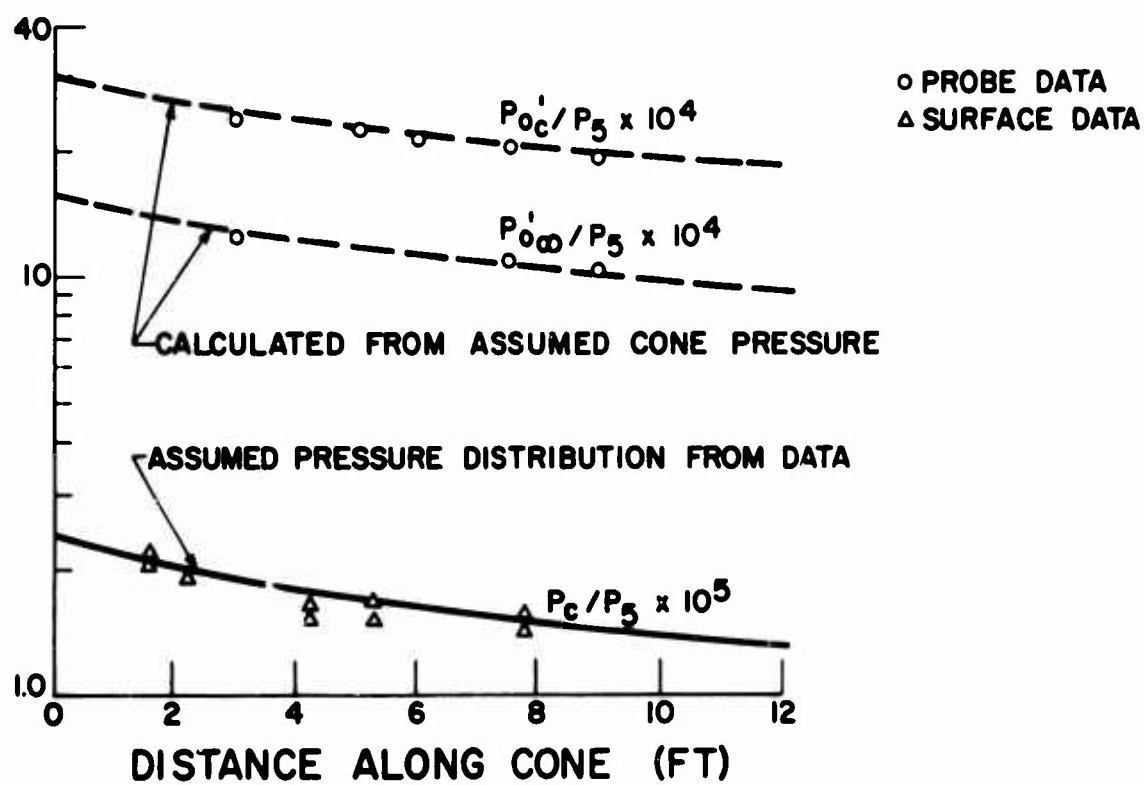


Fig. 2 Typical pressure distributions along sharp cone

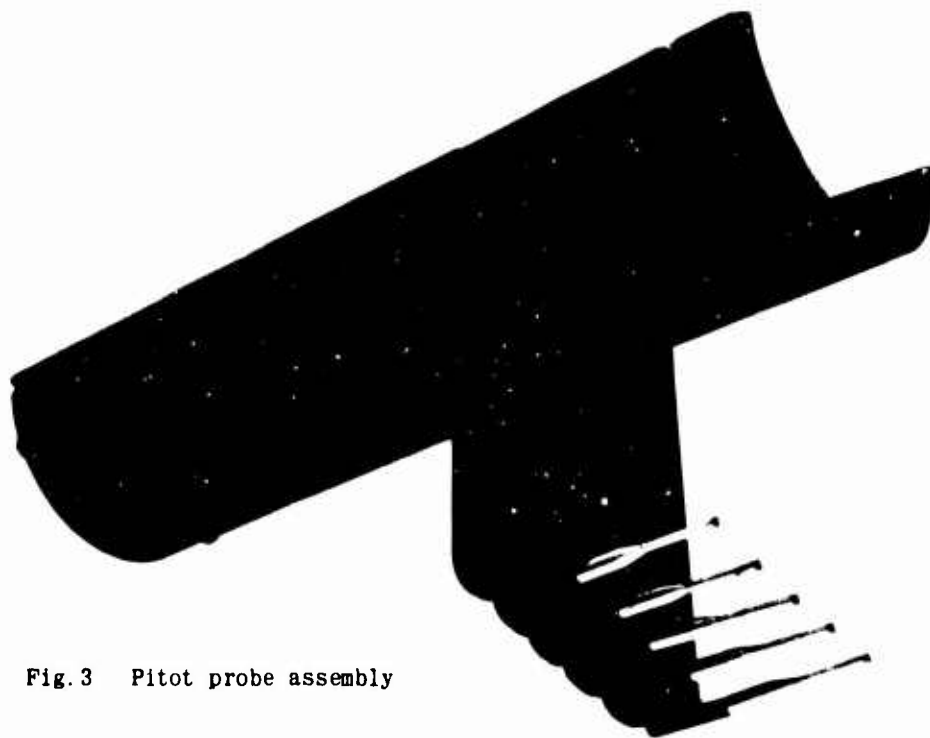


Fig. 3 Pitot probe assembly

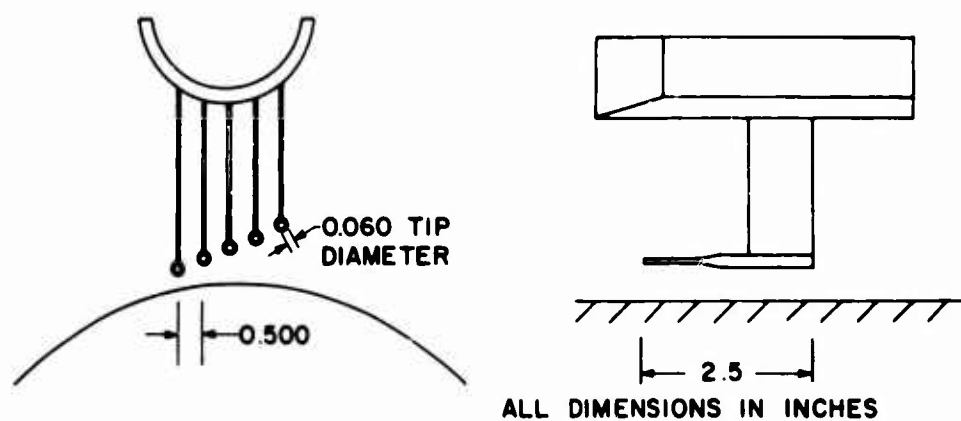


Fig. 4 Pitot probe location in the boundary layer

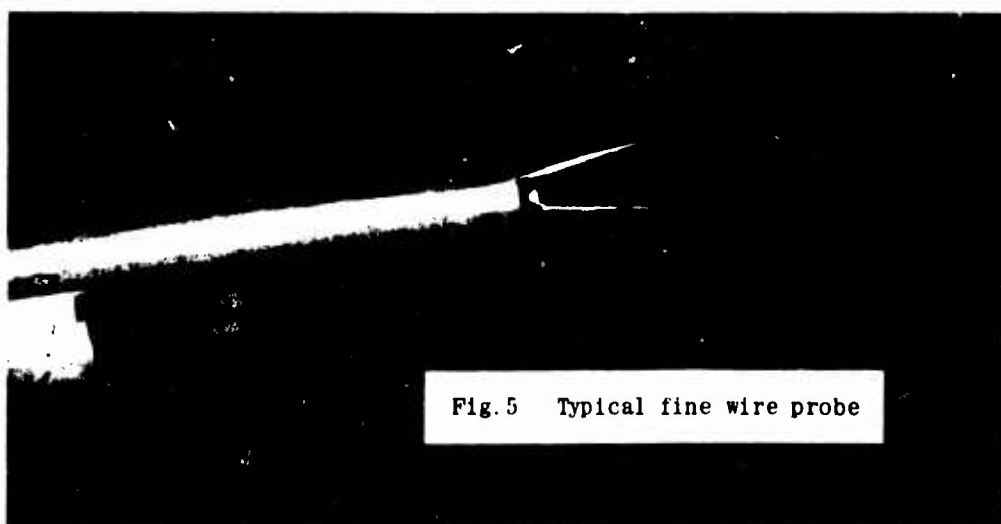


Fig. 5 Typical fine wire probe

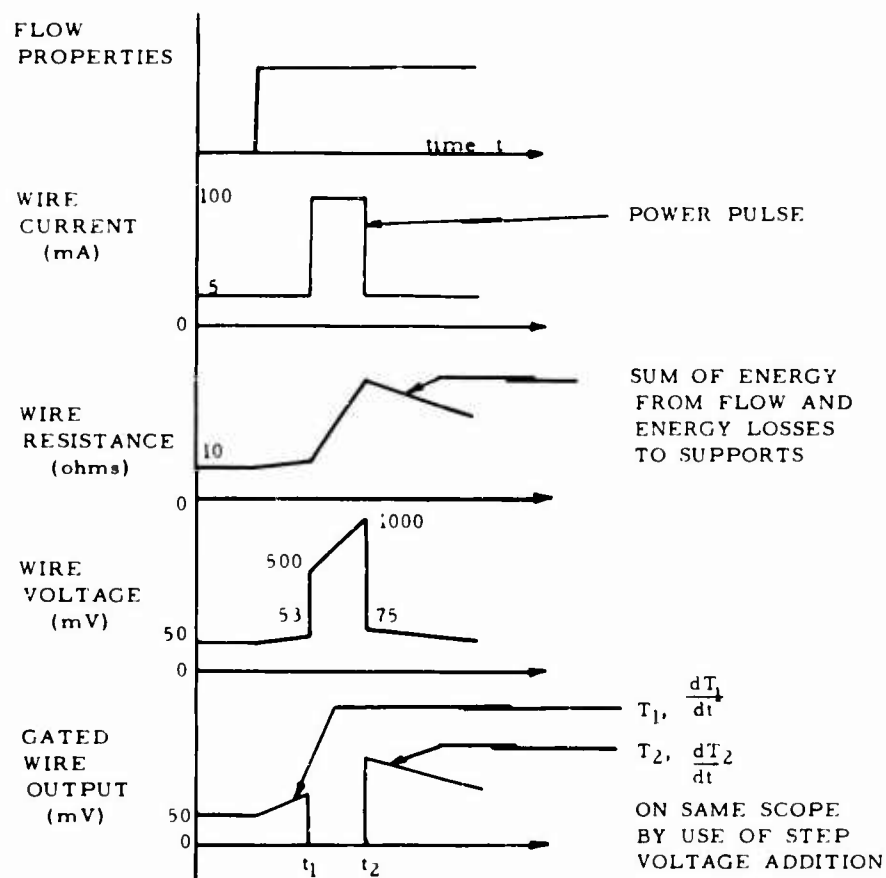


Fig. 6 Typical history of pulsed wire

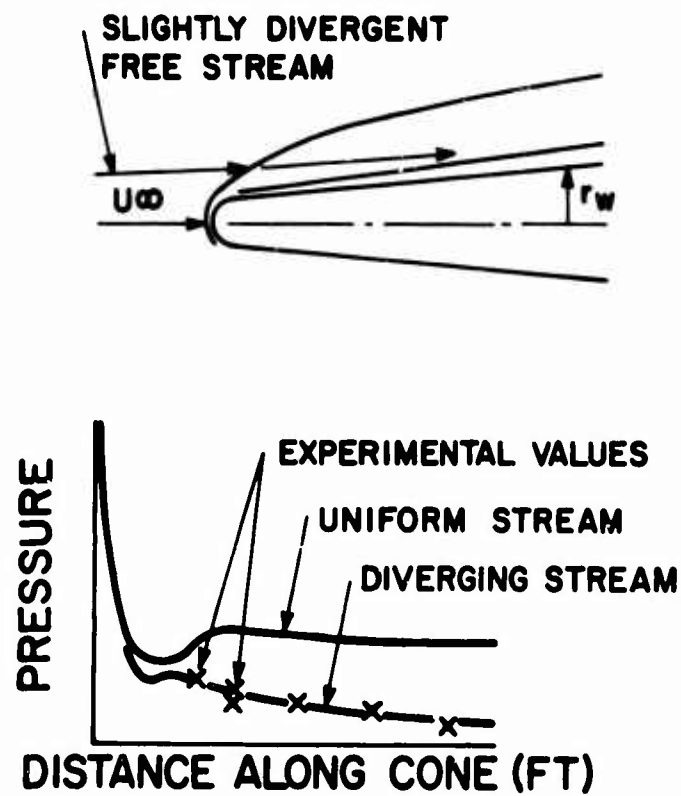


Fig. 7 Flow field and pressure distribution on blunt cone

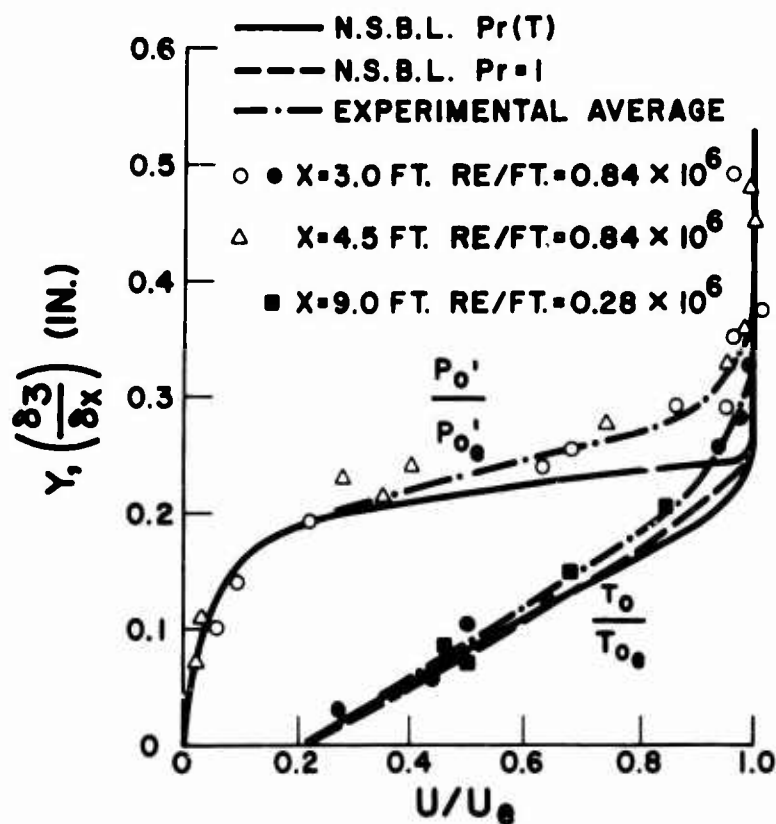


Fig.8 Pitot pressure and total temperature through a laminar boundary layer on a sharp cone

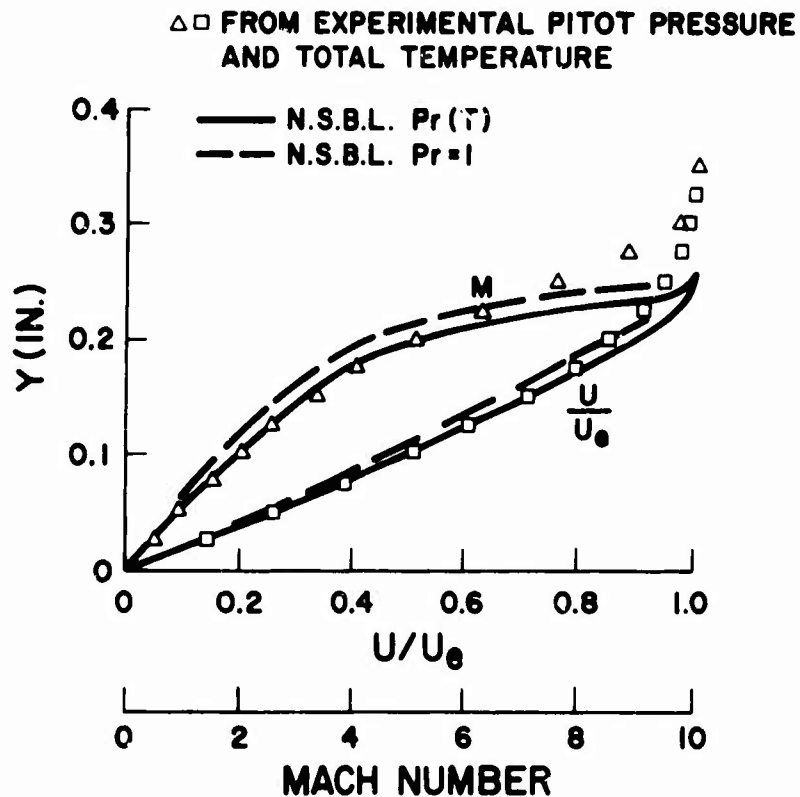


Fig.9 Mach and velocity through a laminar boundary layer on a sharp cone

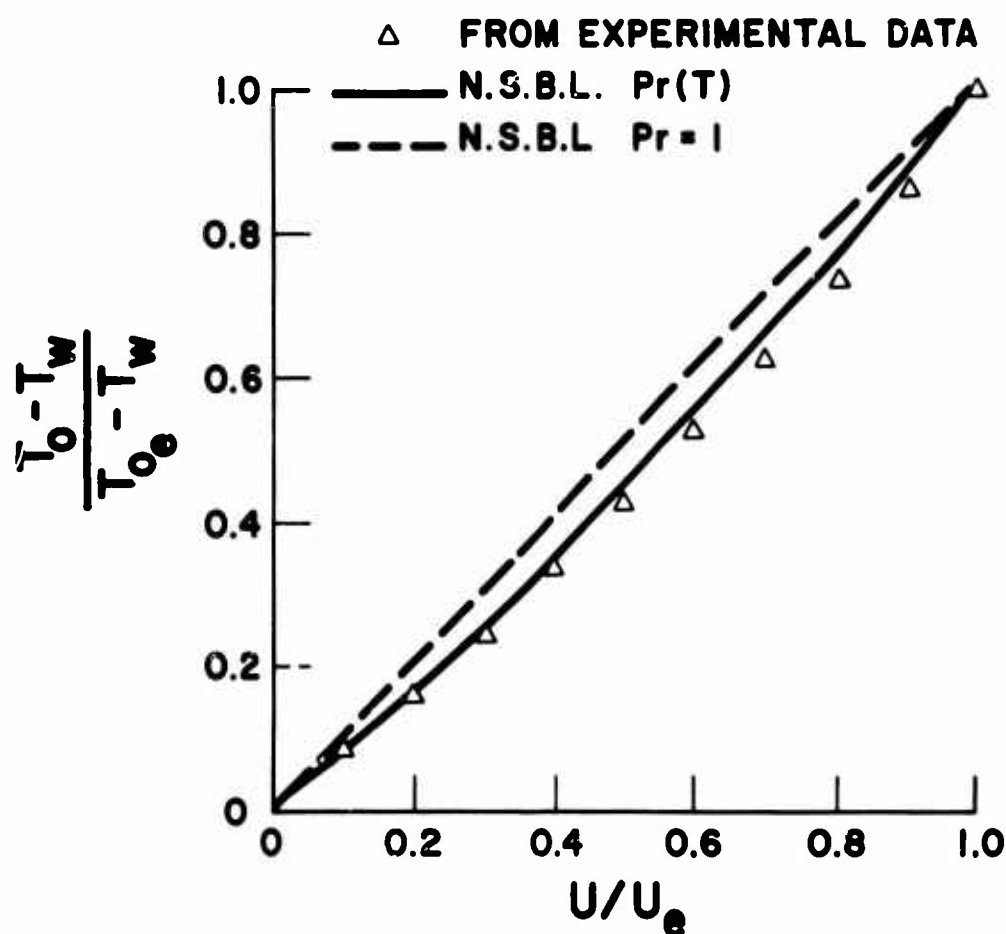


Fig. 10 Total temperature as a function of velocity for a laminar boundary layer on a sharp cone

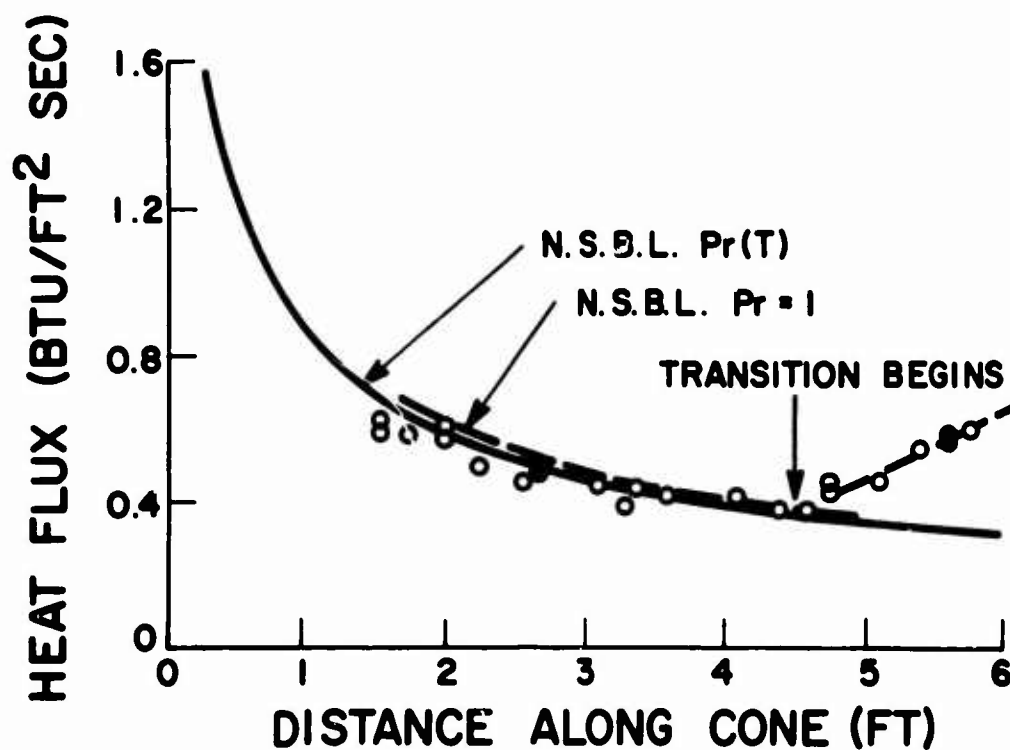


Fig. 11 Laminar heat transfer on a sharp cone

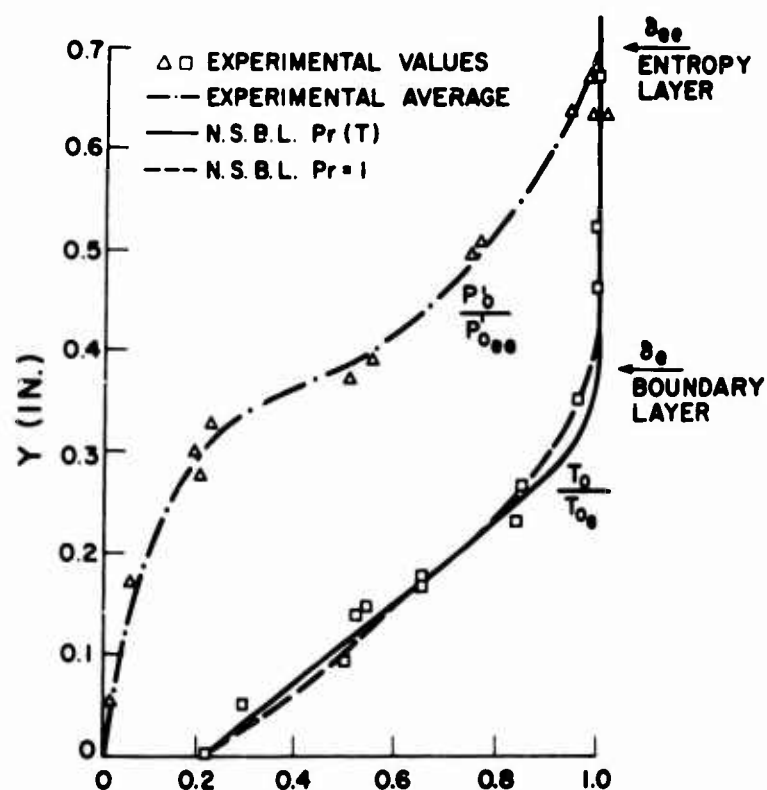


Fig. 12 Pitot pressure and total temperature through a laminar boundary layer on a blunt cone

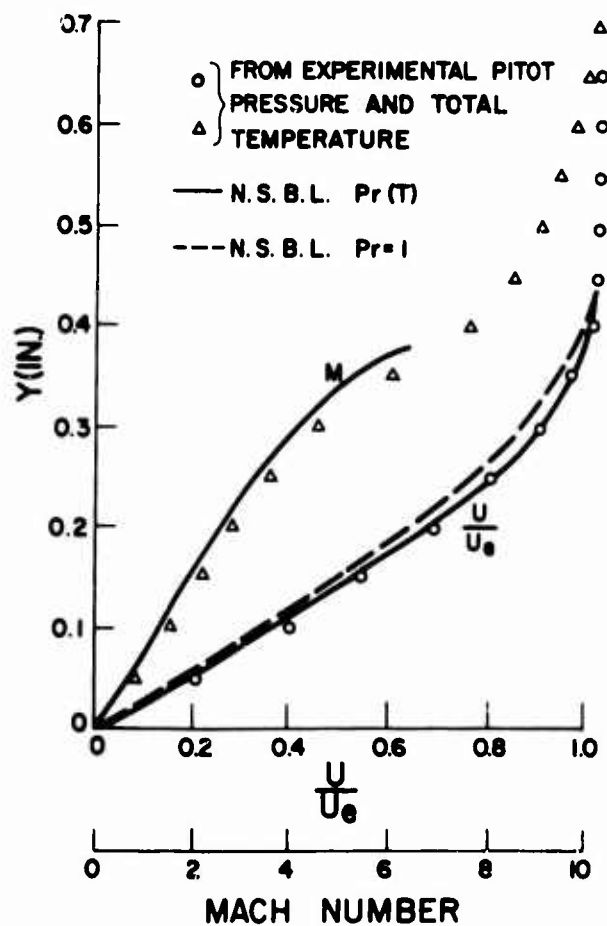


Fig. 13 Mach number and velocity through a laminar boundary layer on a blunt cone

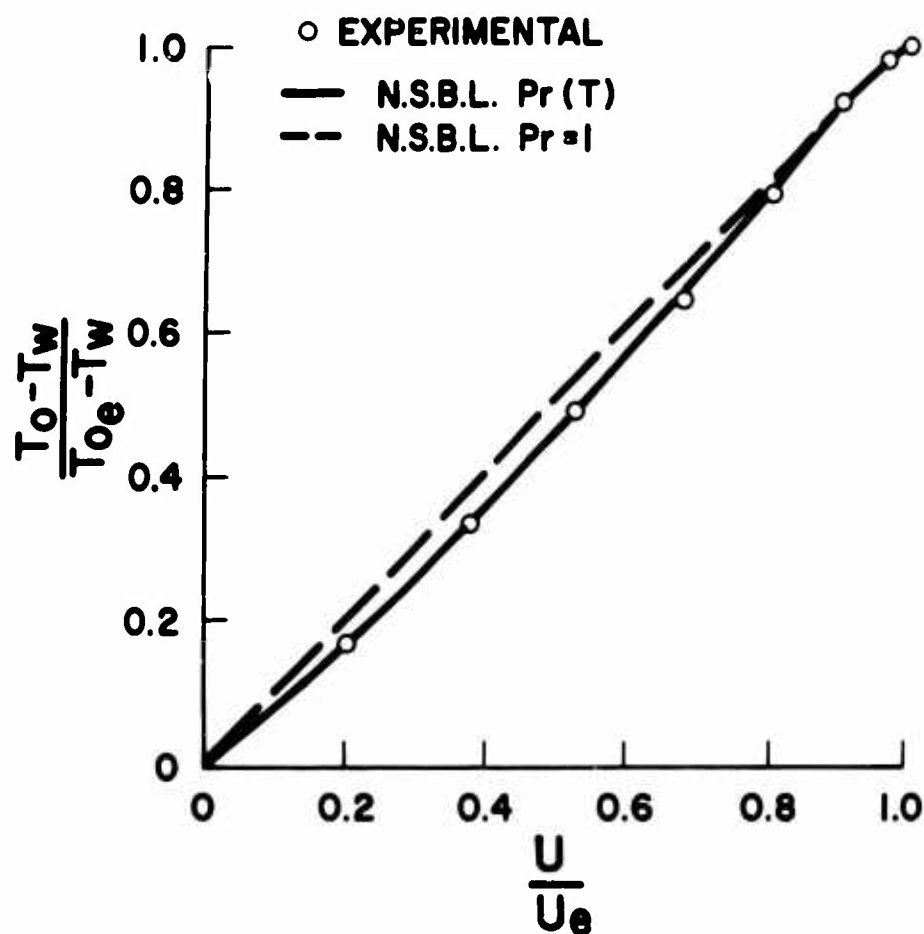


Fig. 14 Total temperature as a function of velocity on a blunt cone

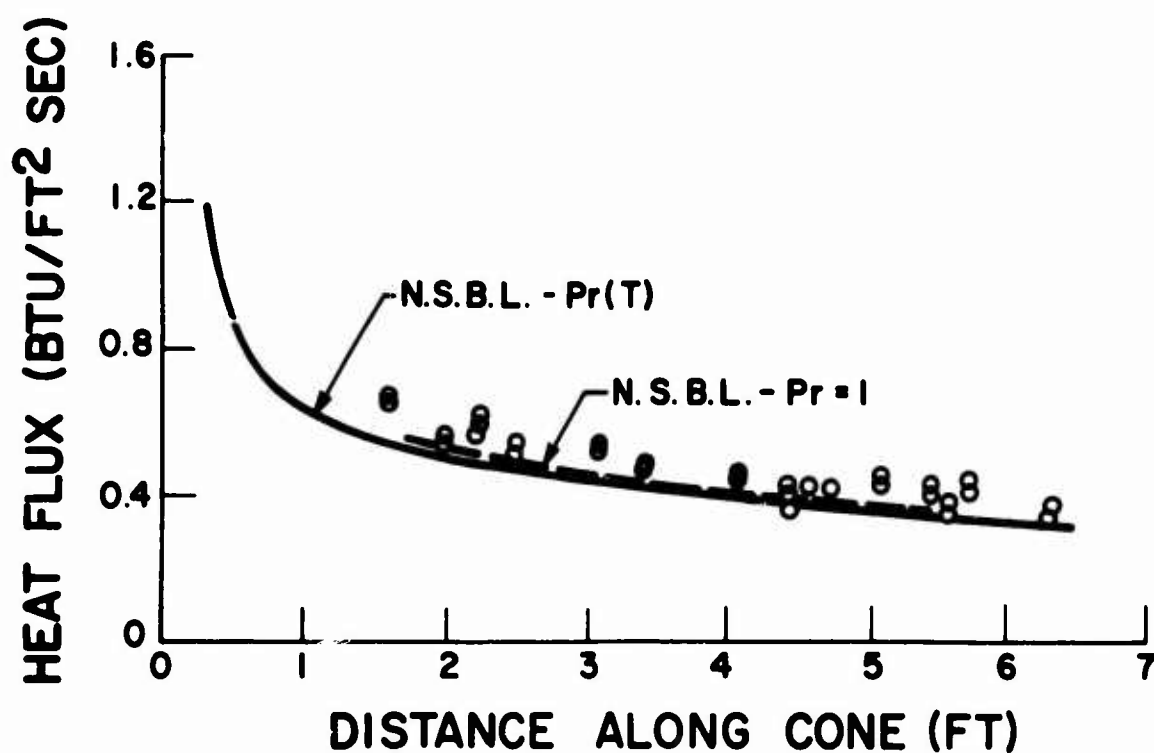


Fig. 15 Heat transfer along a blunt cone

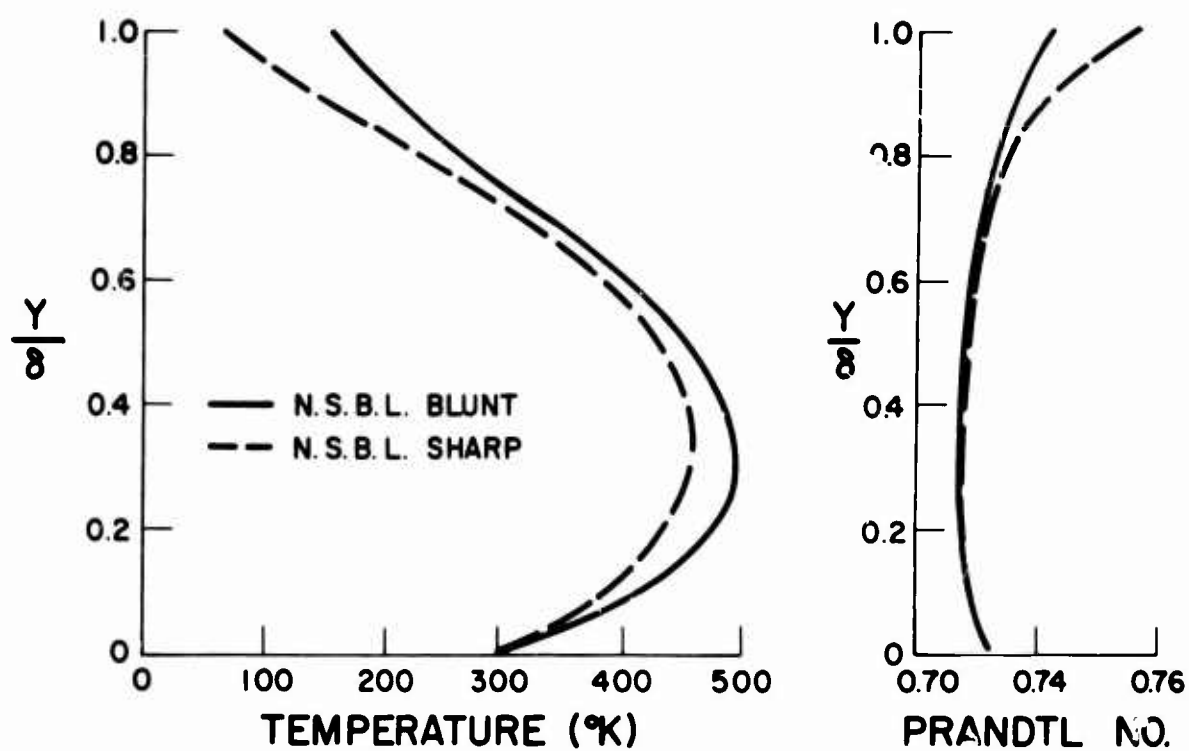


Fig. 16 Temperature and Prandtl numbers through the laminar boundary layers

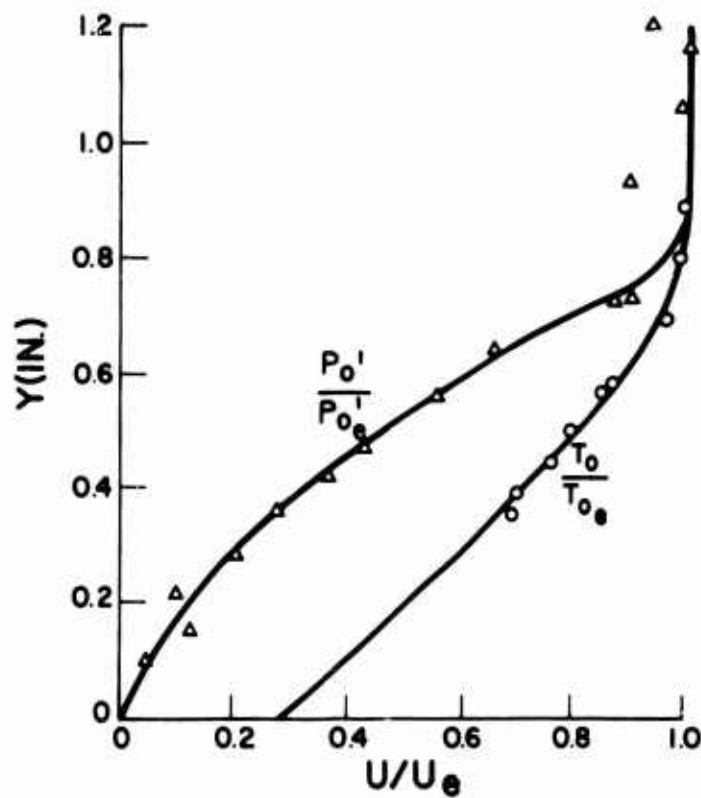


Fig. 17 Pitot pressure and total temperature through a turbulent boundary layer on a sharp cone

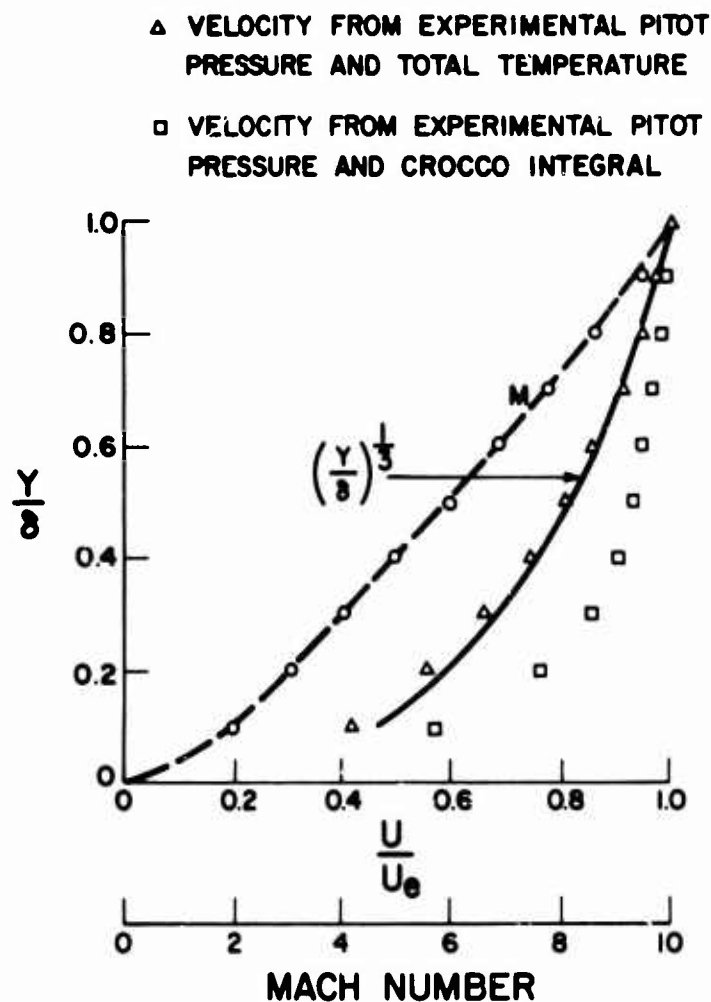


Fig. 18 Mach number and velocity through a turbulent boundary layer

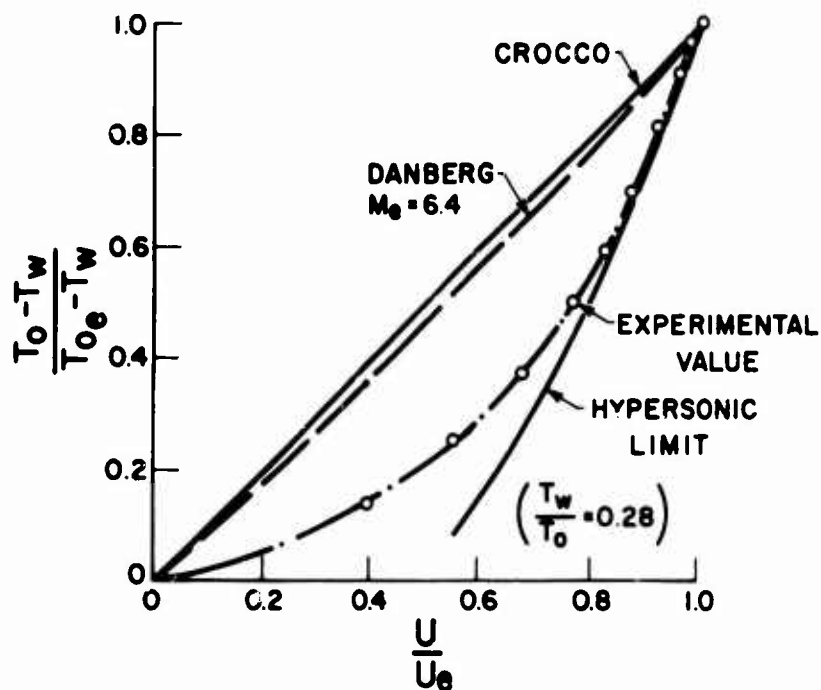


Fig. 19 Total temperature as a function of velocity for a turbulent boundary layer on a sharp cone

THE INTERACTION OF A TURBULENT BOUNDARY
LAYER AND A SHOCK AT HYPERSONIC MACH NUMBERS.

by

D. P. Myring

Royal Aircraft Establishment
Bedford, United Kingdom

Summary

Equations describing the phenomenon of turbulent shock wave boundary layer interaction are presented. The basic model adopted is the conventional one in which the boundary layer displacement effect is assumed to induce streamwise pressure gradients which in turn influence the boundary layer growth. The boundary layer assumption of constant static pressure across the layer is discarded and new hypotheses are invoked concerning the magnitude of the normal pressure gradient. On integration of the final set of simultaneous equations, three solutions are identified. One of these is shown to correspond to the phenomenon of shock interaction and comparisons with experiment are given. The theoretical effects of Reynolds number, Mach number, surface curvature, wall temperature and initial velocity profile on the pressure coefficient at separation are presented. Singularities which appear at low wall temperatures are examined and a simple procedure is presented by which the magnitude of the corresponding discontinuities in the variables may be calculated.

The Interaction of a Turbulent Boundary
Layer and a Shock at Hypersonic Mach Numbers. *

by

D. F. Myring **

Introduction

Shock wave - boundary layer interaction has for many years been the subject of extensive investigation. The fundamental interaction mechanism is at the present time thought to be fairly well understood, and for cases in which the boundary layer remains completely laminar, recent theoretical treatments (1,2) have shown good agreement with the general properties of interactions measured experimentally. However, for cases in which the boundary layer is completely turbulent, theoretical treatments have to date met with little success. This is because in a strong adverse pressure gradient conventional boundary layer analysis predicts downstream decreases in the value of the displacement thickness, with a corresponding tendency to induce favourable pressure gradients. Thus under these conditions the only equilibrium solution is a zero induced pressure gradient. This behaviour is termed by Crocco and Lees (3) as supercritical, but is here attributed to the fact that such theories ignore the variation that exists in the static pressure across the boundary layer. In the present approach an attempt is made to take this variation into account and to predict theoretically the characteristics of shock wave - turbulent boundary layer interaction for the region upstream of the separation point. In particular, the conditions at the separation point will be found theoretically and details of the influence of boundary conditions such as Reynolds number, wall temperature, surface curvature, Mach number and initial velocity profile will be presented.

The basic theoretical model taken makes use of the hypothesis that the streamwise pressure gradients are induced by the displacement effect of the boundary layer. This leads immediately to the requirement that the displacement thickness of the boundary layer should be accurately predicted. The most convenient theoretical approach involves the application of the momentum integral equation coupled with an auxiliary equation. To this end a solution is formulated based on the entrainment method of reference (5). The final compressible entrainment equation is then used in conjunction with the boundary layer momentum equation to predict the displacement thickness measured for a variety of supersonic flows over curved surfaces. The agreement with experiment is generally good. Comparisons are not presented herein. The two latter equations are then coupled with an interaction equation and by simultaneous solution the induced pressure gradients and detailed boundary layer properties up to separation are predicted for shock wave interactions. Sample comparisons with experimental measurements are presented in figures 7 to 10.

Theory

In a recent paper (4) it has been shown that for supersonic boundary layers in streamwise pressure gradients large normal pressure gradients may exist within the boundary layer. These normal pressure gradients may be inferred to have a significant influence on the boundary layer development, and the assumption that they are negligible must be discarded. The external flow in a shock wave - turbulent boundary layer interaction may be regarded, at least up to separation, as a simple wave flow generated by a lower boundary. Under these conditions it was concluded in this paper (4) that to a good approximation the isobars may be taken as linear extensions of the external Mach lines which will themselves be linear. Further, it was shown that by defining integral parameters such as momentum and displacement thicknesses as integrals along isobars, the normal

* This work was carried out by the author at Queen Mary College, London.

** Research Fellow at the Royal Aircraft Establishment, Bedford, England.

pressure gradient effects could be simply included in the momentum integral equation. In the following analysis all integral properties are therefore defined as integrals along isobars which are straight and are inclined at the local external Mach angle to the local external streamline direction. The individual equations concerned will now be discussed.

(1) The Momentum Integral Equation

For turbulent boundary layers it is well known that the pressure rise to separation is much larger than that for corresponding laminar boundary layers. If typical experimental pressure rises are taken with the assumption that the pressure gradients are induced by the boundary layer, it is clear that in the case of shock wave interaction the streamlines near the edge of the boundary layer must be inclined at angles of the order of 20° to the wall near separation. In the following equations account is taken of this by resolving all velocities in a direction locally parallel to the wall. Further, the effects of curvature will be introduced by deriving the momentum equation for a flow over a circular arc. The basic flow element is shown in figure (1), bounded by two linear isobars and a section of the circular arc. Angular momentum about the centre of curvature of the arc will be considered, and by using the methods of reference (4) the momentum integral equation becomes

$$\dot{\bar{\theta}} + \bar{\theta} \left[\left(\frac{\bar{\theta}}{\bar{\theta}_0} + 1 \right) (1 + \tan \lambda (M^2 - 1)^{\frac{1}{2}}) - 1.2 M^2 \right] \frac{\dot{M}}{MA} = cf \frac{M}{2 \cos \lambda} - \bar{\theta} \psi \tan \lambda, \quad 1.$$

where dot denotes differentiation with respect to non-dimensional distance along the surface, \bar{x} , and

$$\bar{\theta} = \int_0^{\bar{x}} \frac{\rho u}{\rho_0 u_0} \left(1 - \frac{u}{u_0} \right) d\ell, \quad 2.$$

$$\delta^* = \int_0^{\bar{x}} \left(1 - \frac{\rho u}{\rho_0 u_0} \right) d\ell, \quad 3.$$

where ℓ is distance measured along an isobar.

$$\lambda = \text{angle between a streamline and the wall;} \quad 4.$$

assumed to be independent of ℓ ,

$$A = 1 + 0.2M^2, \quad 5.$$

$$\bar{\theta} = \theta / \theta_0, \quad 6.$$

where θ_0 is the value of θ at the start of the interaction.

$$\psi = \theta / R, \quad 7.$$

where R is the radius of curvature of the surface. Here the assumption has been made that R is much larger than the boundary layer thickness δ . It is interesting to note that now the streamline angle relative to the wall appears on the left hand side of equation (1) and that there is a cross-coupling between surface

curvature and flow angle on the right hand side. The assumption that λ is independent of l and equal to its external value will not be accurate very close to the wall but it is believed that it will give a good overall description of the flow behaviour.

(2) The Entrainment Equation

In compressible flows the shape parameter δ^*/θ is a function of Mach number and wall temperature, so that in order to remove the dependence on these two parameters a normalized shape parameter G will be defined as

$$G = \left[\frac{\delta^*/\theta}{H} \right]_{M, T_w}, \quad 8.$$

where H is the value of δ^*/θ for a one seventh power law velocity profile at the same Mach number and wall temperature. The value of H at any given Mach number and wall temperature may be found by using a one seventh power law velocity profile and the quadratic relationship between temperature and velocity given in reference (9). Calculated values of H are given in figure (3) in terms of Mach number and wall temperature. A further normalized shape parameter G_1 will be defined as

$$G_1 = \left[\frac{(\delta - \delta^*)/\theta}{H_1} \right]_{M, T_w}, \quad 9.$$

where H_1 is the value of $(\delta - \delta^*)/\theta$ for a one seventh power law velocity profile at the same Mach number and wall temperature. Values of H_1 are given in figure (4), and it will be seen that the variation with Mach number and wall temperature is much less than for the parameter H . This is also true for laminar flows for which it may be simply shown that the parameter H_1 is invariant with both Mach number and wall temperature. For zero pressure gradient compressible turbulent boundary layers in which the velocity profiles are close to a one seventh power law, the values of G and G_1 will thus be close to unity. For adverse pressure gradients G should rise above unity and vice-versa. In incompressible flow Head (5) postulates a unique relationship between δ^*/θ and $(\delta - \delta^*)/\theta$, and here the parallel assumption is that there is a unique relationship between G and G_1 independent of Reynolds number, Mach number, wall temperature and pressure gradient. If a power law family of velocity profiles is assumed in incompressible flow then it can easily be shown that

$$G_1 = \frac{2G}{(9G - 7)}, \quad 10.$$

so that this relationship will be assumed to be true at all Mach numbers and wall temperatures. Experimental evidence of this is shown in figure (5) covering a Mach number range from 0 to 6 and various wall temperatures. It should be noted that much more data is available to confirm this hypothesis but this has been omitted for the sake of clarity.

The non-dimensional rate of change of mass flow rate in the boundary layer, F , is given by

$$F = \frac{1}{e, u_1} \frac{d}{dx} \left[e, u_1 (\delta - \delta^*) \sin \beta \right],$$

so that

$$F = \frac{1}{e, u_1} \frac{d}{dx} \left[e, u_1 \theta G, H, \sin \beta \right], \quad 11.$$

where β is the angle between an isobar and a streamline. Now for a flat plate in supersonic flow it can easily be shown that

$$F \propto R_0^{-0.268} (1 + 0.13M^2)^{-0.762} (1 + 0.0975M), \quad 12.$$

so that this dependence on Reynolds number and Mach number will be assumed to be present in pressure gradients as well. Head's hypothesis, in incompressible flow, that the non-dimensional entrainment rate is a function of $(\delta - \delta^*)/\theta$ only is now extended to the general compressible case by assuming that

$$E = F(1 + 0.13M^2)^{0.762} (1 + 0.0975M)^{-1} R_0^{-0.268} \quad 13.$$

is a function of G , only. Experimental evidence of this is shown in figure (6). Here some discrepancy is evident. It is difficult to determine the precise cause of this discrepancy, but a large proportion of the error may be attached to incorrect data reduction. It is clear however that there is no definite Mach number effect since the Mach 6.0 and Mach 3.0 data points lie on opposite sides of the incompressible data points. A mean line will therefore be taken close to the incompressible data points, which may be inferred to be more reliable, giving

$$F = \frac{0.063}{(G_1 - 0.30)} R_0^{-0.268} (1 + 0.13M^2)^{-0.762} (1 + 0.0975M). \quad 14.$$

Equations (10) (11) and (14) then form the basic entrainment equation. From equation (8) the term δ^*/θ in equation (1) may be replaced by $G.H$, and if the pressure gradient is known equations (1) (10) and (11) may be solved simultaneously for θ , δ^* and δ . In order to predict the pressure gradient as well, a further interaction equation is required to describe the interaction mechanism.

(3) The Interaction Equation

The basic hypothesis is that the induced pressure gradients are directly produced by the displacement effect of the boundary layer. Using the results of reference (4) it is clear that the external flow in the actual shock interaction may be identically reproduced by an inviscid flow over the displacement surface. This latter inviscid flow will have the same free stream Mach number as the actual flow and will consist of a simple wave flow and consequently the Mach lines must be straight and isobaric. It is clear therefore that the displacement surface slope at any point must be the same as the external flow angle at a point on the Mach line passing through that particular point on the displacement surface. The elemental model used to derive the interaction equation is shown in figure (2). Here again the displacement thickness δ^* is defined along a linear isobar and after some algebra the interaction equation may be written

$$\frac{\dot{\delta}^*}{\delta^*} - \frac{1.2M}{A} \dot{M} = M \sin \lambda. \quad 15.$$

The other relation needed to complete the equations is a relation for λ , the flow angle relative to the surface. Basically the simple wave flow relationship between flow angle and Mach number will be used with allowance for the fact that the surface is itself a circular arc with a non-dimensional curvature ψ . The final relationship is

$$\dot{\lambda} = - \frac{(M^2 - 1)^{\frac{1}{2}}}{MA} \dot{M} - \psi. \quad 16.$$

(4) Summary of Describing Equations

The equations to be solved may now be brought together and written after some algebra as

$$\dot{\lambda} \begin{bmatrix} 0 \\ 0 \end{bmatrix} + \dot{M} \begin{bmatrix} \theta N_1 \\ \theta N_2 \end{bmatrix} + \dot{\theta} \begin{bmatrix} 1 \\ 0 \end{bmatrix} + \dot{G} \begin{bmatrix} 0 \\ 0 \end{bmatrix} = \frac{cf}{2} \frac{M}{\cos \lambda} - \theta \gamma \tan \lambda, \quad 17.$$

$$\dot{\lambda} \left[0 \right] + \dot{M} \left[G_1 \bar{\theta} \left(\frac{dH_1}{dM} - \frac{1.2MH_1}{A} \right) \right] + \dot{\bar{\theta}} \left[G_1 H_1 \right] + \dot{G} \left[\frac{-14\bar{\theta}H_1}{(9G-7)^2} \right] = MF, \quad 18.$$

$$\dot{\lambda} \left[0 \right] + \dot{M} \left[G \bar{\theta} \left(\frac{dH}{dM} - \frac{1.2MH}{A} \right) \right] + \dot{\bar{\theta}} \left[G H \right] + \dot{G} \left[\bar{\theta} H \right] = M \sin \lambda, \quad 19.$$

$$\dot{\lambda} \left[1 \right] + \dot{M} \left[\frac{(M^2 - 1)^{\frac{1}{2}}}{MA} \right] + \dot{\bar{\theta}} \left[0 \right] + \dot{G} \left[0 \right] = -\psi, \quad 20.$$

where equation (17) is the momentum integral equation in which

$$N_2 = \frac{1}{MA} \left[(GH + 1)(1 + \tan \lambda (M^2 - 1)^{\frac{1}{2}}) - 1.2M^2 \right]. \quad 21.$$

Equation (18) is the auxiliary entrainment equation and equation (19) is the interaction relationship. Equation (20) is the simple wave flow relation for the flow angle λ . Before these equations may be solved an expression for the skin friction coefficient is required. In this case the Ludwig-Tillmann (5) relationship is used expressed in terms of the normalized shape parameter G and the expression is evaluated using the Eckert reference temperature method (7). The final expression is

$$cf = 0.246 \exp(-2.01G) R_e^{-0.268} \left(\frac{T_1}{T_m} \right)^{0.762}, \quad 22.$$

$$\text{where } \frac{T_m}{T_1} = (1 + 0.18M^2)(0.72 + 0.5S_w) + 0.28, \quad 23.$$

$$\text{and } S_w = \left(\frac{T_w}{T_r} - 1 \right), \quad T_r = \text{recovery temperature}. \quad 24.$$

The shape parameter relationship of equation (10) is also required.

Integration Procedure

The present equations have been formulated in such a way that the velocity profiles are not directly coupled to the local pressure gradient, and this leads to many simplifications in the numerical solution of the equations. In particular the problem is not a boundary value problem. Basically the problem is to determine trajectories in terms of streamwise distance for the Mach number M , the shape parameter G and the non-dimensional momentum thickness $\bar{\theta}$. To do this, one point on the trajectory may be chosen at which to specify boundary conditions of Mach number, shape parameter, momentum thickness, Reynolds number, and external flow angle. Also the wall temperature parameter S_w must be taken as being constant but not necessarily equal to zero. These boundary conditions are completely independent of each other, but they must be specified within practical limits. For instance the Mach number must never fall below unity or else the simple wave flow equation will be violated. The Reynolds number should preferably be characteristic of turbulent flow, although lower values will also give solutions.

Having chosen a particular set of boundary conditions, the equations (17), (18), (19) and (20) may be integrated up and downstream within the physical limits of the problem. For instance the practical upstream limit is the virtual leading edge where $\bar{\theta} = 0$, and downstream the equations as specified will not apply for stations downstream of the separation point. The uniqueness of the solution must also be considered. To date, three different modes of behaviour of the equations have been identified. All of these are easily obtainable, depending on the boundary conditions used. Two of these may be obtained by using boundary conditions corresponding to a station on a flat plate. That is, arbitrary Reynolds number, Mach number, non-dimensional momentum thickness and wall heat transfer parameter, but a value of the shape parameter G close to unity and the external flow angle chosen to produce a zero pressure gradient ($M = 0$). If the equations are now integrated upstream then a very weak interaction solution is obtained with the pressure gradient everywhere small and favourable. This solution can be identified

with the interaction effect of an undisturbed boundary layer on a flat plate. For this flow case the displacement surface may be inferred to be convex, giving small favourable pressure gradients. If on the other hand the equations are integrated downstream then again a favourable pressure gradient is obtained but now it is large in magnitude. This solution may in part be identified with the upstream effect of a convex corner flow, but as yet this has not been fully investigated. The third mode may be obtained by choosing the boundary value of the external flow angle such that the pressure gradient is adverse at the boundary. Integration upstream will then produce an interaction which becomes progressively weaker and eventually blends smoothly with the first mode solution at the zero pressure gradient point. Integration downstream produces large adverse pressure gradients leading to separation. This latter solution may be identified with a shock interaction problem and is the solution which will be more fully discussed at a later stage. In practice it is most convenient to take a boundary value of the shape parameter G close to unity and to take a value of the external flow angle of twice the value required to produce a zero pressure gradient. By doing this the zero pressure gradient point occurs at only a very small distance upstream of the boundary point and the values of shape parameter, Mach number, Reynolds number and momentum thickness may be taken as constant over this small distance. It is thus clear that the zero pressure gradient point may be taken as the start of the pressure rise to separation and the boundary conditions fed in will then be virtually identical to the conditions at the start of the pressure rise. This procedure enables the boundary conditions of any given experiment to be easily specified and fed into the calculation procedure.

Effects of Low Wall Temperatures

An interesting feature of the work described in reference (1) is the effect of large wall cooling on laminar shock interaction theory. Singularities were shown to occur for very cold walls, and in the present analysis similar effects are present. The coefficient determinant, D , of the describing equations (17, 18, 19, 20), is given by

$$D = G \left[\frac{(GH + 1)(1 + \tan\lambda(M^2 - 1)^{\frac{1}{2}})(-9G)}{7MA} + \frac{\frac{dH}{dM}}{H} + \frac{\frac{dH}{dM}}{H_1} \frac{(9G - 7)}{7} \right], \quad 25.$$

and the derivatives \dot{M} , \dot{G} , $\dot{\theta}$ and $\dot{\lambda}$ will have infinite values if the condition arises where D is zero. From the work of Lees and Reeves (1) D may be expected to tend to zero as the wall is progressively cooled or as the initial velocity profile becomes fuller (G falling). The latter tendency may be present if the boundary layer experiences large streamwise favourable pressure gradients immediately prior to the shock interaction region. It is therefore of some interest to determine the roots of equation (25) for $D = 0$.

It is convenient to consider the value of D as a 'property' of the undisturbed boundary layer; that is, the boundary layer on a flat plate with no shock interaction present. In these circumstances the value of $\tan\lambda$ may be accurately found using the relation

$$\tan\lambda = GH_1^{\frac{1}{2}}cf, \quad 26.$$

which in terms of conventional parameters is equivalent to putting

$$\tan\lambda = \frac{d\delta^*}{dx}.$$

In the present analysis a universal Reynolds number based on momentum defect thickness will be taken, having a value of 10^4 . Thus the value of D may be calculated for any value of free stream Mach number, wall temperature, and shape parameter G .

In the integration technique previously described the approach made was to feed in a small perturbation in the value of λ at the start of the interaction region and then to integrate the equations up and downstream. Using this method it was found that downstream, large adverse pressure gradients were predicted as long as D was negative. If D was positive at the start then the initial

perturbation in λ was rapidly damped out and the only solution obtainable was a zero induced pressure gradient at all streamwise stations. This type of behaviour with D positive was termed by Crocco and Lees (3) as supercritical. With D negative the behaviour is subcritical and $D = 0$ is the critical point. Thus D behaves as a stability factor in determining the response of the equations to a small perturbation in λ . If D is negative, then a small perturbation in λ results in a rapidly diverging trajectory depicting an unstable system. Positive D leads to a rapid damping out of disturbances in λ corresponding to a stable system.

Investigations show that the critical point of this particular set of equations will occur at low, but nevertheless realistic, wall temperatures. The velocity profile family assumed indicates that in a strong favourable pressure gradient is applied upstream of the shock interaction region, then as u/u_∞ tends to unity, independent of distance normal to the wall, G tends to 0.778. A solution of equation (25) shows that for an adiabatic wall ($S_w = 0$) and a range of Mach numbers from 1.5 to 10, D will be zero only for $G = 0$ or 0.25. It may therefore be concluded that supercritical flow will not occur under any conditions for adiabatic walls. However, for cold wall cases supercritical flow does occur, and its significance must be examined.

If a shock wave is made to impinge on a supercritical boundary layer, one possible solution is that there is no interaction and that the pressure rises discontinuously at the impingement point. This is feasible if D remains positive at all streamwise stations before and after the impingement point. There is however, a strong possibility that downstream of the discontinuous pressure rise the boundary layer will be in a subcritical state and therefore capable of interaction. It is clear that the solution must contain a discontinuity at the start of the interaction and from experience of physical phenomena this discontinuity is likely to be as small as possible. In other words the discontinuity will be just strong enough to make the transition from a supercritical flow ($D > 0$) to the critical point ($D = 0$). Downstream of this an interaction will occur and D will become negative. Examination of equation (25) at and around the critical point condition shows that the transition from a positive to a zero value of D may be accomplished most efficiently, with the smallest rise in pressure, by considering a discontinuity in the flow angle λ . That is to say that near the critical point the value of D is most sensitive to a change in the value of the flow angle λ . There is thus a strong association between this discontinuity and the appearance of a weak oblique shock wave, the strength of which will be determined by the necessary change in flow angle across it. Thus the following picture has emerged. Considering only the region upstream of separation, it has been assumed that the external flow for the adiabatic wall is a simple wave flow generated by the displacement surface. This simple wave flow will be compressive and in the absence of an upper boundary the Mach lines must therefore converge and eventually coalesce to form a shock wave. The point at which the shock wave forms is usually well away from the boundary layer for adiabatic walls and is therefore of no consequence. However, as the wall is cooled, solutions obtained by the present analysis show that the induced adverse pressure gradients increase and it may be easily shown that the shock formation point must move towards the displacement surface and thus towards the boundary layer. As the wall is progressively cooled it may therefore be inferred that a condition arises in which the induced pressure gradients are so large that the shock formation point will be coincident with the edge of the boundary layer at some streamwise station. It is this physical condition which may be associated with the present mathematical condition defined previously as the critical point ($D = 0$). As the wall is cooled further the shock wave enters the boundary layer producing the observed theoretical singularities. For walls which are only slightly cooler than the critical temperature, the discontinuity, in the form of a weak oblique shock wave, will be weak enough to be adequately described by the incremental simple wave flow relationship.

At the singular point ($D = 0$) the derivatives \dot{M} , \dot{G} , $\dot{\theta}$, $\dot{\lambda}$ will all be infinite, but the ratio of any two of these remains finite. All the variables may be inferred to be discontinuous across the weak shock wave, and the respective increments may be calculated by relationships such as

$$\Delta G = \left[\frac{\dot{G}}{\dot{\lambda}} \right]_{\text{mean}} \cdot \Delta \lambda$$

27.

Thus by a process of iteration the mean values of M , G , θ and λ across the discontinuity may be found simultaneously with the respective increments. The increment $\Delta \lambda$ is defined as the difference between the calculated value of λ from

equation (26) and the value required to produce a zero value of D in equation (25). In the calculation of $\Delta\lambda$ mean values of the variables are not required in equations (26) and (25) but rather the local values before and after the discontinuity respectively.

By this method the discontinuities may be calculated leaving only the downstream subcritical region to be determined. One practical method of starting the relevant downstream integration is to calculate the value of λ in the supercritical region from equation (26) and to find the smallest multiple of this which produces a negative value of D . With D negative the equations may then be integrated downstream to separation. By using the smallest possible multiple of the supercritical value of λ the starting point of the integration is close to the singular point so that again the changes in the values of the variables between the integration starting point and the actual beginning of the interaction region may be neglected.

Numerical Results

Using the procedures previously outlined the describing equations (17), (18), (19) and (20) were solved numerically for a range of boundary conditions using a fourth order Runge - Kutta integration scheme. The downstream limit of the integration must be the separation point, so that some separation criterion must be adopted. Clearly the skin friction coefficient as specified will only be zero for infinite conditions in Reynolds number or shape parameter, so in this sense the definition of separation as the point of zero skin friction is inadequate. Other authors have sought correlations based on a fixed value of the shape parameter δ^*/θ at separation. In the present case this is equivalent to a fixed value of the shape parameter G at separation. For incompressible flows where conditions change relatively slowly the value of G at separation may be inferred from experiment to have an average value of approximately 1.5. However in the present case of shock interaction where rapid streamwise increases in pressure are experienced, it seems likely that separation will occur before the value of G is able to rise to 1.5. For a flat plate G is close to unity, so that in incompressible flows in which an initially zero pressure gradient turbulent boundary layer experiences a streamwise pressure rise, it may be concluded that at separation G has increased by approximately 50% above its zero pressure gradient value. For shock interactions a smaller percentage rise may be expected, and for the following results separation has been defined as the point at which G has increased by 30% above its value at the zero pressure gradient point.

Figures (7) to (10) show experimental and theoretical wall pressure distributions for nominal free stream Mach numbers of 3.0, 5.0, 6.0 and 7.0. The appropriate experimental boundary conditions are shown on each figure and these were used in the calculations. It will be seen that the agreement is fair. In many cases it is difficult to accurately locate the zero pressure gradient point from experiment and the comparisons shown are meant only to indicate that the pressure rises and the streamwise scales are of the correct order.

The pressure coefficient at separation based on conditions at the zero pressure gradient point may be found using the declared definition of separation. The theoretical effects of the boundary conditions on the separation pressure coefficient were found to be as follows.

(1) Reynolds number

There have been several experimental investigations to determine this effect, and of these only the results of reference (8) will be used here. Chapman and colleagues publish data in this reference which show quite a good and distinct correlation between the separation pressure coefficient and Reynolds number based on streamwise distance to the power - 1/10. The present theory predicts a corresponding power of - 1/15, which is in fair agreement. It will be seen that in both cases the effect is relatively small, so that in the following results a universal Reynolds number, based on momentum thickness, of 10^4 will be adopted.

(2) Mach number

The effect of Mach number is shown in figure (11), along with some experimental results. It will be seen that the agreement is good, providing strong confirmation of the separation criterion adopted. Clearly the absolute value of the pressure coefficient at separation will depend on the assumed percentage rise in the shape parameter, but in figure (11) the trend with Mach number is confirmed. Generally it will be seen that the theoretical values are a little larger than the experimental ones, but in some cases it may be inferred that the experimental values are too small owing to premature separation caused by the separation indication device.

(3) Wall curvature

Figure (12) shows this effect which clearly increases with Mach number. It will be seen that concave curvature increases the pressure rise at separation and vice-versa. This result is confirmed experimentally for laminar boundary layers in reference (15).

(4) Initial Velocity Profile

In some practical cases the boundary layer approaching a shock interaction region may be subjected to adverse or favourable pressure gradients imposed by surface geometry alone. At the start of the interaction region it is therefore likely that the velocity profile will already be distorted relative to a characteristic zero pressure gradient profile. This effect may be simulated theoretically by using boundary conditions in the shape parameter G which differ from unity. Figure (13) shows the effect on the pressure coefficient at separation caused by a ten percent increase or decrease in the boundary value of G . Again separation is assumed to occur where G has risen by thirty percent above the starting value. It should be noted that if separation is assumed to occur at the point where G has an absolute numerical value of 1.30, then the effects shown in this figure would become larger.

As might be expected, this figure shows that fuller (low G) initial velocity profiles produce a larger pressure rise at separation. It may be argued therefore that any experimental investigation should include measurements of the initial velocity profile which should consequently be used as correlation parameters.

(5) Wall temperature

Figure (14) shows the effect of heat transfer on the pressure coefficient at separation. Again the results are as expected in that cold walls produce a larger pressure rise at separation. This may be associated with local regions of larger density near the wall producing larger values of momentum flux and consequently a greater resistance to the separating pressure forces.

Also shown in this figure is the critical point line which essentially divides the figure into subcritical and supercritical regions. In the latter region it should be noted that the pressure coefficients are referred to the pressure behind the weak shock at the singular point and not to the pressure at upstream infinity. An estimate of the shock strength required to produce a subcritical flow under conditions of low wall temperature is given in figure (15). In this figure $\Delta\lambda$ represents the difference between the flow angle for a zero pressure gradient and that required to produce a zero value of the coefficient determinant D . Clearly where $\Delta\lambda$ is positive an oblique shock wave is required and the upstream flow is supercritical. Where $\Delta\lambda$ is negative the flow is subcritical and an oblique shock wave is not required. Further calculations with different initial values of the shape parameter G show that as G falls and the velocity profiles fill out, the strength of the discontinuity becomes larger if the other conditions are kept constant. This is to be expected since falling values of G imply a tendency towards an inviscid flow profile and thus a discontinuity tending towards that of an inviscid reflection of the incident shock wave. (i.e. the shock wave producing the interaction).

Figure (16) shows the effect of low wall temperatures on the predicted wall pressure distribution up to separation. For $S_w = -0.2$ and -0.4 the upstream conditions are subcritical and the solutions show increasing pressure gradients as the wall is cooled. At $S_w = -0.6$ the upstream conditions become supercritical and for the boundary conditions as shown the initial discontinuity in pressure ratio was calculated to be 10% giving a pressure ratio across the weak initial shock of 1.1. Downstream the pressure continues to rise sharply as shown. For heated walls the pressure gradients induced by the impinging shock wave become smaller and tend towards those typical of laminar interactions. This may be explained by the fact that as the wall is heated the corresponding decreases in density near the wall produce momentum flux profiles tending towards those of an unheated laminar boundary layer.

Concluding Remarks

The theoretical results presented have been shown to compare fairly well with available experimental results. In regions where little or no concise experimental evidence is available the results may be inferred to be feasible on the grounds of simple physical reasoning.

For shock interaction equations expressed in terms of conventional boundary layer theory in which the normal pressure gradient is assumed to be negligible

it is well known that the supercritical condition is reached at Mach numbers around 2.0. By including the variation of static pressure normal to the surface the present theory for adiabatic walls has overcome this difficulty and has provided sensible predictions when compared with experiment. It is believed that this is possibly the most important result, not only for interaction problems but also for non-interacting flows over curved surfaces. In this latter case normal pressure gradients may again be shown to be extremely important and must be accounted for in theoretical treatments.

A simple physical explanation of the appearance of singularities at low wall temperatures has been presented and a method has been outlined by which the magnitude of the singularities may be calculated. The case in which the incident shock wave reflects as for an inviscid flow can be imagined. The sole requirement for this is that the calculated value of D should be everywhere positive. The appropriate physical conditions for this may be deduced if it is assumed that the shock wave associated with the discontinuity forms part of the reflected shock system. If it is also assumed that the reflected system cannot be stronger than the incident shock wave then clearly the discontinuity shock may not be stronger than the incident shock. Thus the condition at which the interaction just disappears may be inferred to be the condition at which the calculated value of $\Delta\lambda$ is just equal to the flow deflection across the incident shock. For cases such as this the discontinuity shock may no longer be regarded as being weak, and the full oblique shock equations must be used to determine the pressure ratio across it. Even so, the discontinuities in the main variables may still be expected to be given fairly adequately by relations such as that of equation (27) if λ is replaced by the Mach number M . This gives

$$\Delta G = \left[\frac{\cdot}{\frac{G}{M}} \right]_{\text{mean}} \Delta M, \quad 28.$$

where ΔM is the change in Mach number across the discontinuity shock wave.

Although in the previous discussion the singularity in the equations has been interpreted as a physical discontinuity, in reality this is unlikely to be the case. If indeed the singularity is a result of a shock wave forming inside the boundary layer, this shock will certainly have some interaction with the subsonic part of the boundary layer close to the wall, and the consequent variable derivatives will be very large but not infinite. Clearly, the order of accuracy of any solution is governed by the order of accuracy of the mathematical model, and in this case the use of an integral boundary layer analysis effectively implies a one-dimensional boundary layer model. Thus any internal interaction must manifest itself as a mathematical singularity in this particular frame of reference. Nevertheless, the procedures outlined may be expected to give a fair overall picture of the phenomena described, although some experimental evidence for cold walls would be extremely desirable.

Notation

A	: temperature ratio = $1+0.2M^2$.
cf	: coefficient of skin friction.
C	: pressure coefficient at separation.
D^{ps}	: coefficient determinant.
E	: entrainment coefficient independent of Mach and Reynolds numbers.
F	: non-dimensional rate of change of mass flow in boundary layer.
G	: normalized shape parameter based on δ''/θ .
G_1	: normalized shape parameter based on $(\delta-\delta'')/\theta$.
H	: value of δ''/θ for a $1/7$ power law velocity profile.
H_1	: value of $(\delta-\delta'')/\theta$ for a $1/7$ power law velocity profile.
l	: distance measured along an isobar.
M	: Mach number.
N_2	: pressure gradient coefficient defined by equation (21).
P^2	: static pressure.
R	: radius of curvature of surface.
Re	: Reynolds number based on momentum thickness.
S	: wall temperature parameter = $(T_w/T_\infty - 1)$.
T_w	: temperature.
u	: velocity in x - direction.
x, y	: usual boundary layer co-ordinates.
β	: local angle between isobar and streamline.
δ	: boundary layer thickness.
δ^*	: boundary layer displacement thickness.

Notation (cont.)

θ : boundary layer momentum thickness.
 λ : local angle between streamline and wall.
 γ : non-dimensional surface curvature = ϕ/R .
 ρ : density

Subscripts

1 : evaluated just outside boundary layer.
 ∞ : evaluated at upstream infinity.
 - : non-dimensional quantity in terms of θ .
 m : evaluated at reference temperature.
 0 : evaluated at start of pressure rise to separation.
 r : evaluated at recovery temperature.
 w : wall conditions.

References

1. Lees, L. & Reeves, B.L. AIAA Journal Vol 2 No.11. 1964.
2. Nielson, J.N. Lynes, L. & Goodwin, F.K. AGARD Con. Proc. No.4. 'Separated Flows' Part 1. 1966.
3. Crocco, W. & Lees, L. J. Aero. Sci. Vol 19. 1952.
4. Myring, D.F. & Young, A.D. British A.R.C.29 142. 1967.
5. Head, M.R. British A.R.C. - R & M 3152. 1960.
6. Ludwig, H. & Tillmann, W. NACA TM 1285. 1949.
7. Eckert, E.R.G. J. Aero. Sci. Vol 22. No.8. 1955.
8. Chapman, D.R. Kuehn, D.M. & Larson, H.K. NACA TN 3869. 1957.
9. Spence, D.A. British A.R.C. - R & M 3191. 1961.
10. Kepler, C.E. & O'Brien, R.L. United Aircraft Corp. ASD - TDR - 62 - 87. 1962.
11. McLafferty, G.H. & Barber, R.E. United Aircraft Corp. R - 1285 - 11. 1957.
12. Sterret, J.R. & Emery, J.C. NASA TN D - 618. 1960.
13. Bogdonoff, S.M. Princeton University Aero Rpt. No. 222.
14. Gadd, G.E. Proc. Roy. Soc. A226. 1954.
15. Greber, I. NASA TN D - 618. 1960.
16. Jones, J. Arnold Engineering. AEDC - TN - 60 - 189. 1960.
17. Schubauer, G.B. & Klebanoff, P. NACA TN 2133. 1950.
18. Newman, B.G. Australian ACA 53. 1951.
19. Childs, M.E. Paynter, G.C. & Redeker, E. AGARD Con. Proc. No.4. 'Separated Flows' Part 1. 1966.
20. Ackeret, J. Feldmann, F. & Rott, N. NACA TM 1113. 1947.

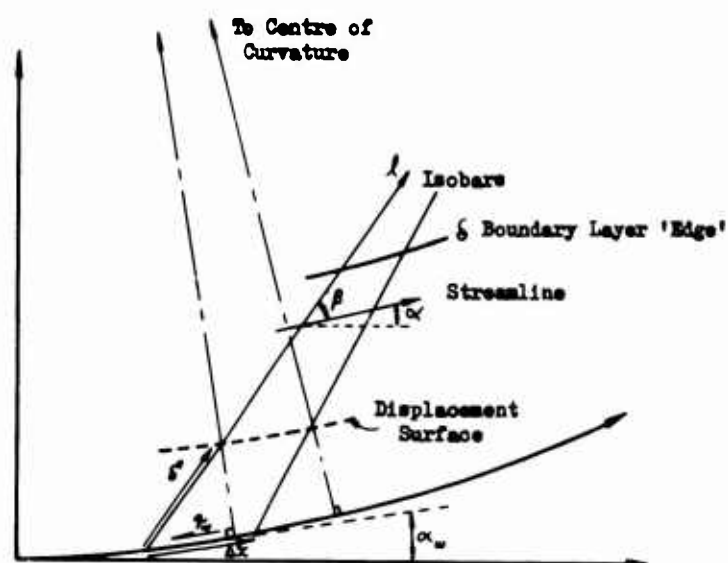


Figure 1. Model Used to Derive the Momentum Integral Equation.

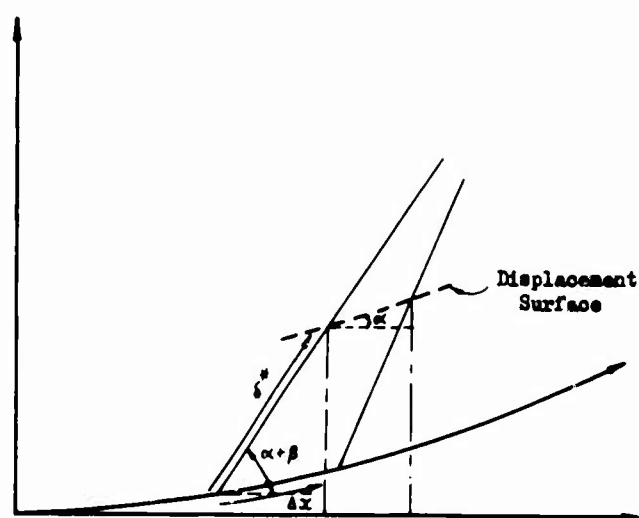


Figure 2. Model Used to Derive the Interaction Equation.

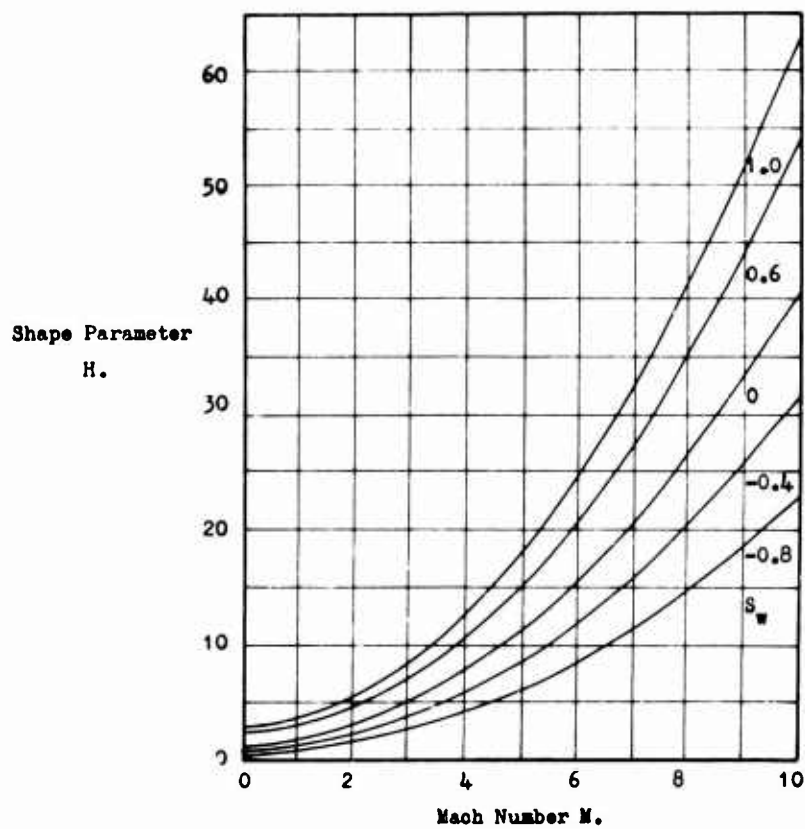
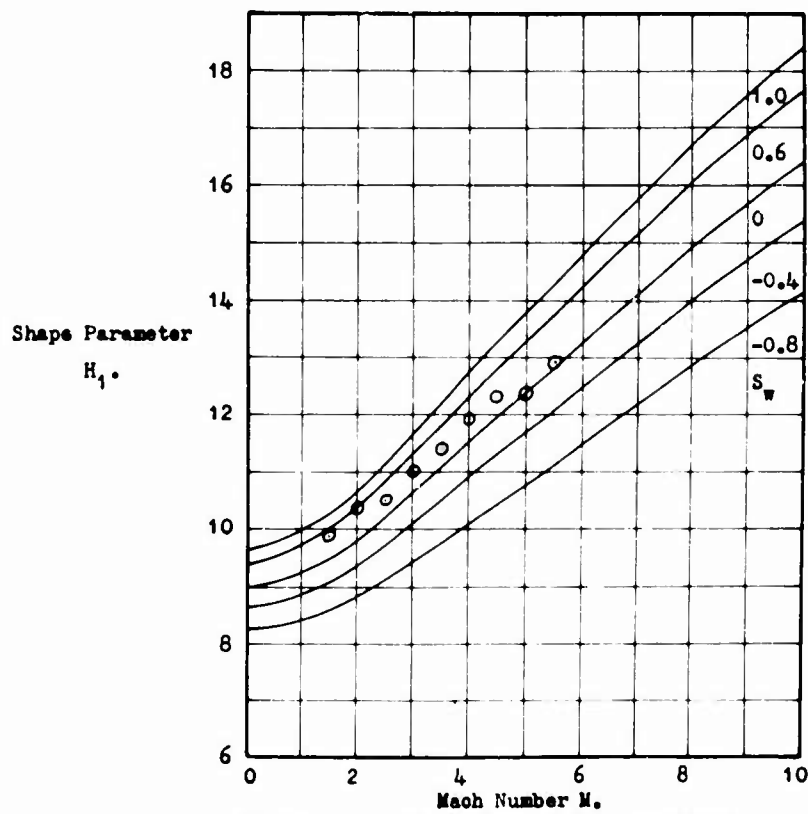


Figure 3. The Effect of Compressibility on the Shape Parameter H .



⊙ Experimental Data:
from ref.16 for
 $S_w=0$, zero pressure
gradient.

Figure 4. The Effect of Compressibility on the Shape Parameter H_1 .

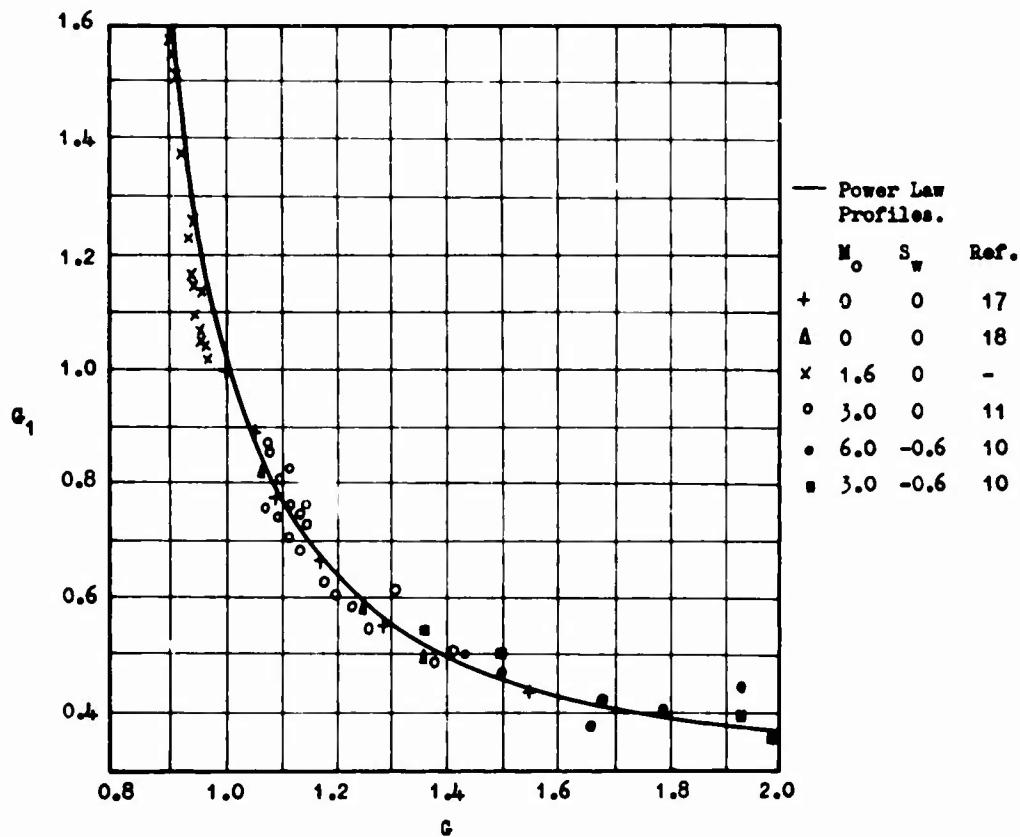


Figure 5. The Relationship between the Shape Parameters G and G_1 .

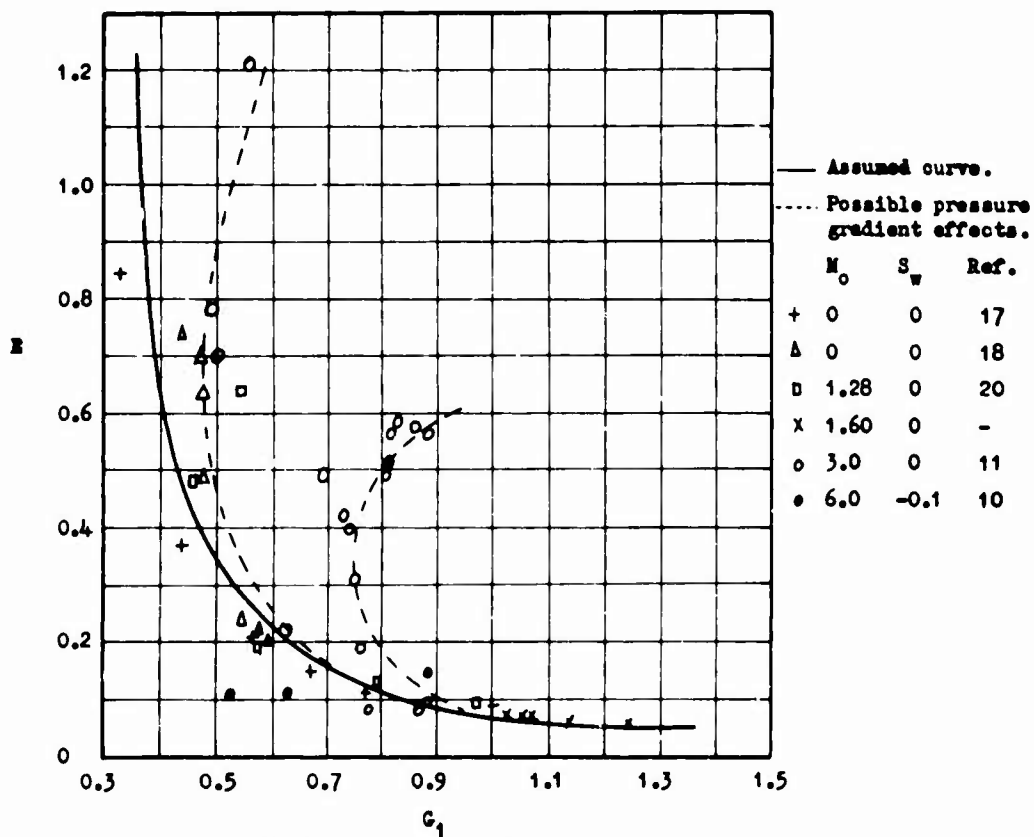


Figure 6. The Entrainment Function E versus the Shape Parameter G_1 .

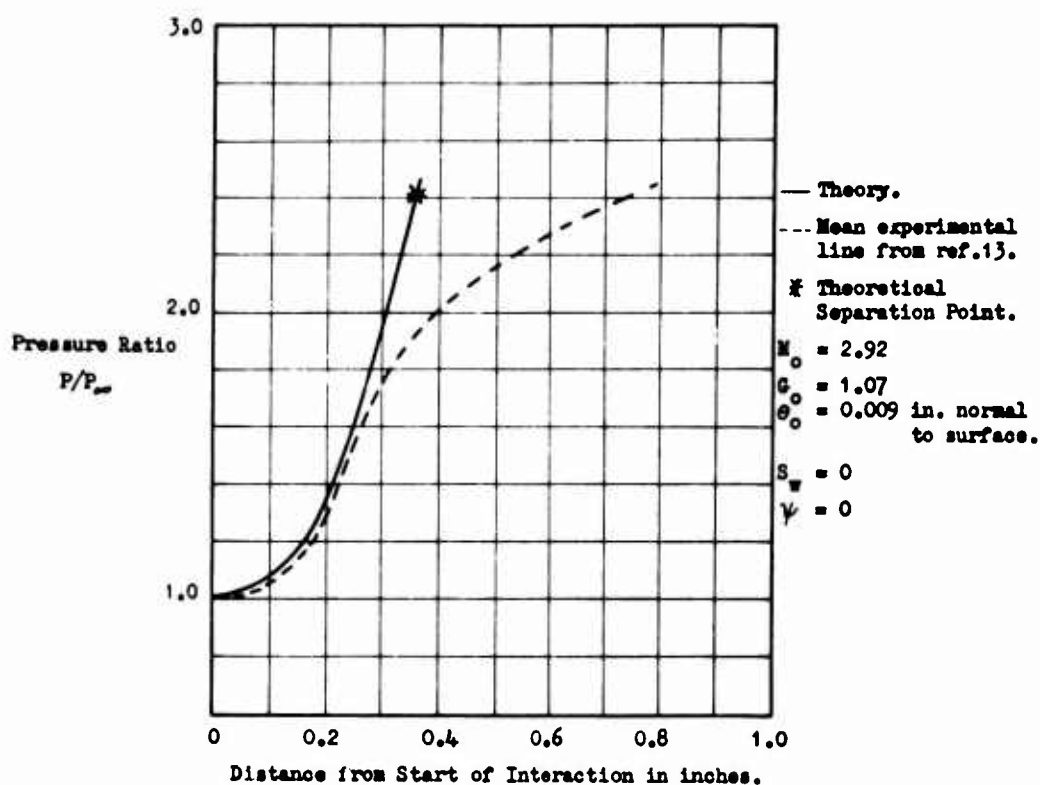


Figure 7. Induced Wall Static Pressure Distribution at Mach 3.0

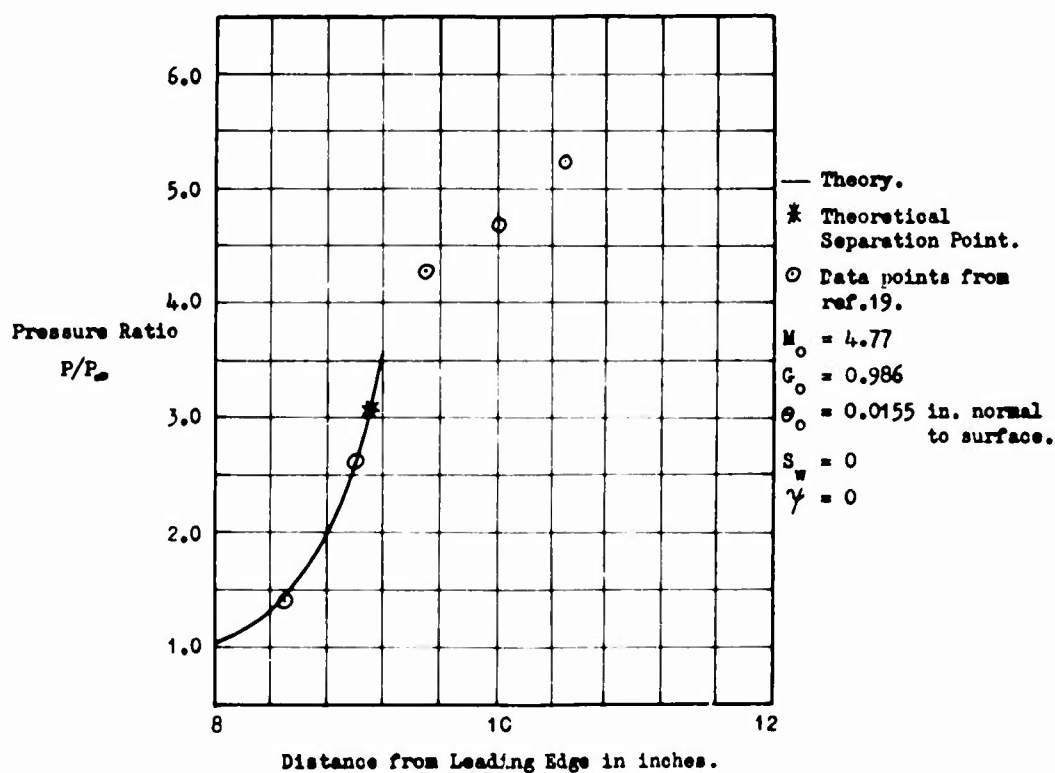
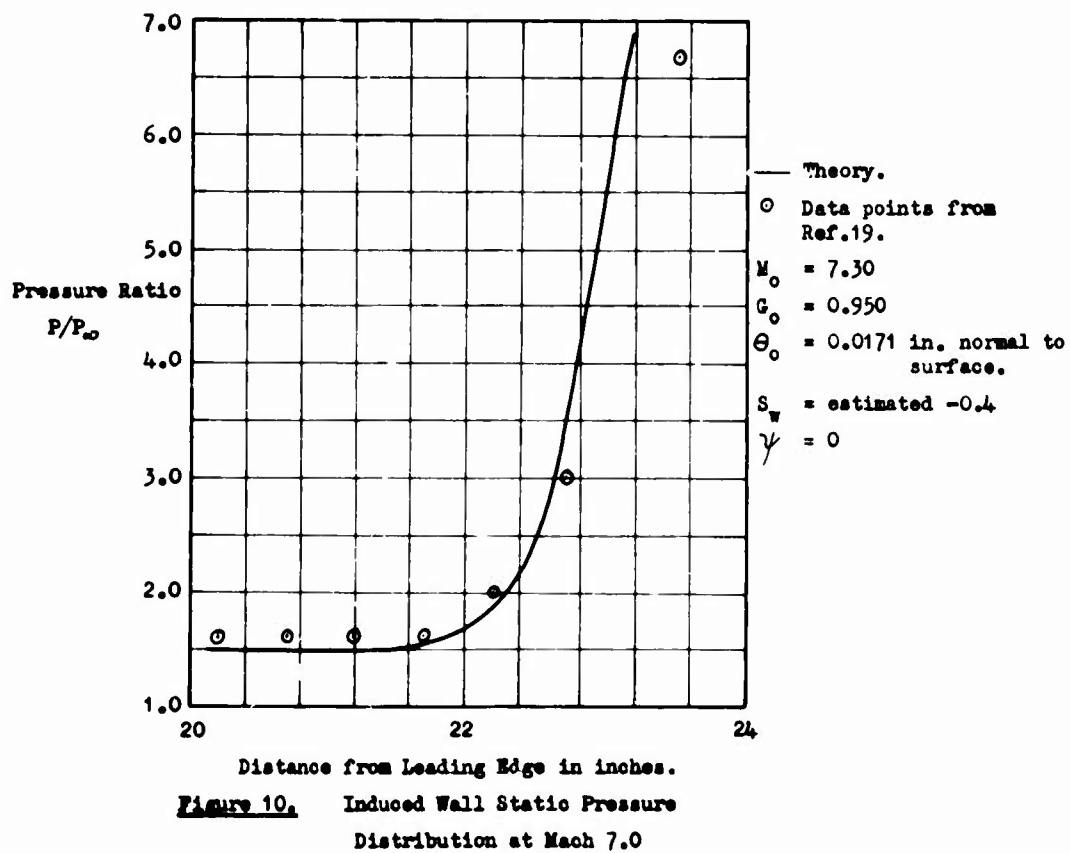
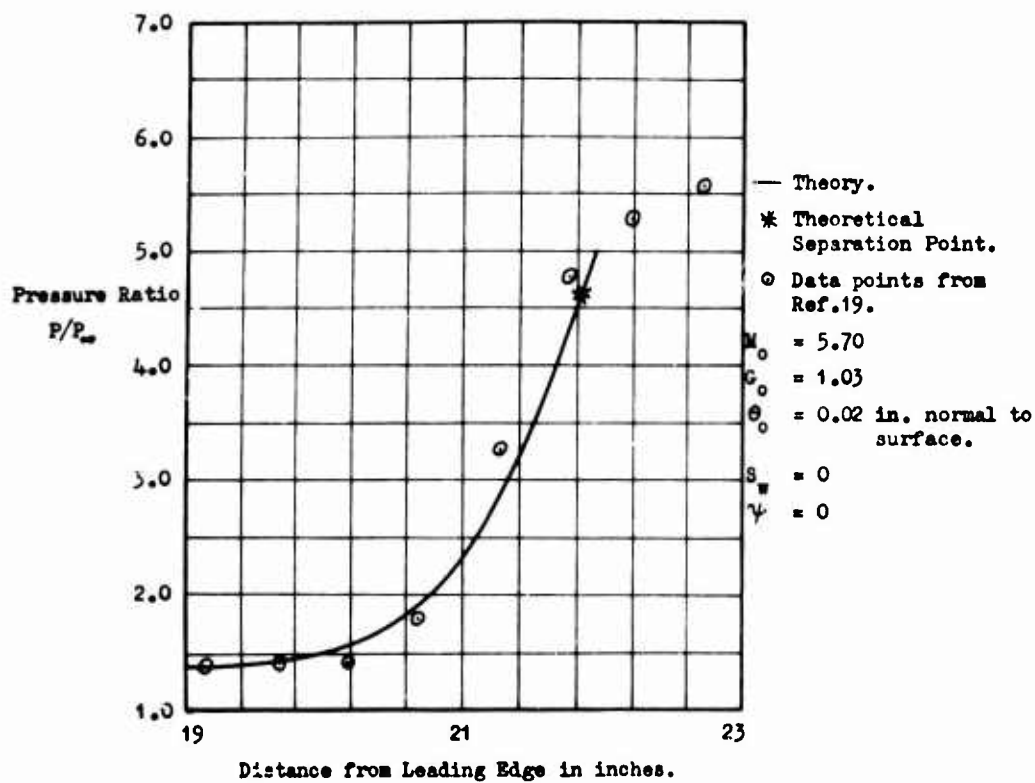


Figure 8. Induced Wall Static Pressure Distribution at Mach 5.0.



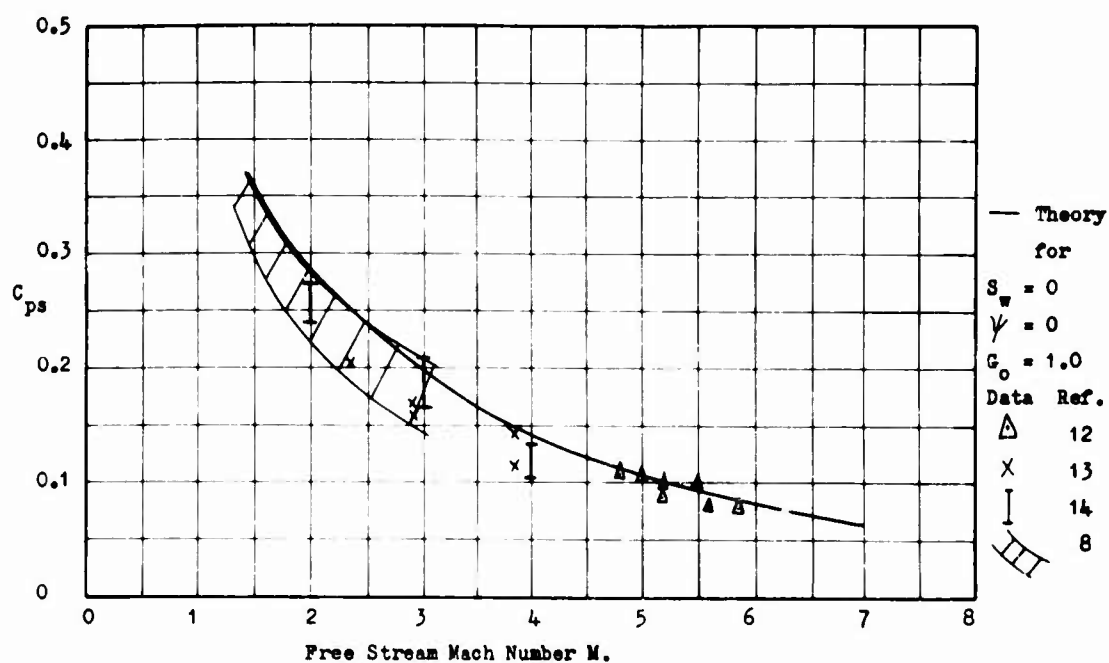


Figure 11.

Correlation between the Experimental Pressure Coefficients at Separation and the Theory.

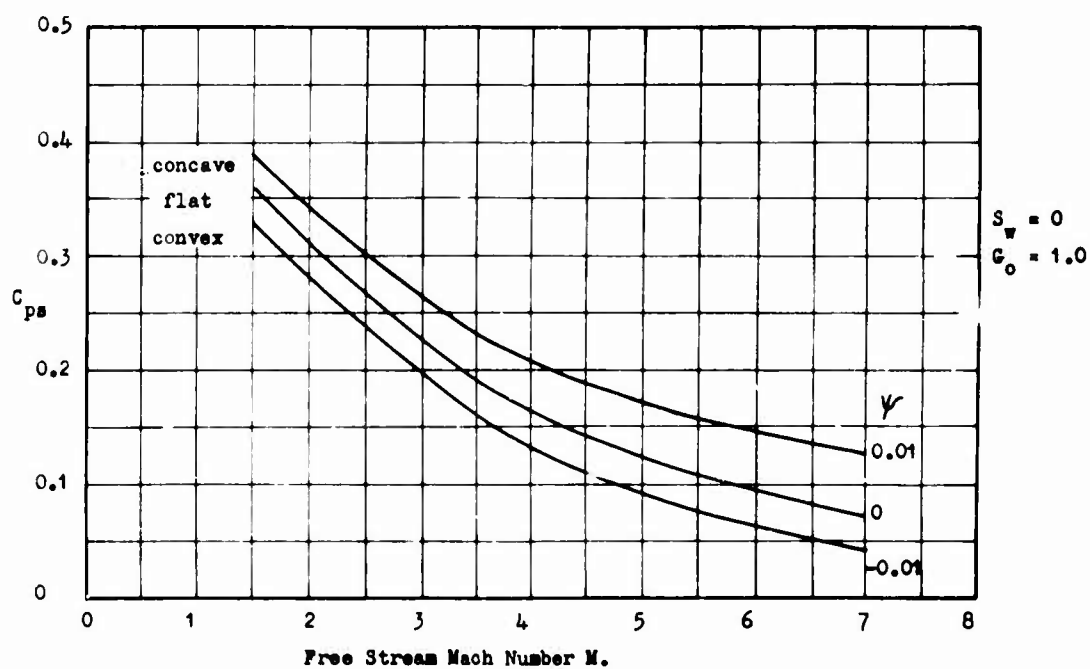


Figure 12.

The Effect of Wall Curvature on the Pressure Coefficient at Separation.

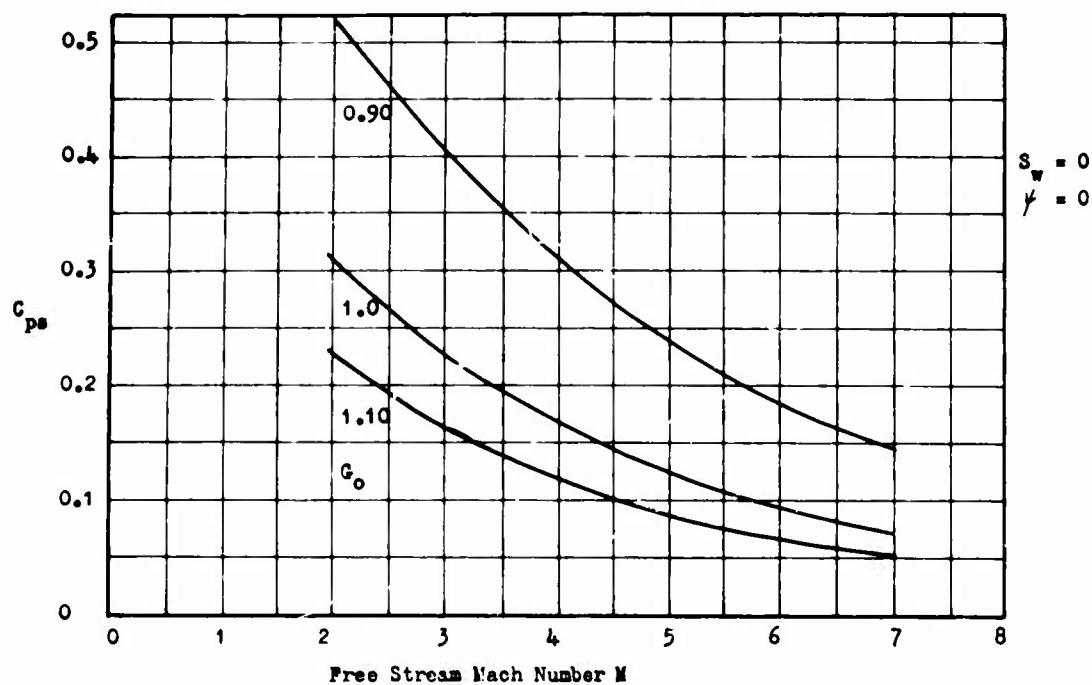


Figure 13. The Effect of the Initial Profile Shape on the Pressure Coefficient at Separation.

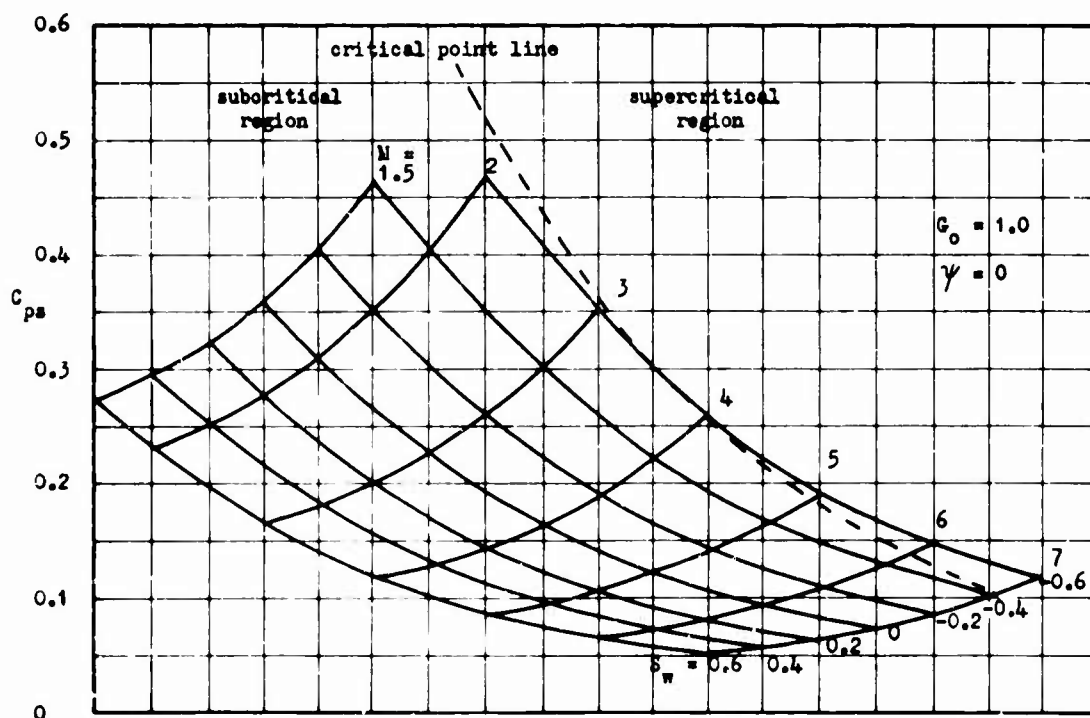


Figure 14. The Effect of Wall Temperature on the Pressure Coefficient at Separation.

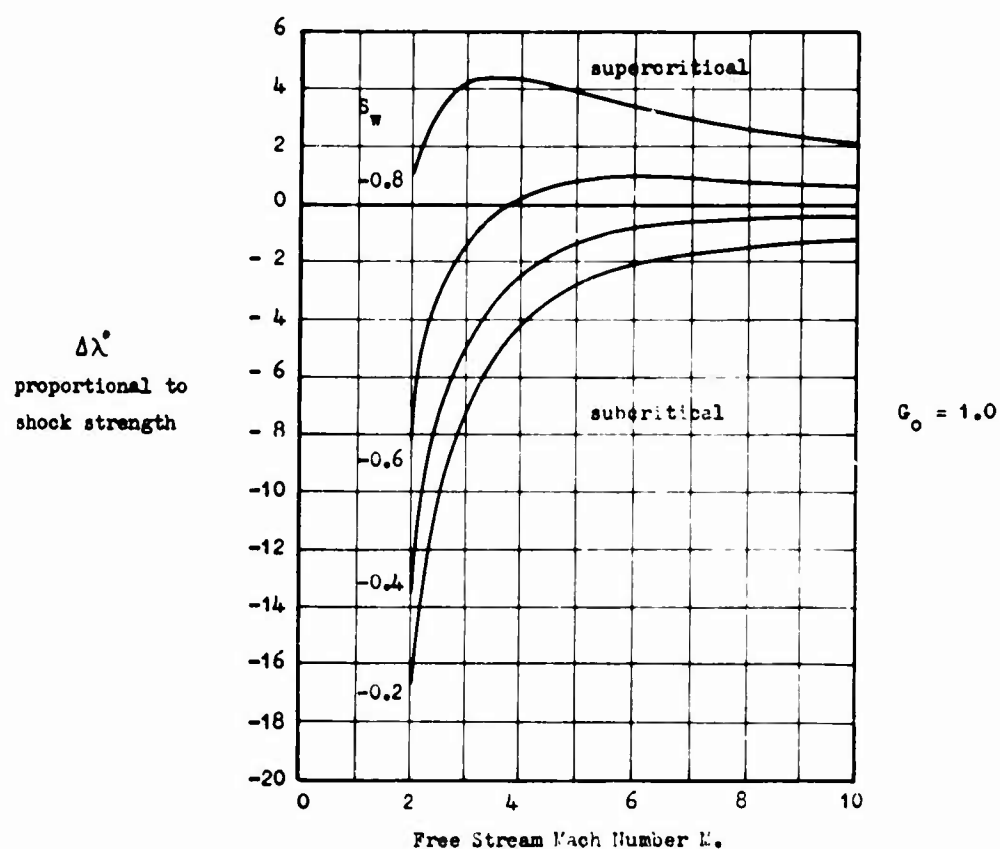


Figure 15. Critical Point Curves.

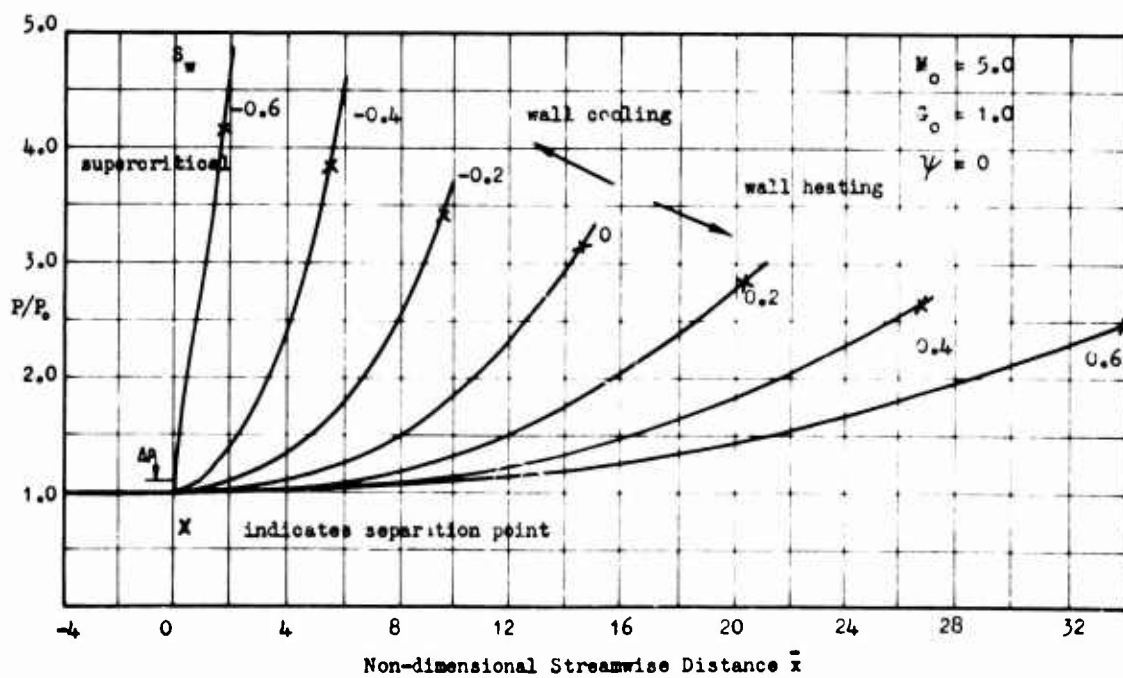


Figure 16.

The Effect of Wall Temperature on the
Wall Static Pressure Distribution at
Mach 5.0

LAMINAR AND TURBULENT FLOW PAST AXISYMMETRIC
CONVEX CORNERS AT HYPERSONIC MACH NUMBERS

Kenell J. Touryan*
Sandia Laboratory, Albuquerque, New Mexico

Thomas J. Tyson**
Dynamic Science, a Division of Marshall
Industries, Monrovia, California

*Supervisor, Reentry Studies Division, Aerothermodynamics Department

**Director, Aerospace Department

SUMMARY

Theoretical and experimental wall pressure distributions on small nose-bluntness ratio cone-cylinder configurations in hypersonic flow are presented. Both laminar and turbulent boundary layers are considered. The expansion over the cone-cylinder shoulder is emphasized. The theoretical computations are comparative studies compiled from various aerospace companies in the U. S. A. including an exact theoretical method for the laminar corner flow developed by one of the authors. The latter is described in some detail. The experiments include hypersonic wind tunnel data and a novel technique using rocket sleds with Mach and Reynolds number ranges of $1.5 \leq M \leq 7$ and $3 \times 10^5 \leq Re/ft \leq 42 \times 10^5$, respectively. A special emphasis is placed on obtaining experimental data with repeatability of better than 5 percent. The measured data are compared with the theoretical calculations and the various discrepancies are analyzed.

INTRODUCTION

The Sandia Laboratory recently evaluated the state-of-the-art for calculating pressure distributions on small nose-bluntness ratio cone-cylinder configurations in hypersonic flow. Both laminar and turbulent boundary layer flows were considered. The expansion over the cone-cylinder shoulder was emphasized and a special effort was made to determine the accuracy with which pressures could be predicted downstream of the corner.

Several aerospace companies participated in calculating the pressure distribution on the cone-cylinder configurations, first using inviscid, ideal gas assumptions, and subsequently including viscous and real gas effects. Because of an unexpectedly large discrepancy among these various calculations it was decided to conduct a set of experimental tests to aid in the selection of the best analytical approach. The experiments included rocket sled tests conducted at Holloman Air Force Base and Naval Ordnance Test Section, and hypersonic wind tunnel tests at the U. S. Naval Ordnance Laboratory. The particular choice of these test facilities was governed by the Mach and Reynolds number requirements described below.

In this paper, the various analytic techniques used are discussed briefly, followed by a description of the experimental apparatus and measurements. The results are then compared, discrepancies are analyzed and an exact theoretical method recently developed by one of the authors is described in some detail.

OUTLINE OF THEORETICAL CALCULATIONS

Table I summarizes the important features in each computation method used by the various aerospace companies (References 1 - 7). These were divided into inviscid and viscous calculations. All inviscid calculations were done both for real gas and perfect gas flow conditions. Because of the very small nose-bluntness in the models under study, there exists a very thin layer close to the corner where large entropy gradients are present. This layer constitutes 5-10 percent of the shock layer thickness and its effect on the corner expansion generated some unexpected computational difficulties which could be traced to the selection of mesh size upstream of the corner.

The viscous calculations included both laminar and turbulent boundary layers. For the latter, it was assumed that transition occurred at $Re = 50,000$, using free stream conditions and the boundary layer displacement thickness. The flow conditions on the conical section, ahead of the corner, were calculated by using either a pseudosurface displacement iteration technique or a simultaneous matching technique of viscous-inviscid boundary conditions. The procedure here was to match conditions at the boundary layer edge to both method of characteristics and boundary layer calculations.

The corner flow calculations were done using three different methods. The first was similar to the method used by Zakkay, Tobak and Kuo (Reference 7). In this technique the velocity and stagnation enthalpy profiles are expanded isentropically around the corner, which is assumed to be sharp ($r=0$) and a new laminar boundary layer is started on the cylinder. The second method adds the extra feature of a finite radius corner to the above method, whereas the third is an exact finite difference solution, restricted to laminar boundary layers only. This method was developed recently by Tyson (Reference 8). The governing equations used in the solution include the transverse (or normal) momentum equation with its attendant pressure gradient. All transverse and longitudinal curvature terms are retained in the equations with the single assumption that the viscous layer is thin and aligned with the surface coordinate. This implies dropping Stokes-like viscous terms which involve $\frac{\partial^2 u}{\partial x^2}$ and $\frac{\partial^2 v}{\partial x^2}$. The reduced equations are solved numerically using a fully implicit finite difference scheme. (See Appendix for reduced equations)

EXPERIMENTS

Two types of experiments were conducted. The first consisted of cone-cylinder models mounted on single-rail high speed rocket sleds at the Holloman Air Force Base 35,000 ft track in Alamogordo, New Mexico, the U. S. Naval Ordnance Test Station 21,500 ft track in China Lake, California, and the Sandia Laboratory 5000 ft track in Albuquerque, New Mexico.

The desirable features inherent in a rocket sled system are: the accuracy with which test conditions can be determined (pressure, temperature, velocity); the possibility of obtaining continuous data over a wide velocity range, and high Mach number and Reynolds number combinations at constant altitudes. Peak values recorded in these tests were $M = 6.6$, $Re = 40 \times 10^6/\text{ft}$.

Details of the sled design, instrumentation, and measurement techniques are given in Reference 9 and will be discussed here only briefly. The models were 1.5 inch base diameter cone-cylinders and cone-cones with nose-to-base radius ratio of 8%. The fore-cone angles varied from 5° to 25° and the aft-cones from 0° (cylinder) to $+2^\circ$ (biconic shape) and -2° (reverse cone). Twenty-four equally spaced holes of 0.063 inch diameter were drilled at four axial stations ranging from 0.2 to 2 cylinder radii aft of the shoulder. The pressures were measured by unbonded strain gauge pressure transducers. The output of each transducer was amplified and telemetered on standard FM-FM channels. The telemetry system contributed the largest single error to the measured model pressure, p . This was equal to or less than $\pm 1\%$. There was no measurable lag time because of the relatively large pressure port size. In fact, the ratio of port size d to displacement thickness δ^* was in the range $5 \leq d/\delta^* \leq 20$. Error estimates based on the experimental work of Pugh (Reference 10) indicate that the maximum expected error in p/p_∞ for this d/δ^* range is ± 2 percent.

The sled speeds were measured by three independent means with an overall accuracy of ± 30 ft/sec. These included image motion (smear) photographs; integration of on-board accelerometer data, and a track side velocity measuring system developed at the Sandia Laboratory. Figure 1 is the photograph of a typical rocket sled shot taken by an image motion camera at 5620 ft/sec (length-dimensions distorted by camera position and image motion rate).

The second set of tests were conducted in Hypersonic Tunnel No. 8 at the Naval Ordnance Laboratory, Silver Springs, Maryland. The Reynolds number ranged from 3 to 30 million/ft at Mach numbers of 5, 6 and 7. The stainless steel models used in the wind tunnel tests were identical to those used on the sleds. In the wind tunnel, five pitot probes and four cone-cylinder models were mounted on a cruciform sting and tested simultaneously. Each of the probe and model pressures was recorded using three separate transducers, calibrated with a dead-weight tester before and after each run. Static pressures, p_∞ , were determined from the pitot probe data assuming isentropic flow. The pressure ratio p/p_∞ was then calculated by computer averaging several hundred data points.

A high speed free-flight rocket test of the 25° cone-cylinder configuration was also conducted at the Sandia Laboratory Tonopah Test Range in Nevada. The rocket was a two-stage Nike-Tomahawk system. The Tomahawk was ignited at the descent stage imparting a burnout velocity of 7400 ft/sec ($M = 6.5$) at 10,000 ft MSL.

RESULTS AND DISCUSSION

When the various inviscid and viscous calculations are compared in the vicinity of the expansion corner, a significant discrepancy is observed among the various techniques used (see Figures 2 and 3). In fact, this discrepancy is a factor of two higher in the corner region than over the cone surface.

Inviscid Flow. As discussed above, the primary cause of this variation in the inviscid solution is believed to be the very thin layer ahead of the shoulder where the streamlines have gone through the curved portion of the bow shock wave. Because of practical limitations on mesh size, etc., variations in the thickness of this layer, with entropy gradients normal to the streamlines, as well as variations in the method of including it in the inviscid corner expansion calculation could account for the observed differences. For example, Figure 4a shows the magnitude of error introduced in p/p_∞ as a result of mesh size selection just ahead of the corner. These errors increase sharply for number of starting points less than 50. Figure 4b, on the other hand, depicts two typical entropy profiles just ahead of the corner for two Mach numbers and shows the effect it has on the pressure gradient immediately past the corner.

Figures 2 and 3 show results based on real gas calculations. Similar studies were done using ideal gas calculations, e. g. Figure 4. Because of relatively low Mach numbers $4 \leq M \leq 8$ and high pressures, the amount of chemical dissociation was low and the flow over the entire body was in chemical equilibrium. In all cases, ideal gas calculations predict a lower pressure past the corner than real gas calculations. Since the boundary layer displacement thickness is roughly proportional to $1/\sqrt{p}$ the boundary calculations utilizing the ideal gas inviscid

solutions will yield a larger displacement thickness which will tend to increase the pressure past the corner. Thus, there is a self-compensation between inviscid and viscous calculations which, when coupled with high pressures and relatively low Mach numbers, made further inclusion of real gas effects unnecessary.

Finally, for the inviscid flow calculations, changing the corner radius from 0 to 0.20 inches amounted to an increase in p_{\min}/p_{∞} of two percent. This change is less for lower Mach numbers.

Viscous Flow. Discrepancies among the various viscous calculations, both laminar and turbulent, are of the same order as the inviscid calculations. Results in Figure 3 indicate that Northrop predictions compare most favorably with experiments in spite of the fact that Lockheed used an intuitively more correct simultaneous matching technique for the flow over the hemisphere-cone portion followed by a corner expansion technique first used by Zakkay et al. (Reference 7). In the Northrop calculations, the flow over the hemisphere-cone incorporates a pseudo-surface displacement iteration technique with locally similar laminar boundary layers and Rose-Probstein-Adams type turbulent boundary layer computations. These computations were stopped just ahead of the corner and re-started on the cylindrical afterbody after carrying out an inviscid expansion over the corner. The displacement thickness on the cone was then faired with the displacement thickness on the cylinder. A numerical technique similar to the Lockheed mass flux matching calculations was also used at the Sandia Laboratory. The axial pressure gradient was approximated by an average pressure parameter defined by: $\bar{p} = \frac{1}{\pi} \int_0^{\pi} p(s) ds$ (where s = distance along body surface), with results that were comparable to those of Lockheed up to the corner. The technique, however, is not suitable for steep pressure gradients as those encountered over corners.

The corner flow was therefore handled using an exact method developed by Tyson. Figure 5 is a schematic of the corner expansion indicating the character of the various flow regions and the stream line and Mach line patterns used in the computation. It is important to note here the various flow regions and the strong interaction between viscous and inviscid flows. In fact, "reflected" waves are generated within the boundary layer due to the Mach number gradient and these waves are propagated downstream. Furthermore, a downstream influence is propagated upstream through the subsonic part of the boundary layer.*

The equations were written in axisymmetric orthogonal surface coordinates and derived under the single assumption that the viscous layer is thin and aligned with the surface coordinate. All transverse and longitudinal curvature terms are retained so the system reduces to the correct polar coordinate formulation at a sharp corner. After writing the equations in curvilinear coordinates and making the "thin viscous layer" assumptions, the coordinate transformation $(x, y) \rightarrow x, \eta = F(y/x^n)$ was introduced to facilitate the numerical treatment (F is an arbitrary analytic function). The transformation allows one to conveniently vary the mesh spacing in the lateral direction depending on the problem at hand.

Experimental and theoretical data for laminar flow over a 9° and a 12.5° corner are shown in Figures 6 and 7. The experimental data were obtained in the NOL Hypersonic Tunnel. The solid curves are the Northrop solutions with simple isentropic expansion and δ^* fairing upstream and downstream of the corner. The dashed curves correspond to the exact corner flow analysis of Tyson, which was based on inputs upstream of the corner using Northrop data. Figure 8 is another interesting plot comparing the 9° cone-cylinder data with the experimental correlation of Victoria (Reference 11), obtained from 10° cone-cylinder and 5° wedge-flat plate

data. The correlation was of the form: $\frac{P - P_{ic}}{P_{ic} - P_{\infty}^{inv}} = P \left(\frac{x - x_c}{\delta^* c} \right)$ where P_{∞}^{inv} is the inviscid pressure for an infinite cylinder at downstream conditions, P_{ic} is the weak interaction pressure for an infinite wedge (or cone) calculated at the corner, P_{inv} is the local inviscid pressure,

*Two more papers have recently come to the authors' attention that deal with expansion corners. The first is by I. I. Glass (Reference 12) and it treats the dissociated-ionized gas flows in two-dimensional corners with an approximate technique used for laminar and turbulent flows, along lines of classical boundary layer theory. The second is by Braylovskaya (Reference 13) and is almost identical to the exact analysis of Tyson, applied to a two-dimensional corner.

δ_c^* is the displacement thickness calculated at the corner and x, x_c are distances from cone tip and corner, respectively. Flow conditions in those tests were $150,000 \leq Re_L \leq 750,000$, and $6.1 < M < 6.8$. A correlation of this type appears quite promising for approximate expanding flow studies.

No "exact" method analogous to the laminar flow of Tyson exists at present for turbulent corner flows. Figures 3 and 9 compare turbulent boundary layer calculations (turbulent flow immediately upstream of the corner) with wind tunnel and sled data. In Figure 9, the differences between the two sets of measurements immediately downstream of the corner can be attributed to differences in T_w/T_o . For wind tunnel models $T_w/T_o = 0.64$ and for sled models T_w/T_o , on the average, was about 0.3 (actually it varied between 0.2 and 0.4 in any given run). This implies thicker boundary layers over the wind tunnel models, and consequently, higher pressures immediately past the corner. In addition, it is not certain that boundary layers were turbulent on the sled models at $M = 5$. This was especially hard to determine because one could not estimate the effect of model vibrations (on the sled runs) on transition.

Figure 10 shows experimental and theoretical plots of p/p_o versus Mach number at 2/3 model diameter behind the corner for corner turning angles of 12.5° , 12° , and 11.5° . The measurements were taken on the rocket sled described above. Dotted lines correspond to inviscid flow calculation with a respective corner angle 0.5° lower than the actual turning angles. The triangles correspond to viscous turbulent computation using the Northrop (Reference 3) approximation, and the actual turning angle. It is interesting to note that a 0.5° increase in afterbody angle (or a 0.5° decrease in turning angle) as used in inviscid hypersonic pressures calculations, has the effect of adding the proper displacement thickness to take into account the pressure increase caused by turbulent boundary layers expanding over convex corners.

CONCLUSIONS

Theoretical and experimental pressure data have been obtained past convex corners on cone-cylinder configurations in laminar and turbulent flows, at hypersonic speeds. The experimental data have been compared to existing analytic techniques that depict the flow past expansion corners using both approximate and exact methods. The latter is limited to laminar boundary layers only. As yet there exists no comparable "exact" method for turbulent boundary layers on convex corners.

However, the analytical method of this paper can be easily extended to accept general eddy diffusivity distributions for turbulent heat and momentum transfers. The quantitative descriptions of such distributions are now felt to be quite well understood for planar incompressible flows (References 14 and 15). The extension to axisymmetric flows should be straightforward. Our ability then to analyze turbulent convex corner flows in detail will rest on the success of current investigations aimed at obtaining the compressible analog of these incompressible eddy diffusivity distributions. In this regard the corner flow problem may well be easier to analyze than more conventional turbulent boundary layer developments. This assertion rests on the fact that the bulk of the boundary layer in the neighborhood of the corner expands in a relatively inviscid manner. That is, the eddy transport terms are comparable to the inertia terms only in a thin sub-layer adjacent to the wall as shown in Figure 5a. Thus the accuracy of the adopted compressible eddy diffusivity model becomes of crucial importance only near the wall. In this new wall domain the compressibility transformation proposed by Coles (Reference 16) and Baronti and Libby (Reference 17) are probably quite adequate. Hence we feel that extension of the analysis of this paper to the turbulent regime will be relatively straightforward. In the meantime, approximate boundary layer fairing techniques if used properly can serve as a first estimate guide in predicting pressure distribution for engineering design purposes.

It has also been demonstrated that in the Mach range $1.5 \leq M \leq 6.6$, p/p_o data from sled tests could be obtained with a repeatability of ± 2 percent. The overall spread in p/p_o data both from wind tunnel and sled tests, including uncertainties introduced by finite transition duration (e. g. Figure 9), were about 8%. The situation is definitely worse for theoretical predictions. The work of Tyson is the most exact with regard to flows over expansive corners; however, it is limited by the accuracy of the upstream inputs, which in turn depend on viscous-inviscid calculations on small-bluntness cones (or wedges).

ACKNOWLEDGMENT

The authors wish to acknowledge Messrs. G. E. Clark and D. J. Rigali of Sandia Laboratory for reducing and compiling the experimental data. Special thanks are due Dr. Irwin Alber of Dynamic Science for his assistance in the corner flow calculations, and to Mr. Andrew Wortman of Northrop Corporation for extensive laminar and turbulent boundary layer computations on various cone-cylinder configurations. This work was supported by the U. S. Atomic Energy Commission.

TABLE 1. SUMMARY OF COMPUTATION METHODS

AGENCY	INVISCID SOLUTION		VISCOUS-INVISCID SOLUTION	CONE-CYLINDER CORNER
	Blunt Body	Afterbody		
General Dynamics ¹ (Fort Worth, Texas)	Real gas, inverse method of Lick ⁶ (modified) and Lomax-Inouye	Real gas, method of characteristics	Laminar δ^* : exact-nonsimilar Turbulent δ^* : modified Reahoko-Tucker. Pseudosurface displacement iteration technique.	Sharp corner-inviscid expansion. Laminar velocity and temperature profiles at corner from nonsimilar program--assumed similar through the corner expansion--average δ^* used at corner. Turbulent δ^* on cone faired with δ^* on cylinder.
Lockheed Missiles ² & Space Company (Huntsville, Ala.)	Perfect gas - real gas, direct method (Dorodnitsyn-Belotserkovskii)	Perfect gas - real gas, method of characteristics	Matching technique for both laminar and turbulent flow to solve Karman momentum-integral equation. Simultaneous matching of viscous-inviscid boundary conditions.	Sharp corner - expansion isentropic along a streamline. No distance travelled by fluid at surface. ⁷
Northrop Corporation ³ Norair Division (Hawthorne, Calif.)	Perfect gas - real gas, inverse method	Perfect gas - real gas, method of characteristics using mass-entropy method	Laminar δ^* : locally similar: Turbulent δ^* : Rose-Probststein-Adams. Pseudosurface displacement iteration technique.	Finite radius - inviscid expansion δ^* on cone faired with δ^* on cylinder.
Sandia Laboratory ⁴	Perfect gas - real gas, inverse method (Lomax-Inouye)	Perfect gas - real gas, method of characteristics	Laminar δ^* : Simultaneous matching of viscous-inviscid boundary conditions.	Exact finite difference solution. ⁹
TRW-Systems ⁵ (Redondo Beach, Calif.)	Equilibrium gas, inverse method	Perfect gas - real gas, method of characteristics	Laminar δ^* : locally similar: Turbulent δ^* : Rose-Probststein-Adams (modified). Pseudosurface displacement iteration technique.	Finite radius. Inviscid expansion with left-running characteristic based on boundary layer properties δ^* zero after expansion.

REFERENCES

1. Benepe, D. B. and Kerr, H. C., "Effects of Viscid-Inviscid Interaction on the Pressure Distribution on Spherically Blunted Cone-Cylinders in Hypersonic Flow," General Dynamics Rep. FZA-409, November 1965.
2. Hamner, R. L., Hoenig, R. J. and Cable, D. F., "Theoretical Hypersonic Pressure Distributions for Blunted 12.5° Cone-Cylinders in Equilibrium Air," Lockheed Missile and Space Company Tech. Rpt. HREC/950B-2, LMSC/HREC A712473, June 1966.
3. Wortman, A. et al., "Pressure Distributions on Blunted 12.5° Cone-Cylinder Configuration at Mach Number 6 and 14," Northrop Corporation, Norair Division, NOR-65-155, July 1965.
4. Hirst, E., "A Description of the NASA-Ames Cone, Blunt Body and Method of Characteristics Flow Field Programs," Sandia Corporation SCL-TM-65-119, February 1966.
5. Vogenitz, F. W., "Final Report on Cone-Cylinder Pressure Distributions," TRW Systems, Rep. No. 4511-6001-R0000, January 1966.
6. Lick, W., "Inviscid Flow Around a Blunt Body of a Reacting Mixture of Gases, Part A. General Analysis," RPI Report TR AE 5810, 1958.
7. Zakkay, V., Toba, K., Kuo, T. J., "Laminar, Transitional, and Turbulent Heat Transfer After a Sharp Convex Corner," AIAA Jour. Vol. 2, No. 8, pp. 1389-1396, August 1964.
8. Tyson, J. Thomas, "Laminar Boundary Layers in the Neighborhood of Abrupt Spatial Disturbances," Ph.D Thesis, GALCIT, Pasadena, California, June 1967.
9. Rigali, D. J. and Feltz, L. V., "The Application of High Speed Monorail Rocket Sleds to Aerodynamic Testing at High Reynolds Numbers," paper presented at AIAA 3rd Aerodynamic Testing Conference, San Francisco, California, April 1968.
10. Pugh, P. G., "A Note on Effect of Hole Size on Measurement of Static Pressures on Models at Supersonic Speeds," Proc. of 23d Supersonic Tunnel Association Conference Vol. 2, May 1965.
11. Victoria, K., Graduate Aeronautical Laboratories, Calif. Inst. of Tech., Private Communication (1968).
12. Glass, I. I., "Research Frontiers at Hypersonic Velocities," Canadian Aeronautics and Space Journal, October 1967, pp. 348-366.
13. Braylovskaya, I. Yu, "Flow of Viscous Gas Along Wall with Discontinuity (in Russian)," Doklady Akademii Nauk SSSR 1967, Tom 176, No. 3, pp. 549-552.
14. Alber, I. E., "Investigations on Nonsimilar Turbulent Boundary Layer Developments," Dynamic Science TR-A-101, 12 Jan. 1968.
15. Mellor, G. L., "Turbulent Boundary Layers with Arbitrary Pressure Gradients and Divergent or Convergent Cross Flows," Gas Dynamics Laboratory, Princeton Univ., Rpt. No. 775, March 1966.

16. Coles, D., "The Turbulent Boundary Layer in a Compressible Flow," Rand Rpt. R-403-PR, September 1962.
17. Baronti, Paolo O. and Libby, Paul A., "Velocity Profiles in Turbulent Compressible Boundary Layers," AIAA Jour., Vol. 4, No. 2, February 1966, pp. 193-202.

APPENDIX: THE "GENERALIZED" LAMINAR
BOUNDARY LAYER EQUATIONS

All quantities below are normalized in the following fashion: r , $(\kappa)^{-1}$, y , and x with respect to an arbitrary length L ; U , V , ρ , T , c_p and μ with their respective undisturbed free stream values; and P with respect to $\rho_\infty U_\infty^2$. κ is the wall curvature; y the normal distance from the surface; and x is coordinate lying along the surface. $j = 0$ for planar flow and $j = 1.0$ in the axisymmetric case. θ is the surface inclination relative to the axis of axisymmetry. Further,

$$Re = \frac{\rho_\infty U_\infty L}{\mu_\infty} \quad \text{and} \quad Pr = \frac{c_{p_\infty} \mu_\infty}{k_\infty}$$

Subscript x and y below refer to partial differentiation.

Continuity

$$\left[(r + y \cos \theta)^j \rho U \right]_x + \left[(1 + \kappa y)(r + y \cos \theta)^j \rho V \right]_y = 0$$

Longitudinal Momentum

$$\begin{aligned} & \left(\frac{1}{1 + \kappa y} \right) \rho U U_x + \rho V U_y + \left(\frac{\kappa}{1 + \kappa y} \right) \rho U V \\ & = - \left(\frac{1}{1 + \kappa y} \right) P_x + \frac{1}{Re} \left\{ \mu (U_y - \frac{\kappa U}{1 + \kappa y}) \right\}_y + \mu \left(\frac{2\kappa}{1 + \kappa y} + \frac{j \cos \theta}{r + y \cos \theta} \right) \left(U_y - \frac{\kappa U}{1 + \kappa y} \right) \end{aligned}$$

Transverse Momentum

$$\left(\frac{1}{1 + \kappa y} \right) \rho U V_x + \rho V V_y - \left(\frac{\kappa}{1 + \kappa y} \right) \rho U^2 = -P_y + \frac{1}{Re} \frac{4}{3} \left[\mu V_y \right]_y$$

Energy

$$\begin{aligned} & \left(\frac{1}{1 + \kappa y} \right) \rho U c_p T_x + \rho V c_p T_y = (\gamma - 1) M_\infty^2 \left\{ \left(\frac{1}{1 + \kappa y} \right) U P_x + V P_y \right\} \\ & + \frac{1}{Re Pr} \left\{ (\mu c_p T_y)_y + \left(\frac{\kappa}{1 + \kappa y} + \frac{j \cos \theta}{r + y \cos \theta} \right) \mu c_p T_y \right\} + \frac{(\gamma - 1) M_\infty^2}{Re} \mu \left(U_y^2 + \frac{4}{3} V_y^2 \right) \end{aligned}$$

State

$$\gamma M_\infty^2 P = \rho T$$

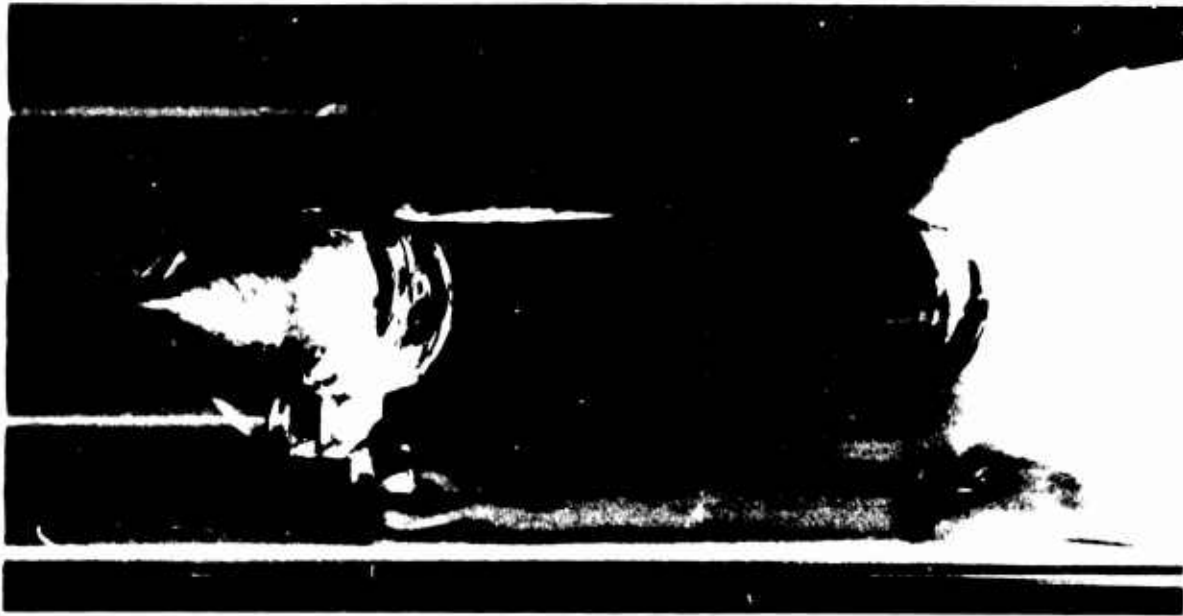


Figure 1 Range Photograph of Rocket Sled with Cone-Cylinder Model. Velocity: 5620 ft/sec, Altitude: 5000 ft above sea level.

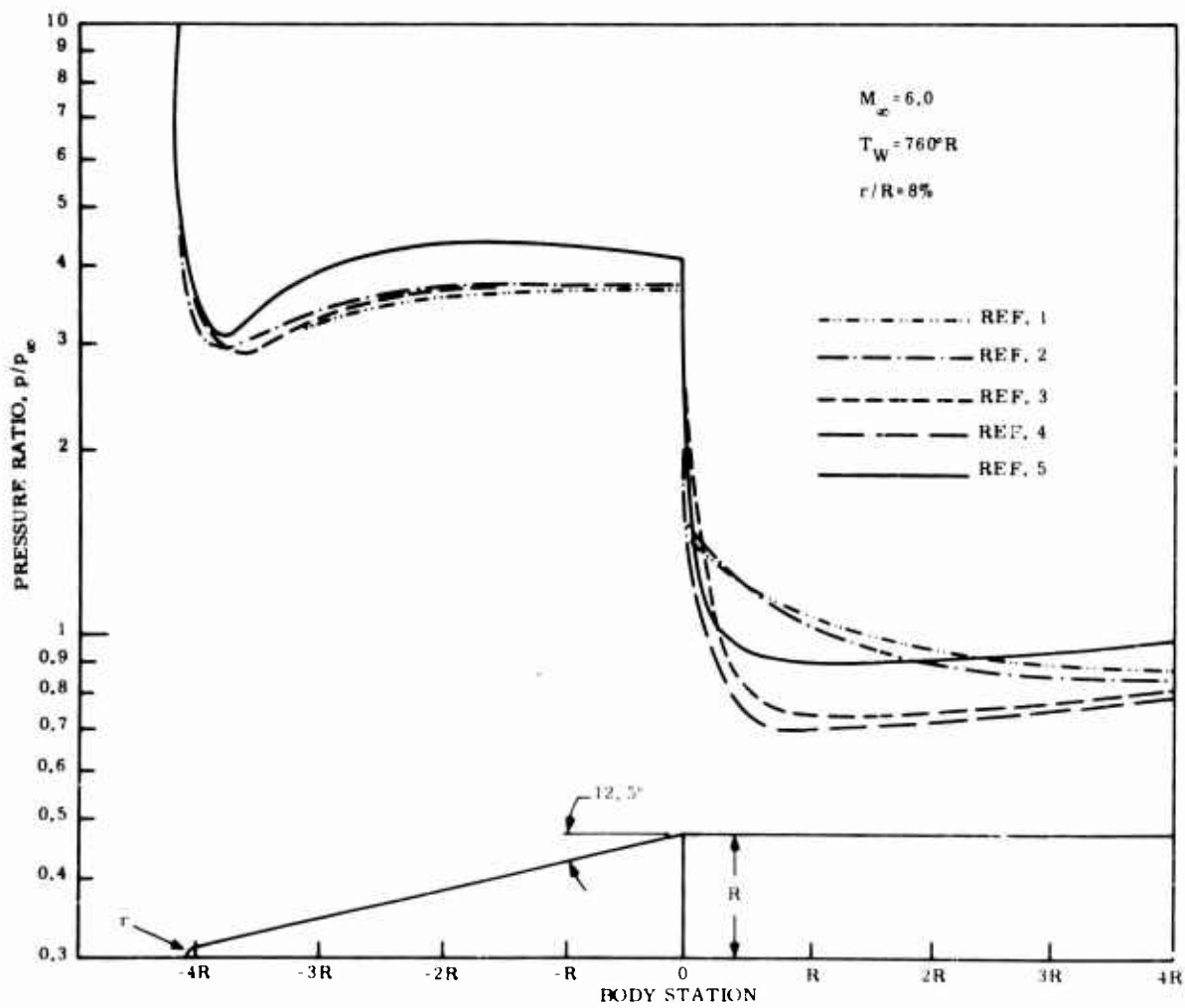


Figure 2 Calculated Inviscid Pressure Distribution Curves on Blunted 12.5° Cone-Cylinder.

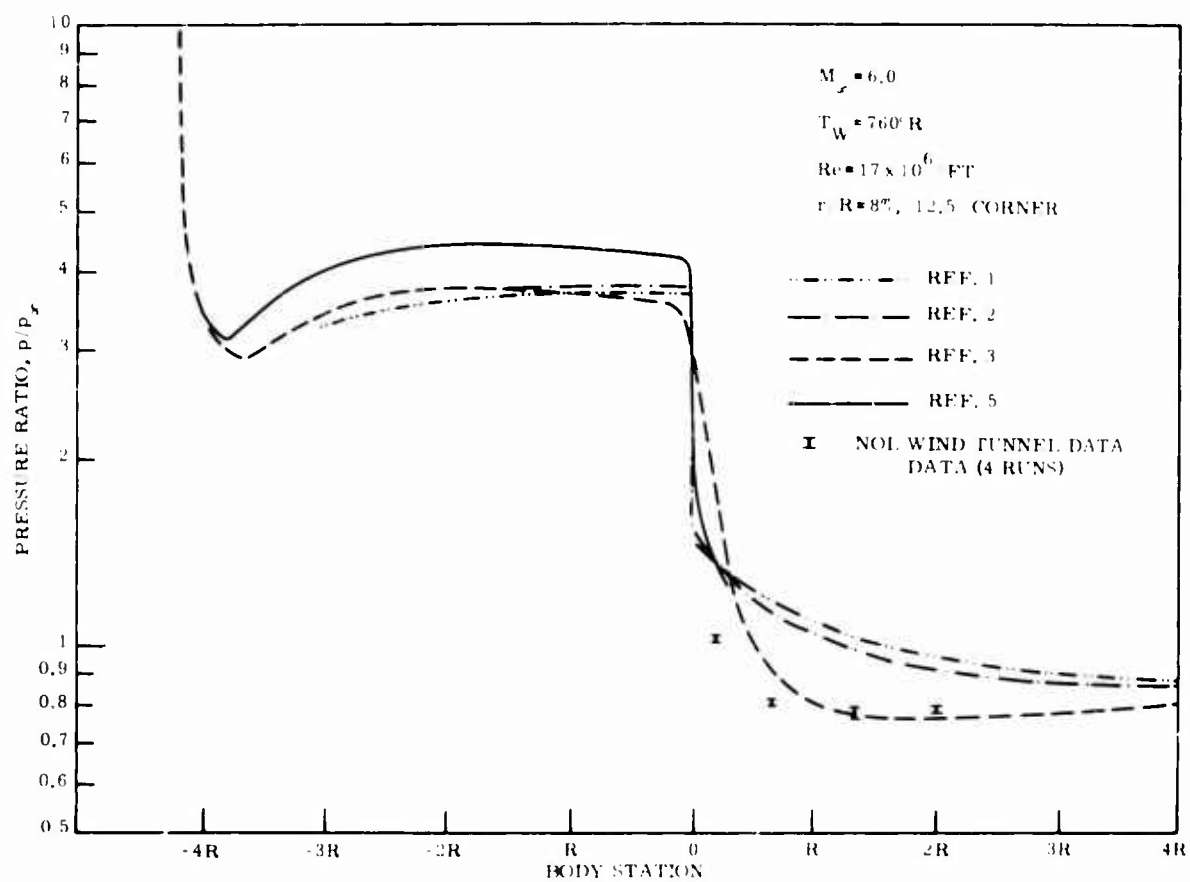


Figure 3 Calculated Viscous, Real Gas Pressure Distributions on Blunted 12.5° Cone-Cylinder Compared with Mach 6 Wind Tunnel Data. Flow Turbulent Upstream of Corner.

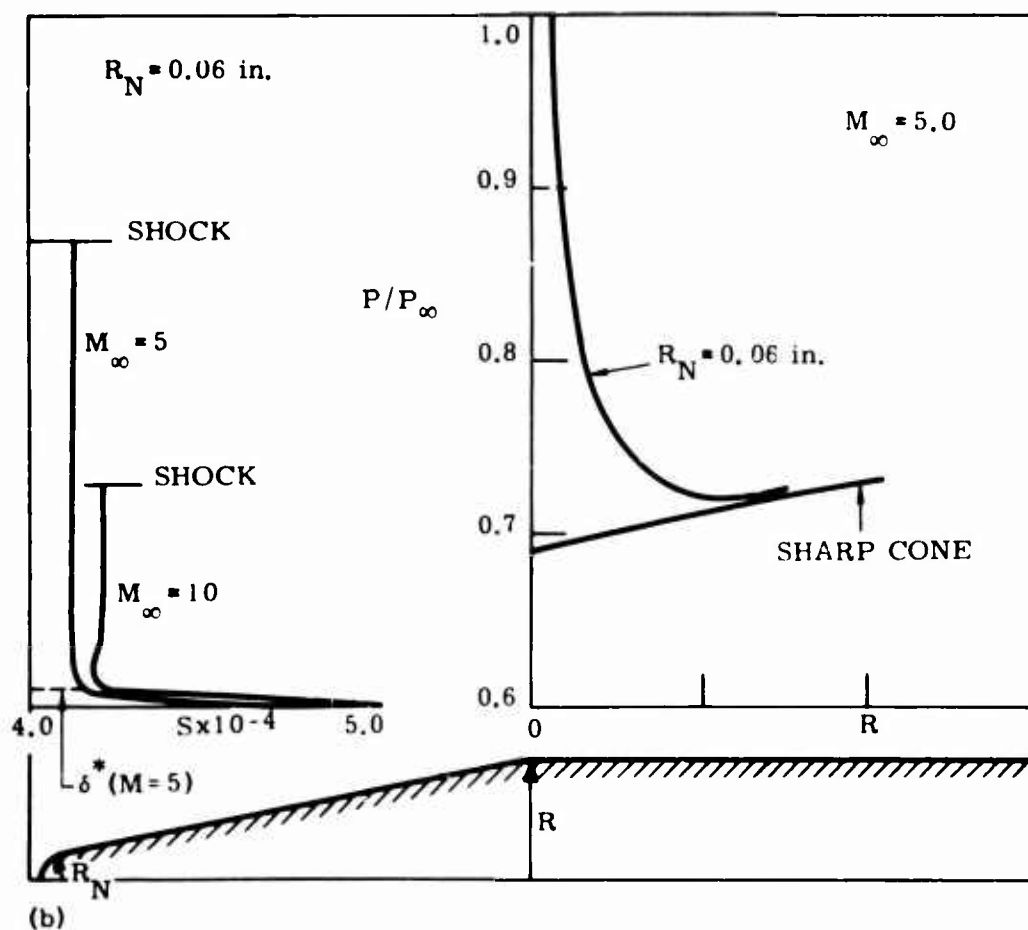
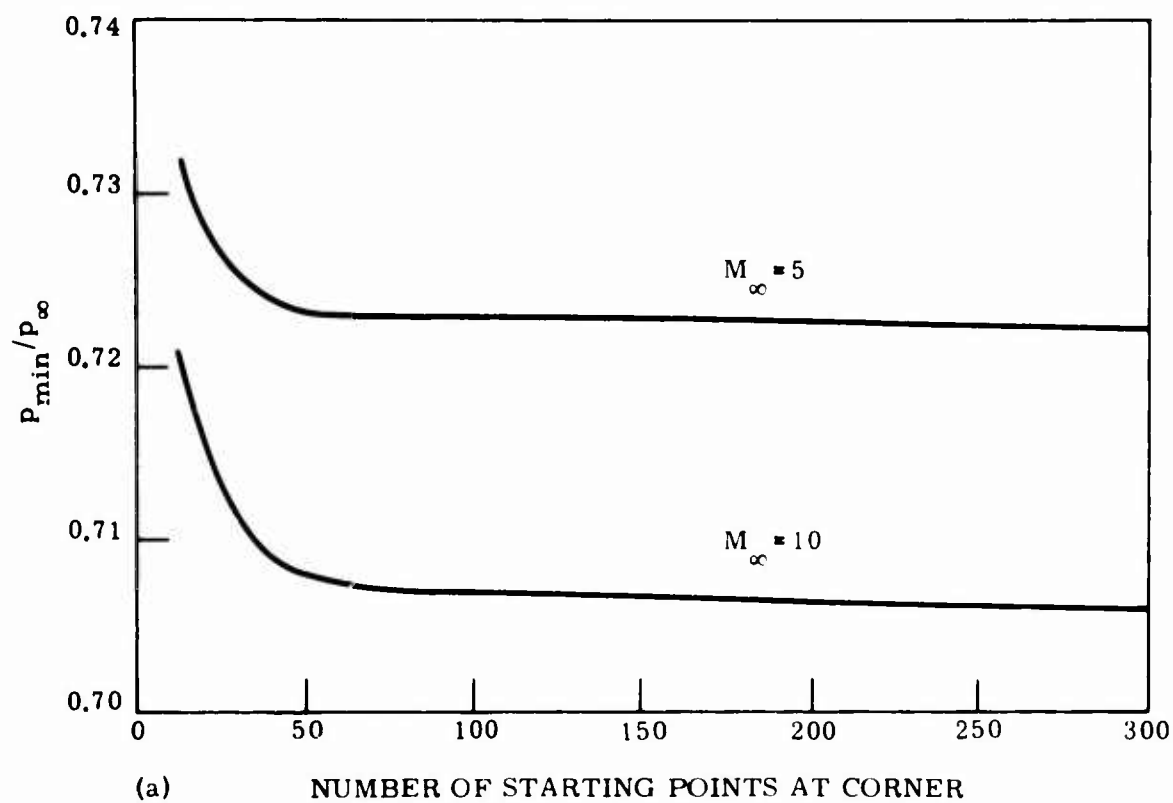


Figure 4 Effect of Entropy Layer on Inviscid Corner Expansion Calculations.

(a) Mesh Size Effect; (b) Entropy Gradient Effect.

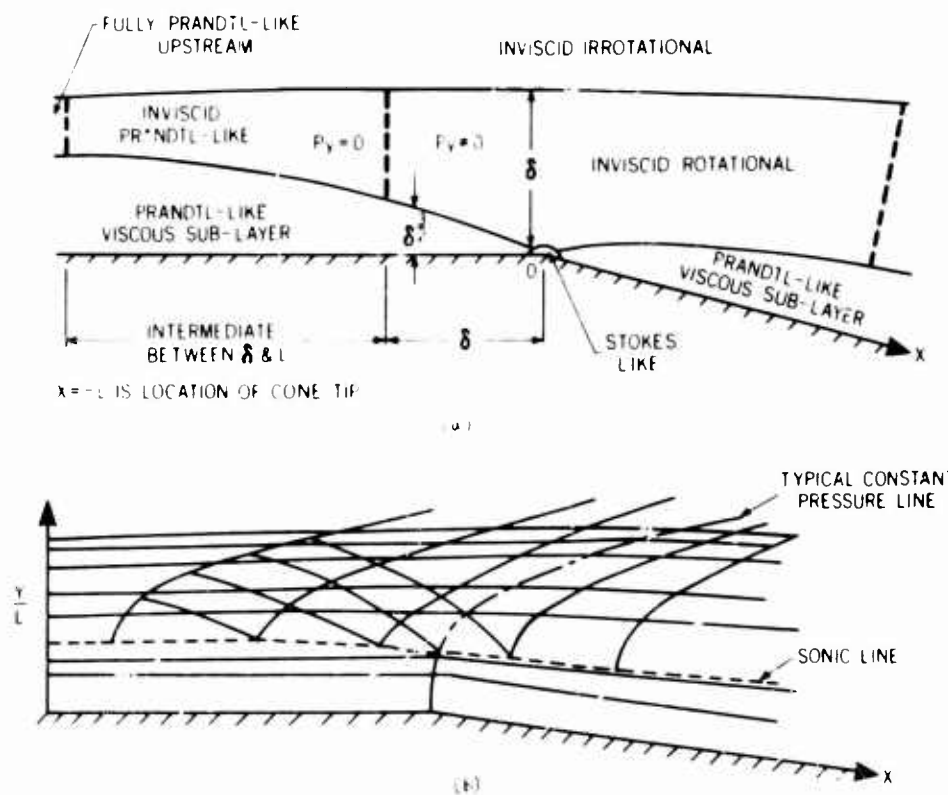


Figure 5 Schematic of Corner Expansion. (a) Character of Various Flow Regions; (b) Stream Line and Mach Line Pattern.

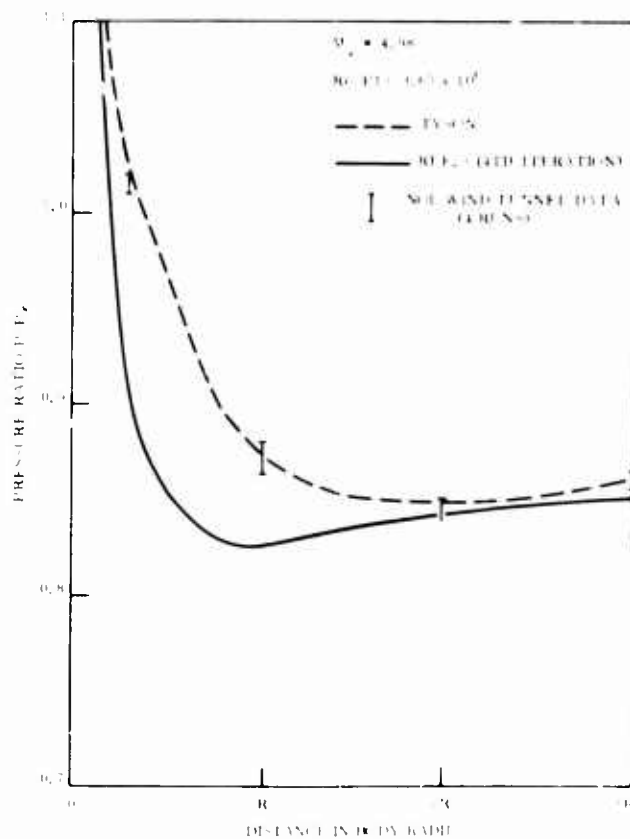


Figure 6 Predicted and Measured Wall Pressure Distribution for Laminar Flow Over 9° Corner.

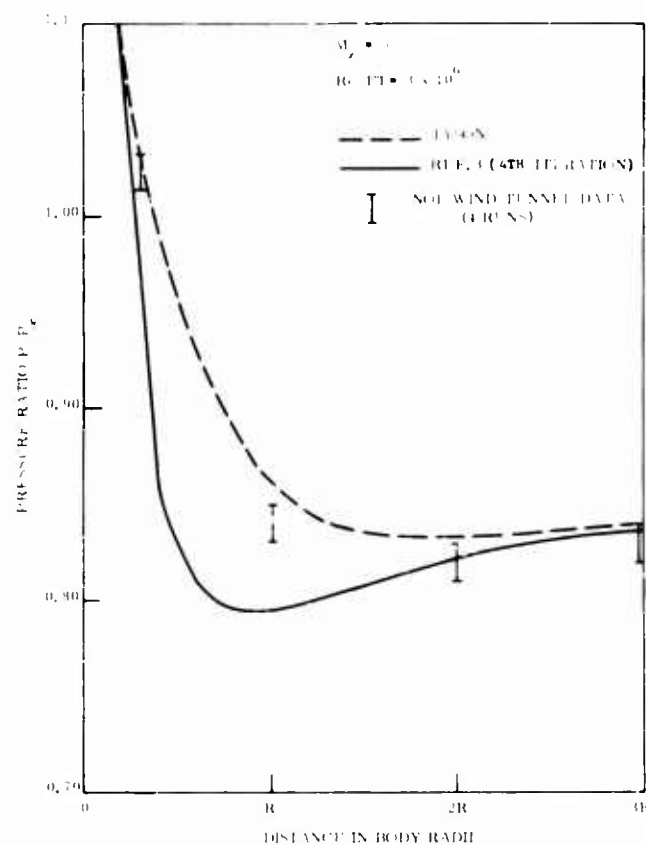


Figure 7 Predicted and Measured Wall Pressure Distribution for Laminar Flow Over 12.5° Corner.

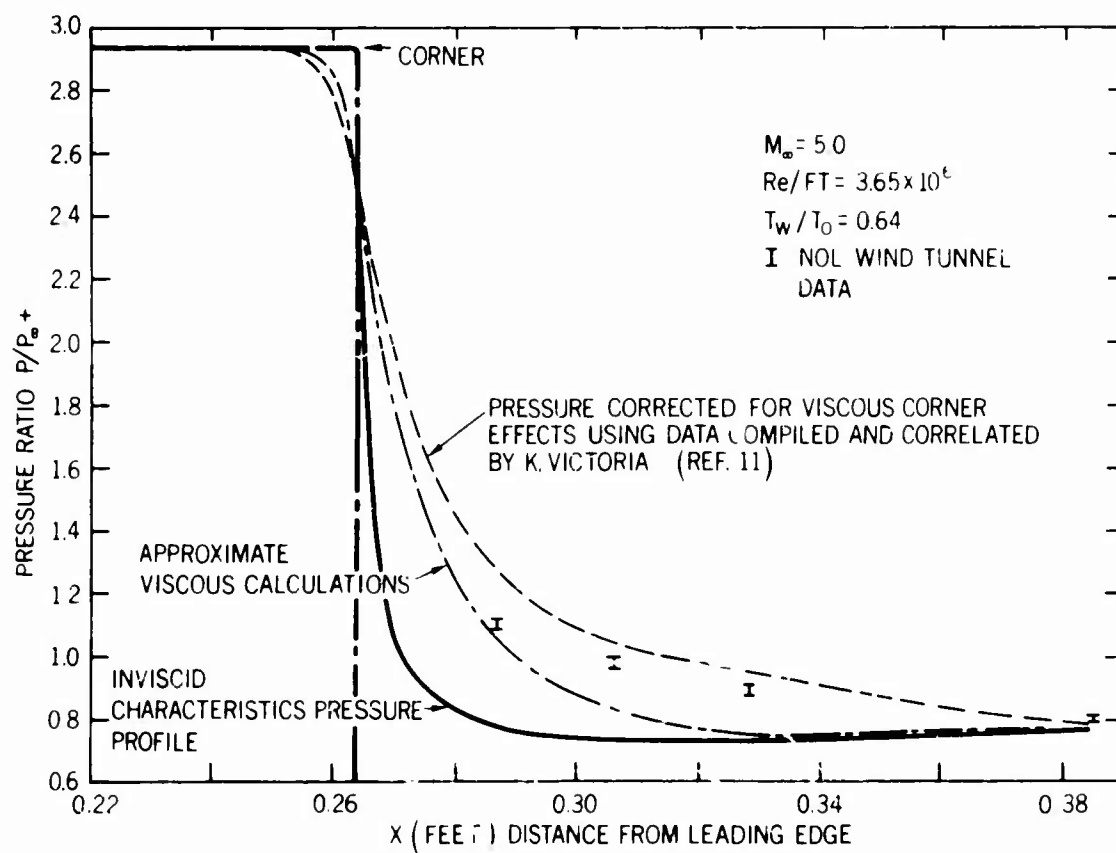


Figure 8 Comparison of 9° Corner Data with Correlation of Victoria (Reference 11).

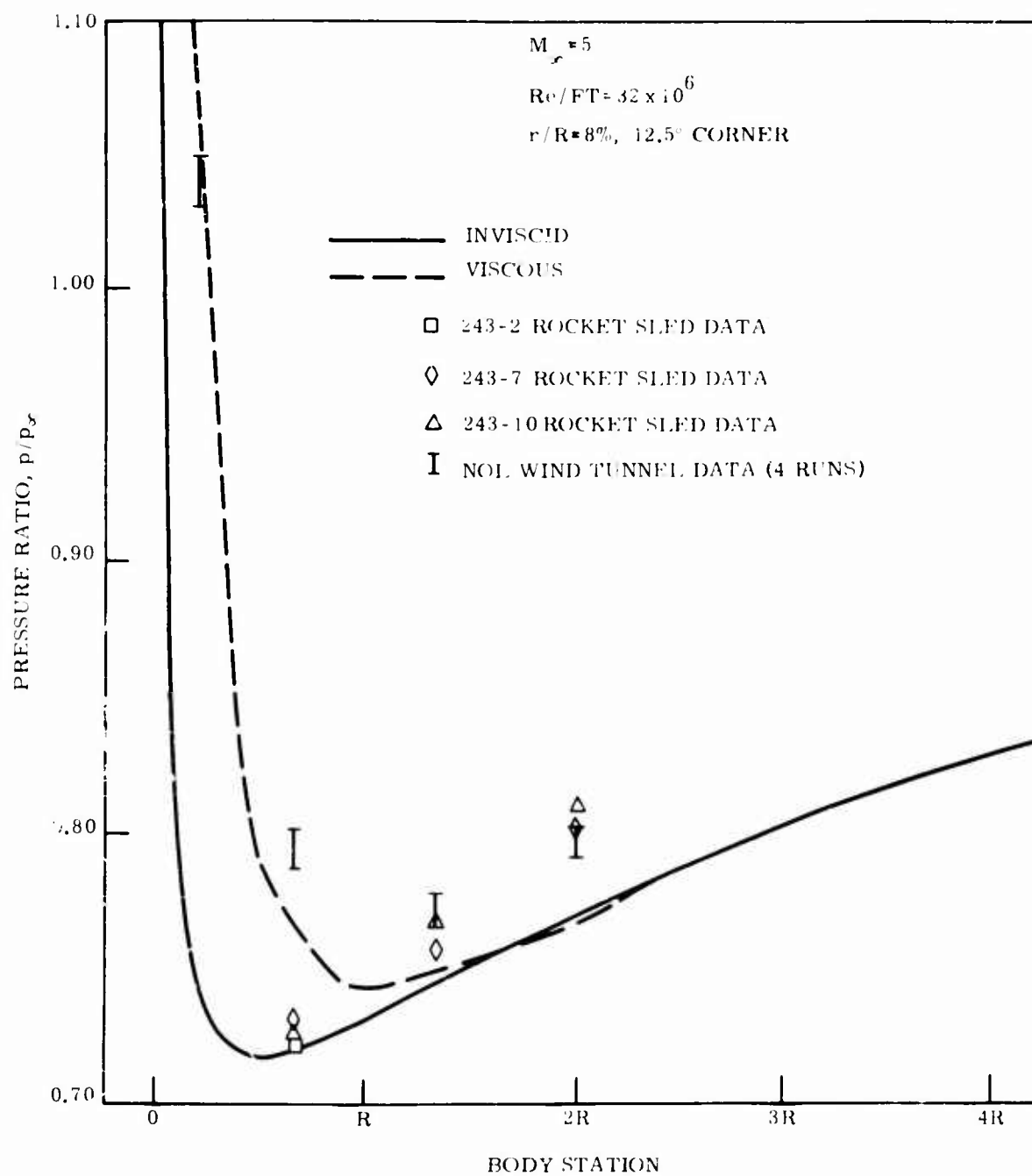


Figure 9 Predicted and Measured Wall Pressure Distribution for Turbulent Flow Over 12.5° Corner.

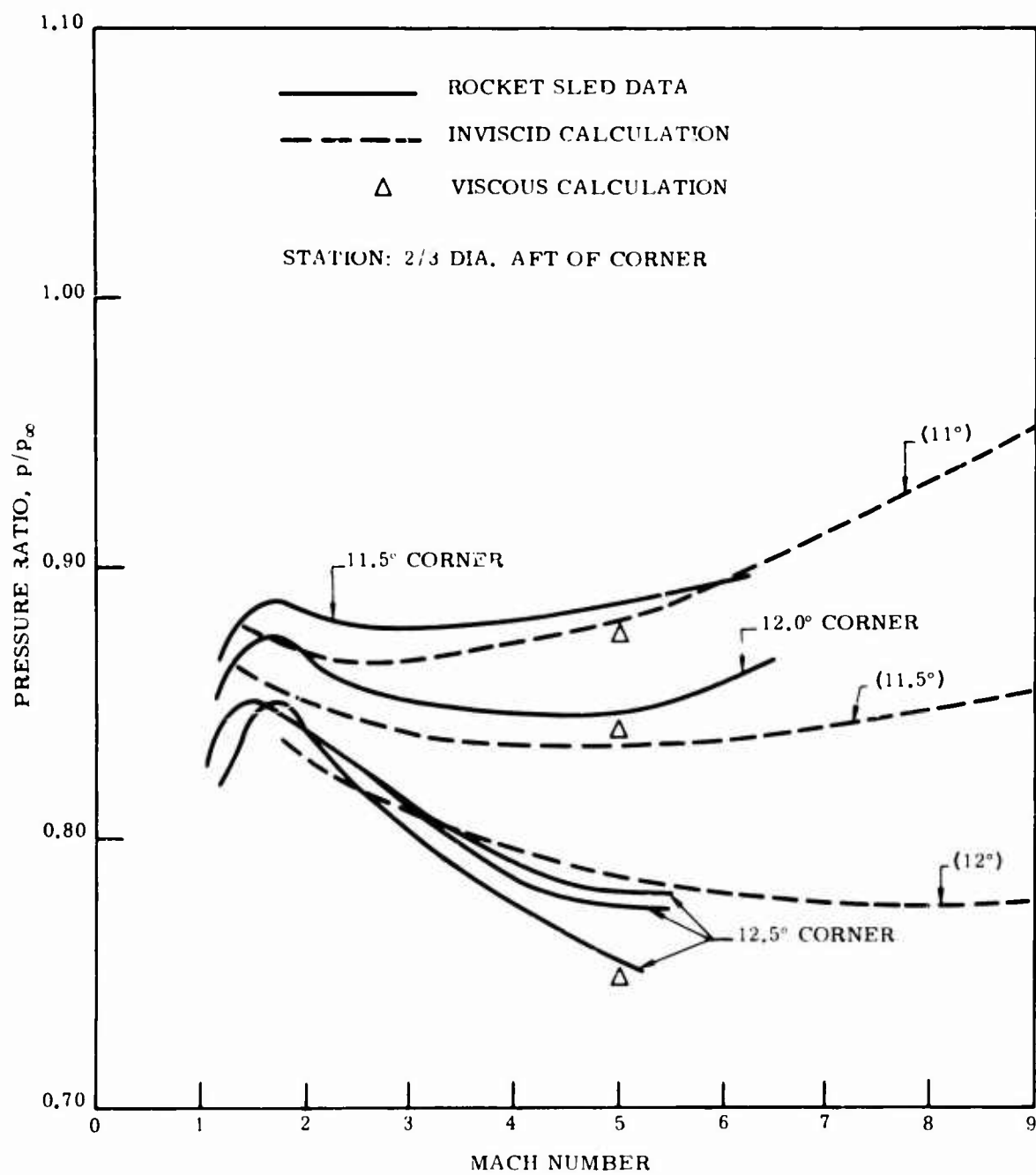


Figure 10 Experimental and Theoretical Plots of p/p_∞ versus Mach Number. Experimental Data from Rocket Sleds. Computations by Northrop (Reference 3).

ORDERLY THREE-DIMENSIONAL PROCESSES IN TURBULENT BOUNDARY LAYERS ON ABLATING BODIES

By Thomas N. Canning,* Michael E. Tauber,** Max E. Wilkins,**
and Gary T. Chapman**

Ames Research Center, NASA, Moffett Field, California, 94035, USA

*Chief, Hypersonic Free-Flight Branch, Vehicle Environment Division.
**Research Scientist.

SUMMARY

Contrary to the frequently made assumption of random behavior, careful experimental studies reported in the literature have revealed a remarkable degree of order in transitional and turbulent boundary layers. Some results are reported here of tests made with biconic, concave, and convex ablating Plexiglas models in a Mach 7 airstream with maximum local Reynolds numbers approaching 10^7 . After they were tested, the model surfaces were carefully examined. In addition to such well-known features as turbulence wedges and streamwise grooves, produced by longitudinal vortices, many parts of the models exhibited a "cross hatching" pattern, which had also been previously observed by the authors under other conditions. It was found that the spiral angle of the cross-hatching is close to the Mach angle based on boundary-layer edge Mach number, while the spacing is typically equal to a few boundary-layer thicknesses. A physical flow model is outlined which could explain the cross-hatching and other observed patterns.

ORDERLY THREE-DIMENSIONAL PROCESSES IN TURBULENT BOUNDARY LAYERS ON ABLATING BODIES

By Thomas N. Canning, Michael E. Tauber, Max E. Wilkins,
and Gary T. Chapman

Ames Research Center, NASA, Moffett Field, California, 94035, USA

1. INTRODUCTION

Careful experimental studies have revealed the presence of a remarkable degree of order in turbulent boundary layers. Two examples of this, which will also be cited as bases for the discussion of the present paper, are the work by Gregory and Walker (1) and by Mochizuki (2,3). These papers illustrate quite clearly that the wedge of turbulent flow produced by affixing a single element of roughness in a flat plate boundary layer contains a highly regular system of longitudinal vortices which extend from the wedge leading edge to great distances downstream.

A number of studies have shown the existence of laterally spaced, time-variant disturbances in transitional subsonic and supersonic flows (4-8). More recently, the present authors (9,10) found what appeared to be regular markings on recovered ballistic-range cone models showing longitudinal as well as lateral periodicity, that is, a cross-hatching of the ablated surface, in addition to longitudinal vortices which ablated streamwise grooves in the surface. An example of this cross-hatching is shown in Fig. 1, taken from Ref. 10.

The possible implications of these crosshatched ablation patterns on the heat-shield performance of entry bodies have prompted the present study. This paper describes an attempt to link the observed sculpturing of the surfaces to the aerodynamic and thermodynamic test conditions under which they were produced.

2. FACILITIES AND TESTS

Most of the data and discussion will concern observations of Plexiglas models (polymethylmethacrylate), as affected by the hot hypersonic flow in the NASA Ames 3.5-foot wind tunnel. Where appropriate, comparison will be made with models recovered after flight in a ballistic range.

The 3.5-foot hypersonic wind tunnel is a blowdown facility, in which air stored at high pressure is heated as it passes upward through a cylindrical tank filled with hot zirconia pebbles. The hot air then passes through an axially symmetric, contoured nozzle ($M_\infty \approx 7$), the walls of which are protected by a thin film of helium injected upstream of the nozzle throat. The tunnel exhausts into four evacuated spheres and can provide test times in excess of 1 minute at the conditions used in the present tests (stagnation pressure of 115 atm and stagnation temperatures of 750° and 1075° K).

The models were mounted on a movable sting, inserted into the test section after steady flow was established, and withdrawn after the desired test interval (before the flow was stopped). Insertion and withdrawal each required only a fraction of a second.

The models used in the experimental study were designed to reveal the influence of both gradual and abrupt, and positive and negative, pressure gradients on the patterns produced by ablation. Shapes were selected that would result in large pressure and heating rate changes on a given model, along with large changes in boundary layer-edge Mach number, M_∞ (1.3 to 3.5) and unit Reynolds number (67,000 per cm to 640,000 per cm). The models (Fig. 2) were solid, homogeneous bodies of revolution (except for laminations) made of Plexiglas. Cone angles at the tip were 25°, 30°, 40°, and 50°; surface inclination was, in every case, changed by a 15° increment, which produced compressions on the two smaller tip angle cones, and expansions on those with larger tip angles. The slope was changed in two ways, discontinuously at a corner, and continuously on surfaces described by cubic equations. Pointed steel tips, about 1.2 cm in diameter, were used on the models to prevent ablation at the apex.

3. DATA

The data presented represent a detailed visual study of the bodies during and after testing. During the tests, the model surfaces were watched by one or more observers and were photographed by a 16 mm motion-picture camera at 128 frames per second. The observers' purpose was to determine the rate of formation of the surface patterns by the airflow and to signal the time for termination of the run by withdrawing the model. Since the plastic material is transparent and the surfaces appear frosted, many subtle details are better revealed by surface replicas than by the original surface. Two types of replica were made.

The more sensitive of the two consisted of epoxy plastic cast in a silicone-rubber mold made from the actual model. The rubber used adheres only weakly to the model and to the epoxy, and is easily separated with a small air jet. The rubber used for making the female impression is Dow Corning 3110 RTV Encapsulant, and the epoxy resin is Epocast Resin No. 4-1 with hardener No. 9111. In the course of making these replicas it was found desirable to provide hollow liners in order to save rubber and epoxy material and make the final bodies light. Liners were made by vacuum forming clear-plastic sheets of 0.508 mm to 1.270 mm thickness over the models. A rather high degree of detail was replicated in both of these processes, and many features difficult or impossible to see

and photograph on the actual models are made easily visible. Photographs of all of the epoxy replicas are shown in Fig. 3. There are more replicas than models since two models were tested twice in the wind tunnel and replicas were made after each test.*

Several techniques were used to measure dimensions and angles of surface patterns from the models and replicas. One very sensitive process was to make pencil rubbings by pressing a piece of bond paper tightly against the model or replica surface and stroking lightly with the side of a lead pencil or a soft, colored pencil. Both longitudinal and lateral strokings were used to get best results. The features were then identified and measured in the flat.

On very subtly sculpted models (Fig. 3(e)) or deeply ablated models (Fig. 3(f)), it was found desirable to hand-mark the features with a grease pencil while studying them with different lighting and viewing angles. After the principal features were thus accentuated, the pencil marks could be either "transferred" using pressure-sensitive tape (and transported to flat paper as in the case of rubbings) or measured in place. Some features, however, were so clearly marked that there was no difficulty in measuring them directly.

In order to minimize any personal bias in the measurement of pattern sizes and shapes, two of the authors made totally independent measurements of the sweep angle and longitudinal and lateral wavelengths of the crosshatch patterns at positions on the bodies selected by each for clarity of markings. Several measurements were made in each region so that the results would have some statistical value, but no averaging has been done in the data presentation. The results of the independent studies were substantially identical.

3.1. Appearance of Ablated Surfaces

After ablation by the hypersonic test stream, the present models exhibited most of the features seen on the earlier ballistic-range models (9). For completeness of the present discussion these features are described briefly herein and related to those reported by other authors, as appropriate.

Each model had small regions of apparently uniform laminar flow, for at least a part of the test time, which produced little in the way of surface sculpting. These regions usually ended at a highly irregular transition front characterized by roughness elements and their resultant more deeply eroded "wedges." The wedges appear similar in planform to those observed in Refs. 1-3, 9, and 10. Their lateral rate of growth is similar as is the occasionally observed longitudinal grooving inside them.**

The most striking feature in the turbulent wedges and elsewhere in the regions of presumably turbulent flow is the cross-hatching produced by the flow. That the patterns result from intersecting grooves which spiral in both directions around the bodies is clearly evident from the slightly ablated bodies (Fig. 3(e)). As the ablation proceeds, the grooves appear to influence the nature of the adjacent flow more and more strongly. Instead of clearly intersecting, the grooves appear to join longitudinally at the spiral intersections and produce a set of wavy longitudinal grooves like those shown in Fig. 3(f) on model 4.

The clarity and depth of the crosshatch patterns is occasionally enhanced by disturbances produced by flaws or joints in the models as seen in Fig. 3(d). A cursory examination showed that new grooves were being created more or less continuously along the surfaces so that the spacing did not increase proportionately with body radius.

3.2. Correlations

In general, the sculpture produced by ablation is seen to be quite complicated, and our first effort at relating the forms produced to the test conditions is necessarily limited. In the present case we have sought to correlate the spiral angle of the grooves, that is, the angle between the groove and the body-generator lines, and the size of the patterns with the boundary-layer-edge flow conditions

3.2.1. Spiral Angle Correlation

Although the influence of material properties has not been ruled out, it was postulated at the outset that the surface patterns were governed by the boundary layer and perhaps the exterior flow. Accordingly, the spiral angle data for all the models were plotted against the boundary-layer-edge Mach number to obtain Fig. 4. A rather convincing correlation is seen between the observed spiral angle and the Mach angle. If the spiral is established by a standing wave, it must of necessity be at a greater angle than the Mach angle at the boundary-layer edge. The quality of the correlation suggests that a standing wave system does in fact exist, and hence that the cross-hatching should

*In general, the replicas do not extend fully to the base of the original model. For the purpose of making the replicas only, in some cases the steel tip was removed from the model nose and replaced with a screw. The apparent blunting of model tips, such as in Fig. 3(c), was caused by air trapped during casting and does not represent the actual condition of the model during the test.

**The bodies also exhibited, in varying degrees, two other types of markings. One consisted of very fine scale longitudinal ridges along body generators (see Fig. 3(h)); these may be a product of small longitudinal vortices. The other markings are small surface craters partly surrounded by crescents immediately downstream of each crater (see Fig. 3(c)); these are thought to be produced by the impact of zirconia dust particles present in the test stream.

not exist in subsonic flow. Mateer and Larson (11) conducted a test series using cones of various materials and a range of apex angles in the same facility and found cross-hatching only on bodies with supersonic flow outside the boundary layer. The points above the Mach angle curve suggest that the disturbance source of the standing wave can be well inside the boundary layer where the Mach numbers are lower than M_∞ . One level in the boundary layer which might be critical is that at which temperature is maximum.

3.2.2 Lateral Spacing Correlation

Since the shape of the pattern, that is, the spiral angle, is related to the flow properties, a length was sought to which the size of the pattern (longitudinal or lateral spacing of grooves) could be satisfactorily related. Several lengths were considered: the various boundary-layer thicknesses, the distance from the surface to the shock wave, the wetted length along the surface from the apex, the radius of curvature of the surface, and the depth of melted surface material, if any. In addition to these lengths, the influence of such factors as absolute heating rate and Mach number on pattern size was checked as well.

Even a cursory examination of the models showed a wide variation of groove spacing at any particular body station. New grooves continuously appear as the flow stretches around the expanding body; this means that the minimum groove spacing is, at the very greatest, half the maximum. Also, since there are doubtless random influences affecting groove initiation, the ratio of maximum spacing to minimum must exceed 2. At a particular streamwise location on model 4 a groove variation of fourfold over the minimum was observed. In view of these variations, only an approximate characterization was possible with the data available. No obvious effect of the pressure gradient on such features as the cross-hatching has been found; however, because of the influence of the pressure on the heat-transfer rate, significant changes occurred in the depth of the surface markings.

Many dimensionless groupings were attempted in the course of studying these data and almost all appeared to yield substantially poorer correlation than that given by a Reynolds number based on boundary-layer-edge conditions and the lateral spacing between the oblique grooves, Re_{λ_y} , plotted as a function of the Reynolds number based on local thickness of the turbulent boundary layer, Re_{λ} . The correlation showed that Re_{λ_y} increased with Re_{λ} (Fig. 5). This finding has two weaknesses: first, it is based on one test of model 3 at higher total temperature (filled symbols). Second, in two-dimensional flow it would be necessary for grooves to disappear selectively in order to permit the spacing to increase so as to avoid passing out of the correlation band. Mateer and Larson found no such selective disappearance in tests with plastic wedges. An alternative to selective disappearance might be that the entire periodic system might simply decay generally and produce imperceptible ablation patterns. In view of the slow decay of longitudinally disposed vortices this might require great distances.

A few measurements of λ_y were made on the ballistic-range models of Ref. 9. Since there is little chance of accurately determining when during the flights the final patterns formed, accurate calculations of Re_{λ_y} and Re_{λ} are not possible. The complications added by the possibility of sizable mass transfer at the surface add to the difficulty of interpretation. Roughly, the values of Re_{λ_y} fell near the bottom of the scatter band in Fig. 5.

The present findings together with those of earlier experiments (clearly defined laterally periodic structure in turbulent boundary-layer flows) lead to a possible model for the inception of cross-hatching and other sculpture of ablated surfaces.

4. POSTULATED MODEL

The flow processes in the boundary layer, which are thought to be capable of sculpting the present patterns (and some other patterns observed earlier as well), are described without qualifying remarks in this section. Subsequently, supporting observations taken from the present experiments and from the literature are presented to lend weight to the description.

4.1. Postulated Flow

The establishment of a turbulence wedge, such as diagrammed in Fig. 6, starts with a single disturbance source *a* (e.g., a roughness element) in a laminar boundary layer *b*. The trailing vortex system *c* from the disturbance may be steady downstream for a distance, depending on such factors as disturbance size and flow Reynolds number, and then suddenly break down into intense oscillation and turbulence at *d* in Fig. 6. The disturbance generated by this breakdown produces a nearly perfectly symmetrical spreading pattern of turbulent flow containing a regular array of discrete longitudinal vortices *e*, which are formed at the wedge leading edge. The disturbance *f* along the leading edge either produces or is produced by a vortex roughly hyperbolic in form near

Near the beginning of the test periods of some of the models a much smaller crosshatch pattern of waves was seen in the thin melt layer. The spiral angle of these wavelets appeared to be the same as that of the grooves produced later, but the spacing of the waves was perhaps smaller by a factor of 3 or 4 than the final markings. They may be like the line cross-hatching shown in Ref. 10. Their smaller size and impermanence suggest that some change in material response, such as temporary development of melt layers of critical thickness, surface tension, or viscosity, may have an important influence on wave spacing in either the small temporary or large permanent patterns observed.

its apex. The longitudinal vortex filaments are regularly spaced. The pressure disturbance resulting from the formation of each filament propagates within the Mach cone g , as indicated in Fig. 6. The array of pressure pulses can excite oscillations in the boundary layer as might a multitude of randomly spaced disturbances in view of the potential for self-aggravation (i.e., feedback) and stabilization introduced by the sculptured pattern. These disturbances do not produce noticeable local increases in heat transfer or ablation outside the wedge h where the flow is laminar; within the wedge, where the flow is turbulent, the wave-boundary layer interaction is concentrated i and yields sharply defined increments in heating. Where the surface contouring by concentrated ablation becomes deep enough, the resulting disturbances become severe enough to supplant the hyperbolic-front vortex mechanism responsible for the earlier spread of turbulence, as shown at j , toward the rear of the sketched flow in Fig. 6. As the boundary layer stretches over the ever-expanding perimeter of the body, new three-dimensional elements (probably vortex pairs) are created and produce additional wave systems (and hence grooves).

4.2. Supporting Evidence

The observations of Gregory and Walker (1) and of Mochizuki (2,3) are examples indicating that the breakdown of the smooth trailing vortex system from a roughness element is hastened either by increasing the free-stream Reynolds number or the size of the roughness element. The suddenness of the breakdown is well documented (2). The disturbance generated by this breakdown is so strong and the resulting breakdown so regular that an almost perfectly symmetrical wedge is produced. Among the scores of turbulence wedges seen by the authors, no highly asymmetric turbulence wedges have ever been seen, so it is concluded that the ensuing spread of turbulence is fully controlled. That transition from laminar to turbulent flow, well known for uncertain behavior, should be so regular in this case attests to the dominance of this mechanism.

Both Refs. 1 and 2 note clearly the regular array of streamwise vortices found in the wedge. The extremely regular breakdown along the wedge leading edge is described in Ref. 3: "... the photographs of the smoke pattern show distinctly the turbulent region behind the sphere [roughness element] and the laminar region outside of it. At the boundary of the two regions, we can see the smoke filaments gather one after another and take winded forms and then become obscure by strong mixing downstream. This state indicates that there might be a longitudinal vortex near the boundary. The measurements of the mean velocity profiles show clearly that a pair of longitudinal vortices appears outside of the four longitudinal vortices existing already, just at the boundaries of the turbulence wedge, and much closer to the flat plate than the former vortices." The indication that all of these outer vortices (in each half of the wedge) are co-rotational also suggests that the mechanism controlling filament formation is not simple induction by the downwash fields of existing vortices, but is the result of a continuous vortex filament or a pressure wave passing obliquely across the flow.

An unusual observation on recovered ballistic-range models (9,10) may be further evidence of this postulated leading-edge vortex. The surface shown in Fig. 7(a) has a clearly visible low ridge called a "hyperbolic front" by the authors; several such fronts have been preserved on ballistic-range models. If the leading-edge vortex described in Ref. 3 does exist, it should induce a lateral flow near the surface such that the surface streamline will trace out a line following the ridge found. The flow detail here is suggested at f in Fig. 6.

The pressure disturbances produced by the start of each vortex filament forming at this front should produce sharp pulses propagating along the Mach cones from each formation point. In subsonic flow no such obvious mechanism exists for concentrating the effect of the pulses, and cross-hatching is not observed. Also, a convincing correlation is found between spiral angle and edge Mach number.

In a laminar boundary layer h (i.e., along the outbound waves, g), the streamwise action of each wave should be spread out over many boundary-layer thicknesses, perhaps over several wave spaces, because of the extensive interaction typical of waves with laminar boundary layers, and therefore produce no important sculpture unless it is strong enough by itself to cause transition (j in Fig. 6), as illustrated in Fig. 7(b). The inward-bound waves, g , on the other hand, are interacting with a boundary layer of much higher shear, so that the interaction is concentrated sharply. This should permit the cutting of grooves in the turbulent-flow area. As the flow is stretched over the body, new grooves appear. That the lateral wavelength does not exceed some poorly defined maximum probably related to the boundary-layer thickness is shown by the present data. The observations using hydrogen-bubble flow visualization in two-dimensional flow (7) show that even at very large Reynolds numbers there is a clear lateral periodicity in turbulent-boundary-layer profiles. Consistent with the results of Ref. 7, Black's analytical formulation (12) points strongly to the possibility of vortex-loop discharges into the outer part of the layer from near the surface at preferred lateral spacings.

This overall flow model for the initiation and development of turbulence and cross-hatching is believed to reconcile many of the observed phenomena in transitional and turbulent flow. The high degree of order found is consistent with the orderliness of the markings.

5. CONCLUDING REMARKS

It has been shown herein that there can be a great deal of order in the supersonic turbulent boundary layer. The presence of both lateral and longitudinal, nearly time-invariant, spatially fixed waves or vortex systems or both has been deduced from studying ablated surfaces under widely varying test conditions, ranging from those of ballistic ranges to wind tunnels. The sizes of the

models ranged over an order of magnitude, while surface pressures and heat transfer rates varied over two to three orders of magnitude. The generally good agreement of "crosshatch" spiral angle with the boundary layer edge Mach angle up to about $M = 2$ and then spreading, at times, at an angle greater than the Mach angle, suggests that the disturbance causing the standing wave system responsible can be near the edge or deeper within the boundary layer as Mach number increases. The attempt to correlate the spacing of the cross hatching against a boundary layer thickness has been only partially successful; typically, the wavelength is equal to a few boundary layer thicknesses. Lastly, the model proposed herein for the formation of the cross hatching is felt to be compatible with many of the critical elements of orderly flow found by earlier investigators.

ACKNOWLEDGMENT

The author would like to acknowledge the contribution of Mr. Hartmut Legner in designing the models and doing many of the flow field calculations.

6. REFERENCES

1. Gregory, N., and Walker, W. S.: "The Effect on Transition of Isolated Surface Excavations in the Boundary Layer." Part I, R. & M. No. 2779, Aeronautical Research Council, London, October 1950.
2. Mochizuki, Masakazu: "Smoke Observation on Boundary Layer Transition Caused by a Spherical Roughness Element." *J. Physical Society of Japan*, vol. 16, no. 5, May 1961, pp. 995-1008.
3. Mochizuki, Masakazu: "Hot Wire Investigations of Smoke Patterns Caused by a Spherical Roughness Element." *Natural Science Report*, vol. 12, no. 2, Ochanomizu University, Tokyo, Japan, 1961.
4. Hama, Francis R.: "Some Transition Patterns in Axisymmetric Boundary Layers." *Physics of Fluids*, vol. 2, no. 6, November-December 1959, pp. 664-667.
5. Hama, Francis R., and Nutant, John: "Detailed Flow Field Observations in the Transition Process in a Thick Boundary Layer." *Proceedings of the 1963 Heat Transfer and Fluid Mechanics Institute* (Stanford University Press, Stanford, California, 1963), pp. 77-93.
6. Coles, Donald: "Transition in Circular Couette Flow." *J. Fluid Mechanics*, vol. 21, part 3, March 1965, pp. 385-425.
7. Schraub, L. A.; Kline, S. J.; Henry, J.; Kunstadler, P. W., Jr.; and Littell, A.: "Use of Hydrogen Bubbles for Quantitative Determination of Time Dependent Velocity Fields in Low Speed Water Flows." Report MD 19, Stanford University, Stanford, California (February 1964).
8. Knapp, C. E., and Roache, P. J.: "A Combined Visual and Hot Wire Anemometer Investigation of Boundary-Layer Transition." *AIAA J.*, vol. 6, no. 1, January 1968, pp. 29-36.
9. Canning, Thomas N.; Wilkins, Max L.; and Lauber, Michael E.: "Boundary Layer Phenomena Observed on the Ablated Surfaces of Cones Recovered After Flights at Speeds Up to 7 km/sec." Presented at AGARD Specialists' Meeting on Fluid Physics of Hypersonic Wakes, Fort Collins, Colorado, May 10-12, 1967.
10. Canning, Thomas N.; Wilkins, Max L.; and Lauber, Michael E.: "Ablation Patterns on Cones Having Laminar and Turbulent Flows." *AIAA J.*, vol. 6, no. 1, 1968, pp. 174-175.
11. Mateer, George G.; and Larson, Howard K.: "Unusual Boundary Layer Transition Results on Cones in Hypersonic Flow." *AIAA Preprint* 68-40, 1968.
12. Black, Thomas J.: "Some Practical Applications of a New Theory of Wall Turbulence." *Proceedings of the 1966 Heat Transfer and Fluid Mechanics Institute*, edited by M. A. Sand and J. A. Miller (Stanford University Press, Stanford, California, 1966), pp. 366-386.

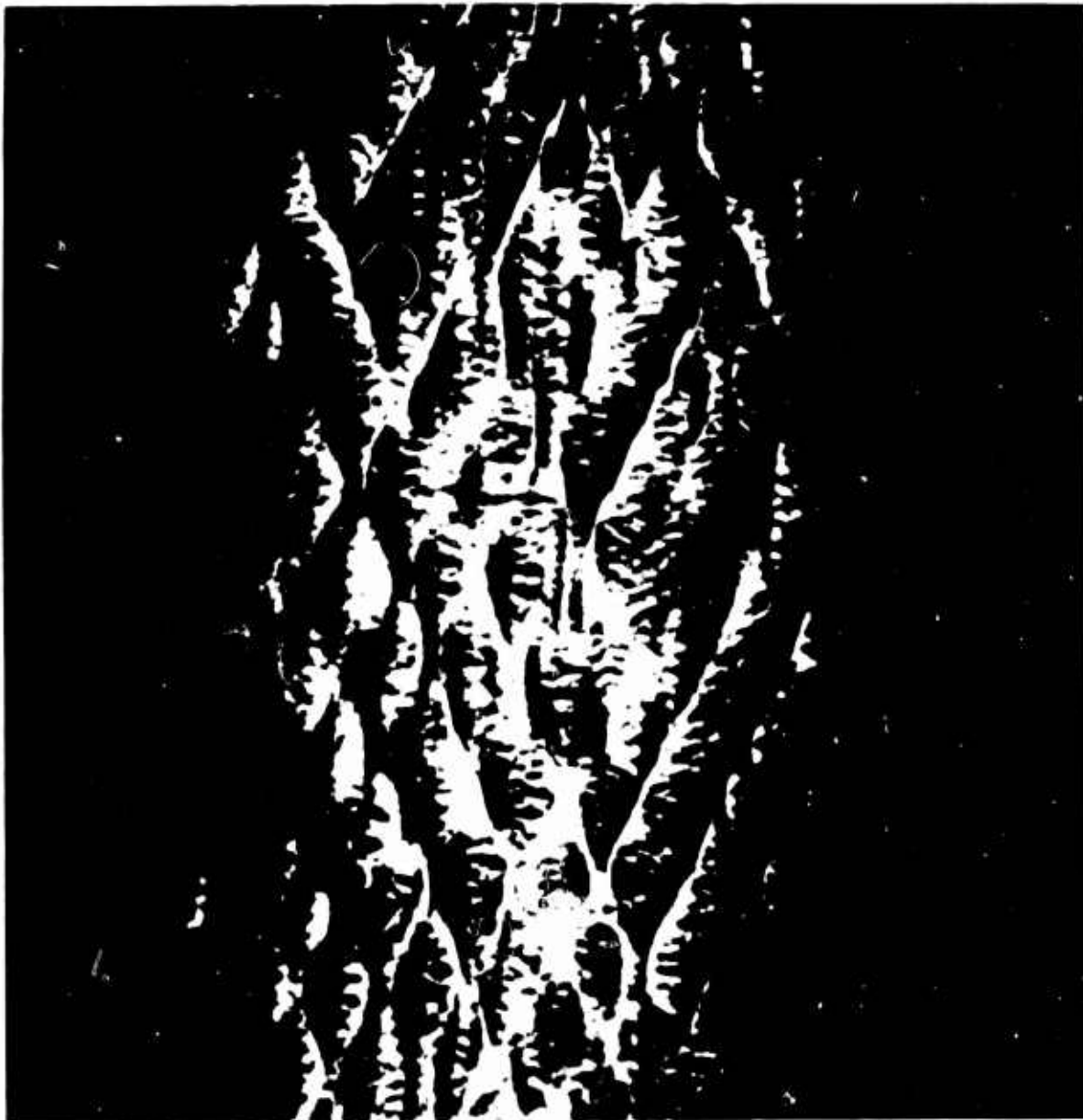
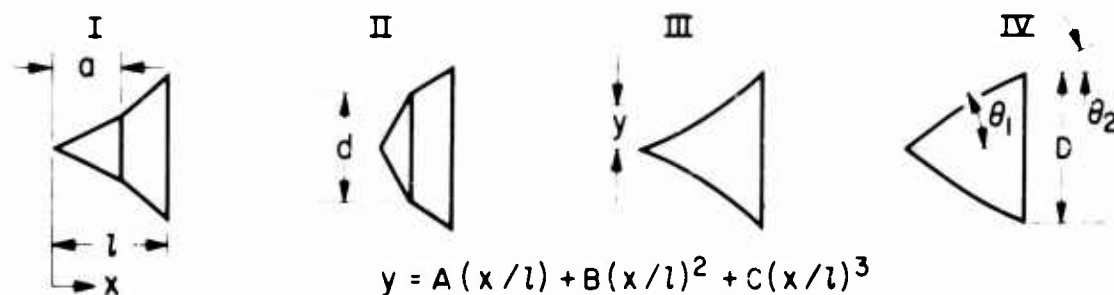


Fig. 1. Example of cross-hatching (Ref. 10).



MODEL No.	CLASS	θ_1 , deg	θ_2 , deg	D , cm	d , cm	l , cm	a , cm	P_s^{**} , atm	T_s^{\dagger} , °K	TEST TIME, sec	A , cm	B , cm	C , cm
1	I	25	40	21.23	9.921	17.38	10.63	120	778	19	—	—	—
2	I	30	45	19.32	10.16	13.38	8.796	118	742	28	—	—	—
3	III	25	40	21.23	—	17.38	—	118	773	21	8.1033	1.0637	1.4502
3*	III	25	40	21.23	—	17.38	—	121	1075	35	8.1033	1.0637	1.4502
4	II	50	35	20.32	11.68	11.07	4.892	122	776	17	—	—	—
4*	II	50	35	20.32	11.68	11.07	4.892	116	764	52	—	—	—
5	IV	50	35	20.32	—	11.07	—	118	761	29	13.195	-3.6627	0.6276
6	IV	40	25	23.50	—	18.97	—	110	743	71	15.918	-5.4400	1.2693
7	III	30	45	19.32	—	13.38	—	117	763	40	7.7254	0.15502	1.7818
8	II	40	25	23.50	13.06	18.97	7.777	114	746	51	—	—	—

* SECOND TEST

** NOMINAL WIND TUNNEL STAGNATION PRESSURE

[†] STAGNATION TEMPERATURE

Fig. 2. Model dimensions and test conditions.



(a) Model No. 1.

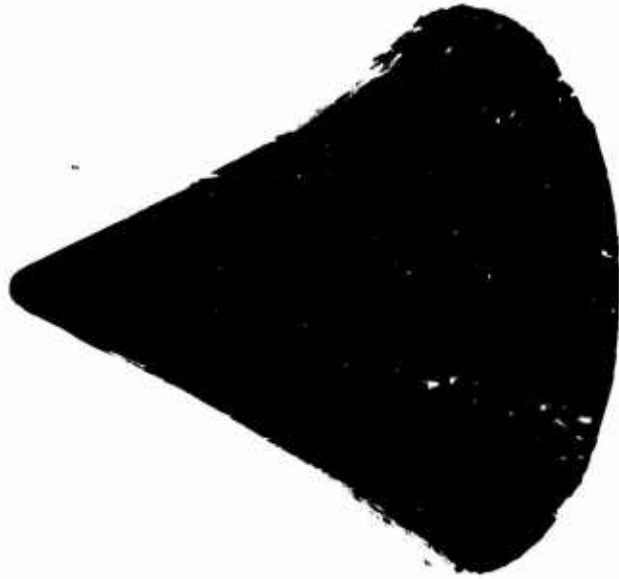


(h) Model No. 2.

Fig. 3. Replicas of ablated models.



(c) Model No. 3 (first test).



(d) Model No. 3 (second test).

Fig. 3. Continued.



(f) Model No. 4 (second test).



(e) Model No. 4 (first test).

Fig. 3. Continued.

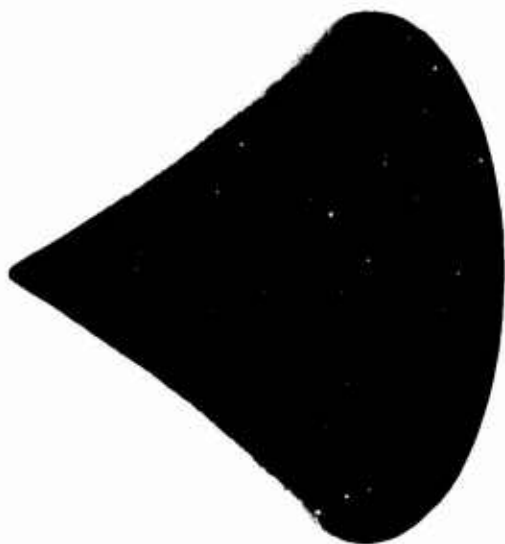


(h) Model No. 6.

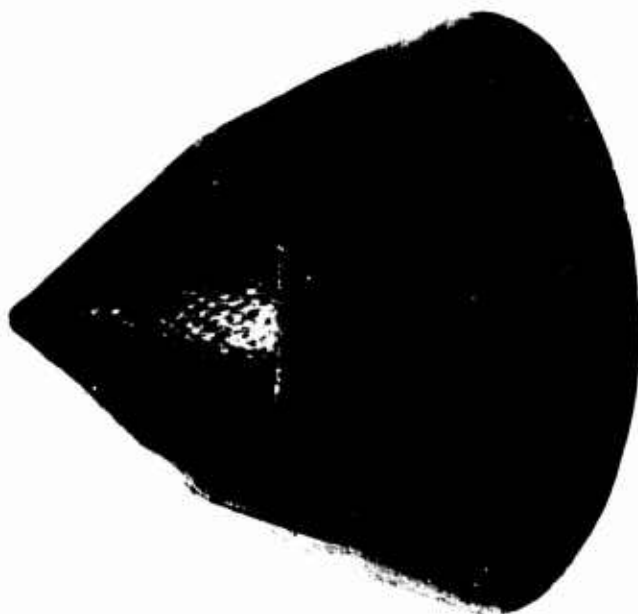


(g) Model No. 5.

Fig. 3. Continued.



(i) Model No. 7.



(j) Model No. 8.

Fig. 3. Concluded.

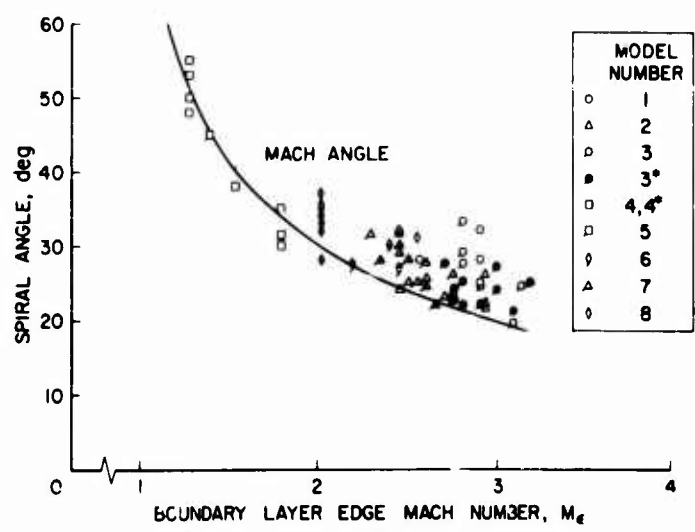


Fig. 4.
Variation of crosshatch spiral angle with boundary-layer-edge Mach number.

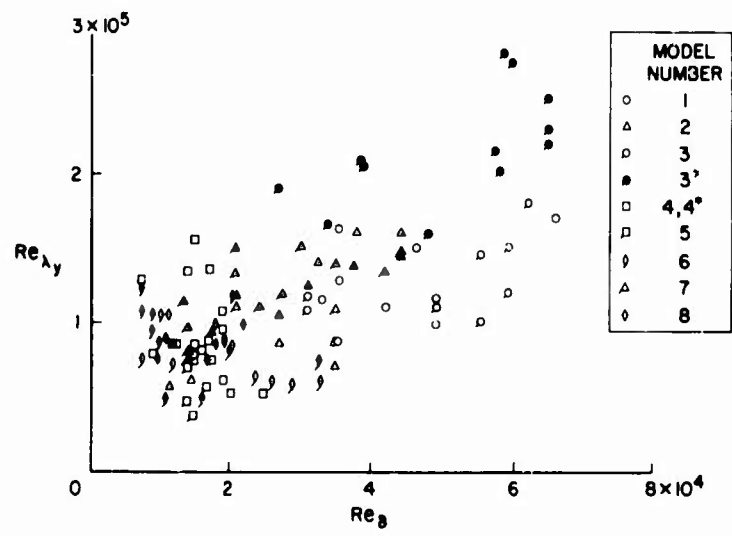


Fig. 5.
Lateral spacing Reynolds number versus boundary-layer thickness Reynolds number.

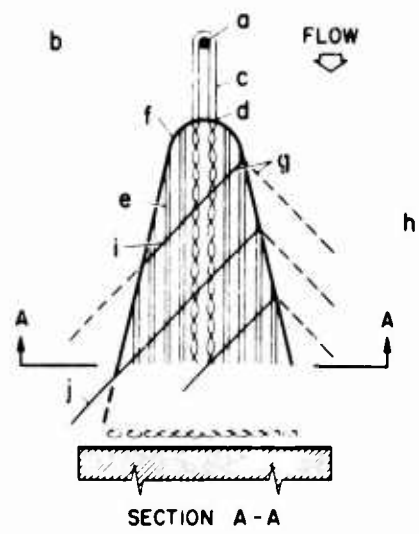
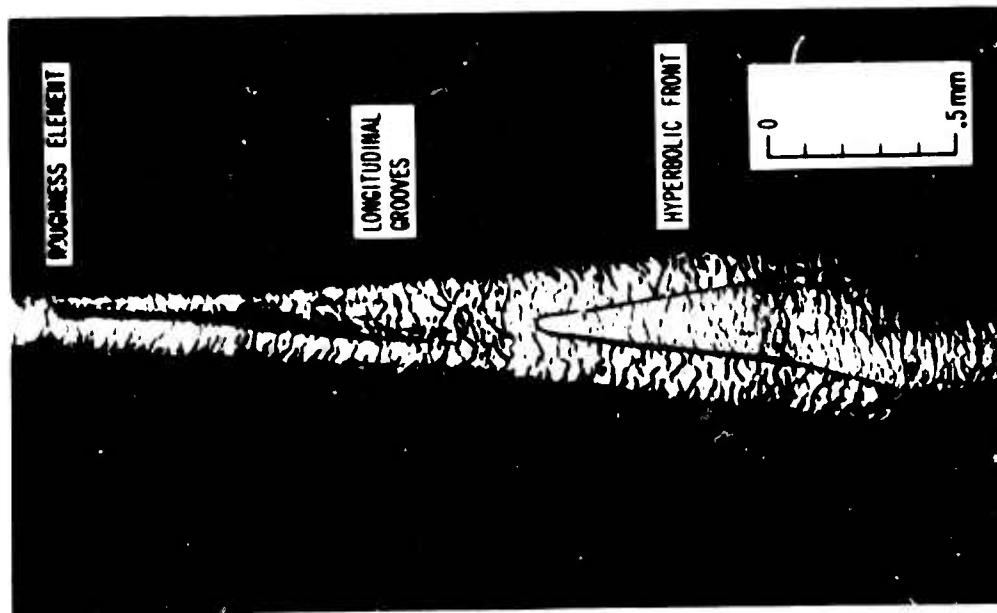
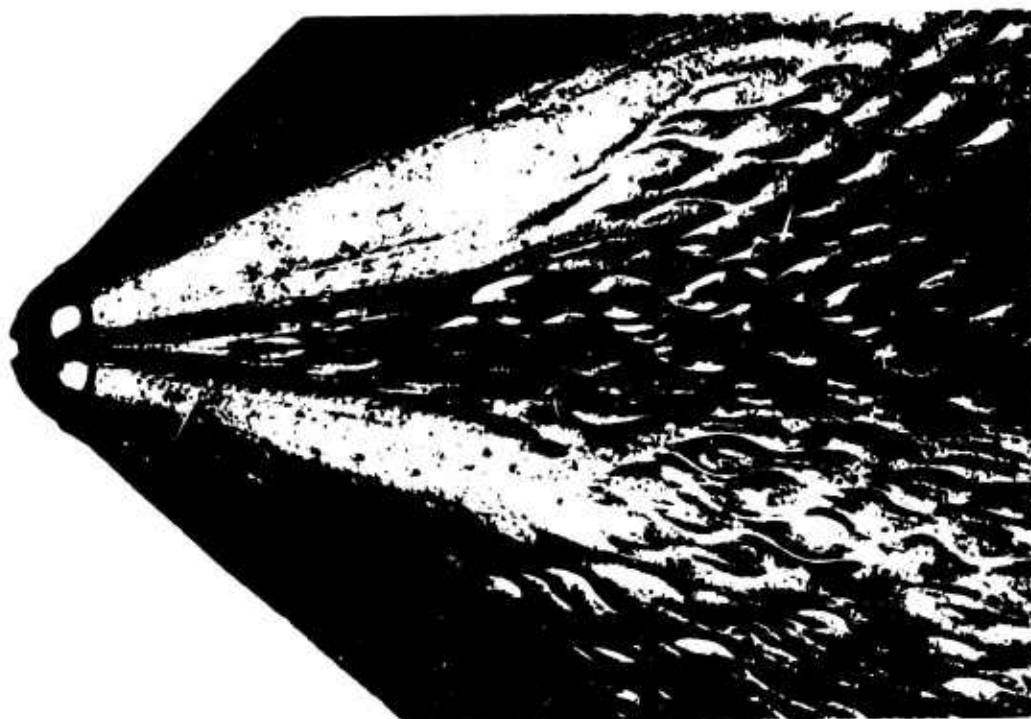


Fig. 6. Diagram of postulated flow model.



(a) Ballistic-range model (Ref. 9).



(b) Nose region of Model No. 8.

Fig. 7. Turbulent wedges.

PAPER 7

This paper has been cancelled
by mutual agreement

REYNOLDS AND MACH NUMBER SIMULATION OF APOLLO AND
GEMINI RE-ENTRY AND COMPARISON WITH FLIGHT

By

B. J. Griffith and D. E. Boylan
ARO, Inc., Arnold Air Force Station, Tennessee

SUMMARY

A comprehensive investigation in the AEDC-VKF wind tunnels was conducted on the Apollo 011 and Gemini 3 spacecraft configurations in order to resolve several anomalies between preflight predictions and flight data. Attention was focused on simulating the actual Apollo Command Module (011) and Gemini spacecraft (GT3) "as flown" in model construction over a Mach number range of 3 to 20.

The investigation indicated that the influence of the ablator (heat shield) geometry of the Apollo Command Module causes a significant change in trim angle of attack and resulting decrease in available lift-to-drag ratio. In addition, a very strong viscous influence exists in the initial portion of re-entry for both the Apollo and Gemini spacecrafts. Also, the Mach number influence extends up to about Mach 14 which is substantially higher than previous blunt body investigations have indicated. Comparisons of the AEDC wind tunnel data with existing flight data are made and generally excellent agreement exists.

REYNOLDS AND MACH NUMBER SIMULATION OF APOLLO AND GEMINI RE-ENTRY AND COMPARISON WITH FLIGHT[†]

By

B. J. Griffith* and D. E. Boylan**
ARO, Inc., Arnold Air Force Station, Tennessee

1.0 INTRODUCTION

The motion of a spacecraft in flight is determined by the propulsive forces supplied, the force of gravity, the inertial characteristics of the spacecraft and the aerodynamic forces. The wind tunnel is generally recognized as being almost indispensable in obtaining the aerodynamic information necessary to define the motion of the spacecraft. However, the validity of wind tunnel data depends on the minimization of the possible sources of error and the simulation of the flow around the spacecraft in flight. The purpose of this paper is to present a direct comparison between flight and wind tunnel data from the Apollo Command Module and the Gemini Spacecraft during the re-entry phase. Attention is focused on (1) simulating Apollo spacecraft 011 (AS-202) and Gemini Spacecraft (GT3) "as flown" in model construction, (2) obtaining consistent pitch plane force measurements in the angle of attack range of interest, (3) defining the effect of Mach number over a range of 3 to 20 for the Apollo tests and 7 to 20 for the Gemini study, (4) defining the effect of Reynolds number, and (5) possible sting effects on the Apollo Command Module.

The aerodynamic model data reported herein were obtained in the 40-in. supersonic Tunnel A, the 50-in. hypersonic Tunnels B and C, the 100-in. hypersonic Tunnel F, the low-density hypersonic Tunnel L, and the hypervelocity Range G of the von Kármán Gas Dynamics Facility (VKF), Arnold Engineering Development Center (AEDC). Other Apollo and Gemini wind tunnel data utilized in this paper were taken from Refs. 1 and 2. The flight test results were obtained from Refs. 2 and 3. A more detailed documentation of the Gemini results is reported in Ref. 2.

2.0 FLIGHT TEST PROGRAM

Apollo mission AS-201 was flown on February 26, 1966 to demonstrate the structural integrity of the spacecraft (009) and to evaluate heat-shield performance during re-entry (see Ref. 4). The spacecraft was not fully instrumented for re-entry flight aerodynamic data. In addition, a failure in the reaction control system resulted in a positive rolling re-entry rather than the planned lifting re-entry. Therefore, spacecraft 009 was not simulated during the post flight investigation. Hence, no comparisons between flight and wind tunnel data are made in this paper.

Apollo mission AS-202 was flown on August 25, 1966. A pre-flight photograph of Spacecraft 011 (prior to flight AS-202) is shown in Fig. 1. A considerable amount of detailed aerodynamic re-entry data resulted from this flight (Ref. 3). Atmospheric data were obtained in the re-entry area. These measurements allowed a quantitative analysis between flight and pre-flight wind tunnel data to be made.

With one exception, comparison of pre-flight Apollo Command Module aerodynamic data and actual flight AS-202 data was good. The one anomaly which resulted was the decreased flight L/D ratio. Post-flight determination of the CM center of gravity confirmed the accurate determination of its location. The decreased flight L/D could then be traced to the fact that the vehicle trimmed at an angle of attack about 3.5 degrees more than pre-flight moment data indicated. The resulting error in L/D was one reason that a large uprange error (205 n.mile) in splash down position occurred.

The Gemini flight test data used in this paper were obtained during the re-entry phase of the GT2, GT3, GT4, and GT5 spacecrafts. The data were collected and analyzed by the McDonnell Aircraft Corporation for NASA. Additional information and data on these flights are given in Ref. 2.

3.0 WIND TUNNEL PROGRAM

3.1 BRIEF HISTORY OF APOLLO WIND TUNNEL PROGRAM (1962-1966)

The earlier Apollo wind-tunnel testing program (AWTTP), conducted prior to the present investigation, was established as part of the design and development program initiated in support of the Apollo spacecraft program. The AWTTP was designed

[†] Research reported in this paper was done at the request of the Arnold Engineering Development Center (AEDC), Air Force Systems Command (AFSC), under Program 920E in cooperation with the NASA Manned Spacecraft Center, Houston, Texas.

* Supervisor, Aerodynamics, Hypervelocity Branch, von Kármán Gas Dynamics Facility.

** Engineer, Aerophysics Branch, von Kármán Gas Dynamics Facility.

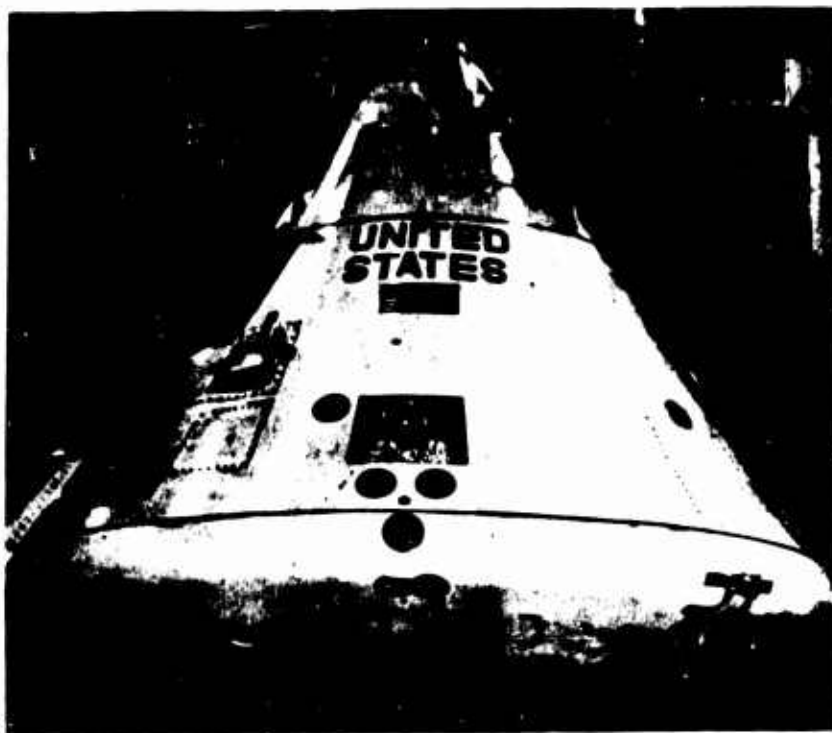
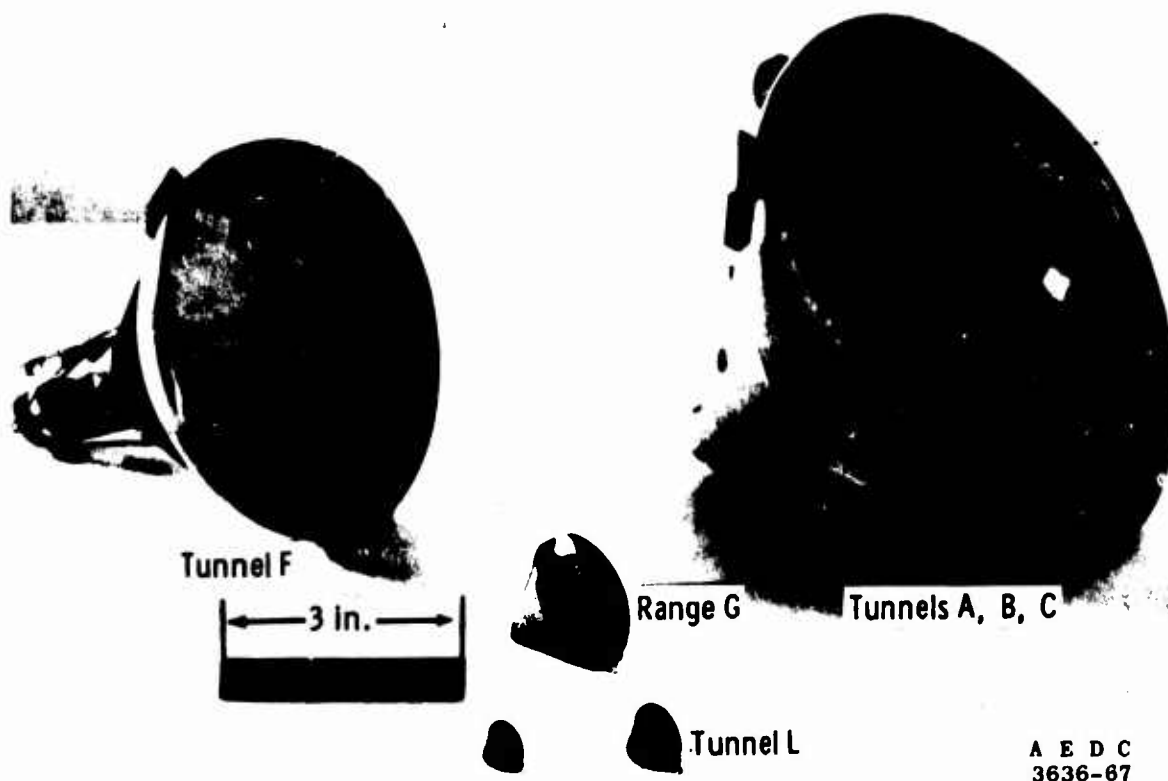


Fig. 1 Photograph of Apollo Spacecraft 011 Prior to Mission AS-202



A E D C
3636-67

Fig. 2 Photograph of AEDC-VKF Apollo Models

to obtain the necessary aerodynamic data for detailed flight planning, flight analyses and abort trajectories to meet various mission requirements. The tests were conducted in 25 different tunnels having Mach number range capabilities from near 0 to Mach number 19. The program was the responsibility of North American Aviation as prime spacecraft contractor. Moseley and Martino (Ref. 5) have given an excellent comprehensive chronological summary of the wind tunnel test program. Moseley, Moore, and Hughes (Ref. 1) present stability characteristics of the Apollo Command Module. A detail summary of these two reports is beyond the scope of the present paper. Rather, attention is drawn only to the Apollo Command aerodynamics in the attitude of heat shield forward, i.e., the re-entry attitude.

The Command Module (CM) aerodynamics are important since the spacecraft is designed to employ a low L/D ratio for flight path control during re-entry into the earth's atmosphere. Since the CM will experience a wide variation of flow regimes from high altitude, high Mach number flight to low altitude, low Mach number flight, many different facilities were employed in an effort to provide the necessary flow regimes. Reference 5 includes a tabulation of the various wind tunnel facilities employed in the investigation of the Apollo CM aerodynamics. In addition, one low density free-flight wind tunnel test (Ref. 6) for which the heat shield was maintained in a forward attitude has been reported in the open literature. Primary parameters studied in these investigations were influence of model configuration, Mach number, and Reynolds number. Various studies have been devoted to the influence of sting mount and base pressure effects, heat shield geometry, and center of gravity location.

Static stability data were taken over a Mach number range of 0.20 to ~ 19. Tests were made using both the smooth command module and models with surface modifications. These modifications included antennas, umbilical fairing (including pad 5 fairing), vent protuberances, window and tower-leg cavities. However on flight AS-202, the 205 miles uprange landing was in some part due to the aerodynamic performance of the spacecraft. The flight lift-to-drag ratio was significantly less than predicted. The reasons have been determined to be: (1) The actual heat shield asymmetry and surface condition of spacecraft 011 were different from that used in the pre-flight wind tunnel program. All wind tunnel models tested during the AWTTP had smooth symmetrical heat shields. (2) The high Mach number data taken during the AWTTP were taken early in the program. Both the Cornell Aeronautical Lab. (CAL) Mach 15.8 data and the AEDC Mach 18.7 data were taken in 1962. The accuracy of these data was such that high Mach number effects could not clearly be defined.

3.2 POST-FLIGHT AEDC-VKF APOLLO (AS-202) WIND TUNNEL PROGRAM

A comprehensive wind tunnel program was undertaken in order to obtain additional wind tunnel data on the command module. Only the command module in the re-entry attitude was tested in order that a systematic and carefully analyzed wind tunnel program could be completed in a short period of time. The program was a correlated effort between NASA and AEDC. Attention was focused on (1) simulating the actual vehicle "as flown" in model construction, (2) obtaining consistent pitch plane force measurements in the angle-of-attack range $150 \leq \alpha \leq 180$ degrees, (3) the effect of Mach number over a range of 3 to 20, (4) the effect of Reynolds number, and (5) possible sting effects. Table 1 presents a brief description of the wind tunnel program and the AEDC-VKF test facilities utilized during the investigation. The first test was initiated in Tunnel L during the month of December, 1966. The final test entry was in Tunnel A during the month of May, 1967. A detailed listing of the test conditions is shown in Table 2.

A number of models were constructed for use in the correlation program. The models, shown in Fig. 2, ranged from 0.60 inches in diameter (heat shield) to 8.01 inches in diameter. For the Tunnel A, B, C, and F tests, the actual vehicle (spacecraft 011) "as flown" was simulated in model construction. Detail templates drawn to model scale were furnished to AEDC by the North American Aviation Company. These templates were computer fairings of actual vehicle measurements (spacecraft 011) after installation of the ablation material over the heat shield and afterbody. Pertinent details of the spacecraft ablation heat shield configuration are shown in Fig. 3. Added ablation material on the windward surfaces of the spacecraft produces an asymmetrical configuration. Ablation material over the pressure pads (supporting structure) makes the heat shield wavy. A view of the asymmetrical wavy heat shield model produced by the classical Toepler-Schlieren technique is shown in Fig. 4. To the authors' knowledge, no previous experimental investigation has been devoted to the asymmetrical wavy heat shield. Symmetrical heat shield models were also studied in the present investigation to provide consistent comparative data.

Pertinent model and sting details are presented in Fig. 5. The asymmetrical configurations were constructed according to templates to station $x/d = 0.30$ (see Fig. 5). Hence, the symmetrical and asymmetrical configurations are identical aft of this station. The asymmetrical model tested in the continuous tunnels included the umbilical housing and surviving antenna. The Tunnel F model included only the umbilical housing while the Tunnel L and Range G models had only symmetrical smooth

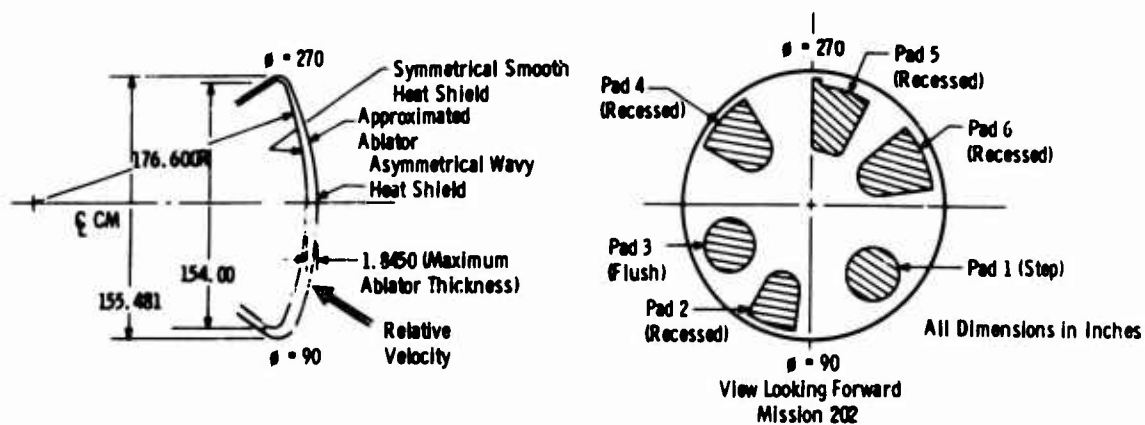
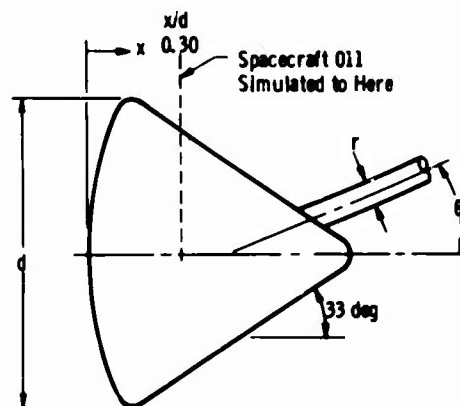


Fig. 3 Apollo 011 Heat Shield Asymmetry

Asymmetrical Wavy
Heat ShieldFig. 4 Optical Photograph of Face
of Tunnel F Model

VKF Facility	d	θ , deg	r , in	Asymmetrical Model
Tunnel A	8.01	20	1.65	Yes
Tunnel B	8.01	20	1.65	Yes
Tunnel C	8.01	20	1.65	Yes
Tunnel F	5.54	0	1.25	Yes
Range G	1.75	-	0	No
Tunnel L	0.60	0	0.16	No
	0.80	0	0.16	No

Fig. 5 Sketch of AEDC-VKF Apollo
Models

heat shields and hence did not include any fairings. Details of these fairings are given in Ref. 3. The sign convention used for the Apollo data is given in Fig. 6.

3.3 AEDC-VKF GEMINI WIND TUNNEL PROGRAM

The AEDC-VKF wind tunnel program is documented by Griffith in Ref. 2. The program, although not as comprehensive as the Apollo study, presents a systematic study of the aerodynamics of the Gemini spacecraft in the re-entry attitude. Figure 7 presents the sign convention used for the Gemini data throughout the paper.

The Gemini investigation was conducted only in AEDC-VKF Tunnels F and L. The Tunnel F model was a 1/15-scale version of the Gemini re-entry module with detailed retaining strap fairings and observation windows. The Tunnel L models were 1/120- and 1/180-scale versions of the re-entry module and did not include fairings or observation windows. The reader is referred to Ref. 2 for additional details.

3.4 TEST FACILITIES FOR CURRENT INVESTIGATION

The Apollo investigation was conducted in the 40-in. supersonic tunnel (Gas Dynamic Wind Tunnel, Supersonic (A)), in the 50-in. hypersonic tunnel (Gas Dynamic Wind Tunnel, Hypersonic (B)), the 50-in. Mach 12 tunnel (Gas Dynamic Wind Tunnel, Hypersonic (C)), the 100-in. Mach 20 tunnel (Gas Dynamic Wind Tunnel, Hypersonic (L)), and the 1000-ft. Hypervelocity Range (G). Only Tunnels F and L were utilized during the Gemini investigation.

Tunnel A is a continuous, closed-circuit, variable-density, supersonic wind tunnel with a Mach number range of 1.5 to 6. The tunnel operates at stagnation pressures between 1.5 to 200 psia and stagnation temperatures of 70 to 290°F.

Tunnel B (a continuous closed-circuit wind tunnel) operates at a nominal Mach number of 6 or 8 at stagnation pressures from 20 to 280 or from 50 to 900 psia, respectively, at stagnation temperatures up to 890°F.

Tunnel C (similar to Tunnel B) operates at a nominal Mach number of 10 or 12 at stagnation pressures from 200 to 2000 or from 600 to 2400 psia, respectively, at stagnation temperatures up to 1440°F. The data presented in this paper at Mach 12 represent the first test (except for calibration) in the Mach 12 nozzle.

Tunnel F is an arc-driven wind tunnel with a 100-in. test section. Nitrogen, initially confined in an arc chamber by a diaphragm located near the throat of an attached 8-deg conical nozzle, is heated and compressed by an electric arc discharge and expanded through the conical nozzle to the test section. A useful run time between 50 and 100 msec is attained.

Tunnel L is a low-density, hypersonic, continuous-flow, arc heated, ejector-pumped facility, normally using nitrogen or argon as the test gas. Nitrogen was used for all the tests reported herein. Contoured nozzles provide gradient free flow at nominal Mach numbers of 4, 9, and 10 at varying free-stream Reynolds numbers.

Hypervelocity Range G is a 1000-ft-long, 10-ft-diameter, variable density tube wholly contained within an underground tunnel. Launching capability ranges from in-gun weights of 498 gms at 12,000 ft/sec to 130 gms at 23,000 ft/sec. Instrumentation includes provisions for pressure and temperature measurements, forty-three dual-axis shadowgraph stations, schlieren photography, microwave and RF cavity measurements, radiometric and spectrographic measurements, and high speed photography.

3.5 PROCEDURE

The broad range of flight conditions during Apollo flight AS-202 demanded that several of the AEDC-VKF tunnels be utilized. In order to keep the experimental program to a minimum, the results of a given test entry were analyzed before the next test was started. For example, tests in Tunnel L were started prior to the Tunnel F tests in order to determine the viscous influence at simulated altitudes up to 350,000 ft. These tests resulted in a more meaningful experimental program in Tunnel F. However, the post-flight tests still required 515 hours of testing. The same general procedure was followed during the Gemini studies. A summary of the Apollo testing program is as follows:

1. Viscous Effects at High Simulated Altitudes

Tests were conducted in Tunnel L at Mach numbers of 9.37 and 10.15. The free-stream Reynolds number (based on heat shield diameter) ranged between 234 and 1283 by varying test conditions and model size. These tests were conducted during the period of 5 December 1966 to 9 January 1967.

2. Viscous and Mach Number Effects at Simulated Altitudes of 220,000 to 280,000 ft, Plus A Study of the Influence of the Ablator (Heat Shield Geometry)

These tests were conducted during the period of 26 December 1966 to 24 January 1967 in Tunnel F. Data were obtained over a Mach number range of 14.6 to 20 at free-stream Reynolds numbers of 13,700 to 377,000.

3. Viscous and Mach Number Effects at Simulated Altitudes of 150,000 to 200,000 ft, Plus A Study of the Influence of the Ablator (Heat Shield Geometry)

The first tests were conducted at Mach 8 in Tunnel B over a Reynolds number range (Re_{∞}) of 0.36×10^6 to 1.8×10^6 on 17 January 1967. The tests were conducted using a small (amplitude ± 3 deg), free oscillation, cross-flexure pivot balance in order to better define the trim angle. The data indicated the need for force coefficients at similar conditions. Additional tests were conducted on 23 February 1967 with a six-component, force-type, strain-gage balance.

4. Additional Data in the High Mach Number, Low Reynolds Number Range

Additional data were obtained in Tunnel F during the week of 15 February 1967 in order to better define the variation of the Apollo force and moment coefficients with Reynolds number.

5. Verification of the Apparent Mach Number Effect

Tests were conducted in Tunnel A on 18 May 1967 at Mach 3, 4, and 6 and on 26 May 1967 in Tunnel C at Mach 12. These data were necessary in order to better define the effect of Mach number on the force and moment coefficients of the Command Module.

6. Sting Effects

Concurrent with the tests on the sting mounted models, configurations with the symmetrical smooth heat shield were being launched in Range G in order to study any possible influence of the sting. Shots were made with models that had full CG offsets (same as spacecraft AS-202), half offsets and zero offsets. The shots were made as near as possible to the Tunnel B test conditions and were made from 25 January 1967 to 25 March 1967.

3.5 ACCURACY AND REPEATABILITY

The accuracy of the data is, of course, a function not only of the uncertainty of the direct measurements but also of the test-section flow properties. Except for the Mach 6 data in Tunnel A the test-section static temperature was kept within a few degrees of the theoretical liquefaction value in order to add validity to the calculated flow properties. Assessments of the estimated uncertainties in the Apollo tunnel and Range data are as follows:

	C_A	C_D	C_N	$C_{m_{cg}}$	α_T
Tunnel A	± 0.01	± 0.01	± 0.002	± 0.0012	- - -
Tunnel F	± 0.01	± 0.01	± 0.002	± 0.0012	- - -
Tunnel C	± 0.01	± 0.01	± 0.002	± 0.0012	- - -
Tunnel F	± 0.04	± 0.04	± 0.005	± 0.0018	- - -
Tunnel L	± 0.03	± 0.03	± 0.02	± 0.0025	- - -
Range G	- -	± 0.01	- -	- - -	± 1.2 deg

The estimated uncertainties for the Gemini wind tunnel data are similar to the above and are given in Ref. 2.

4.0 WIND TUNNEL CORRELATION PARAMETER

The comparison of wind tunnel or range data with flight data requires the determination of a suitable correlation parameter. The need for a correlation parameter, of course, is due to the fact that flight conditions can seldom be duplicated in the wind tunnel. Figure 8 shows the re-entry of Apollo 011 and Gemini 3 in terms of altitude and time. However, Fig. 9 gives (for the same flights) the normal shock stagnation conditions necessary for flight duplication.

Viscous effects are sometimes scaled using free-stream Reynolds number as the scaling parameter, but it is well known that this is not always the best procedure. Higher altitude viscous interaction effects have been successfully accounted for using the parameter \bar{v}_{∞} (Ref. 7). Both a Re_{∞} and \bar{v}_{∞} parameter appear to be applicable to either blunt or sharp slender bodies or for configurations for which viscous effects are of second order importance. However, the flow field of interest about

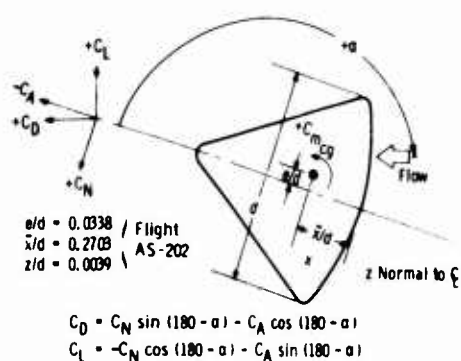


Fig. 6 Apollo Spacecraft 011 - Orientation of Forces and Moments

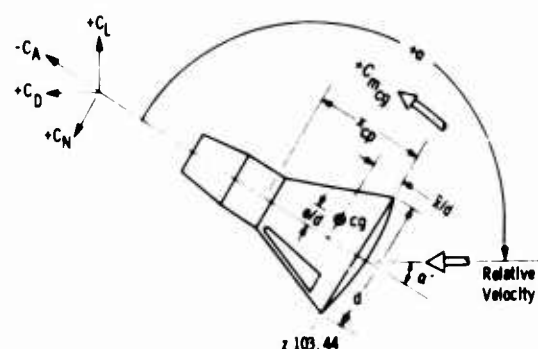


Fig. 7 Gemini 3 Spacecraft - Orientation of Forces and Moments

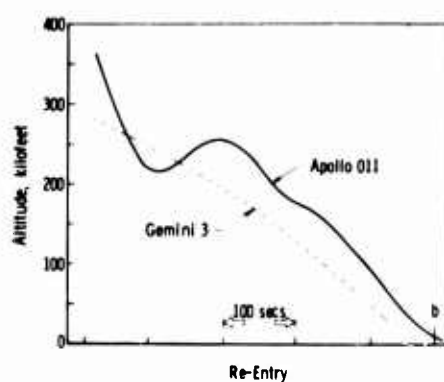


Fig. 8 Re-Entry Trajectory of Apollo 011 and Gemini 3

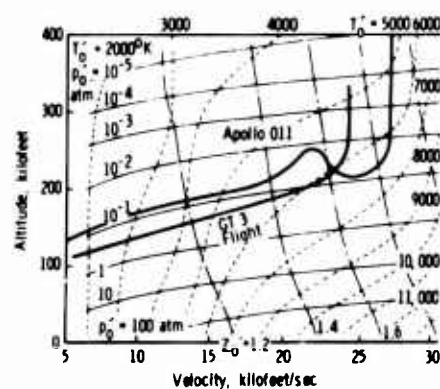


Fig. 9 Normal Shock Stagnation Conditions at Flight Duplication

a very blunt body such as the Apollo CM is the flow which is separated from the free-stream by the bow shock wave.

If the bow shock is strong everywhere ($M_\infty \sin \theta_b \gg 1$), the density ratio ϵ approaches the limit $(\gamma-1)/(\gamma+1)$ and the flow quantities immediately behind the shock become dependent upon only ρ_∞ , U_∞ , and σ .* In addition, the local Mach number M_2 is always a low subsonic value with only about a 2 percent variation between $M_\infty = 10$ and 25. The shock Reynolds number Re_{2d} may be expressed as

$$\begin{aligned} Re_{2d} &= \rho_2 U_2 d / \mu_2 \\ &= (\rho_\infty U_\infty d) / \mu_2 \end{aligned}$$

where d is the characteristic length chosen as the diameter of the heat shield in the present case.

An improved parameter would be one which would account for wall temperature effects (Ref. 8) such as:

$$Re_{wd} = (Re_{2d}) \mu_2 / \mu_w$$

However, lack of adequate wind tunnel and flight wall temperature values and the fact that

$$\mu_\infty / \mu_2 \text{ wind tunnel} \approx \mu_\infty / \mu_2 \text{ flight}$$

in the present case suggests that Re_{2d} should be an adequate correlation parameter between flight and wind tunnel data as long as the free-stream Mach number is high. However, the present data show that the Apollo Command Module aerodynamics are sensitive to variations in free-stream Mach number below a value of approximately fourteen. The data also indicate that above a Re_{2d} value of about 10^4 the aerodynamics of the module are insensitive to further increases in Reynolds number.

Flight values of Re_{2d} for Apollo mission AS-202 are shown in Fig. 10. The velocity profile from the flight data was used in conjunction with the 1962 standard atmosphere and the viscosity values of Ref. 9 and Ref. 10 for the calculation of Re_{2d} . Calculations based on flight values of free-stream pressure and temperature gave essentially the same results. For the flight data, real gas normal shock relationships from Lewis and Burgess (Ref. 10) were employed. VKF wind tunnel data reduction programs include calculation of shock Reynolds number. Nominal facility test conditions (for Apollo) obtained during the present investigation are indicated in Fig. 10 and tabulated in Table 2 to illustrate the regions of flight simulation achieved. Figure 11 compares both the Mach number (M_∞) and Reynolds number variation (Re_{2d}) of mission AS-202 with the facility test conditions. Note that although a variation of nearly five orders of magnitude in Reynolds number is shown, actual Mach number and Reynolds number simulation are achieved only at $M_\infty = 6$ and 8. However, it will be shown that this lack of simulation, although undesirable, is not serious.

The basis of the correlation presented in this report (for the Apollo) is illustrated in Fig. 12. When the pitching-moment data from the present investigation at a given angle of attack are plotted versus Re_{2d} , a consistent trend at values of Re_{2d} above 10^4 does not exist. However, plotting the same data ($Re_{2d} > 10^4$) versus Mach number presents a consistent variation. The other aerodynamic data (C_N , C_A) on the Apollo CM exhibit similar trends. The wind tunnel data at values of $Re_{2d} < 200$ were at Mach numbers of 9.4 and 10.2 (see Fig. 11). However, the strong viscous effects in this regime should make variations in free-stream Mach number rather insignificant.

The lack of a comprehensive set of wind tunnel data on the Gemini configuration prevented a similar type correlation. To circumvent this problem, approximate inviscid values of C_N and center of pressure ($X_{c.p.}$) were obtained by extrapolation of existing data. The reader is referred to Ref. 2 for additional details and information on the correlation procedure used for the Gemini data.

5.0 WIND TUNNEL DATA CORRELATION

The AEDC-VKF data are correlated over a free-stream Reynolds number range of 234 to 1.9×10^6 based on heat shield diameter and a Mach number range of 2.98 to approximately 20. Typical basic data are shown in Fig. 13. The resulting correlations are shown in Figs. 14 through 16. The data points presented represent fairings of the basic data.

*Neglects effects of shock and boundary layer merging at the higher simulated altitudes.

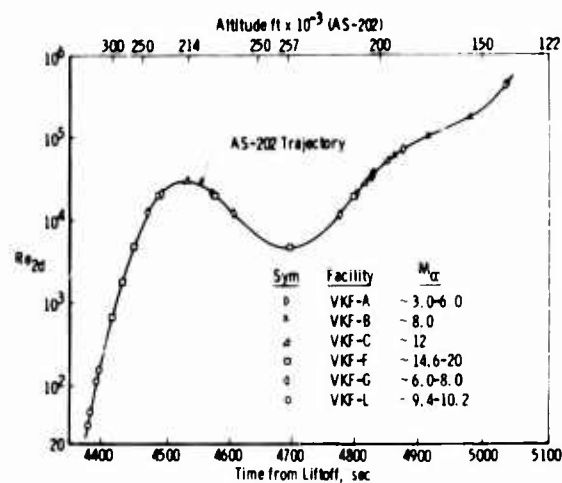


Fig. 10 Shock Reynolds Number Flight Simulation, Apollo

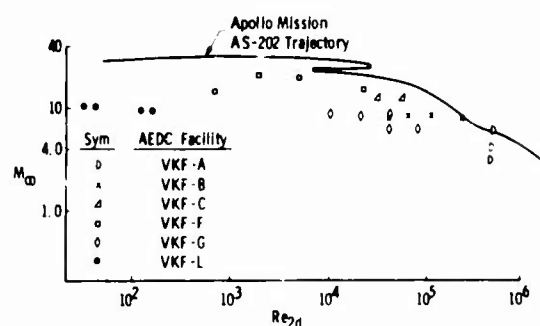


Fig. 11 Mach Number and Shock Reynolds Number Flight Simulation, Apollo

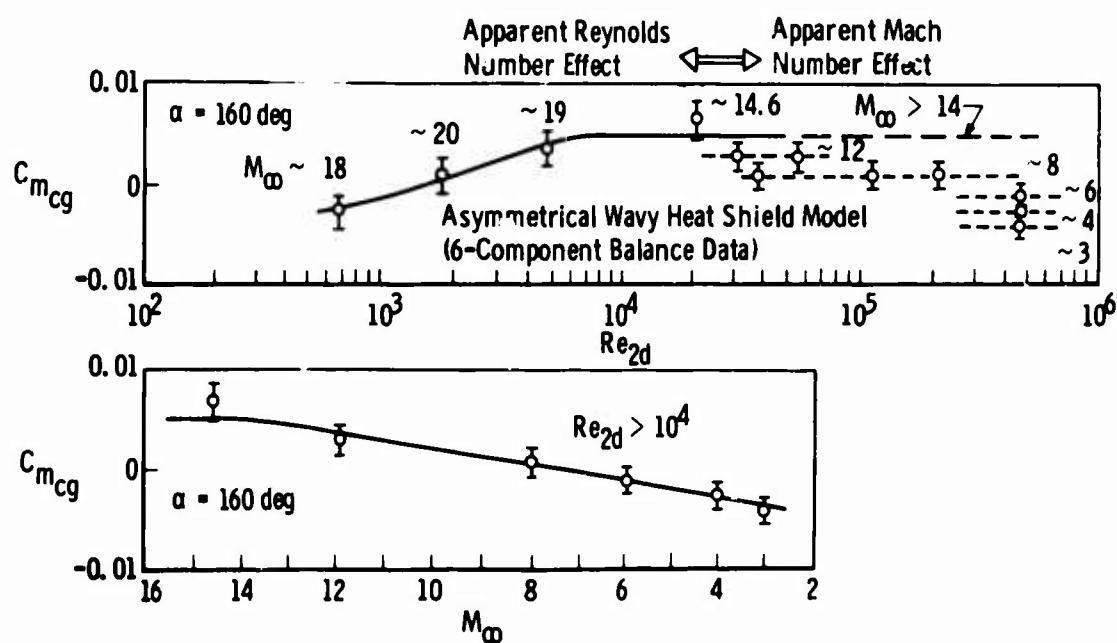


Fig. 12 Typical Data Plot Showing Basis of Data Correlation, Apollo

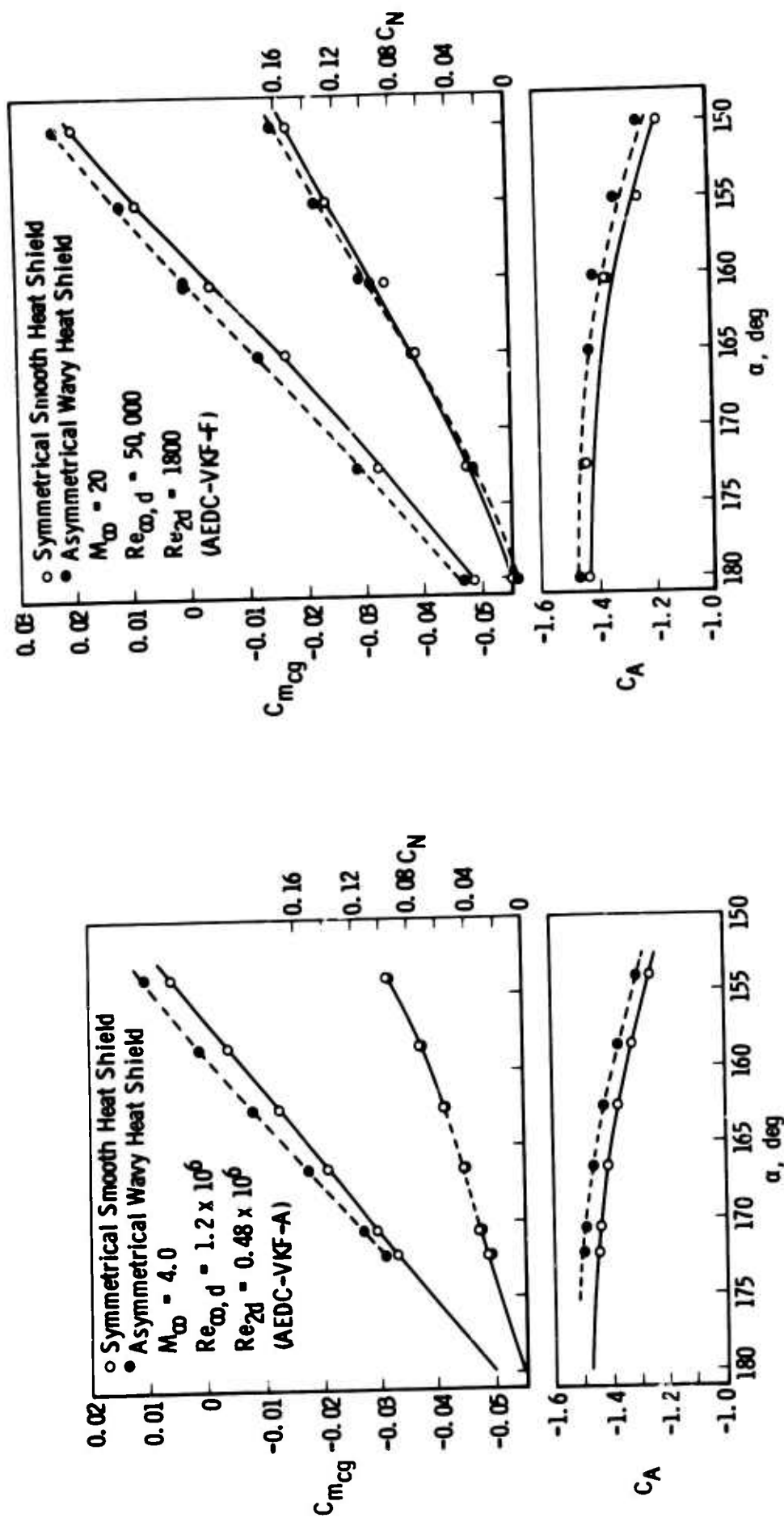


Fig. 13 Typical Basic Data, Apollo

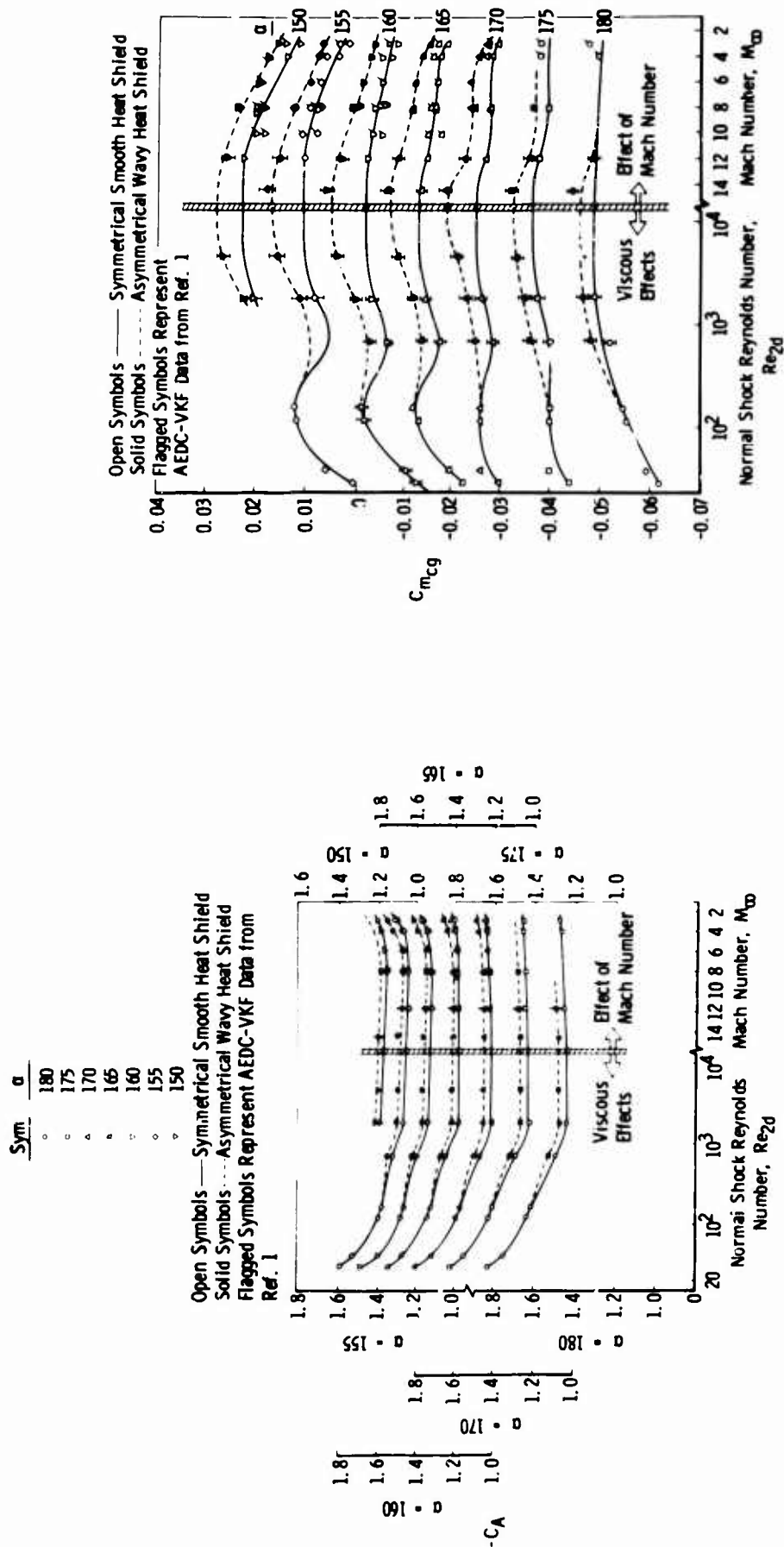


Fig. 14 Variation of Axial-Force Coefficient (C_A) with M_∞ and Re_{2d} , Apollo

Fig. 15 Variation of Pitching-Moment Coefficient ($C_{m_{cg}}$) with M_∞ and Re_{2d} , Apollo

Figure 14 shows the variation of the axial force coefficient of the Apollo CM with Re_{2d} and Mach number. Note the significant increase in C_A at values of Re_{2d} below 1000 and the slight increase at the lower free-stream Mach numbers. The reference area of the symmetrical smooth heat shield is used in data reduction which, in part, accounts for the higher axial force of the asymmetrical wavy heat shield configuration. Model scale limitations did not permit the asymmetrical wavy heat shield to be studied at low values of Re_{2d} . Therefore, the aerodynamics of the symmetrical and asymmetrical models are assumed to be identical below a Re_{2d} of 200 since viscous effects should dominate in this flow regime.

Significant variations in the pitching moment ($C_{m_{cg}}$) of the Apollo CM with Reynolds number, Mach number and heat shield configuration are shown in Fig. 15. The effect of the asymmetrical wavy heat shield is greater at the high Mach number-high Reynolds number flight condition ($M_\infty \geq 14$ and $Re_{2d} \geq 5000$) which represents a major portion of Apollo flight AS-202. Additional data in this important test regime would have been helpful.

The normal force coefficient (C_N) is presented in Fig. 16. Viscous effects are significant below a Re_{2d} value of about 7000 whereas variations of C_N due to Mach number are generally slight. The asymmetrical wavy heat shield causes a decrease in the normal force (C_N) only at angles of attack between 170 and 180 degrees.

The lack of a comprehensive set of wind tunnel data on the Gemini configuration prevented an analysis identical to the Apollo. However, a systematic analysis was possible by working with the center of pressure ($X_{c.p.}$) instead of the moment coefficient $C_{m_{cg}}$. A summary of the C_N and $X_{c.p.}$ correlation versus Re_{2d} is presented in Fig. 17. Note the near order-of-magnitude decrease in C_N between the lower Re_{2d} data and the predicted inviscid level; note also the sudden rearward shift in center of pressure when Re_{2d} was increased from 2400 and 5400. The Apollo data will exhibit a similar trend if plotted in the same manner.

6.0 RESULTS AND DISCUSSION

6.1 APOLLO SPACECRAFT FLIGHT-WIND TUNNEL COMPARISONS

A comparison between the Apollo AS-202 flight trim angle of attack and wind tunnel data is presented in Fig. 18. Note the good agreement of the asymmetrical wavy model wind tunnel data with the flight test data over the regime of trimmed flight. The correlation was made by using Re_{2d} as the correlation parameter from re-entry to an altitude (177,000 ft) at which $M_\infty = 14$ was reached and a Mach number correlation below this altitude. The correlation curves were obtained by cross plots of Fig. 15. The flight test data were obtained from the paper by Hillje (Ref. 3). The post-flight symmetrical model correlation along with the pre-flight estimate (Ref. 3) are given for completeness. The pre-flight estimate was based on previous symmetrical model data. A summary of the lift-to-drag ratios (L/D) for Flight AS-202 is shown in Fig. 19. Again, good agreement is noted between the flight and asymmetrical wavy model wind tunnel data. The offset CG of spacecraft 011 changes during the final re-entry phase due, in part, to fuel usage. The effect of this variation on the correlated wind tunnel data is also shown in Figs. 18 and 19.

Figure 20 compares the present trim angle of attack and corresponding L/D to Apollo Mission AS-202 flight data. However, the comparative data are shown as functions of Re_2 and M_∞ rather than flight time, as used in Figs. 18 and 19, to illustrate the strong viscous influences found in the present study. The strong viscous influence found in the present study is also illustrated in Fig. 21.

In order to determine if the wind tunnel data were free of significant sting effects, several models were launched in the 1000-ft Range G at AEDC-VKF. A comparison of the free-flight Range G data with the wind tunnel data is shown in Fig. 22. Note the good agreement and apparent lack of sting effects.

6.2 GEMINI SPACECRAFT FLIGHT-WIND TUNNEL COMPARISONS

The comparison between the Gemini 3 flight test data and the AEDC-VKF wind tunnel data is shown in Fig. 23. Excellent agreement is noted between the two sets of data. The increase in the predicted trim angle-of-attack curve that occurs near an altitude of 240,000 ft is caused by the center-of-pressure shift shown in Fig. 17. The Gemini 3 flight data do not indicate the increase; however, flight data from GT2 and GT4 give some indication that the shift in center of pressure exists (see Ref. 2). Langley Mach 6.89 data (Ref. 2) are also in excellent agreement with GT3 flight data. The Langley data are correlated on a Mach number basis since insufficient data were available for correlating this lower Mach number with the high Mach number correlation of Fig. 17. A summary of the lift-to-drag ratios versus angle-of-attack for two flight regimes is given in Fig. 25. The Gemini flight and Tunnel F data are in excellent agreement.

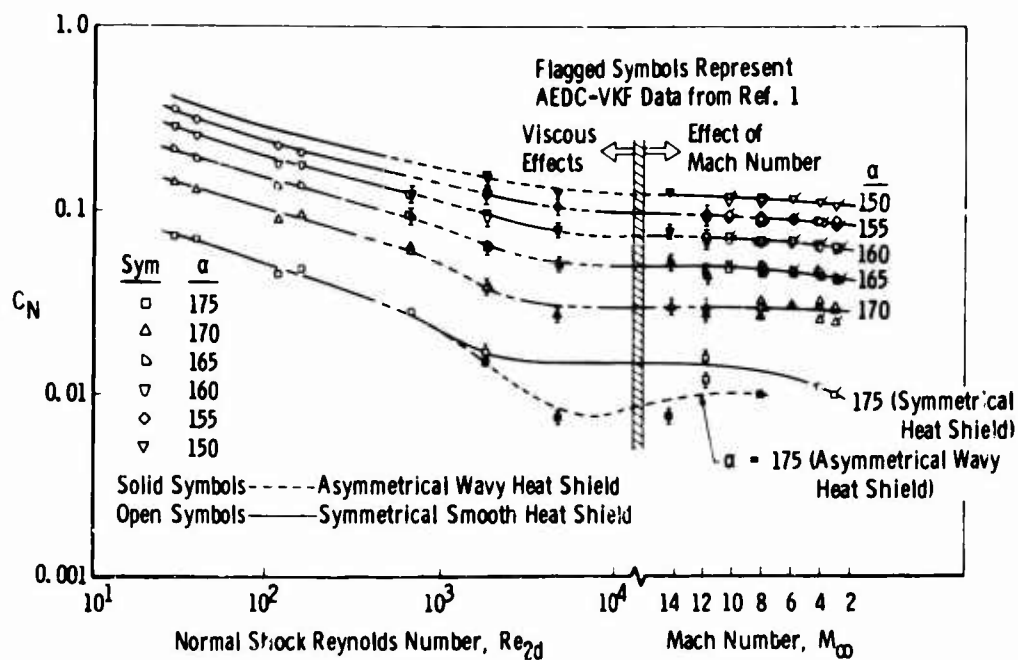


Fig. 16 Variation of Normal-Force Coefficient (C_N) with M_∞ and Re_{2d} , Apollo

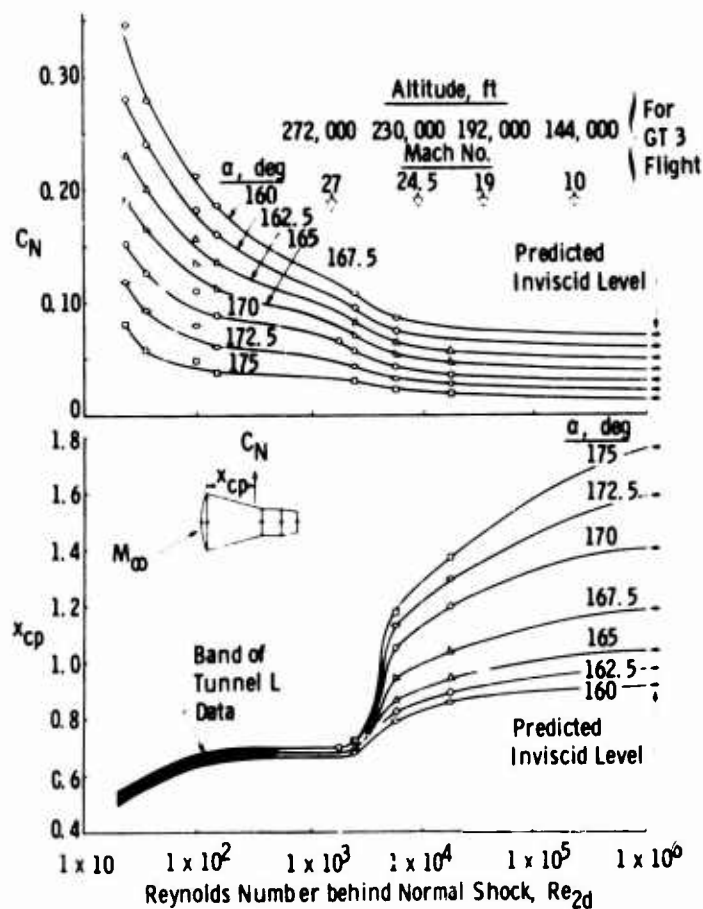


Fig. 17 Correlated Wind Tunnel Data on Gemini

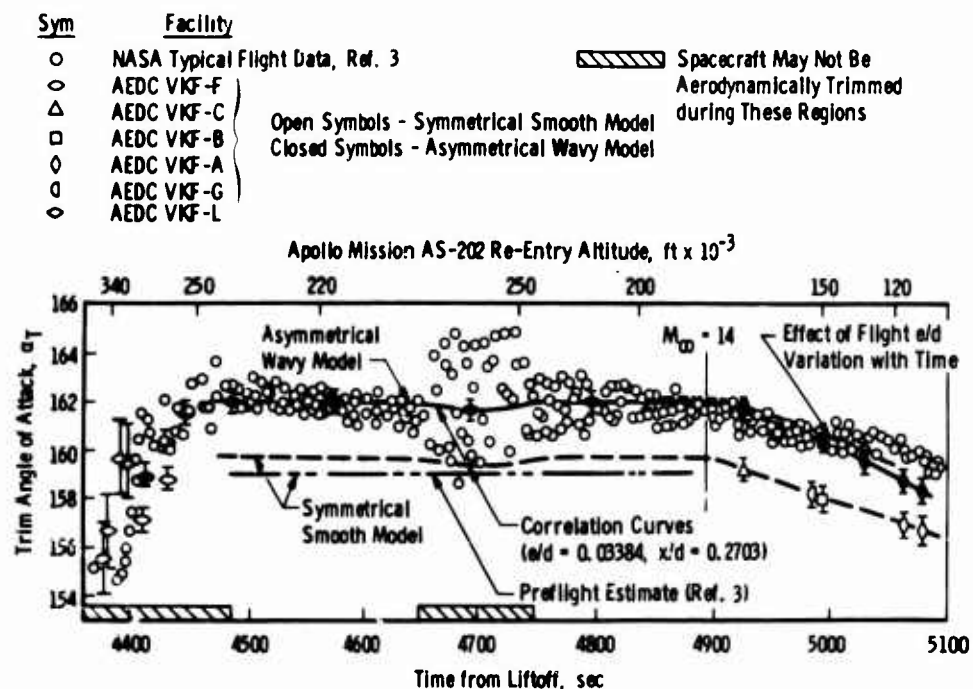


Fig. 18 Comparison of Mission AS-202 Trim Angle of Attack with AEDC-VKF Tunnel Data

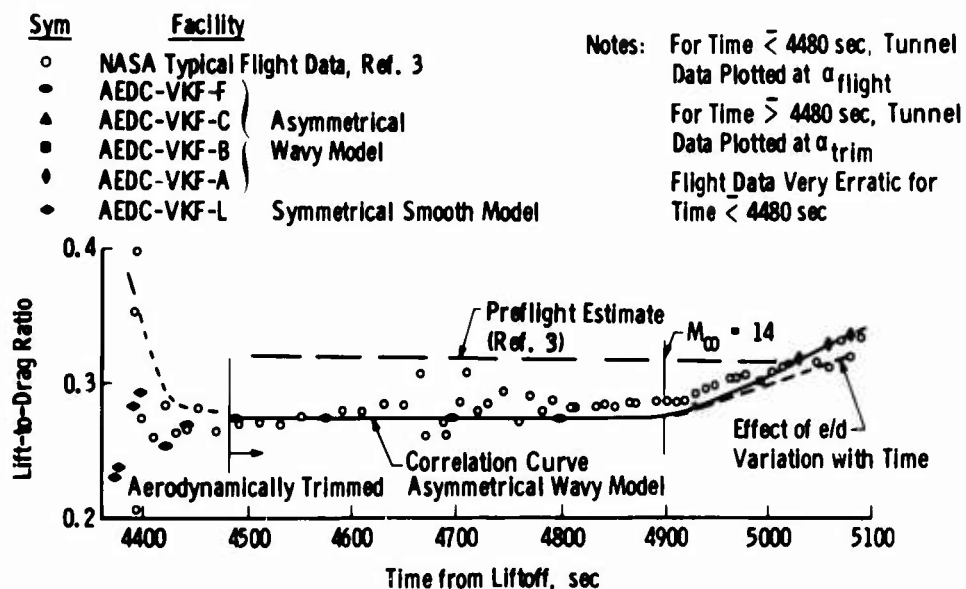


Fig. 19 Comparison of Mission AS-202 Lift-to-Drag Ratio with AEDC-VKF Tunnel Data, Apollo

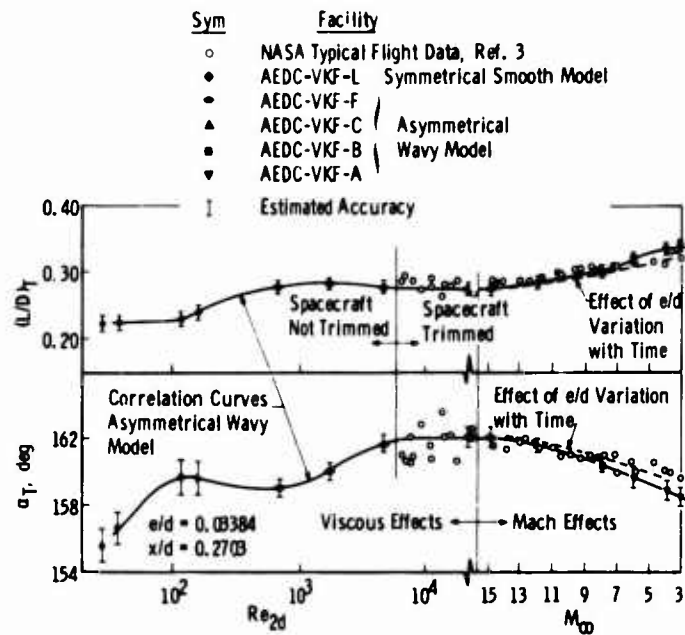


Fig. 20 Summary of Apollo L/D and α_T Data

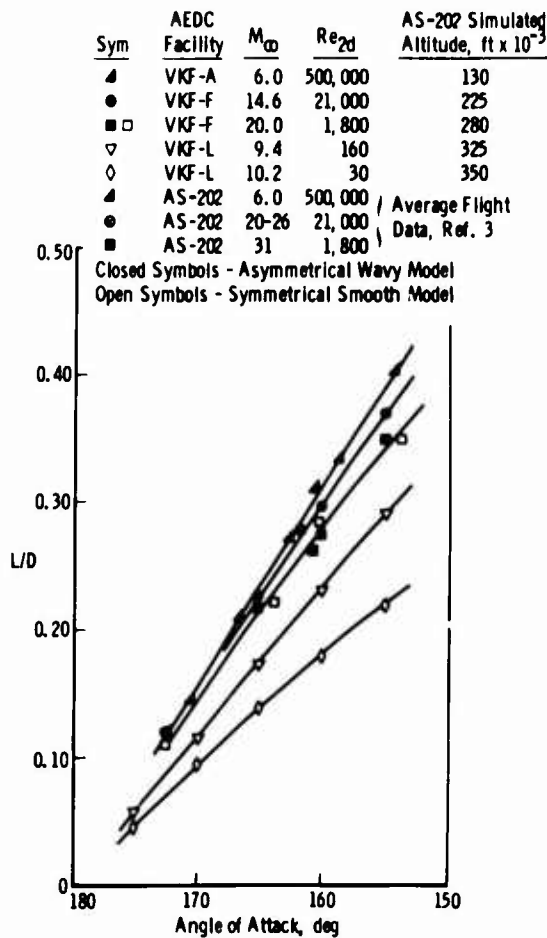


Fig. 21 Effect of Mach Number and Shock Reynolds Number on Lift-to-Drag Ratio, Apollo

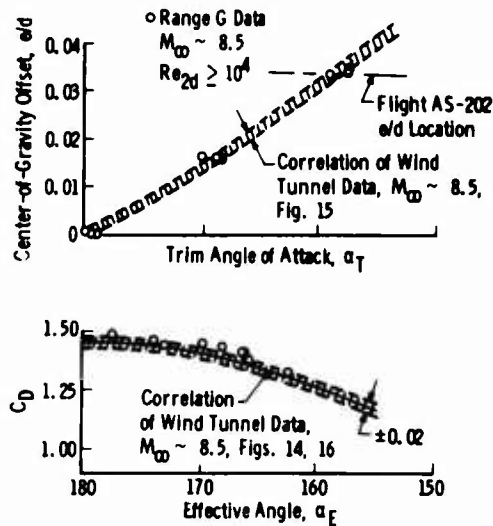


Fig. 22 Comparison of Free-Flight (AEDC-Range G) to Sting Mounted Tunnel Data

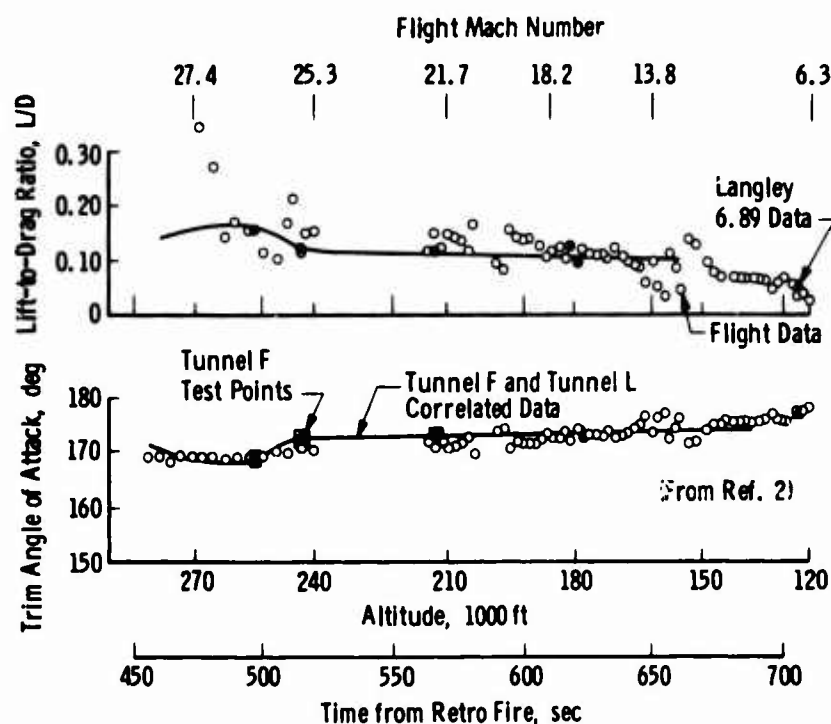


Fig. 23 Comparison of Gemini 3 Flight Data with AEDC and Langley Wind Tunnel Data

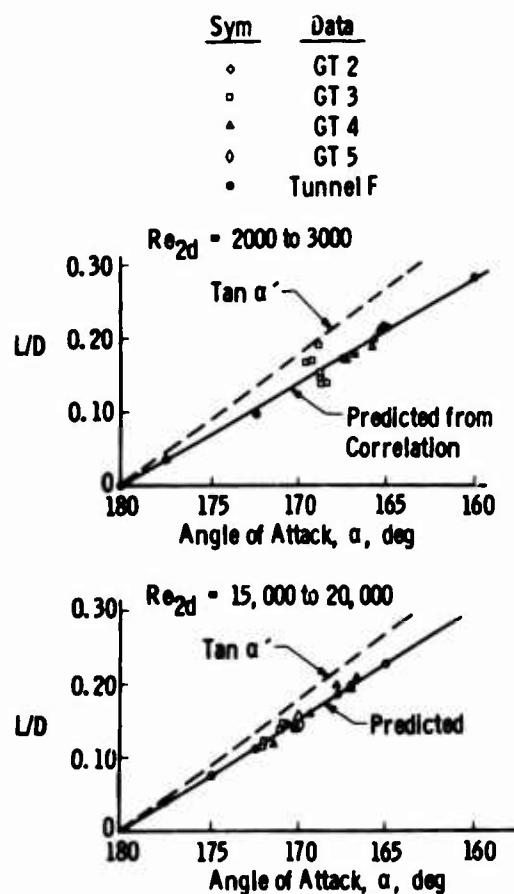


Fig. 24 Comparison of Flight and Tunnel F Lift-to-Drag Ratios for the Gemini

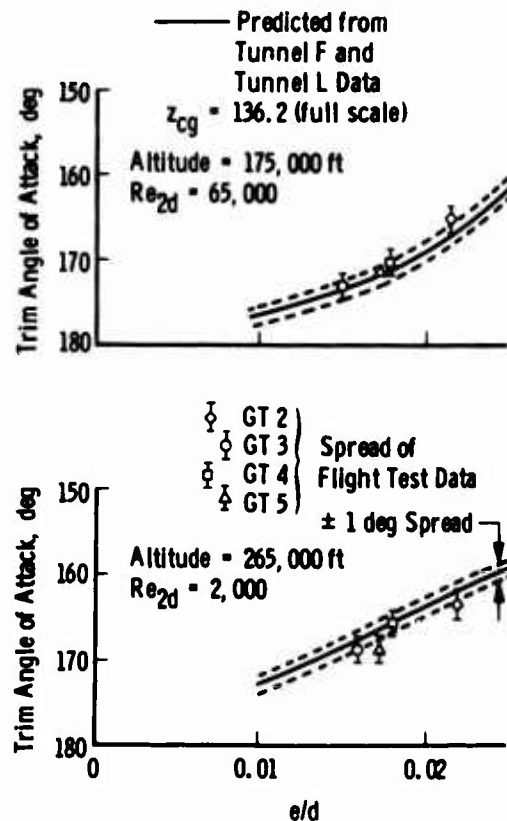


Fig. 25 Comparison of Flight and Wind Tunnel Data for Various Values of e/d

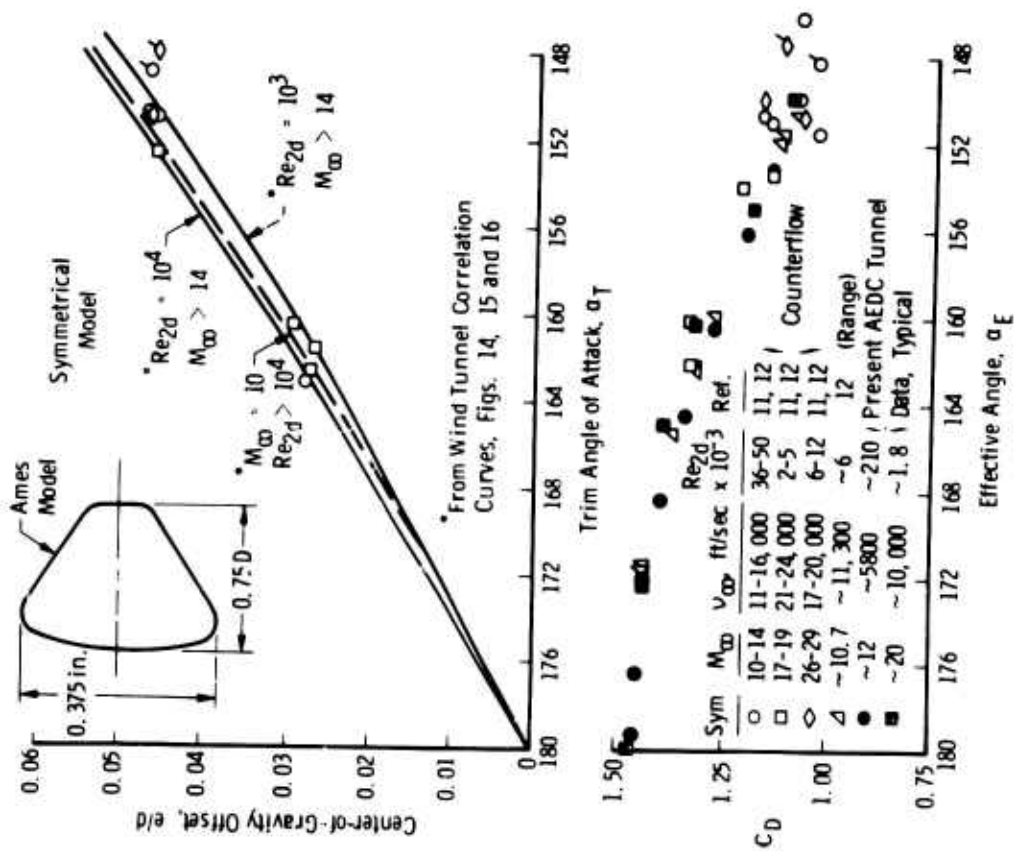


Fig. 27 Comparison of Ames Free-Flight (Counterflow) and AEDC Wind Tunnel Data

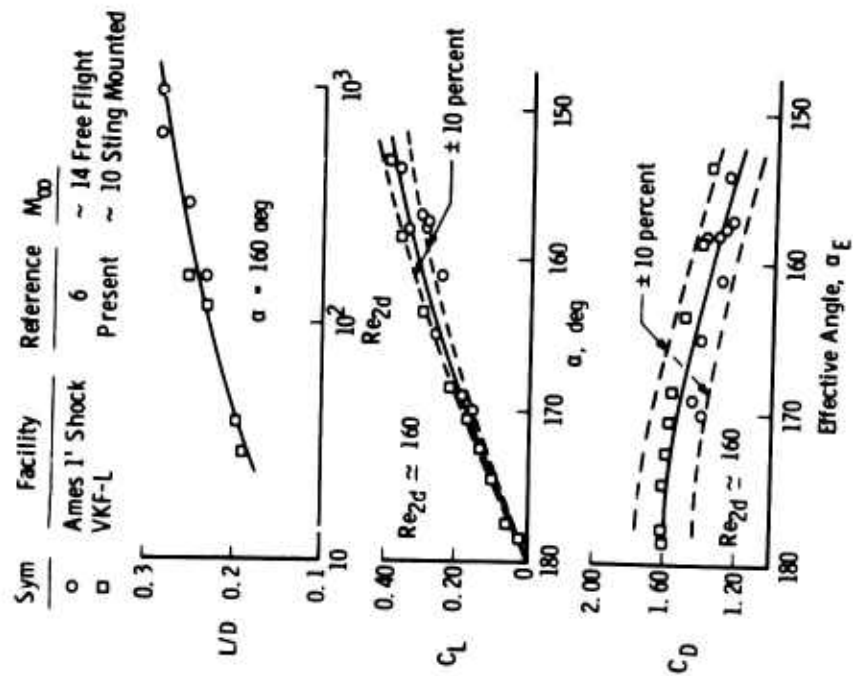


Fig. 26 Comparison of Free-Flight (Ames Shock Tunnel) to Sting Mounted Tunnel Data

The flight test trim angles are plotted in Fig. 25 versus the cg offset (e/d) associated with a number of flights. The data are shown for Re_{2d} values of 2000 and 65,000 and indicate the consistency of the flight results. The trim angle for GT5 at the lower value of Re_{2d} is noted to be somewhat low when compared to the other flights.

6.3 COMPARISON OF AMES FREE-FLIGHT DATA AND AEDC WIND TUNNEL DATA

The low density free-flight data of Horstmann and Kussoy (Ref. 6) from the Ames 1-ft shock tunnel are compared to the AEDC-VKF Tunnel L sting mount data in Fig. 26. Again, as noted in Fig. 24 for the higher density VKF-Range G data, no apparent effect of the support sting is noted.

To investigate the effect of velocity, Mach number, and Reynolds number, DeRose (Ref. 11) measured the trim angle and drag coefficient of Apollo Command Module at speeds up to 24,000 ft/sec in the Ames Counterflow facilities (also see Ref. 12). These data are compared with the AEDC-VKF wind tunnel data in Fig. 27. No apparent effect of velocity, Mach number or Reynolds number is noted. Also general agreement with the AEDC-VKF data is noted, again indicating no apparent sting effects in the AEDC data. An average of the Ames data (at $e/d \sim 0.046$) would indicate a slightly lower trim angle than the tunnel data. The shortened version of the Apollo Command Module used in the Ames tests would have a tendency to produce this trend in the data.

7.0 CONCLUDING REMARKS

Post-flight investigations were undertaken in order to obtain static stability characteristics of the Apollo Command Module "as flown" during flight AS-202 and the Gemini 3 spacecraft. The principle conclusions of the investigation can be summarized as follows:

1. The influence of the ablator (heat shield) geometry causes a significant change in trim angle-of-attack and resulting decrease in available lift-to-drag ratio.
2. A very strong viscous influence exists on the Apollo Command Module in the initial portion of re-entry extending down to an altitude of about 220,000 feet.
3. The Mach number influence extends upwards to a value of about 14 which is substantially higher than previous blunt body investigations have indicated.
4. Based on the agreement between wind tunnel data, where real gas effects were not simulated, and both aeroballistic range and full scale flight data, where real gas effects were present, it may be concluded that real gas effects on the static stability of the Apollo Command Module are not significant at velocities up to 27,000 ft/sec.
5. Generally, excellent agreement exists between the Gemini flight test data and data from the AEDC and Langley wind tunnel facilities. The resulting comparison shows how useful a systematic and carefully analyzed wind-tunnel program could be in the prediction of flight aerodynamics of re-entry spacecraft.

ACKNOWLEDGEMENTS

The authors wish to acknowledge contributions to this research work by many of their colleagues at the von Kármán Gas Dynamics Facility (VKF), AEDC. Among the many who assisted in this work, L. K. Ward of the Supersonic Branch (VKF), R. H. Burt of the Hypersonic Branch (VKF), W. R. Lawrence of the Aerophysics Branch (VKF), and W. S. Norman of the Hypervelocity Branch (VKF), contributed materially in obtaining and analyzing the experimental results. The authors are also grateful to Bass Redd and Ralph Graham of the NASA Manned Space Center for providing helpful information and encouragement during the course of the research and to Jack D. Moote of North American Aviation for providing the pertinent details of Apollo Spacecraft 011.

NOMENCLATURE

AWTTP	Apollo Wind Tunnel Test Program
C_A	Axial force coefficient
C_D	Drag force coefficient
C_L	Lift force coefficient
CM	Command Module

$C_{m_{cg}}$	Pitching-moment coefficient referenced to Apollo Mission AS-202 CM center of gravity (see Figs. 6 and 7)
C_N	Normal force coefficient
C_∞	Chapman-Rubesin viscosity coefficient ($\mu_w/\mu_\infty = C_\infty T_w/T_\infty$)
d	Maximum diameter of Apollo or Gemini Command Module (CM)
e	Center of gravity offset from CM centerline (see Figs. 6 and 7)
e/d	Ratio of offset to CM diameter
L/D	Lift-to-drag ratio
M_2	Mach number downstream of a normal shock
M_∞	Free-stream Mach number
p'_o	Pressure, normal shock stagnation conditions
Re_{2d}	Reynolds number downstream of a normal shock based on CM diameter
$Re_{\infty,d}$	Free-stream Reynolds number based on CM diameter
r	Diameter of model sting (see Fig. 5)
T'_o	Temperature, normal shock stagnation conditions
T_w	Wall temperature
T_∞	Free-stream temperature
U_2	Velocity downstream of a normal shock
U_∞	Free-stream velocity
\bar{v}_∞	Viscous interaction parameter defined as $M_\infty(C_\infty/Re_{\infty,d})^{1/2}$
X	Distance aft of heat shield (see Figs. 5, 6, and 7)
$X_{c.p.}$	Ratio of longitudinal center of pressure location to CM diameter
\bar{x}	Center of gravity location measured longitudinally from aft heat shield (see Figs. 6 and 7)
\bar{x}/d	Ratio of longitudinal center of gravity location to CM diameter
Z	Model or spacecraft station (Gemini)
z	Distance normal to centerline of spacecraft (see Fig. 6)
α	Angle of attack, body axis
α_E	Effective angle of attack = $\sqrt{(180 - \alpha)^2 + \beta^2}$
α_T	Trim angle of attack
α'	$180 - \alpha$
β	Angle of sideslip, body axis
γ	Ratio of specific heats
θ	Angle of model sting referenced to centerline of model
θ_b	Local inclination angle of body
λ_2	Mean free path downstream of a normal shock
μ_∞	Free-stream viscosity
μ_2	Viscosity downstream of a normal shock
μ_w	Viscosity based on wall temperature
ρ_∞	Free-stream density

ρ_2	Density downstream of a normal shock
ϕ	Reference angle of orientation of Apollo heat shield (see Fig. 3)
σ	Shock inclination angle

REFERENCES

1. Moseley, William C., Jr., Moore, Robert H., Jr. and Hughes, Jack E. "Stability characteristics of the Apollo command module," NASA TN D-3890, March 1967.
2. Griffith, B. J. "Comparison of aerodynamic data from the Gemini flights and AEDC-VKF wind tunnels," AIAA J. Spacecraft, Vol. 4, No. 7, pp. 919-924, July 1967.
3. Hillje, Ernest R. "Entry flight aerodynamics from Apollo mission AS-202," NASA TN D-4185, October 1967.
4. Postlaunch Report for Mission AS-201, MSC-A-R-66-4, May 6, 1966.
5. Moseley, William C., Jr. and Martino, Joseph C. "Apollo wind tunnel testing program-historical development of general configurations," NASA TN D-3748, December 1966.
6. Horstmann, C. C. and Kussoy, M. I. "Free-flight measurements of aerodynamic viscous effects on lifting re-entry bodies," AIAA Paper No. 67-165, Presented at the 5th Aerospace Sciences Meeting, January 23, 1967.
7. Whitfield, Jack D. and Griffith, B. J. "Hypersonic viscous drag effects on blunt slender cones," AIAA J., Vol. 2, No. 10, October 1964, pp 1714-1722.
8. Potter, J. Leith "The transitional rarefied-flow regime," Rarefied Gas Dynamics (C. L. Brundin, ed.), Vol. 2, pp. 881-937, Academic Press, New York, 1967.
9. Yos, Jerrold M. "Transport properties of nitrogen, hydrogen, oxygen, and air to 30,000°K," AVCO Report RAD-TM-63-7, March 1963.
10. Lewis, Clark H. and Burgess, E. G., III "Altitude velocity table and charts for imperfect air," AEDC-TDR-64-214 (AD 454078), January 1965.
11. DeRose, Charles E., Ames Research Center, Private communications, December 1967.
12. Seiff, Alvin "Current and future problems in earth and planetary atmosphere entry," AIAA Paper 67-803 (1967).

TABLE 1
POST FLIGHT APOLLO (AS-202)
WIND TUNNEL PROGRAM

(1) EFFECT OF ASYMMETRY HEAT SHIELD AND SIMULATED PRESSURE PADS	AEDC-VKF Tunnels A,B,C and F $M_\infty = 3, 4, 8, 12, 15$ to 20
(2) EFFECT OF FLIGHT ANGLE	$\alpha = 180^\circ$ to 150° (All Tunnels)
(3) MACH NUMBER EFFECTS	$M_\infty = 3, 4, 6, 8, 10, 12, 15$ to 20
(4) EFFECT OF REYNOLDS NUMBER	$Re_{2d} = 29$ to 500,000 (All Tunnels)
(5) POSSIBLE STING EFFECTS	$M_\infty \sim 8$ AEDC-VKF Range G AEDC-VKF Tunnel B

TABLE 2
NOMINAL TEST FLOW CONDITIONS

a. APOLLO

VKF FACILITY	M_∞	$Re_{\infty d}$ $\times 10^{-3}$	Re_{2d} $\times 10^{-3}$	VKF FACILITY	M_∞	$Re_{\infty d}$ $\times 10^{-3}$	Re_{2d} $\times 10^{-3}$
A	6.0	1900	500	C	12.0	730	55
	4.0	1200	480		12.0	420	30
	3.0	870	470	G	6.0	240	80
B	8.0	1800	210		8.5	170	40
	8.0	1000	110		6.0	120	40
	8.0	600	65		8.0	90	20
	8.0	360	40		8.5	50	10
F	14.6	380	21.	L	9.4	1.28	0.16
	19	110	4.7		9.4	0.96	0.12
	20	50	1.8		10.2	0.31	0.04
	18	14	0.68		10.2	0.23	0.03

b. GEMINI

F	15	300	18	L	9.2	1.28	0.15
	19	155	5.4		9.2	0.80	0.10
	20	70	2.4		10.2	0.29	0.32

Langley 11-in. hypersonic (Test Gas - Air)

6.9 360 5

MODULAR HYPERSONIC INLETS

WITH CONICAL FLOW

S. MÖLDER *

J.M. ROMESKIE **

McGILL UNIVERSITY

* Associate Professor, Department of Mechanical Engineering

** Research Engineer, Department of Mechanical Engineering.

SUMMARY

A series of requirements is established for the design of high performance hypersonic air intakes. A method, based on axisymmetric conical flow, is presented for the design of axisymmetric and non-axisymmetric air intakes. Theoretical estimates of the performance of these intakes is presented along with computer drawings of inlet shapes. Geometric construction of modular inlets is presented.

Experimental results are given for an axisymmetric Busemann inlet tested in a gun tunnel at a Mach number of 8.33 and a unit Reynolds number of 6×10^6 per foot. Results of surface static pressures and oil streaks are presented. The surface contour is corrected for a laminar boundary layer displacement thickness and the corrected results are given. Total pressure recoveries are measured.

A modular inlet design is described. This inlet is tested in the gun tunnel. Surface pressure, surface flow visualization, and total pressure recovery results are given.

MODULAR HYPERSONIC INLETS WITH CONICAL FLOW

1. INTRODUCTION

Thermodynamic cycle calculations have shown that the performance of a high Mach number air-breathing engine is critically dependent on the efficient performance of the air intake. It is thus important to have a systematic method for the design of high performance inlets. Before examining such a method, consider a list of desirable qualities for a high performance air intake :

1. The intake should start easily, should not unstart and should operate with steady flow throughout.
2. The intake should have a specified capability in that it should decrease the Mach number, or increase the static pressure, a given desired amount.
3. The task specified in 2. should be performed as efficiently as possible. This efficiency may be measured by total pressure recovery or kinetic energy efficiency and losses in efficiency are due to boundary layers and shock waves. For hypersonic intakes the capability and efficiency are both important considerations since the parameters used to measure them determine aerodynamic performance. The above three qualities are the most important considerations in intake design.
4. It is further desirable to have the flow direction at the exit of the intake in line with the combustion chamber. Another requirement is usually a uniform velocity profile at the exit.
5. From the design standpoint, it is desirable to deal with inlet flows which are easily theoretically predictable.
6. It is desirable not to have performance deterioration with a change in flight Mach number.
7. A change in angle of attack should not produce a performance decrement.
8. There should be no flow spillage within a given operating range of Mach number and angle of attack.
9. The external drag should be as small as possible.
10. There should be a minimum contribution to side forces at angle of attack since these forces would in general be aerodynamically destabilizing because of the intakes forward location.
11. The inlet should be able to withstand high internal pressures, high accelerations and high heat transfer loads. These requirements are not in general compatible with variable geometry.

It is difficult to visualize an inlet possessing all these qualities, because a practical design would invariably compromise one requirement in favour of one or more others. For example, in order to withstand heat transfer the inlet leading edges would have to be blunted. Blunting would create local strong shocks with ensuing loss in total pressure recovery. Another example is that in order to decrease side loads and boundary layer losses one would shorten the intake. However, this would result in higher leading edge shock losses and flow starting difficulties. Thus, no single inlet can be designed to satisfy all requirements completely and a given design entails the making of a series of compromises to achieve an inlet which is best suited for a given mission.

Inlet starting is of paramount importance since an unstarted inlet will result in a lower thrust as well as a greatly increased external drag. Firstly, quasi-steady-state starting can be accomplished by either over-speeding the inlet or by a flow area change (area change is equivalent to flow spillage). Overspeeding is effective only if the inlet has an area ratio (A_0/A_j) less than 1.666 (Ref. 13). This area ratio is not sufficient for a high performance hypersonic inlet, ten to twenty being typical useful area ratios. Thus overspeeding is not a practical method for starting hypersonic inlets. Starting by a change in area would involve going from say $A_0/A_j = 15$ down to at least 1.666. This is likely to pose mechanical problems especially for internal axisymmetric flows. Flow spillage through internal perforations or over the edge of a cowl remains as the only practical solution. It is thus important to perform part of the compression externally so that flow may be spilled during starting. For this reason the modular inlet assumes added importance, in that external compression is employed which allows flow spillage and inlet starting. Yet the design of the modules is such that a simple calculable flow develops after starting has occurred.

This paper presents a theoretical method of finding the inlet geometry required to satisfy the first five aerodynamic requirements listed above. Boundary layer characteristics and losses are then calculated. A method is described whereby portions of axisymmetric conical flows are used to construct non-axisymmetric inlets with swept leading edges. Experimental performance of such inlets is presented.

2. THEORY OF CONICAL FLOWS

The general method of characteristics is not always suitable for internal flow calculations because of the likely formation of Mach discs and consequent mixed flow. Furthermore, the method of characteristics is oriented towards finding the flow over a given body. In a practical intake design, however, one is more interested in finding the body surface shape to produce a desired flow. We make use here of a flow type which was first proposed by Busemann (Ref. 1). This flow was also discussed in Ref. 2 and applied to air inlets in Ref. 3. The flow is internal and has both axial and conical symmetry (Fig. 1). The freestream flow passes through an isentropic compression and then through a conical shock.

Compression is initiated at the freestream Mach angle, and it is isentropic and conically symmetric (i.e. conditions along a ray from the origin "O" are constant.) In this region, the Mach waves start from the surface, bending backwards to intercept the shock wave. Since the shock reflection and Mach waves cancel each other, the flow downstream of the shock is uniform and parallel to the freestream. The flow downstream of the shock may be subsonic or supersonic, depending on whether the conical shock is strong or weak. An inlet can be designed by calculating the aforementioned flowfield and choosing any stream surface as the wall of the inlet duct. An inlet of this type is called the Busemann inlet.

This flow obeys the Taylor-Maccoll equation (Ref. 3,4) for axisymmetric conical flow. The terms U_R and U_θ represent the radial and tangential velocities, nondimensionalized with respect to the escape speed (Fig. 1).

$$U_R^2 (U_R + U_R') = (\gamma - 1)/2 (1 - U_R^2 - U_\theta'^2) \times (U_R'' + U_R' \cot \theta + 2 U_R) \quad (1)$$

where U_θ is obtained from the irrotationality condition,

$$U_\theta = U_R' = dU_R/d\theta \quad (2)$$

This second-order nonlinear differential equation for U_R as a function of θ requires two boundary conditions for a complete solution. These are provided by specifying: 1) the value of the shock angle θ_s and the Mach number M_2 upstream of the shock, and 2) the condition that the flow downstream of the shock is parallel to the freestream flow. Equation (1), together with the two boundary conditions, can now be solved for U_R and U_θ in terms of θ . Once this is done, one can find all the additional useful variables, including the streamline shapes.

Fig. 1 is a drawing of a sample inviscid contoured inlet which diffuses from a freestream Mach number M_∞ of 8.33 to a Mach number M_3 of 5.39 behind the free-standing conical shock. The shock angle θ_s is 12.05, and the Mach number M_2 upstream of the shock is 5.80. The total pressure recovery $P_{t3}/P_{t\infty}$ is .992, the velocity ratio V_3/V_∞ is .9571, and the area ratio A_∞/A_3 is 6.71.

Fig. 2 is a summary of many calculations of the type previously described. For a given freestream Mach number (M_∞) and Mach number after diffusion (M_3), one can find the total pressure recovery, inlet area ratio, and Mach number in front of the shock. The regions of weak and strong shocks occur for $M_3 > 1$ and $M_3 < 1$, respectively. It should be emphasized that this plot is for design point operation as far as freestream Mach number, flow direction, and inlet geometry are concerned, and that no inferences can be made from these results to off-design operation. The inlet described by Fig. 1 is shown on Fig. 2 as a circle.

3. GEOMETRICAL CONSTRUCTION OF MODULAR INLETS

For steady inviscid flow the mathematical "boundary" conditions at a streamline or stream surface are the same as those at a solid wall. This means that a stream surface may be replaced by a surface without in any way affecting the flow contained by the original streamlines. This fact has acquired some practical significance for supersonic flows because the upstream extent of disturbances in supersonic flow is limited by the leading edge wave, thus requiring practical surfaces to extend downstream of the leading edge wave only. Portions of known flowfields have thus been used to construct delta wing shapes (Ref. 5) and even complete aircraft configurations (Ref. 6). An application to missile shapes by Maikapar is discussed in Ref. 7, and 8.

The method consists of tracing a closed curve on the leading edge wave of a known flowfield. In our case, the wave is a Mach wave and the flowfield is the Busemann diffuser flow. The shape of this curve in the front view is the shape of the freestream capture streamtube. From every point on this curve streamlines are traced back to the shockwave at the rear. The resulting

streamline sheet is now replaced by a solid surface, without in any way affecting the flow bounded by the surface. In our example we will choose the shape of the freestream capture area to be that of a 90 degree segment of a circle. This shape is now projected along the flow direction onto the leading edge Mach cone of the full Busemann inlet in such a way that the midpoint of the chord of the segment lies at the centre of symmetry of the original Busemann flow (Fig. 3). The streamline sheet traced back from the leading edge wave intersects the shock-wave at the rear in a similar segment which determines the cross-sectional shape at the exit flow. By this process the surface of a module is developed. Since the leading edges of the module lie in the Mach cone they are sonic leading edges, and consequently flow inside the module does not affect, nor is it affected by, flow outside the module. Thus, while still preserving the flow properties and streamline geometry determined by the full Busemann calculation, one can lay the bottom corners of four of these modules together to form a modular inlet with a circular external shape (Fig. 4). A missile with such an inlet would have four diametrically opposed combustion chambers located at the periphery of the cross-section thus leaving a central free volume. The swept leading edges alleviate problems caused by heat transfer and allow flow spillage and easier starting. Flow starting will be discussed further in section 5.3.

A computer program has been written to calculate and plot module shapes. This program starts by calculating the full Busemann inlet and continues with the geometrical construction described above. Sample plots are shown in Figures 5 and 6.

4.0 EXPERIMENTS ON FULL BUSEMANN INLET

4.1 Full Busemann Inlet without Boundary Layer Correction

All tests were conducted in the National Research Council's Hypersonic Gun Tunnel. The following nominal test conditions were used:

Model size : 2 inches in diameter, 8 to 12 inches long

Total conditions : temperature, $T_t = 2430^\circ\text{R}$; pressure, $P_t = 4800$ psi

Test section conditions : Mach number, $M_\infty = 8.33$; pressure, $p_\infty = 0.333$ psi;
temperature, $T_\infty = 1800^\circ\text{R}$; sp. heat ratio, $\gamma_\infty = 1.4$; Reynolds number per
ft., $Re_\infty = 6.0 \times 10^6/\text{ft.}$

Running time (5% variation in P_t) - 25 milliseconds

Time interval used for tests (2% variation in P_t) - 5 milliseconds

Variations from the nominal conditions from one run to another were too small to affect any nondimensional quantities. A description of this tunnel is given in Ref. 12.

The full Busemann inlet described in Fig. 1 was constructed and subsequently tested in the National Research Council's Hypersonic Gun Tunnel. Measurements of model surface static pressure are shown in Figure 7. The measured pressures are about 50% higher than predicted. There is also qualitative disagreement in that a rapid rise in pressure occurs at $x = 9.9$ inches. Two exploratory tests were performed at this point in order to discover the nature of the internal flow. First a 4 inch length of straight tube was manufactured to conform to the leading edge portion of the inlet. This was then tested with the aim of finding the location of the leading edge wave. At Mach 8.33 a Mach wave emanating from the leading edge would reach the centerline at $x = 9.09$ inches. It was observed, however, that the leading edge wave intersected the center line at $x = 6.5$ inches (Fig. 8). This indicated the presence of a significant shock - boundary layer interaction at the leading edge. It is observed however that the shock is straight which implies that the flow behind it has conical symmetry. Also the reflected shock cone appears straight and there is no visible Mach disc. If this shock system is superimposed on the Busemann inlet flow then the reflected shock meets the inlet surface at 9.9 inches (Fig. 9a). Such superposition is not entirely justified because in Busemann flow the reflected shock would lie in an already compressed flowfield, nevertheless the point of impingement of the weak reflected shock at $x = 9.9$ inches coincides with the observed pressure increase.

A technique of surface flow visualization was used to study the behaviour of the boundary layer along the compression surfaces of all inlets. The method of flow visualization makes use of oil dots of a discrete size (0.020 - 0.030 in diameter) which are evenly spaced over the model surfaces. (The oil dot is composed of a mixture of a low vapour pressure oil and lampblack.) The dot movement is related solely to the local surface shear stress. It is found to give an accurate description of the direction of the limiting streamlines and a good qualitative description of the distribution of the magnitude of surface shear stress. Separation lines, lines of flow attachment, and regions of reversed flow may be readily identified (Ref. 9).

It was found that the oil dot streak pattern, in conjunction with the pressure measurements provided a reliable method for deducing the internal flow structure. The flow picture, as constructed from these measurements is shown in Fig. 10. Discrepancies from the theoretical model are due to boundary layer effects. First, there is the leading edge shock boundary

layer interaction. The measured wave angle and pressure at the leading edge show that the interaction is produced by the equivalent of an average flow deflection of 3.7 degrees. The leading edge wave is reflected from the centre line to intercept the surface at 9.9 inches. The increase in skin friction at 9.9 inches as indicated by the oil streaks was attributed to boundary layer transition probably induced by the incident shock at this location. The second rapid rise in pressure, indicating the presence of another shock wave at the surface, is at 11.8 inches. The general higher level of pressure in the whole inlet is ascribed to the displacement effect of the laminar boundary layer. A displacement thickness correction was calculated and a new inlet was manufactured and tested. This is described in the next section.

4.2 Boundary Layer Corrections on the Full Busemann Inlet

In calculating the boundary layer characteristics one must select a method which accounts for compressibility effects, surface heat transfer and an adverse pressure gradient. With a Reynolds Number per foot of 6.0×10^6 , with high heat transfer to the wall and with the support of oil smear tests described in the previous section, it is reasonable to assume that the boundary layer remains laminar, at least up to the point where the reflected shock is incident on the inlet surface. Based on these considerations it was reasonable to apply the calculation method as described in Ref. 10. Since this reference is not yet generally available a brief description of the method follows: A reference temperature, defined by,

$$T_R = 0.5T_1 + 0.37M_1^2 T_1 + 0.5T_w,$$

is used to transform the compressible boundary layer equations into the incompressible form. These incompressible equations are then solved by a method, similar to Polhausen's method, described in Ref. 11. In the above equation subscript 1 denotes conditions at the boundary layer edge and w denotes wall conditions. The boundary layer edge conditions are calculated from the inviscid flow solution. These are shown in Fig. 1. The remaining quantities required for the boundary layer calculation were the tunnel freestream conditions as given in Section 4.1 and the model wall temperature, taken as $T_w = 300^\circ\text{K}$ (constant). Results of these calculations are presented in Fig. 11. These results show that due to the very high skin friction at the leading edge there is a rapid increase of all boundary layer thicknesses. In practice, the results near the leading edge would be modified by shock boundary layer interaction. Subsequently, in the first 6 inches, the relatively low skin friction and low adverse pressure gradient result in virtually no change in θ and only small changes in δ^* and δ . Because of compressibility, δ^* is actually decreasing slightly. The skin friction coefficient then decreases further and approaches zero at $x = 9.9$ inches and the program terminates calculations here indicating boundary layer separation. Curiously, this point is almost coincident with the rapid surface pressure and oil streak variations observed on the uncorrected model. In an attempt to apply the δ^* correction two problems appear: First, the unrealistically rapid variation of δ^* near the leading edge and secondly the unavailability of δ^* values beyond $x = 10$ inches. In solving the first problem, we use the results found from the straight tube experiment, described previously in Section 4.1, to correct the leading edge by cutting a negative 3.7 degree slope at the leading edge. This cut meets the calculated δ^* curve at $x = 1.6$ inches. From $x = 10$ inches the correction is as calculated. The second problem, beyond $x = 10$ inches, was solved by a reasonable extrapolation shown in Fig. 11. No prior justification exists except if the predicted separation is premature or if transition occurs then the extrapolated curve is not unreasonable. The inlet surface was corrected for δ^* as described above, it was then tested in the Gun Tunnel and the surface pressure, oil streaks and total pressure recovery were measured. Results are presented in Figures 7 and 9b. From Fig. 7, we see that there is now good agreement between the inviscid theory and measured surface pressure values. In particular the leading edge pressure is now down to the freestream value, the rapid rise at $x = 9.9$ inches has completely disappeared and the final value at $x = 12$ inches is 5% above that theoretically predicted. There appears a plateau of pressure when the reflected shock intercepts the surface at $x = 11.8$ inches. This could indicate the presence of a local region of separation or the possibility of a slightly oscillating shock wave.

Oil streaks are shown in Fig. 9. Fig. 9a is for the inlet without boundary layer correction and Fig. 9b is with a laminar boundary layer correction. Only the portions from $x = 6$ inches downstream are shown because upstream of this point there is no significant difference between the two traces. We note that the upper trace indicates a generally higher wall shear. In approaching $x = 11.8$ inches the shear increases substantially. At and beyond $x = 11.8$ inches the streak behaviour is not incompatible with the occurrence of transition. The seeming flow angularity is due to the fact that the oil dots were first placed on a flat paper tape which was then applied to the curved surface of the inlet. In fact, there is natural convergence of the boundary layer flow in this region. With the boundary layer corrected inlet the skin friction is lower and the flow seems smoother right to the exit at $x = 12.8$ inches. There are no obvious regions of separation for either of the two flows.

Pitot pressure was measured at the exit of the corrected Busemann inlet. These measurements were made on the centerline and 0.187 inches from the wall at $x = 12.5$ inches. The measured values were 165 and 179 psi, respectively. These measurements are compared with theory in the following table:

FULL BUSE- MANN INLET		PITOT PRESSURE P_{T4}	STATIC PRESSURE P_3	P_3/P_{T4}		M_3 IDEAL GAS at P_3/P_{T4} and $\gamma = 1.4$	P_{T4}/P_{T3}		P_{T3}	$\frac{P_{T3}}{P_{T\infty}}$	K_D	η_{KE}
				REAL GAS	IDEAL GAS		IDEAL GAS	REAL GAS	REAL GAS		IDEAL GAS	IDEAL GAS
EXPERI- MENT	Center- line	165 †	5.35*	0.0324	0.0329	4.82	0.0710	0.0640	2580.	0.538	.860	.9870
	3/16" from wall	179 †	5.35 †	0.0299	0.0304	5.02	0.0608	0.0549	3265.	0.681	.915	.9910
Theory $\gamma = 1.4$		195	5.17	0.0264	0.0264	5.39	0.0459	0.0414	4720.	0.983	.996	.9989

* ASSUMED
† MEASURED

In this table measured quantities and ratios of measured quantities are reduced to equivalent ideal gas values by the use of correction factors (Ref. 16). The purpose of this is to facilitate comparison with theory. From the table, we see that the static pressure is slightly higher than predicted, the Mach number is lower, and the total pressure recovery is lower. The value of K_D is unusually low here because it reflects the relatively low amount of compression (i.e. from $p_\infty = .333$ to $p_3 = 5.35$) that takes place in this inlet.

5.0 DESIGN, MANUFACTURE AND TESTING OF MODULAR INLETS

5.1 Design and Manufacture

The geometrical method for developing modular inlets meets with some difficulties when one tries to apply it to an actual design. The zero slope of the flow streamlines at the leading edge means that when modules are placed back-to-back an intolerably thin leading edge is required for a considerable leading edge length. The situation becomes even worse when a boundary layer correction is applied because then, for some distance downstream of the leading edge, the surface contours of adjacent modules actually overlap.

The only solution is to have a finite angle leading edge with its adherent shock losses. A finite angle leading edge can be had by simply removing the leading edge portion of the surface streamline contour to the point where the streamline angle is acceptable. Two questions immediately arise: What is acceptable and what are the effects of this truncation on the rest of the flow? An attempt will not be made to answer the first question here, because it involves consideration of structural and heat transfer loads and manufacturing techniques. In answering the second question recall the fact, that for small turning angles and weak shock waves the conditions produced by turning through an isentropic compression and a weak shock are nearly the same. Also a simple look at the geometry of the Busemann streamline will show that at a given flow deflection angle the relationship between freestream Mach number and the resulting finite surface angle is such that the resultant shock wave intercepts the axis of symmetry at the original centre of the conical flow. These two facts mean that removal of a portion of the leading edge contour has the effect of lowering the overall total pressure in the inlet by the amount of the leading edge shock loss without markedly affecting the remaining flow properties or wave structure.

Another difficulty arises when one examines the module shapes in Figures 5 and 6. These shapes, as evidenced by cross-sectional views, are truly three-dimensional, and consequently their manufacture presents considerable problems. In an attempt to circumvent the machining of general three-dimensional surfaces it was assumed that the cross-sectional shapes are almost coincident when their bottom corners are superimposed. This made it possible to use a single (specially shaped) milling cutter to cut four diametrically opposed flutes into an originally circular billet. The bottom corner of each cut was made to the shape of the original Busemann streamline. Another modification of geometry has to be made at the cowl for much the same reasons. Two cowls were manufactured from a straight circular tube (Fig. 4, 18). The external diameter of these cowls is 2.5 inches and their thickness is .0625 inches. Both have four V-cuts with V-angles of 25 degrees. The leading edges are sharp for both cowls. The significant

difference in the two cowls is that Cowl A has an internal leading edge chamfer of 30 degrees (7 degrees when measured in the freestream direction) (Fig. 18). Cowl B has an external chamfer of 30 degrees (Fig. 4). Cowl A was manufactured first because it provided a closer representation of the theoretical cross-section. It was found however that it caused starting difficulties and strong internal shock waves.

The resulting cross-sectional shapes are compared with those of the ideal modular shapes in Figures 5, 6. The largest difference occurs at the exit where, for the Modular Inlet, the actually machined area ratio is 10 to 1 whereas the calculated area ratio is 13 to 1. An attempt was not made to evaluate the effect of these departures from the ideal modular shape because the uncertainties in the boundary layer displacement thickness effects are large and would obscure any effects due to variations in wall geometry. It is noticed however, that a boundary layer correction would result in a larger geometric area in accord with the present geometric deviation.

The Modular Inlet shown in Fig. 4 was manufactured. This four-module Inlet was designed for a freestream Mach number of 8.33, it had an area ratio of 10 to 1 and a leading edge angle of 3 degrees. The outside diameter of the Inlet is 2.5 inches and its length is 8.08 inches. The basic flow conditions of this Modular Inlet are shown by a star on Fig. 2. The next section describes the testing of this Inlet in the NRC Gun Tunnel.

5.2 Test Conditions

The Modular Inlet was tested in the NRC Gun Tunnel at the nominal conditions listed in Section 4.1. In general, the observations consisted of surface static pressure measurements, surface flow visualization by oil streaks and schlieren or shadowgraph flow pictures. Pitot pressures were measured at the exit and some tests were performed at small angles of attack. Some exploratory tests were done to measure inlet drag and base pressure.

5.3 Inlet Starting

In the Gun Tunnel, the starting process is distinctly different in that the airflow suddenly sweeps over the inlet model, and the internal flow is established from the leading edge on downwards. Thus, there is no backpressure to impede flow starting and one would suspect the possibility of impulsively starting high area ratio inlets. This has been observed previously (Ref. 14, 15) as well as in this study. In fact the difficulties encountered with design of variable geometry models for short duration facilities are conveniently eliminated by impulsive flow starting. From our tests on both the axisymmetric and the Modular Inlet we found that the inlet with complete axisymmetric flow was started at an area ratio of 15.7 to 1 (20 to 1 would not start.) From this, it seems that there is no great effect of modules on the starting area ratio. Thus, one may assume that spillage does not play an important role in impulsive starting. In fact it may be that spillage does not even occur during impulsive starting. The above illustrates that impulsive starting is fundamentally different from quasi-steady flow starting and that results of impulsive starting conditions cannot be carried over to α -flight starting situations.

A shadowgraph of the unstarted Modular Inlet with Cowl A is shown in Fig. 12. Strong and unsteady shock waves can be seen emanating from the inlet center spike and the cowl apex. There is clearly a large amount of spillage. In this test, inlet starting was prevented by placing a physical obstruction at the exit. In addition to the unstarting caused by the 7° cowl leading edges, it was found that disturbances produced in one module (e.g., by static pressure tubing) would force adjacent modules to either spill flow or unstart. It was also found that a Module will not start when a large diameter (0.065") pitot tube is inserted at the exit plane.

Figure 13 shows the Modular Inlet with Cowl A at -4 degrees incidence, in this case the inlet is started in the sense that steady supersonic flow appears at the exit, but flow is spilling through the upper V-cut. In this case no strong shocks are emanating from the center spike. The bottom module facing away from the flow is started and is not spilling. Starting was not achieved at larger incidences.

The schlieren photograph shown in Fig. 14 illustrates the external shock structure of the fully started Modular Inlet with Cowl A. As spillage has not occurred, the external shock waves from the module leading edges are weak and lie close to the surface. A second shock wave can be seen at the inlet midsection. This shock wave emanated from the cowl apex. The boundary layer separation shown near the exit plane has been induced by a circumferential groove on the external cowl surface. Full view of the exit flow is obstructed by pressure tubing.

In Figures 13 and 14 starting was achieved by sharpening the leading edges from 7 degrees (measured with respect to the freestream) to approximately 2 degrees. Cowl B (with external chamfer) produced no starting difficulties. The reasons are that the internal shocks were weaker and the effective area ratio was reduced from 10.0 to 9.0.

5.4 Surface Flow Visualization

Oil dot surface flow visualization has been used to study the surface flow behaviour of a fully started inlet, an unstarted inlet, and a started inlet with spillage.

The flow visualization on the surface of the fully started Modular Inlet with no spillage is shown in Figure 15. At the leading edges dot movement is visible due to the high shear stress there. For a considerable distance beyond the leading edge, the surface shear stress is so low that either very little or no dot movement occurs. The surface shear stress starts increasing rapidly on the rear half of the inlet. Near the end of the compression surface, oil streaks are seen to coalesce indicating a separation line. Flow reattachment follows closely behind indicating a small region of separated flow. It seems plausible that this separation is due to a shock wave emanating from the cowl apex. At the horizontal exit section, a very weak separation line can sometimes be seen, indicating a possible shock reflection. The surface flow visualization on the Modular Inlet surface using Cowl B showed a smaller region of separated flow. This is expected, because the shock wave generated from the cowl apex is weaker and is due only to leading edge viscous effects.

The flow visualization on the unstarted inlet shown in Fig. 16, illustrates a recirculating flow with two vortex-like structures. The broadness of some of the dots indicates some flow unsteadiness.

A detailed study of the unsteady starting process of the Modular Inlet has not been undertaken.

The surface flow visualization on the started module with spillage exhibits a pattern of flow streamlines similar to those appearing on the surface of a fully started inlet with no spillage. The case of flow spillage, shown in Fig. 17, was obtained on the upper inlet module when the inlet was tested at -4 degrees angle of attack. The streamlines at half the body length exhibit a sudden upward curvature towards the apex of the cowl leading edges. It is apparent that this flow is approaching separation. The flow, unable to negotiate the increasing pressure gradients in this region, is forced to spill at the cowl apex. Further downstream, a pronounced separation line exists immediately followed by a line of reattachment. This separated region is due to the presence of a shock wave emanating from the cowl apex. Another line of separation occurs downstream, indicating a likely reflected shock wave. The oil streak lengths at the exit show a region of extremely high surface shear stress.

Flow visualization, applied to the internal surface of Cowl A, between the cowl apex and the exit plane is shown in Fig. 18. The resulting oil streak pattern shows two intense separation lines converging in a downstream direction at the inlet centerline. These separations are attributed to the second reflection of the shock wave from the cowl apex. Cowl B exhibited a similar separation region only located close to the exit plane.

5.5 Static Pressure Measurements

Static pressures were measured along the side wall of one module (see Fig. 17, for static pressure holes.) Measurements could not be made at the first six static holes because the presence of pressure tubing and instruments in adjacent modules caused spillage and unstarting of the module being surveyed. Measurements were made, at the 18 aft holes without disturbing the flow fields, by passing tubing through the walls between modules. At the limited wall thickness close to the leading edge prevented such procedures, no static pressure record is available from the first six holes. Static pressures measured in this region exhibited sudden increase immediately behind lines of separation. These increases in pressure, shown in Fig. 19, for both Cows A and B, confirm the presence of the internal shock wave emanating from the apex of the cowl. The static pressure measurements are compared with the theory of Equation 1 in Fig. 19.

Using Cowl A, the pressures measured at the central streamline, before the shock wave, are within 5% of the predicted values. The pressures behind the shock wave are not constant due to the presence of the reflected shock wave. This reflected shock wave, however, appears to be weak since pressures increase between 20 and 50%, whereas the incident shock wave increased the static pressures by 300%. Lower surface static pressures were measured using Cowl B. The static pressures measured at the central streamline, before the shock wave from the cowl apex, are within 6% of the predicted values. Due to the weak shock wave from the cowl the static pressure is increased by 100%. However, the static pressures at the end of the compression surface $x = 7.2$ inches differ by only 9% between tests using the two cowl.

The static pressure measurements made on only a portion of the compression and horizontal exit surface using Cowl A, shown in Fig. 19, are compared in Fig. 20, with the theory (Equation 1) and a method of characteristics solution for the entire surface. Good agreement between theory and experiment can be seen at $x = 7.0$ inches. Beyond this value, the static pressure shows a sudden increase in the region where separation was indicated by flow visualization.

From the measurements it appears that the shock is incident on the surface at a point ahead of the corner and that there is an expansion wave emanating from the corner. Thus, the pressures downstream of the corner exhibit a sudden decrease. Beyond this expansion, at $x = 7.96$, the pressures increase to within 7% of the predicted values.

Static pressures were measured on the internal surface of Cowl A, between the cowl apex ($x = 5.20$) and the exit plane. The static pressure between $x = 5.20$ and $x = 7.20$ remained relatively constant between 9 and 12 psi. At $x = 7.45$ and $x = 7.70$, behind the vertex of the separation, the static pressures were 44.0 and 48.0 psi, respectively. However, the static pressure increase across the shock wave still remained at approximately 300%.

5.6 Pitot Pressure Measurements

Some measurements of exit pitot pressures were made at $x = 7.70$ using Cowl A. The measurement of pitot pressure near the exit was made for two reasons. First, to determine the flow uniformity, and second, to estimate the inlet total pressure recovery, $(P_{t3}/P_{t\infty})$. A summary of pitot pressure measurements is given in Fig. 22.

Measurements made within the boundary layer showed a pitot pressure range between 138 - 174 psi. At approximately 0.070" from the walls near the edge of the boundary layer, pitot pressures were between 294 - 376 psi. The pitot pressure at the inlet centre was 350 psi. A measurement made on the internal cowl surface, immediately behind the vertex of the separation gave an extremely high pitot pressure of 595 psi. Additional pitot measurements in this plane exhibited only slight variations from the value of 350 psi.

An accurate determination of the total pressure recovery of this inlet cannot be obtained without measurement of the static pressure in the exit core. To measure the static pressures in the core of relatively uniform flow with any instrument larger than the cross-sectional area of a pitot tube (0.032"), would be sufficient to prevent inlet starting. Thus, at the exit, the wall static pressure of 16.4 psi was used. The pitot pressure associated with this static pressure measurement is 376 psi. A total pressure recovery, $P_{t3}/P_{t\infty}$, of 0.70 has been calculated by the same method as shown in the table of section 4.2.

6. CONCLUSIONS

A series of requirements for the design of high performance hypersonic air intakes has been outlined. A method has been developed for the rational design of a wide variety of hypersonic air inlet geometries. Inherent in the method is the prediction of all flow quantities, including the total pressure recovery and a uniform and parallel exit stream. The streamline tracing concept has been applied successfully to generate inlets with non-axisymmetric crosssections, swept leading edges and an ability to spill flow at off-design conditions.

Surface static pressure and qualitative shear measurements on an axisymmetric Busemann inlet show substantial effects of leading edge shock-boundary-layer interaction and boundary layer displacement thickness. The same measurements made on an inlet which has been corrected for these viscous effects show good agreement with theory, thus confirming the existence of the postulated conical inviscid flow as well as the correctness of the boundary layer displacement thickness estimations. However, separation, as predicted by the laminar boundary layer calculation, is not observed. The measured total pressure recovery of this inlet is between 0.54 and 0.68.

A modular inlet was tested at Mach 8.33. This inlet had an area ratio of 10 to 1 and reduced the Mach number to 4.14. The measured wall static pressures at the exit plane were within 7% of the theoretical values. Oil dot streaks indicated a region of low surface shear just aft of the leading edge. At -4 degrees angle of attack the module that was turned into the stream spilled some flow. Oil dots indicate that the unstarted flow in a partially blocked module is unsteady and has two vortex-like regions. The measured total pressure recovery of the fully started inlet was 0.70.

It was found that the oil dot streaks, in conjunction with the pressure measurements provided a reliable method for deducing the internal flow structure.

Impulsive starting in the gun tunnel is fundamentally different from quasi-steady flow starting. Results from impulsive starting cannot be carried over to free-flight starting conditions. The largest area ratio started in the present test was 15.7 to 1. It was observed that a high inlet efficiency was conducive to starting.

ACKNOWLEDGEMENTS

Dr. R.F. Meyer of NRC provided the use of the NRC Gun Tunnel, which was employed in all aero-dynamic tests. For this and for his many helpful suggestions - our sincere thanks.

The project was financially supported by NRC Grant A-4190 and The Johns Hopkins University Contract 271798.

REFERENCES

1. Busemann, A. Die Achsensymmetrische Kegelige Überschallströmung; Luftfahrtforschung, 19, 137-144; (1942)
2. Courant, R. Supersonic Flow and Shock Waves; Interscience Publishers Inc., New York; Friedrichs, K.D. (1948)
3. Mölder, S. The Busemann Inlet for Hypersonic Speeds; J. Spacecraft Rockets 13, 1303; Szpiro, E.J. (1966)
4. Taylor, G.I. The Air Pressure on a Cone Moving at High Air Speed; Proc. Roy. Soc., London, A139, 278-311; (1933) Maccoll, J.W.
5. Nonweiler, T. Delta Wings of Shapes Amenable to Exact Shock Wave Theory; J. Roy. Aero. Soc., 67, 39-40; (January 1963)
6. Jones, J.G. A Method for Designing Lifting Configurations for High Supersonic Speeds Using the Flow Fields of Non-Lifting Cones; Royal Aircraft Establishment Report No. Aero 2674; (March 1963)
7. Hayes, W.D. Hypersonic Flow Theory, Vol. I; Academic Press, New York; (1966) Probst, R.F.
8. Maikapar, G.I. On the Wave Drag of Nonaxisymmetric Bodies at Supersonic Speeds; J. Appl. Math. Mech. (Prikl. Mat. Mekh.) 23, 528-531; (1959)
9. Meyer, R.F. A Note on a Technique of Surface Flow Visualization; NRC, NAE Aero. Report LR-457; (July 1966)
10. Camarero, R. A Computer Program for Two-Dimensional and Axisymmetric Laminar Compressible Boundary Layer; McGill University, Mech. Eng., Technical Paper (1965)
11. Tani, I. On the Approximate Solution of the Laminar Boundary Layer Equations; J. Aero. Sciences, 487-495; (1954)
12. Meyer, R.F. The NAE Hypersonic Gun Tunnel: Part I: The Compression Heater; NRC, Et Al. NAE Aero. Report LR-432; (1965)
13. Hermann, R. Supersonic Inlet Diffusers and Introduction to Internal Aerodynamics; Minneapolis-Honeywell Regulator Company, Aeronautical Division, Minneapolis, Minn., (1956)
14. Carrière, P. O.N.E.R.A. Private Communication; (April 1967)
15. Hawkins, R. The Use of a Gun Tunnel for Hypersonic Intake Calibration; Bristol Siddeley Engines Limited, A.P.R.D., Report No. AP5477; (1967)
16. ----- Mach Number Tables ($\gamma = 1.4$) With Correction Factors for Real Air; General Dynamics, OAL Memorandum 147-1, CM 1036-1; (April 1964)

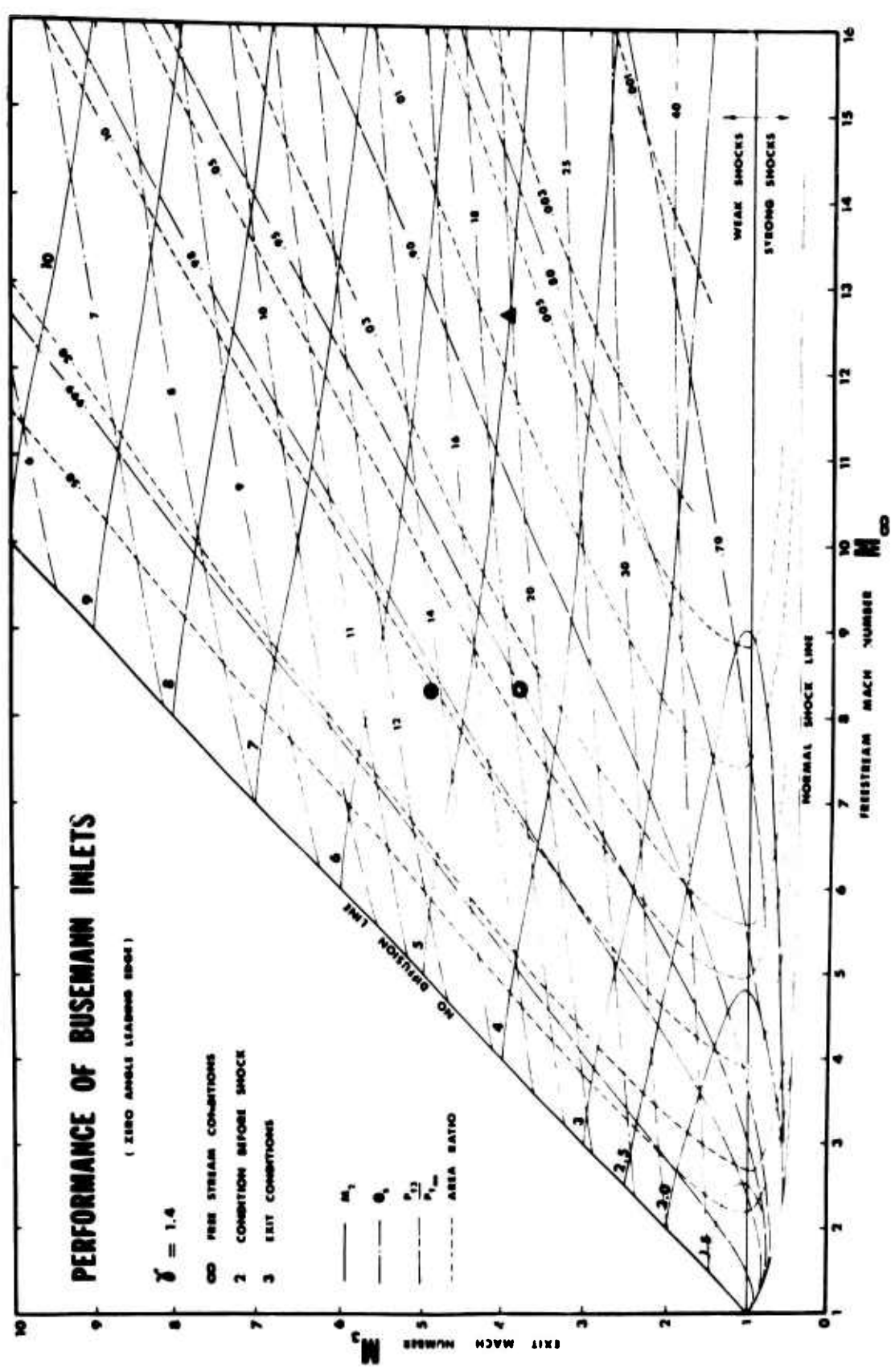


FIG.2 PERFORMANCE OF BUSEMANN INLETS

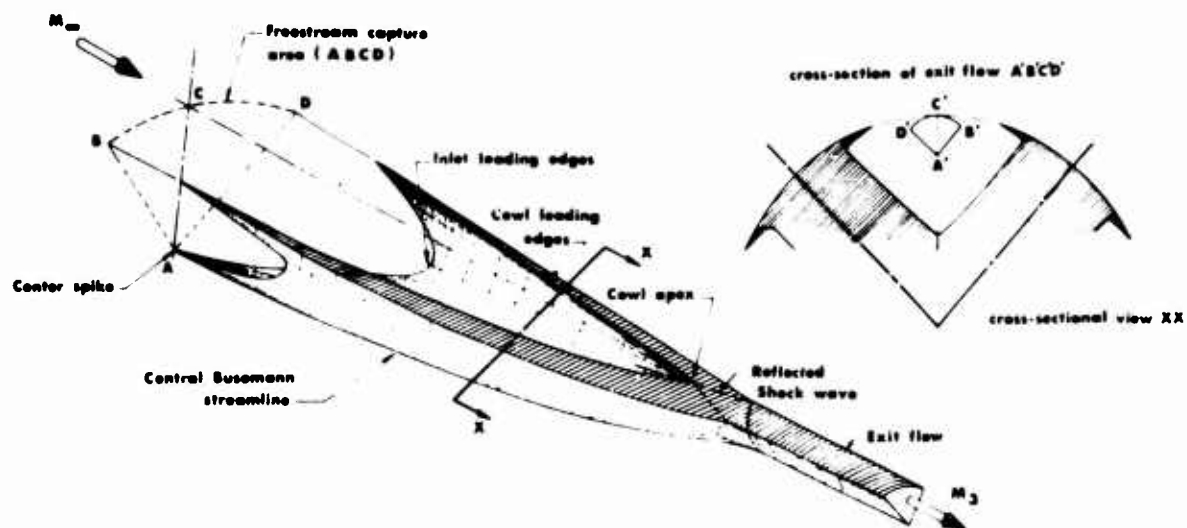


FIG. 3 STREAMLINE SHEET OF MODULAR INLET



FIG. 4 WIND-TUNNEL MODEL OF FOUR-MODULE INLET

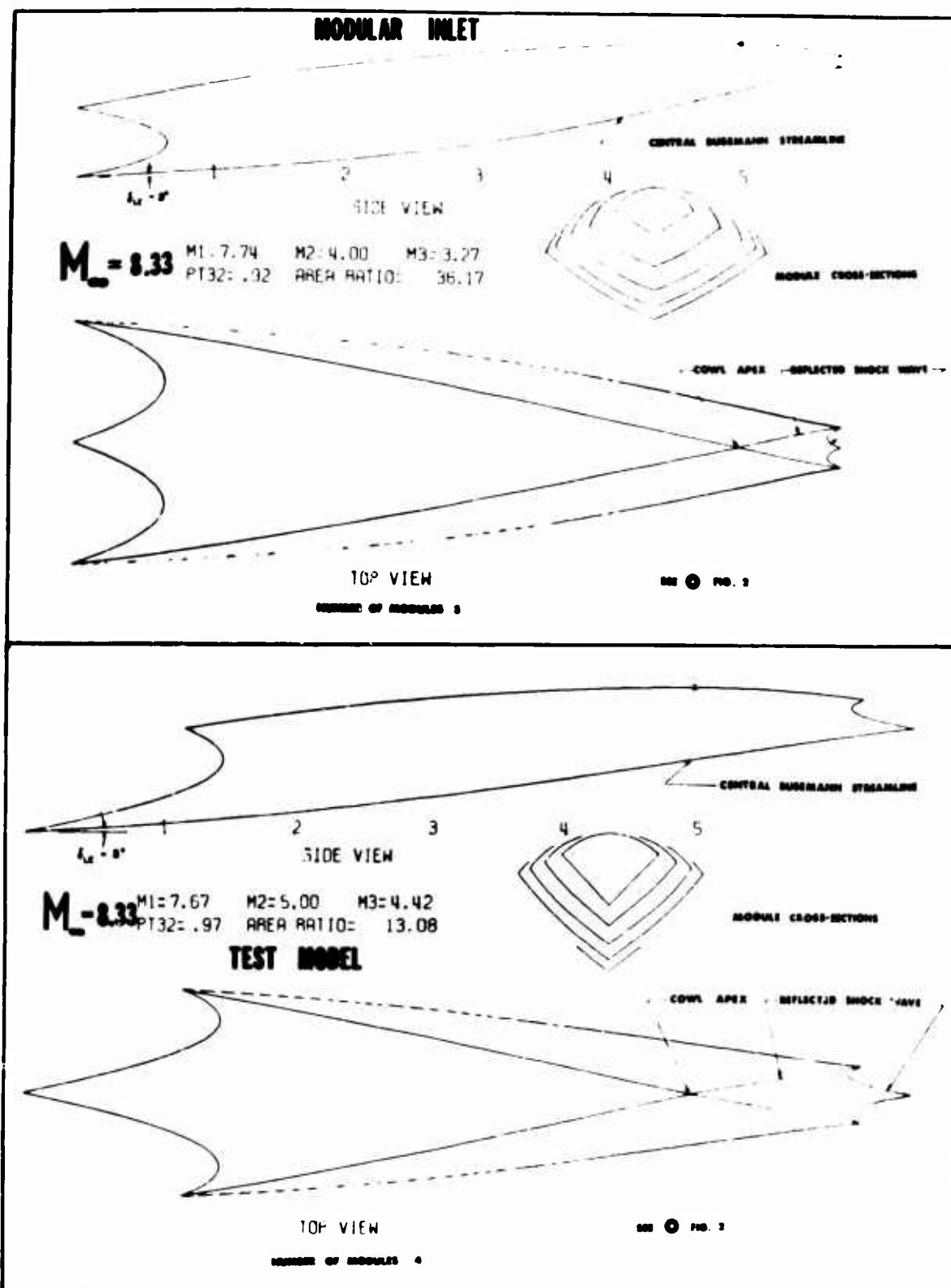


FIG. 5 COMPUTER DRAWING OF MODULAR INLET USED IN PRESENT EXPERIMENTS, TOGETHER WITH ITS THREE-MODULE COUNTERPART

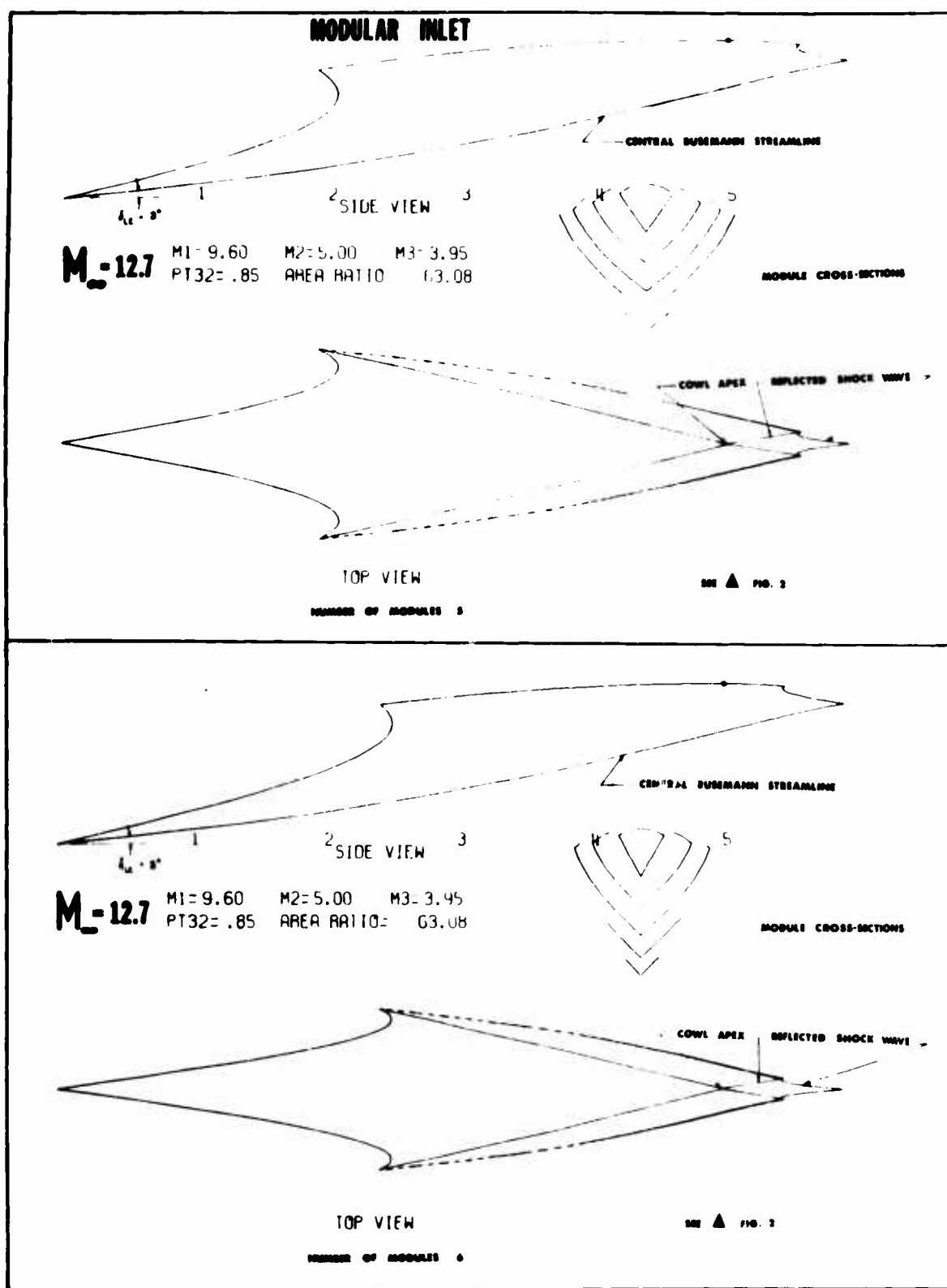


FIG. 6 COMPUTER DRAWINGS OF FIVE AND SIX-MODULE INLETS FOR $M_{\infty} = 12.7$

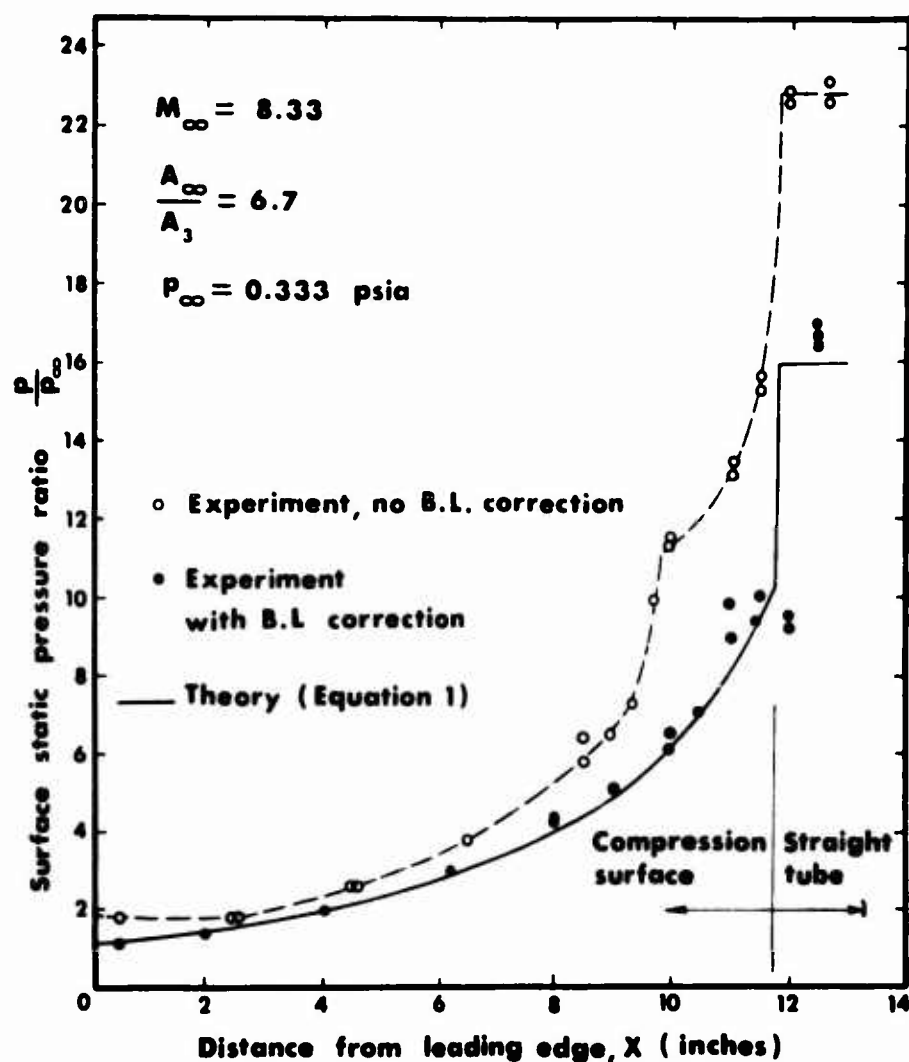


FIG. 7 PRESSURE DISTRIBUTION ON FULL BUSEMANN INLET



FIG. 8 SHOCK WAVES EMANATING FROM THE LEADING EDGE OF A STRAIGHT CIRCULAR TUBE AT MACH 8.33

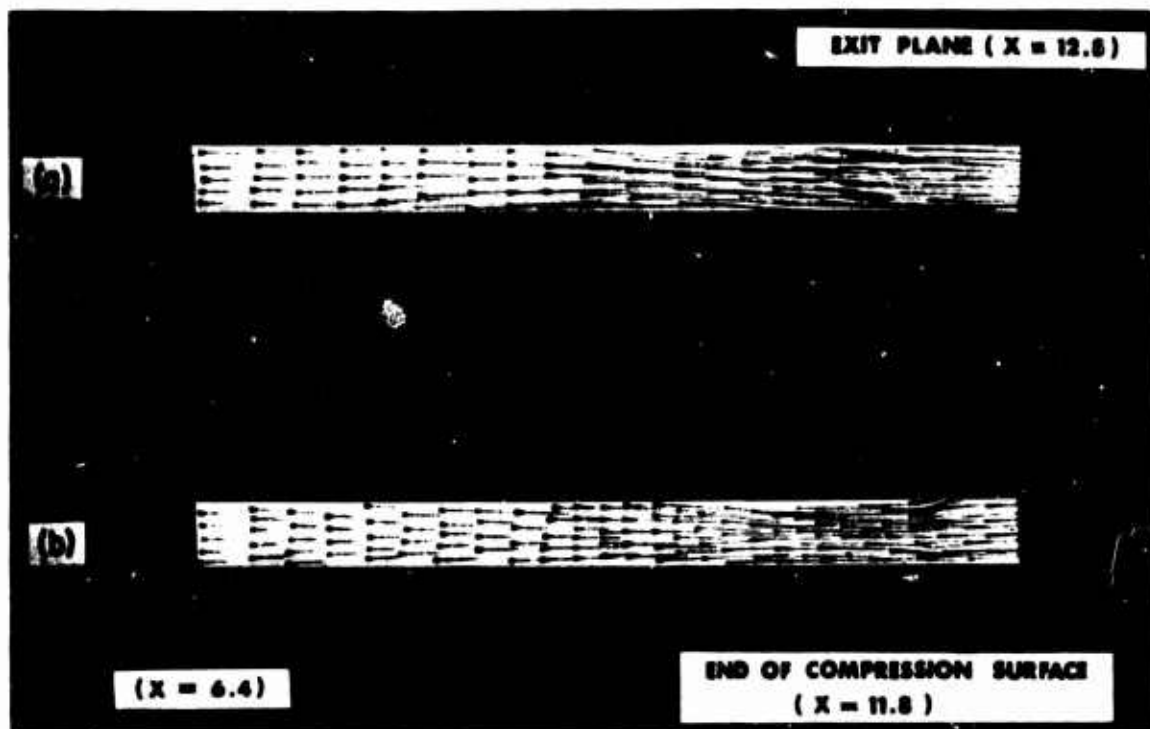


FIG. 9 OIL DOT STREAKS OF FULL BUSEMANN INLET (A) WITHOUT AND (B) WITH BOUNDARY LAYER CORRECTION

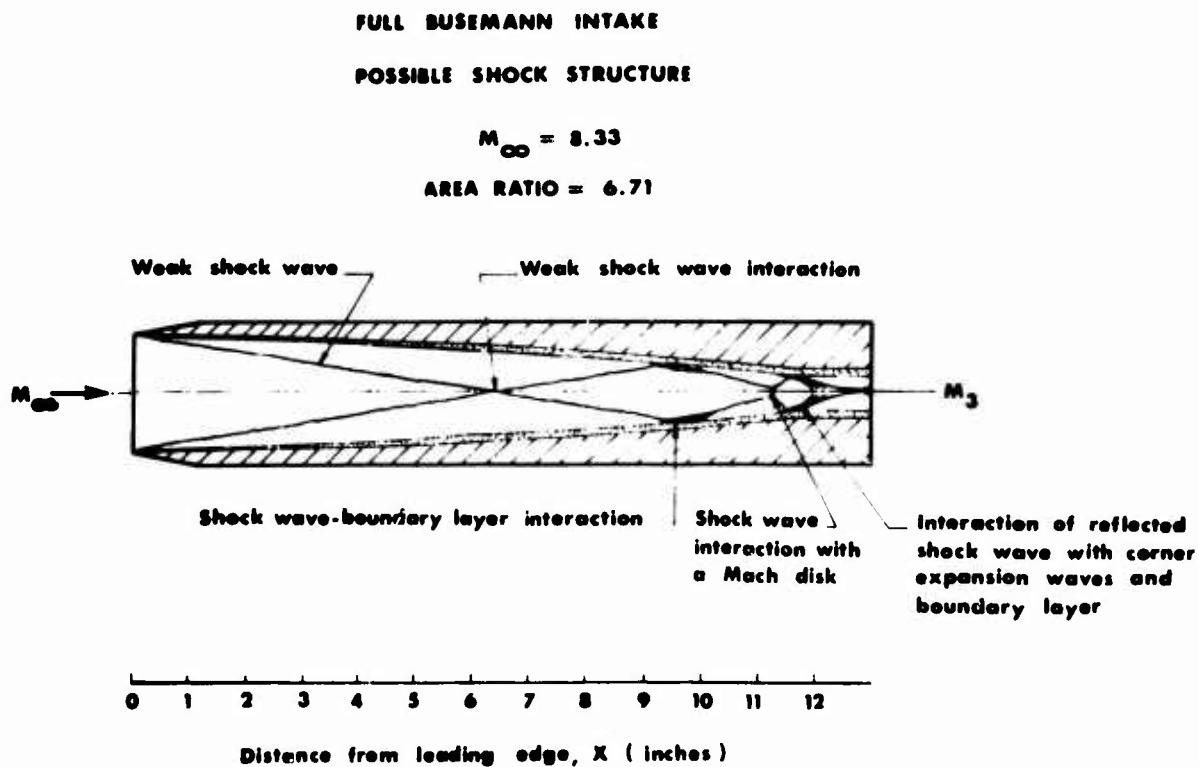


FIG. 10 POSSIBLE FLOW STRUCTURE OF FULL BUSEMANN INLET WITHOUT BOUNDARY LAYER CORRECTION

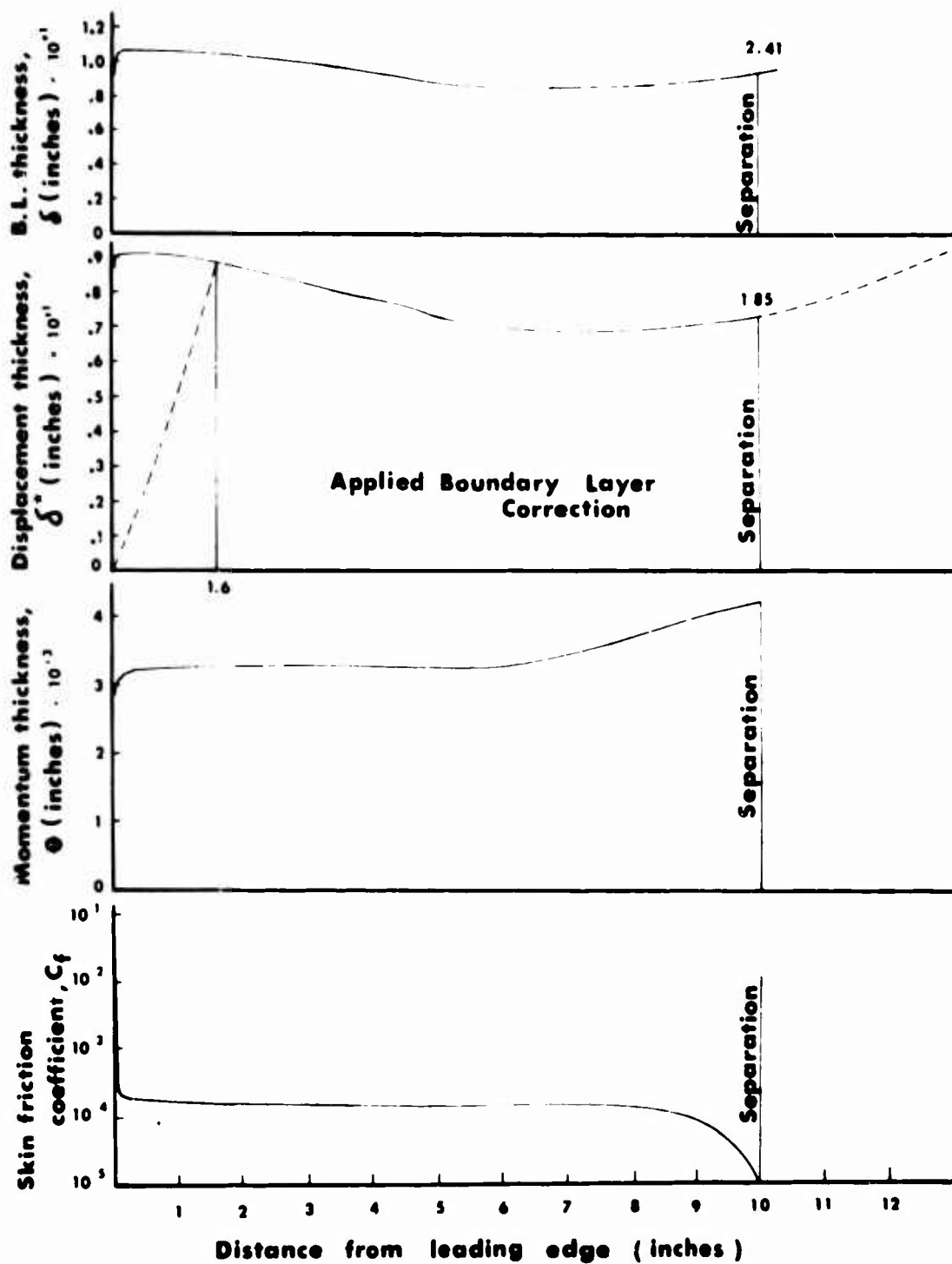


FIG. 11 BOUNDARY LAYER PARAMETERS FOR FULL BUSEMANN INLET AT NOMINAL TUNNEL CONDITIONS



FIG. 12 SHADOWGRAPH OF UNSTARTED FOUR-MODULE INLET WITH COWL A

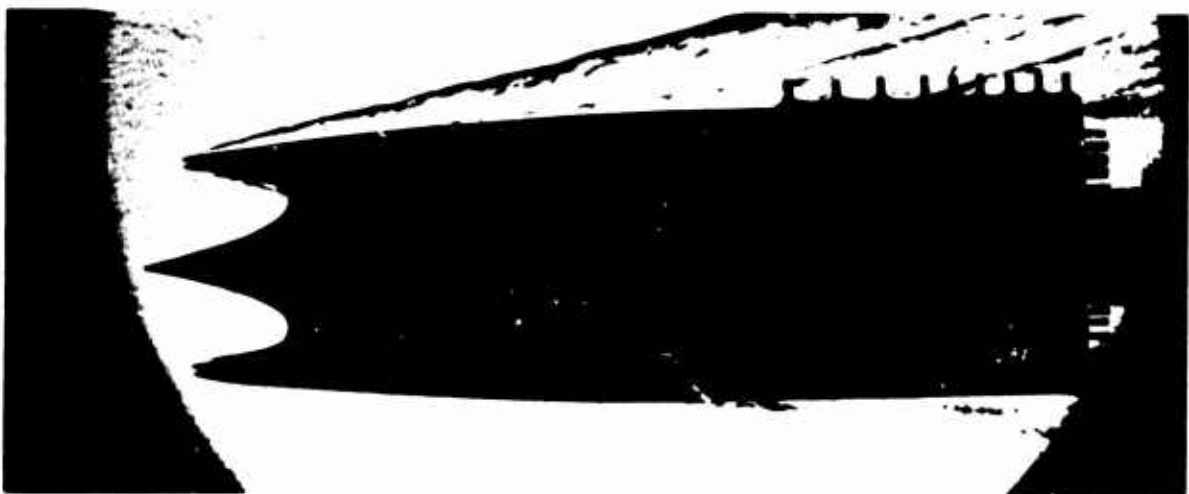


FIG. 13 SCHLIEREN PICTURE OF FOUR-MODULE INLET WITH SOME FLOW SPILLAGE THROUGH THE TOP MODULE



FIG. 14 SCHLIEREN PICTURE OF STARTED MODULAR INLET

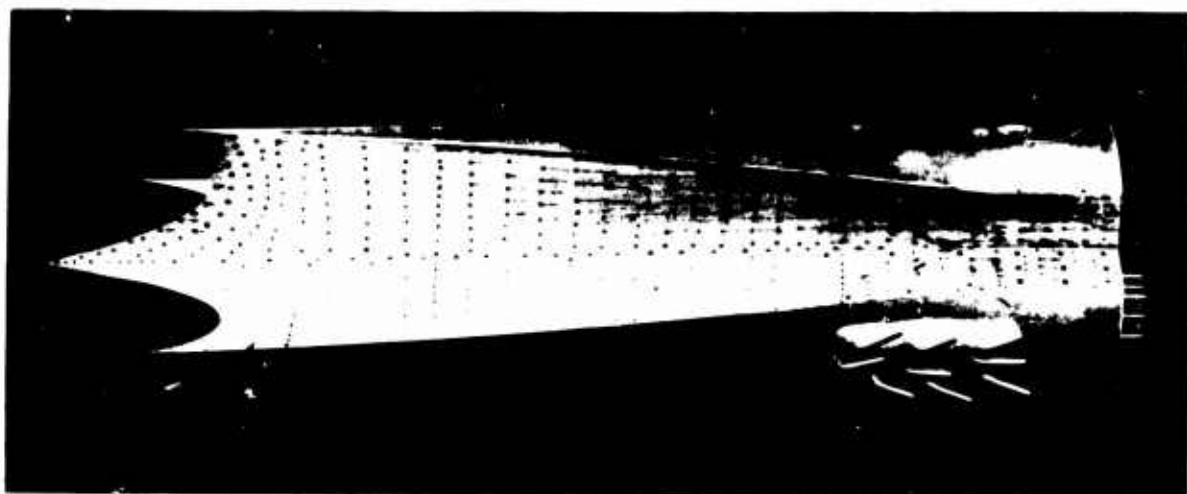


FIG. 15 OIL DOT STREAKS ON SIDEWALLS OF MODULE WITH STARTED FLOW



FIG. 16 OIL DOT STREAKS IN MODULE WITH UNSTARTED FLOW

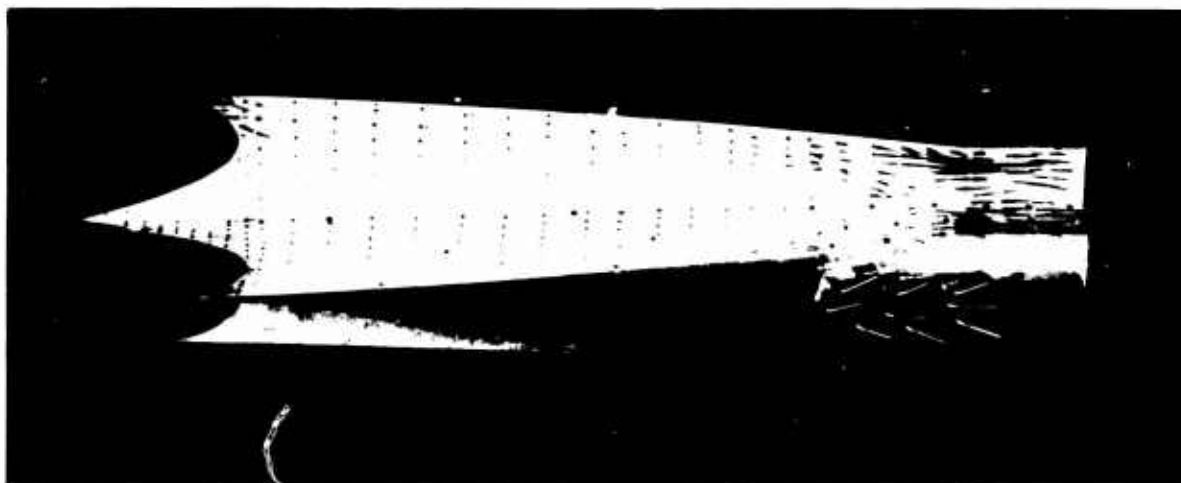


FIG. 17 OIL DOT STREAKS IN MODULE WITH SOME FLOW SPILLAGE (THIS CORRESPONDS TO THE SCHLIEREN PICTURE OF FIG. 13)

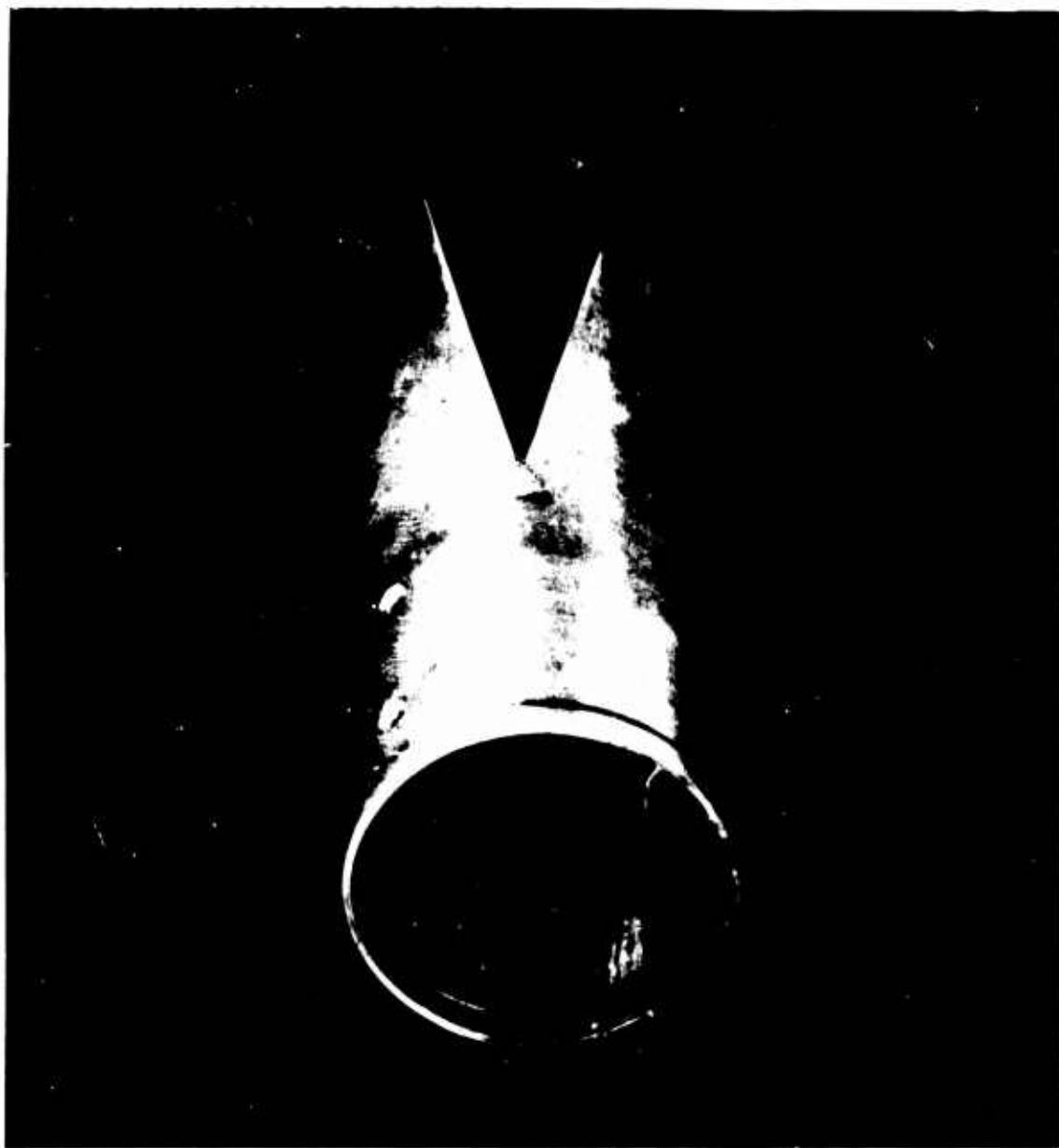


FIG. 18 OIL DOT STREAK ON INTERNAL SURFACE OF COWL A

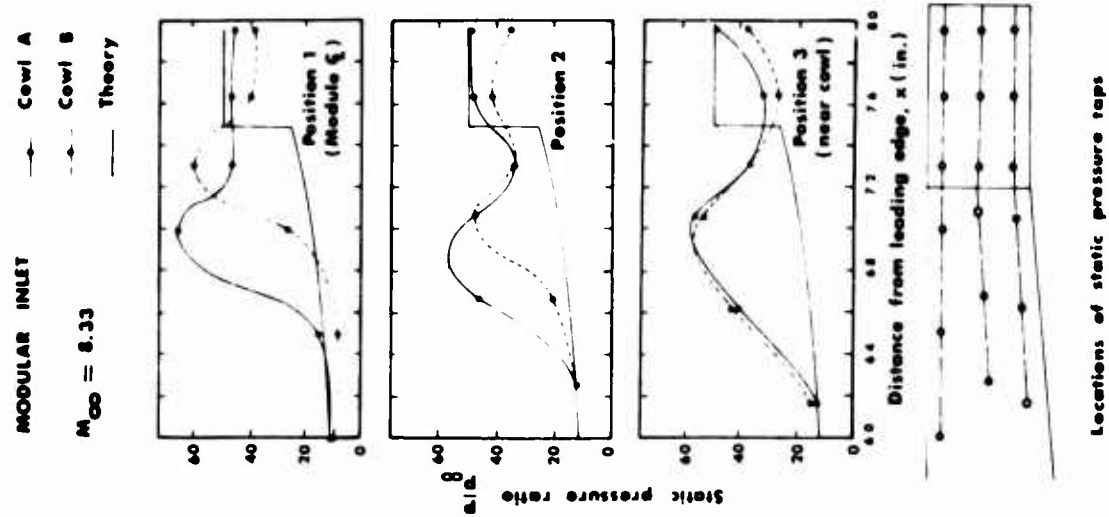


FIG. 19 PRESSURE DISTRIBUTION ON MODULE SIDEWALL NEAR THE EXIT

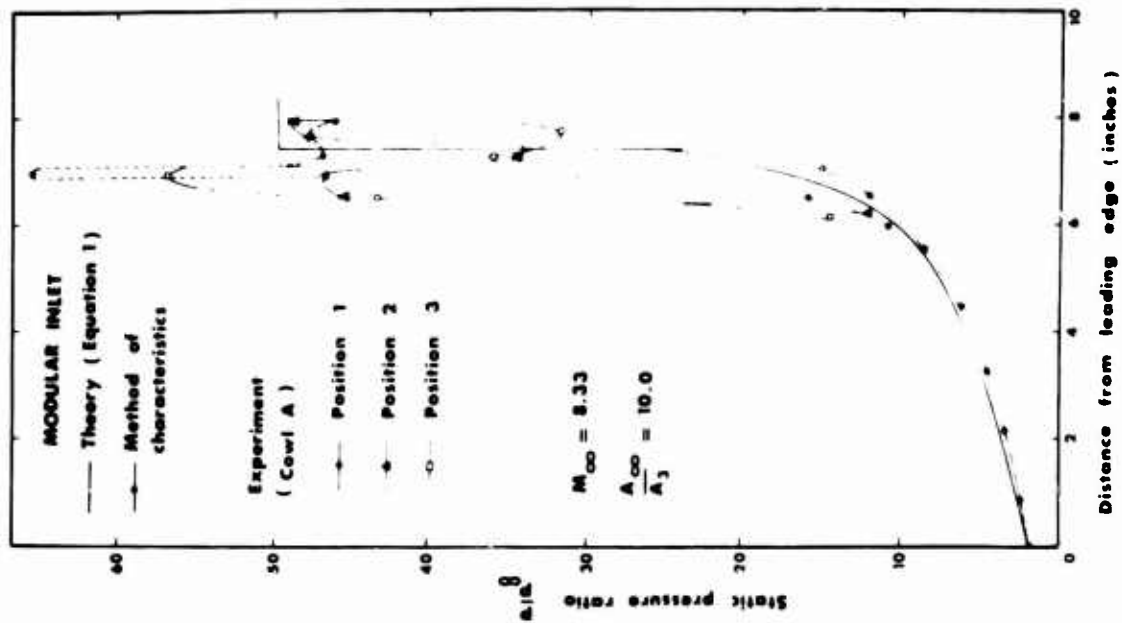


FIG. 20 PRESSURE DISTRIBUTION ON MODULE SIDEWALL

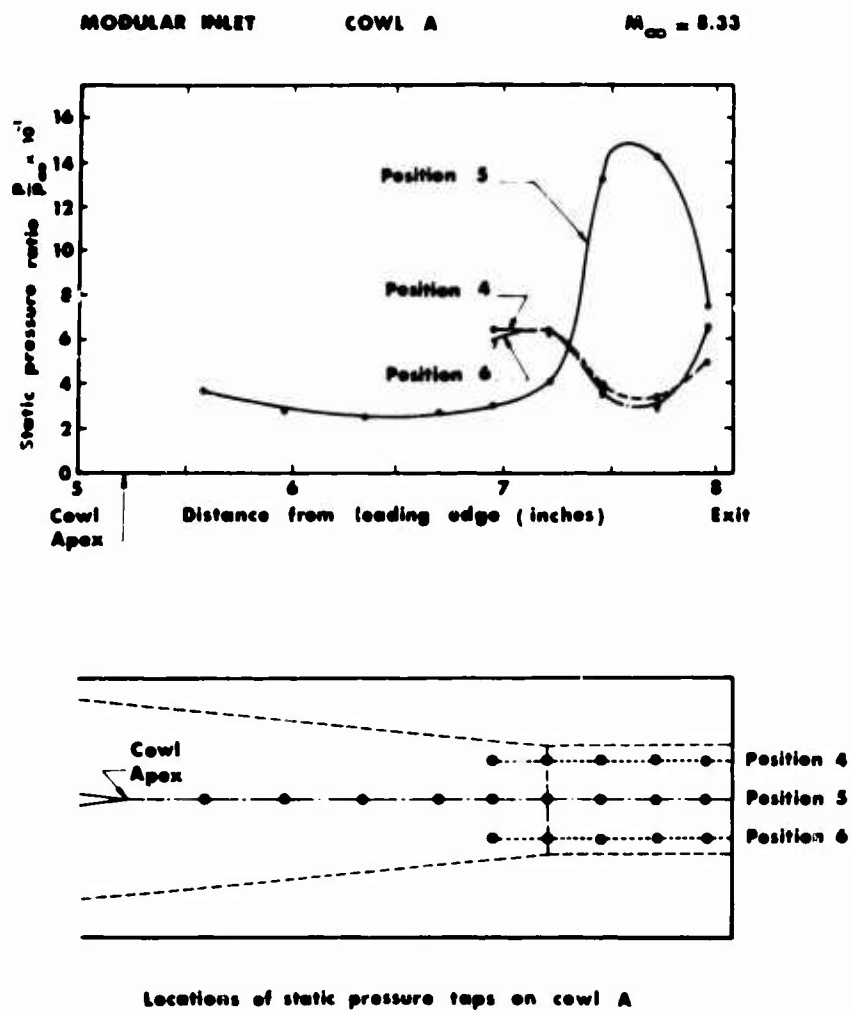


FIG. 21 PRESSURE DISTRIBUTION ON INTERNAL SURFACE OF COWL A

MODULAR INLET
EXIT PITOT PRESSURE (PSI)
AT $X = 7.70$ INCHES

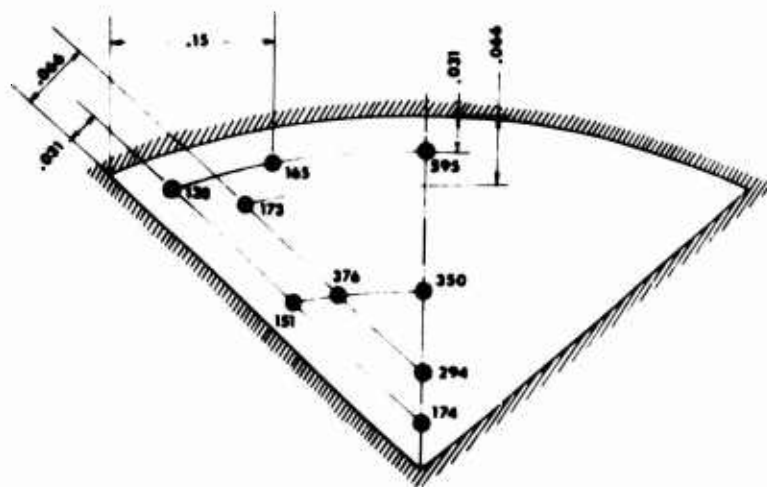


FIG. 22 PITOT PRESSURE MEASUREMENTS AT EXIT OF MODULAR INLET

THE USE OF KNOWN FLOW FIELDS AS AN APPROACH
TO THE DESIGN OF HIGH SPEED AIRCRAFT

by

J. Seddon, Ph.D.* and A. Spence, B.Sc.†

*Director/Scientific Research (Air), Ministry of Technology, London.

†Head of High Speed Division, Aerodynamics Department, Royal Aircraft Establishment, Bedford.

LIST OF SYMBOLS

p	static pressure
p_o	freestream static pressure
q_o	freestream dynamic pressure
C_p	pressure coefficient = $(p - p_o)/q_o$
\bar{C}_p	mean pressure coefficient across span at one fore-and-aft station
C_L	lift coefficient
M	Mach number
L	lift
D	drag
D_p	pressure drag in inviscid flow
C_f	skin friction drag coefficient based on wetted surface area
$\Delta L, \Delta D$	contributions to lift and drag associated with change of momentum along elementary streamtube
ΔA_p	element of planform area associated with elementary streamtube
f_L	lift function of elementary streamtube
f_D	drag function of elementary streamtube
AR	aspect ratio of wing
s	semi-span of wing
l	length of wing
x	longitudinal distance from wing apex
α	incidence
β	$\sqrt{(M^2 - 1)}$
γ	ratio of specific heats (taken as 1.40)
ψ	half included angle between port and starboard halves of wing
τ	volume parameter = $(\text{enclosed volume}) \div (\text{plan area})^{3/2}$
η	fraction of local semi-span from centre line of wing

1. Introduction

The first supersonic airliner of the Western world, the Anglo/French Concorde, is designed around the principles of the slender wing. The central idea of the slender wing is to ensure the maintenance of a single well-behaved flow under all flight conditions (see for example Ref. 1). This is achieved by employing a leading edge sweep-back such that the wing lies well within the Mach cone centred on the apex as in Figure 1. The Mach number normal to the leading edge is subsonic, the flow over the wing is shock-free except at the trailing edge and it follows that many principles of subsonic flow can be adopted to describe the aerodynamics of the shape.

For a cruising Mach number in the region Mach 2 to 2.5, these principles can be used satisfactorily in a fixed wing design because the resulting aspect ratio, or more accurately the span-to-length ratio, of the wing is still high enough to provide good handling and control characteristics in flight at low speeds.

If the cruising Mach number of a long range vehicle, requiring a good aerodynamic lift-to-drag ratio, is to be significantly higher than that of Concorde, say above Mach 3, then alternative sets of aerodynamic considerations come into prominence. Adequate low speed flying characteristics can now be provided, either by employing variable geometry on a slender wing or by using a fixed wing with supersonic velocities normal to the leading edge and thereby being committed to some system of shock waves in association with the general wing shape.

One line of research in the U.K. in recent years has been directed towards the second alternative: that is to say its object has been to study the problem of producing aerodynamic lift efficiently on non-slender planforms, in other words in the presence of shock waves. The chief characteristic of this work has been an approach by the 'inverse' method, that of choosing a known flow field and defining a shape of body which produces it. In the present context this approach has opened up new lines of thought, stimulated considerable discussion, much of it controversial, and provided a degree of definition to the subject of high Mach number aerodynamics, where definition was previously lacking.

The present paper gives a broadly-based account of the beginnings and some of the subsequent progress in this flow field approach to design. The paper is not intended to provide a complete review, nor even a comprehensive bibliography; in particular it deals only with the design point, although the authors fully appreciate the need to ensure good off-design behaviour. The aim has been to present a connected account of the method and its potential, based mainly on particular lines of development of which the authors have had personal experience through their supervision of the group principally involved.

Most of the evidence has been drawn from issued reports written by individual members of that group, whose work is hereby acknowledged: they are L.C. Squire, J.G. Jones, K.C. Moore, J. Pike and P.L. Roe. Whatever its permanent value, it was felt that such a paper would provide a useful background to the discussion of this particular session of the present meeting*.

The need to investigate in basic fashion the aerodynamics of non-slender lifting shapes enters, as already stated, at about Mach 3. The known flow field approach has so far been studied quite generally in terms of supersonic, perfect fluid, aerodynamics; in this form therefore it is applicable up to Mach numbers around 12, beyond which the presence of real gas effects will clearly call for significant changes. The range Mach 3 to 12 is thus established as a natural range of applicability of the ideas and methods involved. Within this range no aerodynamic distinction in kind appears, as for example between what might be termed 'high supersonic' speeds, on the one hand, and 'real hypersonic' speeds on the other.

2. Fundamentals of the method

2.1 Primary considerations: lower surface design

Entry to the method stems from two basic considerations. The first is the recognition that at hypersonic speeds the production of lift on a wing is dominated by pressures on the

*AGARD Fluid Dynamics Panel Specialists' Meeting on 'Hypersonic Boundary Layers and Flow Fields' May 1 - 3, 1968, London.

lower surface, in contra-distinction to the situation at subsonic speeds, where the contribution of suction on the upper surface is all-important. Whatever the shape of wing, suction on the upper surface at hypersonic speeds is severely limited by the approach to absolute vacuum ($C_p = -\frac{2}{\gamma M^2}$). This situation is illustrated in Figure 2.

The second consideration is that introduced by Nonweiler who pointed out (Ref. 2) that a three-dimensional body of triangular planform can be arranged to carry a plane shock wave beneath it, extending across between the leading edges and communicating a constant pressure to all points on the lower surface. In this case the known flow field is that beneath a two-dimensional wedge. The method of construction is illustrated in Figure 3. A pair of swept leading edges is defined in the plane of the shock wave created by the hypothetical wedge and the lower surface of the three-dimensional shape is that generated by the stream-lines proceeding downstream from all points on the leading edges.

If now an arbitrary trailing edge plane is defined and an upper surface is assumed to lie along the mainstream direction, a body of real thickness is obtained as shown in the figure. This body is known as a 'Nonweiler wing' or alternatively a 'caret wing'. In a supersonic stream, at its 'design point', which is determined by the particular combination of Mach number and the angle of the flow field generator wedge, the body produces a single, plane, triangular shock wave, contained underneath between the leading edges, and no other disturbance forward of the base. The lift and pressure drag are immediately calculable and in view of the point made earlier concerning the dominance of lower surface pressures in producing hypersonic lift, one may suggest that an elementary approach to hypersonic design has been made.

Two possible disadvantages of this body as a lifting shape are immediately obvious. The first is the bluff base resulting from the method of construction. This will be ignored for the moment, since it enters into later discussions in an evolutionary manner. The second is the large anhedral, or lower surface concavity, which besides being potentially impractical on an aircraft, clearly implies a large skin friction drag in relation to planform area.

The first extension of the method, due to Jones (Ref. 3), removes any general objection which might otherwise be justified on this second score. Jones showed how the flow past a non-lifting circular cone could be used as the basic flow field, replacing that of the two-dimensional wedge in Nonweiler's construction. The leading edges (not necessarily straight) are now drawn on the conical shock wave and the lower surface of the configuration is obtained, as before, by replacing the stream surface through and downstream of the leading edge by a solid surface. This construction is illustrated in Figure 4. A wider selection of possible shapes, for which the exact flow field is known, is thereby provided. Jones defines two basic types of configuration, depending on whether or not the leading edges are drawn from the apex of the generator cone. In the former case the resulting shape consists of a central 'body' (a sector of the generator cone) and an outer 'wing'. In the latter case the shape is of the type shown in Figure 4. In either case, the lower surface concavity is much less pronounced than with the caret wing.

We are therefore led to the conclusion that the exact knowledge of supersonic flow around bodies of simple shape provides a possible starting point for the development of hypersonic wing theory. Using a selected known flow, a portion of stream surface can be chosen to become the basic lifting surface. The lift and pressure drag characteristics are deducible directly from the knowledge of the generating flow field and the principle of confining shocks to the lower surface should lead to an optimisation of the shockwave system from the aspect of lift-to-drag ratio of a resulting configuration.

The concept of a shape which, on design, rides on a precisely known system of shock waves in the manner described leads to the use of the term 'waverider' to describe such a shape. In practice the term can be applied more generally to distinguish the category of aircraft shapes in which, as distinct from slender wings, the lift is associated primarily with pressures produced by an under-surface shock wave system, whether or not the flow system is precisely calculable. A suitable choice of span-to-length ratio will ensure that the shape behaves as a slender wing at supersonic speeds some way below the design value and also has good flying characteristics at low subsonic speeds.

The Nonweiler and the Jones constructions make use of the simplest and most fundamental known flow fields in two-dimensional and axis-symmetric flow respectively.

2.2 Upper surface design

In the illustrations of Figures 3 and 4, the upper surface of the shape has been taken to be streamwise, i.e. to form a stream surface of the undisturbed flow. It is, however, advantageous for two reasons to design the upper surface to contribute a small share of the lift. First, provided that the inclination of the upper surface is smaller than that of the lower surface, lift can be developed on it at smaller drag; second, because some lift is transferred from the lower surface, the inclination of the latter can itself be reduced. Since the lower surface shock wave is attached to the leading edge, the design of upper surface is generally an independent process. The shape can be evolved in a manner similar to that used for the lower surface but using in this case a stream surface from a known expansion flow field. In principle, any expansion flow field can be used and Flower (Ref. 4) and Moore (Ref. 5) have illustrated the way in which two-dimensional Prandtl-Meyer expansions and axis-symmetric expansions respectively can be employed for this purpose.

In order to be able to combine the upper surface design with that of the lower surface it is necessary only to ensure that the up-stream boundary of the expansion field lies behind the leading edge already chosen for the lower surface. That part of the upper surface lying between the leading edge and the boundary of the expansion field is then a streamwise surface. Figure 5 illustrates a combination of upper and lower surface designs using axi-symmetric flows.

The introduction of an expansion flow for upper surface design, in addition to improving the lift characteristics, also represents a first step in reducing the residual base area of the shape.

3. Types of lower surface flow field

3.1 Flow fields for direct lift

Proceeding from the basic caret or cone-flow wing, it is clear that a number of major steps may be involved in order to arrive at a shape approximating to that of a practical aircraft. Questions arise immediately concerning the distribution of volume and lift, the effect of adding a propulsion system, the nature of surface pressure gradients as affecting boundary layer behaviour, transonic characteristics, structural considerations and so on.

Some of these problems can be studied by the use of more complex flow fields, still with explicitly known or computable characteristics. Keeping in mind the primary aim of designing a lower surface for high lift-to-drag ratio, a number of possible compression flow fields have been examined in greater or lesser degree. These are summarised in Figure 6, to which the following comments apply.

(a) Plain wedge. This is the basic flow field of the Nonweiler or caret wing. The potential disadvantage of large anhedral of the shape (which applies particularly to the lower Mach numbers) has already been mentioned. Additionally it is desirable to be able to provide greater volume near the nose than is given by the caret wing.

(b) Two-dimensional staged compression. The use of more complex two-dimensional flow fields has been studied by Townend (Ref. 6). The chief potential advantage of these is in relation to the design of three-dimensional air intakes, which in turn can be absorbed into the lower surface design so as to preserve two-dimensional flow in the joint lifting-propulsive system.

(c) Plain cone. This is the basic flow field of the Jones or cone-flow wing. Its disadvantages are that the resulting shapes have the centre of lift downstream of the centre of area and too little volume near the nose. Also surface pressure gradients are slightly adverse in the streamwise direction, though this is a point which should be considered along with a refined assessment of skin friction levels. Experiments at $M = 4$ on wings based on this type of flow are reported in Ref. 7.

(d) Cone-cylinder.

(e) Cone-ogive.

Flow fields (d) and (e) both lead to shapes in which both the volume and centre of pressure are further forward than with the cone-flow wings. Studies of these flow fields have been confined to the region of homentropic flow behind the conical shock. The two types give somewhat different indications as to the efficiency of lift production (see Section 4).

(f) Curved shock. This is the first non-homentropic flow field to be studied. It produces the same kind of benefits as do flow fields (d) and (e) but widens the range of possibilities and gives indications of good lifting efficiency of the resulting shapes.

The studies of flow fields (e) and (f) are due particularly to Moore, who has developed computer programmes for evolving the shapes and their pressure distributions.

All the foregoing flow fields are concerned with the problem of lift as produced directly on the derived surface through incidence. It is of interest to consider also the production of lift on a surface by what is usually termed the 'favourable interference' of the pressure field of another component of the configuration; or more generally to consider flow systems whereby direct and interference lift can be combined in an effective manner. Some developments of the theory along these lines are described in the next section.

3.2 Direct and interference lift: comparison and combination

An interesting study by Roe (Ref. 8) has compared the lifting efficiency of a vertical

wedge beneath a plane wing with that of a horizontal wedge producing lift directly through incidence as in the caret wing. His result is that the comparison is favourable or unfavourable to the former (i.e. interference) arrangement according as the parameter $M^4 C_L / \beta^2$ has a value less or greater respectively than 0.65.

The two systems under comparison are illustrated in Figure 7, (a) and (b). The caret wing has the same direct lift characteristic as a two-dimensional wedge, the flow being in both cases deflected vertically downwards by the shock wave. The interference arrangement acquires lift from the pressure field of the vertical wedge acting on the plane wing, the flow being deflected horizontally by the shock wave. Pike (Ref. 9) has analysed the performance of systems containing a combination of direct and interference lift, as obtained from flow fields produced by plane shock waves. A single plane shock wave inclined at an angle to the horizontal gives the deflected air a sideways component of velocity. Shapes equivalent to caret wings but associated with such inclined shock waves may be named more generally V-wings. Pike's analysis shows that V-wings can give significantly better ratios of lift to pressure drag than caret wings. The superiority depends upon exercising freedom in the choice of trailing edge sweepback; with a caret wing this makes no difference to the performance, since pressures and inclinations are the same at all points of the lifting surface; with a general V-wing, however, employing trailing edge sweepback, the favourable interference situation can be optimised to considerable advantage.

An important stage of realism is introduced by joining together two V-wings as a mirror image pair with a common leading edge in the vertical plane of symmetry. This gives a W-wing as illustrated in Figure 7 (c), the performance of which is the same as that of each half or V-wing component. The W-wing configuration may be seen as consisting of a deep central body between lifting wings and from this point of view it is clearly important to assess the potential as defined by study of the flow field characteristics.

Pike's analysis again reveals, now in general terms, the potential advantage of deploying favourable interference at low values of the similarity parameter $M^4 C_L / \beta^2$. A summary picture taken from his report and including some of his worked-out examples is shown as Figure 8.

Generally speaking, the wing-body arrangements emerging are not immediately representative of practical aircraft configurations - to reach the optimum curve in Figure 8 the shapes would become much more extreme than those shown - but the results of the study can be used to indicate the distribution of volume and wing position for obtaining favourable interference when the wing supports an attached shock wave.

4. Considerations of lifting efficiency

4.1 Particular optimisations

As part of the known flow field approach, optimisation studies are frequently possible which, treated in a proper context, i.e. with due regard to the limitations imposed, can provide useful guide lines to design.

Thus in his cone-flow wing study, Jones (loc. cit) shows that with type A configurations, pressure lift is produced more efficiently the smaller the angle ψ (Figure 9). This conclusion has to be weighed against the effect of increase of friction drag with decrease of ψ and the progressive departure from realistic configurations.

A particular study by Pike (Ref. 10) shows that the two-dimensional compression surface with minimum pressure drag for a given lift is a double wedge. The discontinuity in slope is at a point such that disturbances from the discontinuity, on reflection from the shock wave, just fail to affect the surface. The double wedge is generally concave for Mach numbers above 3. The conclusion must be kept in proper context. Thus if a streamwise upper surface is assumed and the enclosed volume per unit span is maintained constant, Bartlett (Ref. 11) has shown that a convex double wedge lower surface gives the best lift-to-drag ratio.

4.2 Momentum analysis

Since the flow beneath a derived lifting surface is known in depth, the lift and drag may be determined from a momentum analysis. An approach on these lines is due to Roe (Ref. 12), who has been able to apply it to both two-dimensional and three-dimensional flow fields.

Briefly, each element of planform area of a given shape is associated with an elementary streamtube in the flow and accordingly with the changes of momentum which take place along that

streamtube. The momentum changes contribute to the overall pressure force by amounts

$$\Delta L = \Delta A_p \cdot f_L$$

$$\Delta D = \Delta A_p \cdot f_D$$

where ΔA_p represents an element of planform area and f_L and f_D are functions which may be computed for each streamline. The lift and drag coefficients are then simply mean values of f_L and f_D .

Roe has developed this method in order to study the generation of lift in a variety of circumstances. An analysis of two-dimensional flow fields leads to a conclusion similar to those of Pike and Bartlett - that optimal lifting shapes are close to doublewedges. The analysis has been extended to three-dimensional flow fields with a vertical plane of symmetry. It is shown how maps of a given flow field may be drawn so as to indicate those parts which from their lifting efficiency seem most suitable for incorporation into a practical lifting system. Some typical maps, relating to axis-symmetric flow fields included in the types discussed in Section 3, are reproduced in Figure 10. The numbers assigned to the contour lines refer to values of a lift efficiency factor for individual streamlines relative to the streamline of the flow through a plane inclined shockwave giving the same f_L .

Since the values of f_L vary throughout the field in each case, it is not possible to deduce overall comparisons of lifting efficiency. Thus a high value of the local efficiency factor may be associated with a relatively small f_L contribution to the overall C_L . Broad qualitative indications are obtained, however, of the relative merits of different flow fields. One would tentatively draw the following conclusions from the results displayed in Figure 10:-

(1) The cone-cylinder flow field is relatively inefficient: this is because the flow over-expands around the shoulder, leading to parallel and even inwardly-directed flow some way downstream in the inner region of the field.

(2) A cone-ogive flow field successfully avoids this characteristic. The high values of local efficiency factor near the vertical plane of symmetry lead to a conclusion similar to that of Jones mentioned above: namely that it is desirable in constructing lifting shapes from this field to employ stream surfaces within a relatively narrow sector around the plane of symmetry. In practice, this conclusion is subject to the same qualification as before in respect of the adverse trend of friction drag with angle of the sector.

(3) The curved shock flow field shown in the third example is worthy of detailed study in relation to practical possibilities, in that it contains an extensive region in which local lifting efficiency factors are greater than unity. This flow field does not exhibit the very high factors which occur locally in the cone-ogive field, the probable explanation being that the leading shock is in this respect now over-strong. That particular fault, however, is compensated by the fact that strengthening the leading shock enables both the volume and centre of pressure of a derived lifting shape to be brought further forward, with consequent benefit in a practical application.

Roe's broad conclusions from this work to date are that optimum flow processes have the following features:-

- (a) The air is initially deflected through a weak shock wave;
- (b) Subsequent flow processes are isentropic;
- (c) Expansion to free-stream pressure occurs in conjunction with a residual deflection angle of the flow.

4.3 Estimates of overall lift-to-drag ratio

It seems appropriate to conclude this section on lifting efficiency with a brief note on the levels of lift-to-drag ratio which it is estimated can be reached by waverider shapes derived from known flow fields, with the effect of skin friction included. The position is depicted in Figure 11. The full curve on the left is estimated for slender wings and its trend towards non-slender span-to-length ratio is confirmed by experimental results from the High Supersonic Speed Tunnel at R.A.E. Bedford. Lying above this, the dotted curve represents a corresponding estimate for slender wings again but assuming, instead of a thin trailing edge, a positive base area equal to the maximum cross section area yet having zero base drag. The conclusions are:-

- (1) Under comparable conditions, waverider shapes at Mach 4 (the speed chosen for this

set of estimates) can give about the same L/D as slender wings;

(2) Forms of waverider utilising trailing edge sweepback show appreciably higher potential than the caret wing;

(3) Since a non-zero base area is an essential feature of basic waverider shapes, the comparisons are made assuming a positive base area but zero base drag: in practice therefore much will depend on how the base drag can be eliminated in a real configuration.

5. Approach to complete aircraft configurations

So far in this account it has been described how the use of known flow fields leads readily to the derivation of efficient lifting shapes with representative volume. The choice of flow field influences such characteristics as the longitudinal distribution of volume, position of centre of pressure and the nature of pressure gradients along the surface. The account would not be adequate, however, without mention of some further significant steps which can be taken in the approach towards complete and acceptable aircraft configurations.

5.1 Engine-airframe integration

At hypersonic speeds, the propulsion system - air intake, engine and nozzle - constitutes a major portion of a total aircraft layout: in particular the area of the propulsion nozzle for complete expansion of the jet grows rapidly with increase of Mach number and by Mach 6, say, is comparable with the total frontal area of the vehicle. Integration of the propulsion system into the total configuration clearly plays an important part in defining the overall aerodynamics. In relation to the flow field approach to design, the first and most obvious point is that concerning the base area of derived shapes. It is recalled that the basic construction of a lifting lower surface and streamwise upper surface (e.g. Figures 3 and 4) defines a base area. By introducing shaping of the upper surface to provide a lift contribution, this base area is reduced. With optimum upper surface lift, however, a substantial base remains. An essential part of the philosophy of the flow field approach is that in a complete configuration this residual base area is occupied by the exhaust nozzle or nozzles of the propulsion system. The extent to which a match can be made will have a significant effect on the ultimate aerodynamic efficiency, as can be seen from Figure 11.

That the flow field method provides a useful approach to the problem of integrating the propulsion system into a configuration has been demonstrated by Pike (Ref. 13). In his worked example for Mach 4 the following steps are incorporated:-

(1) The intake is placed on the lower surface, where it can benefit from the compression through the leading edge shock. In the cruise condition the intake is in a region of known flow and its size is related to the free stream capture area by following forward streamlines. The known flow field is retained behind the intake (assuming, no spillage at the design Mach number) by defining the outer shape of the propulsion box as the stream surface which continues downstream from the intake. At the trailing edge the propulsion box increases to the base area which needs to be absorbed by the nozzle.

(2) Using a cone-cylinder flow field for the lower surface, the base area obtained is about 60% in excess of the nozzle area required. This excess is removed by introducing upper surface expansion. In an interesting modification of the basic method, Pike uses a pair of axis-symmetric expansion flow fields, one on each side of the vertical plane of symmetry, and thereby removes base area towards the tips, leaving the residual nozzle area concentrated around the centre line.

Photographs of a model of the resulting configuration are shown in Figure 12. The vertical 'fin' which can be seen emerges in the form shown as the result of prescribing a solid boundary to prevent the two expansion flows from interfering one with another.

5.2 Lower surface shape

It can of course be argued that shapes precisely as defined by the known flow field approach are generally such as would present significant inconvenience in actual design application. For example, an aircraft designer might justifiably react adversely to the large undersurface concavity which is a feature of the caret wing, at least at the lower Mach numbers, or to the surface curvatures peculiar to the cone-flow wing. This is merely to say, however, that the exact theory is limited in scope to illustrating the principles and providing a first broad approach to particular design. It would seem that the stage has in fact been reached

where the need now is to build up a background of experimental evidence in relation to the details of these more practical points - and there are many - involving departures from exactly derived shapes; and to investigate in parallel the possibilities of introducing perturbation methods to carry the theoretical approach a stage nearer practicality. To take for a moment the question of lower surface detail, it is interesting to compare, as in Figure 13, the lower surface pressure distributions as obtained for some of the known-flow shapes and, in one case, experimental results for a flat-bottomed wing. It is seen that the particular curved-shock design has a spanwise pressure distribution very close to that of the flat-bottomed wing coupled with the advantage of further forward centre of pressure. The results suggest that reconciliation between theory and practice may not be too difficult to achieve. In this respect the work of L.C. Squire (Ref. 14) on the calculation of pressure distributions is important.

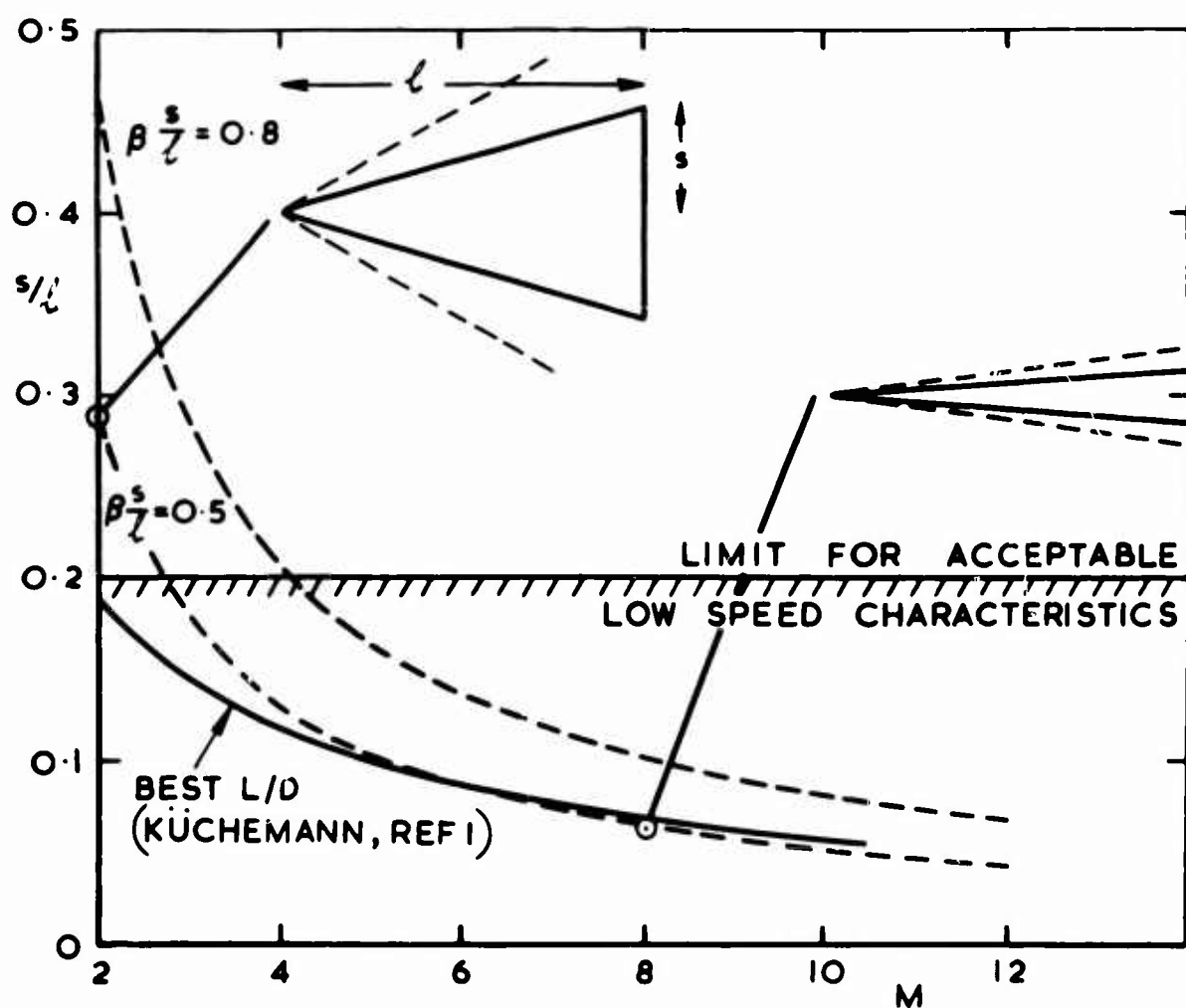
6. Concluding remarks

An account has been given of the method of using known flow fields as an approach to the design of efficient non-slender lifting vehicles at high speeds ($M > 3$). The method is interesting and novel and provides a basis of theoretical design in an area of aerodynamics which is characterized by flow non-linearity resulting from the presence of shock waves. Various types of flow field may be used and the efficiency of the lifting process can be studied in a direct fashion. It seems that extensions of the method, both on an empirical basis and by the use of perturbation theories, could be devised to link the results more closely with design considerations of practical aircraft.

References

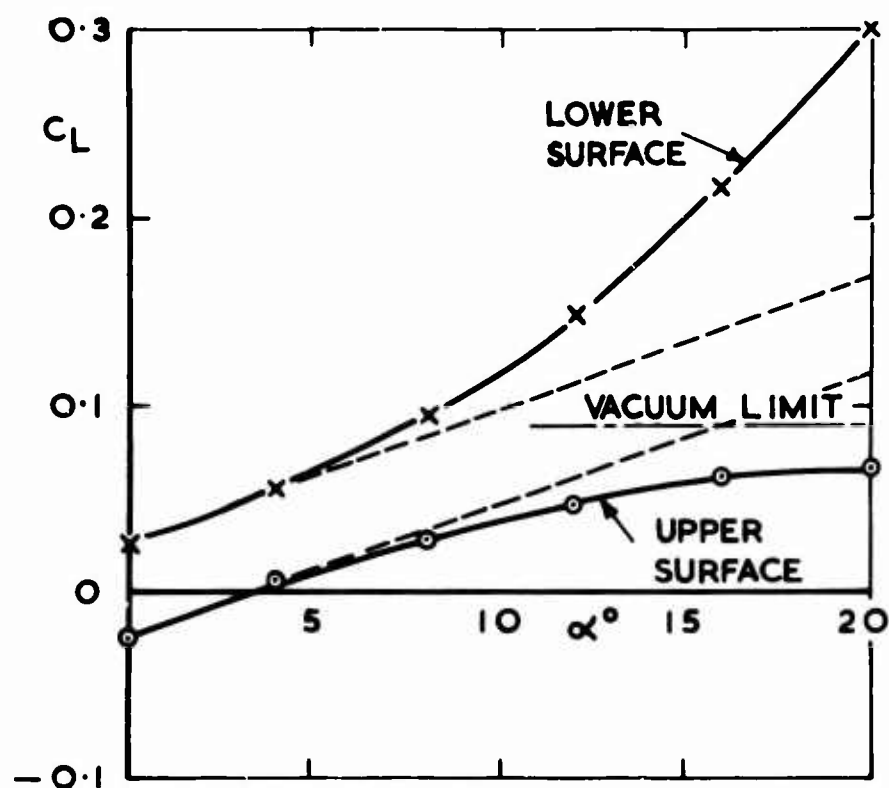
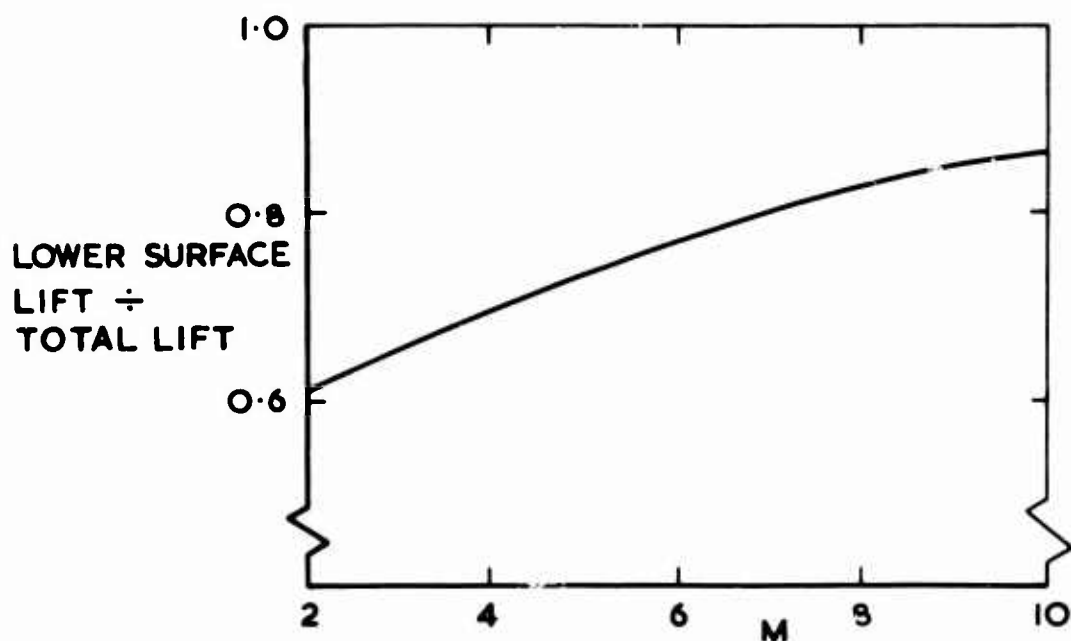
- | <u>No.</u> | <u>Author</u> | <u>Title, etc.</u> |
|------------|-----------------------------|--|
| 1. | Küchemann, D.,
Weber, J. | An Analysis of some Performance Aspects of Various Types of Aircraft Designed to Fly over Different Ranges at Different Speeds.
Prog. Aero. Sci. Vol. 9, Page 329 1968. |
| 2. | Nonweiler, T. | Delta wings of shapes amenable to exact shock wave theory.
J. Roy. Aero. Soc. 67, 39 (1963). |
| 3. | Jones, J.G. | A Method for Designing Lifting Configurations for High Supersonic Speeds using the Known Flow Fields of Non-lifting Cones.
R.A.E. Report No. Aero 2674. ARC 24846, March 1963. |
| 4. | Flower, J.W. | Configurations for High Supersonic Speeds Derived from Simple Shock Waves and Expansions.
J. Roy. Aero. Soc. 67, 287 (1963) |
| 5. | Moore, K.C. | The Application of Known Flow Fields to the Design of Wings with Lifting Upper Surfaces at High Supersonic Speeds.
R.A.E. Tech. Report No. 65034, ARC 26913, February 1965. |
| 6. | Townend, L.H. | On Lifting Bodies which Contain Two-Dimensional Supersonic Flows.
ARC, R & M 3383 (1963). |
| 7. | Pike, J. | Experimental Results from Three Cone-Flow Wave Riders.
A.G.A.R.D. Specialists' Meeting, London, May 1968. |
| 8. | Roe, P.L. | Some Exact Calculations of the Lift and Drag Produced by a Wedge in Supersonic Flow, Either Directly or by Interference.
ARC, R & M 3478 (1967). |
| 9. | Pike, J. | The Analytical Performance of Lifting Surfaces Supporting Plane Shock Waves.
R.A.E. Tech. Report No. 56127, ARC 28452, April 1966. |
| 10. | Pike, J. | Minimum Drag Surfaces of Given Lift which Support Two-Dimensional Supersonic Flow Fields.
R.A.E. Tech. Report No. 66305, ARC 28825, 1966. |
| 11. | Bartlett, R.S. | High Lift-Drag Ratio Double Wedges of Given Volume which Support Two-Dimensional Supersonic Flow Fields.
R.A.E. Tech. Report No. 66306, ARC 28826, 1966. |
| 12. | Roe, P.L. | A Momentum Analysis of Lifting Surfaces in Inviscid Supersonic Flow.
R.A.E. Tech. Report 67124, ARC 29530, 1967. |
| 13. | Pike, J. | A Design Method for Aircraft Basic Shapes with Fully Attached Shock Waves Using Known Axisymmetric Flow Fields.
R.A.E. Tech. Report No. 66069, ARC 28292, March 1966. |
| 14. | Squire, L.C. | Calculation of the Pressure Distributions on Lifting Conical Wings with Applications to the Off-Design Behaviour of Vavriders.
A.G.A.R.D. Specialists' Meeting, London, May 1968. |

FIG. 1.



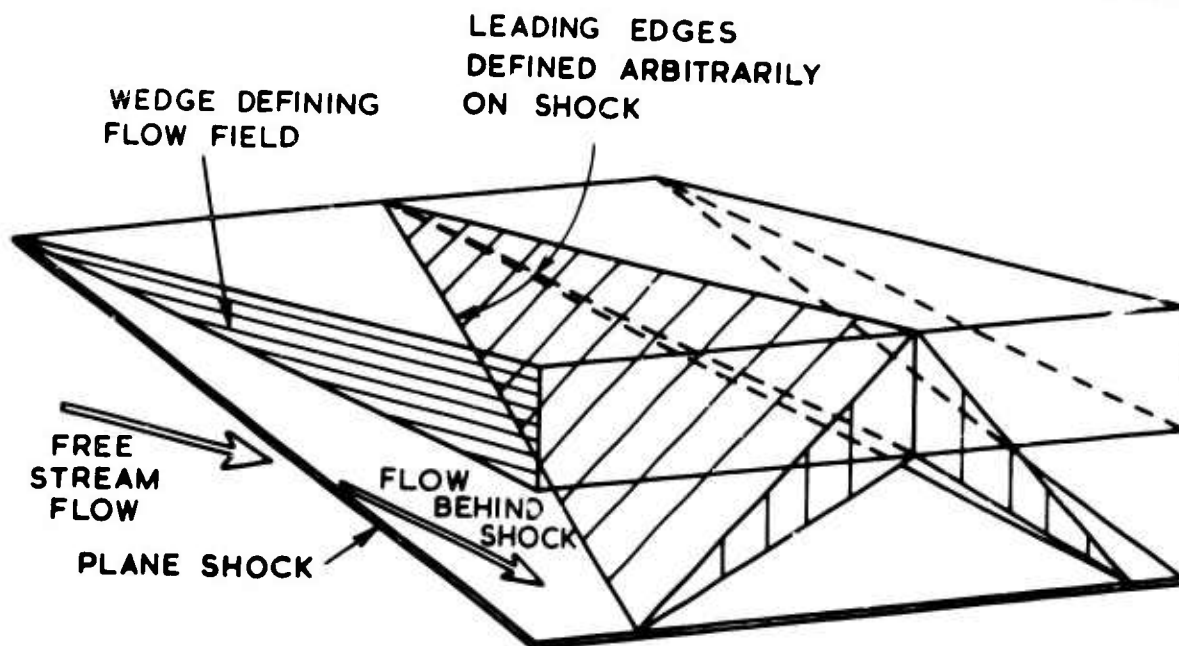
PRINCIPLE OF SLENDER WING

FIG. 2.

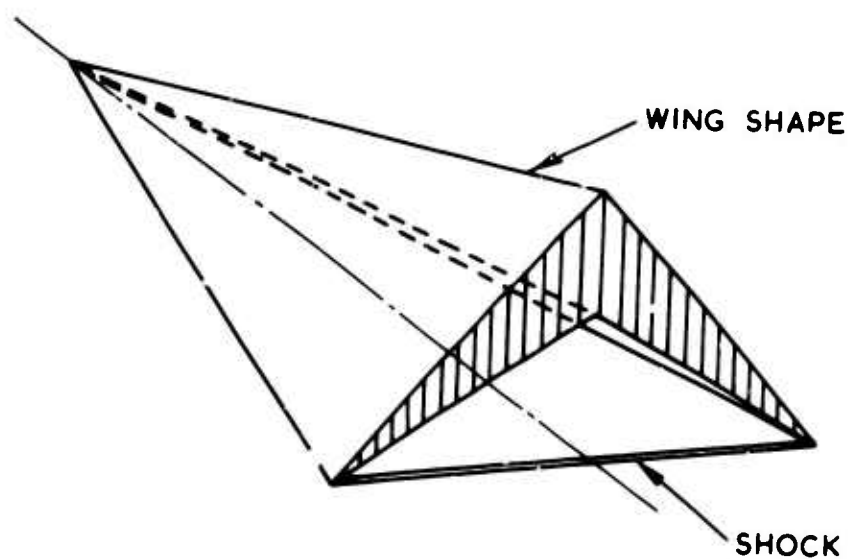
CONICAL WING, $A=2/3$, $M=4$, 3 ft x 4 ft TUNNELTWO-DIMENSIONAL FLAT PLATE AT 10° INCIDENCE

LOWER SURFACE CONTRIBUTION TO LIFT

FIG.3.



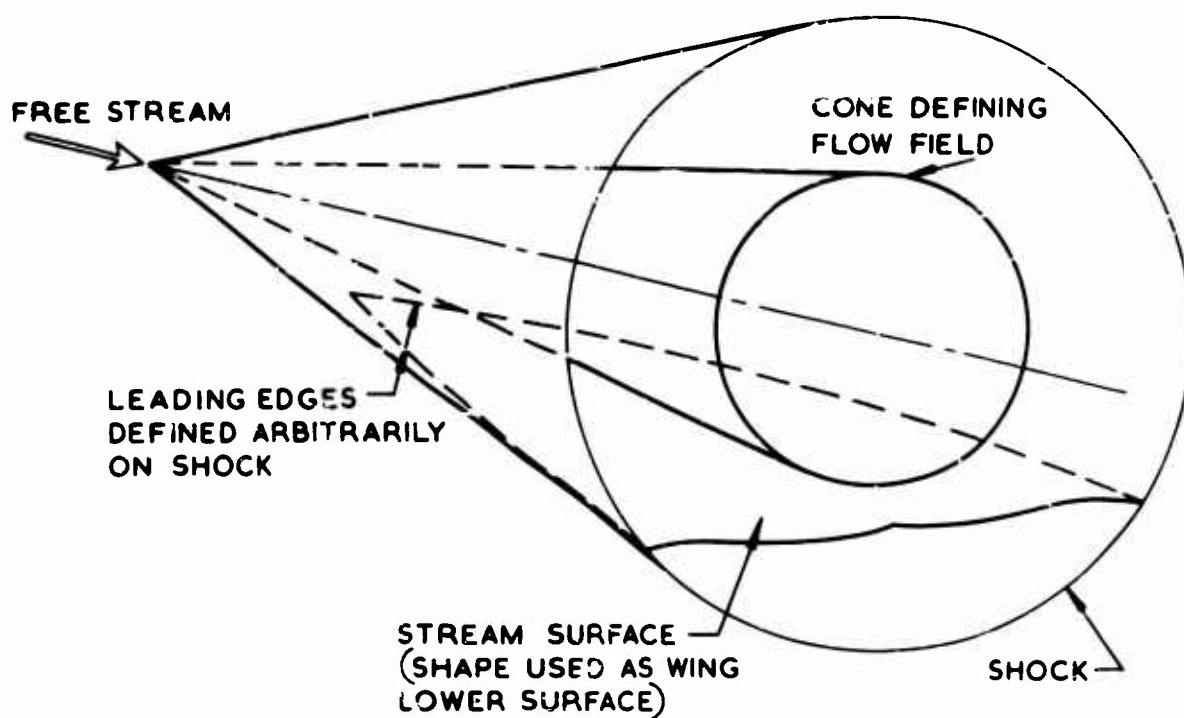
a CONSTRUCTION FROM KNOWN FLOW FIELD



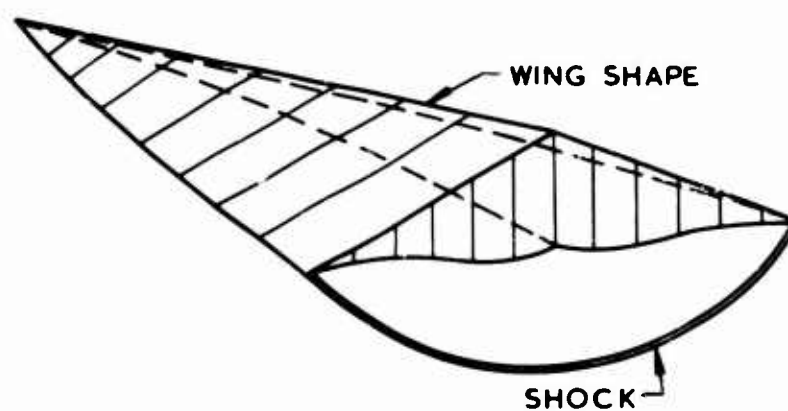
b RESULTING WING AND SHOCK

NONWEILER OR CARET WING

FIG. 4.



a CONSTRUCTION FROM KNOWN FLOW FIELD

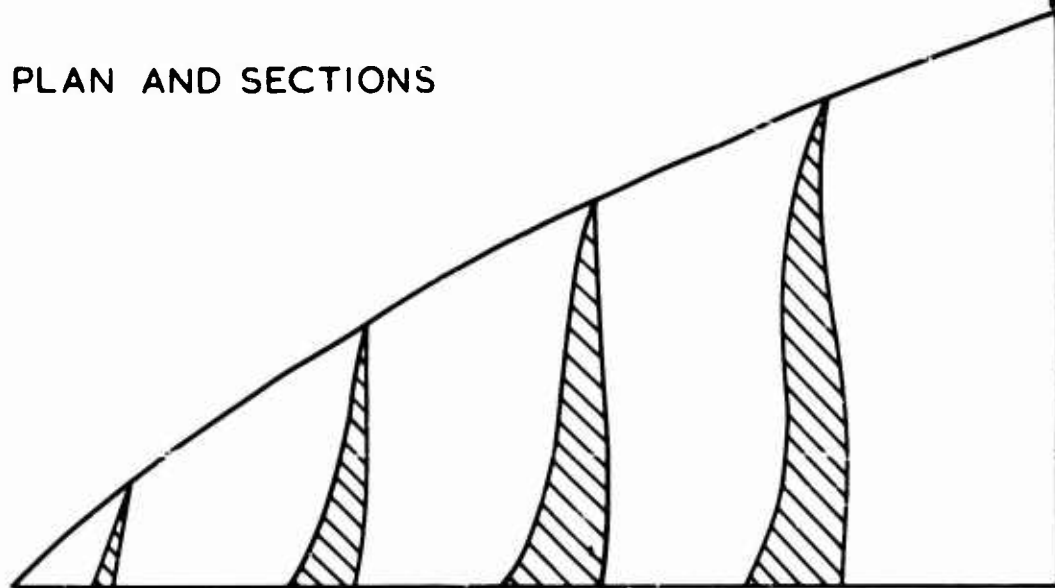


b RESULTING WING AND SHOCK

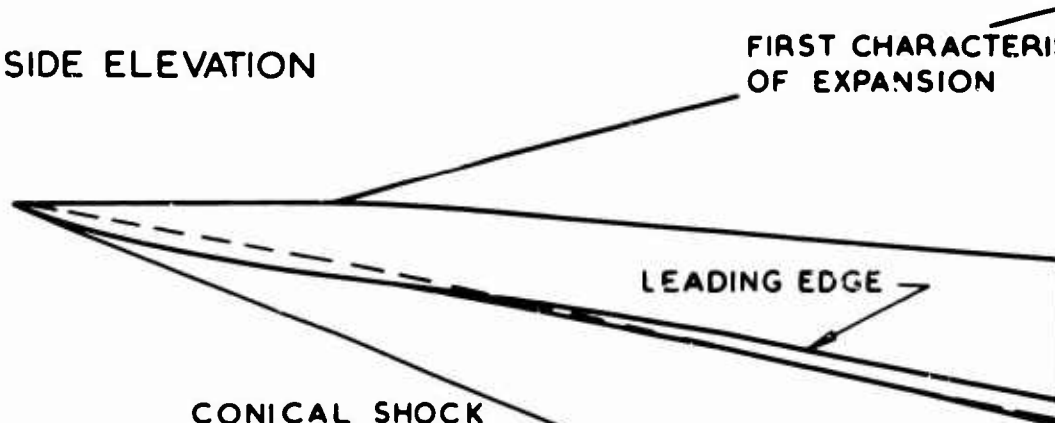
CONE-FLOW WING

FIG. 5

PLAN AND SECTIONS



SIDE ELEVATION

FIRST CHARACTERISTIC
OF EXPANSIONCONICAL SHOCK
WAVE

REAR ELEVATION

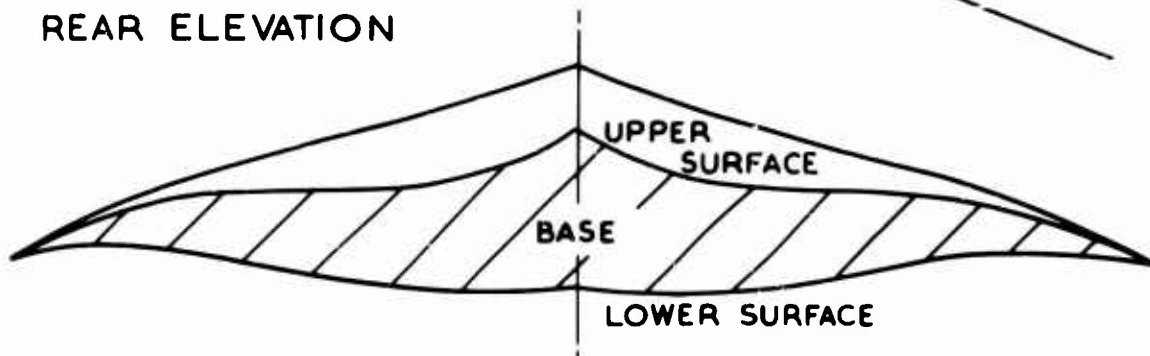
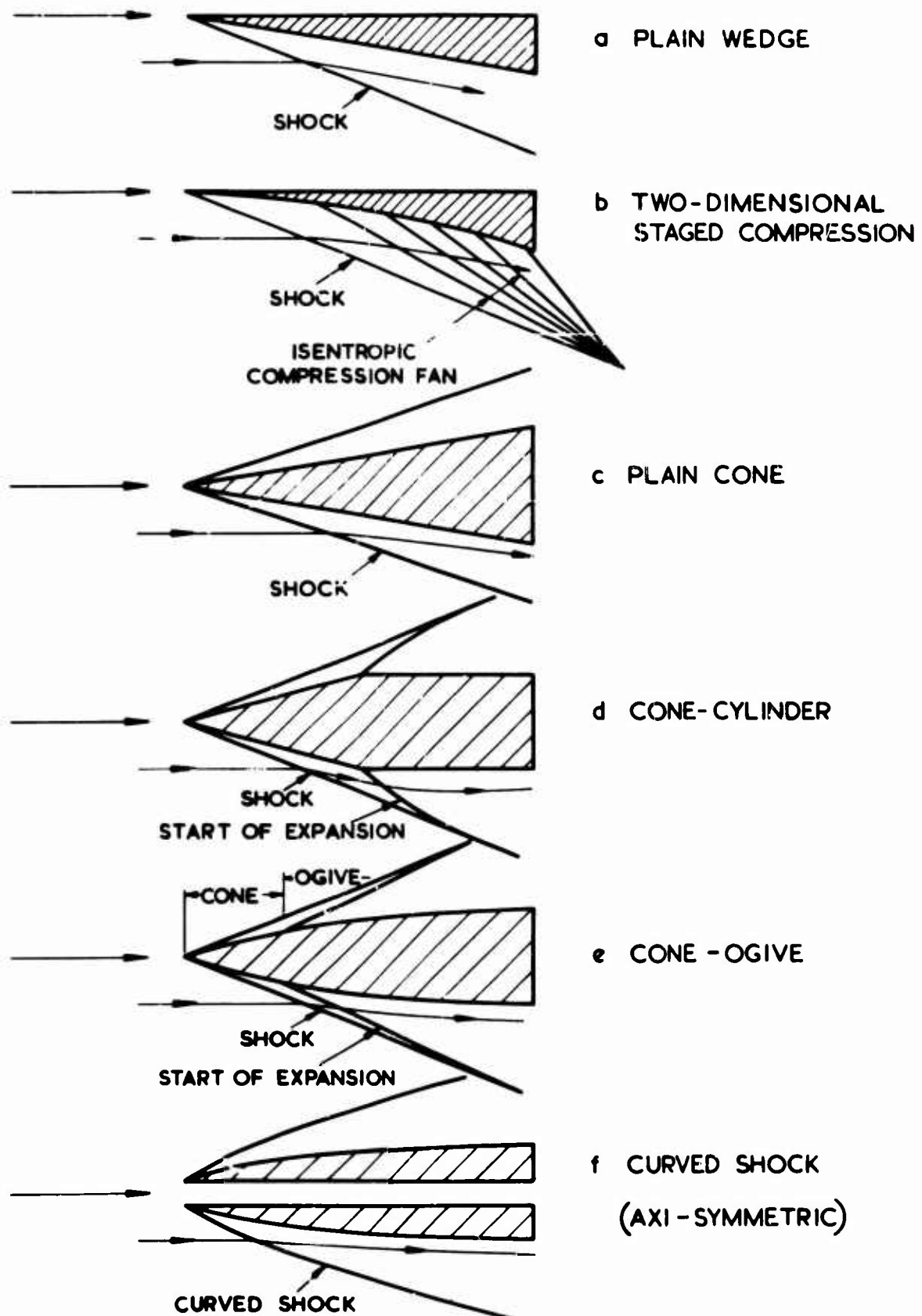
COMBINED LOWER AND UPPER SURFACE
DESIGN

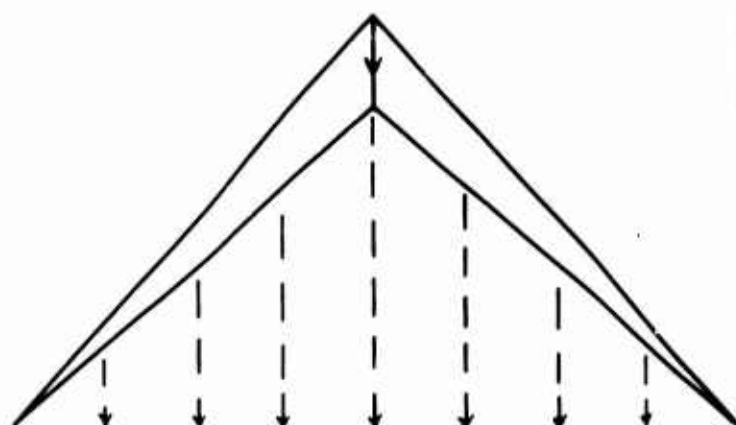
FIG.6



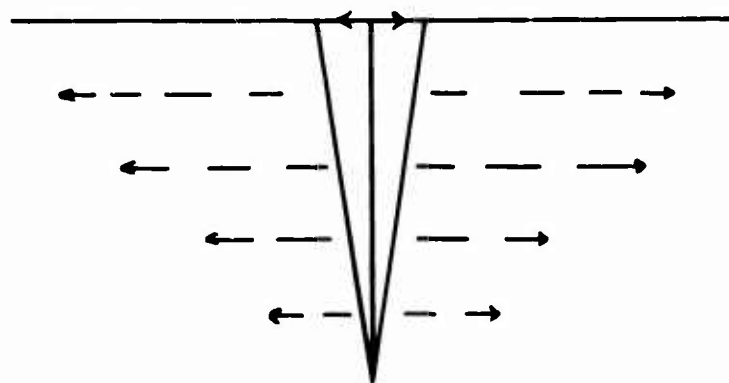
TYPES OF FLOW FIELD

FIG. 7.

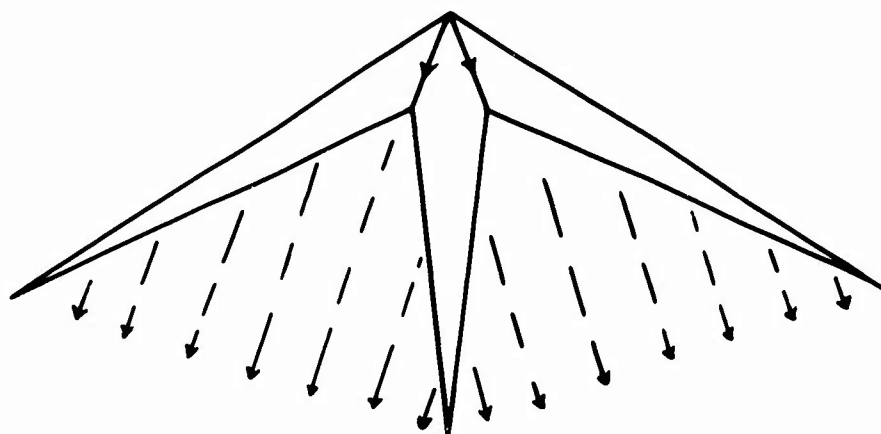
ARROWS SHOW
DIRECTION OF
CROSS-FLOW.



a DIRECT LIFT



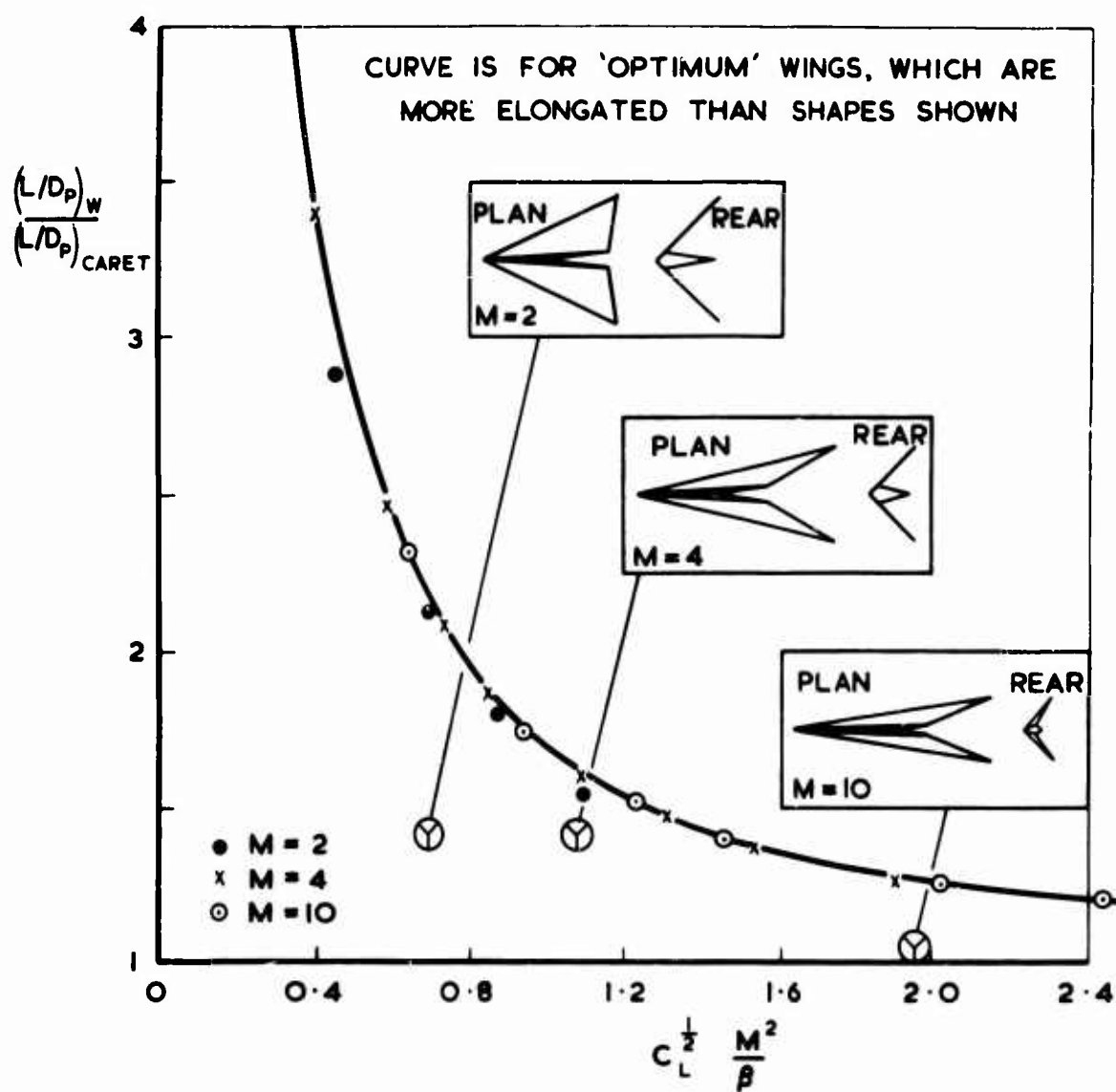
b INTERFERENCE LIFT



c COMBINED LIFT

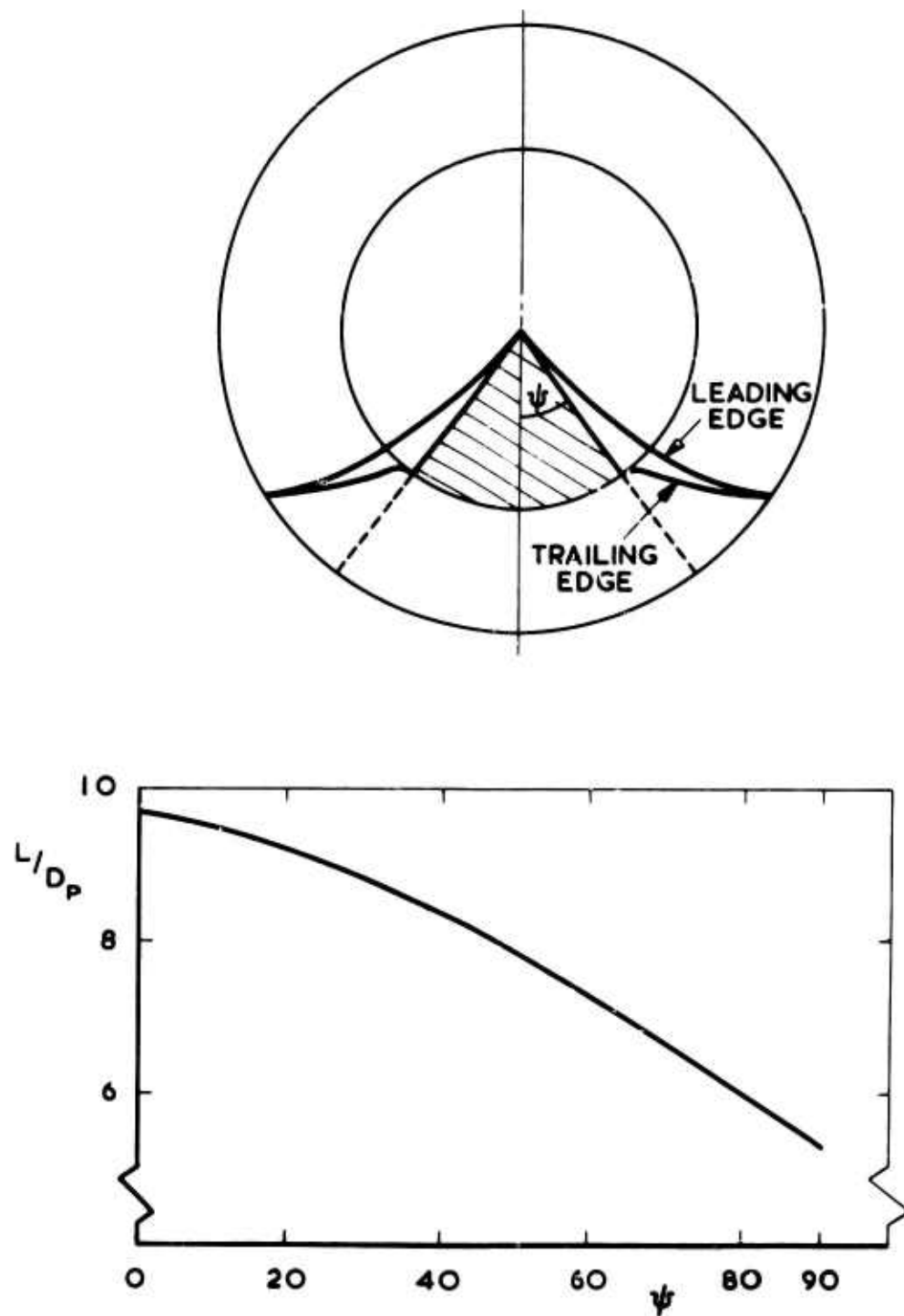
DIRECT AND INTERFERENCE LIFT

FIG. 8.



PERFORMANCE OF W-WINGS
(INVISCID FLOW)

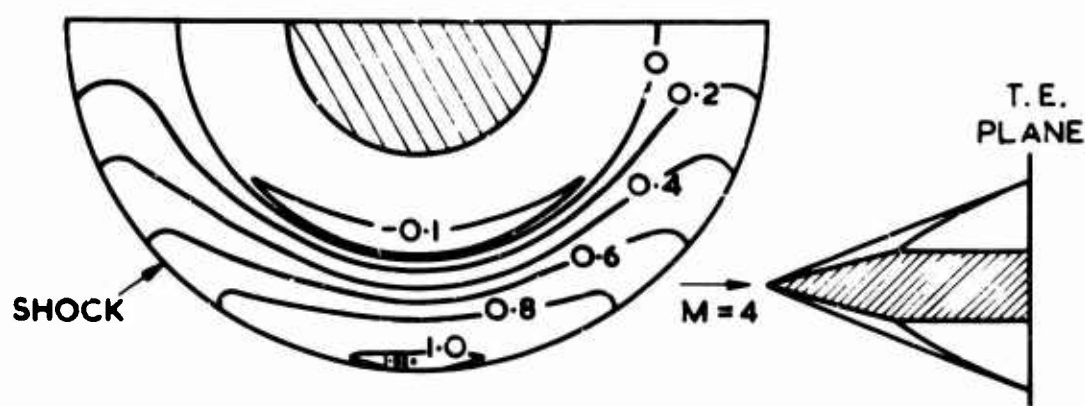
FIG. 9.



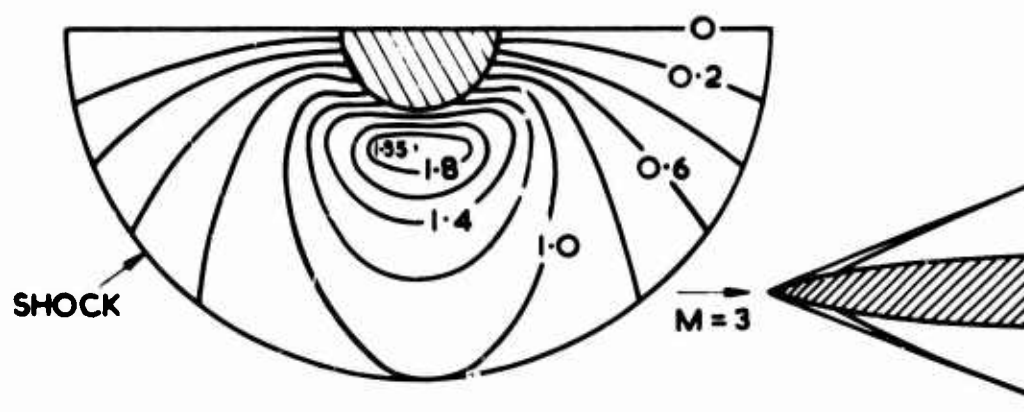
LIFTING EFFICIENCY OF CONE - FLOW SHAPES

FIG.10.

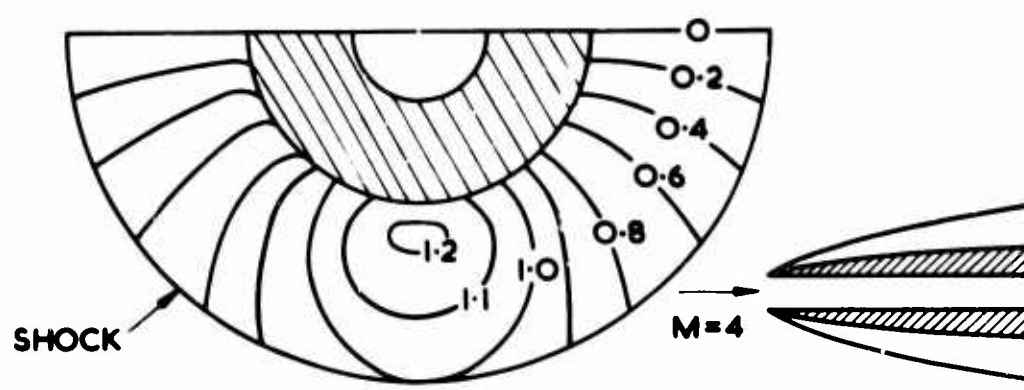
FIGURES ON CURVES ARE VALUES OF THE RATIO OF THE CONTRIBUTION OF A STREAM-LINE TO LIFT AND DRAG (f_L/f_D) COMPARED TO THAT IN WEDGE FLOW AT THE SAME f_L .



a CONE - CYLINDER



b CONE - OGIVE

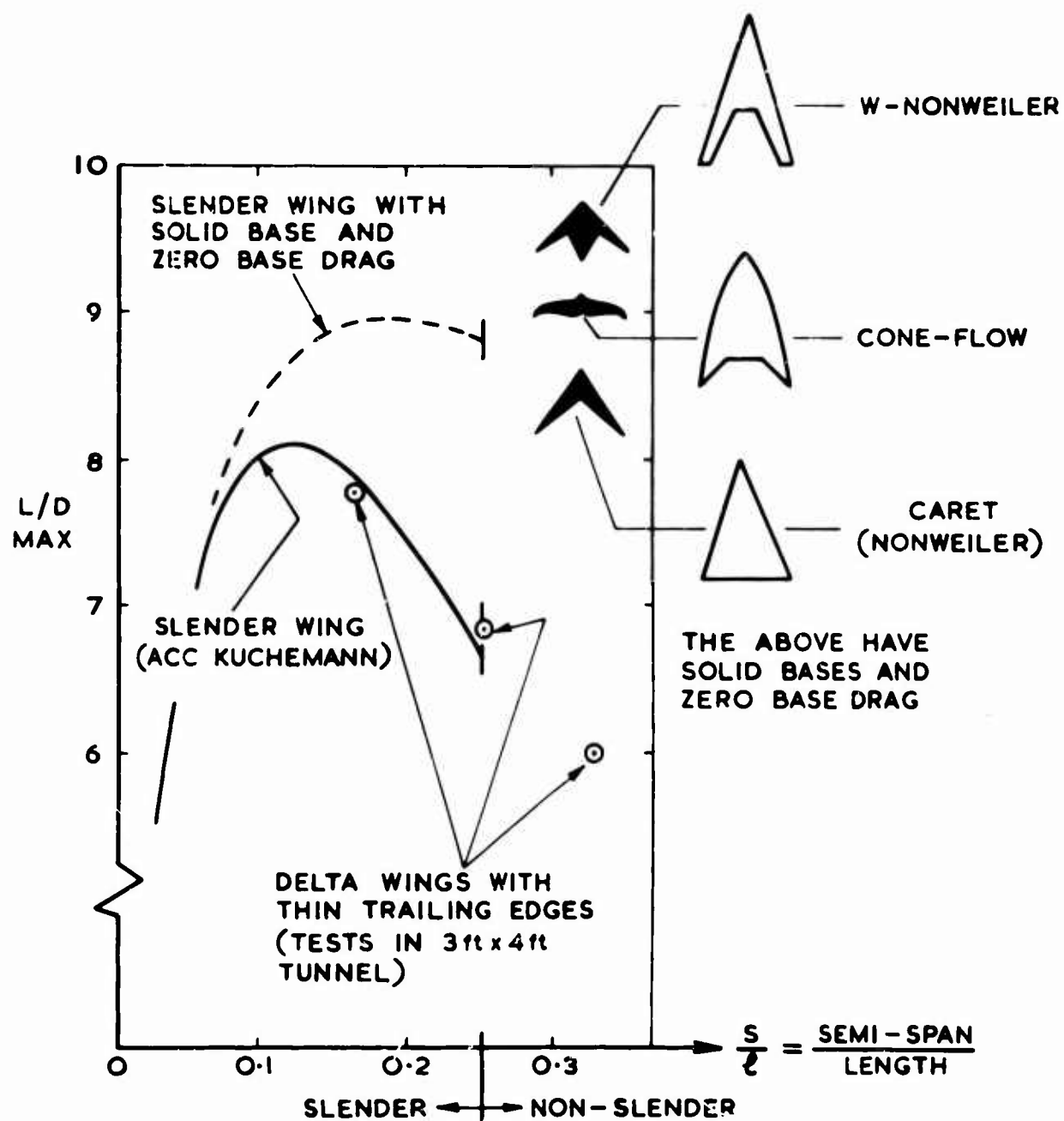


c CURVED SHOCK

FLOW FIELD EFFICIENCY MAPS

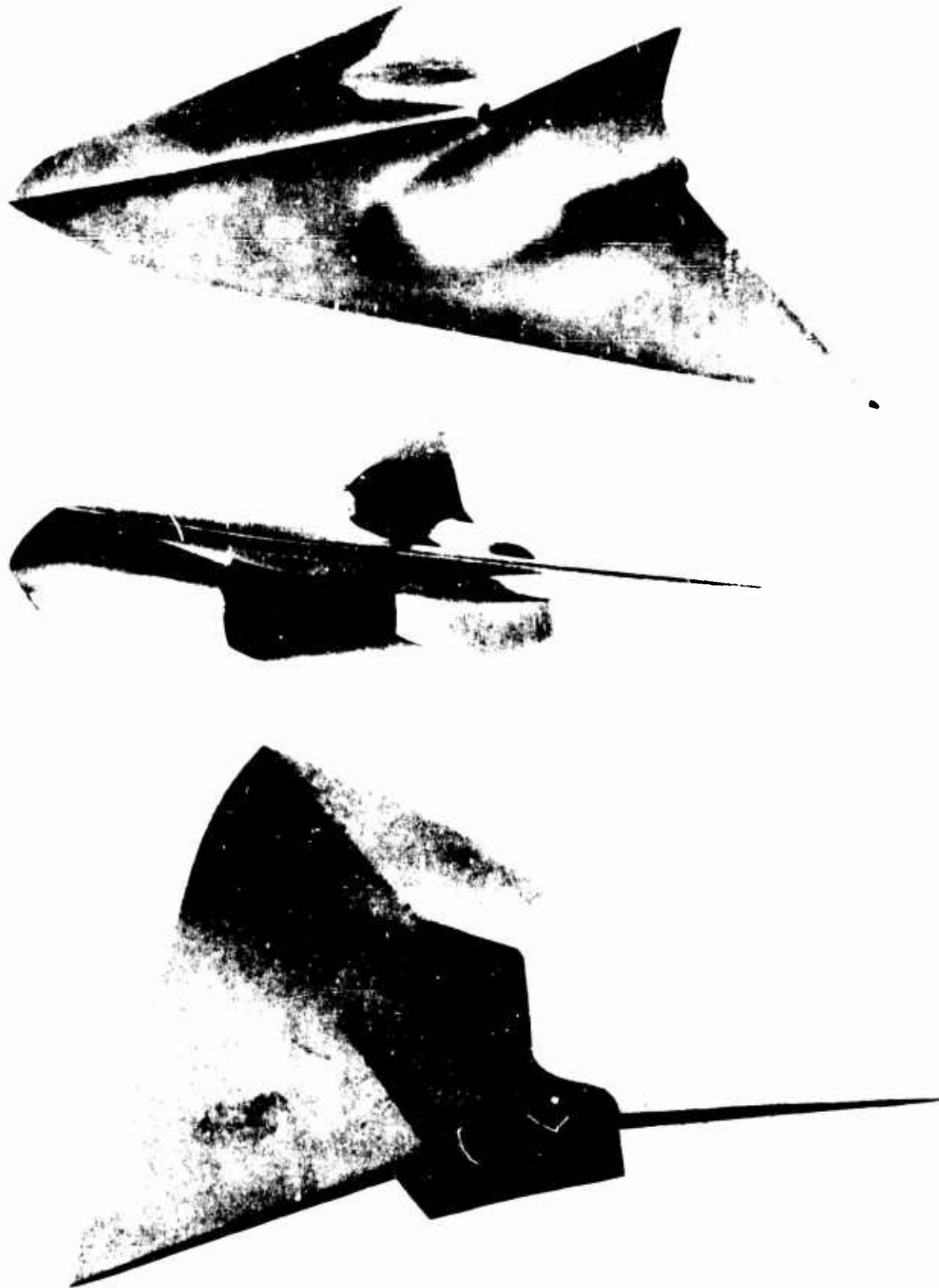
FIG. II.

$$M=4, \tau=0.04, C_f=0.001$$



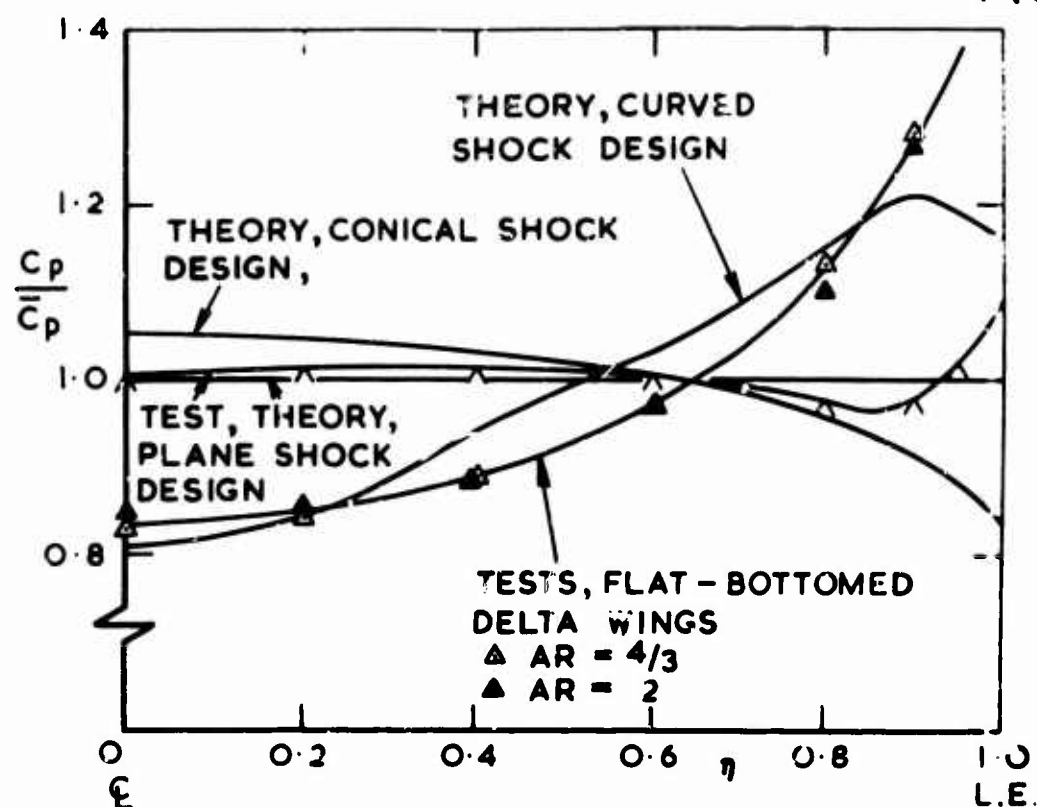
POTENTIAL LIFT/DRAG OF WAVERIDERS

FIG.12.

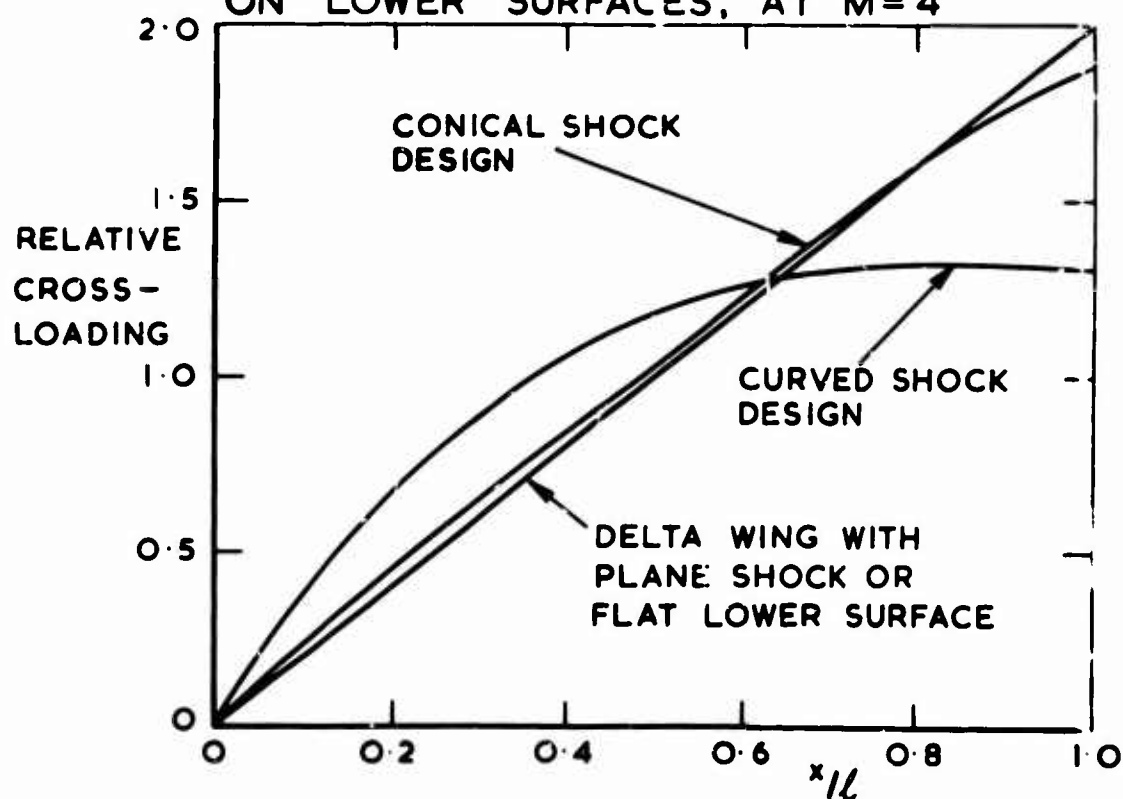


ENGINE-AIRFRAME INTEGRATION BY FLOW FIELD METHOD.

FIG. 13.



a TYPICAL SPANWISE PRESSURE DISTRIBUTIONS ON LOWER SURFACES, AT $M=4$



b THEORETICAL LONGITUDINAL DISTRIBUTIONS OF LOWER SURFACE LIFT LOADING DISTRIBUTIONS

CALCULATIONS OF THE PRESSURE DISTRIBUTION ON LIFTING CONICAL
WINGS WITH APPLICATIONS TO THE OFF-DESIGN BEHAVIOUR OF
WAVE-RIDERS

by

L. C. Squire

Cambridge University Engineering Department
Cambridge, United Kingdom

SUMMARY

Charts are presented for the calculation of pressure distributions and shock shapes on conical wings with diamond and caret (Nonweiler) cross-sections. These charts are based on extensions to Messiter's first order correction to simple Newtonian theory. Comparisons of measured and calculated pressure distributions show good agreement over a wide range of cross-section shapes and Mach numbers. This good agreement allows the theory to be used to build up a systematic description of the off-design behaviour of conical wave-rider wings.

NOTATION

b	tangent of wing semi-apex angle
C	thickness parameter (eqn. (25))
M	Mach number
\bar{p}	static pressure
p_∞	static pressure in free stream
p	correction to Newtonian pressure coefficient, (eqn. (1))
p^*	function in pressure coefficient (eqn. (23))
$\bar{u}, \bar{v}, \bar{w}$	velocity components in physical flow
u, v, w	transformed velocities (eqn. (1))
w_0	constant shock slope near leading edge
$\bar{x}, \bar{y}, \bar{z}$	physical coordinates, Fig. 1: N.B. y is positive downwards
x, y, z	transformed coordinates
y^*	function in physical shock shape (eqn. (24))
z_b	value of transformed \bar{z} on body
z_0	inboard edge of constant pressure
α	incidence of plane of leading edges
γ	angle between shock and surface for wedge flows (Fig. 4(a)): also ratio of specific heats
ϵ	density ratio (eqn. (2))
f	characteristic coordinate (eqn. (3))
ρ	density
ρ_∞	density in free stream
σ	correction to density ratio (eqn. (1))
χ	leading edge sweep
Ω	transformed wing semi-span (eqn. (25))

CALCULATIONS OF THE PRESSURE DISTRIBUTION ON LIFTING CONICAL WINGS WITH APPLICATIONS TO THE OFF-DESIGN BEHAVIOUR OF WAVE-RIDERS

by L.C. Squire

Cambridge University Engineering Department

1. INTRODUCTION

For flight at high supersonic speeds there is considerable interest in lifting body configurations which provide most of the necessary lift and volume and offer the prospect of integration with the power plant¹. However, until recently, most of the methods available for calculating the aerodynamic loads and pressure distributions on these vehicles were rudimentary. This lack of reliable methods for calculating pressure distributions was one of the reasons which led to the current interest in the wave-rider type of vehicle. For these vehicles the complete flow-field is known exactly at the design point; however, reliable methods are still needed to find the off-design characteristics.

Apart from the use of simple Newtonian theory, or the equivalent wedge, or cone, concepts, methods have only been developed for conical shapes. In particular, Walkden² has developed a method for the calculation of the off-design pressure distributions on conical wave-riders by linearisation about the design condition; while the present author^{3,4} has extended Messiter's⁵ first order correction to Newtonian theory to this problem. Crabtree and Treadgold⁶ have also shown that pressure distributions in certain off-design conditions can be predicted by use of certain configurations of oblique shock waves.

The extensions to Messiter's theory produced by the present author require a large amount of computer time. (A typical calculation for a given cross-section at one incidence and speed may need up to 5 minutes on a fast computer). However, for diamond, and caret, cross-sections the solution only depends on two parameters. During the course of the work solutions were obtained for a wide range of these two parameters, and the main purpose of the present paper is to present charts based on these solutions. The charts contain data for both surface pressure distributions and shock shape. The paper also includes more extensive comparisons with experiment than could be included in previous papers. In general the agreement with experiment is very good and the theory is then used to build up a systematic description of the off-design behaviour of conical wave-riders.

2. OUTLINE OF THE THEORY AND DESCRIPTION OF THE CHARTS

2.1 OUTLINE OF THEORY

A full account of Messiter's basic theory can be found in Ref. 5, while the extensions by the present author are described in Refs. 3 and 4. A full account of this work is not necessary here, but a short outline is given for completeness. To derive the equations for the general conical case, Messiter first studied the related problem of the flow over an infinite swept wing with an attached shock. For this case the full solution is known and Messiter recast this solution in terms of the basic Newtonian solution, with the shock lying in the wing surface, together with a series solution in terms of the density ratio across this basic shock. This form of the solution was then used as a guide to treat the conical problem. Using this model Messiter transforms the physical coordinates and the velocities downstream of the physical shock as follows (see Fig. 1 and notation).

$$\begin{aligned}
 x &= \bar{x}, \\
 y &= \bar{y}/\bar{x} \in \tan \alpha \\
 z &= \bar{z}/\bar{x} \in^{\frac{1}{2}} \tan \alpha, \\
 \bar{u}/U_{\infty} &= \cos \alpha + f \sin \alpha \tan \alpha u(y, z), \\
 \bar{v}/U_{\infty} &= f \sin \alpha v(y, z), \\
 \bar{w}/U_{\infty} &= \xi^{\frac{1}{2}} \sin \alpha w(y, z), \\
 C_p &= \frac{\bar{p} - \bar{p}_{\infty}}{\frac{1}{2} \rho_{\infty} U_{\infty}^2} = 2 \sin^2 \alpha (1 + f p(y, z)), \\
 \frac{\rho_{\infty}}{\bar{\rho}} &= \xi + \xi^2 \sigma(y, z),
 \end{aligned} \tag{1}$$

where barred symbols denote physical coordinates and velocities, and $\bar{\epsilon}$ is the density ratio across the basic shock lying in the plane of the leading edges, of incidence α ; i.e.

$$\bar{\epsilon} = \frac{\gamma - 1}{\gamma + 1} + \frac{2}{(\gamma + 1)M^2 \sin^2 \alpha} \quad (2)$$

Substitution of these expressions into the equations of motion and into the jump conditions across the shock lead to a consistent system of equations. In particular it is found that the equations for v , w and p are independent of u and $\bar{\phi}$. Furthermore the equations for v , w and p have two real characteristics given by $z = \text{constant}$ and $\xi = \text{constant}$, where

$$(v - y) \frac{d\xi}{dy} + (w - z) \frac{d\xi}{dz} = 0. \quad (3)$$

Thus the lines $\xi = \text{constant}$ are conical projections of the streamlines. Messiter fixes the constant on these characteristics by putting $\xi = z$ on the shock. The equations of motion and the jump conditions across the shock then show that w is a function of ξ only and that

$$\frac{dy_s(z)}{dz} = -w(\xi) = -w(z), \quad (4)$$

where $y_s(z)$ is the equation of the shock.

Messiter was then able to integrate the equations for v , w and p to obtain

$$y(\xi, z) = y_s(z) - \int_{\xi}^z \frac{w(s) - z}{(w(s) - s)^2} ds, \quad (5)$$

$$v(\xi, z) = y(\xi, z) + (w(\xi) - z) \left\{ \int_{\xi}^z \frac{ds}{(w(s) - s)^2} - w(z) - \frac{1}{w(z) - z} \right\}, \quad (6)$$

$$p(\xi, z) = -1 + 2y_s(z) + 2zw(z) - w^2(z) +$$

$$\left\{ -1 + \frac{1}{(w(z) - z)^2} \right\} \frac{dw(z)}{dz} \int_{\xi}^z \frac{(w(s) - z)^3}{(w(s) - s)^2} ds. \quad (7)$$

In the present approximation the condition that the body is a stream-surface reduces to

$$\left(\frac{dy}{dz} \right)_{\text{body}} = \frac{v - y}{w - z}, \quad (8)$$

or, by substitution from eqn. (6) to

$$\left(\frac{dy}{dz} \right)_{\text{body}} = \int_{\xi}^{z_b} \frac{ds}{(w(s) - s)^2} - w(z_b) - \frac{1}{w(z_b) - z_b}. \quad (9)$$

In this equation ξ is the value of the constant on the characteristic passing through z_b , that is, it is the value of z where the projected streamline from z_b crosses the shock. Thus, in order to solve eqn. (9) for w , we need another equation to relate ξ and z_b . This relation can be obtained by differentiation of eqn. (5) with respect to ξ and by regarding z_b as a function of ξ so that

$$z'_b(\xi) \left[\int_{\xi}^{z_b} \frac{ds}{(w(s) - s)^2} - w(z_b) - \frac{1}{w(z_b) - z_b} - \left(\frac{dy}{dz} \right)_{\text{body}} \right] + \frac{w(\xi) - z_b}{(w(\xi) - \xi)^2} = 0. \quad (10)$$

Since the term in square brackets is zero by eqn. (9) we must have

$$w(\xi) = z_b, \text{ or } 1/z'_b(\xi) = 0. \quad (11)$$

If $z_b = w(\xi)$, then a projected streamline ends at a point on the body surface, and the surface streamlines lie along conical rays from the wing apex. Messiter suggests that this corresponds to a detached shock, when $w(\xi)$ is the solution of the equation

$$\int_{\xi}^{w(\xi)} \frac{ds}{(w(s) - s)^2} - w(w(\xi)) - \frac{1}{w(w(\xi)) - w(\xi)} = \left(\frac{dy}{dz} \right)_{\text{body}}, \quad (12)$$

with $w(0) = 0$, and $w(\Omega) = 1 + \Omega$. Here $\Omega \left(= \frac{b}{\xi^2 \tan \alpha} \right)$ is the transformed

semi-span and the boundary condition at the leading edge (i.e. at $z = \Omega$) corresponds to a singularity in the shock curvature (see Messiter for a full discussion of this boundary condition). Messiter obtained some solutions of

eqn. (12) for flat wings, i.e. $\left(\frac{dy}{dz} \right)_{\text{body}} = 0$, and the present author has described a numerical method of solution³ for non-zero $\left(\frac{dy}{dz} \right)_{\text{body}}$. This numerical method of solution requires a large amount of computer time. However, for wings with rhombic cross-sections (diamond, or Nonweiler, cross-sections) $\left(\frac{dy}{dz} \right)_{\text{body}}$ is constant and is equal to $-\frac{h}{b \xi^2} = -C$ (say). In this case, as pointed out

in the introduction, the solution depends on the two parameters Ω and C and it has been possible to produce charts for the surface pressure distribution and shock shape covering a wide range of these parameters. These charts are described in section 2.3 below, and are presented in Figs. 2 and 3.

Messiter also pointed out that the condition $1/z'_b(\xi) = 0$ corresponded to the flow near the leading edge with an attached shock, but he was unable to match this solution to the non-uniform flow near the centre-line. An approximate method of carrying out this matching is described by the present author in Ref. 4. This matching follows from the fact that near the leading edge of a wing with an attached shock all the surface streamlines cross the conical rays from the apex, and so a projected streamline runs across the wing surface and crosses the shock at the leading edge. Thus near the leading edge $\xi = \Omega$ for all z_b and eqn. (9) becomes

$$\int_{\Omega}^{z_b} \frac{ds}{(w(s) - s)^2} - w(z_b) - \frac{1}{w(z_b) - z_b} = \left(\frac{dy}{dz} \right)_{\text{body}}, \quad (13)$$

with $\int_{\Omega}^{\Omega} w(s) ds = 0$, i.e. the shock is attached.

If we confine our attention to wings with constant $\left(\frac{dy}{dz} \right)_{\text{body}}$ ($= -C$ (say)), that is, to flat wings, wings with diamond cross-sections and Nonweiler wings, we

would expect the flow to be uniform, and the shock to be plane, near the leading edge. Thus by eqn. (4) $w(z)$ will be constant (w_0 , say) for $z > z_0$, where z_0 is as yet unknown. Substitution into eqn. (13) then gives, for $z > z_0$,

$$\int_{\Omega}^z \frac{ds}{(w_0 - s)^2} - w_0 - \frac{1}{w_0 - z} = -C, \quad (14)$$

$$\text{or, } \frac{1}{(w_0 - z)} - \frac{1}{w_0 - \Omega} - w_0 - \frac{1}{w_0 - z} = -C, \quad (15)$$

so that eqn. (13) holds for all $z > z_0$, provided w_0 , Ω and C are related by

$$\frac{1}{w_0 - \Omega} + w_0 = C, \quad (16)$$

$$\text{or, } w_0 = \frac{1}{2} \left\{ (\Omega + C) \pm ((\Omega - C)^2 - 4)^{\frac{1}{2}} \right\}. \quad (17)$$

At $(\Omega - C) < 2$ w_0 is imaginary and so $(\Omega - C) = 2$ is the condition for shock detachment. In general we would expect to take the negative sign in eqn. (17) as corresponding to the weak shock. However, as shown below, the strong shock may occur on Nonweiler wings at the design condition.

A solution of eqn. (9), inboard of the uniform region, may be obtained by noting that Babaev's¹¹ numerical solution for a flat delta wing with an attached shock shows that at the inboard edge of the uniform flow the shock, and the shock slope, are continuous, but that the shock curvature may be discontinuous. In the present notation this implies that $w'(z)$ may be discontinuous at the inner edge of the uniform flow region. It is possible to show that this type of discontinuity does not invalidate solutions (5), (6) and (7), so that eqn. (9) still holds. It can then be shown (Ref. 4) that $w = w_0$ for all $z > 1 + w_0$, provided $w_0 > 0$; so that $z = (1 + w_0)$ corresponds to the inner edge of the uniform flow region. Inboard of this point $w(z)$ is given by

$$w(z) = z - 1. \quad (18)$$

This solution can then be matched approximately to a solution of eqn. (12) to give the flow in the central region of the wing. As pointed out in Ref. 4 this matched solution is not completely satisfactory. However, the results obtained are in good agreement with Babaev's numerical solution (see Fig. 11). Results from this matched solution are included in the charts of Figs. 2 and 3.

Near the leading edge the shock shape, and the pressure, can be found explicitly in the form

$$y_s(z) = (\Omega - z)w_0, \quad (1 + w_0) \leq z \leq \Omega$$

$$y_s(z) = (\Omega - 1)w_0 - w_0^2/2 + (z - 1)^2/2, \quad z \leq (1 + w_0), \quad (19)$$

$$\text{and } C_p = 2\sin^2\alpha(1 + \epsilon p),$$

$$\text{where } p = -1 + 2w_0\Omega - w_0^2 \quad (1 + w_0) \leq z \leq \Omega$$

$$p = -1 + 2w_0\Omega - w_0^2 + 2(z - 1 - w_0) \quad z \leq (1 + w_0). \quad (20)$$

Finally it should be noted that at the design point of a conical wave-rider, the incidence of the plane of the leading edges, α , and the inclination of the central ridge line to this plane, γ ($= \tan^{-1}(-h)$) (Fig. 1) are related by the oblique shock relations for a shock inclined at an angle α producing a flow deflection of $(\alpha - \gamma)$, see Fig. 4(a).

$$\text{Thus } \frac{\tan\gamma}{\tan\alpha} = \frac{p_\infty}{p} = \epsilon,$$

$$\text{so that } C\Omega \cong \frac{h}{\epsilon^{\frac{1}{2}}b} \cdot \frac{b}{\epsilon^{\frac{1}{2}}\tan\alpha} = -\frac{\tan\gamma}{\epsilon\tan\alpha} = -1. \quad (21)$$

Thus for all Nonweiler wings at design the product of the parameters C and Ω lie on a hyperbola in the (C, Ω) plane: this line is drawn in Fig. 4(b). As can be seen this line lies above the line $(\Omega - C) = 2$, so that the shock is attached; and by eqn. (17) $w_0 = 0$, so that the shock lies in the plane of the leading edges, as would be expected. It should be noted that to make $w_0 = 0$ in eqn. (17) we need to take the negative root for $\Omega > 1$ and the positive root for $\Omega < 1$; this corresponds to the physical fact that if we regard the Nonweiler wing from the viewpoint of oblique shock waves attached to a swept edge, then it is the weak shock which lies in the plane of the edges if the edges are supersonic with respect to flow inside the caret shape, whereas the strong shock lies in this plane if the edges are subsonic with respect to this flow. A study of a large number of Nonweiler wings using the oblique shock relations showed that this changeover does occur very near $\Omega = 1$.

For $w_0 \neq 0$, eqn. (7) gives $p = -1$, so that the pressure coefficient, as given by eqn. (1), is

$$\begin{aligned} C_p &= 2 \sin^2 \alpha (1 + \epsilon p) = 2 \sin^2 \alpha (1 - \epsilon), \\ &= \frac{2}{\gamma M^2} \cdot \frac{2\gamma}{\gamma + 1} (M^2 \sin^2 \alpha - 1), \end{aligned} \quad (22)$$

which is the exact pressure coefficient as given by the oblique shock relations. Thus the present approximation is exact for the Nonweiler wing at design.

2.2 SIGNIFICANCE OF THE PARAMETERS C AND Ω

As can be seen from Fig. 4(b), the lines $C\Omega = -1$ and $(\Omega - C) = 2$, divide the C - Ω plane into the four regions labelled A, B, C and D. Also positive C corresponds to conical wings with diamond cross-sections, whereas negative C corresponds to Nonweiler wings (see Fig. 1). Fig. 4(b) thus shows two types of flow over wings with diamond cross-sections, i.e. flow with attached shocks, region D, and flow with attached shocks, region B: but four types of flow on Nonweiler wings. Region D is again the case of flow with a detached shock, and the flow field is fully given by the solution of eqn. (12). To find the significance of the other three regions it is first helpful to consider a wing designed for an incidence α_D and a Mach number M_D , so that γ , and hence h , is given by the oblique shock relations. If M is now kept fixed and the incidence changed to another incidence α' , then, in general, it is possible to find a new equivalent design Mach number M' , so that M' and α' give the same value of γ (see Fig. 4(a)). (Note that in all this discussion we assume that the flow on the under surfaces is independent of the shape of the upper surface). Thus the case of a wing at design Mach number, but off-design incidence, is equivalent to that on a wing at design incidence, but off-design Mach number. At the equivalent design point $C\Omega = -\tan \gamma / \epsilon \tan \alpha' = -1$, and at off-design speed α' and γ remain fixed, so that $C\Omega$ behaves like $1/\epsilon$. However, at fixed incidence $1/\epsilon$ behaves like M^2 , so that $|C\Omega| > 1$ for wings flying above the equivalent design speed. Thus region A corresponds to wings at design incidence but at Mach numbers above design, whereas regions B, C and D correspond to flight below the equivalent design speed.

The flow regimes in regions B and C are best understood by considering the values of w_0 (eqn. (17)) on their boundaries. At design, i.e. at $C\Omega = -1$, w_0 is zero since the shock lies in the plane of the leading edges, thus by eqn. (17)

$$\begin{aligned} 0 = w_0 &= \frac{1}{2} \left\{ (\Omega - 1/\Omega) \pm ((\Omega + 1/\Omega)^2 - 4)^{\frac{1}{2}} \right\} \\ &= \frac{1}{2} \left\{ (\Omega - 1/\Omega) \pm |\Omega - 1/\Omega| \right\}. \end{aligned}$$

Therefore, if $\Omega > 1$ the design shock corresponds to the weak attached shock, whereas if $\Omega < 1$ the design shock corresponds to the strong attached shock. Along the line $(\Omega - C) = 2$, $w_0 = (\Omega - 1)$. Thus $w_0 > 0$ for $\Omega > 1$, and this condition holds for all region B. On the other hand $w_0 < 0$ in region C. Also, as shown in Ref. 4, eqn. (12) gives physically possible solutions for $C < -1$, $(\Omega - C) > 2$, (Region C), whereas for $C > -1$, $(\Omega - C) > 2$ (Region B) the solutions obtained are physically meaningless since the calculated shock cuts the wing surface inboard of the leading edge, i.e. the 'detached' shock is not detached. However, in region B it is

possible to obtain the matched solution described in section 2.1 since $w_0 > 0$. Thus it would appear that region B corresponds to the type of flow shown in Fig. 4(c) with the weak shock at the design condition and with an attached shock below the plane of the leading edges for a certain Mach number range below design. On the other hand region C corresponds to flight below the design speed, with the strong attached shock occurring at design. In this condition both eqn. (17), and the oblique shock relations, show that the shock wave attached to the leading edges lies inside the 'caret' shape (see Fig. 4(d)), whereas the two-dimensional shock corresponding to the equivalent wedge lies below this plane. It is suggested in Ref. 4 that in these conditions no matching of the shock system is possible, and that the shock detaches immediately the speed falls below design, so that we revert to the detached shock type of flow as in Region D. It must be admitted that this interpretation of the flow in region C is rather tentative, but it is supported by the fact that we can get solutions of eqn. (12) in this region, and these solutions are in good agreement with experiment (see, for example, Fig. 7).

2.3 DESCRIPTION OF THE CHARTS

In presenting charts based on the above solutions it is most convenient to re-write the pressure coefficient in the form

$$C_p = 2\sin^2\alpha \left[1 + \epsilon(2\Omega C + p^*(\Omega, C, \bar{z}/b\bar{x})) \right], \quad (23)$$

and the physical shock shape as

$$\bar{y}/\bar{x} = \epsilon \tan\alpha y^*(\Omega, C, \bar{z}/b\bar{x}), \quad (24)$$

where, as mentioned above, α is the incidence of the plane containing the leading edges of the wing, or body, and ϵ is the ratio of upstream to downstream density across a shock lying in this plane (eqn. (2)). C and Ω are parameters, as defined above, depending on the wing geometry and density ratio, they are given by

$$C = \frac{h}{b\epsilon^{\frac{1}{2}}}, \quad \Omega = \frac{b}{\epsilon^{\frac{1}{2}}\tan\alpha}. \quad (25)$$

It should be remembered that y is measured downwards normal to the plane of the leading edges so that C is positive for diamond cross-sections, and negative for Nonweiler wings.

The calculations showed that the functions p^* (eqn. (23)), and y^* (eqn. (24)) varied slowly near the centre-line, and more rapidly near the leading edges. Also, as explained in Ref. 3, the numerical values near the leading edges are relatively inaccurate for the detached shock solution. In the light of this behaviour it is convenient to plot p^* and y^* against C at fixed values of Ω in four separate charts for $\bar{z}/b\bar{x} = 0, 0.4, 0.7$ and 0.9 . To allow accurate interpolation the actual values of Ω vary in the different charts. The charts for p^* are given in Figs. 2(a) to 2(g) and the charts for y^* in Figs. 3(a) to 3(d). In general, the values of p^* and y^* at

$\bar{z}/b\bar{x} = 0, 0.4, 0.7$ and 0.9 should be sufficient to determine the complete pressure distribution and shock shape across the span, except very close to the leading edge. However, if there is any doubt about the shape of the curve through the four points, guidance can be obtained from the typical plots of p^* and shock shape presented in Refs. 3 and 4.

It should be noted that the charts generally stop for $C > 1.5$ since it was difficult to obtain accurate solutions for $C > 1.5$. Also results for region B are shown dotted since they are slightly less accurate than the results in regions C and D. Near the leading edges of wings in region B the shock shape and pressure coefficients can be calculated directly from the formulae given above (eqns. (19) and (20)). These results are not included in the charts. Alternatively results near the leading edges of wings in region B can be obtained exactly from the oblique shock relations.

2.4 ACCURACY OF THE CHARTS

It is shown in Ref. 1 that the method of solution for the detached shock case is capable of giving values of p^* with an accuracy of better than ± 0.015 , whereas the error in the approximate matched solution for the attached shock case may be slightly larger. The interpolation to produce the present

charts, and interpolation from these charts for given values of C and Ω , probably doubles this error. Thus p^* , as derived from the charts, should be accurate to ± 0.03 . This gives an error in pressure coefficient of

$$\begin{aligned} & \pm 0.03(\epsilon 2 \sin^2 \alpha), \\ & = \pm 0.01(\sin^2 \alpha + 5/M^2), \text{ for } \gamma = 1.4. \end{aligned}$$

Except at low Mach numbers ($M < 4$, say) and high incidence ($\alpha > 25^\circ$, say) this gives a maximum error of ± 0.005 in C_p . However, at very low incidence ϵ itself tends to be large so that the neglected higher order terms become significant.

It is also estimated that the charts for y^* are accurate to ± 0.02 , thus for $\epsilon < 0.5$, the shock angle should be accurate to $\pm 0.6^\circ$.

3. COMPARISON BETWEEN THEORY AND EXPERIMENT

Some comparisons between the present theory and experimental results are included in Refs. 3 and 4. Since these papers were written a large amount of experimental data on Nonweiler wings has become available and this data is compared with the present theory in Figs. 5 to 8. For completeness some of the comparisons included in previous papers are given in Figs. 8 to 11. The range of the parameters C and Ω corresponding to the experimental results used in the comparisons are shown in Fig. 4(b). This figure also includes the figure numbers of the various comparisons. It should be noted that in the figures for Nonweiler wings α' is measured relative to the design incidence and so does not correspond to the incidence used in eqn. (1). Also the theoretical curves drawn in Fig. 9 correspond to values of C greater than 1.5, and therefore had to be obtained by extrapolation from the curves of Fig. 2. This extrapolation gives larger errors in p^* than the values quoted in section 2.4, however, for these wings $2\epsilon \sin^2 \alpha$ is small (< 0.12) so that C_p should still be accurate to ± 0.01 .

Let us first consider the comparisons between theory and experiment in regions C and D for Nonweiler wings, Figs. 5, 6 and 7. As can be seen the agreement is very good at $M = 4.3$, except at very high incidence, but is less good at $M = 2.47$, where the agreement between theory and experiment is still good over the outer 40% of the span, but where the measured pressures are above the theoretical curve near the centre-line. This is also true at the design condition (Fig. 7, $\alpha' = 0$), where the present theory is exact. At the design condition the pressures measured on two wings of different aspect ratios both show an almost linear fall of about 0.04 in C_p from centre-line to leading edges. This type of variation is not present on the wing designed for $M = 4.3$ (Fig. 6(a)), where the measured pressures are constant across the span and are in excellent agreement with the theoretical value. (Note that in Fig. 6(a) $\alpha' = 4^\circ$ is also a design incidence). It seems unlikely that the discrepancies at $M = 2.47$ indicate a breakdown in the present theory at low values of Ω , since some of the results on Fig. 5(a) correspond to almost as low values of Ω , yet the agreement between theory and experiment is very good in this case. Rather it would appear that some viscous effect is present at this low Mach number which is virtually independent of incidence. This behaviour calls for further study.

Results* for Nonweiler wings in region B are shown in Fig. 8. This figure also includes the ranges of the parameters C and Ω covered by the tests in the bottom right-hand figure. This latter figure also includes the line of exact shock detachment as calculated by the oblique shock relations. As will be seen the exact and approximate lines of shock detachment are close together at $M = 3.97$ ($\epsilon = 0.33$), but slightly further apart at $M = 3.5$ ($\epsilon = 0.47$). At $M = 3.5$ exact shock detachment occurs at about 1° above the approximate value. The pressures calculated by the present method are close to the measured pressures in cases where the shock is detached (the higher incidences);

* These results were recently obtained in the high supersonic speed tunnel at the R.A.E. Bedford. The author would like to thank the staff of the tunnel for their help in arranging and in carrying out the tests.

but when the shock is attached the present method overestimates the pressure in the uniform flow region near the edge. The discrepancy increases as the line of shock detachment is approached. Thus calculated results for $M = 3.5$, $\alpha' = 0.7^\circ$, and $M = 3.75$, $\alpha' = 4.7^\circ$ and 8.9° , which are near the condition for shock detachment, are very high, whereas results for $M = 3.75$, $\alpha' = 0.7^\circ$ and $M = 3.97$, $\alpha' = 0.1^\circ$, 4.1° and 8.2° are in good agreement with the measured values. In all cases the present matched solutions are in very good agreement with the measured pressures near the centre-line in spite of the large errors near the leading edge. As might be expected, the pressures calculated from the oblique shock relations are very close to the pressures measured near the edge. Thus it would appear that the pressures in region B can be predicted over the whole span by using the present matched solution near the centre-line (this solution is included in the charts), and by using the exact oblique shock relations near the edge.

Measured results for wings with diamond cross-sections and with flat surfaces are compared with the present theory for detached shocks in Figs. 9 and 10. In general the comparisons are very good except in Fig. 10(a) at the higher aspect ratio. The shapes of the pressure distributions for the bodies of Fig. 10(a) suggest that as the aspect ratio increases the flow over the body becomes more 'winglike'. However, the large discrepancy between theory and experiment at $\Omega = 1.76$ suggests that the present theory tends to predict too rapid an approach to the 'winglike' flow. Thus, in cases where the physical type of flow is changing rapidly the present method may be in error. The results for the flat wings (Fig. 10(b)) are particularly encouraging since they include some results at approximately the same value of Ω (1.82), but different values of ϵ (0.42 and 0.71); in both cases the agreement between experiment and theory is excellent.

Finally Fig. 11 (extracted from Ref. 4) shows a comparison of Babaev's numerical solution for flat wings with attached shocks, with the present matched solution. As can be seen the agreement is very good at $\alpha = 15^\circ$, where $\epsilon = 0.51$, but less good at $\alpha = 9^\circ$ and $\alpha = 21^\circ$. The discrepancy at $\alpha = 9^\circ$ can be explained by the high value of ϵ (= 1.11) which means that the present theory is not strictly valid. The discrepancy at $\alpha = 21^\circ$, is due to the fact that the condition for shock detachment has been approached and so, as shown in the last comparison, we might expect the present method to be in error. However, in spite of these discrepancies the present results are quite good.

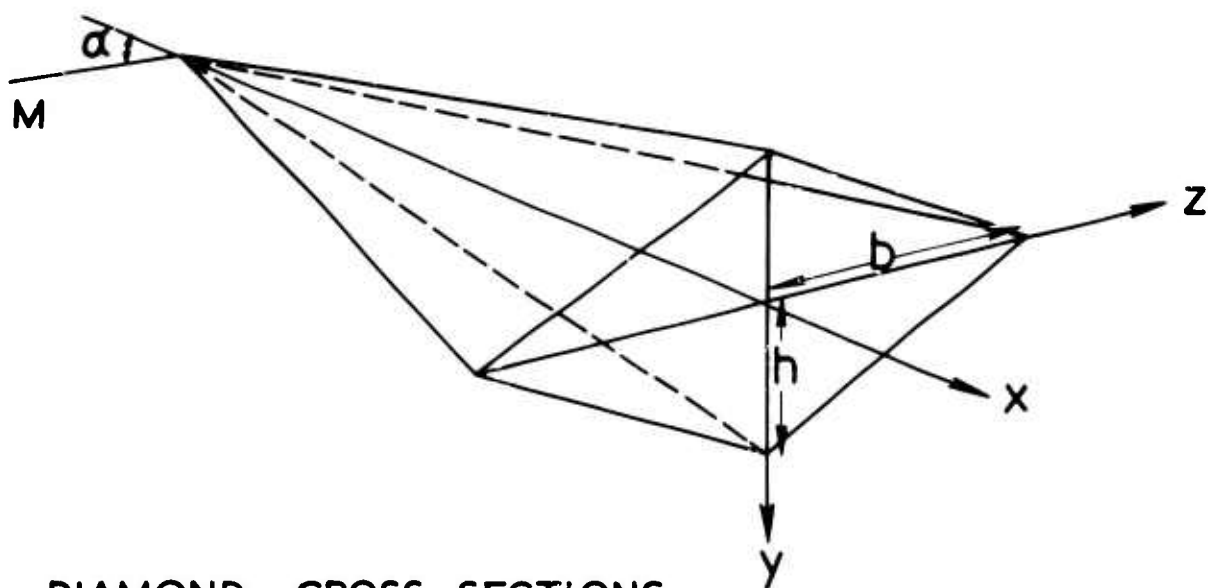
4. CONCLUSIONS

The comparison between theory and experiment discussed in section 3 show that the charts presented in this paper can be used to predict accurate pressure distributions on a wide range of conical bodies at high supersonic speeds. In particular, the charts can be used to predict the off-design characteristics of Nonweiler wings, except in conditions near shock detachment. However, here the charts can be combined with the exact oblique shock relations to give accurate predictions of the pressure distribution. The overall good agreement between theory and experiment shows that the flow regions of Fig. 4(b) which are predicted by the present theory correspond closely with the real flow regimes, and so the real flow may be conveniently classified in terms of the two parameters C and Ω . These two parameters depend on the wing geometry, and incidence, and on the ratio of upstream to downstream density across a shock wave inclined to the flow at an angle equal to the incidence of the plane containing the leading edges of the wing. In all the cases considered in this paper this ratio has been found from the perfect gas relationships. However, it seems likely that the theory will still apply in its present form in cases where real gas effects are significant, provided these real gas effects are included in the calculation of the basic density ratio.

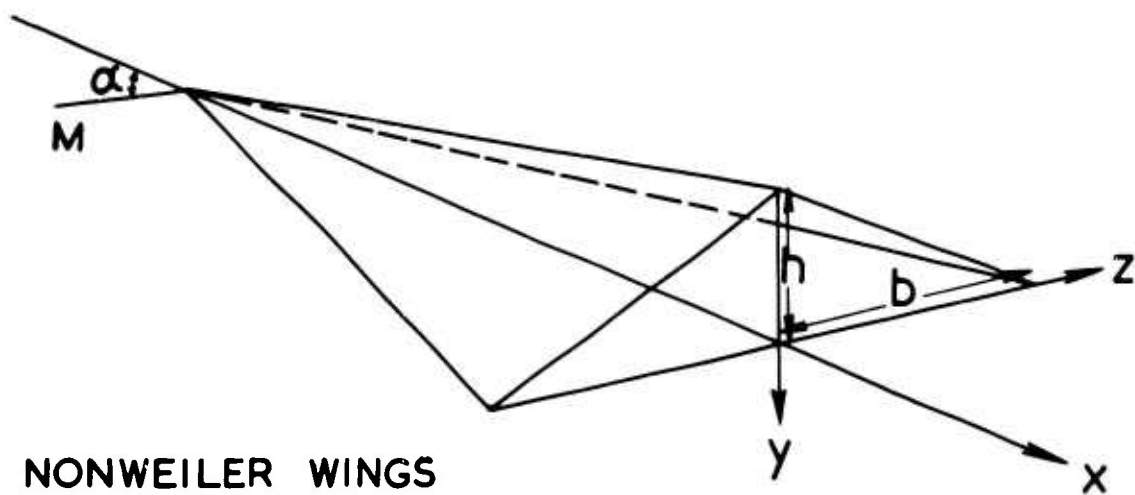
Finally it should be noted that the work so far only applies to conical bodies, and that calculations have only been made for cross-sections with straight edges. Although it would require much more computer time, eqn. (12) for the detached shock, could be solved for more complicated cross-sections, such as biconvex sections, or Nonweiler wings with blunted leading edges and work on this topic is in progress. The extension of the present work to non-conical shapes is more difficult, but it should be noted that many lifting bodies will be conical near the nose and so the present solution should provide initial conditions for a marching type of solution in the stream direction.

REFERENCES

1. D. Küchemann Hypersonic aircraft and their aerodynamic problems.
Progress in Aeronautical Sciences, Vol. 6, 1965. (Pergamon Press)
2. F. Walkden and R.H. Eldridge Waveriders under off-design conditions.
Aero. Res. Coun. 28,728, 1967.
3. L.C. Squire Calculated pressure distributions and shock shapes on thick conical wings at high supersonic speeds.
Aero. Quart. Vol. XVIII, pp.185-206, 1967.
4. L.C. Squire Calculated pressure distributions and shock shapes on conical wings with attached shock waves.
To be published in Aero. Quart.
5. A.F. Messiter Lift of slender delta wings according to Newtonian theory.
A.I.A.A. Journal, Vol. 1, pp.794-802, 1963.
6. L.F. Crabtree and D.A. Treadgold Experiments on hypersonic lifting bodies.
Fifth Congress of the International Council of the Aeronautical Sciences, 1966.
ICAS paper 66-24.
7. L.C. Squire Pressure distributions and flow patterns at $M = 4.0$ on some delta wings.
Aero. Res. Coun. R & M 3374, 1963.
8. L.C. Squire Pressure distributions and flow patterns on some conical shapes with sharp leading edges at $M = 4.0$.
Aero. Res. Coun. R & M 3340, 1962.
9. D.H. Peckham Pressure distribution measurements on a series of slender body shapes at Mach numbers of 6.85 and 8.60.
Aero. Res. Coun. C.P. 791, 1962.
10. D.A. Treadgold Unpublished R.A.E. results.
11. D.A. Babaev Numerical solution of the problem of the supersonic flow past the lower surface of a delta wing.
Translated from Russian in A.I.A.A. Journal, Vol. 1, pp.2224-2231, 1963.

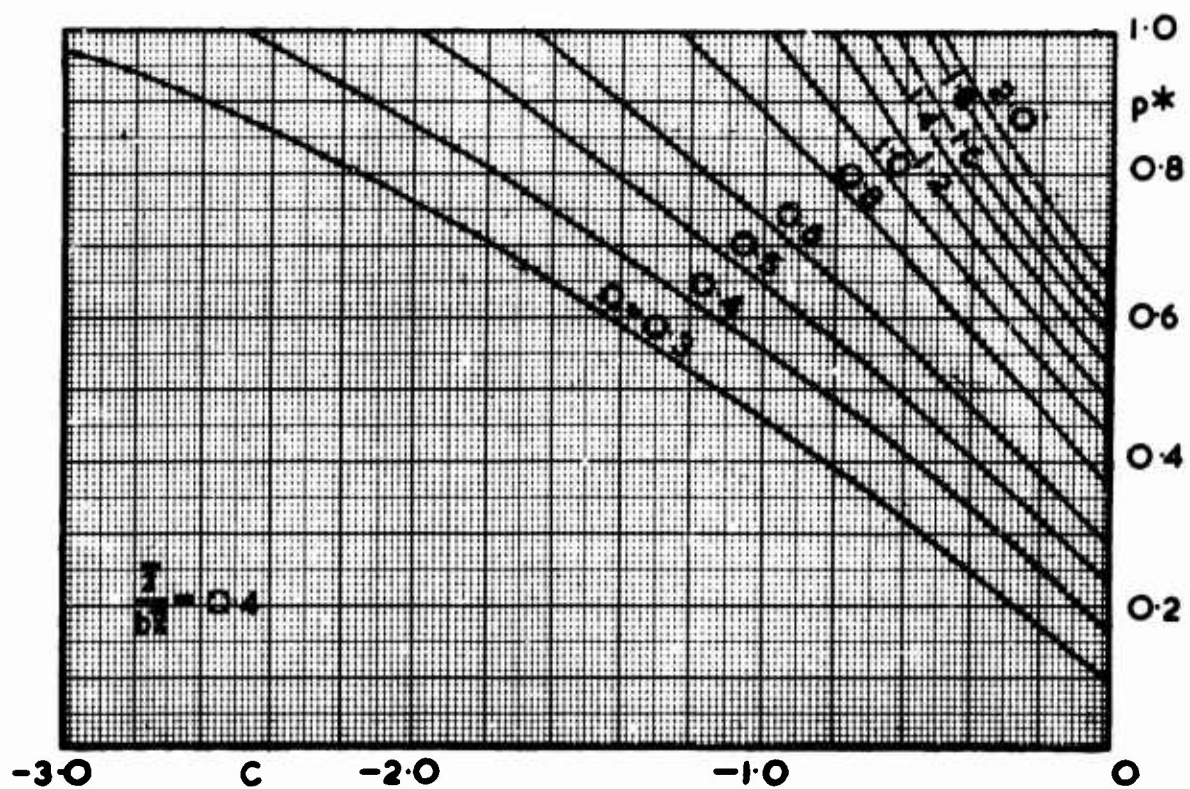
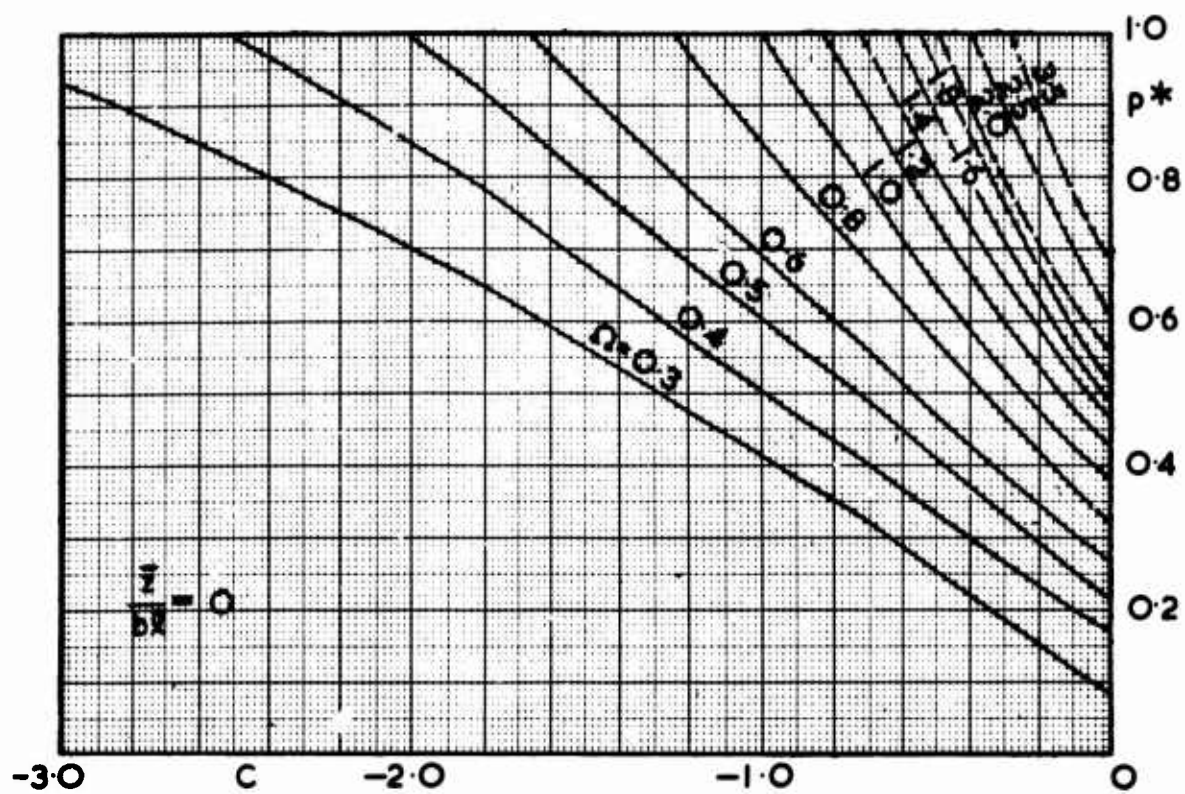


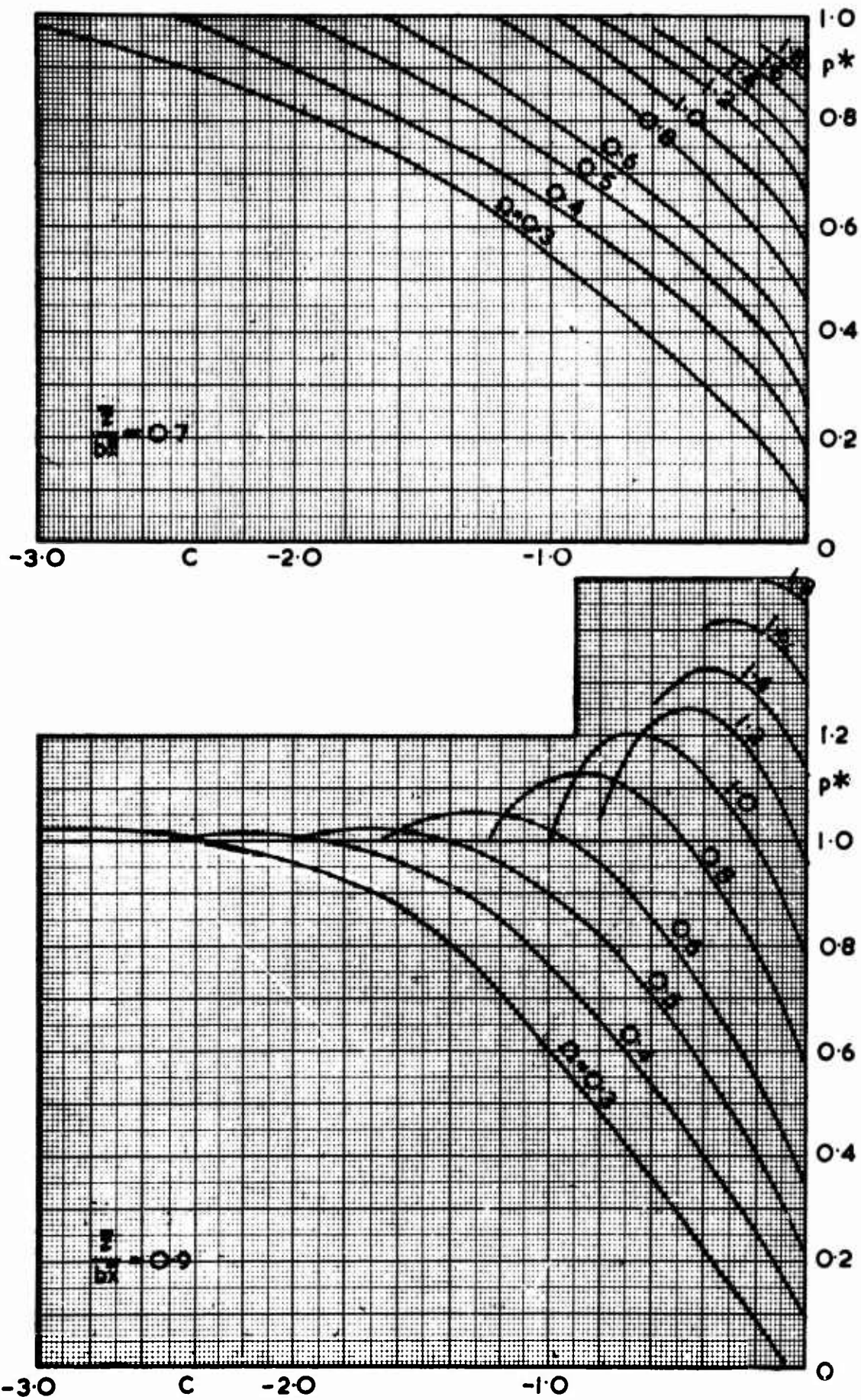
DIAMOND CROSS SECTIONS

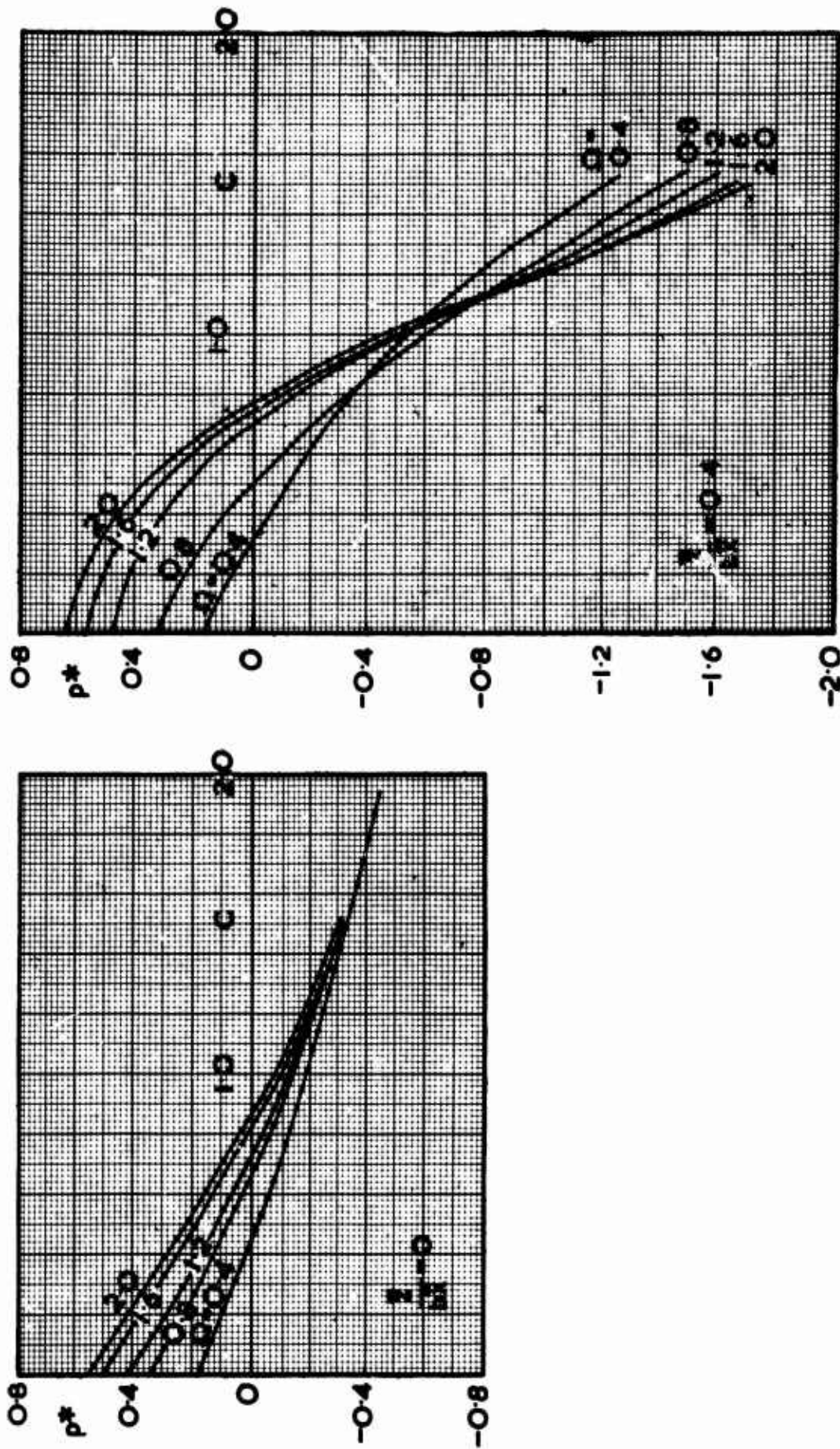


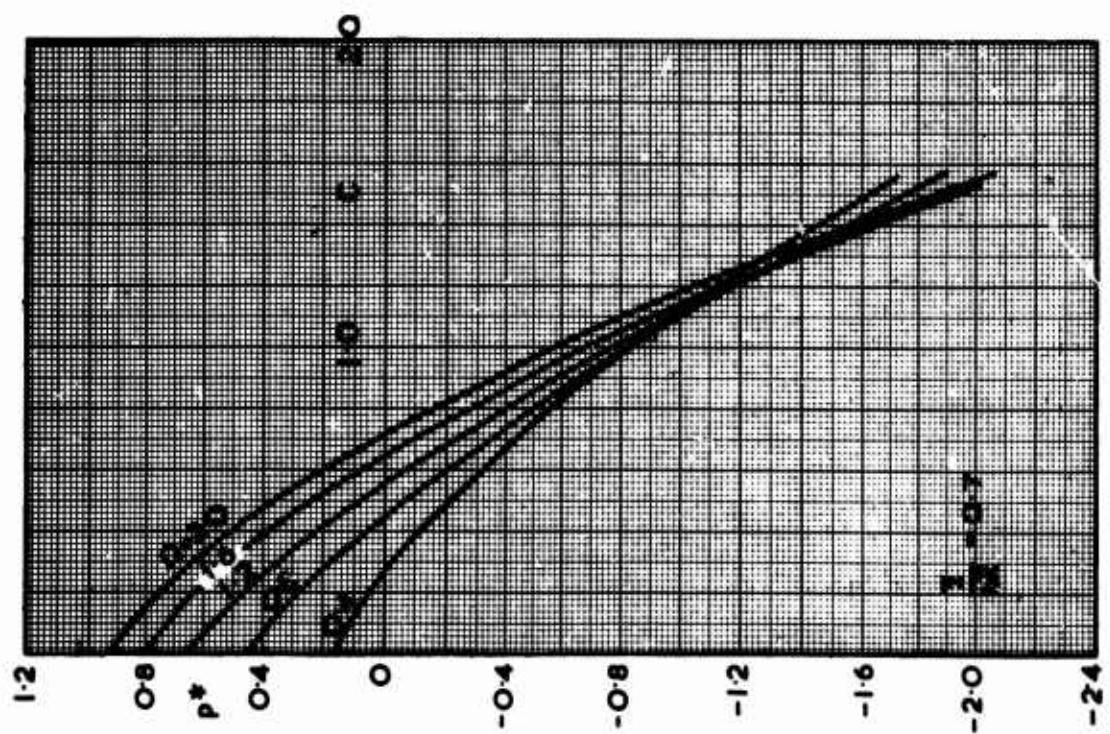
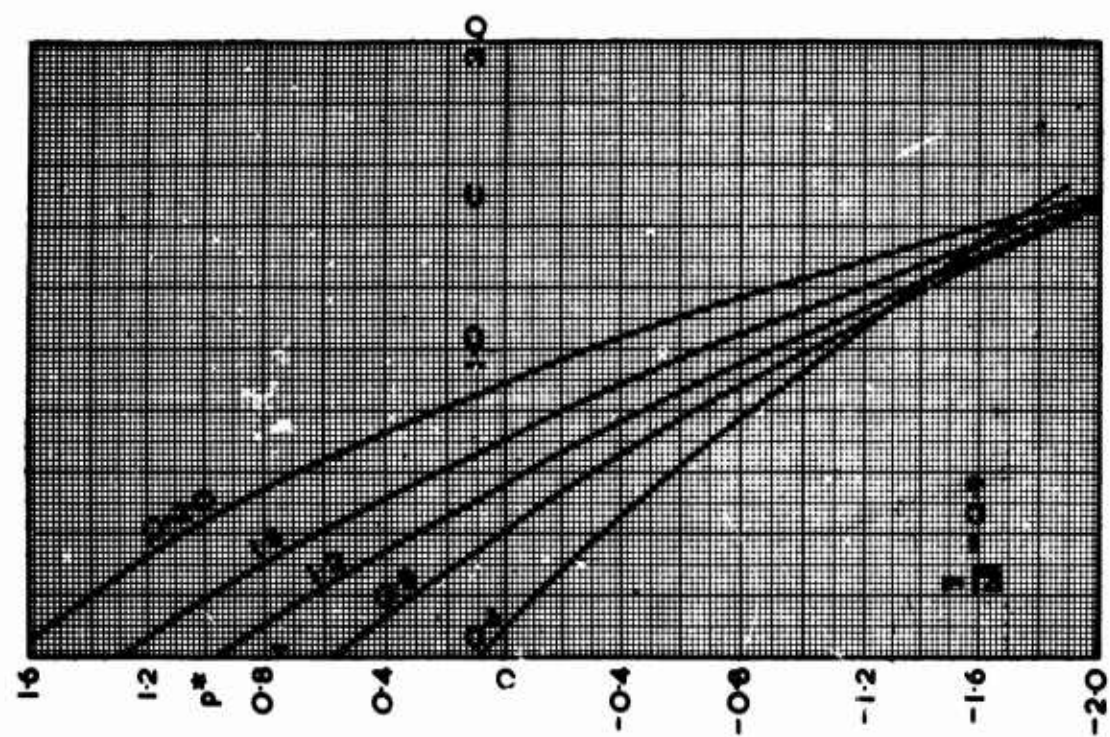
NONWEILER WINGS

Fig. 1 Notation

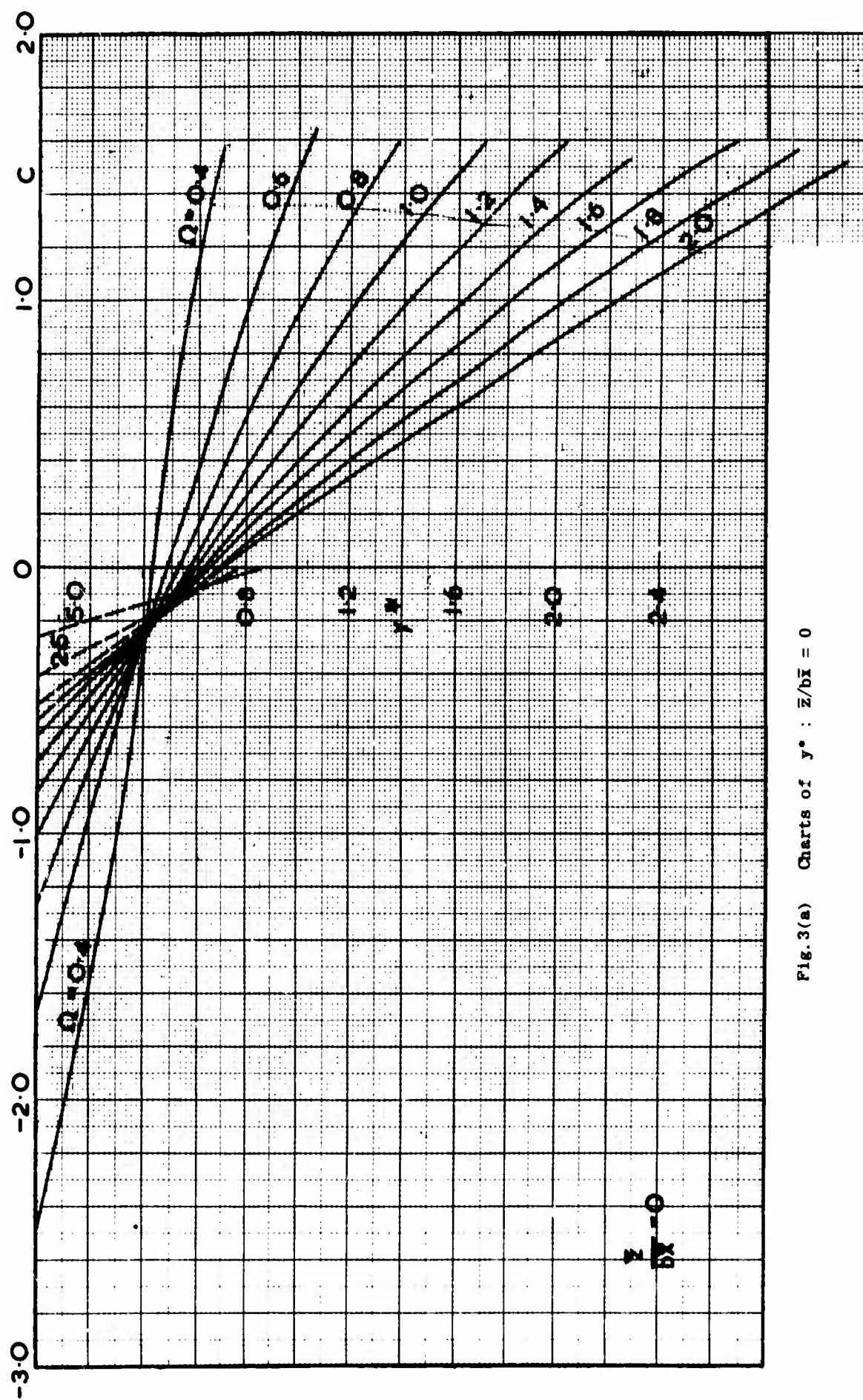
Figs. 2(a) and (b) Charts of p^* : $C < 0$

Figs. 2(c) and (d) Charts of $p^* : C < 0$

Figs. 2(e) and (f) Charts of $p^* : C > 0$



Figs. 2(g) and (h) Charts of p^* : $C > 0$

Fig. 3(a) Charts of $y^* : z/bx = 0$

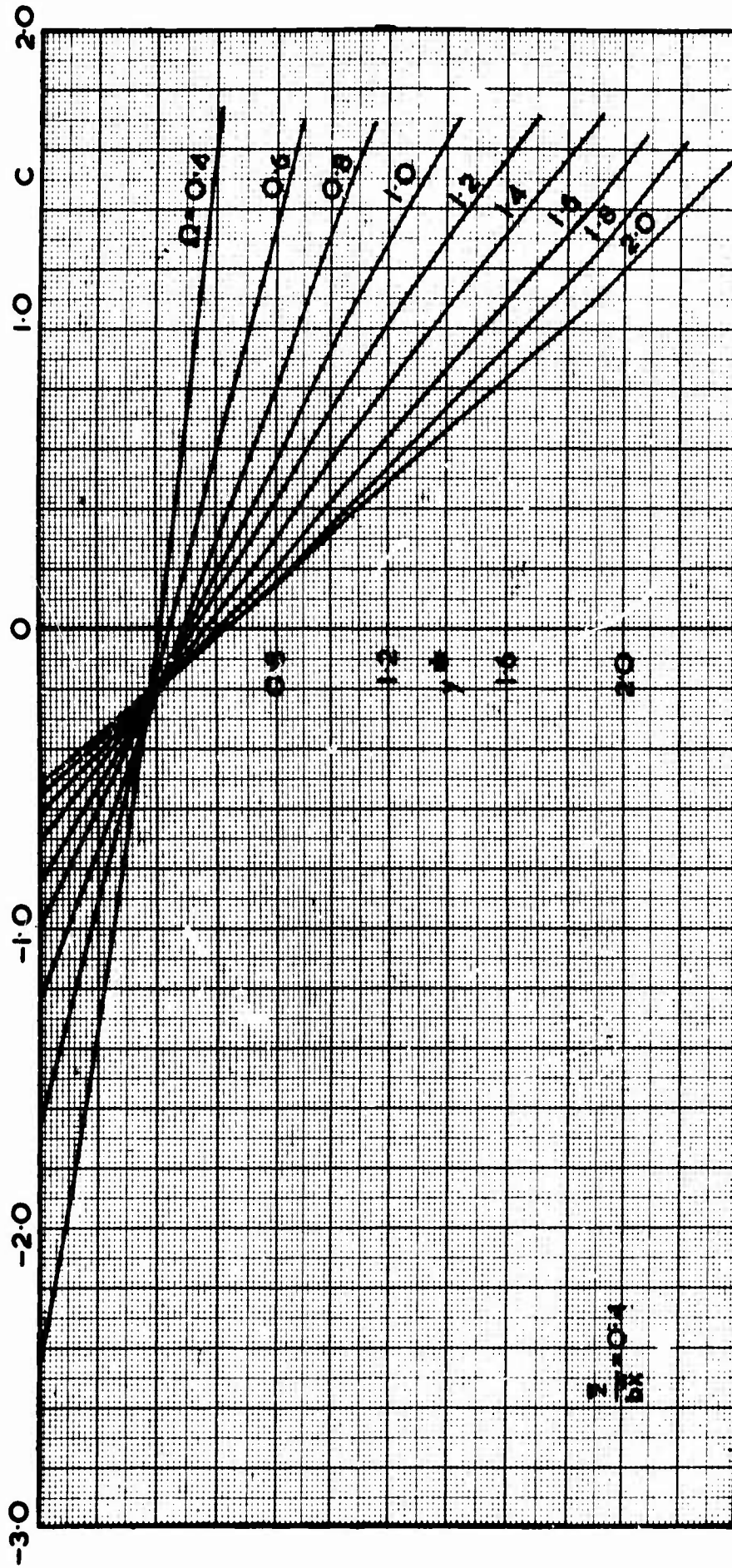
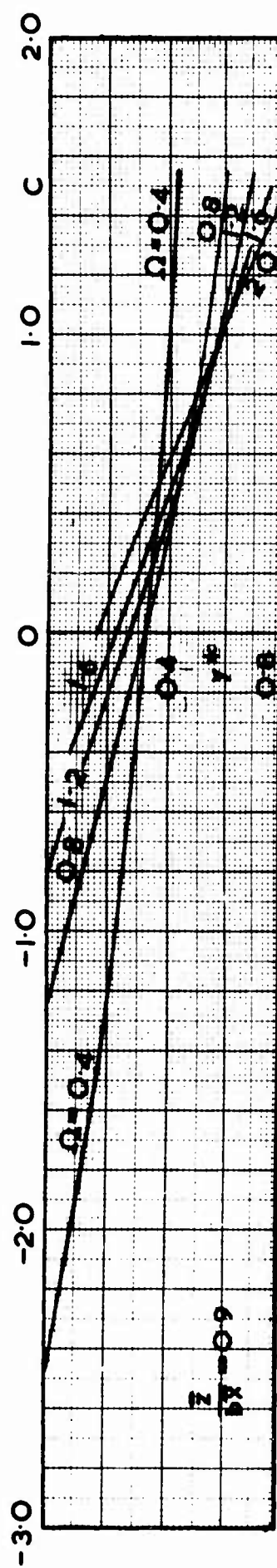
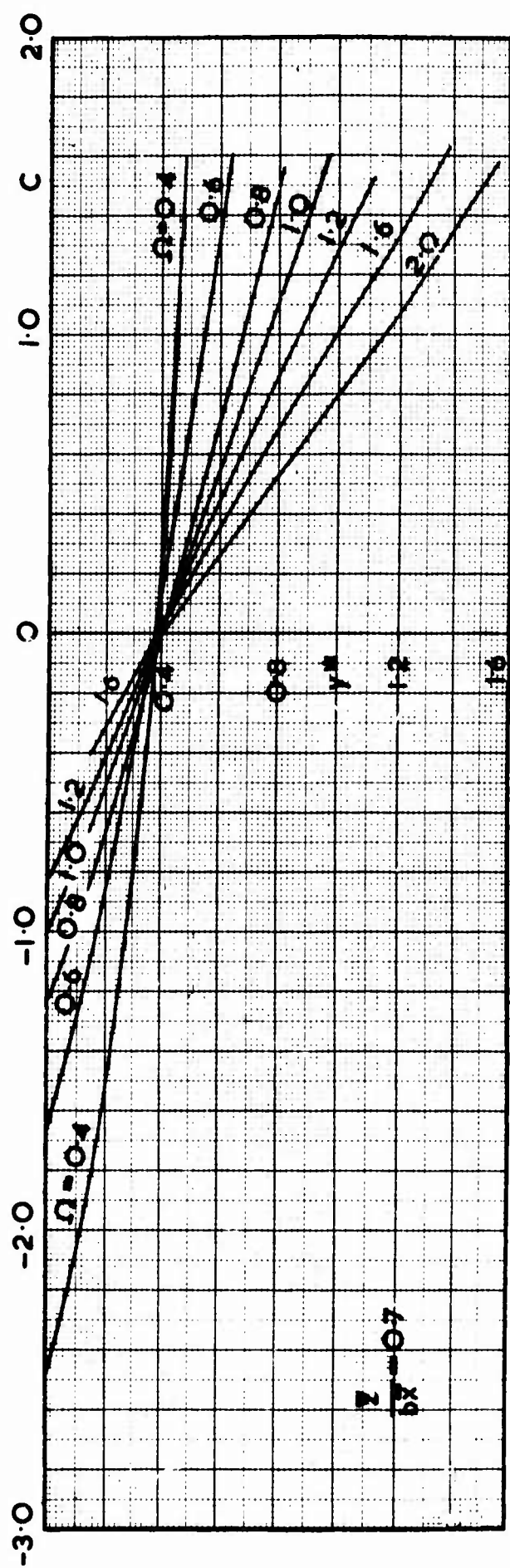


Fig. 3(b) Charts of $y^* : z/bx = 0.4$



Figs. 3(c) and (d) Charts of y^* : $z/b\bar{x} = 0.7, 0.9$

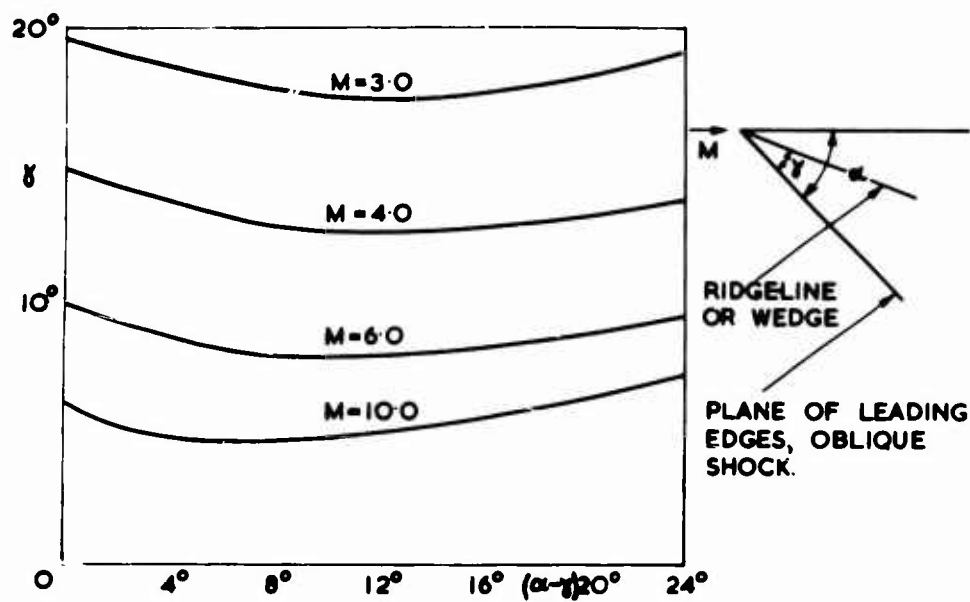


Fig. 4(a) Deflection angles on Nonweiler wings

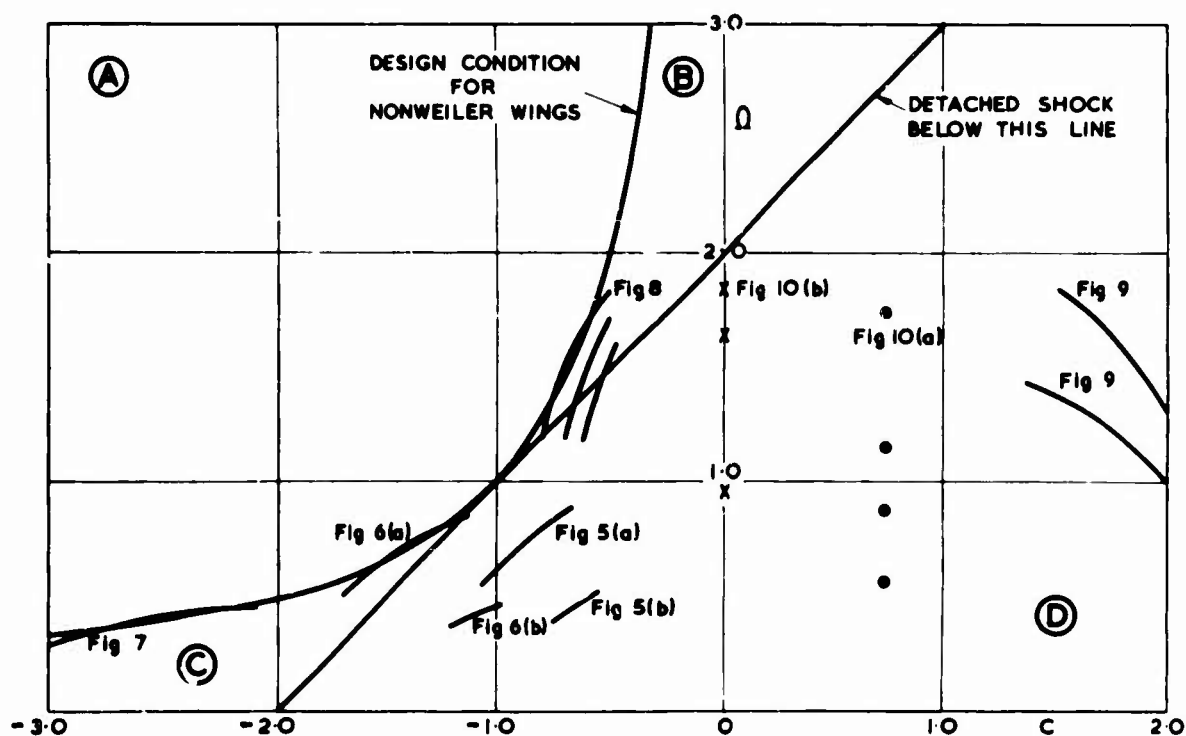


Fig. 4(b) Flow regions and range of comparisons

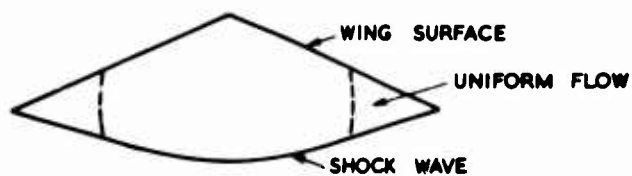


Fig. 4(c) Flow pattern in region B



Fig. 4(d) Flow pattern in region C

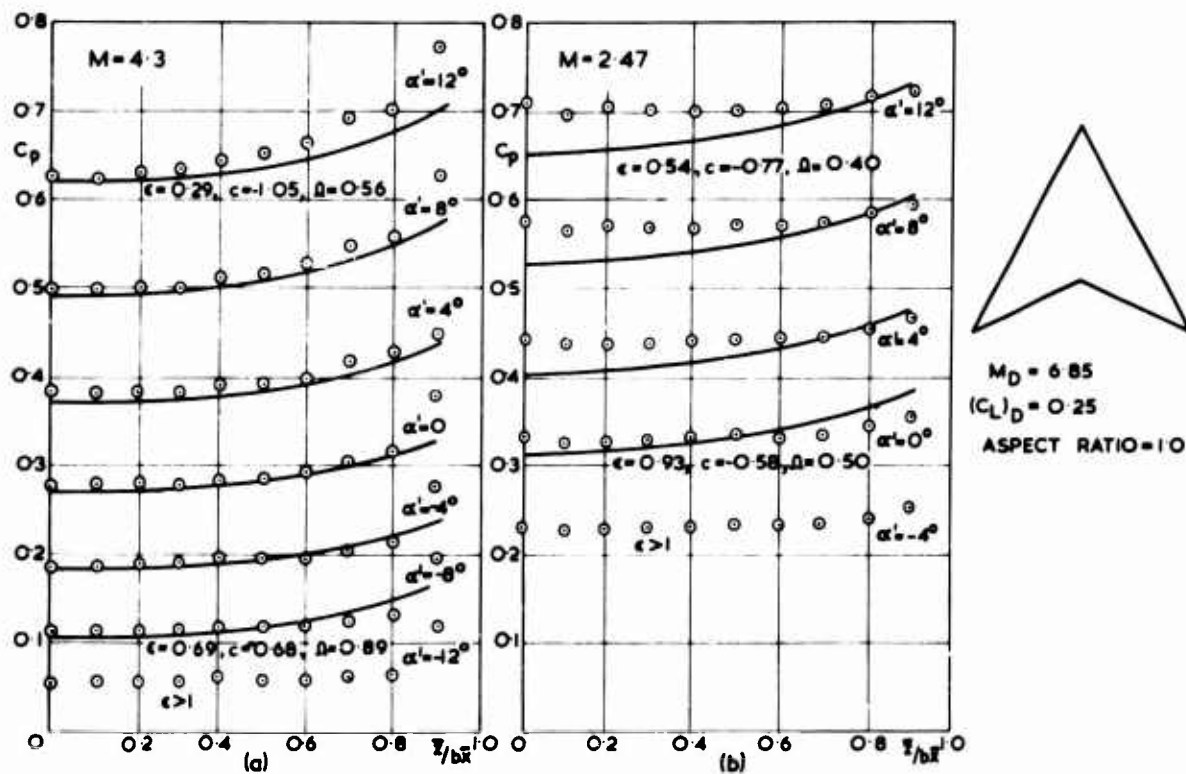


Fig. 5 Comparison of theory and experiment. Nonweiler wings

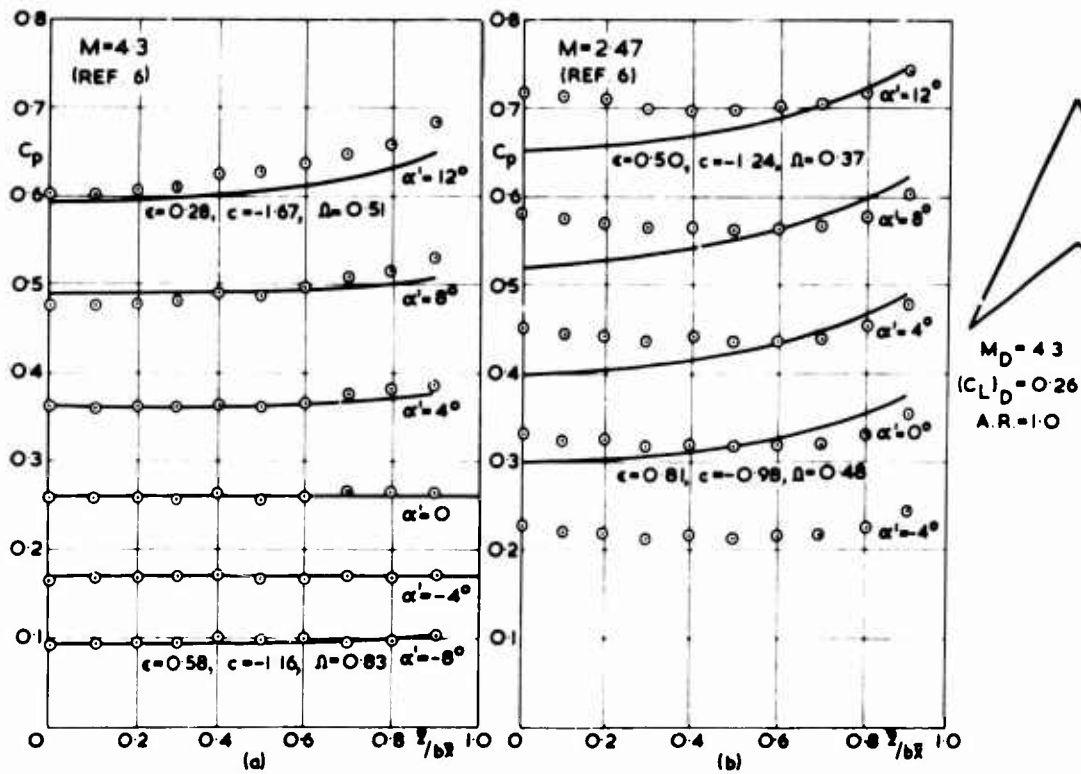


Fig. 6 Comparison of theory and experiment: Nonweiler wings

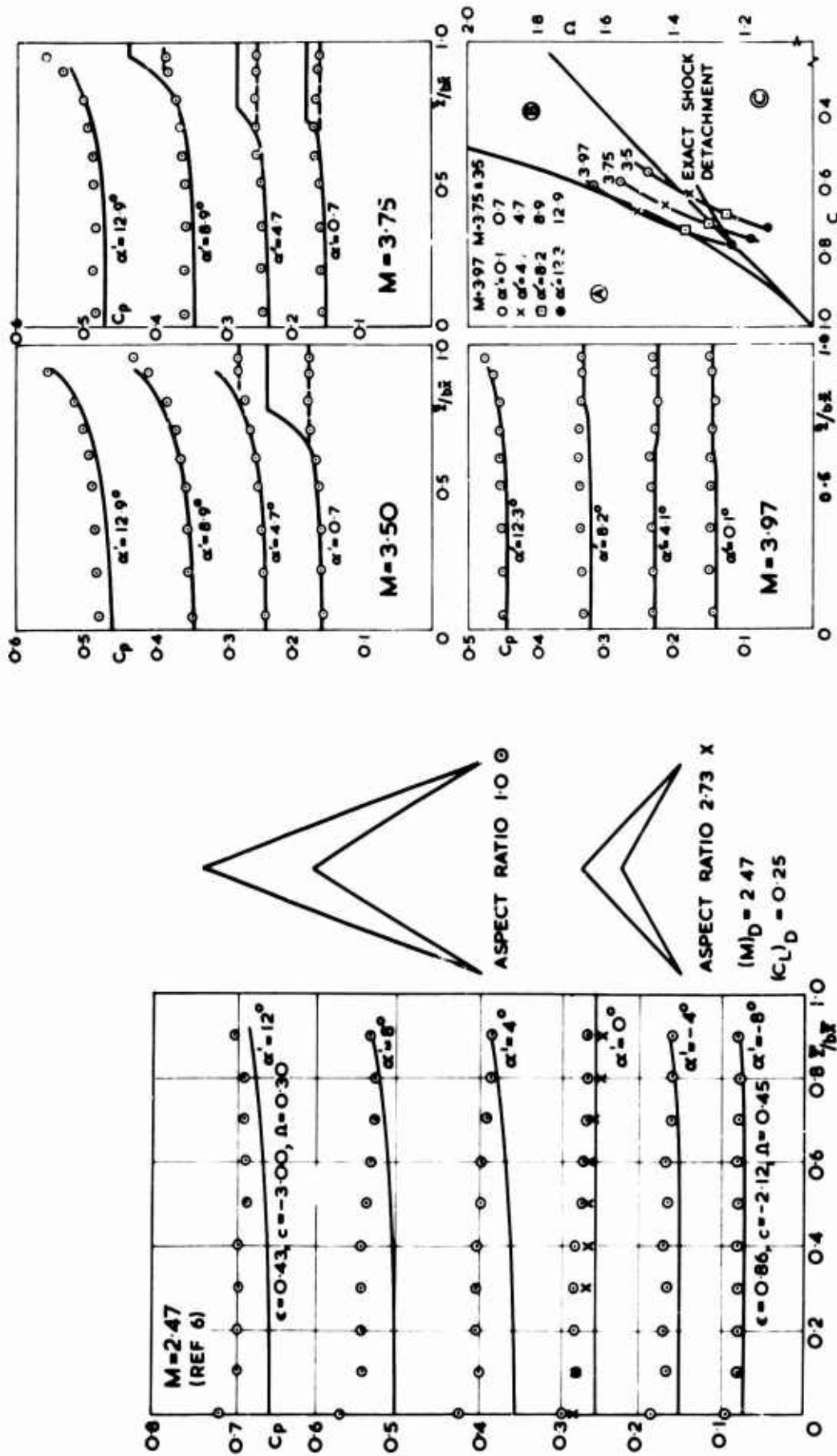


Fig. 7 Comparison of theory and experiment: Nonweiler wings

Fig. 8 Results for Nonweiler wings in Region B
 $M_D = 4.0$, $(C_L)_D = 0.135$,
 Aspect ratio = 2.0

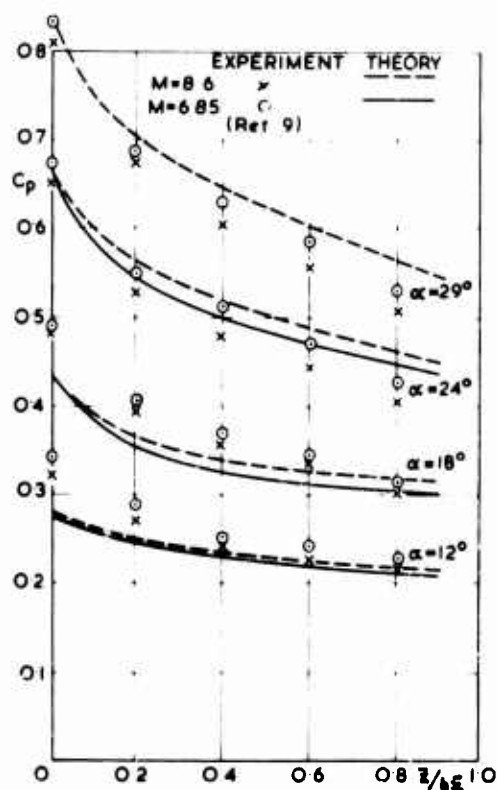


Fig. 9 Comparison of theory and experiment: wings with diamond cross-sections

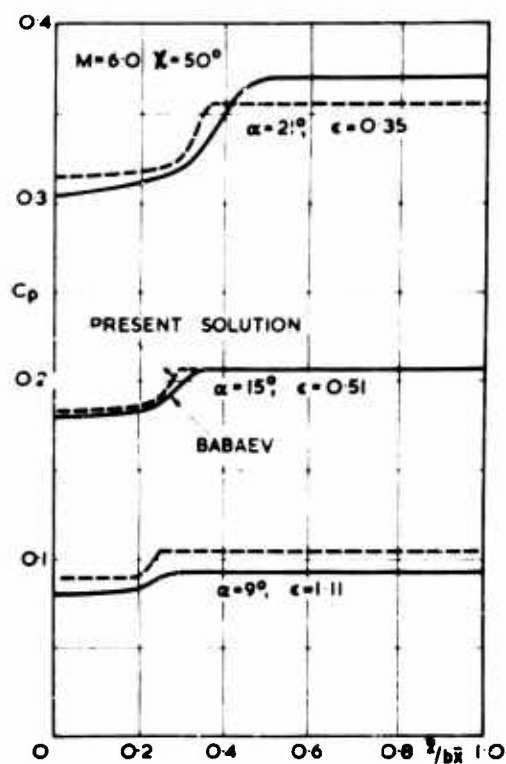


Fig. 11 Comparison with Babaev's numerical solution.

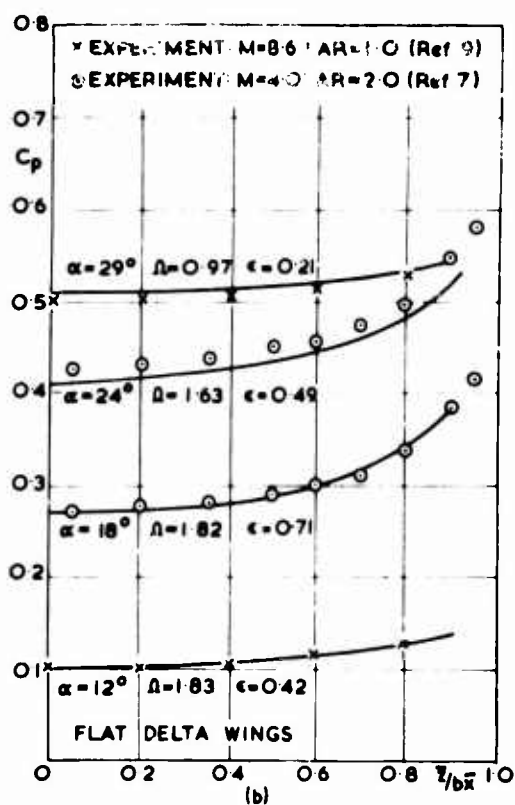
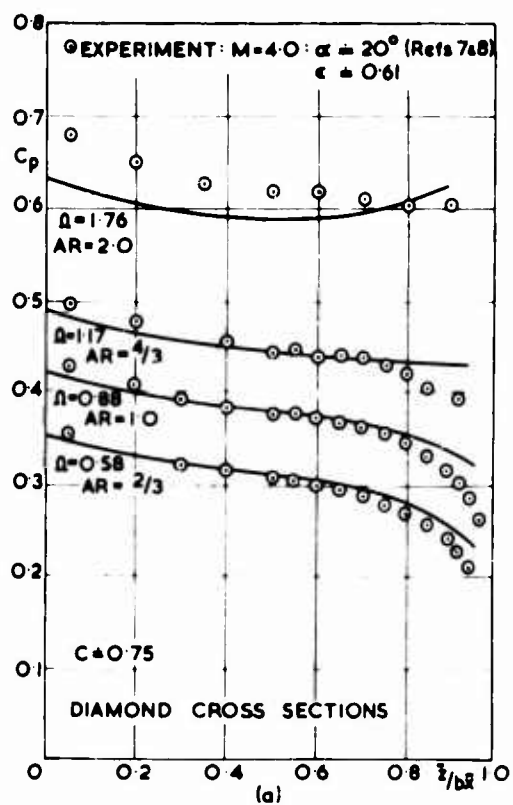


Fig. 10 Comparison of theory and experiment: wings with diamond cross-sections and flat wings

EXPERIMENTAL RESULTS FROM THREE

CONE-FLOW WAVERIDERS

by

J. Pike

Royal Aircraft Establishment,

Bedford, U.K.

Summary

Experimental results from three cone flow waveriders.

The 3ft x 4ft high supersonic speed tunnel at R.A.E. Bedford has been used to obtain experimental results from two waverider models with sharp leading edges and a third with a rounded leading edge. At a particular incidence and Mach number ($M = 4$) the flow supported by the compression surfaces of the models can be predicted theoretically. This predicted flow is shown to agree closely with experimental measurements of lower surface pressures, the shock wave shape and the surface streamline pattern.

At other incidences or Mach numbers the flow cannot be predicted theoretically. The experimental results show however, that for high incidence at $M = 4$ the pressures are remarkably uniform, and at constant incidence with Mach number decreasing, the shape of the shock wave changes smoothly, including its detachment from the leading edge.

Leading edge rounding is shown to affect pressures only close to the leading edge.

Introduction

It has been suggested,¹ that lifting configurations may be designed, which at a particular incidence and supersonic Mach number, have a theoretically predictable flow. The design technique involves fitting together compression and expansion surfaces which are the same shape as stream surfaces in known axisymmetric flow fields, to form a 'closed' configuration which has supersonic leading edges, and commonly a bluff base. This design technique is described in more detail in reference 2.

Two models have been constructed whose compression surfaces are the same shape as stream surfaces from the flow about unyawed cones of 11° and 16° semi-angles at $M = 4$. These models have been tested in the 3ft x 4ft high supersonic speed tunnel at R.A.E. Bedford, to verify that the predicted flow exists, and to investigate the flow at other incidences and Mach numbers.

A third model with a rounded leading edge has also been tested to investigate the effect of leading edge rounding, in case this is necessary for structural reasons.

2. Experimental details.

Planforms, sections and pressure hole positions for two of the models are shown at $1/4$ scale in figure 1. The compression surfaces are the same shape as stream surfaces in the flow about unyawed circular cones of 11° or 16° semi-vertex angle, in a free stream at $M = 4$. The surfaces were generated by defining the leading edge in a conical shock wave with vertex 14.35 inches ahead of the nose of the model, and obtaining the surface coordinates by following streamlines in the flow downstream from the leading edge.

All the models were constructed of glass cloth and araldite covering a steel core. Small pressure holes (diameter ~ 0.010 in.) in the compression surface were connected via tubes buried in the glass cloth and araldite to the pressure measuring system pick-up points at the base of the model. The pressures were measured by Midwood manometers³ with an accuracy of 0.015 in.Hg.

Most of the tests were made with the tunnel at a fixed Mach number of $M = 3.977$. A variation in Reynolds number from about 10^6 per foot to about 10^7 per foot could be obtained by varying the total pressure in the working section from 20 in. Hg to 220 in. Hg. A few tests were made with the variable Mach number facility in operation, giving a Mach number range of 2.5 to 5.

3. Comparison of the experimental results with the theoretically predicted flow.

The experimental results are compared with the theoretical flow in three ways, firstly from a comparison of surface pressures along theoretical isobars, secondly from schlieren photographs of the shock wave at various roll angles, and thirdly from oil flow patterns giving the surface streamline pattern.

The position of the pressure holes and theoretical isobars are shown in figure 1. In the isometric view of figure 2, the vertical axis shows pressure coefficients, and the experimental values associated with the pressure holes are compared with theoretical values shown by the 'broken' lines. We see that the experimental pressures closely confirm the theoretical distribution.

Errors in the experimental pressures can come from a number of causes. These can be grouped under five headings, namely errors in model shape, errors in tunnel conditions, deflection of the model in the tunnel, boundary layer effects and errors in the pressure measuring system. The errors in model shape have most significance when measured as errors in model slope. A series of checks showed errors of order 0.002 in/inch as typical, with the model shown in figure 1a having somewhat smaller errors than those of the model shown in figure 1b. The errors in slope could account for up to half the difference between the experimental and theoretical pressure coefficients shown in figure 2. Flow misalignment in the tunnel was allowed for by taking measurements at 0° and 180° of roll. The tunnel incidence measurements were accurate to within 0.05 degree, which is equivalent to about 0.001 in per inch. The test Mach number was 3.977. The reduction of 0.023 in Mach number below the design value would tend to increase the pressures by a small amount. The pressure coefficients have been corrected for sting deflection due to aerodynamic force. Deflection of the glass cloth and araldite near the leading edge of the model due to aerodynamic forces, were eliminated from the model shown in figure 1a by shaping the upper surface to have balancing pressures. The leading edge of the model shown in figure 1b was thick enough to give only small deflections. No correction has been applied for the change in slope due to boundary layer displacement thickness. The boundary layer growth must be expected to increase the pressure slightly near the leading edge. Pressure measuring system inaccuracies could come from pressure holes not perpendicular to the surface, pressure holes which are chipped round the edge, leaks in the pressure tubes or errors in the manometers. The significant effect was found to be the leaks in the pressure tubes, causing a number of pressure holes to be abandoned before the tests

started. This accounts for the raps in the pressure hole distributions shown in figure 1. The total effect of the errors are such that they could account for the differences in the experimental and theoretical pressure coefficients shown in figure 2.

Figure 3 shows schlieren photographs of the 11° cone flow model at various roll angles. The theoretical shock wave is conical and inclined at 18.5° to the free stream direction. The shock wave shown in figure 3 is straight and in the theoretically predicted position in all three views.

The surface streamlines are illustrated for the 16° cone-flow model in figure 4, by oil flow technique. The line aa is the cone axis. As the flow is axisymmetric aa is also a theoretical streamline on the surface of the body. The slight deviation of the flow from this line may be accounted for by the boundary layer modifying the direction of the flow near the surface.

The comparisons discussed here, demonstrate clearly, that the theoretically predicted flow does occur in practice.

4. Further experimental results

At conditions other than that for which the compression surface was designed, the flow is not predictable theoretically, and we rely solely on the experimental results for information about the flow.

In figure 5, the pressure distribution for various incidences, with Mach number constant at $M = 4$, is shown. Zero incidence as shown in figure 5, is the incidence for which the flow is known theoretically. When the surface is inclined to the free stream at less than this incidence, the pressure coefficients are not only small but vary considerably across the surface. For example, in figure 5a we see that at -4° the pressure coefficient has become zero near the wing tips, slightly larger near the nose and reaches a maximum at the centre of the base. This pressure distribution tends to correspond to the local inclination of the compression surface to the free stream. The wing tips of the compression surface are nearly streamwise, the nose is inclined at 3.7° to the free stream and the inclination of the surface increases progressively along the centre line to reach a maximum of 6° at the base.

At positive incidences, the pressure coefficients are remarkably constant across the wing. The characteristic over-compression near the leading edge and resulting expansion in the centre of a flat delta wing with an attached shock wave, does not occur for the shapes tested here. The caret shape near the nose, the smaller incidence of the tips and higher incidence inboard are instrumental in producing the nearly constant pressure.

The ratio of the lift to pressure drag has been obtained by integrating the experimental pressures over the surface. In figure 6 the values obtained are compared with the envelope for plane two-dimensional wedges or caret compression surfaces chosen to be on design at each lift coefficient. The ratio of lift to pressure drag for the cone flow wing is found to be very close to the caret value for a wide range of lift coefficient. For zero lift the pressure drag of any curved surface is finite. Hence the ratio of lift to pressure drag of the cone-flow wing tends to zero as the lift coefficient tends to zero, whereas that of the plane wedge becomes large. The experimental values suggest this divergence at low values of lift coefficient.

With variation of Mach number, the effect of particular interest is the detachment of the shock wave from the leading edge. In figure 3 schlieren photographs of the model and shock wave are shown at various roll angles. From such photographs a series of tangents to the shock wave may be obtained, whose envelope represents the shock wave shape. Shock wave shapes obtained thus at various Mach numbers are shown in figure 7. The main sources of errors in determining the shapes, result from difficulty in exactly locating the edge of the shock wave in some of the photographs, and in constructing the envelope from the finite number of tangents available. However these errors are in general small and give only small changes in the shape, except possibly near the ends of the detached shock waves where the errors may be significant.

At $M = 4$ the shock wave approximates to an arc of a circle. At higher Mach numbers the shock wave as expected, becomes less convex, and remains firmly attached to the leading edge. As the Mach number decreases below Mach 4, the shock wave detaches smoothly from the leading edge at about $M = 3.5$ and progressively becomes more remote from the surface.

The rounded leading edge model has a shock wave which is, of course, detached at all Mach numbers. In figure 8, comparison between the sections of the rounded leading edge model and the model derived from the 11° cone-flow are shown. We see that the only difference occurs near the leading edges. The rounded leading edge is semi-circular with $1/4"$ radius. This radius is large to emphasize the effect of the leading edge rounding. The nose of the rounded leading edge model is part-spherical.

A comparison of the pressures for the two models appears on the left of figure 8. The rounded leading edge has very high pressures on the areas most inclined to the flow, and a rapid

expansion round the leading edge until it meets the compression surface. Recompression to near the original value is complete by about three leading edge diameters inboard or about ten diameters downstream.

Leading edge blunting then makes little difference to the lift coefficient, but the high pressures on forward facing areas will contribute to the drag.

5. Conclusions

At the correct conditions of incidence and Mach number, the compression surfaces support the predicted flow to within the limits of experimental error.

Increasing the incidence, whilst keeping the Mach number constant, results in a pressure distribution which is remarkably uniform. The lift to pressure drag ratio is found to be very close to that of a two-dimensional wedge of the same lift coefficient.

The shock wave shape, it is found, becomes increasingly convex with decreasing Mach number, detaching from the leading edge smoothly and becoming remote from the surface at low supersonic Mach numbers.

Leading edge rounding does not affect the pressures on the wing significantly, except over a region of three diameters width from the leading edge, or ten diameters downstream.

References

1. Jones, J.C. A method for designing lifting configurations
 Moore, K.C. for high supersonic speeds using axisymmetric
 Pike, J. flow fields.
 Roe, P.L. Ingenieur Archiv
 To be published.

2. Seddon, J. The use of known flow fields as an approach
 Spence, A. to the redesign of high speed aircraft.
 Agard Conference Proceedings.
 Hypersonic Boundary Layers and Flow Fields.
 Paper No: 10, May 1968.

3. Anderson, J.R. Short note on some recent calibrations of
 R.A.E. automatic self balancing capsule
 manometers.
 Agard Report 163, Note 19, March 1958.

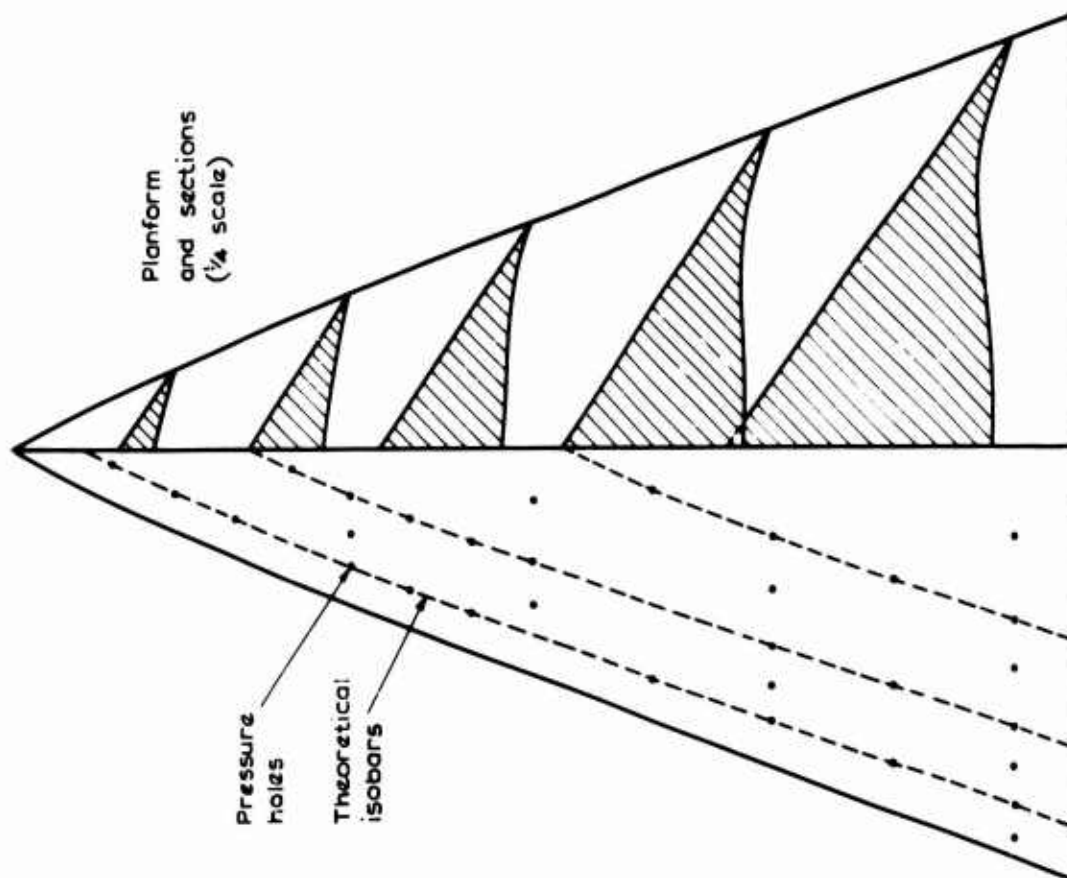


Fig. 1a Planform, sections and pressure hole positions for the model derived from an 11° cone flow

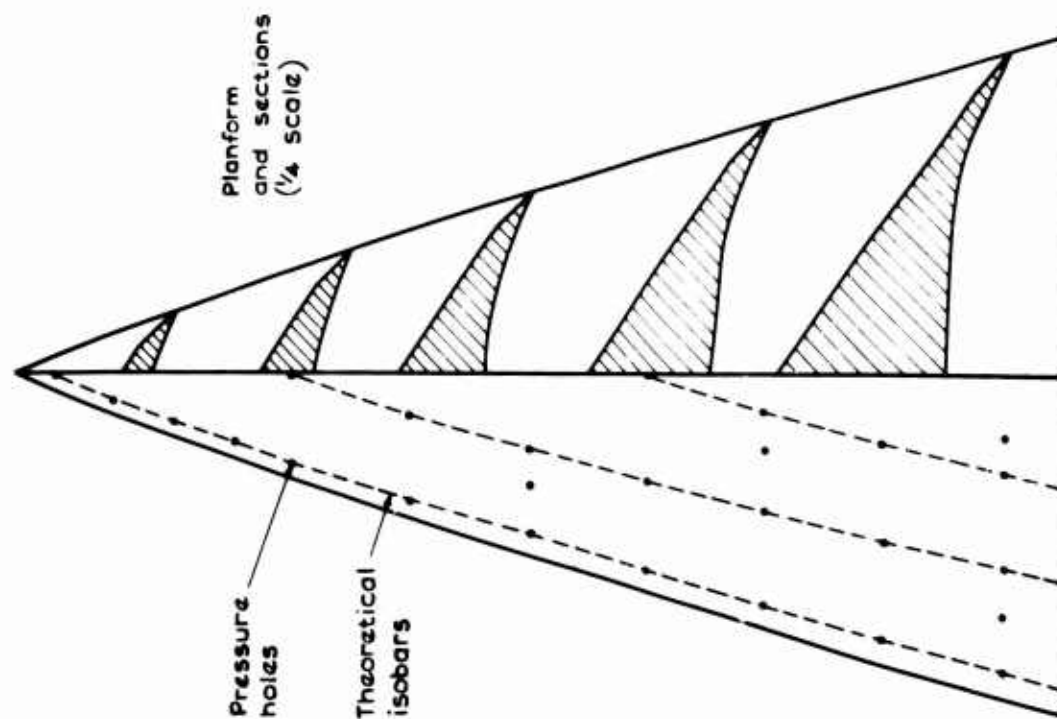
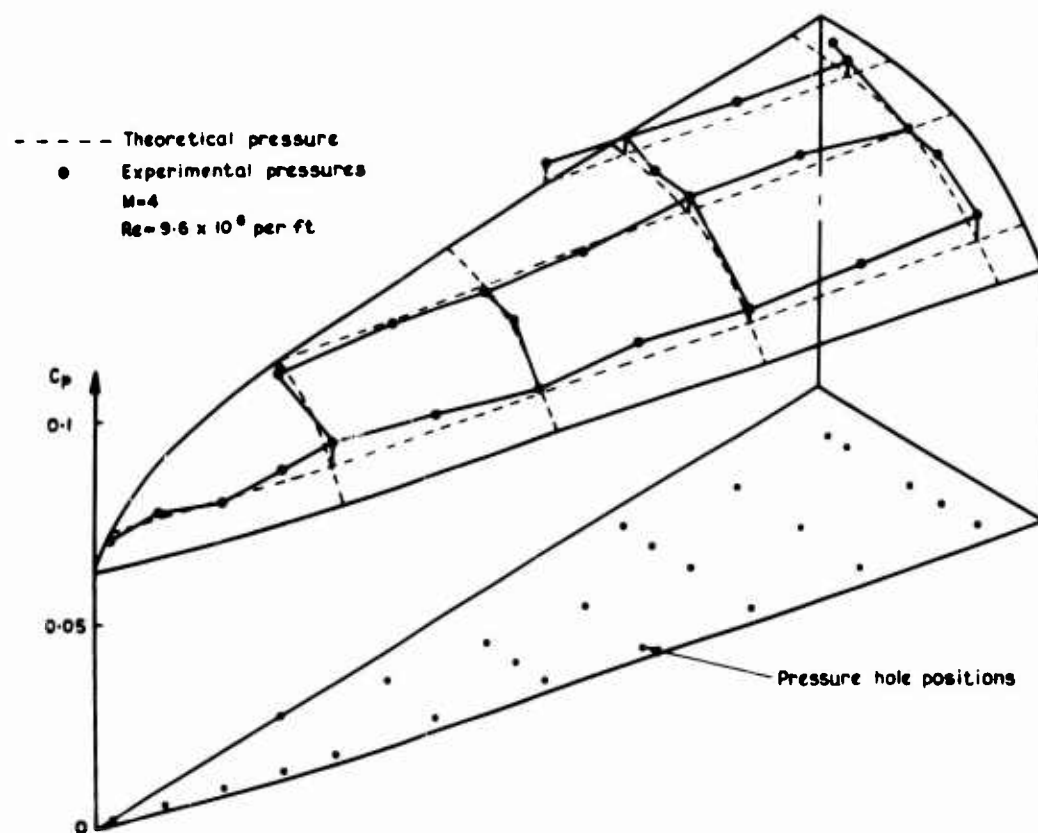
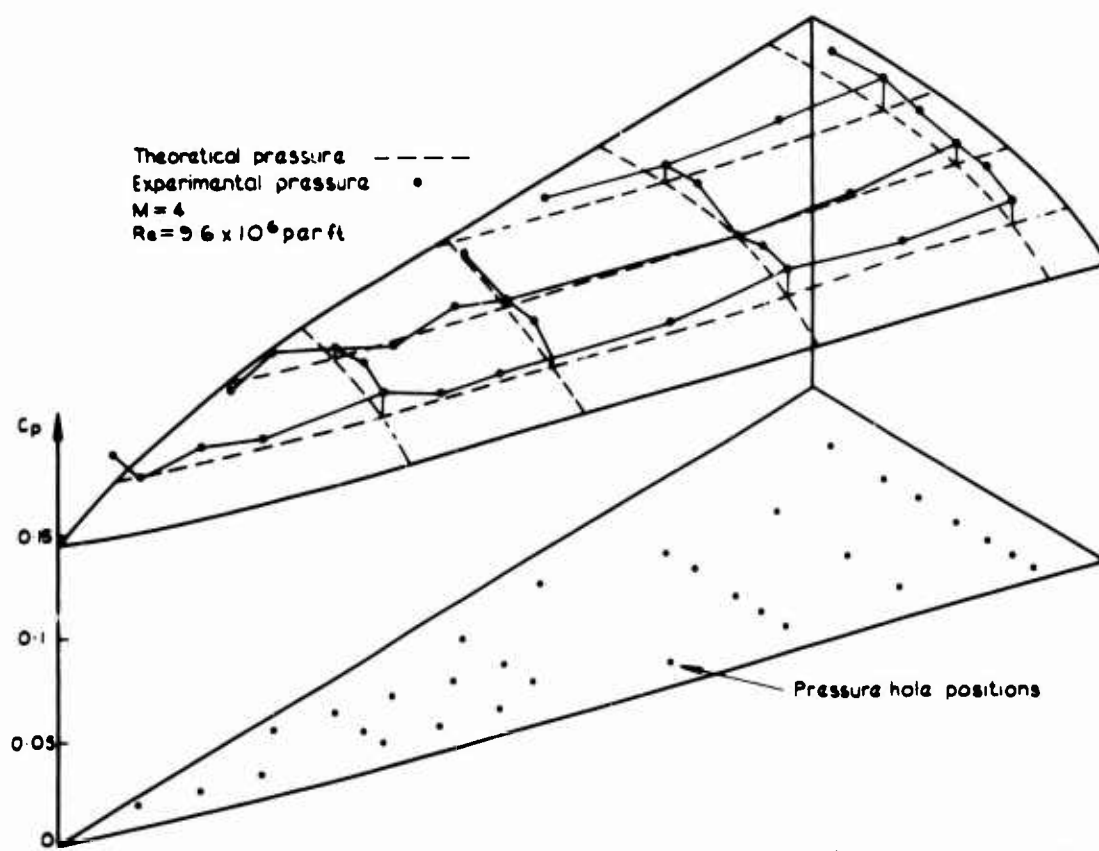


Fig. 1b Planform, sections and pressure hole positions for the model derived from a 16° cone flow

Fig. 2a Comparison of experimental and theoretical pressures (11° cone flow model)Fig. 2b Comparison of experimental and theoretical pressures (16° cone flow model)

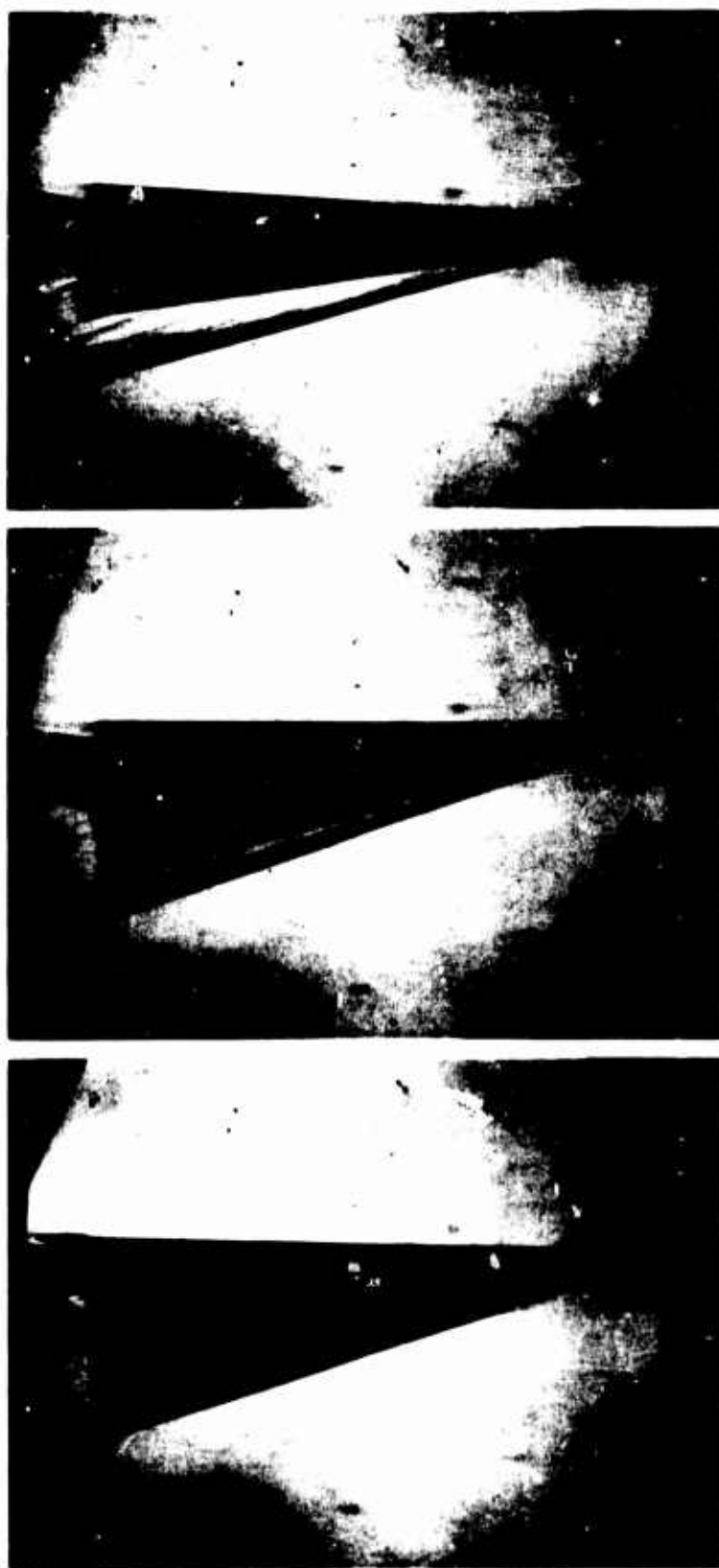


FIG. 3. SCHLIEREN PHOTOGRAPHS OF THE MODEL
SUPPORTING A CONICAL SHOCK WAVE, AT $M=4$ AND
AT 0° , 10° AND 20° OF ROLL.

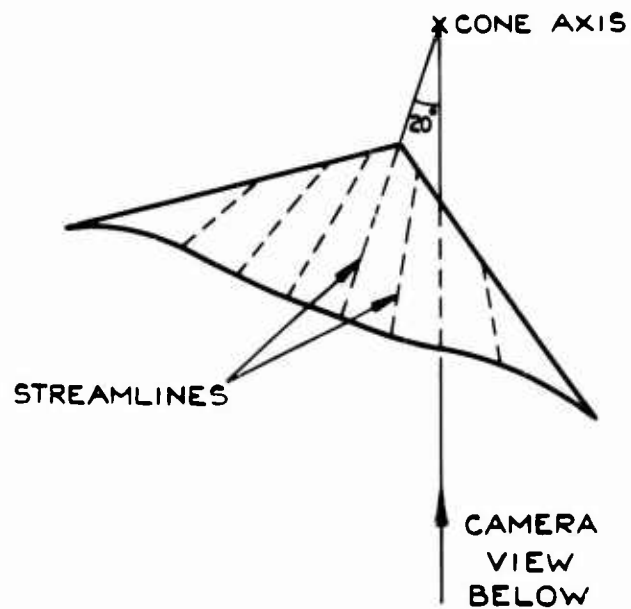
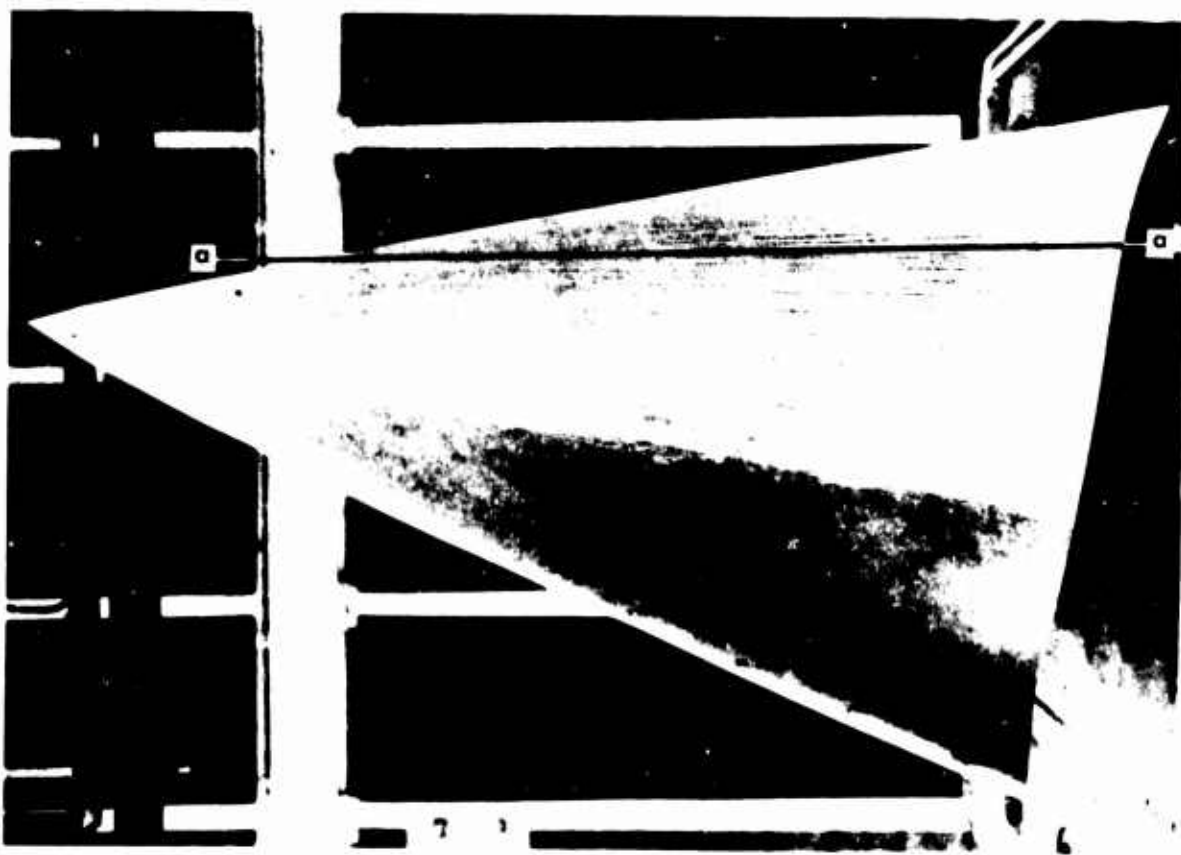


FIG 4A. FRONT VIEW OF MODEL.

FIG. 4B. OIL FLOW PHOTOGRAPH SHOWING STREAMLINE PATTERN AT $M=4$ (16° CONE FLOW MODEL).

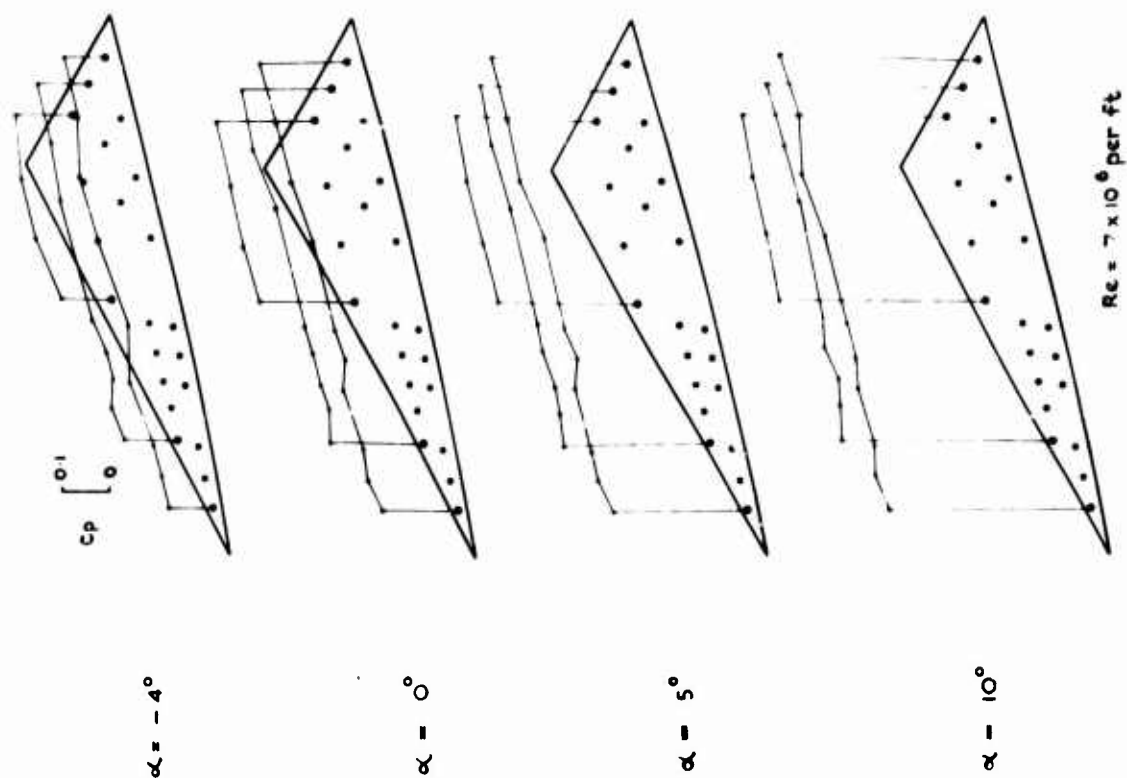


Fig. 5a Experimental pressures on a wing from an 11° cone flow at $M=4$

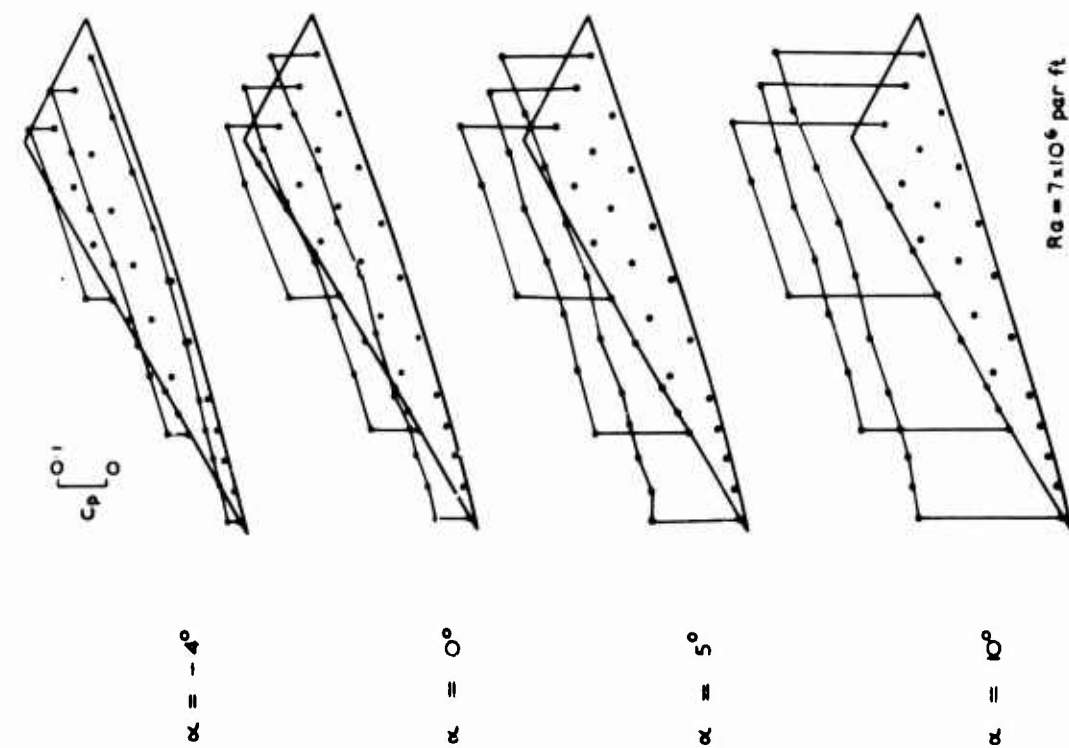


Fig. 5b Experimental pressures on a wing from a 16° cone flow at $M=4$

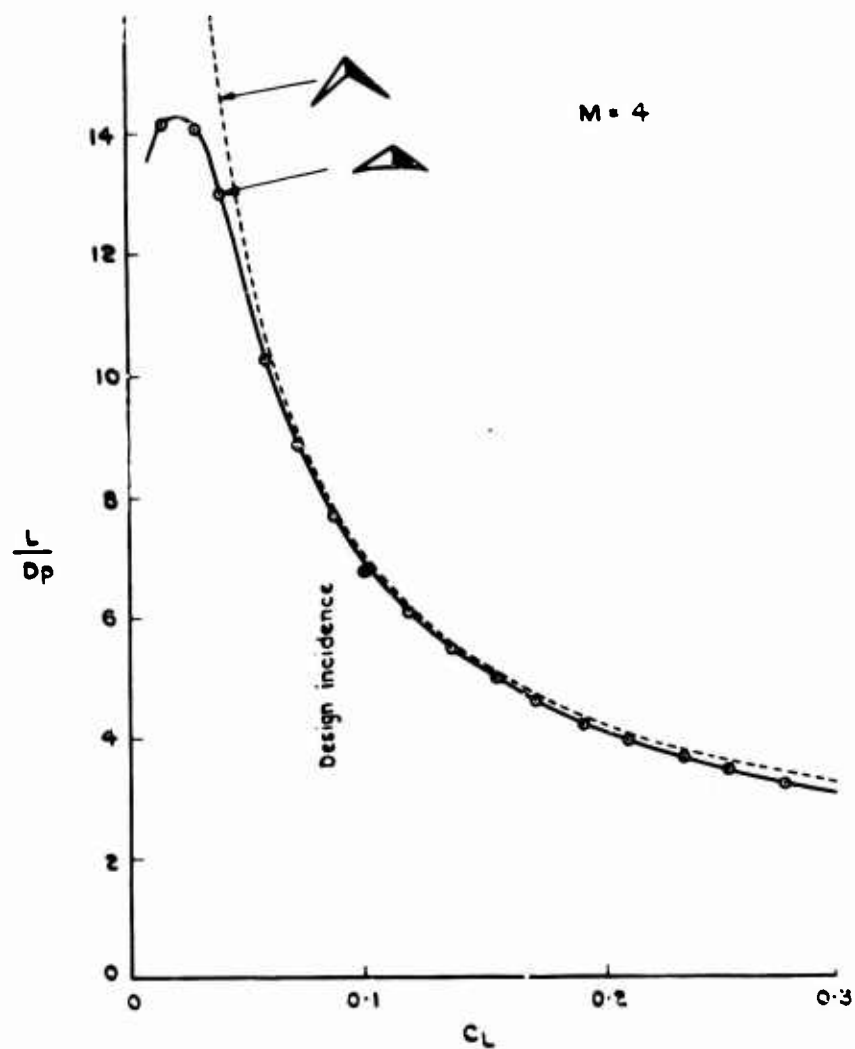


Fig. 6 Lift over pressure drag v lift coefficient
(11° cone flow model)

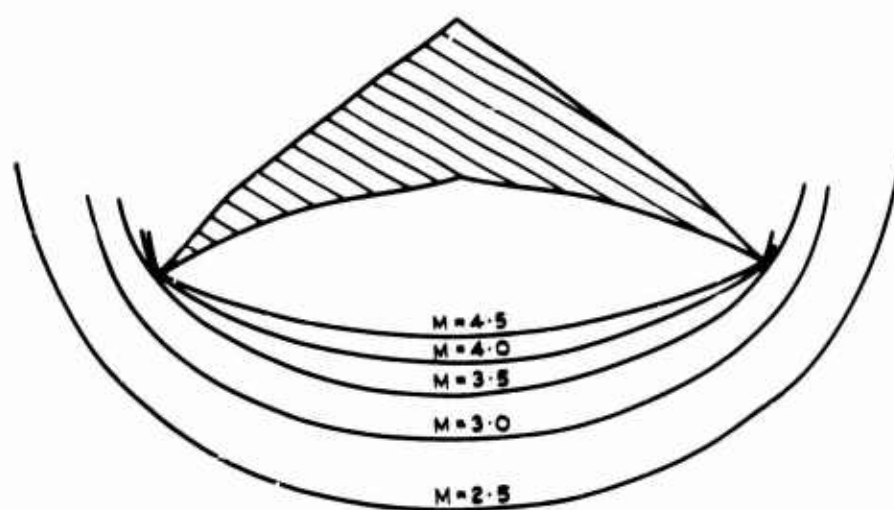


Fig. 7 Shock wave shape at various Mach numbers
(11° cone flow model at 0.52 chord)

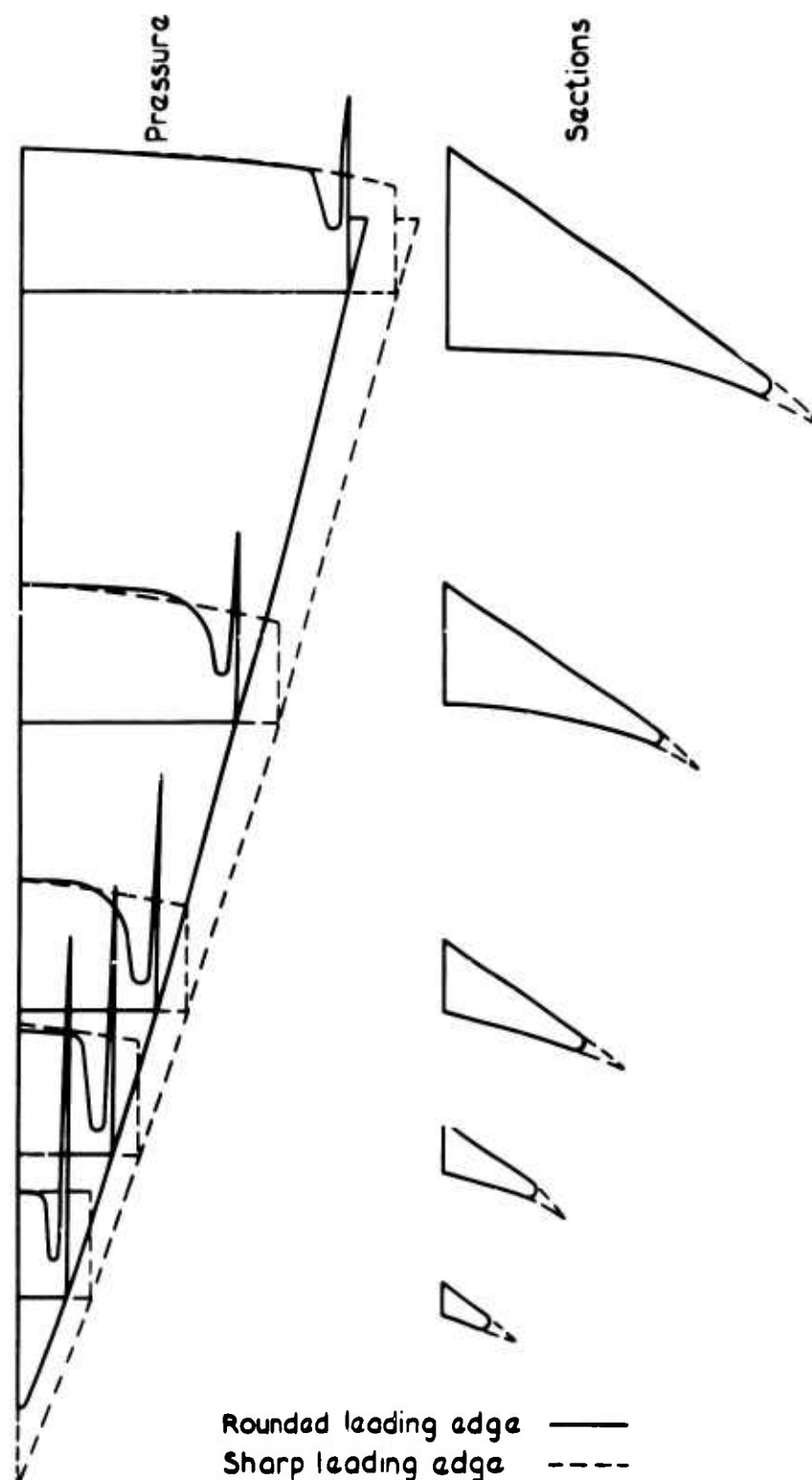


Fig. 8 Comparison of sections and pressures on rounded and sharp leading edge cone flow wings at $M = 4$

EXPERIMENTAL INVESTIGATION OF WAVE EFFECT

IN THE MACH NUMBER RANGE FROM 0 TO 10

BY

V. K. KILB

U.S. AIR FORCE, WRIGHT-PATTERSON AIR FORCE BASE, OHIO

SUMMARY

A series of wave riders (caret wings) have been investigated in the DFL hypersonic gun tunnel in the Mach number range from $Ma = 7.9$ to 15.5 , and at corresponding Reynolds numbers from $2.7 \cdot 10^6$ to $1.4 \cdot 10^5$. The tests included three-component-force measurements, pressure distribution measurements and determination of the shock wave angle by flow visualization. The experimental data have been compared with simple wedge theory, and wedge theory including viscous effects and also with an extended Newtonian theory depending on two hypersonic similarity parameters only.

It has been shown that large viscous interaction effects have considerable influence on the lift-to-drag ratio, on the pressure distribution and on the shock wave angle.

RESUME

Une série de planeurs hypersoniques (caret wings) ont été examinés dans la soufflerie à choc (gun tunnel) de la DFL. Les nombres de Mach réalisés sont compris entre 7.9 et 15.5 et les nombres de Reynolds sont compris entre $2.7 \cdot 10^6$ et $1.4 \cdot 10^5$. Les recherches expérimentales comprenaient des mesures de force, la détermination des angles de choc et des distributions de la pression. Les résultats expérimentaux ont été comparés avec la théorie de coin, une fois sans et l'autre fois avec considération des effets visqueux. Une comparaison a été faite avec une théorie de Newton modifiée, qui dépend seulement de deux paramètres hypersoniques. Il a été démontré que les effets de viscosité ont une influence considérable sur les paramètres caractéristiques suivants:

Portance/trainée, l'angle de choc et la distribution de la pression.

ACKNOWLEDGEMENT

The author is greatly indebted to Professor Dr. Ing. K. Gersten for having proposed these investigations and for the great amount of help in carrying out this research work.

NOTATION

A	aspect ratio, $A = 4 s/l$
s	semispan of wing
l	upper surface ridge-line length of models
S_p	planform area of wing, $S_p = s l$
S_w	wetted surface area of wing, $S_w = S_p \left[\left(1 + \left(\frac{\tan \delta_{des}}{s/l} \right)^2 \right)^{1/2} + \left(1 + \tan^2 \delta + \left(\frac{\tan \delta_{des} - \tan \delta}{s/l} \right)^2 \right)^{1/2} \right]$
V	total volume of wing, $V = \frac{1}{3} F \tan \delta$
r	volume coefficient, $r = V/S_p^{3/2}$
δ	angle between the upper and lower ridge-line
δ_{des}	angle between the upper ridge-line and the leading-edge plane (Fig.1)
ψ	anhedral angle of the upper surface
γ	angle between the two planes of the lower surface (Fig.1), also ratio of specific heats ($\gamma = 1.4$)
α	angle of attack (see Fig.1)
δ_1	deflection angle, $\delta_1 = \delta + \alpha$
θ	shock wave angle (Fig.1)
x, y, z	coordinate system (Fig.1)
η	non-dimensional semispan, $\eta = y/s(x)$
x_M/l	position of pressure holes
Ma	Mach number, $Ma = \frac{U}{a}$
Re	Reynolds number, $Re = \frac{U l}{\nu}$
L	lift
D	drag
M	pitching moment
N	normal force
c_L	lift coefficient, $c_L = L/q_\infty S_p$
c_D	drag coefficient, $c_D = D/q_\infty S_p$
c_m	pitching moment coefficient, $c_m = M/q_\infty S_p l$
c_N	normal force coefficient, $c_N = N/q_\infty S_p$
x_{cp}/l	center of pressure
L/D	lift-drag ratio, $L/D = c_L/c_D$
c_f	skin-friction coefficient
c_{Df}	coefficient of drag due to skin-friction, $c_{Df} = c_f S_w/S_p$
p	static pressure

q	dynamic pressure, $q = \rho U^2/2 = \frac{\gamma}{2} Ma^2 p$
U	velocity
a	velocity of sound
ρ	density
T	temperature
c_p	pressure coefficient, $c_p = (p-p_\infty)/q_\infty$
ϵ	density ratio across a shock wave (equ.9)
χ	hypersonic viscous interaction parameter, $\chi = Ma^3/\sqrt{Re}$
ν	kinematic viscosity
μ	dynamic viscosity
C_S	Sutherland constant, $C_S = \mu T_1/\mu_1 T$
δ^*	displacement thickness of boundary layer
C	thickness parameter (equ.10)
Ω	wing semispan parameter (equ.11)
p^*	correction to Newtonian pressure coefficient (equ.8)
$\overline{c_N}$	reduced normal force coefficient, $\overline{c_N} = (c_N - (c_N)_{\text{Newton}})/(c_N)_{\text{Newton}}^\epsilon$

Subscripts

∞	free stream
0	stagnation state
1	behind an oblique shock wave
eff	effective
des	design condition
L.E.	leading edges
vis	viscous
iv	inviscid
c	compression
e	expansion
L	lower surface
U	upper surface
Newton	Newtonian theory
w	wall
max	maximum

EXPERIMENTAL INVESTIGATIONS OF WAVE RIDERS IN THE MACH NUMBER RANGE FROM 8 TO 15

K. Kipke

1. INTRODUCTION

Wave riders represent the connecting link between supersonic aircraft and spacecraft. As a result of the high Mach numbers the disturbances of the flow fields due to the body do not remain small and shock waves of finite strength become effective. A wave rider produces a shock system on which it seems to ride. T. NONWEILER (Ref.1) has made proposals for lifting bodies which produce plane shock waves. The simplest of these bodies is a surface of triangular planform, comprising two flat panels which meet with an anhedral angle. Such a body having undersurfaces of inverted-V section is called a caret wing. At its design condition a plane shock wave is lying in the plane of the leading edges and hence leads to a uniform pressure over its lower surface equal to the pressure behind the shock in the two-dimensional wedge flow. The essential parameters for designing a caret wing are as follows:

1. Design Mach number Ma_{des}
2. Aspect ratio $A = 4 \frac{s}{t}$
3. Volume parameter $\tau = \frac{V}{s^{3/2} p}$

Fig.1 shows the notation of a caret wing at an arbitrary free-stream condition. The design condition is given by $Ma_{\infty} = Ma_{des}$ and $\alpha = 0^\circ$. For a given design Mach number Ma_{des} and a wedge angle δ the angle θ_{des} which determines the position of the leading edge plane can be calculated by the oblique shock relation:

$$\cot \delta = \tan \theta_{des} \left[\frac{(\gamma+1) Ma_{des}^2}{2(Ma_{des}^2 \sin^2 \theta_{des} - 1)} - 1 \right] \quad (1)$$

The third free geometric parameter can be either the aspect ratio A or the volume parameter τ which are connected by

$$\tau \sqrt{A} = \frac{2}{3} \tan \delta \quad (2)$$

The overall forces of caret wings in inviscid flow can be calculated from the pressure coefficients as follows:

$$c_N = c_{p_L} - c_{p_U} \quad (3)$$

$$c_T = c_{p_L} \tan \delta \quad (4)$$

At design condition the exact formula for the pressure coefficients can be given by

$$c_{p_L} = 2 \frac{\sin \theta_{des} \sin \delta}{\cos(\theta_{des} - \delta)} \quad (5)$$

with θ_{des} from equ.(1)

$$c_{p_U} = 0 \quad (6)$$

At off-design conditions the following approximations have been used to calculate the pressure coefficients.

(a) Wedge Theory

It is assumed that the caret wing has the same aerodynamic characteristics as a two-dimensional wedge-typed wing with the same planform area and a wedge angle δ . Therefore the pressure coefficients can be calculated by oblique shock relations and by Prandtl-Meyer-expansion relations. The formulas for the pressure coefficients throughout the incidence range on the lower and upper surface can be taken from Table 1a.

(b) Hypersonic Slender Body Theory

Under the assumption that the caret wings considered here are slender, i.e. $\delta \ll 1$; $A \ll 1$; $\alpha \ll 1$; $Ma_{\infty} \gg 1$; the general dependence

$$c_p = f(Ma_{des}, A, \tau, \alpha, Ma_{\infty})$$

can be reduced to

$$\frac{c_p}{\delta^2} = F(K, \frac{\alpha}{\delta}, A Ma_{des}, \tau \sqrt{Ma_{des}}) \quad (7)$$

where $K = Ma_{\infty} \delta$ is the hypersonic similarity parameter.

(c) Simple Newtonian Theory

By assuming that at all off-design conditions the shock wave is lying in the plane of the leading edges in the case $\alpha > -\delta_{des}$ and on the upper surface in the case $\alpha < 0$ the pressure coefficients on the upper and lower surface can be calculated by simple Newtonian theory. The equations can be taken from Table 1b.

(d) Extended Newtonian Theory

In recent papers, A.F. MESSITER (Ref.2) and K. HIDA (Ref.3) have proposed a first order correction of simple Newtonian theory for the pressure distributions on lifting conical bodies with detached shocks. L.C. SQUIRE (Ref.4) has extended this method to caret wings at off-design when the shock wave is detached from the leading edges. Hence the pressure coefficient on the lower surface of a caret wing can be written as follows:

$$c_{pL} = 2 \sin^2(\alpha + \delta_{des}) [1 + \epsilon p^*(Q, C, \eta)] \quad (8)$$

The first term represents simple Newtonian flow and the second the correction term. The density ratio ϵ and the parameters C and Q are defined as

$$\epsilon = \frac{\gamma-1}{\gamma+1} + \frac{2}{(\gamma+1)Ma_{\infty}^2 \sin^2(\alpha + \delta_{des})} \quad (9)$$

$$C = - \frac{4 \tan(\delta_{des} - \delta)}{A \cos \delta_{des} \sqrt{\epsilon}} \quad (10)$$

$$Q = \frac{A \cos \delta_{des}}{4 \sqrt{\epsilon} \tan(\alpha + \delta_{des})} \quad (11)$$

The essential advantage of this extended Newtonian flow theory is that the correction function p^* for a fixed value of η depends only on these parameters C and Q , that means C and Q are hypersonic similarity parameters with regard to the difference between the Newtonian and the real flow field. The C - Q -diagram of caret wings at all conditions is divided into two different parts which correspond to different types of off-design conditions as shown in Fig.2. The dividing line corresponding to the design condition is determined by $|CQ| = 1$. In the region $|CQ| > 1$, the wave pattern includes two plane attached shock waves which have moved inwards and closer to the surface, as compared with the design pattern. These two plane waves are joined by a nearly plane wave in the middle. As the pressure in the conically subsonic region is appreciably higher than the value obtained for a two-dimensional flow deflection through the same angle, a simple conjecture has been drawn in Fig.2 including two further discrete shocks and two singular points where three waves intersect. For the case $|CQ| < 1$ the shock wave is detached from the leading edges. Due to shock wave curvature the pressure distribution on the lower surface will show an increase towards the leading edges, as can be seen from Fig.2.

Detailed surveys on wave rider aerodynamics are given by D. KUECHEMANN (Ref.5), L.F. CRABTREE (Ref.6) and D.H. PECKHAM (Ref.7). Hence it follows that experimental investigations have been carried out mainly in the supersonic range. The tests presented in this paper have been undertaken to obtain experimental data on wave riders at hypersonic Mach numbers.

2. TEST ARRANGEMENT

The tests were made in the hypersonic gun tunnel of Deutsche Forschungsanstalt für Luft- und Raumfahrt (DFL), Braunschweig, in the Mach number range from $Ma_\infty = 7.9$ to 15.5. The stagnation pressure was 150 at and the stagnation temperatures ranged from approximately 700°K to 1500°K. The corresponding Reynolds numbers in the test section based on model length varied between $Re = 2.7 \cdot 10^6$ at $Ma_\infty = 7.9$ and $Re = 1.4 \cdot 10^5$ at $Ma_\infty = 15.5$. A conical axisymmetric nozzle with an exit diameter of 160 mm (6.3") was used in these tests. The average total testing time amounts to 35 milliseconds. The models investigated are shown in Table 2. It was necessary to restrict the model length to $l = 90$ mm (3.54") for keeping the models in the central core of uniform flow in the working section. The design Mach number varied between $Ma_{des} = 6$ and 10, the aspect ratio between $A = 0.8$ and 1.6 and the volume parameter between $v = 0.0675$ and 0.1. Model 1 was made out of steel, whereas models 2-6 were made out of duralumin. Three-component force data were obtained by use of two strain-gage balances in an angle-of-attack range of about -20° to $+20^\circ$. Pressures were measured by four strain-gage pressure transducers. The measurements were carried out in a plane of the wings in a distance of about $x_M/l = 0.834$ from the apex along the semispan on the lower surface in the incidence range from 0° to 17.5° . The pressure holes on the surface had 1.5 mm (0.059") diameter. Differential-interferometer photographs were used to estimate the shock wave angle σ (see Fig.1) in the plane of symmetry of the models.

3. PRESENTATION AND DISCUSSION OF RESULTS

3.1 Force Measurements

The experimental results presented in this paper are only some typical results taken from a more comprehensive report on the experimental data, Ref.8. Fig.2 shows the aerodynamic coefficients c_L , c_D , and c_m of all six models at Mach number $Ma_\infty = 10.9$ plotted against the "two-dimensional" deflection angle $\delta_1 = \alpha + \delta$. The solid curves represent inviscid two-dimensional wedge theory. As can be seen, there is good agreement between the measured lift coefficients and theory nearly throughout the positive deflection angle range, except at high values of δ_1 . However, in the negative region of the angle of attack, that is, at values of $\delta_1 - \delta < 0$ simple wedge theory completely fails to predict the lifting forces. The main reason for this is that in this case the upper surface of the caret wing becomes a compression surface and the basic assumption of a plane shock wave is no longer valid because of the convex shape of the upper surface. Thus, model 1 which has the lowest value of the anhedral angle Ψ (see Fig.1 and Table 1) shows the best agreement between experiment and theory at negative angles of attack, whereas model 2, having the largest anhedral angle Ψ of all models, shows the largest difference. It is worth noting that the lifting force characteristic is nearly independent of wing geometry in the positive range of deflection angles.

The comparison between the experimental drag coefficients and simple wedge theory indicates that throughout the positive range of the deflection angle theory predicts drag coefficients generally somewhat lower than the experiment. These differences are obviously due to viscous effects not included in the simple wedge theory. A simple approximation of the skin-friction drag, which has to be added to the inviscid drag, could be obtained by using the skin-friction coefficients c_f of a flat plate. Assuming $c_f = 0.0018$ the skin-friction drag coefficient is about $c_{Df} = 0.0041$ considering an average wetted surface-to-projected plan area ratio of 2.3 for all models. Thus, by including viscous effects there will be a better agreement between experiment and theory at least for small values of positive angles of attack. Large deviations between experiment and theory are to be seen in Fig.3 in the negative region of the angles of attack due to the strong curvature of the shock waves on the upper surface. These large discrepancies also occur with respect to the pitching moment coefficients and can also be seen from Fig.2. It should be noted that in the total positive incidence range the experimental pitching moment coefficients are somewhat smaller than predicted by simple wedge theory, except at lower values of the deflection angle. From this it may be concluded that the center of pressure has slightly moved forward, because the c_L -values have shown good agreement with theory.

To study the influence of Mach number and Reynolds number Fig.4 presents aerodynamic coefficients obtained from model 1 in the Mach number range from 7.9 to 15.5 plotted against the angle of attack. It is shown that throughout the Mach

number range simple wedge theory, drawn as a solid curve, fails completely at negative angles of attack, however, in the positive angle-of-attack range agrees quite well with the experimental lift force coefficients. At small angles of attack the experimental data are somewhat higher than predicted by theory whereas at high α -values wedge theory overpredict the lifting forces especially by an increase of Mach number and a decrease of Reynolds number. A similar trend is noted with respect to the pitching moment. Apparently viscous effects are the reason for the large discrepancies between experimental and calculated drag forces particularly observed at high Mach numbers and low Reynolds numbers. In order to include viscous effects the simple assumption of a constant skin-friction drag coefficient throughout the incidence range has been made. The total drag coefficients, calculated for c_f -values of 0.0006 at $Ma_\infty = 7.9$ and 0.0018 in the Mach number range from 10.9 to 15.5, are shown in Fig.4 as the dotted lines. As can be seen good agreement is obtained at small angles of attack up to Mach numbers of $Ma_\infty = 13.6$ whereas for the case $Ma_\infty = 15.5$ the experimental data are considerable higher than predicted.

Fig.5 presents the center of pressure of models 1, 3, 4 and 5 plotted against the angle of attack at various Mach numbers. It is to be seen that in all cases the theoretical value of $x_{cp}/l = 2/3$ predicted from inviscid conical flow theory is not verified by the experimental data. The values of x_{cp} vary between 0.6 and 0.63, thus, it may be inferred that there will be a non-conical flow due to viscous effects which induce a pressure gradient in chordwise direction. It can be taken from the measurements that in spite of some scatter the center of pressure is nearly independent of Mach number, angle of attack, and wing geometry.

An essential aspect for suggesting wave riders as hypersonic vehicles has been the expectation to achieve high lift-to-drag ratios at hypersonic speeds. Experimental lift-to-drag ratios obtained from wing 2 in the Mach number range from 7.9 to 15.5 are presented in Fig.6 plotted against the lift coefficients. As can be seen the experimental data considerably scatter at low c_L -values, that is, in a region where the maximum L/D-values are expected. Although viscous wedge theory predicts a nearly independence of hypersonic Mach numbers for the case $c_f = \text{const}$ the experimental L/D-values show large differences at various Mach numbers. From this it may be inferred that this is an effect due to Reynolds number. The solid curves shown in Fig.6 represent viscous wedge theory calculated with c_f -values empirically found from measurements. As can be seen the c_f -values considerably increase with decreasing Reynolds number. These empirical skin-friction coefficients are higher than those of a flat plate, probably because of three-dimensional effects occurring in the boundary layer on the upper and lower surface of the wave riders.

Maximum lift-to-drag ratios are obtained at c_L -values ranging from about 0.05 to 0.1, i.e. at angles of attack from about $\alpha = 1^\circ$ to 2.5° . In spite of the large scatters of the experimental data in the region of maximum lift-to-drag ratios the values of $(L/D)_{max}$ of all six models are plotted in Fig.7 against the Mach number and the corresponding Reynolds numbers. A comparison between model 4 and 5 which differs only by the volume parameter ($\tau = 0.08$ and $\tau = 0.1$) shows that the $(L/D)_{max}$ -values for the thicker wing (model 5) are slightly smaller than those obtained from model 4. The effect of aspect ratio on $(L/D)_{max}$ can be taken from Fig.7 by comparing the data of model 4 ($A = 1.2$) and model 6 ($A = 1.6$). It may be seen that the $(L/D)_{max}$ -values of model 1 are higher than those obtained from model 6 which has the larger aspect ratio. Furthermore, it may be seen that $(L/D)_{max}$ of all models tends to decrease with decreasing Reynolds numbers as already seen in Fig.6.

3.2 Shock Wave Angle Measurements

It has been pointed out in the previous chapter that viscous effects have a significant influence on drag force characteristics and particularly on lift-to-drag ratios. It may be expected that there is also an essential effect of the boundary layer on the shock wave pattern. At hypersonic speeds the influence of boundary layer is connected with special displacement effects. In fact, it can be shown that the boundary layer thickness is proportional to $0.5(\gamma-1) Ma^2/\sqrt{Re}$, where suffix 1 represents the state behind the shock wave. Thus interactions between the boundary layer and the external flow become more and more important as the Mach number increases. With respect to the displacement effect of the boundary layer, two regions can be distinguished, a zone of strong interaction near the leading edges and a zone of weak interaction further downstream. The interaction parameter $X = Ma^3/Re^{1/2}$ determines which type of interaction will occur. In case of $X \gg 1$ there will be a strong interaction and in case of $X \ll 1$ a weak interaction, respectively. In the present tests at small angles of incidence the values of X ranged from about $X = 0.2$ at $Ma_\infty = 7.9$ to the value of $X = 2.5$ at $Ma_\infty = 15.5$. Thus, it may be inferred that due to the high values of X in the upper Mach number range there is a large influence of viscous effects on the shock wave pattern.

The geometry of model 3 and 5 was chosen such that at test Mach numbers of $Ma_{\infty} = 7.9$ and 10.9 , respectively, a nearly plane shock wave lying in the plane of the leading edges should be obtained at $\alpha = 0^\circ$. But, differential interferometer photographs show, that the plane shock wave condition is not achieved at $\alpha = 0^\circ$.

In Fig. 8 the experimental data of shock wave angles taken from differential interferometer photographs of model 1 are plotted against the angle of attack at various Mach numbers and Reynolds numbers, respectively. The solid curve represents the theoretical shock wave angle σ after inviscid wedge flow theory. It is clearly to be seen that there are great differences between theory and experiment especially for low angles of attack and at low Reynolds numbers. The maximum difference of about 4° is obtained at $Ma_{\infty} = 15.5$ and $\alpha = 0^\circ$, whereas at very high angles of attack the experimental data tend to be smaller than predicted by theory. The dash-and-dot line represents the position of the leading edge plane $\sigma_{L.E.} = \alpha + \sigma_{des}$. Having in mind Fig. 2 in which the various shock wave pattern at off-design conditions have been shown it can be seen from Fig. 8 that for the case of $Ma_{\infty} = 10.9$, i.e. nearly design condition, the shock wave is lying almost in the leading edge plane over a rather wide range of angles of attack. In the case of $Ma_{\infty} > Ma_{des}$ the shock wave has moved inwards at low angles of attack. If, however, the angle of attack increases the shock wave tends to move outwards until a definite angle of attack is reached where the shock is lying in the leading edge plane and thus, design condition is obtained. In the negative incidence range there is another definite angle of attack at which design condition occurs. Thus, in the case $Ma_{\infty} > Ma_{des}$ there will be always two different angles of attack at which design condition is obtained. If the Mach number Ma_{∞} is decreased both angles begin to approach until they meet at $\alpha = 0^\circ$ in the case $Ma_{\infty} = Ma_{des}$. For $Ma_{\infty} < Ma_{des}$ no design condition occurs in the total incidence range. These predictions by inviscid wedge theory are not fulfilled as can be taken from Fig. 8. In no case the shock wave has moved inwards.

In order to improve the theory viscous effects have been included by a simple two-dimensional boundary layer calculation based on the equation for the displacement thickness on a flat plate given in Ref. 8:

$$\delta^* = \frac{\gamma-1}{\gamma+1} \left(0.664 + 1.73 \frac{T_w}{T_o} \right) Ma_{\infty}^2 \left(\frac{C_s x}{U_{\infty} \nu_{\infty}} \right)^{1/2} \quad (12)$$

For a blunted wedge or for the compression surface of an inclined flat plate δ^* can be calculated from this simple flat plate result provided free stream conditions are taken to be those behind the oblique shock. The effective body slope due to the displacement effects of the boundary layer results from:

$$\delta_{eff} = \delta + \frac{d\delta^*}{dx} = \delta + \frac{1}{2} \frac{\gamma-1}{\gamma+1} \left(0.664 + 1.73 \frac{T_w}{T_o} \right) Ma_{\infty}^2 \left(\frac{C_s}{Re_{1x}} \right)^{1/2} \quad (13)$$

An average angular slope was taken as that at the quarterchord point of the wedge to represent the conditions over the entire plate (Ref. 9). With an iteration procedure the "viscous" shock angle can be estimated from $(\delta_{eff})^{1/4}$ and Ma_{∞} . Near the leading edges the slope of the boundary layer displacement surface becomes large and this viscous theory is therefore not valid, at least at very small deflection angles, where strong interactions take place. Nevertheless it can be taken from Fig. 8 that even at small angles of attack rather good agreement between experiment and theory has been obtained. The theoretical curve is drawn as the dotted line, which has been calculated with the assumption of a wall temperature of $T_w = 293^\circ K$. At higher angles of attack there are slight disagreements due to failing of the assumption, that the shock has no transverse curvature. An essential result is the decrease of viscous effects with increasing angles of attack.

Fig. 9 presents experimental shock wave angles of model 1, 2, 4 and 5 plotted against the deflection angle δ_1 at various Mach numbers compared with inviscid wedge theory and viscous wedge theory, respectively. Good agreement between measurement and viscous theory is obtained up to deflection angles of about $\delta_1 = 20^\circ$. At higher values the experimental data are somewhat smaller than predicted by theory due to the strong shock curvature. It is remarkable that in spite of different wing configurations the experimental shock angles are lying on one single curve. Only model 2, which has the lowest design Mach number ($Ma_{des} = 6$) of all models, shows slight differences. This might be a result of corner effects as this wing has the lowest value of γ (see Fig. 1). The interference effects of a corner are such as to displace the flow near the corner additionally compared to the displacement effect of the flat plate boundary layer.

3.3 Pressure Distribution Measurements

From the previous chapters it could have been assumed that simple wedge theory including viscous effects is sufficient to describe the flow field of a caret wing over a relative wide range of angles of attack and Mach numbers. But, although this method gives surprisingly good estimates of the overall lifting forces, pitching moments, shock wave angles in the symmetry plane and under certain circumstances also drag forces, it often fails completely to predict pressure distributions.

Fig. 10 presents some typical pressure distributions at various angles of attack obtained from model 5 in the Mach number range from 7.9 to 15.5 plotted against the non-dimensional semispan coordinate. The dotted lines represent inviscid wedge theory, and as can be taken from Fig. 10 there is a complete disagreement between theory and measurement particularly at high angles of attack. The different regions $|CQ| \leq 1$ are shown as hatched boundaries. It is clearly to be seen that in the region $|CQ| > 1$, where a pressure rise near the plane of symmetry ($\eta = 0$) should be expected (see Fig. 2) an increase of pressure near the leading edges occurs, particularly noted at low Reynolds numbers, $Re = 2.1 \cdot 10^5$ ($Ma_\infty = 13.6$) and $Re = 1.4 \cdot 10^5$ ($Ma_\infty = 15.5$). After the inviscid flow theory the shock wave on the lower surface should have been displaced inwards and hence the distance between the shock and the lower surface would be much smaller than in cases $|CQ| \leq 1$. Therefore much larger viscous interaction effects might be expected for $|CQ| > 1$ rather than for $|CQ| \leq 1$. Including viscous effects the ratio of displacement thickness of the boundary layer and the shock distance from the lower surface will increase towards the leading edges which means that strong interaction and hence shock detachment will occur.

In the case of $|CQ| < 1$ inviscid extended Newtonian theory predicts already shock detachment and it is assumed that viscous effects will not have such a strong influence as in the case $|CQ| > 1$ because of the larger distance of the shock wave from the lower surface. As a first approximation it is assumed that the flow past the wave rider including viscous effects is the same as the inviscid flow past a wave rider having a larger wedge angle δ . The increase of δ , shown in Fig. 11 as δ_{vis} , is equivalent to the displacement of the boundary layer.

Under this assumption the similarity parameter C can be written as follows:

$$C_{vis} = - \frac{4 \tan(\delta_{des} - (\delta + \delta_{vis}))}{A \cos \delta_{des} \sqrt{\epsilon}} \quad (14)$$

The other parameter Q is independent of viscous effects. Assuming that $(\delta_{des} - \delta) \ll 1$ and $\delta \ll 1$, equation (14) can be rewritten as

$$C_{vis} = C_{iv} + \text{const } \delta_{vis} \quad (15)$$

$$(CQ)_{vis} = (CQ)_{iv} + \text{const } \delta_{vis} Q \quad (16)$$

Thus, the position of the design curve, $(CQ)_{vis} = -1$, in the inviscid $C-Q$ diagram is given by the expression:

$$(CQ)_{iv} = -1 - \text{const } Q \delta_{vis} \quad (17)$$

This result is shown schematically in Fig. 11 and as can be seen the design curve including viscous effects is shifted towards higher values of Q for a constant C with increasing δ_{vis} -values.

That means, if measured pressure distributions are reduced to the correction function p^* for a fixed value of C and Q the reduced experimental data will lie on a single curve only in the case of $\delta_{vis} = \text{const}$ of all reduced data. If the experimental data obtained under the condition $C, Q = \text{const}$ show different viscous effects the reduction to p^* will show large scatter. A reduction has been carried out for the case $C = -0.75$ and $Q = 1.23$ result of which is presented in Fig. 12. The pressure distribution $c_p(\eta)$ obtained from wing 3 at $Ma_\infty = 10.9$ and an incidence of $\alpha = 15^\circ$ is in good agreement with the corrected Newtonian theory drawn as the solid curve and even after having reduced to p^* the good agreement remains considering that slight errors in measurement are increased by the roughening character of this procedure. However, reducing model i with the condition $Ma_\infty = 9.55$ and $\alpha = 7.5^\circ$, which presents the same $C-Q$ -combination $Q = 1.23$ and $C = -0.75$ shows clearly that there are large discrepancies between theory and experiment particularly to be noted in the $p^* - \eta$ -diagram. In the case of $C = -0.56$ and $Q = 1.79$, that is a design condition, the same effect is to be seen. Model 4 at $Ma_\infty = 12.2$ and $\alpha = 7.5^\circ$, that is at a relative high Mach number

with a corresponding low Reynolds number, shows large discrepancies from the theoretical value $p^*(\eta) = -1$ especially towards the leading edges. A further viscous effect which is representative for all models investigated at $Ma_\infty = 7.9$ ($Re = 2.7 \cdot 10^6$) can be seen from a pressure rise near the lower ridge line. As the corresponding Reynolds number presents the highest value of all test Reynolds numbers it has been assumed that there might be a transition of boundary layer supported by corner interferences. Due to the considerably greater displacement effect of a turbulent boundary layer compression waves might be produced which are responsible for the increase of pressure near the lower ridge line, which is impossible due to inviscid theory in the case $|CQ| < 1$. Integration of equ. 8 shows, that, as in the case of pressure measurement, a reduction of the experimental normal force coefficients can be carried out in the same way. The result is shown in Fig. 13 for the case $C = -0.6$ and it is clearly to be seen that as in the case of pressure reduction some scatter occurs due to different viscous effects.

4. CONCLUSIONS

Analysis of experimental data obtained from six caret wings in a Mach number range from 7.9 to 15.5 and corresponding Reynolds numbers from $2.7 \cdot 10^6$ to $1.4 \cdot 10^5$ leads to the following conclusions:

- (a) Good predictions of overall lifting forces and pitching moments by inviscid wedge theory in the positive range of incidence are found.
- (b) By assuming a constant value of skin-friction drag throughout the incidence range using flat plate results, the drag-force coefficients can be predicted by wedge-type analysis for small angles of attack in good agreement with the experiments.
- (c) Large deviations of the aerodynamic coefficients c_L , c_D and c_m from two-dimensional wedge theory occur in the negative incidence range due to strong transverse curvature of the shock wave.
- (d) A severe decay of maximum lift-drag ratio occurs with decreasing Reynolds numbers due to increasing viscous effects.
- (e) Pressure distribution measurements and shock wave angle determinations show that due to considerable viscous effects the shock wave is displaced outwards from the leading edges, particularly in the case $|CQ| > 1$. Obviously the shock wave is detached from the leading edges due to strong interaction effects.
- (f) Good agreement was obtained with regard to experimental shock wave angles by a simple two-dimensional boundary layer calculation including displacement effects.

REFERENCES

1. Vonweiler, T. Delta Wings of Shapes amenable to Exact Shock-Wave Theory, Journ. Roy. Aeron. Soc. 67, 1963
2. Messiter, A.F. Lift of Slender Delta Wings according to Newtonian Theory. AIAA Journal, Vol. 1, 1963
3. Hida, K. Thickness effects on the Force of Slender Wings in Hypersonic Flow. AIAA Journal, Vol. 3, 1965
4. Squire, L.C. Calculated Pressure Distributions and Shock Shapes on Thick Conical Wings at High Supersonic Speeds. The Aeronautical Quarterly, Volume XVII, Part 2, May 1967
5. Küchemann, D. Hypersonic Aircraft and Their Aerodynamic Problems. Progress in Aeronautical Sciences Vol. 6, Pergamon Press, Oxford, 1965
6. Crabtree, L.F. Boundary-Layer Effects on Hypersonic Aircraft. RAE Report Tech. Memo Aero 902
7. Peckham, D.H. On Three-Dimensional Bodies of Delta Planform which can Support Plane Attached Shock Waves. A.R.C. C.R. No. 640
8. Kipke, K. Experimentelle Untersuchungen an Wellenreiter-Flügeln im Hyperschallbereich. DFL-Bericht 67/39, 1967
9. Cox, R.N. Elements of Hypersonic Aerodynamics. English Universities Press Ltd., London, 1965
10. Crabtree, L.F. Hypersonic Aerodynamics. The Ronald Press Company, New York, 1959

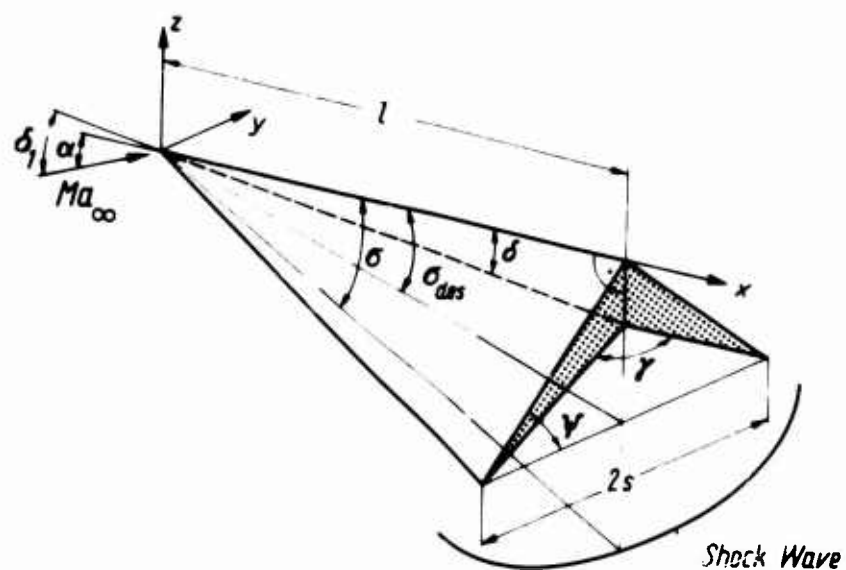


Fig. 1 Notation of a caret wing

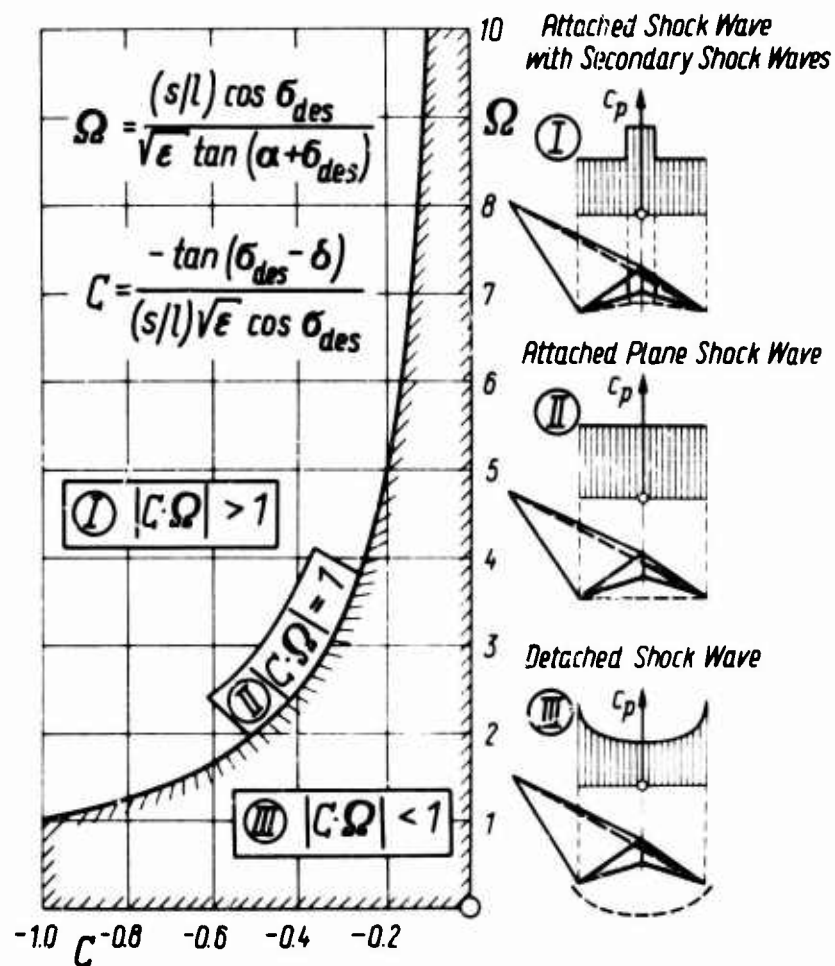


Fig. 2 Typical shock shapes and pressure distributions of a caret wing

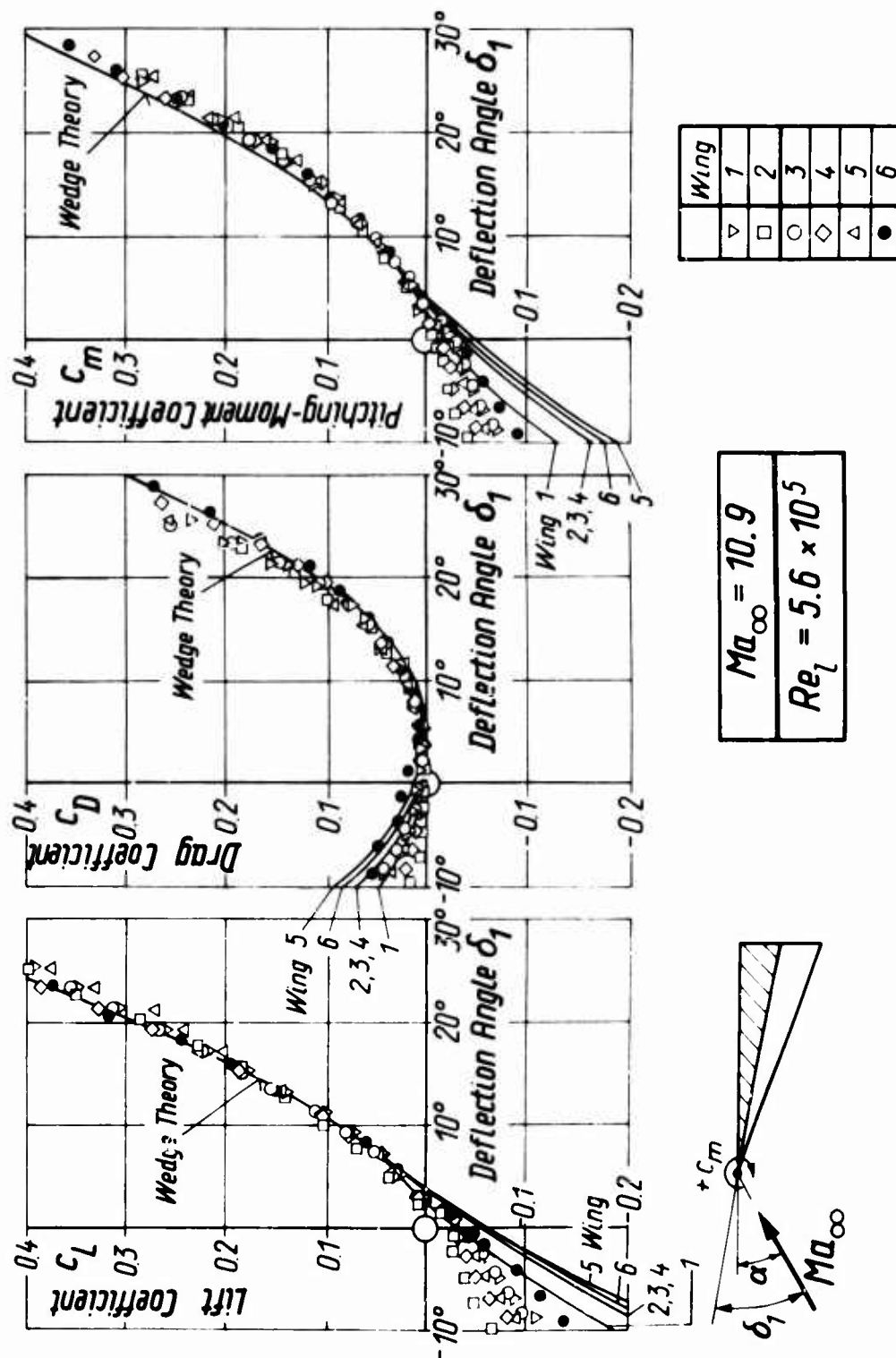


Fig. 3 Aerodynamic coefficients c_l , c_D , c_m versus deflection angle δ_1 for curved wings at $Ma_\infty = 10.9$

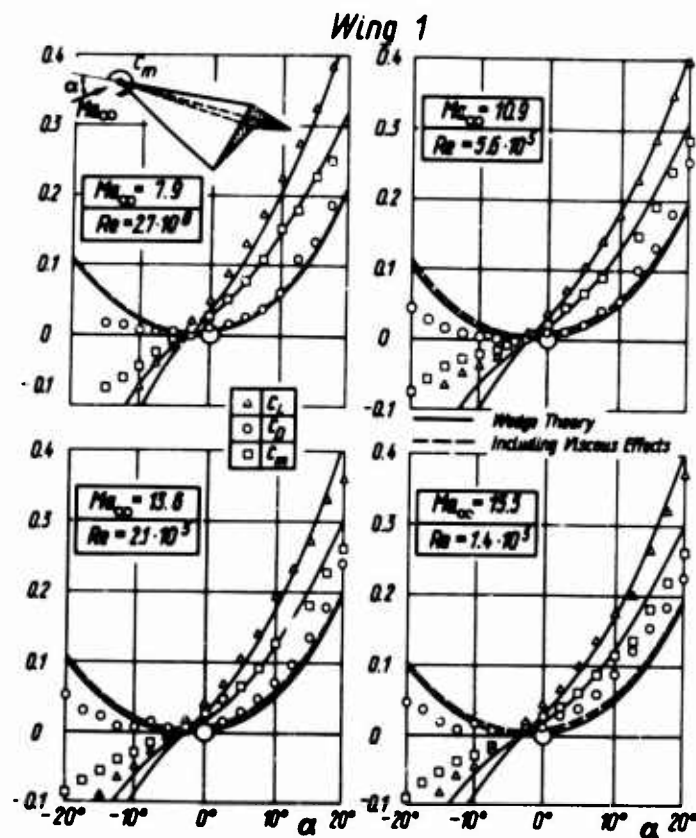


Fig.4 Aerodynamic coefficients c_L , c_D , c_m of wing 1 at various Mach numbers

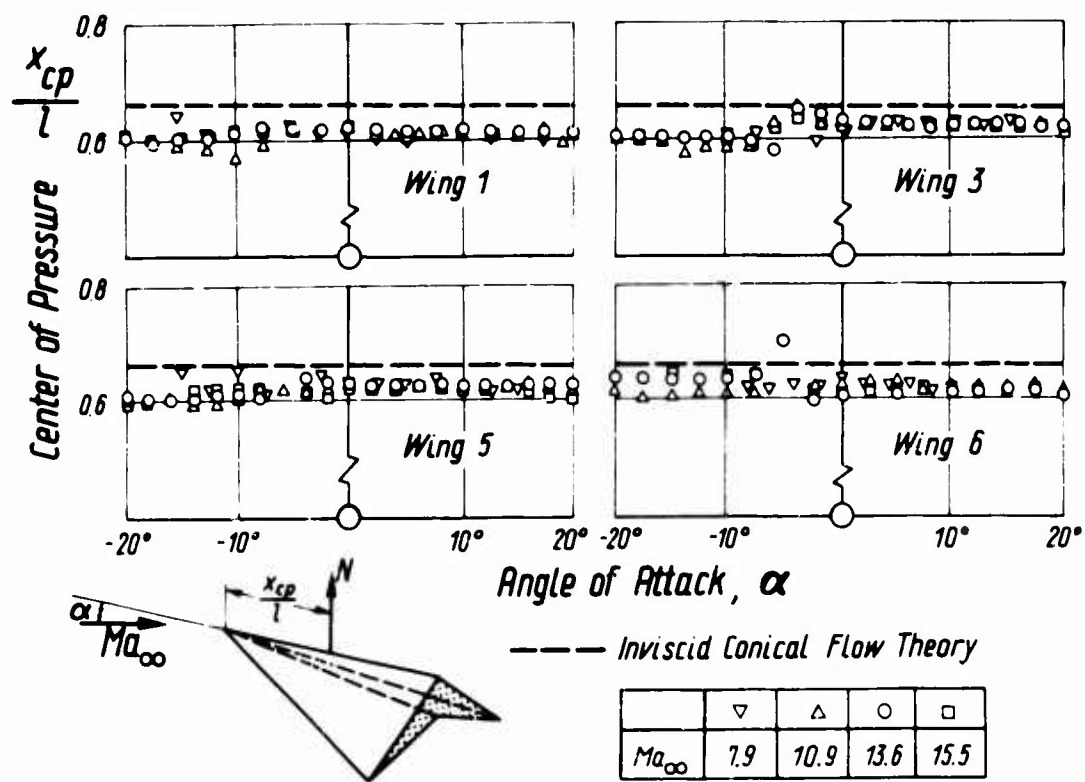


Fig.5 Center of pressure versus angle of attack for caret wings at various Mach numbers

Wing 2

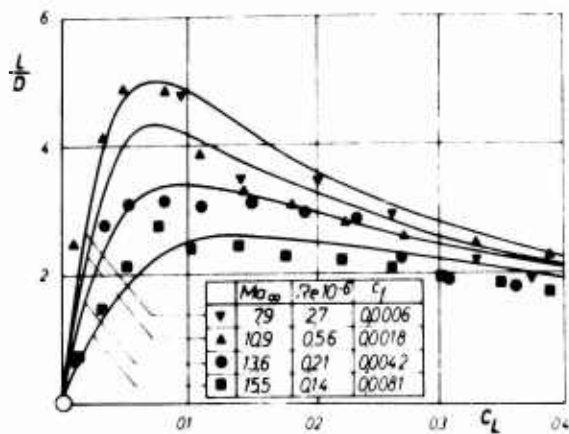


Fig.6 Lift-to-drag ratios of wing 2 at various Mach numbers and Reynolds numbers

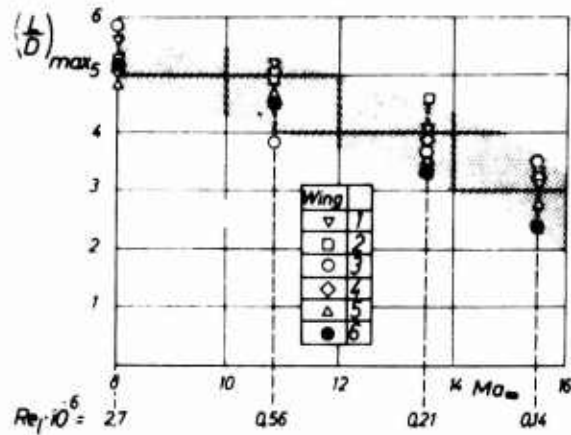


Fig.7 Maximum lift-to-drag ratios of models investigated at various Mach numbers and Reynolds numbers

Wing 1

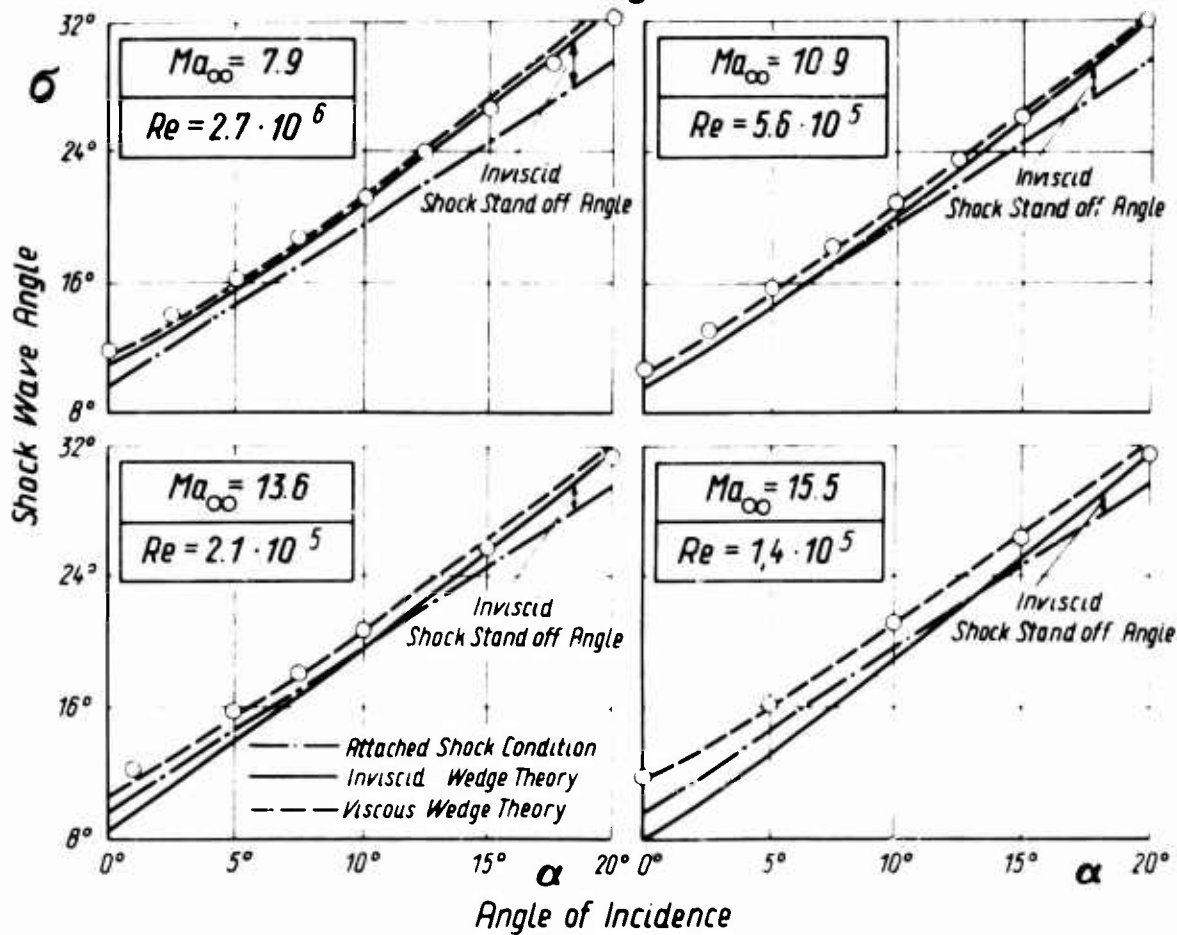


Fig.8 Shock wave angles of wing 1 at various Mach number.

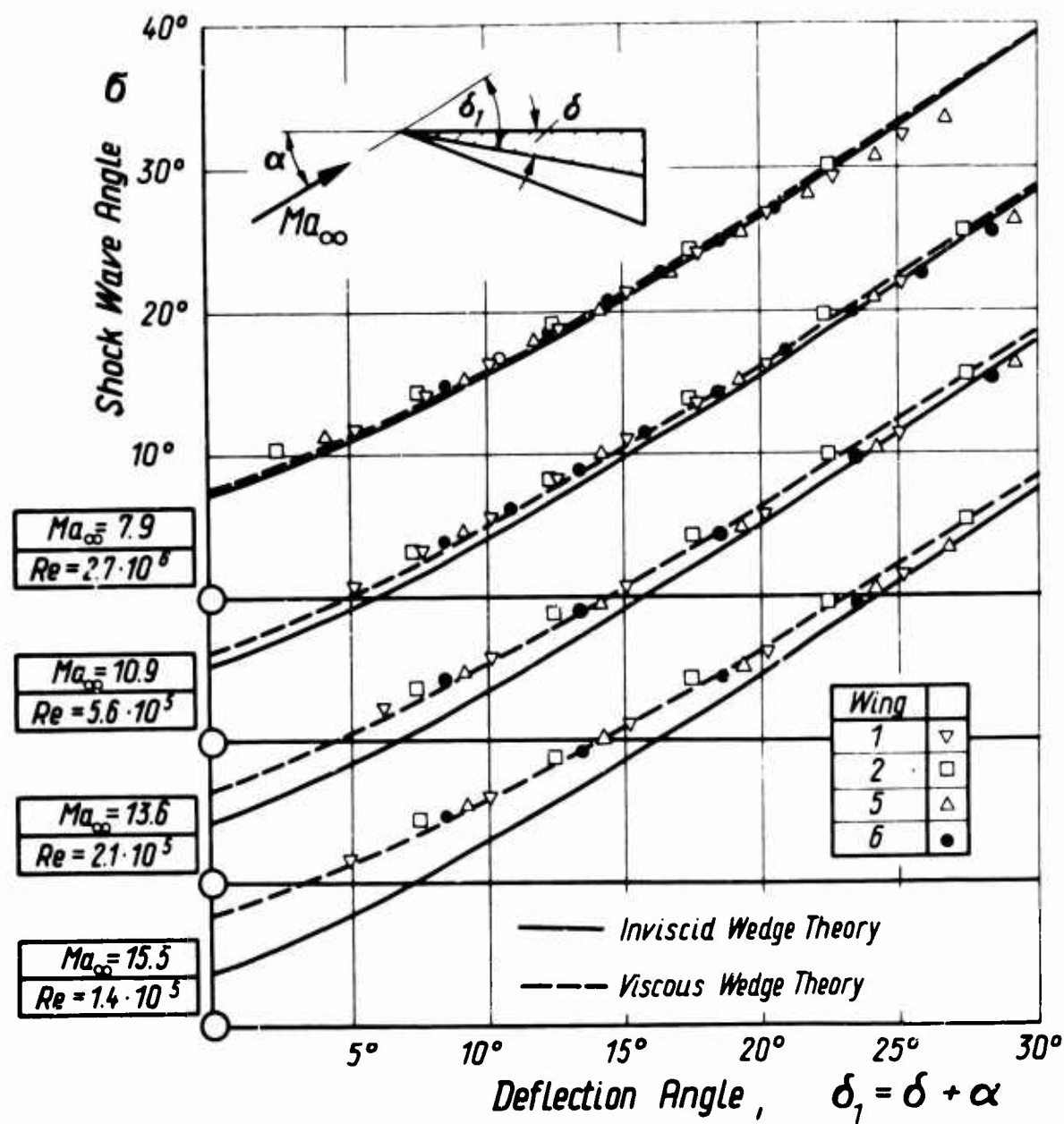


Fig.9 Shock wave angles of wing 1, 2, 5 and 6 versus deflection angle at various Mach numbers

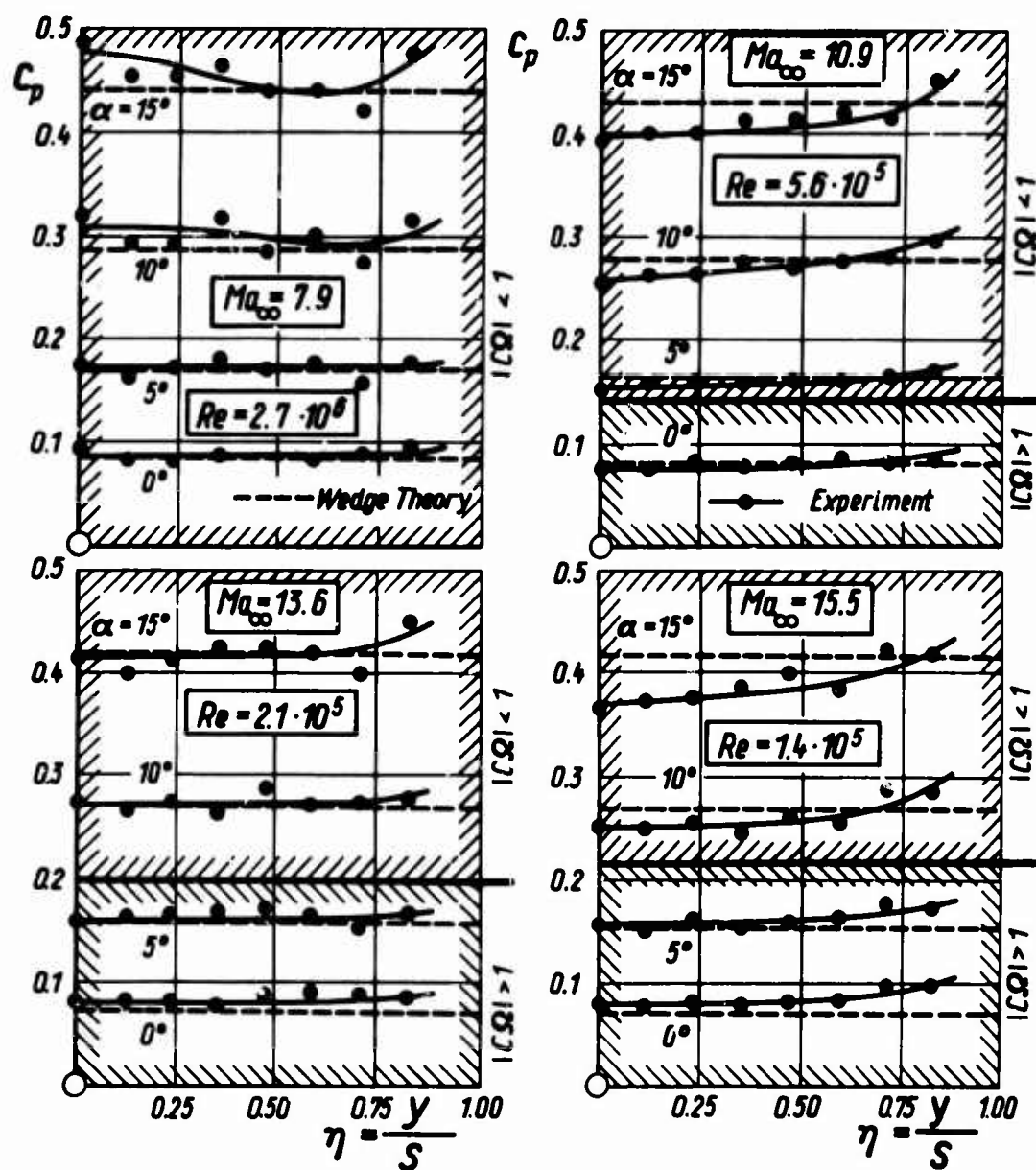


Fig.10 Pressure distributions on the lower surface of wing γ at various Mach numbers and Reynolds numbers

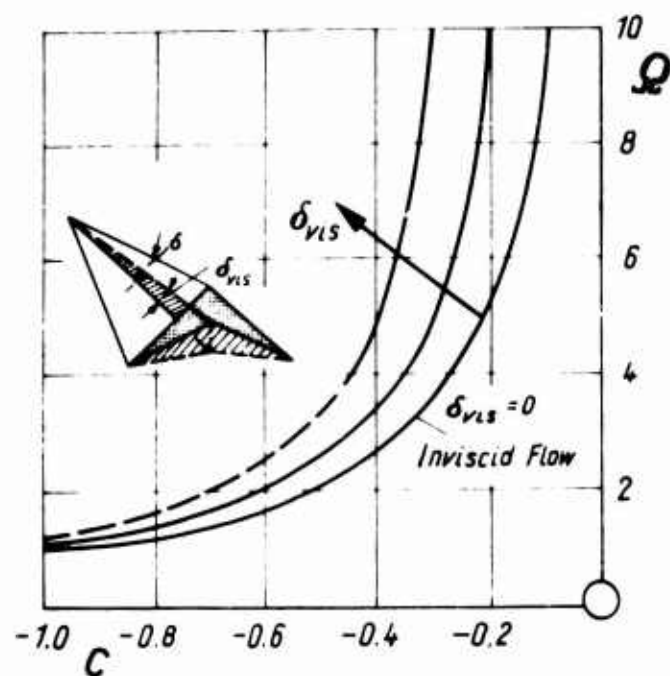
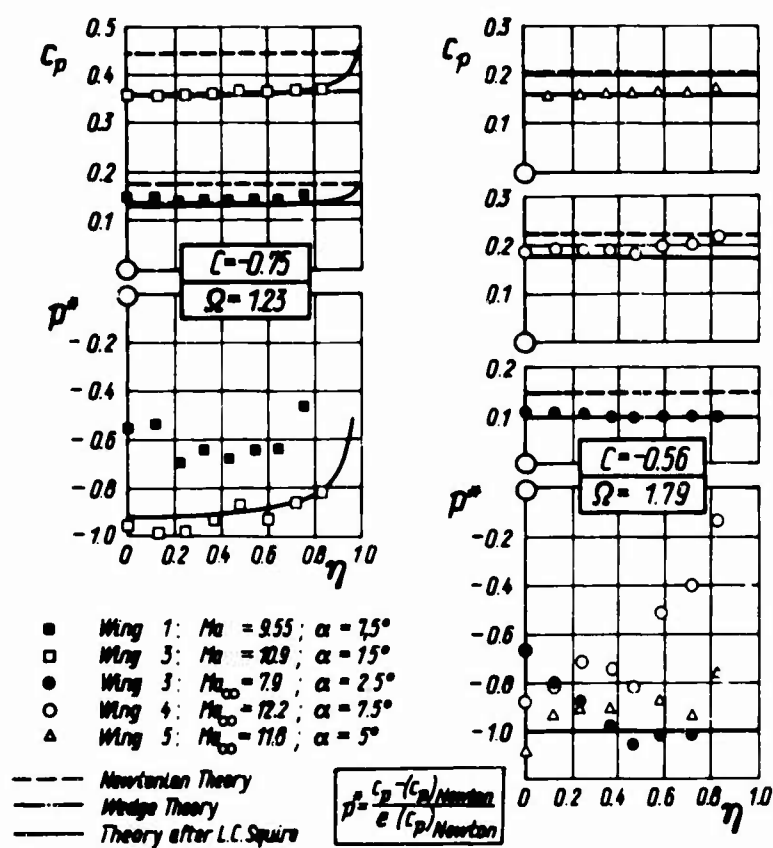
Fig. 11 C- Ω -diagram including viscous effects

Fig. 12 Reduction of measured pressure distributions

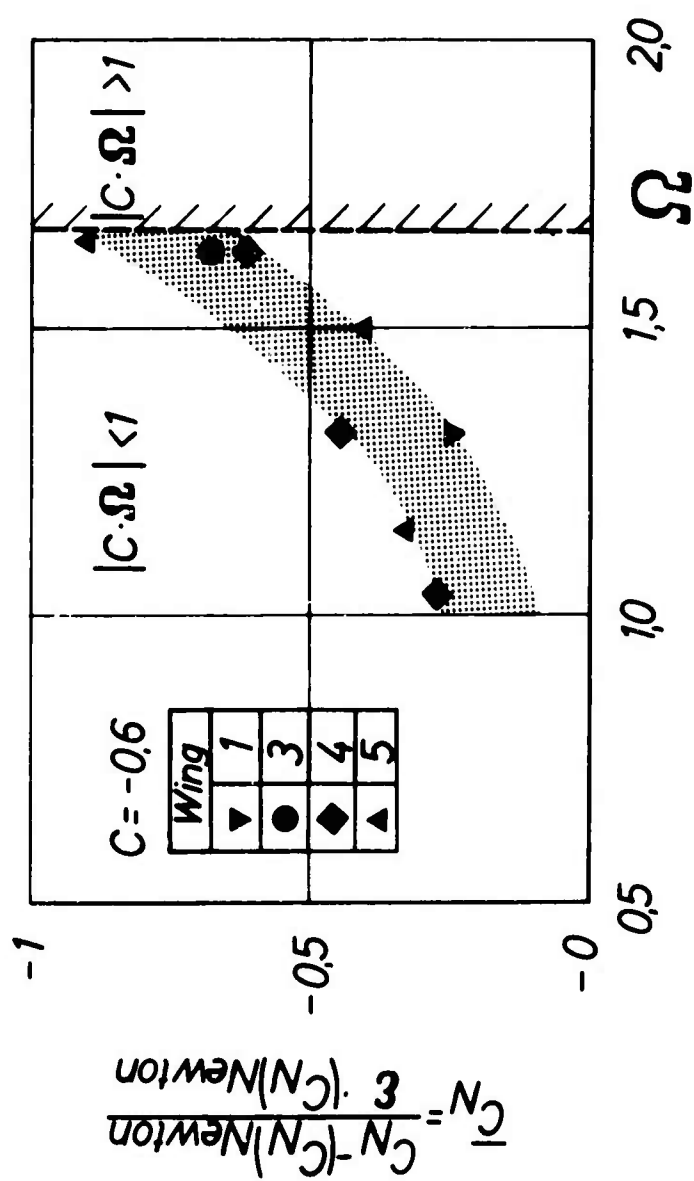








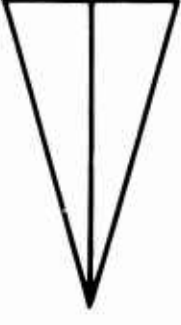
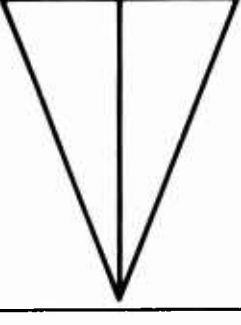


Fig.13 Reduction of normal forces

a) Wedge Theory			b) Simple Newtonian Theory		
Incidence Range	Pressure Coefficient on the Lower Surface c_{pL} on the Upper Surface c_{pU}		Incidence Range	Pressure Coefficient on the Lower Surface c_{pL} on the Upper Surface c_{pU}	
$\alpha > 0$	$2 \frac{\sin \delta \cdot \sin(\alpha + \delta)}{\cos(\delta - \alpha + \delta)}$ with δ from Equ ① ($\delta_L = \alpha + \delta$)	$2 \frac{\left[\left(\frac{Ma_e}{Ma_\infty} \right)^{\frac{\gamma}{\gamma-1}} - 1 \right]}{\gamma Ma_\infty^2}$ with Ma_e from Equ ② ($\delta_e = \alpha$)	$\alpha > 0$	$2 \sin^2(\alpha + \delta_{des})$	0
$-\delta < \alpha < 0$	$2 \frac{\sin \delta \cdot \sin(\alpha + \delta)}{\cos(\delta - \delta - \alpha)}$ with δ from Equ ① ($\delta_L = \alpha + \delta$)		$-\delta_{des} < \alpha < 0$	$2 \sin^2(\alpha + \delta_{des})$	$2 \frac{\sin^2 \alpha}{1 + 16 \left(\frac{\tan \delta_{des}}{R} \right)^2}$
$\alpha < -\delta$	$2 \frac{\left[\left(\frac{Ma_e}{Ma_\infty} \right)^{\frac{\gamma}{\gamma-1}} - 1 \right]}{\gamma Ma_\infty^2}$ with Ma_e from Equ ② ($\delta_e = -(\alpha + \delta)$)	$2 \frac{\sin \delta \cdot \sin \alpha}{\cos(\delta - \alpha)}$ with δ from Equ ① ($\delta_L = -\alpha$)	$\alpha < -\delta_{des}$	0	$2 \frac{\sin^2 \alpha}{1 + 16 \left(\frac{\tan \delta_{des}}{R} \right)^2}$
$\cos \delta_L = \tan \delta \left[\frac{(\gamma+1) Ma_\infty^2}{2 (Ma_\infty^2 \sin^2 \delta - 1)} - 1 \right]$ ① $\delta_e = \sqrt{\frac{\gamma+1}{\gamma-1}} \left[\arctan \sqrt{\frac{\gamma-1}{\gamma+1} (Ma_\infty^2 - 1)} - \arctan \sqrt{\frac{\gamma-1}{\gamma+1} (Ma_e^2 - 1)} \right] - \left[\arctan \sqrt{Ma_\infty^2 - 1} - \arctan \sqrt{Ma_e^2 - 1} \right]$ ②					

Table 1: Calculation of pressure coefficients after wedge theory and Newtonian theory

Wing No	①	②	③	④	⑤	⑥
Cross-Section						
Plan Form						
Aspect Ratio	$A = 0.8$	1.2				1.6
Design Mach-No	$Ma_{des} = 10$	6	8	10	10	10
Volume Param.	$\tau = 0.0675$	0.08	0.08	0.08	0.10	0.08
γ	136.4°	125.7°	143°	151.3°	151.1°	158.2°
δ	5.2°	7.5°	7.5°	7.5°	9.3°	8.5°

Effect of Aspect Ratio: Wing ④, ⑥
Effect of Design Mach Number: Wing ②, ③, ④
Effect of Volume Parameter: Wing ④, ⑤

Table 2 Wing geometry of models

HYPERSONIC VISCOUS - INVISCID INTERACTIONS BY A NEW
TYPE OF ANALYSIS *

by

S. G. Rubin, S. Rudman, T. C. Lin, and M. Pierucci

Department of Aerospace Engineering
and Applied Mechanics
Polytechnic Institute of Brooklyn
Farmingdale, New York

* This study was supported by the Air Force Office of Scientific Research under Contract No. AF 49 (638) - 1623, Project No. 9781 - 01.

SUMMARY

Hypersonic viscous-inviscid interactions are treated by the finite-difference solution of a single set of equations valid throughout the boundary layer and shock wave structure, as well as inviscid regions. Primary interest is concerned with the flow structure and surface properties in the continuum merged layer, near a sharp leading edge, and the strong-interaction domain further downstream.

Several geometries are considered. Among these are (1) axisymmetric flow over sharp cones, (2) two-dimensional channel flow with interior oblique shock wave interaction, and for a finite length channel, the exhaust interaction with the hypersonic flow outside the channel, and (3) the three-dimensional geometry of a finite width flat plate having a sharp leading edge.

Results are presented for flow structure, wall pressure and heat transfer. For the three-dimensional geometry, shock wave patterns are described and comparisons with two-dimensional flat plate results are shown.

NOMENCLATURE

C	Chapman viscosity constant $\mu=CT$
C_f	Skin friction coefficient $C_f=2(\mu\partial u/\partial y)_{y=0}/\rho_\infty U_\infty^2$
C_H	heat transfer coefficient $C_H=(kTy+\bar{u}\bar{u}_y)_{y=0}/\rho_\infty U_\infty C_p(T_\infty-T_w)$
C_p	specific heat at constant pressure
C_v	specific heat at constant volume
k	coefficient of thermal conductivity
l	length scale in tangential direction
M	Mach number
r	pressure
R	gas constant
Re_∞	Reynolds number based on free stream conditions
T	temperature
u	tangential velocity component
v	normal velocity component
V_∞	Rarefaction parameter $M\omega\sqrt{C}/\sqrt{Re}$
w	lateral velocity component for three-dimensional geometry
x	tangential body coordinate
y	normal body coordinate
z	lateral direction for three-dimensional geometry
α	angle of attack
γ	ratio of specific heats $\gamma=C_p/C_v$
δ	length scale in normal direction
ϵ	order of higher approximation in Eq. (5)
λ	mean free path
μ	coefficient of viscosity
ρ	density
σ	Prandtl number
θ_c	Cone half-angle
χ_∞	interaction parameter
<u>Superscripts</u>	
()	average dimensional
()	dimensional
()	nondimensional
<u>Subscripts</u>	
max	maximum value
ref	local reference conditions
RH	Rankine-Hugoniot
s	shock wave
stag	stagnation conditions
o	initial value
∞	free stream quantities

HYPERSONIC VISCOUS - INVISCID INTERACTIONS BY A NEW TYPE OF ANALYSIS *

by

S. G. Rubin, [‡] S. Rudman ^{*}, T. C. Lin ^{**}, and M. Pierucci ^{***}

Polytechnic Institute of Brooklyn

I. INTRODUCTION

The hypersonic flow over slender bodies having sharp leading edges involves a complex interaction between the vorticity created at the surface, and diffused in the form of a boundary layer, and the outer compressive region or "shock-wave" that bounds the disturbed flow domain.

Due to the complexity of the coupling, theoretical investigations have been concerned almost exclusively with the interaction that occurs in the hypersonic flow over a sharp flat plate or sharp nose cone. In particular, the following model for these flows has evolved: ⁽¹⁾ a small kinetic region occurs at the leading edge and precedes a continuum merged layer throughout which viscous effects are significant. The length of this region increases appreciably for increasing Mach number and inverse unit Reynolds number, i. e., increasing Knudsen number. The merged layer asymptotes into the strong interaction flow. It is here that a distinct outer Rankine-Hugoniot shock wave has formed and is separated from an inner low density boundary layer by an inviscid core. The solutions for the different layers remain closely coupled until further downstream the shock wave becomes sufficiently weak so that iterative techniques become possible in the so-called weak interaction flow. From a practical point of view, this division of the flow reflects the significant differences in both the magnitudes and functional variations of surface pressure, skin friction and heat transfer at different locations along the surface. Fig. 1a depicts the various flow regimes for typical flow conditions on a sharp flat plate.

The different flow regimes are generally treated separately. Typical models for the strong interaction flow include the use of local similarity ⁽²⁾ or integral methods ⁽³⁾ for the inner boundary layer and tangent wedge theory ⁽²⁾ or similarity solutions ⁽³⁾ for the outer inviscid flow. For the fully viscous merged layer a two layer description has also been employed ^(4, 5). An inner boundary layer is assumed to merge into a compressive, thick shock layer that forms the outer portion of the disturbed region. A local similarity ⁽⁴⁾ or integral boundary layer ⁽⁵⁾ solution is matched, along some dividing line, to a shock structure solution for the outer compressive flow.

The purpose of this paper is to utilize a new single layer model, that does not presuppose the existence of shock waves or boundary layers, in order to study the flow in the merged and strong interaction regimes. Previous results have been reported for the flow over flat plates and wedges ⁽⁶⁾ and are in good agreement with the available experimental data ^(1, 7). The simplicity of obtaining numerical solutions to a single set of equations valid throughout the entire continuum flow domain allows for the treatment of more complex body shapes, in particular, of three-dimensional geometries.

The flow over sharp cones, the viscous-inviscid interactions in a two-dimensional internal channel flow, as well as the wake region for a finite length channel, and the flow over a sharp flat plate of finite width will be discussed in the sections to follow. Results for wall pressure, heat transfer and skin friction, as well as the entire flow structure, including the shock-layer for the three-dimensional geometry, shall be discussed. Comparisons with experimental data shall be described whenever possible.

* This research was supported by the Air Force Office of Scientific Research under Contract No. AF 49 (638) - 1623, Project No. 9781-01.

‡ Associate Professor of Aerospace Engineering

* Currently, Propulsion Technology Engineer, Propulsion Dept., Grumman Aircraft Engineering Corporation, Bethpage, New York.

** Research Fellow

***Research Associate

II. ANALYSIS

Slender bodies at small angles of attack, moving with hypersonic velocities, create disturbances that are confined to a thin layer adjacent to the surface. Outside of this region the fluid is unaffected by the body and the free stream conditions are applicable. Therefore the various viscous and inviscid layers within the disturbed region, shock waves, boundary layers, etc., are all relatively thin so that normal gradients are everywhere much greater than gradients along the surface direction. From the familiar boundary layer and hypersonic small disturbance theories it is apparent that the respective viscous and inviscid layers are thin when the square root of the local Reynolds number $Re_x^{1/2}$, and the Mach number M are large. With these parameters assumed to be large, a uniformly valid expansion for the entire continuum hypersonic flow regime can be formulated. A complete description of the flow field under consideration and derivation of the governing equations is presented in Ref. 6. The general technique, using a two-dimensional model, shall be outlined below.

In order to estimate the magnitude of the various terms in the governing Navier-Stokes equations, within the different layers described above, all the flow variables are non-dimensionalized with respect to local reference conditions at an arbitrary point. This expansion technique is used here only to determine the order of the terms in the different layers. Ultimately, constant reference values shall be prescribed in a final expansion. Using an (x, y) coordinate frame, where x is measured along the surface and y normal to the surface, with velocity components (u, v) , the following expansion is assumed.

$$\begin{aligned}\bar{u} &= \bar{u}_\infty (u + \epsilon u_1 + \dots) \\ \bar{v} &= \bar{u}_\infty \delta (v + \epsilon v_1 + \dots) \\ \bar{p} &= \bar{p}_\infty p_{ref} (p + \epsilon p_1 + \dots) \\ \bar{\rho} &= \bar{\rho}_\infty \rho_{ref} (\rho + \epsilon \rho_1 + \dots) \\ \bar{T} &= \bar{T}_\infty T_{ref} (T + \epsilon T_1 + \dots) \\ \bar{\mu} &= \bar{\mu}_\infty \mu_{ref} (\mu + \epsilon \mu_1 + \dots) \\ \bar{x} &= x, \bar{y} = y \delta, \delta = \delta / \bar{x}\end{aligned} \quad (1)$$

The subscript $()_{ref}$ is used here to denote the local magnitude of all the dimensional properties. In this manner nondimensional reference parameters can be formed in order to estimate the relative magnitude of the terms in various regions of the flow field. These parameters are estimated on the basis of boundary layer and hypersonic flow requirements. δ is assumed to be a small parameter and the order of ϵ is yet to be determined.

The two-dimensional Navier-Stokes equations for non-reacting gases with expansions (1) become

$$\rho u u_x + \rho v u_y = -\Delta^2 p_x + (\delta^2 Re_{ref})^{-1} (\mu u_y)_y + O(N_1) \quad (2)$$

$$\rho u v_x + \rho v v_y = -(\delta / \delta^2) p_y + (\delta^2 Re_{ref})^{-1} \left[\frac{4}{3} (\mu v_y)_y + (\mu u_y)_x - \frac{2}{3} (\mu u_x)_y \right] + O(N_2) \quad (3)$$

$$\Delta^2 \left(\rho u T_x + \rho v T_y + (v-1) p (u_x + v_y) - \frac{\gamma}{\sigma} (\delta^2 Re_{ref})^{-1} (\mu T_y)_y \right) = (\delta^2 Re_{ref})^{-1} \left[(\gamma-1) \left(\mu u_y^2 + \delta^2 \frac{4}{3} \mu v_y^2 - \frac{4}{3} \mu u_x v_y \right) + \epsilon \left(\mu_1 u_y^2 + 2 \mu u_y u_{1y} \right) \right] + O(N_3) \quad (4)$$

$$(\rho u)_x + (\rho v)_y = O(N_4) \quad (5)$$

where $Re_{ref} = (\bar{\rho}_\infty \bar{u}_\infty \bar{x} / \bar{\mu}_\infty) \rho_{ref} / \mu_{ref}$, $\sigma = \bar{u}_\infty C_p / k$ and $\Delta^2 = T_{ref} / \gamma M_\infty^2$. It will be assumed that σ , γ , C_p , C_v are constant, although these conditions are not essential for the final calculations. The N_i represent the order of all higher order terms and include ϵ , δ^2 and small body curvature effects.

From these equations the following can be concluded⁶: (1) δ^2 is a small parameter, of order M_∞^{-2} in the outer portions of the disturbed layer and of order $(\gamma-1) (2\gamma A)^{-1}$ in the inner boundary layer; $A = \sigma^{-1/2}$ for adiabatic wall conditions and $A \approx 4$ for cold wall conditions. With δ^2 small the streamwise pressure gradient p_x would not appear in the zeroth-order equations. This approximation is not essential in this theory but is useful in that it leads to a substantial reduction in the time required for a typical calculation. This approximation will be used throughout this paper.

The effects of including the streamwise pressure gradient in the leading approximation have been considered (6). In order to avoid the difficulties associated with the sonic singularity, where the streamwise velocity component equals the sonic velocity, the two layer model of Denison and Baum⁹ was prescribed. In this model, the normal pressure gradient is assumed to be zero in the subsonic portion of the flow near the wall (usually when $(u/\delta)^2 \leq 1.2$). In the cases treated here, where slip boundary conditions are required, this approximation is particularly good since a subsonic flow layer near the surface does not appear until a point downstream where a constant pressure boundary layer has already formed. For cold wall conditions, with $\gamma=1.4$, differences of about 5% result when terms of order δ^2 are retained in the zeroth-order equations. A complete first-order calculation leads to corrections of from 5%-8%. These calculations have been carried down as far as the beginning of the strong interaction flow.

(2) The normal pressure gradient p_y is not necessarily small throughout the inner portion of the merged layer where $(\Delta/\delta)^2=O(1)$. As δ decreases in magnitude further downstream $(\Delta/\delta)^2$ increases and a typical boundary layer forms near the surface, i.e., $p_y \approx 0$. In the outer portion of the disturbed flow $(\Delta/\delta)^2=O(1)$ throughout. This depicts the outer compressive or shock wave region.

(3) From the energy equation (4), in the outer portion of the flow where $\Delta^2=O(M_\infty^{-2})$, the leading approximation is $u_y=0$,

or in view of the x-momentum equation (2), $u=1$. Terms of $O(\delta^2)$ must be included in order to describe the outer compressive flow. This leads to the retention of the term $\frac{4}{3}\mu u_y^2$. For the inner region where Δ achieves its largest values a typical boundary layer balance between the left hand side of equation (4) and μu_y results.

(4) In regions where viscous effects are significant $(\delta^2 Re_{ref})^{-1}=O(1)$. For inviscid regions $(\delta^2 Re_{ref})^{-1} \rightarrow 0$ and the hypersonic small disturbance equations result.

Based on the discussion just concluded, the following non-dimensionalized equations should describe the entire flow field to zeroth-order. Higher order approximations can be obtained in a similar manner.

$$\begin{aligned} (\rho u)_x + (\rho v)_y &= 0 \\ \rho u u_x + \rho v u_y &= (\mu u_y)_y \\ \rho u v_x + \rho v v_y &= p_y + \frac{4}{3}(\mu v_y)_y - \frac{2}{3}(\mu u_x)_y + (\mu u_y)_x \\ \rho u T_x + \rho v T_y &= -(\gamma-1)p(u_x + v_y) + \frac{\gamma}{Pr} T_y + \gamma(\gamma-1)M_\infty^2 \mu u_y^2 + \frac{4}{3}(\gamma-1)\mu v_y^2 \\ p &= \rho T, \mu = \mu(T), k = k(T) \end{aligned} \quad (6)$$

$P_{ref}, T_{ref}, \rho_{ref}$ were taken to be unity; $u_{ref} = M_\infty$; $\bar{x} = \gamma M_\infty^3 (\bar{\mu}_\infty / \bar{\rho}_\infty \bar{u}_\infty)$; $\delta = (\gamma M_\infty)^{-1}$.

The Sutherland viscosity law will be used throughout. We note that \bar{x} and δ are proportional to M_∞^{-1} and $M_\infty^{-1/2}$ respectively, where λ_∞ is the free stream mean free path. The equations are independent of the unity Reynolds number but not the Mach number, or interaction parameter $\chi_\infty = \sqrt{C} M_\infty^3 / \sqrt{Re_\infty}$.

Neglecting body curvature effects, the error in this approximation, and hence the order of ϵ , will most probably be determined by the largest values of Δ^2 . For $\gamma=1.4$, these are 4% for the cold wall conditions treated here, and 12% for the adiabatic flow. These values are in agreement with those obtained from first-order calculations (6). The modifications of the equations for axial symmetry and three-dimensionality are described on section IV and V.

The equations are boundary layer like with only the streamlines as real characteristics. Numerical solutions were obtained on a CDC 6600 computer using an explicit finite difference scheme, in view of its simplicity. Since exact initial data was not available for the calculations, the effects of different initial conditions were examined in detail for the flat plate flow (6). It was found that all solutions were essentially indistinguishable when the rarefaction parameter $V_\infty = \sqrt{C} M_\infty / \sqrt{Re} = \chi_\infty / M_\infty^2$ decreased below 0.4. * Nothing definitive can be concluded about the results prior to this point. For $M_\infty=20$ this corresponds to a distance $60\lambda_\infty$ from the leading edge. Initial conditions for which the surface heat transfer was prescribed as the free molecular value are chosen in sections III and IV. This condition was prescribed in view of the available experimental data for the flat plate and cone geometries. These solutions were then in good agreement with the data for $V_\infty < 1.0$ or $10\lambda_\infty$ from the leading edge. Uniform initial conditions were chosen for the three dimensional geometry in view of the simplicity and a lack of any experimental data. For the flat plate solution the use of uniform initial data led to initial differences of about 10-20%. All differences vanished when $V_\infty \leq 0.4$.

* It is interesting that some recent experimental data (8) depicts significant initial deviations due to extremely small leading edge blunting, but that these variations vanish when $V_\infty \leq 0.35$. The strong interaction flow begins when $V_\infty \approx 0.15-0.25$.

The details of the numerical finite difference procedure are given in Ref. 6. The grid spacing in the y direction was prescribed to be about one free stream mean free path, while the step size in the x direction was dictated by stability criteria. A typical calculation with slip boundary conditions required about 50 seconds to reach $M_\infty \sqrt{C}/Re_{x_\infty} = 0.2$ for the two dimensional flat plate geometry.

III. CHANNEL FLOW

In this section the two-dimensional hypersonic flow over two finite flat plates of equal length is considered (Fig. 1b). The flow is symmetric about the center line between the plates; however, asymmetric geometries do not create added complexity within the scope of the theory described herein. This class of problems, involving two or more adjacent surfaces was suggested by Prof. M. H. Bloom who terms them "hypersonic interference" problems.

The flow field can be divided into three distinct regions, the flow outside of the plates, equivalent to the flat plate considerations of Rudman and Rubin (6), the interior channel flow, and the interaction of these two domains in the wake region behind the plates. The geometry and flow solutions are restricted in several ways by the nature of the governing equations. First, it is clear that only initial conditions and boundary values along the plates can be prescribed. Therefore channel flows with arbitrary back pressure cannot be considered. The exit conditions must be accepted as a part of the total solution. This restriction is a result of the parabolization of the elliptic Navier-Stokes equations. Upstream influence is limited to a negligible domain. It is apparent that if incompatible downstream conditions are imposed the elliptic nature of the equations must be restored. Therefore, if choked flows, flows involving strong normal shock waves or separated flow regions are to be treated, suitable modification of the theory must be advanced. Second, the error analysis in Section II must be modified for the interior channel flow. Free stream quantities should be replaced in favor of centerline conditions so that the error in the neglect of the streamwise pressure gradient is now of the order of the maximum value of $\frac{y-1}{2VA}$ and $(\gamma M_{CL})^{-1}$. First-order solutions are determined throughout the interior flow in order that the error here is comparable to that outside of the plates. It is significant that the first-order results provide corrections of 5%-7% for $M_{CL} > 5$, 20% for $M_{CL} = 2$, and increasingly larger deviations as M_{CL} decreases further. This problem can be resolved completely by retaining p_x in the leading approximation. Of course when M_{CL} approaches unity a choking condition might also become a factor and the elliptic nature of the problem must be restored. The plate length for the ensuing discussion is such that M_{CL} achieves a minimum of somewhat less than five.

For these calculations, as well as those to be described in the next two sections, flow conditions identical to those used previously for the flat plate flow (6) were chosen. These are $M_\infty = 25$, $T_{stag} = 3600^\circ$, $T_w/T_{stag} = 0.15$, $\sigma = 0.75$, $\gamma = 1.4$, $\sqrt{C} = 0.85$. As discussed above, exact initial values are not available so that initial conditions were chosen such that the leading edge heat transfer coefficient, on both the upper and lower surfaces, corresponded to the free molecular value. Slip boundary conditions are used throughout, as slip effects are significant in the merged layer and even the beginning portion of the strong interaction flow (6).

Boundary Data:

$$0 \leq x \leq L$$

$$y = \pm h: v = 0, u = \pm \lambda u_y, T = T_w \pm \frac{2\gamma}{\gamma+1} \frac{1}{\sigma} (\lambda T_y)$$

$$y = \infty: v = 0, u = 1, T = 1, p = 1$$

Symmetry conditions at $y = 0$

Thermal accommodation and scattering coefficients are both assumed to be unity. $\lambda = 1.26 u / \rho T^{1/2}$.

$$x > L$$

$$y = \pm \infty: v = 0, u = 1, T = 1$$

At $x = L$, the outer flow is prescribed by the flat plate solution for $|y| > h$ and by the channel solution for $|y| < h$. The calculation was divided into three parts: (1) the outside flat plate solution of Rudman and Rubin (6), the interior channel interactions and the mixing or wake region. Upstream influence due to the trailing edge of the plates is not included in this "boundary layer" theory so that all three regions can be treated independently. If separation does not occur, it is expected that this effect will be no greater than that occurring at the leading-edge. It is possible that modifications of the theory, similar to methods now used for near wake and corner point calculations (9, 10), might allow for the inclusion of certain upstream influences when these become significant.

The interior development is probably the most interesting of the three calculations. The flow on the upper and lower plates proceeds two-dimensionally until the bounding shock waves intersect at the center line. For the chosen geometry the interaction begins when $V_\infty = 0.22$ or near the end of the merged layer. The flow is still fully viscous but bounded by what is now almost a fully developed Rankine-Hugoniot shock wave. Therefore an essentially inviscid shock interaction takes place at the center line, with viscous diffusion important thereafter. The reflected wave is imbedded within the viscous boundary layer and attenuates as it approaches the subsonic inner layer. These results are depicted in Figs. 2-6. The center-line pressure attains a maximum value of 320 after the initial shock intersection. For a calculated incident shock angle of 14° (15°) with $M=25$, a fully inviscid intersection leads to a final pressure of 280 (340). The reflected wave travels inward until it reflects off the inner subsonic layer causing a sudden rise in the wall pressure, skin friction and heat transfer. The wave pattern continues to the center-line where a much weaker intersection takes place just prior to the channel exit. It is interesting that when the channel was continued beyond the length described herein, down to M_{CL} equal to 1.5, the transverse pressure distribution approached a uniform state and it appeared as if a fully developed compressible flow was being approached, Fig. (7). In the exhaust region behind the plates typical wake profiles result.

IV. FLOW OVER A SHARP CONE

Axi-symmetric flow problems can be treated in a manner identical to that used for the two-dimensional geometries. The procedure has been outlined in Section II.

Once again an (x, y) coordinate system is employed, where x is measured along the surface and y is locally normal to the surface. With the expansion procedure of Section II, the effect of transverse curvature is to modify the governing equations (6) by adding the following terms to the right hand side of each of the respective equations.

$$\begin{aligned} \text{Continuity:} & -r^{-1}(Bu+v) \\ x\text{-Momentum:} & r^{-1}\mu u_y \\ y\text{-Momentum:} & 2(3r)^{-1}(Bu+v)u_y + \mu(3r)^{-1}(Bu_y + 4u_y - 4r^{-1}(Bu+v)) \\ \text{Temperature:} & -(v-1)r^{-1}p(Bu+v) + (v-1)(r-2(Bu+v)^2 - r^{-1}(Bu+v)v_y) + \mu(\sigma)^{-1}T_y \end{aligned}$$

Where $B = \theta_c / 6$, θ_c = cone half angle, $r = y + x\theta_c / 6$

The Sutherland viscosity law, slip boundary conditions at the cone surface and initial data as discussed in Section II are prescribed. The outer boundary conditions must be modified such that $v \rightarrow B$ as $y \rightarrow \infty$

Unless otherwise specified all of the calculations are for free stream and surface conditions as described in Section III.

Due to the singular nature of the governing equations as $r \rightarrow 0$, the starting point for the calculations was chosen somewhat downstream of the leading edge. In order to determine the effect of different starting locations, several starting points were selected, in particular $x_0 = 0.005$, 0.01, 0.02, and 0.04. These points correspond to distances ranging from $2\lambda_\infty$ to $20\lambda_\infty$ from the leading edge; corresponding initial cone radii vary from $\lambda_\infty/5$ to $2\lambda_\infty$. All of the solutions were indistinguishable when $V_\infty < 0.4$, the point at which initial conditions are no longer significant for the two-dimensional and axi-symmetric geometries.

The results to be discussed below are for initial data prescribed at $x_0 = 0.02$ or $10\lambda_\infty$ from the leading edge. The cone radius is about λ_∞ at this point. The error in the zeroth-order calculation is dependent on the parameters mentioned previously and in addition on the magnitude of θ_c^2 , as terms of this order have been neglected.

Some of the results are depicted in Figs. 8-14. Flow profiles are given in Figs. 8 and 9. On the same figures are wedge solutions for the same half-angle $\theta_c = 5^\circ$. As might have been anticipated, the cone shock layer is much thinner than that for the equivalent wedge solution and the outer compression is considerably weaker in the axi-symmetric case. The temperature profiles indicate that the cone flow is also much cooler than that for the comparable wedge geometry. The stagnation enthalpy exhibits an overshoot in the outer shock structure portion of the profile for both flows.

These solutions are significantly different than those for the two-dimensional flat plate in two respects. First, a second compression region below the outer shock does not occur for either the wedge or cone. Such a region was observed for the flat plate, although no experiments have indicated the existence of this compression. Refinements of the normal grid size did not eliminate this effect and altered it only moderately. As it does not occur here, it is still questionable as to whether it was due to numerical inaccuracy or actually occurs as a very weak compression for the flat plate. Second, the pressure profiles show only a moderate decrease in magnitude behind the shock while a substantial expansion occurs in the flat plate solution. This result is perhaps not unexpected, as the inviscid surface pressure is considerably higher in the cone or wedge flow than for the flat plate case.

Fig. 10 compares pitot pressure and density profiles with the experimental data of Horstman and Kussow (11). There is good agreement in the lower 70% of the shock layer, but substantial differences in the outer shock structure. These differences may be a result of the use of a Navier-Stokes model without bulk viscosity in the calculations discussed here. A more refined normal grid, about 1/5 the size considered here, improves the shock structure solution by about 5% (6), affecting surface conditions by less than 2%. This improvement is insignificant since it is within the error of the calculation; it also increases the time required for a typical calculation by a factor of 125*. Finally, the smearing effect, due to probe size, in the high gradient compressive region must be evaluated in order to determine the experimental accuracy in measuring the shock structure profile. Calculation time for the axis-symmetric flow is roughly equivalent to that for the two-dimensional case.

Figs. 11 and 12 compare surface pressure, heat transfer, and skin friction on the cone and wedge, while Figs. 13-14 provide comparisons with the bulk of the available experimental data. (11-14)

V. FINITE WIDTH FLAT PLATE

The simplest flow geometry that accounts for three-dimensional effects is the finite width flat plate having a sharp leading edge**. With x measured along the surface in the streamwise direction, y normal to the surface, and z along the transverse surface direction, the governing equations can be derived by the order of magnitude analysis described in section II. The z coordinate is non-dimensionalized with δ , and w with $U_{\infty} \delta$. All lateral velocities (w) and gradients in the z direction having counterparts in the surface normal direction in equations (6) are retained to zeroth order. In addition all cross products involving velocity components v and w are also retained.

The right hand sides of the governing equations (6) must be modified with the inclusion of the following terms:

Continuity: $-(\rho w)_z$

x-Momentum: $(\mu_z)_z - \rho w u_z$

y-Momentum: $-\rho w v_z + \mu v_{zz} + \frac{1}{3} \mu w_y y_z - \frac{2}{3} \mu_y w_z + \mu_z v_z + \mu_z w_y y_z$

Energy: $\rho w T_z - (\gamma-1) \rho w_z + \frac{\gamma}{\sigma} (\mu T_z)_z + (\gamma-1) M_{\infty}^2 \mu u_z^2 + \frac{4}{3} \mu (\gamma-1) (w_z^2 - v_y v_z) + \mu (\gamma-1) (w_y + v_z)^2$

The z-momentum equation is: $\rho w_x + \rho v w_y + \rho w w_z = -p_z + \frac{4}{3} (\mu w_z)_z - \frac{2}{3} (\mu u_x)_z + (\mu u_z)_x + (\mu w_y)_y + \frac{1}{3} \mu v_y z - \frac{2}{3} \mu_z v_y + \mu_y v_z$

The above equations contain all the terms necessary to account for boundary layer, merged layer, and compression layer development in the (y, z) plane. The equations are of the same type as in the two-dimensional flow, with the streamlines as the only real characteristics. Once again a solution is obtained numerically by prescribing appropriate initial and boundary data. Uniform initial conditions are used at all points except at the surface where slip boundary conditions are enforced. These conditions allow for a maximum of simplicity, and due to a lack of any experimental data no other correlations are possible.

Boundary Data:

$y=0, z$ on the plate; $u=\lambda u_y, w=\lambda(w_y + (\beta-T)^{-1/2} T_z), v=0, T=T_w + \frac{2\gamma}{\gamma+1} \frac{\lambda}{\sigma} T_y$

$y=0, z$ off the plate; v is anti-symmetric, and u, w, T, ρ are symmetric

$(y^2 + z^2) \rightarrow \infty; v \rightarrow 0, w \rightarrow 0, u \rightarrow 1, \rho \rightarrow 1.$

The effect of lateral surface temperature creep (T_z) on the lateral slip velocity should be retained to zeroth order; however, solutions with and without this term indicate that its effect is less than a maximum of 8%. For other geometries, such as a corner, where the z gradients are larger, this effect might become more important. At higher Mach number its magnitude should also be increased in proportion with M_{∞} . The stream conditions used in this calculation are those of Section III.

The calculation time for the three-dimensional geometries is appreciably greater (approximately n times) than for the two dimensional flow; n is the number of lateral mesh points. In addition, the streamwise step size had to be reduced somewhat, for stability purposes, due to the large lateral gradients off the side edge of the plate; this further increased the calculation time. It was possible to proceed downstream to a point at which $V_{\infty}=0.25$ in 60 minutes.

*From stability considerations the x -wise step size is proportional to the square of the normal grid spacing.

**A corner geometry is discussed in another paper to be presented at this meeting. Hypersonic Flow in Rectangular and Non-Rectangular Corners, -Cresci, R. J., Rubin, S. G., and Nardo, C. T.

In order to maintain the maximum degree of simplicity the lateral and normal grid spacings are chosen to be equivalent and approximately equal to λ_∞ . The calculation is restricted by the storage capacity of the computer (CDC-6600); it is possible to prescribe a maximum of 100 mesh points in both the y and z directions. Even this requires some rather ingenious programming devices in order to reduce the storage of several flow variables and their derivatives. For this reason the plate width is rather small, about $40\lambda_\infty$ in these calculations. Ultimately a variable grid size in the lateral direction will allow for solutions for larger geometries. However, the results described herein should be indicative of those to be found for larger plates as one might expect similar qualitative trends to appear for all of the solutions.

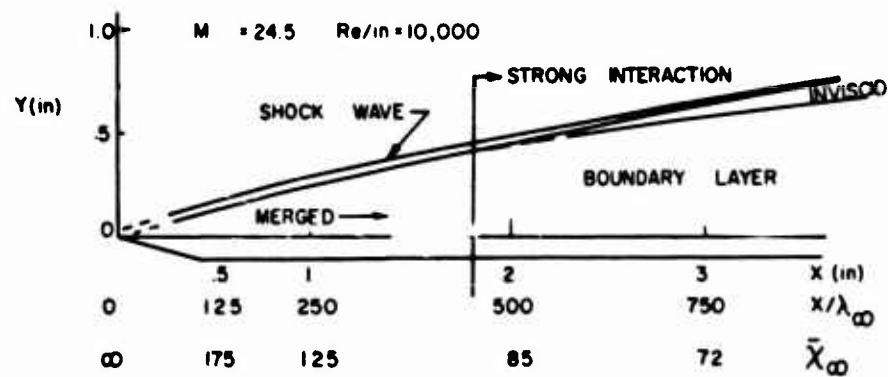
The results to date are shown in Figs. 15-17. The point furthest downstream corresponds to $V_\infty=0.5$ or a distance somewhat greater than one plate width. The results indicate that the flow remains two-dimensional along the centerline for a distance of about 0.6 of a plate width, after which the surface pressure and density maximum decrease below their two-dimensional values. Surprisingly, even after the apparent loss of two-dimensionality near the centerline, the lateral gradients of surface pressure and heat transfer are rather small; when $V_\infty=0.5$ there is only a 5% deviation in these results for one-third of the plate width about the centerline. There are considerable variations near the side edge.

Fig. 17 is a pressure contour diagram and depicts the highly compressive region that envelops the plate. The compression is strongest at the centerline, decreasing in strength around the side edge. Further calculations are now in progress.

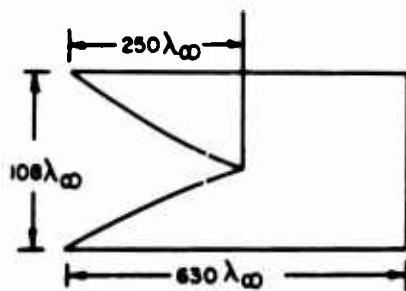
From the results of sections III-V, we conclude that the method described herein, which is an extension of that used previously to determine the flow near the leading edge of a two-dimensional sharp flat plate, ⁽⁶⁾ can account for certain shock interactions, axial symmetry and three-dimensionality. Studies concerning more complex geometries are under consideration.

REFERENCES

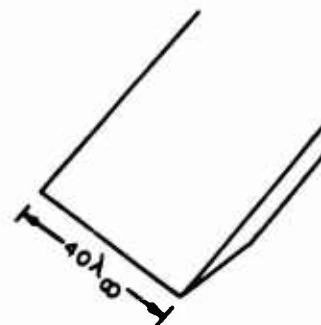
1. McCroskey, W. J., Bogdonoff, S. M., and McDougall, J. G. "An Experimental Model for the Sharp Flat Plate in Rarefied Hypersonic Flow", AIAA Journal Vol. 4, No. 9, 1966, pp. 1580-1587.
2. Hayes, W. D., and Probstein, R. F., Hypersonic Flow Theory, Academic Press, New York, 1959, pp. 353-365.
3. Stewartson, K., "On the Motion of a Flat Plate at High Speed in a Viscous Compressible Fluid - II. Steady Motion", J. Aeronautical Sci., Vol. 22, No. 5, 1955, pp. 303-309.
4. Shorenstein, M. L., and Probstein, R. F., "Hypersonic Leading Edge Problem", AIAA 6th Aerospace Sciences Meeting, New York, 1968 AIAA Pre-Print 68-4.
5. Chow, W. L., "Hypersonic Rarefied Flow Past the Sharp Leading Edge of a Flat Plate", AIAA Journal, Vol. 5, No. 9, 1967, pp. 1549-1557.
6. Rudman, S. and Rubin, S. G. "Hypersonic Flow over Slender Bodies with Sharp Leading Edges", PIBAL Report No. 1018, AFOSR 67-1118, Polytechnic Institute of Brooklyn, 1967, also; AIAA 6th Aerospace Sciences Meeting, New York 1968, AIAA Pre-Print 68-3.
7. Vidal, R. J. and Bartz, J. A. "Surface Measurement on Sharp Flat Plates and Wedges in Low-Density Hypersonic Flow", Cornell Aero Lab Report No. AF-2041-A-2, 1967.
8. Joss, W. W., Vas, J. E. and Bogdonoff, S. M. "Studies of the Leading Edge Effect on the Rarefied Hypersonic Flow over a Flat Plate", AIAA 6th Aerospace Sciences Meeting, New York 1968, AIAA Pre-Print 68-5.
9. Baum, E. and Denison, M. R. "Interacting Supersonic Laminar Wake Calculations by a Finite Difference Method", AIAA Journal, Vol. 5 No. 7, 1967, pp. 1224-1230.
10. Holden, M. S. "An Analytical Study of Separated Flows Induced by Shock Wave - Boundary Layer Interaction", Cornell Aero Lab Report No. AI, 1972-A-3, 1965.
11. Horstman, G. C. and Kussoy, M. I. "Hypersonic Viscous Interaction on Slender Cones", AIAA 6th Aerospace Sciences Meeting, New York, 1968, AIAA Pre-Print 68-2.
12. Waldron, H. F., "Viscous Hypersonic Flow over Pointed Cones at Low Reynolds Numbers", AIAA Journal, Vol. 5, No. 2, 1967, pp. 208-218.
13. McCroskey, W. J., Bogdonoff, S. M., and Genchi, A. P. "Leading Edge Flow Studies of Sharp Bodies in Rarefied Hypersonic Flow", Rarefied Gas Dynamics, Supplement No. 4, Vol. II, Academic Press, New York 1967.
14. Hickman, R. S. "An Experimental Study of Hypersonic Rarefied Flow over a 10° Cone", Rarefied Gas Dynamics, Supplement No. 4, Vol. II, Academic Press, New York, 1967.



a. FLAT PLATE



b. CHANNEL FLOW



c. FINITE FLAT PLATE

FIG.1 FLOW GEOMETRIES

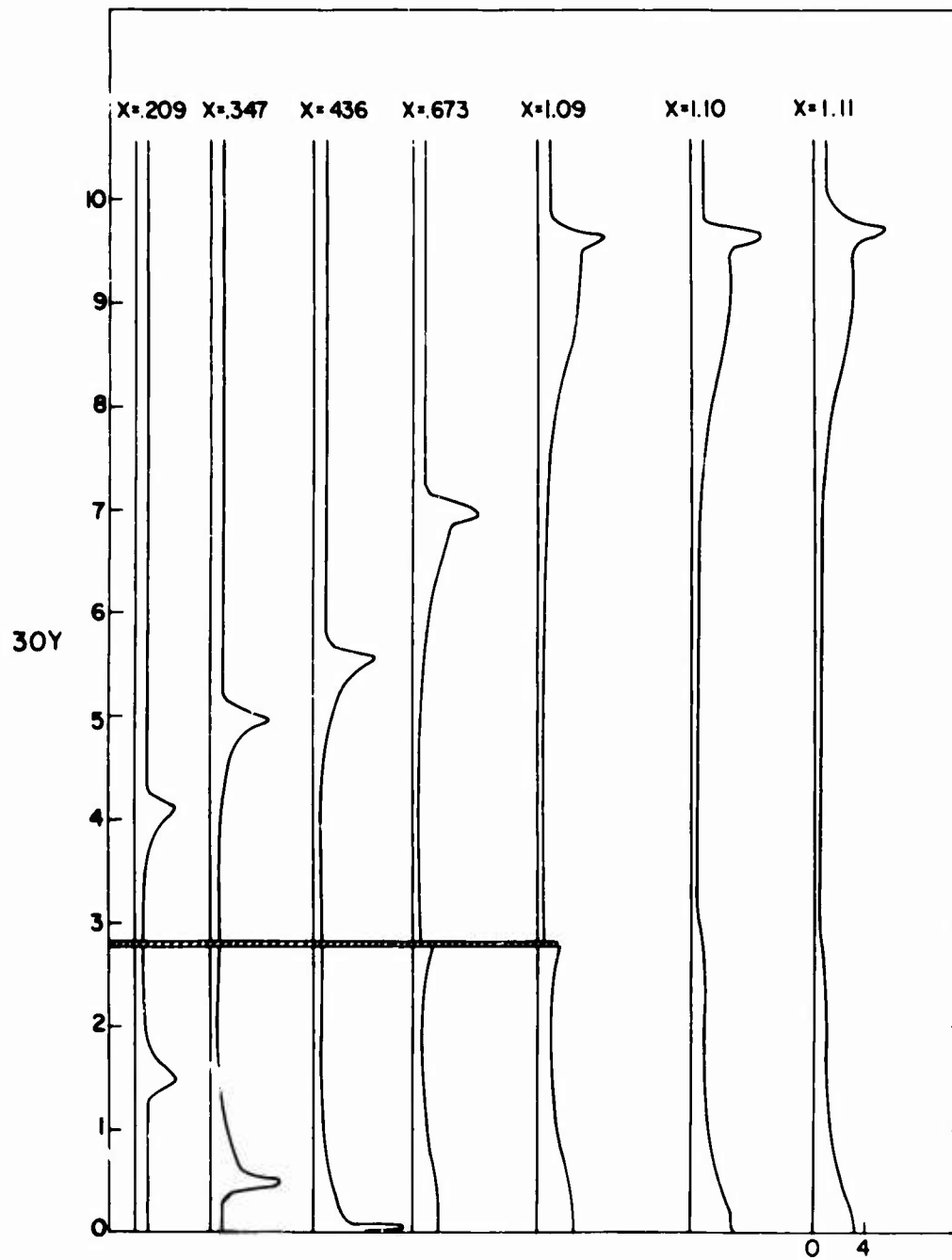


FIG.2 DENSITY PROFILES FOR CHANNEL FLOW

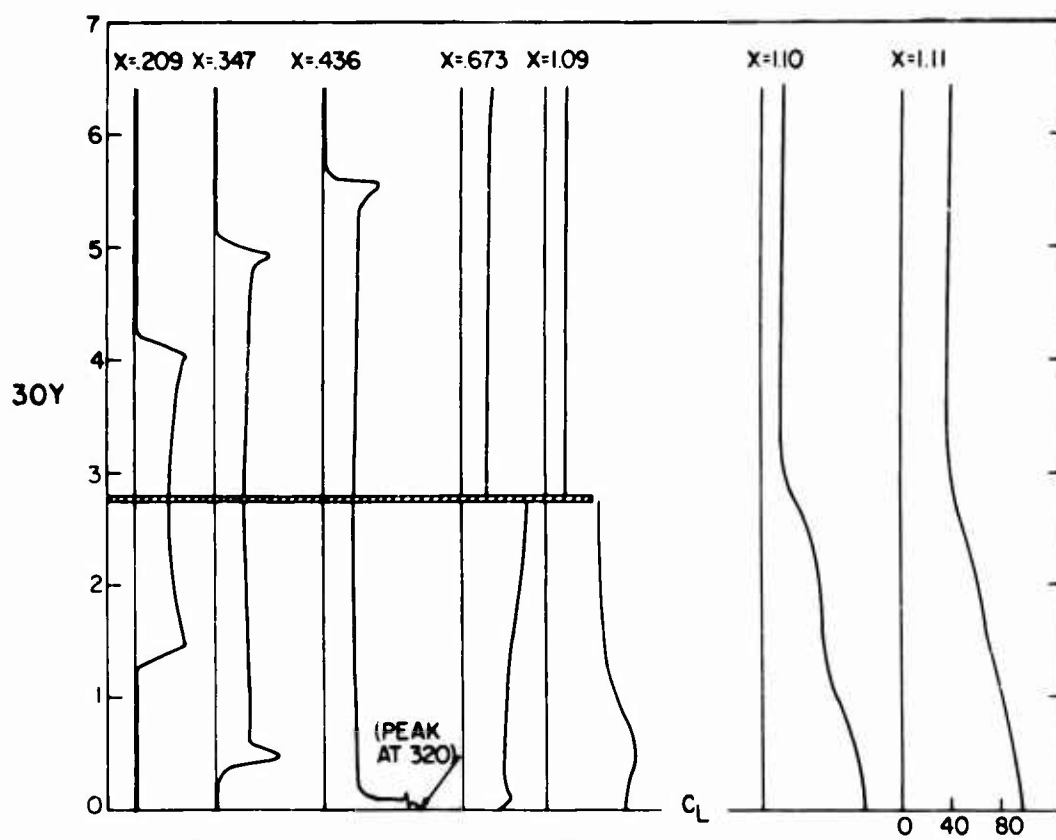


FIG.3 PRESSURE PROFILES FOR CHANNEL FLOW

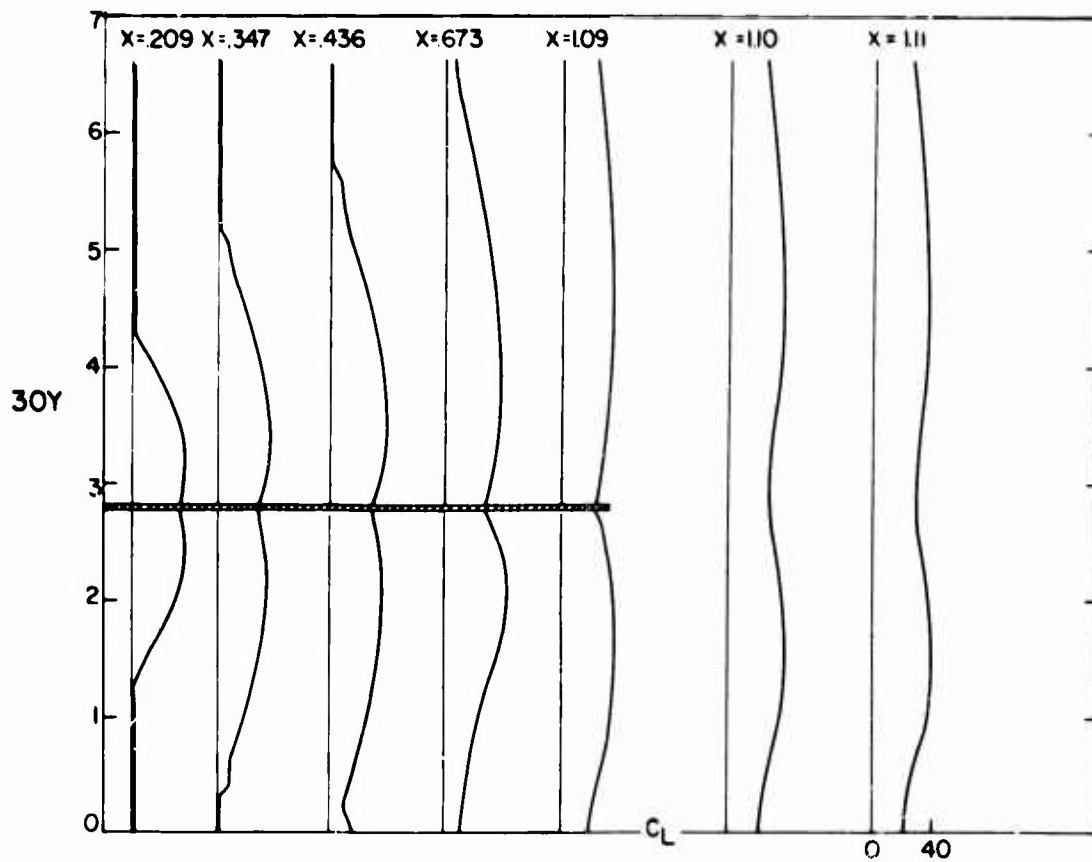


FIG. 4 TEMPERATURE PROFILES FOR CHANNEL FLOW

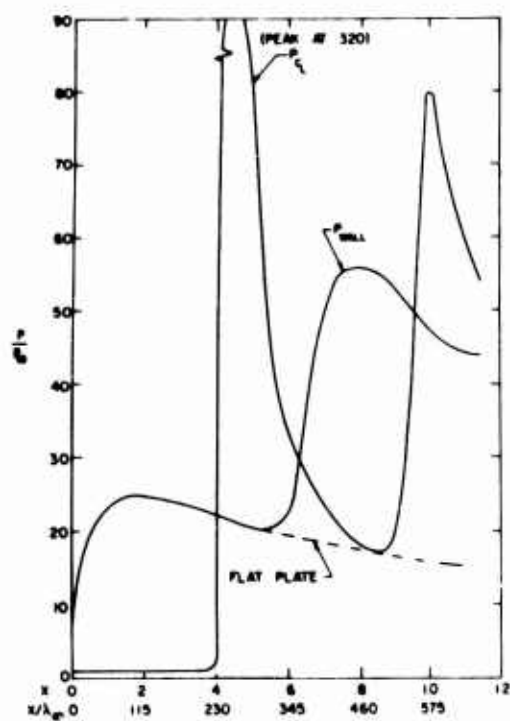


FIG 5 SURFACE AND CENTERLINE PRESSURE DISTRIBUTIONS IN A CHANNEL

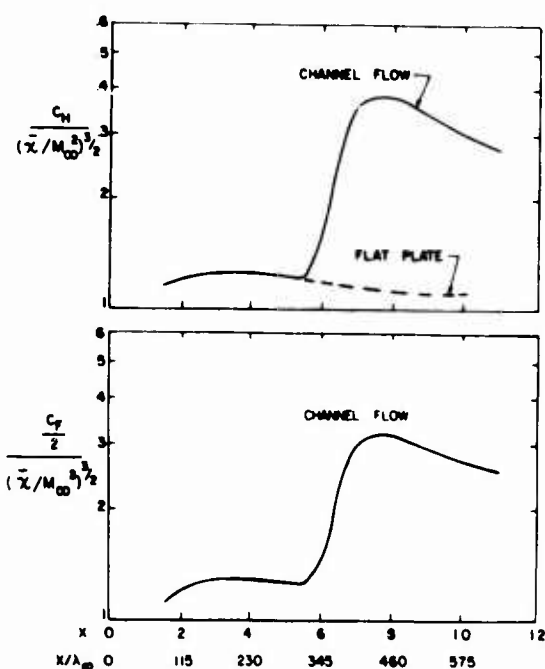


FIG 6 HEAT TRANSFER AND SKIN FRICTION DISTRIBUTIONS IN A CHANNEL

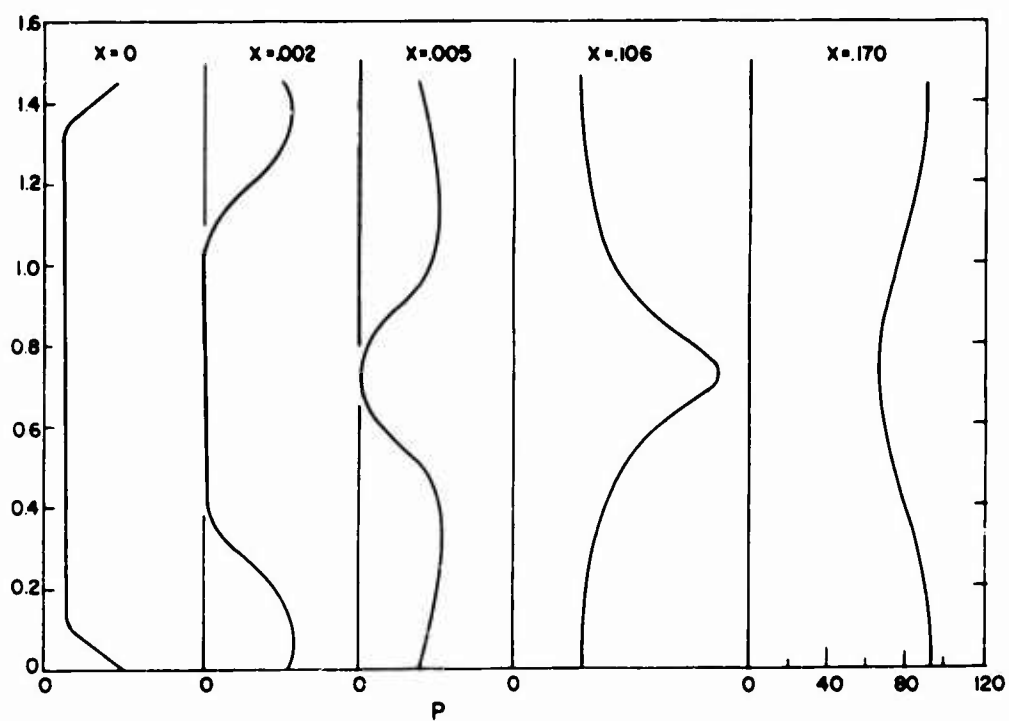
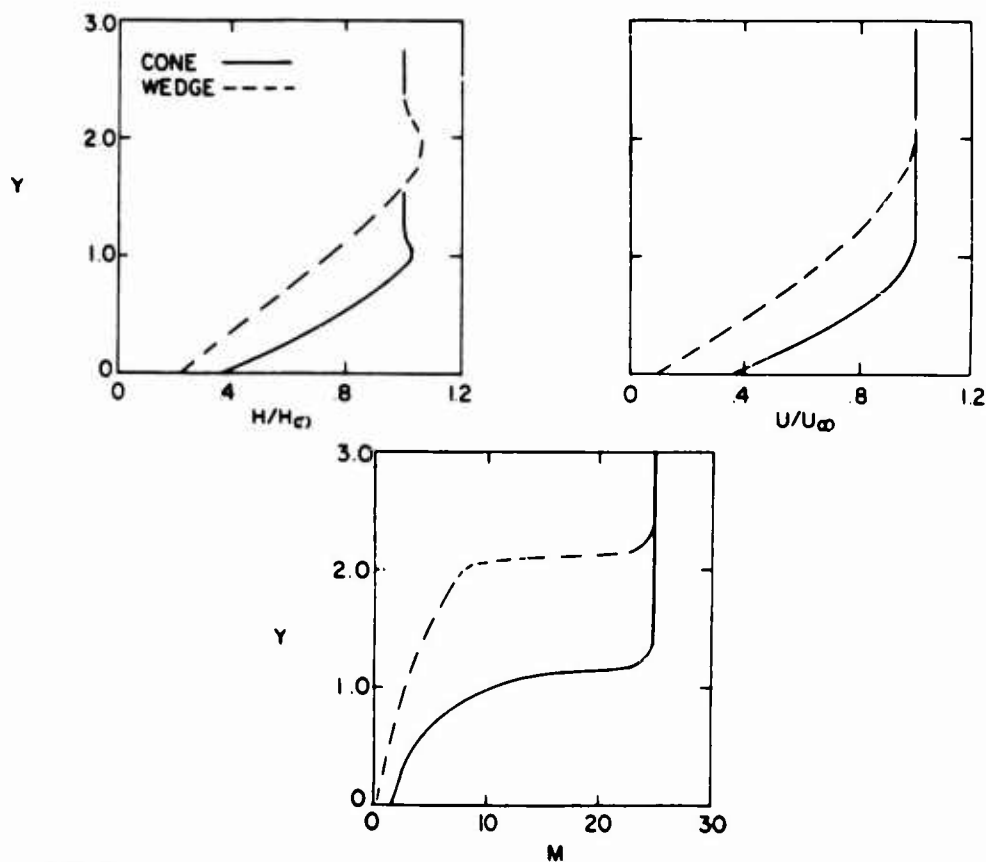
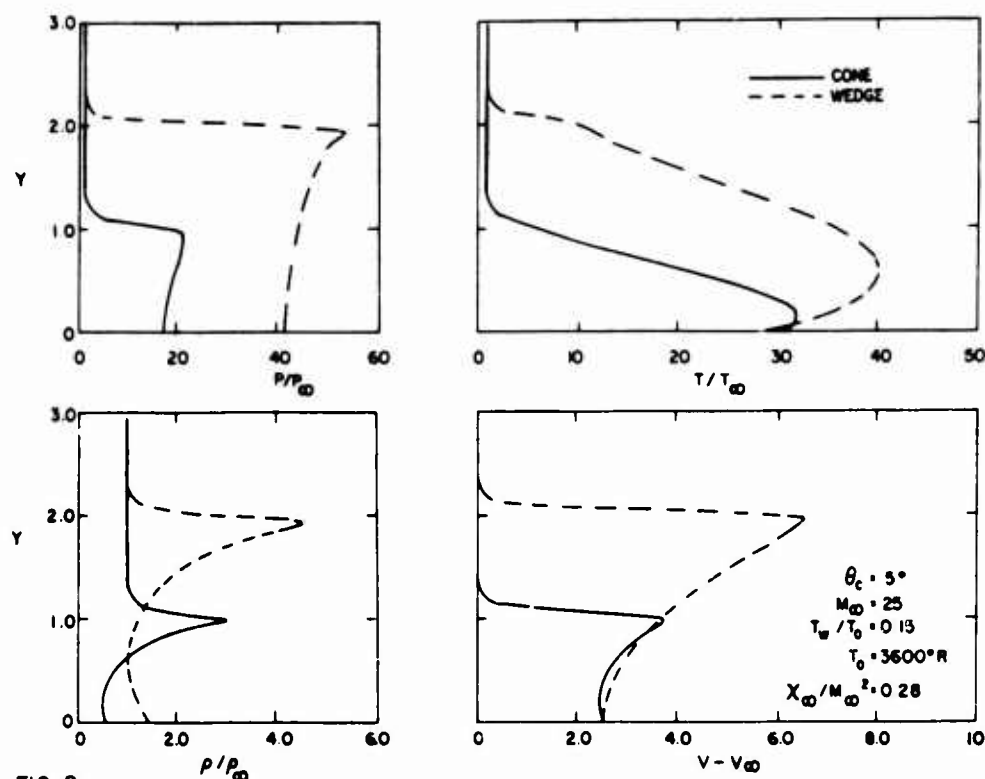


FIG.7 PRESSURE PROFILES IN A LONG CHANNEL



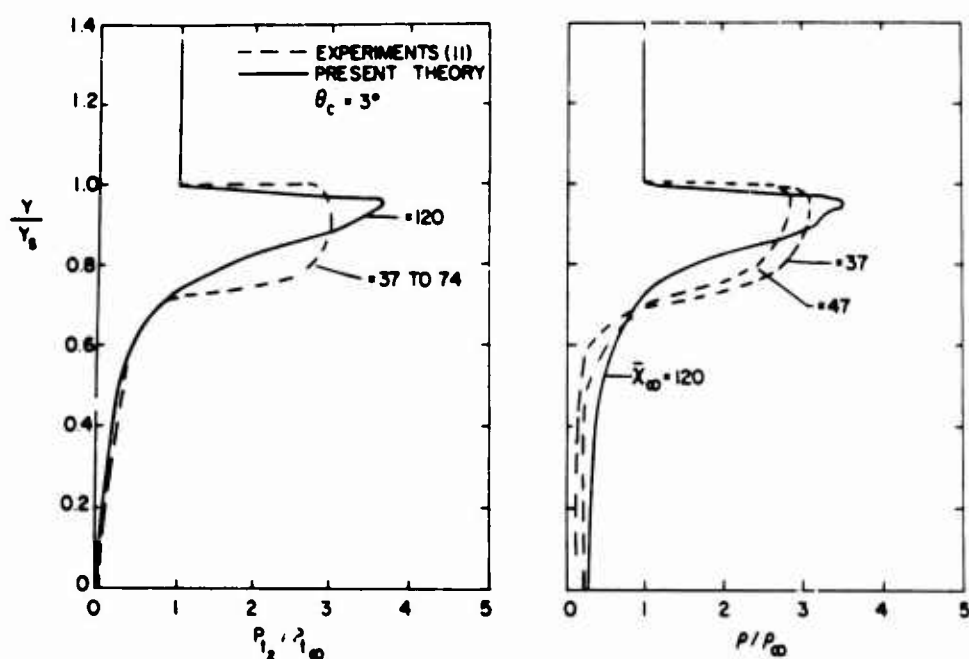


FIG. 10
PITOT PRESSURE AND DENSITY PROFILES FOR A CONE

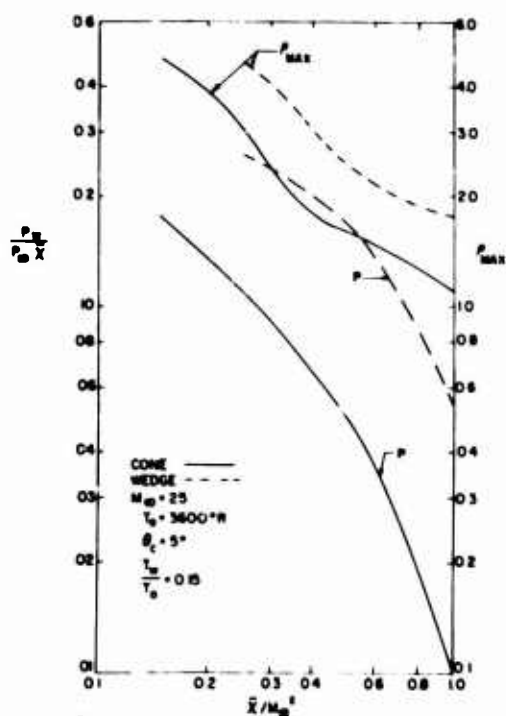


FIG. 11
PRESSURE AND MAXIMUM DENSITY DISTRIBUTION
FOR CONES AND WEDGES

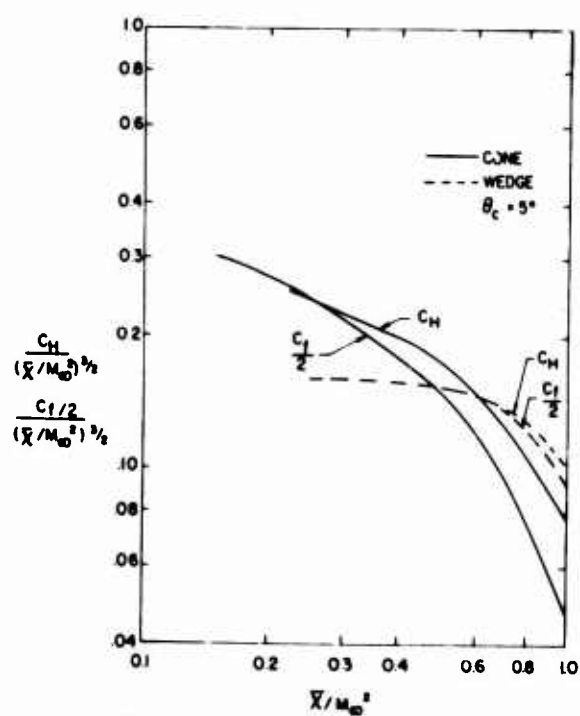


FIG. 12
HEAT TRANSFER AND SKIN FRICTION ON
CONES AND WEDGES

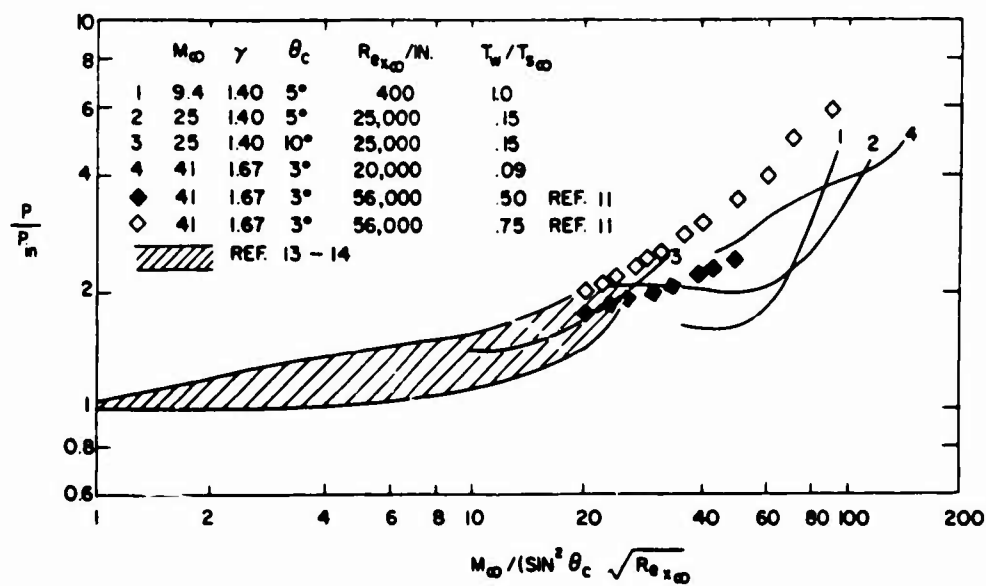


FIG. 13
SURFACE PRESSURE DISTRIBUTION ON CONES

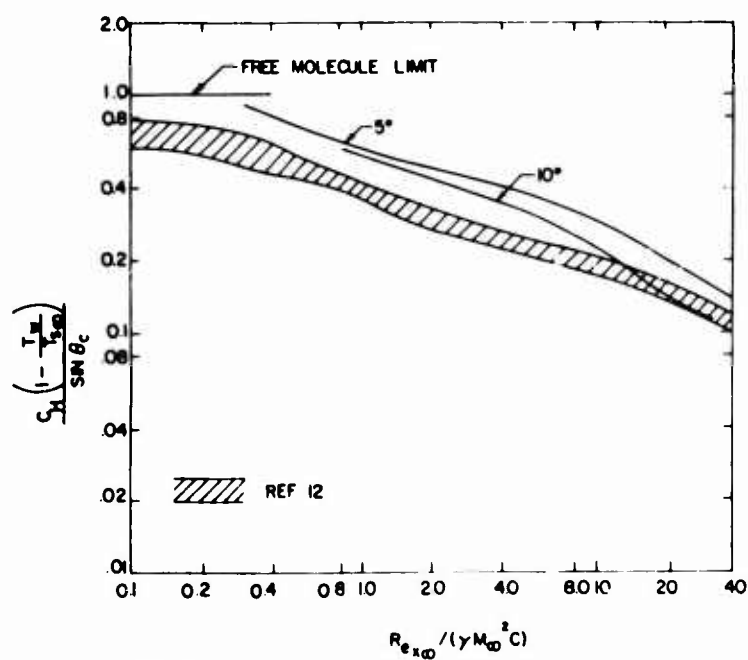


FIG. 14
COMPARISON OF HEAT TRANSFER WITH EXPERIMENTS
ON CONES

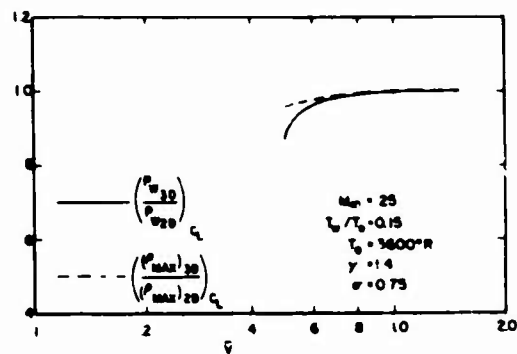


FIG 15 CENTERLINE PRESSURE AND MAXIMUM DENSITY FOR FINITE FLAT PLATE

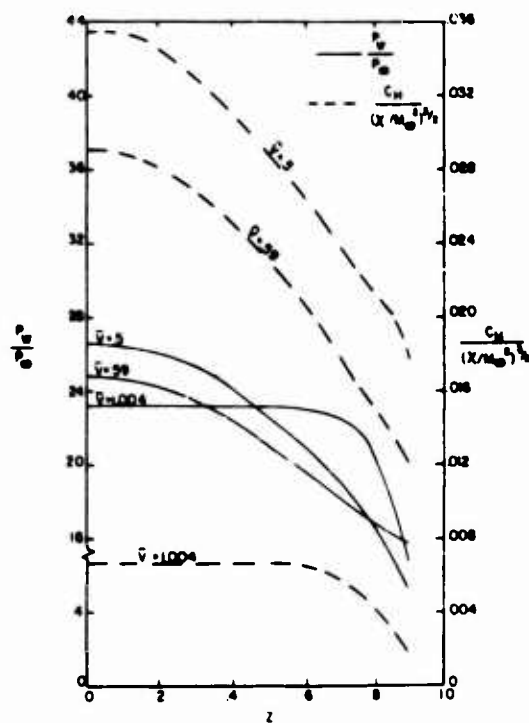


FIG 16 SURFACE PRESSURE AND HEAT TRANSFER FOR FINITE FLAT PLATE

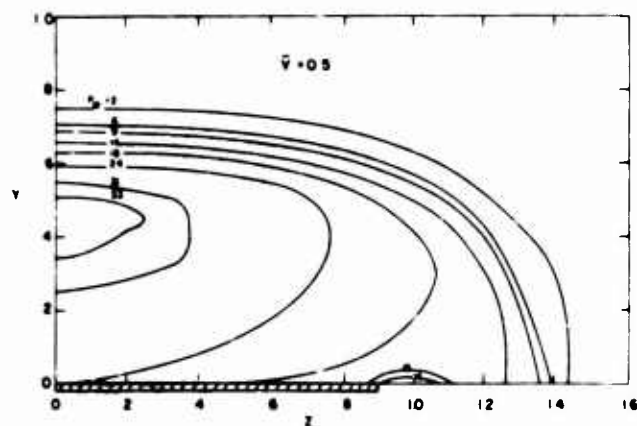


FIG 17 PRESSURE CONTOURS FOR FINITE FLAT PLATE

PAPER 15

This paper has been cancelled
by mutual agreement

AN INVESTIGATION OF THREE-DIMENSIONAL JET CONTROL
INTERACTION ON A CONICAL BODY*

by

V. Zakkay⁺, J. Erdos⁺⁺ and W. Calarese⁺⁺⁺

Department of Aeronautics & Astronautics
New York University
Bronx, N. Y.

* This work was supported by Aeronautical Research Laboratory, Office of Aerospace Research,
United State Air Force, Wright-Patterson Air Force Base, Ohio under Contract No. F33(615)68-C-1184

⁺ Professor

⁺⁺ Associate Research Scientist

⁺⁺⁺ Assistant Research Scientist

SUMMARY

An experimental investigation of the interaction of a finite-span jet issuing normal to the surface of a 7° semi-vertex angle sharp cone at a free stream Mach Number = 6 is performed. The jet slot is contained within a peripheral angle of 60° , and located at a distance midway along the length of the cone surface. A range of unit Reynolds number of 2×10^6 to 4×10^7 per foot is covered. This permits the study of the interaction for laminar, transitional and fully turbulent flows over the conical surface of the body. Jet penetration heights are varied, and the results compared to two-dimensional flows and to equivalent fences normal to the surface. Data are also obtained for three-dimensional separation and reattachment lines by injecting a dye at the surface.

The results of this experimental study indicate that the total normal force coefficient produced by a finite-span jet is not degraded by three-dimensional effects. In fact, the normal force coefficient measured in these tests equals or exceeds the normal force per unit span obtained in experiments with two-dimensional flows at the same Mach number and jet mass flux ratio. This behavior is attributed to a favorable interaction between the cross-flow and the mainstream that substantially increases the effective span of the jet. It is also noted that a positive contribution to the total normal force is received from the flow downstream of the jet location, contrary to previous results at lower Mach numbers. However, experiments were also performed with finite-span and full-span fences (rings) in which a negative contribution is produced downstream of the fence location. In general, it is emphasized that the results obtained by examining only the pressure distribution along the plane of symmetry through the jet may not be representative of the actual normal force produced, and are definitely misleading when cross-flow occurs.

A new theoretical model is proposed to describe the structure of the jet interaction flow field. The fluid mechanics is essentially inviscid, but the effects of viscosity and heat conduction are implicitly introduced through the nonuniformity of the upstream flow. The flow field is calculated numerically by a time-dependent technique. The method is clearly extendable to three-dimensional flow fields, but only two-dimensional flows are presently considered.

NOTATION

A	Surface area
a	Sound speed
b	Slot span
C_{N_A}	Normal force coefficient, $2 \int (p - p_i) dA / \rho_\infty u_\infty^2$
C_{N_R}	Thrust coefficient, $2T / \rho_\infty u_\infty^2$
d	Slot width
F_i	Normal force due to interaction with a forward-facing step or transverse fence
h	Step or fence height, or height of Mach disc above the surface
H	Total enthalpy, $C_p T + \frac{1}{2} q^2$
l	Length of separated flow region
L	Surface length from cone apex to slot or fence
M	Mach number
p	Static pressure
P_o	Total pressure
q	Velocity vector
R	Gas constant
R_e	Reynolds number, $\rho u x / \mu$
T	Thrust, or static temperature
T_o	Total temperature for the sonic jet $T = (1.27 P_{o_j} - P_i) b d$
t	Time
u_i	Velocity component in the x_i direction
u	Streamwise component of velocity
v	Normal component of velocity
w	Transverse component of velocity
\dot{m}	Mass flux
x	Streamwise or axial coordinate
y	Normal coordinate
z	Transverse coordinate
δ	Boundary layer thickness
γ	Ratio of specific heats
μ	Viscosity coefficient
ν	Kinematic viscosity coefficient, μ / ρ
ρ	Density
θ	Momentum defect thickness
ψ	Stream function
ϕ	Azimuthal angle

Subscripts

c	Conical, cone surface value
e	Boundary layer edge
i	Initial or undisturbed cone surface value
j	Jet
w	Wall or surface value
∞	Reservoir condition, or evaluated at upstream infinity
2D	Two-dimensional
3D	Three-dimensional
bl	Boundary layer
sp	Separation point
tr	Transition point

AN INVESTIGATION OF THREE-DIMENSIONAL JET CONTROL INTERACTION ON A CONICAL BODY

V. Zakkay, J. Erdos and W. Calarese

1. INTRODUCTION

Secondary jets have received attention as a possible alternative to conventional aerodynamic surfaces (e.g., ailerons, flaps, flares, etc.) for supersonic or hypersonic flight control systems. The forces generated by an underexpanded jet issuing normal to a surface are known to be amplified considerably over the in vacuo thrust of the jet, due to a complex interaction with the main, supersonic stream. Also, the severe heating and loading problems associated with the exposure of a control surface to a supersonic or hypersonic stream may be avoided. These considerations have motivated a number of investigations of the "jet interaction" phenomenon, and have renewed (or expanded) the interest in boundary layer separation and reattachment. A bibliography containing several hundred entries can be found in Refs. 1 to 17.

The structure of the two-dimensional jet-interaction flow field has been inferred by a number of investigators, from schlieren photographs and surface pressure distributions. There appears to be a general consensus of opinion about the general features of the flow field, although some disagreement has arisen in regard to the effects of various parameters on its structure and the resultant forces.¹⁸ It should also be pointed out that the structure is usually depicted for a jet that penetrates into the stream to a height many times the thickness of the upstream boundary layer. A somewhat different behavior pertains to the case where the penetration height is of the same order as the boundary layer thickness. The case where the boundary layer is very thin is shown schematically in Fig. 1a. A large, clockwise rotating vortex and a small counter-rotating vortex occur in the separated region upstream of the jet plume, and a single clockwise rotating vortex occurs downstream of the plume. As the boundary layer becomes thicker, or the jet penetration height is reduced, the plume and adjacent vortices will probably become more nearly symmetric, and eventually all three vortices should disappear as the jet is submerged in the boundary layer.

The jet interaction flow field of a finite-span jet, on the other hand, is essentially three-dimensional. In fact, only an axially-symmetric body (at zero angle of attack) can assuredly produce a two-dimensional flow; with a planar geometry spurious three-dimensional effects can be subtle, and difficult to eliminate. Spaid and Zukowski¹⁸ attribute the relative reduction in amplification of two-dimensional jet interaction forces with increasing ratio of jet to main stream total pressure to three-dimensional effects rather than any basic dependence of the amplification factor on this parameter. It is implied that the three-dimensional effects associated with finite span jets can reduce the beneficial induced forces³; indeed, on a conical body circumferential cross-flow may nearly cancel the induced normal force. The present investigation is primarily concerned with the three-dimensional problem of a finite span jet or a forward facing step on a conical body. The results of an experimental study are presented, and compared with previous data regarded as two-dimensional. A basis for correlation of two-dimensional and three-dimensional data is proposed, based on the penetration height of this plume.

The need for a detailed analysis of the flow field, particularly in the three-dimensional case, is considered apparent. A new theoretical approach has been developed based on an inviscid, rotational flow model. Calculations are performed by Lax's time-dependent method, and results are presented for several examples of separated flows.

2. EXPERIMENTAL INVESTIGATION

2.1 Experimental Apparatus and Test Conditions

All the tests were conducted in an axially symmetric Mach 5.8 nozzle having a test section diameter of 1', with a uniform flow of 3' in length and 9" in diameter.

The model consisted of a sharp axially symmetric conical body with a cone half angle of 7°, and a base diameter of 4.6". This provided an overall surface length of approximately 20" and therefore allowed a large variation of the transitional to turbulent flow on the model ahead of the injection region. For the condition of jet injection, the slot was 0.015" and 0.030" wide and extended over a peripheral angle of 60°. The slot was machined perpendicular to the surface of the cone, and located at an axial distance of 14-1/8" from the tip of the model. For the injection tests the complete inner chamber of the model was used as the stagnation chamber. Experiments were also performed with the fences perpendicular to the model. The fences were placed at the same location as the slot, and also extended within a peripheral region of 60°. Various heights were used, 3/4", 1/2", 3/8" and 1/4". In order to compare the results of the three-dimensional flow field to that of a two-dimensional flow, some tests were performed with a complete ring around the body at the same location. Again for this case the heights of the rings were 0.6", 0.5", 0.375" and 0.25".

Pressure taps were provided at 60 points on the model, and measured by means of two Scannivalve transducers. The normal and axial force coefficients were calculated from the overall pressure distributions.

The test conditions were performed at a stagnation temperature of 820°R and a wall temperature of 520°R. The stagnation pressure of the tunnel was varied between 1,800 p.s.i.a. and 60 p.s.i.a. These conditions provided a large variation over a wide range of Reynolds numbers and on the parameter Po_j/Po_∞ .

2.2 Experimental Results: Finite Span Jet

At first it was desirable to investigate the nature of the boundary layer over the surface of the cone, with no interaction over the full range of stagnation conditions. The transition point, determined from heat transfer measurement, is presented in Fig. 2. For the test conditions presented in this report, correlation of all the data resulted in the following relationship:

$$Re_\theta = 0.4 \sqrt{\frac{\rho_e u_e x}{\mu_e}}$$

A value of Re_θ equal to 750 was obtained for the full range of stagnation conditions. It is clearly seen from Fig. 2 that for the highest stagnation pressure $Po_\infty = 1,800$ p.s.i.a., transition occurs within a distance of less than one inch from the tip of the cone. Therefore, the boundary layer is turbulent well ahead of the slot. For the lowest stagnation pressure ($Po_\infty = 60$ p.s.i.a.) transition does not occur over the entire length of the cone, and therefore, a laminar boundary layer exists over the entire surface of the cone. A discussion of the jet interaction will be made at first, and comparison to two-dimensional results obtained in Ref. 11 will be made. For all the test conditions presented here M_∞ was equal to 1. The interaction and the observed structure of the flow field will be explained with the aid of Schlieren pictures, flow diagrams, ink tracing, and pressure distributions. A typical set of schlieren photographs are presented in Fig. 3, and the corresponding pressure distributions in Fig. 4. The test conditions for the results which are presented in these figures are $M_\infty = 6.0$, $To_\infty = 820^\circ R$, $Tc = 520^\circ R$. The diagram of the flow along the line of symmetry shown in Fig. 1 was constructed from this data. Fig. 6 presents the flow streamlines along the body surface which are traced by ink injected through pressure taps. Along the symmetric plane the flow pattern is similar to the one obtained for the two-dimensional jet interaction problem as has been discussed in Ref. 11. However, as it may be seen in Figs. 1, 3 and 6, there is a large divergence of the flow from the axis of symmetry which is analogous to the flow of a cone at an angle of attack. Therefore, there is a large cross-flow component which tends to minimize the upstream extent of the separation region. In order to understand the complete flow field, it is desirable to follow the flow from the region ahead of the separation point. Fig. 3a is a schlieren of the jet without the secondary air stream, and Figs. 3b and 3c are the schlieren pictures of the interaction phenomena between the two streams. The jet itself has acted like a step or protrusion normal to the surface of the body, and has an effective height of 0.6 times the height of the jet without the interaction (Figs. 3a and 3b). The jet without interaction may be analyzed from a two-dimensional point of view and the jet boundaries may be obtained by the method of characteristics, assuming no mixing along the boundaries. Free jet studies were not made here since the phenomenon is two-dimensional and has been discussed in detail in Refs. 11, 15 and 16. Analogous to the flow field in Ref. 11, the flow in the central core passes through a strong shock, which is usually called the "Mach disc". Such a shock may be observed in Figs. 3a and 3b. The "Mach disc" in this case is three-dimensional, with a maximum height "h" at the symmetry plane and reducing to height zero at the two edges of the slot. The test results presented in Figs. 3 and 6 are summarized below:

$L = 1.6''$	$\delta^* = 0.04''$ (for $L = 13''$)
$L = 14.5''$	$\dot{w}_{b.1.} = 0.1170 \text{ #/sec}$ (for $\varphi = 360^\circ$) (for $L = 13''$)
$d = 0.030''$	$\dot{w}_{b.1.} = 0.791$
$h = 0.295''$	

A plot of $\dot{w}_{b.1.}/\dot{w}_j$ versus Po_j/Po_∞ is presented in Fig. 7, for the slot width of 0.030" and a fully developed turbulent boundary layer, which is assured at $Po_\infty = 400$ p.s.i.a. The boundary layer undergoes a sudden deflection, as indicated in Fig. 1 and is contained within the separation shock and the separated region, and then penetrates through the bow shock and mixes with the jet. The jet itself is equivalent to a solid boundary, which previously has been correlated in terms of a forward facing step (Ref. 17). An analogous correlation for the three-dimensional jet penetration may be done and will be described later in the report. Two three-dimensional separation bubbles, labelled 1 and 2 in Fig. 1, are produced as a result of the separation upstream of the slot, as shown clearly by Fig. 6, and the two plateaus of pressure shown in Fig. 4. The first separation bubble (1) has an upstream flow direction at the surface while separation bubble (2) has a downstream direction. In order to establish this, ink was injected in the region of separation bubble (1) and the ink traversed upstream. When the ink was injected in the region of bubble (2) the ink traversed downstream. Some of these results may be seen in Fig. 3d. The extent of the separation region ahead of the jet was L/h equals to 5.4 which compares to a value of 4 for a two-dimensional step. The angle formed between the wall and a line drawn from the separation point to the top of the Mach disc was equal to 11°. This compares to a value of 13° for a two-dimensional jet with the same conditions.

In two-dimensional separated flows the plateau pressure and separation shock are usually calculated for an equivalent wedge. In the present case, it is of interest to consider such a calculation, although the flow is clearly three-dimensional, and to compare the result with the two-dimensional case. With a jet penetration height of 0.295" the ratio of slot span to jet height is 6.65 so the phenomenon may be locally two-dimensional near the plane of symmetry. Using $M_c = 5.35$ and a wedge angle of 11° , corresponding to the observed angle of the separated boundary layer, two-dimensional oblique shock relations give a shock angle of 20° and a plateau pressure of $P_c/P_i = 3.7$. These compare very well with the shock angle of 19.5° measured from the schlieren photograph and the plateau pressure ratio of 4.0 shown in Fig. 4. Therefore, it appears the flow field is locally two-dimensional and can be compared with two-dimensional experiments on the basis of a corrected effective penetration coefficient $P_{o,j}/P_{o,\infty}$. Or, in other words, the penetration height, h , can be used to relate the two-dimensional and three-dimensional phenomena, at least near the axis of symmetry, and in this sense the problem is reduced to relating $(P_{o,j})_{3D}$ to $(P_{o,j})_{2D}$ for the same penetration height, h . $(P_{o,j})_{3D}$ is of course much larger than $(P_{o,j})_{2D}$ for the same h due to the cross-flow. (The oncoming flow is effectively more energetic, since the low energy flow moves laterally around the jet.) To estimate the ratio $(P_{o,j})_{3D}/(P_{o,j})_{2D}$ the results of the present tests are compared with the data of Ref. 11, which are also for $M_\infty = 6$, in Fig. 8. For example, in the present experiments at $(P_{o,j,d})/(P_{o,\infty,L}) = 0.465 \times 10^{-3}$ a value of $h/L = 0.0204$ is obtained, and for this same h/L Ref. 11 has $(P_{o,j,d})/(P_{o,\infty,L}) = 0.11 \times 10^{-3}$. Therefore, $(P_{o,j})_{3D}/(P_{o,j})_{2D}$ is approximately 4. At these conditions, Ref. 11 has $t/L = 0.13$ while in the present experiment $t/L = 0.12$, confirming the premise that h/L is a basic correlation parameter. However, four times the mass must be injected in the three-dimensional case to obtain the same separated flow pattern, and thus the same normal force per unit span, along the plane of symmetry. The value of C_{N_A} obtained by integrating the measured pressure distributions over the entire cone surface are also plotted in Fig. 8. It can be seen that the total normal force coefficients obtained in these experiments are nearly the same as the centerline values of Ref. 11, with the same jet mass flux, which is quite remarkable. This implies that the cross-flow produces a favorable interaction with the mainstream and thus forming a three-dimensional separated region well beyond the boundaries of the slot. An explanation of this behavior is presented below, in connection with the discussion of the amplification factor C_{N_A}/C_{N_R} .

The surface pressure along the line of symmetry is presented in Fig. 4a for various test conditions. Care must be exercised in interpreting this data since for the conditions of $P_{o,\infty}$ below 200 p.s.i.a. transition occurs ahead of the slot, as may be seen from Fig. 2. However, the plateau reached in each case is clearly shown in the diagram. Immediately downstream of the slot, the flow behaves like a wake with an associated recirculation region, labelled 3 in Fig. 1, a neck, and a reattachment shock. Analogous to wake flow, the pressure immediately downstream of the slot corresponds to the base pressure and is below the undisturbed cone pressure. However, it subsequently recompresses and reaches a value of almost twice the undisturbed cone pressure at a distance of approximately four h . Although unfavorable interaction has been observed in a lower range of Mach numbers for the downstream portion of the jet, it seems that a favorable interaction can be obtained with increasing Mach numbers. Similar results were obtained in Ref. 18 for two-dimensional configurations. The results of Ref. 18 indicate that considerable unfavorable interaction (a decrease downstream of the jet) was obtained at $M = 2.61$ and 3.5. Results at $M_\infty = 4.54$ indicated a net interaction force of zero for the portion downstream of the jet. Ref. 18, in addition, obtained a recompression pressure of p_c/p_i of 1.5. Since this recompression pressure is a function of Mach number, it may be that a considerable interaction may be obtained for the downstream region for Mach numbers above 5. Lateral distributions of surface pressure are shown in Figs. 4b and c, for $s = 14.0$ " and 14.5 ". (The slot is at $s = 14.3$ ") Attention is called to the high pressure region downstream of the slot where the cross-flow passes, as opposed to the low pressure trough that exists immediately behind the slot. Schlieren photographs of the jet interaction for the range of conditions discussed are presented in Figs. 5a-g. The boundary layer is laminar or transitional in Figs. 5e, f and g.

The amplification factor C_{N_A}/C_{N_R} has been computed from the integrated pressure distribution on the cone and the calculated thrust of the sonic jet. The present results are plotted in Fig. 9 and are comparable to the data presented in Ref. 11 for two-dimensional flow. Both the value obtained by considering the normal force acting only up to the slot location and that obtained by integration over the entire surface are shown. It can be seen that a positive net contribution is received from the region downstream of the slot* although the pressures are locally below the undisturbed cone value immediately behind the plume. The trend of decreasing C_{N_A}/C_{N_R} with increasing $P_{o,j,d}/P_{o,\infty,L}$ is obtained in these experiments, as previously observed by Sterrett et al.^{11,13,35} Spaid and Zukowski¹⁸ correctly point out that this trend is due to three-dimensional effects rather than a basic dependence on the jet momentum (beyond a certain threshold value), however they do not offer an explanation of the nature of the three-dimensional effects. The explanation is apparent if the surface streamline patterns are examined. For example, in Fig. 6 it can be seen that the boundaries of the separation region have been extended, due to the cross-flow, from the end of the slot, point A in Fig. 6, to the point B. The span of the separation region has been increased from the slot span of 1.96" to nearly 5". Thus, the cross-flow has more than doubled the effective span of the jet, or reduced the value of C_{N_R} per unit span by more than a factor of two. This same phenomenon is evident in Maurer's oil streak data³. Therefore, to obtain the true amplification factor C_{N_A}/C_{N_R} either of the following procedures are recommended:

*The opposite result has been reported at lower Mach numbers, e.g. Ref. 11.

- a) C_{NA} must be calculated by integrating the pressure distribution over the entire surface area, or
- b) an effective C_{NR} per unit span must be used, which is in the same ratio to the actual C_{NR} as AC/BC (in Fig. 6).

These considerations are not intended to imply that a constant value of C_{NA}/C_{NR} will be obtained without three-dimensional effects, however, the decreasing trend observed in the flat-plate experiments will be substantially reduced. It is emphasized that in the present study (which involves a cone rather than a plate) the behavior is somewhat different due to the axial symmetry. The normal force is defined as the component of the force acting parallel to the plane of symmetry through the jet ($\phi = 0$) as well as normal to the axis of symmetry of the cone. Therefore, the relative contribution to the normal force due to the cross-flow decreases as the lateral extent of the separation region increases. (For example, the pressure acting at $\phi = 90^\circ$ makes no contribution to the normal force.) Since the lateral extent of the separation region increases with increasing $P_{01}/P_{0\infty}$, it is understandable that the amplification factor C_{NA}/C_{NR} decreases. The included peripheral angle of the jet is 60° in these experiments; the amplification factor can be expected to depend on this angle to some extent. Similar results for C_{NA}/C_{NR} have been presented in Ref. 35.

2.3 Experimental Results: Transverse Fences

For this part of the investigation the interaction will be studied for both axially symmetric transverse fences and for finite span fences of the same included peripheral angle as the slot (60°). Figs. 10a,b,c and d present the schlieren photographs for finite step heights of $h = 3/4"$, $1/2"$, $3/8"$ and $1/4"$. It is of interest to determine if the separation region has a geometric similarity analogous to the two-dimensional case. In this case, the value of l/h has been measured from schlieren photographs, for all the various step heights. Values of l/h of 4.26, 4.3, 4.35 and 4.2 were obtained for the above step height. This value compares to a value of 4.3 for the two-dimensional case (Ref. 19). In addition, the angle of the separation shock as well as the plateau pressure reached is given by the equivalent wedge angle of 13.1° which is in quite good agreement with the value obtained in the two-dimensional case. The pressure distribution for all the above conditions are presented in Fig. 11. The results have been correlated in terms of s/h , and it is seen that there is good agreement for all the tests. However, one may also observe that, unlike the case of the slot injection, the pressure in the wake region of the fence has no overshoot and in fact is always below the undisturbed conical pressure, thus resulting in an unfavorable interaction at the centerline of the body. However, pressure away from the plane of symmetry of the fence recovered and was above the undisturbed conical value. The full pressure distributions over the entire surface of the model will be presented in Ref. 14. The pressure along the centerline in the wake of the fence recovers completely at an l/h of 3. The normal force for the interaction was calculated by integrating the entire pressure distribution over the model. The results are compared to the two-dimensional interaction as given in Ref. 19. The values of F_l/p_{1hb} obtained in these tests have been calculated and are shown in Fig. 12. These values include the interaction upstream and downstream of the fence. An average value of F_l/p_{1hb} of 11 was obtained for an M_∞ of 5.3. The value corresponding to the same conditions for the two-dimensional interaction as calculated from the correlations of Ref. 19 (Eq. 2) gives a value of 11.2. It is pointed out here that normal forces which are obtained by integrating the centerline pressure distribution are misleading; the full span of the separation region, beyond the boundary of the fence, must be included.

It may be of interest to compare the interaction obtained by the step to the one obtained by the jet for the same value of h . The results of the jet interaction indicated that the same penetration height was obtained in the present experiments as in the two-dimensional experiments when four times the amount of mass flow was injected through the slot. However, this resulted (approximately) in $(C_{NA})_{3D}/(C_{NA})_{2D} = 4$. In other words, the value of C_{NA} was approximately the same as in the two-dimensional case for the same mass flow. In the case of the fence there is a favorable interference which results in a larger normal force due to the fence than due to the jet with an equivalent penetration height, h . However, a larger drag force is obtained with the fence than with the slot, therefore resulting in approximately the same C_N/C_D .

It has been indicated in the literature that a true two-dimensional separation is hard to achieve, and therefore the separation point is sensitive to cross flow gradients. For this purpose a study of two-dimensional separation is studied on an axially symmetric configuration, by placing a full-span fence (or ring) over the surface of the body. For this type of configuration, a more realistic comparison may be made between finite and infinite fences. The results with the full ring are presented in Figs. 10e, f and g. Only the main results will be given here, and the details will be included in Ref. 14. The tests were performed with a full ring of height, h , corresponding to the finite fences. For $h = 3/4"$, $1/2"$ and $3/8"$, the pressure gradients produced were too severe, and unfortunately the flow detached completely at the tip of the cone (see for example Fig. 6e). A study of the separation region could only be made for step heights equal to or smaller than $1/4"$. The schlieren photographs corresponding to a step height of $1/4"$ are presented in Figs. 10f and g. An increase in the value of l/h was observed, over that of the finite fence for the same h . A value of l/h of 4.5 was measured; this compares to a value of l/h of 4.2 for the finite fence. The results for the conditions presented in Fig. 10f are for a fully turbulent boundary layer well ahead of the separation region, which results presented in Fig. 10g are for a laminar boundary layer ahead of the separation region. A more detailed description of the full fence with associated pressure distributions will be given in Ref. 14.

3. THEORETICAL ANALYSIS OF THE JET INTERACTION FLOW FIELD

3.1 Background and Motivation

Previous analyses of the jet interaction flow field have been primarily concerned with determining the parameters that directly affect the phenomenon and correlate the experimental data. Certain parts of the flow field have been analyzed in some detail, for example Sterret et al.^{11,21} have constructed the supersonic portion of the jet plume by the method of characteristics. Spaid and Zukowski^{18,19} have developed a correlation of the separated turbulent flow upstream of the plume by analogy with the flow upstream of a forward-facing step. This approach has also proved successful in the present experimental study, which has shown the jet penetration height to be basic correlation parameter for both two-dimensional and three-dimensional flows. Nevertheless, a unified, theoretical description of the entire flow field is still lacking. The present investigation is addressed to this problem as well as to the experimental study of the phenomenon. Motivation for the theoretical study lies partly in the need to clarify the complex structure of the three-dimensional flow field of a finite jet, and partly to determine the extent to which the phenomenology of two-dimensional separated flows is applicable to the problem. However, the study has not yet progressed to the point where a definitive answer to either question is provided. The purpose of the following discussion is to demonstrate the proposed theoretical model is valid and a workable method of solution has been developed. Primary attention is directed toward the description of the separated flow upstream of the plume which is considered to be a crucial part of the flow field and certainly the least amenable to theoretical treatment.

3.2 A New Approach to Separated Flow Problems

A qualitative description of the mechanism by which separation occurs, in general, is well known: the flow near the wall lacks sufficient energy to continue in the same direction as the flow in the mainstream, due to the imposition of an adverse pressure gradient. If the flow is constrained to remain two-dimensional by some physical consideration then the pressure gradient causes the low energy flow near the wall to reverse direction, and the presence of the disturbance is propagated far upstream. On the other hand, if cross-flow is permitted (i.e., the flow is allowed to move laterally) the low energy flow is easily diverted away from or around the disturbance, and the extent of upstream propagation is reduced considerably. Although separation can occur in both the two-dimensional and three-dimensional cases, the flow pattern is very much different, and the location of the separation line in the latter case cannot be identified by vanishing the wall shear stress, or by the presence of flow reversal.

The point to be noted in the above qualitative picture is that the description can be made completely in terms of opposing pressure and inertial forces, that is, without explicit introduction of viscous forces. As pointed out by Batchelor^{22,23} a physically plausible solution of the Navier-Stokes equations for flows of this type with closed streamlines is possible in the limit of infinite Reynolds number, i.e., inviscid flow. The word plausible is emphasized because such flows have never been observed due to the occurrence of instabilities and turbulence at large Reynolds numbers. Nevertheless, a mathematical model for such flows is important in that it "would allow the determination, by some kind of asymptotic expansion, of the flow at the upper end of the range of Reynolds numbers at which the flow is stable, more readily than by an expansion valid in the neighborhood of zero Reynolds number."²³ In other words, it would provide the inviscid flow field with which Prandtl's boundary layer equations could be used to evaluate the effects of viscosity in the thin regions near the wall and along vortex sheets in the flow. Within the framework of Batchelor's model, it is of interest to examine further the role of viscosity in separation. Clearly, viscosity is essential to the phenomenon in the sense that separation is a consequence of the momentum defect in the flow near the wall resulting from viscous dissipation. Viscous forces also act in opposition to changes due to inertial or pressure forces. Thus, viscosity can be thought of as playing a dual role, that is, causing the required momentum defect but nevertheless opposing the adverse pressure gradient acting on the low energy flow near the wall. It must be emphasized, however, that in the latter role, the effects of the viscosity may be crucial only in certain confined regions, outside of which they can be neglected. In particular, the shear stress at the wall is essential in truncating the upstream propagation of the pressure rise due to the disturbance (e.g., a control surface or jet) at the separation point in a two-dimensional flow, while the recirculation and reattachment may be essential inviscid processes. (However, in a three-dimensional separated flow the cross-flow may be more significant than the viscous stresses in limiting the extent of upstream propagation.) Therefore, in the absence of explicit consideration of viscous stresses, the point of separation must be fixed empirically. In the case of base flow behind a sharp-cornered body, such as Batchelor²³ considered, the separation point is clearly fixed at the corner (i.e. a "Kutta-condition"). In the flow upstream of a jet plume, or a forward-facing step, the separation point must be determined a priori by correlation of experimental data.

In the proposed model the control surface or jet is immersed in an inviscid, rotational stream that includes the nonuniform velocity and total enthalpy distributions of the finite (nonvanishing) upstream boundary layer profile, especially the important subsonic flow near the wall. The effects of viscous dissipation and (finite) free stream Reynolds number are assumed to be fully accounted for by the upstream boundary layer thickness and velocity distribution. Thus, the flow field is governed by the Euler equations.

It should be noted that this model includes a mixed (subsonic/supersonic) flow, separated by a free boundary; but as is well known, the steady state form of the Euler equations is elliptic in the subsonic domain, hyperbolic in the supersonic domain, and parabolic (but singular) along the $M = 1$ plane. However, the time-dependent form of the equations is hyperbolic regardless of the Mach number. These equations can be solved by the application of well-known²⁴⁻³⁰ finite-difference techniques. The particular scheme used here is outlined below.

3.3 Method of Analysis

A powerful numerical technique for solving fluid dynamic problems was first suggested by von Neumann²⁴ and developed by von Neumann and Richtmyer²⁵ in connection with the calculation of strong shock waves. In essence, the technique is simply an application of the method of finite differences to the unsteady (time-dependent) conservation equations. The method was put on a formal mathematical basis by Lax²⁶ and developed further by Lax and Wendroff²⁷. The idea of obtaining steady-state solutions in this manner, i.e., as the asymptote in time, also occurred to Crocco²⁸, who pointed out that the intermediate solution i.e. the time dependent results, need not have any physical meaning, and, in fact, need not even satisfy the unsteady equations, as long as the asymptotic solution satisfies the steady-state equations. (This latter observation allows considerable freedom in formulation of the finite-difference scheme, however, this latitude will not be exploited in the present analysis) Comparable methods have also been developed independently by Godunov^{31,32}. The calculation of separated flows by a time-dependent technique using the full Navier-Stokes equations has been considered by Thommen and Magnus³³ but they do not present any results.

The governing equations in the present analysis are:

$$\frac{\partial \rho}{\partial t} + \frac{\partial}{\partial x_i} (\rho u_i) = 0$$

$$\frac{\partial}{\partial t} (\rho u_i) + \frac{\partial}{\partial x_j} (\rho u_i u_j + \delta_{ij} p) = 0$$

$$\frac{\partial}{\partial t} (\rho H - p) + \frac{\partial}{\partial x_i} (\rho u_i H) = 0$$

where $i = 1, 2, 3$

$$\delta_{ij} = 1 \quad \text{for } i = j \text{ and } 0 \text{ for } i \neq j$$

$$H = \frac{\gamma RT}{\gamma - 1} + \delta_{ij} \frac{u_i u_j}{2}$$

The pressure is eliminated using the equation of state $p = \rho RT$, yielding five equations and five unknowns; ρ , u_1, u_2, u_3 and H . ($\gamma = 7/5$ is assumed in the following calculations.) Lax's method of casting the equations in difference form is adopted here. The equations are all of the form $\partial w / \partial t + \partial / \partial x_i (f_i) = 0$. The time derivative is approximated by a forward difference and the spatial derivatives by centered differences:

$$w(x_1, x_2, x_3, t + \Delta t) = w(x_1, x_2, x_3, t) - \frac{\Delta t}{\Delta x_i} \left[f(x_1 + \Delta x_i, x_j, x_k, t) - f(x_1 - \Delta x_i, x_j, x_k, t) \right]$$

$$i = 1, 2, 3$$

$$k \neq j \neq i$$

To obtain conditional stability $w(x_1, x_2, x_3, t)$ is replaced by $\bar{w}(x_1, x_2, x_3, t)$ namely

$$\bar{w}(x_1, x_2, x_3, t) = \frac{1}{2} [w(x_1 + \Delta x_i, x_j, x_k, t) + w(x_1 - \Delta x_i, x_j, x_k, t)]$$

Stability is then achieved by observing the Courant-Friedrichs-Lewy (CFL) criteria:

$$\frac{\Delta t}{\Delta x_i} \leq \frac{1}{|u_i| + a}$$

(This is related to the requirement that disturbances must propagate at least as fast numerically as they do physically.) The appearance of an "artificial viscosity" in the difference equation is clear if it is rewritten as the difference analog of the differential equation:

$$\frac{\partial w}{\partial t} + \frac{\partial}{\partial x_i} (f_i) = - \frac{(\Delta x_i)^2}{6 \Delta t} \frac{\partial^2 w}{\partial x_i^2}$$

The only characteristic length scales in the problem are the thickness of the upstream boundary layer, δ , and the mesh size, Δx_i . A square mesh ($\Delta x = \Delta y = \Delta z$) is needed to keep the "artificial viscosity" coefficient isotropic. The order of the "artificial viscosity" coefficient is estimated, using

the CFL stability criteria:

$$\nu_{\text{artificial}} = 0 [\Delta x_i (u_i + a)_{\text{max}}]$$

Therefore the "artificial viscosity" can be reduced to the order of the true molecular viscosity by choosing $\Delta x = 0(\delta^2)$. The upstream boundary layer thickness, δ , is then the only characteristic length scale in the problem. The only characteristic time scale in the problem is the "relaxation time" to reach the steady-state solution from a given set of initial data. However, the maximum permissible time step as determined by the CFL criteria can be written as

$$\Delta t = 0 [\nu_{\text{artificial}} / (u_i + c)_{\text{max}}^2]$$

Thus the magnitude of the "artificial viscosity" is reduced at the cost of a proportional increase in the number of time steps to reach the steady-state asymptote.

The boundary conditions at a solid surface are obtained by considering the surface to be impermeable membrane or contact surface. Impermeability is obtained numerically by requiring the velocity normal to the surface to be equal and opposite at a mesh point above the surface and at a corresponding "virtual point" inside the surface. (Lax²⁶ termed this "reflection".) The same technique is usually applied to all the other variables as well, without the sign reversal^{29,30}. However, this implies the first derivative of these variables at the wall is numerically zero, which is clearly unacceptable in the present application. Therefore, the velocity and mass flux tangential to the surface are extrapolated to a "virtual point" inside the surface assuming their second derivative is zero at the wall. (This procedure effectively eliminates the influence of the "artificial viscosity" at the wall. It is also equivalent to evaluating the first derivative at the surface by a backward difference rather than a centered difference.) The temperature at the "virtual point" is then determined by requiring the pressure to be the same at the "virtual point" inside the surface as it is one point above the surface. The points at the outer boundaries of the domain are handled by the usual "reflection" technique.

3.4 Numerical Examples

The two-dimensional flow of a supersonic stream impinging on a flat-faced step is considered here to demonstrate several salient features of the method and the nature of the results. Two cases are postulated, namely: a uniform stream at $M_\infty = 5$ and a rotational stream with a maximum Mach number of 5 and zero velocity at the wall. The two velocity profiles are plotted in Fig. 13. The first case is obviously equivalent to the supersonic blunt body problem for a semi-infinite flat plate normal to the stream. The particular Mach number is chosen because results by the method of integral relations are available for comparison.³⁴ A mesh size 1/10 the step height was used in the present calculation. The stagnation point pressure obtained is shown in Fig. 14 as a function of the number of time cycles the calculation was performed. The steady-state value is approached very closely after about 80 cycles, and the flow field may be considered fully converged after about 100 cycles.* Contours of constant Mach number are plotted in Fig. 15. The bow shock is "smeared" over several mesh points, which is a fairly large distance due to the coarse mesh used, however it can be seen that the Mach 1 contour is in very good agreement with the shock location predicted by the integral method. The calculated pressure distribution on the face of the step is shown in Fig. 16 and compared with the integral method results. The fact that the sonic line does not terminate at the corner, and the discrepancy in pressures near there, is attributed to the fact that the boundary conditions are not imposed precisely at the point of the corner but only at the nearest mesh points. The impreciseness is presumably present in other calculations of flows around sharp-cornered bodies³⁰, and will be manifested in the case with rotational flow also. (This point has not been pursued further as the sharp cornered step is only considered here to demonstrate the method, and will not be encountered in the applications for which the method is intended.)

In the rotational flow the temperature profile for the initial conditions was calculated from the Crocco integral relation

$$H = H_w + (H_\infty - H_w) u/u_\infty$$

where H_w was evaluated assuming the wall was at the free stream static temperature (i.e., a "cold" wall). The convergence of stagnation point pressures for this case is shown in Fig. 17. The constant Mach number contours (after 200 cycles)** are plotted in Fig. 18. The shock location has been estimated by considering the location of the Mach contour and by examining the entropy variation along streamlines. The computed streamline pattern is plotted in Fig. 19. The presence of the closed streamline ($\omega = 0$) and the "bubble" or recirculating fluid is of particular interest. Profiles of the u - and v -components of velocity at the station $x/h = -1$ are plotted in Fig. 20. The wall pressure distribution and the distribution on the face of the step are given in Fig. 21. The reattachment pressure rise is essentially merged with the separation point rise, so the pressure plateau typical of extensively separated flows is not evident here.

*Less than five minutes was required to compute 120 cycles on an IBM 360/75, including printing of all variables at each mesh point every 10th cycle. The value of $\Delta t/\Delta x$ used was 0.58.

**The maximum permissible $\Delta t/\Delta x$ was computed before each cycle and 3/4 of this value was then used. The initial value was 0.625, and after 75 cycles a constant value of 0.514 was obtained.

The above results are presented primarily to demonstrate that the theoretical model embodies the essential physical mechanism needed to describe separated flows, except for the previously discussed inability to predict the location of the separation point. Calculations that can be compared with experimental data are being carried out, but results are not presently available. Calculations of the jet plume are also planned; as a purely inviscid phenomenon with an imbedded strong shock (the "Mach disc"), it is ideally suited to calculation by this technique. A unified, theoretical description of the complete jet interaction flow field can then be undertaken. The extension to three-dimensional flow fields requires only the inclusion of another difference equation and dependent variable, the transverse velocity component. These calculations will provide not only detailed information regarding the structure of the flow field, but also quantitative predictions of normal forces and moments for finite span jets.

4. CONCLUSIONS

The interaction of a finite-span, transverse jet on a 7° cone in an $M_\infty = 6$ stream has been studied experimentally. Pressure distribution have been measured over the surface of the cone, separation lines have been determined by injecting ink on the surface, and the structure of the flow field has been recorded on schlieren photographs. Based on these observations it has been concluded that along the plane of symmetry the separated region upstream of the jet correlates very well with two-dimensional experiments in terms of the jet penetration height as the basic scale length. (The aspect ratio of the jet plume, b/h , is of order 6 or larger. The quasi-two-dimensional behavior will probably diminish as the aspect ratio is decreased.) However, four times the jet mass flux is required in the case of the finite-span jet to obtain the same jet penetration height as an infinite span (two-dimensional) jet. But the remarkable feature of the three-dimensional phenomenon is that integration of the pressure distribution over the cone surface shows that the normal force coefficient obtained is the same as the normal force coefficient per unit span of a two-dimensional jet with the same jet mass flux. This behavior is attributed to a favorable interaction between the cross-flow and the main stream that increases the effective span of the jet. It is clearly misleading to consider only the pressure distribution along the centerline when cross-flow may be present (although small) due to end effects. If correlated in terms of the jet penetration height, rather than mass flux, the total normal force coefficient of a finite-span jet exceeds the normal force per unit span coefficient of a two-dimensional jet, implying that a finite-span solid control surface, e.g., a transverse fence or forward-facing step, of a given height will produce a larger normal force than predicted by two-dimensional considerations. When the jet is replaced by a transverse fence, the two-dimensional and three-dimensional normal forces are comparable. It is also noted, however, that a larger low pressure region occurs behind the fence than behind the jet plume, so the net interaction force due to the jet is relatively larger than due to the fence. On the basis of these experiments, it is suggested that a combination of a secondary jet and transverse fence may prove to be a more efficient control system than either individually.

The proposed theoretical model, based on an inviscid, rotational flow has been shown to embody the necessary physical mechanism to determine the structure of the jet interaction flow field, except at the point of separation, where viscous stresses are crucial. Several numerical examples, based on a finite-difference solution of time-dependent equations demonstrate the importance of the subsonic, rotational portion of the upstream boundary layer in formation of the separation bubble and the bow shock ahead of the jet or transverse fence. The structure of the plume, Mach disc, and reattachment region, and their mutual interaction are currently being studied.

Acknowledgement

The authors wish to acknowledge the participation of Dr. A. Pallone, formerly Professor of Aeronautics and Astronautics at New York University, in the early stages of this experimental investigation, and his suggestion of an inviscid theoretical model.

REFERENCES

1. Morkovin, M. V.
Pierce, Jr., C. A.
Craven, C. E. "Interaction of a Side Jet with a Supersonic Main Stream", Bull. 35, Engineering Res. Inst., Univ. of Mich., (September 1952).
2. Ferrari, C. "Interference between a Jet Issuing Laterally from a Body and the Enveloping Supersonic Stream", Bumblebee Series Rept. 286, Applied Physics Lab., John Hopkins Univ., (April 1959).
3. Maurer, F. "Three-Dimensional Effects in Shock-Separated Flow Regions ahead of Lateral Control-Jets Issuing from Slot Nozzle of Finite Length", AGARD Conference Proceedings No. 4, Separated Flows, p. 597 (May 1966).
4. Strike, W. T.
Schueler, C. J. "Investigation of Interference Effects Produced by Lateral Jets on Surfaces in a Supersonic Stream", AIAA Paper 63-184 (1963).
5. Sehgal, R.
Wu, J. "Thrust Vector Control by Liquid Injection into Rocket Nozzles", J. Spacecraft Rockets 1, pp. 545-551 (1964).
6. Zukoski, E. E.
Spaid, F. W. "Secondary Injection of Gases into a Supersonic Flow", AIAA J. 2, pp. 1689-1696 (1964).
7. Vranos, A.
Nolan, J. J. "Supersonic Mixing of a Light Gas and Air", AIAA Propulsion Joint Specialists Conference, Colorado Springs, Colorado (1965).
8. Schetz, J. A.
Billig, F. S. "Penetration of Gaseous Jets Injected into a Supersonic Stream", J. Spacecraft Rockets 3, 11, pp. 1658-1665, (November 1966).
9. Kaufman, II, L. G.
Hartofilis, S. A.
Evans, W. J.
Oman, R. A.
Meckler, L. R.
Weiss, D. "Review of Hypersonic Flow Separation and Control Characteristics" Grumman Aircraft Engineering Corp., Rept. No. ASD-TDR62-168, (March 1962).
10. Spring, D. J.
Street, T. A.
Amick, J. L. "Transverse Jet Experiments and Theories - A Survey of the Literature", U. S. Army Missile Command, Redstone Arsenal, Alabama, Rept. No. RD-TR-67-4 (June 1967).
11. Sterret, J. R.
Barber, J. B. "A Theoretical and Experimental Investigation of Secondary Jets in a Mach 6 Free Stream with Emphasis on the Structure of the Jet and Separation ahead of the Jet", AGARD Conference Proceedings No. 4. "Separated Flows", Part II (May 1966).
12. McDonald, R. D.
Garbrick, M. W. "Research Study to Verify and Extend High Speed Mach Model for Jet Reaction Control Effectiveness", Final Report OR 8439, Martin Marietta Corporation, Orlando, Florida (August 1966).
13. Romeo, D. J.
Sterret, J. R. "Aerodynamic Interaction Effects ahead of a Sonic Jet Exhausting Perpendicularly from a Flat Plate into a Mach Number 6 Free Stream", NASA TN-D 743 (1961).
14. Zakkay, V.
Erdos, J.
Calarese, W. "An Investigation of Three-Dimensional Jet Control Interaction on a Conical Body", Department of Aeronautics & Astronautics, New York University, Bronx, N. Y., Rept. No. NYU-AA-69-2 (April 1968).
15. Adamson, T. C., Jr. "The Structure of the Rocket Exhaust Plume without Reaction at Various Altitudes" Supersonic Flow, Chemical Processes and Radiative Transfer, edited by D. B. Olfe and V. Zakkay, Pergamon Press, Oxford (1964).
16. Love, E. S.
et al "Experimental and Theoretical Studies of Axisymmetric Free Jets" NASA TR-R (1959).
17. Sterrett, J. R.
Holloway, P. F. "On the Effect of Transition on Parameters within a Separation Region at Hypersonic Speeds - with Emphasis on Heat Transfer", Symposium on Fully Separated Flows, ASME Proceedings, pp. 15-26 (1964).
18. Spaid, F. W.
Zukoski, E. E. "A Study of the Interaction of Gaseous Jets from Transverse Slots with Supersonic Streams", AIAA J., 6, 2, pp. 205-211 (1968).
19. Zukoski, E. E. "Turbulent Boundary Layer Separation in Front of a Forward Facing Step", AIAA J., 5, 10, pp. 1746-1753 (1967).

20. Barnes, J. W.
Davis, J. G.
Tang, H. H. "Control Effectiveness of Transverse Jets Interacting with a High Speed Free Stream", Air Force Flight Dynamics Laboratory Report AFFDL-TR-67-90, I (September 1967).
21. Sterrett, J. R.
Barber, J. B.
Alston, D. W.
Romeo, D. J. "Experimental Investigation of Secondary Jets from Two-Dimensional Nozzles with Various Exit Mach Numbers for Hypersonic Control Application", NASA TN-D-3795 (January 1967).
22. Batchelor, G. K. "On Steady Laminar Flow with Closed Streamlines at Large Reynolds Number", JFM 1, pp. 177-190 (1956).
23. Batchelor, G. K. "A Proposal concerning Laminar Wakes behind Bluff Bodies at Large Reynolds Number", JFM, 1, pp. 388-398 (1956).
24. Von Neumann, J. "Proposal and Analysis of a Numerical Method for Treatment of Hydrodynamic Shock Problems", Nat'l Def. and Res. Comm. Report AM-551 (1944).
25. Von Neumann, J.
Richtmyer, R. D. "A Method for Numerical Calculations of Hydrodynamic Shocks", J. Appl. Physics, 21, pp. 232-237 (1950).
26. Lax, P. D. "Weak Solutions on Nonlinear Hyperbolic Equations and their Numerical Computations", Comm. Pure and Appl. Math., 7, pp. 159-193 (1954).
27. Lax, P. D.
Wendroff, B. "Systems of Conservation Laws", Comm. Pure and Applied Math., 13, pp. 217-237 (1960).
28. Crocco, L. "A Suggestion for the Numerical Solution of the Steady Navier-Stokes Equations", AIAA J. 3, pp. 1824-1832 (1965).
29. Burstein, S. Z. "Numerical Methods in Multidimensional Shocked Flows", AIAA J. 2, pp. 2111-2119 (1964).
30. Bohachevsky, I.
Rubin, E. "A Direct Method for Computation of Nonequilibrium Flows with Detached Shock Waves", AIAA J. 4, pp. 600-606 (1966).
31. Gudonov, S. K. "Difference Method for the Numerical Calculation of Discontinuous Solutions of the Equations of Hydrodynamics", Mathematic Sbornik, 47, pp. 271-306 (1959).
32. Gudonov, S. K.
Zabrodin, A. V.
Prokopov, G. D. "A Difference Scheme for a Two-Dimensional Unsteady Problem in Gas Dynamics and the Calculation of a Flow with a Detached Shock Wave", USSR Comp. & Math. and Math. Phys. 1, 6 (1961).
33. Thommen, H. U.
Magnus, R. J. "Numerical Calculation of Separated Flows" AGARD Conf. Proc. No. 4, Separated Flows, (May 1966).
34. Hayes, W.
Probstein, R. Hypersonic Flow Theory, Second Edition, I, pp. 426-429, Academic Press, New York (1966).
35. Barber, J.
Staylor, F. "Investigation of Secondary Jets on a Cone at a Mach Number of 6", J. Spacecraft Rockets, 3, 10, pp. 1554-1555 (October 1966).

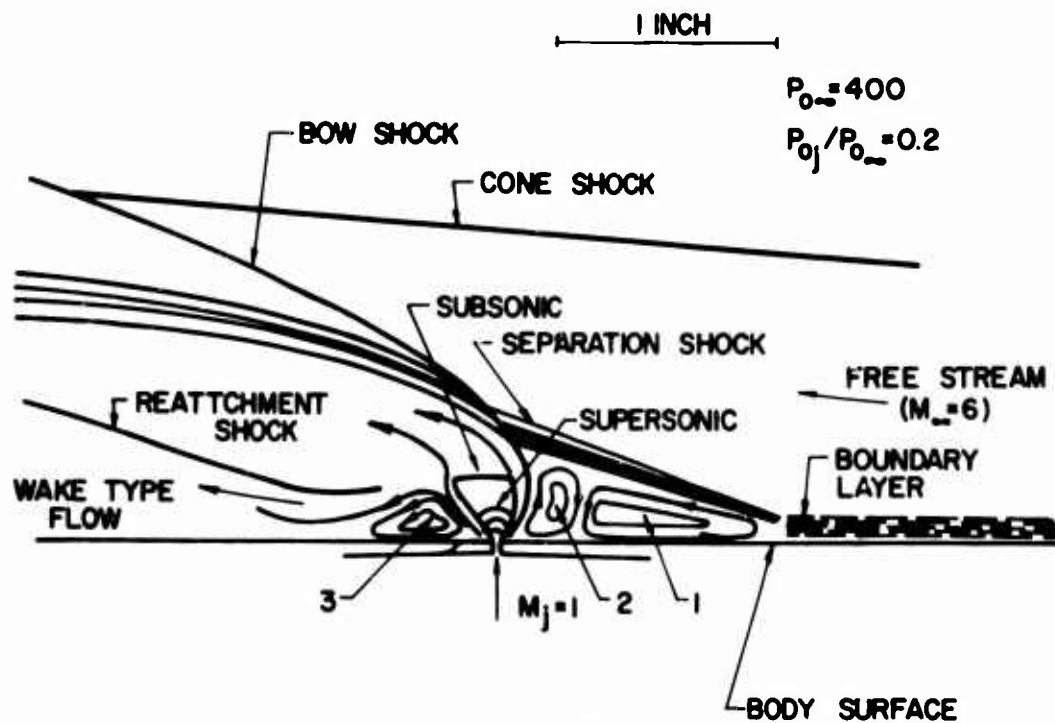


Fig. 1 Schematic of Jet Interaction Flow Field Along the Plane of Symmetry

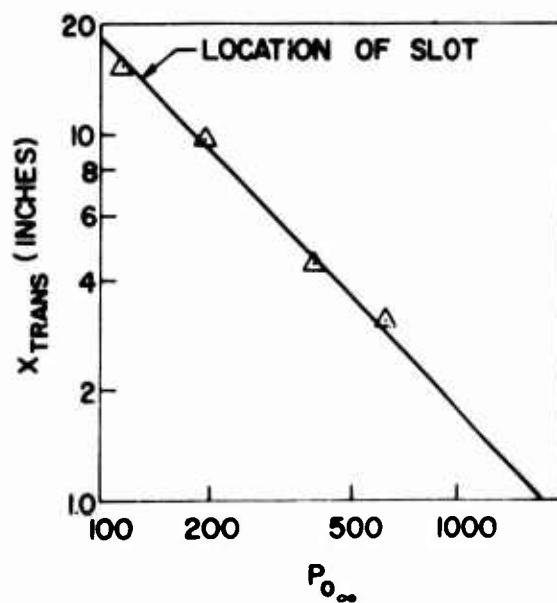


Fig. 2 Transition Location on the Cone

(a) $Po_{\infty} = 0 : Po_j = 90$ (b) $Po_{\infty} = 300 : Po_j = 90$ (c) $Po_{\infty} = 400 : Po_j = 90$ (d) $Po_{\infty} = 400 : Po_j = 90$

Fig. 3 Schlieren Photos of Jet Interaction Flow Field, & Picture of Ink Pattern on Model Surface

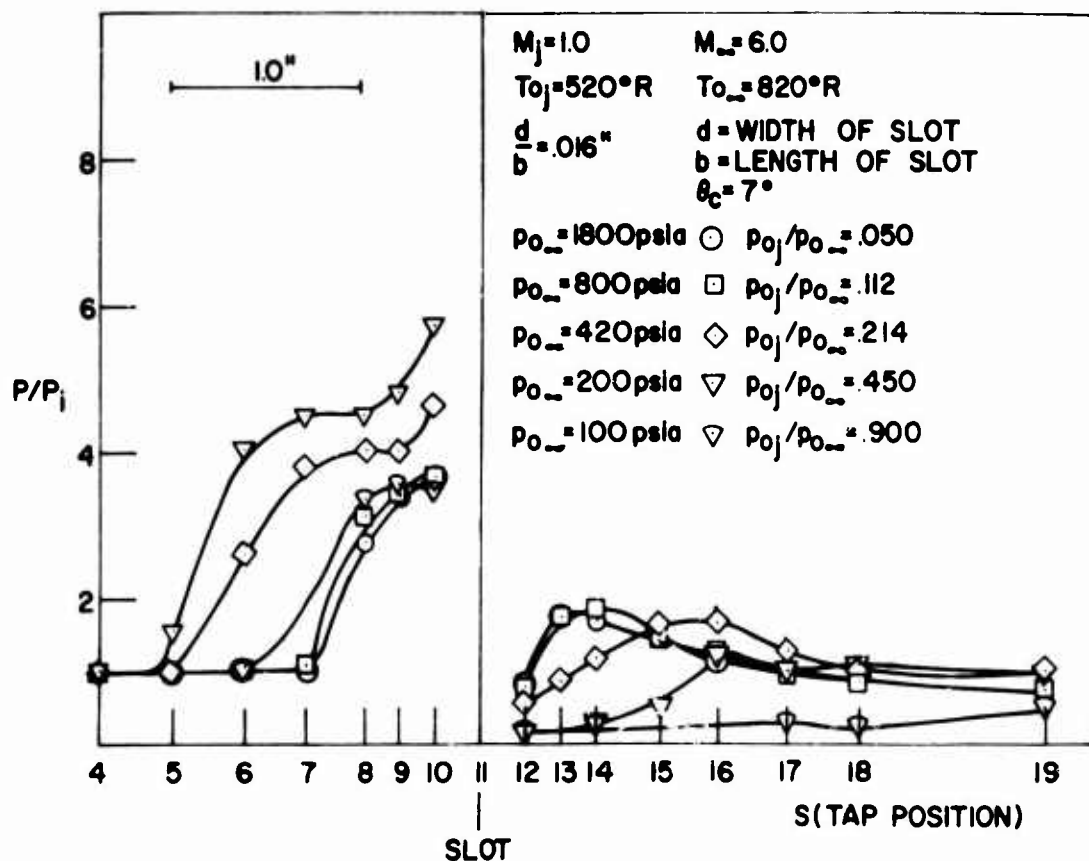
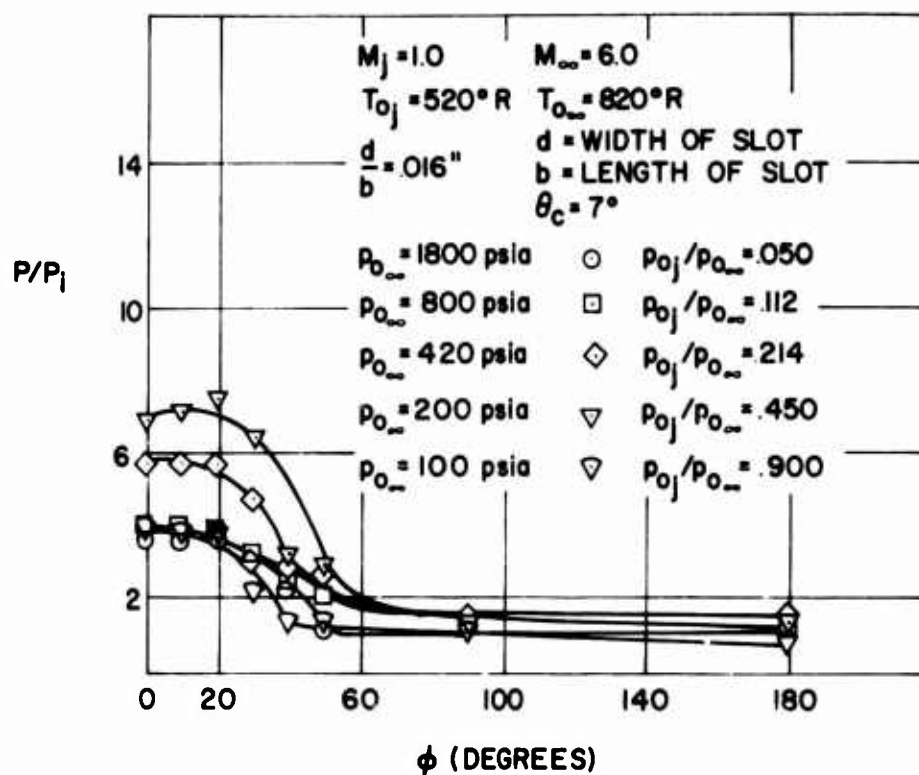
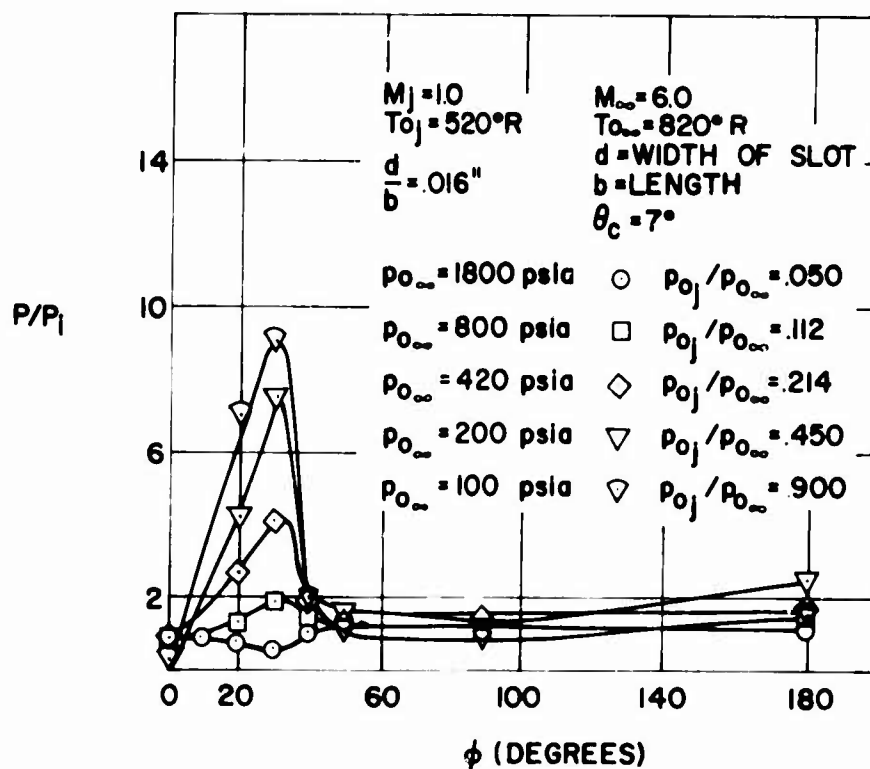


Fig. 4a Surface Pressure Distribution Along Plane of Symmetry For Jet Interaction

Fig. 4b Transverse Distribution of Surface Pressure at $s = 14.0$ inchesFig. 4c Transverse Distribution of Surface Pressure at $s = 14.5$ inches



(a) $Po_{\infty} = 1800 : Po_j = 90$



(b) $Po_{\infty} = 800 : Po_j = 90$



(c) $Po_{\infty} = 420 : Po_j = 90$



(d) $Po_{\infty} = 200 : Po_j = 90$



(e) $Po_{\infty} = 160 : Po_j = 70$



(f) $Po_{\infty} = 100 : Po_j = 90$



(g) $Po_{\infty} = 60 : Po_j = 90$

Fig. 5 Schlieren pictures of interaction of finite jets
for various jet to free stream stagnation conditions

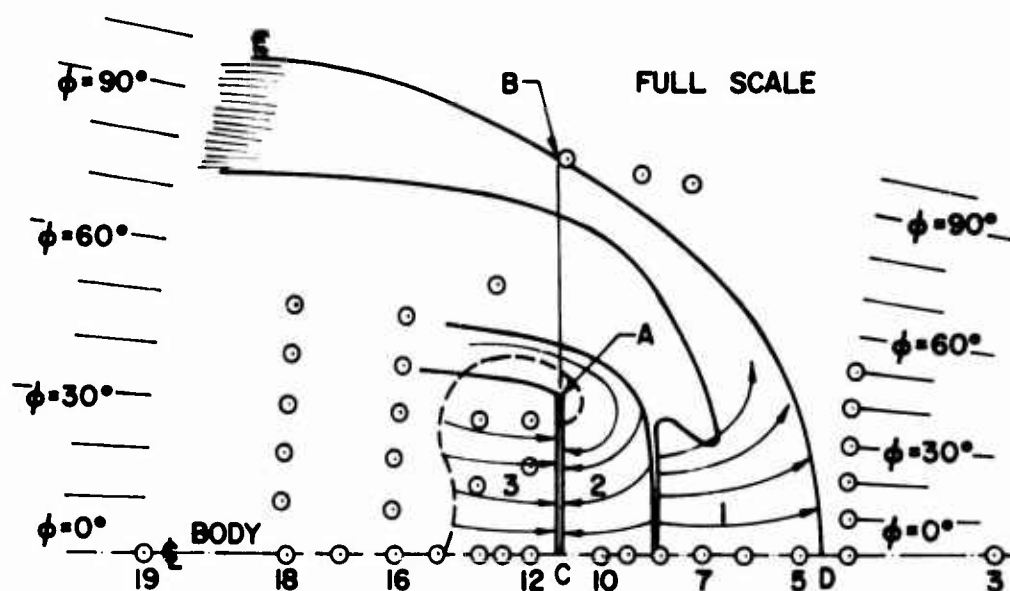


Fig. 6 Tracing of Ink Pattern on Model Surface

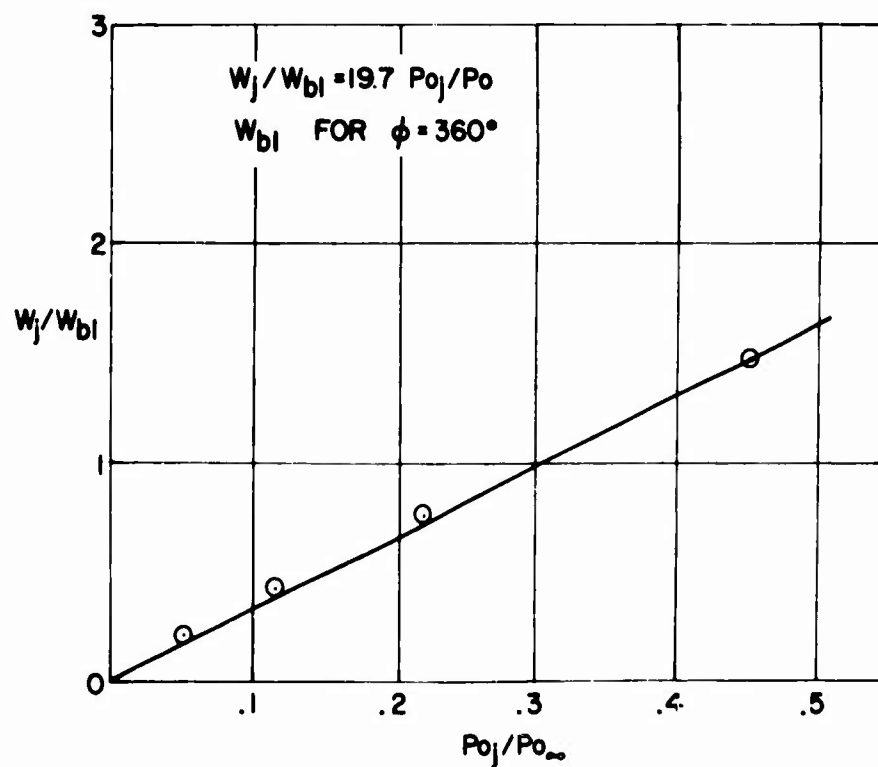


Fig. 7 Ratio of Jet Mass Flux to Boundary Layer Mass Flux

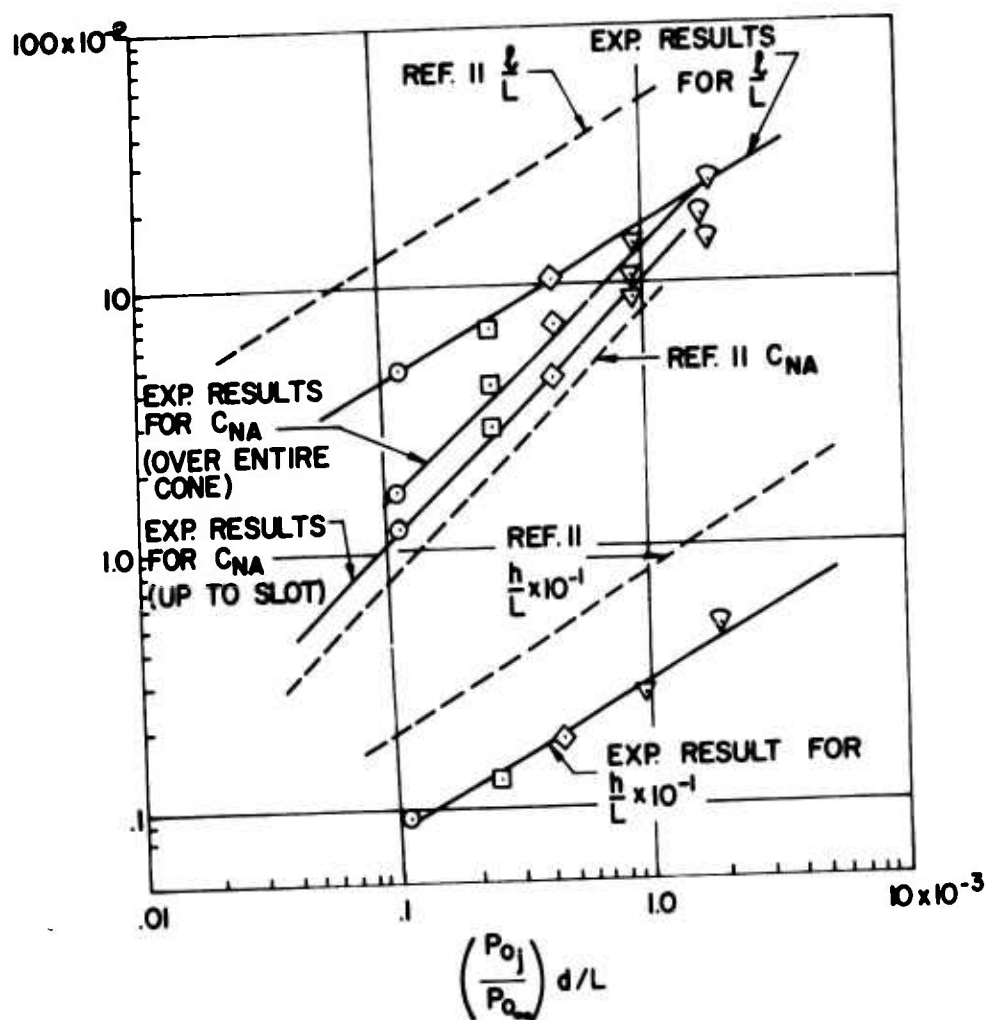


Fig. 8 Jet Penetration Height, Length of Separated Flow Region, & Normal Force Coefficient

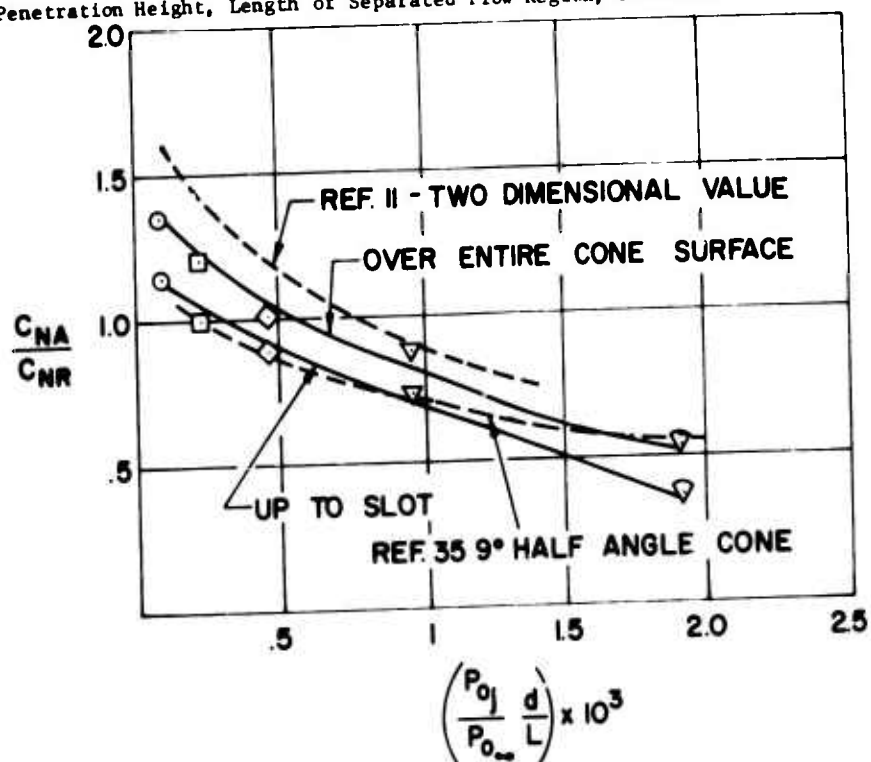


Fig. 9 Normal Force Amplification Factor

(a) $Po_{\infty} = 1800$ $h = 3/4"$ (b) $Po_{\infty} = 1800$ $h = 1/2"$ (c) $Po_{\infty} = 1800$ $h = 3/8"$ (d) $Po_{\infty} = 1800$ $h = 1/4"$ (e) $Po_{\infty} = 1800$ FULL RING $h = 3/8"$ (f) $Po_{\infty} = 1800$ FULL RING $h = 1/4"$ (g) $Po_{\infty} = 100$ FULL RING $h = 1/4"$

Fig.10 Schlieren pictures of interaction for various
axially symmetric and finite step heights

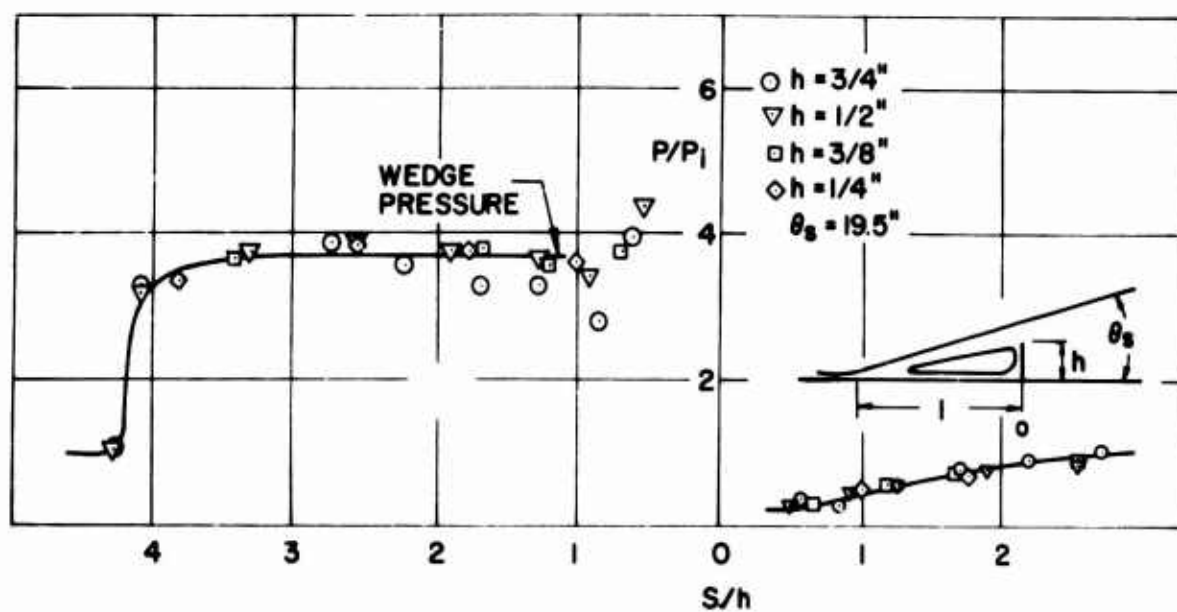


Fig. 11 Surface Pressure Distribution Along Plane of Symmetry for Transverse Fences

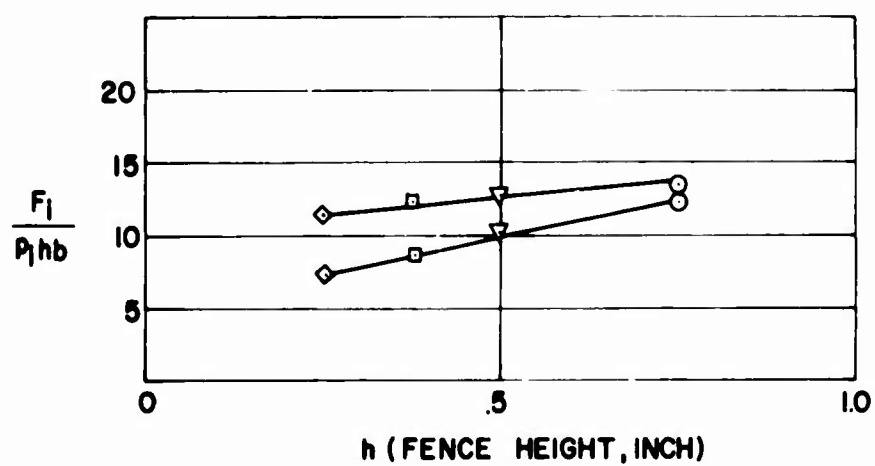


Fig. 12 Normal Force Parameter Due to Fence

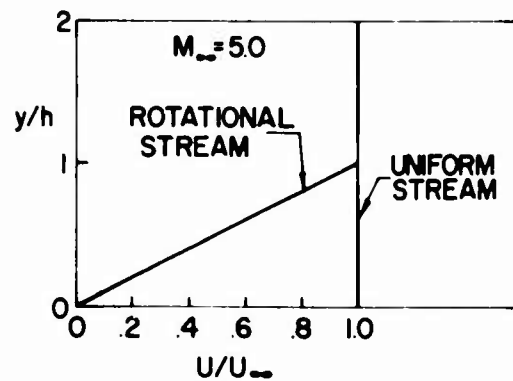


Fig. 13 Upstream Velocity Profiles for Two Postulated Flow Fields

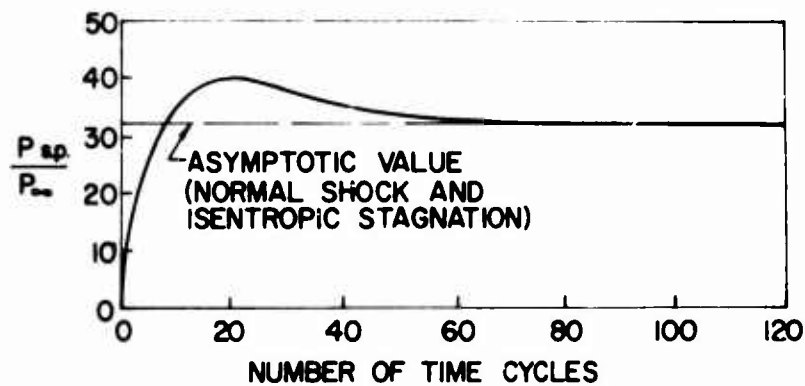


Fig. 14 Stagnation Point Pressure for the Uniform Stream

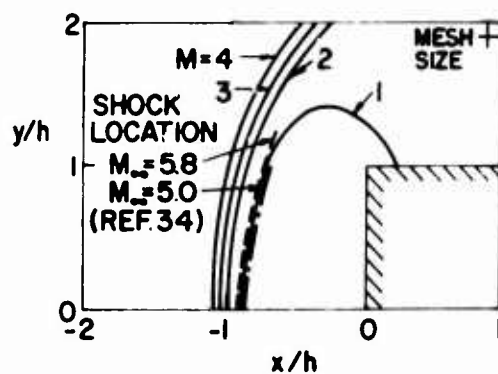


Fig. 15 Constant Mach Number Contours for Uniform $M_{\infty} = 5$ Stream

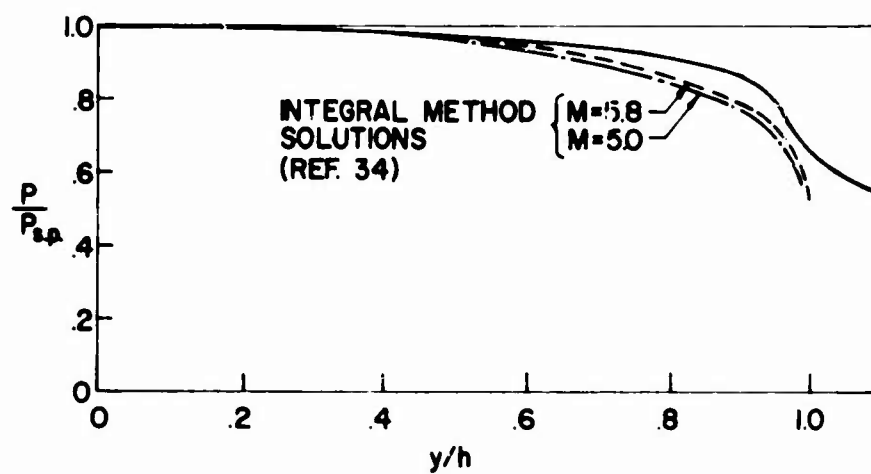


Fig. 16 Pressure Distribution on the Face of the Step (Uniform Stream)

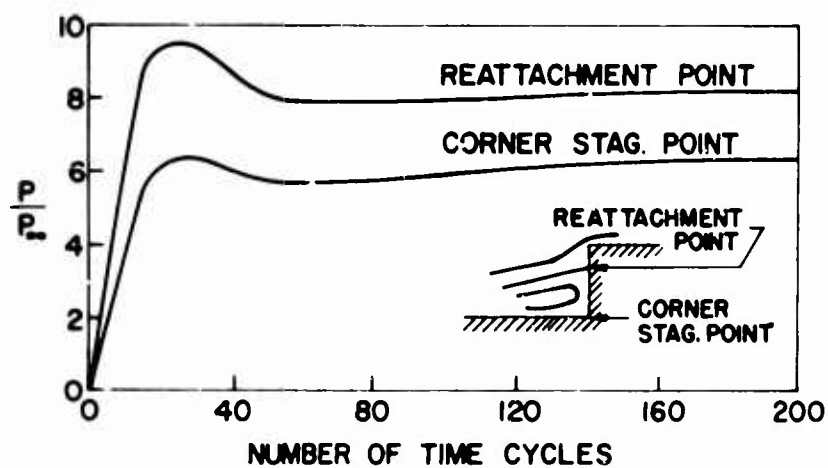


Fig. 17 Stagnation Point Pressures for the Rotational Stream

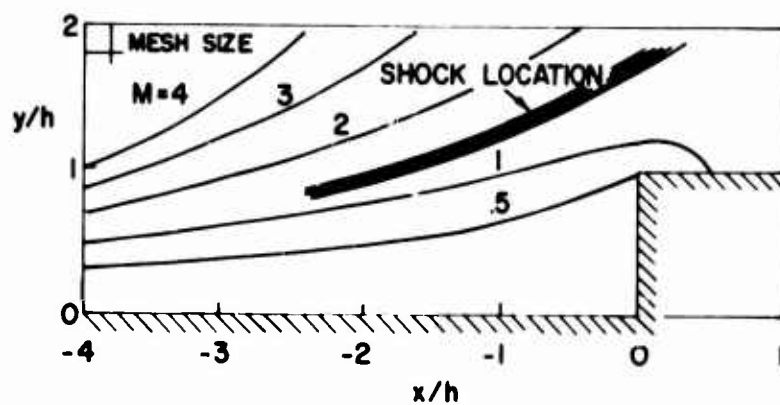


Fig. 18 Constant Mach Number Contours for the Rotational Stream

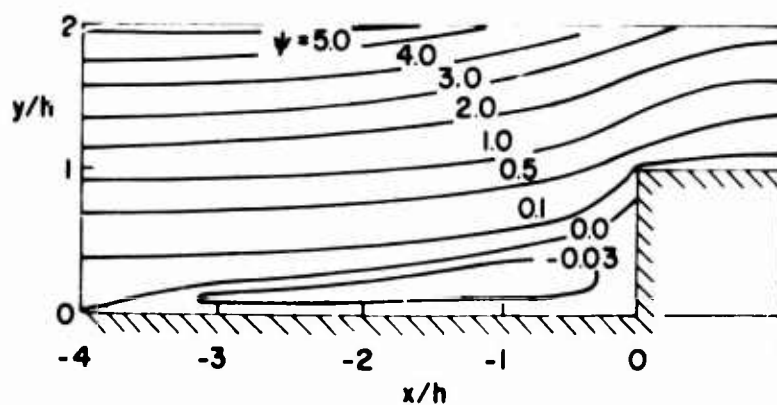


Fig. 19 Streamline Pattern for the Rotational Stream

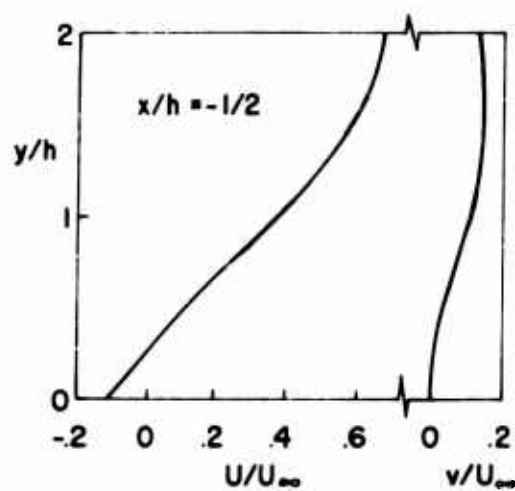


Fig. 20 Velocity Profiles Ahead of Step, for the Rotational Stream

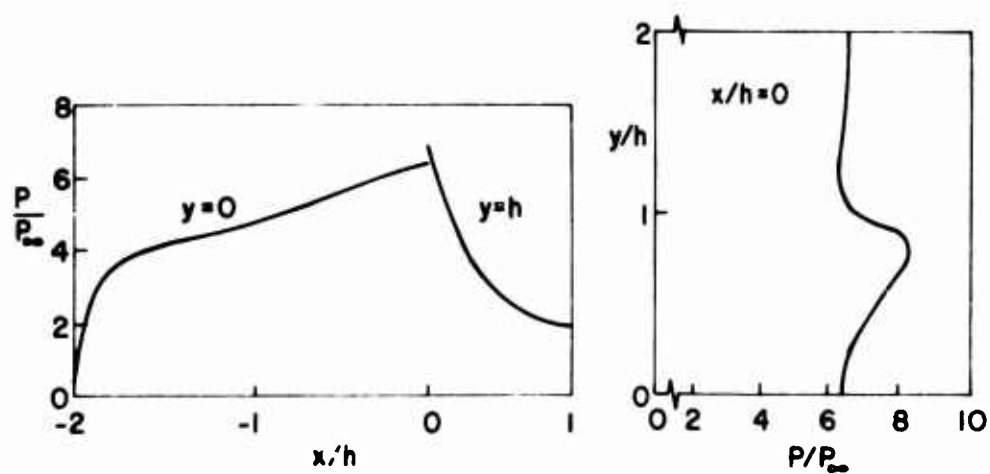


Fig. 21 Pressure Distributions on the Wall and Face of the Step

HYPERSONIC INTERACTIONS ABOUT A SLENDER CONE
INDUCED BY RADIAL MASS INJECTION

by

P. G. Simpkins*

Aerophysics Laboratory
Avco Space Systems Division
Wilmington, Mass. 01897

*Senior Staff Scientist

SUMMARY

The interaction between a two-dimensional underexpanded jet and the hypersonic flow over a cone at a freestream Mach number of thirteen is reported. The jet emanates radially from a slot which is normal to the axis of symmetry of the right circular cone which has a semi-angle of five degrees. The influence of variations in freestream Reynolds number, jet pressure ratio, secondary mass flux and yaw angle are investigated, for a regular and blunted cone configuration.

Measurements of the surface heat transfer and pressure distributions far upstream of the jet are consistent with accepted boundary layer separation predictions in the free interaction region. In the immediate vicinity of the efflux, on both the upstream and downstream side, the measurements indicate the existence of reattachment regions. These are associated with the substantial increases observed in both the local pressure and heat transfer distribution. Throughout the length of the cone behind the jet, the heat transfer is found to be less than the undisturbed cone value. This is attributed to a film cooling effect.

When the jet pressure ratio is maintained at a constant value, the separation length ahead of the efflux is found from schlieren photographs to be independent of the freestream Reynolds number. This implies that the geometrical features of the separated flowfield are similar and that the free shear layer is thin enough for the viscous parameters to be unimportant. Further observations indicate that when the secondary mass flux is constant, the separation length decreases with increasing freestream Reynolds number.

NOMENCLATURE

C - constant of proportionality in linear viscosity-temperature relationship

C_H - Stanton number = $\dot{q} / \rho_\infty u_\infty (H_\infty - H_w)$

D - cone base diameter

h - jet penetration height

H - total specific enthalpy

l - separation length

M - Mach number

Pr - Prandtl number

p - pressure

q - heat transfer rate

R - radius

R_0 - nose radius

Re - Reynolds number

S - distance measured from forward stagnation point

T - temperature

u - velocity

α - angle of attack

β - cone half angle

γ - ratio of specific heats

δ - shear layer separation angle

θ - separation shock angle

ρ - density

SUBSCRIPTS

- a - ambient conditions
- e - conditions at boundary layer edge
- J - jet reservoir conditions
- j - conditions at the exit plane of the jet
- O - atmospheric conditions
- R - conditions upstream of jet Riemann wave
- s - incident shock conditions
- t - stagnation conditions
- w - surface conditions
- 5 - reservoir conditions in the reflected region of the shock tunnel
- ∞ - freestream conditions

HYPERSONIC INTERACTIONS ABOUT A SLENDER CONE INDUCED BY RADIAL MASS INJECTION

P. G. Simpkins

1. INTRODUCTION

The interaction between a two-dimensional jet of air emanating from a long narrow slit set at right angles to the flow was first studied by Taylor (1954). In that analysis, Taylor considered an inviscid incompressible flowfield, and proposed using an equivalent body approach to evaluate the conditions downstream of the jet. Since that time the number of publications dealing with secondary flowfield interactions has grown steadily as various applications of the technique have been proposed. Extensive data is now available, for example, dealing with the control of the thrust vector of rocket exhausts. With this application in mind, emphasis has been placed on flowfields in which the primary stream is supersonic and the interaction three-dimensional; for example, a typical flowfield considered is a circular jet penetrating a nozzle flow. The investigations by Broadwell (1963), Charwat & Allegre (1965) and Hsia, Seifert & Karamcheti (1965), to name a few, are representative of the approaches used to determine the salient features of such a jet-nozzle interaction process. Because of the obvious complexity of this three-dimensional interaction a number of investigators have restricted themselves to flows over flat plates in order to simplify the flowfield. The studies of Zukowski & Spaid (1964) have illustrated that when the jet is underexpanded and has a circular cross section, the interaction regime is highly three-dimensional even though the primary flow is two-dimensional. By extending their earlier studies to include the case where the jet issues from a transverse slot Spaid & Zukowski (1968) have more closely approximated a two-dimensional interaction, but even then found evidence of three-dimensional effects. Similar results have been reported by Maurer (1966) who has noted that at large jet pressure ratios and high aspect ratios, the centerline flowfield ahead of the jet exhibits three-dimensional effects. Studies of the planar free jet structure by Gregorek & Luce (1966) may well shed some light on the reasons for some of the three-dimensional effects noted above. The appearance of strong wave systems originating at the ends of the slots have been observed in planar jets at high pressure ratios. Gregorek & Luce found that under these conditions the wave systems often intersect each other and eliminate the normal shock that is characteristic of underexpanded axi-symmetric jets.

Two points of interest are apparent from the above discussion. Firstly, while extensive studies have been undertaken with regard to the technique of thrust vectoring, very little attention has been paid to the hypersonic interaction which is of interest as a means of attitude control. A number of studies of the finite span two-dimensional interaction process have been reported by Sterrett and his co-workers; who initially examined the transitional and turbulent boundary layer interaction ahead of an underexpanded jet, see Romeo & Sterrett (1961). More recently, Sterrett & Barber (1966) and Sterrett, Barber & Alston (1967) have concentrated on the turbulent boundary layer interaction, and included detailed examination of the jet structure. These authors suggest that before the interaction process can be fully understood, the parameters that determine the jet structure must be defined. Other aspects of the same problem have been described by Poisson-Quinton & Ceresuela (1966) and Kaufman (1967). The former work examined the three-dimensional interaction between a circular jet and the flow over a flat plate at $M_\infty = 10$, and compared the results with similar conditions created by forward facing steps. Kaufman (1967) used a two-dimensional situation of finite aspect ratio to study the interaction at freestream Mach numbers from 14 to 21. The latter studies revealed that the interactions with hypersonic streams can produce considerable overpressures downstream of the efflux. The limited number of investigations of the hypersonic interaction problem, have been only partially successful in describing the mechanics of the process. Hence, some disparity exists between the predictions, which are somewhat restrictive, and the observations. Indeed, at the present time, comparison between various sets of experimental results show that the data are generally inconsistent.

The second point mentioned earlier, is that the presence of three-dimensional effects has been noted in all of the cited references. Many of the investigators using finite span slots note that side plates modify their results; an observation which is not entirely unexpected, but one which could be a contributing factor in explaining the lack of agreement in currently available data. These inconsistencies could also be due to a number of other factors, such as the onset of transition in the free shear layer and the variation in wall to free stream temperature ratio during different studies. Because of the uncertainties due to three-dimensional effects, the model in the present series of tests was fabricated as a cone with an injection slot of infinite aspect ratio. The absence of three-dimensional effects associated with this configuration at zero yaw angle, simplifies the study of the hypersonic interaction flowfield by eliminating one of the undesirable features of finite span flat plate models.

2. EXPERIMENTAL METHODS

The interaction study was undertaken at a nominal freestream Mach number of thirteen in a hypersonic shock tunnel which has a $7\frac{1}{2}$ degree conical nozzle and a test section diameter of 51 cm. The shock tunnel operates in a tailored interface mode ($M_0 \approx 3.8$) using helium as the driver gas and air as the test gas. The performance of the tunnel from total and static pressure surveys compares favorably with real gas nozzle predictions based on the conditions in the reflected region. Variation of the test section parameters with the pressure in the reflected region, p_5 , are shown in figure (1). In the present tests the driver pressure p_4 has been varied between 28×10^6 and $110 \times 10^6 \text{ Nm}^{-2}$ which yields a corresponding variation in freestream unit Reynolds number from 1.5×10^4 to $6.5 \times 10^4 \text{ cm}^{-1}$.

A double-pass or coincident schlieren system similar to the type described by Holder & North (1956) is used for flow visualization. The method employs a non-parallel light beam which passes through the test section twice. Since the source and its image are not truly coincident in this method, even in the absence of any density gradients, the image quality is affected by the production of two slightly offset images. The greater sensitivity produced by the beam's double passage through the test section is, however, advantageous when operating at low density levels.

2.1 Mass Injection Technique

Because of the limited volume of the shock tunnel test section, substantial changes in ambient density occur when mass injection is initiated prior to firing; figure (2) shows the variation of test section density as a function of time for various injection rates. This figure illustrates the necessity of obtaining accurate timing in the experiment in order to avoid blockage of the shock tunnel nozzle in the starting process. The threshold levels shown represent the maximum allowable density in the test section to achieve starting the tunnel at driver pressures between 14×10^6 and $110 \times 10^6 \text{ Nm}^{-2}$. It is clear from figure (2) that 3 milliseconds prior to firing the shock tunnel is the maximum lead time available to initiate the secondary mass injection process. This is insufficient to consider a repeatable sequence in which mass injection commences prior to starting the shock tunnel. Thus the necessity arises of undertaking the more repeatable sequence of using a fast acting valve which is actuated after the diaphragms of the shock tunnel have burst.

The technique selected for the program utilizes an exploding valve which is triggered from a speed station on the driven section of the shock tunnel. Tests on the valve characteristics showed that the operating time is 1.2 milliseconds and is repeatable within $\pm 10\%$. A sequential timing operation in the shock tunnel can thus be achieved with this valve without difficulty. The electronic switching of the exploding valve consists of a two stage transistor network shown in figure (3). The bias on the transistor T_1 is set so that a pulse of greater than 3 volts saturates T_2 , and the valve primer which is part of the collector circuit for T_2 then experiences a potential similar to the D.C. supply. The nominal resistance of the primer is 0.9 ohms so that it draws a current in excess of 13 amps until ignition occurs.

2.2 Model Description

The model used throughout the experiments is a right circular cone with a five degree semi-angle and a base diameter of 10 cms. The model is constructed such that the injection can occur around the entire periphery from a slot situated at the half chord point. The slot width can be adjusted by using spacing washers, however, in these tests it had a fixed value of 0.25 mm. The configuration of the model eliminates all three-dimensional effects from the interaction when it has zero yaw angle, a photograph of the components parts is shown in figure (4). The efflux of the injectant issues from the slot which has its minimum area at the cone surface. By operating the slot in an underexpanded condition so that the flow is choked, the mass flux may be computed from the jet reservoir pressure, which is recorded by two piezo-electric pressure transducers.

Thin film thermometers and surface pressure gauges are mounted along three meridians as shown in figure (4), together with an auxiliary set of instruments on the opposite side of the model. This ensures that in the immediate vicinity of the jet the outputs of the instrumentation are similar so that the repeatability of the data can be examined within each test. The model is sting mounted from its base, and a high pressure supply line is connected to the nozzle reservoir. Commercial grade compressed air is used throughout the tests, the reservoir being a standard high pressure bottle the pipeline from which is regulated to a selected lower pressure, and terminates at the normally closed explosive valve.

3. RELEVANT THEORETICAL RESULTS AND PHYSICAL FLOWFIELD MODELS

3.1 Transverse Curvature Effects on a Cone

Transverse curvature effects for compressible axisymmetric laminar boundary layers on slender cones have been studied by Probstein & Elliot (1961). Their results show that when transverse curvature is taken into account, the heat transfer to the surface may be expressed as

$$(q/q_\infty) = 1 + (C/3)^{\frac{1}{2}} (Re)_0^{\frac{1}{2}} \cot \beta \left\{ 0.52 + 0.91 \frac{T_w}{T_0} + 0.12 (Y-1) M_0^2 \right\}$$

for $Pr = 1$. The value of q_m is the heat transfer rate obtained from the Prandtl boundary layer equations using the Mangler transformation as,

$$q_m = 0.332 \sqrt{3} \rho_e u_e (H_r - H_w) (c_e / Re_{x_e})^{1/2}$$

In the slender cone case, the effects of transverse curvature on the surface pressure are negligible. The above results are applicable when the boundary layer thickness is less than the local radius of curvature of the cone.

3.2 Bluntness: Effects on the Flow over Cones

The changes in surface pressure distribution on a conical body due to nose bluntness are well known. Recently, the case of spherical bluntness on conical bodies has been extensively tabulated for ideal gas flows by Roberts, Lewis and Reed (1966). The results that are appropriate to the present tests being described are reproduced in figure (5), which illustrates the extent of the downstream region of influence of the nose bluntness. From this figure we see that for the model used in the present test program, the effect of nose bluntness is felt over the entire body length. The surface pressure distribution is reduced by the overexpansion at the shoulder to about 60 per cent of the inviscid sharp cone values. It is therefore, to be expected that for the same free-stream conditions the jet pressure ratio will be greater on the blunt cone than on the sharp cone configuration. The penetration of the jet into the primary flow will therefore be greater in the former case, and consequently the induced separated region is expected to be larger.

3.3 Separated and Reattaching Flows

Considerable theoretical analysis of separated compressible laminar boundary layer flows are available in the literature. The models which give the qualitative features of the separation interaction are those of Chapman, Kuehn & Larson (1958) and Lees & Reeves (1964). When the boundary layer is separated the flowfield near the separation point is controlled by the interaction between the resultant free shear layer and the external stream. This is generally known as the "free-interaction" region, and is insensitive to the disturbance, or obstacle, which creates the separation. The location of the separation point, however, is a function of the disturbing mechanism, which in the present case is the jet efflux. In the forward region of the separated flowfield, the pressure distribution, and the local surface heating, are controlled by the free-interaction process and are comparable with those due to steps and wedges, etc. The distributions in the neighborhood of the disturbance, are however dependent on the phenomena creating the separation and are therefore closely related to the details of the jet characteristics.

The interaction between a secondary jet and a hypersonic flowfield creates a more complex flow pattern than the classical step or shock induced separated flows. The gross aerodynamic features of such an interaction are given in figure (6) for the case where the jet is highly under-expanded. The boundary layer separates from the surface at S at an angle δ . Part of the jet efflux turns upstream and stagnates the free shear layer at the point P. Fluid contained between the jet boundary and the streamline which terminates at P is thus turned towards the surface forming a region with vorticity opposed to that associated with the free shear layer. A dividing streamline therefore exists between P and the reattachment point R at the surface. Another dividing streamline passes through P and separates the freestream fluid from the effluent. Thus the free stagnation point P has the characteristics of a classical saddle point. Downstream of the jet the flow may reattach to the surface at Q, thus creating a reattachment shock as illustrated. This situation is similar to the flow over a rearward facing step, and is a consequence of the freestream flow becoming over-expanded as it passes across the plume of the jet. It is conceivable that the plume could become sufficiently distorted by the freestream that very little expansion occurs; under these conditions the reattachment shock will be weak or possibly non-existent.

The surface pressure and heat transfer distribution between the points S and R can be expected to be in qualitative agreement with either the simplified Chapman (1958) model or the more refined Lees-Reeves theory. From the former the heat transfer in a separated laminar mixing layer is 1/5 of that for the corresponding attached laminar boundary layer. On the other hand one can expect a rather substantial change to occur between the reattachment point R and the jet exit E.

3.4 Underexpanded Free Jet Analysis

Experimental investigations by Vick et al (1964) have shown that the effects of viscous dissipation and heat conduction are confined to a thin layer along the jet boundary which is small compared to a characteristic jet dimension. The essential features of the jet flowfield can thus be found from inviscid theory by assuming the jet boundary to be a vortex sheet across which the pressure is continuous but the temperature, density and velocity are discontinuous. The method of characteristics has been used by Vick et al (1964), and Love et al (1966), to calculate the inviscid jet boundaries and the results have compared favorably with experimental observations. For a fixed nozzle geometry, exit Mach number and ratio of specific heats, the extent of the jet boundaries are dependent only on the jet pressure ratio. A number of investigators have shown how the interesting characteristics of the same family coalesce to form shock waves inside the jet boundary, which are terminated by a normal shock or Riemann wave. By assuming the pressure downstream of the shock is

equal to the ambient pressure p_a , Lord (1959) derived an expression for the location of the Riemann wave in terms of the jet pressure ratio. The Mach number M_R ahead of the shock can be written in terms of the static pressure ratio across it as

$$(p_a/p_R) = (\gamma+1)^{-1} [2\gamma M_R^2 - (\gamma-1)]$$

Since p_R is related to the jet exit pressure p_j by the isentropic equations, we have

$$(p_R/p_j) = \left[1 + \frac{1}{2}(\gamma-1)M_j^2\right]^{\frac{\gamma}{\gamma-1}} \left[1 + \frac{1}{2}(\gamma-1)M_R^2\right]^{\frac{-\gamma}{\gamma-1}}$$

and hence

$$(p_a/p_j) = \left[\frac{2\gamma M_R^2 - (\gamma-1)}{\gamma+1}\right] \left[1 + \frac{1}{2}(\gamma-1)M_j^2\right]^{\frac{\gamma}{\gamma-1}} \left[1 + \frac{1}{2}(\gamma-1)M_R^2\right]^{\frac{-\gamma}{\gamma-1}}$$

This equation relates the pressure ratio to the Mach number ahead of the Riemann wave and the jet exit Mach number M_j . If we expand for $M_R \gg 1$ we find

$$(p_a/p_j) = 2\gamma(\gamma+1)^{-1} \left[\frac{2}{(\gamma-1)} + M_j^2\right]^{\frac{\gamma}{\gamma-1}} M_R^{\frac{-2}{\gamma-1}} + \dots$$

Now for distances that are large compared to the nozzle dimension, the streamlines have a source like character and Lord (1959) has shown, that to the first-order,

$$M_R = K(x_R/d)^{\frac{\gamma-1}{2}} \quad \text{where} \quad K = K(M_j; \gamma).$$

Combining these two results we find that

$$(x_R/d) = L(M_j; \gamma) (p_j/p_a)^{\frac{1}{2}} + \dots$$

Thus the location of the strong shock wave is proportional to the square root of the jet pressure ratio. For a perfect gas with $M_j = 1$ the value of $L(M_j; \gamma) = 1.45$. A comparison of this result with the experimental data due to Vick et al (1964) is shown in figure (7), where it can be seen that Lord's approximation overestimates the shock location by approximately 50 per cent. A recent analysis by Sibulkin and Gallaheer (1963) has yielded a modified value for $K(M_j, \gamma)$ which for the case under consideration gives a value of $L = 0.95$. This curve is also plotted on figure (7) and is in excellent agreement with the experimental measurements. The agreement between the analysis and the experimental data quoted above is for axi-symmetric jets, and it is not clear at this time whether two-dimensional jets exhibit a similar dependence of the pressure ratio.

4. DISCUSSION OF RESULTS

Typical schlieren photographs taken of the flowfield interaction are shown in figure (8) for both sharp and blunt cone configurations. In order to aid identification in these pictures the shock waves, etc. on one half of each plate have been traced with dashed lines, the other half of the photographs have been directly reproduced. Both plates show similar features to those described earlier, namely a highly underexpanded jet, terminated by a strong shock, which separates the boundary layer ahead of it. The presence of the interaction shock wave ahead of the efflux will undoubtedly cause a modification of the surface heating rate in the jet vicinity, from that predicted by the classical separation analyses.

4.1 Heat Transfer Measurements

The normalized heat transfer results for the sharp cone flowfield with and without the secondary mass injection are shown in figure (9). The results are compared with the analytical predictions for the attached and separated flows due to Frobenstein & Elliot (1950), and Chapman (1956), respectively. The comparison shows that the agreement is very good in the case of the undisturbed

conical flow. For the interaction flowfield, the comparison of the experiment with the Chapman (1954) theory is qualitatively reasonable in the region ahead of the injection point. Note that a region of high heat transfer exists which is attributed to the reattachment ahead of the jet discussed earlier. This phenomena has been previously observed for the three-dimensional flowfield interaction by Poisson-Quinton & Cerenuela (1966). Downstream of the injection annulus the heat transfer rate to the surface is somewhat less than one half the undisturbed cone value throughout the remaining length of the model. The maximum heat transfer occurring just downstream of the efflux is indicative of a reattachment region in that vicinity. The effects on the interaction of varying the freestream Reynolds number while maintaining a constant secondary mass flux are shown in figure (10). The heating in the free interaction regime is seen to decrease substantially with increasing Reynolds number; when the region in close proximity to the injection is reached, the heat transfer rate increases rapidly. With exception of this somewhat confined reattachment zone the Stanton number remains substantially less than the undisturbed conical value. It should be emphasized that maintaining a constant secondary mass flux and changing Re_∞ results in the jet pressure ratio being altered. The ramifications of this effect will be discussed further below.

The effect of nose bluntness on the surface heat transfer rate is given in figure (11) for the same freestream conditions as those in figure (10). It is of interest to note that the efflux occurs in a region where the effect of nose bluntness is most pronounced. Throughout the regime shown by Roberts, Lewis & Reed (1966) to experience the greatest effect of the pressure undershoot, the local heat transfer rate is seen to be considerably less than predicted by the Probstein-Elliott analysis. This prediction is included to illustrate that the blunt cone data asymptotically approach the sharp cone values far from the nose, when there is no efflux. The results obtained with mass injection show that in the upstream separated region the heat transfer rates are similar to those given in figure (10) for the sharp cone, although the Reynolds number dependence appears to be more significant. Downstream of the injection the local Stanton number is less than the undisturbed value but greater than the results shown in figure (10). The appearance of a crest in the heat transfer distribution suggests the presence of a reattachment region, however, there is no evidence of this on any of the schlieren photographs.

4.2 Surface Pressure Measurements

Typical results of the surface pressure distribution on the sharp cone configuration are shown in figure (12) for constant freestream Reynolds number and varying jet pressure ratio. Increasing the jet strength causes a growth in the separation region ahead of the plume. Downstream of the injection annulus an overpressure which extends for some six hundred slot widths, (15 cms), is observed. Near the base of the model the surface pressure is found to be consistently lower than the undisturbed cone values, which are included in figure (12), and illustrate the repeatability of the data. The modification of the downstream surface pressure distribution with secondary mass flux is interesting in that it conflicts with measurements taken with supersonic freestreams, where a significant pressure drop has been observed; see for example Spaid & Zukoski (1968). The present results confirm Kaurtman's (1967) observations of a downstream overpressure at hypersonic freestream Mach numbers. Similar trends in pressure distribution have been found for the case where the jet efflux has been retained constant and the freestream Reynolds number systematically varied. In this case the appearance of peaks and troughs in the pressure distribution similar to those reported by Sterrett and Barber (1966) are observed.

4.3 Schlieren Observations

Measurements of the separation length L due to the mass injection have been made from the schlieren pictures taken during the tests. The separation length is defined as the distance from where the free shear layer intersects the body surface to the forward plane of the injection annulus; viz. the distance SE in figure (6). It must be noted that by varying the Reynolds number in the shock tunnel, the freestream conditions and hence the surface pressure distribution over the cone are proportionately altered, as shown in figure (1). Thus although the mass flux is maintained at a constant value during such tests, the plume pressure ratio changes proportionately with the Reynolds number. The variation of separation length with freestream Reynolds number for both cone configurations is shown in figure (13).

When the secondary mass flux is constant the results in figure (13) show that the separation length diminishes with increasing Reynolds number. If the mass flux is increased at a given Reynolds number, the separation length is seen to increase proportionately. Nose bluntness effectively increases the jet strength by reducing the local surface pressure. Hence for a given mass flux the separation length is greater for the blunted configuration than for the sharp cone case.

Observations of the separation length with constant injection strength for jet pressure ratios at a constant value show that the separation length is independent of the freestream Reynolds number. The implication of this independence is that the geometrical features of the separated region are similar and that the free shear layer is thin enough for the flow parameters to be unimportant. Needham (1966) using the free interaction relationship has demonstrated that the similarity with the Reynolds number independence of the flow geometry must be similar; the only alternative is that the separation angle changes, implicitly requiring a variation in the local Reynolds number. The significance of the free shear layer thickness being small enough for the flow parameters to be unimportant has been demonstrated by Chapman, Kuehn & Larson (1958) who showed that the reattaching edge laminar separation where the secondary layer formed is independent of the Reynolds number. Although the separation length of the jet is independent of the Reynolds number, the independence of Reynolds number effect is not observed for the separation length of the cone apex, the independence of Reynolds number effect is observed for the separation length of the

ness at separation is negligibly small compared to the separation length. The variation of separation length with the jet strength is given in figure (14) which indicates a linear dependence throughout the range of the tests. The freestream Reynolds number dependence is also shown to illustrate the coupling which exists between figures (13) and (14).

4.4 Yaw Effects

The effect of yaw angle may be expected to radically alter the interaction process. This is because the jet penetration will no longer be symmetric about the cone axis, since the undisturbed surface pressure distribution is substantially modified. On the windward side of the cone, therefore, the jet penetration is reduced while on the leeward side the penetration and hence the separation length is increased. Preliminary data obtained for yaw angle effects is given in figure (15) for a constant jet mass flux. The data shows that on the windward side of the cone separation length diminishes rapidly with increasing yaw angle, while on the leeward side the converse is true. On the leeward side of both cone configurations, the separation extends to practically the tip of the model when the cone half angle is equal to the yaw angle. Thus, a large separated region is created which exhibits very strong three-dimensional interactions. Evidence is found on the schlieren pictures of the existence of a reattachment shock downstream of the jet on the windward side of the cone.

5. COMMENTS ON A FLOWFIELD MODEL

A representative flowfield model can be constructed for the underexpanded secondary jet issuing into a primary stream from examination of the schlieren photographs. The primary difficulty is to realistically represent the coupling that exists between the two individual flowfields. In particular, it is necessary to establish the effective pressure ratio that the jet experiences in this type of interaction process. This essentially reduces to achieving a pressure downstream of the jet shock which is compatible with that obtained from the separated flowfield downstream of the interaction shock. This compatibility requirement can be achieved by an iterative procedure between the two individual flowfields.

To illustrate this approach, consider the sketch given in figure (6). When the boundary layer separates from the surface, the angle δ may be determined from the separation shock angle θ and the freestream Mach number. Thus the pressure distribution between the points S and R, which is similar to that along SP is given to a first approximation by the wedge or cone angle formula. The Mach number along the dividing streamline SP has been shown by Chapman, Kuehn & Larson (1958) to be approximately 60 per cent of inviscid value downstream of the separation shock, and can be computed in terms of θ and the freestream conditions. The pressure rise across the interaction shock is estimated by assuming the shock to be normal to free shear layer SP. An effective jet pressure is thus estimated and will yield a value for the jet shock height h , from figure (7). This technique has been applied to the present results and those of Sterrett and Barber (1966) to compare the estimated jet shock height with the observed values. In all cases the comparison showed that the observed jet height exceeded the estimated value by a factor of approximately two. These calculations have assumed that the coefficient of proportionality between the jet shock height and the pressure ratio is identical for the two-dimensional and axis-symmetric jets. Such an assumption appears to be intuitively questionable however until evidence is found to the contrary it is the most logical to use. The agreement between the procedure described and the experimental observations can be improved by relaxing the assumption that the interaction shock is normal to the free shear layer. When this is done, one seeks the oblique shock angle which allows the pressure downstream of the interaction shock to be compatible with the observed jet shock height.

6. CONCLUSIONS

The following conclusions are based primarily on the experimental observations.

1. In the free interaction region ahead of the jet, the heat transfer distribution has been shown to be qualitatively in agreement with the simple separation analysis proposed by Chapman (1957). It is to be expected that the more refined analysis due to Lees & Reeves (1964) would show a more quantitative agreement throughout the free interaction regime.
2. In the vicinity immediately upstream of the jet a reattachment region exists which is characterized by a significant increase in the heat transfer rate. This region corresponds to the high pressure regime observed downstream of the plateau pressure associated with the free shear layer.
3. Downstream of the jet a substantial region is observed in which pressure is found to be greater than the undisturbed inviscid cone value. This is believed to be caused by a reattachment of the primary flow which overexpands as it traverses the plume of the jet. Within this region the local heat transfer rate is observed to be greater than elsewhere on the cone downstream of the jet.
4. The surface heat transfer rate downstream of the jet has been found to be less than the undisturbed flow values. This is attributed to a cooling effect introduced by the secondary fluid which has a recovery temperature significantly less than the primary flow.
5. Measurements of the upstream separation length have shown that it decreases with increasing Reynolds number, when the secondary mass flux is maintained at a constant level. The effect of nose bluntness is to increase the separation length by about 60 percent. This is attributed to an increased jet pressure ratio caused by the local pressure drop resulting from the nose bluntness.

6. When the jet pressure ratio is held constant the separation length is observed to be independent of freestream Reynolds number. This observation implies that the free shear layer downstream of separation is thin enough for viscous parameters to be unimportant.

7. Estimates of the jet shock height based on a number of simplifying assumptions have been found to agree with the observed values to within a factor of two. Relaxing the assumption that the interaction shock is normal to the free shear layer allows this agreement to be considerably improved, and forms the basis for an iterative procedure to couple the two individual flowfields.

ACKNOWLEDGMENTS

I am indebted to Drs. H. Gold and B. Reeves for their helpful remarks concerning the analysis of jets and interaction flowfields. The advice and assistance offered by Dr. C. E. Smith and the cooperation of a number of my colleagues is also gratefully acknowledged. The work described herein has been supported by a company sponsored IRAD Program.

REFERENCES

- Broadwell, J. E., (1963) AIAA Journal 1, 1067-1075.
- Chapman, D. R. (1956) NACA TN 3792
- Chapman, D. R., Kuehn, D. M. and Larson, H. K. (1958) NACA TR 1356.
- Charvat, A. F. and Allegre, J. (1965) AIAA Journal 2, 1965-1971.
- Gregorek, G. M. and Luce, R. G. (1966) ARL Rept 66-0068.
- Holder, D. W. and North, R. J. (1956) AGARDograph 23.
- Hsia, H. T., Seifert, H. S. and Karamcheti, K. (1965) J. Spacecraft 2, 67-72.
- Kaufman, L. G. (1967) AIAA Preprint 67-190. Presented at 5th Aerospace Sciences Meeting.
- Lees, L. and Reeves, B. L. (1964) AIAA Journal 2, 1907-1920.
- Lord, W. T. (1959) RAE Farnborough Rept. Aero 2626.
- Love, E. S., et al (1959) NASA TR R-6.
- Maurer, F. (1966) AGARD Conference Proceedings No. 4.
- Needham, D. A. (1966) University of London Ph.D. Thesis.
- Poisson-Quinton, P. and Ceresuela, R. (1966) ONERA Rept TP365 (presented at 5th ICAS Congress, London).
- Probstein, R. F. and Elliot, D. (1956) J. Aero Sci. 28, 208-224.
- Romeo, D. J. and Sterrett, J. R. (1961) NASA TN D-743.
- Roberts, J. F., Lewis, C. H. and Reed, M. (1966) AEDC-TR-66-121.
- Sibulkin, M. and Gallaher, W. H. (1963) AIAA Journal 1, 1452-1453.
- Spaid, F. W. and Zukoski, E. E. (1968) AIAA Journal 6, 205-212.
- Sterrett, J. R. and Barber, J. B. (1966) AGARD Conference Proceedings No. 4.
- Sterrett, J. R., Barber, J. B. and Alston, D. W. (1967) NASA TN D-3795.
- Taylor, G. I. (1954). Scientific Papers 3, 537-540 ed. G. K. Batchelor. Cambridge University Press.
- Vick, A. K. et al (1964) NASA TN D-2327.
- Zukoski, E. E. and Spaid, F. W. (1964) AIAA Journal 2, 1689-1696.

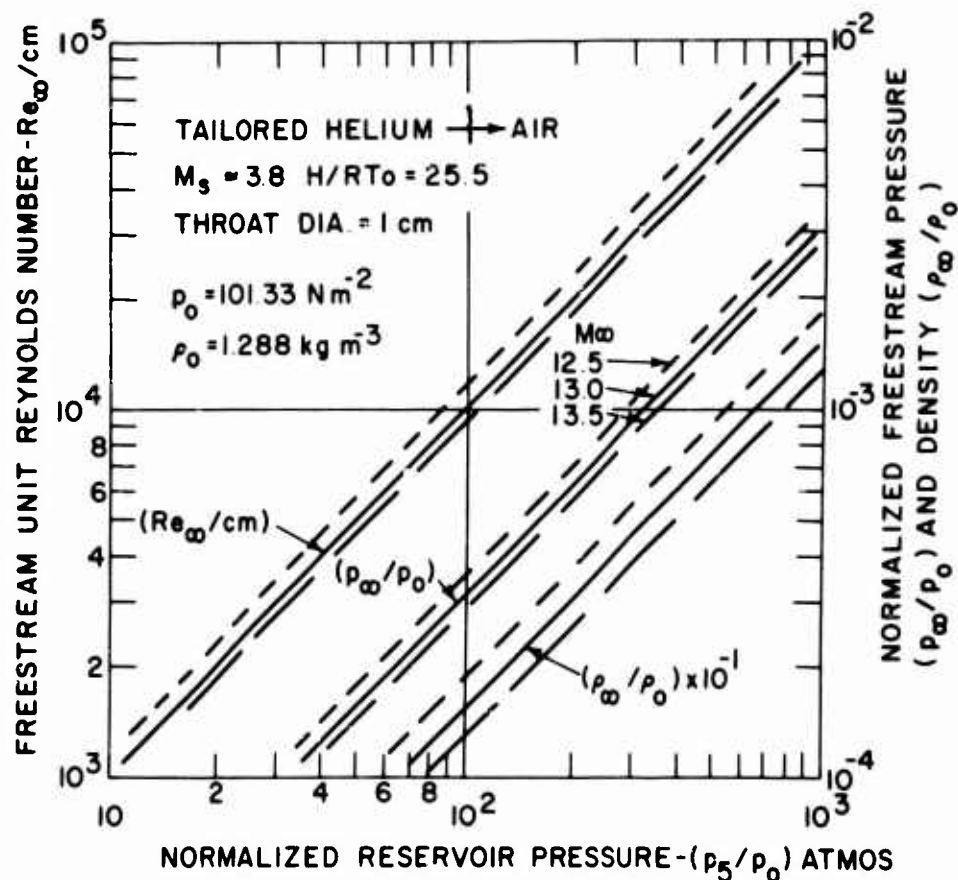


Fig. 1 Variation of the Shock Tunnel Test Section Conditions with Reservoir Pressure for Tailored Interface Operation.

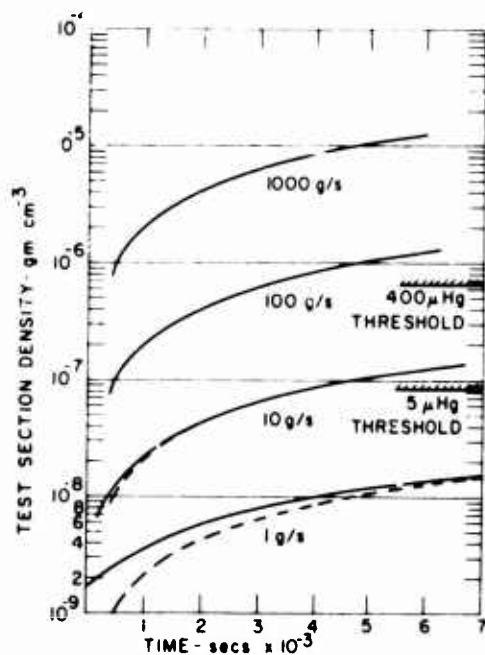


Fig. 2 Change in Test Section Density Due to Mass Injection Based on an Initial Vacuum of 1 micron

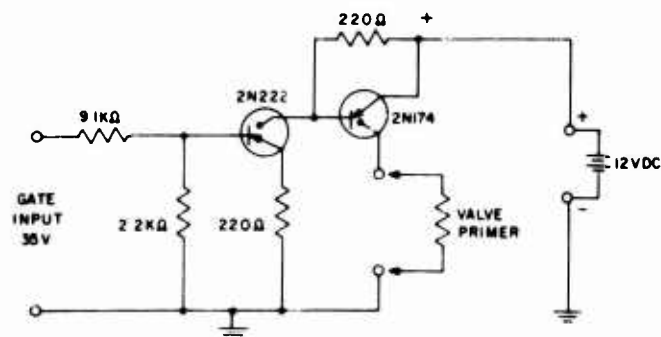


Fig. 3 Transistor Network Used for Switching the Explosive Valve

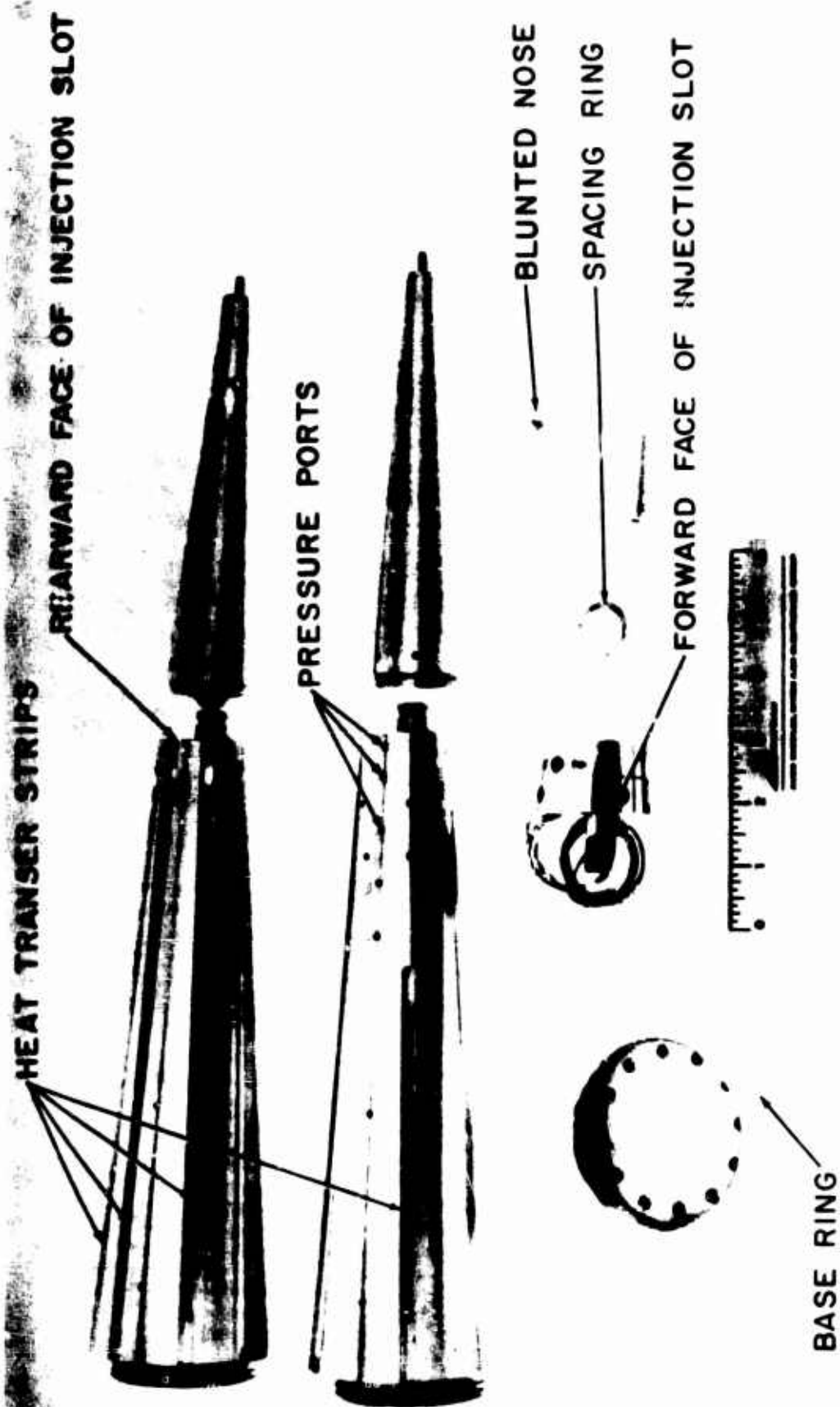


Fig. 4 Photograph of the Dismantled Model

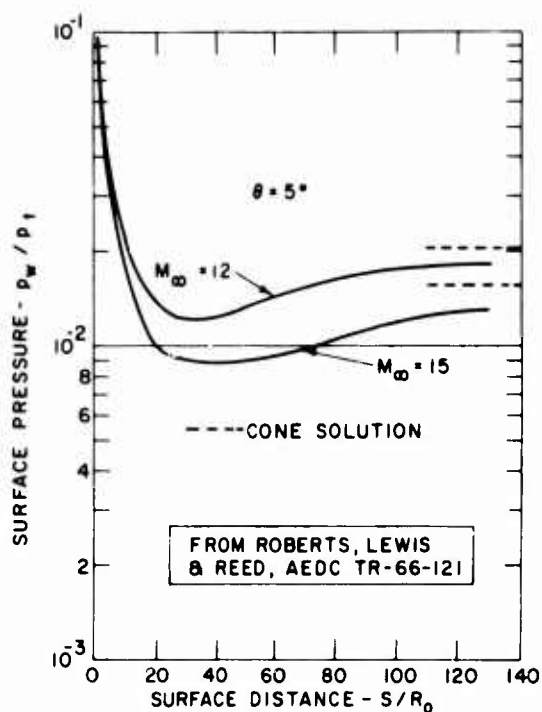


Fig. 5 Surface Pressure Distribution Along a Spherically Blunted Right Circular Cone

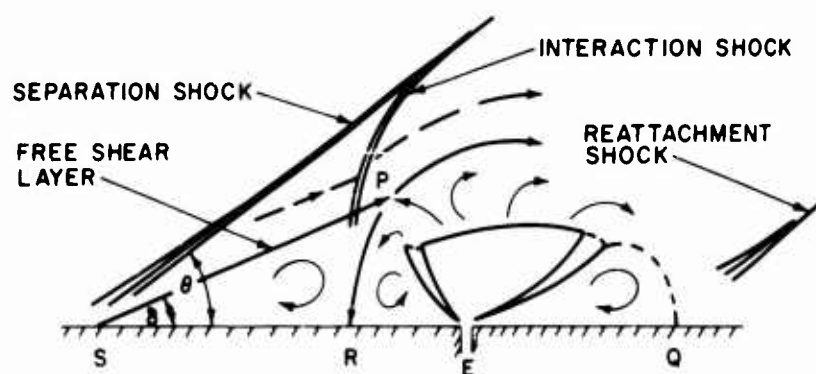


Fig. 6 Schematic of the Interaction Flow Field for an Underexpanded Jet

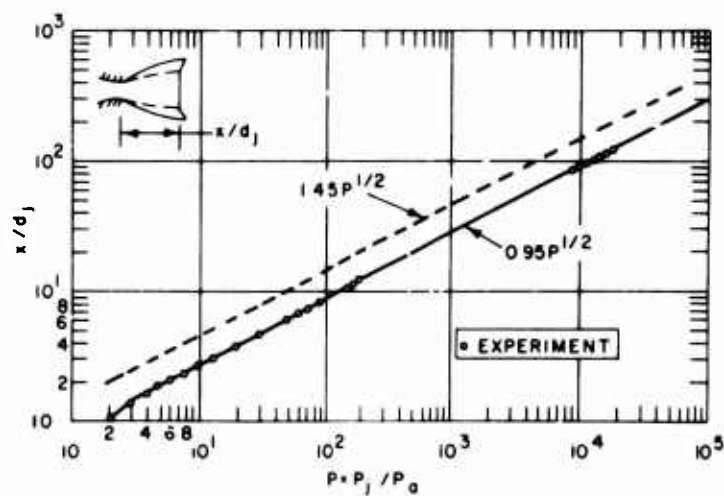


Fig. 7 Effect of Jet Pressure Ratio on the Axial Location of the First Riemann Wave in an Underexpanded Plume; $M_j = 1.0$; $\gamma = 1.4$

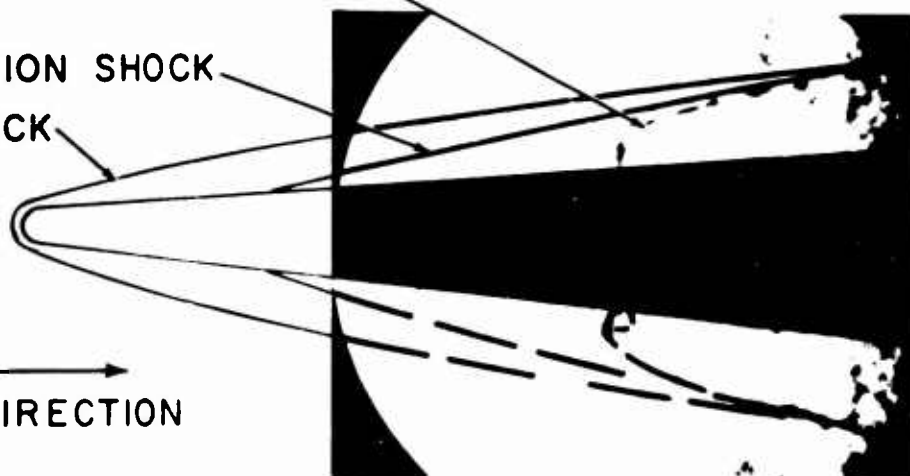
INTERACTION SHOCK
SEPARATION SHOCK
SHEAR LAYER



a) $M_\infty = 13$; $Re_{\omega_D} = 4 \times 10^5$; $\dot{m} = 3.4 \text{ gm sec}^{-1}$

INTERACTION SHOCK
SEPARATION SHOCK
BOW SHOCK

FLOW DIRECTION



b) $M_\infty = 13$; $Re_{\omega_D} = 2.2 \times 10^5$; $\dot{m} = 3.4 \text{ gm sec}^{-1}$

Fig.8 Typical Schlieren Photographs of the Jet Interaction Flow Field
(a) Five Degree Cone (b) Blunted Cone

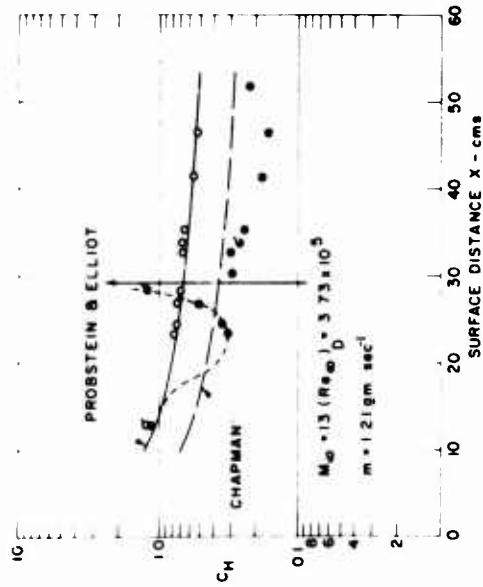


Fig. 9 Heat Transfer Distribution Along the Five Degree Cone Showing the Effect of Secondary Mass Injection

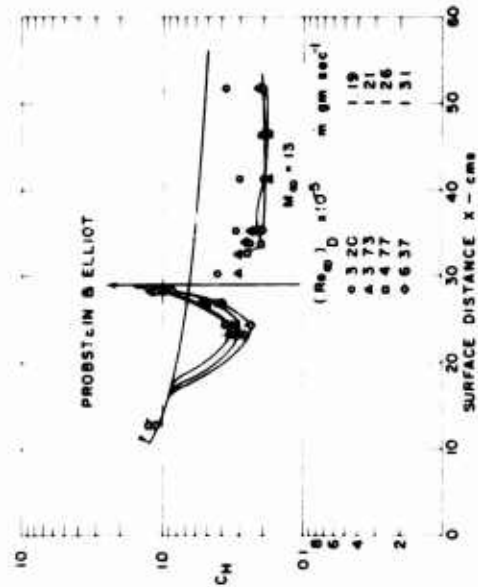


Fig. 10 Heat Transfer Distribution for Various Freestream Reynolds Numbers and Constant Secondary Mass Flux

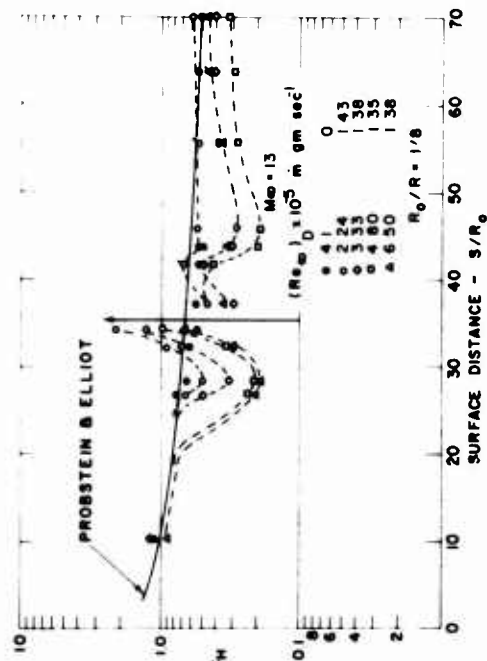


Fig. 11 Heat Transfer Distribution Along the Blunted Cone Surface for Various Freestream Reynolds Numbers and Constant Secondary Mass Flux

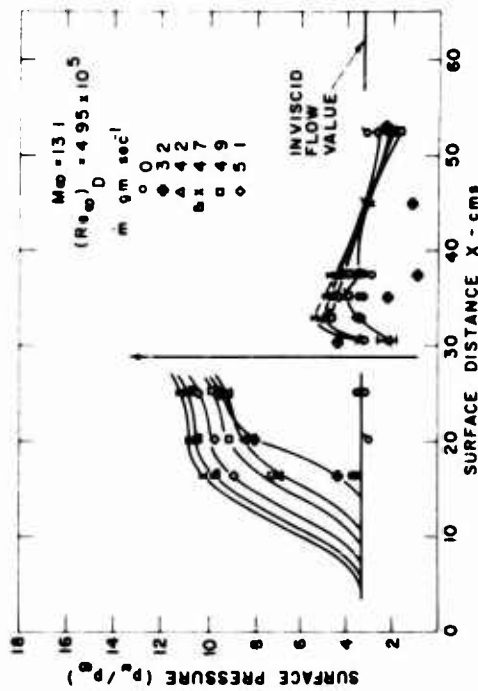


Fig. 12 Surface Pressure Distribution On the Cone for Various Jet Pressure Ratios and Constant Reynolds Number

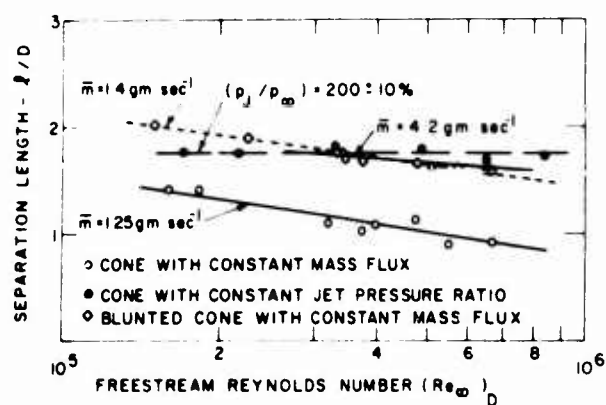


Fig. 13 Variation of Separation Length with Free-stream Reynolds Number

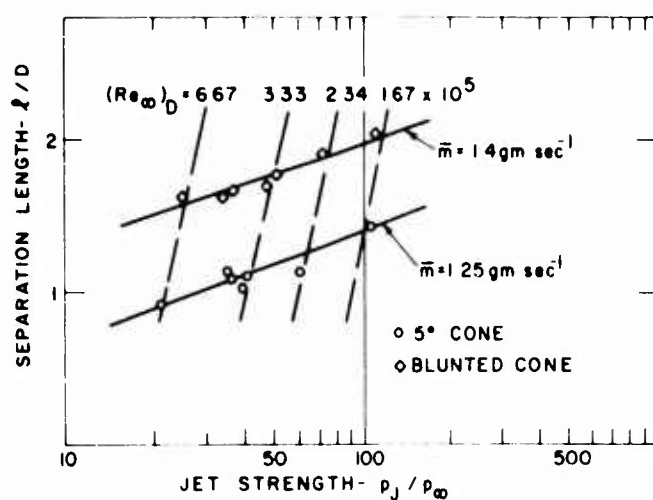


Fig. 14 Variation of Separation Length with Jet Pressure Ratio

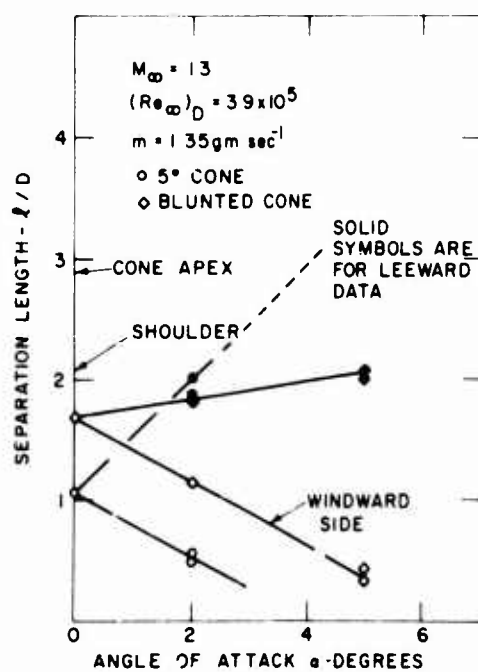


Fig. 15 Variation of Separation Length with Angle of Attack at Constant Mass Flux

HYPERSONIC FLOW IN RECTANGULAR
AND NON-RECTANGULAR CORNERS

by

R. J. Cresci, S. G. Rubin, and C. T. Nardo

Department of Aerospace Engineering
and Applied Mechanics
Polytechnic Institute of Brooklyn
Farmingdale, New York

This research was supported by the Air Force Office of Scientific
Research Under Contract No. AF 49(638)-1623, Project No. 9781-01.

SUMMARY

An investigation of the behavior of the three-dimensional hypersonic flow along intersecting planes has been conducted, considering both the viscous and inviscid flows and their mutual interaction.

The experimental program involves measurements of surface pressures and heat transfer rates in the vicinity of corners with various included angles. The local forces and shear stresses can be obtained thereby, yielding some information on the nature of the three-dimensional boundary layer behavior in this region. Pitot pressure profiles are also obtained and utilized in the determination of the complex intersecting shock structure in the corner. The test data were obtained at a nominal free stream Mach number of 12 and a Reynolds number producing values of $\bar{\chi}$ as high as 15.

A theoretical analysis of the corner flow is obtained by using the finite difference solution technique previously proposed by Rubin and extended here to the three-dimensional corner configuration. The results are compared to the experiments where applicable.

NOMENCLATURE

$C = T_{\infty} \mu / T \mu_{\infty}$	Chapman-Rubesin constant
$C_f = \tau_w / \rho_{\infty} U_{\infty}^2$	skin friction coefficient
$C_F = C_f / \bar{V}^{1/2}$	normalized skin friction coefficient
$C_p = [p/p_{\infty} - 1] / \bar{\chi}$	normalized pressure coefficient
H	stagnation enthalpy
k	coefficient of thermal conductivity
M	Mach number
p	pressure
$q = (k \partial T / \partial y)_w$	heat transfer rate
$Re_x = \rho u x / \mu$	Reynolds number based on x
$Re_{\infty} = \rho_{\infty} U_{\infty} / \mu_{\infty}$	free stream Reynolds number
$St = q_w / \rho_{\infty} U_{\infty} (H_{\infty} - H_w)$	Stanton number
T	temperature
u	velocity in the streamwise direction
$\bar{V} = \bar{\chi} / M_{\infty}^2$	rarefaction parameter
x	coordinate in the streamwise direction
y	coordinate along vertical surface normal to x axis
Y_s	shock displacement thickness
z	coordinate along horizontal surface normal to x axis
γ	ratio of specific heats
δ	boundary layer thickness
$\bar{z} = z / \delta_{1-D}$	z coordinate normalized with respect to boundary layer thickness
$\eta = y Re_{\infty} / \sqrt{x} M_{\infty}^2$	non-dimensionalized surface coordinate along vertical plate
μ	coefficient of viscosity
$\xi = z Re_{\infty} / \sqrt{x} M_{\infty}^2$	non-dimensionalized surface coordinate along horizontal plate
σ	Prandtl number
$\tau = (\mu \partial u / \partial y)$	shear stress
φ	corner included angle
$\bar{\chi} = M_{\infty}^3 \sqrt{C / Re_{x_{\infty}}}$	viscous-inviscid interaction parameter

SUBSCRIPTS

e	conditions external to boundary layer
s	stagnation conditions
w	conditions evaluated at the surface
$z \rightarrow \infty$ $y \rightarrow \infty$ zD	flat plate conditions
∞	free stream condition
2	conditions behind a normal shock

I. INTRODUCTION

An investigation of the detailed behavior of three-dimensional hypersonic flow along intersecting planes has been conducted for free stream conditions corresponding to the strong interaction regime. This problem, in addition to its basic scientific interest is directly applicable to lifting configurations traveling at high velocities and high altitudes. Although the general problem of flow along a corner has been studied quite extensively in the past as is evidenced by the comprehensive review of ref. (1), there is not a great deal of information available in the regime of viscous-inviscid interaction. Theoretical treatments of the boundary layer flow have been restricted to uniform external flow conditions⁽²⁻⁴⁾ while even for low supersonic velocities it has been shown both theoretically⁽⁵⁾ and experimentally⁽⁶⁾ that the outer inviscid flow is highly non-uniform in the corner region.

As a result, most of the information that has been obtained concerning corner flows has relied heavily on experimental data due to the difficulties connected with a theoretical treatment of the problem by standard techniques, i.e., by matching a three-dimensional boundary layer flow with a highly non-uniform inviscid flow in which strong shock waves may be present.

Recently, a new technique has evolved for analyzing high Mach number, low density flows⁽⁷⁾ over a sharp, flat plate. Therein it was shown that streamwise pressure gradients and streamwise velocity gradients appearing in the viscous terms are negligible in the streamwise momentum equation, thus allowing the governing equations to be formulated in such a manner that a forward integration scheme is possible. The boundary conditions applicable to the problem are specified at the body surface and in the undisturbed stream such that "matching" of boundary layer, inviscid layer, and shock layer is unnecessary. The location of the shock and the flow conditions in the inviscid layer, therefore, need not be known a priori since the same system of equations apply throughout the entire region between the body and the undisturbed free stream. As a result, the shock formation and configuration will be generated in the solution of the equations. Although this is a distinct advantage even for two-dimensional or axisymmetric flows, it is quite essential for analysis of the complex three-dimensional flows of interest here.

The present paper, therefore, presents the results of a combined experimental and theoretical program concerning the hypersonic, strong interaction flow in a corner formed by two sharp, flat plates. The experimental study was conducted at a free stream Mach number of 11.2 and a Reynolds number of $1.5 \times 10^4/\text{in.}$ The configuration tested consists of two sharp, flat plates intersecting to form a corner of various included angles. Data taken consist of surface pressures and heat transfer rates and also pitot pressure and total temperature surveys in a cross plane corresponding to a value of $X = 5$. Shock shapes and some indication of the boundary layer behavior can be inferred from these measurements. The theoretical analysis corresponding to these free stream conditions was performed using the three-dimensional counterpart of the Rubin-Rudman⁽⁸⁾ analysis which is described briefly in Section IV.

The authors are pleased to acknowledge the assistance of the staff of the Gas Dynamics Laboratory in conducting the experiments and analyzing the data and in particular to Prof. M. H. Bloom for his interest and suggestions throughout the program. The authors would also like to thank Mr. Tony C. Lin for his help with the computations.

II. EXPERIMENTAL APPARATUS

The wind tunnel used for the present test program is a Mach 12 (nominal) variable Reynolds number blowdown tunnel, a detailed description of the complete facility including the tunnel design, heater, air supply, etc. is given in ref. (9). Fig. (1) shows a schematic of the test model which is the same as that used in ref. (10), with an additional modification which allows the corner angle to be varied. Further details of the model and probe design can be found in ref. (11). The present tests were run for interior angles of 60° , 90° , and 120° , at a free stream Mach number of 11.2 which corresponds to the particular test Reynolds number of the present program ($Re_\infty = 1.5 \times 10^4/\text{in.}$). Each test duration is on the order of 3-4 seconds, thus providing an essentially constant model surface temperature during the test. For the range in stagnation temperatures achieved (1650°R - 1800°R), the wall to stagnation temperature ratio was between 0.30 and 0.33.

Surface heat transfer rates were obtained using thin plates with thermocouples spot-welded to the unexposed surface, cf. Fig. (1). For the plate thickness and range of heat rates obtained, the uniform temperature distribution across the plate permitted the heat transfer rate to be computed from the back-side temperature history.

Stagnation temperature profiles are obtained using open tip thermocouples. The response of the thermocouple wire (0.001 inch diameter) is sufficiently rapid to achieve the adiabatic wall temperature well within the run duration. No corrections are made in the raw

data to convert from adiabatic wall to stagnation temperature since (i) the scatter in the measured data is greater than the error incurred in neglecting the correction, and (ii) all the data is normalized with respect to the free stream stagnation temperature which is obtained from the same type of probe. This normalization will tend to eliminate (or at least decrease) the overall error. On the basis of repeatability and the method of data reduction, the overall accuracy of the temperature data is believed to be within $\pm 5\%$.

Pitot pressure profiles are obtained with standard type, blunt probes mounted on a movable rake. In order to determine the shock location within the desired degree of accuracy, the probes used have an OD of 0.060" and an ID of 0.045". This was found to be the smallest tube size that could be used with good response in the test times available. Since the measured pressure level extended over a range of three orders of magnitude between the surface and the free stream, several different types of pressure sensing instruments were necessary. In the vicinity of the surface, where the pressure is on the order of the free stream pressure, Hastings type, heated thermopile, high vacuum gauges are used, for pressures between 5 and 40mm of mercury, variable reluctance type diaphragm transducers are used, while in regions adjacent to intersecting shock waves, the pitot pressures are sufficiently high to require the use of Statham strain gauge transducers. Whenever the transducer type was changed, several points in the profile were overlapped to assure continuity between the different instruments. The overall accuracy of the pressure measurements is $\pm 5\%$.

Alignment of the model in the tunnel is quite critical since even a small angular change can produce a change in the shock location. The horizontal plate was aligned to within $\pm 10'$ of angular deflection; the fin, however, presented more of a problem, particularly for the 60° and 120° configurations. As will be noted in the pitot profile data obtained for the 60° included angle, there is sufficient misalignment to alter the two-dimensional shock location by approximately 10%. Even though this does create some asymmetry about the bisecting plane, it is not considered sufficient to alter the general flow behavior in the corner region. For the 90° corner, the asymmetry is considerably less.

III PRESENTATION OF EXPERIMENTAL DATA

The surface heat rates are presented in figures (2a) through (2d), as a function of distance from the corner, for various values of \bar{X}_0 and included angles of 60° to 120° . Similar data were obtained in reference (10) for the 90° configuration. The typical behavior can be observed in figure (2a); the heat transfer increases from zero at the corner to a peak value above that of an infinite flat plate and then decreases to the flat plate value away from the corner. For the smaller included angle, higher peak heating rates result and, in addition, the location of the peak occurs further from the corner. As \bar{X} decreases (as one proceeds downstream) the peak decreases and also moves away from the corner. As the included angle increases, the overall heat transfer approaches that of a two-dimensional plate with only an extremely small region of low heat transfer in the immediate corner region. The peak heating rates in terms of the Stanton number are shown in figure (3) as a function of \bar{X} including the data of reference (10) and the lower Mach number ($M_\infty = 8.0$) data of reference (1). The theoretical analysis of reference (12) is also shown for comparison. It can be observed that two different theoretical curves result for the two sets of data obtained at different free stream Mach numbers. This results since the heat transfer parameter that correlates with the viscous interaction parameter (χ) is $M_\infty St$ rather than the Stanton number alone. In either case, the two-dimensional data agrees quite well with the boundary layer theory for low \bar{X} . The experimental data for the 60° and 90° corner angles, however, appear to correlate directly in terms of \bar{X} for the two sets of data, indicating that the peak heating is dominated more by the three-dimensional, strong interaction effects in the corner than by usual boundary layer behavior even at lower values of \bar{X} . The location of the peak value of Stanton number with respect to the local two-dimensional boundary layer thickness is noted in Fig. (2) where the boundary layer thickness on an infinite plate is included for each value of \bar{X} . As observed in ref. (10), where $\Phi = 90^\circ$, the peak seemed to occur approximately at a distance equal to the two-dimensional boundary layer thickness from the corner. In the present case, the peak is farther from the corner for $\Phi = 60^\circ$ and slightly closer than the local δ_{2D} for $\Phi = 120^\circ$. In fact, the location of maximum heating appears to correspond to the position of intersection of the undisturbed two-dimensional boundary layer edges on each surface.

In addition to the surface heat transfer data, profiles of pitot pressure and total temperature were obtained in a cross plane corresponding to a value of $\bar{X} = 5.0$ for $\Phi = 90^\circ$ and $\Phi = 60^\circ$. In order to compute the local velocities and velocity gradients, the surface static pressures were also obtained. These are shown in Fig. (4) for the two corner angles. The pressure was not measured exactly in the corner; however, from the data close to the line of intersection, it is observed that the surface pressure increases slightly at first before decreasing to the local two-dimensional value away from the corner. Comparison of the data at interior angles of 60° and 90° indicates a much higher overpressure for the smaller angle and also a slower decay to the local two-dimensional value. This is consistent with the surface heat transfer data where the corner region of disturbance is also more extensive for the smaller included angle.

Typical pitot pressure profiles are shown in Figs. (5a) through (5e) for both the 60° and 90° corners at $\bar{x} = 5.0$. The value indicated for the "y" coordinate is measured from the fin surface; therefore, for the 60° corner, constant values of "z" do not correspond to a profile perpendicular to the plate but to one inclined at 60° to the surface. Fig. (5e) shows the complete two-dimensional pitot profile at $\bar{x} = 5.0$ taken at a value of "y" sufficiently far from the corner to correspond to a completely two-dimensional flow. Since the data for $\phi = 60^\circ$, along a line of constant "y", does not correspond to a profile normal to the fin surface, the data was plotted as a function of the actual normal coordinate ($z \sin \phi$) to facilitate comparison between the two sets of data. It is observed that the shock location on the fin for the 60° corner is slightly less than in the 90° corner; this is due to some misalignment of the fin during the model assembly.

From the surface static pressure distribution of Fig. (4) and the pitot pressures close to the wall, the local skin friction coefficient can be obtained. These data are shown in Fig. (6) for $\phi = 60^\circ$ and $\phi = 90^\circ$, with the skin friction normalized with respect to the local two-dimensional value and the surface coordinate normalized with respect to the two-dimensional boundary layer thickness. It is observed that the peak does not change significantly; however, the distribution does. For the smaller corner angle, the peak skin friction moves outward and exhibits a slower decay to the local two-dimensional value. This effect was also observed in the surface pressure and heat transfer rates.

The location of the imbedded shocks can be determined quite closely from the pitot pressure plots as the region where a discontinuity in pitot pressure results. In Fig. (5c), for example, the $\phi = 90^\circ$ configuration indicates a shock wave at $z \approx 1.15$ inches and a weaker shock at $z \approx 1.05$ inches. Comparison of the data for the two different corner angles shows a distinct difference in the flow behavior. For the 60° angle, the shock waves are significantly stronger as characterized by the greater jump in pitot pressure across them. Due to the complicated nature of the flow in the corner, it is difficult to establish the overall shock pattern and general flow behavior from these plots. One can get a better picture of the entire flow pattern if one examines, for example, a physical cross section of the corner region with contours of constant pitot pressure. This is shown in Fig. (7) for both corner angles at $\bar{x} = 5$. The differences in the shock pattern for the two corner angles is made more obvious in these plots. For the 90° corner, the bifurcated shock in the corner intersects the two-dimensional shock and appears to generate two additional shock waves at each end, one approaches the plane of symmetry and is rapidly attenuated while the other approaches the plate surface and extends into the boundary layer. In the 60° configuration, however, the extent of the bifurcated shock is decreased considerably and generates only one additional shock at its point of intersection with the two-dimensional shock wave. This shock also extends into the boundary layer and is considerably stronger than in the 90° case. The two pitot pressure peaks existing in the 90° corner have also degenerated into one peak (of larger size) in the 60° corner region.

Stagnation temperature profiles were also obtained and are shown in Figs. (8a) through (8d) for $\phi = 60^\circ$, and $\bar{x} = 5$. The region of influence on the stagnation temperatures is considerably smaller than either the pitot pressures or the heat transfer since here the variation is confined to the boundary layer in the corner. The behavior in this case is quite similar to that obtained in the 90° corner, cf., ref. (10), where a high temperature core occurred in the immediate vicinity of the corner. This is believed to be caused by the streamwise vortices existing on either side of the corner plane of symmetry.

IV THEORETICAL ANALYSIS

The theoretical analysis used in the corner flow problem is analogous to that presented in ref. (7), where a detailed description of the method as it applied to two-dimensional flow appears. An outline of the technique, as well as the complete three-dimensional equations, is given in ref. (8) where a finite width flat plate is considered. The calculation discussed herein was performed on the CDC 6600 computer and required 40 minutes to reach $V = 0.34$. For the present problem, rather than consider the entire corner region and specify the boundary conditions at ∞ and at the surface, the plane of symmetry was chosen as a boundary surface in order to reduce the calculation time and required storage capacity by one-half. Across this surface (a plane inclined at 45° with respect to the horizontal surface), the components of velocity in the "y" and "z" directions are symmetric with respect to one another. This permits the computation to be initiated in the corner (for a given value of the streamwise coordinate "x") and extended outward for increasing "y" and "z". Once the free stream conditions are realized in the y direction, or the plane of symmetry, is reached, the analysis continues outward (in the "z" direction) until the two-dimensional profile is obtained, i. e., flow properties change with z by less than a specified amount, say 10^{-5} .

The non-dimensional governing equations are:

$$\text{Continuity: } (\rho u)_x + (\rho v)_y + (\rho w)_z = 0$$

$$\text{x-Momentum: } \rho u u_x + \rho v u_y + \rho w u_z = (\mu u_y)_y + (\mu u_z)_z$$

$$\text{y-Momentum: } \rho u v_x + \rho v v_y + \rho w v_z = -p_y + \frac{4}{3} (\mu v_y)_y + (\mu w_z)_z + (\mu u_x)_x - \frac{2}{3} (\mu u_x)_y + (\mu w_y)_z - \frac{2}{3} (\mu w_z)_y$$

$$\text{z-Momentum: } \rho u w_x + \rho v w_y + \rho w w_z = -p_z + \frac{4}{3} (\mu w_z)_z + (\mu v_y)_y + (\mu u_x)_x - \frac{2}{3} (\mu v_y)_z - \frac{2}{3} (\mu u_x)_z + (\mu v_z)_y$$

$$\text{Energy: } \rho u T_x + \rho v T_y + \rho w T_z = -(\gamma-1)p(u_x + v_y + w_z) + \frac{\gamma}{\sigma} (\mu T_y)_y + \frac{\gamma}{\sigma} (\mu T_z)_z + \gamma(\gamma-1)M_\infty^2 \left(u \frac{\partial}{\partial x} (u^2 + v^2 + w^2) + \frac{4}{3} \mu (\gamma-1) (v \frac{\partial}{\partial y} w^2 + w \frac{\partial}{\partial z} v^2) + (\gamma-1) \mu (w_y + v_z)^2 \right)$$

$$\text{State: } p = \rho T$$

p, ρ, T and u are non-dimensionalized with free stream conditions, u with $u_\infty M_\infty$, v and w with $u_\infty \delta$, x with \bar{x} , and y and z with δ . Where $\delta = (\gamma M_\infty^2)^{-1/2}$.

$$\bar{x} = \gamma M_\infty^2 (u_\infty / \rho_\infty U_\infty); \quad \bar{\delta} = \delta \bar{x}$$

The Sutherland viscosity law, and constant values of $\gamma=1.4$ and $\sigma=\mu c_p/k=0.75$, were used throughout. Uniform initial conditions, except at the surface where slip conditions prevailed, were prescribed.

$$\text{Boundary Data: } y=0, z>0: v=0, T=T_w + \frac{2\gamma}{\gamma-1} \frac{1}{\sigma} T_y, u=\lambda u_y, w=\lambda (w_y + (8\pi T)^{-1/2} T_z).$$

Across $y=z$: u, ρ, T are symmetric, $v(y, z)=w(z, y)$

The velocities v and w are not set equal along the diagonal but remain so throughout the calculation. The lateral temperature slip effect (T_z) on the lateral slip velocity w was rather small, less than 7%, but for higher stream Mach numbers this effect might prove more significant.

The analysis was applied to the current test conditions for the 90° corner. To date, numerical computations have been carried downstream to a value of \bar{V} of 0.34, which corresponds to $\bar{x}=42$. The analysis will be extended to lower values of \bar{V} to attempt to reach the strong interaction region of the present wind tunnel tests. Although the analysis at $\bar{x}=42$ corresponds to a region which is still characterized as a "merged" layer, the data was compared to the theoretical results and reasonably good qualitative agreement results. The experimental data are normalized in the same manner as the analytical, nondimensional, coefficients for surface pressure and skin friction coefficient in Figs. (9) and (10), respectively. Fig. (9) presents the surface pressure as a function of distance from the corner where the nondimensional coordinate, \bar{s} , is the physical distance normalized with respect to the local two-dimensional boundary layer thickness. It should be noted that since the analytical results correspond to $\bar{V}=0.34$, which is still in the merged layer regime, there is little difference between the viscous layer and the shock layer. Notwithstanding these differences, the agreement between the surface pressure data for $\bar{x}=5-9$ and the analytical results for $\bar{x}=42$ appears to be quite good both qualitatively and quantitatively. Even the initial increase in pressure going away from the corner, which was noted in the experiments, is indicated in the theoretical curve only to a much lesser degree.

The comparison of measured and computed skin friction, as seen in Fig. (10), is qualitatively consistent but somewhat disparate in the magnitude of the predicted peak level. It may also be noted that the theoretical skin friction coefficient is not equal to zero at the corner intersection since there is still some surface slip at these values of the rarefaction parameter. The theoretical surface heat transfer distribution exhibits the same type of behavior as the skin friction except that the peak is considerably higher than the local two-dimensional value; this was also observed in the experimental data.

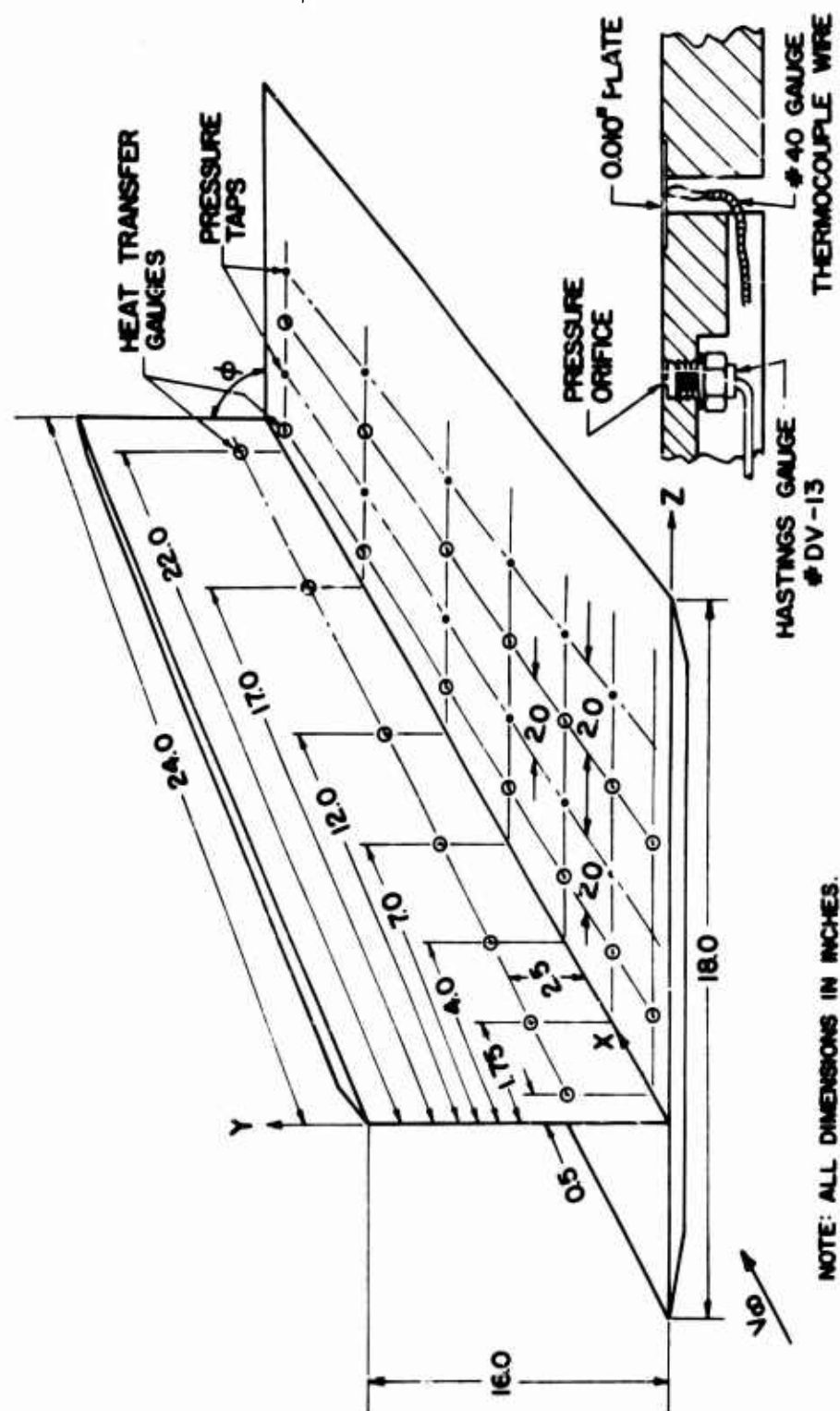
Some indication of the nature of the corner flow field predicted by the analysis can be observed by constructing a contour map of isobars. This is shown in Fig. (11) where an immediate, if not exact, correspondence can be seen in comparison with the experimental pitot pressure contours of Fig. (7). The two-dimensional shock wave is displaced as it approaches the corner and forms a bifurcated shock with branches extending toward the plane surfaces through the boundary layer. A more complete comparison in terms of total temperatures and pitot pressures will be performed when the analytical results have been extended downstream into the strong interaction regime.

V. CONCLUDING REMARKS

A combined theoretical and experimental program has been carried out in connection with the viscous-inviscid interaction of corner flows. Surveys of surface data and flow field data have been obtained experimentally in the PIB hypersonic tunnel in an attempt to provide a better understanding of the corner flow phenomena and also to compare with analytical results. The three-dimensional analysis initially proposed in two-dimensional form in ref. (7) has been applied to the corner problem with the corresponding free stream conditions. Despite the fact that the analysis was not extended sufficiently far downstream to correspond to the physical location on the model at which data were obtained, the agreement between the analytical and experimental results is remarkable. Surface pressure distributions are predicted quite accurately while the skin friction and heat transfer are qualitatively similar in behavior. The overall flow field is also seen to agree quite well with the experiments, both in the prediction of the type of shock intersection and the imbedded shock locations within the viscous-interaction layer. Clearly, it is desirable to extend the analytical computations further downstream to obtain a more quantitative comparison and also to run some additional experiments in the "merged layer" regime which can be compared to the present theoretical predictions.

REFERENCES

1. Stainback, P. C. and Weinstein, L. M. "Aerodynamic Heating in the Vicinity of Corners at Hypersonic Speeds". NASA TN D-4130, November 1967.
2. Carrier, G. F. "The Boundary Layer in a Corner", Quarterly Appl. Math., Vol. IV, No. 4, pp. 367-370, January 1947.
3. Bloom, M. H. and Rubin, S. G. "High-Speed Viscous Corner Flow", J. Aero. Sci., Vol. 28, No. 2, pp. 145-157, February 1961.
4. Rubin, S. G. "Incompressible Flow Along a Corner. Part I: Boundary Layer Solutions and Formulation of Corner Layer Problem". Polytechnic Institute of Brooklyn, PIBAL Report No. 876, AFOSR 65-1420, AD 621987, May 1965.
5. Wallace, J. and Clarke, J. H. "Uniformly Valid Second-Order Solutions for Supersonic Flow Over Cruciform Surfaces". Brown University, Report No. CM-1019, June 1962.
6. Charwat, A. F., and Redekopp, L. G. "Supersonic Interference Flow Along the Corner of Intersecting Wedges". The Rand Corporation Santa Monica, Calif., AIAA Paper No. 66-128.
7. Rudman, S. and Rubin, S. G. "Hypersonic Viscous Flow Over Slender Bodies Having Sharp Leading Edges". Polytechnic Institute of Brooklyn, PIBAL Report No. 1018, AFOSR 67-1118, May 1967.
8. Rubin, S. G., Rudman, S., Lin, T. C. and Pierucci, M. "Hypersonic Viscous-Inviscid Interactions by a New Type of Analysis". Paper presented at the AGARD Specialists' Meeting on "Hypersonic Boundary Layers and Flow Fields, London, England, May 1-3, 1968.
9. Staff, Aerospace Research Laboratory "Description of the Aerospace Research Laboratories at the Long Island Graduate Center". Polytechnic Institute of Brooklyn, PIBAL Report No. 982, April 1966.
10. Cresci, R. J. "Hypersonic Flow Along Two Intersecting Planes". Polytechnic Institute of Brooklyn, PIBAL Report No. 895, AFOSR 66-0500, March 1966; also, presented at the 1966 Heat Transfer and Fluid Mechanics Institute, Univ. of Santa Clara, Calif. June 22-24, 1966.
11. Nardo, C. T. "Hypersonic Interaction Effects Along the Interior Corner of Two Intersecting Flat Plates". Master's Thesis, Polytechnic Institute of Brooklyn, June 1967.
12. Eckert, E. R. G. "Survey on Heat Transfer at High Speeds". Wright Air Development Center, TR 54-70, 1954.
13. Lees, L. and Probstein, R. F. "Hypersonic Viscous Flow over a Flat Plate". Princeton University, Report No. 195 (Contract AF 33 (038)-250), Aero. Eng. Lab., April 1952.
14. Bertram, M. H. and Blackstock, T. A. "Some Simple Solutions to the Problem of Predicting Boundary-Layer Self-Induced Pressures". NASA TN D-798, April 1961.



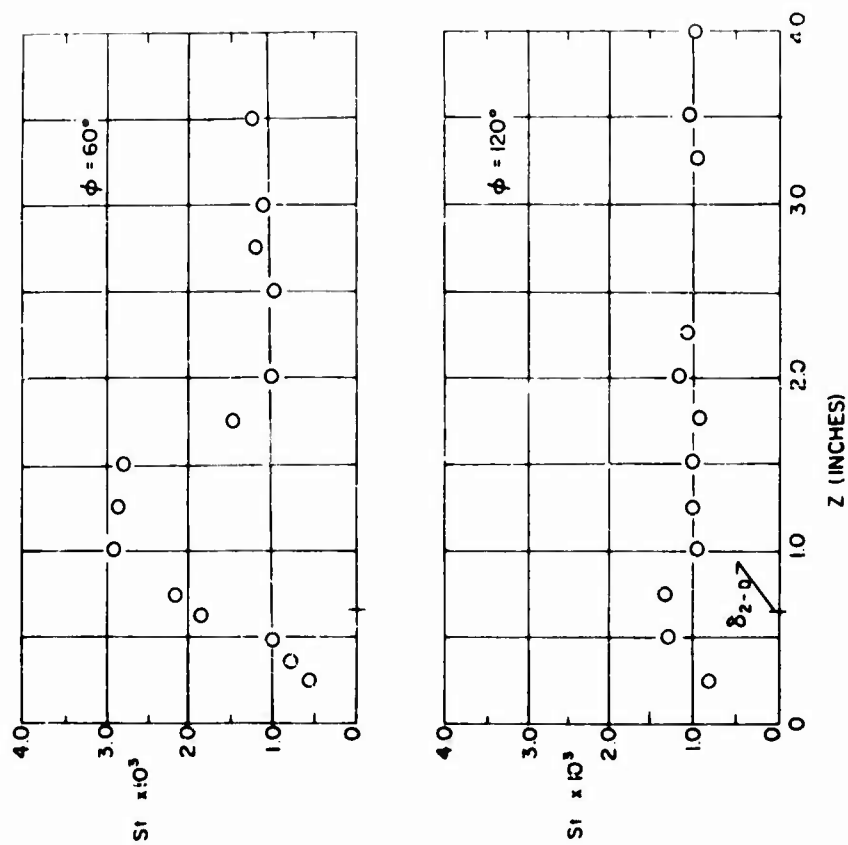


FIG (2) SURFACE HEAT TRANSFER DISTRIBUTION
(b) $\bar{X} = 4.1$

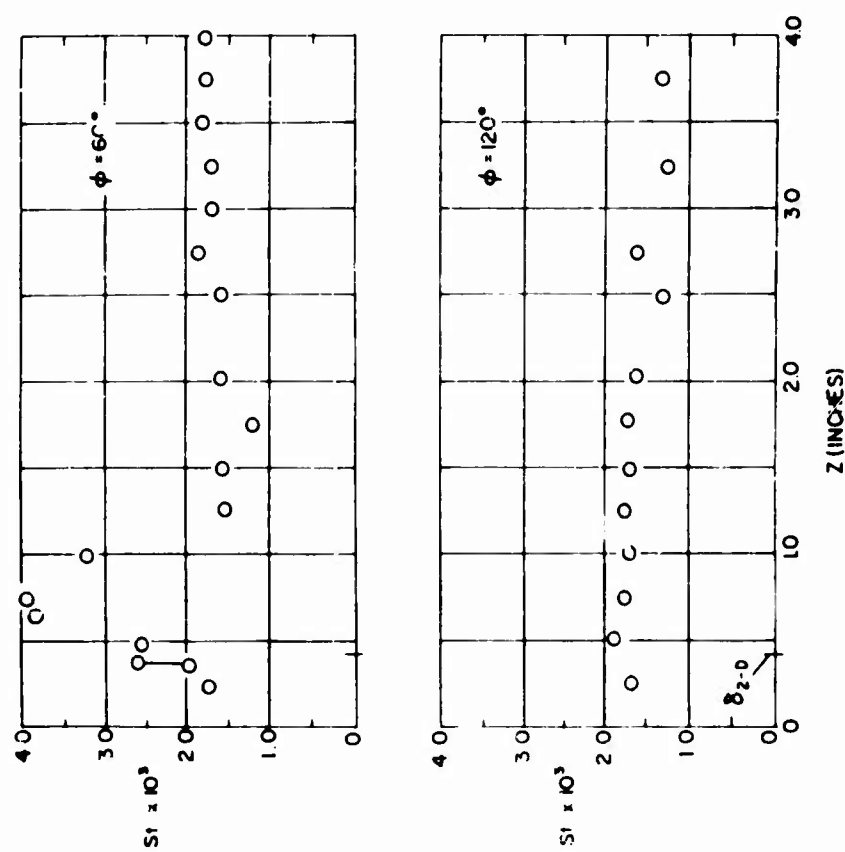


FIG (2) SURFACE HEAT TRANSFER DISTRIBUTION
(a) $\bar{X} = 5.6$

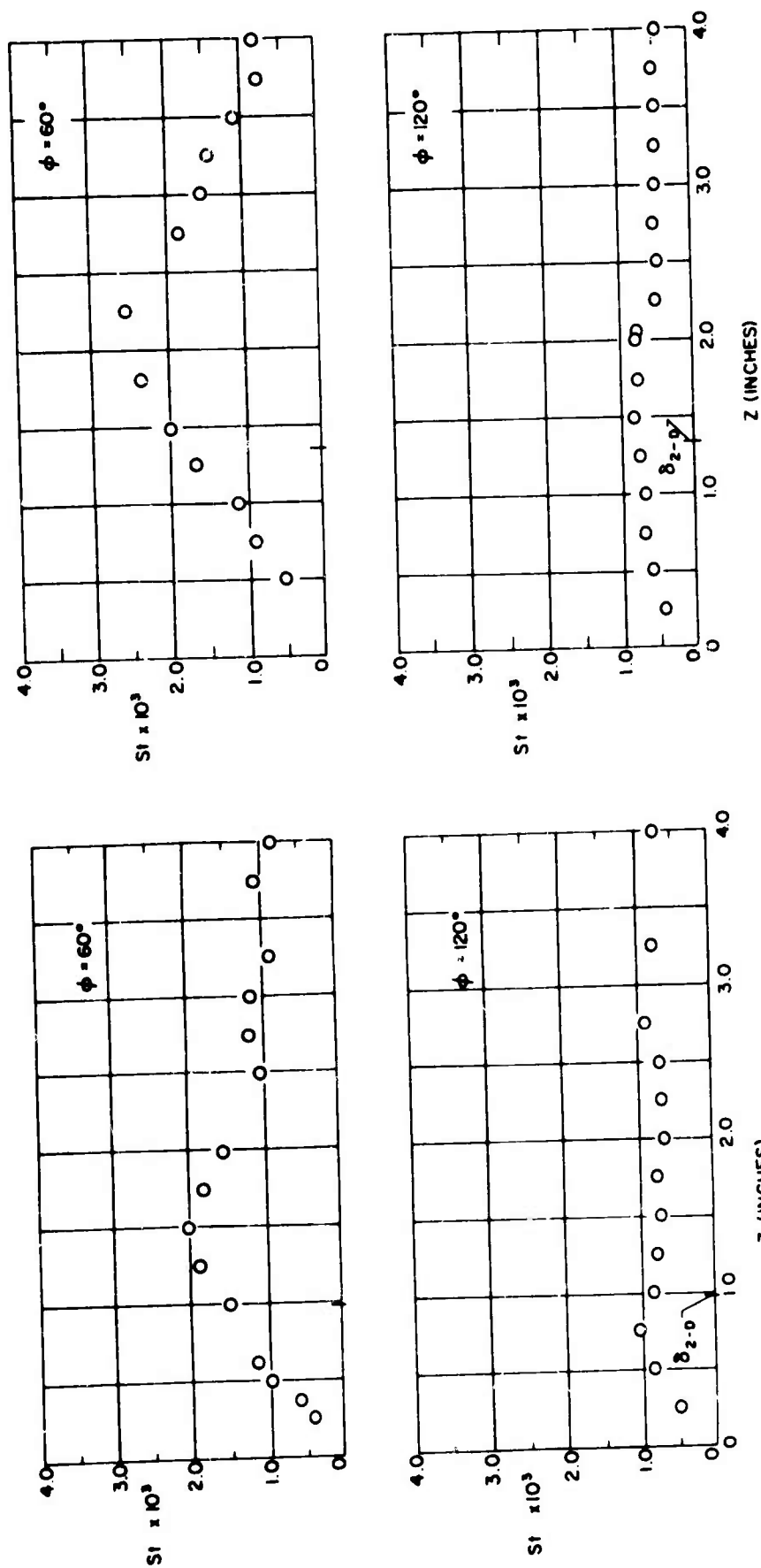


FIG (2) SURFACE HEAT TRANSFER DISTRIBUTION
(d) $\bar{X} = 2.5$

FIG (2) SURFACE HEAT TRANSFER DISTRIBUTION
(c) $\bar{X} = 3.1$

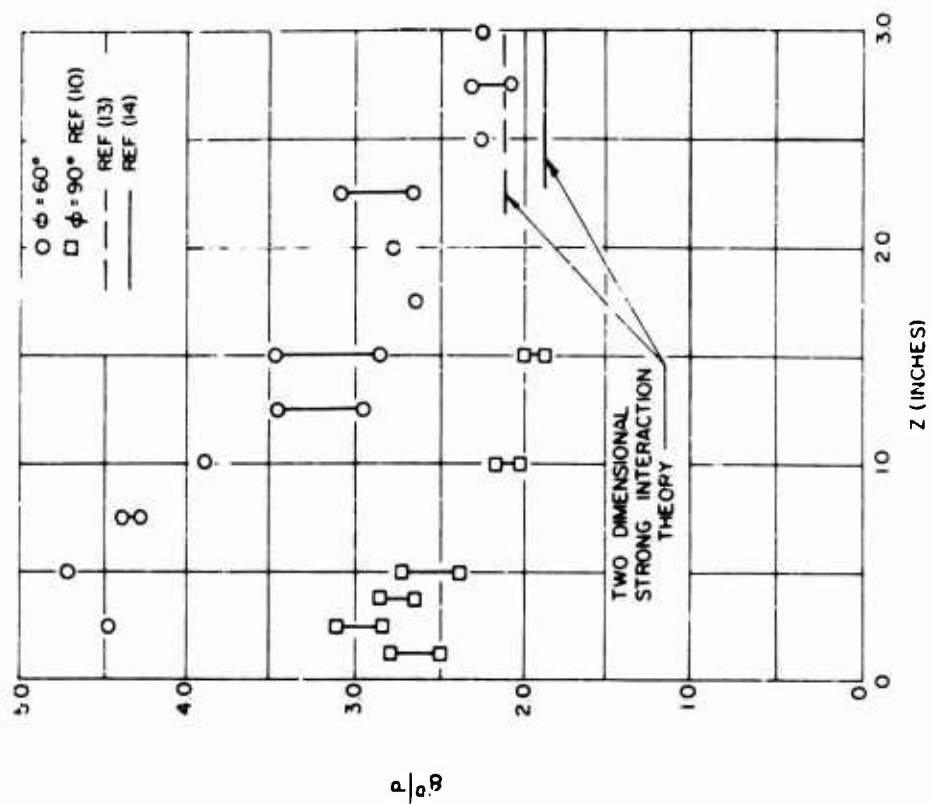


FIG (4) STATIC PRESSURE DISTRIBUTION IN CORNER REGION - $\bar{x} = 5.0$

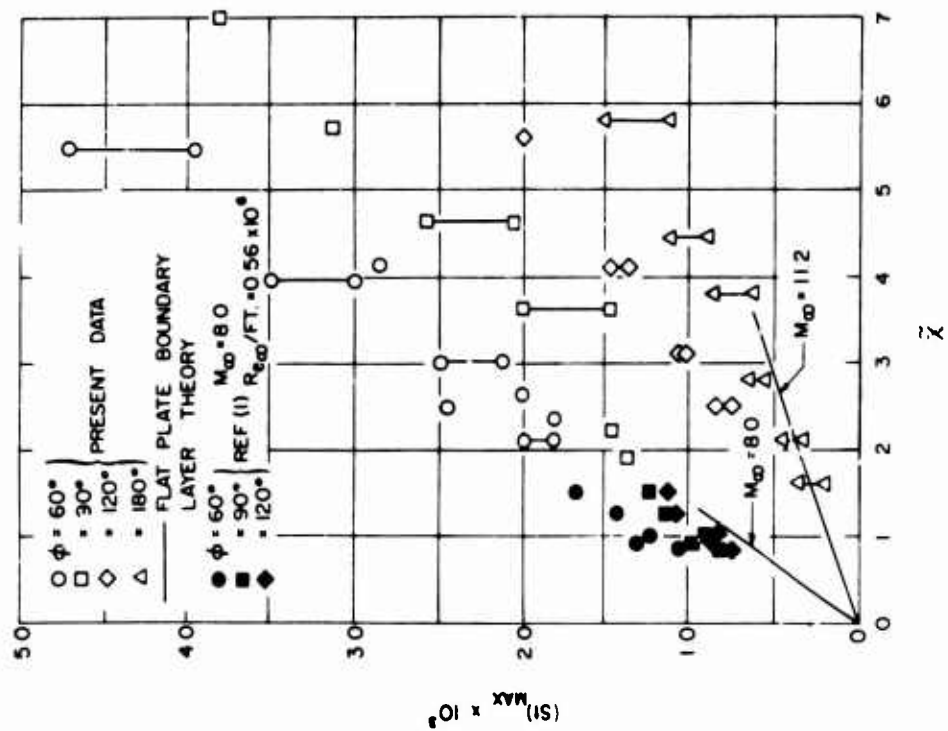


FIG (3) MAXIMUM HEAT TRANSFER IN CORNER

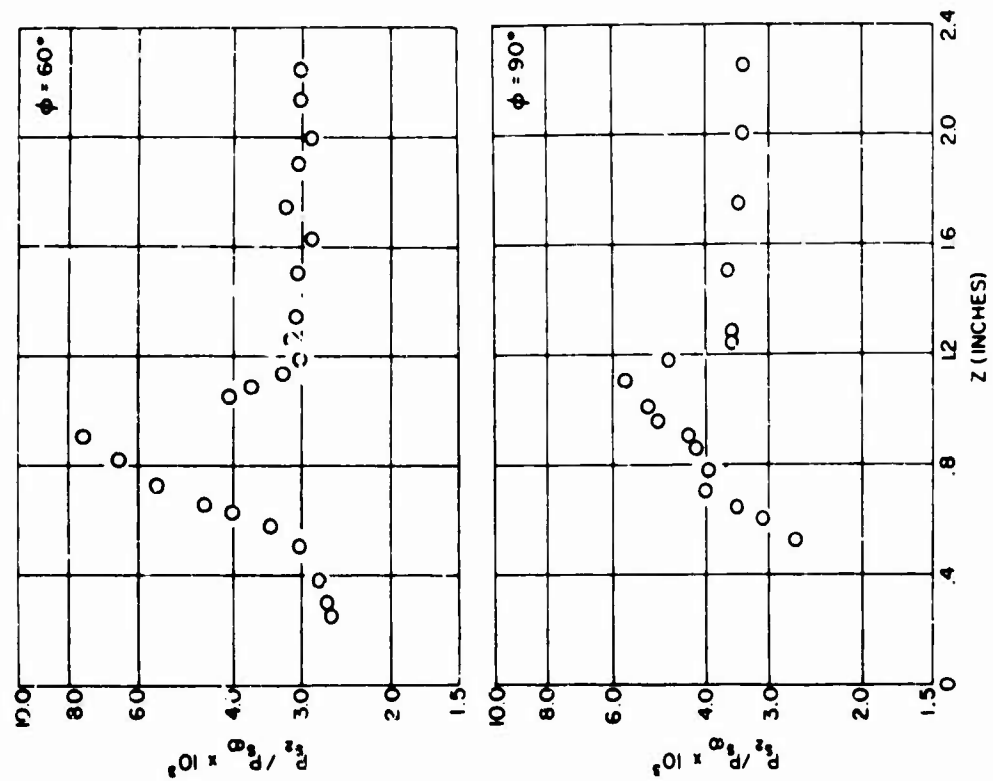


FIG. (5) PITOT PRESSURE PROFILES
(b) $Y = 0.90$ INCHES

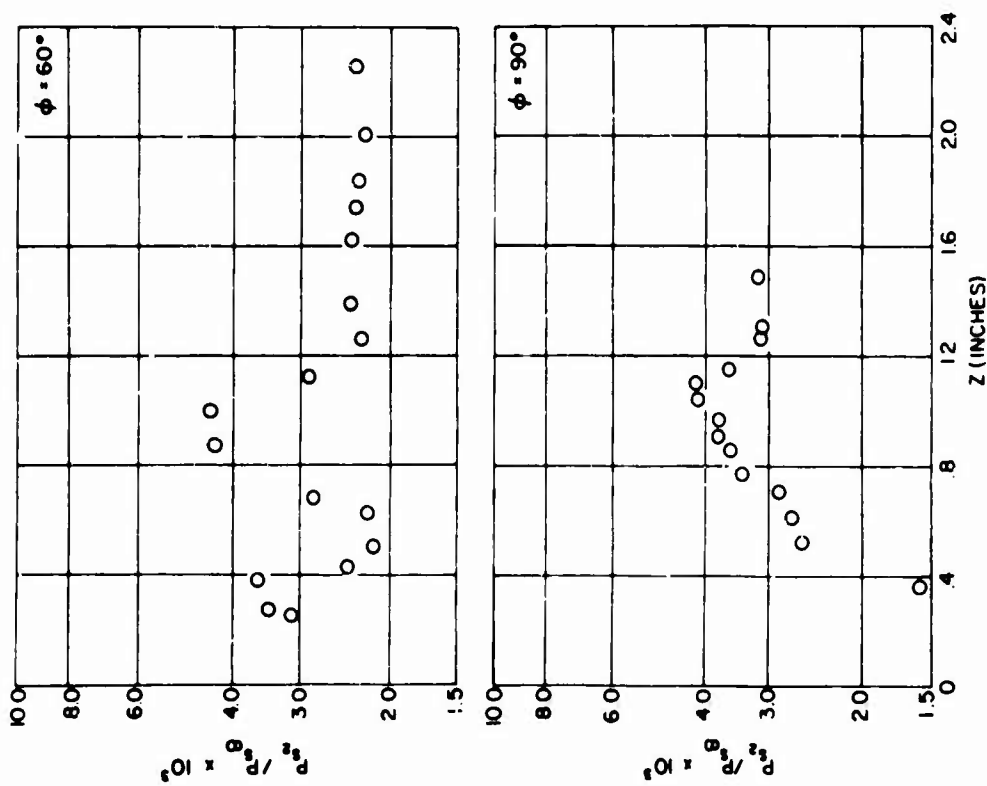


FIG. (5) PITOT PRESSURE PROFILES
(a) $Y = 0.75$ INCHES

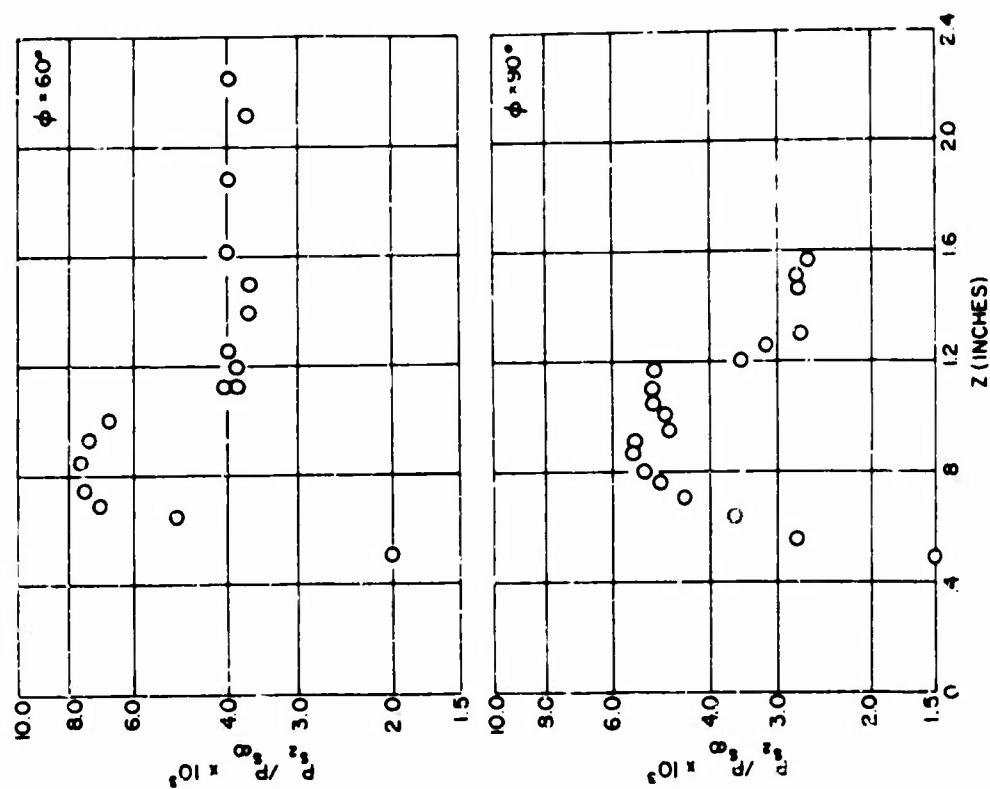


FIG (5) PITOT PRESSURE PROFILES
(d) $Y = 1.10$ INCHES

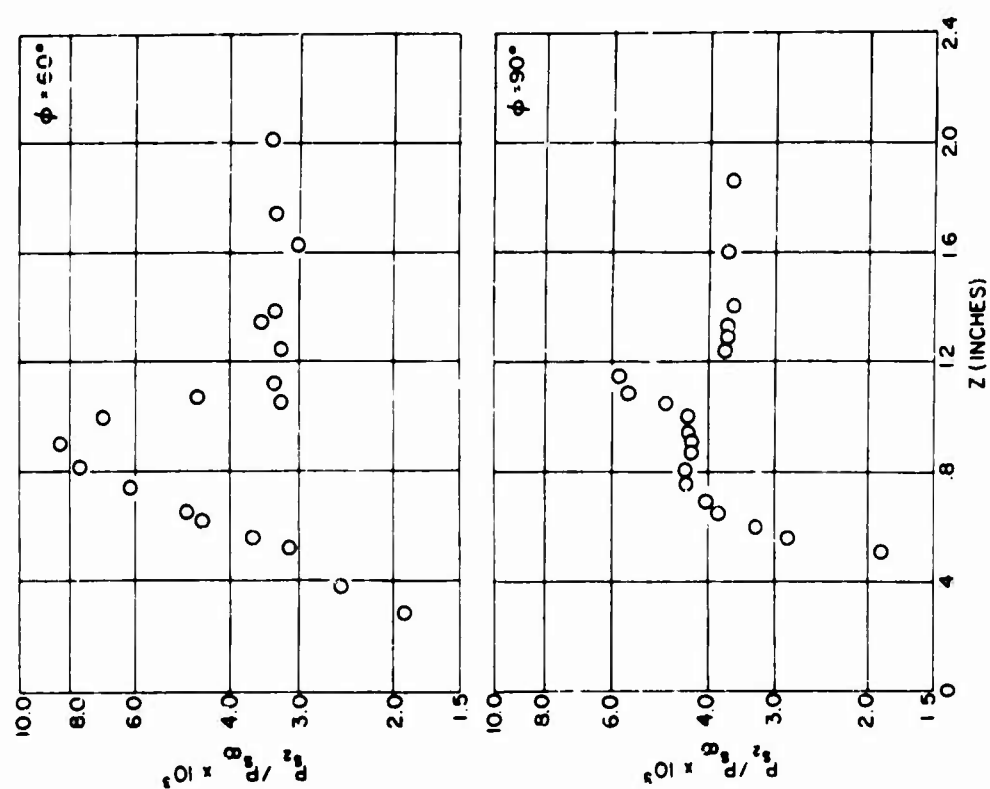


FIG (5) PITOT PRESSURE PROFILES
(c) $Y = 1.00$ INCHES

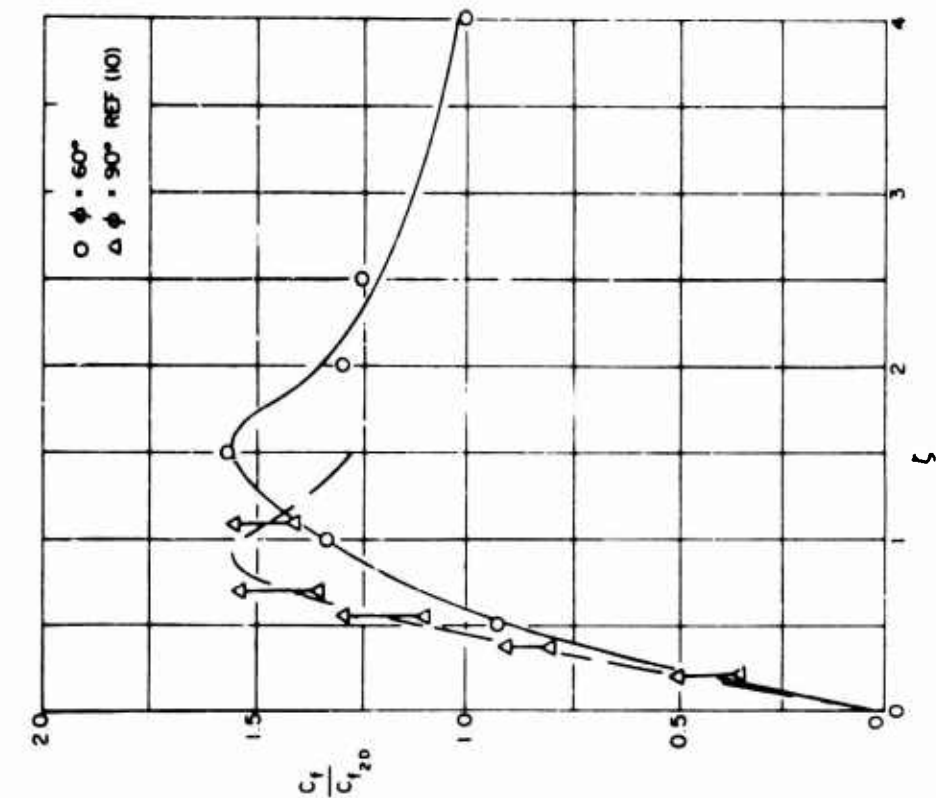


FIG (6) SKIN FRICTION VARIATION IN CORNER

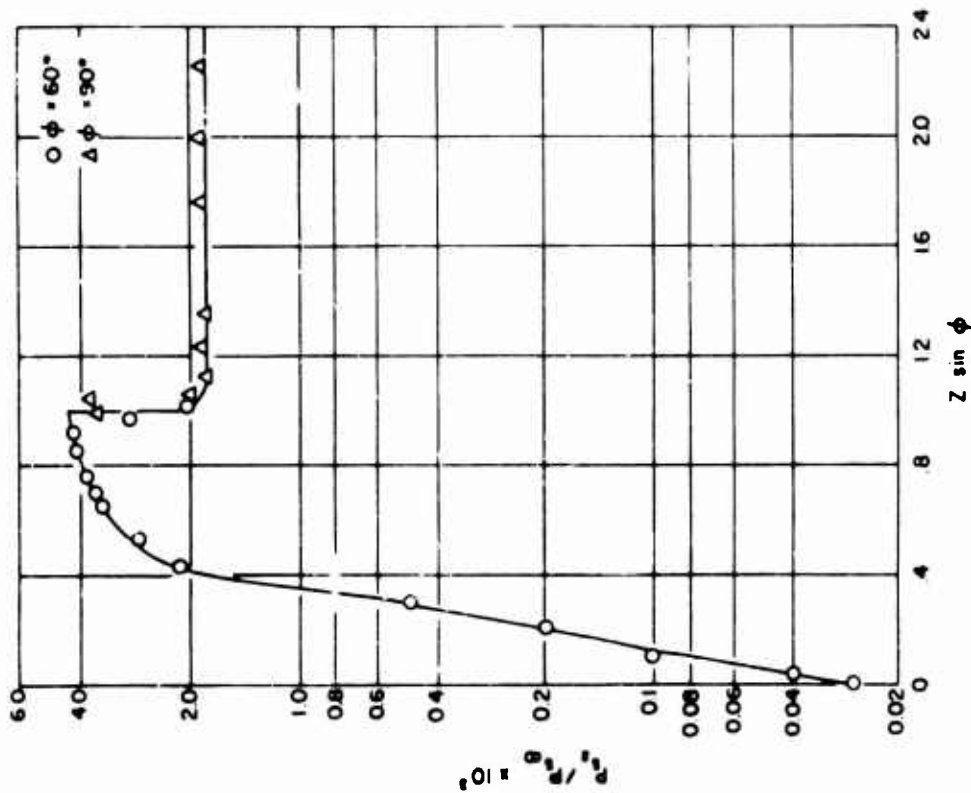
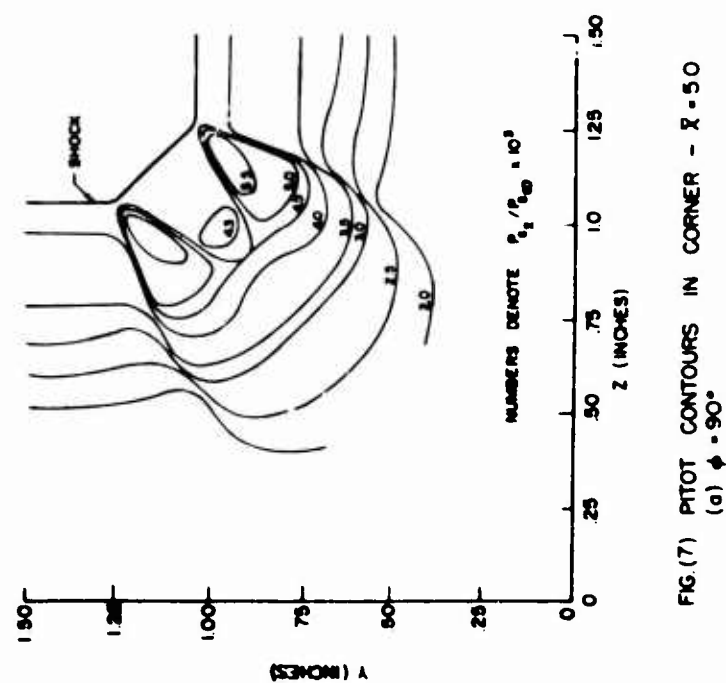
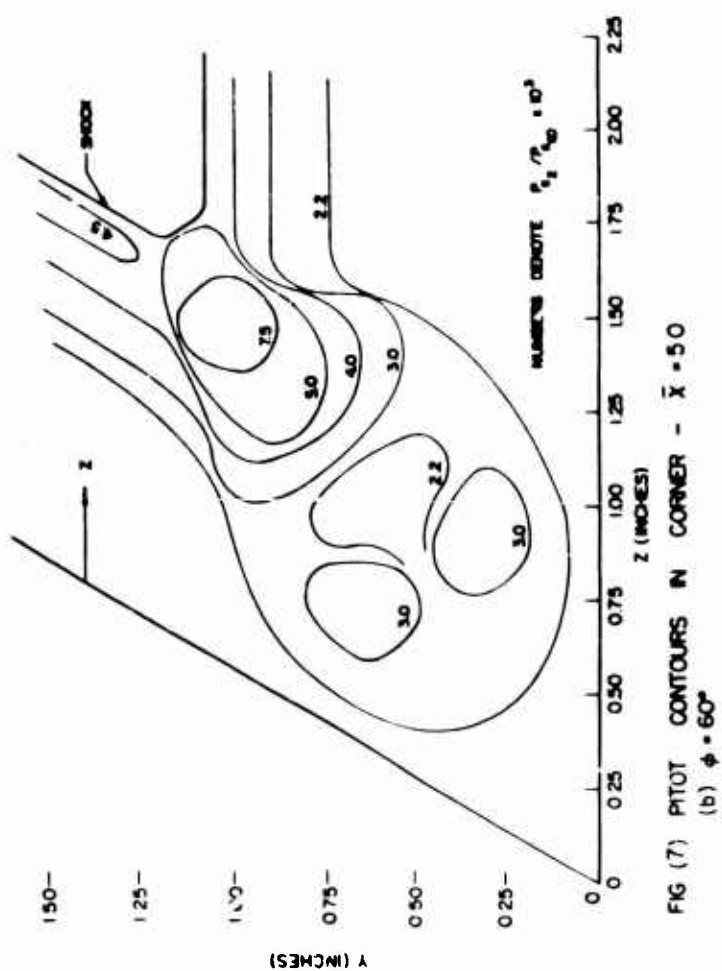


FIG. (5) PITOT PRESSURE PROFILES
(e) TWO DIMENSIONAL ($Y \rightarrow \infty$)



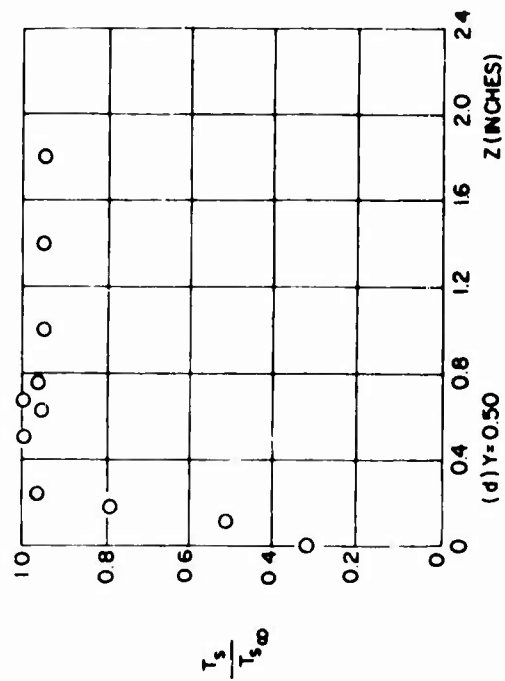
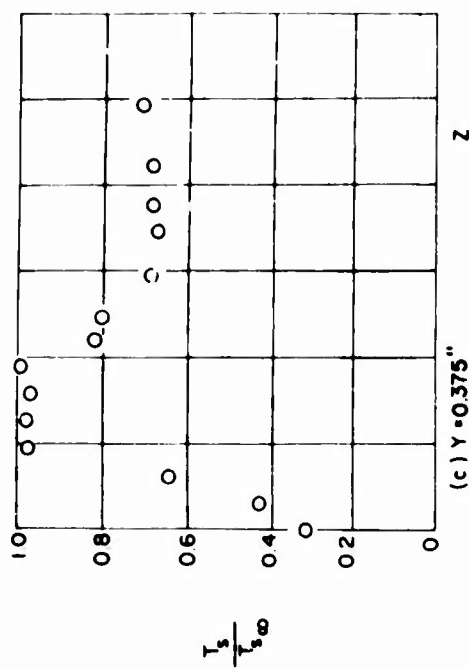


FIG. (8) STAGNATION TEMPERATURE PROFILES
 $\bar{X} = 5.0, \phi = 60^\circ$

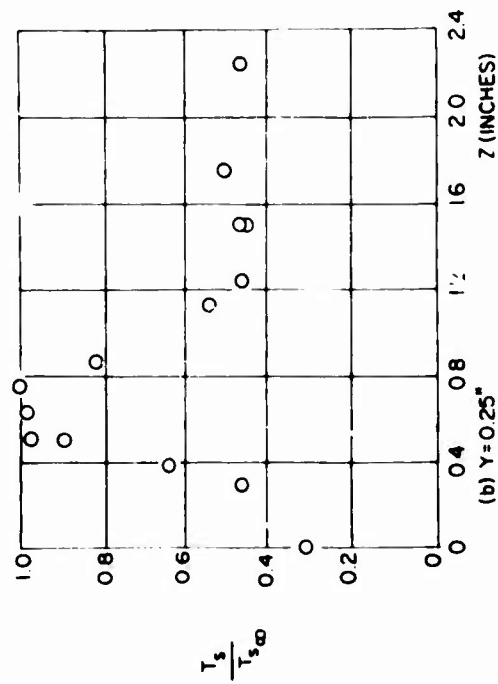
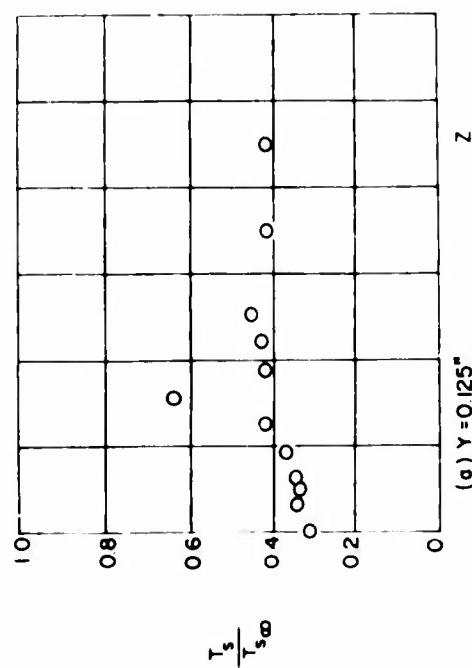
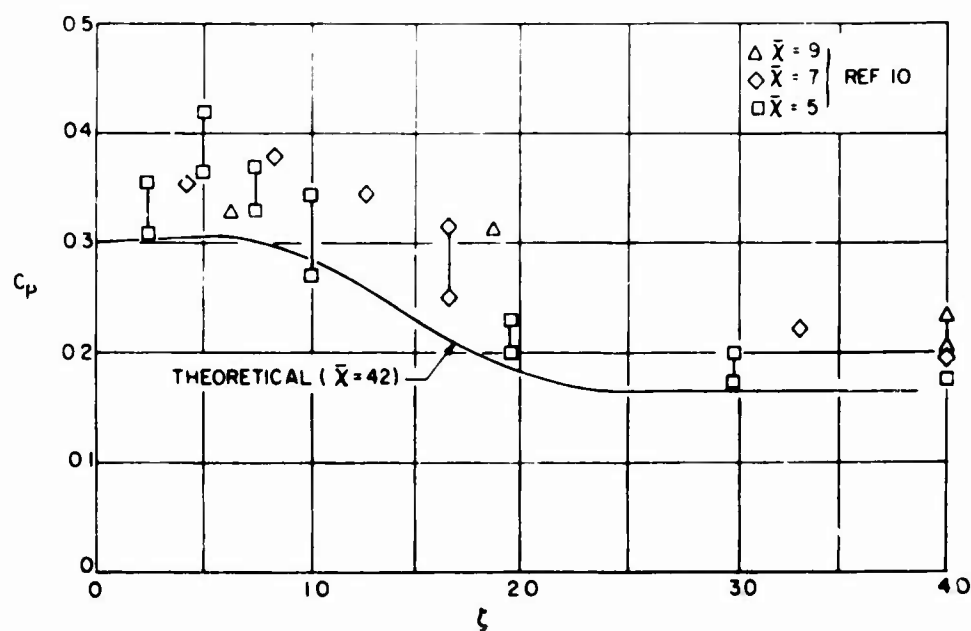
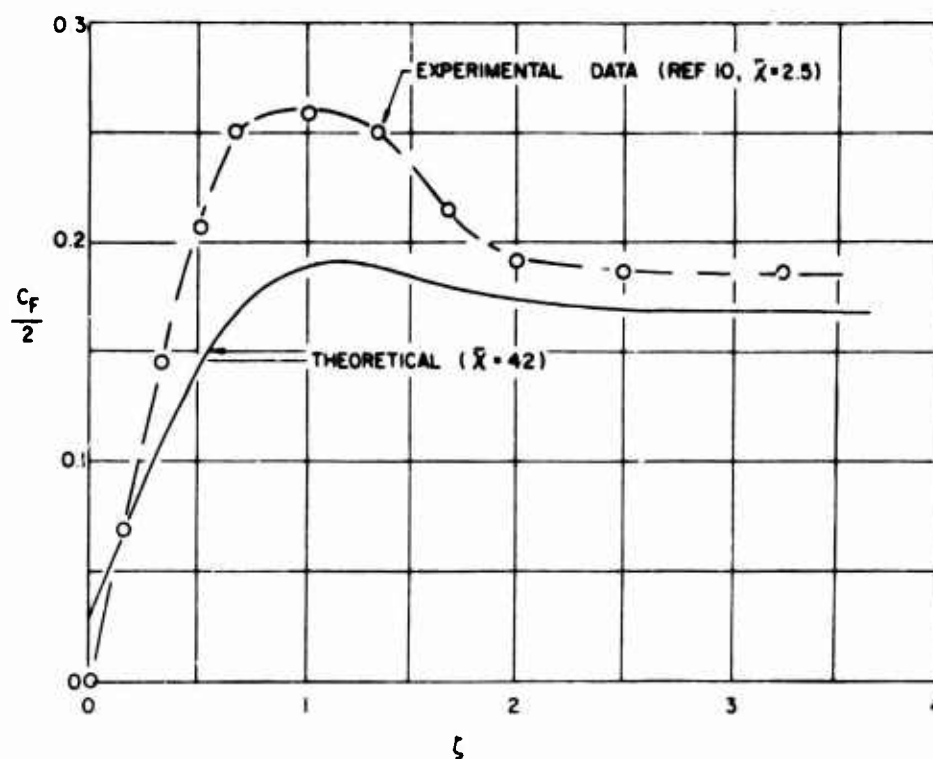
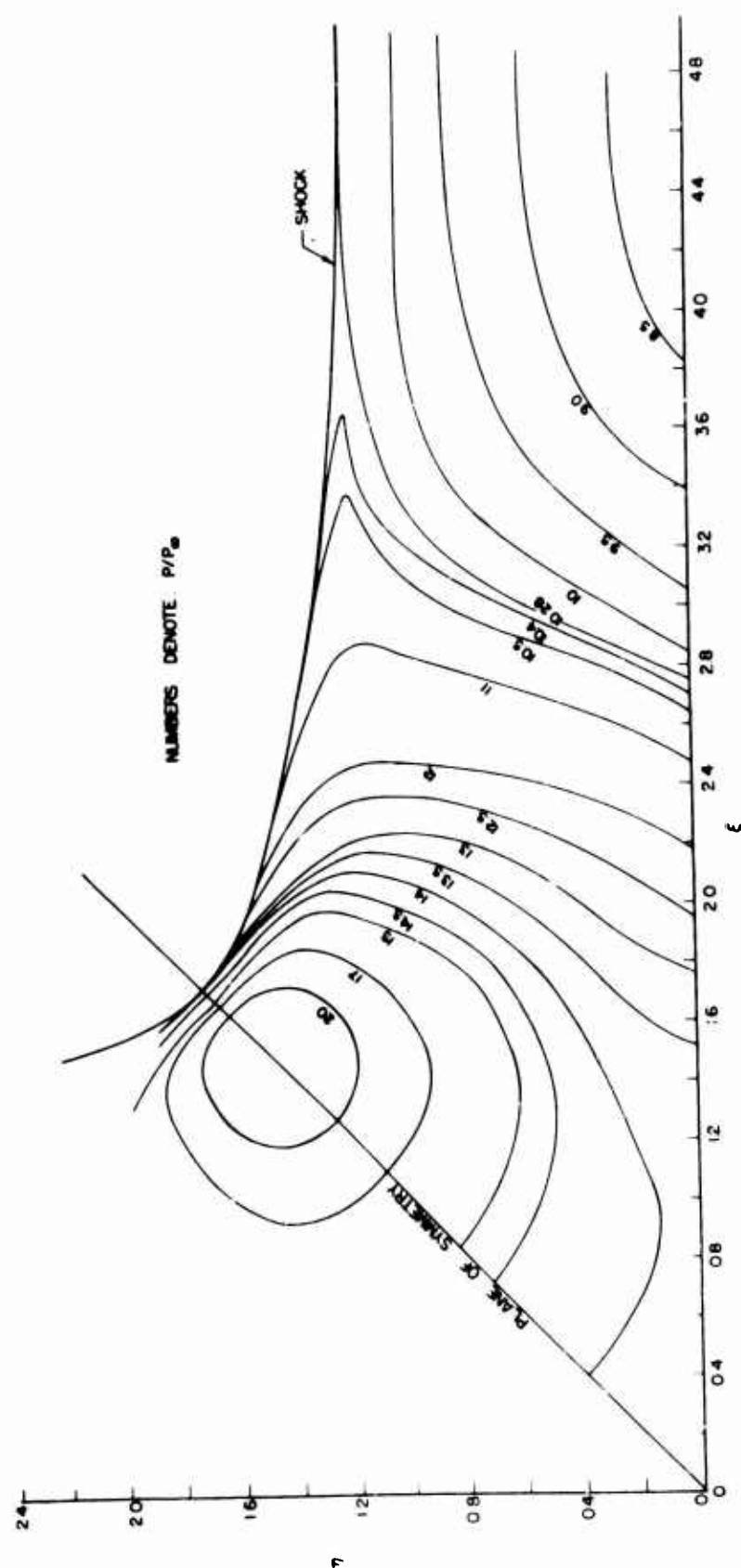


FIG. (8) STAGNATION TEMPERATURE PROFILES
 $\bar{X} = 5.0, \phi = 60^\circ$

FIG (9) NORMALIZED SURFACE PRESSURE ($\phi = 90^\circ$)FIG (10) NORMALIZED SKIN FRICTION ($\phi = 90^\circ$)

FIG. (11) THEORETICAL ISOBARS IN CORNER REGION ($\bar{x} = 42$)

THE EXTERNAL FLOW FIELD ABOUT YAWED CIRCULAR CONES

W. J. Rainbird*

National Aeronautical Establishment
 National Research Council
 Ottawa, Canada

Summary

Experimentally determined pressure distributions, surface shear stresses and detailed external flow field measurements on a yawed, 54-inch-long, 5° semiangle cone, are presented. The cone was tested in the NAE 5-ft intermittent blowdown wind tunnel under high Reynolds number conditions ($Re_\infty = 3.4 - 6.8 \times 10^7$) at Mach numbers of 1.80 and 4.25 and up to large relative incidence. Some additional results from a 40.6-inch-long, $12\frac{1}{2}^\circ$ semiangle cone, tested under similar conditions, are also included.

The development of the viscous flow and separation about circular cones, with increasing relative incidence, and at high Reynolds number, is shown to be a gradual process involving the formation of symmetrically disposed lobes of vortical fluid which develop into vortices and which remain comparatively close to the cone surface on either side of, and near, the leeward generator. Numerical methods for the solution of the inviscid supersonic flow about yawed circular cones give excellent predictions up to moderate relative incidence (about 1.2), provided mixed flow conditions with internal shock waves do not occur. An inviscid flow model with free vortex sheets is needed to approximate the real flow with separation at larger relative incidence ($\alpha/\theta_c > 1.5$).

*Head, High Speed Aerodynamics Section: On leave at the Department of the Aerospace and Mechanical Engineering Sciences, University of California, San Diego; La Jolla, California.

List of Symbols

(See Figure 23 for definition of some of the symbols used.)

C_{fe}	local skin friction coefficient, $\tau_w/0.7 p_e M_e^2$
C_n	local normal force coefficient from integrated surface pressures
C_N	overall normal force coefficient from balance measurements
C_p	local surface pressure coefficient, $(p_e - p_\infty)/0.7 p_\infty M_\infty^2$
C_{pe}	local surface pitot pressure coefficient
C_{p0}	surface pressure coefficient at zero incidence
d_o, d_i	outside and inside diameters of Preston surface pitot tubes
$f_2(T_w)$	viscosity density function used in compressibility correlation of Preston tube calibrations, Ref. 20.
F_0, F_1, \dots, F_m	coefficients of Fourier cosine series describing shock wave shape, $\tan \theta_s$
h	height of flow field probe above cone surface
$\bar{h} = h/R$	nondimensional height of flow field probe above cone surface measured in local cone radii
L	cone axial length
M_e	local Mach number outside boundary layer
M_r	radial component of Mach number, cylindrical coordinates
M_ϕ	circumferential component of Mach number
M_∞	Mach number of undisturbed stream
P_B	inviscid surface pressure predicted by Babenko numerical solution
P_e	local static pressure on cone surface
P_J	inviscid surface pressure predicted by Jones numerical solution
P_0'	pitot pressure of undisturbed flow
P_1	pitot pressure from flow field survey probe
P_2, P_3, P_4, P_5	pitch and yaw pressure differences from flow field survey probe
P_6	averaged surface static pressure from flow field survey probe
P_∞	static pressure of undisturbed flow
R	local radius of cone
R_d	Reynolds number based on Preston tube diameter and local external flow conditions
RL_∞	Reynolds number based on cone length and undisturbed conditions
Rx_∞	Reynolds number based on local axial distance and undisturbed conditions
T_o	stagnation temperature of undisturbed flow ($\approx 530^\circ R$)
T_w	cone wall temperature ($\approx T_o$)
u, v, w	velocity components parallel to spherical polar coordinate directions r, θ, ϕ
U_J, U_B	velocity components along rays (i.e., in r -direction) according to Jones and Babenko, respectively, normalized with respect to the critical speed of sound
x	cone axial length from the apex
α	angle of incidence of cone, or flow pitch angle measured by probes
α/θ_c	relative angle of incidence
$(\alpha/\theta_c)_a$	minimum relative angle of incidence for separation
β_∞	$(M_\infty^2 - 1)^{1/2}$
γ	circumferential angle of resultant velocity vector relative to flow field probe
δ	resultant angle of attack of probe
δ^*	boundary layer displacement thickness
$\Delta\xi$	grid spacing in ξ direction
$\Delta\phi$	grid spacing in ϕ direction
θ_c	cone semiangle

$\theta_s(\varphi)$	shock wave angle, measured from cone axis
θ_v	vortex angle
θ_v/θ_c	$= 1 + \bar{h}_v$, nondimensional vortex height
ξ	coordinate measured between cone surface and shock wave, $\xi = (\tan \theta - \tan \theta_c)/(\tan \theta_s - \tan \theta_c)$
τ_w	wall shear stress
φ	circumferential angle
$\varphi_{s1}, \varphi_{s2}$	primary and secondary separation angles
ω_e	direction of external streamlines relative to a cone generator
ω_s	direction of limiting streamlines, surface shear stress

1. Introduction

One promising approach to the design of hypersonic aircraft is to consider lifting bodies whose shape can be derived from parts of known flow fields (Ref. 1). In particular, known conical flow fields have been studied in some detail and J. G. Jones (Ref. 2) has given a method for deriving lifting surfaces from the flow field of a circular cone at zero incidence. Since boundary layer interaction effects are especially important at hypersonic speeds, it is necessary to consider lifting surfaces with either constant or slightly falling pressure along the streamlines defining the surface and to avoid strong transverse pressure gradients which might lead to three-dimensional separation. The Jones lifting surfaces and also those derived from reversed Prandtl-Meyer flow (Townend, Ref. 3) do not satisfy this requirement. However, lifting surfaces derived from the flow field of cones at incidence could be chosen to avoid serious viscous effects.

Considerable progress has recently been made using numerical methods to solve the nonaxisymmetric inviscid supersonic flow about circular and elliptical cones (Refs. 4-8). Provided the flow fields are "conically subsonic"* it has been possible to find numerical solutions up to incidences where the vortical singularity lifts off the surface (i.e., to α/θ_c of the order of 1.3 for circular cones). No computations have so far been made with mixed flow field conditions which properly allow for "conically supersonic" regions.

Methods for calculating the compressible laminar and turbulent boundary layers on slightly yawed circular cones were given some time ago by Moore (Ref. 9) and Braun (Ref. 10), respectively, and Moore (Ref. 11) also considered the laminar boundary layer in the plane of symmetry at large yaw. Recently Cooke (Ref. 12) has published an implicit finite difference method for the compressible laminar case which can be used for general conical surfaces at large yaw with heat transfer and suction, and can predict, among other things, separation. In applying his method to a circular cone of $7\frac{1}{2}^\circ$ semiangle at large relative incidence ($\alpha/\sin \theta_c = 1, 2$) Cooke used an inaccurate external flow field based on perturbation methods (Sims, Ref. 13), with a modification to ensure irrotationality. Measurements of the turbulent boundary layer growth and a description of the gradual development of separation on a $12\frac{1}{2}^\circ$ semiangle circular cone have been given by the present author (Ref. 14).

While flow separation about yawed circular cones represents one of the simplest cases in the general problem area of three-dimensional separation, little progress has been made in constructing an inviscid flow model to describe the flow field and to predict the vortex positions and nonlinear lift. Bryson's incompressible flow model (Ref. 15) represents, in the simplest mathematical form, the effects of the separated flow by two straight vortex sheets emanating from arbitrarily specified positions on the body, each feeding a discrete vortex, and imposes the condition of zero net force on the system. This gives unrealistic pressure distributions. A more adequate treatment, similar to that used by Smith (Ref. 16) for the equivalent delta-wing problem, is needed using, perhaps, the experimentally determined separation positions at each relative incidence (see Ref. 17 and Fig. 14 of the present report).

Tracy (Ref. 18) has made very extensive measurements of the hypersonic flow ($M_\infty = 8$) about a 10° semiangle cone with laminar boundary layers ($Re_{L_\infty} = 0.5 - 4.2 \times 10^5$) up to large relative incidence ($\alpha/\theta_c = 2.4$). By slowly rolling his model he is able to present continuous trace records of surface static pressure and heat transfer and measurements of the external flow field using a single fixed direction pitot tube. For incidences above about 12° mixed flow conditions prevail and the positions of the internal shock waves are clearly indicated by his surveys. It can be noted that the leeward part of the nose shock wave and the outer parts of the internal shock waves are very weak, becoming tangential to a free stream Mach cone with apex coincident with the cone apex. Also at incidences of 12° and above, boundary layer separation is present and the pitot probe measurements indicate a single large lobe of vortical fluid above the leeward generator.

The objective of the present work was to experimentally determine, under high Reynolds number conditions, cone surface quantities (pressure, and shear stress magnitude and direction) and the flow field above a cone, at both moderate and large relative incidence. From these results the range of application of the numerical methods for calculating the inviscid flow field can be assessed and a description given of the nature of the separated flow field at large relative incidence.

*Conically subsonic flows exist when the component of Mach number normal to rays is subsonic, otherwise conically mixed (transonic) conditions are present.

2. Experimental Method

Measurements were made on a 54-inch-long, 5° semiangle cone, sting mounted in the National Aeronautical Establishment (NAE) 5-ft trisonic intermittent blowdown wind tunnel at nominal Mach numbers of 1.80 and 4.25. Stagnation pressures of 25 and 166 psia, respectively, were used giving Reynolds numbers based on cone axial length and undisturbed conditions of 34×10^6 and 68×10^6 . No boundary layer trip was used but it is expected that transition takes place quite close to the apex (certainly at $x/L < 0.1$) due to the high stream turbulence level resulting from noise generated by the control valve and working section wall boundary layers. The initial cone surface temperature before a wind tunnel run was approximately equal to the stream stagnation temperature ($\approx 70^\circ\text{F}$) and so all tests were made under very small heat transfer conditions. With typical wind tunnel run durations of 20 to 30 seconds, the change in surface temperature was less than 5°F for the 1/2-inch-thick aluminum wall of the cone.

Because of the conicity and symmetry of the flow all detailed measurements were confined to an axial station 0.85 of the cone length aft of the apex and to one-half (0° to 180°) of the cone. Circumferential pressure distributions were measured using up to eight unbonded strain-gauge pressure transducers closely coupled pneumatically to 0.020-inch holes spaced 45° apart at the 0.85 station. The model was pitched to the desired incidence and slowly rolled during a wind tunnel run while the transducer outputs were digitized at 0.8-second intervals to give data at about $2\frac{1}{2}^\circ$ circumferential intervals from $\phi = -5^\circ$ to about 185° . Pitot pressure outside the boundary layer (actually at a height of 3/8 inch above the cone surface) and in the windward plane of symmetry ($\phi = 0$), was also measured thus enabling the circumferential distribution of Mach number, M_e , to be calculated.

Surface shear stress direction, ω_s , was measured from flow visualization traces taken with an oil-dot technique (Ref. 19). This method is particularly useful in intermittent wind tunnels and defines, among other things, flow separation and attachment lines. Surface shear stress magnitude was measured using small Preston surface pitot tubes ($d_0 = 0.0165$ inch)—see Fig. 1. These tubes were aligned using the flow visualization results and measurements were made every 5° of circumferential angle. The surface pitot pressure difference was converted to the local skin friction coefficient using a calibration given in Fig. 6 of Ref. 20, namely

$$C_{fe} = \frac{C_{pe}^{0.8606}}{21.66 [f_2(T_w)]^{0.1394} R_d^{0.2788}}$$

Local Mach number, pitot pressure and flow direction in the external flow above the cone were measured using a pair of flow field probes mounted at various heights above the surface with the measuring heads adjacent to the 0.85-length station—see Fig. 2. Again slow rotation during a wind tunnel run, with the cone at fixed incidence, enabled the leeward flow field to be surveyed. The flow field probe head (Fig. 3) consists of a 30° semiangle cone blunted by a pitot tube. Four pressure differences $P_1 - P_0'$, $P_1 - P_6$, $P_2 - P_3$ and $P_4 - P_5$ are measured from which the local Mach number, stagnation pressure and resultant flow direction can be iteratively calculated using probe calibration data. Typical calibration curves are shown in Figs. 4 and 5. The probes were separately calibrated at several Mach numbers between 1.8 and 4.25 and the calibration curves were fitted by simple empirical functions.

Overall force measurements were made with an internal strain-gauge balance.

Some surface pressure distribution results for a 40.6-inch-long, $12\frac{1}{2}^\circ$ semiangle cone tested under similar conditions are also included in this report.

3. The Inviscid Flow Field for the Circular Cone at Incidence

3.1 Perturbation Methods

The original attempts to find the inviscid flow field about a cone at small incidence were based on perturbation methods and used the exact Taylor-Maccoll flow for circular cones at zero incidence (first tabulated for air by Kopal, Ref. 21, and more recently, in convenient form, by Sims, Ref. 22). The perturbation theory, for both the first- and second-order effects of incidence, was formulated by Stone (Refs. 23, 24) and after extensive numerical integrations the results were tabulated by Kopal (Refs. 25, 26). Again Sims, using modern digital computers rather than the desk calculators available to Kopal, has recalculated the first-order Stone theory and presented the results for air, at convenient values of cone semiangle and Mach number, in body-fixed coordinates in Ref. 13. The second-order tabulations of Kopal contain uncertainties, are of limited range, and in practice are rather inconvenient to use.

Ferri (Ref. 27) pointed out a fundamental error in the Stone results and gave a method for correcting the surface velocity components. He observed that the body surface must be a surface of constant entropy wetted by streamlines that cross the nose shock wave in the windward plane of symmetry ($\phi = 0$) and that because of this there must be a region of high vorticity near the cone

surface, "the vortical layer." All the streamlines which cross the nose shock wave terminate at a singular point ($\phi = \pi$, $\theta = \theta_c$) at which the entropy is multivalued, "the vortical singularity." Such singularities are present in all nonaxisymmetric supersonic flows over conical bodies and represent the final directions into which particles moving along streamlines are deflected. Munson (Ref. 28) and Melnik (Ref. 29), among others, have studied the vortical layer in detail and, using the technique of matched asymptotic expansions, have obtained inner expansion for the vortical layer which match Stone's solution (outer expansion). In addition, Melnik (Ref. 30) has examined vortical singularities in conical flow and has given a condition on the curvature of the pressure distribution which marks the liftoff from the surface of the vortical singularity. This critical condition has not been related back to relative incidence, Mach number and cone semi-angle but this could be done by examining the results of recent numerical flow field calculations.

With the advent of high-speed computing machines and the use of sophisticated techniques in numerical analysis, perturbation methods for calculating the flow field about circular cones at incidence have now been superseded by numerical methods.

3.2 Numerical Solutions

In the last few years a number of numerical methods (Refs. 4-7) have been developed, some of which are quite general, and which have been applied, in particular, to the circular cone at incidence to an inviscid supersonic stream. A brief review of these methods, their similarities and limitations, will be given.

Stocker and Mauger's method (Ref. 4) uses basically the elliptic equations transformed to use a stream function as one of the independent variables. Starting from an assumed shock shape ($\sin^2 \theta_s$ expressed as a Fourier cosine series of the circumferential angle, ϕ) the method integrates inward along streamlines using the inverse marching process developed for blunt-body problems. The streamlines "envelope" to define the body shape and converge toward the vortical singularity. For direct cases (given body shape) an iterative procedure was used, the shock shape being successively modified empirically to obtain a closer approximation to the given body. Circular cone solutions were presented for $\theta_c = 20^\circ$, $M_\infty = 3.53$, $\alpha = 5^\circ$ and 10° which showed good agreement with experiment at the smaller incidence but only fair agreement for $\alpha/\theta_c = 1/2$. Indeed difficulties were experienced with the iteration at $\alpha = 10^\circ$ and no solution could be obtained for $\alpha = 15^\circ$. It was thought at the time that the difficulties that were experienced in matching the inner boundary condition were due to the vortical singularity lifting off the surface, but we will see below that this could not have occurred at such a small relative incidence (2/3).

A very general and obviously powerful method to deal with three-dimensional supersonic flows has been developed by a Russian school of mathematicians under K. I. Babenko (available in translation as Ref. 5). This method, termed the BVLR method by the French, is discussed by Germain (Ref. 31) and its advantages stressed. When applied to conical bodies the full three-dimensional equations are used, giving a hyperbolic system--the downstream direction along the cone axis being used like the time variable in an unsteady two-dimensional problem. Starting from an assumed initial shock shape and a given conical body at the required incidence the equations are numerically integrated downstream until a conicity condition on, say, the velocity components is sufficiently satisfied. This is similar, then, to finding the solution of a steady two-dimensional problem from the asymptotic behavior at long times, of the equivalent unsteady problem.

Extensive tables of results for circular cones are given in Ref. 5 for Mach numbers of 2, 3, 4, 5, 6, 7, cone semiangles from 5° to 45° in 5° steps and for relative incidences up to at most 0.8. The results for Mach numbers of 4 and 6 have mostly been obtained by interpolation. In practice, the use of such tables is always rather tedious and invariably involves interpolation or extrapolation. There is a great need to collapse such results (at least for surface conditions) into a more directly usable form, using generalized correlation parameters, as was done for $\alpha = 0$ in Ref. 32. An example of a typical correlation is shown in Fig. 6 for surface pressure coefficient (the interpolated results for $M_\infty = 4$ and 6 contain errors and have been excluded from the figure since they do not show a smooth variation with the parameter $\beta_\infty \sin \theta_c$).

Some very interesting examples of the application of the BVLR method to circular and elliptic cones are given by Gonidou in Ref. 8. It is clear that the method can be used well beyond the largest relative incidence of 0.8 given in Babenko tables and is limited only by the vortical singularity lifting off the surface (provided that the flow is still conically subsonic). Typical computer times on a CDC 3600 for a grid of $\Delta\phi = \pi/32$ and $\Delta\xi = 1/10$ involving about 500 downstream steps range from 1/2 to 1 hour (Ref. 8).

Moretti (Ref. 6) has independently given a similar method for circular cones. The flow field is obtained as the asymptotic stage of a three-dimensional flow computed, in a spherical frame of reference, by means of a finite difference technique associated with a method of characteristics on the shock and body. For a given case (i.e., given incidence) the initial shock is chosen as an ellipse whose shape is determined iteratively from the appropriate $\alpha = 0$ solution and integrations of the equations in the plane of symmetry. Again about 500 downstream steps yield a good solution and take about 1/2 hour on an IBM 360/50. Figure 7 compares the surface pressure distributions for a given case, $M_\infty = 7$, $\theta_c = 10^\circ$, $\alpha/\theta_c = 1/2$, obtained using the Babenko, BVLR, method

(17 x 21 mesh) and McCrety's method (11 x 7 mesh). The differences are very small, less than 1%, and are likely due to the different mesh sizes used.

The most recent method, for general conical bodies, is that due to D. J. Jones (Ref. 7) who solves the elliptic equations by iteration. Like Babenko and Moretti, Jones uses a grid formed by equally spaced meridional planes ($\phi = \text{constant}$) and equally spaced points between cone surface and shock. The shock shape ($\tan \theta_s$), represented by a Fourier cosine series $F_0 + F_1 \cos \phi + \dots + F_m \cos m\phi$, enables conditions at the outer boundary to be determined. Circumferential derivatives are approximated by a finite difference scheme and the resulting coupled ordinary differential equations are numerically integrated inward to the mesh points closest to, but not on, the body. Conditions on the body surface needed for the iteration process, specifically the normal velocity component, are obtained by extrapolation. This iterative procedure, used to minimize the sum of the squares of the residual normal velocities on the body with respect to the F_m 's defining the shock shape, is a modification of the generalized least squares method and is due to Powell (Ref. 33).

Jones uses for the starting point of all his calculations the known shock shape about a circular cone at zero incidence, i.e., F_0 known and $F_m = 0$, $m > 0$. Then, for the circular cone case, he uses a small incidence step $\alpha_1 = 0.01 \theta_c$ and iterates to find the F_m . The flow for $\alpha_2 = 0.1 \theta_c$ is next found with first approximations for the F_m obtained by extrapolation. Iteration reduces the squares of the residual normal velocities to an acceptable minimum, produces a new set of F_m and solves the flow field. The calculations can be continued in steps of say $0.1 \theta_c$ until the vortical singularity leaves the surface and approaches the first mesh point from the body in the plane $\phi = \pi$, or the flow field becomes conically mixed. The method is general and it is easily possible to perturb the body shape rather than, or in addition to, attitude.

Final surface conditions for each case are found from the extrapolated pressures, conditions at the saddle point of attachment and the condition of constant entropy. Table 1 gives a comparison of the Jones method with Babenko and shows excellent agreement of shock shape (and hence the outer part of the flow field) and only small differences, less than 1%, on the surface, even though the mesh used by Jones in this case has twice the spacings used by Babenko. The computer time per case on an IBM 360/50 for the Jones method is typically between 1/2 and 3 minutes (the time increasing as the incidence increases), a dramatic reduction when compared with the other methods.

Figures 8 and 9 show a comparison of the Jones method with the present experimental results for the $12\frac{1}{2}^\circ$ and 5° cones, respectively, at Mach numbers of 1.80 and 4.25 and for a relative incidence of unity. The results for $M_\infty = 4.25$ have been shifted up one unit for clarity. For the $12\frac{1}{2}^\circ$ cone cases, where the relative influence of viscosity at these high Reynolds numbers is small, the agreement is very good. The scatter of the experimental results for the 5° cone is much greater due to the much smaller pressure differences that have to be measured, but again the agreement with the Jones calculation at $M = 4.25$ is very good. Difficulties were experienced with the numerical flow field calculations for the other case given on Fig. 9, namely $M_\infty = 1.80$, $\theta_c = 5^\circ$, due to the shock wave being very close to a Mach wave. For such cases $[(M_\infty^2 - 1)^{1/2} \sin \theta_c \ll 1]$ it would be more appropriate to represent the shock wave shape as a Fourier cosine series in angle about the wind axis rather than the cone axis.

From the above survey it is clear that we have available powerful numerical methods for solving the flow field about cones inclined to an inviscid supersonic stream, up to relative incidences where the vortical singularity lifts off the surface (≈ 1.2 to 1.3 for the present cases) or where the flow becomes conically mixed. It still remains to define these limits in terms of Mach number and cone angle and to extend the methods beyond them. Such extensions to higher relative incidence are however of limited practical importance since the effects of viscosity will already have become important in the further development of the flow field.

4. The Flow with Viscosity

The present experimental results, together with those of a related investigation already reported by the author in Ref. 14, will be used to describe the effects of viscosity on the supersonic flow about slender circular cones.

4.1 Overall Effects

The overall effects of viscosity on the normal force characteristics of the 5° cone are illustrated in Fig. 10, which shows both balance and integrated pressure results up to a very large relative incidence of almost 6. The normal force slopes near $\alpha = 0$ are not much affected and are slightly greater than given by the Stone theory (it is estimated that $(\delta^*/x)/\theta_c \approx 1.8\%$ and 3.3% for $M_\infty = 1.8$ and 4.25 , respectively). It can be seen, however, that significant nonlinear lift is generated above a relative incidence of about $1\frac{1}{2}$ due to flow separation. Initially the magnitude of this nonlinear lift increases more rapidly with α/θ_c at the higher Mach number. This is due to the development of mixed flow conditions and internal shock waves causing earlier (in terms of ϕ) separation with a stronger vortex system. At the lower Mach number, 1.8, conditions near the surface are conically subsonic (Figs. 9, 12 and 13) and above a certain relative incidence, about 3.1, the vortex system becomes unstable and asymmetric, generating appreciable side force.

At Mach number 4.25, with mixed flow conditions and separation produced by internal shock waves, no such asymmetry was present.

The excellent agreement between the integrated pressures and balance measurements, together with extensive flow visualization and center of pressure measurements not presented here, establish the conicity and symmetry of the flow up to $\alpha/\theta_c \approx 3$ which is beyond the maximum relative incidence of the remainder of the results discussed below.

4.2 The Surface Pressure Distribution and Separation

The development of the pressure distribution with incidence can be followed from Figs. 9, 12 and 13. At small relative incidence (α/θ_c smaller than about 0.6 for the present tests) the surface pressure gradient is favorable (roughly proportional to $\sin \phi$), the external streamlines do not have an inflection point, and the boundary layer grows in a regular manner from the windward to the leeward generator. Only very small crossflows are developed in the boundary layer. With increase of incidence the pressure gradient first becomes adverse near the leeward generator. The relative incidence at which

$$\left(\frac{d^2 p_c}{d\phi^2} \right)_{\phi=\pi} = 0$$

which might be said to define the minimum relative incidence for separation, $(\alpha/\theta_c)_a$, can be approximately calculated from the velocity components given in the Sims tables (Ref. 13) and is shown on Fig. 11.* It has the correct slender body value of 0.5 for small values of the similarity parameter, $\beta_\infty \sin \theta_c$, but is not reliably estimated for hypersonic conditions [and large $(\alpha/\theta_c)_a$]. Examination of the numerical inviscid flow field solutions will have to be made to define this relative incidence $(\alpha/\theta_c)_a$ accurately at large $\beta_\infty \sin \theta_c$.

As the relative incidence exceeds $(\alpha/\theta_c)_a$ the point of minimum pressure moves rapidly around the cone. Notice, from Fig. 9, that this point has moved from $\phi = 180^\circ$ to about $\phi = 130^\circ$ for a relative incidence change from, say, 0.6 to 1.0. At the pressure minimum the external streamlines have an inflection point and beyond this angle the boundary layer encounters an adverse pressure gradient and thickens rapidly. The crossflow within the boundary layer is first reduced and then reversed by the adverse pressure gradient until the limiting streamlines very close to the surface are turned along a generator of the cone ($\omega_s = 0$ at $\phi = \phi_{s1} \approx 168^\circ$ for $\alpha/\theta_c = 1$ on Fig. 9). At the same time, the boundary layer thickness on the leeward generator is reduced due to the draining away of low energy fluid toward the pressure minima. The streamlines of this boundary layer growing away from the leeward generator pass under the separated outer boundary layer coming from the windward side of the cone and form two symmetrically disposed lobes of vortical fluid on either side of the leeward generator. However, there is no general eruption of vortical fluid from the cone surface and at high Reynolds number these lobes are still thin compared, say, to the local cone radius.

At still larger relative incidence (Figs. 12 and 13) the adverse pressure gradient following the pressure minimum intensifies and primary separation angle ϕ_{s1} occurs much earlier, Fig. 14. Between the circumferential angles for which ω_s is zero there is a plateau of essentially constant pressure followed by a second pronounced pressure minimum and finally a recompression to zero pressure gradient at the leeward generator. We shall see below that, under these conditions, the scale of separated flow is more extensive and the shear layers roll up to form a pair of symmetrically disposed vortices close to the cone surface (Fig. 19, for example). The second pressure minima at $\phi \approx 180^\circ + 14^\circ$, produced by these vortices, also causes a marked thinning of the boundary layer and a very strong outflow away from the leeward generator. Secondary separation of this leeward boundary layer also occurs in the neighborhood of $\phi = \phi_{s2} \approx 159^\circ$ (Figs. 12, 13, 15 and 16). Many of these flow features are qualitatively similar to the laminar boundary layer separation about circular cones at low speeds discussed in Ref. 17.

At the higher Mach number, $M_\infty = 4.25$, mixed flow conditions are present at $\alpha/\theta_c = 2.1$ and 2.5 and the sharp pressure rise following the first pressure minimum is caused by internal shock waves. As expected, the development of mixed flow conditions with internal shock waves causes much earlier separation as can be seen from Fig. 14 where flow visualization measurements of ϕ_{s1} are given for 5° and $12\frac{1}{2}^\circ$ cones.

4.3 The Surface Shear Stress

The surface shear stress directions (that is the direction of the limiting streamlines at the base of the boundary layer flow) have been measured by oil streak flow visualization and are

*It is perhaps worth noting that a rough estimate for the relative incidence at which the vortical singularity lifts off the surface is given by $2(\alpha/\theta_c)_a$.

given, for various relative incidences, in Figs. 15 and 16. Data measured at two lengthwise positions $x/L = 0.65$ and 0.85 , are given at the largest relative incidence, and within the scatter, show no systematic influence of lengthwise location. For all conically subsonic cases the limiting streamline directions are reduced smoothly to zero (separation) by the adverse pressure gradient but, with internal shocks present, the boundary layer cross flow near the wall is reversed, and separation is produced, extremely rapidly. The large boundary layer outflows from the leeward generator under the vortex core and the subsequent secondary separation are also shown.

The magnitude of the local skin friction coefficient, determined from the Preston surface pitot tube measurements, are shown in Figs. 17 and 18 for Mach numbers 1.8 and 4.25, respectively. It was noted earlier that the Preston tubes were aligned against the surface streamlines for each circumferential angle. Also the assumption is made in reducing the data that the two-dimensional calibration of these tubes (Ref. 20) applies, that is, in effect, that the boundary layer crossflows are small. The turbulent boundary layer results in Ref. 14 show that this condition will be satisfied except perhaps near primary separation.

For a relative incidence of about unity the magnitude of the local skin friction coefficient decreases smoothly to a minimum but finite value at separation and at the leeward generator has a value that is close to the zero incidence skin friction coefficient. At $\alpha/\theta_c \approx 2.1$ there are minima at both primary and secondary separations and very high values due to the strong outflow, near the leeward generator. It should be noted, however, that while the actual surface shear stress ($\tau_w = C_{fe} 0.7 p_e M_e^2$) on the leeward generator exceeds that on the windward generator for $M_e = 1.80$, the reverse is true for $M_{\infty} = 4.25$ due to the low density on the leeward side in this latter case. In fact,

$$(\tau_w)_{180} = 1.11 (\tau_w)_0 \quad \text{for } M_{\infty} = 1.80, \alpha/\theta_c = 2.12$$

while

$$(\tau_w)_{180} = 0.65 (\tau_w)_0 \quad \text{for } M_{\infty} = 4.25, \alpha/\theta_c = 2.10$$

4.4 The External Flow

Measurements of the symmetrical external flow field were made, using the flow field probes, up to relative incidences of 2.5. Attempts to measure asymmetric conditions at $M_{\infty} = 1.8$ and $\alpha/\theta_c = 4$ were frustrated by insufficient height adjustment on the probe support and by unsteady conditions (perhaps vortex bursting).

Pitot pressure contours (i.e., lines of constant values of the ratio of local pitot pressure divided by pitot pressure of the undisturbed uniform stream) have been constructed from surveys made at various probe heights and are shown in Figs. 19 and 20 for Mach numbers 1.80 and 4.25. The probe pitot pressures have been corrected for the measured local flow angularities. Notice that while the probe head size seems rather large, representing about 2.9° of circumferential angle, the pitot tube opening is only $1/10$ of this and so the steep pitot pressure gradients are readily measured.

For moderate relative incidence, $\alpha/\theta_c = 1.01$ and 1.26 , the contours show the lobes of vortical fluid accumulating near the leeward generator, the maximum thickness occurring some distance downstream (larger ϕ) of where the windward boundary layer has separated ($\omega_s = 0$). At the larger relative incidences the centerline of the separating shear layer (indicated by a dash-dot line) can be seen starting from the primary separation angle ϕ_{s1} (approximately tangentially) and merging into the well-defined but rather extensive vortex core. The boundary layer near the leeward generator and under the vortex core is too thin to be penetrated by the present probes but the lobe of vortical fluid from it can be seen, for $\alpha/\theta_c = 2.5$, just beyond the secondary separation angle ϕ_{s2} . It is noted that fluid of high total pressure flows down onto the leeward generator (forming an attachment line there) and out under the vortex core. For the conically mixed flow case, $M_{\infty} = 4.25$, $\alpha/\theta_c = 2.49$, shown in Fig. 20, the position of the internal shock wave is also shown.

Figure 22 shows an example of the circumferential distribution of the transverse components of Mach number and flow direction at a height above the cone surface ($\bar{h} = 0.212$) slightly in excess of the center of the vortex core ($\bar{h} \approx 0.205$). Rapid changes of these quantities through the separated shear layer (indicated as SSL on the figure) and near the vortex core, VC, are shown, together with the strong downflow near the leeward generator. It is interesting to compare the vortex cone heights with those given for low speed flow with laminar separation in Ref. 17. From Fig. 21 it can be seen that the vortex cores occur at very nearly the same circumferential position but are nearer the cone surface, at a given α/θ_c , for the present results involving higher Mach number and turbulent separation. This is partly due, of course, to the much later separation positions.

The structure of the external flow which emerges from the present high Reynolds number measurements at large relative incidence, with its well-defined symmetrical vortices and high skin friction coefficient near the leeward generator (Fig. 23), contrasts strongly with Tracy's measurements (Ref. 16) taken at much lower Reynolds numbers ($Re_{L_{\infty}} = 0.5 - 4.2 \times 10^5$) with laminar boundary layers. His results show only a single massive lobe of vortical fluid above the leeward generator.

5. Conclusions

Based on high Reynolds number measurements on the surface and in the external flow field above yawed 5° and $12\frac{1}{2}^\circ$ semianple cones, at Mach numbers of 1.80 and 4.25, it is concluded that:

(a) Numerical methods (such as that proposed by D. J. Jones, Ref. 7) for the solution of the unseparated inviscid supersonic flow about yawed circular cones give an excellent prediction of the flow up to moderate relative incidence (say $\alpha/\theta_c < 1.2$). Such methods are presently restricted to conically subsonic flow and to relative incidences below those resulting in liftoff of the vortical singularity. The boundaries defining the onset of mixed flow conditions and/or the liftoff of the vortical singularity need to be calculated.

(b) The development of the viscous flow and separation about circular cones, with increasing relative incidence, is a gradual, progressive, steady and essentially conical process involving the formation of symmetrically disposed lobes of vortical fluid ($0.8 < \alpha/\theta_c < \text{about } 1.5$) which develop into vortices and which remain comparatively close to the cone surface on either side of and near, the leeward generator. At high Reynolds numbers there is no general eruption of vortical fluid from the cone surface which would cause sudden changes to the external inviscid flow.

(c) The construction of an inviscid flow model with free vortex sheets, similar to the corresponding slender delta-wing case, is needed to describe the flow at large relative incidence ($\alpha/\theta_c > \text{about } 1.5$).

References

1. D. Küchemann, "Hypersonic aircraft and their aerodynamic problems," Part 5 of Progress in Aeronautical Sciences, Vol. 6 (eds. D. Küchemann and L. H. G. Sterne), Pergamon Press, 1965.
2. J. G. Jones, "A method for designing lifting configurations for high supersonic speeds using the flow fields of non-lifting cones," Royal Aircraft Establishment, Farnborough, U.K., Report No. Aero 2674, 1963.
3. L. H. Townend, "On lifting bodies which contain two-dimensional supersonic flows," Royal Aircraft Establishment, Farnborough, U.K., Report No. Aero 2675, 1963.
4. P. M. Stocker and F. E. Mauger, "Supersonic flow past cones of general cross section," Journal of Fluid Mechanics **13**, 383-399 (1962).
5. K. I. Babenko, et al., "Three-dimensional flow of ideal gas past smooth bodies," NASA TT F-380, April 1966.
6. G. Moretti, "Inviscid flow field past a pointed cone at an angle of attack. Part I--Analysis," General Applied Science Lab., Inc., Westbury, New York, Tech. Report No. 577, December 1965.
7. D. J. Jones, "Numerical solutions of the flow field for conical bodies in a supersonic stream," to be published as a National Research Council, NAE Aero Report.
8. René Gonidou, "Écoulements supersoniques autour de cônes en incidence," ONERA, La Recherche Aérospatiale, No. 120, pp. 11-19, September-October 1967.
9. F. K. Moore, "Laminar boundary layer on a circular cone in supersonic flow at a small angle of attack," NACA TN 2521, October 1951.
10. W. K. Braun, "Turbulent boundary layer on a yawed cone in a supersonic stream," NACA TN 4208, 1958.
11. F. K. Moore, "Laminar boundary layer on a cone in supersonic flow at large angle of attack," NACA TN 2844, 1952.
12. J. C. Cooke, "Supersonic laminar boundary layers on cones," Royal Aircraft Establishment, Farnborough, U.K., Tech. Report No. 66347, November 1966.
13. J. L. Sims, "Tables of supersonic flow around right circular cones at small angle of attack," NASA SP-3007, 1964.
14. W. J. Rainbird, "Turbulent boundary layer growth and separation on a yawed cone at Mach numbers 1.8 and 4.25," Preprint No. 68-98, AIAA 6th Aerospace Sciences Meeting, New York, January 1968.
15. A. E. Bryson, "Symmetric vortex separation on circular cylinders and cones," Journal of Applied Mechanics **26**, pp. 643-648 (1959).

16. J. H. B. Smith, "Improved calculations of leading-edge separation from slender delta wings," Royal Aircraft Establishment, Farnborough, U.K., Tech. Report 68070, March 1966.
17. W. J. Rainbird, R. S. Crabbe and L. S. Jurewicz, "A water tunnel investigation of the flow separation about circular cones at incidence," National Research Council, NAE Aero. Report LR-385, September 1963.
18. R. R. Tracy, "Hypersonic flow over a yawed circular cone," Graduate Aeronautical Labs., California Institute of Technology, Hypersonic Res. Proj. Memo. No. 69, August 1963.
19. R. F. Meyer, "A note on a technique of surface flow visualisation," National Research Council, NAE Aero. Report LR-457, July 1966.
20. E. J. Hopkins and E. R. Keener, "Study of surface pitots for measuring turbulent skin friction at supersonic Mach numbers--adiabatic wall," NASA TN D-3478, July 1966.
21. Z. Kopal, "Tables of supersonic flow around cones," Massachusetts Institute of Technology, Dept. of Electrical Engineering Tech. Report No. 1, 1947.
22. J. L. Sims, "Tables of supersonic flow around right circular cones at zero angle of attack," NASA SP-3004, 1964.
23. A. H. Stone, "On the supersonic flow past a slightly yawing cone, Part I," Journal of Mathematics and Physics 27, pp. 67-81 (1948).
24. A. H. Stone, "On the supersonic flow past a slightly yawing cone, Part II," Journal of Mathematics and Physics 30, p. 200 (1951).
25. Z. Kopal, "Tables of supersonic flow around yawing cones," Massachusetts Institute of Technology, Dept. of Electrical Engineering Tech. Report No. 3, 1947.
26. Z. Kopal, "Tables of supersonic flow around cones of large yaw," Massachusetts Institute of Technology, Dept. of Electrical Engineering Tech. Report No. 5, 1949.
27. A. Ferri, "Supersonic flow around circular cones at angles of attack," NACA TN 2236, November 1950.
28. A. G. Munson, "The vortical layer on an inclined cone," Journal of Fluid Mechanics 20, pp. 625-643 (1964).
29. R. E. Melnik, "A conical thin-shock-layer theory uniformly valid in the entropy layer," U. S. Air Force Flight Dynamics Lab., Report No. FDL-TDR-64-82, 1965.
30. R. E. Melnik, "Vortical singularities in conical flow," AIAA Journal 5, pp. 631-637 (1967).
31. P. Germain, "Recent evolution in problems and methods in aerodynamics," Journal of the Royal Aeronautical Society 71, No. 682, October 1967.
32. M. H. Bertram, "Correlation graphs for supersonic flow around right circular cones at zero yaw in air as a perfect gas," NASA TN D-2339, June 1964.
33. M. J. D. Powell, "A method for minimizing a sum of squares of non-linear functions without calculating derivatives," Computer Journal 7, p. 303 (1965).

Table 1. Babenko-Jones Comparison: $M_\infty = 7$, $\theta_c = 25^\circ$, $\alpha = 15^\circ$, $\gamma = 1.4$

ϕ°	Surface Values				Shock Wave Shape	
	U_J	U_B	P_J	P_B	$(\tan \theta_s)_J$	$(\tan \theta_s)_B$
0	1.5203	1.5202	2.3817	2.3822	0.5654	0.5656
22.5	1.5299	1.5299	2.2471	2.2474	0.5665	0.5667
45	1.5583	1.5585	1.8897	1.8896	0.5698	0.5699
67.5	1.6033	1.6042	1.4249	1.4242	0.5752	0.5752
90	1.6609	1.6633	0.9775	0.9768	0.5820	0.5820
112.5	1.7258	1.7305	0.6314	0.6312	0.5883	0.5884
135	1.7906	1.7976	0.4138	0.4149	0.5906	0.5902
157.5	1.8423	1.8509	0.3207	0.3203	0.5818	0.5816
180	1.8647	1.8646	0.3025	0.3025	0.5734	0.5734

Mesh Size: Babenko; $\Delta\phi = 11.25^\circ$, $\Delta\xi = 0.05$
 Jones; $\Delta\phi = 22.5^\circ$, $\Delta\xi = 0.1$

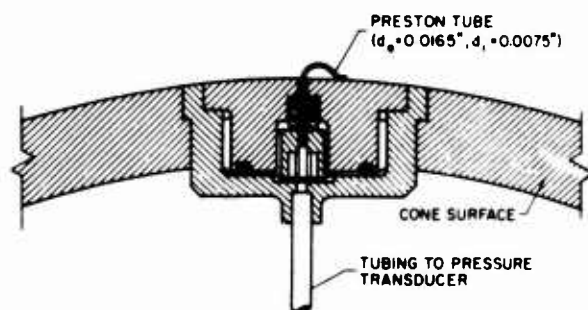


Fig. 1. Installation of Preston Surface Pitot Tubes

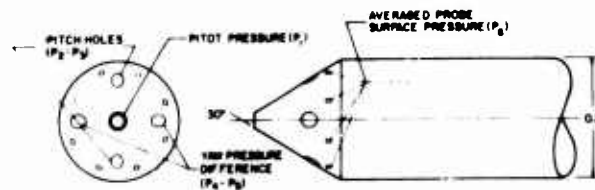


Fig. 3. Flow Field Probe Head

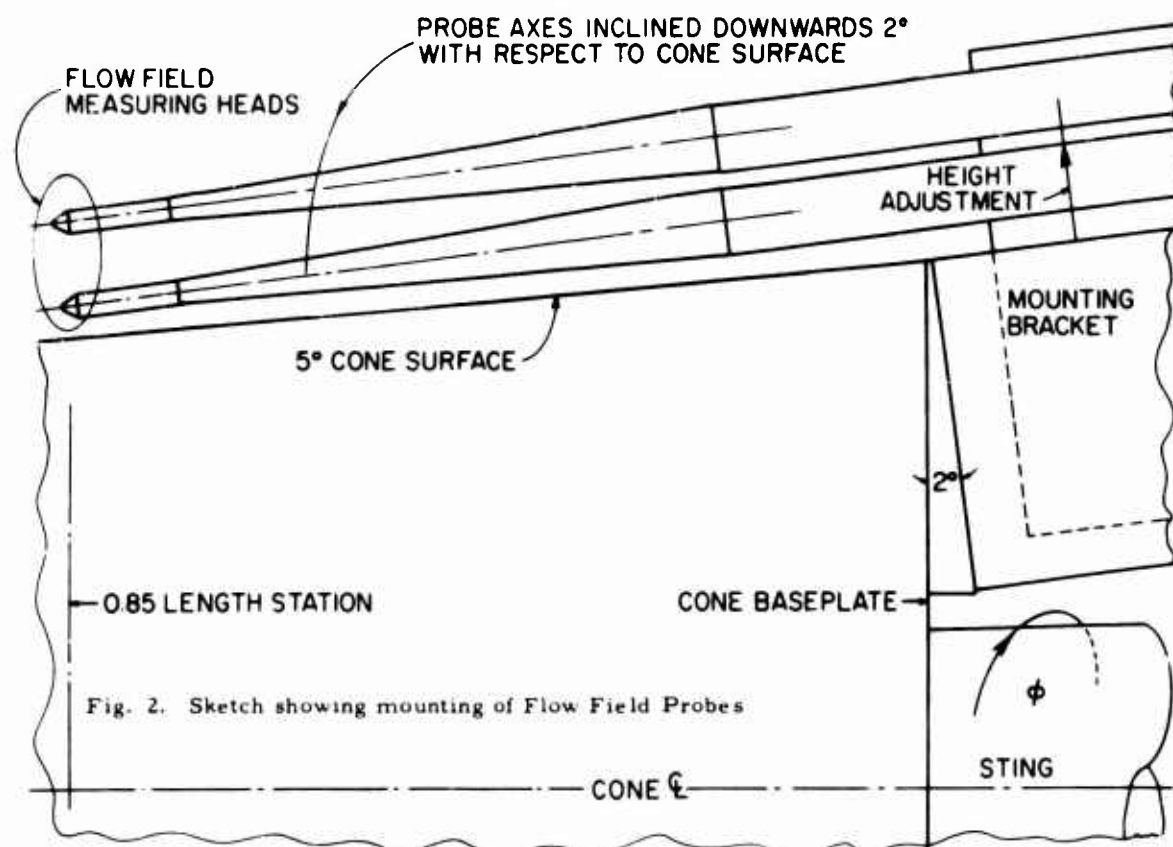


Fig. 2. Sketch showing mounting of Flow Field Probes

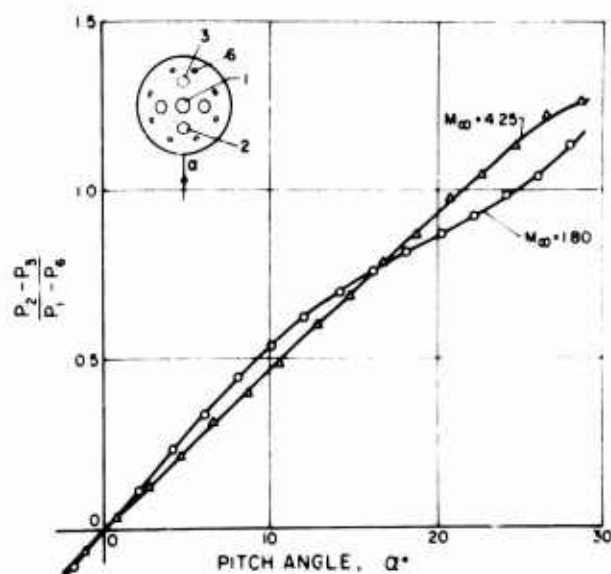


Fig. 4. Typical Probe Pitch Calibration

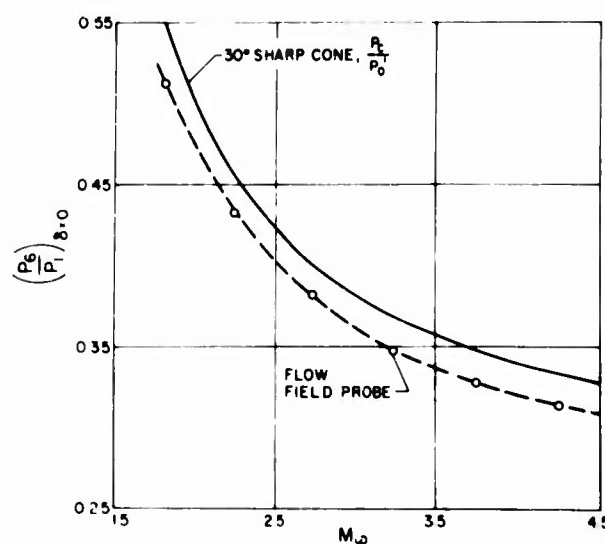


Fig. 5. Typical Probe Mach Number Calibration

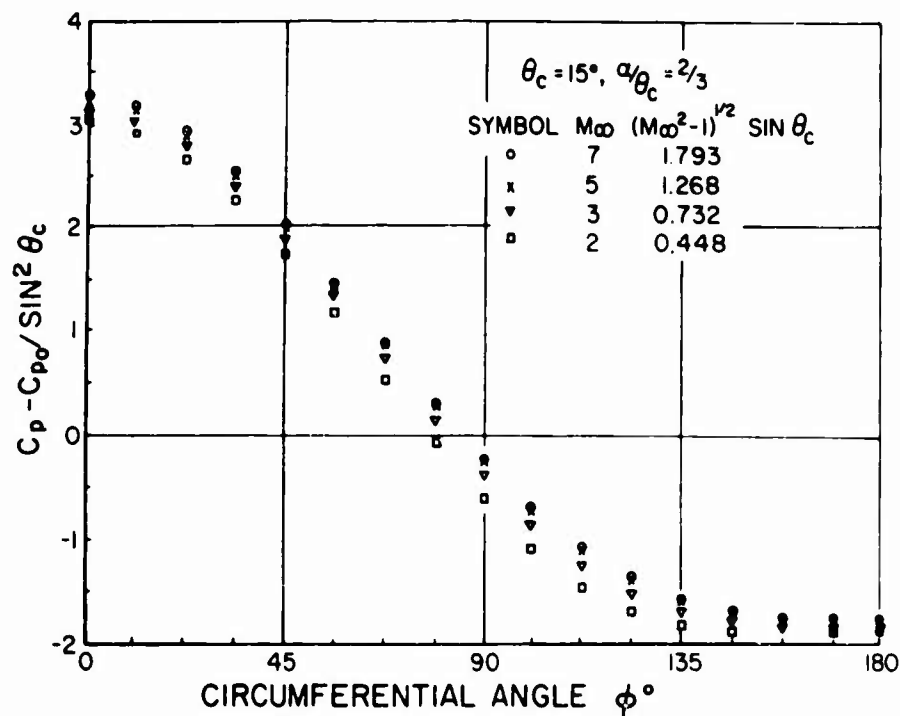


Fig. 6. Pressure Distributions in Similarity Form, from Babenko

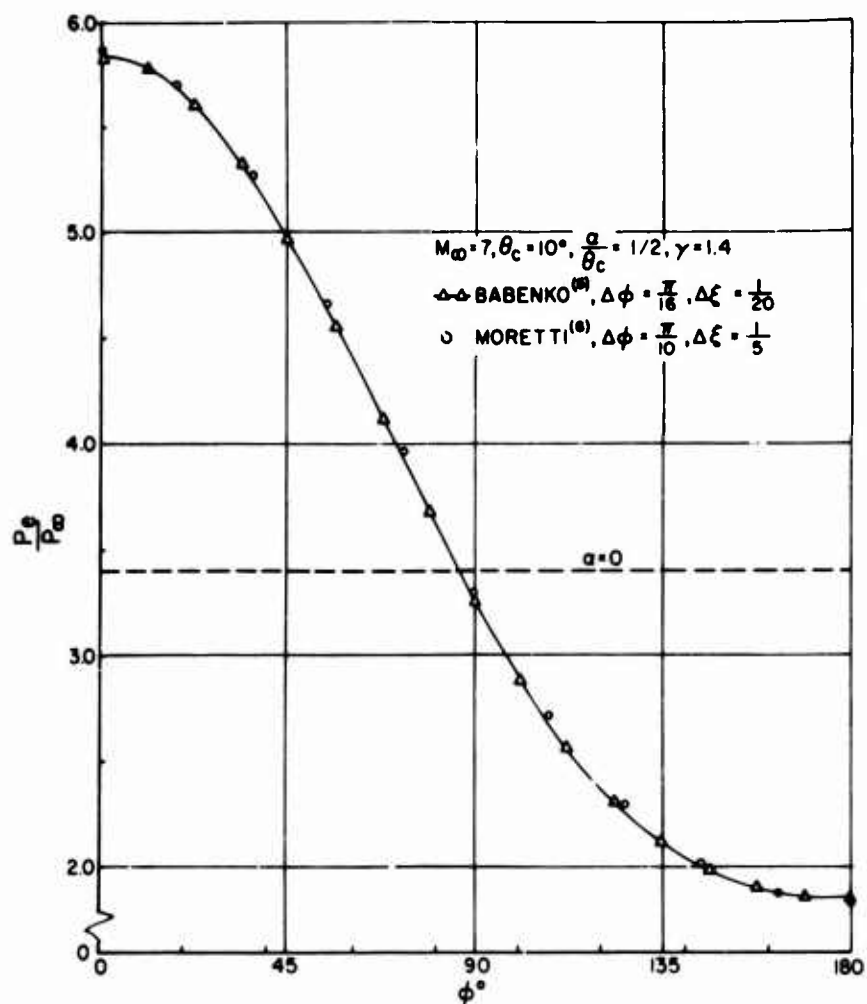


Fig. 7. Comparison of Numerical Calculation Methods (Babenko and Moretti)

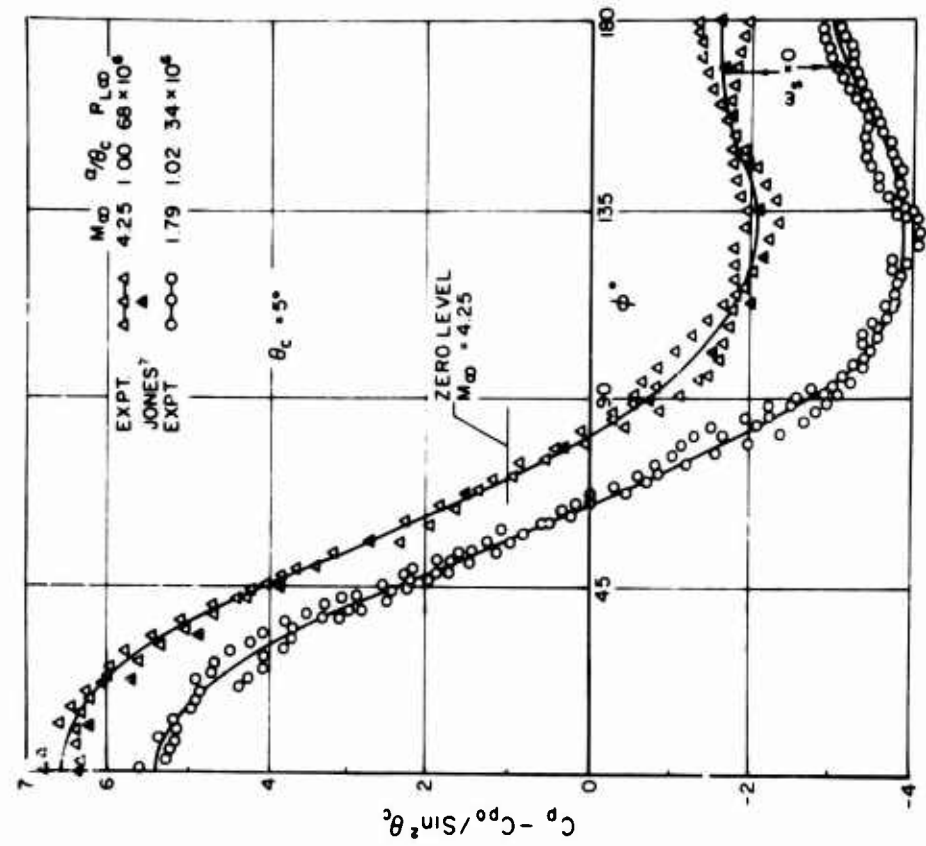


Fig. 9. Comparison of Experimental Pressure Distributions with Numerical Solution of Jones for 5° Cone

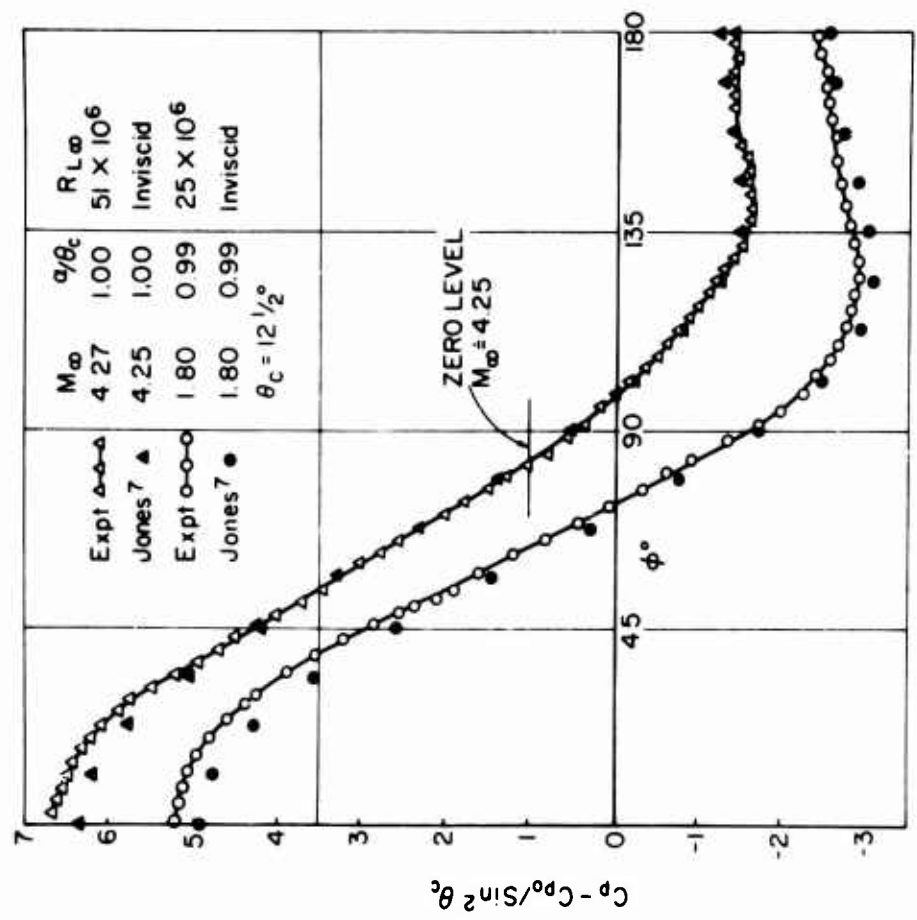


Fig. 8. Comparison of Experimental Pressure Distributions with Numerical Solutions of Jones for 12½° Cone

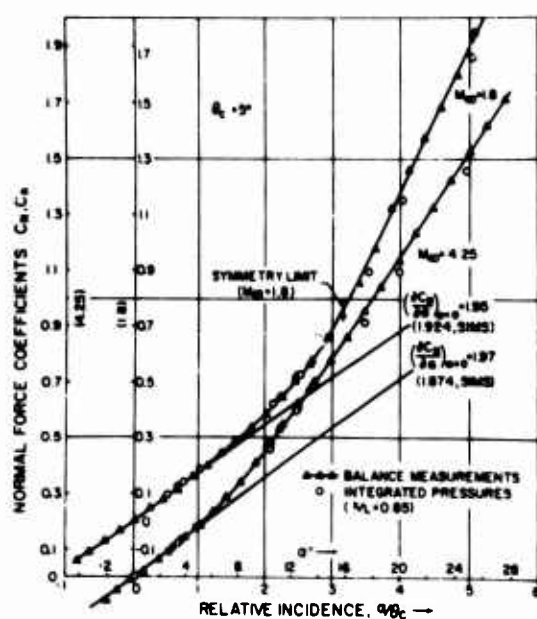


Fig. 10. Normal Force Characteristics: 5° Cone

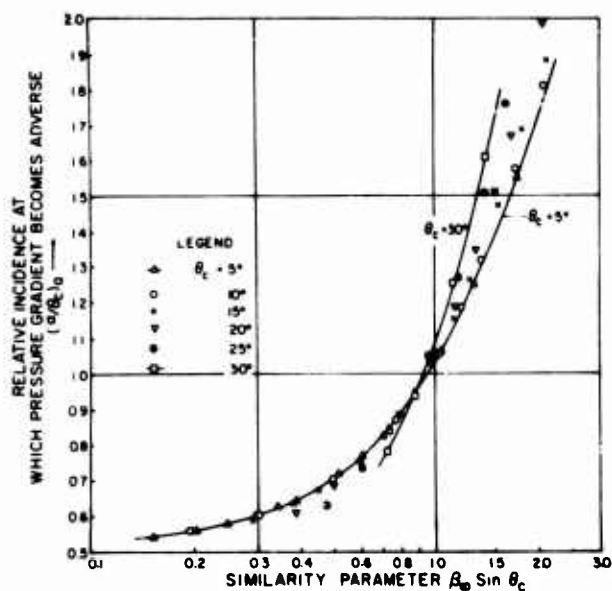


Fig. 11. Minimum Relative Incidence for Separation [based on Sims (13)]

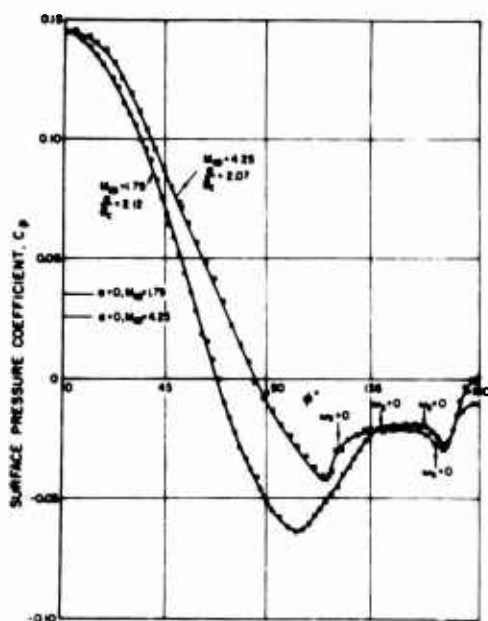


Fig. 12. Circumferential Pressure Distributions around a 5° Cone at a Relative Incidence of 2.1

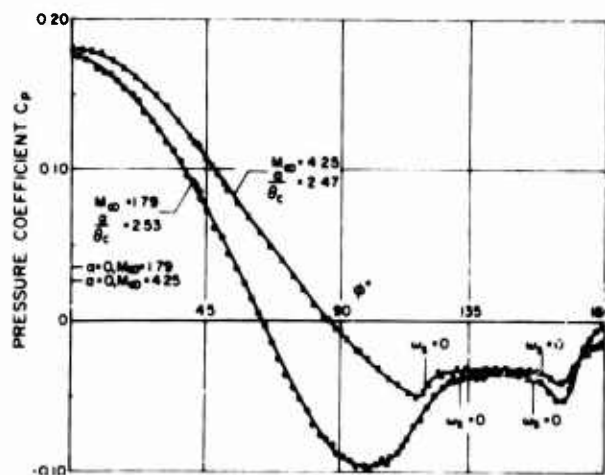


Fig. 13. Circumferential Pressure Distributions around a 5° Cone at a Relative Incidence of 2.5

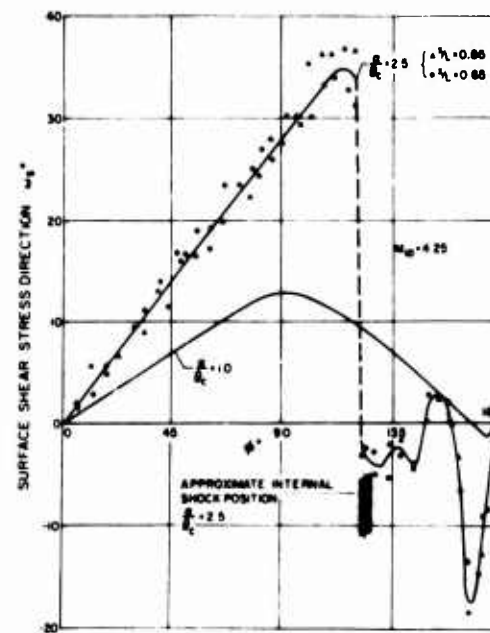
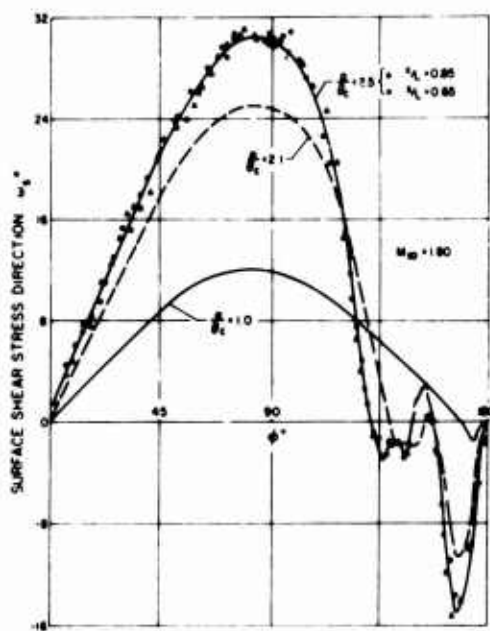
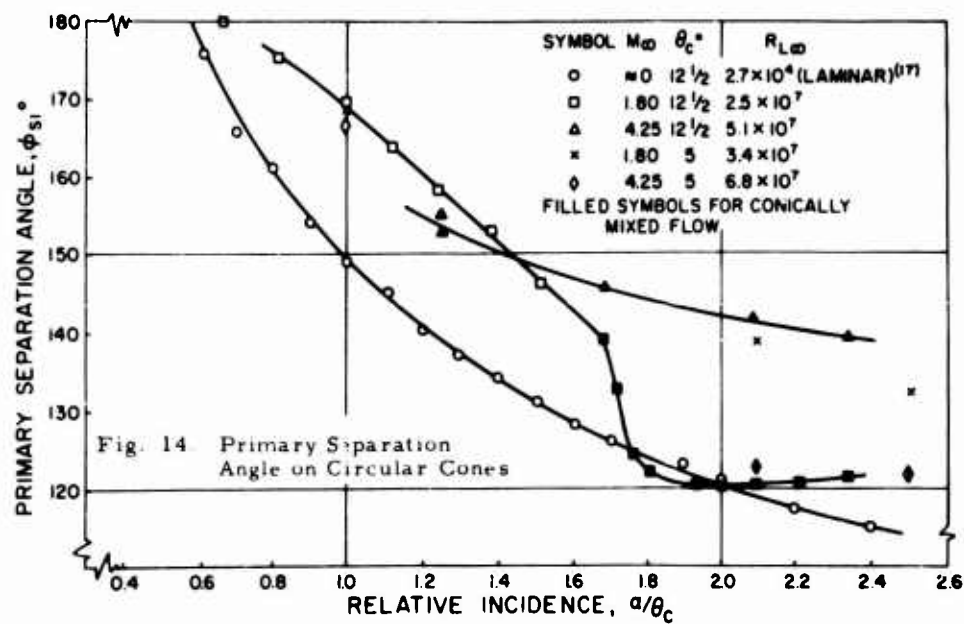
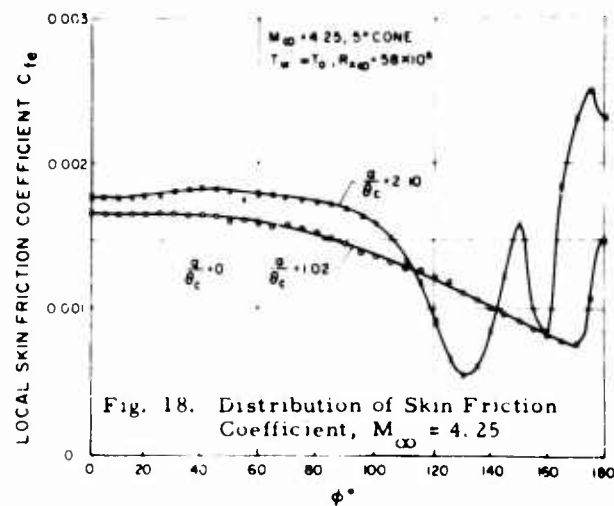
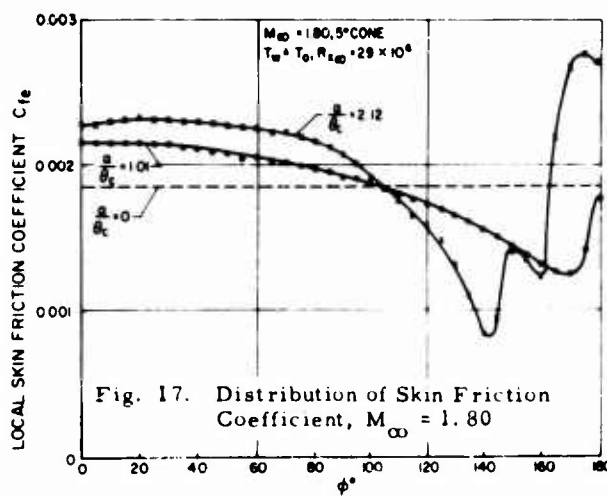


Fig. 15. Surface Shear Stress Direction on 5° Cone at $M_\infty = 1.80$

Fig. 16. Surface Shear Stress Direction on 5° Cone at $M_\infty = 4.25$



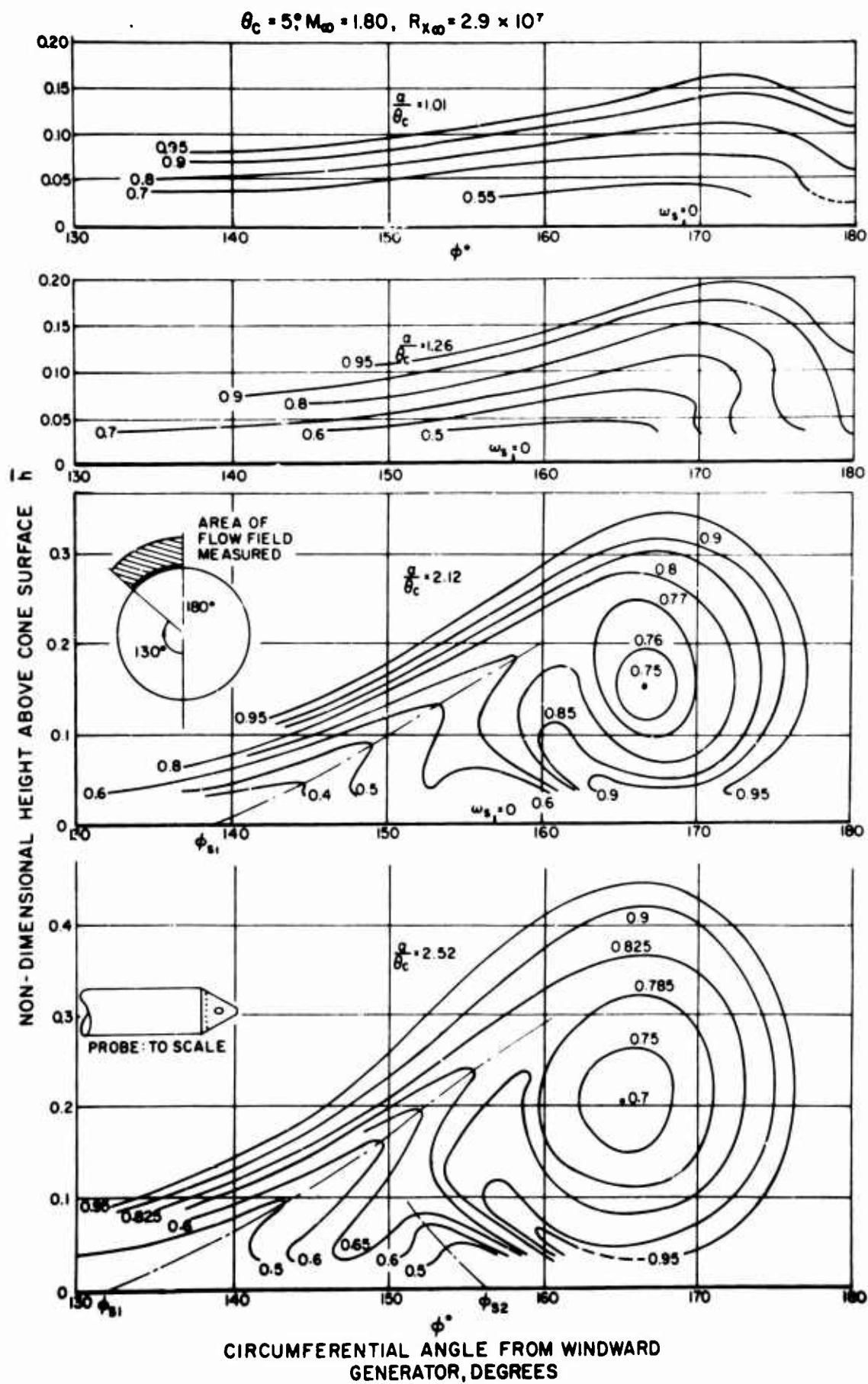
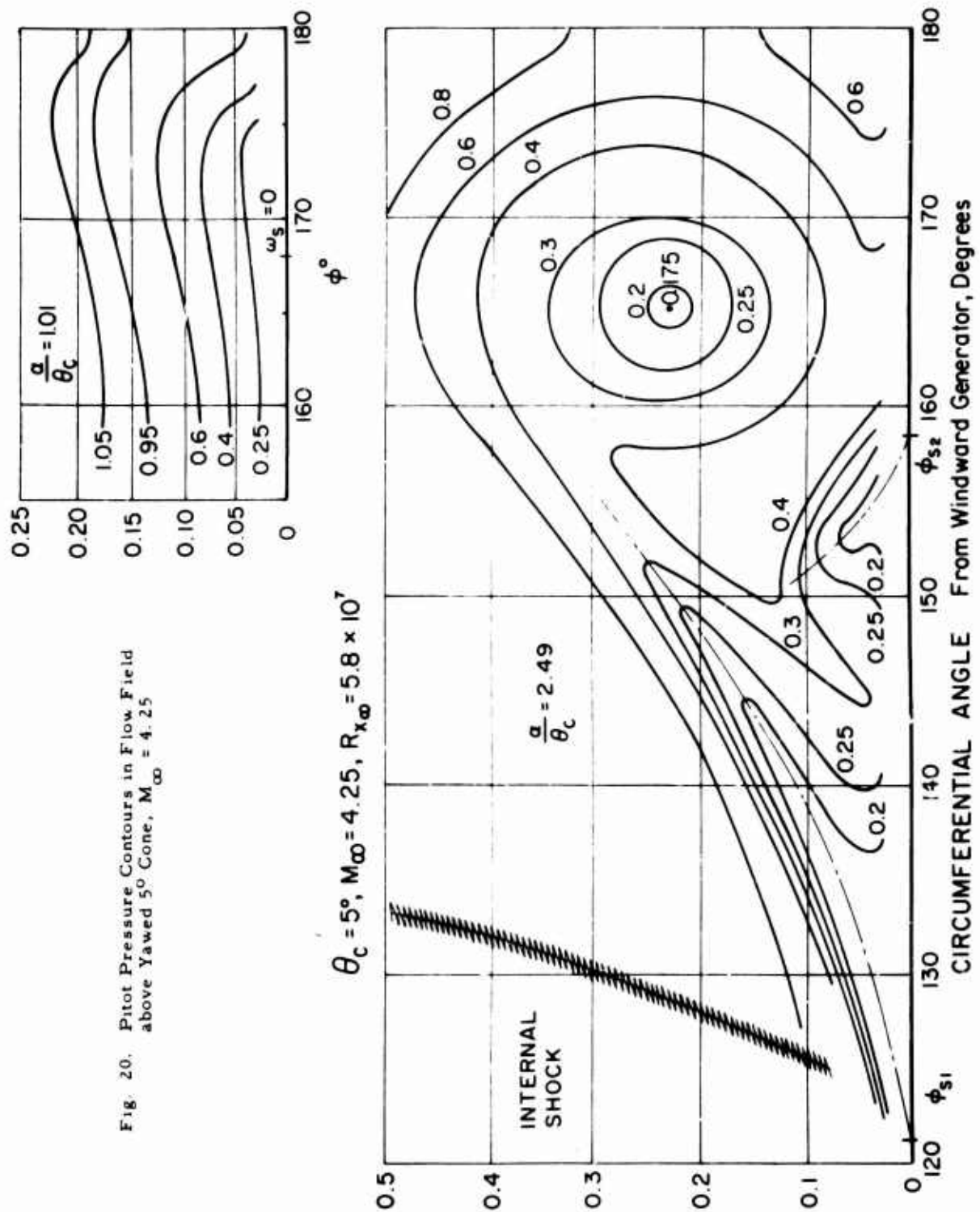


Fig. 19. Pitot Pressure Contours in Flow Field above Yawed 5° Cone, $M_\infty = 1.80$

NON-DIMENSIONAL HEIGHT ABOVE CONE SURFACE, \bar{h} 

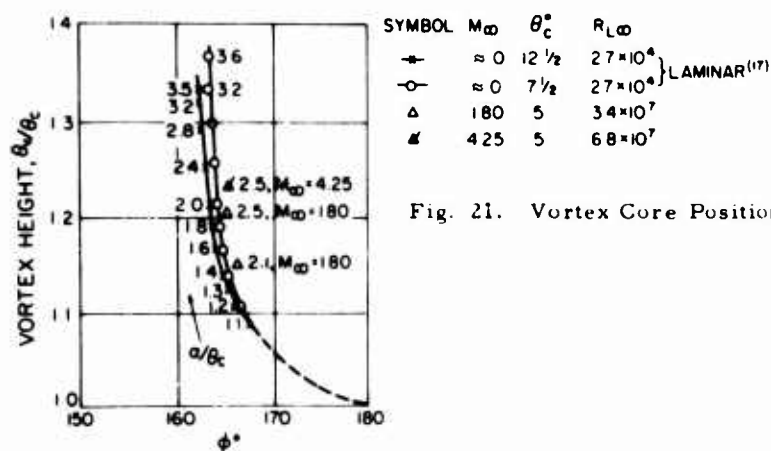


Fig. 21. Vortex Core Positions at Various Relative Incidences

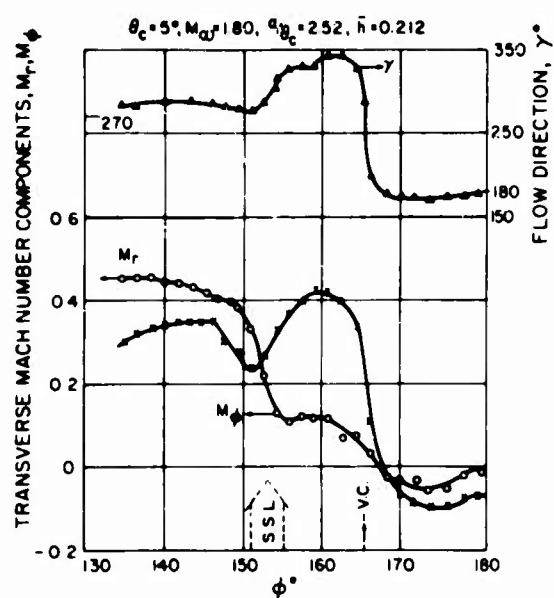
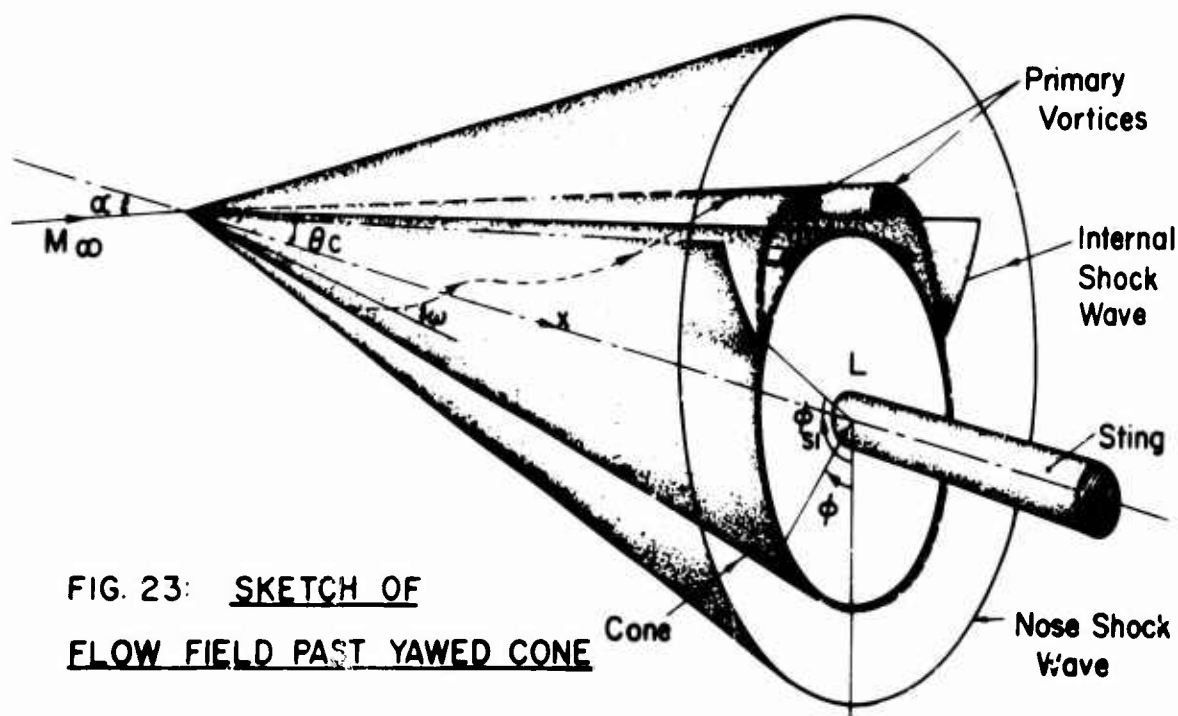


Fig. 22. Circumferential Distribution of Mach Number Components

FIG. 23: SKETCH OF
FLOW FIELD PAST YAWED CONE

ETUDE THEORIQUE ET EXPERIMENTALE DE LA COUCHE
LIMITE AUTOUR D'UN CONE CIRCULAIRE PLACE EN
INCIDENCE DANS UN COURANT HYPERCONIQUE

par

D. Guffroy, B. Roux, J. Marcillat, R. Brun et J. Valensi

Institute des Fluides,
Marseille, France

SOMMAIRE

Le mémoire rend compte des résultats théoriques et expérimentaux obtenus à la suite d'essais effectués dans une soufflerie à rafales ($M = 7$, $Re = 110000/cm$ et $25000/cm$) d'une part, et dans une soufflerie à chocs à haute enthalpie d'arrêt ($M = 9$, $Re = 12000/cm$) d'autre part, en vue de déterminer les caractères de l'écoulement autour d'un cône de demi-angle 9° .

L'étude de l'écoulement pariétal a été réalisée par des mesures de pression statique et de densité de flux de chaleur convectée et par les visualisations des lignes de courant. Un décollement est mis en évidence dans la région la moins exposée au vent pour des incidences très inférieures au demi-angle. La couche limite non décollée reste partout laminaire pour $Re = 25000/cm$ et $12000/cm$ alors que, pour $Re = 110000/cm$, la transition entraîne un recollement turbulent.

En ce qui concerne l'écoulement extérieur, des explorations à la sonde de Pitot ont permis d'obtenir la forme de l'onde de choc pour différentes incidences et de localiser les deux tourbillons d'apex.

Dans le présent mémoire, figurent des résultats constituant une partie des thèses de Doctorat d'Etat qui seront soutenues par M. D. Guffroy (en ce qui concerne la théorie) et M. J. Marcillat (en ce qui concerne les essais dans la soufflerie à rafales).

NOTATIONS

C	fonction de Chapman-Rubensin
H	enthalpie d'arrêt
i	incidence
k	coefficient de conductivité thermique
M	nombre de Mach
p	pression statique
p_0'	pression d'arrêt (Pitot)
Pr	nombre de Prandtl
q	densité de flux de chaleur
r	coordonnée normale à l'axe du cône
Re	nombre de Reynolds
T	température statique
T_f	température de frottement
u	composante de vitesse longitudinale
V	angle d'une ligne de courant pariétale et d'une génératrice
w	composante de vitesse transversale
x	abscisse le long du cône (à partir du sommet)
y	ordonnée normale à la surface du cône
ρ	masse spécifique
n	variable sans dimension ⁽⁸⁾
θ	demi-angle au sommet du cône
φ	angle d'azimut
ν	coefficient de viscosité

INDICES

O	conditions réservoir
-	conditions en amont de l'onde de choc
c	conditions immédiatement en aval de l'onde de choc
e	conditions à la frontière de la couche limite
p	conditions à la paroi du cône
a	conditions sur la ligne de décollement
+	conditions à la température de référence

1. INTRODUCTION

Une étude expérimentale a été conduite en vue de déterminer les caractères principaux de l'écoulement autour d'un cône en dérapage, en particulier dans la couche limite. Les mesures effectuées concernent la distribution de la pression à la surface du cône ainsi que celle de la densité de flux de chaleur convectée.

Dans le but d'étudier l'influence du nombre de Reynolds sur les caractères de l'écoulement ainsi que, dans une certaine mesure, celui de l'enthalpie d'arrêt, les essais ont été effectués, d'une part dans une soufflerie hypersonique "froide" où la température d'arrêt de l'écoulement est suffisamment élevée pour éviter la liquéfaction et, d'autre part, dans une soufflerie à chocs à haute enthalpie d'arrêt.

Dans la soufflerie hypersonique, des explorations à la sonde de Pitot, effectuées pour certaines incidences, ont permis d'obtenir avec précision la forme de l'onde de choc et de localiser les tourbillons d'apex. La configuration de l'écoulement à la paroi (forme des lignes de courant pariétales, délimitation des régions séparées, transition) a pu être déterminée grâce à des visualisations complémentaires obtenues par la méthode du film d'huile.

Les mesures, en particulier celles effectuées dans le plan de symétrie de l'écoulement, ont été confrontées avec la théorie, l'écoulement dans la couche limite supposée laminaire étant déterminé à l'aide d'une méthode de calcul précédemment mise au point et exposée dans un précédent mémoire (1).

Les essais ont été effectués avec le concours, dans la soufflerie à rafales, de MM. R. Guillaume et L. Galles et, dans la soufflerie à choc, de MM. J.P. Guibergia et R. Marmey.

Les résultats obtenus dans la soufflerie à rafales sont extraits d'une étude effectuée au titre d'une collaboration confiée à l'Institut de Mécanique des Fluides de Marseille par l'Office National d'Etudes et Recherches Aérospatiales. Ceux obtenus dans la soufflerie à chocs sont extraits d'une étude qui a fait l'objet d'un contrat de recherches confié à l'Institut de Mécanique des Fluides par la Direction des Recherches et Moyens d'Essais (Direction des études techniques).

2. CONDITIONS DES ESSAIS ET TECHNIQUES DE MESURE

2.1. Soufflerie à rafales

2.1.1. Conditions des essais

Les essais ont été effectués dans la soufflerie hypersonique à rafales de l'I.M.F.M. dans les conditions suivantes :

Pression génératrice : 23.89 bars (respectivement 5.16 bars)
 Température génératrice : 600 °K
 Diamètre de la section d'essai : 20 cm
 Nombre de Mach : 6.85 (respectivement 6.67)
 Nombre de Reynolds par cm : 110000 (respectivement 25000)
 Température initiale de la maquette : 295 °K

2.1.2. Techniques de mesure et maquette

La maquette utilisée est un cône circulaire, de demi-angle au sommet 9°. Elle est équipée de 18 pastilles calorimétriques déjà décrites (2) destinées aux mesures de densité de flux de chaleur et régulièrement réparties le long d'une génératrice, la première étant à 55 mm du sommet. Les visualisations de l'écoulement pariétal ont été réalisées en déposant le long de parallèles, à différentes distances du sommet, de l'huile en couche très mince, puis en développant la surface du cône après la rafale.

2.2. Soufflerie à chocs

2.2.1. Conditions des essais

Les expériences à enthalpie d'arrêt élevée ont été réalisées dans la soufflerie à chocs TC 3 de l'I.M.F.M. dans les conditions énumérées ci-dessous :

Gaz d'essai : azote
 Gaz moteur : hydrogène
 Nombre de Mach du choc incident (tube à chocs) : 6
 Pression réservoir : 290 bars
 Température réservoir : 4000 °K
 Nombre de Mach de l'écoulement libre : 8.9
 Nombre de Reynolds par cm de l'écoulement libre : 12000/cm
 Durée de rafale : 3 millisecondes

2.2.2. Techniques de mesure et maquette

Des mesures de pression et de flux de chaleur ont été effectuées à la paroi d'un cône, de demi-angle au sommet 9° , placé à des incidences comprises entre $1^\circ 30'$ et 9° .

La pression est mesurée à l'aide de capteurs piézoélectriques(3) placés dans la maquette et préalablement étalonnés dans un tube à chocs auxiliaire. Quant au flux de chaleur, il est mesuré par des sondes thermométriques à film de platine.

3. ETUDE DE L'ÉCOULEMENT PARIÉTAL

3.1. Pression statique

La distribution de la pression déterminée dans les différents cas d'écoulement est représentée sur les figures 1a, 1b, 1c. Les valeurs moyennes de p/p_∞ relevées le long de chaque génératrice varient régulièrement en fonction de l'azimut.

Comme il était aisément prévisible, les rapports de pression pour $\varphi = \pi/2$ sont voisins de ceux correspondant à l'incidence nulle. Il faut également noter, dans le cas de la soufflerie à rafales (Fig. 1b et 1c), un minimum de pression atteint pour $\varphi < \pi$ aux incidences les plus fortes.

Pour effectuer une comparaison entre les figures 1b et 1c, il faut tenir compte, d'une part de l'augmentation de l'épaisseur de déplacement sur l'obstacle, d'autre part, de la variation du nombre de Mach de l'écoulement (probablement due à la couche limite de la tuyère).

L'effet du nombre de Reynolds ne devient important qu'aux fortes incidences et dans la région la moins exposée au vent. En particulier, pour $i = 20^\circ$, le rapport p/p_∞ passe de la valeur 0.76 au nombre de Reynolds 110000/cm à la valeur 1.11 au nombre de Reynolds 25000/cm.

3.2. Lignes de courant pariétales (méthode du film d'huile)

3.2.1. Etude à $M_\infty = 6.85$, $Re_\infty = 110000/cm$

Les spectres de l'écoulement pariétal, pour quatre configurations caractéristiques suivant la valeur de l'incidence, sont reproduits sur la figure 2. A l'incidence 2° , aucun décollement n'est observé. Il faut cependant noter que, si la répartition azimutale du frottement présente sur $\varphi = \pi$ un minimum près de la pointe, elle est maximale sur cette génératrice vers l'extrémité de la maquette.

Pour les incidences supérieures et jusqu'au demi-angle du cône, on observe un léger décollement tridimensionnel dans une zone étroite et fermée entourant la génératrice la moins exposée au vent. Cette zone, d'abord confinée au voisinage du sommet du cône aux faibles incidences (Fig. 2b) gagne de l'étendue vers l'aval lorsque l'incidence croît (Fig. 2c).

Pour $i > 10^\circ$, la frontière de la zone de décollement est bien marquée par l'accumulation d'huile le long de deux génératrices symétriques par rapport au demi-plan $\varphi = \pi$. Une région d'écoulement faiblement divergent apparaît également au voisinage de $\varphi = \pi$, limitée par deux génératrices symétriques, lignes d'accumulation d'huile, mettant en évidence un décollement secondaire (Fig. 2d). Cette configuration de l'écoulement est liée à la présence de deux tourbillons d'apex dont l'étude sera précisée plus loin.

3.2.2. Etude à $M_\infty = 6.67$, $Re_\infty = 25000/cm$

Le frottement pariétal étant plus faible que dans le cas précédent, les visualisations sont un peu moins nettes. L'interprétation des spectres est délicate, en particulier pour les incidences faibles (Fig. 3a). On constate bien que l'huile se trouve très peu entraînée lorsque l'incidence est inférieure à 3° , au voisinage de $\varphi = \pi$, mais il est difficile de distinguer s'il y a ou non décollement. Par contre, aux incidences supérieures à 3° , on distingue très bien un décollement (Fig. 3b). La région décollée est nettement délimitée par deux génératrices symétriques par rapport à $\varphi = \pi$, ces génératrices étant des lignes d'accumulation d'huile pour les fortes incidences (Fig. 3c et 3d).

Les figures 2 et 3, ainsi que la figure 4 où sont reproduits pour $i = 7^\circ$ et $i = 11^\circ$ les spectres obtenus pour $Re_\infty = 110000/cm$ et $Re_\infty = 25000/cm$, montrent que la couche limite est, à une incidence donnée, décollée sur une plus grande longueur au nombre de Reynolds le plus bas et, dans ce cas, aucun décollement n'est observé sur la maquette.

3.2.3. Etude du décollement

La figure 5 rend compte de l'évolution de l'azimut des génératrices de décollement de part et d'autre du plan de symétrie de l'écoulement en fonction de l'incidence et pour les deux nombres de Reynolds. Les deux courbes présentées, distinctes aux faibles incidences, se confondent pour une incidence voisine de 7° qui correspond approximativement à l'incidence à partir de laquelle différents auteurs ont prévu l'apparition du décollement en le supposant dû au seul effet du gradient de pression transversal (4)(5). Pour des incidences supérieures à 14° environ, l'azimut des génératrices de décollement devient indépendant de l'incidence. De plus, la valeur limite atteinte correspond à l'azimut de la génératrice de décollement sur un cylindre circulaire placé à une incidence correspondante. Ce résultat remarquable a été mentionné par Avdoulevsky et Miedviediev (4).

D'après ces mêmes auteurs, il n'est pas nécessaire, pour qu'il y ait décollement, que le frottement soit nul et qu'il existe une surface de courant ayant la ligne de décollement en commun avec la surface de l'obstacle. Il suffit que les lignes de courant pariétales admettent une enveloppe passant, soit par un point où le frottement est nul, soit par un point singulier de la surface (ce sera ici le sommet du cône).

Le profil de la composante de la vitesse normale à la ligne de décollement présente alors un point d'inflexion dont la présence peut entraîner l'instabilité de la couche limite susceptible de provoquer la transition et un recollement turbulent. Une telle interprétation se trouve confirmée aux incidences inférieures au demi-angle, pour $Re_\infty = 110000/cm$, par l'aspect des traînées de films d'huile dont la longueur est évidemment fonction du frottement à la paroi.

3.3. Flux de chaleur convectée pariétal dans le plan de symétrie

3.3.1. Résultats expérimentaux

Les résultats, rapportés aux valeurs théoriques à l'incidence zéro, sont représentés en fonction de l'incidence sur les figures 6, 7, 8 (à l'exception de ceux relatifs à $\varphi = \pi$ pour $Re_\infty = 110000/cm$ et $x > 95 mm$), la génératrice $\varphi = 0$ correspondant aux incidences positives et la génératrice $\varphi = \pi$, aux incidences négatives. Le flux de chaleur croît régulièrement en fonction de l'incidence.

En ce qui concerne plus particulièrement la génératrice $\varphi = \pi$ au nombre de Reynolds le plus fort, la figure 9 montre que, pour une incidence positive donnée, le flux de chaleur, en fonction du nombre de Reynolds local Re_x , passe par un minimum. La valeur de Re_x correspondant à ce minimum est de l'ordre de $2 \cdot 10^6$ pour $i = 1^\circ 5$, décroît avec l'incidence et devient sensiblement constante et de l'ordre de 10^6 pour $i > 4^\circ 5$. Après ce minimum, une remontée brutale de flux de chaleur est observée qui semble due à la transition dans la couche limite (6).

3.3.2. Calcul théorique en couche limite laminaire (paroi isotherme)

La densité de flux de chaleur convectée à la paroi s'exprime aisément en utilisant la méthode de calcul déjà exposée par ailleurs qui tient compte de la composante transversale de la vitesse (1).

Il vient :

$$\frac{q}{q_{i=0}} = \left[\frac{\rho_e u_e u_e C}{(\rho_e u_e u_e C)_{i=0}} \left(1 + \frac{4}{3} \frac{\partial w}{u_e \sin \theta \partial \varphi} \right) \right]^{\frac{1}{2}} \frac{H_f - H_p}{(H_f)_{i=0} - H_p}$$

où $C = \frac{\rho_e u_e}{\rho_e u_e}$ est la fonction de Chapman-Rubesin évaluée pour l'enthalpie de référence donnée par Eckert (7).

Le flux de chaleur à incidence nulle est donné par :

$$q_{i=0} = \frac{(H_f)_{i=0} - H_p}{Pr} (\rho_e u_e u_e C)_{i=0}^{\frac{1}{2}} \sqrt{\frac{3}{2} \left(\frac{dS}{dn} \right)_{\substack{n=0 \\ \theta=0}}}$$

où $S = \frac{H}{H_0} - 1$ et $\left(\frac{dS}{dn} \right)_{\substack{n=0 \\ \theta=0}}$ est évalué à partir de l'intégration d'un système d'équations différentielles qui se déduit du système des équations aux dérivées partielles de l'écoulement réel par application des transformations de Mangler et Stewartson et après changement de variables sur le système transformé en vue de l'obtention de solutions de similitude locale (8).

L'enthalpie de frottement H_f peut être calculée à partir de la température statique locale en évaluant le facteur de récupération $r = \sqrt{Pr}$.

Les conditions locales de l'écoulement peuvent être déterminées à l'aide de la méthode B.V.L.R. (9) ou, pour une incidence faible, par la méthode de Sims (10) dérivée de celle de Kopal (11).

3.3.3. Discussion

L'examen des figures 6, 7 et 8 montre que la couche limite est laminaire dans tous les cas pour $\varphi = 0$. Sur la génératrice $\varphi = \pi$, le décollement observé paraît ne pas avoir d'influence notable sur le flux de chaleur pour $Re_x = 110000/cm$. L'effet est plus net pour $Re_x = 25000/cm$. Dans ce dernier cas, les valeurs expérimentales sont nettement inférieures aux valeurs théoriques.

En ce qui concerne le décollement, dans le cas des essais dans la soufflerie à chocs, on peut observer qu'il y a deux influences qui s'opposent. D'une part, la faible valeur du nombre de Reynolds favorise le décollement ainsi qu'il vient d'être constaté. D'autre part, le gradient de pression limite qui correspond au décollement (8) et la composante transversale de vitesse décroissant avec le rapport T/T_0 , la valeur élevée de l'enthalpie d'arrêt tend à retarder ce décollement. La méthode des films d'huile n'ayant pu être appliquée dans la soufflerie à chocs, il n'est pas possible de conclure en utilisant seulement les mesures de flux de chaleur dont les résultats paraissent cependant en bon accord avec ceux donnés par la théorie pour une couche limite laminaire non décollée.

La transition n'a pas été observée à l'incidence nulle sur la maquette pour $Re_\infty = 110000/cm$. Cependant, des essais complémentaires, effectués à des nombres de Reynolds légèrement plus élevés, ont montré que la valeur critique Re_{x_t} , évaluée en admettant que l'abscisse du minimum des répartitions de x flux de chaleur correspond avec celle du début de la transition, est voisine de $3.8 \cdot 10^5$. Ce résultat est en bon accord avec la valeur correspondant au début de la transition indiquée par Nagamatsu, Graber et Sheer (12) qui ont rassemblé les résultats expérimentaux donnés par différents auteurs en les complétant par des essais effectués à des nombres de Mach compris entre 8.5 et 10.5.

A partir de cette valeur critique de Re_{x_t} , il est alors possible de prévoir la position du point de transition à l'incidence zéro dans le cas étudié. Ce point devrait se trouver légèrement en aval du culot de la maquette.

Stetson et Rushton (13) ont étudié le phénomène de transition sur un cône de demi-angle 8° au nombre de Mach 5.5 en appliquant à toute incidence le critère indiqué plus haut pour l'incidence nulle.

La figure 10 montre que les résultats obtenus pour l'abscisse du minimum de flux de chaleur, notée x_t et rapportée à $(x_t)_{i=0}$, sont en bon accord avec ceux de ces auteurs.

Toutefois, il résulte de la présente étude que l'interprétation des observations relatives à ce minimum doit tenir compte du décollement et du recollement éventuels de la couche limite.

4. ETUDE DE L'ECOULEMENT EXTERIEUR

4.1. Forme de l'onde de choc

Sur la figure 11, sont représentées les sections des surfaces de choc par un plan perpendiculaire à l'axe du cône à $x = 195$ mm de la pointe ($Re_\infty = 110000/cm$), déterminées à l'aide d'exploration à la sonde de Pitot.

Il faut remarquer que l'onde de choc subsiste dans la région la moins exposée au vent pour des incidences légèrement supérieures au demi-angle du cône. Ce résultat avait été obtenu théoriquement par Gonidou (14). A l'incidence 15° , l'onde de choc n'est plus une surface fermée et la région la moins exposée au vent est en détente par rapport à l'écoulement infini amont.

Il est facile de déduire de ces résultats la variation de l'angle du plan tangent à la surface du cône en fonction de l'azimut, puis l'intensité de l'onde de choc définie par le rapport $\frac{P_c - P_\infty}{P_\infty}$. La figure 12b montre l'effet de l'incidence et de l'azimut sur l'intensité de l'onde de choc et la figure 12a montre, dans le cas particulier de l'incidence 5° , une comparaison avec la courbe théorique donnée par Gonidou. Un bon accord est observé jusqu'à $\varphi = 120^\circ$; l'écart devenant ensuite important en raison de l'effet de déplacement dû au décollement de la couche limite.

4.2. Cas d'une forte incidence ($i = 20^\circ$)

L'onde de choc n'étant plus une surface fermée et la couche limite étant décollée, il est important d'étudier plus complètement l'écoulement extérieur. L'examen de la figure 13 montre que l'on peut supposer l'onde de choc conique (13b) et que l'effet du nombre de Reynolds est peu important (13a). Une représentation commode est fournie par le tracé des courbes d'égale pression d'arrêt déterminées expérimentalement dans une section normale à l'axe du cône (Fig. 14 et 15). On distingue ainsi très bien la surface de décollement ainsi que l'allure des tourbillons d'apex.

5. CONCLUSION

Des essais ont été effectués dans une soufflerie hypersonique froide et dans une soufflerie à chocs à haute enthalpie d'arrêt en vue de déterminer les caractères principaux de l'écoulement autour d'un cône élané en dérapage. Les mesures ont été effectuées, non seulement à la paroi, mais également entre la surface du cône et l'onde de choc. L'effet du nombre de Reynolds a été étudié. Les essais ont permis de déceler l'apparition de la transition dans la couche limite ainsi que celle du décollement. La localisation et l'étendue des régions séparées ont été déterminées d'une façon précise.

Les résultats des mesures de la densité de flux de chaleur convectée à la paroi ont été comparés avec les résultats du calcul effectué avec une méthode théorique valable lorsque la couche limite tridimensionnelle est laminaire.

L'étude expérimentale a été complétée par l'observation visuelle de l'écoulement pariétal à l'aide de la méthode des films d'huile.

REFERENCES

- (1) J. VALENSI, D. GUFFROY, B. ROUX
"Sur le calcul du coefficient de convection local le long de la ligne d'arrêt d'un corps de révolution en dérapage (écoulements hypersoniques, couche limite laminaire)"
Comptes rendus t. 263, p. 425, Septembre 1966
- (2) R. GUILLAUME, D. GUFFROY, R. MARMEY, J.P. GUIBERGIA
"Méthodes de mesure des flux de convection thermique dans les souffleries à rafales et les tubes à chocs"
Communication présentée au Congrès A.F.I.T.A.E. à Toulouse, Novembre 1965
- (3) P. ISSARTIER, R. MARMEY
"Mesure de la pression à la paroi des obstacles dans les souffleries hypersoniques à chocs réfléchis"
Comptes rendus t. 263, série A, p. 304, 1966
- (4) V.S. AVDOUIEVSKY, K.I. MIEDVIEDIEV
"Décollement d'une couche limite tridimensionnelle"
Mekhanika Zhidkosti i Gaza, n° 2, 1966
- (5) F.K. MOORE
"Laminar boundary layer on cone in supersonic flow at large angle of attack"
N.A.C.A. Report 1132, 1952
- (6) J. VALENSI, R. GUILLAUME
"Transition dans la couche limite autour d'un cône à pointe vive placé en incidence"
Comptes rendus t. 263, série A, p. 396, 1966
- (7) E.R.G. ECKERT
"Engineering relations for friction and heat transfer to surfaces in high velocity flow"
J.A.S. Vol. 22, p. 585, 1955
- (8) C.B. COHEN, E. RESHOTKO
"Similar solutions for the compressible laminar boundary layer with heat transfer and pressure gradient"
N.A.C.A. Report 1293, 1956
- (9) K.I. BABENKO, G.P. VOSKRESSENSKY, A.M. LIUBIMOV, V.V. ROUSSANOV
"Three dimensional flow of an ideal gas past ideal smooth bodies"
N.A.S.A. TT F 380, 1965
- (10) J.L. SIMS
"Tables for supersonic flow around right circular cones at small angle of attack"
N.A.S.A. SP 3007, 1964
- (11) Z. KOPAL
"Tables of supersonic flow around yawing cones"
M.I.T. TR n° 3, 1947
- (12) H.T. NAGAMATSU, R.C. GRAPER, R.C. SHEER
"Roughness, bluntness and angle of attack effects on hypersonic boundary layer transition"
Journal of Fluid Mechanics, Vol. 24, part 1, 1966
- (13) K.F. STETSON, G.H. RUGHTON
"Shock tunnel investigation of boundary layer transition at $M = 5.5$ "
A.I.A.A. J. Vol. 5, n° 5, Mai 1967
- (14) R. GONIDOU
"Écoulements supersoniques autour de cônes en incidence"
La Recherche Aéronautique, n° 120, Sept-Oct. 1967

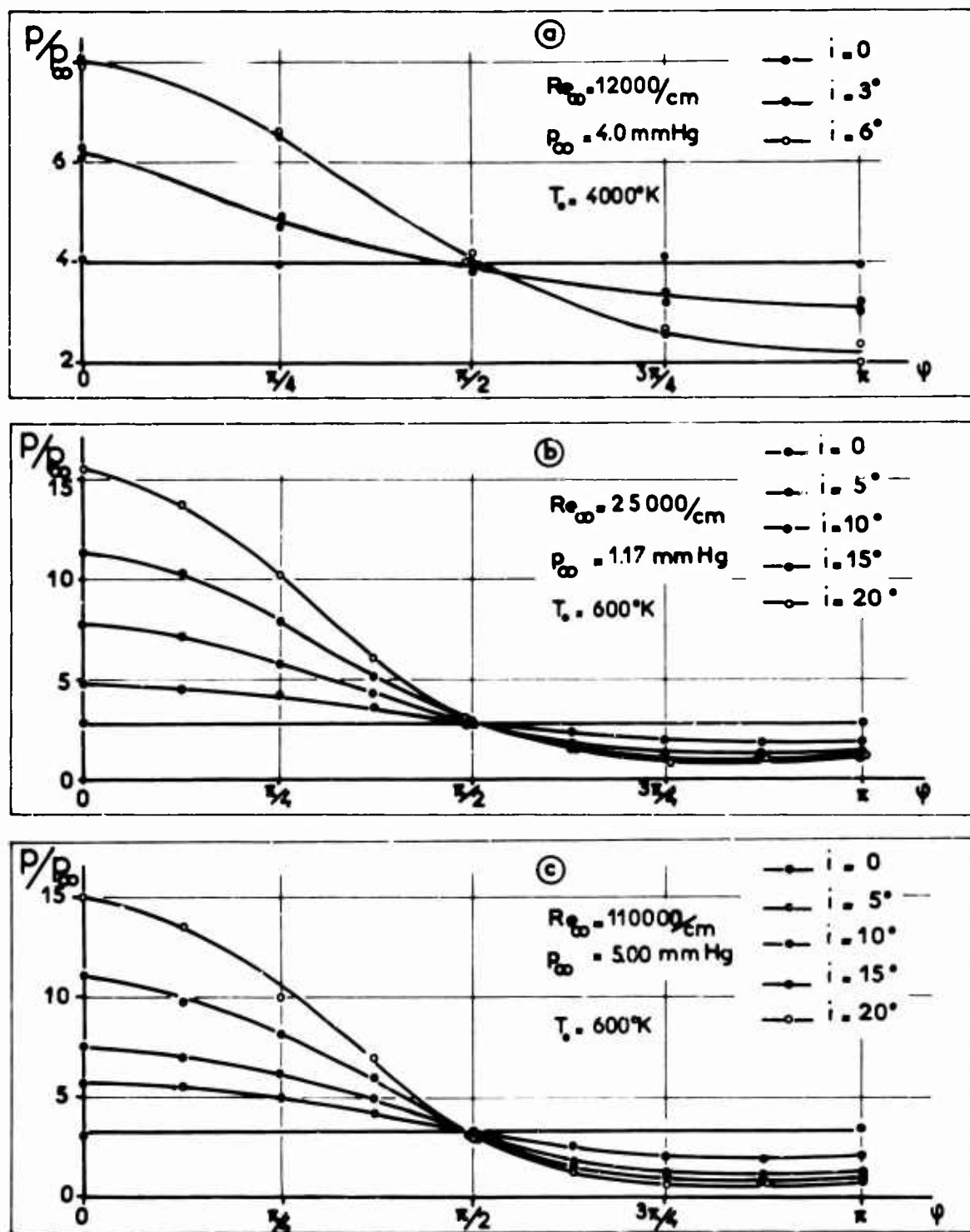
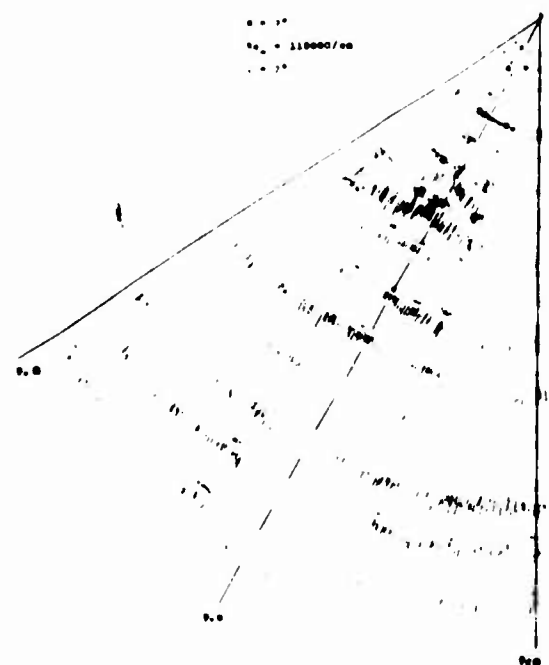
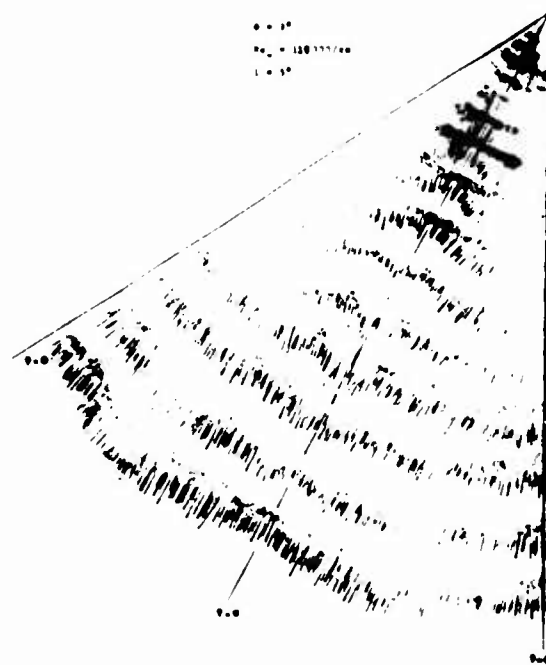


Fig. 1 Pression à la paroi en fonction de l'azimut



(a)

 $i = 2^\circ$ 

(b)

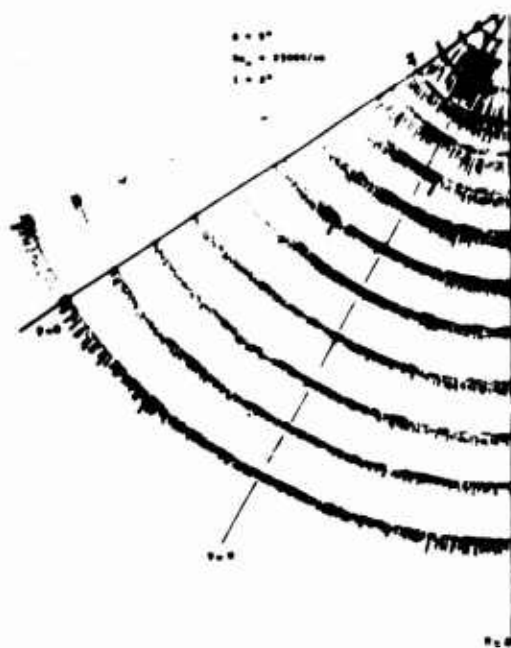
 $i = 5^\circ$ 

(c)

 $i = 9^\circ$ 

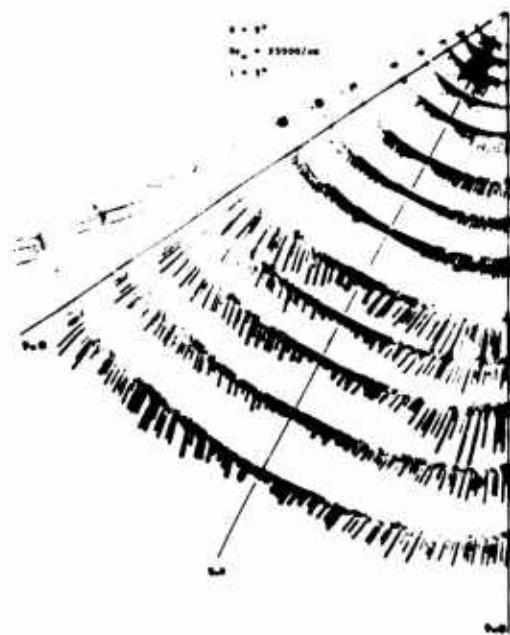
(d)

 $i = 15^\circ$ Fig. 2 Visualisations de l'écoulement pariétal ($Re = 110\,000/\text{cm}$)



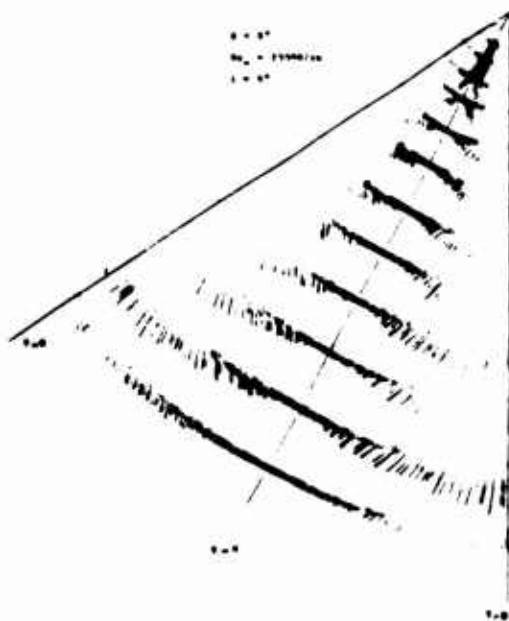
(a)

$i = 2^\circ$



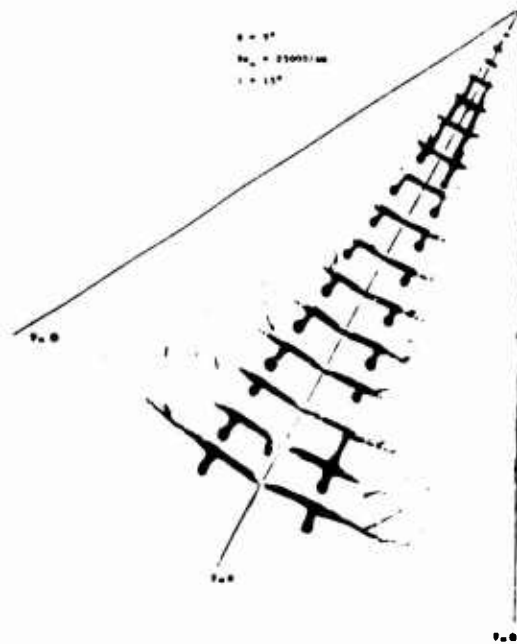
(b)

$i = 5^\circ$



(c)

$i = 9^\circ$



(d)

$i = 15^\circ$

Fig. 3 Visualisations de l'écoulement pariétal ($Re_\theta = 25000/cm$)

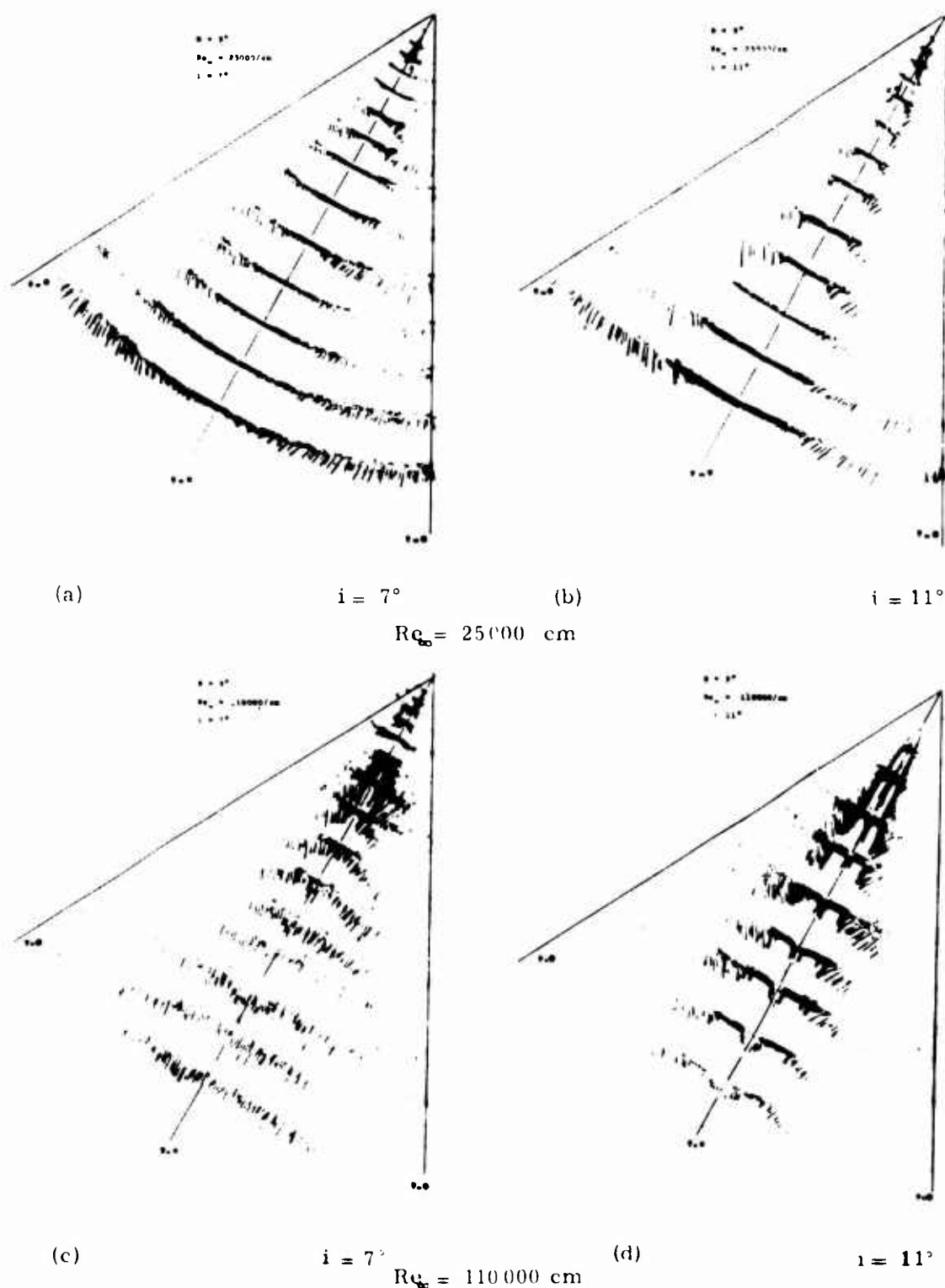


Fig. 4 Visualisations de l'écoulement pariétal ($i = 7$ et 11°)

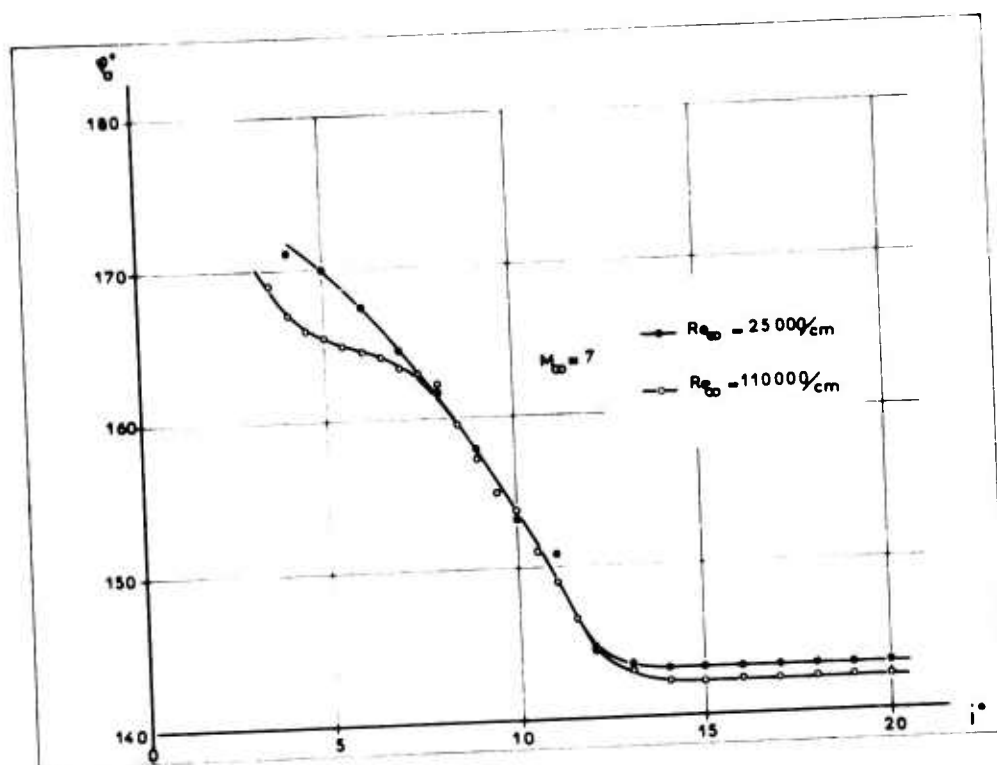


Fig.5 Position de la génératrice de décollement

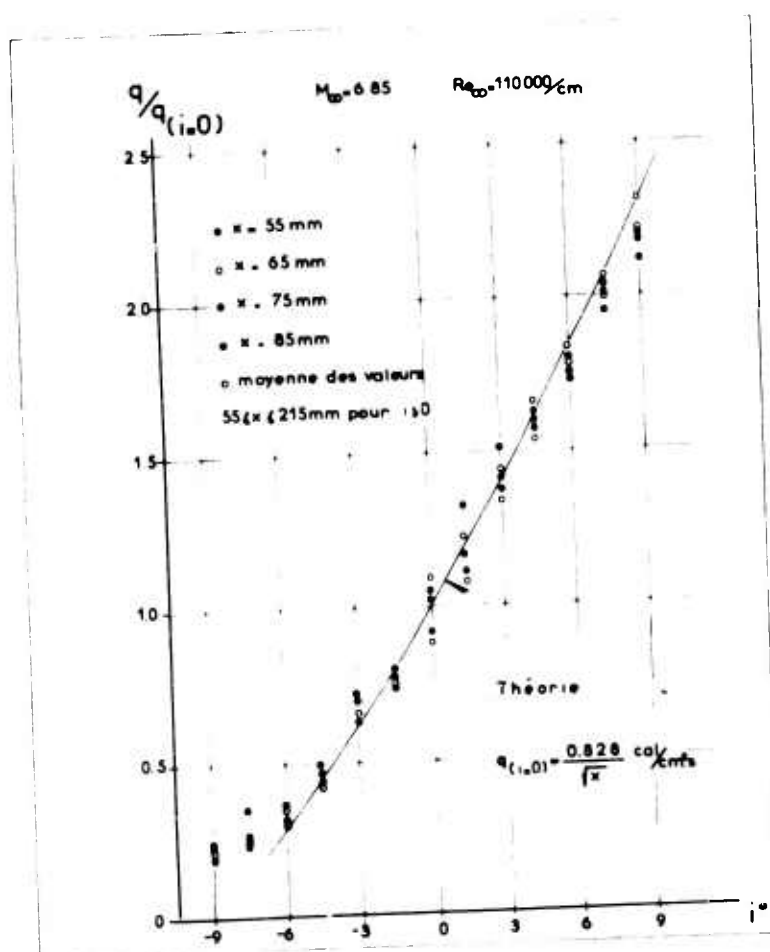


Fig.6 Densité de flux de chaleur convectée à la paroi

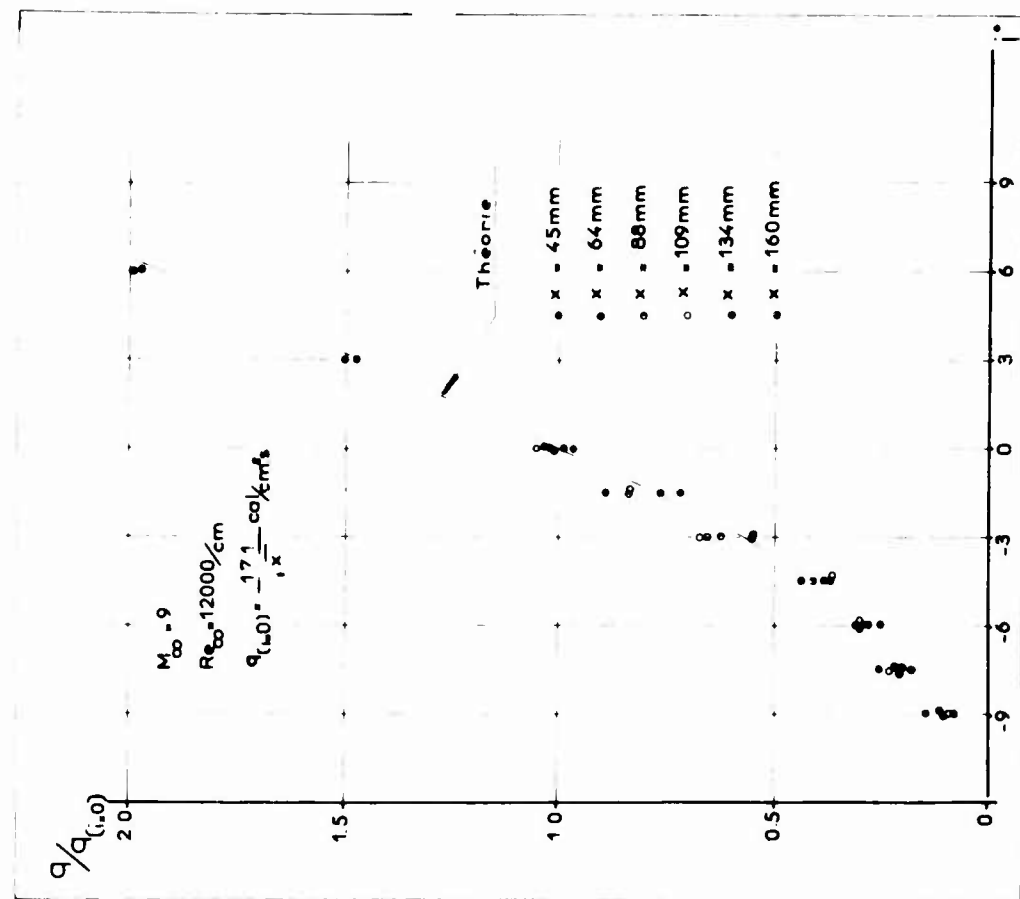


Fig.8 Densité de flux de chaleur convectée à la paroi

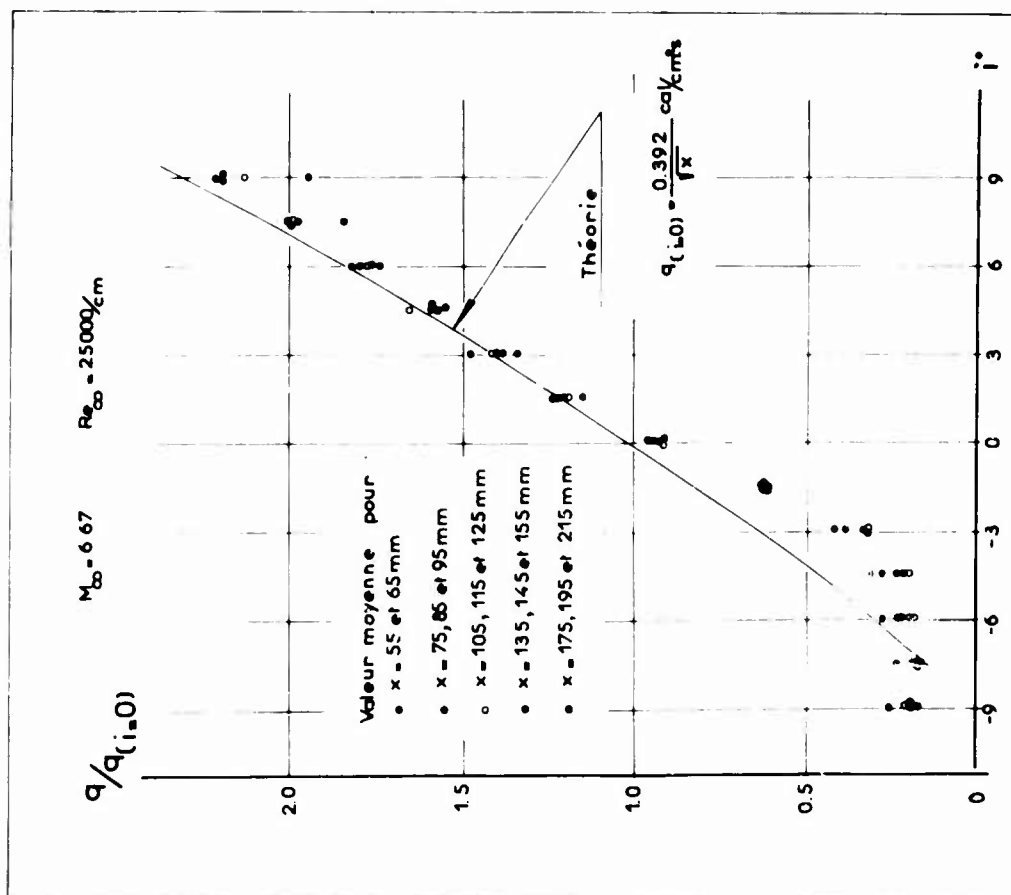


Fig.7 Densité de flux de chaleur convectée à la paroi

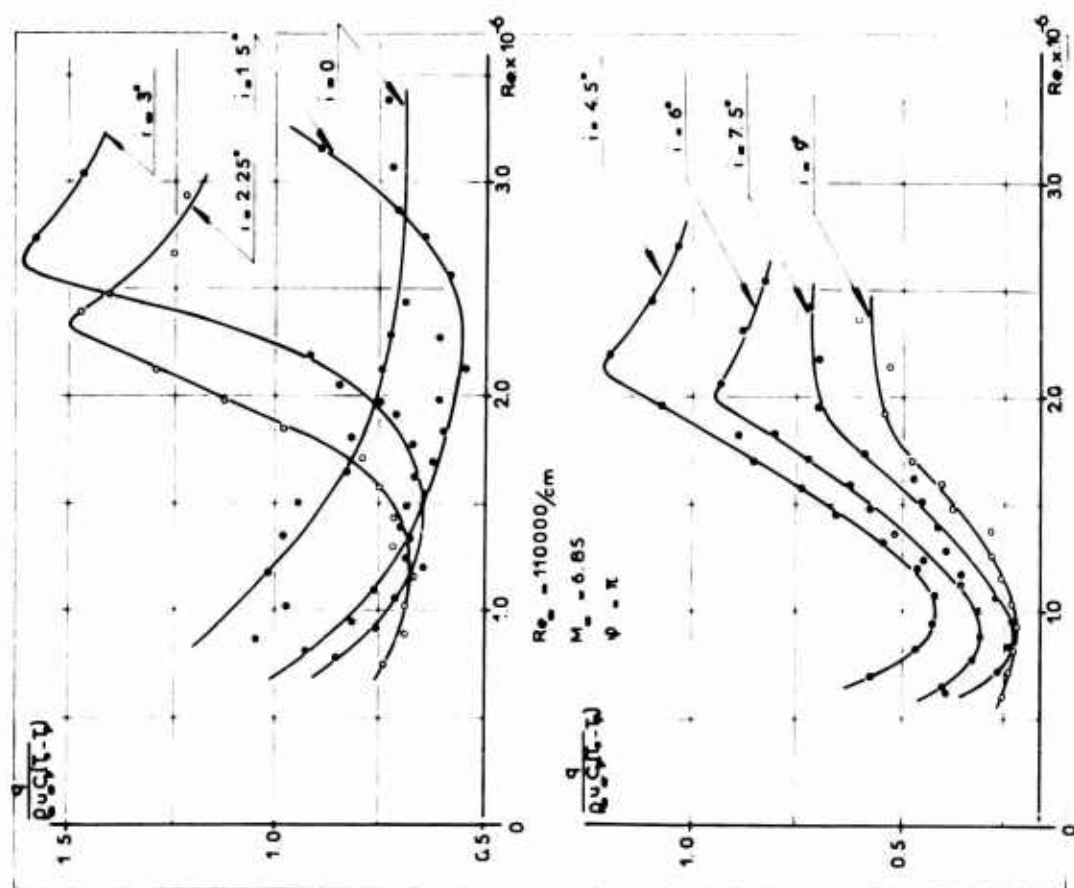


Fig.9 Densité de flux de chaleur convectée à la paroi

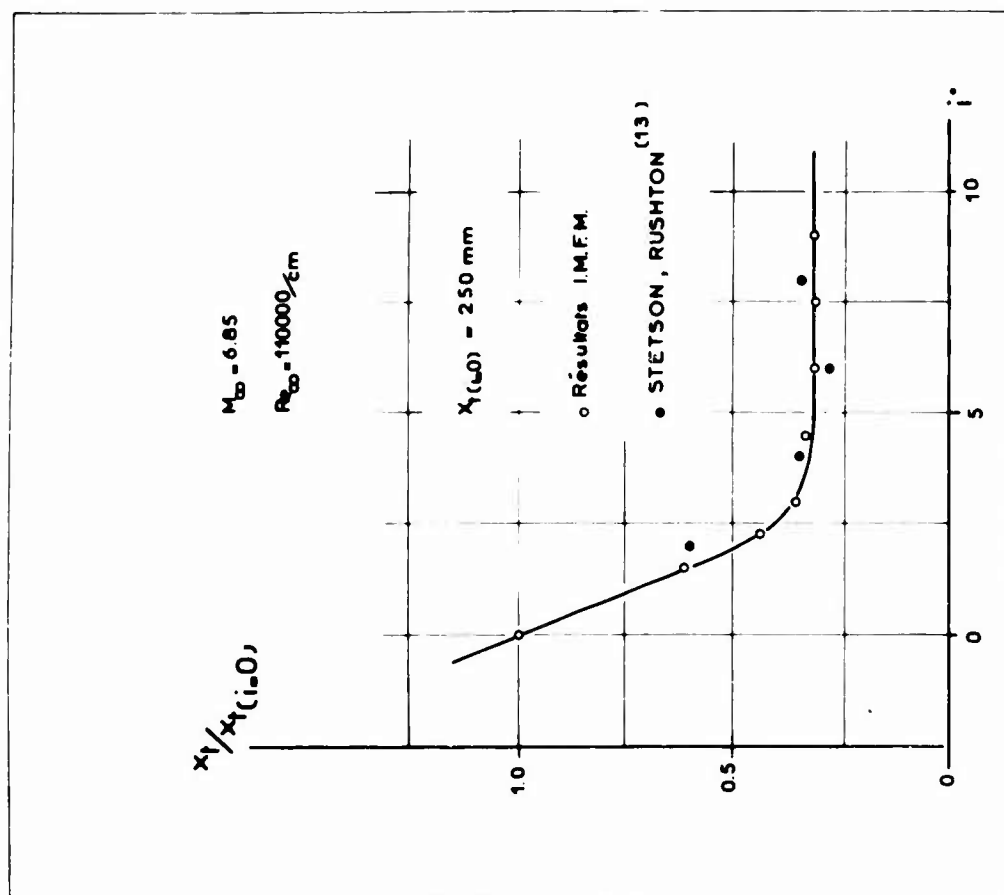


Fig.10 Abscisse du minimum de flux de chaleur

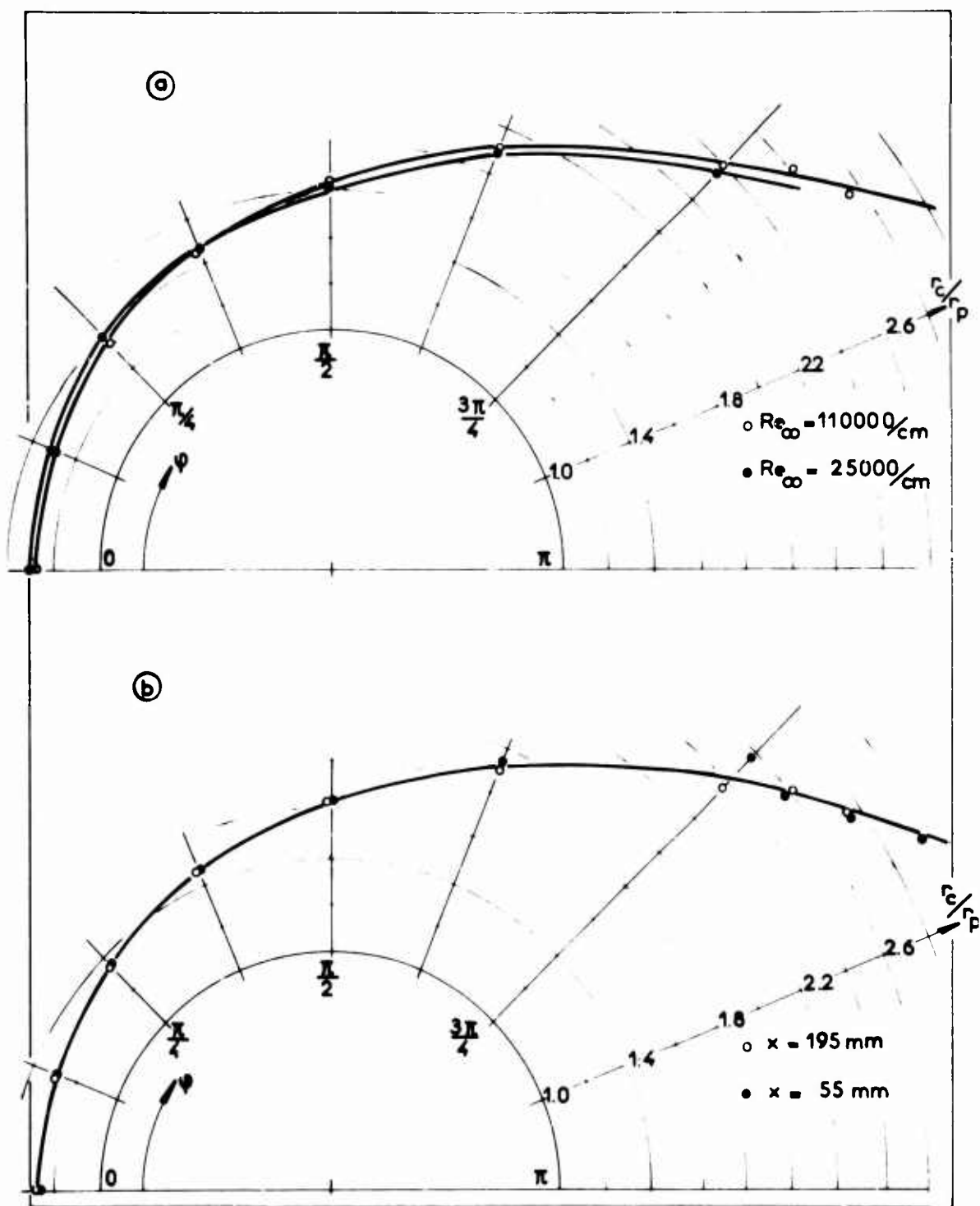
Fig. 13 Forme de l'onde de choc ($i = 20^\circ$)

Fig. 14: REPARTITION TRANSVERSALE
DE LA PRESSION D'ARRET

$Re_{\infty} = 25000/cm$

$M_{\infty} = 7$

$\theta = 9^\circ$

$i = 20^\circ$

$x = 195mm$

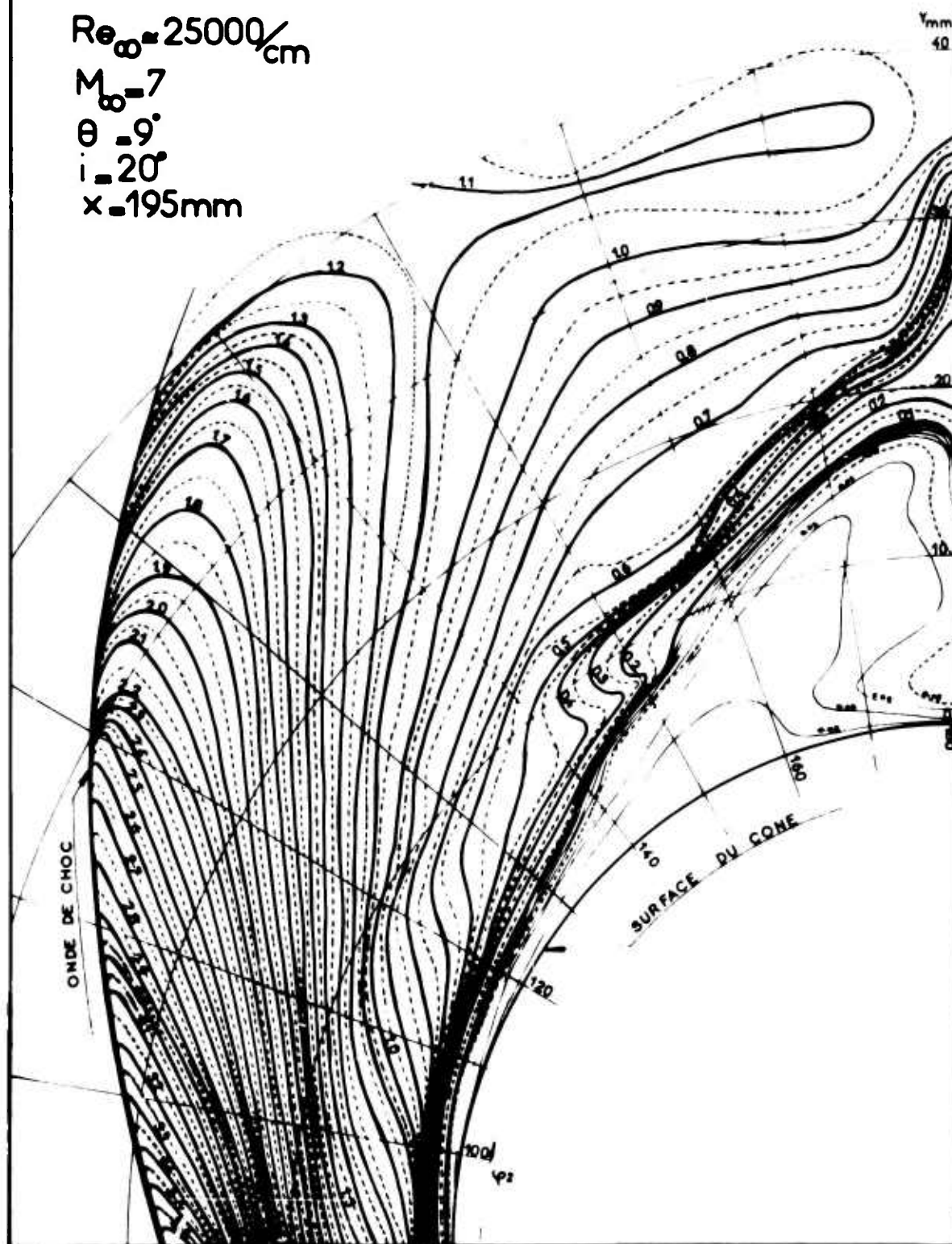
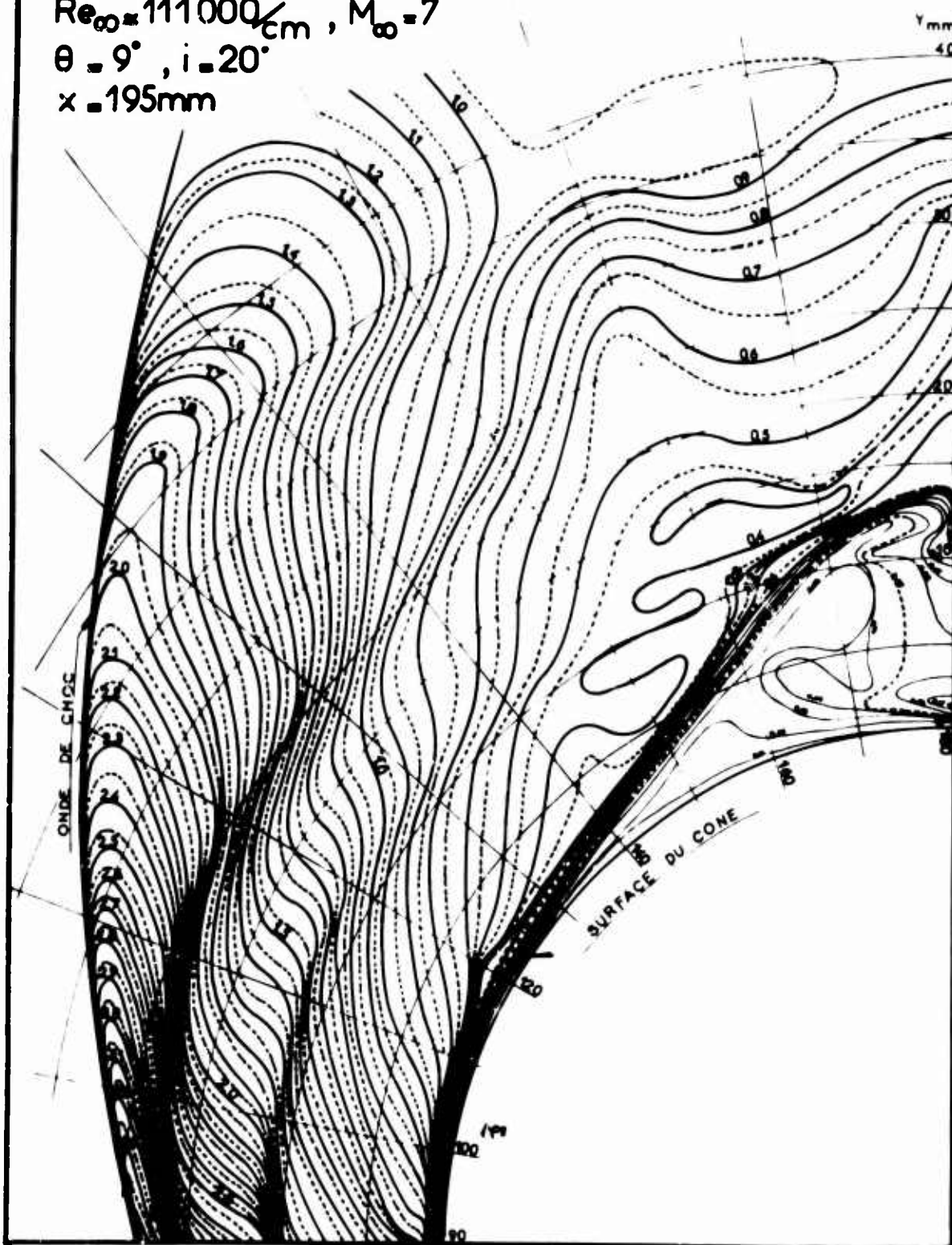


Fig. 15 : REPARTITION TRANSVERSALE
DE LA PRESSION D'ARRET

$Re_{\infty} = 111000/cm$, $M_{\infty} = 7$
 $\theta = 9^\circ$, $i = 20^\circ$
 $x = 195mm$



DISPLACEMENT INTERACTION AND FLOW SEPARATION ON CONES
AT INCIDENCE TO A HYPERSONIC STREAM

by

Terstein K. Fannelop* and George D. Waldman**

Reentry Technology Directorate
Avco Missile Systems Division
Wilmington, Massachusetts

*Section Chief

**Senior Consulting Scientist

SUMMARY

A theoretical analysis is presented for the boundary-layer flow about a blunted cone at incidence to a hypersonic stream. The boundary-layer problem is formulated in terms of streamline coordinates and the equations which result are solved exactly by means of an implicit finite-difference procedure. Methods available for solving the three-dimensional inviscid flow field are examined and found to be inefficient relative to the present boundary-layer method. A semi-empirical method for calculating the inviscid surface pressure rapidly and accurately is presented together with details of the corresponding streamline tracing procedure. The method can account for changes in the local inviscid pressure due to boundary layer displacement effects. Converged solutions of the displacement pressure interaction problem are obtained by coupling the boundary layer and inviscid methods in a step-by-step iteration procedure. The effects of displacement interaction are particularly important on the leeward side. The relationship between these effects and incipient separation is discussed.

NOMENCLATURE

Symbols

A	$\cos \delta \left. \frac{\partial \delta}{\partial \phi_1} \right _{x_c}$
c_p^*	Specific heat at constant pressure (assumed constant)
c_s^*	Speed of sound at stagnation point
E	$\left. \frac{\partial \phi}{\partial \phi_1} \right _{x_c}$
e_2	Metric for lateral coordinate ($e_2 = dn d\phi_1$)
i	Enthalpy (referenced to c_s^{*2})
k(x)	Curvature function
K	Curvature of inviscid streamline in the tangent plane
M_∞	Free-stream Mach number
n	Surface distance normal to streamline
p	Pressure (referenced to $\rho_s^* c_s^{*2}$)
Pr	Prandtl number (assumed constant)
\dot{q}_w	Heat-transfer rate.
Q_1, Q_2, Q_3	Functions defined by Equations (2.9a, b, c)
r	Body radius (normal to axis of symmetry)
R_N^*	Nose radius
R_s	Reference Reynolds number, $R_s = \frac{\rho_s^* c_s^* R_N^*}{\mu_s^*}$
u	Velocity component in the x-direction
v	Velocity component in the y-direction
w	Velocity component in the boundary layer directed transverse to the inviscid streamline
x	Surface distance along an inviscid streamline
x_c	Distance from nose along axis of symmetry
y	Coordinate normal to surface
z	Coordinate along surface normal to inviscid streamline
α	Angle of attack
γ	Ratio of specific heats, $\gamma = \frac{c_p^*}{c_v^*}$
δ	Angle between a surface streamline and the local meridian
δ^*	Mass-flow defect thickness
Δ^*	Effective displacement thickness. Equation (2.14) ($\Delta^* = \delta^*$ with no mass transfer)
ϵ	Perturbation parameter
θ	Local inclination of surface relative to wind vector
θ_c	Cone half-angle

NOMENCLATURE (CONT'D)

μ	Viscosity
ρ	Density
τ	Wall shear (τ_t = tangential, τ_c = crossflow)
ϕ	Meridian angle ($\phi = 0$ on the most leeward generator)
ϕ_i	Meridian angle at which the streamline intersects the cone-sphere juncture. (Also independent lateral variable)

SUBSCRIPTS

b	Body surface
e	Conditions at edge of boundary layer
i	Value at cone-sphere junction; also, number of iterations
s	Stagnation (reference) condition
v	Viscous (displacement) effect
w	Condition at wall
0,1	Zeroth- and first-order quantity

SUPERSCRIP^TTS

A	Assumed value in iteration process (Equation (4.1))
C	Calculated value in iteration process (Equation (4.2))
*	An asterisk () [*] denotes a dimensional quantity

DISPLACEMENT INTERACTION AND FLOW SEPARATION ON CONES AT INCIDENCE TO A HYPERSONIC STREAM

Terstein K. Fannelop and George L. Waldman

1. INTRODUCTION

A blunt nose or leading edge is generally required for survival during reentry, but the availability of new materials and improved design sophistication have led to ever more slender shapes and smaller bluntness ratios. Blunt conical shapes are presently favored in normal (nonlifting) reentry applications. Slender blunted cones are also of interest for lifting reentry since their hypersonic lift-to-drag ratio compares favorably to that of other configurations.

The effects of viscous-inviscid interaction are increasingly important with a decreasing bluntness ratio, however, and ablation of the surface material tends to enhance the interaction effects due to the contribution of mass transfer to the effective displacement thickness. For a fixed angle of attack the interaction effects become more and more important as the cone half-angle is reduced. The sweeping of gas in the crossflow direction during yawed flight results in a great increase in displacement thickness on the leeward side. Hence, viscous-inviscid interaction effects are much more important at angle of attack than in symmetric flight. It is a matter of experience that boundary-layer separation occurs with increasing angle of attack generally at values near the cone half angle. The occurrence of separation drastically alters the lift, drag and stability characteristics. To understand why separation occurs and to locate the separation front are therefore of considerable importance. The separation of the boundary layer for hypersonic flow over cones at incidence is believed to be the result of a complex viscous-inviscid interaction process. One ingredient here is undoubtedly boundary-layer displacement interaction which becomes appreciable even at relatively high Reynolds numbers in the critical leeward region. The present study is an attempt to augment our understanding of the separation phenomenon through calculations of the three-dimensional displacement-pressure interaction effects. It falls short, however, of an actual prediction of the occurrence of separation.

2. BOUNDARY LAYER METHOD

In the analysis of three-dimensional boundary-layer problems the choice of coordinate system is crucial. The so-called "streamline coordinates" are now preferred in many applications, in particular for flows characterized by small lateral curvature of the inviscid surface streamlines. For such flows Hayes¹ has shown that the crossflow, i.e., the boundary-layer flow across the inviscid streamlines, will in general be small. It can therefore be neglected to a first approximation in the conservation equations for mass, tangential momentum and energy. The crosswise momentum equation can furthermore be linearized. Fannelop² has recently embedded Hayes' "small crossflow approximation" in a systematic perturbation procedure in terms of a parameter related to the (small) lateral streamline curvature. The present investigation will be based on Fannelop's analysis and the numerical methods he developed for solving the perturbation equations of zeroth- and first-order. The relevant features of Fannelop's approach are reviewed below.

The basic three-dimensional laminar compressible boundary-layer equations in terms of an orthogonal set of streamline coordinates have been given for instance by Hayes¹ and Cooke and Hall³. As independent variables, the arclength x along the inviscid streamline and the normal distance y from the surface are used; this choice effectively eliminates the explicit appearance of the metric coefficients associated with the tangential and normal coordinates. The lateral variable z and its associated metric coefficient e_z are as yet unspecified. The velocity components associated with the (x, y, z) coordinates are (u, v, w) respectively. For convenience a set of nondimensional variables are introduced based on the reference conditions at the forward stagnation point (subscript s). The reference quantities chosen are c_s^* (speed of sound-reference velocity), ρ_s^* (reference density), μ_s^* (reference viscosity), R_n^* (nose radius), e_s^* (reference entropy). The derived quantities c_s^{*2} and $\rho_s^* c_s^{*2}$ represent respectively the reference enthalpy and pressure. (An asterisk is used here and in what follows to identify dimensional quantities).

By inspecting the momentum equation governing the crossflow w and its associated boundary and initial conditions, it is found that it admits the solution $w = 0$ whenever the lateral streamline curvature K vanishes provided $w = 0$ initially. It is natural therefore to consider a perturbation expansion in terms of K . The value of this parameter is known from the inviscid momentum equation

$$K \rho_e u_e^2 = - \frac{1}{e_z} \frac{\partial r_e}{\partial z} \quad (2.1)$$

For the purpose of our perturbation expansion, the curvature function K is considered to be the product of a small quantity ϵ and a function κ of order unity. For an axisymmetric body at incidence, ϵ is identified with the angle of attack α . A formal expansion of the dependent

variables appearing in the three-dimensional laminar boundary-layer problem, results in the following sets of equations:

Zeroth Order

$$\text{Continuity: } \frac{\partial}{\partial x} (\rho_0 u_0) + \frac{\partial}{\partial y} (\rho_0 v_0) = 0 \quad (2.2)$$

$$\text{x-Momentum: } \rho_0 u_0 \frac{\partial u_0}{\partial x} + \rho_0 v_0 \frac{\partial u_0}{\partial y} = -\frac{dp}{dx} + \frac{\partial}{\partial y} \left(\mu \frac{\partial u_0}{\partial y} \right) \quad (2.3)$$

$$\begin{aligned} \text{Energy: } \rho_0 u_0 \frac{\partial}{\partial x} \left(i_0 + \frac{1}{2} u_0^2 \right) + \rho_0 v_0 \frac{\partial}{\partial y} \left(i_0 + \frac{1}{2} u_0^2 \right) \\ = \frac{1}{Pr} \frac{\partial}{\partial y} \left[\mu \frac{\partial i_0}{\partial y} \right] + \frac{\partial}{\partial y} \left[\mu u_0 \frac{\partial u_0}{\partial y} \right] \end{aligned} \quad (2.4)$$

First Order

$$\begin{aligned} \text{Crossflow: } \rho_0 u_0 \frac{\partial w_1}{\partial x} + \rho_0 v_0 \frac{\partial w_1}{\partial y} + \frac{\rho_0 u_0 w_1}{e_2} \frac{de_2}{dx} \\ = k \rho_0 u_e^2 \left(\frac{u_0^2}{u_e^2} - \frac{\rho_e}{\rho_0} \right) + \frac{\partial}{\partial y} \left(\mu \frac{\partial w_1}{\partial y} \right) \end{aligned} \quad (2.5)$$

$$\text{Continuity: } \frac{\partial}{\partial x} \left[\rho_0 (u_1 + \rho_1 u_0) \right] + \frac{\partial}{\partial y} \left[\rho_0 (v_1 + \rho_1 v_0) \right] = q_1 \quad (2.6)$$

$$\begin{aligned} \text{x-Momentum: } \rho_0 u_0 \frac{\partial u_1}{\partial x} + \rho_0 v_0 \frac{\partial u_1}{\partial y} + (\rho_0 u_1 + \rho_1 u_0) \frac{\partial u_0}{\partial x} \\ + (\rho_0 v_1 + \rho_1 v_0) \frac{\partial u_0}{\partial y} \\ = \frac{\partial}{\partial y} \left(i_1 \mu' \frac{\partial u_0}{\partial y} + \mu \frac{\partial u_1}{\partial y} \right) + q_2 \end{aligned} \quad (2.7)$$

$$\begin{aligned} \text{Energy: } \rho_0 u_0 \frac{\partial}{\partial x} (i_1 + u_0 u_1) + \rho_0 v_0 \frac{\partial}{\partial y} (i_1 + u_0 u_1) \\ + (\rho_0 u_1 + \rho_1 u_0) \frac{\partial}{\partial x} \left(i_0 + \frac{u_0^2}{2} \right) \\ + (\rho_0 v_1 + \rho_1 v_0) \frac{\partial}{\partial y} \left(i_0 + \frac{u_0^2}{2} \right) \\ = \frac{1}{Pr} \left\{ \frac{\partial}{\partial y} \left[\mu \frac{\partial i_1}{\partial y} + i_1 \mu' \frac{\partial i_0}{\partial y} \right] \right\} \\ + \frac{\partial}{\partial y} \left[\mu \frac{\partial}{\partial y} (u_0 u_1) + i_1 \mu' \frac{\partial}{\partial y} \left(\frac{u_0^2}{2} \right) \right] + q_3 \end{aligned} \quad (2.8)$$

where

$$\begin{aligned} q_1 &= - \frac{\partial}{\partial z} \left(\rho_0 w_1 \right), & q_2 &= - \frac{\rho_0 w_1}{e_2} \frac{\partial u_0}{\partial z}, \\ q_3 &= - \frac{\rho_0 w_1}{e_2} \frac{\partial}{\partial z} \left(i_0 + \frac{u_0^2}{2} \right) \end{aligned} \quad (2.9a, b, c)$$

The equations of state of zeroth- and first-order

$$p = \frac{\gamma - 1}{\gamma} \rho_0 i_0, \quad \rho_1 i_0 + \rho_0 i_1 = 0 \quad (2.10a, b)$$

and the constitutive relations

$$\mu = \mu(i_0), \quad \mu' = \frac{d\mu}{di} \Big|_{i=i_0} \quad (2.11a, b)$$

complete the system of equations.

The relevant boundary conditions are:

$$\begin{aligned} \text{Zeroth Order:} \quad u_0 &= v_0 = 0, \quad i_0 = i_w \text{ at } y = 0 \\ u_0 &= u_e, \quad i_0 = i_e \text{ as } y \rightarrow \infty \end{aligned} \quad (2.12)$$

$$\begin{aligned} \text{First Order:} \quad u_1 &= v_1 = i_1 = w_1 = 0 \text{ at } y = 0 \\ u_1 &= i_1 = w_1 = 0 \text{ as } y \rightarrow \infty \end{aligned} \quad (2.13)$$

For flows with ablation the conditions $v_0 = v_1 = 0$ are replaced by the mass-transfer rates specified by the zeroth- and first-order energy balance.⁶

The derivation of the zeroth- and first-order expressions for wall shear and heat-transfer rate is straightforward. The displacement thickness represents a quantity of special interest here, and in view of some erroneous results for the effective displacement thickness Δ^* with mass transfer which exist in the literature⁷, the complete zeroth- and first-order expressions are given below:

$$\Delta_0^* = \int_0^x \left(1 - \frac{\rho_0 u_0}{\rho_e u_e} \right) dy + \frac{1}{\rho_e u_e e_2} \int_0^x \rho_w v_{0w} e_2 dx \quad (2.14)$$

$$\begin{aligned} \Delta_1^* &= \frac{1}{\rho_e u_e e_1} \frac{\partial}{\partial z} \left\{ \int_0^x \left[\int_0^\infty \rho w_1 dy \right] dx \right\} \\ &\quad + \int_0^\infty \frac{\rho w_1 + \rho_1 u_0}{\rho_e u_e} dy + \frac{1}{\rho_e u_e e_2} \int_0^x \rho_w v_{1w} e_2 dx \end{aligned} \quad (2.15)$$

The last terms in Equations (2.14) and (2.15) represent the contributions due to surface mass transfer. The contribution to the displacement thickness due to crossflow (the first term in (2.15)) was first given in this form by Lighthill⁵.

Along a given inviscid streamline (i.e., with z fixed), the zeroth-order equation can be considered as two-dimensional, i.e., the quantities u_0, v_0, i_0 , etc. depend only on x and y . The crossflow equation is also two-dimensional and it is, moreover, uncoupled from the other first-order equations and can be solved independently. The other first-order equations contain derivatives with respect to z but they can nevertheless be written in a two-dimensional form (as shown in Equations (2.6) through (2.8)). The z -dependent "forcing functions" q_1, q_2, q_3 defined by (2.9) can be evaluated prior to calculating u_1, v_1 and i_1 provided u_0, v_0, i_0 and w_1 are already known along two or more adjacent streamlines. It therefore becomes possible to compute both the zeroth- and first- (as well as higher-) order terms by means of a suitable two-dimensional numerical procedure. Fannelop

developed for this purpose an implicit finite-difference method by which the zeroth- and the first-order equations can be solved exactly. The method was applied to the case of interest here, i.e., a blunted cone at incidence to a hypersonic stream. The numerical results show that of the first-order terms, u_1 and i_1 and the associated wall shear and heat transfer values are always small. The crossflow velocity w_1 and the associated transverse shear stress are numerically larger and hence more important than the other first-order terms. The crossflow profile is also more sharply peaked than the corresponding u_1 - and i_1 -profiles, and the peak occurs closer to the wall where the zeroth-order velocity component u_0 is very small. In view of the fact that the crossflow plays a crucial role in the three-dimensional separation process, it seems reasonable to include the crossflow term in the first-order displacement thickness, Equation (2.15) while neglecting the second term which is associated with the nonvanishing values of u_1 and i_1 . The numerical results of Fannelop show, however, that the two terms are numerically of about equal magnitude and of opposite sign. For this reason, only the zeroth-order value Δ^* has been used in the present viscous-inviscid interaction studies.

3. INVISCID METHOD

The problem of determining the inviscid input for the three-dimensional boundary-layer solution cannot realistically be separated from that solution. The present boundary-layer procedure, which solves the initial-value problem by marching step-by-step along the inviscid streamlines, is relatively straightforward and efficient. We therefore look for an equally straightforward and efficient inviscid method rather than a sophisticated numerical approach such as the three-dimensional method of characteristics. There are two alternatives. The first includes methods which are based on rational approximations, such as Newton-Busemann theory or the method of linearized characteristics. The former is known, however, to give rather poor results for blunt bodies, while the latter has been found to be accurate only when the angle of attack is a small fraction of the cone half-angle. The second category includes empirical or semi-empirical methods which can be shown to agree well with the exact numerical and experimental results. The second alternative is chosen for this study.

The inviscid input required in the boundary-layer program are the pressure distribution and the streamline geometry, i.e., location, curvature and spreading metric e_2 . The geometric quantities can be derived from the pressure distribution through the transverse-momentum equation, as will be described in what follows, so that the primary input needed is the pressure distribution. The configurations of interest here are blunted cones at incidence to a hypersonic stream with free-stream Reynolds numbers sufficiently low to warrant the inclusion of displacement-thickness interaction effects.

The effects of boundary-layer displacement can be accounted for in the first-order boundary-layer solution by adjusting the inviscid pressure distribution. The usual practice is to perform a global iteration. The boundary-layer thickness calculated without considering interaction is added to the body thickness. An improved pressure distribution is calculated which in turn leads to a better boundary-layer solution. This procedure would be acceptable if convergent; the calculations of Blottner and Flügge-Lotz⁶ (flat plate) show, however, that it may well be divergent so that results which are obtained from a limited number of iterations are suspect. For three-dimensional flow fields the method is also somewhat impractical due to the complexity of the general inviscid method. For this reason an approximate numerical method must be developed which allows local corrections due to displacement along individual streamlines. The convergence of the local iterations can be assured by a suitable numerical technique (see Blottner and Flügge-Lotz⁶).

The inviscid method which we shall consider can be thought of in two parts; one applicable to the cone region and the other to the blunt nose. In each case, the method represents a generalization of the idea behind the tangent-cone method. For sharp axisymmetric bodies in supersonic flow, the tangent-cone method is known to give reasonably accurate results even though it is difficult to justify on a rational basis. The generalized method for the cone region, dubbed the "effective-cone method", will be shown to be accurate for yawed blunted cones and for blunted non-conical bodies as well. In the nose region the method becomes the tangent-sphere method and this will likewise be shown to be accurate for nonspherical forebodies. Hence, the generalized method will be suitable to predict complete pressure distributions over yawed axisymmetric blunt bodies including boundary-layer displacement effects.

In the effective-cone method, the pressure at some point on a blunt body is equated to the pressure at the corresponding point on an unwaved cone with the same blunt nose shape and with a half-angle equal to the local inclination angle of the body surface. Figure 1 illustrates this idea for the windward meridian of a yawed cone. The pressure on unwaved blunted cones is a function of both the axial distance x_c and the half-cone angle θ_c for given free-stream conditions; in this effective-cone method the pressure distribution on the yawed body becomes the same function of the equivalent axial distance x'_c and the local inclination angle θ .

Cleary⁷ has pointed out the general accuracy of this idea in comparison with experimental data for a 15° blunted cone at Mach 10 in the plane of symmetry only. Figures 2a, b and c compare his experimental data for various angles of attack with effective-cone and linearized characteristics results generated from Avco computer programs. The linearized characteristics pressure distributions are inaccurate for all but the smallest angles of attack, while the effective-cone results are reasonably accurate for all angles of attack. The linearized characteristics program predicts negative

pressure coefficients (and negative pressures) on the leeward side of the cone at 10° angle of attack. The failure of the linearized characteristics method in this case is due to the fact that at each point on the body it assumes a linear variation of the pressure with the angle of attack, whereas the experimental data show the pressure variation to be definitely nonlinear.

Also plotted on Figure 2b is the experimental pressure distribution along the 90° meridian at 10° angle of attack, which agrees quite well with the pressure distribution over the cone at zero angle of attack.

In Figure 3 are plotted the meridional pressure distributions versus ϕ for various axial locations. Shown here are the experimental data of Cleary for $\alpha = 10^\circ$ and the effective-cone results. The accuracy of these effective-cone pressure distributions is adequate.

Figure 4 illustrates a distribution at a higher Mach number. Lewis and Knox^{8,9} present Mach 18 data for a 90° blunted cone at 10° angle of attack and compare it with results of the three-dimensional characteristics program developed at General Applied Science Laboratory.¹⁰ Figure 4 shows this data together with the results of the effective-cone method as described above. The gas is frozen with $\gamma = 1.4$; a meridional plot is shown at the axial station $x_c = 11.7$. Both the GASL program and the effective-cone method appear to yield adequate agreement with the experimental data, except perhaps on the leeward side where viscous effects may be important.

It may be noted here that the effective-cone method fails at some point on the leeward side of a cone at an angle of attack greater than the cone half-angle. The reason is that the effective cone for the leeward meridian has a negative angle and collapses to a vertex beyond which the pressure distribution is no longer meaningful. This failure is not serious from the point of view of the present analysis, however, since such a yawed body will have a region of thick viscous flow on its leeward side. The effective body then resembles more closely a cylinder than a cone on the leeward side, and it is more appropriate for the viscous-inviscid interaction computations described in Section 4 to use the cylinder pressure distribution as the reference distribution.

In order to check the accuracy of the effective-cone method on nonconical bodies, a method-of-characteristics calculation was carried out on a blunt unyawed axisymmetric ogive-type body. In a meridional plane, the section of this body consisted of a circular forebody followed by a parabolic arc. The slopes of nose and parabolic afterbody were matched at the $\theta = 20^\circ$ point, and the parabola was constrained to pass through the point $x_c = 15.7$, $r = 6$, roughly simulating a thick boundary layer on a 15° cone with base radius $r = 5$. The effective-cone pressure was calculated at each value of x_c simply by linear interpolation in θ between the calculated pressures on blunt 15° and 20° cones. The agreement with the numerical calculation shown on Figure 5 is very good.

It is worth mentioning that a half-dozen other schemes, variations of shock-expansion theory and the tangent-cone method, some taking the 15° -cone pressure distribution as a base, were also tried with the hope that something even simpler than the effective-cone method would be found. Not one of these schemes came even reasonably close to matching the numerical results. It can therefore be stated with some confidence that no scheme which attempts to relate pressure variations on a nonconical contour to strictly local changes in body geometry will be successful. The property which distinguishes the effective-cone method from other schemes of this sort is that the method takes account of the downstream influence of the nose on the pressure distribution over a blunted cone. The influence is essentially nonlinear as a function of cone half-angle θ ; as θ increases, the overexpansion region is compressed toward the nose. In this sense the effective-cone method, although apparently local in application, takes into account the global influence of a change in body slope, for it equates the resulting pressure to the pressure on a new cone with a different upstream pressure distribution.

The pressure distribution on a sphere is a function of the local angle only and not of the axial distance. For a nonspherical nose then, it is logical to equate local pressure to the pressure on a sphere at the same surface slope. Hence, this application of the inviscid method becomes simply a tangent-sphere method. It is applied locally at each point on the body (Figure 6a) and hence is more general than the idea suggested by Maslen¹¹ of representing the effective body in the subsonic region by a shifted and expanded sphere. It reduces to Maslen's method at the stagnation point.

The accuracy of the method in the nose region was checked by comparing pressure distributions for a perfect gas at $M_\infty = \infty$ on a sphere and an oblate ellipsoid with major-to-minor axis ratio of 1.5. If the method is applicable, the pressure distributions on sphere and ellipsoid when plotted versus local body angle should coincide. Figure 6b indicates that the deviation is not serious for bodies with this degree of oblateness, so that the method is quite suitable for boundary-layer interaction calculations on spheres; of course the method would fail for the extreme case of a flat disk. The numerical calculation shown on Figure 6b was carried out by Belotserkovskii.¹²

In conclusion, the effective-cone method is seen to provide an accurate means of predicting supersonic pressure distributions over blunt yawed bodies and nonconical bodies, and the tangent-sphere method works well for nonspherical noses. These inviscid techniques can be applied in a step-by-step manner to the calculation of pressures for viscous-inviscid interaction. The remaining problem is the determination of the streamline geometry on the effective body surface.

Streamline shapes and the metric e_2 are computed from a given pressure distribution by integrating the momentum equation transverse to inviscid streamlines on the surface (2.1), which, expressed in terms of axial distance x_c and the angle δ between a surface streamline and the local meridian, is

$$\frac{\partial \delta}{\partial x_c} = - \frac{1}{\cos \theta \cos \delta} \left[\frac{1}{\rho_e u_e^2} \frac{\partial p_e}{\partial n} + \frac{\sin \theta \sin \delta}{r} \right] \quad (3.1)$$

together with the geometrical relationship

$$\frac{\partial \phi}{\partial x_c} = - \frac{\tan \delta}{r \cos \theta} \quad (3.2)$$

These equations are numerically integrated along each streamline, subject to the initial condition at the sphere-cone junction (subscript 1)

$$\tan \delta_1 = \frac{\sin \alpha \sin \phi_1}{\sin \theta_1 \sin \alpha \cos \phi_1 + \cos \theta_1 \cos \alpha}$$

resulting from the fact that the streamlines on the nose are great circles originating at the stagnation point.

The lateral coordinate z is defined as ϕ_1 , the meridian angle of a streamline at the sphere-cone junction. The lateral metric then becomes $e_2 = \delta n / \delta \phi_1$, where n measures surface distance normal to streamlines, i.e., e_2 is the ratio of the distance separating two adjacent streamlines to the initial difference between the meridian angles at the points where they cross the sphere-cone junction. The metric reduces to r in the case of axisymmetric flow. If we define $E = \delta \phi / \delta \phi_1 |_{x_c}$ (here $\delta \phi$ is the difference between meridian angles of adjacent streamlines at the same value of x_c), then $e_2 = r E \cos \delta$. The equation for E can be found by differentiating equations (3.1) and (3.2) in the ϕ -direction (i.e., between adjacent streamlines). Letting $A = \cos \delta \delta \delta / \delta \phi_1 |_{x_c}$, the following two differentiated equations result:

$$\frac{\partial A}{\partial x_c} = \frac{1}{\cos \theta} \left[A \left(\frac{\tan \delta}{\rho_e u_e^2 \cos \delta} \frac{\partial p_e}{\partial n} - \frac{\sin \theta}{r} \right) - E \cos \delta \frac{\partial}{\partial \phi} \left(\frac{1}{\rho_e u_e^2 \cos \delta} \frac{\partial p_e}{\partial n} \right) \right], \quad (3.3)$$

$$\frac{\partial E}{\partial x_c} = \frac{-A}{r \cos \theta \cos^3 \delta}, \quad (3.4)$$

subject to the initial conditions

$$A_1 = \frac{\cos^3 \delta_1 \sin \alpha (\sin \theta_1 \sin \alpha + \cos \theta_1 \cos \alpha \cos \phi_1)}{(\sin \theta_1 \sin \alpha \cos \phi_1 + \cos \theta_1 \cos \alpha)^2}, \quad (3.5)$$

$$E_1 = 1 \quad (3.6)$$

There is a certain arbitrariness in the application of the effective-cone method to three-dimensional flow over axisymmetric bodies, having to do with the choice of the value of the local body slope θ which is to be substituted into the pressure relation $p = p(x_c, \theta)$. Here we took a hint from Newtonian theory and equated θ to the complement of the angle between the normal to the body surface and the free-stream vector. This leads to the relation

$$\sin \theta = \sin \theta_c \cos \alpha - \cos \theta_c \sin \alpha \cos \phi, \quad (3.7)$$

where θ_c is the surface slope and ϕ the meridian angle in body-fixed coordinates. The pressure derivatives appearing in Equations (3.1) and (3.3) can be related to derivatives with respect to

x_c and θ , the latter, in turn, being related to derivatives in ξ through chain differentiation:

$$\frac{\partial p}{\partial \xi} = \frac{\partial p}{\partial \theta} \frac{\partial \theta}{\partial \xi}, \quad \frac{\partial^2 p}{\partial \xi^2} = \frac{\partial^2 p}{\partial \theta^2} \left(\frac{\partial \theta}{\partial \xi} \right)^2 + \frac{\partial p}{\partial \theta} \frac{\partial^2 \theta}{\partial \xi^2} \quad (3.8)$$

The derivatives of p with respect to x_c and θ are evaluated by curve-fitting axisymmetric method-of-characteristics results.

Figure 7 shows a comparison of streamline shapes over a 4° half-angle cone at 10° angle of attack for $M_\infty = 18$. The results of the analysis described here are shown as solid curves. The dashed curves are taken from Reference 9 and represent the results of a method-of-characteristics inviscid flow program developed at GASL. The agreement between the two sets of curves is seen to be excellent for x_c less than about 5 and adequate for larger values of x_c .

4. VISCOUS-INVISCID INTERACTION

Several methods have been proposed for the solution of problems in weak boundary-layer interaction theory. These methods consist of numerical or analytic solutions for one or more of the various second-order boundary-layer effects for isoeenergetic flow: namely, longitudinal and transverse curvature, external vorticity, slip and temperature jump and displacement. Of these effects, that of displacement should be studied separately since it is the only one which requires additional consideration of the external inviscid flow.

The other effects are associated with terms of order $Re_s^{-1/2}$ which appear explicitly in the equations and boundary conditions for the boundary layer. They may be separated out, as has been done by Van Dyke¹³, by means of a systematic perturbation procedure. One advantage of this approach is that for a given configuration, a single boundary-layer solution is valid for all Reynolds numbers in the permissible range. This apparent advantage becomes rather illusory, however, if the displacement problem is introduced, since then it is necessary to find a perturbation solution of the inviscid flow field.¹⁴ Such inviscid perturbation solutions, which must be linear in the parameter $Re_s^{-1/2}$ and give the displacement effect of the boundary layer for all Reynolds numbers, are difficult to obtain and have poor accuracy. (The question of accuracy and the limited range of validity of one candidate method, the method of linearized characteristics, were discussed in Section 3. The effective-cone method could be made to yield solutions for all Reynolds numbers by means of interpolation. This scheme is promising but is not pursued further here.)

Regardless of how the various second-order boundary-layer effects are treated, they need not all be included for blunted cones. Numerical calculations show that slip and transverse curvature effects are small for $Re > 10^3$, whereas the displacement effect can be substantial, especially on the leeward side. The effect of vorticity cannot be disregarded in comparison with the displacement effect, but the problem of including vorticity is complicated by the fact that there is no rational method for dealing with entropy-layer entrainment at the present time. The effect of entropy-layer entrainment is to make vorticity interaction negligible far downstream and to minimize its importance over the rest of the cone surface. The longitudinal curvature effect is important over the spherical nose, a region of secondary interest, but is unimportant over the cone. These effects have been neglected in the present analysis.

For the displacement effect, an alternative to the use of an inviscid perturbation solution is a global iteration as discussed in Section 3. A single iteration leads to a result equivalent to that of Van Dyke's second-order theory for displacement, but the result is valid only at the specified Reynolds number. Attempts to improve the accuracy of this solution by additional iterations are potentially dangerous, since there is evidence that such a procedure is divergent.

Convergence can be assured by a suitable numerical technique, even for strong interactions, if a local iteration procedure is combined with a step-by-step integration of the boundary-layer equations. Such a procedure requires a method of determining the inviscid pressure locally as opposed to globally. Blottner and Flügge-Lotz⁶ successfully used this procedure for flat-plate flow by employing the tangent-wedge formula to predict the local pressure at the edge of the boundary layer. In this paper we will adapt the method of Blottner and Flügge-Lotz to three-dimensional interacting flows, using the effective-cone method to predict the pressure.

The variable to be iterated at any point on the body is θ , the effective body slope. In this scheme, values of the assumed slope θ^A used in the effective-cone method to predict the local pressure are compared to values of the calculated slope θ^C evaluated from the difference between the displacement thickness at successive points on the body. The iteration is carried out numerically at a point on an inviscid streamline until the difference between two successive values of the calculated slope is less than a specified small value, and then the next point on the streamline is computed.

The iteration procedure is illustrated in Figure 7, a hypothetical plot of θ^C versus θ^A . The solution must lie on the line $\theta^C = \theta^A$; substituting a series of values of θ^A into the equations will yield a solution-curve as shown which intersects the line $\theta^C = \theta^A$ at a single point. Several methods are available for numerically determining the intersection point; we have chosen the method of false position

used by Flugge-Lotz and Blottner, in which the solution-curve is approximated by a straight line drawn through the two previous iteration points (subscripts 1-1 and 1-2). The intersection of this straight line with the line $\theta^C = \theta^A$ gives the next guess for the assumed slope:

$$\theta_1^A = \frac{\theta_{1-2}^C \theta_{1-1}^A - \theta_{1-1}^C \theta_{1-2}^A}{\theta_{1-1}^A - \theta_{1-2}^A - \theta_{1-1}^C + \theta_{1-2}^C} \quad (4.1)$$

The first two guesses of θ^A which are used to start the iterative calculation are the value at the previous point along the streamline, and that value minus one degree. The corresponding values θ^C are computed in the same way for all iterations:

$$\theta^C = \theta_b + \theta_v \quad (4.2)$$

The first term θ_b is the local slope of the body surface and is taken to be the complement of the angle between the normal to the body and the free stream velocity vector as mentioned in Section 3:

$$\sin \theta_b = \sin \theta_c \cos \alpha - \cos \theta_c \sin \alpha \cos \phi \quad (4.3)$$

The second term θ_v is the local viscous slope due to displacement:

$$\tan \theta_v = \frac{d\Delta^*}{dx} \quad (4.4)$$

It is evaluated by numerical differentiation between adjacent points on the streamline. The displacement thickness is computed from a finite-difference solution of the boundary-layer equations, using the local value of the effective-cone pressure.

A number of pressure distributions must be computed for blunted axisymmetric cones whose half-angles span the expected range of effective-cone angles. Five-degree increments in the effective-cone angle θ are used in the present case. These distributions are curve-fitted as functions of x_c and read into the computer program which carries out the numerical solution. The local pressure at any point on the yawed cone surface as a function of the assumed effective-body slope θ^A is then computed by quadratic interpolation in θ between these distributions.

The geometry of the inviscid streamline at the edge of the boundary layer (that is, the location $\phi(x_c)$ of each point on the streamline and the value of the metric e_c) is determined by the method described in the previous section. In this calculation, the local value of the pressure is taken to be the value computed at the previous point rather than the pressure without displacement effect. In a sense, therefore, the effect of boundary-layer displacement on the inviscid streamline pattern is taken into account, although the method was derived only for streamlines on axisymmetric bodies. It is not possible to use this method to compute streamline turning due to a nonuniform circumferential boundary-layer thickness distribution.

5. NUMERICAL RESULTS

The first example to be considered is a 15 degree half-angle blunted cone at $M = 10$. This configuration has been the subject of an extensive experimental program (Cleary⁷), and both pressure and heat-transfer measurements are available at several angles of attack. Fannelop² has already published a comparison between the experimental heat-transfer data and the heat-transfer results calculated on the basis of the experimental pressure distribution for the case $\alpha = 10^\circ$. The present calculations will, of course, be based on the inviscid methods discussed in Section 4.

The Reynolds number in Cleary's experiments is quite high ($Re_\delta = 25,300$) and the wall temperature rather low ($T_w/T_\infty = 0.265$). It is therefore known from the outset that the displacement interaction effects will be relatively small, at least on the windward side. Cleary's case appears worthwhile for comparison purposes, in spite of the expected small displacement-pressure interaction effects, in view of the fact that the occurrence of separation depends primarily on the angle of attack. For purely laminar or turbulent flows the Reynolds number is believed to be of secondary importance. We will restrict the present considerations, for reasons of economy and space, to two streamlines ($\phi_1 = 175^\circ$ and 140°) and three angles of attack ($\alpha = 10^\circ, 15^\circ$ and 20°). Figure 9 shows the calculated pressure distribution along the two streamlines at $\alpha = 10^\circ$. The incremental pressures due to viscous-inviscid interaction are seen to be small, but the contribution is not negligible on the leeward side. Cleary's experimental data are also shown whenever the streamlines cross

a meridian for which data are available. (Interpolation in x was necessary for some of the points.) The agreement between the experimental and the retical pressure values is quite good, although rather inconclusive as regards the validity of the calculated interaction effects. Figure 10 shows the corresponding heat-transfer results. (The theoretical values are normalized with respect to $\dot{q}_{s0} = 2.03$, the stagnation value without interaction effects.) The agreement is satisfactory for the $\beta_1 = 14^\circ$ streamline and somewhat less so for the single point shown for the $\beta_1 = 13^\circ$ streamline. A detailed comparison with the results previously obtained by Fannelop for this streamline shows the present results to be somewhat lower for $x > 1$. The difference in the theoretical calculations is due to numerical problems encountered in evaluating the transverse pressure gradient $\partial p / \partial \theta^2$ which in turn affects the calculation of the metric e . The present method requires evaluation of $\partial p / \partial \theta^2$ from the numerical pressure fits for the various cone half-angles - (see Equation (4.3)). Along the windward meridian, the metric coefficient e grows nearly exponentially with the exponent proportional to $\int_{x_0}^x (\partial^2 p / \partial \theta^2) dx$, so that the numerical accuracy of this second derivative is particularly important very far downstream on the windward side. It appears that a more careful curve-fitting of the axisymmetric pressure distributions will yield better agreement with the experimental data here, and this is currently being attempted.

Figure 11 shows the calculated wall shear components, tangential (τ_c) as well as crosswise (τ_θ), for the two streamlines considered. The tangential wall shear peaks on the spherical forebody with the value $\tau_c \approx 1.2$ and falls thereafter with the decreasing pressure along the streamline. The crossflow wall shear builds up rapidly to a near constant value starting at the cone-sphere juncture in response to the suddenly applied lateral pressure gradient. For $\beta_1 = 13^\circ$ the ratio τ_θ / τ_c is small everywhere, thus indicating that the perturbation procedure is valid in the range considered. For $\beta_1 = 14^\circ$ we find, however, that $\tau_\theta > \tau_c$ for $x_0 > 0.8$, $x < 1.2$, thus indicating that the crossflow may exceed the tangential flow in magnitude in the boundary layer. This violates, at least locally, the assumptions underlying the present boundary-layer analysis. Calculations of higher-order terms for tangential velocity and enthalpy and comparisons with experiments both indicate, however, that the zeroth-order solution can represent a fair approximation of the boundary-layer flow even when w exceeds u locally. (This abnormal behavior is limited to a very narrow region near the wall.) It is also of interest to note the rather large corrections in the crossflow wall shear due to displacement interaction effects. This indicates, in view of the crucial role played by the crossflow in a three-dimensional separation process, that displacement interaction may influence the separation location.

Figures 12a,b,c show the location of the streamlines and the direction of the resultant wall shear stress on the developed cone for $\alpha = 12^\circ$, 14° and 16° respectively. (Only the interacting streamlines are shown; the differences between these and the inviscid streamlines are insignificant.) As expected, the streamlines approach the leeward side more rapidly as the angle of attack is increased. The progressive steepening of the wall shear vector with angle of attack is somewhat more surprising. (A more exact boundary-layer analysis would give results which differ from the present in degree but not in character, for reasons already noted.) The existence of a separation front, across which the surface shear vanishes, requires the surface shear vectors to be asymptotic to a single line which is parallel with a generator far downstream. The present results show no tendency to coalesce even at $\alpha = 16^\circ$, for which separation certainly occurs. The reason is that the present approximate inviscid method, as well as available exact or nearly exact methods, generally predict a favorable circumferential pressure gradient in the critical leeward region, contrary to experimental results. There is therefore no obvious inviscid mechanism available for reversing the direction of the crossflow relative to the inviscid streamline. The displacement effects accounted for in the present analysis are relatively small and cannot by themselves explain why separation occurs. It appears that a very strong localized disturbance such as an internal shock is required to reverse the crossflow to the desired direction. Such shocks do in fact occur according to recent experiments by Rainbird¹⁵. He contends that these shocks (which for a sharp cone are parallel to a generator) are caused by inviscid effects and occur when the velocity component normal to conical rays becomes supersonic. (For the hypersonic flows presently considered, this would occur at quite small angles of attack.) Another possibility is that the shock observed is simply the lip shock associated with separation, and that the separation process is dictated by a complex viscous-inviscid interaction process involving the conditions downstream in the near wake. The situation is then analogous to that of hypersonic flow over a circular cylinder. A purely inviscid analysis indicates a favorable pressure gradient everywhere on the cylinder, so that the first-order boundary-layer solution predicts no separation, contrary to existing experiments. Reeves and Lees¹⁶ have shown, however, that separation is in fact controlled by conditions in the near wake. The boundary layer must separate in a prescribed manner in order to allow the flow to pass smoothly through the critical "throat" region. If the three-dimensional analog of a "throat" condition exists, a prediction of the separation location is not possible on the basis of considerations which involve only the boundary layer upstream of separation, even if an exact three-dimensional method is used.

For cones of finite length, another problem which should be considered is base interference. It is possible that signals from the near wake in the base region can propagate upstream through the thick leeward boundary layer and thus trigger, or at least influence, the separation process. (17) The supersonic and hypersonic cases may be rather different as regards base interference. Tracy's⁽¹⁷⁾ experiments ($M \approx 8$) indicate that the base pressure for $\alpha \approx 1$ is substantially lower than the pressure on the leeward side, thus ruling out possible base effects. Rainbird¹⁵ ($M = 1.8$ and 4.25) moreover found the flow in the separated region to be essentially conical. Recent hypersonic experiments at Avco (Stetson, $M = 13.6$, unpublished) indicate, however, that the base and leeward pressures are nearly equal at $\alpha \approx 1$, raising the question whether a coupling exists between the flow in the two regions at sufficiently high Mach numbers.

In the preceding example we have concentrated on flows with no mass transfer at the wall. Because very little work on this subject has appeared in the literature, in our second example we will examine the effect of large rates of mass transfer on viscous-inviscid interaction in three-dimensional flow. The configuration will be a 7 degree half-angle blunted cone at $M_\infty = 18$. Two Reynolds numbers, $Re_\delta = 1000$ and $Re_\delta = 5000$, are considered. (A tabulation of available low Reynolds number wind-tunnel tests in Ref. 7 shows that Re_δ falls in the range $10^3 - 10^4$ for these tests.)

The mass-transfer rates in the calculations which follow are governed by a simplified energy balance for the ablation process of the form

$$\rho_w v_w = - \frac{\dot{q}_w}{L_v} \quad (5.1)$$

where L_v represents the latent heat of the wall material. The nonsimilar blowing parameter f_w is given by the following integral expression:

$$f_w = - \frac{1}{\sqrt{2\eta}} \int \frac{\rho_w v_w}{\rho_w \mu_w^{1/2} e^{c_2}} d\eta \quad (5.2)$$

The transformed coordinate η in this expression is the usual Lees-Levy variable with e_2 replacing r^2 in accord with the axisymmetric analogy. For further details the reader is referred to Ref. 2.

The values of Re_δ and L_v^{-1} for the various cases which were computed are indicated in Table 1. All cases follow the external streamline which starts at the sphere-cone junction at $\theta_1 = 18.0^\circ$. The inviscid streamlines for $\alpha = 10^\circ$ are already shown in Figure 7. The stagnation temperature for these cases is 6500°R. (The numerical solutions are nearly independent of the temperature level as long as it is high.) The value $L_v^{-1} = 0.8$ corresponds to a dimensional latent heat of ablation $L_v^* = 780$ BTU/lb, which together with a wall temperature at ablation of $T_w^* = 12000^\circ\text{F}$ is representative of a low-temperature ablator such as Teflon. The value $L_v^{-1} = 3.2$ does not correspond to the latent heat of any known substance, and is used here as an artifice to produce a large mass-transfer rate.

The streamline traces with interaction differ only slightly from those given for $Re_\delta = \infty$ in Figure 7, but the difference increases with increasing axial distance. To illustrate the magnitude of the deviation due to interaction effects, the calculated streamline meridian positions at a representative axial station are shown in Table 1.

Re_δ	L_v^{-1}	θ , deg.
∞	0	11.0
5000	0	10.3
5000	0.8	87.9
5000	3.2	89.6
100	0	87.8

Table 1. Position of $\theta_1 = 18.0^\circ$ External Streamline at Station $x_c = 13.85$

It is perhaps surprising that the displacement-interaction effects push the streamlines towards the leeward side. Physically this can be explained, at least in part, by the fact that the pressure level is increased on the cone and the inviscid velocity reduced in the streamwise direction. The streamlines are therefore less "stiff" and tend to bend more for a given lateral pressure gradient. For the purpose of calculating the circumferential pressure gradient, it was expressed in Section 4 in the form

$$\frac{\partial p}{\partial \eta} = \frac{\partial p}{\partial \theta} \frac{d\theta}{d\eta}$$

Inspection of the derivative $\partial p / \partial \theta$ shows that it becomes larger with increasing θ , and therefore increases due to interaction effects. (The geometric factor $d\theta/d\eta$ is evaluated here on the equivalent cone surface rather than at the displacement surface and hence is unaffected by interaction.) The asymmetry of the "effective" body surface will give an opposite contribution to the circumferential pressure gradient, but this cannot be accounted for without considering the complete

circumferential distribution of the displacement thickness. An attempt has been made, however, to estimate the orders of magnitude of this asymmetry effect and other effects neglected in the analysis, and it is concluded that these effects are probably small relative to the terms which have been retained and in any event will not alter the general behavior of the streamlines. It therefore appears that the effect of boundary-layer displacement is to increase the curvature of the streamlines and hence cause them to migrate somewhat more rapidly toward the leeward side of the body.

This conclusion must be qualified by the remark that boundary-layer entrainment of inviscid fluid has not been included in the present analysis. Entrainment would have the effect of increasing the "stiffness" of the streamlines appearing at the edge of the boundary layer, and these streamlines would make smaller angles with respect to the local meridian direction than the original streamlines. Therefore the effect of entrainment would be opposite to the effect of displacement in altering the direction of the external streamlines. Unfortunately, no rational approach to the problem of boundary-layer entrainment is presently available, even for flows at zero angle of attack.

The calculated surface pressures along the $\eta_1 = 1$ streamline, with and without interaction effects, are shown in Figure 14. As expected, the pressure increases with increasing mass-transfer rate and decreasing Reynolds number. (The cases $Re_{\infty} = 10^5$, 10^6 , and 10^7 and $h_{\infty} = 10^{-3}$, 10^{-4} , and 10^{-5} gave nearly identical results.) The interaction effects appear to become less important for $x_2 > 15$. There are two reasons for this: First, the streamlines with boundary-layer interaction migrate more to the leeward side for large x_2 than do the undisplaced streamlines; at $x_2 = 15$, for example, there is a 10° difference in the meridian angles of the undisplaced streamline and the streamline for $h_{\infty} = 10^{-3}$. More important, however, is the fact that the pressure varies relatively slowly as a function of η in the leeward region, so that a large change in displacement surface slope will induce a relatively small change in local pressure.

Figure 14 shows the variation of the η wall parameter η_w for 10^5 and 10^7 , respectively. The value of the η wall parameter is seen to remain nearly constant over the range considered. (The nonsimilar value calculated differs markedly, however, from that calculated on the basis of "similarity", except in the first case.) The calculated heat-transfer rates are shown in Figure 15. The stagnation heat-transfer rate without interaction $q_{s,0}$ is used as the reference value. If the actual stagnation q_s (at values for 10^5 and 10^7 , respectively) are used as reference for the cases with interaction, the curves in Figure 15 are nearly identical. (At the stagnation point, $q_s = 1.0$ and 1.0 for 10^5 and 10^7 , respectively.) Figure 16 shows the calculated displacement thickness δ^* and Δ^* along the streamline. The direct contribution to δ^* (i.e., the second term in Equation (14a)) is seen to be of the same order of magnitude when compared with the "marginal" mass-flow defect thickness δ^* .

The calculated tangential and crossflow wall shear distributions are shown in Figure 17 for the cases 10^5 and 10^7 at $h_{\infty} = 10^{-3}$. The tangential wall shear τ_w decreases as expected when the blowing rate is increased, whereas the crossflow wall shear τ_{η} is nearly unaffected by blowing. (The slight difference between the cases 10^5 and 10^7 can be attributed in large measure to viscous-inviscid interaction effects.) The apparent lack of coupling between the primary flow and the crossflow in the region near the wall, which is illustrated by the present example is of considerable interest. It has already been noted that the fourth-order boundary-layer solution can approximate the actual flow even when the crossflow shear exceeds the tangential shear, because the variation of the crossflow in the boundary layer is limited to a narrow region near the wall. Now it may be concluded that both the crossflow and tangential flow components develop independently near the wall, with the crossflow primarily influenced by the external pressure gradients.

This suggests the possibility of a new and simpler analytic treatment of the flow in the region near the wall. In addition, approximate (internal) methods for calculating three-dimensional boundary-layer flows should take this property into account. For instance, a crossflow profile which has the correct behavior near the wall for an impermeable surface could probably be used as well for problems with mass transfer.

From the viewpoint of lifting-body research, the present result indicates that the primary effect of ablation is to reduce the lift. The viscous contribution to lift is nearly unchanged relative to the nonablating wall.

The actual crossflow profiles, with and without mass transfer, are shown at two different stations along the $\eta_1 = 1$ streamline in Figures 18a and b. An increase in mass transfer tends to increase the crossflow velocity and at the same time shift the velocity peak outward from the wall in such a way that the velocity gradient near the wall remains nearly constant. These results corroborate earlier findings discussed in Ref. 1.

CONCLUSIONS

A method has been developed for the analysis of the effects of boundary-layer displacement-pressure interaction over yawed blunt cones. The three-dimensional laminar compressible boundary-layer equations are written in terms of a streamline coordinate system determined from the inviscid pressure distribution, which in turn is calculated from the effective-cone method. The boundary-layer equations are perturbed with respect to a parameter ϵ which is related to the inviscid streamline curvature and proportional to the angle of attack, and only the leading term is retained. The resulting "small ϵ " equations are solved exactly by means of an implicit finite-difference procedure. Converged solutions of the displacement-interaction problem are obtained by coupling the

boundary-layer and inviscid computations at each point on the body surface in a local iterative procedure. The effective-cone method is shown to represent the inviscid flow accurately in the downstream region for both blunt yawed and nonconical bodies, and it is readily adapted to the local iterative calculation of pressure. In the blunt nose region an analogous tangent-sphere method is used.

Numerical calculations have shown that the displacement interaction analysis is stable and efficient for blunt cones at moderate angles of attack for Reynolds numbers down to $Re_\delta = 1000$. High rates of mass transfer at the wall have been included in some of these calculations, using a simplified energy balance at the wall and a constant latent heat of the wall material. In general, a tendency is noted for the crossflow wall shear to build up rapidly as streamlines migrate to the leeward side of the cone, particularly for the larger angles of attack, to such an extent as to exceed the tangential wall shear in the leeward region. In these cases, it is argued that although the assumption underlying the expansion of the boundary-layer equations in ϵ is violated, nevertheless the calculations for the zeroth-order heat transfer and wall shear represent a fair approximation of the actual boundary-layer flow. A related phenomenon is observed in the remarkable insensitivity of the crossflow wall shear to the mass transfer rate at the wall. It appears that the crossflow wall shear is primarily a function of the applied lateral pressure gradient, and that, in a narrow sublayer near the wall, the two flow components develop practically independently. This lack of coupling between the crossflow and the tangential components is interesting from a fundamental point of view, and it points to the possibility of a simplified theoretical analysis of the flow in the "inner" boundary layer region.

The calculations demonstrate a rapid boundary layer growth toward the leeward side, accentuated by increasing the mass flow rate and decreasing the Reynolds number. The boundary layer growth is accompanied by an increase in pressure due to the displacement effect, but this increase is moderated somewhat by two effects: First, the relative pressure change due to variations in boundary-layer slope is less toward the leeward side; and second, the external streamlines tend to move more rapidly toward the leeward side as the interaction is increased. The latter effect is found to be small, however. Because the wall shear vector steepens progressively with increasing angle of attack in these calculations, the behavior which would be associated with separation is not observed. It is concluded that the method formulated here, although more complete than competing methods published to date, does not take into account all the factors which control leeward separation on cones in hypersonic flow. (It may well be impossible to account for all the important effects in a "classical" analysis which considers only the attached flow upstream of the separation line.) Apparently one ingredient in separation is an internal shock, caused either directly by the supersonic crossflow or indirectly by the viscous-inviscid interaction process linked to the near wake.

ACKNOWLEDGMENT

This research is a part of the Avco Reentry Environment and Systems Technology (REST) Program which is supported by the U. S. Air Force Systems Command, Space and Missile Systems Organization under the ABRES Program, Contract No. F04(694)-67-C-0060.

The authors are indebted to Messrs. S. Mazzola and P. Smith of Avco MSD for computational assistance.

REFERENCES

1. Hayes, W. D., "The Three-Dimensional Boundary Layer," NAVORD Report 1313, (NOTS 384) May 1951.
2. Fannelop, T. K., "A Method of Solving the Three-Dimensional Laminar Boundary Layer Equations with Application to a Lifting Reentry Body," AIAA Paper No. 67-159, January 1967 (To appear in AIAA J.)
3. Cooke, J. C. and Hall, M. G., "Boundary Layers in Three-Dimensions," Progress in Aeronautical Sciences, Vol. II, "Boundary Layer Problems," (Editors: D. Kuchemann and A. Ferri) pp. 221-285, Pergamon Press, 1962.
4. Fannelop, T. K., "Displacement Thickness for Boundary Layers with Surface Mass Transfer," AIAA J. Vol. 4, No. 6, pp. 1142-1144; and "Reply to O. R. Burggraf," AIAA J. Vol. 4, No. 6, p. 1147, June 1966.
5. Lighthill, M. J., "On Displacement Thickness," J. Fluid Mech. Vol 4, pp. 383-392, 1958.
6. Blottner, F. G. and Flügge-Lotz, I., "Finite-Difference Computation of the Boundary Layer with Displacement Thickness Interaction," Journal de Mecanique, Vol II, No. 4, 1963.
7. Cleary, J. W., "Effects of Angle of Attack and Nose Bluntness on the Hypersonic Flow Over Cones," AIAA Paper No. 66-414, June 1966. (See also Tb. NASA TN D-2969).
8. Lewis, C. H. and Knox, E. C., "A Spherically Blunted Cone at Angle of Attack," AIAA J. Vol. 4, No. 6, pp. 1110-1111, June 1966.
9. Knox, E. C. and Lewis, C. H., "A Comparison of Experimental and Theoretically Predicted Pressure Distributions and Force and Stability Coefficients for a Spherically Blunted Cone at $M_\infty \sim 18$ And Angles of Attack," AEDC TR 65-234, February 1966.
10. Sanlorenzo, E. and Petri, F., "Programs for the Analyses of Flow Fields Around Spherically Capped Three-Dimensional Bodies at Angles of Attack," GASL-TR-462, September 1964.
11. Maslen, S. H., "Second-Order Effects in Laminar Boundary Layers," Martin Co., R.R. 29, 1962.
12. Belotserkovskii, O. M., "The Calculation of Flow Over Axisymmetric Bodies with a Decaying Shock Wave," Academy of Sciences, U.S.S.R. (Moscow), Computation Center Monograph, 1961; Translated by J. F. Springfield, Avco RAD-TM-62-64, September 1962.
13. Van Dyke, M., "Second-Order Compressible Boundary-Layer Theory with Application to Blunt Bodies in Hypersonic Flow," Hypersonic Flow Research, (Editor: F. R. Riddell), Progress in Astronautics and Rocketry, Vol. 7, Academic Press, pp. 37-76, 1962.
14. Marchand, E. O., Lewis, C. H. and Davis, R. T., "Second-Order Boundary-Layer Effects on a Slender Blunt Cone at Hypersonic Conditions," AIAA Paper No. 68-54, AIAA 6th Aerospace Sciences Meeting, New York, 1968.
15. Kainbird, W. J., "Turbulent Boundary Layer Growth and Separation on a Yawed $12\frac{1}{2}^\circ$ Cone at Mach Numbers 1.8 and 4.25," AIAA Paper No. 68-98, 1968.
16. Reeves, B. and Lees, L., "Theory of the Laminar Near Wake of Blunt Bodies in Hypersonic Flow," AIAA J. Vol 3, p. 2061, 1965.
17. Tracy, K., "Hypersonic Flow Over a Yawed Circular Cone," Galtit Memo. No. 69, 1963.

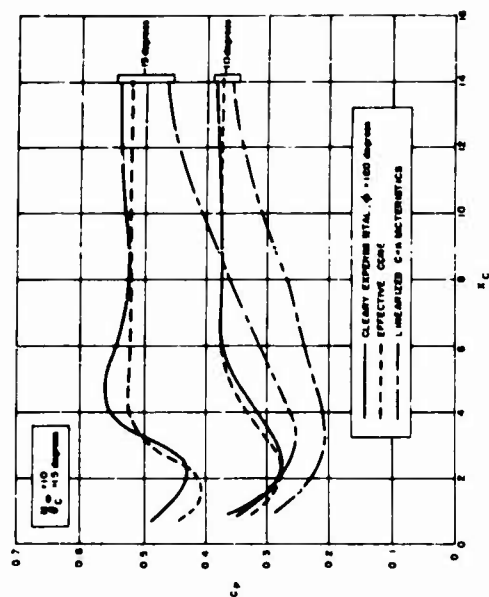


Figure 2a Comparison of Linearized Characteristics and Effective-Cone Results with Cleary Data, $\alpha = 10^\circ, 150^\circ$

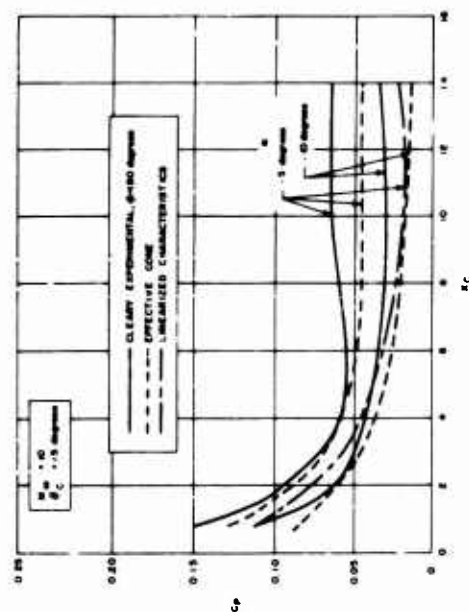


Figure 2c $\alpha = -5^\circ, -100^\circ$

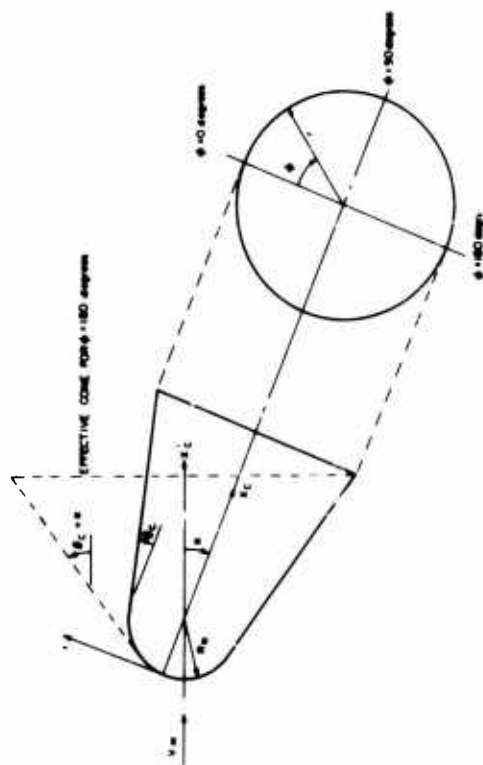


Figure 1 Effective-Cone Method

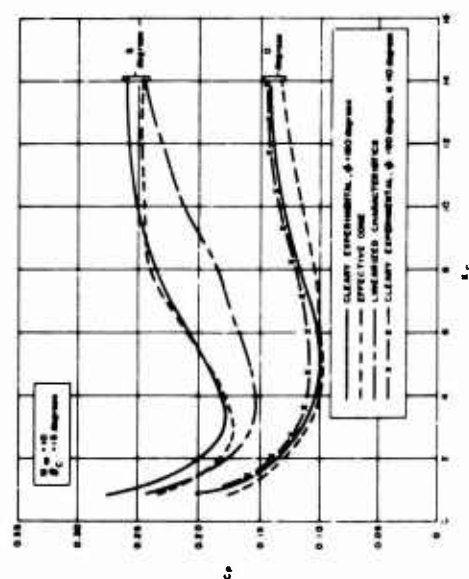


Figure 2b $\alpha = 0^\circ, 50^\circ$

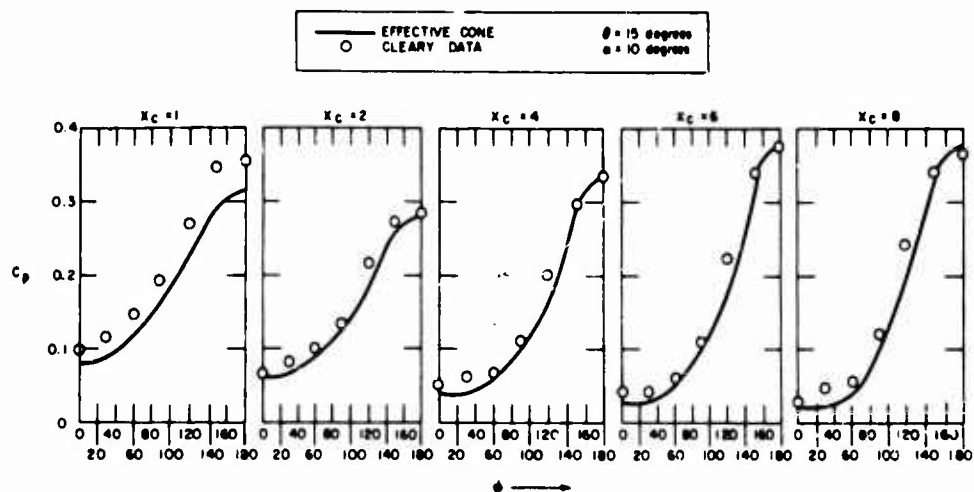
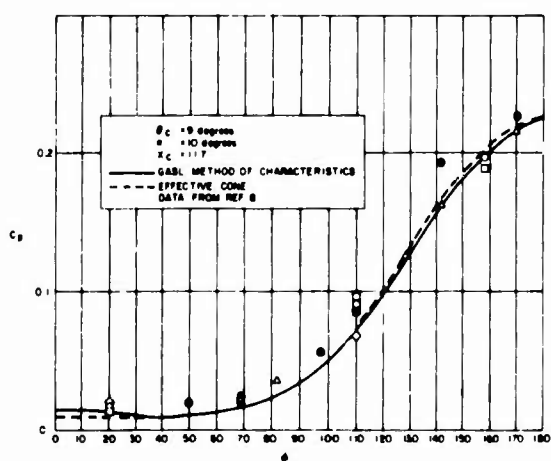
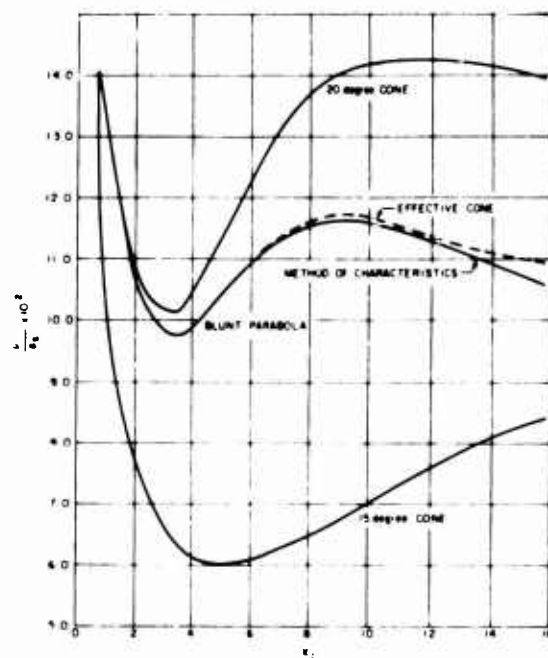
Figure 3 Comparison of Circumferential Pressure Distribution, $M_\infty = 10$ Figure 4 Comparison of Circumferential Pressure Distribution, $M_\infty = 18$ 

Figure 5 Pressure Distribution Over Blunted-Ogive Body

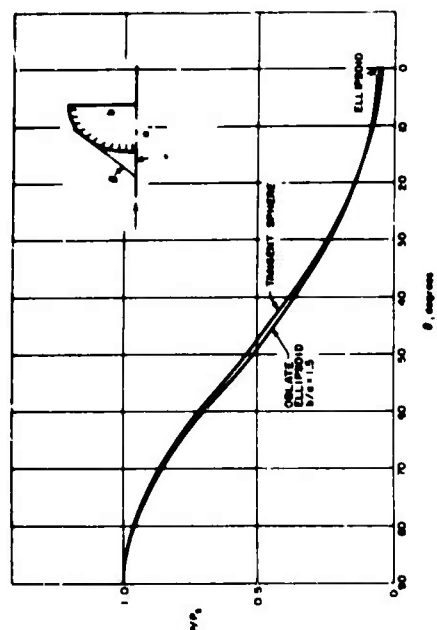


Figure 6a Tangent-Sphere Method



Figure 6b Comparison of Pressure Distribution Over Sphere and Oblate Ellipsoid, $M_\infty = \infty$

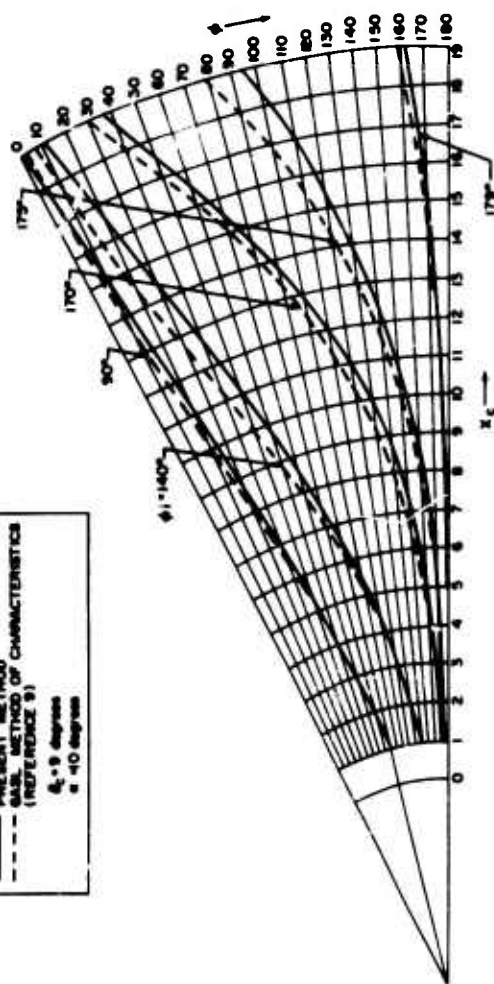


Figure 7 Comparison of Streamline Shapes, $M_\infty = 18$

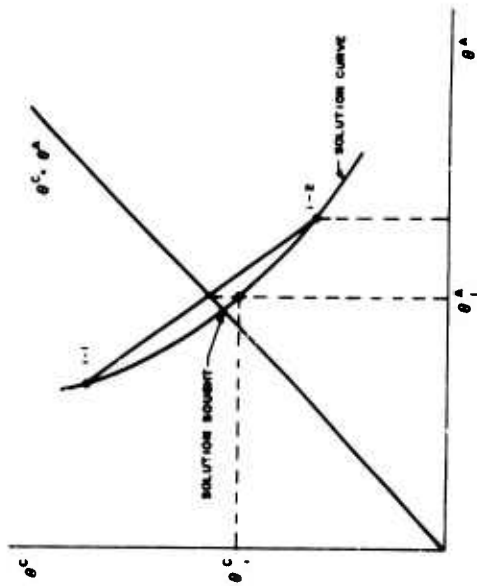


Figure 8 Method of Iteration

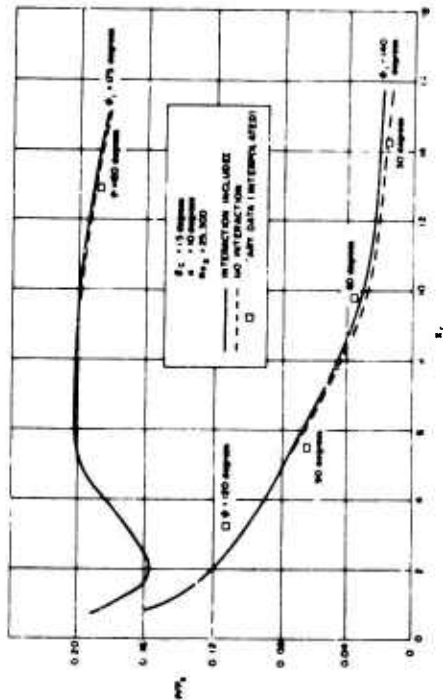


Figure 9 Pressure Distribution Along External Streamlines, $M_\infty = 10$

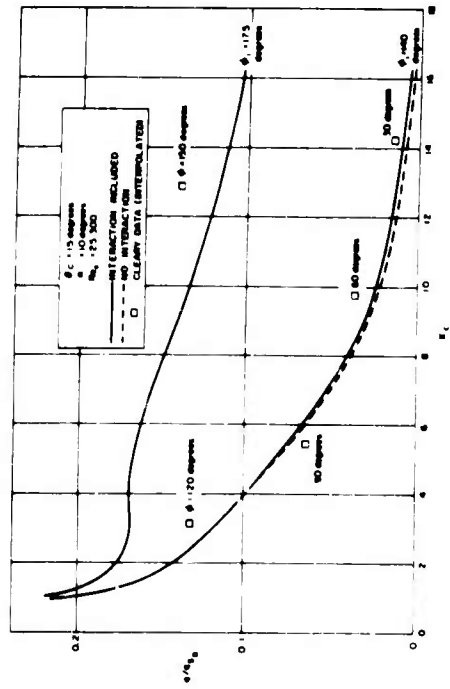


Figure 10 Heat-Transfer Distribution Along External Streamlines, $M_\infty = 10$

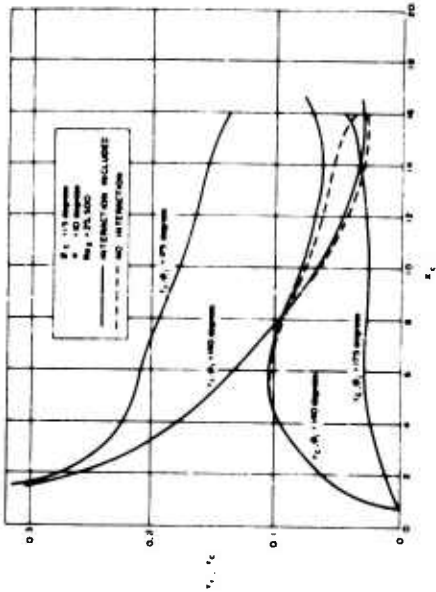


Figure 11 Tangential and Crossflow Wall-Shear Distributions Along External Streamlines, $M_\infty = 10$

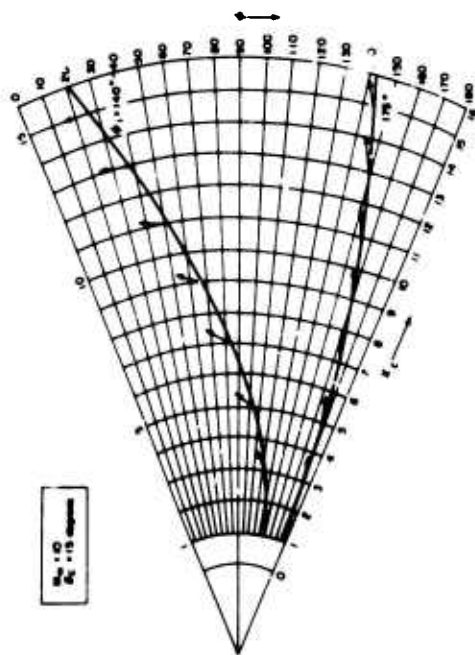


Figure 12a External Streamline Shapes and Directions of Surface Shear
Stress, $\alpha = 10^\circ$

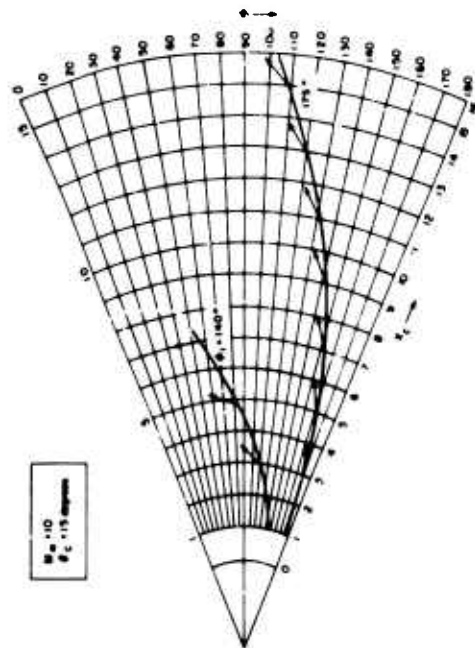


Figure 12b $\alpha = 15^\circ$

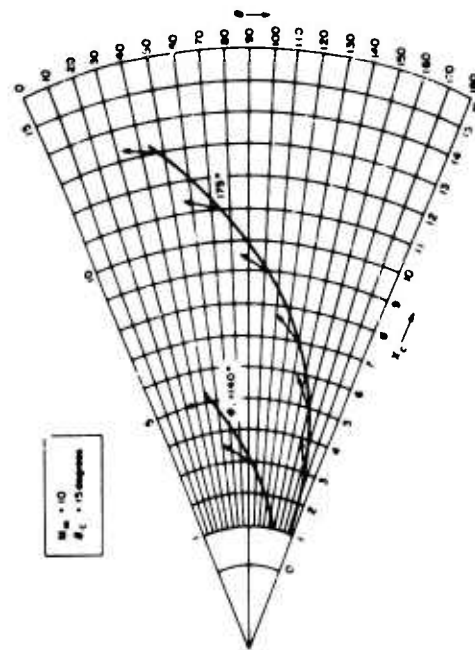


Figure 12c $\alpha = 20^\circ$

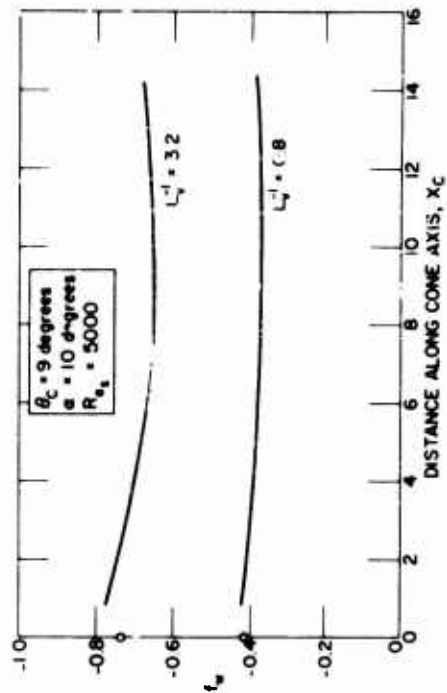


Figure 14 Distributions of Wall Flowing Parameter Along External Streamline, $\phi_1 = 170^\circ$, $M_\infty = 18$

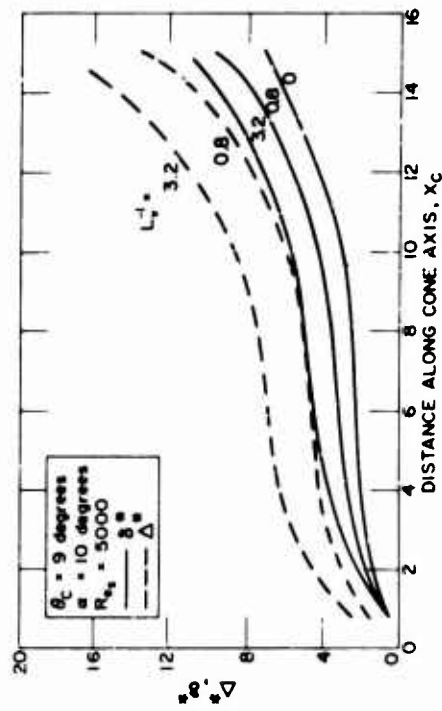


Figure 16 Distributions of Displacement Thickness Along External Streamline, $\phi_1 = 170^\circ$, $M_\infty = 18$

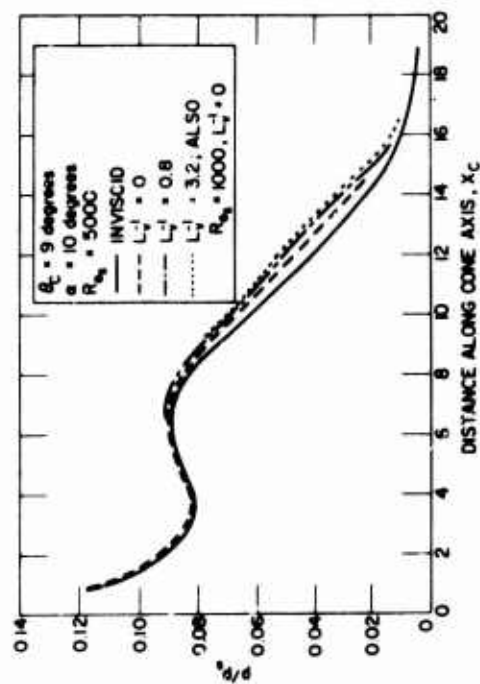


Figure 13 Pressure Distributions Along External Streamline, $\phi_1 = 170^\circ$, $M_\infty = 18$

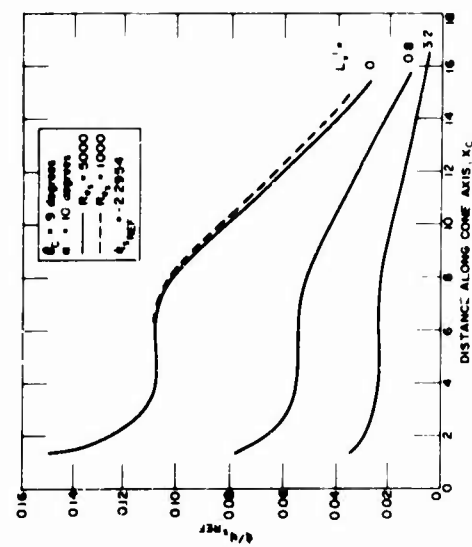


Figure 15 Heat-Transfer Distributions Along External Streamline, $\phi_1 = 170^\circ$, $M_\infty = 18$

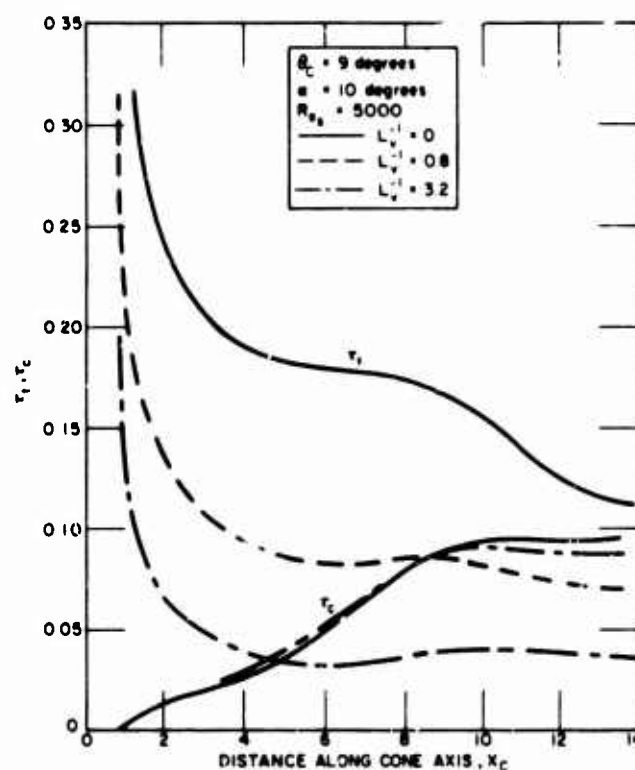


Figure 17 Tangential and Crossflow Wall Shear Distributions Along External Streamline, $\phi_1 = 170^\circ$, $M_\infty = 18$

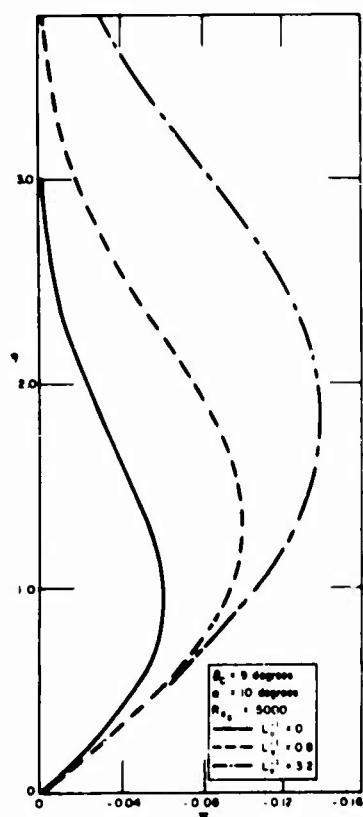


Figure 18a Crossflow Velocity Profiles Through Boundary Layer at Point $x_c = 6$, $\phi = 155^\circ$ on $\phi_1 = 170^\circ$ Streamline, $M_\infty = 18$

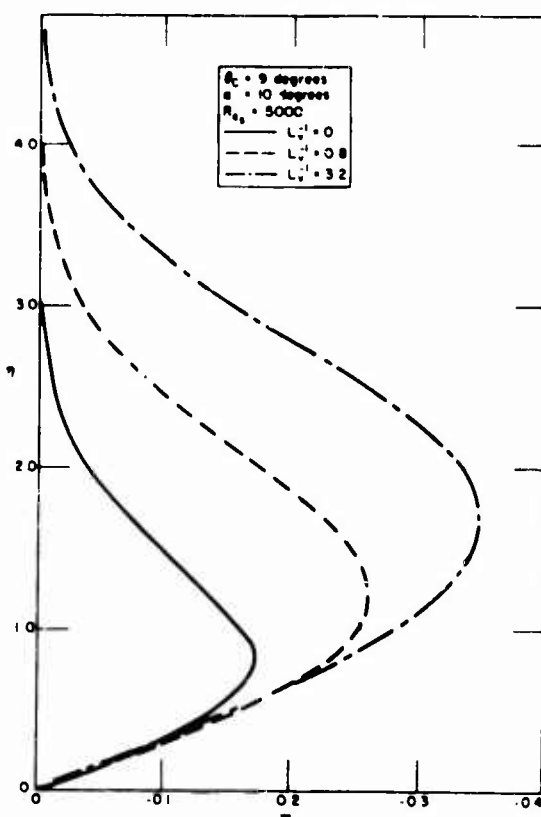


Figure 18b Crossflow Velocity Profiles Through Boundary Layer at Point $x_c = 12$, $\phi = 110^\circ$ on $\phi_1 = 170^\circ$ Streamline, $M_\infty = 18$

ETUDE THEORIQUE ET EXPERIMENTALE DE L'ECOULEMENT HYPERSONIQUE
AUTOUR D'UN CORPS EMBOUSSE EN INCIDENCE

par René CERESUELA (*)
Günter KRETZSCHMAR (**)
Colmar REHRACH (***)
O.N.E.R.A. (France)

(*) Chef de Groupe de Recherches
(**) Chef de Groupe de Recherches
(***) Ingénieur de Recherches

R E S U M E

Le champ aérodynamique à Mach 10 autour d'un cône fortement émoussé et peu ouvert ($2\delta = 10^\circ$) a été calculé par la méthode de BABENKO à 5° , 10° et 20° d'incidence; pour cette dernière le calcul numérique a divergé et abouti à des pressions négatives.

La comparaison avec des mesures en soufflerie a montré que :

- a) le profil de l'onde de choc est prédit avec une excellente précision,
- b) les pressions locales théoriques et expérimentales se recoupent, sauf aux incidences élevées, sur la partie supérieure où existe un écoulement tourbillonnaire en cornet lié au décollement de la couche limite,
- c) dans les conditions des présents essais (couche limite laminaire) les flux thermiques mesurés excèdent généralement les flux calculés.

Ce résultat est discuté.

En général, les divergences entre calcul et mesures restent confinées dans les zones où flux et pressions sont très faibles; la méthode de BABENKO conduit donc, aux incidences notables, à une évaluation assez approchée des charges aérodynamiques et thermiques globales sur un corps de révolution fortement émoussé.

S U M M A R Y

The aerodynamic field at Mach 10 around a very blunt cone of low apex angle ($2\delta = 10^\circ$) was calculated by BABENKO's method for incidence angles of 5° , 10° and 20° ; the numerical calculation diverged and gave negative pressures in the case of the latter incidence angle.

The comparison with wind-tunnel results showed that :

- a) the shock-wave was predicted with an excellent precision,
- b) the theoretical and experimental local pressures were in good agreement except for high incidence angles on the upper part of the body, where a boundary-layer separation induced a horse-shoe shaped vortex,
- c) in the conditions of the present tests (laminar boundary-layer) the heat rates measured were greater than those predicted in most cases. This result is discussed.

Generally, the divergence between theoretical and experimental results remained confined into zones where the heat rates and the pressure levels were low; therefore BABENKO's method leads to an evaluation sufficiently close to the real thermal and aerodynamic loads on a very blunt axisymmetrical body at fairly high angles of incidence.

NOTATIONS

A, B, C	Matrices carrées.
c_{cr}	Vitesse critique du son.
C_p	Chaleur spécifique de l'air à pression constante.
e	Largeur d'un tube de courant.
h_i	Enthalpie d'arrêt.
L	Longueur totale de l'obstacle.
\bar{p}	Pression rapportée au produit de la densité amont par c_{cr}^2 ; $\frac{p}{p_\infty} = 24,5 \bar{p}$ pour $M = 10$.
M_∞	Nombre de Mach à l'infini amont.
P	Nombre de PRANDTL.
q	Flux thermique par unité de surface.
q_i	Flux au point d'arrêt.
$r = G(x, \varphi)$	Equation de l'obstacle.
$r = F(x, \varphi)$	Equation du choc.
R	Rayon de la partie sphérique.
s	Abscisse curviligne le long d'une ligne de courant.
(A, n, b)	Système d'axes utilisés dans l'étude de la couche limite.
S	Facteur d'analogie de Reynolds.
T	Température.
T^*	Température de référence.
T_p	Température de paroi.
T_f	Température de frottement athermane.
(u, v, w)	Composantes axiale, radiale et circonférentielle de la vitesse.
$(\bar{u}, \bar{v}, \bar{w})$	Composantes axiale, radiale et circonférentielle de la vitesse rapportées à c_{cr}
(x, r, φ)	Système de coordonnées cylindriques lié à l'axe du corps.
\bar{x}	Vecteur de composantes $(\bar{u}, \bar{v}, \bar{w}, \bar{p})$.
α, β, σ	Paramètres servant à stabiliser le schéma aux différences.
$\xi = \frac{r-G}{F-G}$	Variable auxiliaire utilisée pour faciliter l'écriture des conditions aux limites.
Γ	Vecteur de quatre composantes.
δ	Epaisseur de la couche limite.
Δ	Epaisseur d'énergie.
ρ	Masse spécifique.
μ	Viscosité.
<u>Indices</u>	
e	Désigne l'état à la frontière de la couche limite.
∞	Désigne l'état à l'infini amont.

1 - INTRODUCTION

Le calcul de l'écoulement supersonique de gaz parfaits autour de corps de révolutions émoussés et sans incidence est résolu depuis de nombreuses années par la méthode des caractéristiques à partir de conditions initiales soniques, elles mêmes déduites d'une solution approchée du champ subsonique autour de l'émoussement sphérique. Le champ d'application de la méthode a été ensuite étendu aux écoulements de gaz à chaleurs spécifiques variables, à l'équilibre ou figés, et plus récemment avec cinétique chimique. Par ailleurs, une méthode de calcul de l'écoulement autour de corps de révolution émoussés, aux incidences faibles, dite méthode des caractéristiques linéarisée, a été établie [1] ; elle permet en particulier d'accéder aux gradients de force normale et à la stabilité des ogives au voisinage de l'incidence nulle.

Mais la détermination du champ d'écoulement autour de cônes (circulaires ou non) et à des incidences voisines du demi-angle du cône n'a été rendue possible que par la méthode numérique proposée par quatre auteurs russes [2], désignée ici brièvement par méthode de BABENKO.

Cette méthode a été programmée à l'O.N.E.R.A. et une première exploitation autour de cônes en a été publiée [3] ; cette exploitation a dégagé l'une des limitations de la méthode, qui apparaît sous la forme de divergence numérique, lorsque l'onde de choc dégénère en ligne de Mach, ce qui se produisait pour l'incidence 12° , dans le cas cité d'un cône de 9° de demi-angle à Mach 7.

Ces observations ont suggéré d'éprouver la méthode de calcul dans le cas d'un cône émoussé de faible ouverture, assurant la présence d'une onde de choc intense, tandis que de fortes détentes seraient observées en incidence à la partie supérieure du corps ; on visait ainsi à dégager d'autres limites de validité du calcul, que la seule évanescence de l'onde de choc. Les calculs ont été effectués pour Mach 10, avec un rapport des chaleurs spécifiques $\gamma = 1,4$.

Parallèlement à ces calculs a été effectuée une série de mesures dans la soufflerie Mach 10 de Chalais-Meudon, pour mettre en évidence les limitations d'ordre physique (viscosité et tourbillons) qui venaient à leur tour limiter le domaine d'application du schéma de calcul.

La présente communication relate les premiers résultats obtenus et les observations faites lors de cette étude.

2 - CONDITIONS DE CALCUL DU CHAMP D'ECOULEMENT

La méthode utilisée pour le calcul du champ aérodynamique autour du corps en incidence, et de la forme de l'onde de choc, est due à BABENKO, VOSKRESSENSKIY, LIOUBIMOV et ROUSSANOV [2].

Son analyse et l'élaboration du programme qui permet son exploitation sur ordinateur ont été effectuées à l'O.N.E.R.A. avec la collaboration de la S.E.M.A. (Société d'Economie et de Mathématique Appliquées, Paris) [3]. Les calculs numériques ont été exécutés sur l'ordinateur CONTROL DATA 6600 de la S.I.A. (Société d'Informatique Appliquée, Paris).

2.1 - Résumé de la méthode -

L'écoulement supersonique autour d'un obstacle de forme quelconque est donné par une solution du système aux dérivées partielles

$$A \frac{\partial X}{\partial x} + B \frac{\partial X}{\partial \xi} + C \frac{\partial X}{\partial \varphi} + \Gamma = 0 \quad (1)$$

où x est l'abscisse d'un plan normal à l'axe du corps, ξ la cote réduite d'un point le long d'un rayon de ce plan, et φ la position angulaire de ce rayon, voir la Fig. 1.

Les matrices carrées A , B , C et le vecteur Γ sont fonctions du vecteur inconnu X ; la matrice B contient en outre des termes dépendant de la forme du choc, autre inconnue du problème. Le système à résoudre est donc quasi linéaire.

Dans le cas du gaz parfait (seul traité par l'O.N.E.R.A.), les matrices A , B et C sont d'ordre 4 et les vecteurs X et Γ ont 4 composantes.

Le domaine où la solution est cherchée est défini par :

$$\begin{aligned} x_0 &\leq x \leq x_M \\ 0 &\leq \eta < 1 \\ 0 &\leq \varphi < 2\pi \end{aligned} \quad (2)$$

Les conditions initiales sont données dans le plan x_0 , les conditions aux limites pour :

$$\begin{aligned} \eta &= 0 \quad (\text{condition de vitesse tangente à la paroi de l'obstacle}) \\ \eta &= 1 \quad (\text{conditions de RANKINE-HUGONIOT sur le choc}). \end{aligned}$$

La solution cherchée doit en outre être périodique en φ .

Pour la résolution numérique on remplace le système (1) par un schéma aux différences qui permet le calcul des inconnues aux points d'une grille rectangulaire à pas fixe :

$$\Delta x = \tau \quad \Delta \eta = \frac{1}{M} \quad \Delta \varphi = \frac{2\pi}{L} \quad (3)$$

Ce schéma, joint aux conditions aux limites, constitue l'algorithme de passage du plan $x = x_0 + n\tau$ ($n = 0, 1, 2 \dots N-1$), où l'écoulement est supposé connu, au plan $x = x_0 + (n+1)\tau$, où il est inconnu, et permet en principe une solution complète du problème.

Le fait que le système ainsi obtenu n'est pas linéaire par rapport aux inconnues, et qu'il y a donc plus d'une solution, amène les auteurs russes à proposer un procédé itératif grâce auquel le système non linéaire aux différences se décompose en L systèmes linéaires indépendants. Chacun de ces systèmes permet la détermination des inconnues sur un rayon $\varphi = \text{const.}$ de la grille. La convergence des itérations vers la solution cherchée n'est pas établie théoriquement, mais son existence est constatée par de nombreux résultats de calcul.

La solution du système sur un rayon du plan $x = x_0 + (n+1)\tau$ est obtenue de la façon suivante :

- On y suppose connue l'itération (i) et l'on cherche l'itération (i+1) (l'itération (0) peut, par exemple, être constituée par la solution dans le plan précédent, mais il est certainement avantageux d'utiliser un "prédicteur", ici une extrapolation linéaire, plus précis pour lier au maximum le nombre des itérations). Pour ce faire on amène par un calcul qui utilise l'itération (i) et qu'on appelle progression directe la condition d'obstacle sur le choc. Le système d'équations ainsi obtenu fournit l'itération (i+1) pour la position du choc et la valeur du vecteur X sur celui-ci. La progression inverse donne à partir des informations sur le choc l'itération (i+1) du vecteur X pour les autres points du rayon considéré.

Ce procédé appliqué à chacun des L rayons du plan $x = x_0 + (n+1)\tau$ y donne l'itération (i+1). Cette dernière sert au cours de la progression directe suivante qui aboutit à l'itération (i+2) sur le choc et à l'aide de la progression inverse à l'itération (i+2) sur tout le rayon. On passe au rayon suivant et ainsi de suite.

On répète de cette façon le calcul dans le plan considéré jusqu'à convergence. Celle-ci atteinte, on passe au plan suivant.

2.2 - Application numérique -

Avant d'examiner les résultats numériques obtenus dans le cas particulier traité, il est intéressant de faire quelques remarques concernant l'exploitation du programme.

Le problème étant symétrique par rapport au plan médian (dérapage nul), on n'a traité que le demi-plan

$$\begin{aligned} 0 &\leq \eta < 1 \\ 0 &\leq \varphi < \pi \end{aligned}$$

La grille définie plus haut est, pour les calculs en question, caractérisée par

$$L = 32$$

$$M = 10$$

τ variant au cours du calcul de

$$\tau = 0,00125 L$$

dans la zone de forte courbure, à

$$\tau = 0,0125 L$$

dans la partie conique du corps.

Les auteurs russes ont introduit dans leur schéma aux différences des paramètres stabilisateurs

$$\alpha, \beta \text{ et } \sigma$$

visant à assurer la convergence du procédé de calcul ; nous avons adopté pour ces paramètres les valeurs :

$$\alpha = 0,505$$

$$\beta = 0,495$$

et

$$\sigma = 10^{-4}$$

La préparation des données dans le plan initial x_0 nécessite un travail considérable. Il s'agit d'y fournir les composantes de vitesse $\bar{u}, \bar{v}, \bar{w}$, la pression \bar{p} et la forme du choc pour tous les points de la grille adoptée. Nous avons choisi le plan x_0 dans la partie du corps où l'écoulement est encore sphérique, ce qui a permis d'utiliser une table d'écoulement de BIELOTSEKOVSKY [4]. Les valeurs aérodynamiques y sont tabulées pour différents nombres de Mach en coordonnées polaires. Il suffit donc de passer aux coordonnées cylindriques utilisées dans le programme.

Le cône étudié est tel que son émoussement reste sphérique jusqu'à un angle de 65° (le raccord avec le cône de $4,66$ degrés de demi-ouverture est un secteur de clothoïde assurant la continuité de courbure, Fig. 2) ; les conditions initiales du calcul sont donc des conditions sphériques, de révolution autour de la vitesse amont, jusqu'à une incidence de 24° (point sonique voisin de $40,1^\circ$ à Mach 10 [4]). Les calculs ont été effectués pour les angles d'incidence $5^\circ, 10^\circ$ et 20° .

Les résultats se présentent sous la forme suivante :

- Pour chaque incidence, on obtient pour une soixantaine de plans $x = \text{const.}$ les composantes de vitesse $\bar{u}, \bar{v}, \bar{w}$ et la pression \bar{p} en tous les points de la grille (3,4) adoptée pour le calcul. Pour chacun des rayons ($\psi = \text{const.}$) de la grille, on obtient également la forme du choc définie par sa cote polaire F et la dérivée $\partial F / \partial x$, qui exprime sa pente locale par rapport à l'axe du corps.

Le temps d'utilisation du C D C 6600 est, par incidence calculée, de l'ordre de

16 minutes d'unité centrale* (calcul proprement dit)

et de

13 minutes d'unités périphériques (entrée des données, sortie des résultats).

Remarque -

L'un des buts de la présente étude, mettre en évidence des limites d'utilisation de la méthode numérique, non liées à l'évanescence de l'onde de choc, a été atteint : en effet le calcul pour l'incidence 20° n'a pu aller au delà du plan d'abscisse $x/L = 0,475$ où la progression inverse (du choc au corps) est devenue instable dans la zone de forte détente sur l'extrados ; le calcul mécanographique y a été arrêté par l'apparition d'une pression négative (introduite par le prédicteur linéaire évoqué plus haut), dans le plan situé à environ $\psi = 155^\circ$, voir la Fig. 3. Une étude détaillée des raisons de cette instabilité numérique, et des procédés éventuels pour la lever, est en cours à l'O.N.E.R.A.

L'intégration des composantes de la vitesse issues du calcul, en vue de calculer la géométrie des lignes de courant, a été demandée à un programme d'IBM 704.

Utilisé dans le cas présent pour le calcul des lignes de courant pariétales (3 minutes d'ordinateur fournissent 17 lignes de courant couvrant le demi-corps de l'intrados à l'extrados), ce programme peut être adapté pour calculer toutes les lignes de courant entre le corps et le choc.

* Rappelons que le calcul autour d'un cône pointu sur machine C D C 3600, avec le même programme, dure environ 1 heure.

2.3 - Méthode de calcul des flux thermiques -

2.3.1 - Principe

On se propose de calculer les flux de chaleur à la paroi du corps dans le cas d'une couche limite laminaire et dans l'hypothèse d'un gaz parfait à chaleurs spécifiques constantes. Une solution approximative est obtenue par l'application de la méthode de MICHEL et DUONG [5], méthode qui est fondée sur l'intégration de l'équation globale de l'énergie. D'après le "principe de prévalence" de RICHELIEUX et OUDART [8], un traitement "bidimensionnel" est appliqué à la couche limite tridimensionnelle ; à cet effet on choisit un système d'axes orthogonaux défini par

- la projection normale des lignes de courant à la frontière extérieure de la couche limite sur la paroi (s), (lignes de courant pariétales de l'écoulement du fluide parfait),
- la normale à la paroi (n),
- la perpendiculaire à s, n (b).

Dans ce système, la composante (w) suivant b du vecteur vitesse, est nulle en $n = 0$ et $n = \delta$.

Entre ces deux limites, w est faible par rapport à la composante longitudinale u . Ceci suggère de négliger en première approximation w et toutes les dérivées par rapport à b dans les équations de la couche limite. Celles-ci se réduisent alors à celles d'un écoulement bidimensionnel. La divergence des lignes de courant, nulle en écoulement plan et seulement fonction du rayon transversal en écoulement de révolution, dépend à la fois de la forme géométrique du corps et du champ d'écoulement qui s'établit autour.

Dans les équations globales on voit apparaître le terme

$$\frac{1}{e} = \frac{de}{ds}$$

où e désigne la largeur d'un pinceau de courant défini par deux lignes de courant extérieures voisines. Le calcul préalable de l'écoulement parfait fournit l'intersection des lignes de courant à la paroi avec des plans $\alpha = c\theta$, dans des coordonnées cylindriques (r, φ). Pour la ligne de courant numérotée " m " on calculera alors $e = e_m$ par la relation

$$e_m = \frac{1}{2} r (\varphi_{m+1} - \varphi_{m-1}) \cos \theta_m$$

θ_m est l'angle que forme la ligne de courant avec le plan méridien passant par le même point. Il se calcule à l'aide des composantes du vecteur vitesse (issues ici du calcul de BABENKO) :

$$\tan \theta = \frac{w}{u}$$

2.3.2 - Equation globale de l'énergie, hypothèses nécessaires à sa résolution.

L'équation globale de l'énergie s'obtient en intégrant l'équation aux dérivées partielles de $n = 0$ à $n = \delta$:

$$\frac{q}{\rho_e u_e h_{ie}} = \frac{d\Delta}{ds} + \Delta \frac{1}{\rho_e u_e e} \frac{d\rho_e u_e e}{ds} \quad (4)$$

L'état de l'écoulement à la frontière de la couche limite, ρ_e, u_e, h_{ie} étant connu, une hypothèse doit être introduite pour relier le flux de chaleur q à la paroi à l'épaisseur d'énergie

$$\Delta = \int_0^\delta \frac{\rho u}{\rho_e u_e} \left(\frac{h_i}{h_{ie}} - 1 \right) dn.$$

Les solutions semblables de la couche limite laminaire suggèrent d'exprimer ce flux, rendu convenablement sans dimension, en fonction du nombre de Reynolds défini avec l'épaisseur Δ sous la forme

$$\frac{q}{\rho_e u_e h_{ie}} = \frac{B}{\rho_e u_e \Delta / \mu_e} \quad (5)$$

Le coefficient B dépend, en principe, des paramètres caractérisant l'écoulement : nombre de Mach, température de paroi, gradient de pression. En fait, on montre dans la réf. [5] que l'effet du gradient de pression sur B n'affecte guère le flux calculé. Une relation de "plaque plane" sera donc retenue pour B . Tenant compte des effets de la compressibilité par le concept de la "température de référence"

$$T^* = T_e + 0,54 (T_p - T_e) + 0,16 (T_f - T_e)$$

on écrira

$$B = 0,2205 \frac{\rho^* \mu^*}{\rho_e \mu_e} \left(S \frac{T_f - T_p}{T_e} \right)^2 \quad (6)$$

où $\rho^* = \rho(T^*)$, $\mu^* = \mu(T^*)$. Pour le facteur d'analogie de Reynolds S on utilisera l'approximation habituelle, valable également pour un écoulement sans gradient de pression,

$$S = P^{-2/3} = 1,24.$$

Le facteur de récupération laminaire r qui intervient dans le calcul de T_f est donné par

$$r = P^{1/2} = 0,85.$$

L'équation globale (4), après la substitution des relations (5), (6) peut être intégrée sous la forme

$$(\Delta \rho_e u_e e)^2 = (\Delta \rho_e u_e e)^2_{s=0} + 0,441 \int_{s=0}^s \frac{\rho^* \mu^*}{\rho_e \mu_e} \rho_e u_e \mu_e \left(S e \frac{T_f - T_p}{T_e} \right)^2 dA \quad (7)$$

L'épaisseur Δ étant ainsi calculée, on obtient le flux de chaleur par la relation (5).

Au point d'arrêt où u_e et e sont nuls, un passage à la limite appropriée conduit à

$$\left. \begin{aligned} \Delta(0) &= \sqrt{0,4403 \frac{\rho^* \mu^*}{\rho_e \mu_e} \frac{\mu_e}{\rho_e} S \frac{T_f - T_p}{T_e}} \\ q(0) &= \sqrt{0,441 \frac{\rho^* \mu^*}{\rho_e \mu_e} \rho_e \mu_e \frac{du_e}{dA} S c_p (T_f - T_p)} \end{aligned} \right\} \quad (8)$$

2.3.3 - Intégration numérique

L'intégrale qui apparaît au deuxième membre de l'équation (7) est calculée numériquement, pas à pas. Pour intégrer d'un point A_n au point suivant A_{n+1} l'intégrand est approché par un polynôme du second degré en s , dont les coefficients sont déterminés par les valeurs de l'intégrand aux points A_{n-1} , A_n et A_{n+1} espacés de façon quelconque.

Au tout premier pas cette méthode n'est évidemment pas applicable. On utilise alors la formule des trapèzes. Sachant qu'au voisinage du point d'arrêt

$$u_e \sim \Delta, \quad e \sim \Delta$$

on applique un facteur correctif pour améliorer la précision de l'intégration. Ce facteur tient compte également de la nature de la couche limite (laminaire ou turbulente).

2.3.4 - Approximation améliorée pour le calcul des flux

Les erreurs, dues aux hypothèses simplificatrices introduites dans la méthode de calcul, s'éliminent en grande partie lorsqu'on forme le quotient $q(\Delta)/q(0)$, les deux quantités $q(\Delta)$ et $q(0)$ étant affectées sensiblement des mêmes erreurs. On l'a vérifiée réf. [5] en comparant les distributions de flux relatifs $q(\Delta)/q(0)$ obtenues par la méthode globale avec celles calculées à l'aide de méthodes plus exactes.

Il est alors facile d'améliorer la précision des flux en multipliant le rapport $q(\Delta)/q(0)$ par le flux au point d'arrêt q_{FR} donné par exemple par la formule de FAY et RIDDELL :

$$q = q_{FR} \frac{q(\Delta)}{q(0)} \quad (9)$$

2.3.5 - Programmation de la méthode

La résolution de l'équation globale de l'énergie sous la forme (7), et l'obtention des flux à l'aide des relations (5), (8) et (9) a fait l'objet d'une programmation en FORTRAN pour l'ordinateur IBM 704. Plusieurs options sont possibles selon la nature de la couche limite (laminaire, turbulente) et la géométrie de l'écoulement (plan, de révolution, tridimensionnel).

Un calcul complet (17 lignes de courant avec 60 à 70 points de calcul sur chacune) demande environ 10 minutes.

3 - VERIFICATIONS EXPERIMENTALES

Les essais ont été effectués dans la soufflerie R3 de Chalais-Meudon, à un nombre de Mach $M = 9,95$ dans une veine d'un diamètre utile d'environ 30 cm. La pression génératrice est de 120 bars et la température de 1 020°K environ. Le nombre de Reynolds correspondant, rapporté à l'écoulement non perturbé et à la longueur de la maquette (25 cm) est $Re = \frac{V_\infty L}{\nu} = 2,3 \cdot 10^6$; les couches limites sont donc très probablement laminaires sur toute la longueur du modèle.

3.1 - La détermination de la forme de l'onde de choc est obtenue par striescopie normale ; une tentative de détermination de la forme tridimensionnelle de l'onde de choc, en présentant la maquette dans des positions d'incidence et dérapage combinés n'a pas réussi, à cause de difficultés de restitution.

3.2 - Mesures de pressions pariétales -

On a utilisé une maquette équipée de micro-capteurs de pression à réponse rapide situés directement sous la paroi ; les essais étaient effectués au cours d'une même rafale par paliers d'incidence ($5^\circ - 10^\circ - 15^\circ - 20^\circ$) pour des valeurs fixes de l'angle polaire ψ de la génératrice considérée. Sur la figure 3 les points d'une même verticale sont donc issus d'une unique rafale.

3.3 - Mesures d'échauffement cinétique -

Une première série d'essais au moyen de maquettes en silastène revêtue de peintures thermovirantes, selon la technique décrite dans la réf. [6], a donné des valeurs numériques exploitables sur la seule moitié inférieure de la maquette, siège des échauffements les plus forts, voir la figure 4 a ; les mesures ont été reprises sur une maquette à paroi mince calibrée, munie de thermocouples. Ce sont ces dernières mesures, qui ont confirmé et prolongé les premières, qui ont été retenues et fournies ici.

3.4 - Visualisation des lignes de courant sur la paroi -

Le programme d'analyse numérique permettant le calcul des lignes de courant, n'a été recherché une visualisation de ces lignes au cours des essais ; l'emploi des sillages de billes sur peinture thermovirante est limité, comme on le voit sur la photographie de la figure 4 a, aux parties les plus exposées. Des résultats plus nets ont été obtenus au moyen de gouttes d'huile aux silicoles colorées, et déposées avant l'essai sur la maquette peinte en blanc - Figure 4 a, b, c, d.

4 - RESULTATS

4.1 - Forme de l'onde de choc - figure 5

La méthode de BABENKO fournit des formes de choc qui recoupent remarquablement les striescopies. A l'incidence 5° le calcul repris par la méthode des caractéristiques linéarisée définit une onde de choc située à l'extérieur de la première. Une analyse des résultats semble indiquer que les méthodes de calcul (BABENKO ou caractéristiques) n'expliquent pas cet écart, qui serait dû à de très faibles écarts sur les conditions initiales (soniques) des calculs.

4.2 - Répartitions de pression -

Les pressions calculées sur les génératrices inférieure et supérieure sont comparées sur la figure 2. Considérant le calcul de BABENKO (courbes en traits interrompus), on note une surdétente suivie d'une recompression, d'intensités croissantes avec l'incidence, sur le début de la partie conique, côté extradors ; vers les 2/3 arrière du corps les courbes 10° et 5° se confondent. La courbe $i = 20^\circ$ en particulier indique, après une très forte surdétente, une recompression suivie d'une nouvelle détente accentuée jusqu'au plan $x/L = 0,475$ où le calcul a été arrêté par annulation de la pression (voir 2.2).

Côté intrados, on note à $i = 10^\circ$ une légère recompression sur la moitié arrière du corps. Cette évolution qui s'accroît à $i = 20^\circ$, est à rapprocher du changement de courbure de l'onde de choc, qui traduit le raccord de l'écoulement régi par le nez émoussé, à l'écoulement conique asymptotique.

Les répartitions calculées par la méthode des caractéristiques semi-linéarisées - traits pleins - surestiment la détente et sous-estiment la compression, ce qui montre qu'à 5° d'incidence déjà cette méthode perd toute signification.

Remarque - Il a cependant été constaté que la méthode des caractéristiques semi-linéarisées donne le gradient de force normale à l'incidence nulle et la position du foyer aérodynamique fournis par l'expérience à Mach 10.

Les répartitions de pressions autour du corps à différentes abscisses - figure 3 - montrent que le calcul de BABENKO prédit remarquablement les pressions mesurées à l'abscisse $x/L = 0,11$ origine de la partie conique (courbes (a)). Pour $x/L = 0,445$, (courbes b) les courbes théoriques interprètent encore exactement les valeurs mesurées pour $i = 5^\circ$ et $i = 10^\circ$, mais à l'incidence 20° on constate un écart dans le secteur de $\psi = 170^\circ$ à $\psi = 125^\circ$, dont les visualisations - figure 4 (c) - montreront le rapport avec le décollement tourbillonnaire.

Pour $x/L = 0,95$, courbes (c), ce même phénomène apparaît dès l'incidence 10° , vers $\psi = 116^\circ$. La courbe théorique pour $i = 20^\circ$ n'est pas disponible comme il est dit plus haut, mais l'allure de la courbe expérimentale confirme qu'un décollement s'y produit également au voisinage de $\psi = 120^\circ$.

Tracé des isobares dans un plan normal à l'axe du corps - Figure 6

Les courbes des pressions locales le long des rayons passant par l'axe, données directes du calcul de BABENKO, permettent à leur tour le tracé des isobares dans le plan contenant ces rayons, ici le plan du culot $x/L = 1$.

N.B. - Ces courbes sont graduées en valeurs de \bar{P} , paramètre de calcul tel que $P/P_\infty = 24,5 \bar{P}$.

On note que les courbes relatives à l'incidence 5° sont monotones entre intrados et extrados ; à $i = 10^\circ$ apparaissent 2 minima de pression pour $\psi = 135^\circ$; pour $i = 20^\circ$, et dans le plan $x/L = 0,45$ (qui est le dernier plan où le calcul a convergé) cette zone de faibles pressions s'est accentuée et les minima se sont rapprochés du plan de symétrie. On remarquera que ces zones de faible pression restent au contact du corps ; le sondage en soufflerie des pressions d'arrêt entre le choc et le corps, complément indispensable des présents tracés est en cours au moment de la rédaction.

Lignes de courant calculées à la paroi

La figure 7 représente, sur un plan développé d'un demi-corps, les lignes de courant calculées pour les incidences 5° , 10° et 20° . Ces lignes de courant ont servi de base au calcul du flux thermique.

Comparaison entre les échauffements calculés et mesurés

La figure 8 compare les échauffements mesurés et calculés sur la génératrice inférieure (en compression). L'allure des deux courbes est bien la même, mais les calculs sous-estiment d'environ 10% les valeurs mesurées.

On note qu'au delà de 10° d'incidence, l'échauffement sur la partie arrière augmente après un minimum qui se rapproche du nez à i croissant ; cette allure est très voisine de celle constatée le long du bord d'attaque cylindrique d'une aile en flèche à émoussement sphérique essayée précédemment dans les mêmes conditions expérimentales [5].

La figure 9 compare les strioscopies obtenues et les flux mesurés rapportés au flux au point d'arrêt, portés en fonction des abscisses réduites x/R dans les cas

- a) du corps de révolution à $i = 15^\circ$,
- b) d'une aile en flèche de 75° en dérapage de 5°

où les génératrices exposées au vent ont donc une inclinaison égale de 20° . Les deux courbes sont remarquablement voisines, ainsi que les champs d'écoulement donnés par la strioscopie. Le calcul exposé dans la réf. [5] rend bien compte de l'existence d'un minimum dû à l'effet d'émoussement.

Sur la figure 10 on a comparé les flux mesurés à $i = 20^\circ$ sur les génératrices à $30^\circ - 60^\circ$ et 90° de l'intrados ; on note la déformation très progressive des courbes, qui rappelle celle des courbes des pressions mesurées (figure 10 b). Il semble donc que les flux locaux dépendent assez étroitement des pressions locales, ce qui avait déjà été constaté par GRIFITH [7] dans le cas de corps émoussés à l'incidence nulle, essayés en hypersonique.

Mais sur la génératrice d'extrados - figure 11 - la comparaison entre calcul et mesures, correcte à $i = 5^\circ$, montre que les flux mesurés sur la partie arrière ne suivent pas la décroissance monotone calculée mais augmentent de nouveau à partir d'un point qui avance à i croissant.

En se reportant aux visualisations de la figure 4 on voit que les hypothèses de calcul ne sont pas respectées par l'écoulement réel dans cette zone : la ligne de courant qui suit la génératrice supérieure n'est pas le confluent de toutes les lignes de courant qui ont contourné le corps mais au contraire l'origine de lignes de courant divergentes. Cette divergence est provoquée par le décollement tourbillonnaire.

Les répartitions des flux mesurés et calculés autour du corps - figure 12 - sont en désaccord croissant quand on s'éloigne de la génératrice inférieure : pour $x/L = 0,425$ et $\varphi = 90^\circ$ par exemple, l'écart est voisin de 50%, bien que cette zone ne soit le siège d'aucun décollement.

Cet écart peut être imputé à ce que les lignes de courant pariétales réelles ne sont pas celles calculées en écoulement non visqueux. La figure 4 groupe quelques-unes des photographies de lignes de courant visualisées par deux procédés différents : le premier employé a consisté à garnir la maquette en silastène, revêtue de peinture thermochromique, de billes de 1,9 mm de diamètre, dont le sillage serait visualisé par les plus forts échauffements qui règnent à son voisinage, ainsi que l'avaient signalé des observations précédentes. Mais la photographie 4 e montre que les sillages ne sont plus visibles pour $\varphi > 90^\circ$, où les flux deviennent inférieurs à 2 Watts/cm², donc au-dessous de la limite de virage de la peinture* pour les durées ($t < 7$ s) considérées.

Le second procédé a consisté à déposer sur la maquette métallique, peinte en blanc pour le contraste, des gouttes de résines polyester colorées. Les photographies montrent que les trajectoires obtenues vont cette fois jusqu'à l'extrados pendant les 7 secondes d'essai ; après l'essai le liquide visqueux se fige de nouveau et le schéma obtenu peut être conservé plusieurs jours.

Les inclinaisons des lignes ainsi obtenues ont été relevées et comparées avec celles issues du calcul de BABENKO. La figure 13 compare calcul et sillages sur peinture virante à $i = 10^\circ$ (13 a), avec les traces d'enduit visqueux à la même incidence (13 b), et à $i = 20^\circ$ avec la méthode de l'enduit visqueux (13 c); les inclinaisons sur la partie supérieure des maquettes n'ont pas été tracées, mais sont de signe opposé aux valeurs théoriques.

Deux remarques s'imposent :

- d'abord les deux méthodes de visualisation utilisées à $i = 10^\circ$ conduisent à des inclinaisons de lignes de courant très voisines ; bien qu'il s'agisse dans un cas de sillages d'obstacles émergeant de la couche limite, et dans l'autre cas de filets liquides épais d'environ 1/10 de mm, on peut suspecter que les deux expériences indiquent les directions à la partie inférieure de la couche limite, donc probablement différentes des directions des lignes de courant externes, ce qui expliquerait que les inclinaisons sont dans tous les cas beaucoup plus fortes que celles calculées, du double au quadruple selon l'abscisse ;
- on note par ailleurs que les inclinaisons maximales restent au voisinage de $\varphi = 90^\circ$ alors que les maxima théoriques sont plus voisins de l'extrados.

Ces remarques apportent peut-être l'explication de l'écart constaté entre les flux mesurés et ceux calculés car le calcul basé sur le principe de prévalence n'est pas applicable quand les composantes transversales de la vitesse sont très importantes. Une série de mesures clinométriques locales visera à préciser les directions vraies des lignes de courant extérieures à la couche limite.

On espère que le sondage des pressions d'arrêt entre le choc et le corps, en cours au moment de la rédaction, attirera l'attention sur des différences fondamentales entre le champ d'écoulement théorique et le champ réel régi par la présence de deux tourbillons libres symétriques issus de la couche limite décollée aux incidences excédant la demi-ouverture du cône.

5 - CONCLUSIONS

Le champ d'écoulement autour d'un cône fortement émoussé et peu ouvert (demi-ouverture environ 5°) à Mach 10 et à des incidences de 5° , 10° et 20° , a été calculé par la méthode d'analyse numérique de BABENKO ; le calcul à $i = 20^\circ$ a été interrompu à mi-longueur du corps par un défaut de convergence de calcul.

Une série d'essais en soufflerie a permis de comparer les formes des ondes de choc, les répartitions de pressions, les répartitions de flux thermiques, et les formes des lignes de courant pariétales avec les résultats du calcul théorique.

*On trouvera dans la réf. [6] le détail de la mise en oeuvre de la méthode des peintures thermocolorées, telle qu'elle est appliquée à l'O.N.E.R.A.

Cette comparaison a montré que la méthode de calcul prévoit avec une excellente précision les répartitions de pressions aux incidences telles que n'existent pas de décollements à l'extrados ; aux incidences plus élevées les prévisions théoriques sont erronées sur la partie supérieure mais néanmoins exactes sur la partie inférieure du corps.

Les flux thermiques mesurés s'écartent également de ceux calculés dans l'hypothèse d'une couche limite laminaire, non seulement dans la partie supérieure du corps où le champ réel est différent du champ théorique, mais encore sur l'ensemble du corps, en exceptant la partie inférieure où l'écart n'est plus que de 10% environ ; les écarts constatés ne permettent cependant pas de mettre en doute l'hypothèse de laminarité.

Par contre la visualisation des lignes de courant pariétales, par deux méthodes différentes, a mis en évidence que ces lignes ont des composantes transversales beaucoup plus importantes que les lignes calculées, ce qui expliquerait l'échec relatif des calculs d'échauffement effectués par intégration le long de ces dernières.

Des mesures de pression d'arrêt sont actuellement en cours entre le corps et l'onde de choc en vue de comparer avec plus de détails le champ réel et le champ théorique fourni par la méthode de BABENKO.

LISTE DES REFERENCES

- [1] P. DIRINGER Calcul d'écoulements supersoniques autour de corps de révolution
P. LAVAL ou de profils, avec ou sans incidence, par la méthode des caractéristiques.
N.T. O.N.E.R.A. à paraître.
- [2] K.I. BABENKO Ecoulement à trois dimensions d'un gaz parfait autour d'un corps régulier.
et al. Editions NAOUKA - Moscou (1964).
- [3] R. GONDOU Ecoulements supersoniques autour de cônes en incidence.
Rech. Aér. n° 120 (1967).
- [4] O.M. BIELOTSEKOVSKIY Calcul de l'écoulement autour du corps de révolution avec onde
de choc détachée.
Centre de Calcul de l'Académie des Sciences de l'U.R.S.S. - Moscou (1961).
- [5] R. MICHEL Flux de chaleur au bord d'attaque d'une aile à forte flèche en hypersonique.
DUONG VINH HUNG T.P. O.N.E.R.A. n° 116 (1966).
- [6] R. CERESUELA Mesures de flux thermiques en hypersonique.
A. BETREMIEUX T.P. O.N.E.R.A. n° 293 (1965).
- [7] B.J. GRIFFITH Laminar heat transfer to spherically blunted cones at hypersonic conditions.
A.I.A.A. Journal, Vol. 2, N° 3 - March 1964.
- [8] E.A. EICHELEBENNER Méthode de calcul de la couche limite tridimensionnelle.
A. OUDART Publication O.N.E.R.A. n° 76 (1955).

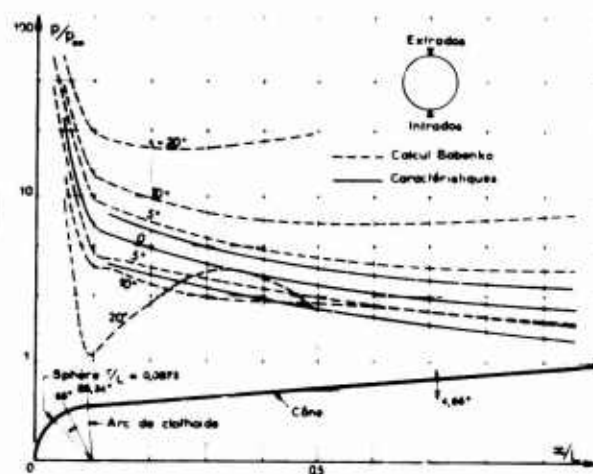
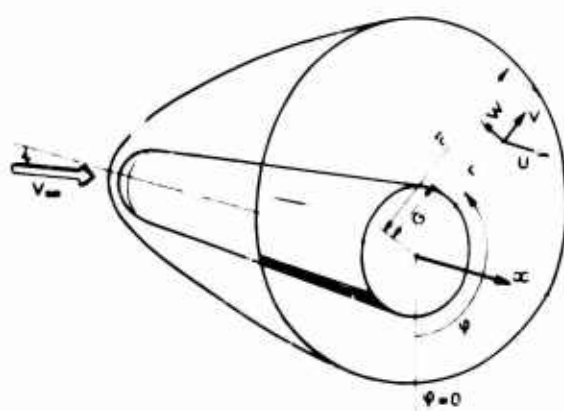


Fig. 1 - Notations géométriques du calcul numérique de BABENKO

Fig. 2 - Répartition des pressions théoriques sur les génératrices supérieure et inférieure

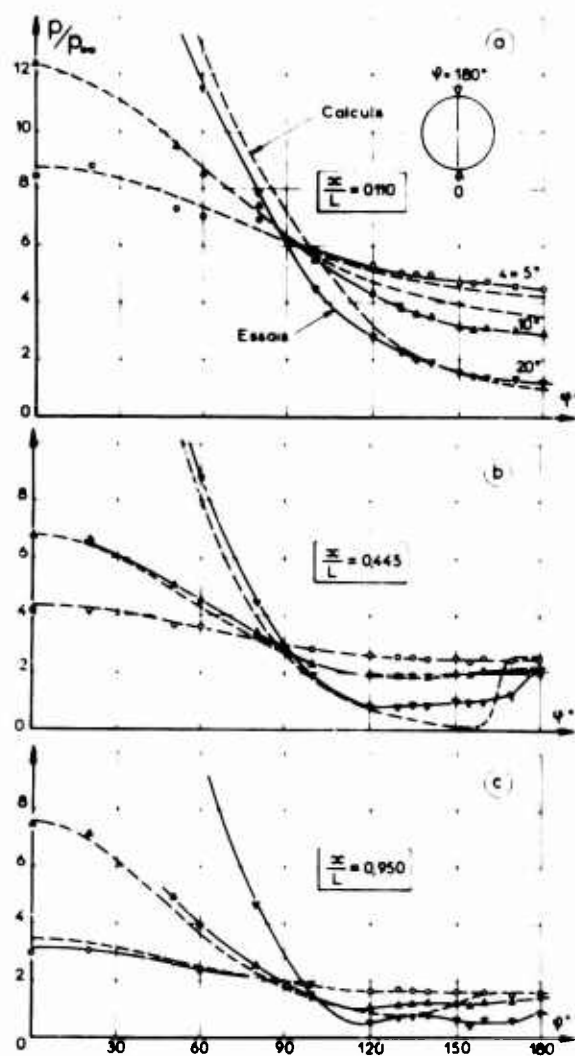
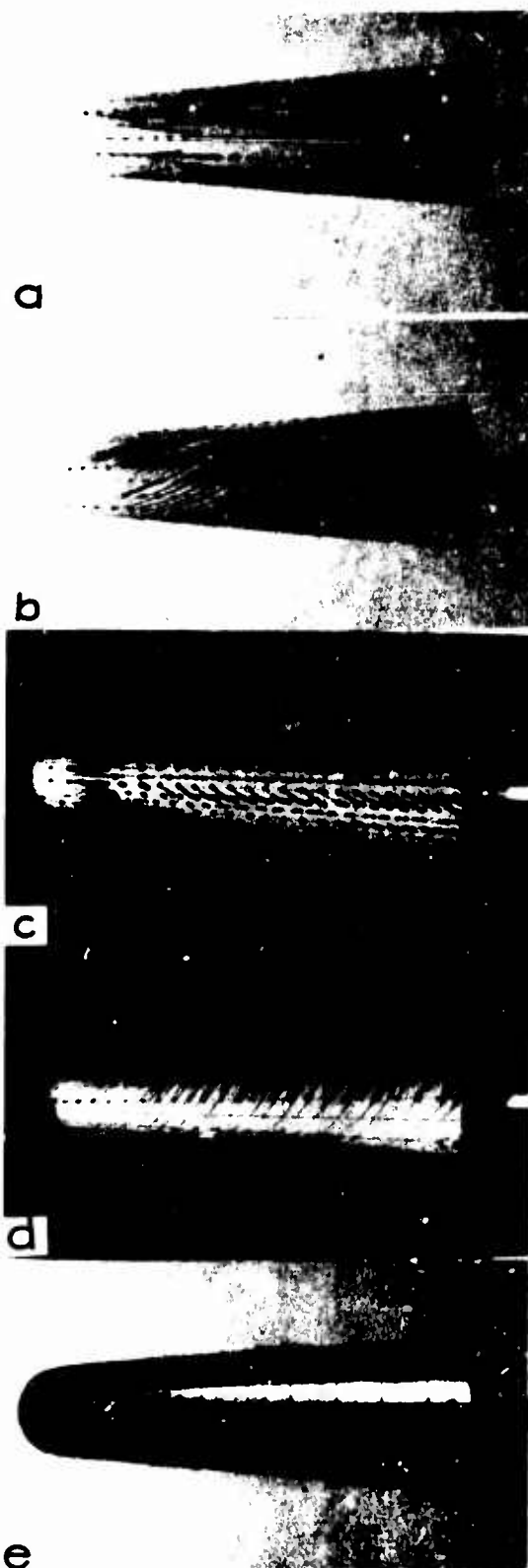


Fig. 3 - Répartitions de pressions calculées et mesurées dans des plans normaux à l'axe.

Fig. 4 - Visualisation de l'écoulement pariétal



- Méthode de l'enduit plastique

a) $i = 10^\circ$, vue de dessus

b) $i = 10^\circ$, vue de profil

c) $i = 20^\circ$, vue de dessus

d) $i = 20^\circ$, vue de profil

- Méthode des sillages sur peinture thermovirante

e) $i = 10^\circ$, vue de profil



Fig. 5 - Forme de l'onde de choc à Mach 10.

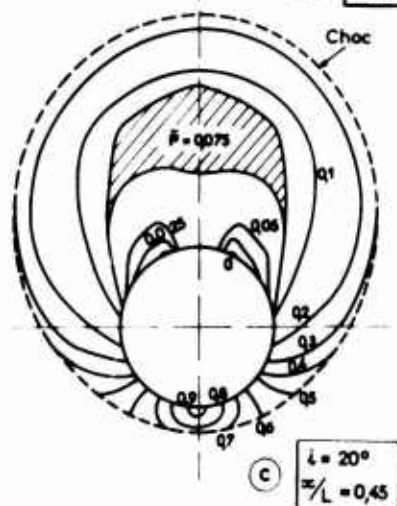
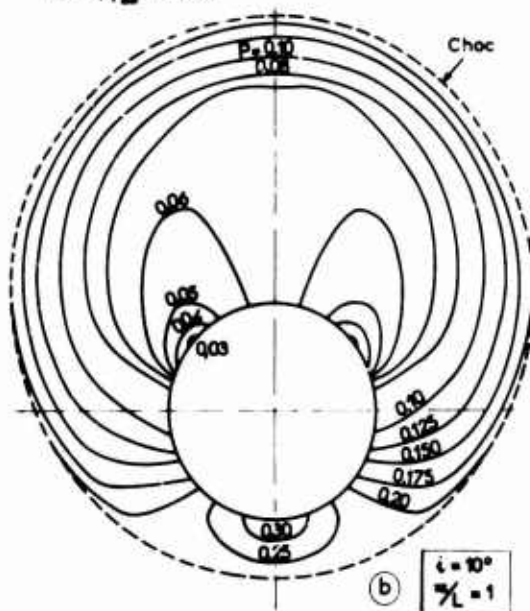
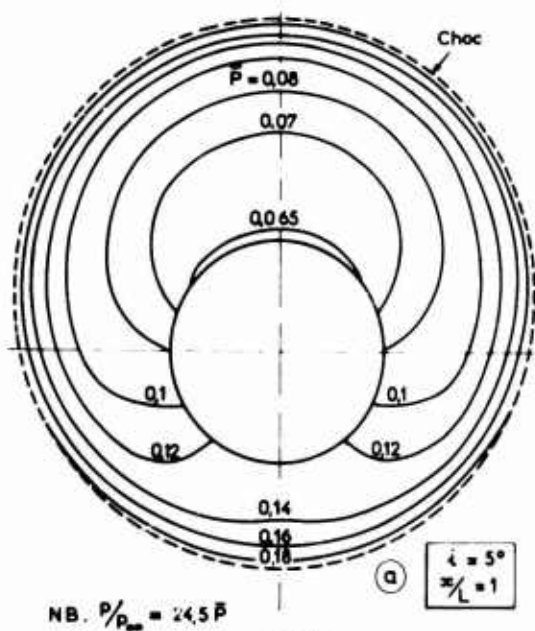


Fig. 6 - Section de l'onde de choc et tracé des courbes isobares dans des plans normaux à l'axe
a) $i = 5^\circ$ $x/L = 1$
b) $i = 10^\circ$ $x/L = 1$
c) $i = 20^\circ$ $x/L = 0.45$

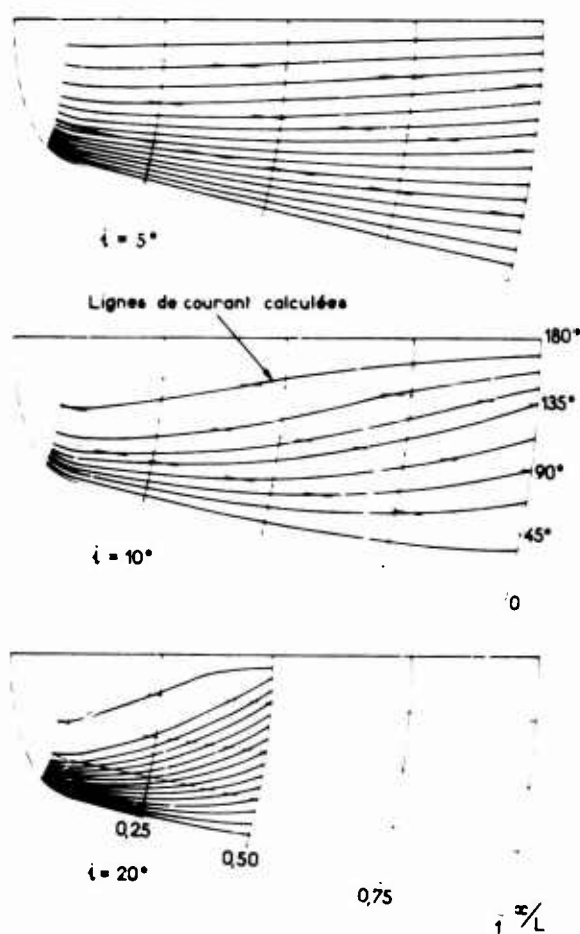


Fig. 7 - Tracé des lignes de courant pariétales calculées.

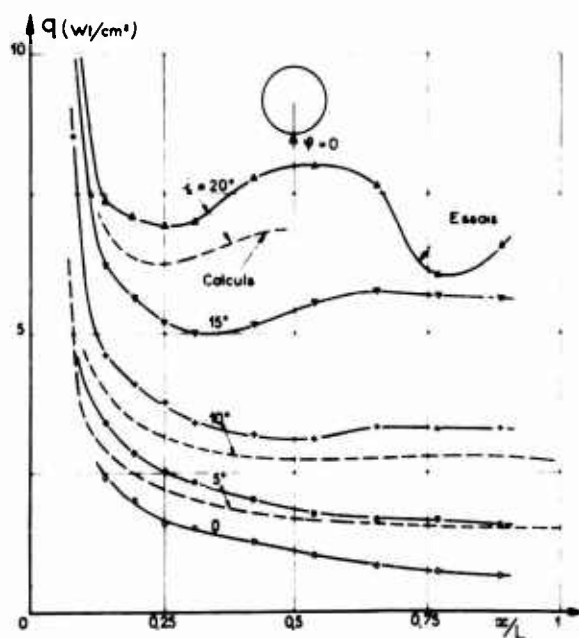


Fig. 8 - Flux thermiques mesurés et calculés sur la génératrice inférieure.

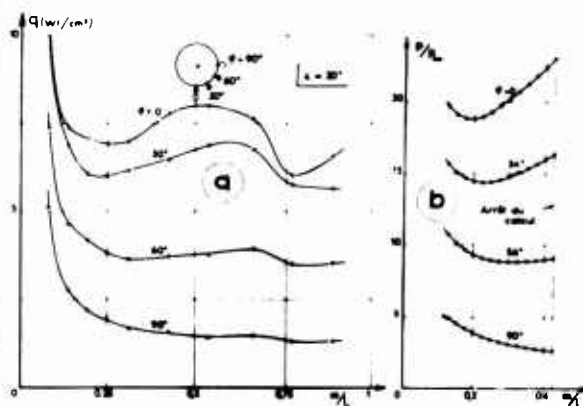
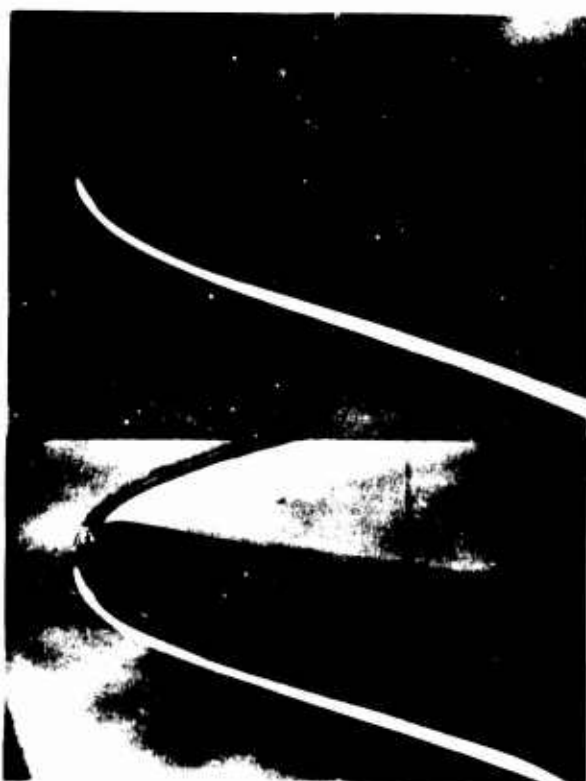


Fig. 10 - Evolution des flux et pressions mesurés à $i = 20^\circ$ sur le flanc inférieur du corps

- a) flux
- b) pressions

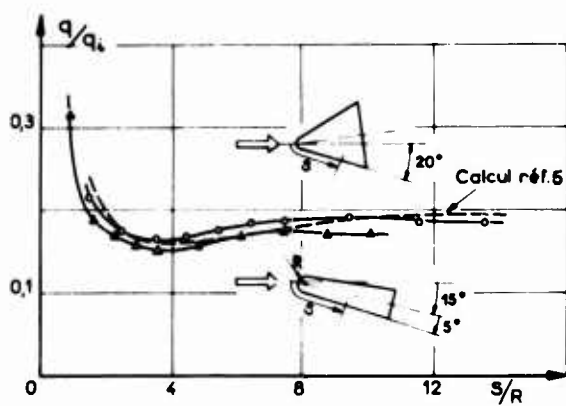


Fig. 9 - Comparaison des flux thermiques mesurés sur la génératrice inférieure à $i = 15^\circ$, et au bord d'attaque d'une aile en flèche de 70° ($\delta = 75^\circ$ en dérapage de 5°).

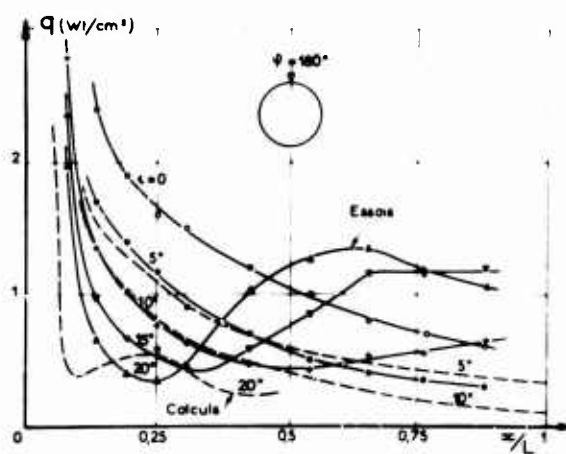


Fig. 11 - Distribution des flux thermiques mesurés sur la génératrice supérieure.

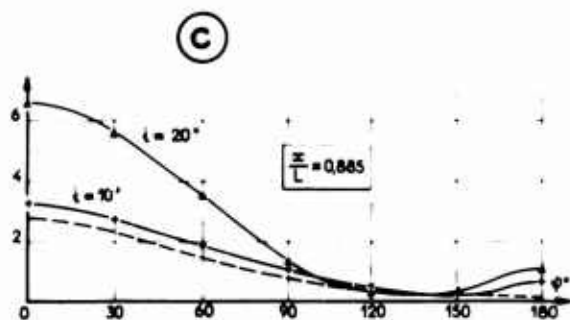
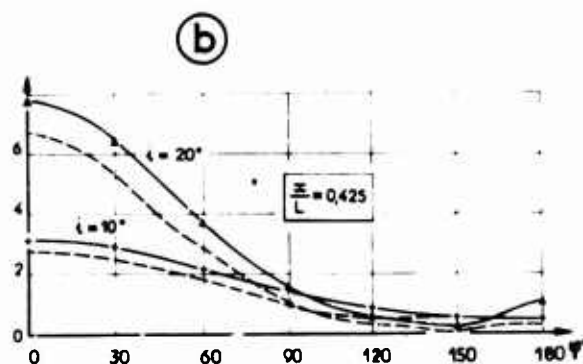
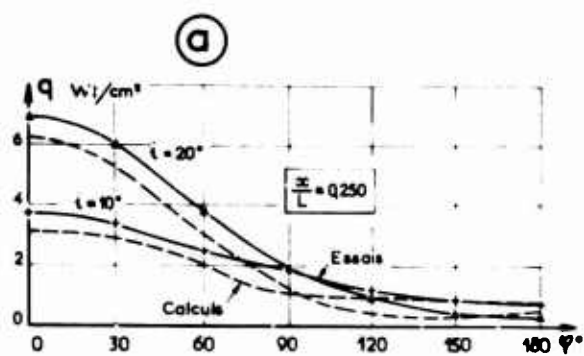


Fig. 12 - Distribution des flux thermiques calculés et mesurés le long des méridiennes :

- a) $x/L = 0,250$
- b) $x/L = 0,425$
- c) $x/L = 0,885$

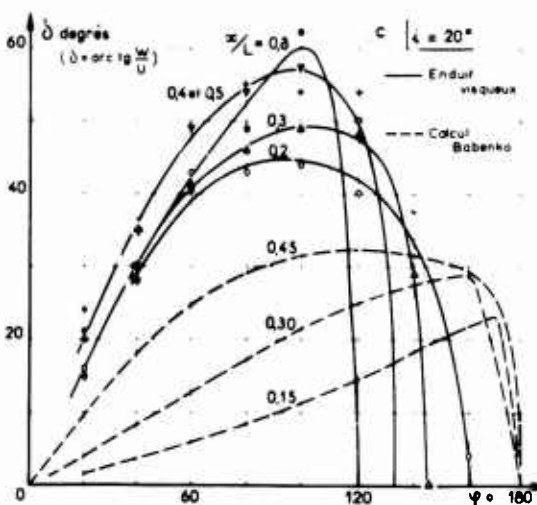
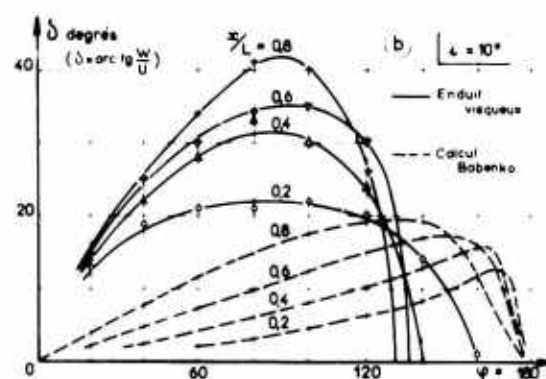
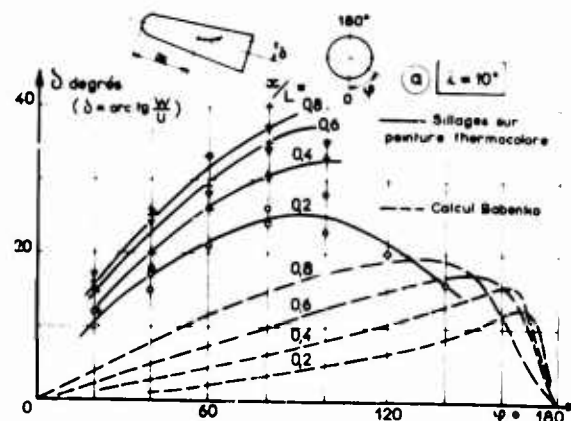


Fig. 13 - Angles des lignes de courant à la paroi, calculés et mesurés :

- a) méthode des sillages $i = 10^\circ$,
- b) méthode de l'enduit plastique $i = 10^\circ$,
- c) méthode de l'enduit plastique $i = 20^\circ$.

ETUDE DE L'ECOULEMENT SUPERSONIQUE & HYPERSONIQUE

AUTOUR D'UNE AILE ELANCEE EN INCIDENCE

par Bernard MONNERIE (*)

Henri MERLE (**)

O.N.E.R.A. (France)

(*) Ingénieur de Recherche - Chef de Groupe

(**) Ingénieur de Recherche - Chef de Groupe

RESUME

L'étude du champ aérodynamique autour d'une aile de 75° de flèche à bord d'attaque aigu a été effectuée à des nombres de Mach M_0 égaux à 1,9 - 4 et 7 qui correspondent à des valeurs du nombre de Mach M_n normal au bord d'attaque respectivement subsonique, sonique et supersonique.

L'analyse des résultats obtenus par visualisation et sondage de pression d'arrêt permet de présenter une description schématique de l'écoulement à l'extrados de l'aile, et notamment des zones de décollement.

ABSTRACT

The study of the aerodynamic field around a 75° degree-sweepback wing with sharp leading edge has been carried out at Mach numbers 1.9 - 4 and 7, which correspond to values of the Mach number M_n , normal to the leading edge, respectively subsonic, sonic and supersonic.

The analysis of the results obtained by visualization and surveys of the total pressure leads to the presentation of a schematic description of the flow on the upper surface of the wing, and in particular of the separated zones.

1 - INTRODUCTION

L'étude de l'écoulement autour d'une aile élancée, dans un domaine étendu d'incidences et de nombres de Mach constitue le point de départ de recherches plus générales consacrées par la Direction Aérodynamique de l'ONERA aux problèmes du décollement et du recollement tridimensionnel ; les résultats préliminaires, présentés dans cette communication, ont été obtenus avec un modèle expérimental unique (aile delta élancée) et donnent essentiellement une analyse détaillée du champ aérodynamique en fonction du nombre de Mach et de l'incidence.

Ces phénomènes intéressent :

- soit la région du bord d'attaque où des effets marqués, enregistrés en écoulement incompressible se retrouvent en écoulement supersonique lorsque le nombre de Mach normal au bord d'attaque est subsonique,
- soit le voisinage du bord de fuite (confluence des écoulements d'extrados et d'intrados),
- soit enfin, un domaine intérieur à l'aile lorsqu'il y a interaction entre la couche limite de l'aile et une onde de choc issue de l'apex.

Les résultats présentés ici ont été obtenus à des nombres de Mach variant assez largement depuis des valeurs supersoniques modérées ($Mo = 1,95$, aile à bord d'attaque subsonique) jusqu'à des valeurs hypersoniques ($Mo = 7$, aile à bord d'attaque supersonique).

2 - TECHNIQUES EXPERIMENTALES ET CONDITIONS D'ESSAIS

2.1 - Installations d'essais

Etant donné le large domaine de nombres de Mach impliqué par cette étude, il a été nécessaire d'utiliser plusieurs souffleries [1]. Celles-ci sont répertoriées avec leurs principales caractéristiques dans le tableau ci-contre.

A ces installations, il y a lieu d'ajouter le tunnel hydrodynamique de l'ONERA qui a fourni les éléments de comparaison avec l'incompressible ($V_0 = 20 \text{ cm/s}$ - Reynolds $= 4.10^4$).

Soufflerie	Type	Mach	P. bar	T. °K	Corde maquette l mm	Re_l
S ₀	continu	1,95	1	288	70	$0,95 \cdot 10^6$
R ₁	rafale 30 s	1,90	2,5	330	90	$2,5 \cdot 10^6$
GR ₀	rafale 60 s	4	5	310	70	$1,5 \cdot 10^6$
R ₂	rafale 30 s	7	65	600	150	$4,5 \cdot 10^6$

2.2 - Maquettes et montages

Les maquettes étudiées sont des ailes delta de 75° de flèche à bord d'attaque aigu (fig. 1). Elles sont tenues en veine par un support conçu de façon à laisser dégagée la face plane qui constitue l'extrados de l'aile et à réduire les interactions dans ce domaine. Néanmoins lorsque l'incidence croît, le support crée de petites perturbations visibles à la striescopie, toutefois assez faibles pour ne pas modifier sensiblement la conicité de l'écoulement d'extrados.

2.3 - Moyens d'étude

Pour cette étude consacrée à une description qualitative de l'écoulement, les techniques de visualisation ont été largement employées.

Quelques sondages de pression ont cependant été effectués pour tenter d'obtenir des informations plus détaillées sur la structure de l'écoulement dans un plan transversal normal à l'aile.

2.3.1 - Visualisations striescopiques

La striescopie classique à simple traversée a été utilisée systématiquement dans toutes les souffleries avec une source lumineuse continue. En outre, à la soufflerie R₁, une source éclair a permis d'obtenir des temps d'exposition très courts, de l'ordre de la microseconde. L'axe d'observation est soit normal, soit parallèle au plan de symétrie de l'aile et la position des crouteaux parallèle à la direction de la vitesse amont.

2.3.2 - Interférométrie holographique

Dans le but de préciser l'allure du champ aérodynamique une technique d'interférométrie holographique mise au point par la Direction de la Physique de l'ONERA [2] a également été employée. Celle-ci consiste à superposer sur la même plaque photographique deux hologrammes de la veine d'expérience, l'un pris en cours d'essai et l'autre au repos.

A la restitution du double hologramme, on observe un tableau de franges identique à celui qu'on aurait obtenu avec un interféromètre à deux ondes, équipement volumineux et onéreux par rapport au montage optique très simple, nécessaire pour réaliser les hologrammes (fig. 2).

2.3.3 - Visualisations pariétales

Elles ont été effectuées en déposant sur la maquette peinte en blanc, un réseau de petites taches d'huile silicone colorée. Lorsque l'écoulement est établi, les particules liquides se déplacent sous l'action du courant d'air et dessinent sur fond blanc, les lignes de courant pariétales.

2.3.4 - Etude thermocolor

En hypersonique, des précisions supplémentaires sur la structure de l'écoulement ont été acquises grâce à l'emploi d'une peinture thermocolor dont le changement de teinte permet de mettre en évidence les zones où le flux thermique pariétal est maximum [3].

Une maquette spéciale, comportant à l'extrados d'un logement parallélépipédique de 5 mm de profondeur rempli d'un matériau plastique isolant (silastène) a été réalisée pour cet essai.

2.3.5 - Sondage de pression

Des explorations au tube de pitot ont été effectuées pour tous les nombres de Mach d'essai dans un plan transversal normal à l'aile situé à environ 80 % de la profondeur, la sonde étant maintenue parallèle à l'axe de l'aile.

Par suite de l'importance des incidences locales de l'écoulement par rapport à la direction de la sonde, l'exploitation des résultats obtenus ne fournit qu'une première approximation du champ des pressions d'arrêt. L'exploration de l'écoulement avec une sonde de pression statique beaucoup plus sensible à l'effet d'incidence que la sonde de pression d'arrêt, ne pouvant donner qu'une très vague représentation du champ réel, a de ce fait été écartée.

Parmi les difficultés expérimentales rencontrées, la plus importante concerne l'interaction de la sonde et de son support avec le champ de l'aile, notamment lorsque l'incidence est élevée. Ce problème a été en partie résolu en éloignant le plus possible du bord de fuite, le support de l'explorateur. Toutefois, dans certains cas et notamment en écoulement hypersonique, la présence de la sonde a pu altérer la structure des domaines décollés, sans modifier profondément l'allure des phénomènes.

3 - ANALYSE DES RESULTATS EXPERIMENTAUX

3.1 - Etude de l'écoulement à des nombres de Mach modérés ($M_0 = 1.95$, bord d'attaque du type subsonique)

3.1.1 - La description du champ aérodynamique à l'extrados de l'aile est présentée tout d'abord dans le cas où le nombre de Mach normal M_n au bord d'attaque est subsonique ($M_n = 0,5$ pour $M_0 = 1,95$).

L'analyse de l'écoulement à l'extrados de l'aile a été effectuée pour des incidences i comprises entre 0 et 30°. Lorsque i croît à partir de la valeur 0, la structure de l'écoulement, symétrique par rapport au plan médian de l'aile, subit une évolution continue :

3.1.2 - Au voisinage de $i = 0$, l'écoulement pariétal d'extrados est très sensiblement parallèle au plan de symétrie sur la majeure partie de l'aile ; on décèle toutefois des perturbations intéressant le voisinage immédiat du bord d'attaque qui correspondent à un décollement transversalement peu étendu.

3.1.3 - Ce décollement de bord d'attaque devient très visible lorsque l'incidence atteint 5°. Dans un premier temps, (incidence comprise entre 5° et 17° env.) il se développe de façon régulière en conservant une organisation dont l'analyse peut être faite à partir des éléments présentés fig. 3, pour une incidence de 10°.

La structure tourbillonnaire du décollement est mise en évidence aussi bien par le sondage des pressions d'arrêt (fig. 3C) que par la visualisation stroboscopique à étincelle (fig. 3A) et l'observation des lignes de courant pariétales (fig. 3B).

La comparaison avec les résultats obtenus en écoulement incompressible au tunnel hydrodynamique pour des plans d'observations identiques (fig. 4), révèle une similitude totale dans la structure tourbillonnaire de ces deux écoulements ($M_0 = 0$ et $M_0 = 1,95$).

Cette structure dont une représentation perspective est donnée par la fig. 7 peut être décrite de la façon suivante, en s'appuyant sur des études détaillées, effectuées antérieurement au tunnel hydrodynamique [4 et 5] :

- la nappe de courant venant de l'intrados et se détachant du bord d'attaque, s'enroule en cornet [6] pour constituer l'ossature du tourbillon principal (1) ;
- une seconde nappe aboutit sur l'aile suivant la ligne de recollement (M) et constitue la frontière extérieure entre le domaine tourbillonnaire et l'écoulement sain sensiblement radial sur la partie centrale de l'aile (3) ;
- les lignes de courant qui forment cette seconde nappe longent la paroi en (4), suivant des trajectoires très déviées par rapport à la direction de référence Ox et décollent en (5) pour former l'ossature d'un tourbillon secondaire (2) moins intense que le premier et de sens opposé ;
- le fluide circulant entre ces deux nappes, alimente les deux tourbillons : le partage des débits d'alimentation s'effectue le long de (M). Lorsque l'incidence i augmente, l'étendue transversale de ce domaine tourbillonnaire croît et corrélativement, la région (3) diminue, elle disparaît lorsque i atteint une valeur de l'ordre de 17° .

3.1.4 - On obtient alors la configuration dite de tourbillons rejoins dont les principales caractéristiques sont présentées pour $i = 25^\circ$ fig. 5 à $M_0 = 1,95$ et fig. 6 en écoulement incompressible ; l'organisation correspondante de la zone tourbillonnaire est analogue à celle de la figure 7 mais le domaine (3) a disparu et la ligne (M) est confondue avec l'axe ainsi que le montre la figure 8.

On remarquera qu'en écoulement supersonique la trace (A), dans le plan de symétrie de l'aile, d'une onde de choc apparaît sur les clichés strioscopiques.

Cette onde de choc est engendrée par la déviation brutale que doit subir l'écoulement pour retrouver une direction parallèle à la paroi. Cette déviation a été mise en évidence par une méthode de perturbation à l'aide d'une sonde aplatie de petites dimensions dont la section droite est un dièdre de faible ouverture. Lorsque l'axe de la sonde est orienté suivant une direction voisine de la tangente à la ligne de courant locale, la strioscopie permet de visualiser un système d'ondes de choc quasi symétrique à partir duquel il est possible d'obtenir la direction de l'écoulement au point considéré. Les résultats obtenus lors de sondages effectués dans le plan de symétrie de l'aile à une distance $X_0/L = 0,75$ du bord d'attaque, sont présentés figure 9. On notera l'inclinaison importante des vitesses locales, par rapport à la vitesse amont (60°) et par rapport à l'aile (35°).

3.1.5 - Evolution de la position des axes des tourbillons avec l'incidence

Compte tenu de l'analogie existant dans l'organisation du domaine tourbillonnaire à $M_0 = 0$ et $M_0 = 1,95$, il a paru intéressant de comparer les positions respectives des traces du tourbillon principal dans un plan transversal normal à l'aile et leur évolution en fonction de l'incidence. La détermination précise des axes T et T' des tourbillons est obtenue en écoulement incompressible à partir des photographies de visualisations fines par émission colorée et par bulles d'air (fig. 4 et 5).

En écoulement supersonique, les différentes techniques utilisées (strioscopie, interférométrie, sondages de pression) conduisent à l'excellent recoupement présenté fig. 11.

Il est intéressant de remarquer, que l'exploitation des clichés interférométriques et strioscopiques permet d'obtenir rapidement et continuellement la projection commune (t) de T et T' sur le plan de symétrie de l'aile.

Compte tenu des dépressions dont ils sont le siège, T et T' correspondent à un minimum de densité locale ($\partial\rho/\partial z = 0$) qui se traduit en interférométrie par une cassure en V dans le tableau de franges serrées présenté fig. 12.

En strioscopie, la condition $\partial\rho/\partial z = 0$ le long de T et T' entraîne que le taux de noircissement local du cliché sur (t) est identique à celui que l'on trouve dans la partie uniforme de l'écoulement.

Le dépouillement des striogrammes au microdensitomètre (fig. 11) a permis de définir cette ligne avec précision.

La figure 14, montre également que (t) est très sensiblement rectiligne, ce qui confirme la conicité de l'écoulement tourbillonnaire au régime supersonique étudié. Il est alors possible de

repérer la position du tourbillon par l'angle α_1 de (t) avec l'axe de l'aile. L'évolution $\alpha_1 = f(i)$ est donnée fig. 15. Sur la même figure est également portée la courbe $\alpha_2(i)$ représentant les variations de l'inclinaison sur l'aile du choc (A) qui se produit à l'extrados à grande incidence.

L'évolution avec l'incidence des traces de T et T' dans un plan transversal normal à l'aile ainsi déterminées aussi bien en écoulement incompressible qu'en écoulement supersonique à $M_0 = 1,95$, est comparée figures 16 et 17 d'une part aux prévisions théoriques existantes [7 à 12], d'autre part à différents résultats expérimentaux obtenus pour des conditions d'essais voisines [13 à 15].

Les expériences mettent en évidence, une évolution des traces de T et T' dans le plan Z Y beaucoup plus marquée à $M_0 = 1,95$ que celle qui est obtenue en incompressible.

Dans un premier temps, T et T' s'éloignent de l'aile en se rapprochant du plan de symétrie (S) ; lorsque la configuration dite des tourbillons rejoins est obtenue, T et T' tout en continuant à s'éloigner de l'aile s'écartent alors de S.

Ce phénomène n'est prévu que par la théorie proposée par PERSHING [10].

Une étude systématique de l'influence du nombre de Reynolds sur cette évolution n'a pas été entreprise jusqu'à présent. Toutefois, compte tenu des résultats actuellement disponibles, il ne semble pas qu'une augmentation sensible du nombre de Reynolds d'essai modifie beaucoup l'évolution indiquée figure 16.

3.1.6 - Remarque

Dans la gamme d'incidences étudiées de 0 à 30°, l'écoulement d'extrados reste sensiblement conique jusqu'au bord de fuite. Le domaine d'interaction lié à la confluence des écoulements d'intrados et d'extrados est limité à une zone étroite au voisinage du bord de fuite. Le développement de ce domaine d'interaction, qui survient lorsque l'incidence croît au delà de $i = 30^\circ$, ne sera pas examiné dans cette communication.

3.2 - Etude de l'écoulement en supersonique élevé ($M_0 = 4$) et en hypersonique ($M_0 = 7$)

3.2.1 - Généralités

L'étude effectuée à $M_0 = 1,95$ dans un cas où le nombre de Mach normal au bord d'attaque est nettement subsonique ($M_n \sim 0,5$) a clairement mis en évidence un décollement de bord d'attaque générateur d'un système tourbillonnaire bien organisé jusqu'à des incidences élevées ($i \sim 30$ à 35°) intéressant une partie importante de l'écoulement.

Nous allons maintenant examiner comment peuvent être modifiées la situation et l'organisation de ce décollement lorsque le nombre de Mach augmente jusqu'à des valeurs hypersoniques.

Les expériences présentées dans cette communication ont été effectuées à deux valeurs du nombre de Mach $M_0 = 4$ (bord d'attaque sonique $M_n = 1,03$) et $M_0 = 7$ (bord d'attaque supersonique $M_n = 1,81$).

Avant de commenter les résultats obtenus, il convient de préciser que le profil en épaisseur de la maquette comporte au bord d'attaque un dièdre de 15 ou 20° qui ne permet pas d'obtenir dans le domaine de nombre de Mach étudié une configuration de choc attaché, même lorsque l'incidence est modérée (fig. 18 B et 19 B).

Dans ces conditions, une interaction entre les écoulements d'extrados et d'intrados de l'aile est possible par le bord d'attaque, bien que ces configurations soient dites "à bord d'attaque supersonique" au sens de la théorie linéarisée.

3.2.2 - Etude de l'écoulement à $M_0 = 4$

Les différentes techniques de visualisation (fig. 18 et 20) ainsi que les sondages de pression d'arrêt (fig. 22) mettent en évidence l'existence d'un décollement à l'extrados de l'aile qui prend naissance dès le bord d'attaque et s'étend au fur et à mesure que l'incidence augmente.

La zone tourbillonnaire de faible épaisseur ainsi créée (zone blanche du cliché strioscopique fig. 18 A), est limitée latéralement par une ligne de recollement sensiblement droite et issue de l'apex, qui constitue une frontière d'accumulation pour les lignes de courant pariétales qui la bordent (fig. 20).

Dans la partie centrale de l'aile où la couche limite est mince, ces lignes de courant sont bien dessinées et prennent une forte courbure lorsque l'incidence i atteint une valeur de l'ordre de 10° ; cette tendance résulte de la recompression importante qui se produit dans cette région et peut être observée à l'occasion du sondage des pressions d'arrêt (Fig. 22). Cette recompression est confirmée par l'évolution très marquée des pressions statiques à la paroi (Fig. 24) depuis un niveau élevé

sur l'axe jusqu'à des valeurs faibles dans la zone décollée sensiblement isobare.

L'exploration détaillée de ce dernier domaine, rendue difficile par le faible niveau des pressions et les perturbations apportées par la sonde d'arrêt ne permet pas toutefois d'affirmer l'existence d'une organisation tourbillonnaire aussi caractérisée qu'à $M_0 = 1,9$ (fig. 18 C). Par suite de l'épaisseur relativement mince de ce décollement, les effets visqueux deviennent prépondérants et la faible inclinaison sur l'axe des lignes de courant pariétales fournit un indice supplémentaire de la rotation peu intense qui l'anime.

Cette organisation se conserve jusqu'à des valeurs de i comprises entre 10 et 15° ; l'effet de l'incidence se traduit :

- 1) par une ouverture progressive de l'onde de choc conique issue de l'apex.
- 2) par une évolution lente de la ligne de recollement vers le plan de symétrie.
- 3) par un élargissement du domaine d'interaction lié à la recompression importante dont la zone de recollement est le siège (courbure des lignes de courant pariétales fig. 20 A B C au voisinage de la ligne de recollement).

Lorsque i atteint et dépasse 15° , l'onde de choc produite par la confluence des écoulements d'intrados et d'extrados au bord de fuite provoque à l'arrière de l'aile une modification profonde de la structure du décollement dont l'épaisseur croît de façon notable ; cette désorganisation progresse rapidement vers l'amont lorsque l'incidence augmente (Fig. 20 C et D).

3.2.3 - Etude de l'écoulement à $M_0 = 7$

Une aile de 75° de flèche possède à $M_0 = 7$ un bord d'attaque B supersonique. Lorsque le dièdre qui constitue B est suffisamment aigu et l'incidence assez faible, l'écoulement est recomprimé à l'intrados par une onde de choc attachée au bord d'attaque.

A l'extrados, peuvent être alors distingués :

- 1) un domaine uniforme correspondant à une détente autour de B qui provoque une déviation de l'écoulement vers le plan de symétrie S de l'aile.
- 2) un second domaine où l'écoulement reprend une direction parallèle à S.

Les deux domaines sont séparés par une ligne droite issue de l'apex qui est la trace d'une onde de choc normale à l'aile dont l'interaction avec la couche limite peut donner lieu à des phénomènes très importants, notamment lorsque celle-ci est laminaire.

Dans le cas étudié (dièdre de 20°), il n'existe pas de choc attaché le long de B ; malgré cela pour les petites incidences ($i \leq 5^\circ$), la configuration de l'écoulement est très voisine de celle qui vient d'être discutée ; en particulier, contrairement à ce qui se produisait à $M_0 = 4$, l'écoulement reste attaché à l'aile au voisinage de B. Lorsque l'incidence dépasse 5° , l'intensité de l'onde de choc normale à l'aile est suffisante pour provoquer un décollement local de la couche limite. Ce décollement D s'étend rapidement vers le bord d'attaque, plus lentement vers le plan de symétrie et, en même temps, la distance de détachement du choc conique extérieur augmente.

La structure de D présente une grande analogie avec celle qui a été rencontrée lors de l'étude de l'aile à $M_0 = 4$ bien que son apparition soit localisée en un point différent. En particulier :

- a) la zone décollée est très aplatie sur l'aile et faiblement tourbillonnaire (fig. 19-21) ;
- b) elle est limitée au centre par une portion d'écoulement recollé, à forte pression (fig. 23 et 24) particulièrement bien mise en évidence par l'utilisation d'une peinture thermosensible (fig. 25) qui détecte les zones (claires sur la figure) où le flux thermique est maximum
- c) l'interaction au bord de fuite des écoulements d'intrados et d'extrados est considérable lorsque l'incidence est élevée. A $i = 10^\circ$ par exemple (fig. 21 B) la perturbation de bord de fuite est déjà très sensible ; à $i = 20^\circ$, l'écoulement à l'extrados de l'aile est complètement désorganisé.

3.2.4 - Remarque

Dans cette étude préliminaire, l'influence du nombre de Reynolds sur l'évolution de ces phénomènes n'a pas été examinée ; il est vraisemblable qu'elle est importante compte tenu du rôle très grand que peut jouer la viscosité dans un domaine proche de la paroi notamment dans les problèmes d'interaction couche limite-onde de choc.

Cette influence peut, en particulier, être déterminante sur les conditions de passage de la configuration avec décollement le bord d'attaque à la configuration avec décollement sur l'aile. Le nombre de Mach normal au bord d'attaque B proposé réf. [19] pour caractériser ce passage est

vraisemblablement insuffisant. Toutefois, les résultats obtenus sont sensiblement en accord avec la courbe empirique de la réf. 19 pourvu que les incidences normales à B soient comptées par rapport à l'intrados du profil de l'aile.

4 - CONCLUSION

L'étude de l'écoulement à l'extrados d'une aile delta de 75° de flèche à bord d'attaque aigu, dans le domaine supersonique et hypersonique a montré que :

- 1°) A $M_0 = 1,9$ l'organisation de l'écoulement est très voisine de celle observée en incompressible : l'écoulement décolle au bord d'attaque et vient former un tourbillon très structuré et très intense.
- 2°) A $M_0 = 4$ la séparation se produit toujours au bord d'attaque, mais le nombre de Mach étant plus élevé, la zone décollée est aplatie sur l'aile et l'intensité tourbillonnaire est réduite par la viscosité.
- 3°) A $M_0 = 7$ l'écoulement reste attaché dans la région voisine du bord d'attaque, tout au moins aux incidences modérées, mais il décolle sur l'aile pour donner naissance à une zone tourbillonnaire de faible intensité très analogue à celle observée à Mach 4.

Ces configurations d'écoulement se conservent jusqu'à des incidences d'autant plus élevées que le nombre de Mach est plus faible (environ 30° à $M_0 = 1,9$, 12° à $M_0 = 4$ et 7° à $M_0 = 7$).

Au delà de ces incidences, les recompressions importantes qui se produisent dans la région du bord de fuite provoquent une désorganisation du décollement qui gagne la totalité de l'extrados de l'aile lorsque l'incidence croît.

° °
°

- REFERENCES -

- [1] - P. REBUFFET - J.D. VAGNER & J.P. CHEVALLIER
Souffleries hypersoniques de recherches de Chalais-Meudon
O.N.E.R.A. N.T. n° 83 (1965).
- [2] - M. PHILBERT & J. SURGET
Application de l'interférométrie holographique en soufflerie
Rech. Aér. n° 122 (1968).
- [3] - J. PONTEZIERE & A. BETREMIEUX
Méthode de mesures des flux thermiques pariétaux par peinture thermosensible
Communication à l'ATMA (Session 1967).
- [4] - H. WERLE
Méthodes d'étude, par analogie hydraulique, des écoulements subsoniques, supersoniques et hypersoniques.
AGARD Rapport 399 (Octobre 1960).
- [5] - H. WERLE
Etude physique des phénomènes tourbillonnaires au tunnel hydrodynamique.
Communication à l'ATMA (Session 1961).
- [6] - M. ROY
Sur la théorie de l'aile delta. Tourbillons d'apex et nappes en cornet.
Rech. Aér. n° 56 (1957).
- [7] - R. LEGENDRE
Ecoulement au voisinage de la pointe avant d'une aile à forte flèche aux incidences moyennes.
Rech. Aér. n° 30 (1952) et 31 (1953).

- [8] - C. BROWN & W. MICHAEL
On slender delta wings with leading-edge separation
NACA Report TN 3430 (April 1955).
- [9] - K.W. MANGLER & J.H.B. SMITH
Calculation of the flow past slender delta wings with leading-edge separation.
R.A.E. Rep. Aéro. 2593 (May 1957).
- [10] - B. PERSHING
Separated flow past slender delta wings with secondary vortex simulation.
Report TDR 269 (4560-10) - 4 (August 1964).
- [11] - J.H.B. SMITH
Improved calculations of leading-edge separation from slender delta wings.
R.A.E. Techn. Rep. n° 66 070 (Mars 1966).
- [12] - E. CARAFOLI & St. STAIU
Sur un modèle théorique concernant l'aile delta mince avec décollement aux bords d'attaque.
Journal de Mécanique - vol. 6 n° 2 (Juin 1967).
- [13] - J. BERGESEN & J. PORTER
An investigation of the flow around slender delta wings
with leading-edge separation.
Off. Nav. Res. Princeton Univ. Report 510 (Mai 1960).
- [14] - P.B. EARNshaw & J.A. LAWford
Low-speed wind-tunnel experiments on a serie of sharp-edged delta wings.
Aero. Res. Council R. et M. n° 3424 (1964).
- [15] - W.H. MICHAEL
Flow studies on flat-plate delta wings at supersonic speed.
Langley NASA Techn. Note 3472 - July 1955.
- [16] - H. WERLE
Sur l'éclatement des tourbillons d'apex d'une aile delta aux faibles vitesses.
Rech. Aéro. n° 74 (1960).
- [17] - J.J. ELLE
On the breakdown at high incidences of the leading edge vortices on delta wings.
Journal of Roy. Aero. Soc. (August 1960).
- [18] - A.H. CRAVEN & A.J. ALEXANDER
An investigation of vortex breakdown at Mach 2
Cranfield C. OA. Note Aero. 758 (Nov. 1963).
- [19] - A. STANBROOK & L.C. SQUIRE
Possible types of flow at swept leading edges
The Aeron. Quarterly (Fév. 1964) - vol. XV - Part. 1.
- [20] - W.M. MURRAY & R.L. STALLINGS
Heat-Transfer and pressure distributions on 60° and 70° swept delta
wings having turbulent boundary layers.
Langley NASA T.N. D-3644 (Octobre 1966).
- [21] - D.M. SYKES
Flow visualisation studies of plane and cusp delta wings
at supersonic and hypersonic Mach numbers.
R.A.R.D.E. Memorandum (B) 59/62 (Dec. 1962).

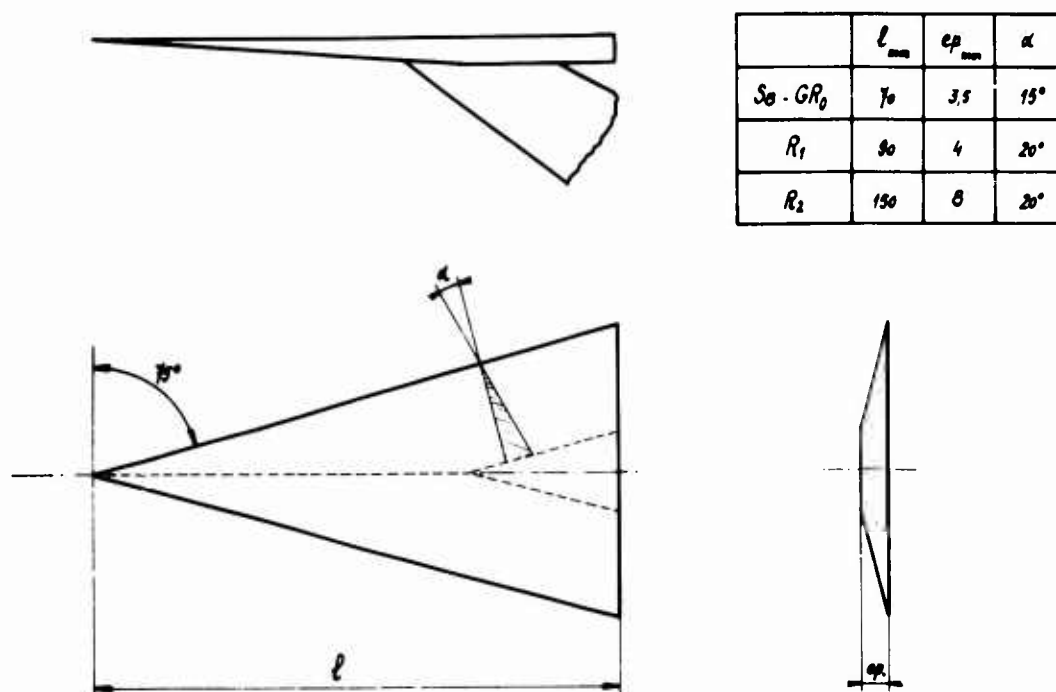


Fig. 1 - Maquette

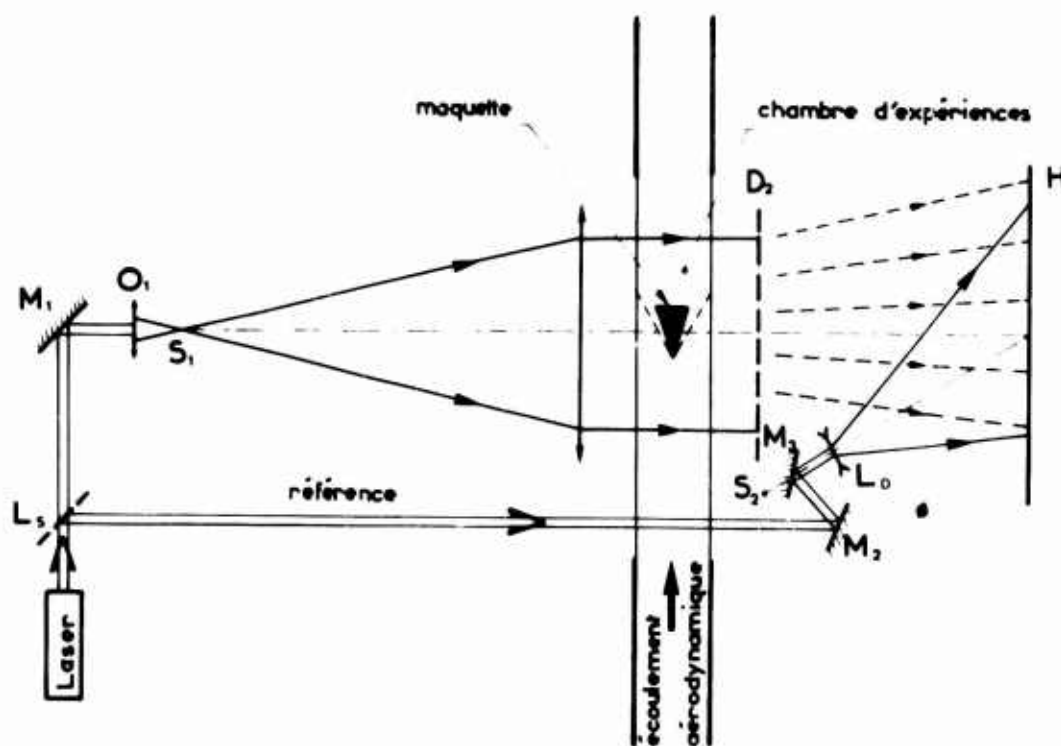


Fig. 2 - Schéma de l'interféromètre

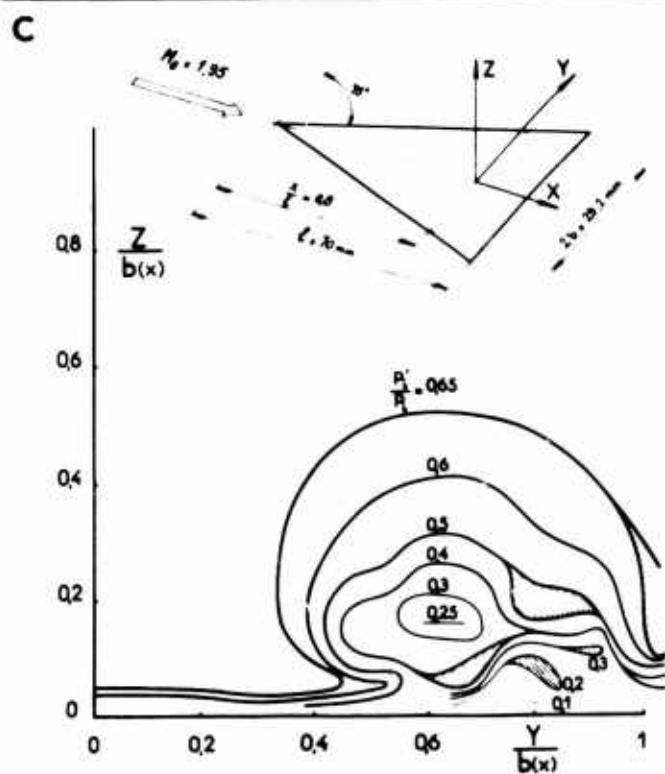
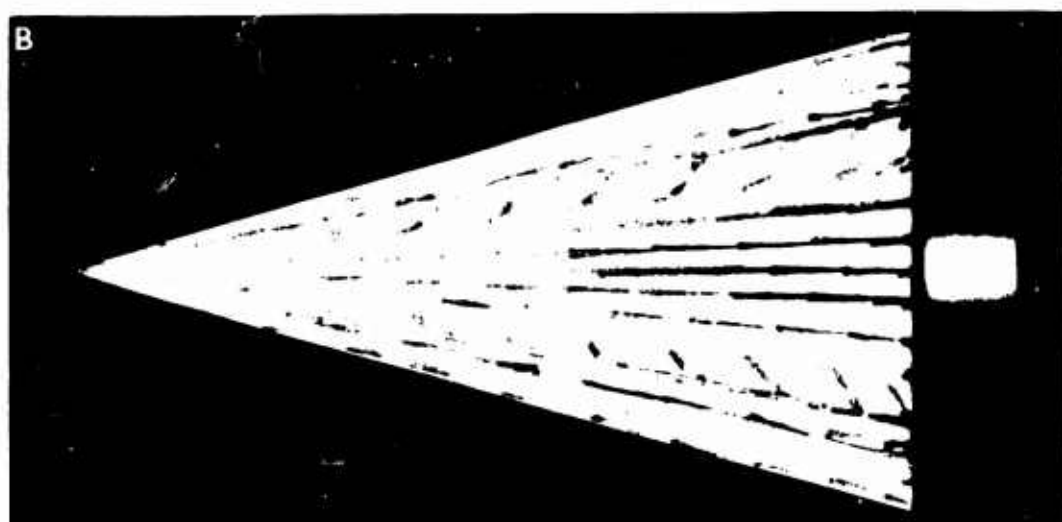


Fig. 3

Ecoulement à l'extrados
d'une aile delta ($\varphi = 75^\circ$)

$$M_0 = 1,95$$

$$i = 10^\circ$$

- A Strioscopie
B Ecoulement pariétal
C Répartition des pressions
d'arrêt.

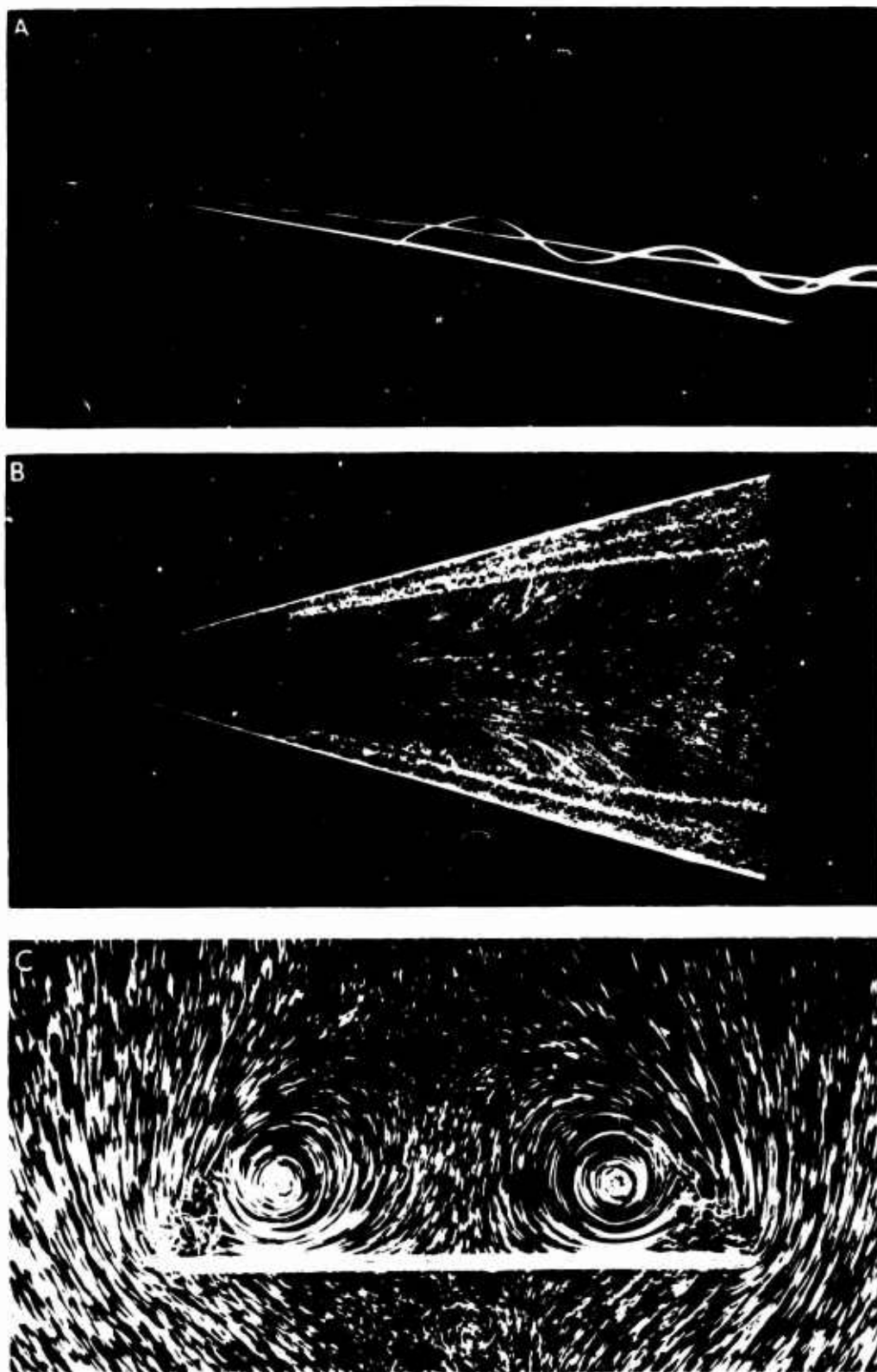


Fig. 4 - Ecoulement à l'extrados d'une aile delta ($\varphi = 75^\circ$)

$M_0 = 0$
 $i = 10^\circ$

- A Vue de profil (visualisation par émissions colorées).
B Ecoulement au voisinage de l'extrados.
C Tranche d'écoulement transversale située au bord de fuite (axe de prise de vues parallèle à l'axe de la maquette).

Visualisation par bulles d'air en suspension dans l'eau.

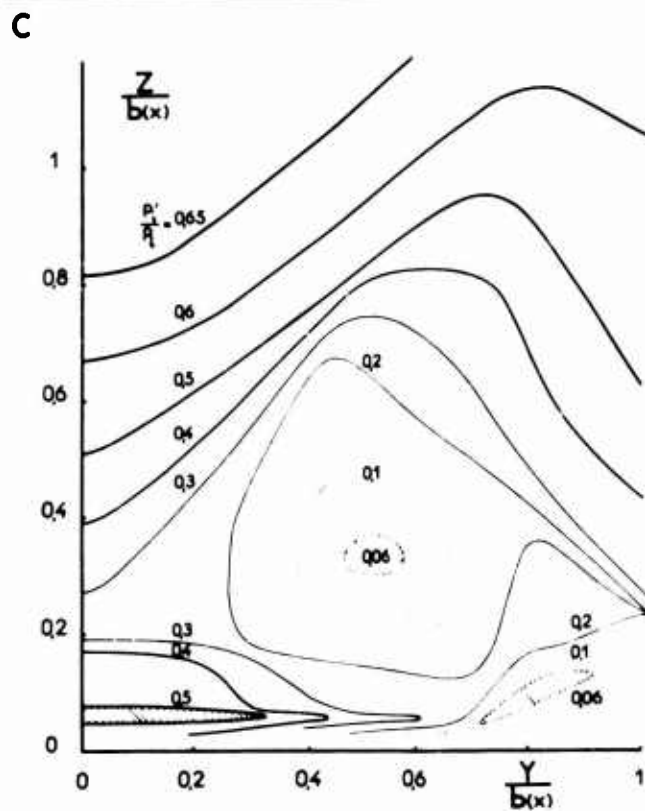
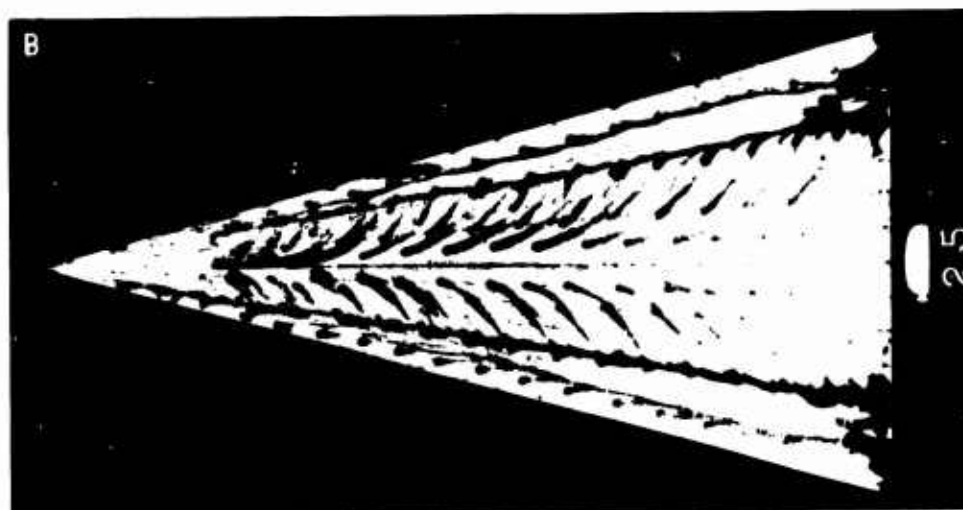


Fig. 5

Ecoulement à l'extrados
d'une aile delta ($\varphi = 75^\circ$)

$$M_0 = 1,95$$

$$\Gamma = 25^\circ$$

- A Strioscopie
B Ecoulement pariétal
C Répartition des pressions d'arrêt.

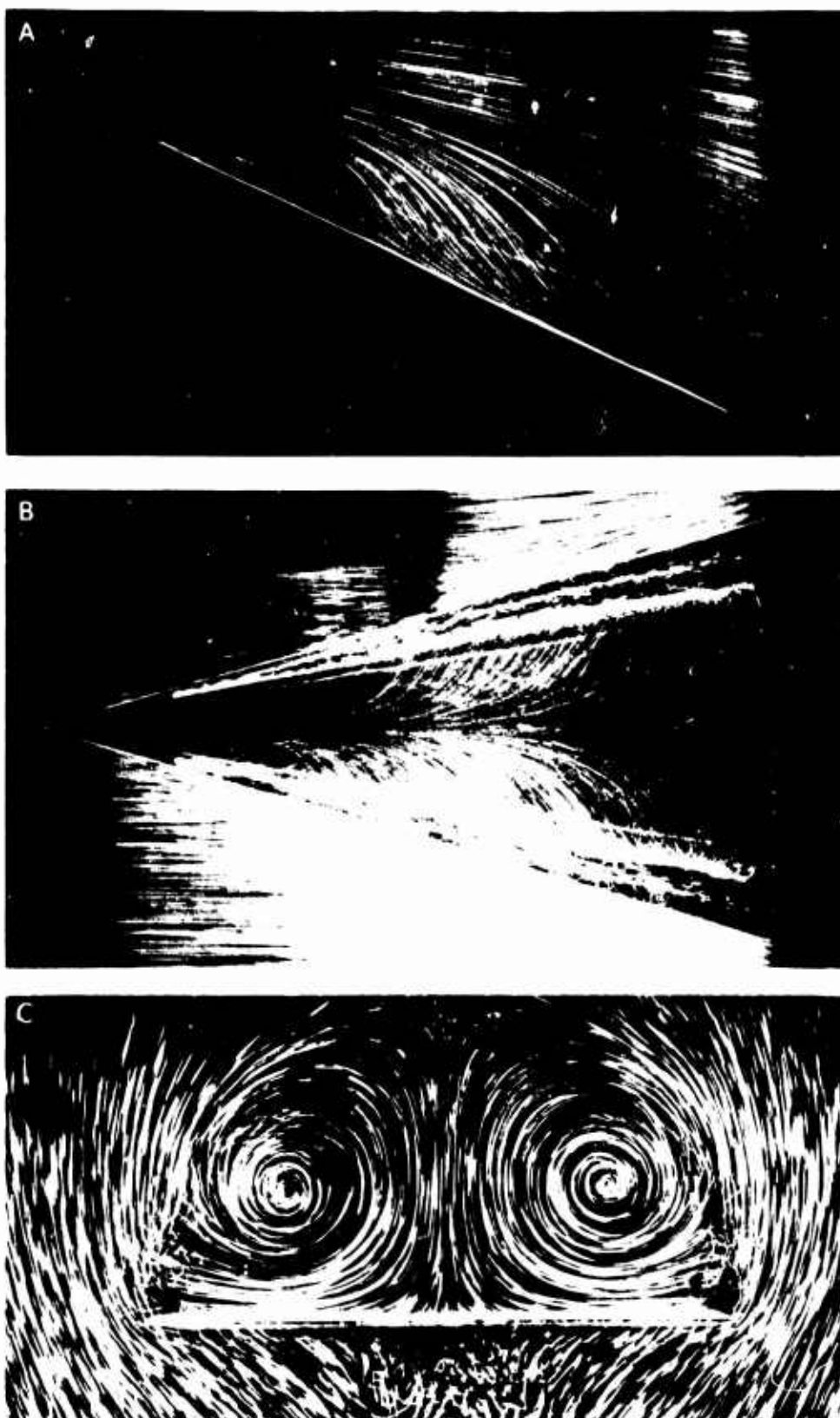


Fig. 6 - Écoulement à l'extrados d'une aile delta ($\alpha = 75^\circ$)

$K_0 = 0$
 $i = 25^\circ$

- A Écoulement dans le plan de symétrie
- B Écoulement au voisinage de l'extrados
- C Tranche d'écoulement transversale située au bord de fuite
 (axe de prise de vues parallèle à l'axe du modèle).

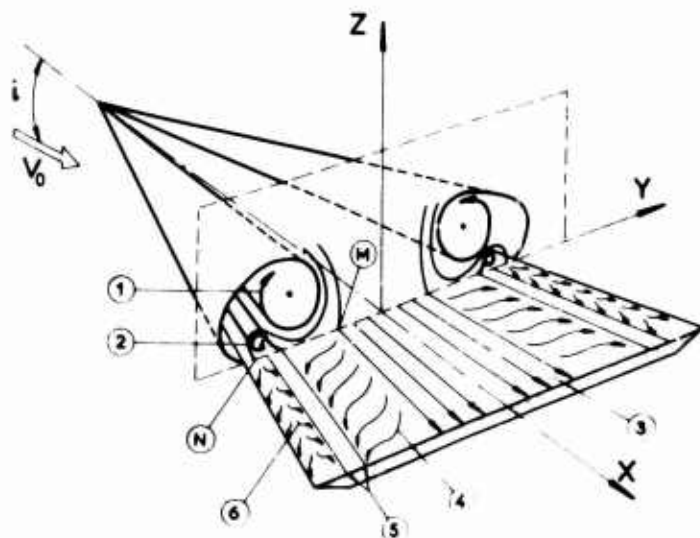


Fig. 7

Schéma de l'écoulement sur l'extrados d'une aile delta mince aux incidences moyennes.

Légende

- ① Nappe en "cornet" formant le tourbillon principal d'extrados.
- ② Nappe en "cornet" formant le tourbillon secondaire.
- ③ Zone médiane non tourbillonnaire.
- ④ Zone balayée par le tourbillon principal.
- ⑤ Lignes d'accumulation d'enduit (ou de bulles d'air) situées entre zones ④ et ⑥
- ⑥ Zone balayée par le tourbillon secondaire.
- M Frontière entre les zones ③ et ④ (ou entre les 2 zones ④ après disparition de la zone ③ aux incidences élevées).
- N Frontière entre la zone ⑥ et la zone située près du bord d'attaque et soumise à l'effet de la nappe ①.
- A Trace, dans le plan de symétrie, de l'onde de choc d'extrados se formant dans l'écoulement supersonique fortement dévié au voisinage du modèle.
- B Trace, dans le plan de symétrie côté extrados, du cône de Mach issu de l'apex.

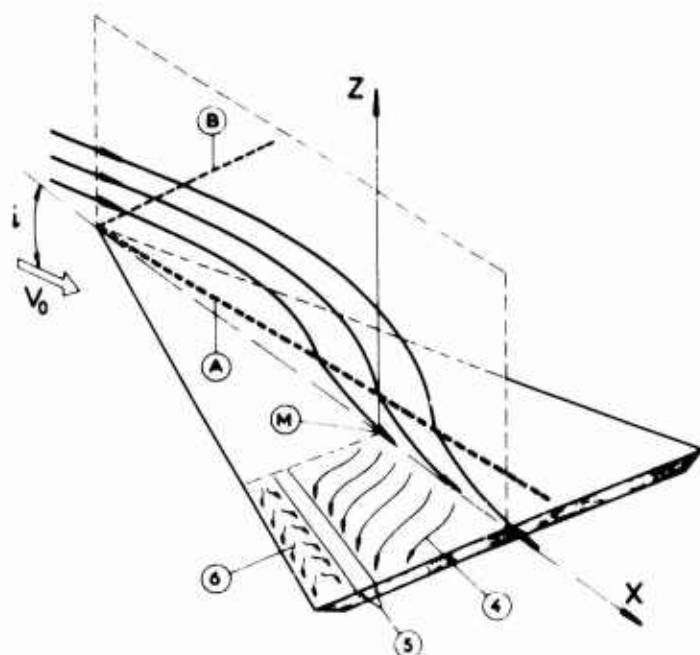


Fig. 8

Schéma de l'écoulement dans le plan de symétrie et sur l'extrados d'une aile delta mince aux incidences élevées.

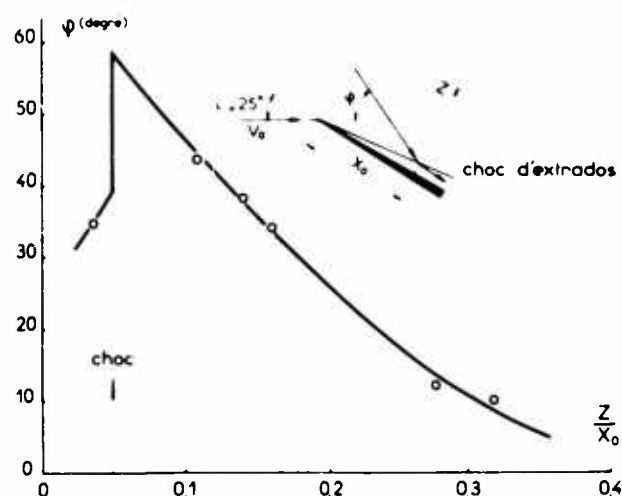


Fig. 9

Evolution de l'inclinaison de la vitesse locale par rapport à V_0 le long d'une normale à l'extrados située dans le plan de symétrie.

Essais en supersonique

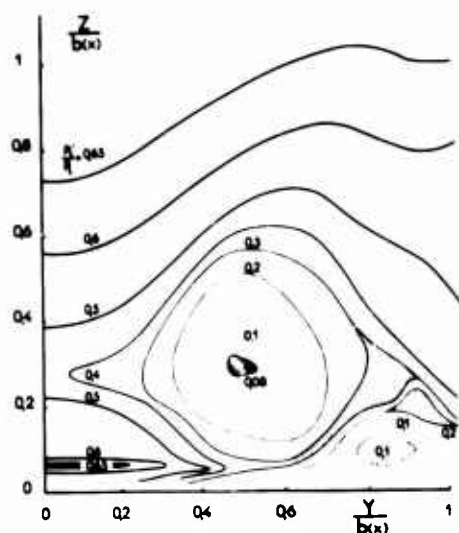
 $M_0 = 1,95 - i = 20^\circ$ 

Fig. 10 - Répartition des pressions d'arrêt.

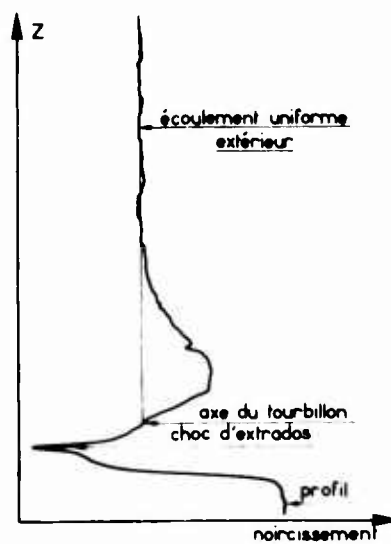


Fig. 11 - Dépouillement d'un striogramme au microdensitomètre.



Fig. 12 - Interférogramme.



Fig. 13 - Strioscopie.

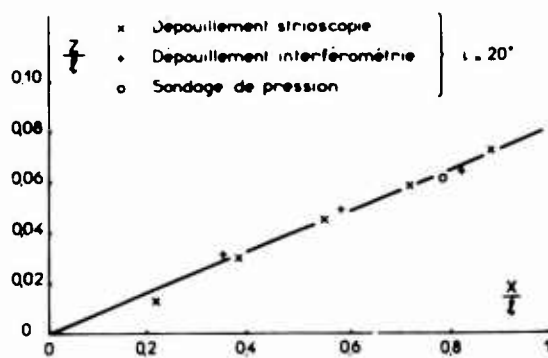


Fig. 14 - Comparaison des diverses déterminations.

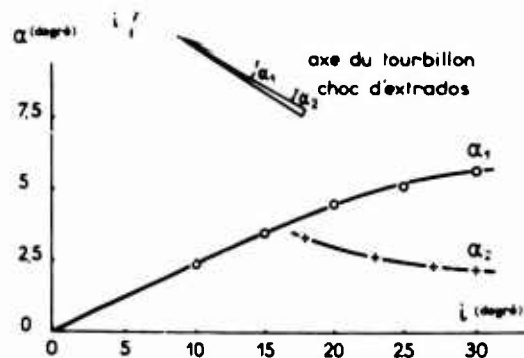


Fig. 15 - Evolution de la position de l'axe en fonction de l'incidence.

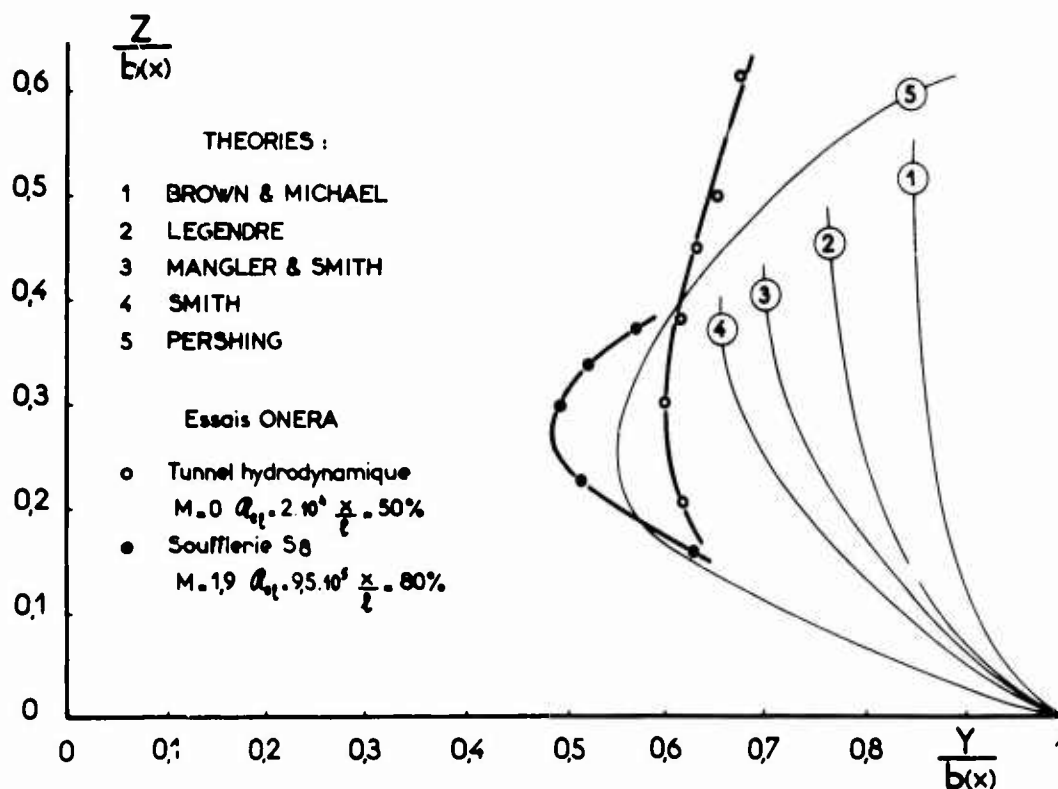


Fig. 16 - Position de l'axe du tourbillon dans un plan transversal

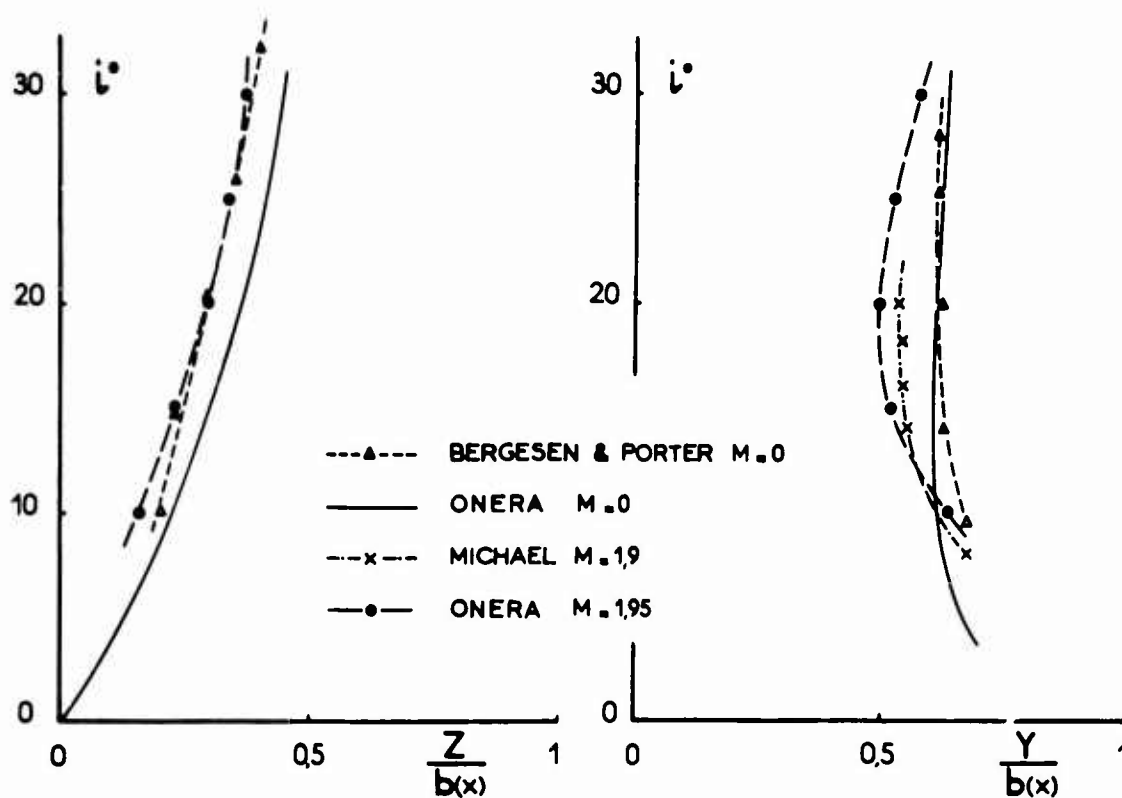


Fig. 17 - Influence de l'incidence sur la position de l'axe du tourbillon

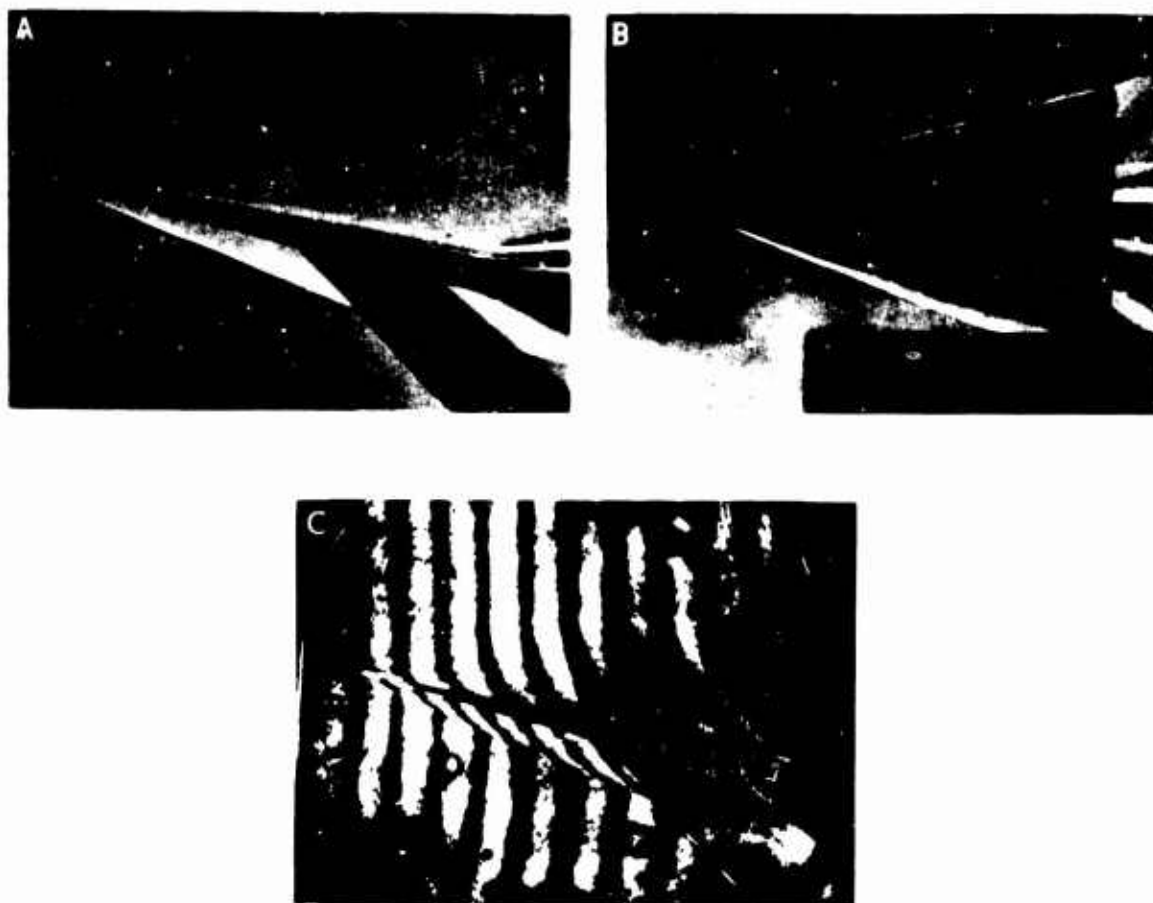


Fig. 18 - Visualisation de l'écoulement à $M_0 = 4$ et $i = 10^\circ$
A et B Strioscopie, C Interférométrie

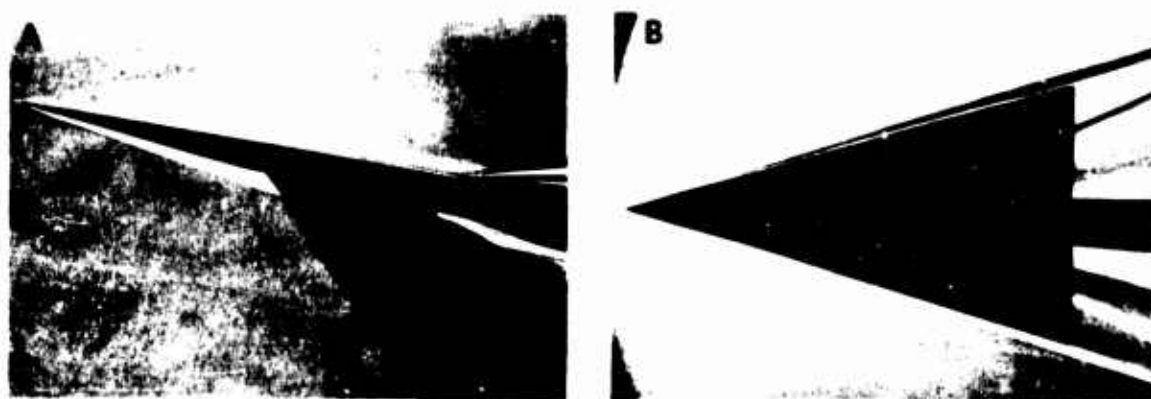


Fig. 19 - Visualisations de l'écoulement à $M_0 = 7$ et $i = 10^\circ$

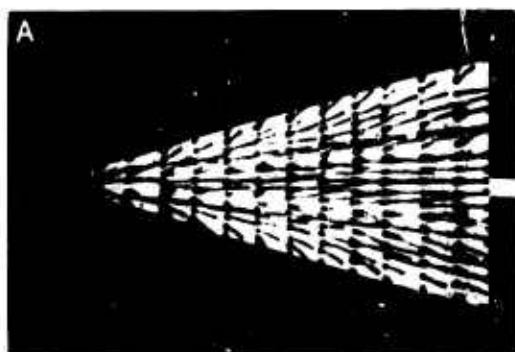
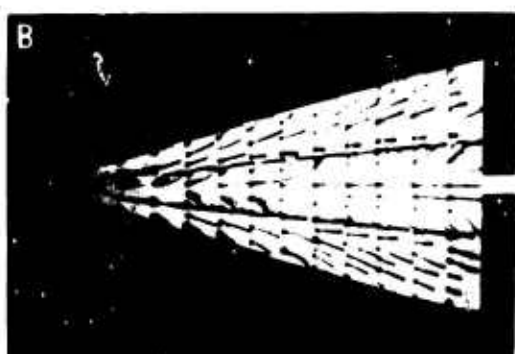
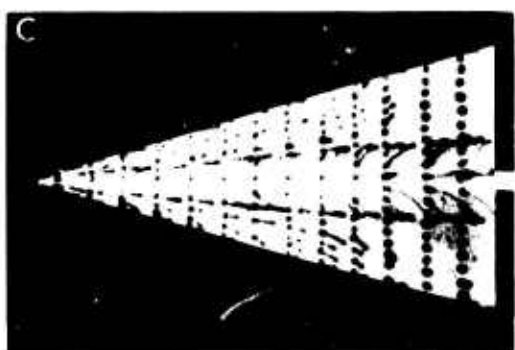
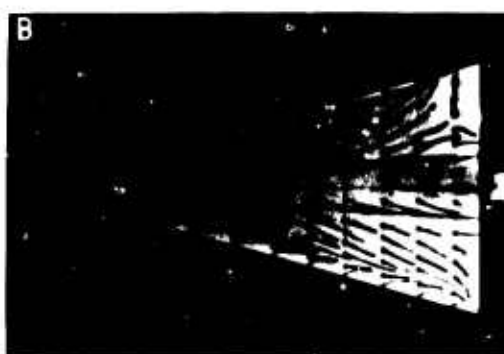
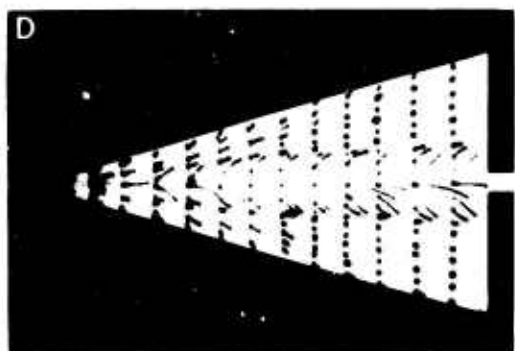
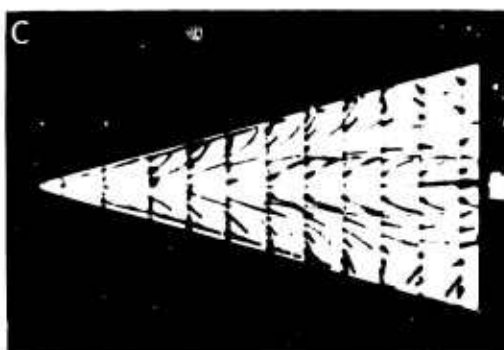
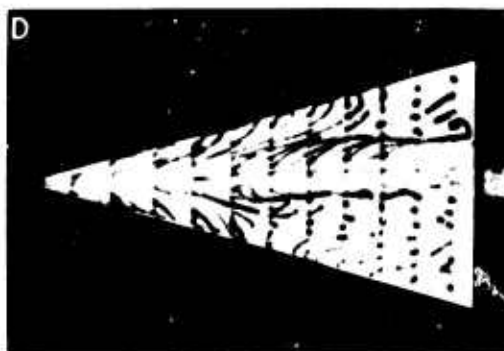

 $1 = 5^\circ$

 $1 = 10^\circ$

 $1 = 15^\circ$

 $1 = 20^\circ$


Fig. 20 - Visualisations pariétales $M_0 = 4$

Fig. 21 - Visualisations pariétales $M_1 = 7$

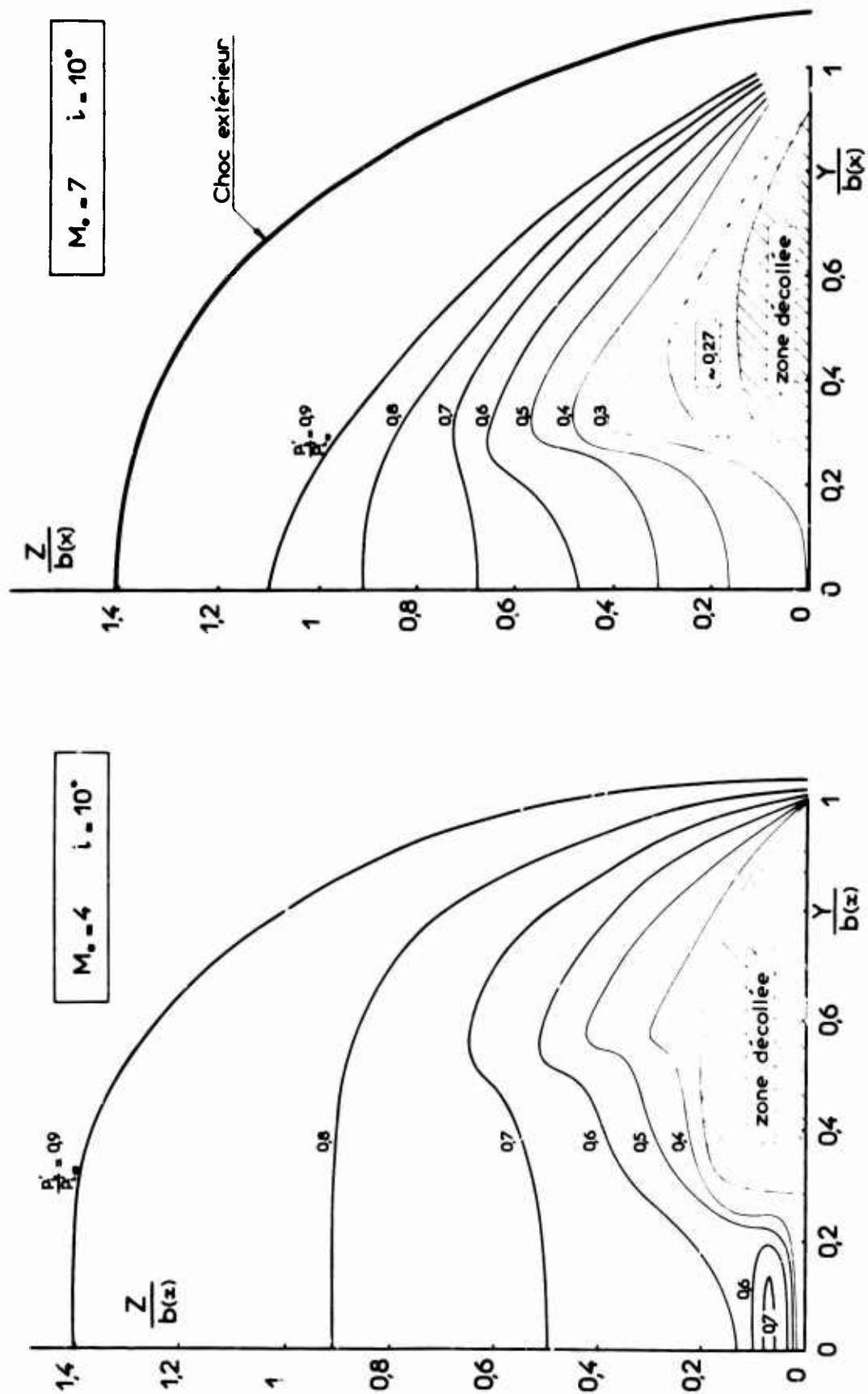


Fig. 22 - Répartition des pressions d'arrêt.

Fig. 23 - Répartition des pressions d'arrêt.

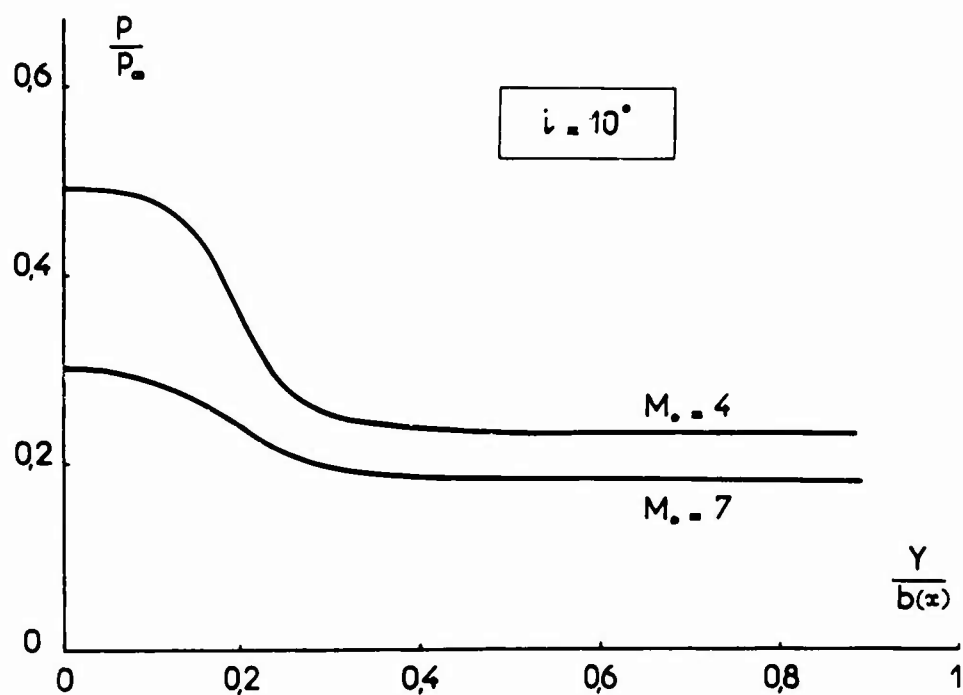


Fig. 24 - Répartition de pression statique suivant l'enveloppe.

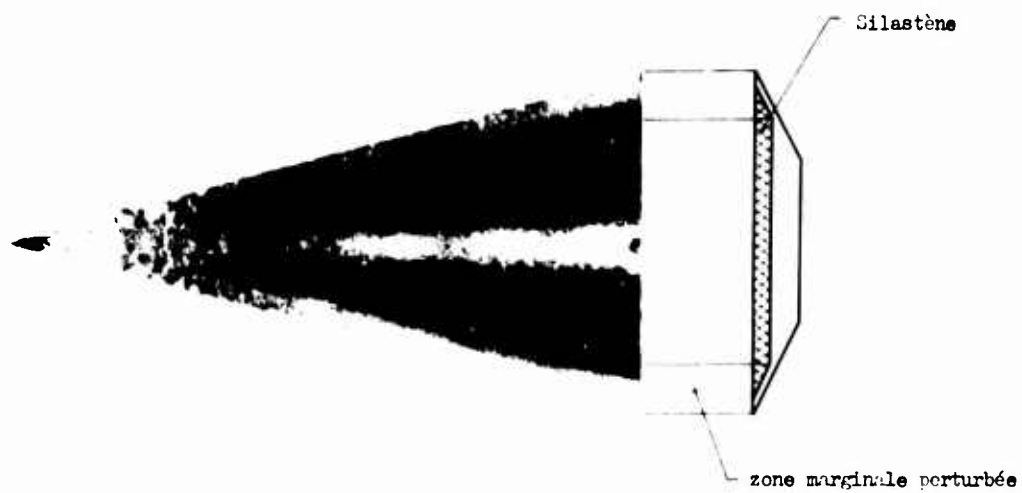


Fig. 25 - Recherche des zones où le flux thermique est maximum :
visualisation par peinture thermosensible.

HYPERSONIC LAMINAR BOUNDARY LAYER GROWTH
IN AN ADVERSE PRESSURE GRADIENT

by

Henry A. Fitzhugh*
Imperial College, London University

*Research Student, Department of Aeronautics

SUMMARY

The paper is concerned with testing a number of laminar boundary layer theories against each other and against experiment. In the course of this work, a comprehensive set of exact solutions to the boundary layer equations have been computed using the finite-difference computer programme of Sells in the range $M = 2-10$, with and without wall cooling. Part two is concerned with testing several theories against experimental results. The theories tested are those of Chen₁ (strong interaction), Monaghan (correlation technique) the Discontinuity/Analogy Method of Stroud and Miller as extended by the author, and the method of Hankey for shock wave-boundary layer interactions and compression corner flows. The exact computer results show the errors in many of the more appropriate methods available for the case where $U_0 = U_\infty(1 - X/L)$, but no comparison with experiment was possible. The theories tested in Part two against experimental results were all shown to be inadequate, and the final conclusion is that no theory has been tested sufficiently to warrant its acceptance as a prediction method.

Special thanks are due to the author's supervisor, Mr. J.L. Stollery, for his valuable inspiration, moral support, and criticism in the course of this work; thanks are also due to Dr. C.C.L. Sells for providing a copy of his computer programme, and for subsequent helpful discussions.

HYPERSONIC LAMINAR BOUNDARY LAYER GROWTH IN AN ADVERSE PRESSURE GRADIENT

by

Henry A. Fitzhugh

A wide variety of laminar boundary layer theories have been published, most of which have the ability to predict behaviour in an adverse pressure gradient. Few of these theories have been adequately tested and the main aim here is to compare various theoretical predictions with each other and, where possible, with experiment.

Part I of this paper contains the results and discussion of laminar boundary layer calculations using the finite difference computer programme of Sells (1).

Part II contains predictions from four other theories, namely those of Monaghan (5), Stroud and Miller (10), Cheng (11), and Hankey (12), and some comparisons with experimental data.

Part I

Computer Programme experiments on the hypersonic boundary layer

These numerical experiments were intended to be comprehensive and as many effects were studied as possible. Much more information is given than in previous exact solutions, including boundary layer profiles and the displacement thickness.

The computer solutions serve two purposes. They provide a standard against which the various approximate theories can be measured and they indicate trends. Until now, very few exact solutions have been published for the supersonic and hypersonic boundary layer equations with wall cooling.

Sells' (1) computer programme solves the boundary layer momentum, energy, and continuity equations assuming only a perfect diatomic gas of constant Prandtl number flowing over a wall of constant temperature. The inviscid solution over the body in question is specified before calculation begins. His method of solution of two coupled non-linear partial differential equations employs an implicit finite difference scheme and a technique of estimating the non-linear terms. The resulting non-homogenous linear equations are solved by matrix inversion, the non-linear terms are re-evaluated and the process is repeated until the solution converges to within some pre-set limit. The programme then marches downstream utilising the parabolic nature of the equations. Sells finds that results are accurate to four places, three near separation. The programme is capable of integrating close to separation and usually fails to converge at some point less than one step length from the extrapolated separation point. Occasionally the programme integrates one step length beyond separation, but errors in calculation using a reversed flow velocity profile are thought to be so great that convergence cannot be obtained any further downstream.

The programme as published did not converge at Mach numbers above four, and a great deal of time was spent trying to force convergence by numerical techniques less accurate than those originally employed. However, it was later realized that in the scaled variables used in the machine code, the boundary layer thickness decreases with increasing Mach number, which is the opposite trend to the physical growth. When the input parameters were adjusted accordingly, it was found that the original programme worked perfectly well at any Mach number up to the limit tested i.e. $M = 22$.

Cases Studied

By far the most common, relevant problem reported in the literature is the growth of a laminar boundary layer in a linearly retarded velocity field, i.e. $u_0 = u_\infty(1 - x/L)$. Morduchow (2) has given an excellent summary of the results of such calculations available before 1965, a few have appeared since then. The method of Sells has now been used to solve the same problem in order to compare the results with those reported previously.

The body shapes that generate a linearly retarded velocity field are shown in figures 1a and 1b depending on whether tangent wedge or Prandtl-Meyer compression is assumed.

In the solution of the linearly retarded velocity distribution the body contour varies with Mach number. Therefore, in order to see trends more clearly the boundary layer growth over a circular arc of unit semi-circumference was calculated. The external (adverse) pressure gradient was determined assuming isentropic Prandtl-Meyer compression.

* The cases studied are listed in tables 1,2,3. The properties calculated were $\delta/L\sqrt{R_x}$, $C_f\sqrt{R_x}$ and $S_t\sqrt{R_x}$ from the leading edge to the separation point. Velocity, stagnation temperature, and static temperature profiles are shown at $M = 6$ and 10 , for the linearly retarded velocity distribution, cold wall, at two Prandtl numbers.

The recovery factor was assumed to be $\sqrt{P_r}$ and the adiabatic wall temperature is defined by

$$T_{aw} = T_\infty + \sqrt{P_r} \frac{u_\infty^2}{2C_p}$$

This assumption is correct for zero pressure gradient. Its validity was tested for adverse pressure gradients by calculating the magnitude of the heat transfer rate in these cases. In this paper solutions labelled adiabatic wall imply $T_w = T_R = T_{aw}$ as defined above and do not necessarily imply zero heat transfer. Of course, if $P_r = 1.0$ then $T_R = T_{aw}$ and the heat transfer is identically zero.

Although the computer programme can use the Sutherland viscosity law, all calculations except one were made assuming a linear variation of viscosity with temperature. The use of the Sutherland law requires the specification of the stagnation temperature independently, and this is too much of a restriction to put on an otherwise general set of exact solutions. However, one case of $M = 10$, $T_w = T_\infty$, $P_r = .725$, and $T_{0\infty} = 1000^\circ K$ was calculated using the Sutherland law.

Comparisons with other Results

For the linearly retarded velocity distribution with zero heat transfer at $P_r = 1.0$, the present computer results give separation points at $x/L = .062, .043, .026$, for $M = 4, 6$ and 10 respectively. For $M = 4$, Morduchow (2) lists six values between .060 and .065, in addition to .056, .066, .067. Head (3) lists values of .067, .054, .055, .056. It should be noted that the NPL "exact" solution value of .045 is in error, the finite difference integration was done by hand and carried to only three place accuracy in skin friction. For $M = 6$ Morduchow lists six values of x_s between .040 and .050, and .057, .037. For $M = 10$, Morduchow gives .020 and .025, in addition to many scattered outside this range. For the case $M = 4$, $P_r = 1.0$, $T_w = T_\infty$, the computer results give $(x/L)_s = .205$; Morduchow lists three values between .20 and .23, .25, .173, .177. Finally, Terrill (4) gives the incompressible separation point on a cylinder as $x/r = .91$ compared with the computer results of .920 for the same Prandtl number i.e. $P_r = .70$ and the computer result is .935 at $P_r = 1.0$.

It should be noted that all of the above separation points were extrapolated by taking the last three points prior to separation and finding the power of n to make C_f linear in $((x/L)_s - x/L)^n$. It is expected (Morduchow (2)) that n should equal 0.5, but it was found always to be slightly larger.

The only exact non-similar solution known to this author prior to this study was that for $M = 4$, $T_w = T_\infty$, $P_r = 1.0$ and $U_0 = U_\infty(1 - x/L)$. Figure 2 shows this solution compared with our own, plus three approximate methods.

Results from Present Study

Tables 1,2,3 list the separation point positions for the cases mentioned previously. Figure 3 shows the variation of $(x/L)_s$ for the linearly retarded velocity distribution and includes unpublished data of Beadle and Sells (as referenced in Cooke and Mangler (8)) together with the predictions of Gadd (9) for $P_r = 1.0$. The figure shows that increasing the Prandtl number moves the separation point forward markedly for the case $u_0 = u_\infty(1 - x/L)$. The percentage shift defined by $1 - (x_{1.0}/x_{.725})_s$ is greater for the hot wall than the cold and increases with Mach number, whereas the percentage shift levels off above $M = 5$ for the cold wall cases. However, in an absolute sense the separation point movement with Prandtl number is much greater in the cold wall cases.

It should be pointed out that it is wrong to conclude that, for adiabatic wall, increasing Mach number moves the separation point upstream because in this example of a linearly retarded velocity distribution the body geometry is changing with Mach number.

Gadd (9) gives an upper limit on $(x/L)_s$ as M tends to infinity and T_w tends to zero. This value was calculated using the Cohen and Reshotko method. However, the results of Beadle and Sells mentioned earlier, indicate that for $T_w = 0$, even at low M , $(x/L)_s$ is greater than the value of .34 given by Gadd, and the results lie well above Gadd's curve for $T_w = 0$, $P_r = 1.0$.

Calculations with the computer programme at $M = 11, 12, 13, 14, 15$, with $T_w = T_\infty$, and $P_r = 1.0$ show that there was no separation at all above $M = 12$, and the separation points for $M = 11, 12$ are far above the asymptotic limit given by Gadd. No amount of coaxing could make the solution separate; C_f would decrease to a very small value and then rise slowly. The locations of the C_f minimum were much farther downstream than any of the separation points calculated for lower M .

As stated earlier, the programme can calculate with either the Sutherland law or linear viscosity law. The one case run at $T_\infty = 1000$ K, $M = 10$, $P_r = 0.725$, and $T_w = T_\infty$, is shown in fig. 3 and table 3.

Figures 4 and 5 show the non-dimensionalized boundary layer displacement thickness for the linearly retarded velocity distribution. The effect of Prandtl number can be seen to increase markedly as Mach number increases, and the effect of cooling can be seen by comparing, say, the $M = 10$ curves at the same x/L . The boundary layer is thinned dramatically reaching one quarter of its hot wall thickness for $T_w = T_\infty$. The boundary layer thinning at high Mach numbers as shown in figure 4 is due to the fact that the flow proceeds far enough downstream so that the local density is high enough to cause this effect.

Figures 6 and 7 show the distribution of C_f for the linearly retarded velocity distribution for both values of P_r , and for hot and cold walls. The vast difference in numerical value of C_f , R_x and the difference in shape of the distribution near the leading edge for the adiabatic wall case are easily discernible. The reader is reminded of the great difference in scale between figure 6 and figure 7.

Figure 8 shows the variation of Stanton number for the linearly retarded velocity distribution. The curves show qualitatively the same behaviour as the corresponding trends in C_f (Fig. 6) but S_t never approaches zero, and inspection of figures 6 and 8 together show that C_f/S_t starts at 2.0 at $x/L = 0$ and proceeds smoothly to zero at separation.

The linearly retarded velocity distribution was also calculated for $M = 0.5$, $T_w = 0.5 T_\infty$ at $P_r = 1.0$ and .70 in order to compare its trends with a previously solved case for a subsonic cylinder, i.e. $U_e = U_\infty (2 \sin x/r)$ at the same conditions, and figure 9 shows the variation in C_f , S_t and δ^* for the cylinder. For the linearly retarded velocity distribution a higher Prandtl number leads to lower Stanton number, lower skin friction, higher values of displacement thickness and earlier separation. However, for the subsonic cylinder it was found that the trends in Stanton number and displacement thickness were the same as the linearly retarded velocity distribution, but that a higher Prandtl number gave a higher skin friction and later separation. The reversal of trends is probably due to the difference in pressure gradients, i.e. the cylinder produces a pressure gradient which is initially favourable and later turns adverse, while the linearly retarded velocity distribution is continuously adverse.

Figures 10 and 11 show at $M = 6, 10$ respectively, the velocity, stagnation temperature, and static temperature profiles across the boundary layer for Prandtl numbers of 1.0 and .725. In these graphs, separation refers to the last profile calculated by the programme, the actual separation point is slightly farther downstream. The effect of P_r is marked, especially on the static temperature. It should be noted when the velocity gradient at the wall approaches zero, the stagnation and static temperature gradient is still nonzero. Near separation, the curves for corresponding values of x/L cease to coincide at all, because one flow is much nearer separation than the other.

Figure 12 shows the separation points on the circular arc for cold and adiabatic walls. The separation point is very insensitive to Mach number for the adiabatic cases, but moves rearward as M increases for the cold wall case. The value of this study is that the circular arc is of constant geometry unlike the $U_e = U_\infty(1 - x/L)$ distribution and shows that at constant Mach number, cooling the wall delays separation, all other parameters remaining constant. Figures 13, 14, 15 show the variation in δ^* , C_f , and S_t for the circular arc. Again dramatic thinning of the boundary layer with cooling can be seen in figure 13, where the difference between hot and cold wall displacement thickness can be as much as a factor of 3. The marked thinning of the boundary layer as it proceeds downstream in the cold wall cases is also evident. The curves for C_f and S_t show again that S_t does not approach zero as C_f does.

If we compare the flows at the same Mach number, each near separation (different x/L therefore) then we see that at $M = 2$ the value of $S_t \sqrt{R_x}$ for the "adiabatic" wall (not graphed) is about 30% of its cold wall ($T_w = T_\infty$) value, while the figure is 3% at Mach 10, with the flow at 4,6,8, being 15%, 7%, 5% respectively. It should be realized that the high figure at low Mach numbers is partly accounted for by the low heat transfer rate even at cold wall conditions. Even with $T_w = T_\infty$, i.e. $T_w = .444 T_{O_\infty}$, the wall is not very cold at low M .

For the circular arc case, at $M = 2$, where the cold wall is colder ($T_w = 0.25 T_{O_\infty}$), the maximum value of $S_t \sqrt{R_x}$ near separation for the adiabatic case is about 20% of its corresponding cold wall value. From the above examples we can see that assuming recovery factor equal to $\sqrt{P_r}$ is a better assumption at high Mach number than at low. It should be remembered that the above conclusions were drawn from considerations of $S_t \sqrt{R_x}$, not from S_t alone.

Figures 6,8,9,14,15 show that the skin friction maximum does not occur at the same point as the heat transfer maximum, thus discrediting the often-made assumption that heat transfer and skin friction behave similarly, although not necessarily in accord with Reynolds analogy. Far more important, however, is the fact that the heat transfer is definitely not zero at the separation point. Inspection of figures 8,9,15 show that $S_t \sqrt{R_x}$ cannot logically be extrapolated to zero at the same point that $C_f \sqrt{R_x}$ can. Moreover, on the occasions when the computer programme managed to converge beyond separation, the heat transfer was definitely positive and only slightly reduced from its separation point value, even though C_f was negative.

To conclude this part, it is felt that the above results form a set of solutions which provide a comparison for future approximate methods, as well as indicating the trends of separation point with wall temperature and Mach numbers.

M	$T_w = T_R$		$T_w = T_\infty$	
	$P_r = 1.0$	$P_r = .725$	$P_r = 1.0$	$P_r = .725$
2	.091	.096	.141	.143
4	.062	.073	.204	.232
6	.043	.055	.282	.325
8	.029	.039	.324	.372
10	.026	.036	.351	.405 (.383)
11	-	-	.360	-
12	-	-	.365	-
13,14,15	-	-	No Separation	-

Table 1. Separation points for $U_e = U_\infty(1 - x/L)$, linear viscosity law. (Sutherland Law $T_{O_\infty} = 1000^\circ K$, $P_r = .725$)

M	$T_w = 0.25 T_{O_\infty}$	$T_w = T_R$
2	.096	.046
4	not calculated	not calculated
6	.24*	.072
8	.27*	not calculated
10	.28*	.080*

Table 2. Separation points for circular arc, $P_r = 0.725$, Linear viscosity law. * These values accurate only to $\pm 5\%$, due to the step length used.

	$(x/L)_s$
$P_r = 1.0$.935
$P_r = .70$.920

Table 3. Separation points for cylinder, $U_e = 2U_\infty \sin x/r$; $T_w = 0.5 T_{O_\infty}$, $M = 0.5$, Linear viscosity law.

Part II

Comparison of four boundary layer methods with experiment

The methods listed in the Introduction are each felt to include the highest state of development along a particular line of attack. The methods of Monaghan (5) and Stroud and Miller (10) predict heat transfer as well as skin friction and boundary layer thickness. The method of Hankey and Cross (12) predicts pressure, and, although not strictly applicable to flows with pressure gradient, the method of Cheng et al (11) predicts pressure as well as heat transfer.

Monaghan's method is the last in a series of momentum integral correlation techniques, which descended through Cohen and Reshotko (6) and Luxton and Young (7). These techniques depend on correlation of known exact solutions to the boundary layer equations, and on using these correlations for general problems.

Monaghan reduces the boundary layer equations to a form where they can be integrated stepwise downstream, provided that some relationship can be found between the first and second derivative, with y , of the velocity at the wall. He achieves this by using the incompressible correlation of Flawites, having previously used a transformation to the incompressible plane. It was decided to apply Monaghan's method to the attached flow over a compression corner which had been "faired in" in order to produce a smooth inviscid Mach number distribution. From other experimental evidence on this type of flow we would expect the heat transfer rate to drop slightly, relative to a flat plate, near the corner, and then to rise. However, at $M = 8$, it can be seen in figure 16 that the heat transfer rate rises immediately. It should also be said that in order to perform this calculation at all, it was necessary to extrapolate the relevant curves in Monaghan's report, an extrapolation that, due to the nature of the curves, is difficult to do with confidence.

Hankey and Cross (12) have proposed a momentum integral technique which reduces the problem of the boundary layer equations in a compression corner or shock wave/boundary layer interaction to the solution of a second order linear ordinary differential equation with constant coefficients. The energy equation is not included, nor is it possible to predict heat transfer by this method. Hankey and Cross assume that $d\theta_1/dx \gg d\theta_1/dx$ and dM/dx and that $H = \delta_1/\theta_1$ varies linearly with $\theta_1^2 dM/dx$. Figure 17 compares predictions by this method with experimental data obtained by Lewis et al (13) on a compression corner at $M = 6.06$ and a shock wave/boundary layer interaction at Needham (14). Hankey's method automatically gives the right final pressure rise, dictated by inviscid flow considerations, and the quantities left to calculate are the value of the pressure plateau and the length of the total interaction. In both examples the estimates are poor, the plateau region is too high and the interaction as calculated is much longer than experiments show. One of the difficulties is that Hankey's method calculates Mach numbers while experiments give pressures. At $M = 6$, a 10% error in M gives a 100% error in pressure; we are not surprised that this effect lessens the accuracy of this method at high M . The author would like to acknowledge Hankey's excellent and comprehensive private communication with respect to the above examples.

The method of Stroud and Miller was originally set forth for treatment of turbulent boundary layers, but has been extended by the present author to cover laminar flows as well. This method is of interest because it can cope with any effect likely to happen in a boundary layer, including normal pressure gradients and non-uniform wall temperature. The provisions for treating normal pressure gradients were not used in any calculations for this paper and will not be discussed here. This method is known as the discontinuity analogy because it assumes that the Mach number distribution can be broken down into a series of constant Mach number elements (flat plates) with discontinuities connecting adjacent elements. Flat plate relationships, either laminar or turbulent, are used along the constant Mach number elements. Mass, momentum, and energy are conserved across the discontinuities, and thus the calculation procedure is to march along alternating flat plate regions and discontinuities.

Figure 18 compares our exact solution at $M = 4$, $U_e = U_\infty(1 - x/L)$ and $T_w = T_\infty$ with the prediction of the discontinuity analogy. The performance of the latter is disappointing. Moreover, tests at other Mach number showed that this formulation always thinned the boundary layer in an adverse pressure gradient at any Mach number. Experimental evidence and the results of the previous section show that this effect occurs only above about $M = 5$, depending on the pressure gradient, of course. The discontinuity analogy is more sensitive to pressure gradient than anything else, and cannot be relied upon even in the range $M = 6-10$, where it does predict the correct trends.

The Cheng theory applies to flat plates at incidence, either positive or negative, in the strong interaction regime. The author has carried out experiments at $M = 15.1$ on a power-law concave body given by $Y = X^3/150$, in inches, mated to a wedge of slope 28° , so that the total turning angle from the sharp leading edge was 28° at $X = 5.1'$. This model was instrumented with film gauges for heat transfer measurement and was inclined so that the leading edge was at -6° incidence in order to ensure that the leading edge shock did not impinge on the rear of the model and $X = 14$ at $X = 1'$.

Inspection of Cheng's assumptions concerning small deflections, slenderness, etc. show that none of the assumptions of the theory has been violated except one: the inviscid flow has a pressure gradient over the above cubic surface, and is not a flat plate flow as assumed by the theory. Still it will be informative to compare our results against this theory, as in figures 19 and 20 where the experimental heat transfer is plotted against the appropriate correlation parameters of Cheng's theory. Near the leading edge, the agreement is quite good; in fact, the Cheng theory predicts the heat transfer correctly up to $X = 3.5''$, where the body has already turned through some 14° . However, from there on the theory predict heat transfer which is far too high (not shown). Moreover, it was found that when the boundary layer reached the wedge described above, the heat transfer went on rising dramatically, even though the inviscid pressure gradient ceased. Schlieren photographs showed that the boundary layer went through a "neck" region thereafter, and this points to the reason for increased heat transfer. No theory can account for this as yet. Unfortunately, the Cheng flat plate theory cannot account for this delayed thinning of the boundary layer, nor for the fact that the flow is near separation, although it never separates. The above discussion will be clearer if reference is made to figure 21, which is partly a drawing of a schlieren photograph of the above model and flow pattern.

Concluding Remarks

All of the above comparisons point to a rather bleak picture - it appears that none of the theories tested can predict boundary layer growth in an arbitrary adverse pressure gradient or in the strong interaction regime. Moreover, there is not enough laminar data in the range $M = 2-10$ with heat transfer to afford a direct test of, say, the computer programme of Part I. It has been shown that this computer programme agrees well with many other theories, there is no doubt that the solutions presented are solutions to the boundary layer equations. However, whether that programme will predict results which agree with experiment is another question. Until it is resolved positively, there seems to be no theory available for the hypersonic laminar boundary layer which can be used with any degree of confidence.

Symbols

C_f	Skin friction coefficient, based on free stream conditions
C_p	Specific heat at constant pressure
L	Length of body
M	Free stream Mach number
p	Pressure
Pr	Prandtl number
q	Heat transfer to the wall
S	$T_0/T_{0c} - 1$
St	Stanton number $q / \rho_\infty U_\infty C_p (T_{0c} - T_w)$
T	Absolute temperature
T_R	Recovery temperature
r	Radius of circular arc body
R_x	Reynolds number based on X
U	Velocity in streamwise direction
X, Y	Cartesian coordinates
α	Local turning angle of surface
δ^*	Boundary layer displacement thickness
γ	C_p / C_v
ζ	$\zeta = 1/\gamma + \lambda$
η	Similitude normal coordinate $\int_0^y \rho/\rho_\infty dy$
θ	Momentum thickness
ρ	Density
$\bar{\gamma}$	$u^3 / \sqrt{\mu x}$
$\bar{\gamma}_e$	$\bar{\gamma}_e = (4.66) + 1.73 T_w / T_\infty \bar{\gamma}_e$

Subscripts

i	Incompressible plane
e	Edge of boundary layer
∞	Free stream conditions
o	Stagnation conditions
w	Wall conditions
s	Separation point

References

1. Sells, C.C.L., Two-dimensional laminar compressible boundary layer programme for a perfect gas. RAE. Pt. 66243, August 1966.
2. Morduchow, M. Review of Theoretical Investigations on Effect of Heat Transfer on Laminar Separation. AIAA J. August 1965, P. 1377.
3. Head, M.R. and Hayasi, N. Approximate Calculation of the Incompressible Laminar Boundary Layer. Aero. quarterly, August 1967, P. 259.
4. Terrill, R.M. Laminar Boundary Layer Flow Near Separation with and without Suction. Phil. Trans. Royal. Soc. A. 253, P.55 (1960).
5. Monaghan, R.J. Effects of Heat Transfer on Laminar Boundary Layer Development under Pressure Gradients in Compressible Flow. A.R.C. R and M. No. 3218, 1961.
6. Cohen, C.B. and Heshotko E. The Compressible Laminar Boundary Layer with Heat Transfer and Arbitrary Pressure Gradient. NACA TN 3226, April 1955.
7. Luxton, R.E. and Young, A.D. Generalized Methods for Calculation of the Laminar Compressible Boundary-Layer. Characteristics with Heat Transfer and Non-Uniform Pressure Distribution. ARC R and M 3233, 1962.
8. Cooke, J.C. and Mangler K.W. The Numerical Solution of the Laminar Boundary Layer Equations for an Ideal Gas in two and three Dimensions. RAE Tech Memo. Aero 989.
9. Gadd, T.E. A Review of Theoretical Work Relevant to the Problem of Heat Transfer Effects on Laminar Separation. ARC CP 331, 1957.
10. Stroud, J.F. and Miller L.D. An Experimental and Analytical Investigation of Hypersonic Inlet Boundary Layers. AFFDL TR-65-123, Vol 1, Aug. 1965.
11. Cheng, H.K. and Hall, J.G. and Golian, T.C. and Hertzberg, A. Boundary Layer Displacement and Leading Edge Bluntness Effects in High Temperature Hypersonic Flow. J. Aero and Sciences, May 1961, P.353.
12. Hankey, W.I. and Cross, Jr., E.J. Approximate Closed-Form Solutions for Supersonic Laminar Separated Flows. AIAA J. April 1967, P.651.
13. Lewis, J.L., Kubota, T. and Lees, L. Experimental Investigation of Supersonic Laminar Two-dimensional Separation in a Compression Corner with and without Cooling. AIAA J. Jan. 1968, P.7.
14. Needham, D.A. Laminar Separation in Hypersonic Flow. London University Ph.D. Thesis (1965).

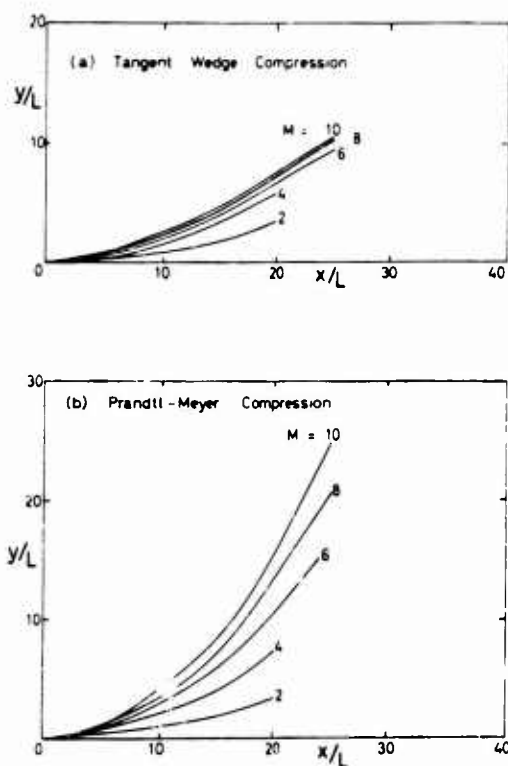


Figure 1 Contours which generate a velocity distribution $U_e = U_\infty(1 - x/L)$, for isentropic and non-isentropic compression.

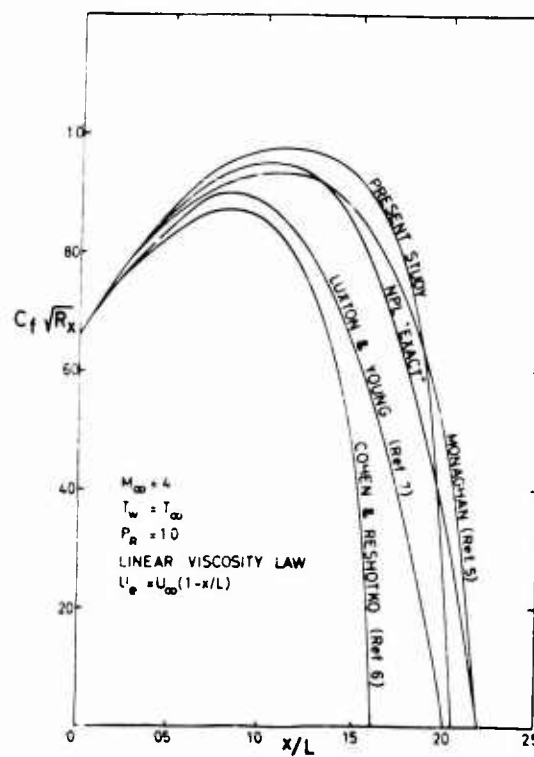


Figure 2 Results of present study compared to four other methods.

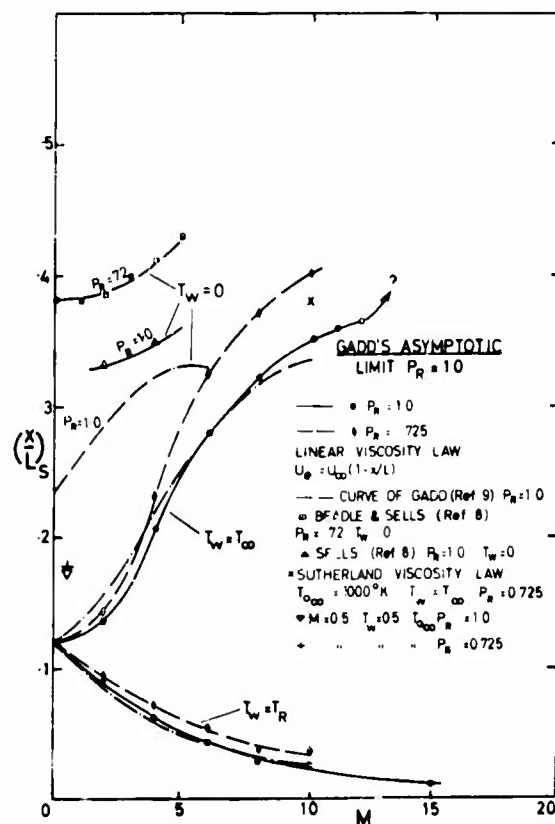


Figure 3 Separation points for the linearly retarded velocity distribution.

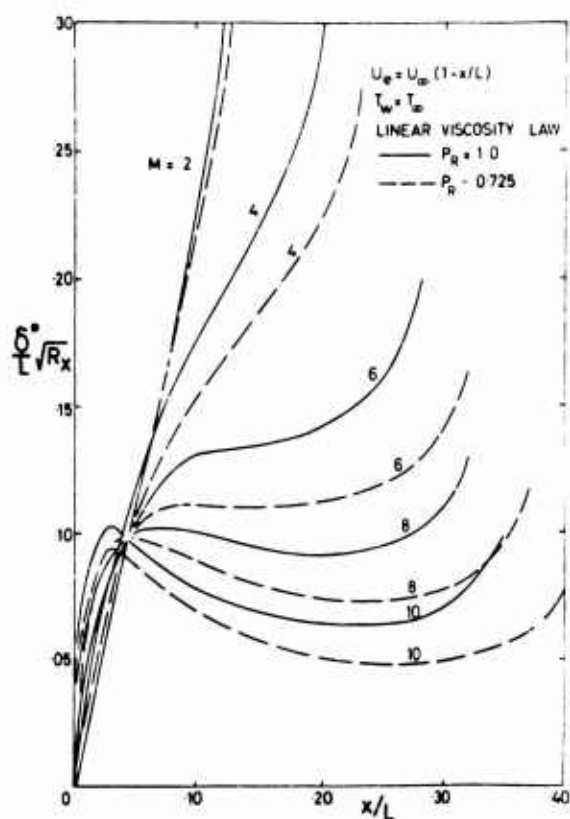


Figure 4 Displacement thickness for the linearly retarded velocity distribution, cold wall.

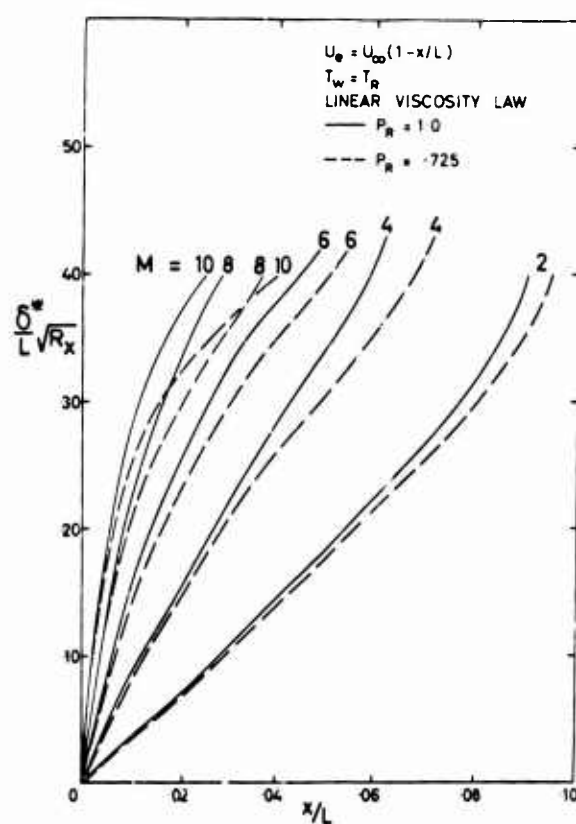


Figure 5 Displacement thickness for the linearly retarded velocity distribution, adiabatic wall.

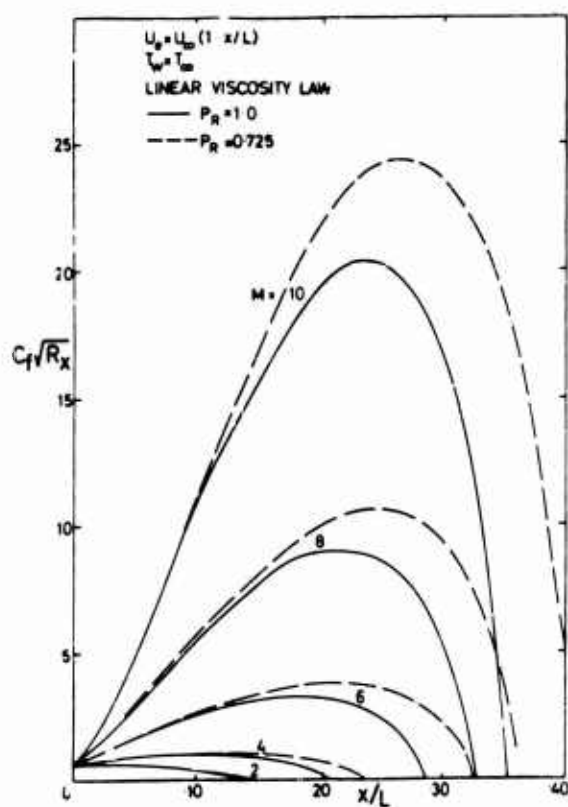


Figure 6 Skin friction for the linearly retarded velocity distribution, cold wall.

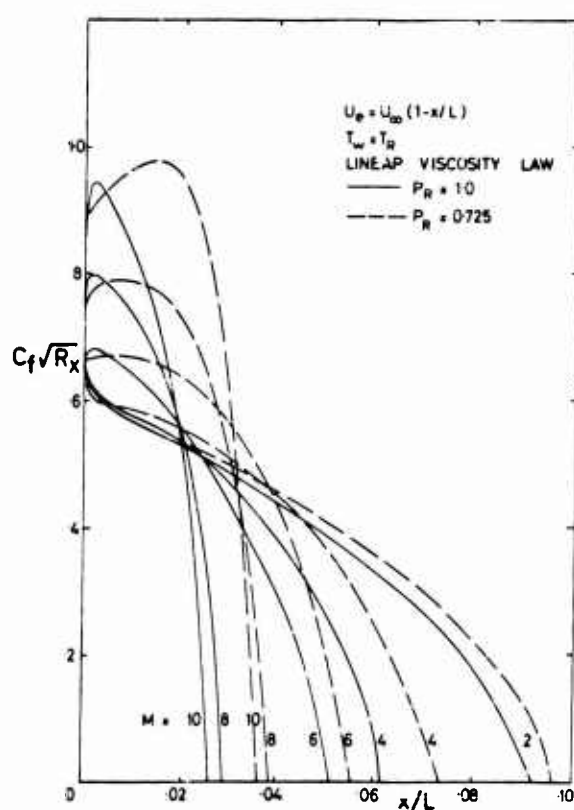


Figure 7 Skin Friction for the linearly retarded velocity distribution, adiabatic wall.

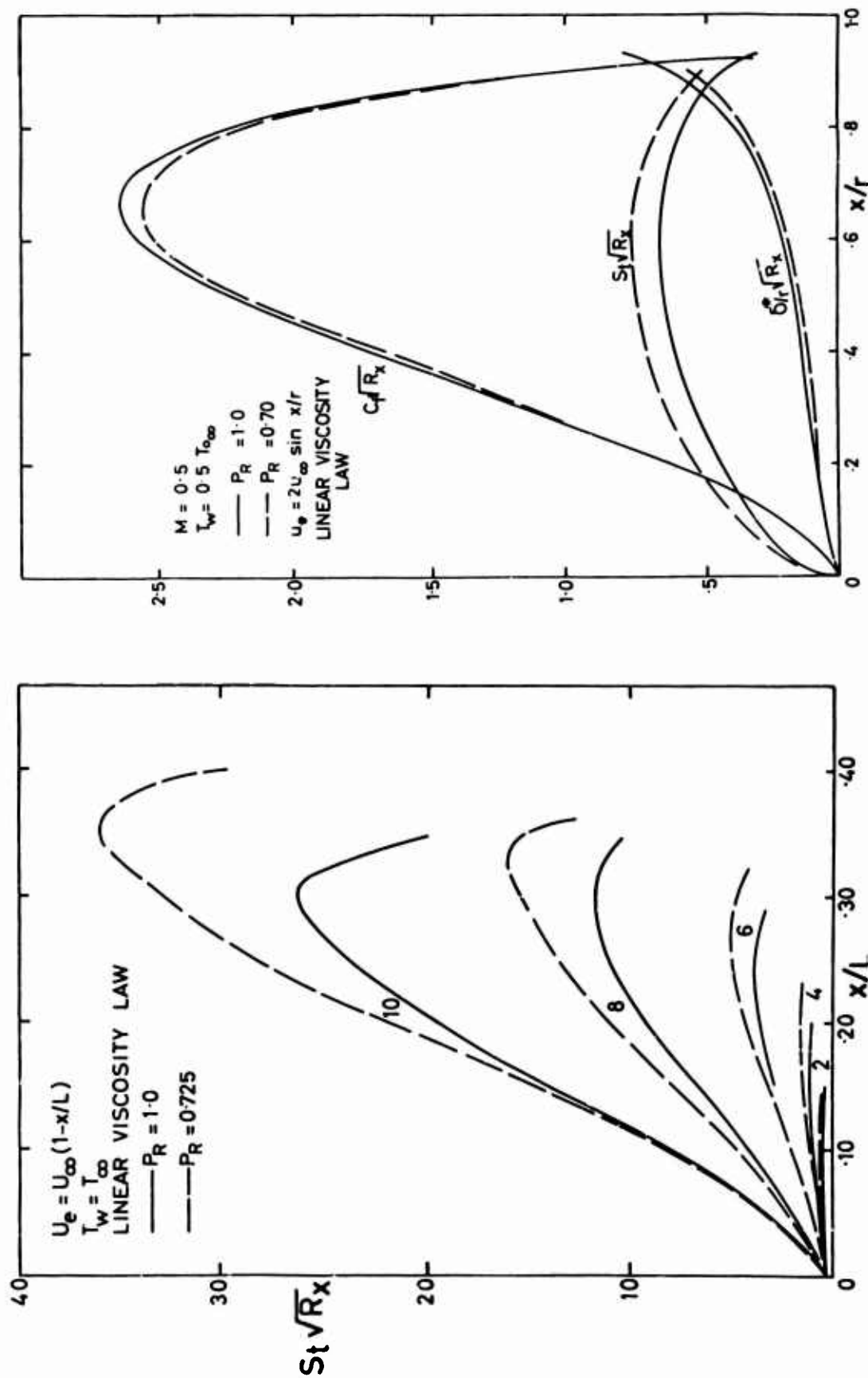


Figure 8 Heat transfer for the linearly retarded velocity distribution.

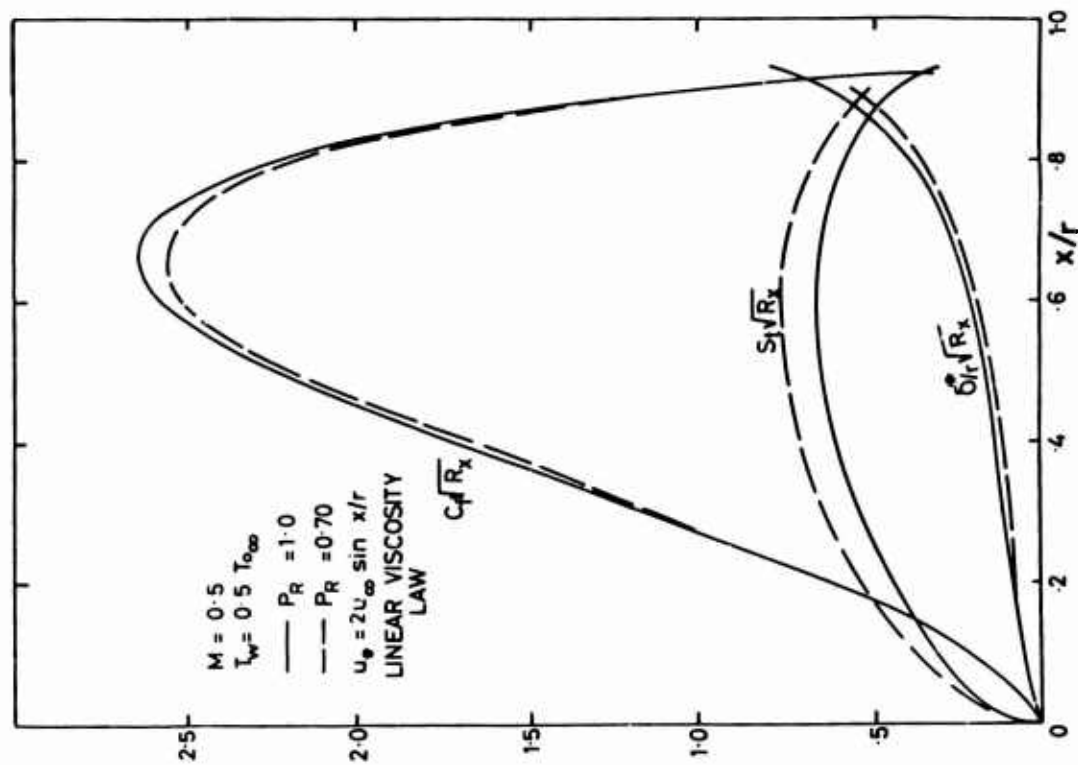


Figure 9 Displacement thickness, skin friction, and heat transfer for a cooled cylinder.

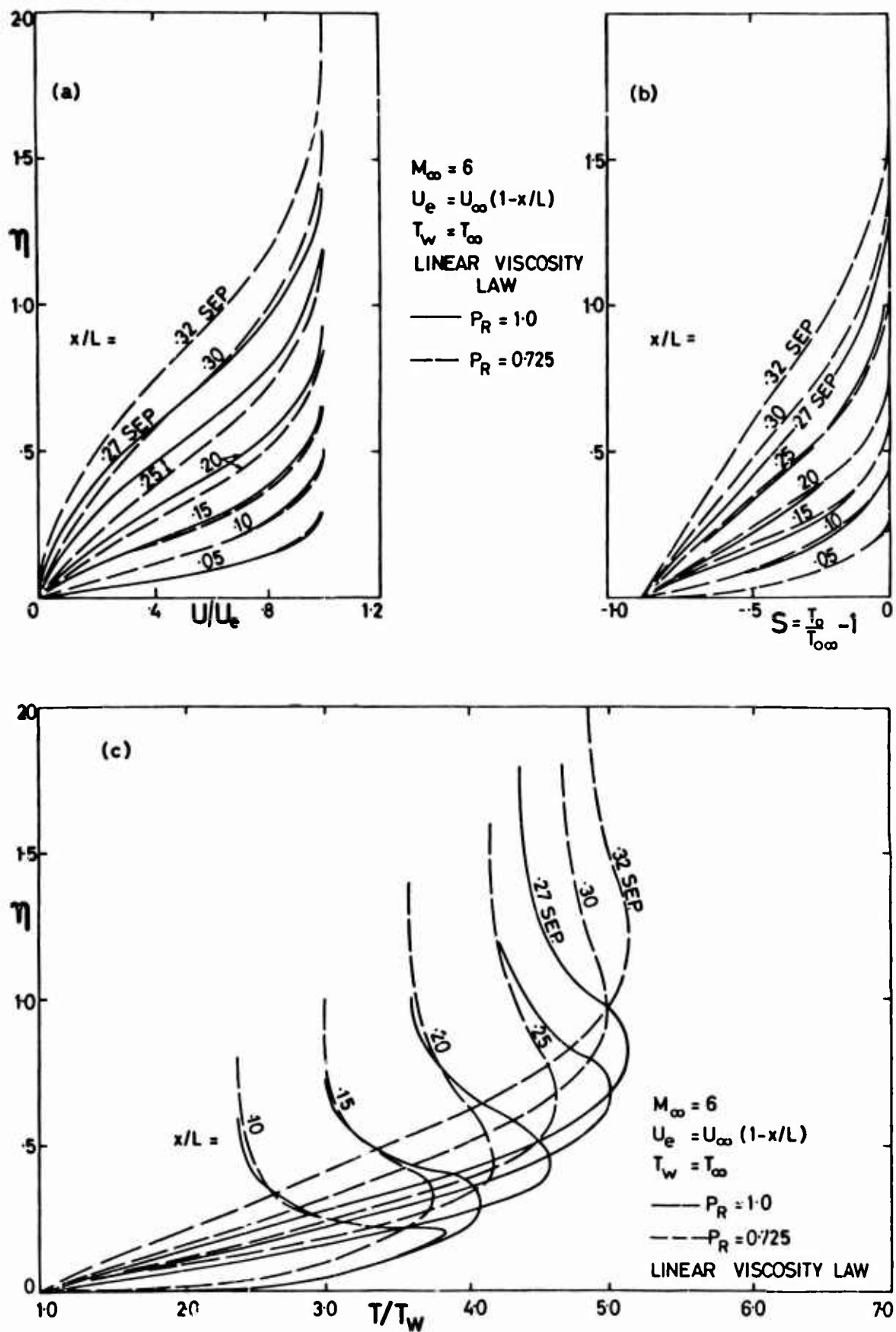


Figure 10 Velocity, stagnation and static temperature profiles for the linearly retarded velocity distribution $M = 6$.

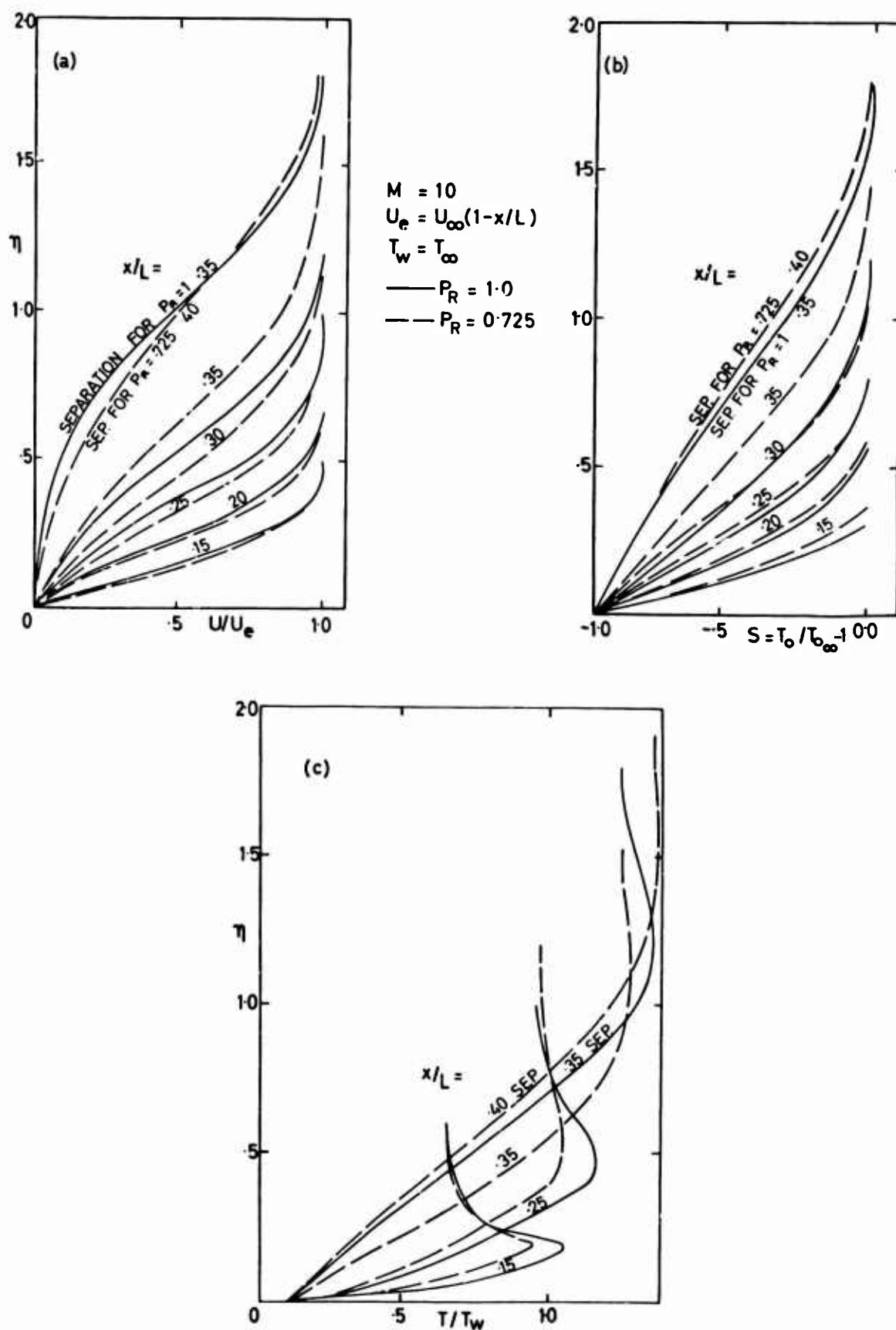


Figure 11 Velocity, stagnation and static temperature profiles for the linearly retarded velocity distribution $M = 10$.

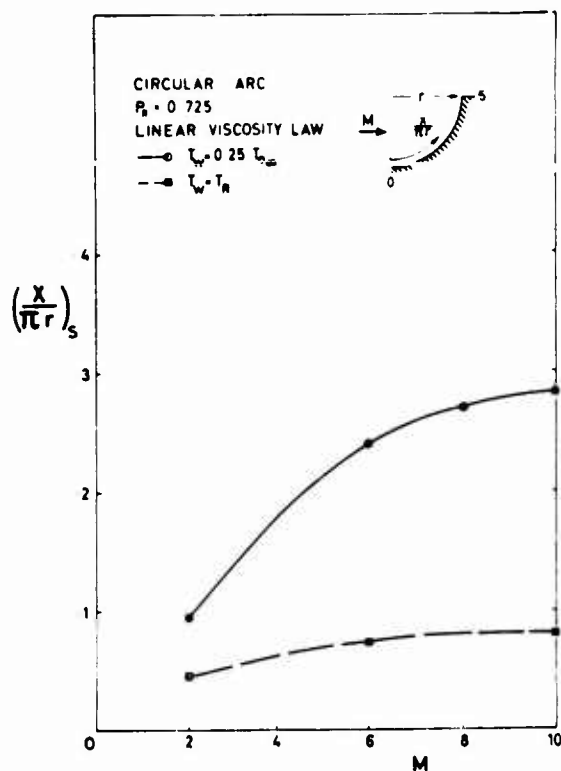


Figure 12 Separation points on a circular arc for adiabatic and cold walls.

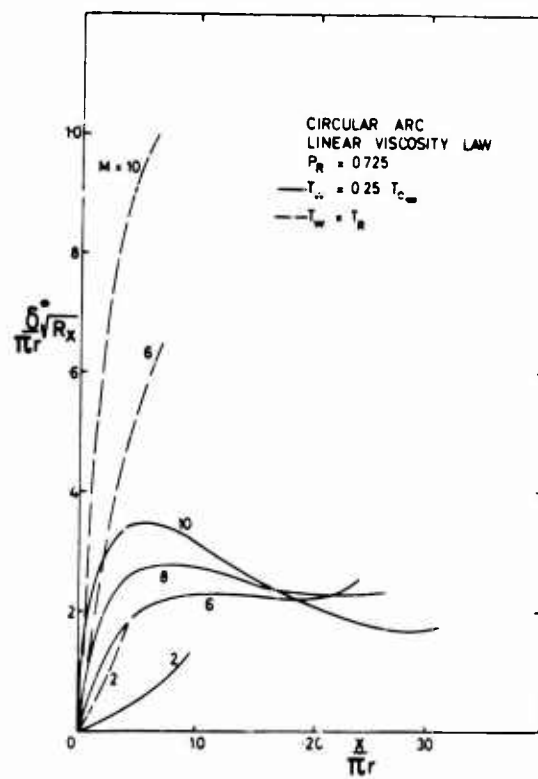


Figure 13 Displacement thickness on the circular arc for adiabatic and cold walls.

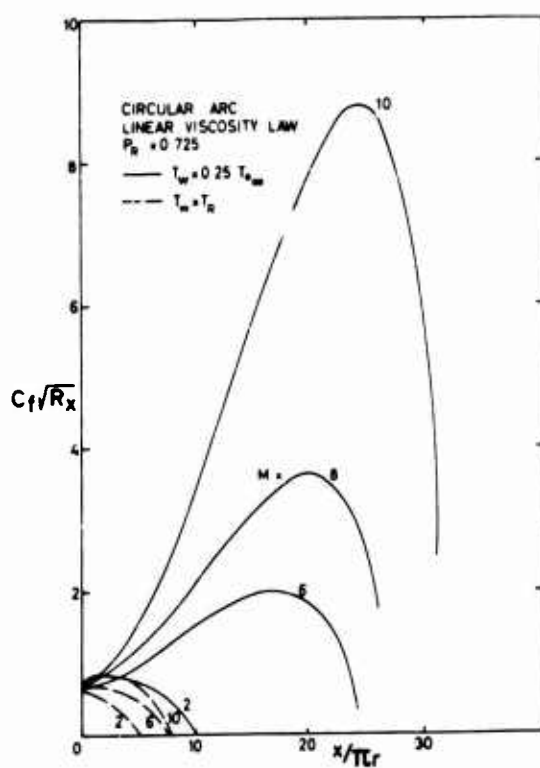


Figure 14 Skin friction on the circular arc for adiabatic and cold walls.

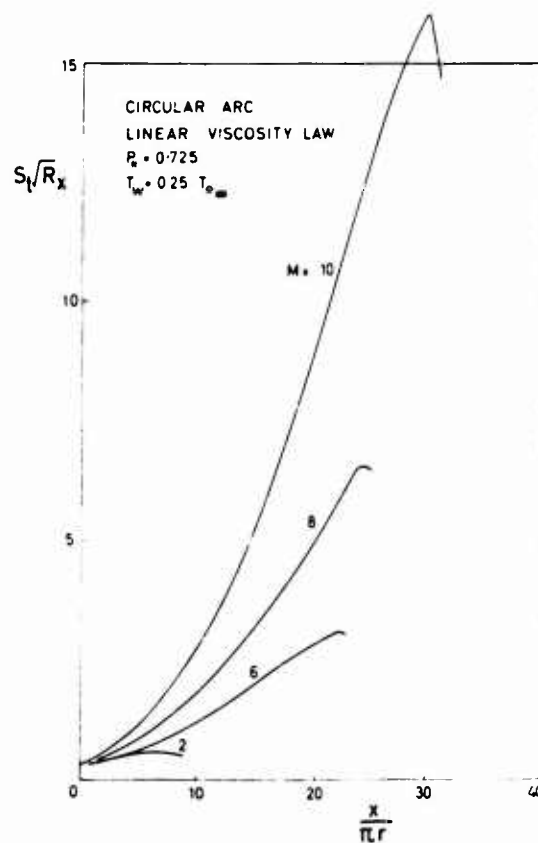


Figure 15 Heat transfer on the circular arc for adiabatic and cold walls.

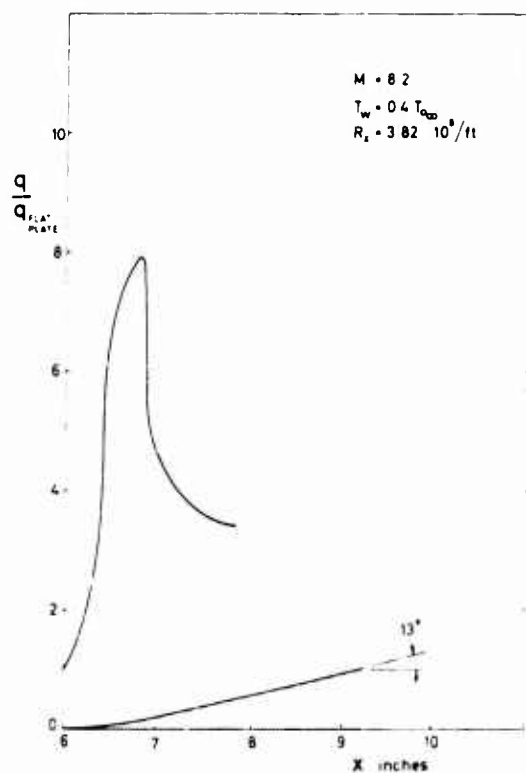


Figure 16 Heat transfer prediction of Monaghan's method on a smoothed-in ramp.

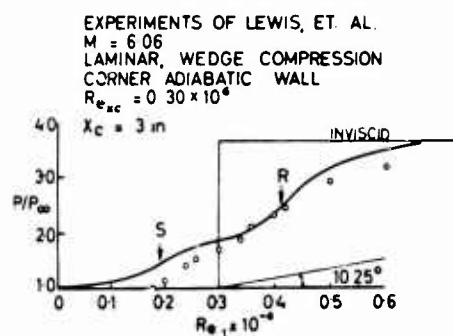
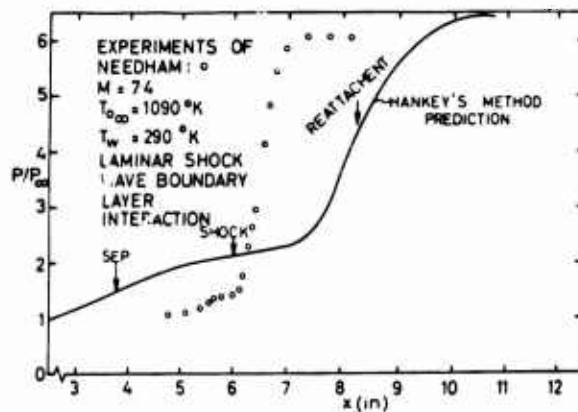


Figure 17 Pressure predictions of Hankey's method for a compression corner and a shock-wave/boundary layer interaction.

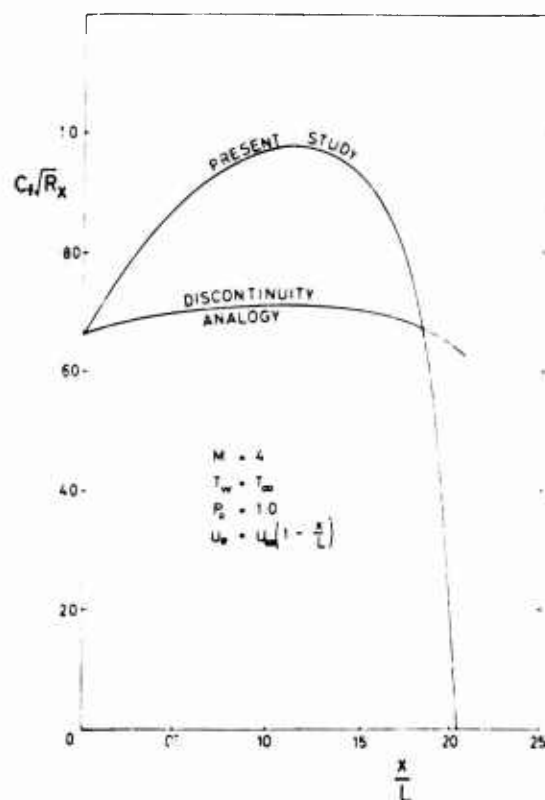


Figure 18 Comparison of present study and discontinuity analogy for a linearly retarded velocity distribution.

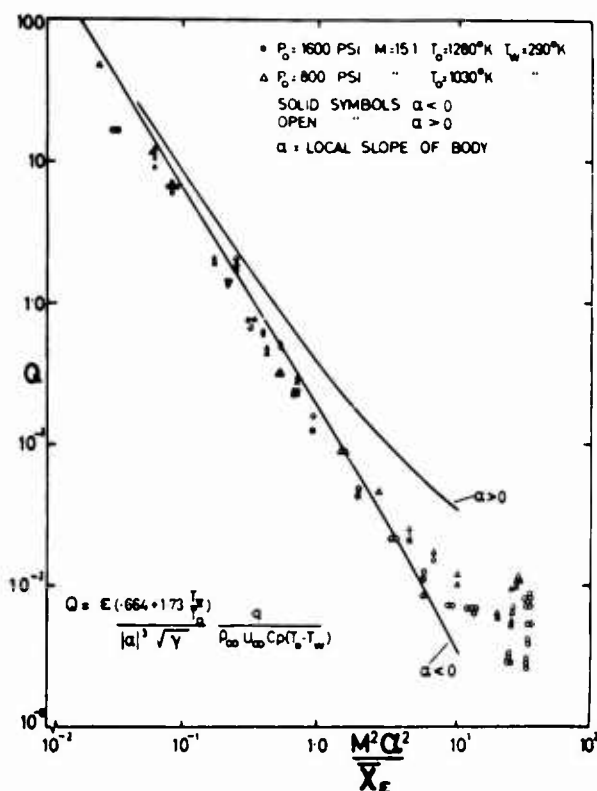


Figure 19 Heat transfer measurements on cubic surface compared to Cheng's theory for flat plates at positive and negative incidence.

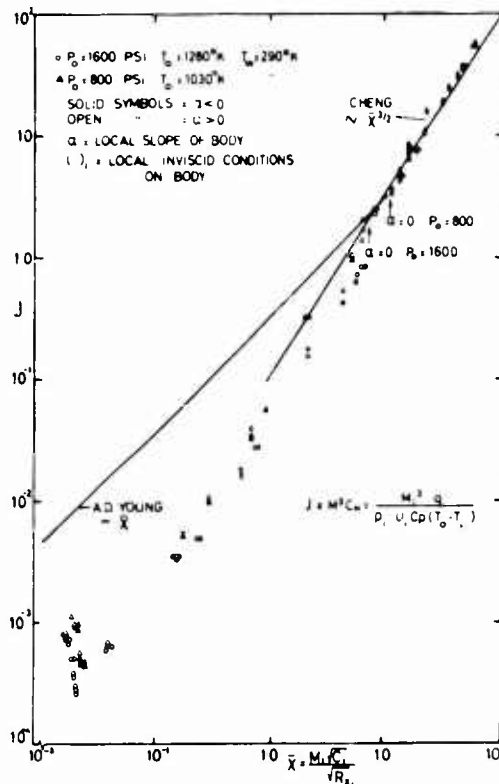


Figure 20 Heat transfer measurements on cubic surface compared to Cheng's theory evaluated at local inviscid conditions.

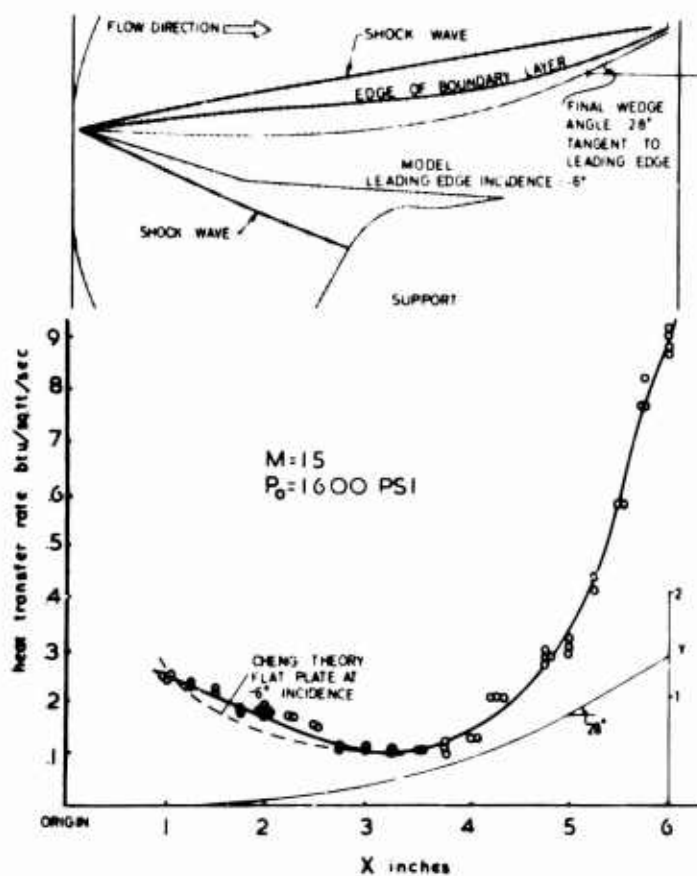


Figure 21

Heat transfer measurements on cubic surface and Cheng's theory for flat plate at incidence. Drawing of schlieren photograph of flow is shown above.

VISCOUS HYPERSONIC FLOW PAST SLENDER
BODIES AT INCIDENCE*

by

Roberto Vaglio-Laurin⁺

Department of Aeronautics & Astronautics
New York University
Bronx, N. Y.
U.S.A.

*The paper is based on research sponsored by the U. S. Air Force Office of Scientific Research (OAR) under Grant AF-AFOSR-818-66

⁺Professor of Aeronautics & Astronautics

SUMMARY

A physical model and a simplified analysis applicable to three-dimensional hypersonic laminar boundary layers with large cross flow are presented. It is shown that the boundary layers in question can be divided into two regions, namely: 1) an outer region where the local density and momentum flux per unit area are comparable to those in the inviscid stream while the cross flow is negligible; 2) an inner region, comprising the major portion of the boundary layer, where the local density and momentum flux per unit area are very small (compared to those in the inviscid flow), the cross flow is important, and the state of motion is controlled by the viscous forces. The flow in the inner region is Couette-like in the streamwise direction and Poiseuille-like in the direction normal to the streamlines of the inviscid flow; the velocity and enthalpy profiles there are governed by ordinary differential equations with solutions that depend parametrically on the local pressure gradients, the local geometry of the inviscid flow streamlines, the local wall temperature ratio and the local thickness of the boundary layer. The only unknown parameter, the boundary layer thickness, can be determined either by matching the solutions in the two regions or by integral momentum considerations employing the aforementioned "exact" profiles for the inner region. A preliminary assessment of the integral method for a two-dimensional flow indicates good agreement between theory and experiments.

VISCOUS HYPERSONIC FLOW PAST SLENDER BODIES AT INCIDENCE

Roberto Vaglio-Laurin

1. INTRODUCTION

Recent studies¹ have indicated that thigh altitude aerodynamics has important effects on lifting reentry performance. The degradation of aerodynamic characteristics at low flight Reynolds number (viz. $Re_{\infty} \approx 2 \times 10^6$, for a slender body) results in appreciable reductions of lateral and longitudinal range. Performance (i.e. lateral range) and flight program (i.e. longitudinal range) exhibit different trends of dependence upon degraded characteristics; hence, realistic mission analyses require detailed consideration of high altitude aerodynamics.

The conditions of interest are characterized by values of the hypersonic viscous parameter $v_{\infty} \geq 10^{-2}$, where $v_{\infty} = M_{\infty}(C/Re_{\infty})^{1/2}$, M_{∞} being the flight Mach number, C the Chapman-Rubesin constant, and Re_{∞} the Reynolds number based on freestream conditions and wetted length L . Theoretical analysis of the flow field becomes increasingly complex as $v_{\infty} > 10^{-2}$. A fundamental understanding of the flow patterns and a quantitative determination of viscous effects has been obtained only for simple two-dimensional (wedges) and axisymmetric (circular cones, ~~powerbodies~~ configurations in the interaction regime^{1,3}. The more complex three-dimensional flow fields of practical interest have received limited theoretical consideration.

Theoretical analyses of hypersonic viscous interactions for two-dimensional sharp wedges² show that maximum lift/drag ratio is attained at large angles of attack, $\alpha \approx v_{\infty}$, such that weak interaction prevails over a major portion of the windward surface of the airfoil. Approximate considerations for three-dimensional bodies indicate a similar trend; again optimum aerodynamic performance is attained at large incidences, e.g. $\alpha \approx 25^\circ$ for $v_{\infty} \approx .25$, with attendant strongly three-dimensional flows. Under conditions of large incidence and large local external Mach number the laminar boundary layer tends to develop a large cross flow relative to the local inviscid streamlines^{3,4}; analysis of the flow then becomes quite complex. Previous studies of three-dimensional hypersonic boundary layers have sought simplification of the problem either by confining attention to similar flows in the neighborhood of symmetry planes⁴ or by introducing the assumption of small cross flow⁷, which is strictly applicable only for moderate Mach number flows over highly cooled surfaces^{5,6}.

In the present paper the general problem is approached by yet another point of view. A simplified physical and mathematical model is constructed by dividing the boundary layer into two regions, namely: 1) a thin outer region of negligible cross flow where the fluid velocity is nearly the same as the external velocity and the density is comparable to the external density; 2) an inner region where the cross flow can be appreciable but the inertia forces are small compared to the viscous forces. The subdivision into two regions has been used previously in connection with two-dimensional problems, viz. Stewartson's study¹⁰ of the strong-interaction region in viscous hypersonic flow past a slender circular cone and Clauser and Lighthill's analysis¹¹ of the axial viscous flow over a long circular cylinder; however, the application to three-dimensional hypersonic boundary layers has not been exploited.

The paper presents a heuristic derivation of the physical and mathematical models. Physical considerations are submitted first (Section 2). Subsequently the simplified analytical statements valid in the two regions are set forth and the determination of matched solutions is discussed; also an approximate method of solution is outlined employing integral method considerations in conjunction with the "exact" profiles appropriate to the inner region (Section 3). Finally a preliminary assessment of the integral method is presented in connection with the viscous interaction problem over an insulated flat plate (Section 4).

2. THE HYPERSONIC LAMINAR BOUNDARY LAYER

It is well known^{8,9} that two-dimensional hypersonic laminar boundary layers exhibit the following characteristics (Fig. 1): 1) a thin outer region, adjacent to the edge, where the density and the momentum flux per unit area rapidly decrease from their inviscid stream values while the streamwise velocity remains essentially undisturbed; 2) an inner region, which encompasses the major portion of the boundary layer, where the local density and momentum flux per unit area are much smaller than the density and the momentum flux per unit area in the inviscid stream.

Associated with these features, forcibly demonstrated also by experiments (Fig. 2), are a particular physical model of the boundary layer flow and a consistent simplified analytical description. On physical grounds it is apparent that the high density fluid in the outer region plays the role of an equivalent solid plate with respect to the low density fluid in the inner region. The equivalent plate, which moves parallel to the actual body surface at the inviscid flow velocity, drags the low-density, low-inertia gas into a Couette flow. This physical model is substantiated by determination of reduced equations and matched solutions valid in the two regions¹⁰; in the inner region the inertia terms may be neglected compared to the viscous terms and the Couette-like behavior of the flow is confirmed.

Obviously three-dimensional hypersonic laminar boundary layers also exhibit two regions characterized by momentum fluxes per unit area of different order of magnitude. The three-dimensional behavior becomes readily apparent if the flow is viewed in a system of orthogonal curvilinear coordinates (x_1, x_2, x_3) having the surface $x_3 = 0$ coincident with the outer surface of the boundary layer* and the lines $(x_2 = \text{constant}, x_3 = 0)$ coincident with the streamlines of the inviscid flow. In this frame of reference the outer region maintains the role of an equivalent solid plate moving parallel to the surface of the body with velocity v_{1e} in the x_1 -direction; the cross flow in this region is small because a) the momentum flux per unit area is comparable to that in the free stream and b) the thickness of the region itself is small compared to the overall boundary layer thickness. The fluid in the inner region moves under the simultaneous action of the equivalent outer plate, of the actual wall and of the transversal pressure gradient $\partial p / \partial x_2$; because of the low density and inertia of this fluid the motion is dominated by the viscous forces and, therefore, is Couette-like in the x_1 -direction (of the inviscid streamlines) and Poiseuille-like in the x_2 -direction (orthogonal to the inviscid streamlines, see Fig. 3).

Qualitative corroboration of the three-dimensional model is obtained by inspection of the velocity profiles for "exact" solutions, e.g. the similar solutions for the boundary layer near a plane of symmetry⁴. If a sketch of the equivalent solid plate is superposed on typical profiles of this family, the Couette- and Poiseuille-like behaviors in the inner region are quite apparent. Also apparent are the boundary conditions for the inner flow; in accord with the physical model one requires no slip relative to the body surface ($x_3 = -\delta$) and to the equivalent outer plate ($x_3 = 0$), which moves with velocity v_{1e} . It should be noted that the profiles in Fig. 4 are plotted versus the Howarth-transformed variable η ; inverse transformation to physical coordinates would shrink dramatically the thickness of the outer region, again in accord with the proposed model.

The aforementioned physical considerations provide straightforward guidelines for deriving a simplified mathematical statement of the problem; this is discussed in the following section.

3. THE MATHEMATICAL STATEMENT

With a view toward the analysis of three-dimensional problems encompassing the complete spectrum from strong-to, weak-to, negligible- interaction, the governing equations are stated here in a form that fully accounts for transverse curvature effects. Simultaneous consideration of regions of strong- and weak- interaction is often required in the analysis of viscous hypersonic flows past slender bodies at incidence; the typical example of $M_\infty = 41$ flow over a 3° half-angle circular cone at 10° incidence (Fig. 5) clearly exhibits weak interaction on the windward side and strong interaction on the leeward side. Under such conditions the metric elements (e_1, e_2, e_3) associated with the streamline-fixed orthogonal curvilinear coordinate system defined in the previous section are functions of all three space variables. The appropriate form of the boundary layer equations for a perfect gas follows immediately from the derivation outlined in Ref. 6.

$$\frac{\partial}{\partial x_1} (e_2 e_3 \rho v_1) + \frac{\partial}{\partial x_2} (e_1 e_3 \rho v_2) + \frac{\partial}{\partial x_3} (e_1 e_2 \rho v_3) = 0 \quad (1)$$

$$e_1 e_2 \rho \left(v_1 \frac{\partial v_1}{e_1 \partial x_1} + v_2 \frac{\partial v_1}{e_2 \partial x_2} + v_3 \frac{\partial v_1}{e_3 \partial x_3} \right) + \rho \left(v_1 v_2 \frac{\partial e_1}{\partial x_2} - v_2^2 \frac{\partial e_2}{\partial x_1} \right) - \quad (2)$$

$$e_2 \rho e v_{1e} \frac{\partial v_{1e}}{\partial x_1} = \frac{\partial}{\partial x_3} \left(\mu e_1 e_2 \frac{\partial v_1}{e_3 \partial x_3} \right)$$

$$e_1 e_2 \rho \left(v_1 \frac{\partial v_2}{e_1 \partial x_1} + v_2 \frac{\partial v_2}{e_2 \partial x_2} + v_3 \frac{\partial v_2}{e_3 \partial x_3} \right) + \quad (3)$$

$$\rho \left[v_1 v_2 \frac{\partial e_2}{\partial x_1} - v_{1e}^2 \frac{\partial e_1}{\partial x_2} \left(\frac{v_1^2}{v_{1e}^2} - \frac{\rho}{\rho_e} \right) \right] = \frac{\partial}{\partial x_3} \left(\mu e_1 e_2 \frac{\partial v_2}{e_3 \partial x_3} \right)$$

*Parallel to the body surface for a non-interacting boundary layer.

$$e_1 e_2 \rho \left(v_1 \frac{\partial H}{e_1 \partial x_1} + v_2 \frac{\partial H}{e_2 \partial x_2} + v_3 \frac{\partial H}{e_3 \partial x_3} \right) = \frac{\partial}{e_3 \partial x_3} \left[\mu e_1 e_2 \left(\frac{\partial H}{e_3 \partial x_3} + \frac{1-Pr}{Pr} \frac{\partial h}{e_3 \partial x_3} \right) \right] \quad (4)$$

$$\frac{\rho}{\rho_e} = \frac{h}{h_e} ; \quad h + \frac{v_1^2 + v_2^2}{2} = H ; \quad \mu = \mu(h) \quad (5)$$

where x_i ($i = 1, 2, 3$) denotes the curvilinear coordinates, e_i the associated metric elements, v_i the associated components of velocity, ρ the density, μ the viscosity, h the enthalpy, H the stagnation enthalpy, Pr the Prandtl number, and the subscript e identifies properties of the inviscid flow. Associated with the Eqs. (1) through (5) are the boundary conditions (for impermeable wall)

$$x_3 = x_{3 \text{ wall}} , \quad v_1 = v_2 = v_3 = 0 , \quad H = H_w \quad (6a)$$

$$x_3 \rightarrow \infty , \quad v_1 \rightarrow v_{1e} , \quad v_2 \rightarrow 0 , \quad H \rightarrow H_e \quad (6b)$$

The possibility of further simplifying the equations (1) through (5) into forms appropriate to the different regions of the boundary layer must now be assessed. The effort is warranted if, ultimately, the solutions of the approximate equations valid in the different regions can be matched consistently to provide a complete description of the overall boundary layer. Thus, the consistency proof can only be obtained a posteriori.

According to the physical model discussed in Section 2 the outer region is characterized by

$$\left. \begin{aligned} \bar{v}_1 &= (v_{1e} - v_1)/v_{1e} \ll 1 ; & \bar{v}_2 &= v_2/v_{1e} \ll 1 \\ \bar{H} &= (H_e - H)/H_e \ll 1 ; \\ \rho &= O(\rho_e) ; & \rho v_1^2 &= O(\rho_e v_{1e}^2) \end{aligned} \right\} \quad (7)$$

The consistency of the small cross flow assumption is verified by substitution of (7) into (3) and order of magnitude analysis. The governing equations can then be reduced to the form

$$\frac{\partial}{\partial x_1} (e_2 e_3 \rho v_{1e}) + \frac{\partial}{\partial x_3} (e_1 e_2 \rho v_3) = 0 \quad (8)$$

$$e_1 e_2 \rho \left(v_{1e} \frac{\partial \bar{v}_1}{e_1 \partial x_1} + v_3 \frac{\partial \bar{v}_1}{e_3 \partial x_3} \right) + e_2 \rho_e \frac{\partial v_{1e}}{\partial x_1} = \frac{\partial}{e_3 \partial x_3} \left(\mu e_1 e_2 \frac{\partial \bar{v}_1}{e_3 \partial x_3} \right) \quad (9)$$

$$e_1 e_2 \rho \left(v_{1e} \frac{\partial \bar{H}}{e_1 \partial x_1} + v_3 \frac{\partial \bar{H}}{e_3 \partial x_3} \right) = \frac{\partial}{e_3 \partial x_3} \left[\mu e_1 e_2 \left(\frac{\partial \bar{H}}{e_3 \partial x_3} - \frac{1-Pr}{Pr} \frac{1}{H_e} \frac{\partial h}{e_3 \partial x_3} \right) \right] \quad (10)$$

$$\frac{\rho}{\rho_e} = \frac{h}{h_e} ; \quad \frac{h-h_e}{H_e} = \frac{v_{1e}^2}{H_e} \bar{v}_1 - \bar{H} ; \quad \mu = \mu(h) \quad (11)$$

for the streamwise velocity, the density and the enthalpy. The (small) cross flow velocity is determined subsequently from the equation

$$e_1 e_2 \rho \left(v_{1e} \frac{\partial \bar{v}_2}{e_1 \partial x_1} + v_3 \frac{\partial \bar{v}_2}{e_3 \partial x_3} \right) + \rho \left[v_{1e} \bar{v}_2 \frac{\partial e_2}{\partial x_1} - v_{1e} \frac{\partial e_1}{\partial x_2} \left(\frac{v_1^2}{2} - \frac{\rho_e}{\rho} \right) \right] = \frac{\partial}{e_3 \partial x_3} \left(\mu e_1 e_2 \frac{\partial \bar{v}_2}{e_3 \partial x_3} \right) \quad (12)$$

The boundary conditions for equations (8) through (11) are

$$\eta \rightarrow 0 \quad ; \quad \bar{v}_1 \rightarrow \left(\frac{v_{1e} - v_1}{v_{1e}} \right)_{\text{inner}} \quad ; \quad v_3 \rightarrow 0 \quad ; \quad \bar{H} \rightarrow \left(\frac{H_e - H}{H_e} \right)_{\text{inner}} \quad (13-a)$$

$$\eta \rightarrow \infty \quad ; \quad \bar{v}_1 \rightarrow 0 \quad ; \quad \bar{H} \rightarrow 0 \quad (13-b)$$

with η a Levy-Lees-like variable (except for the density transformation) defined by

$$\eta = \frac{v_{1e}}{(2\xi)^{1/2}} \int_{x_3 \text{ wall}}^{x_3} e_2 e_3 dx_3 \quad ; \quad \xi = \int_0^{x_1} \rho^* \mu^* v_{1e} e_2^2 e_1 dx_1 \quad (14)$$

The boundary conditions for the cross flow equation (12) are

$$\eta \rightarrow 0 \quad ; \quad \bar{v}_2 \rightarrow \left(\frac{v_2}{v_{1e}} \right)_{\text{inner}} \quad (15-a)$$

$$\eta \rightarrow \infty \quad ; \quad \bar{v}_2 \rightarrow 0 \quad (15-b)$$

The equations (8) through (12) can further be reduced to ordinary differential equations if local similarity is assumed valid; within these limits typical solutions can be determined and their matching with the inner solutions can be tested.

In the inner region the momentum flux per unit area becomes very small and the viscosity very large, viz. $\rho(v_1^2 + v_2^2)/\rho_e v_{1e}^2 \ll 1$ and $\mu/\mu_e \gg 1$. If the rates of convergence (divergence) of the streamlines $(\partial e_2/\partial x_1)$ and $(\partial e_1/\partial x_2)$ are $O(1)$ the viscous terms then dominate in equations (2)* and (4) while the viscous and pressure gradient terms dominate in equation (3). However, if the particular inviscid flow pattern is characterized by $(\partial e_i/\partial x_j)$, $(i, j = 1, 2)$, with magnitude comparable to the density ratio $(\rho_e/\rho)_{\text{inner}}$, the Coriolis terms must be retained in the momentum equations. With allowance for inviscid flow patterns having strongly converging (or diverging) streamlines, the equations for the inner region take the form

$$\frac{\partial}{e_3 \partial x_3} \left(\mu e_1 e_2 \frac{\partial v_1}{e_3 \partial x_3} \right) = \rho v_2 \left(v_1 \frac{\partial e_1}{\partial x_2} - v_2 \frac{\partial e_2}{\partial x_1} \right) \quad (16)$$

$$\frac{\partial}{e_3 \partial x_3} \left(\mu e_1 e_2 \frac{\partial v_2}{e_3 \partial x_3} \right) - \left(\rho v_1^2 \frac{\partial e_1}{\partial x_2} \right)_e = - \rho v_1 \left(v_1 \frac{\partial e_1}{\partial x_2} - v_2 \frac{\partial e_2}{\partial x_1} \right) \quad (17)$$

$$\frac{\partial}{e_3 \partial x_3} \left[\mu e_1 e_2 \left(\frac{\partial H}{e_3 \partial x_3} + \frac{1 - \text{Pr}}{\text{Pr}} \frac{\partial h}{e_3 \partial x_3} \right) \right] = 0 \quad (18)$$

$$\frac{\rho}{\rho_e} = \frac{h_e}{h} \quad ; \quad h + \frac{v_1^2 + v_2^2}{2} = H \quad ; \quad \mu = \mu(h) \quad (19)$$

with the boundary conditions

$$x_3 = x_3 \text{ wall} \quad ; \quad v_1 = v_2 = 0 \quad ; \quad H = H_w \quad (20-a)$$

*The pressure gradient term in equation (2) can be neglected because at hypersonic velocities, the derivative $(\partial v_{1e}/\partial x_1)$ is small.

$$x_3 \rightarrow 0 \quad ; \quad v_1 \rightarrow (v_1)_{\text{outer}} \quad ; \quad v_2 \rightarrow (v_2)_{\text{outer}} \quad ; \quad H \rightarrow (H)_{\text{outer}} \quad (20-b)$$

If the quantities $(\partial e_1 / \partial x_1)$ are small compared to (ρ_e / ρ) the righthand sides of equations (16) and (17) can be set to zero. Among the other cases it is of interest to note those characterized by $(\partial e_2 / \partial x_1)$ negative with magnitude comparable to (ρ_e / ρ) ; equation (17) has then harmonic character and may exhibit oscillatory solutions⁷ for the cross flow velocity v_2 .

The equations (16) through (18) are ordinary differential equations; hence, the flow in the inner region satisfies a form of local similarity. The history of the boundary layer manifests itself parametrically through the thickness of the inner region, viz. the coordinate x_3 of the wall, which is unknown a priori and must be determined by matching of inner and outer solutions.

As noted above the matching process also provides the ultimate test of the proposed two-layer model. Obviously the test is most conveniently carried out for self-preserving flows where the motion in the outer region is also governed by ordinary differential equations. A successful example of matching in a two-dimensional flow is provided by Stewartson's solution for the strong-interaction region near the tip of a slender cone¹⁰; a straightforward extension of Stewartson's results gives as a second example the strong-interaction region on a flat plate with a sharp leading edge. A comparable test for three-dimensional problems consists in applying the method of this paper to reproduce the solutions of Ref. 4 for boundary layers near a symmetry plane; this investigation is currently underway.

If the boundary layer flow is not self-preserving the determination of the outer solution and its matching with the inner solution become somewhat laborious. The assumption of local similarity would provide some simplification; however, its range of applicability for three-dimensional problems remains to be demonstrated by comparison with either experiment or careful numerical solutions of the full equations. An alternative is provided by an integral method approach, viz. an extension of the method successfully employed by Glauert and Lighthill¹¹ in the study of two-dimensional boundary layers over very slender bodies*. For the class of boundary layers investigated by those authors, as well as for the hypersonic boundary layers considered here, the momentum defect is concentrated in the inner region; accordingly, integral method considerations based on the "exact" profiles determined by integration of the equations for the inner region (with the thickness $\delta = x_{3, \text{wall}}$ as parameter) lead to accurate results, e.g. within 15% for the problem of Ref. 11.

In integral method analyses of three-dimensional boundary layers with heat transfer and $Pr \neq 1$ three thicknesses must be considered, viz. δ_1 for the streamwise motion, δ_2 for the cross flow and δ_H for the energy. If $Pr = 1$ and the streamwise pressure gradient and Coriolis accelerations are negligible, δ_H may be set equal to δ_1 ; for these conditions two partial differential equations in δ_1 and δ_2 are readily obtained by applying integral considerations to the x_1 - and x_2 -momentum equations

$$\begin{aligned} \frac{\partial}{\partial x_1} \int_{x_3 w(\delta_1)}^0 e_2 e_3 \rho v_1 (v_1 - v_{1e}) dx_3 + \frac{\partial v_{1e}}{\partial x_1} \int_{x_3 w(\delta_1)}^0 e_2 e_3 (\rho v_1 - \rho_e v_{1e}) dx_3 \\ - \left(\mu e_1 e_2 \frac{\partial v_1}{\partial x_3} \right)_{x_3} = x_{3w}(\delta_1) \end{aligned} \quad (21)$$

$$\begin{aligned} - \frac{\partial}{\partial x_2} \int_{x_3 w(\delta_1)}^0 e_1 e_3 \rho v_2 (v_1 - v_{1e}) dx_3 - \int_{x_3 w(\delta_1)}^0 e_3 \rho v_2 \left(v_1 \frac{\partial e_1}{\partial x_2} - v_2 \frac{\partial e_2}{\partial x_1} \right) dx_3 \\ \frac{\partial}{\partial x_1} \int_{x_3 w(\delta_2)}^0 e_2 e_3 \rho v_1 v_2 dx_3 + \frac{\partial}{\partial x_2} \int_{x_3 w(\delta_2)}^0 e_1 e_3 \rho v_2^2 dx_3 + \\ \left(\frac{\rho v_1^2}{e_1 e_2} \frac{\partial e_1}{\partial x_2} \right)_e \int_{x_3 w(\delta_2)}^0 e_1 e_2 e_3 dx_3 - \int_{x_3 w(\delta_2)}^0 e_3 \rho v_1 \left(v_1 \frac{\partial e_1}{\partial x_2} - v_2 \frac{\partial e_2}{\partial x_1} \right) dx_3 \\ \left(\mu e_1 e_2 \frac{\partial v_2}{\partial x_3} \right)_{x_3} = 0 \end{aligned} \quad (22)$$

*Stewartson¹⁰ has previously suggested such extension for two-dimensional interaction problems

The terms at the righthand side of (21) represent the effect of the cross flow on the streamwise momentum balance.

Equations (21) and (22) can be integrated upon stipulation of appropriate initial conditions, e.g. δ_1 given on $(x_1 = x_1^{(0)}, 0 \leq x_2 \leq l)$, and of boundary conditions, e.g. $(\partial\delta_1/\partial x_2)$ given on $(x_1 \geq x_1^{(0)}, x_2 = 0)$ and on $(x_1 \geq x_1^{(0)}, x_2 = l)$. In the absence of viscous interactions the pressure field is prescribed a priori and δ_1, δ_2 are the only unknown quantities in (21), (22). If viscous interactions are present the pressure field can be related directly to the displacement thickness δ^* by typical approximations, e.g. tangent cone; in turn, δ^* can be identified with either δ_1 or δ_2 (whichever is larger) since for the considered hypersonic conditions

$$\delta^* = \text{div} \left\{ \int_0^{\delta} \left[\vec{v}_{1e} \cdot \frac{\rho}{\rho_e} (\vec{v}_1 + \vec{v}_2) \right] e_3 dx_3 \right\} / \text{div} \vec{v}_{1e} \approx \delta \quad (23)$$

4. SOME PRELIMINARY RESULTS

A preliminary assessment of the accuracy afforded by the integral method has been obtained in connection with the problems of strong- and weak- pressure interactions on a flat plate with a sharp leading edge. Integration of equation (21), reduced to two-dimensional form, yields the following equations for the pressure on an insulated flat plate in a perfect gas ($\gamma = 7/5$) stream

$$p/p_\infty = 1 + 0.438 \bar{\chi} \quad p/p_\infty = 0.624 \bar{\chi}$$

$$\bar{\chi} = M_\infty^3 (C/Re_{\infty X})^{1/2}$$

for weak- and strong- interaction, respectively. These predictions compare favorably with experiments, as shown in Fig. 6, and thus provide some confidence for more extensive applications.

5. CONCLUDING REMARKS

A simplified physical model and a mathematical description have been set forth for three-dimensional hypersonic laminar boundary layers with cross flow of arbitrary magnitude. According to the model the flow over the major portion of the boundary layer is dominated by viscous forces and, therefore, is Couette-like in the streamwise direction and Poiseuille-like in the cross flow direction. The point of view leads to drastic simplifications in the analysis and substantially lifts its dependence from laborious numerical solutions. The simplicity and physical grounding of the model suggest the possibility of interesting extensions, e.g., to turbulent flows, and of numerous applications, e.g. internal as well as external three-dimensional hypersonic flows.

REFERENCES

1. Hidalgo, H.
Vaglio-Laurin, R. "High Altitude Aerodynamics and Its Effects on Lifting Reentry Performance", Proceedings of the XVIII Astronautical Congress, Pergamon Press (in publication).
2. Mirels, H.
Lewellen, W. S. "Hypersonic Viscous Interaction Theory for Wedge Wings", J. of Spacecraft and Rockets 4, 492-497 (1967).
3. Cheng, H. K. "The Shock Layer Concept and Three-Dimensional Hypersonic Boundary Layers", Cornell Aeronautical Lab. Inc., Rept. AF-1285-A-3 (January 1961).
4. Trella M.
Libby, P. A. "Similar Solutions for the Hypersonic Laminar Boundary Layer Near a Plane of Symmetry", AIAA J. 3, 75-83 (1965).
5. Vaglio-Laurin, R. "Laminar Heat Transfer on Three-Dimensional Blunt Nosed Bodies in Hypersonic Flow", ARS J. 29, 123-129 (1959).
6. Vaglio-Laurin, R. "Turbulent Heat Transfer on Blunt Nosed Bodies in Two-Dimensional and General Three-Dimensional Hypersonic Flow", J. Aero. Sci. 27, 27-36 (1960); also WADC TN 58-301 (September 1958).
7. Kang, S. W.
Rae, W. J.
Dunn, M. G. "Effects of Mass Injection on Compressible, Three-Dimensional, Laminar Boundary Layers", AIAA J. 5, 1738-1745 (1967).
8. Hayes, W. D.
Probstein, R. F. "Viscous Hypersonic Similitude", J. Aero. Sci. 26, 815-824 (1959).
9. Stewartson, K. Theory of Laminar Compressible Boundary Layers. Oxford University Press, London, (1964).
10. Stewartson, K. "Viscous Hypersonic Flow Past a Slender Cone", Physics of Fluids 7, 667-675 (1964).
11. Glauert, M. B.
Lighthill, M. J. Proc. Roy. Soc. (London) A230, 188 (1955).
12. Horstman, C. C.
Kussoy, M. I. "Hypersonic Viscous Interaction on Slender Cones" AIAA Paper 68-2 (January 1968).
13. Hayes, W. D.
Probstein, R. F. Hypersonic Flow Theory, Academic Press Inc., New York (1959).

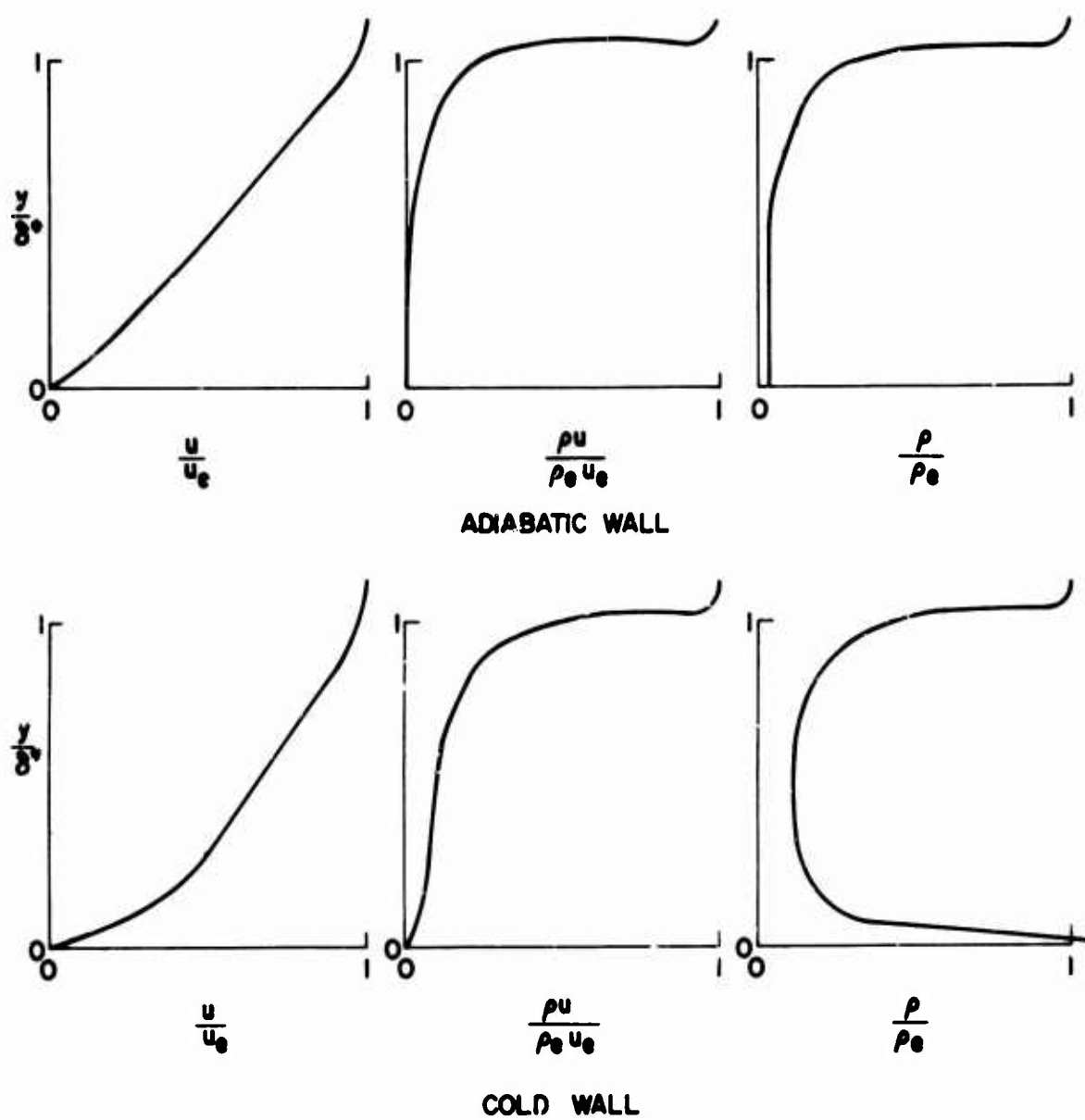


Fig. 1 SCHEMATIC DIAGRAMS OF TYPICAL PROFILES FOR TWO-DIMENSIONAL HYPERSONIC LAMINAR BOUNDARY LAYERS (From Ref. 8)

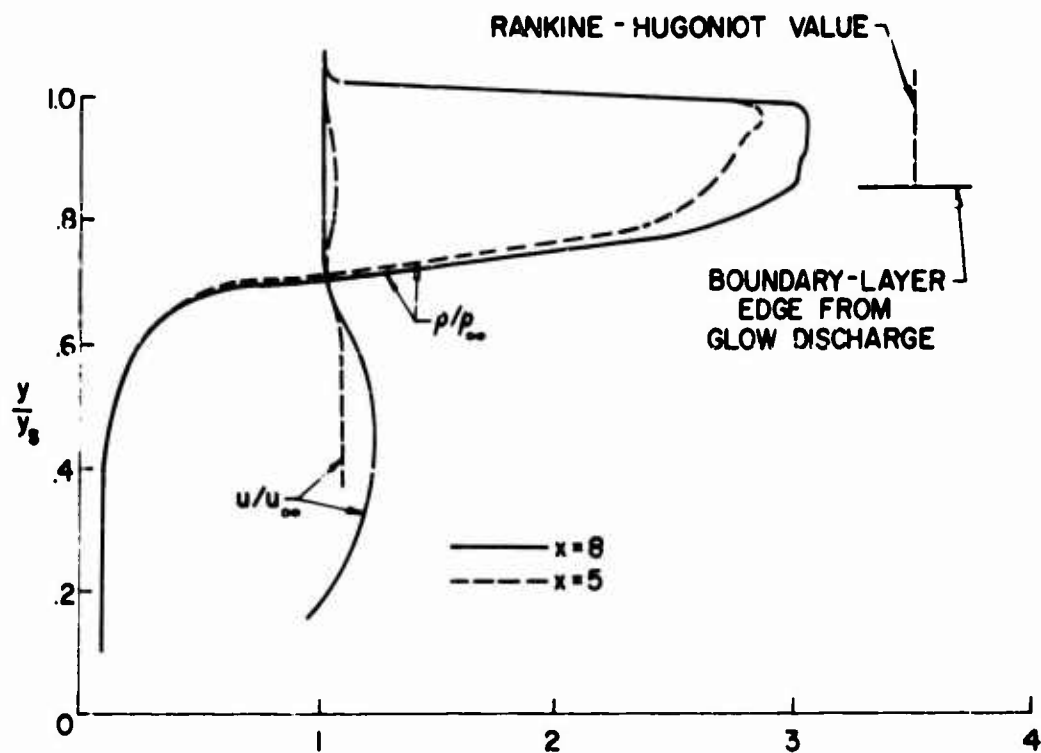
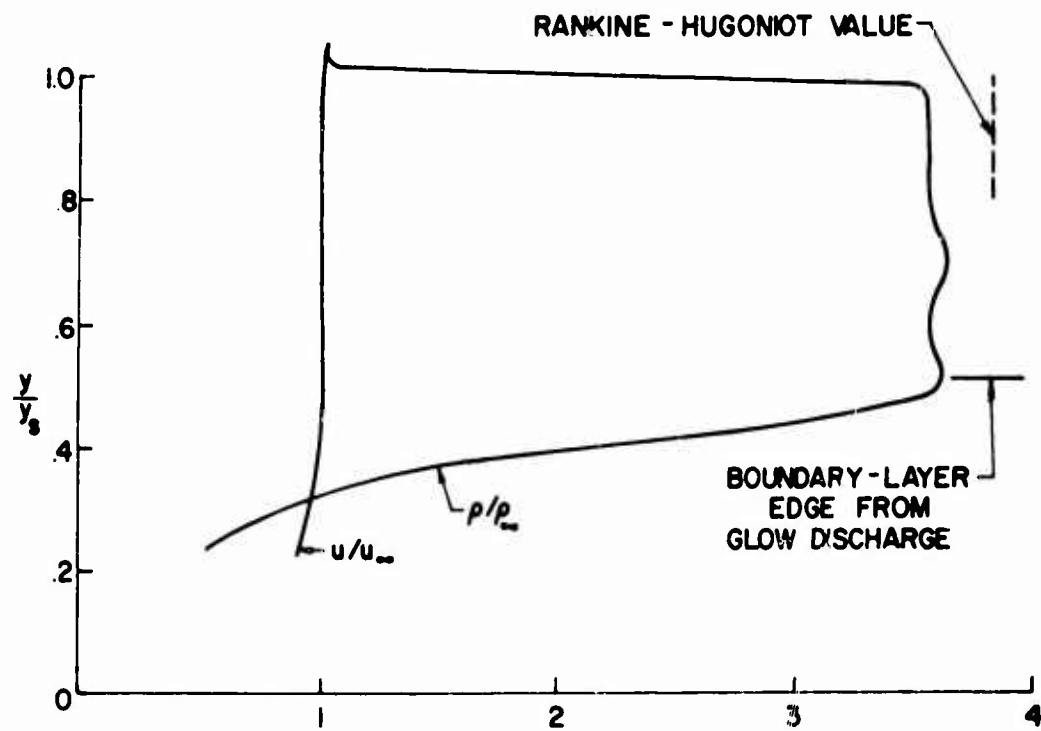
(a) $\alpha = 0^\circ$ (b) $\alpha = 10^\circ$

Fig. 2 TYPICAL EXPERIMENTAL PROFILES OF DENSITY AND VELOCITY IN HYPERSONIC FLOW WITH VISCOUS INTERACTIONS. MEASUREMENTS THROUGH THE SHOCK LAYER ON A SLENDER CIRCULAR CONE (3° HALF-ANGLE) UNDER THE CONDITIONS $M_\infty = 41$, $\gamma = 5/3$, $T_w/T_0 \approx 0.75$. DATA FROM REF. 12

TOP: ZERO INCIDENCE

BOTTOM: WINDWARD SIDE AT 10° INCIDENCE

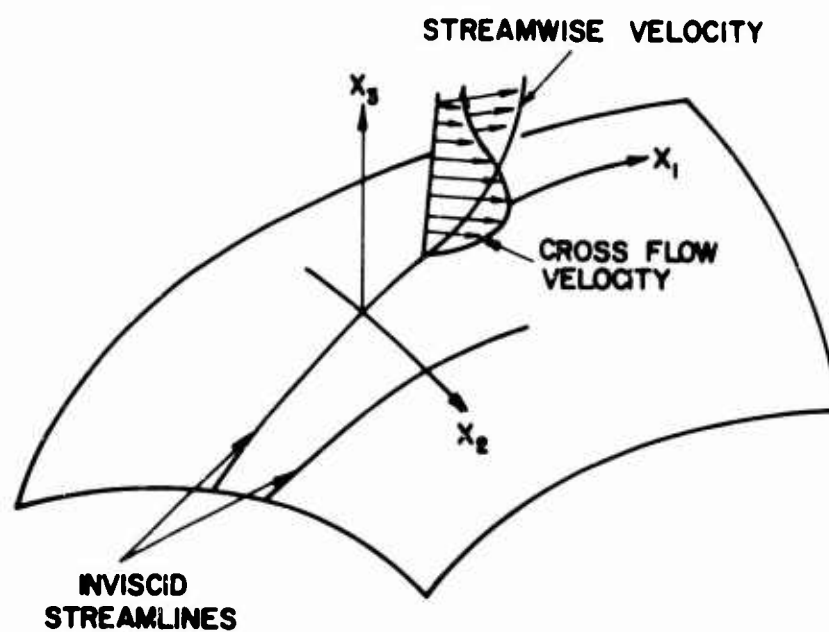
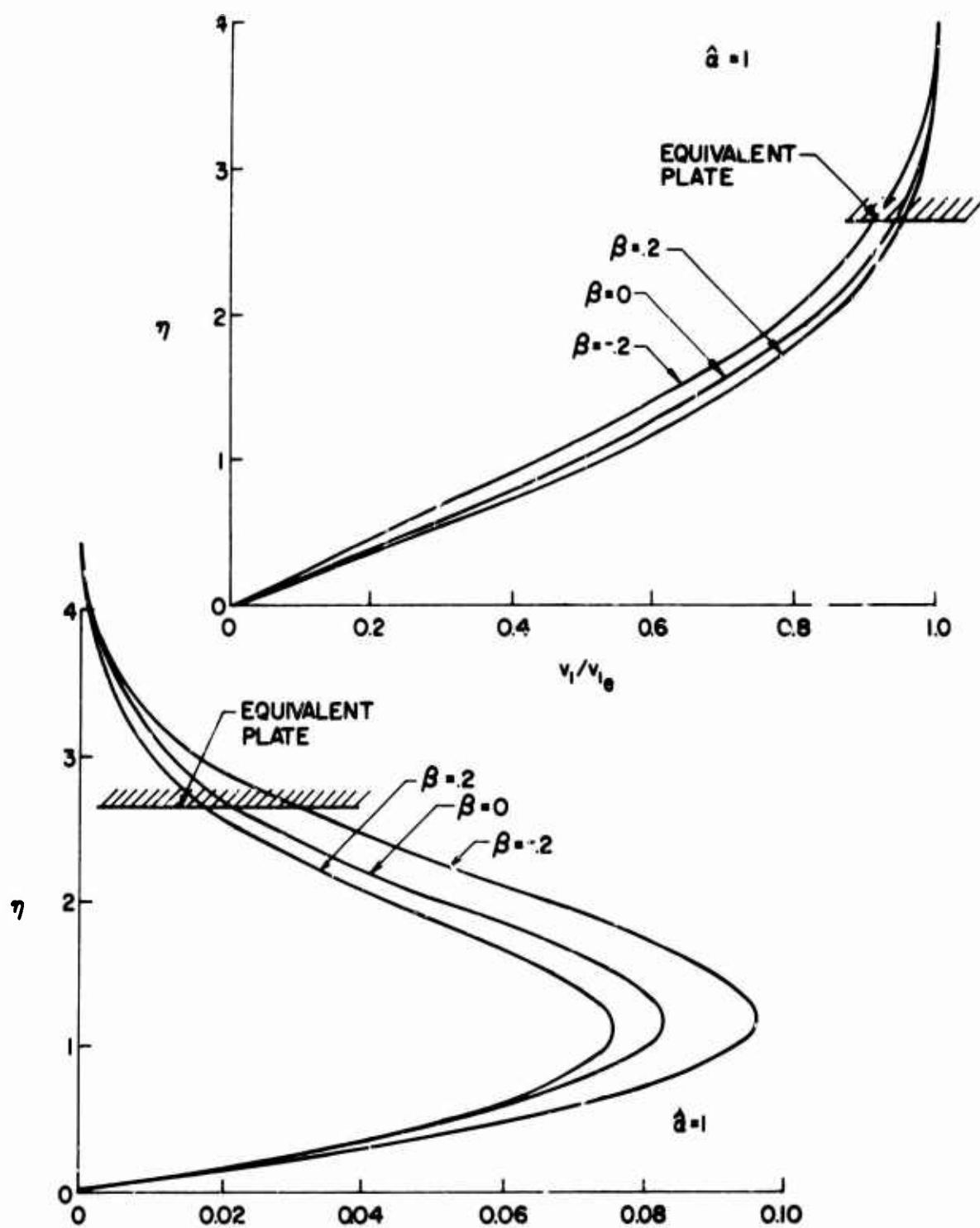


Fig. 3 SCHEMATIC DIAGRAM OF ORTHOGONAL CURVILINEAR COORDINATE SYSTEM



$$\left[1 - \frac{v_{1e}^2}{2H_0} \right] \left[\frac{\partial v_2 / \partial x_2}{\partial v_{2e} / \partial x_2} \right]$$

Fig. 4 SCHEMATIC DIAGRAM OF VELOCITY PROFILES FOR THE HYPERSONIC LAMINAR BOUNDARY LAYER NEAR A PLANE OF SYMMETRY. PROFILES FROM REF. 4. β STREAMWISE PRESSURE GRADIENT PARAMETER; \hat{a} CROSS FLOW PARAMETER ($\hat{a} > 0$ FOR DIVERGING STREAMLINES)

TOP: STREAMWISE VELOCITY

BOTTOM: CROSS FLOW VELOCITY

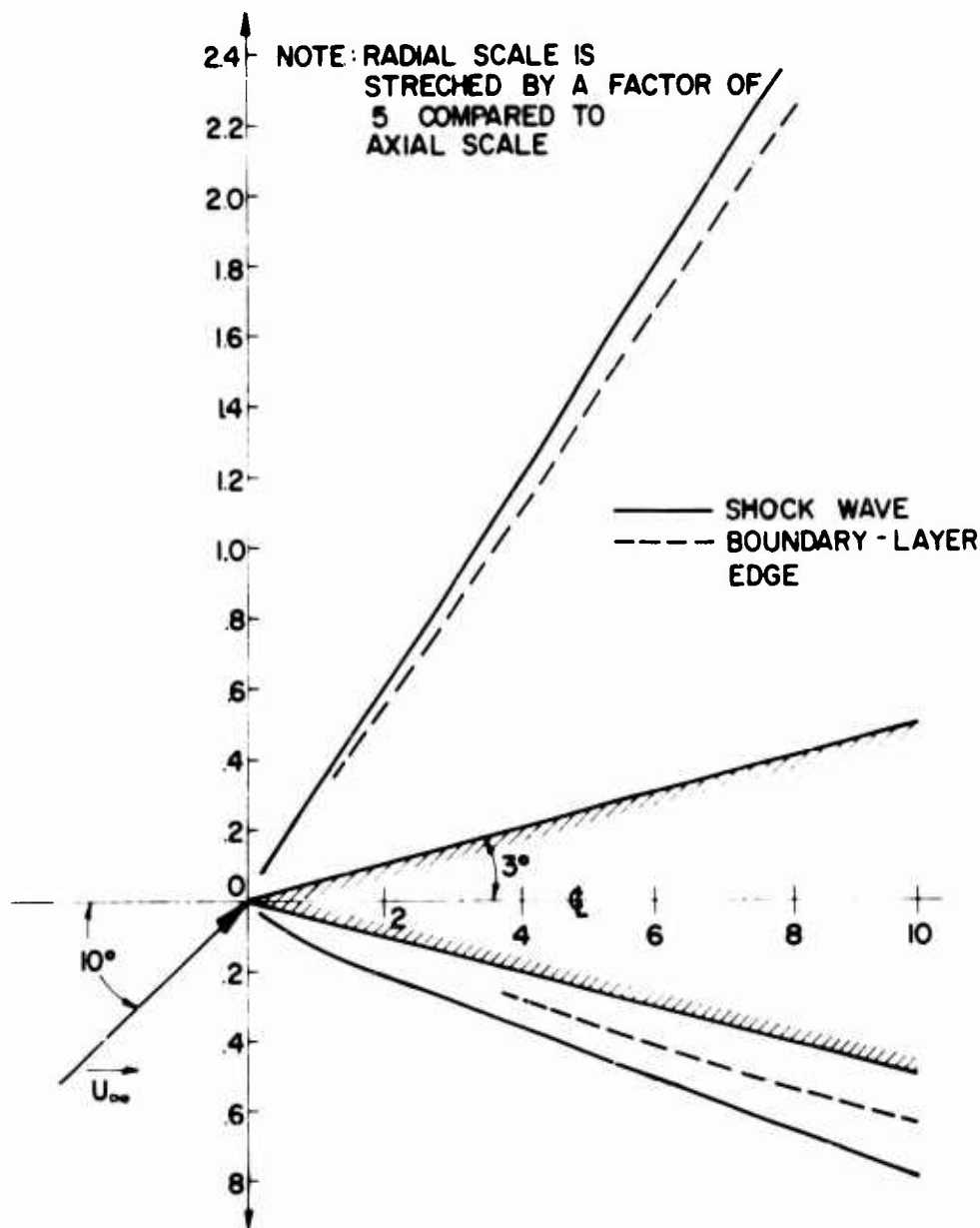


Fig. 5 SCHEMATIC DIAGRAM OF THE HYPersonic FLOW FIELD OVER A SLENDER CIRCULAR CONE AT INCIDENCE IN THE PRESENCE OF VISCOUS INTERACTION. EXPERIMENTAL DATA FOR SHOCK-LAYER AND BOUNDARY LAYER THICKNESSES FROM REF. 12. EXPERIMENTS ON A 3° HALF-ANGLE CONE AT INCIDENCE $i = 10^\circ$ IN A HELIUM STREAM ($\gamma = 5/3$) AT MACH NUMBER $M_\infty = 41$; WALL TEMPERATURE RATIO $T_w/T_0 \approx 0.75$.
NOTE AT A GIVEN DISTANCE FROM THE APEX THE SIMULTANEOUS OCCURRENCE OF WEAK-INTERACTION ON THE WINDWARD SIDE AND STRONG-INTERACTION ON THE LEEWARD SIDE.

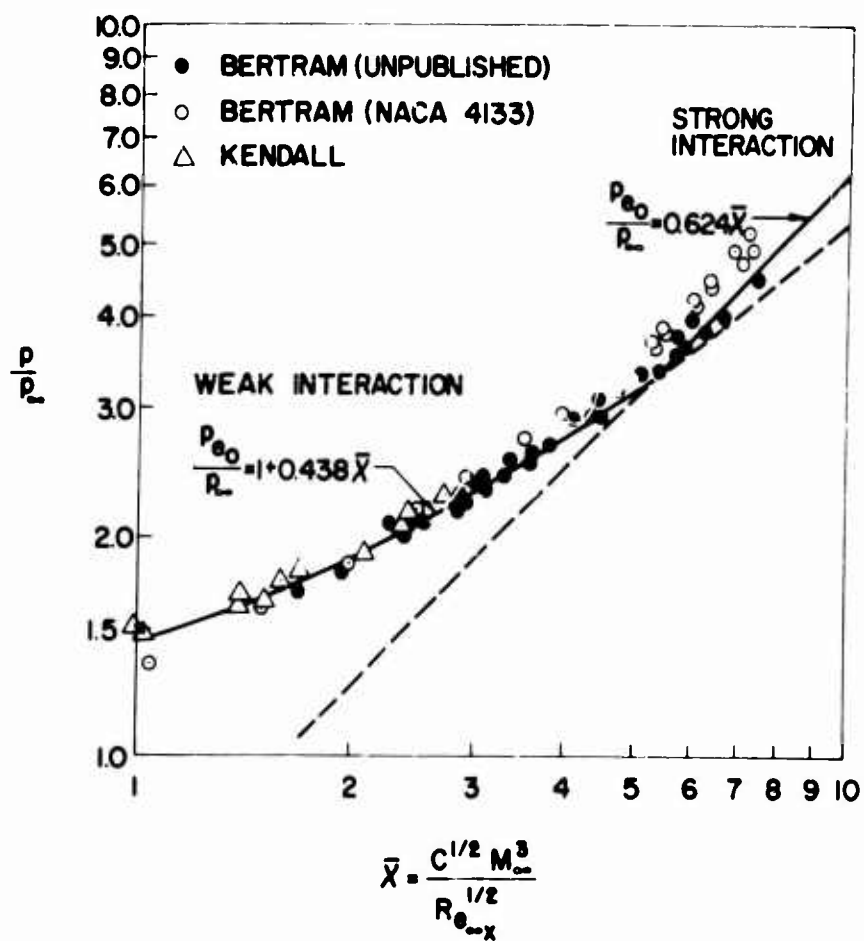


Fig. 6 WEAK- AND STRONG- INTERACTION PRESSURES ON AN INSULATED FLAT PLATE IN AIR. THEORETICAL PREDICTIONS BY INTEGRAL METHOD, EQUATION (21); EXPERIMENTS FROM FIGURE 9-5 OF REF. 13.

VORTICAL LAYERS IN SUPERSONIC CONICAL FLOW

by

R. F. Melnik

Grumman Aircraft Engineering Corporation

SUMMARY

A theoretical analysis of supersonic flow over slightly yawed conical surfaces is presented. The cross section of the cone is assumed to be nearly circular, but otherwise arbitrary. The method of matched expansions is employed and a solution is obtained by a systematic expansion from the known solution for supersonic flow over an unyawed circular cone.

The behavior of the uniformly valid solution at vortical singularities is closely analyzed. The solution is found to be a formal asymptotic solution at these points. There is no indication of the lift-off behavior of the vortical singularity suggested by Ferri.

Analytic results are given for the second order uniformly valid solutions for a yawed circular cone. Numerical results for the first order composite solution for the entropy distribution on an elliptic cone are also presented.

VORTICAL LAYERS IN SUPERSONIC CONICAL FLOW

R. E. Melnik*

Grumman Aircraft Engineering Corporation

1. INTRODUCTION

In this paper, we consider supersonic conical flows without axial symmetry by expanding about the known exact solution (Taylor-Maccoll, 1933) for a circular cone at zero incidence. This method was originally developed by Stone (1948, 1952) for circular cones at small incidence and was extended by Ferri (1954) to cones of nearly circular but otherwise arbitrary cross section. Ferri (1954) pointed out that Stone's solution for the yawed circular cone broke down at the cone surface where the first order solution for entropy, density and radial velocity are discontinuous. He introduced the notion of a vortical or entropy layer, across which these quantities varied rapidly from the Stone values outside to the correct values at the surface. Cheng (1962), Bulakh (1962a, 1962c), Woods (1962), and Sapunkov (1963) investigated the structure of the solution in the vortical layer for the special case of a circular cone and obtained the leading term of the solution in this region. Cheng (1962), Sapunkov (1963), and Bulakh (1962b) considered the hypersonic case and introduced an additional expansion in terms of the density ratio across the shock wave and obtained somewhat simpler solutions.

In the present investigation, we treat this problem and also the problem of flow over cones of nearly circular cross section by the method of matched expansions (see Van Dyke, 1964). We recover the first order uniformly valid solutions obtained by the above authors for circular cones and extend these results to cones with other cross sections. Uniformly valid composite expansions are given up to second order in terms of a parameter defining the asymmetry of the flow field.

Woods (1963) and Munson (1965) also treated the circular cone problem by the method of matched expansions. These investigations and the present one were all carried out independently and completed at about the same time in 1963. However, the methods differ in a number of important details and the resulting solutions for circular cones are not entirely equivalent as will be discussed in the main text.

2. EXACT EQUATIONS OF CONICAL FLOW

The problem is formulated in the orthogonal curvilinear coordinate system (r, ξ, η) shown in Fig. 1. The body surface lies along a coordinate surface, $\eta = \eta_b = \text{constant}$. The surfaces $r = \text{constant}$ are spheres centered about the apex, and the surfaces $\xi = \text{constant}$ are planes passing through the generators of the cone which are normal to the body surface. The remaining surfaces $\xi = \text{constant}$ are given by a family of conical surfaces similar to the body surface which are orthogonal to the planes $\xi = \text{constant}$. It is convenient to define ξ so that on the body surface it is equal to the azimuthal angle, ϕ of the spherical polar coordinate system (r, θ, ϕ) (see Fig. 1). Then the equation for the body surface can be given by an equation of the usual form $\theta = \theta_b(\phi) \equiv \theta_b(\xi)$.

This investigation is part of a dissertation submitted to the Polytechnic Institute of Brooklyn in 1965 in partial fulfillment of the requirements of Doctor of Philosophy in Astronautics. The author is indebted to R. Vaglio-Laurin for numerous discussions and for his guidance during the study.

* Research Scientist

The velocity at infinity is taken to lie in the $\xi = 0$ plane and have a magnitude U_∞ . The velocity components u, v and w in the directions of increasing r, η and ξ respectively are nondimensionalized with respect to U_∞ . The pressure, p , the density, ρ , and the entropy, s , are nondimensionalized with respect to $\rho_\infty U_\infty^2$, ρ_∞ and γR respectively, where ρ_∞ is the free stream density, γ is the ratio of specific heats, and R is the gas constant. The exact equations of inviscid conical flow of a perfect gas are given in (r, ξ, η) coordinates by:

$$\frac{\partial \rho v \chi}{\partial \eta} + \frac{\partial \rho w}{\partial \xi} + 2 \rho u \chi = 0 \quad (1a)$$

$$v \frac{\partial u}{\partial \eta} + w \frac{\partial u}{\chi \partial \xi} = v^2 + w^2 \quad (1b)$$

$$v \frac{\partial v}{\partial \eta} + w \frac{\partial v}{\chi \partial \xi} + uv + \kappa w^2 = - \frac{1}{\rho} \frac{\partial p}{\partial \eta} \quad (1c)$$

$$v \frac{\partial w}{\partial \eta} + w \frac{\partial w}{\chi \partial \xi} + uw - \kappa v w = - \frac{1}{\rho} \frac{\partial p}{\chi \partial \xi} \quad (1d)$$

$$v \frac{\partial s}{\partial \eta} + w \frac{\partial s}{\chi \partial \xi} = 0 \quad (1e)$$

$$p \rho^{-\gamma} = \frac{1}{\gamma M_\infty^2} \exp \gamma(\gamma - 1)(s - s_\infty) \quad (1f)$$

for later reference we give Bernoulli's equation which is an integral of the above equations

$$u^2 + v^2 + w^2 + \frac{2\gamma}{\gamma - 1} \frac{p}{\rho} = 1 + \frac{2}{(\gamma - 1) M_\infty^2} \quad (2)$$

where M_∞ and s_∞ are the free stream Mach number and entropy. The scale factor χ and the curvature of the $\eta = \text{constant}$ surfaces, κ , are given by

$$\chi = \chi_b [\cos(\eta - \eta_b) - \kappa_b \sin(\eta - \eta_b)] \quad (3a)$$

$$\kappa = [\kappa_b \cos(\eta - \eta_b) + \sin(\eta - \eta_b)] \chi / \chi_b \quad (3b)$$

where

$$\chi_b = \sin \theta_b / \cos \sigma_b \quad (3c)$$

and

$$\kappa_b = \left(\frac{d\sigma_b}{d\xi} - \cos \theta_b \right) / \chi_b \quad (3d)$$

The quantity σ_b is the angle between the body surface and a $\eta = \text{constant}$ surface. Thus,

$$\sigma_b = \tan^{-1} \left(\frac{d\theta_b}{\chi_b d\xi} \right) \quad (3e)$$

The condition of tangent flow at the cone surface is given by

$$v(\eta_b, \xi) = 0 \quad (4)$$

The formulation is completed by giving the boundary conditions at the shock wave, $\eta = \eta_s(\xi)$, which can be derived from the standard Rankine-Hugoniot jump conditions. The explicit form of the shock conditions in the present coordinate system is quite lengthy and hence, they will not be written out. They are, however, given in the thesis version of this paper (Melnik, 1965) along with many other details omitted here. We note that for the special case of a circular cone, $\theta_b = \text{constant}$, the present coordinate system reduces to a spherical polar coordinate system with axis along the cone axis and the above formulation becomes the familiar one using body axis.

It is perhaps important to point out that the present coordinate system was not chosen on the basis of convenience alone but plays an essential role in the analysis. The outer solution must be given in a coordinate system which fixes the body surface to a coordinate surface $\eta = \text{constant}$ or strong moving singularities associated with the vortical layer will arise in the outer solution and prevent matching with the inner solution.

3. OUTER SOLUTION

Following Stone and Ferri, we seek an outer solution of the general problem formulated in the previous section by expanding about the exact solution for the axisymmetric flow over a circular cone. We assume the body surface is specified by the following Fourier series

$$\theta_b(\xi) = \tau + \epsilon f(\xi) \quad (5a)$$

where

$$f(\xi) = \sum_n b_n \cos n\xi + \sum_m b_m \sin m\xi \quad (5b)$$

τ is the half angle of the basic circular cone and ϵ is a small parameter which serves as a measure of the asymmetry of the flow field. We also assume that the incidence, α (which enters in the present formulation via the shock conditions) is $O(\epsilon)$ and formally introduce a stretched angle of attack by the equation $\alpha = \epsilon \bar{\alpha}$. The coefficients b_n and $\bar{\alpha}$ are assumed to be $O(1)$.

The outer expansion is taken in the form of a power series in ϵ with ξ, η fixed. As suggested by Eq. (5) each term of the series is expanded in a Fourier series in terms of ξ with coefficients depending on η . For example the outer solution for u is given by

$$u = u_0(\eta) + \sum_n \left[\epsilon \lambda_n u_{1n}(\eta) + \epsilon^2 \mu_n u_{2n}(\eta) + \dots \right] \cos n\xi + \text{similar terms in } \sin m\xi \quad (6a)$$

with similar expansions for v, p, ρ, s and an obvious extension of the above notation. The expansion for w is given by

$$w = \sum_n \left[\epsilon \lambda_n w_{1n}(\eta) + \epsilon^2 \mu_n w_{2n}(\eta) + \dots \right] n \sin n\xi + \text{similar terms in } \cos m\xi \quad (6b)$$

The equation for the shock wave is sought in the form

$$\eta_s = \eta_{s0} + \sum_n \left[\epsilon \Delta_{1n} + \epsilon^2 \Delta_{2n} + \dots \right] \cos n\xi + \text{similar terms in } \sin m\xi \quad (6c)$$

The parameters λ_n and μ_n are constants introduced for normalization purposes.

Substituting Eqs. (6) into Eqs. (1)-(4) and the shock conditions we obtain successively, ordinary differential equations for the basic flow, the first order Fourier coefficients and the second order coefficients. Except for the difference in notation, the lowest order equations are identical with the usual equations governing the supersonic flow over a circular cone at zero angle of attack. Solutions to these equations have been obtained numerically by Kopal (1947a) and are tabulated for a number of Mach numbers and cone angles in the first volume of the MIT cone tables. Thus, the functions $u_0(\eta)$, $v_0(\eta)$, $p_0(\eta)$, $\rho_0(\eta)$ and s_0 defining the basic flow in the present scheme can be obtained from these tables by replacing θ by η and by dividing the tabular values of the velocities by \bar{U} and the pressure by \bar{U}^2 to account for the difference in reference velocity. Here

$$\bar{U} \equiv U_\infty / U_{1im} = \left[1 + 2/M_\infty^2(\gamma - 1) \right]^{-1/2} \quad (7)$$

We call attention to the change of meaning of the basic flow implied by this change of variables. In the present study, the basic shock wave is parallel to the actual body and hence is generally noncircular. The zeroth order functions are assumed to approximate the exact profiles along normals to the body surface. It turns out that this zeroth-order solution is not a ξ independent solution to the exact conical flow equations.

The ordinary differential equations governing the first order Fourier coefficients appearing in the representation given in Eqs. (6) are exactly the same as the equations derived by Ferri, and employed by Ness and Kaplita (1954) in generating their tables except for the presence of a single nonhomogeneous term in the present system. However, a particular solution for this term and an additional term appearing in the shock conditions, is easily found which leads to the following representation of the first order solution,

$$u_{1n} = \bar{u}_{1n}(\eta) + c_n v_o(\eta) \quad (8a)$$

$$v_{1n} = \bar{v}_{1n}(\eta) + c_n v_o'(\eta) \quad (\text{prime denotes } d/d\eta) \quad (8b)$$

$$w_{1n} = \bar{w}_{1n}(\eta) - c_n v_o(\eta) \csc \eta \quad (8c)$$

$$s_{1n} = \bar{s}_{1n} = d/\gamma(\gamma - 1) \quad (8d)$$

$$p_{1n} = \bar{p}_{1n}(\eta) + c_n p_o'(\eta) \quad (8e)$$

$$\rho_{1n} = \bar{\rho}_{1n}(\eta) + c_n \rho_o'(\eta) \quad (8f)$$

where the barred quantities are obtained from Ness and Kaplita's tables by changing their independent variable from θ to η and by dividing the velocities by \bar{U} the pressure by \bar{U}^2 and the entropy by $\gamma\bar{P}$. The quantity d is the same constant appearing in the Kopal tables. The constant c_n is to be determined by matching the above solution to the inner solution. In the next section, we show that it is consistent to determine this constant from the condition

$$v_{1n}(\tau) = 0 \quad (9)$$

If we define λ_n by the relation

$$\lambda_n = b_n + \Delta_{1n} - \bar{\alpha}\delta_{1n}$$

where $\delta_{1n} = 1$ for $n = 1$ and is zero for $n \neq 1$, Eqs. (8b) and (9) yields

$$c_n = \bar{v}_{1nb}/2u_{ob} \quad (10a)$$

where the subscript, b , denotes surface values (i.e., $\eta = \tau$). Then the shock coefficients, Δ_{1n} , are given by

$$\Delta_{1n} = - (b_n - \bar{\alpha}\delta_{1n})(1 - 2u_{ob}/v_{1nb}) \quad (10b)$$

We should point out that the computations for the first order circular cone perturbations tabulated in the MIT and PIBAL tables have been carried out with different normalization. The relation between the two sets of tables is given by

$$F^* = [\bar{\alpha}/(\bar{\alpha} - \Delta_{11})]F^{**} \quad (10c)$$

where F^* denotes for the PIBAL values and F^{**} the corresponding MIT values.

The differential equations for the second order Fourier coefficients are also identical to Ferri's except for some additional nonhomogeneous terms which depend on the lower order solutions. These equations have not been extensively treated and the only numerical results available are Kopal's (1949) tables for the quadratic terms for the yawed circular cone. The application of these tables to the present

work is discussed in a later section. It is shown in the following section that the correct matching condition to be used with these equations is given by

$$v_{21}(\tau) = 0 \quad (11)$$

It can be shown that this condition holds to all orders. Hence, there is no displacement effect and the outer solution is completely determined, independent of the inner solution. This is a consequence of an exponentially thin inner layer.

The behavior of the outer solution near the cone surface is easily ascertained. For the basic flow we have $s_o = \text{constant}$ and

$$(u_o, p_o, \rho_o) = (u_{ob}, p_{ob}, \rho_{ob}) + O(\eta - \tau)^2 \quad (12a)$$

and

$$v_o = -2u_{ob}(\eta - \tau) + O(\eta - \tau)^3 \quad (12b)$$

The behavior of the higher order terms follows from an analysis of the ordinary differential equations governing the perturbation together with the condition of the vanishing of v_{1n} and v_{2n} . The results are, for the first order solution:

$$u_1 = u_{ob} l_1(\xi) + O(\eta - \tau) \quad (13a)$$

$$v_1 = -2u_{ob} n_1(\xi)(\eta - \tau) + O(\eta - \tau)^2 \quad (13b)$$

$$w_1 = -u_{ob} j_1(\xi) \sin \tau + O(\eta - \tau)^{\frac{1}{2}} \quad (13c)$$

$$\rho_1 = \rho_{ob} t_1(\xi) + O(\eta - \tau) \quad (13d)$$

$$s_1 = [d/\gamma(\gamma - 1)] \left[\sum_n \lambda_n \cos n\xi + \text{similar terms in } \sin m\xi \right] \quad (13e)$$

and for the second order solution

$$u_2 = u_{ob} \left[l_2(\xi) - \frac{\Gamma_1(\xi)}{(\gamma - 1)M_{ob}^2} \ln\left(\frac{\eta - \tau}{\eta_{os} - \tau}\right) \right] + O(\eta - \tau) \quad (14a)$$

$$v_2 = -2u_{ob} \left[n_2(\xi) - \frac{\Gamma_1(\xi)}{(\gamma - 1)M_{ob}^2} \ln\left(\frac{\eta - \tau}{\eta_{os} - \tau}\right) \right] (\eta - \tau) + O(\eta - \tau)^2 \quad (14b)$$

$$w_2 = -u_{ob} j_2(\xi) \sin \tau + O(\eta - \tau)^{\frac{1}{2}} \quad (14c)$$

$$s_2 = \frac{1}{\gamma - 1} \left[\Gamma_2(\xi) + \Gamma_1(\xi) \ln\left(\frac{\eta - \tau}{\eta_{so} - \tau}\right) \right] + O(\eta - \tau)^{\frac{1}{2}} \quad (14d)$$

$$\rho_2 = \rho_{ob} \left[t_2(\xi) - \Gamma_1(\xi) \ln\left(\frac{\eta - \tau}{\eta_{so} - \tau}\right) \right] + O(\eta - \tau)^{\frac{1}{2}} \quad (14e)$$

where

$$M_{ob} = u_{ob}(\rho_{ob}/\gamma p_{ob})^{\frac{1}{2}} \quad (15)$$

and the functions $l_1(\xi)$, $l_2(\xi)$, $n_1(\xi)$, $n_2(\xi)$, etc., are nonsingular functions of ξ listed in an appendix to this paper. Thus, we see that the first order solution is discontinuous and the second order solution is logarithmically infinite at the surface. The higher order solutions involve only higher powers of the logarithm. This type of solution can be matched to the inner solution given in the next section. However, if body orientated coordinates were not employed, additional pole type

singularities would arise which would prevent matching. In addition, we would find that w_2 would be infinite and behave like

$$w_2 \sim (\eta - \tau)^{-\frac{1}{2}} \quad (16)$$

in other coordinate systems.

4. INNER SOLUTION

From the results of the previous section, we see that the outer solution breaks down in a region near the body surface defined by the condition

$$|\epsilon \ln(\eta - \tau)| = O(1)$$

This suggests that an appropriate inner variable for describing the solution in the inner region is

$$\tilde{\eta} = -\epsilon \ln[(\eta - \tau)/(\eta_{so} - \tau)] \quad (17)$$

We note that $\tilde{\eta} = O(\epsilon)$ in the outer region and $\tilde{\eta} \rightarrow -\infty$ at the body. It also follows that an appropriate inner variable for the normal component of velocity is

$$V = -v/(\eta - \tau) \quad (18)$$

The remaining inner variables U, W, P, R , and S are unstretched and are denoted by upper case letters. The inner solution could be taken as a power series expansion of the upper case quantities in terms of ϵ keeping $\xi, \tilde{\eta}$ fixed. However, we find it is convenient to follow a slightly different procedure. First we introduce $\xi, \tilde{\eta}$ as independent variables into the exact equations [Eqs. (1)] and then neglect a number of terms which are exponentially small in the inner region. We find the pressure is constant to all orders across the inner layer. Matching the pressure to the outer solution immediately determines the inner pressure distribution to all orders,

$$P(\xi, \eta; \epsilon) = p_b(\xi; \epsilon) \quad (19)$$

With the pressure now known it is convenient to introduce a von Mises type streamline coordinate system to treat the rest of the problem. Accordingly, we introduce a function, ψ , which is constant on crossflow streamsurfaces (Fig. 1) and is defined by the equation

$$\epsilon V(\partial\psi/\partial\tilde{\eta}) + W(\partial\psi/\partial\xi) = 0 \quad (20)$$

and the boundary condition $\psi = \xi$ at $\eta = \eta_{so}$. The entropy, density, and radial velocity are determined from the following algebraic relations,

$$S = G(\psi; \epsilon) \quad (21a)$$

$$R^\gamma = \gamma M_\infty^2 P_b \exp \gamma(\gamma - 1)(s_\infty - S) \quad (21b)$$

$$U^2 = \bar{U}^2 - W^2 - (2\gamma/\gamma - 1)(P_b/R) \quad (21c)$$

The remaining quantities V, W and $\tilde{\eta}$ are determined from the following system of partial differential equations,

$$V = 2U + W(D \ln \Lambda / \chi_b D\xi) \quad (21d)$$

$$W(DW/D\xi) + \chi_b WU = -(1/R) dP_b/d\xi \quad (21e)$$

$$D\tilde{\eta}/D\xi = \epsilon \chi_b V/W \quad (21f)$$

where

$$\Lambda \equiv RW\partial\tilde{\eta}/\partial\psi \quad \text{and} \quad D/D\xi \equiv (\partial/\partial\xi)_{\psi} \quad (21g)$$

The inner solution is expanded in the form:

$$U = U_0(\xi, \psi) + \epsilon U_1(\xi, \psi) + \dots \quad (22a)$$

$$V = V_0(\xi, \psi) + \epsilon V_1(\xi, \psi) + \dots \quad (22b)$$

with similar expansions for W, P , and R . The streamlines are determined from the expansion,

$$\tilde{\eta} = \tilde{\eta}_0(\xi, \psi) + \epsilon \tilde{\eta}_1(\xi, \psi) + \dots \quad (22c)$$

These expansions are then substituted into the Eqs. (21). The equations governing each term of the series are easily integrated. Two arbitrary functions of ψ , one arising from the expansion of $G(\psi; \epsilon)$ and the other from the integration of Eq. (21f), are introduced at each order of the expansion. However, these functions are easily determined by matching the inner and outer expansions. The matching is carried out as follows: The inner solution for the streamlines, $\tilde{\eta}(\psi, \xi; \epsilon)$ is expanded in powers of $(\psi - \xi)$ and the result inverted to give a series solution for the inner stream function, $\psi(\xi, \tilde{\eta}; \epsilon)$, which is valid in the outer region. This function is substituted into the remaining terms of the inner solution which is then written in terms of outer variables ξ, η and expanded in powers of ϵ . The matching is completed by comparing this result with the outer solution expressions given by Eqs. (12)-(14).

Following this procedure, we find that the leading term of the inner solution is given by $W = 0$ and

$$U_0 = u_{ob}, \quad V_0 = 2u_{ob}, \quad S_0 = s_0, \quad I_0 = \rho_{ob} \quad (23)$$

To lowest order the streamlines are normal to the body and hence $\psi = \xi$.

The first order inner solution is

$$U_1 = -u_{ob}t_1(\xi) + \left[u_{ob}^2/M_{ob}^2\right] \left[s_1(\xi) - s_1(\psi)\right] \quad (24a)$$

$$V_1 = 2u_{ob}n_1(\xi) + 2\left[u_{ob}^2/M_{ob}^2\right] \left[s_1(\xi) - s_1(\psi)\right] \quad (24b)$$

$$W_1 = -u_{ob}j_1(\xi) \sin \tau, \quad S_1 = s_1(\psi) \quad (24c, d)$$

$$R_1 = \rho_{ob}t_1(\xi) + (\gamma - 1)\rho_{ob} \left[s_1(\xi) - s_1(\psi)\right] \quad (24e)$$

where the function $G_1(\psi)$ has been evaluated from the matching condition

$$G_1(\psi) = s_1(\psi) = [d/\gamma(\gamma - 1)] \left[\sum \lambda_n \cos n\psi + \sum \lambda_m \sin m\xi \right]$$

The equation for the streamlines up to first order is actually given by the zeroth order function $\tilde{\eta}_0(\xi, \psi)$, where,

$$\tilde{\eta}_0(\xi, \psi) = I_0(\xi) - I_0(\psi) \quad (25a)$$

and

$$I_0(\xi) = -2 \int_{\xi_{ref.}}^{\xi} [1/j_1(t)] dt \quad (25b)$$

or in unstretched variables

$$(\eta - \tau)/(\eta_{so} - \tau) = [B(\psi)/B(\xi)]^{1/\epsilon} \quad (25c)$$

where

$$B(\xi) = \exp I_0(\xi) \quad (25d)$$

The second order inner solution is given by

$$U_2 = u_{ob} L_2(\xi, \psi), \quad V_2 = 2u_{ob} N_2(\xi, \psi) \quad (26a, b)$$

$$W_2 = -u_{ob} J_2(\xi, \psi) \sin \tau \quad (26c)$$

$$R_2 = \rho_{ob} T_2(\xi, \psi), \quad S_2 = s_{2s}(\xi) \Big|_{\xi=\psi} \quad (26d, e)$$

where the functions L_2 , N_2 , J_2 , and T_2 are given in terms of the outer solution by expressions in the appendix. The solution for the second order inner streamlines is given by

$$\begin{aligned} \tilde{\eta}_1(\xi, \psi) &= E_2(\psi)/j_1(\psi) + 3 \ln j_1(\xi)/j_1(\psi) \\ &- \left[(\gamma - 1) + 2/M_{ob}^2 \right] \left[I_0(\xi) - I_0(\psi) \right] G_1(\psi) + \left[I_1(\xi) - I_1(\psi) \right] \end{aligned} \quad (26f)$$

where

$$I_1(\xi) = \int_{\xi_{ref.}}^{\xi} \left[H_1(t)/j_1(t) \right] dt \quad (26g)$$

The functions $E_2(\psi)$ and $H_1(\xi)$ are listed in the appendix.

In general, we can combine the inner and outer expansions to form a "composite" expansion which is uniformly valid in the entire flow field. The usual rule for forming a composite expansion is applicable here:

$$\begin{aligned} \text{composite expansion} &= \text{inner expansion} + \text{outer expansion} \\ &- \text{inner expansion of (outer expansion)} \end{aligned}$$

In the present study this prescription is implemented by subtracting the limit forms of the outer solution given in Eqs. (13) and (14) from the outer solution and adding the result to the inner solution. The result is a power series expansion in ϵ with the coefficients depending on three independent variables ξ, η, ψ . In the first order composite solution the stream function is determined implicitly by Eqs. (25) and in the second order solution by Eqs. (26). Hence the present procedure leads to a parametric representation for a uniformly valid solution. To first order we have,

$$u_c = u_o + \epsilon \left\{ u_1 + (u_{ob}/M_{ob}^2) \left[s_{1s}(\xi) - s_{1s}(\psi_1) \right] \right\} \quad (27a)$$

$$v_c = v_o + \epsilon \left\{ \eta - \tau \right\} \left\{ \frac{v_1}{\eta - \tau} - (2u_{ob}/M_{ob}^2) \left[s_{1s}(\xi) - s_{1s}(\psi_1) \right] \right\} \quad (27b)$$

$$w_c = w_1 \quad (27c)$$

$$p_c = p_o + \epsilon p_1 \quad (27d)$$

$$\rho_c = \rho_o + \epsilon \left\{ \rho_1 + \rho_{ob}(\gamma - 1) \left[s_{1s}(\xi) - s_{1s}(\psi_1) \right] \right\} \quad (27e)$$

$$s_c = s_{os} + \epsilon s_{1s}(\psi_1) \quad (27f)$$

where the stream function ψ_1 is determined from Eqs. (25).

The second order composite solution is easily formed by the above procedure and has a similar form to the first order solution. The expressions are quite lengthy and therefore will not be written out here for the general case. However, a second order composite solution for the yawed circular cone is given in the following section.

It is of some interest to determine the behavior of the inner solution near crossflow stagnation points. These occur on the cone surface at places where the surface pressure gradient vanishes. If each term in the expansion for the surface pressure gradient vanishes at the same point the stagnation point is fixed, independent of ϵ , and its location is determined by the first order solution for the pressure distribution. If this is not the case the crossflow stagnation point is said to be movable, with its position shifting as more terms are included in the solution for the pressure distribution.

At a fixed stagnation point, located at $\xi = 0$, the inner solution for $\tilde{\eta}(\xi, \psi; \epsilon)$ has the following expansion

$$\tilde{\eta} = (4/3k) c(\psi; \epsilon) \ln(\xi/\psi) + A(\psi; \epsilon) + O(\xi) \quad (28a)$$

or in outer variables

$$\xi = \frac{\psi}{\bar{A}(\psi; \epsilon)} \left[\frac{\eta - \tau}{\eta_{so} - \tau} \right]^{-(3\epsilon k/4)c(\psi; \epsilon)} \quad (28b)$$

where k is a crossflow parameter given by

$$k = \frac{2}{3\gamma M_{ob}^2 \sin^2 \tau} \frac{d^2(p_{1b}/p_{ob})}{d\xi^2} \bigg|_{\xi=0} \quad (28c)$$

and

$$c = 1 + \epsilon c_1(\psi) + \epsilon^2 c_2(\psi) + \dots \quad (28d)$$

$$c_1(\psi) = - (9k/4) + H(0) + \left[(\gamma - 1) + 2/M_{ob}^2 \right] G_1(\psi) \quad (28e)$$

The functions $A(\psi)$ and $\bar{A}(\psi)$ are lengthy expressions involving the entropy and surface pressure distributions. The main point to note is that the asymptotic solution for the streamlines is given by an expression of the form in Eq. (28b). The exponent depends on the stream function and is given by a formal power series expansion in ϵ . At a maximum of the pressure $k > 0$ and the streamlines form a saddle point (point B', Fig. 1). At a minimum, $k < 0$, and the streamline pattern is a node with streamlines tangent to the body surface (point A', Fig. 1). Equation (28b) gives no indication of the lift-off of vortical singularities first suggested by Ferri (1954). This is consistent with the findings of Melnik (1967) which shows that lift-off of vortical singularities is a large yaw effect.

At a movable stagnation point the second order pressure gradient does not vanish and as a consequence it is easy to show that $\tilde{\eta}_1$ must have a pole singularity at the origin. The ratio of the first two terms of the inner solution for $\tilde{\eta}$ is of the form,

$$\epsilon \tilde{\eta}_1 / \tilde{\eta}_0 \sim \left[\frac{dp_{2b}/d\xi}{d^2 p_{1b}/d\xi^2} \right]_{\xi=0} \left[\frac{\epsilon}{\xi \ln \xi} \right] \quad (29)$$

Hence the inner solution breaks down at movable crossflow stagnation points. This difficulty is caused by a shift of the zeros of the surface pressure gradient and the consequent development of moving singularities. This suggests the introduction of a PLK coordinate straining (see Van Dyke, 1964),

$$\xi(z; \epsilon) = z + \epsilon \xi_1(z) + \epsilon^2 \xi_2(z) + \dots \quad (30)$$

where we subject the straining functions, $\xi_n(z)$, to the condition that zeros of the surface pressure gradient be fixed in the z plane. Detailed analysis shows that this

condition is equivalent to the requirement that the ratio of successive terms in the expansion for $\tilde{\eta}$ be $O(\epsilon)$ as we approach a stagnation point. Substituting Eq. (30) into the (known) expression for the surface pressure gradient and expanding the result for small ϵ we obtain the following expression for the surface pressure gradient in the z plane,

$$\frac{dp_b(\xi; \epsilon)}{d\xi} = \epsilon \left[\frac{dp_{1b}(\xi)}{d\xi} \right]_{\xi=z} + \epsilon^2 \left[\frac{dp_{2b}(\xi)}{d\xi} + \xi_1(z) \frac{d^2 p_{1b}(\xi)}{d\xi^2} \right]_{\xi=z} + \dots \quad (31)$$

If the first order pressure gradient vanishes at $z = z_1$ the condition that the zeros of the pressure gradient be fixed in the z plane, independent of ϵ , is satisfied by requiring each group of terms of the same order in Eq. (31) to vanish at $z = z_1$. This results in the following set of conditions to determine $\xi_1(z)$,

$$\left[\frac{dp_{2b}(z)}{dz} + \xi_1(z) \frac{d^2 p_{1b}(z)}{dz^2} \right]_{z=z_1} = 0 \quad (32)$$

The choice of the straining function is otherwise arbitrary. For convenience we choose the following polynomial, which satisfies Eq. (32),

$$\xi_1(z) = - \sum_{k=1}^n \left[\frac{dp_{2b}}{d\xi} / \frac{d^2 p_{1b}}{d\xi^2} \right]_{\xi=z_1} \left[\prod_{i=1, i \neq k}^n \frac{z - z_i}{z_k - z_i} \right] \quad (33)$$

where n is equal to the number of stagnation points. A detailed analysis given in Melnik (1965) shows that a similar straining of the stream function is also required,

$$\psi = \zeta + \epsilon \xi_1(\zeta) + \dots \quad (34)$$

where ζ is the strained stream function and the first order straining function is the same as that appearing in the $\xi(z)$ expansion. It is also shown that a second order inner solution which is uniformly valid at movable stagnation points can be obtained by simply replacing (ξ, ψ) by (z, ζ) and $H_1(t)$ by $\hat{H}_1(t)$ in the first two terms for $\tilde{\eta}$, where

$$\hat{H}_1(t) = H_1(t) + \xi_1(t) - \frac{d\xi_1(t)}{dt} \quad (35)$$

Since the straining functions are regular we can invert the expansion for $\xi(z)$ and $\psi(\zeta)$ to obtain the following parametric representation for the second order stream function, $\psi_2(\xi, \eta; \epsilon)$

$$\tilde{\eta} = I_0(z) - I_0(\zeta) + \epsilon \left\{ \frac{E_2(\zeta)}{j_1(\zeta)} + 3 \ln \frac{j_1(z)}{j_1(\zeta)} - \left[\gamma - 1 + \frac{2}{M_{ob}^2} \right] [I_0(z) - I_0(\zeta)] G_1(\zeta) + [I_1(z) - I_1(\psi)] \right\} \quad (36a)$$

where

$$I_1(z) = \int_{z_{ref.}}^z \left[\hat{H}_1(t) / j_1(t) \right] dt \quad (36b)$$

$$z = \xi - \epsilon \xi_1(\xi) \quad ; \quad \zeta = \psi_2 - \epsilon \xi_1(\psi_2) \quad (36c, d)$$

The inner solution for the remaining independent variable is unchanged and is given by Eqs. (24) and (26). The local behavior of the streamlines near movable crossflow stagnation is of the same general form as Eqs. (28) with (ξ, ψ) replaced by (z, ζ) . The effects of movable stagnation points only arise in the second and higher order solutions. The only second order outer solutions currently available are for the yawed circular cone. These contain only fixed stagnation points for the small angles

of attack for which the theory is valid. Hence we will not pursue this matter further. Details are given in Melnik (1965) where a second order composite solution is constructed which is uniformly valid at movable stagnation points.

5. APPLICATIONS

In this section we will apply the general results given in the previous sections to the problem of supersonic flow over a yawed circular cone and over an elliptic cone. Corresponding to the availability of numerical data for the outer solution we present only first order solutions for the elliptic cone but include the second order terms in the solution for the circular cone.

5a. Circular Cone Solutions

In the circular cone solutions only the first Fourier coefficients, u_{11} , v_{11} , etc., appear in the linear terms of the expansion and only the first two Fourier coefficients u_{20} , u_{22} , v_{20} , v_{22} , etc., arise in the quadratic terms. These coefficients can be obtained by applying a number of transformations to the numerical data given in the MIT tables (Kopal, 1947a,b,1949). First, as previously mentioned, the tabulated velocities and pressures must be divided by \bar{U} and \bar{U}^2 , respectively, in order to obtain a consistent nondimensionalization. The normalization constants λ_1 , μ_0 and μ_2 are set equal to one. Finally, we use the formula given by Roberts and Riley (1954) to transform from the wind axis used in the MIT tables to the body axis required in the present analysis. We should mention the fact that a number of practical difficulties arise in carrying out this program. In performing his computations Kopal did not take special care to control the influence of the logarithmic singularities present in the second order solution. Hence his tables are probably quite inaccurate near the cone surface. Further inaccuracies are introduced by the treatment of the square root infinity appearing in the solution for w_{22} in wind axis [see Eq. (16)]. Because of numerical truncation this singularity is not exactly cancelled by the Roberts and Riley transformation and the transformed solution for w_{22} is likely highly in error. In addition we have uncovered an error in the formula given by Roberts and Riley for the determination of a quantity, $z'^* \equiv \partial w_1 / \partial \theta$. Their results yields a finite value at the cone surface while the present study shows it actually behaves like $(\theta - \tau)^{-1/2}$. For these reasons one should be very cautious about using the existing tables for the quadratic terms.

The outer solution for the pressure distribution is uniformly valid and is given by (setting $\epsilon = 1$, $\eta = \theta$, and $\xi = \phi$)

$$p = p_0 + \alpha p_{11} \cos \phi + \alpha^2 (p_{20} + p_{22} \cos 2\phi) \quad (37)$$

The equation for the first order streamlines can be obtained from the first two terms of Eq. (37). Carrying out the quadrature defining the quantity I_0 in Eq. (25b) and rearranging the results yields

$$\frac{\theta - \tau}{\theta_{so} - \tau} = \left[\frac{\tan \phi/2}{\tan \psi_1/2} \right]^{-4/3\alpha k} \quad (38a)$$

where the crossflow parameter, k , is given by

$$k \equiv \frac{2}{3} \frac{w_{11b}}{u_{ob} \sin \tau} = \frac{2}{3} \frac{p_{11b}/p_{ob}}{M_{ob}^2 \sin^2 \tau} \quad (38b)$$

The subscript was added to the stream function to indicate that Eq. (38a) determines the first order solution for the streamlines. Equation (38a) can be inverted to obtain an explicit representation,

$$\zeta_1 = \left[(1 + \cos \phi) / (1 - \cos \phi) \right]^{1/2} \left[(\theta - \tau) / (\theta_{so} - \tau) \right]^{-3\alpha k / 4} \quad (38c)$$

where $\zeta_1 \equiv \cot(\psi_1/2)$ is the stream function employed by Cheng (1962). Using Eq. (38c) the first order composite solution can be written in the following explicit form,

$$u_c = u_o + \alpha u_{11} \cos \phi + \alpha (s_{11} u_{ob} / M_{ob}^2) (\cos \phi - \cos \psi_1) \quad (39a)$$

$$v_c = v_o + \alpha v_{11} \cos \phi - 2\alpha (s_{11} u_{ob} / M_{ob}^2) (\theta - \tau) (\cos \phi - \cos \psi_1) \quad (39b)$$

$$w_c = \alpha w_{11} \sin \phi \quad (39c)$$

$$p_c = p_o + \alpha p_{11} \cos \phi \quad (39d)$$

$$\rho_c = \rho_o + \alpha \rho_{11} \cos \phi + \alpha (\rho_{ob} s_{11}) (\gamma - 1) (\cos \phi - \cos \psi_1) \quad (39e)$$

$$s_c = s_o + \alpha s_{11} \cos \psi_1 \quad (39f)$$

A number of profiles of $\Delta s \equiv (s_c - s_o) / \alpha s_{11} = \cos \psi_{11}$ are plotted for various stations, $\phi = \text{constant}$, in Fig. 2 for a 20° half angle cone at a Mach number of 3.3694 which corresponds to $k = 1.96429$. Calculations are given for $\alpha = 4^\circ$ and 20° . We call attention to the very large gradients near the body surface particularly on the leeward side even at the relatively large incidence of 20° . We see that the entropy layer is extremely thin at the lower angles of attack but is relatively thick for $\alpha = 20^\circ$. We note that these profiles are also indicative of the correction terms for the density, radial and normal components of velocity.

The second order solution for the streamlines can be obtained by using Eq. (37) in Eqs. (26). This yields

$$\frac{\theta - \tau}{\theta_{so} - \tau} = \left[\exp - \frac{2E_{21}}{3k} \right] \left[\frac{1 + \cos \phi}{1 + \cos \psi_2} \right]^{-4a_2/3k} \times \left[\frac{\tan \phi/2}{\tan \psi_2/2} \right]^{-(4/3ak)(1 - \alpha a_2 - \alpha a_1 \cos \psi_2)} \quad (40a)$$

where

$$a_1 = [(\gamma - 1) - (2/M_{ob}^2)] s_{11} \quad (40b)$$

$$a_2 = (9k/4) - (4p_{22b}/p_{11b}) + [1 - (2/M_{ob}^2)] [p_{11b}/\gamma p_{ob}] \quad (40c)$$

$$E_{21} = - \int_{\tau}^{\theta_{so}} \left[\frac{2(\theta - \tau)w_{11}}{v_o \sin \tau} + \frac{w_{11b}}{u_{ob} \sin \tau} \right] \frac{d\theta}{\theta - \tau} \quad (40d)$$

Following the usual prescription the rest of the second order composite solution is found to be given by:

$$\begin{aligned} u_c = u_o + \alpha \left\{ u_{11} \cos \phi + (u_{ob} s_{11} / M_{ob}^2) (\cos \phi - \cos \psi_2) \right\} \\ + \alpha^2 \left\{ \left[u_{20} + \frac{3k}{8} \left(\frac{u_{ob} s_{11}}{M_{ob}^2} \right) \ln \left(\frac{\theta - \tau}{\theta_{so} - \tau} \right) \right] + \left[u_{22} + \frac{3k}{8} \left(\frac{u_{ob} s_{11}}{M_{ob}^2} \right) \ln \left(\frac{\theta - \tau}{\theta_{so} - \tau} \right) \right] \cos 2\phi \right. \\ + \frac{u_{ob}}{M_{ob}^2} \left[s_{22s} (\cos 2\phi - \cos 2\psi_2) + \frac{s_{11} E_{21}}{2} \sin^2 \phi \right. \\ \left. \left. + \left(\gamma - 1 + \frac{1}{M_{ob}^2} \right) \left(\frac{p_{11b} s_{11}}{\gamma p_{ob}} \right) (\cos \phi - \cos \psi_2) \cos \phi \right] \right\} \end{aligned} \quad (41a)$$

$$\begin{aligned}
v_c = v_o + \alpha[\theta - \tau] & \left\{ \frac{v_{11} \cos \phi}{\theta - \tau} - \left(\frac{2u_{ob}s_{11}}{M_{ob}^2} \right) (\cos \phi - \cos \psi_2) \right\} \\
& + \alpha^2[\theta - \tau] \left\{ \left[\frac{v_{20}}{\theta - \tau} - \frac{3k}{4} \left(\frac{u_{ob}s_{11}}{M_{ob}^2} \right) \ln \left(\frac{\theta - \tau}{\theta_{so} - \tau} \right) \right] \right. \\
& + \left[\frac{v_{22}}{\theta - \tau} - \frac{3k}{4} \left(\frac{u_{ob}s_{11}}{M_{ob}^2} \right) \ln \left(\frac{\theta - \tau}{\theta_{so} - \tau} \right) \right] \cos 2\phi - \frac{2u_{ob}}{M_{ob}^2} \left[s_{22s}(\cos 2\phi - \cos 2\psi_2) \right. \\
& + \frac{s_{11}E_{21}}{2} \sin^2 \phi - \left(\gamma - 1 + \frac{1}{M_{ob}^2} \right) \left(\frac{p_{11b}s_{11} \cos 2\tau}{2p_{ob}\gamma \sin^2 \tau} \right) (\cos \phi - \cos \psi_2) \cos \phi \\
& \left. \left. + \left(\gamma - 1 + \frac{1}{M_{ob}^2} \right) \left(\frac{s_{11}^2}{2} + \frac{p_{11b}s_{11}}{2p_{ob} \sin^2 \tau} \right) (\cos^2 \phi - \cos^2 \psi_2) \right] \right\} \quad (41b)
\end{aligned}$$

$$w_c = \alpha w_{11} \sin \phi + \alpha^2 \left\{ 2w_{22} \sin^2 \phi + \left(\frac{u_{ob}s_{11}}{\gamma M_{ob}^2 \sin^2 \tau} \right) \left(\gamma - 1 + \frac{1}{M_{ob}^2} \right) (\cos \phi - \cos \psi_2) \right\} \quad (41c)$$

$$p_c = p_o + \alpha p_{11} \cos \phi + \alpha^2 (p_{20} + p_{22} \cos 2\phi) \quad (41d)$$

$$\begin{aligned}
\rho_c = \rho_o + \alpha \left\{ \rho_{11} \cos \phi + \rho_{ob} s_{11} (\gamma - 1) (\cos \phi - \cos \psi_2) \right\} \\
& + \alpha^2 \left\{ \left[\rho_{20} + \rho_{ob} (\gamma - 1) \left(\frac{3}{8} k s_{11} \right) \ln \left(\frac{\theta - \tau}{\theta_{so} - \tau} \right) \right] \right. \\
& + \left[\rho_{22} + \rho_{ob} (\gamma - 1) \left(\frac{3}{8} k s_{11} \right) \ln \left(\frac{\theta - \tau}{\theta_{so} - \tau} \right) \right] \cos 2\phi - \rho_{ob} (\gamma - 1) \left[s_{22s}(\cos 2\phi - \cos 2\psi_2) \right. \\
& \left. \left. + \left(\frac{s_{11}E_{21}}{2} \right) \sin^2 \phi + \left(\frac{p_{11b}s_{11}}{\gamma p_{ob}} \right) (\cos \phi - \cos \psi_2) \cos \phi - \left(\frac{\gamma - 1}{2} \right) s_{11}^2 (\cos^2 \phi - \cos^2 \psi_2) \right] \right\} \quad (41e)
\end{aligned}$$

$$\begin{aligned}
s_c = s_o + \alpha s_{11} \cos \psi_2 + \alpha^2 \left\{ \left[s_{20} - \frac{3}{8} k s_{11} \ln \left(\frac{\theta - \tau}{\theta_{so} - \tau} \right) \right] \right. \\
& + \left[s_{22} - \frac{3}{8} k s_{11} \ln \left(\frac{\theta - \tau}{\theta_{so} - \tau} \right) \right] \cos 2\phi - \frac{s_{11}E_{21}}{2} \sin^2 \phi - s_{22s}(\cos 2\phi - \cos 2\psi_2) \left. \right\} \quad (41f)
\end{aligned}$$

Equations (40)-(41) provide a parametric representation for the second order composite solution. We note that the equation for the second order streamlines is too complicated to be inverted and no further simplifications are possible.

5b. Elliptic Cone at Zero Angle of Attack

The main difficulty in applying the first order composite solution given in Section 4 to noncircular cones is associated with the evaluation of the function $I_0(\xi)$. In general the function $j_1(\xi)$ is given by Fourier series and the quadrature

defining $I_0(\xi)$ must be carried out numerically. The numerical integration is complicated by the presence of pole type singularities in the integrand at crossflow stagnation points. In order to deal with finite quantities in the numerical integration we first subtract out these singular terms. If we restrict ourselves to flows with two planes of symmetry only four crossflow stagnation points arise at $\phi = 0, \pi/2, 3\pi/2$, and 2π . Taking $\xi_{ref} = 0$ in Eq. (25b) and subtracting out these singularities we obtain the following equation for the first order streamlines

$$\frac{\eta - \tau}{\eta_{so} - \tau} = B(\psi_1)/B(\xi) \quad (42a)$$

$$B(\xi) = \left(\frac{1 - \cos \xi}{\sin \xi} \right)^{3A_1/4} \left(\frac{1 + \sin \xi}{\cos \xi} \right)^{3A_2/4} \exp h(\xi) \quad (42b)$$

where

$$A_1 = \left(\sum_n n k_n \right)^{-1} ; \quad A_2 = - \left(\sum_n (-1)^{n/2} n k_n \right)^{-1} \quad (42c,d)$$

$$k_n = \frac{2n \lambda_n p_{lnb}/p_{ob}}{3\gamma M_{ob}^2 \sin^2 \tau} \quad (42e)$$

$$h(\xi) = \left[A_2 + \frac{(A_1 + A_2)\xi^2}{\pi} \right] + \frac{4}{3} \int_0^\xi \left[\left(\sum_n k_n \sin nt \right)^{-1} + \frac{A_1}{\sin t} + \frac{A_2}{\cos t} + \frac{2(A_1 + A_2)t}{\pi} - A_2 \right] dt \quad (42f)$$

The integrand is now free of singularities and the function $h(\xi)$ is regular and can be determined numerically without difficulty. The composite solution for the entropy distribution is given by

$$(s_c - s_{os})/as_{11} = \sum_{n=0} \lambda_n \cos n\psi_1 \quad (43a)$$

(only even terms in n arise under the assumed symmetry). The remainder of the solution is given by

$$u_c = u_o + \sum_{n=0} \lambda_n \left[u_{ln} \cos n\xi + \frac{u_{ob}s_{11}}{M_{ob}^2} (\cos n\xi - \cos n\psi_1) \right] \quad (43b)$$

$$v_c = v_o + \sum_{n=0} \lambda_n \left[v_{ln} \cos n\xi - \frac{2u_{ob}s_{11}}{M_{ob}^2} (\eta - \tau)(\cos n\xi - \cos n\psi_1) \right] \quad (43c)$$

$$w_c = \sum_{n=0} n\lambda_n w_{ln} \sin n\xi ; \quad p = p_o + \sum_{n=0} \lambda_n p_{ln} \cos n\xi \quad (43d,e)$$

$$\rho_c = \rho_o + \sum_{n=0} \lambda_n \left[\rho_{ln} \cos n\xi + (\gamma - 1) \rho_{ob} (\cos n\xi - \cos n\psi_1) \right] \quad (43f)$$

In Fig. 3 we plot the first order entropy profiles obtained from Eqs. (42, 43a) for an elliptic cone with semiaxis ratio $a/b = 1.24$, and with an equivalent base area, $\sqrt{ab} = .36397b$ (L = length of cone). The calculation was done for a Mach number of $M = 3.3694$ and $\gamma = 1.405$. It was found that the first four Fourier coefficients b_2, b_4, b_6 , and b_8 were sufficient to represent the body to four place accuracy. The boundary layer character of the solution is clearly evident in the figure. The results for the entropy are also indicative of the boundary layer behavior of the

quantities u_c , ρ_c , and $v_c/(\eta - \tau)$.

6. DISCUSSION

The expansions constructed in the present study lead to an implicit representation of a uniformly valid solution. For example, the inner solution for the radial velocity, u , has the following parametric form for a yawed circular cone,

$$U(\psi, \phi) = \sum \alpha^n U_n(\psi, \phi) \quad (44a)$$

$$\tilde{\theta}(\psi, \phi) \equiv -\alpha \ln \left(\frac{\theta - \tau}{\theta_{so} - \tau} \right) = \sum \epsilon^n \tilde{\theta}_n(\psi, \phi) \quad (44b)$$

The first order solution for $\tilde{\theta}_1$ can be inverted [see Eq. (38c)] and an explicit first order uniformly valid solution can be obtained for this problem [see Eqs. (38)-(39)]. The inverted solution is in agreement with the previous work discussed in the introduction (except for Bulakh's solutions in which he missed a term associated with v_1). The second order solution cannot be similarly treated because inversion of Eq. (40a) introduces additional logarithmic singularities into the second order solution at vortical singularities (located at the leeward ray on a circular cone). These singularities can be identified with the log terms that arose in Munson's (1965) and Woods (1963) inner solution at the leeward ray. Both these investigators constructed their inner expansions in the physical plane. For example, their inner solution for U was of the form

$$U_{\text{Woods}} = \sum \alpha^n U_n(\tilde{\theta}, \phi) \quad (45)$$

$$U_{\text{Munson}} = \sum \alpha_n U_n(\theta, \phi) \quad (46)$$

where Munson used a slightly different stretching,

$$\theta = \left(\frac{\sin \theta - \sin \tau}{\sin \tau} \right)^\alpha \sim \exp(-\tilde{\theta})$$

These expressions should be compared with Eqs. (44) which is the representation used in the present study. Hence the breakdown of both Woods and Munson's inner solution at vortical singularities is caused by the use of physical coordinates, θ, ϕ respectively, as independent variables. Munson attempted to remedy his inner solution by using the expansion

$$\theta^\alpha = 1 + \alpha \ln \theta + \dots$$

to rearrange his expansion and eliminate the unwanted log singularities. However, comparison of his second order solution for the streamlines [Eq. (5.16b) of his paper] with the corresponding result of the present study [Eq. (40)] shows that, although his modified solution is of the right form, it contains at least two errors. Munson's modified solution for the streamlines can be written in the form

$$\frac{\theta - \tau}{\theta_{so} - \tau} = F(\psi_2) (\tan \phi/2)^{-(4/3\alpha k)(1-\alpha a_2)}$$

Comparison with Eqs. (40) shows that Munson's solution is missing the second term in brackets in Eqs. (40) and the a_1 term in the exponent. We note that this missing term introduces a ψ dependence into the exponent which is entirely missing in Munson's solution. This discussion points to the essential role of the parametric representation using streamline coordinates in the present analysis. Using this representation the solution in each region could be expressed by simple power series expansions. The composite solution is also given by a power series in ϵ but contains three independent variables ξ, η , and ψ in this representation.

The present results agree in form with Sapunkov's (1963) solution. In particular, the form of the equation for the streamlines given in Eqs. (40) corresponds very closely to Eq. (9.6) of Sapunkov's paper (with $\zeta_2 = \cos \psi_2$ and $\omega = \theta - \pi/2$). They both have exponents which depend on the stream function in an identical manner. (This is a further indication that Munson is missing a ψ dependent term in his exponent.) Although the details have not been carried out Sapunkov's solution is apparently the correct Newtonian limit of the present second order composite solution for the yawed circular cone. However we should point out that Sapunkov's solution was obtained by an iterative analysis that is considerably more complicated than the present procedure which employed simple power series expansions in conjunction with appropriate independent variables.

We should also call attention to an unresolved discrepancy between the present small asymmetry solution and the solution given in Melnik (1967) for the local behavior near vortical singularities. The present solution for the streamlines has the following behavior near vortical singularities

$$\xi \sim (\eta - \tau)^{-(3\epsilon k/4)(1+\epsilon c_1+\dots)}$$

and hence is a formal asymptotic solution. The results given in Melnik (1967) indicate that the correct local behavior should be

$$\xi \sim \left[\frac{\eta - \tau}{(\ln \eta - \tau)^{1/2}} \right]^{-(3\epsilon k/4)(1+\epsilon c_1+\dots)}$$

The reason for this discrepancy is not understood at present.

Before concluding this study we should indicate some of the implications the present results have on the behavior of viscous boundary layers on slightly yawed cones. On a pointed cone the thickness of the viscous and entropy boundary layers grow as follows

$$\delta_{\text{viscous}} \sim \sqrt{r}, \quad \delta_{\text{entropy}} \sim r$$

with a rate that depends on the Reynolds number and yaw angle respectively. Hence near the tip of the cone the viscous boundary layer is thicker than the entropy layer while downstream the entropy layer eventually becomes thicker. Hence we expect classical boundary layer theory to be valid near the tip. The boundary layer solution in this region can then be described by Moore's (1951) similarity solutions. However, downstream the entropy layer becomes thicker than the boundary layer and similarity no longer applies.

In addition we must also consider the more fundamental question of the matching of the viscous and inviscid solutions in these regions. The outer boundary conditions used in viscous boundary layer theory are derived from the matching conditions (see Van Dyke, 1964). In imposing the matching conditions it is assumed that the outer inviscid solution is analytic at the body surface and can be expanded in powers of the normal distance from the wall. In the present analysis we have shown that the inviscid solution is not analytic at the body surface, has infinite gradients at the wall and cannot be expanded in a power series as required in the matching conditions. Hence, a careful analysis of the matching of the inviscid and viscous boundary layer solutions is called for in the case of asymmetric supersonic flow over pointed bodies.

REFERENCES

- Bulakh, B. M., 1962, a Prikl. Mat. i Mech., 26, 430.
- Bulakh, B. M., 1962, b Prikl. Mat. i Mech., 26, 1200.
- Bulakh, B. M., 1962, c Prikl. Mat. i Mech., 26, 1473.
- Ferri, A., 1954, Article in High Speed Aero. Jet Prop., VI Princeton U. Press.
- Ferri, A., Ness, N., and Kaplita, T. T., 1952, J. Aero. Sci., 20, 563.
- Kopal, Z., 1947, a Mass. Inst. Tech. Dep. Elec. Eng., Technical Report No. 1.

- Kopal, Z., 1947, b Mass. Inst. Tech. Dep. Elec. Eng., Technical Report No. 3.
 Kopal, Z., 1949, Mass. Inst. Tech. Dep. Elec. Eng., Technical Report No. 5.
 Melnik, R. E., 1965, Ph.D. Dissertation, Polytechnic Institute of Brooklyn.
 Melnik, R. E., 1967, AIAA Journal, 5, 631.
 Moore, F. K., 1951, NACA Tech. Note, 2521.
 Munson, A. G., 1965, J. Fluid Mech., 20, 645.
 Ness, N. and Kaplita, T. T., 1954, Polytechnic Institute of Brooklyn Report No. 220.
 Sapunkov, I. A., 1963, Prikl. Mat. i Mech., 27, 1422.
 Stone, A. H., 1948, J. Math. and Phys., 27, 67.
 Stone, A. H., 1952, J. Math. and Phys., 30, 200.
 Taylor, G. I. and Maccoll, J. W., 1933, Proc. Roy. Soc. A, 139, 278.
 Van Dyke, M. D., 1964, Perturbation Methods in Fluid Mechanics, Academic Press.
 Woods, B. A., 1962, Aero. Quart., XIII, 115.
 Woods, B. A., 1963, R.A.E. Technical Note No. Aero 2939.

APPENDIX

The following functions arise in the study of the behavior of the outer solution near the cone surface (Section 3).

$$j_1(\xi) = \left(\frac{1}{\gamma M_{ob}^2 \sin^2 \tau} \right) \frac{dp_{1b}(\xi)/p_{ob}}{d\xi} \quad (A.1a)$$

$$l_1(\xi) = - \left(1/\gamma M_{ob}^2 \right) \left[p_{1b}(\xi)/p_{ob} + \gamma s_{1s}(\xi) \right] \quad (A.1b)$$

$$n_1(\xi) = l_1(\xi) - \frac{1}{2} dj_1(\xi)/d\xi \quad (A.1c)$$

$$t_1(\xi) = p_{1b}(\xi)/\gamma p_{ob} + (\gamma - 1) s_{1s}(\xi) \quad (A.1d)$$

$$\Gamma_1(\xi) = \frac{1}{2} (\gamma - 1) j_1(\xi) ds_{1s}(\xi)/d\xi \quad (A.2a)$$

$$\Gamma_2(\xi) = (\gamma - 1) s_{2s}(\xi) - \left[\frac{1}{2} (\gamma - 1) E_2(\xi) \right] ds_{1s}(\xi)/d\xi \quad (A.2b)$$

$$j_2(\xi) = \left(\frac{1}{\gamma M_{ob}^2 \sin^2 \tau} \right) \frac{dp_{2b}(\xi)/p_{ob}}{d\xi} - \left[\left(1 - \frac{1}{M_{ob}^2} \right) \frac{p_{1b}(\xi)}{p_{ob}} - \left(\gamma - 1 - \frac{1}{M_{ob}^2} \right) s_{1s}(\xi) + f(\xi) \cot \tau \right] j_1(\xi) + j_1(\xi) dj_1(\xi)/d\xi \quad (A.3a)$$

$$l_2(\xi) = - \frac{\Gamma_2(\xi)}{(\gamma - 1) M_{ob}^2} - \frac{1}{\gamma M_{ob}^2} \left[\frac{p_{2b}(\xi)}{p_{ob}} - \frac{1}{2\gamma} \left(\frac{M_{ob}^2 - 1}{M_{ob}^2} \right) \left(\frac{p_{1b}(\xi)}{p_{ob}} \right)^2 + \left(\gamma - 1 + \frac{1}{M_{ob}^2} \right) \left(\frac{p_{1b}(\xi)}{p_{ob}} + \frac{\gamma}{2} s_{1s}(\xi) \right) (s_{1s}(\xi)) \right] + \frac{1}{2} j_1^2(\xi) \sin^2 \tau \quad (A.3b)$$

$$n_2(\xi) = l_2(\xi) - \left[\Gamma_1(\xi) / (\gamma - 1) M_{ob}^2 \right] - \frac{1}{2} M_{ob}^2 \sin^2 \tau j_1^2(\xi) - \frac{1}{2} dj_2(\xi)/d\xi + \frac{1}{2} f(\xi) \cot \tau dj_1(\xi)/d\xi \quad (A.3c)$$

$$t_2(\xi) = \left[\frac{p_{2b}(\xi)}{\gamma p_{ob}} - \Gamma_2(\xi) \right] - \frac{\gamma - 1}{2} \left[\left(\frac{p_{2b}(\xi)}{\gamma p_{ob}} \right)^2 + 2 \frac{p_{1b}(\xi)}{p_{ob}} s_{1s}(\xi) - (\gamma - 1) s_{1s}^2(\xi) \right] \quad (A.3d)$$

$$\text{where } E_2(\xi) = - \int_{\tau}^{\eta_{so}} \left[\frac{2(\eta - \tau) w_1(\xi)}{v_o \sin \tau} + \frac{w_{1b}(\xi)}{u_{ob} \sin \tau} \right] \frac{d\eta}{\eta - \tau} \quad (A.4)$$

The following functions appear in the second order inner solution (Section 4).

$$H_1(\xi) = \left[\frac{dp_{2b}(\xi)}{d\xi} / \frac{dp_{1b}(\xi)}{d\xi} \right] - \left[1 - \frac{\gamma}{M_{ob}^2} \right] \frac{p_{1b}(\xi)}{p_{ob}} - 2f(\xi) \cot \tau \quad (A.5)$$

$$J_2(\xi) = j_2(\xi) - \left[(\gamma - 1) + \frac{1}{M_{ob}^2} \right] [s_{1s}(\xi) - s_{1s}(\psi)] \quad (A.6a)$$

$$L_2(\xi, \psi) = - \frac{s_{2s}(\psi)}{M_{ob}^2} - \frac{1}{\gamma M_{ob}^2} \left[\frac{p_{2b}(\xi)}{p_{ob}} - \frac{1}{2\gamma} \left(\frac{M_{ob}^2 - 1}{M_{ob}^2} \right) \left(\frac{p_{1b}(\xi)}{p_{ob}} \right)^2 + \left(\gamma - 1 + \frac{1}{M_{ob}^2} \right) \left(\frac{p_{1b}(\xi)}{p_{ob}} + \frac{\gamma}{2} s_{1s}(\psi) \right) (s_{1s}(\psi)) \right] - \frac{1}{2} J_1^2(\xi) \sin^2 \tau \quad (A.6b)$$

$$N_2(\xi, \psi) = L_2(\xi, \psi) - \frac{1}{2} \left(\gamma - 1 + \frac{2}{M_{ob}^2} \right) j_1(\psi) \frac{ds_1(\psi)}{d\psi} - \frac{1}{2} M_{ob}^2 \sin^2 \tau j_1^2(\xi) - \frac{1}{2} dJ_2(\xi, \psi)/d\xi + \frac{1}{2} f(\xi) \cot \tau dj_1(\xi)/d\xi \quad (A.6c)$$

$$T_2(\xi, \psi) = \left[\frac{p_{2b}(\xi)}{\gamma p_{ob}} - (\gamma - 1) s_{2s}(\psi) \right] - \frac{\gamma - 1}{2} \left[\left(\frac{p_{1b}(\xi)}{\gamma p_{ob}} \right)^2 + 2 \frac{p_{1b}(\xi)}{p_{ob}} s_{1s}(\psi) - (\gamma - 1) s_{1s}^2(\psi) \right] \quad (A.6d)$$

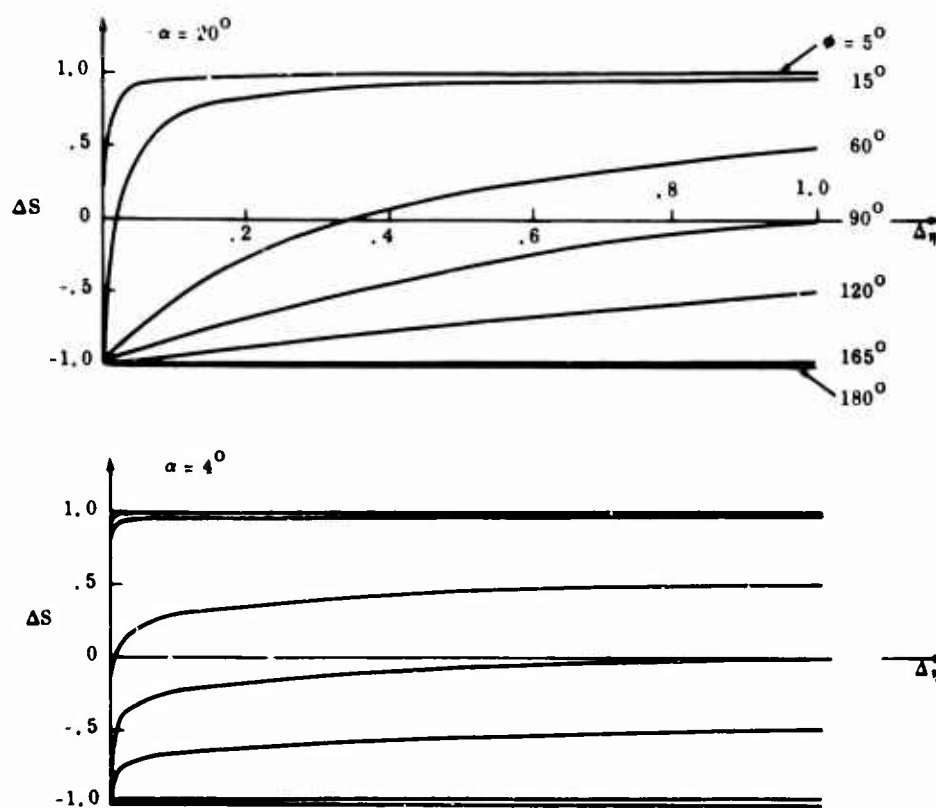


Fig. 2 Entropy Profiles for a Yawed Circular Cone

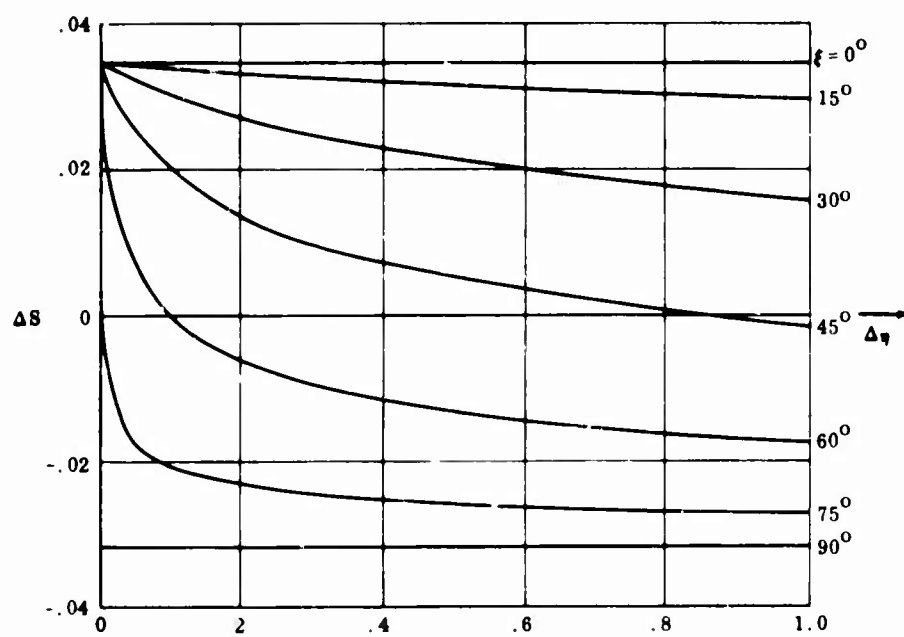


Fig. 3 Entropy Profile for an Elliptic Cone at Zero Angle of Attack

Etude de l'Ecoulement
à un nombre de Mach de 18 autour
d'une plaque plane en incidence et à
bord d'attaque variable

par

J. Allègre et Ch. Bisch
Laboratoire d'Aérodynamique
du C.N.R.S.
Meudon - France

SOMMAIRE

Si les études expérimentales à nombre de Mach élevé sur des plaques planes sont nombreuses, elles sont généralement limitées au cas de l'incidence nulle. Les expériences présentées comprennent des mesures de la pression pariétale et de la pression d'arrêt au-dessus d'une plaque plane dont l'incidence varie de -6° à $+9^\circ$ et dont l'épaisseur du bord d'attaque est comprise entre 0,07 mm et 1,5 mm. Ces mesures mettent en évidence les variations de l'emplacement et de l'intensité du choc, variations qui entraînent d'importantes modifications des valeurs de la pression pariétale. Enfin, des photographies de visualisation par effluves électriques permettent de vérifier la position et la forme du choc.

NOMENCLATURE

C	- constante de Chapman Rubesin,
e	- épaisseur du bord d'attaque,
i	- angle d'incidence de la plaque; $i > 0$ pour les écoulements en compression sur la surface,
k	- coefficient de traînée du bord d'attaque,
M_∞	- nombre de Mach de l'écoulement non perturbé, mesuré dans la section de veine passant par le bord d'attaque,
p	- pression statique de l'écoulement non perturbé,
$p_{t2}, p_{t2\infty}$	- pression d'arrêt locale et pression d'arrêt de l'écoulement non perturbé,
Re	- nombre de Reynolds,
T_0	- température génératrice de l'écoulement,
T_p	- température pariétale de la plaque,
\bar{v}	- paramètre de raréfaction : $\bar{v} = M_\infty (C/Re_x)^{1/2}$,
$\bar{\chi}$	- paramètre d'interaction visqueuse : $\bar{\chi} = M_\infty^3 (C/Re_x)^{1/2}$,
χ_e	- paramètre d'effet de déplacement de la couche limite : $\chi_e = (\gamma-1)/(\gamma+1) [0,664 + 1,73 (T_p/T_0)] M_\infty^3 (C/Re_x)^{1/2}$,
ϵ	- $\epsilon = (\gamma-1)/(\gamma+1)$,
x,y	- coordonnées rectangulaires ayant pour origine le bord d'attaque, respectivement parallèles et perpendiculaires à la plaque,
x_1, y_1	- coordonnées rectangulaires ayant pour origine le bord d'attaque, respectivement parallèles et perpendiculaires à l'écoulement.

.../...

1. INTRODUCTION.

Au cours de ces dernières années, les problèmes d'ondes de choc et de développement de couche limite à des nombres de Mach élevés, sur une plaque plane à angle d'incidence nul, ont fait l'objet de nombreuses recherches; par exemple, les références 1, 2, 3, 4 et 5 se rapportent aux régimes de faible et forte interactions et, plus récemment, les références 6 et 7 ont trait à la région d'écoulement proche du bord d'attaque pour laquelle la couche limite fusionne avec l'onde de choc, zone appelée "merged layer". Cette dernière région assure la liaison entre le modèle d'écoulement cinétique au bord d'attaque, d'une part, et la couche limite hypersonique classique à l'aval, d'autre part. En même temps, plusieurs théories étaient suggérées, références 8, 9, 10 et 11, et il est possible de calculer, par exemple, les pressions pariétales et les flux thermiques avec une approximation raisonnable.

Pour des incidences positives ou négatives, d'importants changements apparaissent dans l'épaisseur de déplacement de la couche limite le long de la plaque. Ceci entraîne une variation de l'intensité de l'onde de choc incidente et, en conséquence, affecte très sensiblement les valeurs des pressions induites. La connaissance de l'interaction couche limite onde de choc sur la plaque plane en incidence nulle n'est pas suffisante pour prédire avec certitude les caractéristiques de l'écoulement sur une plaque en incidence; il est nécessaire de connaître avec exactitude quelques quantités utiles telles que la localisation de l'onde de choc et les distributions de pressions pariétales. De plus, les effets de déplacement de couche limite dépendent considérablement de la température de paroi; à cet égard, nous noterons les travaux théoriques de CHENG[8] et OGUCHI[10] qui tiennent compte de la température de paroi.

2. CONDITIONS EXPERIMENTALES.

2.1. Soufflerie.

Les présentes expériences ont été effectuées dans la soufflerie SH3 du laboratoire d'Aérodynamique[16]. Bornons-nous à rappeler que cette soufflerie, à fonctionnement continu, utilise un réservoir d'azote à haute pression, un surpresseur à membrane et une pompe à vide rotative à deux étages. La chambre de tranquillisation est conçue pour supporter plus de 200 bars et des températures du gaz pouvant atteindre 2 000°K. L'azote est chauffé par effet Joule au moyen d'un réchauffeur en graphite à double traversée. La tuyère tronconique, de 20° d'angle d'ouverture, a un diamètre au col de 1,2 mm et un diamètre de sortie de 100 mm.

Dans les expériences actuelles, la pression génératrice p_0 et la température génératrice T_0 sont respectivement de 100 bars et de 1 400°K; à ces conditions, correspondent, dans la veine d'expérience, un nombre de Mach de 18, un nombre de Reynolds de 10 500 par cm, une pression statique de 32 microns de mercure et une température de 21°K.

Des études antérieures ont été effectuées pour définir l'influence de la condensation du gaz sur les caractéristiques de pression de l'écoulement. Les résultats présentés par GRIFFITH[19] concordent avec les expériences de DAUM[20]. Ils montrent que, si l'on considère la pression de l'écoulement libre obtenue dans les expériences actuelles, la limite de la condensation correspond à une température inférieure à 15°K. Par conséquent, aucun effet de condensation n'a lieu dans ces conditions particulières.

2.2. Modèle.

Le modèle utilisé est une plaque plane en laiton, refroidie par circulation d'eau, de 40 mm d'envergure, 60 mm de long et 5 mm d'épaisseur. Les angles des dièdres du bord d'attaque et du bord de fuite sont respectivement de 20° et 30°.

Initialement, l'épaisseur minimale moyenne du bord d'attaque, mesurée au microscope, est de 0,07 mm; ensuite, le bord d'attaque est épaissi, en le limant perpendiculairement à la surface de la plaque, afin d'obtenir une épaisseur maximale de 1,5 mm.

La plaque est tenue latéralement par un bras cylindrique qui traverse un des hublots de la soufflerie; il permet de positionner la plaque dans l'axe de l'écoulement à l'incidence choisie. Le bras sert également de passage aux sept tubes de prise de pression reliant la plaque à l'appareil de mesure et aux deux tubes de circulation d'eau permettant de maintenir la température de paroi de la plaque à environ 300°K. Les sept prises de pression sont situées sur deux lignes distantes de 5 mm de l'axe longitudinal de la plaque, de 5 mm en 5 mm, entre les abscisses 10 mm et 40 mm; leur diamètre est de 0,8 mm.

Une visualisation par dépôt d'huile a permis de vérifier qu'aucune perturbation marginale n'affecte la zone explorée.

2.3. Mesures statiques et dynamiques.

La pression génératrice est mesurée à $\pm 2\%$ près avec un manomètre à membrane; dans la veine, les pressions ont été relevées à l'aide d'un alphanon avec une précision de lecture de $\pm 5\%$; les temps de réponse pour les mesures de pressions pariétales sont de l'ordre de trois minutes. Avant toute expérience, l'ensemble des conduits de pression est dégazé pendant plusieurs heures; cette précaution est une condition indispensable pour obtenir une bonne fidélité des mesures.

Les explorations dynamiques sont réalisées avec un tube de Pitot de 1,2 mm de diamètre extérieur et de 0,7 mm de diamètre intérieur; ces dimensions permettent d'obtenir un temps de réponse relativement court. L'ordonnée de l'axe du tube, comptée à partir de la plaque, est lue au moyen d'une lunette assurant une précision de lecture de $\pm 0,05$ mm.

.../...

L'angle d'incidence de la plaque est vérifié pendant le fonctionnement de la soufflerie, car les efforts aérodynamiques sont susceptibles de modifier le calage initialement choisi; cette vérification consiste à projeter l'ombre d'un rapporteur à vernier sur le profil de la plaque jusqu'à l'obtention d'un parallélisme vérifiable à la lunette; la précision est de $\pm 0,04^\circ$.

3. RESULTATS.

3.1. Plaque plane à bord d'attaque effilé.

Initialement, l'épaisseur du bord d'attaque est de 0,07 mm. Rapporté à cette épaisseur, le nombre de Reynolds n'est que de 70, et les effets majeurs intervenant dans la pression pariétale et le transfert de chaleur sont dus surtout à la viscosité.

Les valeurs des pressions pariétales corrigées, rapportées à la pression statique de l'écoulement non perturbé, sont données sur la figure 1 en fonction du paramètre d'interaction visqueuse $\bar{\chi} = M_\infty^3 (C/Re_x)^{1/2}$ pour l'incidence nulle; elles sont comparées à des résultats expérimentaux antérieurs et à quelques théories existantes.

Il semble que les pentes des courbes des variations théoriques définies par OGUCHI[10], CHENG[8] et AROESTY[9] soient trop grandes pour les valeurs considérées du paramètre. La grande différence constatée entre les résultats expérimentaux présentés et la loi d'AROESTY provient du fait que, dans ses calculs, l'auteur considère une paroi adiabatique.

La constante de Chapman-Rubesin, calculée suivant la méthode de CHENG[8], a pour valeur 0,76 dans les conditions de l'expérience.

La pression de paroi est corrigée selon la méthode présentée en référence 21 afin de tenir compte des effets résultant du transfert de chaleur entre l'écoulement et la paroi refroidie et des conditions de raréfaction du gaz.

On a négligé les effets dus au gradient longitudinal du nombre de Mach $(1/M)(dM/dx)$ qui est de l'ordre de 1% par centimètre. En fait, il semble très difficile de prédire de quelle manière la pression pariétale mesurée dépend de la variation longitudinale du nombre de Mach; en tenant compte de la courbure des lignes de courant en aval de l'onde de choc, il est probable que seule la valeur du nombre de Mach à la partie frontale du choc incident doit être prise en considération. Pour toutes les expériences, le nombre de Mach de référence de l'écoulement libre est mesuré à la verticale du bord d'attaque.

Les pressions pariétales, rapportées à la pression statique de l'écoulement non perturbé, sont portées sur la figure 2 en fonction de l'abscisse de la plaque. Leurs valeurs augmentent en même temps que l'angle d'incidence. Cependant, à l'incidence -6° , on observe une très forte élévation de la pression à l'aval de la section située à 20 mm du bord d'attaque; ceci est probablement dû au décollement local de la couche limite.

Les explorations dynamiques faites au tube de Pitot près de la surface de la plaque et à 20 mm du bord d'attaque sont représentées, sur la figure 3, pour six angles d'incidence. Compte tenu de la grande dimension du tube de Pitot comparée à l'épaisseur de la couche de choc, toutes les mesures se réfèrent à la position de son axe. Comme on l'a indiqué sur la même figure 3, l'ordonnée y_c du choc est positionnée au milieu de la partie approximativement linéaire des courbes de pression. Aux incidences croissantes correspond une augmentation de l'intensité du choc et son rapprochement corrélatif de la paroi; les photographies de l'écoulement visualisé par effluves montrent que la trace de l'onde de choc atteint une pente minimale quasi constante pour les valeurs de l'angle d'incidence supérieures à environ 12° .

3.2. Plaque plane à bord d'attaque tronqué.

L'influence de l'épaisseur du bord d'attaque est indiquée sur les figures 4, 5 et 6 où les pressions pariétales, rapportées à la pression statique de l'écoulement non perturbé, sont portées en fonction de l'abscisse de la plaque pour trois valeurs de l'angle d'incidence. A l'incidence -6° (fig. 4), la forte élévation de pression enregistrée pour le bord d'attaque effilé n'apparaît plus avec le bord d'attaque tronqué. Des différences sensibles dans les niveaux de pressions mesurées sont observées, surtout dans la région voisine du bord d'attaque; par exemple, à angle d'incidence nul (fig. 5), à l'abscisse $x = 10$ mm, la valeur de p/p_∞ double presque lorsque l'épaisseur du bord d'attaque croît de 0,07 à 1,5 mm.

Les explorations dynamiques faites au tube de Pitot sont présentées sur les figures 7 et 8 aux angles d'incidence de 0° et 6° pour différentes valeurs de l'épaisseur du bord d'attaque. Les emplacements correspondants du choc sont indiqués sur la figure 9, en fonction de l'épaisseur du bord d'attaque, pour six valeurs de l'incidence.

La figure 10 montre les photographies de visualisation par effluves électriques correspondant aux deux épaisseurs 0,07 mm et 1,5 mm du bord d'attaque et aux incidences -6° , 0° et $+6^\circ$. On peut y constater les très nettes différences de forme et de position du choc suivant les cas considérés. Nous avons pu aussi vérifier que les positions déduites de la visualisation concordent avec celles obtenues au tube de Pitot, à la précision de lecture près.

Remerciements

Les auteurs tiennent à exprimer à Monsieur le Professeur Edmond A. BRUN, Directeur du Laboratoire d'Aérodynamique, leur profonde gratitude pour le soutien qu'il a bien voulu leur apporter au cours de cette étude.

REFERENCES

- [1] - I.E. VAS, J.G. Mc DOUGALL, G. KOPPENWALLNER, S.M. BOGDONOFF : "Some exploratory experimental studies of hypersonic low density effects on flat plates and cones". Rarefied Gas Dynamics, Fourth Symposium, vol. 1, Academic Press, New York, 1965, p. 508-534.
- [2] - S.M. BOGDONOFF, I.E. VAS : "Preliminary studies of the flow around two-dimensional bodies at high Mach numbers and low Reynolds numbers". Report 754, Gas Dynamics Laboratory, Princeton University, N.J.
- [3] - R.J. VIDAL, J.C. GOLIAN, J. BARTZ : "An experimental study of hypersonic low density viscous effects on a sharp flat plate". AIAA Paper 435, 1963.
- [4] - H.T. NAGAMATSU, D.C. WISLER, R.E. SHEER Junior : "Continuum to free molecule flow in the vicinity of the leading edge of a flat plate at Mach numbers of 19,4 and 24,1". General Electric (RADG) Report n° 67-C-247, June 1967.
- [5] - N.I. YUSHENKOVA, A.A. POMERANTSEV and V.I. NEMCHENKO : "Influence of real gas effects on the hypersonic rarefied flow near the sharp leading edge of a thin plate". Int. Journal of Heat and Mass Transfer, vol. 10, n° 1, January 1967, p. 5-14.
- [6] - W.J. Mc CROSKY, S.M. BOGDONOFF, J.G. Mc DOUGALL : "An experimental model for the sharp flat plate in rarefied hypersonic flow". AIAA Journal, sept. 1966, p. 1580-1587.
- [7] - I.E. VAS, J. ALLEGRE : "The N-4 hypersonic low density facility and some preliminary results on a sharp flat plate". Rarefied Gas Dynamics, Fifth Symposium, vol. II, Academic Press, New York, 1967, p. 1015-1030.
- [8] - H.K. CHENG, J.G. HALL, T.C. GOLIAN, A. HERTZBERG : "Boundary layer displacement and leading edge bluntness effects in high temperature hypersonic flow". J.A.S., n° 5, vol. 28, May 1961, p. 353-381.
- [9] - J. AROESTY : "Strong interaction with sl p boundary conditions". A.R.L. Report 64, 1961.
- [10] - H. OGUCHI : "The sharp leading edge problem in hypersonic flow". Rarefied Gas Dynamics, Second Symposium, Academic Press, New York, 1961, p. 501-524.
- [11] - W.D. HAYES, R.F. PROBSTEN : "Hypersonic flow theory". Academic Press, New York, 1959.
- [12] - R.J. VIDAL, J. BARTZ : "Experimental studies of low density effects in hypersonic wedges flows". Rarefied Gas Dynamics, Fourth Symposium, vol. 1, Academic Press, New York, 1965, p. 467-486.
- [13] - FELDHUHN, PARSAPOUR : Aeronautical Reports, Princeton University, N.J.
- [14] - W.J. Mc CROSKY, S.M. BOGDONOFF, A.P. CENGHI : "Leading edge flow studies of sharp bodies in rarefied hypersonic flow". Rarefied Gas Dynamics, Fifth Symposium, Academic Press, New York, 1967, p. 1047-1060.
- [15] - J.E. WALLACE, A.F. BURKE : "Cornell Aeronautical Laboratory, ASD-TDR 63-772.
- [16] - J. ALLEGRE, C. BISCH, D. FAULMANN : "La soufflerie hypersonique SH3 du Laboratoire d'Aérodynamique du C.N.R.S.". Laboratoire d'Aérodynamique, Rapport n° 66-4, 1966.
- [17] - I.E. VAS, G. KOPPENWALLNER : "The Princeton university high pressure hypersonic nitrogen tunnel N3". Report 690-1964, Gas Dynamics Laboratory, Princeton University, N.J.
- [18] - "Equations, Tables and Charts for Compressible Flow". NACA, Report 1135.
- [19] - B.J. GRIFFITH, H.E. DESKINS, H.R. LITTLE : "Condensation studies in hotshot tunnels". AIAA J. 2, Sept. 1964, p. 1645-1647.
- [20] - F.L. DAUM : "Air Condensation in hypersonic wind tunnel". AIAA J. 1, May 1963, p. 1043-1046.
- [21] - J.L. POTTER, M. KINSLOW, D.E. BOYLAN : "An influence of the orifice on measured pressures in rarefied flow". Rarefied Gas Dynamics, Fourth Symposium, vol. II, Academic Press, New York, 1965, p. 175-193.

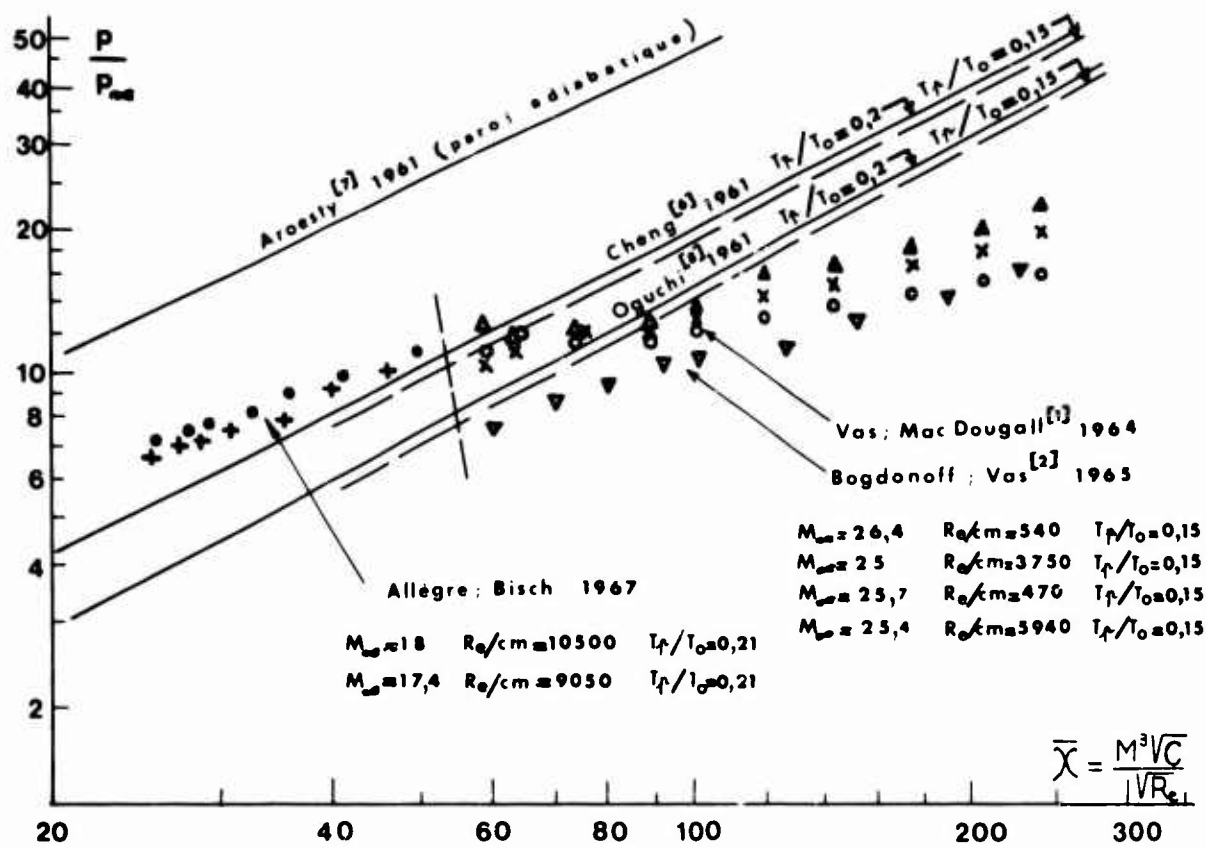


Fig. 1 - Distribution de la pression pariétale de la plaque plane effilée en fonction du paramètre d'interaction visqueuse.

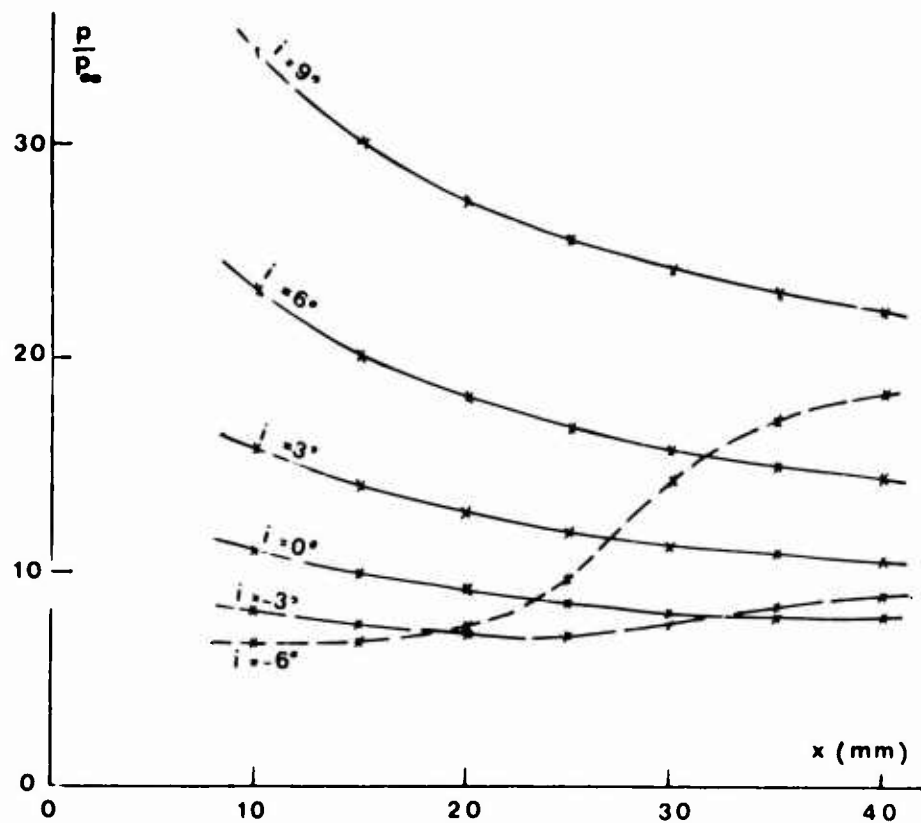


Fig. 2 - Distribution de la pression pariétale le long de la plaque plane effilée pour six angles d'incidence.

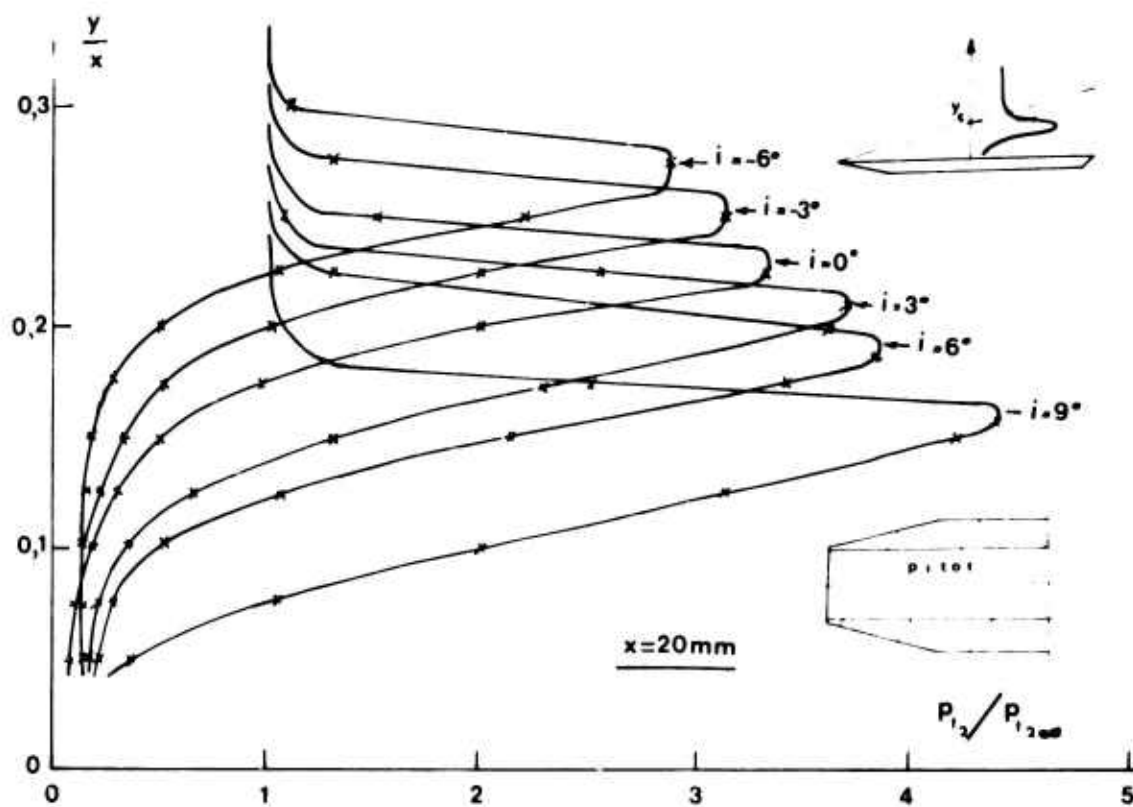


Fig. 3 - Explorations au tube de Pitot effectuées à 20 mm du bord d'attaque de la plaque plane effilée, pour six angles d'incidence.

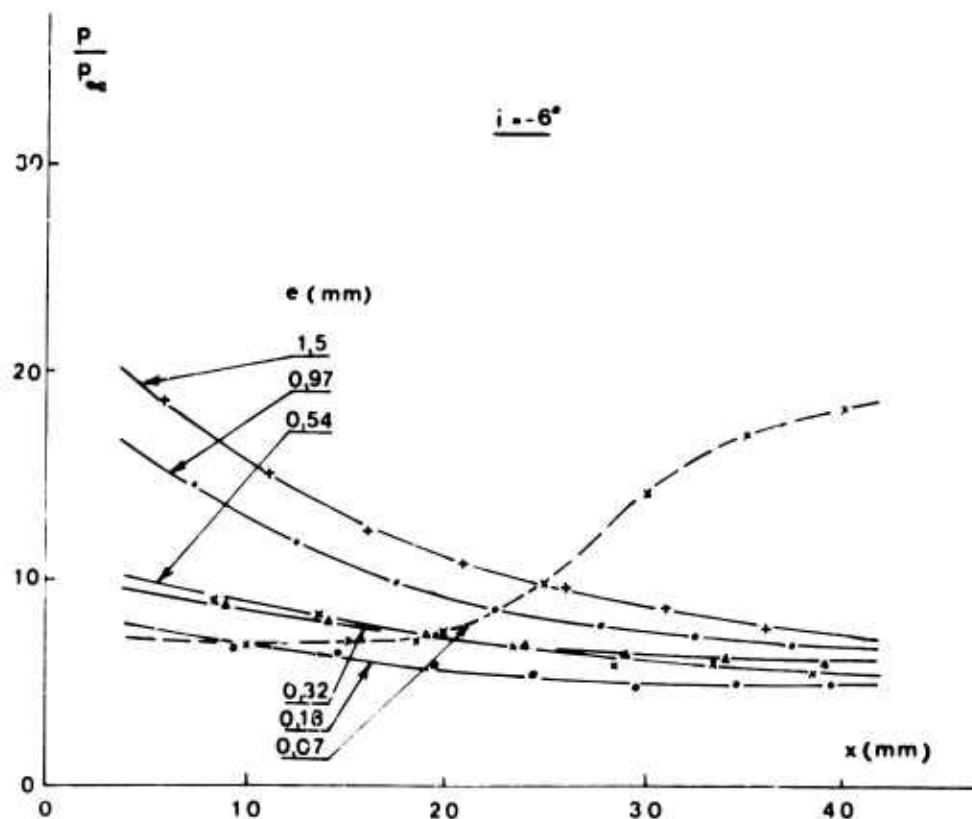


Fig. 4 - Distribution de la pression pariétale le long de la plaque plane émoussée pour l'incidence -6° .

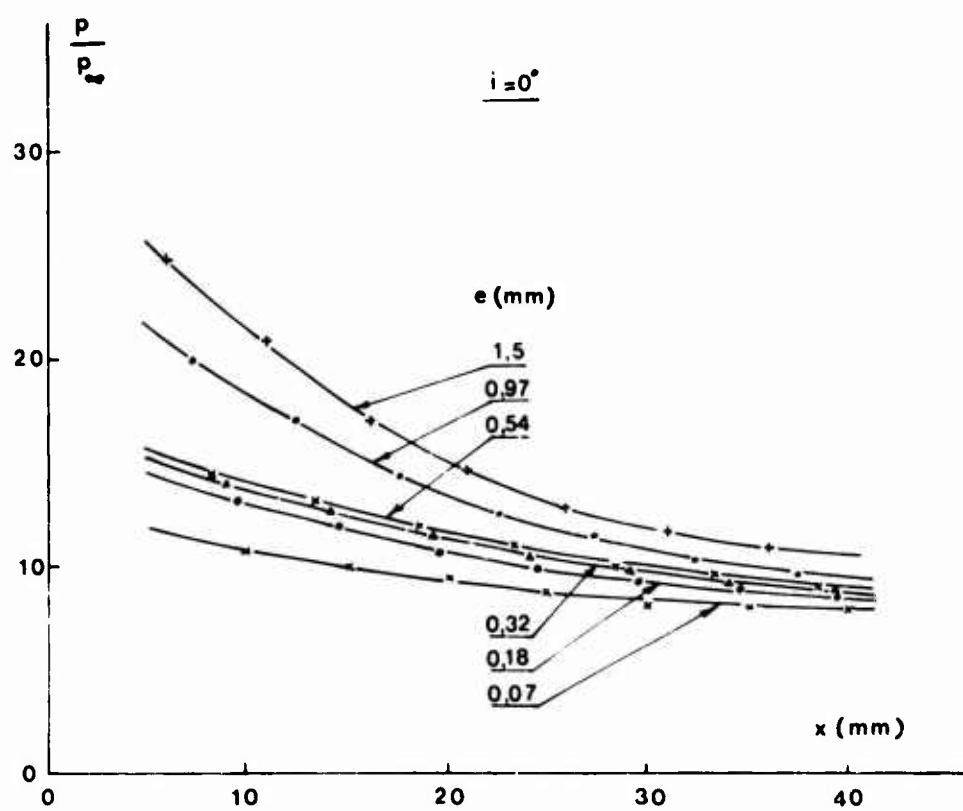


Fig. 5 - Distribution de la pression pariétale le long de la plaque plane émoussée pour l'incidence nulle.

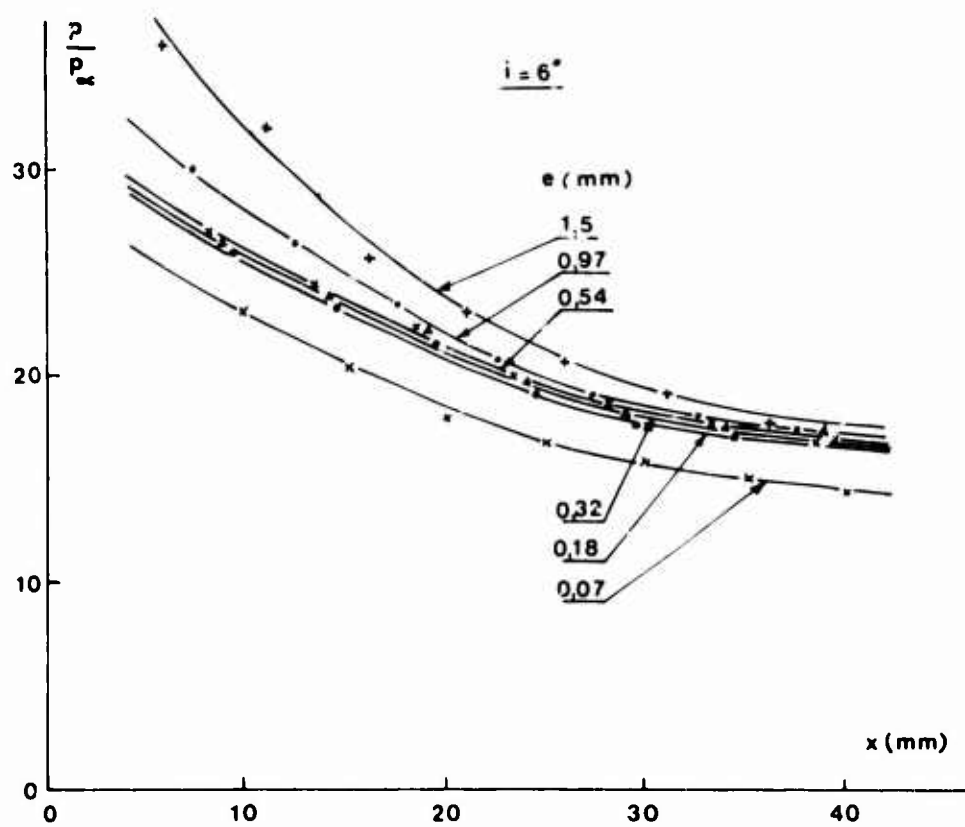


Fig. 6 - Distribution de la pression pariétale le long de la plaque plane émoussée pour l'incidence $+6^\circ$.

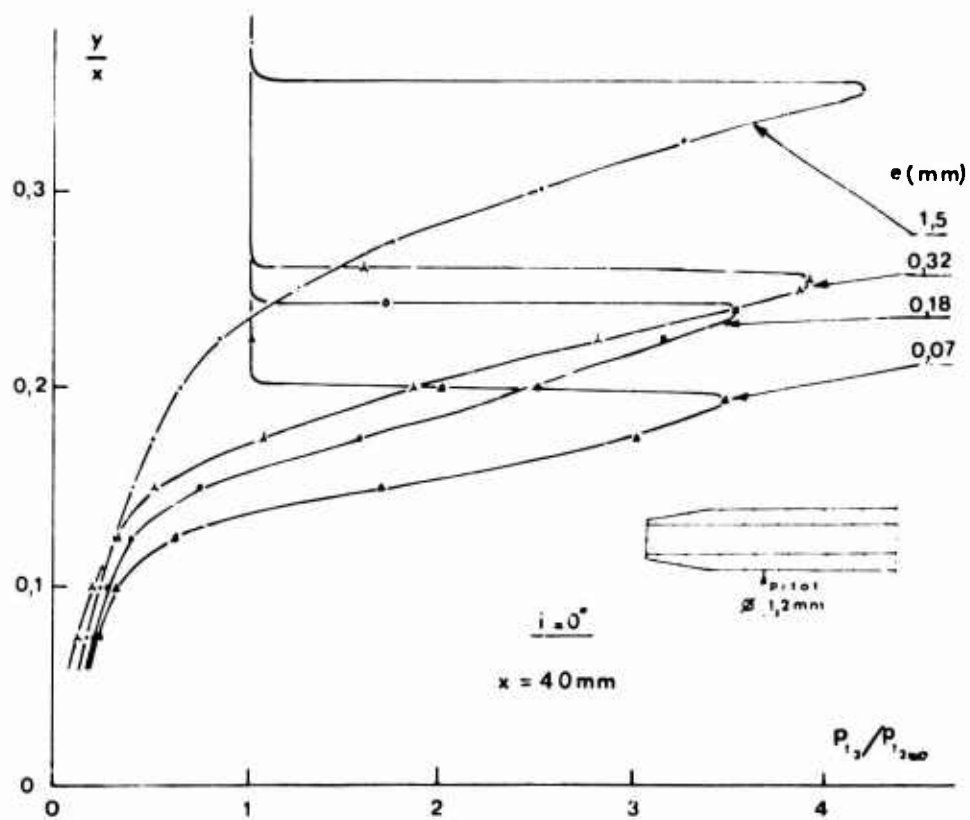


Fig. 7 - Explorations au tube de Pitot effectuées à 40 mm du bord d'attaque pour l'incidence nulle.

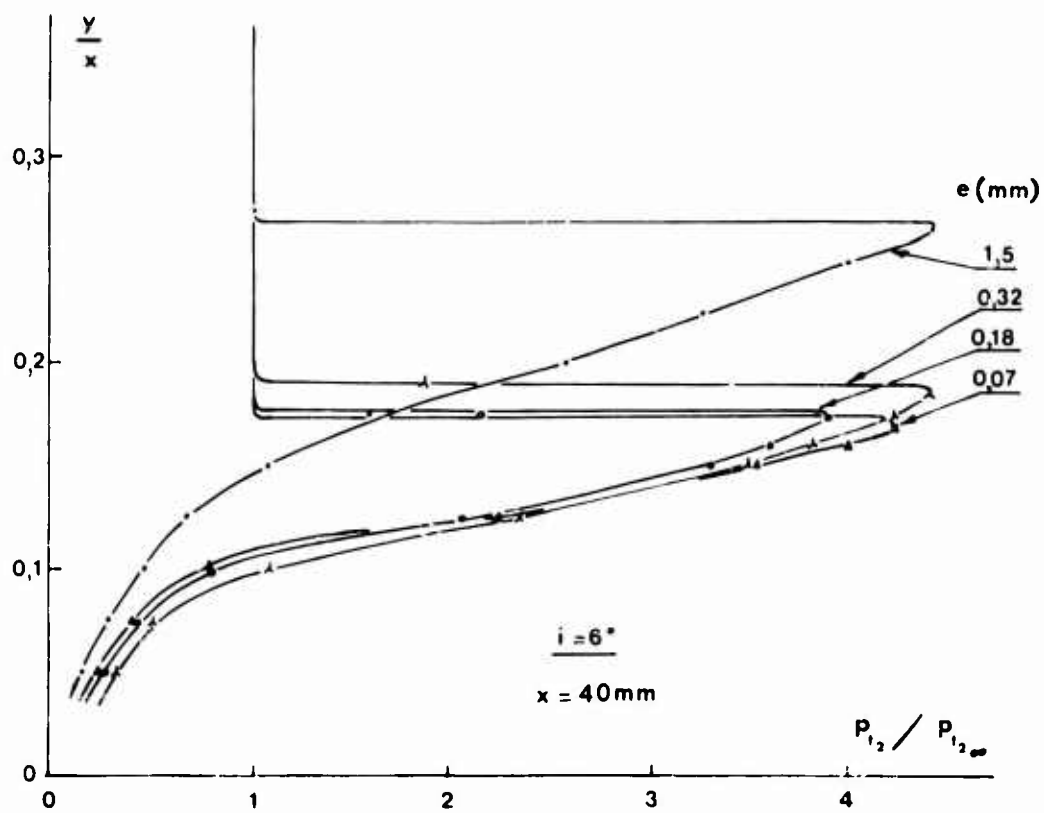


Fig. 8 - Explorations au tube de Pitot effectuées à 40 mm du bord d'attaque pour l'incidence 6° .

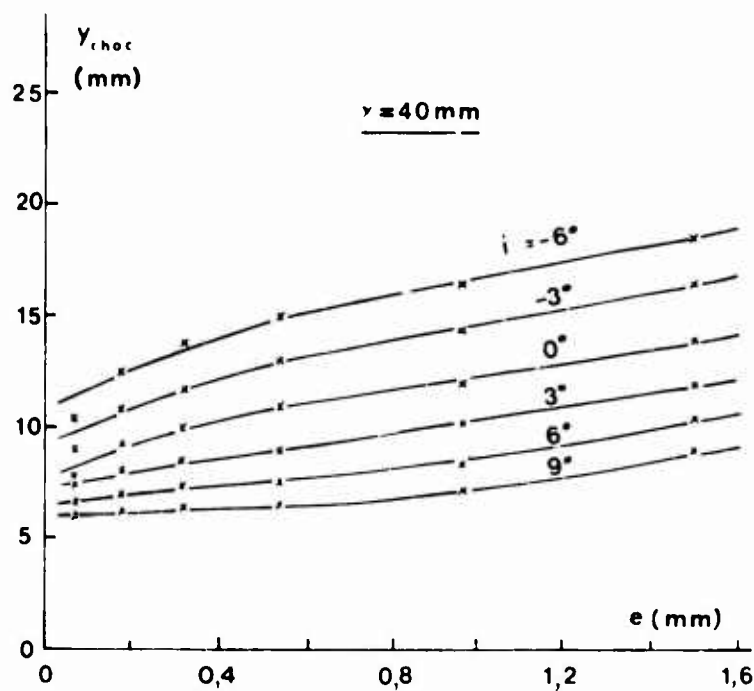


Fig. 9 - Position de l'onde de choc en fonction de l'épaisseur du bord d'attaque pour six angles d'incidence.

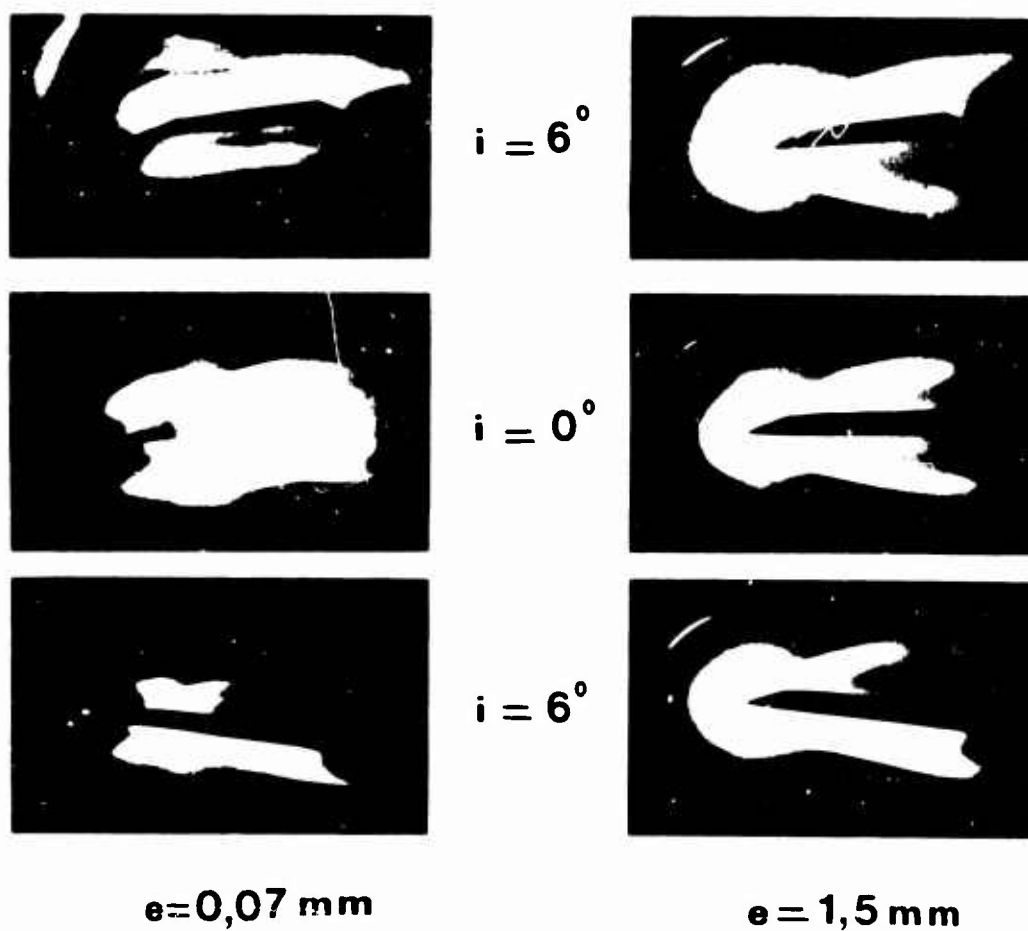


Fig. 10 - Photographies d'effluves électriques correspondant aux deux épaisseurs du bord d'attaque de 0,07 et 1,5 mm et aux incidences de -6° , 0° et 6° .

STUDIES OF THREE-DIMENSIONAL, COMPRESSIBLE BOUNDARY
LAYERS ON BLUNT LIFTING ENTRY BODIES*

by

Sang-Wook Kang**, William J. Rae*, and Michael G. Dunn**

CORNELL AERONAUTICAL LABORATORY, INC.
Buffalo, New York, U.S.A.

*This work was supported by the National Aeronautics and Space Administration, Goddard Space Flight Center, under Contract NAS 5-9978.

**Research Mechanical Engineer, Aerodynamic Research Department

*Principal Research Engineer, Aerodynamic Research Department

**Principal Mechanical Engineer, Aerodynamic Research Department

SUMMARY

Theoretical studies of the three-dimensional, laminar, compressible boundary layer with mass injection are reported. Applications are given to cases typical of the heat shield of the Apollo vehicle during lifting reentry. The studies are divided in two parts. The first part, reviewed only briefly here, is restricted to the case of small secondary flow. The second part, which makes up the major content of this paper, consists of an integral method in which the small-secondary-flow restriction need not be made. Applications of the latter method are described; significant nonsimilar effects associated with mass injection and inviscid-streamline curvature are observed.

NOTATION

A	Streamwise wall-shear parameter, $\left(\frac{\partial U}{\partial \eta}\right)_b$
a	Constant, $\frac{3/\pi}{2}$
B	Heat-transfer parameter, $\left(\frac{\partial \theta}{\partial \eta}\right)_b$
C	Secondary-flow wall-shear parameter, $\left(\frac{\partial V}{\partial \eta}\right)_b = \frac{c^2 G - Q}{a^2 + W}$
C'	Coefficient for viscosity; Eq. (13)
D	Dimensionless streamline curvature, $K_1 l$, Eq. (14)
E_2	Dimensionless metric coefficient, e_2/e_{2r}
e_1, e_2	Metric coefficients in curvilinear coordinate system
F_i	Functions defined in Section 3.3
f	Dimensionless (Howarth-Dorodnitsyn) stream function in Section 2
G, F	Profile parameters for secondary-flow velocity, Eq. (28)
$g(\eta)$	Profile function for the secondary-flow velocity
H	Total enthalpy, $\lambda + \frac{u^2 + v^2}{2}$
λ	Static enthalpy
H_i	Total enthalpy-defect thickness, Eq. (11)
$\lambda(\eta)$	Profile function for the secondary-flow velocity
K_1, K_2	Geodesic curvature of streamlines, $K_1 = \frac{1}{e_1 e_2} \frac{\partial e_1}{\partial y}$, $K_2 = \frac{1}{e_1 e_2} \frac{\partial e_2}{\partial x}$
l	Body nose radius
M_i	Dimensionless displacement thickness, Eq. (32), $\frac{\delta_i}{\Delta}$
M_j	Dimensionless momentum-defect thickness, Eq. (31), $\frac{\delta_{ij}}{\Delta}$
m_i	Profile functions, Section 3.2
N	Mass injection ratio, $\frac{\rho_b w_b}{\rho_\infty u_\infty}$
P	Dimensionless pressure-gradient parameter, Section 3.1
P_i	Constants defined in Appendix
Pr	Prandtl number
p	Pressure
Q	Dimensionless streamline-curvature parameter, Section 3.1
Q_i	$\frac{Q}{a^2 + W}$, Section 3.2
r	Distance from the body surface to the axis of symmetry
Re	Reynolds number, $\frac{\rho_\infty u_\infty l}{\mu_\infty}$
S	Sutherland constant, Eq. (13)
Δ	Line element
T_i	Dimensionless total enthalpy-defect thickness, Eq. (31) $\frac{H_i}{\Delta}$
U	Dimensionless streamwise velocity, $\frac{u}{u_\infty}$
V	Dimensionless secondary-flow (transverse) velocity, $\frac{v}{u_\infty}$

W	Dimensionless mass-injection parameter, Eq. (14)
W_p	$P_r W$
W_i	$\frac{a W}{a^2 + W}$, Section 3.2
u, v, w	Velocities in curvilinear coordinate directions
x, y, z	Curvilinear coordinates
X	Dimensionless distance along streamline, $\frac{e, d \psi}{l}$
Z	Transformed coordinate normal to the body surface, Eq. (12)
α	Defined in Eq. (43), $\tan^{-1} \left(\frac{C}{A} \right)$
σ	Defined in Eq. (39)
β	Pressure-gradient parameter, $\frac{2 \xi}{u_e} \cdot \frac{H_e}{h_e} \cdot \frac{du_e}{d\xi}$
γ	Specific-heat ratio
Δ	Transformed boundary-layer thickness, Section 3.1
δ	Physical boundary layer thickness
δ_i	Displacement thickness, Eq. (11)
δ_{ij}	"Momentum-defect" thickness, Eq. (11)
η	$\frac{Z}{\Delta}$
θ	Total enthalpy ratio, $\frac{H}{H_e}$
μ	Viscosity
ν	Kinematic viscosity
ξ, η^*	Howarth-Dorodnitsyn transformation coordinates, Section 3.4
ρ	Mass density
τ_i	Wall-shear stress, Eq. (46)
ϕ	Coordinate normal to streamlines
ψ	Stream function
Ω	Dimensionless boundary-layer thickness, $\frac{\Delta}{l} \sqrt{Re}$

Subscripts

b	Surface condition
e	Local value at the outer edge of the boundary layer
r	Reference condition
o	Condition behind a normal shock
∞	Free-stream condition

Note: Bar over symbol signifies dimensionless variables.

STUDIES OF THREE-DIMENSIONAL, COMPRESSIBLE BOUNDARY LAYERS ON BLUNT LIFTING ENTRY BODIES

S.W. Kang, W.J. Rae, and M.G. Dunn

1. INTRODUCTION

The objective of the research described in this paper was to investigate the boundary layers on the heat shield of a blunt lifting entry body. These boundary layers are three-dimensional in character and, because of the energy dissipated in the heat shield during entry, the influence of mass injection on their development must be included in the analysis.

The essential features of three-dimensional boundary-layer flows were first discussed by Hayes¹, Moore², and Mager³. These papers were followed by an extensive literature⁴⁻²⁶. Analyses have been performed for special geometries, where simplifications in the governing equations are possible, such as yawed infinite cylinders⁴⁻⁶ and flat plates⁷⁻¹⁰. Numerous analyses are also available for other special cases, for example, flows where the secondary-flow (transverse) velocity component is assumed to be small compared with the streamwise velocity¹¹⁻²¹, flows in the stagnation region²²⁻²⁵, and flows over a blunt-nosed cold body²⁶. Techniques are available²⁷⁻³¹ for studying the influence of mass injection on the boundary-layer characteristics for axisymmetric or two-dimensional flow fields with or without pressure gradient. However, analyses^{18,32} dealing with the influence of mass injection on three-dimensional boundary layers are considerably more limited in scope in that they are restricted to the case of small secondary flow.

The purpose of the present paper is to analyze the effects of mass injection on general three-dimensional boundary-layer flows. The studies were performed in two parts. In the first³², the objective was to estimate the magnitude of the three-dimensionality under conditions typical of an Apollo reentry. In making these estimates, it was assumed that the boundary layer was laminar and that the secondary flow was small. By application of a local-similarity assumption, solutions were obtained for the secondary-flow velocity profiles, the streamwise velocity profiles and the total-enthalpy profiles. The results of this work showed that the three-dimensionality of the flow was too large to be adequately treated by a small-secondary-flow assumption. Therefore, the second part of the study³³ was initiated in which an integral method, which eliminated the constraints of small secondary flow and local similarity, was applied to obtain a general analysis of the three-dimensional, compressible boundary layer. The profiles used for the velocity components and the enthalpy are patterned after those found in the previous analysis³². No assumptions are made concerning similarity of the flow characteristics or the magnitude of the secondary-flow velocity component, however. This integral method has been applied to a specific flight condition typical of an Apollo-type body and the results are briefly discussed.

For the studies described above, calculations were performed for the limiting case of no mass injection and the more practical case of mass injection. The analysis deals principally with the fluid dynamics of the problem, and thus the gas is assumed to be nonreacting. The material contained in this paper includes material from Ref. 32 not previously reported in the open literature (Section 2) and a detailed treatment of the material reported in Ref. 33 (Section 3). It is recognized that knowledge of the afterbody separated-flow region is also important for blunt lifting vehicles. To this end, an approximate analysis has been conducted by Rae³⁴ to estimate separated-flow profiles over an axisymmetric afterbody. Further discussion of this work is not included in the present paper.

2. LOCALLY SIMILAR FLOWS WITH SMALL SECONDARY FLOW

The three-dimensional nature of the inviscid flow field³⁵ for a blunt lifting entry body suggests that significant three-dimensional effects may also be present in the boundary layer. The analysis described in this section was undertaken as the initial step in determining the importance of the secondary flow in the following way. The secondary-flow momentum equation is linearized to estimate the size of the three-dimensional effect, and then these estimates are put back into the complete equations in order to determine if the linearized theory is sufficient.

In dealing with the three-dimensional boundary layer, it is convenient to use the inviscid streamlines at the body surface as the coordinate system. In such a coordinate system, the three-dimensional nature of the boundary layer manifests itself as a secondary flow, i.e., a component parallel to the body surface and normal to the inviscid streamline direction.

Generally speaking, secondary flows over highly cooled bodies tend to be small. The reason is that the layer near the cold wall is relatively dense; thus, pressure gradients in any direction (normal to streamlines as well as along them) have a limited effect. For this reason, a good approximation can be found by neglecting the secondary flow altogether. The resulting equations, when written in the inviscid-streamline coordinate system, can be transformed into an equivalent two-dimensional problem, as shown by Hayes¹, Vaglio-Laurin²⁶, and Cooke and Hall³⁶. A first estimate of the secondary-flow component can then be found by solving the linear equation which it satisfies. Solutions of this sort are considered by Hayes¹, by Vaglio-Laurin³⁷, and by Beckwith¹⁶. This latter analysis, based on the assumption of local similarity, is especially appropriate for the present problem. The differential equations employed in this analysis have

been developed in detail in Ref. 32. Thus, in the following paragraph only a brief review of the equations utilized is presented.

2.1 Brief Review of Governing Equations

For small secondary flow, the boundary-layer equations can be written in terms of the transformed variables as follows:

$$\xi = \int_0^s \rho_b \mu_b u_e e_1 ds \quad \eta = \frac{u_e e_2}{\sqrt{2\xi}} \int_0^\eta \rho dz$$

Subscripts e and b denote conditions in the free stream and at the wall; ρ is the density, μ the viscosity, u the velocity component in the inviscid-streamline direction, s is the distance along the body surface in the streamline direction, z is the distance normal to the body surface, and e_1 is the metric coefficient relating incremental changes in distance normal to streamlines (π) to incremental changes in the coordinate y , which is constant along a streamline i.e., $d\pi = e_1 dy$. (See Fig. 1.) The local-similarity approximation is made by neglecting derivatives with respect to ξ , while ξ -variations are retained whenever they appear parametrically. The resulting equations, for a Prandtl number of one and a constant $\rho\mu$ product, are

Streamwise-Momentum:

$$f''' + ff'' = \beta(\xi) [f'^2 - \theta] \quad (1)$$

Energy

$$\theta'' + f\theta' = 0 \quad (2)$$

Secondary-Flow Momentum

$$V'' + fV' - \lambda(\xi) f'V = \theta - f'^2 \quad (3)$$

where

$$f' = u/u_e, \quad \theta = H/H_e, \quad V = \frac{v/u_e}{-\beta \frac{\partial p/\partial \pi}{\partial p/\partial s}}$$

and where primes designate derivatives with respect to π . H is the total enthalpy, v is the velocity component in the π -direction, and

$$\beta = \frac{2}{1 - \frac{u_e^2}{2H_e}} \frac{d \ln u_e}{d \ln \xi}, \quad \lambda = \frac{d \ln \left\{ -\beta u_e e_2 \frac{\partial p/\partial \pi}{\partial p/\partial s} \right\}}{d \ln \xi}$$

The term β is defined to be the streamwise pressure-gradient parameter. The term λ is the secondary-flow parameter, and is a measure of the Coriolis force in the flow.

These equations must satisfy the boundary conditions

$$\begin{aligned} f'(0) &= 0, & f'(\infty) &= 1 \\ \theta(0) &= H_b/H_e, & \theta(\infty) &= 1 \\ V(0) &= V(\infty) = 0, & f(0) &= f_b = -\frac{u_b \sqrt{2\xi}}{u_e e_2 \mu_b} \end{aligned}$$

The quantities $e_1, \beta, \frac{\partial p/\partial \pi}{\partial p/\partial s}$, and λ were calculated for a typical inviscid streamline on the fore-body of an Apollo-type body at 20° angle of attack using the results of Bohachevsky and Mates³⁵. The resulting values of these parameters along the streamline were used in conjunction with the locally similar solutions to calculate the boundary-layer velocity profiles at a series of points along the streamline.

2.2 Results of Restricted Analysis

Figure 2 shows the range of parameters for which solutions are reported in Ref. 32. As may be seen from the figure, the integration scheme failed to converge for values of the wall-blowing parameter, f_b , less than -1.1 in the cold wall case, $\theta_b = 0$. For larger values of θ_b , solutions were obtained for substantially more negative values of f_b , as illustrated.

Figures 3 and 4 show the influence of the variation in wall temperature on the velocity profiles for $f_b = 0$ and -1.0, respectively. In both cases, it is seen that as the wall temperature is increased, the secondary-flow component is greater in magnitude than the cold-wall case. This is physically reasonable, since the cooler the wall, the greater the fluid density near the wall and

hence, the fluid is sluggish in responding to influences such as blowing. This greater sensitivity for the $\theta_b = 0.5$ case is shown in Figure 4, where a sizable increase in the maximum value of V is observed.

Figures 5 and 6 illustrate the influence of β , which is allowed to vary from 0.5 to 2.0, on the boundary layer for blowing-rate parameters of 0 and -2.0, respectively, while all other parameters remain fixed. It may be seen from these results that β significantly affects the flow. In particular, decreasing values of β result in increasing effects on the secondary flow. That is, the maximum value of the secondary-flow velocity increases by a factor of approximately three as the streamwise pressure-gradient parameter decreases from 2.0 to 0.5. Also, the maximum values of the secondary-flow velocity are located at greater distances from the body surface as β decreases. Further, decreasing the value of β is shown to thicken the boundary layer, thus increasing the region of viscous influence. Such an effect of β is reasonable, since the more favorable the pressure gradient is in the streamwise direction, the smaller is the magnitude of mass flux existing in the secondary-flow direction. The relative influence of β on these two flow characteristics becomes magnified at greater blowing rates, as can be seen by comparing Figures 5 and 6.

The secondary-flow parameter, λ , is a measure of the Coriolis force in the flow. This parameter does not appear in the streamwise momentum equation or the energy equation, but only in the secondary-flow momentum equation. This stems from the assumption of small secondary flow. As illustrated in Figures 7 and 8, increasing the value of λ causes a reduction in the maximum value of the secondary-flow velocity, as well as the boundary-layer thickness, for a given value of the blowing-rate parameter, f_b . Physically, a positive λ signifies diverging streamlines. Therefore, for a given mass-injection rate, greater values of λ tend to spread the effect of blowing over a greater region consistent with the diverging streamlines.

The results of the approximate analysis discussed above suggested that the influence of secondary flow and mass addition on the boundary-layer development was sufficiently large to merit the formulation of a less restrictive analysis. To this end, the integral technique discussed in the following section was formulated.

3. NON-SIMILAR FLOW ANALYSIS BY APPLICATION OF THE INTEGRAL METHOD WITH ARBITRARY SECONDARY-FLOW VELOCITY

3.1 Basic Equations

In this section, an integral method will be applied to obtain a general analysis of the three-dimensional, thin, laminar boundary layer with mass injection. The equations are expressed in terms of the streamline coordinate system and profile parameters are introduced for the streamwise velocity, the total enthalpy and the secondary-flow velocity profiles. As an illustration, the present formulation will be applied to three-dimensional flow in the forebody region of a blunt body. The effects of mass injection and streamline curvature, including the effect of an inflection point in the outer inviscid streamline, will also be analyzed.

For the case of a nonreacting gas, the equations for a compressible, three-dimensional boundary layer are^{20,38}

$$\text{Continuity} \quad \frac{1}{e_1 e_2} \frac{\partial}{\partial x} (\rho u e_1) + \frac{1}{e_1 e_2} \frac{\partial}{\partial y} (\rho v e_2) + \frac{\partial}{\partial z} (\rho w) = 0 \quad (4)$$

x -momentum

$$\frac{\rho u}{e_1} \frac{\partial u}{\partial x} + \frac{\rho v}{e_1} \frac{\partial u}{\partial y} + \rho w \frac{\partial u}{\partial z} + K_1 \rho u v - K_2 \rho v^2 = \frac{\rho e_1}{e_1} \frac{\partial u_e}{\partial x} + \frac{\partial}{\partial z} \left(\mu \frac{\partial u}{\partial z} \right) \quad (5)$$

y -momentum

$$\frac{\rho u}{e_1} \frac{\partial v}{\partial x} + \frac{\rho v}{e_2} \frac{\partial v}{\partial y} + \rho w \frac{\partial v}{\partial z} + K_1 \rho u v = K_1 \rho e_1^2 \left[\left(\frac{u}{e_1} \right)^2 - \frac{p}{\rho} \right] + \frac{\partial}{\partial z} \left(\mu \frac{\partial v}{\partial z} \right) \quad (6)$$

Energy

$$\frac{\rho u}{e_1} \frac{\partial H}{\partial x} + \frac{\rho v}{e_2} \frac{\partial H}{\partial y} + \rho w \frac{\partial H}{\partial z} = \frac{\partial}{\partial z} \left(\frac{\mu}{Pr} \frac{\partial H}{\partial z} \right) - \frac{\partial}{\partial z} \left[\frac{\mu (1-Pr)}{2 Pr} \frac{\partial}{\partial z} (u^2 + v^2) \right] \quad (7)$$

where it is assumed that $\partial p / \partial y = 0$, so that $\rho e_1 u_e (\partial u_e / \partial x) = -\partial p / \partial x$ and $e_2 K_1 \rho e_1^2 = \partial p / \partial y$.

The boundary conditions are

$$\begin{aligned} u(x, y, 0) &= v(x, y, 0) = 0 & \text{and} & & u(x, y, \infty) &= u_e(x, y) \\ w(x, y, 0) &= w_b(x, y) & & & v(x, y, \infty) &= 0 \\ H(x, y, 0) &= H_b = h_b(x, y) & & & H(x, y, \infty) &= H_e = h_e + \frac{u_e^2}{2} \end{aligned}$$

When the Equations (5), (6), and (7) are integrated from $y = 0$ to $y = \delta$ using continuity, Equation (4), they become

$$\begin{aligned} & \frac{1}{\rho_e u_e^2 e} \frac{\partial}{\partial x} (\rho_e u_e^2 \delta_{11}) + \frac{1}{e} \frac{\partial \delta_{12}}{\partial y} + \frac{\delta_{11}}{u_e e} \frac{\partial u_e}{\partial x} + K_1 (\delta_{11} + \delta_{12}) \\ & + \delta_{12} \left(K_1 + \frac{2}{u_e e} \frac{\partial u_e}{\partial y} + \frac{1}{\rho_e e} \frac{\partial \rho_e}{\partial y} \right) - \delta_{11} \left(K_1 + \frac{1}{u_e e} \frac{\partial u_e}{\partial y} \right) \\ & = \frac{\mu_b}{\rho_e u_e^2} \left(\frac{\partial u}{\partial y} \right)_b + \frac{\rho_b w_b}{\rho_e u_e} \end{aligned} \quad (8)$$

$$\begin{aligned} & \frac{1}{\rho_e u_e^2 e} \frac{\partial}{\partial x} (\rho_e u_e^2 \delta_{21}) + \frac{1}{e} \frac{\partial \delta_{22}}{\partial y} + 2K_2 \delta_{21} + K_1 (\delta_{11} + \delta_{12}) \\ & + \delta_{22} \left(K_1 + \frac{2}{u_e e} \frac{\partial u_e}{\partial y} + \frac{1}{\rho_e e} \frac{\partial \rho_e}{\partial y} \right) = - \frac{\mu_b \left(\frac{\partial v}{\partial y} \right)_b}{\rho_e u_e^2} \end{aligned} \quad (9)$$

and

$$\begin{aligned} & \frac{\partial H_1}{e_1 \partial x} + \frac{\partial H_1}{e_1 \partial y} + H_1 \left(K_1 + \frac{1}{\rho_e e_1} \frac{\partial \rho_e}{\partial x} + \frac{1}{u_e e_1} \frac{\partial u_e}{\partial x} \right) \\ & + H_2 \left(K_1 + \frac{1}{u_e e_1} \frac{\partial u_e}{\partial y} + \frac{1}{\rho_e e_1} \frac{\partial \rho_e}{\partial y} \right) \\ & = \frac{\mu_b}{\rho_e u_e R_b} \left(\frac{\partial \theta}{\partial y} \right)_b + \frac{\rho_b w_b}{\rho_e u_e} \theta_b \end{aligned} \quad (10)$$

where

$$\begin{aligned} \delta_1 &= \int_0^\delta \left(\frac{\rho_e}{\rho} - \frac{u}{u_e} \right) \frac{\rho}{\rho_e} dy & \delta_2 &= \int_0^\delta \frac{v}{u_e} \frac{\rho}{\rho_e} dy \\ \delta_{11} &= \int_0^\delta \left(1 - \frac{u}{u_e} \right) \frac{u}{u_e} \frac{\rho}{\rho_e} dy & \delta_{12} &= \int_0^\delta \frac{v}{u_e} \left(1 - \frac{u}{u_e} \right) \frac{\rho}{\rho_e} dy \\ \delta_{21} &= \int_0^\delta \frac{u}{u_e} \frac{v}{u_e} \frac{\rho}{\rho_e} dy & \delta_{22} &= \int_0^\delta \left(\frac{v}{u_e} \right)^2 \frac{\rho}{\rho_e} dy \\ H_1 &= \int_0^\delta (1 - \theta) \frac{u}{u_e} \frac{\rho}{\rho_e} dy & H_2 &= \int_0^\delta (1 - \theta) \frac{v}{u_e} \frac{\rho}{\rho_e} dy \end{aligned} \quad (11)$$

and

$$\theta = H/H_e$$

The momentum boundary-layer thickness (δ) is taken to be the same for both the streamwise and the secondary flows^{14,32,39}. Further, the thermal boundary-layer thickness is assumed to be the same as the momentum boundary-layer thickness^{40,41}. The term $\rho_b w_b$ signifies the mass-injection flux at the body surface. When this term is equal to zero, i.e., the solid-wall case, Equations (8), (9), and (10) reduce to the equations obtained in previous analyses, e.g., Refs. 20 and 32.

The y -coordinate is now transformed by introducing the variable

$$Z = \int_0^y \frac{\rho}{\rho_e} dy \quad (12)$$

from which follows the boundary-layer thickness in the transformed plane

$$\Delta = \int_0^\delta \frac{\rho}{\rho_e} dy$$

In addition, the viscosity is assumed to vary with temperature⁴², as follows

$$\frac{\mu}{\mu_r} = C' \frac{T}{T_r} \quad (13)$$

where the subscript r denotes reference conditions and the coefficient is taken such that the Sutherland viscosity-temperature relation is exactly satisfied at the wall temperature T_b . Thus,

$$C' = \sqrt{\frac{T_b}{T_r}} \left(\frac{T_r + S}{T_b + S} \right)$$

where S is the Sutherland constant.

In order to make the formulation as general as possible, the equations are nondimensionalized with respect to a reference condition. A suitable reference point is, for example, the point immediately behind the shock on the stagnation streamline. Thus, we introduce

$$\begin{aligned} \Omega &= \frac{\Delta}{l} \sqrt{Re} & Re &= \frac{\rho_b u_b l}{\mu_b} \\ U &= \frac{u}{u_b} & \bar{u}_e &= \frac{u_e}{u_b} \\ V &= \frac{v}{u_b} & D_i &= K_i l \\ W &= N \frac{\bar{\rho}_e \sqrt{Re}}{\bar{\rho}_b \bar{\mu}_b} \Omega & N &= \frac{\rho_b u_b l}{\rho_e u_e} \\ M_{i,j} &= \frac{\delta_{i,j}}{\Delta} & T_i &= \frac{H_i}{\Delta} \\ M_i &= \frac{\delta_i}{\Delta} & \eta &= \frac{z}{\Delta} \end{aligned} \quad (14)$$

where terms with bars signify normalization with respect to the reference condition, e.g., $\bar{\rho}_e = \rho_e/\rho_b$ etc. In addition, the term E_2 will be introduced as $E_2 = e_2/e_{2r}$ where e_{2r} is the metric coefficient at some convenient point in the flow and is a constant. Then Equations (8), (9), and (10) become, after some rearrangements,

$$\begin{aligned} & \frac{\partial \Omega^2}{\partial(x/l)} + \Omega^2 \frac{2}{e_1} \frac{\partial}{\partial(x/l)} \left[\ln \bar{\rho}_e \bar{u}_e^{2 + \frac{M_{11}}{M_{11}}} M_{11} E_1^{1 + \frac{M_{11}}{M_{11}}} \right] \\ &= \frac{2}{M_{11}} \left(\frac{\rho_b}{\rho_e} \right) \frac{\bar{\mu}_b}{\bar{\rho}_e \bar{u}_e} \left[\left(\frac{\partial U}{\partial \eta} \right)_b + W \right] + \frac{2\Omega^2}{e_2} \frac{M_{12}}{M_{11}} \frac{\partial}{\partial(y/l)} (\ln e, u_e) \\ & - \frac{2\Omega^2}{e_2} \frac{M_{12}}{M_{11}} \frac{\partial}{\partial(y/l)} [\ln e, u_e^2 \bar{\rho}_e] - \frac{2\Omega}{M_{11} e_2} \frac{\partial [\Omega M_{12} \sqrt{Re}/l]}{\partial(y/l)}, \end{aligned} \quad (15)$$

$$\begin{aligned} & \frac{\partial(M_{21} \Omega)}{e_1 \partial(x/l)} + \frac{M_{21} \Omega}{e_1} \frac{\partial}{\partial(x/l)} \left[\ln \bar{\rho}_e \bar{u}_e^2 E_1^2 \right] \\ &= -D_i \Omega (M_{11} + M_{12}) - \left(\frac{\rho_b}{\rho_e} \right) \frac{\bar{\mu}_b}{\bar{\rho}_e \bar{u}_e} \Omega \left(\frac{\partial V}{\partial \eta} \right)_b \\ & - \frac{M_{22} \Omega}{e_1} \frac{\partial}{\partial(y/l)} [\ln e, u_e^2 \bar{\rho}_e] - \frac{1}{e_1} \frac{\partial [\Omega M_{22} \sqrt{Re}/l]}{\partial(y/l)}, \end{aligned} \quad (16)$$

and

$$\begin{aligned}
& \frac{\partial(T_e \Omega)}{e, \partial(x/l)} + \frac{T_e \Omega}{e,} \frac{\partial}{\partial(x/l)} \left[\ln \bar{\rho}_e \bar{u}_e E_e \right] \\
& = \left(\frac{\rho_e}{\bar{\rho}_e} \right) \frac{\bar{\mu}_b}{\bar{\rho}_e \bar{u}_e \Omega} \left[\frac{1}{R_b} \left(\frac{\partial \theta}{\partial \eta} \right)_b + W \theta_b \right] \\
& - \frac{T_e \Omega}{e,} \frac{\partial}{\partial(y/l)} \left[\ln e_e u_e \bar{\rho}_e \right] - \frac{\partial(T_e \Omega)}{e, \partial(y/l)}
\end{aligned} \tag{17}$$

It may be noted here that the integral equations, Equations (15), (16), and (17), have the following properties: 1) They can accommodate mass injections at the body surface. The term W contains the mass-injection flux and appears in Equations (15) and (17). 2) They can be used for both laminar and turbulent boundary-layer flows. In the case of a turbulent flow, some suitable correlations may be used for the reference temperature, $(\partial u / \partial \eta)_b$, $(\partial v / \partial \eta)_b$ and $(\partial \theta / \partial \eta)_b$ to obtain the solutions^{43,44}.

The integral equations yield integrated effects of the flow characteristics from an upstream location to a point of interest in the flow field. In obtaining meaningful solutions, however, it is also important to account for local effects such as mass injection at the body surface and local pressure gradients tangent and transverse to the streamline. For this latter purpose, the so-called "compatibility conditions" at the wall are introduced, by specializing the differential Equations (5), (6), and (7) to the body surface. Thus, we obtain, in dimensionless forms,

$$W \left(\frac{\partial u}{\partial \eta} \right)_b = P + \left(\frac{\partial^2 u}{\partial \eta^2} \right)_b \tag{18a}$$

$$W \left(\frac{\partial v}{\partial \eta} \right)_b = -Q + \left(\frac{\partial^2 v}{\partial \eta^2} \right)_b \tag{18b}$$

$$W \left(\frac{\partial \theta}{\partial \eta} \right)_b = \frac{1}{R_b} \left(\frac{\partial^2 \theta}{\partial \eta^2} \right)_b - \left(\frac{u_e^2}{H_e} \right) \left(\frac{1 - Pr}{Pr_b} \right) \left[\left(\frac{\partial u}{\partial \eta} \right)_b^2 + \left(\frac{\partial v}{\partial \eta} \right)_b^2 \right] \tag{18c}$$

where

$$P = \left(\frac{\rho_e}{\bar{\rho}_e} \right)^2 \frac{\bar{\rho}_e}{\bar{\mu}_b} \frac{\Omega}{e,} \frac{\partial \bar{u}_e}{\partial(x/l)}$$

$$Q = D_e \Omega^2 \frac{\bar{\rho}_e \bar{u}_e}{\bar{\mu}_b} \left(\frac{\rho_e}{\rho_b} \right)^2$$

For the region near the stagnation point in hypersonic flows, u_e^2 / H_e is much smaller than unity and, thus, the last term in Equation (18c) may be neglected without loss in accuracy, although the Prandtl number may not be unity. In the case where the Prandtl number is unity, of course, the term is identically zero. In obtaining the examples included in this paper, the term containing u_e^2 / H_e is neglected. Thus, we have

$$W \left(\frac{\partial \theta}{\partial \eta} \right)_b \cong \frac{1}{Pr_b} \left(\frac{\partial^2 \theta}{\partial \eta^2} \right)_b \tag{19}$$

We now have derived six equations, viz., Equations (15), (16), (17), (18a), (18b), and (19). Thus, six unknown parameters describing the flow characteristics may be introduced and, theoretically, the problem is determinate.

3.2 Choice of Profiles

Application of the integral method to the boundary-layer flow involves assuming forms of the velocity and total enthalpy profiles in terms of parameters which characterize the fluid motion. In what follows, these various profiles will be separately considered.

The Streamwise Velocity Profile

We introduce the fourth-degree polynomial form

$$U = \frac{u}{u_e} = \sum_{m=0}^4 a_m \eta^m \quad (20)$$

The boundary conditions are

$$\begin{aligned} \eta = 0 : \quad U &= 0 \\ \eta = 1 : \quad U &= 1 \\ \frac{\partial U}{\partial \eta} &= 0 \\ \frac{\partial^2 U}{\partial \eta^2} &= 0 \end{aligned} \quad (21)$$

In addition, we have the compatibility condition at the wall, i.e., Equation (18a). Substitution of Equation (20) in Equations (18a) and (21) gives

$$\begin{aligned} a_0 &= 0 \\ a_1 &= \frac{12+P}{6+W} = A \\ a_2 &= \frac{W a_1 - P}{2} \\ a_3 &= 4+P - a_1(3+W) \\ a_4 &= -3 - \frac{P}{2} + a_1 \left(2 + \frac{W}{2}\right) \end{aligned} \quad (22)$$

Therefore, we have

$$U = m_1(\eta) + A m_2(\eta) \quad (23)$$

where

$$m_1(\eta) = \eta^4(6-8\eta+3\eta^2), \quad m_2(\eta) = \eta(1-\eta)^3$$

Thus, the streamwise velocity is expressed as a function of only one parameter, A . The physical significance of A is that it expresses the magnitude of the velocity gradient at the body surface and, therefore, is a measure of the streamwise shear stress. It is interesting to note here that when there is no mass injection at the wall, $W = 0$, then A is dependent only on P , the pressure-gradient parameter. On the other hand, if the mass injection is very great, the other limiting case is obtained, i.e., $A \rightarrow 0$, as $W \rightarrow \infty$. In other words, as mass injection increases, the streamwise skin friction decreases and in the limit approaches zero, a physically reasonable result. Another interesting result is that when there is no streamwise pressure gradient, i.e., $P = 0$, $A = 12/(6+W)$. It may also be seen that regardless of the value of W , $A = 0$ for $P = -12$, signifying the separation of the flow due to adverse pressure gradient. Later, numerical comparison of the value of A will be made with other results for the more general case of finite pressure gradient and mass injection.

We have thus expressed the streamwise velocity profile in terms of one parameter, which combines the pressure-gradient characteristic and the mass-injection characteristics in the flow. It should be noted here that based on previous analyses⁴⁵⁻⁴⁷, the above one-parameter expression is expected to yield reasonable results.

The Total-Enthalpy Profile

Here, we introduce the fifth-degree polynomial form such that

$$\theta = \frac{H}{H_e} = \sum_{m=0}^5 b_m \eta^m \quad (24)$$

The reason for taking this particular form is discussed later.

The boundary conditions are

$$\begin{aligned}
 \eta = 0 & : \quad \theta = \theta_b \\
 \eta = 1 & : \quad \theta = 1 \\
 \frac{\partial \theta}{\partial \eta} = 0 & , \quad \frac{\partial^2 \theta}{\partial \eta^2} = 0
 \end{aligned}
 \tag{25}$$

The compatibility condition for the total enthalpy is given in Equation (19). We thus obtain

$$\begin{aligned}
 b_0 &= \theta_b \\
 b_1 &= B \\
 b_2 &= \frac{W_P}{2} b_1 \\
 b_3 &= 10(1 - b_0) - \left(6 + \frac{3}{2} W_P\right) b_1 \\
 b_4 &= -15(1 - b_0) + \left(8 + \frac{3}{2} W_P\right) b_1 \\
 b_5 &= 6(1 - b_0) - \left(3 + \frac{W_P}{2}\right) b_1
 \end{aligned}
 \tag{26}$$

where

$$W_P = P_r W$$

and Equation (24) becomes

$$\frac{\theta - \theta_b}{1 - \theta_b} = m_s(\eta) + \frac{B}{1 - \theta_b} [m_4(\eta) + W_P m_5(\eta)]
 \tag{27}$$

where

$$\begin{aligned}
 m_1(\eta) &= \frac{\eta^2}{2} (1 - \eta)^2 \\
 m_4(\eta) &= \eta (1 - 6\eta^2 + 8\eta^3 - 3\eta^4) \\
 m_5(\eta) &= \eta^3 (10 - 15\eta + 6\eta^2)
 \end{aligned}$$

In contrast to the streamwise flow case, where the fourth-degree polynomial form is used, the total-enthalpy profile here is expressed in fifth-degree polynomial form. The reason is as follows: when the fourth-degree form is used, all b_m 's can be determined in terms of W , P , θ_b and A and, thus, the problem is reduced to obtaining the solutions to the streamwise-momentum integral equation. Once the solutions are obtained for A , W , P from this equation, then, it is a simple matter to construct the total-enthalpy characteristics, and the energy equation, i.e., the total-enthalpy integral equation, is ignored. This procedure has been used by Cohen and Roshko⁴⁸ using Thwaites' approach⁴⁹ and the results show, in some cases, poor accuracy in the energy field while yielding the velocity field accurately. Others (such as Tani⁵⁰ and Poots⁴⁰) use the energy equation and the fourth-degree form. They then drop the compatibility condition, but in its place use the "kinetic-energy" integral equation and obtain good results. Physically, the energy equation and the compatibility condition serve two functions: the energy integral equation describes the integrated effects of the energy of the flow from upstream to the point of interest along the streamline, while the compatibility condition describes the local flow effects. It is thus recognized that meaningful results may be obtained by considering both equations. This procedure has, in fact, been followed in two-dimensional cases^{41, 46}. In the present analysis, therefore, both the energy integral equation and the compatibility conditions are retained and considered by assuming a fifth-order polynomial form for the total-enthalpy profile. It should be noted, however, that the results for the energy field can be interpreted only in conjunction with the streamwise momentum results, as well as the secondary-flow momentum results.

The Secondary-Flow Velocity Profile

In the present analysis, we assume a modified form of Timman's⁵¹⁻⁵³ profile, such that

$$V = \frac{u}{u_c} = G \lambda(\eta) - F g(\eta)
 \tag{28}$$

where

$$\begin{aligned}
 k(\eta) &= a \eta e^{-a^2 \eta^2} \\
 g(\eta) &= \frac{1}{2} \left[\operatorname{erfc}(a \eta) + (\eta - 1) e^{-a^2 \eta^2} \right] \\
 a &= 3\pi/2
 \end{aligned}$$

The terms G and F are two free parameters which will be determined from the integral equations and the compatibility conditions. In fact, the compatibility condition can be used at this juncture to eliminate one parameter, thus leaving the integral equation to solve for the remaining parameter along the streamline.

Substitution of Equation (28) in Equation (18b) yields

$$W(aG + F) = -Q - a^2 F \quad (29)$$

Thus,

$$F = -\frac{Q + aWG}{a^2 + W}$$

Since the wall shear for the secondary flow is $\left(\frac{\partial v}{\partial \eta}\right)_b = aG + F$, we obtain

$$C = \left(\frac{\partial v}{\partial \eta}\right)_b = \frac{a^2 G - Q}{a^2 + W}$$

The profile becomes, using the definition of

$$V(\eta) = G k(\eta) + (W_1 G + Q_1) g(\eta) \quad (30)$$

where

$$W_1 = \frac{aW}{a^2 + W}, \quad Q_1 = \frac{Q}{a^2 + W}$$

It should be noted that presence of an inflection point along the streamline may cause the secondary flow velocity profile to be S-shaped ("cross-over" profile) near the inflection point. Thus, in order to obtain realistic velocity distributions, it is necessary for the profile to exhibit the S-shaped form, as well as the C-shaped form. This requirement is satisfied by the profile form assumed in Equation (28) or Equation (30), and the problem now is to determine from the integral equations the values of these parameters, i.e., G and F , along the streamline.

With the chosen profile forms, it is now possible to calculate various characteristic "thicknesses" from these profiles in terms of parameters A, B, G , etc.

From Equations (11) and (14), we have

$$\begin{aligned}
 M_{11} &= \int_0^1 U(1-U) d\eta = P_1 + P_2 A - P_3 A^2 \\
 M_{11} &= \int_0^1 U V d\eta = G(P_2 + A P_3 + W_1 P_6 + A W_1 P_7) + Q_1 (P_6 + A P_7) \\
 M_2 &= \int_0^1 V d\eta = G(P_6 + W_1 P_9) + Q_1 P_9 \\
 M_{12} &= \int_0^1 V(1-U) d\eta = M_2 - M_{11} \\
 M_{22} &= \int_0^1 V^2 d\eta = G^2(P_6^2 + 2W_1 P_{11} + W_1^2 P_{12}) + Q_1^2 P_{12} + 2GQ_1(P_7 + W_1 P_{12}) \\
 T_1 &= \int_0^1 U(1-\theta) d\eta = (1-\theta_b)(P_3 + A P_4) - B(P_3 + A P_6 + W_1 P_7 + A W_1 P_8) \\
 T_2 &= \int_0^1 V(1-\theta) d\eta = (1-\theta_b) [G(P_7 + W_1 P_{10}) + Q_1 P_{10}] \\
 &\quad - B[G(P_6 + W_1 P_{12} + W_1 P_{13} + W_1^2 P_{14}) + Q_1(P_7 + W_1 P_{12})]
 \end{aligned} \quad (31)$$

and

$$M_i = \int_0^1 \left(\frac{\rho}{\rho_e} - U \right) d\eta = \frac{H_e}{A_e} M_i^* + \left(\frac{H_e}{A_e} - 1 \right) (M_{ii} - M_{22}) \quad (32)$$

$$M_i^* = \int_0^1 (\theta - U) d\eta = P_{25} - A P_{26} + \theta_i P_{27} + B (P_{28} + W P_{29})$$

where the ideal-gas relationship

$$\frac{P_e}{\rho} - U^2 = \frac{H_e}{A_e} (\theta - U^2) - \left(\frac{H_e}{A_e} - 1 \right) V^2$$

has been used. The coefficients, i.e., P_{2i} , are included in the Appendix.

3.3 Integral Equations

Substitution of the profiles chosen in Section 3.2 into the integral Equations (15), (16), and (17) yields, substituting ϕ and ψ for α and γ , respectively³⁸,

$$\begin{aligned} \frac{\partial \Omega}{\partial(\phi/l)} + \frac{2\Omega}{e_i} \frac{\partial}{\partial(\phi/l)} \left[\ln \bar{\rho}_e M_{ii} \bar{u}_e^2 E_2^* \frac{M_{ii}}{e_i} \right] &= \frac{2F_i}{M_{ii}} (A + W) \\ &+ \frac{2\Omega M_{21}}{e_i M_{ii}} \frac{\partial \ln e_i u_e}{\partial(\psi/l)} - \frac{2\Omega M_{12}}{e_i M_{ii}} \frac{\partial \ln e_i u_e \bar{\rho}_e}{\partial(\psi/l)} - \frac{2\Omega}{M_{ii}} \frac{\partial(\Omega M_{12} \sqrt{A_e}/l)}{e_i \partial(\psi/l)} \end{aligned} \quad (33)$$

$$\begin{aligned} \frac{\partial(M_{21}\Omega)}{e_i \partial(\phi/l)} + \frac{M_{21}\Omega}{e_i} \frac{\partial [\ln \bar{\rho}_e \bar{u}_e^2 E_2^*]}{\partial(\phi/l)} &= -D_i \Omega (M_{ii} + M_i) - \frac{F_i}{\Omega} \left(\frac{2G}{a^2} - Q \right) \\ &- \frac{M_{22}\Omega}{e_i} \frac{\partial [\ln e_i u_e \bar{\rho}_e]}{\partial(\psi/l)} - \frac{1}{e_i} \frac{\partial(M_{12}\Omega)}{\partial(\psi/l)} \end{aligned} \quad (34)$$

$$\begin{aligned} \frac{\partial(T_i\Omega)}{e_i \partial(\phi/l)} + \frac{T_i\Omega}{e_i} \frac{\partial [\ln \bar{\rho}_e \bar{u}_e^2 E_2^*]}{\partial(\phi/l)} &= \frac{F_i}{\Omega} \left(\frac{B}{A_e} + W \theta_i \right) \\ &- \frac{T_i\Omega}{e_i} \frac{\partial [\ln e_i u_e \bar{\rho}_e]}{\partial(\psi/l)} - \frac{1}{e_i} \frac{\partial(T_{12}\Omega)}{\partial(\psi/l)} \end{aligned} \quad (35)$$

where

$$F_i = \left(\frac{\rho_e}{\rho} \right) \frac{\bar{\mu}_b}{\bar{\rho}_e \bar{u}_e}$$

The term ψ takes on a physical meaning of stream function while ϕ can, in the case of irrotational outer flow, signify the velocity potential³⁸. Since the compatibility conditions have already been incorporated in Section 3.2, they are not written here. Thus, there are three integral equations, and the parameters to be determined from these equations are Ω , G and B and the problem is mathematically determinate. When specialized to incompressible flow with small secondary flow and no mass injection, the present formulation reduces to that of Cooke¹⁵, while for axisymmetric flow it reduces to Truckenbrodt's result⁵⁴.

3.4 Solutions and Discussion of Results

We now consider the method of solving the integral Equations (33), (34), and (35). From the inviscid flow-field analysis, the quantities at the outer edge of the boundary layer are assumed known, including the streamline-curvature distribution (D_i) and the streamline divergence-convergence function (E_2). With known initial conditions, integration of the equations is then carried out along individual external streamlines ($\psi = \text{constant}$). The last term in each equation is of the form $\frac{\partial}{\partial \psi} \{ \}$ and is not known a priori. Thus, this term is dropped at first⁵⁵⁻⁵⁷ and is accounted for after solutions have been obtained along several streamlines. It should be remarked here that

because only the gradient term is dropped at first, this method does not involve the assumption of small secondary flow, but rather is an iterative method of solving the equations.

As an application of the integral method formulated in Equations (33), (34), and (35), analysis will be made of a hypersonic flow around a blunt body at angle of attack with mass injection at the body surface assuming irrotational, inviscid outer flow and an ideal gas. Any other conditions or assumptions required will be introduced as the analysis proceeds. From the condition of irrotational flow we get^{20,38}

$$e_1 = u_e^{-1}$$

and thus

$$K_1 = \frac{1}{e_1 e_2} \frac{\partial e_1}{\partial \psi} = -\frac{1}{u_e e_2} \frac{\partial u_e}{\partial \psi} \quad (36)$$

We shall now estimate the term $\partial \rho_e / \partial \psi$. Using the ideal-gas relationship, we obtain

$$\frac{1}{\rho_e} \frac{\partial \rho_e}{\partial \psi} = \frac{1}{p} \frac{\partial p}{\partial \psi} - \frac{1}{h_e} \frac{\partial h_e}{\partial \psi} \quad (37)$$

Since

$$\frac{\partial p}{\partial \psi} = c_2 K_1 \rho_e u_e^2$$

and $h_e = H_e - \frac{u_e^2}{2}$, we have, for $H_e = \text{constant}$,

$$\frac{\partial h_e}{\partial \psi} = -u_e \frac{\partial u_e}{\partial \psi} = c_1 K_1 u_e^2 \quad (38)$$

Combination of Equations (37) and (38) yields the following result

$$\frac{1}{\rho_e e_2} \frac{\partial \rho_e}{\partial \psi} = K_1 \left(\frac{H_e}{h_e} - 1 \right) \frac{2}{(\gamma-1)\gamma} = K_1 \beta \quad (39)$$

Thus, the transverse gradient of ρ_e may be conveniently expressed in terms of K_1 . It is noted that near the stagnation point the term σ is usually much less than unity and, thus, for air Equation (39) is smaller than K_1 .

Applying the relationships derived above in the integral Equations (33), (34), and (35), we obtain

$$\frac{\partial(\Omega^1 F_2)}{\partial X} = \frac{2F_1 F_2}{M_{11}} (A+W) + \frac{2(1-\beta)\Omega^1 D_1 F_2 M_{12}}{M_{11}} \quad (40)$$

$$\frac{\partial}{\partial X} (M_{11} \Omega F_3) = -F_3 F_4 - \frac{F_1 F_2}{\Omega} \left(\frac{a^1 G - Q}{a^1 + W} \right) \quad (41)$$

$$\frac{\partial}{\partial X} (T_1 \Omega F_5) = \frac{F_1 F_2}{\Omega} \left(\frac{B}{\rho_r b} + W \theta_b \right) + \beta T_2 \Omega D_1 F_5 \quad (42)$$

where

$$F_1 = \left(\frac{\rho_b}{\rho_e} \right) \frac{\bar{\mu}_b}{\bar{\rho}_e \bar{u}_e}$$

$$F_2 = \left[\bar{\rho}_e M_{11} \bar{u}_e^{2 + \frac{M_{11}}{M_{11}}} E_1^{1 + \frac{M_{11}}{M_{11}}} \right]^2$$

$$F_3 = \bar{\rho}_e \bar{u}_e^2 E_2^2$$

$$F_4 = \frac{H_e}{h_e} D_1 \Omega \left[M_{11} + M_{11}^* - \left(1 - \beta \frac{h_e}{H_e} \right) M_{12} \right]$$

$$F_5 = \bar{\rho}_e \bar{u}_e E_3$$

and, as discussed previously, the last term in Equations (33), (34), and (35) has been dropped and will later be accounted for from the solutions obtained along the streamlines. A new variable X is introduced such that $X = e, \alpha r/l$ and signifies the length along the streamline. From the inviscid outer-flow field, distributions of the various terms, such as $\bar{\rho}_e$, D , \bar{u}_e etc., are considered known. The dependent variables are

1. Ω , from which Δ , A , W , M_{II} can be calculated,
2. M_{21} , which in turn depends on G and Ω , and
3. T , which will enable calculation for B .

Thus, there are three essential unknowns, Ω , G , and B . Since there are three equations, (40), (41), (42), the problem is now, mathematically speaking, solvable. Because of the complexity of the equations, numerical solution on a digital computer is carried out in the present analysis. Computation time for a typical case was about one minute on IBM 7044 computer.

In order to start the integration, it is necessary to know the initial values. If the integration were to start from an arbitrary point along the streamline, the initial conditions at that point would be presumed to be given from the upstream conditions. However, if the integration starts from the stagnation point, the initial conditions can be determined from the integral equations themselves. Essentially, this involves dropping the slope terms for Ω , T , and M_{21} for the first approximation and then, by numerically differentiating these terms, obtaining the second-order approximation; the iteration is repeated until convergence in these values is achieved. Further details are included in Refs. 13 and 58. It has been repeatedly found by Cooke¹⁵ that the main part of the solution is not sensitive to the way in which the solution is started. This conclusion was reinforced by Head⁵⁹ who used, as initial conditions, the Blasius velocity profile despite the fact that the pressure gradient at the initial point was not zero. He found that after a very short distance the solutions approached those obtained using the more elaborate, iterative technique. In the present analysis, both the iterative technique and an approximate technique have been tested for a specific problem. For the approximate technique, the initial values used were obtained by taking a limit of the Equations (40), (41), and (42) to the stagnation point. It was found that both techniques yielded equally reasonable results for the main part of the solution along the streamline and it was decided to apply the approximate technique in obtaining the initial conditions in the present analysis because of the saving in the computation time and simplicity in application.

Examples

The formulation derived in Equations (40), (41), and (42) will be applied to a flow on an Apollo-type blunt body entering the atmosphere. Specifically, the conditions assumed are:

Altitude: 200,000 ft

Velocity (u_∞): 30,000 ft/sec (0.915×10^6 cm/sec)

Body radius (l): 15.5 ft (474 cm)

Angle of attack: 20 degrees

Under these conditions, the properties of equilibrium air behind a normal shock wave are⁶⁰

$$\rho_0/\rho_\infty = 16.81$$

$$p_0/p_\infty = 1099$$

$$T_0/T_\infty = 33$$

with

$$p_\infty = 2.26 (10^{-2}) \text{ (dyne/cm}^2\text{)}$$

$$u_\infty = 0.915 (10^6) \text{ (cm/sec)}$$

$$\rho_\infty = 3.14 (10^{-7}) \text{ (gr/cm}^3\text{)}$$

$$\mu_\infty = 1.6 (10^{-4}) \text{ (gr/cm-sec)}$$

$$T_\infty = 2.5 (10^2) \text{ (}^\circ\text{K)}$$

$$Re_\infty = 8.8 (10^5) = \rho_\infty u_\infty l / \mu_\infty$$

and

$$\begin{aligned}
 p_0 &= 2.49 (10^5) \text{ (dyne/cm}^2\text{)} \\
 w_0 &= 5.45 (10^4) \text{ (cm/sec)} \\
 \rho_0 &= 5.27 (10^6) \text{ (gr/cm}^3\text{)} \\
 \mu_0 &= 0.916 (10^{-3}) \text{ (gr/cm-sec)} \\
 T_0 &= 8.25 (10^3) \text{ (}^\circ\text{K)} \\
 Re &= 1.44 (10^5) = \rho_0 w_0 l / \mu_0
 \end{aligned}$$

where $\mu_0/\mu_\infty \approx (T_0/T_\infty)^{1/2}$ was used across the normal shock. With these property values, the Equations (40), (41), and (42) were integrated along the streamline from the stagnation point assuming an ideal gas for cases of arbitrarily chosen mass-injection rates, ranging from the solid-wall case, ($N = 0$), to a uniform 15 percent injection rate ($N = 0.15$). Variable mass-injection fluxes along the streamline were also analyzed. In all the examples considered, the wall temperature was assumed constant at one-tenth of the free-stream stagnation temperature. The distributions along the streamline of D , \bar{u}_e , $\bar{\rho}_e$, E_2 , etc. were assumed expressible in analytic forms, e.g., $\bar{u}_e = \alpha_m X - \beta_m X^2$. This is strictly for convenience, since these distributions can be easily put on the digital computer in tabular forms or in curve-fit expressions. Specifically, the following distribution forms are assumed in the present example, based on an inviscid analysis³⁵:

$$\begin{aligned}
 \bar{u}_e &= 5.65 X - 20 X^2 \\
 E_2 &= 1.0 - \exp(-15X) \\
 D_1 &= 30X \left[\exp(-100X^2) - \frac{0.6}{X + 1.0} \right] \\
 \bar{\rho}_e &= 1.022 - 0.8 X^2 \\
 \bar{p}_e &= 10.22 \\
 \bar{\mu}_e &= 0.1022 \\
 \theta_b &= 0.10
 \end{aligned}$$

These distributions are shown in Figure 9. The streamline curvature function D , is expressed in the particular form shown above in order to allow for the change in the sign of D , $D = 0$ denoting the streamline inflection point. The above appears to be a reasonable general form. It should be noted in passing that the local radius of streamline curvature can be obtained simply as l/D .

The results obtained are shown in Figures 10 through 16. Figure 10 shows the distributions of Ω , the dimensionless "boundary-layer thickness" in the transformed plane, for various mass-injection rates. It is noted that Ω increases with increasing values of the mass-injection ratio, N , a physically reasonable result that has been obtained in previous analyses^{28,32}. It may also be seen from Figure 10 that Ω , for large mass-injection rates, at first increases, then decreases along the streamline. This results primarily from the second term in Equation (40), containing D , and Ω^2 . Because, for increasing injection rates, Ω increases and because, in the present example, D , is comparatively large far downstream from the stagnation point, this term is seen to influence the magnitudes of the boundary-layer thickness along the streamline. When $\Delta = \Omega l / R_0$ is transformed back into the physical plane by the relationship $\delta = \int_0^{\Omega} (\rho_e / \rho) dz$, with ρ_e decreasing with X and ρ_b held constant in the example, the thickening rate of δ is not as great as that of Δ . Thus, this demonstrates the greater sensitivity of Δ to the flow conditions in the transformed plane than in the actual physical plane, a useful result, enabling determination of the effects of various conditions in an exaggerated manner in the transformed plane.

Figures 11 and 12 describe the variations of the pressure-gradient parameter (p) and the mass-injection parameter (W) along the streamline. These are combined to yield the streamwise wall-shear parameter (A) from the relationship $A = (12 + P)/(6 + W)$. It may be seen that P and W exert opposite influences on the streamwise skin friction. The parameter A can be related to the physical streamwise wall-shear stress τ_{wb} by $A/\Delta = \tau_{wb} \rho_e / (\rho_b \mu_b u_e)$. Figure 13 shows the effects of various mass-injection rates on the streamwise wall shear. Consistent with previous analyses^{28,32}, the results show lower values of wall shear for greater injection rates.

Figure 14 shows the results for the heat-transfer distribution along the streamline for various mass-injection rates. In particular, the heat-transfer parameter B may be related to the conventional heat-transfer term, i.e., Nusselt number, by $B\Delta = Nu[(\lambda_e/\lambda_0) - \theta_w] \rho_e \beta_b l$. It shows that the heat-transfer rate decreases for increasing injection rates and, at uniform 15 percent mass flux at the wall, the heat transfer rate is practically zero, signifying a nearly insulated condition. It is noted that the decrease in B with increasing mass-injection rate is greater than that of A , so that for a certain value of mass flux, the body may be practically insulated, while there is still a finite skin friction. This result was also obtained in a previous analysis in Ref. 32.

Figure 15 describes the distribution of the transverse wall-shear stress along the streamline. Also shown in the figure is the prescribed streamline-curvature distribution D , which goes through zero, which indicates streamline inflection point, at $X \approx 0.076$, corresponding to a distance of 36 cm. from the stagnation point in the present example. It is seen that D , is at first increasing and then becomes negative, while the wall shear is negative and later becomes positive. This is a reasonable result, since it follows from $\partial p / \partial y = K_e \rho_e u_e^2$ that $D = K_e l$ and the transverse pressure gradient $\partial p / \partial y$ have the same signs. Since the transverse (or secondary-flow) velocity component is in the direction of lower pressure, this means that v and $\partial p / \partial y$ possess opposite signs. The results in Figure 16 confirm this conclusion. An interesting result is noted immediately after the inflection point in the figure where the transverse wall shear, denoting the direction of v near the wall, and D , (and thus $\partial p / \partial y$) both have the same signs. This signifies the non-similarity effect of the flow taken into account in the present analysis, where the influence of the upstream momentum is still present at the inflection point. After some distance beyond the inflection point, this flow sufficiently adjusts to the change in the streamline curvature D , so that v and D , again possess opposite signs. This result was also observed by Cooke¹⁵ in his approximate analysis and by Hansen and Herzig¹⁰ in their exact solutions for the incompressible, solid-wall case. Thus, the present analysis describes the nonsimilar effects of the inflection point on the flow even in the case of mass injection.

Another interesting result is observed in Figure 16 where increased mass-injection rates bring about decrease in the distance between the streamline inflection point and the point at which the secondary flow reverses its direction, so that the two points virtually coincide for uniform 15% injection rate. Physically, this signifies that the lower-velocity mass being injected into the flow responds more quickly to the change in the streamline curvature than the outer fluid.

As in the results for the streamwise flow and the total enthalpy, the magnitude of the transverse velocity gradient at the wall, i.e., the transverse wall shear, decreases with increasing mass-injection rates. The angle between the inviscid external streamline and the limiting streamline at the body surface may be determined from the relationship

$$\alpha = \tan^{-1} \left(\frac{C}{A} \right) \quad (43)$$

Figures 13 and 15 show that the absolute magnitude of α increases with increasing mass-injection rate, a result obtained due to a slower decrease in C compared to a more sensitive change in A with increasing mass flux. Thus, the limiting streamlines tend to diverge more with mass injection than without, exhibiting greater three-dimensionality of the flow. This result has also been obtained in a previous analysis¹⁶ where small secondary flow was assumed. It is to be noted that α reaches a certain finite value as mass-injection rate is further increased, signifying that the surface streamline has a limiting angle with the outer inviscid streamline in the case of very large mass-injection rates. This is due to the fact that both A and C vary only slightly as N becomes very large.

Comparisons will now be made with other solutions for Δ , the boundary-layer thickness, and A , the shear-stress parameter in the streamwise direction. In particular, the values at the stagnation point will be compared. Using the Howarth-Dorodnitsyn similarity transformation⁶¹, i.e.,

$$\xi = \int_0^y \rho_e \mu_e u_e r_b^2 dy$$

$$\eta^* = \frac{\rho_e u_e r_b}{\sqrt{2\xi}} \int_0^y \frac{\rho}{\rho_e} dy$$

and Equation (12), we obtain

$$\eta_e^* = \frac{\rho_e u_e r_b}{\sqrt{2\xi}} \Delta$$

In the stagnation region, we may use approximately $r_b \sim y$, $u_e \sim \left(\frac{\partial u_e}{\partial y} \right)_{y=0}$. Hence, we have

$$\eta_e^* \approx \Delta \left(\frac{2 \rho_e^2 \left(\frac{\partial u_e}{\partial y} \right)_{y=0}}{\rho_b \mu_b} \right)^{1/2} \quad (44)$$

For the example used in the present analysis, the value of the square-root quantity in Equation (44) is approximately 2.80. Now, from the results, Δ for $N = 0$ is 1.20 at the stagnation point, while $\Delta \approx 2.1$ for $N = 0.01$. On the other hand, the similarity solution obtained in Ref. 32 gives, for $\theta_b = 0.1$ and $\beta = (2\xi/u_e)(H_e/\mu_e)(\partial u_e/\partial \xi) = 0.5$, $\eta_e^* \approx 3.30$ for $f_b = 0$ ($N = 0$), and $\eta_e^* \approx 6.0$ for $f_b = -0.5$ ($N \approx 0.01$). It is thus demonstrated from Equation (44) that the results for Δ obtained in the present analysis are reasonable.

We shall now compare the streamwise wall-shear parameter, which is termed A in the present analysis, and its corresponding quantity, f_b'' , in the similarity analyses. Specifically, we wish to determine the actual streamwise skin friction defined to be $\tau_{ib} = \mu_b (\partial u / \partial y)_b$. In the present formulation, τ_{ib} is expressible as

$$\tau_{ib} = \frac{\rho_b u_e \mu_b}{\rho_e \Delta} A \quad (45)$$

while similarity transformation of Howarth-Dorodnitsyn gives, from

$$\gamma_{1b} = \frac{\mu_b \rho_b u_e r_b u_e}{\sqrt{2\xi}} f_b'' = \frac{\mu_b \rho_b u_e}{\rho_e \Delta} \eta_e^* f_b'' \quad (46)$$

Thus, from Equations (45) and (46), the comparison to be made is between A and $\eta_e^* f_b''$. The case of zero pressure gradient and zero mass injection gives $P = 0$ and $N = 0$, and therefore A is identically 2.0. On the other hand, from similarity analysis, this case corresponds to $f_b = 0$ (no mass injection) and $\beta = 0$ (zero pressure gradient). From Cohen and Reshotko's analysis⁶², we obtain $\eta_e^* \approx 4.20$, $f_b'' \approx 0.47$, and hence $\eta_e^* f_b'' \approx 1.98$, which is close to 2.0, a value for A obtained from the present analysis. The mass-injection cases are now compared. Specifically, 5% injection rate, i.e., $N = 0.05$ gives, at the stagnation point, $A \approx 0.27$, while from similarity analysis³², $\eta_e^* \approx 11.0$ and $f_b'' = 0.025$, and hence $\eta_e^* f_b'' = 0.275$ for $\beta^* = 0.5$ and $\theta_b = 0.1$, confirming the reasonableness of the results obtained in the present analysis.

It is thus shown that solutions can be obtained along any streamline based on the integral method formulated in the present analysis. After calculations have been obtained along several streamlines, the suppressed terms, viz., $\partial/\partial \eta \{ \}$, in Equations (33), (34), and (35) can be determined, and, if these terms are not small compared to other terms in the equations, the calculations can be performed once more along the streamlines until convergence is reached. This has not been carried out in the present analysis, since this type of iterative procedure has already been shown by others to be tractable⁵⁵⁻⁵⁷, and since the conditions in the present examples were rather arbitrarily assigned in order to test the applicability of the integral method.

Finally, it is to be remarked that the present formulation may be extendable to the case of dissociated flow. It will require assuming a suitable form for the species profiles, and the modification of the definition of M , and other property terms. Thus, simultaneous integration of the equations along the streamlines should yield approximate, nonsimilar solutions for the flow characteristics, including the species concentrations.

4. CONCLUDING REMARKS

As noted in the Introduction, the primary motivation for the research described in this paper was the need for information about three-dimensional effects in the boundary layer on the Apollo heat shield. The most notable features of this physical situation are the presence of mass addition at the ablating surface, and the fact that the curvature of the inviscid streamlines is relatively pronounced for conditions typical of Apollo reentry. The existing body of theory, in which a small secondary flow is accounted for to linear approximation, was extended to accommodate mass injection. It was found that this effect generally emphasized the three-dimensional character of the boundary layer. Application of this theory to typical Apollo conditions yielded values of the secondary flow that were too large to justify the use of the linear approximation.

To remedy this defect, the integral method which comprises the main content of this paper was developed. The families of profiles used were patterned after those which had been found in the small-secondary-flow work described above. Perhaps the most interesting feature observed in the applications of this method that have been made to date is the occurrence of a lag between the reversal of the transverse pressure gradient and the reversal of the secondary-flow velocity component, with mass injection at the body surface.

Recent years have witnessed the production of an increasing number of three-dimensional solutions for the inviscid flow external to the boundary layer. Particularly for the case of large ablating heat shields, the increasing volume of these solutions has created the need for a complementary boundary-layer analysis of commensurate accuracy. The integral method described in this paper is felt to be a first step in contributing to that need. Future developments of the method should include applications to other configurations of interest, the incorporation of more complex transport and chemical-kinetic properties, and an extension to the case of turbulent flow.

REFERENCES

1. Hayes, W.D. The Three-Dimensional Boundary Layer. AVORD Rept. 1313, China Lake, Calif. (1951)
2. Moore, F.K. Three-Dimensional Compressible Laminar Boundary-Layer Flow. NACA TN-2279 (1951)
3. Mager, A. Generalization of Boundary-Layer Momentum-Integral Equations to Three-Dimensional Flows Including Those of Rotating System. NACA Rept. 1067 (1952)
4. Reshotko, E. Heat Transfer to a Yawed Infinite Cylinder in Compressible Flow. 1956 Heat Transfer and Fluid Mechanics Institute, Stanford, Calif., p. 205
5. Tinkler, J. Effect of Yaw on the Compressible Laminar Boundary Layer. ARC, R & M 3005 (1957)

6. Reshotko, E.
Beckwith, I.E. Compressible Laminar Boundary Layers Over a Yawed Infinite Cylinder with Heat Transfer and Arbitrary Prandtl Number. NACA TN 3986 (1957)
7. Mager, A.
Hansen, A.G. Laminar Boundary Layer Over a Flat Plate in a Flow Having Circular Streamlines. NACA TN 2658 (1952)
8. Sowerby, L. Secondary Flow in a Boundary Layer. RAE Rep*. No. Aero 2512 (March 1954)
9. Loos, H.G. A Simple Laminar Boundary Layer with Secondary Flow. J. Aero. Sci., 22, 1, pp. 35-40 (1955)
10. Hansen, A.G.
Herzig, H.Z. Cross Flows in Laminar Incompressible Boundary Layers. NACA TN 3651 (1956)
11. Eichelbrenner, E.
Oudart, A. Méthode de Calcul de la Couche Limitée Tridimensionnelle. Application à un Corps Fuselé Incliné sur le Vent. U.N.E.R.A. Pub. No. 76 (1955)
12. Mager, A. Three-Dimensional Laminar Boundary Layer with Small Cross Flow. J. Aero. Sci., 21, pp. 835-845 (1954)
13. Zaat, J.A. A Simplified Method for the Calculation of Three-Dimensional Laminar Boundary Layers. NLL Report F. 184 (1956)
14. Cooke, J.C. An Axially Symmetric Analogue for General Three-Dimensional Boundary Layers. ARC, R & M No. 3200 (June 1959)
15. Cooke, J.C. Approximate Calculation of Three-Dimensional Laminar Boundary Layers. RAE Rept. No. Aero. 2658 (1959)
16. Beckwith, I.E. Similarity Solutions for Small Cross Flows in Laminar Compressible Boundary Layers. NASA TR R-107 (1961)
17. Chan, Y.Y. An Approximate Method for Three-Dimensional Compressible Laminar Boundary Layers with Small Cross Flow. NRC Aero. Rept. LR-455 (1966)
18. Fannelop, T.K. A Method of Solving the Three-Dimensional Laminar Boundary-Layer Equations with Application to a Lifting Reentry Body. AVCO Rept. AVMSD-0209-66-RM (August 1966) Also AIAA Paper 67-159
19. Tsen, L.F. Contribution à l'étude de la Couche Limitée Tridimensionnelle Laminaire Compressible Avec Transfert de Chaleur (a Dissertation) De L'université de Poitiers, France, 1965
20. Cooke, J.C.
Hall, M.G. Boundary Layers in Three Dimensions. Section in Progress in Aeronautical Sciences, Vol. 2, Pergamon Press, 1962. Edited by A. Ferri, D. Kuchemann and L. Sterne
21. Trella, M.
Libby, P.A. Similar Solutions for the Hypersonic Laminar Boundary Layer Near a Plane of Symmetry. AIAA J., 3, 75-83 (1965)
22. Howarth, L. The Boundary Layer in Three-Dimensional Flow. Part II - The Flow Near a Stagnation Point. Phil. Mag., 42, pp. 1433-1440 (1951)
23. Davey, A. Boundary-Layer Flow at a Saddle Point of Attachment. J. Fluid Mech., 10, pp. 593-610 (1961)
24. Poots, G. Compressible Laminar Boundary-Layer Flow at a Point of Attachment. J. Fluid Mech., 22, pp. 197-208 (1965)
25. Libby, P.A. Heat and Mass Transfer at a General Three-Dimensional Stagnation Point, AIAA J., 5, pp. 507-517 (1967)
26. Vaglio-Laurin, R. Laminar Heat Transfer on Three-Dimensional Blunt-Nosed Bodies in Hypersonic Flow. ARS J., 29, pp. 123-129 (Feb. 1959)
27. Brown, W.B.
Donoughe, P.L. Tables of Exact Laminar Boundary-Layer Solutions when the Wall is Porous and Fluid Properties are Variable. NACA TN-2479 (Sept. 1951)
28. Libby, P.A. The Homogeneous Boundary Layer at an Axisymmetric Stagnation Point with Large Rates of Injection. J. Aero. Sci., 29, pp. 48-60 (1962)
29. Beckwith, I.E. Similar Solutions for the Compressible Boundary Layer on a Yawed Cylinder with Transpiration Cooling. NASA TR R-42 (1959)

30. Aroesty, J.
Cole, J.D. Boundary-Layer Flows with Large Injection Rates. Rand Corp. Memo RM-4620-ARPA (Aug. 1965)
31. Eckert, E.R.G.
Donoughe, P.L.
Moore, B.J. Velocity and Friction Characteristics of Laminar Viscous Boundary Layer and Channel Flow over Surfaces with Ejection or Suction. NACA TN-4102 (Dec. 1957)
32. Kang, S.W.
Rae, W.J.
Dunn, M.G. Effects of Mass Injection on Compressible, Three-Dimensional, Laminar Boundary Layers with Small Secondary Flow. Cornell Aeronautical Laboratory Report No. AI-2187-A-2 (August 1966). Condensed version of this work appears as Effects of Mass Injection on Compressible, Three-Dimensional, Laminar Boundary Layers, AIAA Journal, Vol. 5, No. 10, pp. 1738-1745 (October 1967)
33. Kang, S.W. An Integral Method for Three-Dimensional, Compressible Laminar Boundary Layers with Mass Injection. Cornell Aeronautical Laboratory Report No. AI-2187-A-5 (May 1967)
34. Rae, W.J. A Method for Estimating Separated-Flow Profiles Over An Axisymmetric Afterbody. Cornell Aeronautical Laboratory Report No. AI-2187-A-7 (October 1967)
35. Bohachevsky, I.O.
Mates, R.E. A Direct Method for Computation of Nonequilibrium Flows with Detached Shock Waves, Part II. Axisymmetric Blunt-Body at Angle of Attack. AIAA Paper No. 65-24, AIAA 2nd Aerospace Sciences Meeting, New York (25-27 January 1965)
36. Cooke, J.C.
Hall, M.G. Boundary Layers in Three Dimensions. RAE Rept. Aero 2635 (1960)
37. Vaglio-Laurin, R. Three-Dimensional Laminar Boundary Layer with Small Cross Flow About Blunt Bodies in Hypersonic Flight. GASL Tech. Rept. 59 (April 1958)
38. Mager, A. Three-Dimensional Laminar Boundary Layers. Section C in Theory of Laminar Flows, High Speed Aerodynamics and Jet Propulsion. Vol. IV, pp. 286-394. Edited by F.K. Moore, Princeton 1954
39. Hansen, A.G. On Possible Similarity Solutions for Three-Dimensional Incompressible Laminar Boundary Layer Flows Over Developable Surfaces and with Proportional Mainstream Velocity Components. NACA TM 1437 (1958)
40. Poots, G. A Solution of the Compressible Laminar Boundary Layer Equations with Heat Transfer and Adverse Pressure Gradient. Quart. J. Mech. and Appl. Math., 13, pp. 57-84 (1960)
41. Libby, P.A.
Pallone, A. A Method for Analyzing the Heat-Insulating Properties of the Laminar Compressible Boundary Layer. J. Aero. Sci., 21, pp. 825-834 (1954)
42. Libby, P.A.
Morduchow, M. Method for Calculation of Compressible Laminar Boundary Layer with Axial Pressure Gradient and Heat Transfer. NACA TN 3157 (1954)
43. Eckert, E.R.G. Engineering Relations for Friction and Heat Transfer to Surfaces in High Velocity Flow. J. Aero. Sci., 22, 8, p. 585 (1955)
44. Cooke, J.C. A Calculation Method for Three-Dimensional Turbulent Boundary Layers. RAE Rept. Aero. 2576 (1958)
45. Morduchow, M. On Heat Transfer Over a Sweat-Cooled Surface in Laminar Compressible Flow with a Pressure Gradient. J. Aero. Sci., 19, pp. 705-712 (1952)
46. Tien, C.L.
Gee, C. Hypersonic Viscous Flow Over a Sweat-Cooled Flat Plate. AIAA J., 1, pp. 159-167 (1963)
47. Liu, S.W.
Kuby, G.H. Interaction of Surface Chemistry and Mass Transfer in Nonsimilar Boundary-Layer Flows. AIAA J., 5, pp. 526-534 (1967)
48. Cohen, C.B.
Reshotko, E. The Compressible Laminar Boundary Layer with Heat Transfer and Arbitrary Pressure Gradient. NACA Rept. 1294 (1956)
49. Thwaites, B. Approximate Calculation of the Laminar Boundary Layer. Aero. Quart., 1, Part III, Roy. Aero. Soc., London, pp. 245-280 (Nov. 1949)

50. Tani, I. On the Approximate Solution of the Laminar Boundary-Layer Equations. *J. Aero. Sci.*, 21, pp. 487-495 (1954)
51. Timman, R.A. A One-Parameter Method for the Calculation of Laminar Boundary Layers. National Aero. Res. Inst., Amsterdam, (NLL) Rept. F35 (1949)
52. Timman, R.A. The Theory of Three-Dimensional Boundary Layers. Symposium on Boundary Layer Effects in Aerodynamics, National Physical Laboratory (1955)
53. Timman, R.A.
Zaat, J.A. Eine Rechenmethode für dreidimensionale laminare Grenzschichten. 50 Jahre Grenzschichtforschung (1955). Friedr. Vieweg. u. Sohn Braunschweig.
54. Truckenbrodt, E. Ein Quadraturverfahren zur Berechnung der laminaren und turbulenten Reibungsschicht bei ebener und rotationssymmetrischer Strömung. *Ing. Arch.*, 20, 14, pp. 211-228 (1952)
55. Lindfield, A.W.
Pinsent, H.G.
Pinsent, P.A. Approximate Methods for Calculating Three-Dimensional Boundary Layer Flow on Wings. Boundary Layer and Flow Control, edited by G.V. Lachmann, Pergamon Press, London (1961)
56. Eichelbrenner, E.A. La Couche Limité Tridimensionnelle en Régime Turbulent d'un Fluide Compressible: Cas de la Paroi Athermale. AGARD Specialists' Meeting, Part 2, pp. 795-828, Naples, Italy (May 1965)
57. Eichelbrenner, E.A.
Peube, J.L. Theoretical and Experimental Investigations on Three-Dimensional Boundary Layers, in Particular on Problems of Transition, Separation and Reattachment. Final Report, ONR Contract N62558-3863 (Sept. 1966)
58. Zaat, J.A.
van Spiegel, E.
Timman, R.A. The Three-Dimensional Laminar Boundary Layer Flow About a Yawed Ellipsoid at Zero Incidence. NLL Rept. F 165 (1955)
59. Head, M.R. An Approximate Method of Calculating the Laminar Boundary Layer in Two-Dimensional Incompressible Flow. ARC, R & M 3123 (March 1957)
60. Marrone, P.V. Normal Shock Waves in Air: Equilibrium Composition and Flow Parameters for Velocities from 26,000 to 50,000 ft/sec. CAL Rept. AG-1729-A-2 (1962)
61. Hayes, W.D.
Probstein, R.F. Hypersonic Flow Theory. Academic Press, New York, 1959
62. Cohen, C.B.
Reshotko, E. Similar Solutions for the Compressible Laminar Boundary Layer with Heat Transfer and Pressure Gradient. NACA Rept. 1293 (1956)

APPENDIX

From the profile functions defined in Section 3.2 we have:

$P_1 = \int_0^1 (1-m_1) m_1 d\eta = 0.114286$	$P_{15} = \int_0^1 m_1 m_4 d\eta = 0.047519$
$P_2 = \int_0^1 (1-2m_1) m_2 d\eta = 0.00953$	$P_{16} = \int_0^1 m_2 m_4 d\eta = 0.0075397$
$P_3 = \int_0^1 m_1^2 d\eta = 0.00396825$	$P_{17} = \int_0^1 m_1 m_3 d\eta = 0.0045535$
$P_4 = \int_0^1 k m_1 d\eta = 0.0756331$	$P_{18} = \int_0^1 m_2 m_3 d\eta = 0.00059524$
$P_5 = \int_0^1 k m_2 d\eta = 0.015252$	$P_{19} = \int_0^1 (1-m_5) k d\eta = 0.139727$
$P_6 = \int_0^1 g m_1 d\eta = -0.0064069$	$P_{20} = \int_0^1 (1-m_5) g d\eta = -0.0219595$
$P_7 = \int_0^1 g m_2 d\eta = -0.0021876$	$P_{21} = \int_0^1 m_4 k d\eta = 0.0289805$
$P_8 = \int_0^1 k d\eta = 0.187303$	$P_{22} = \int_0^1 m_3 k d\eta = 0.00228809$
$P_9 = \int_0^1 g d\eta = -0.0252027$	$P_{23} = \int_0^1 m_4 g d\eta = -0.0037695$
$P_{10} = \int_0^1 k^2 d\eta = 0.0589253$	$P_{24} = \int_0^1 m_3 g d\eta = -0.00026364$
$P_{11} = \int_0^1 k g d\eta = -0.0083928$	$P_{25} = \int_0^1 (m_5 - m_1) d\eta = -0.1$
$P_{12} = \int_0^1 g^2 d\eta = 0.0014283$	$P_{26} = \int_0^1 m_2 d\eta = 0.050$
$P_{13} = \int_0^1 m_1 (1-m_5) d\eta = 0.169047$	$P_{27} = \int_0^1 (1-m_5) d\eta = 0.50$
$P_{14} = \int_0^1 m_2 (1-m_5) d\eta = 0.036905$	$P_{28} = \int_0^1 m_4 d\eta = 0.10$
	$P_{29} = \int_0^1 m_3 d\eta = 0.008333$

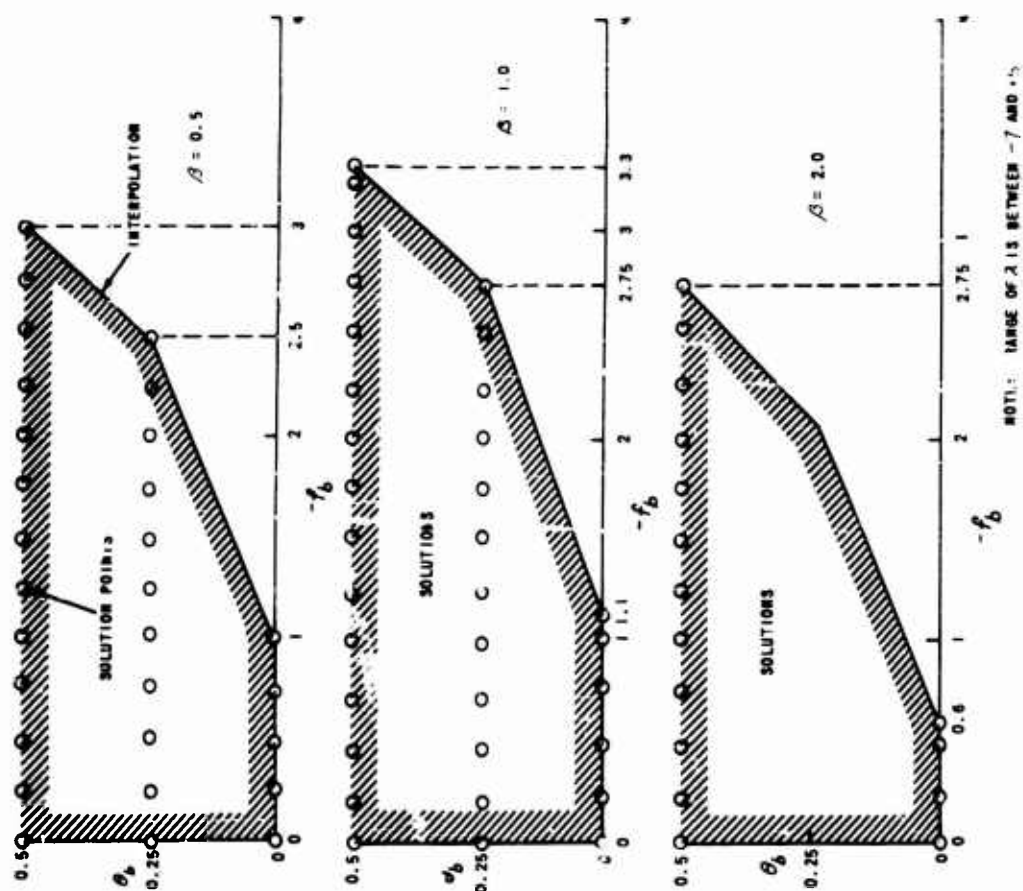


Fig. 2 Solutions that have been completed in Section 2

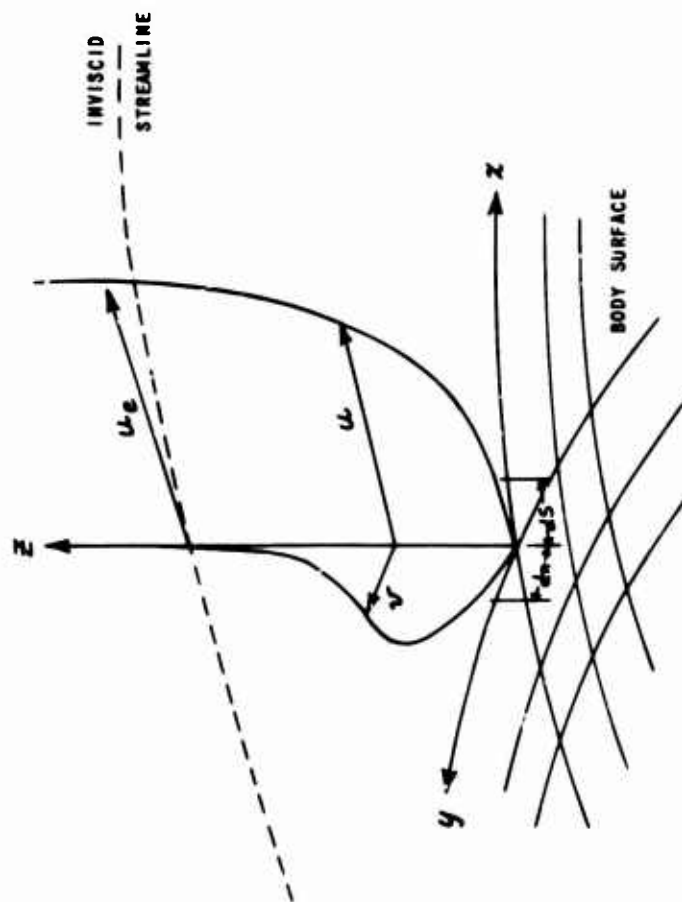


Fig. 1 Coordinate System

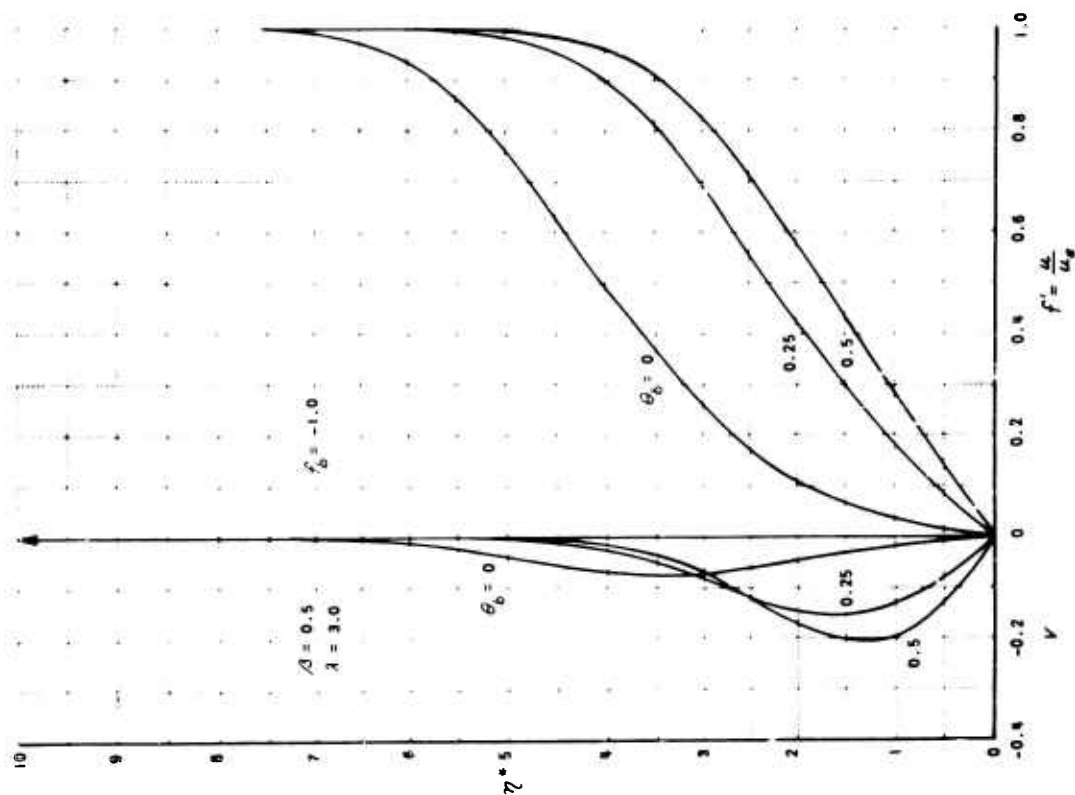


Fig. 3 Velocity Profiles for Various Wall Temperatures ($f_b = 0$)

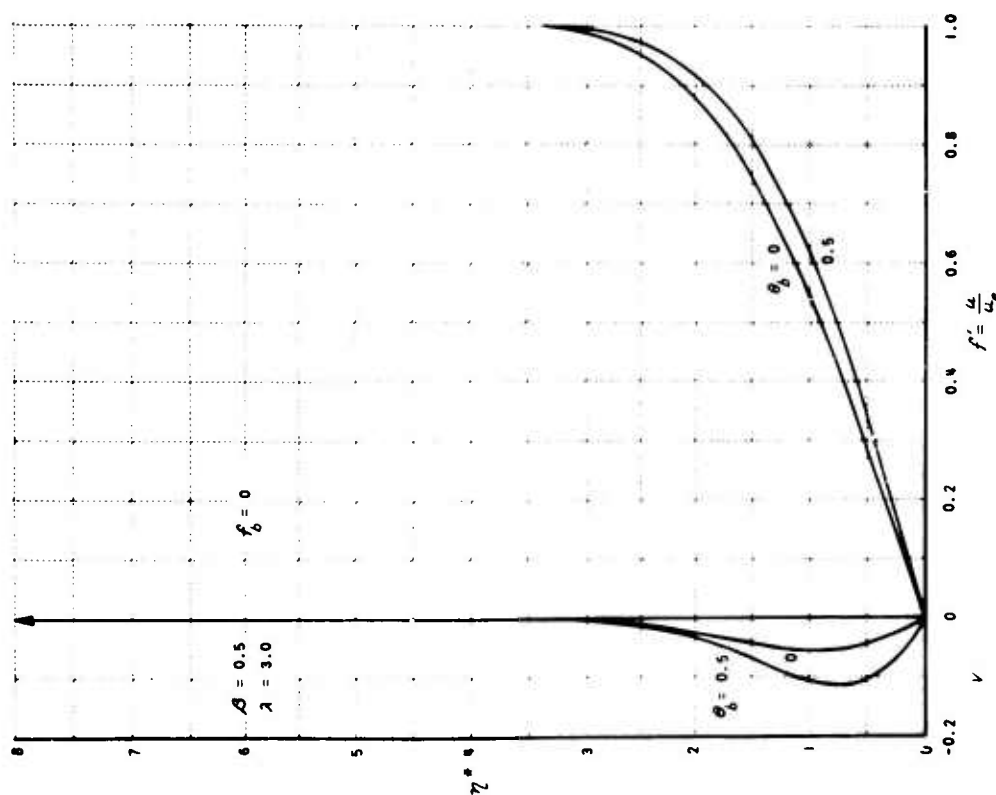


Fig. 4 Velocity Profiles for Various Wall Temperatures ($f_b = -1.0$)

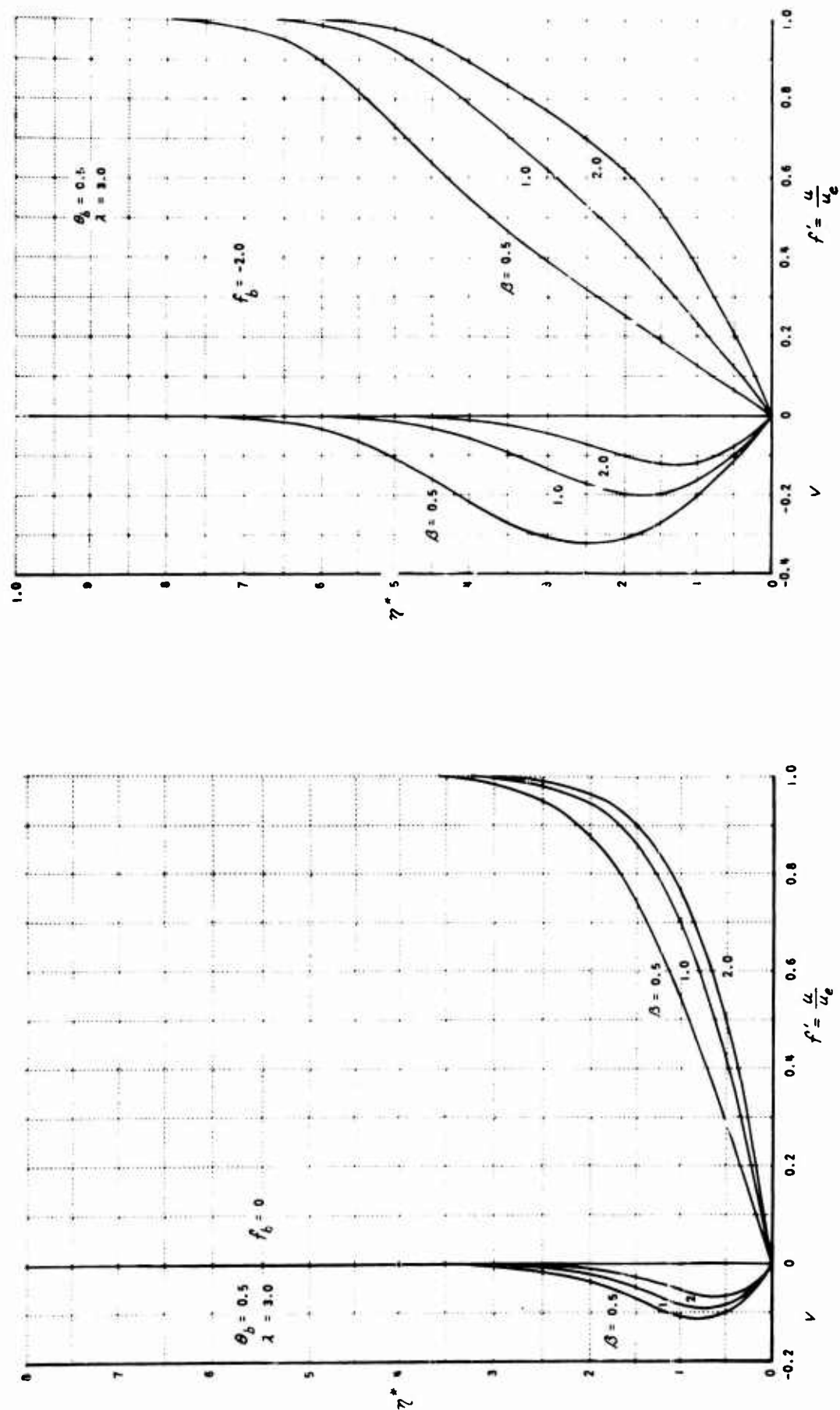


Fig. 5 Velocity Profiles for Various Values of Streamwise Pressure-Gradient Parameter ($f_b' = 0$)

Fig. 6 Velocity Profiles for Various Values of Streamwise Pressure-Gradient Parameter ($f_b' = -2.0$)

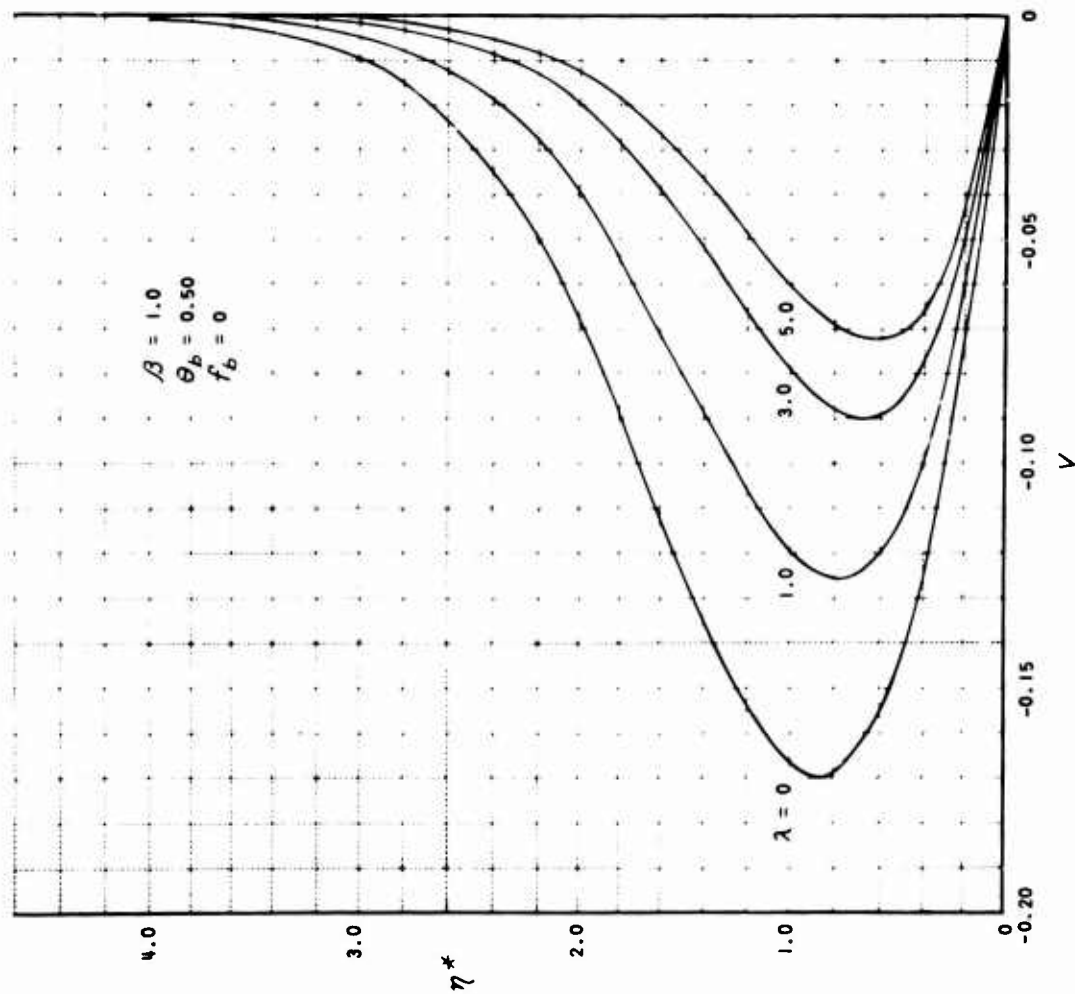


Fig. 7 Profiles of the Secondary-Flow Velocity Parameter for Positive Values of λ ($f_b = 0$)

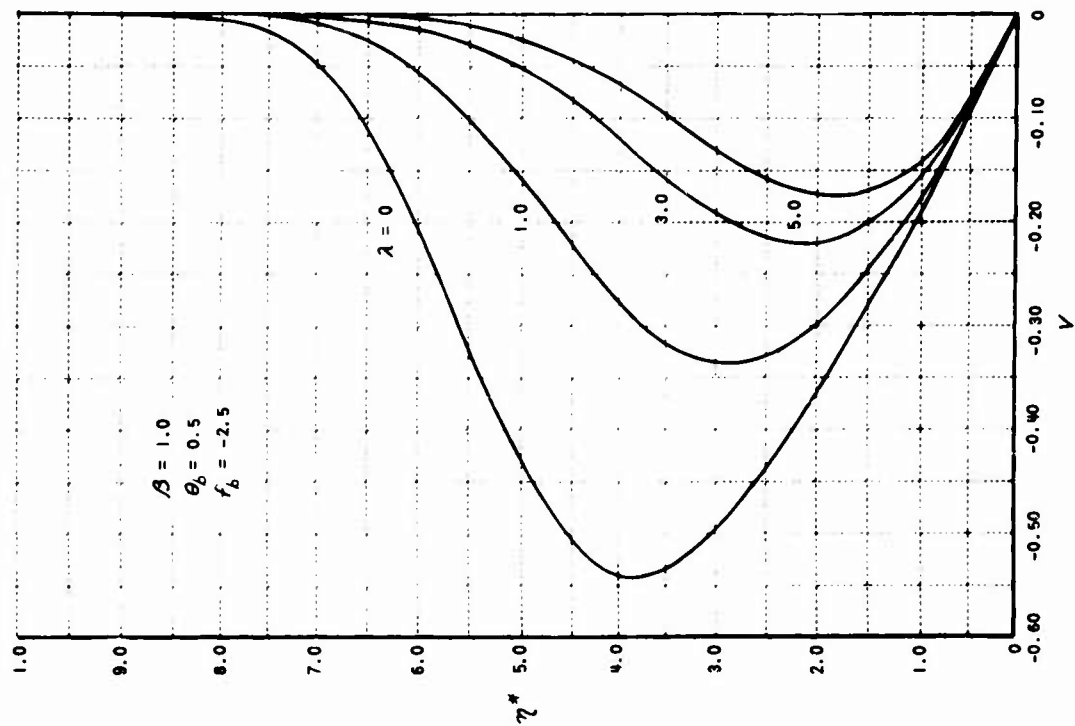


Fig. 8 Profiles of the Secondary-Flow Velocity Parameter for Positive Values of λ ($f_b = -2.5$)

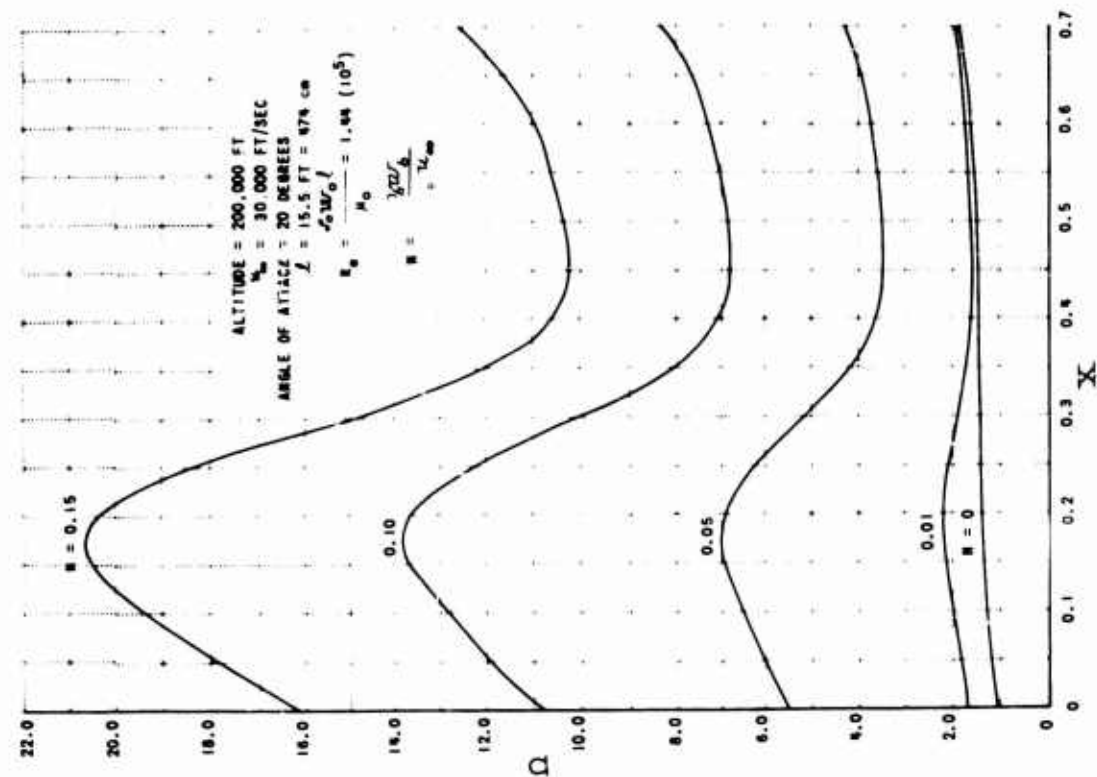


Fig. 10 Distributions of "Boundary-Layer Thickness" along Streamline for Various Mass-Injection Rates

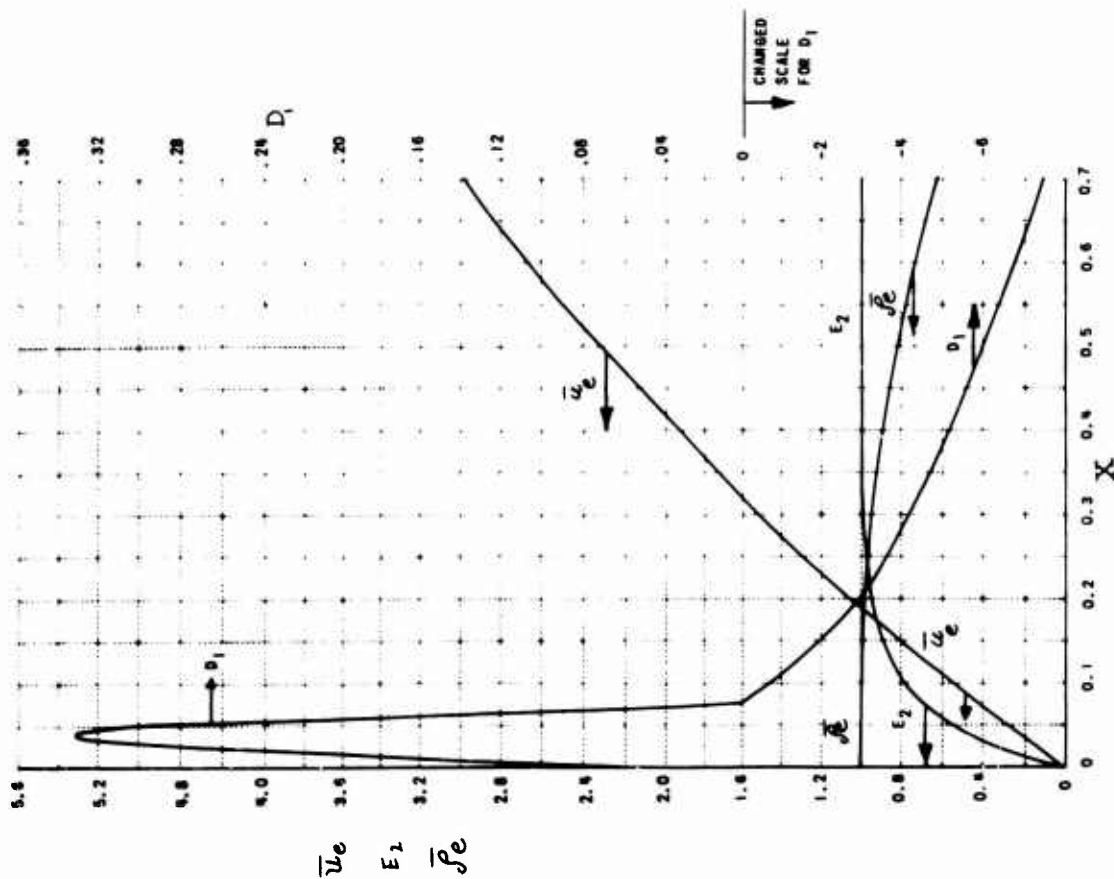


Fig. 9 Distributions of Flow Properties along Streamline

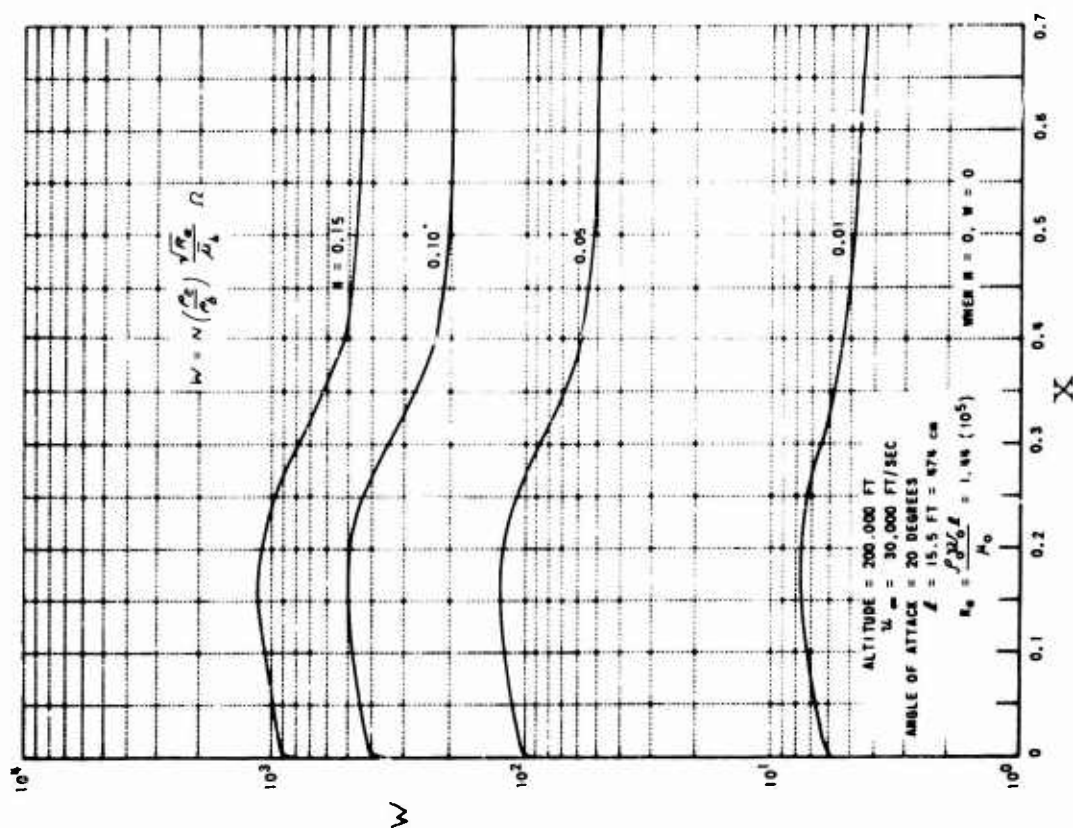


Fig. 12 Distributions of Mass-Injection Parameter along Streamline

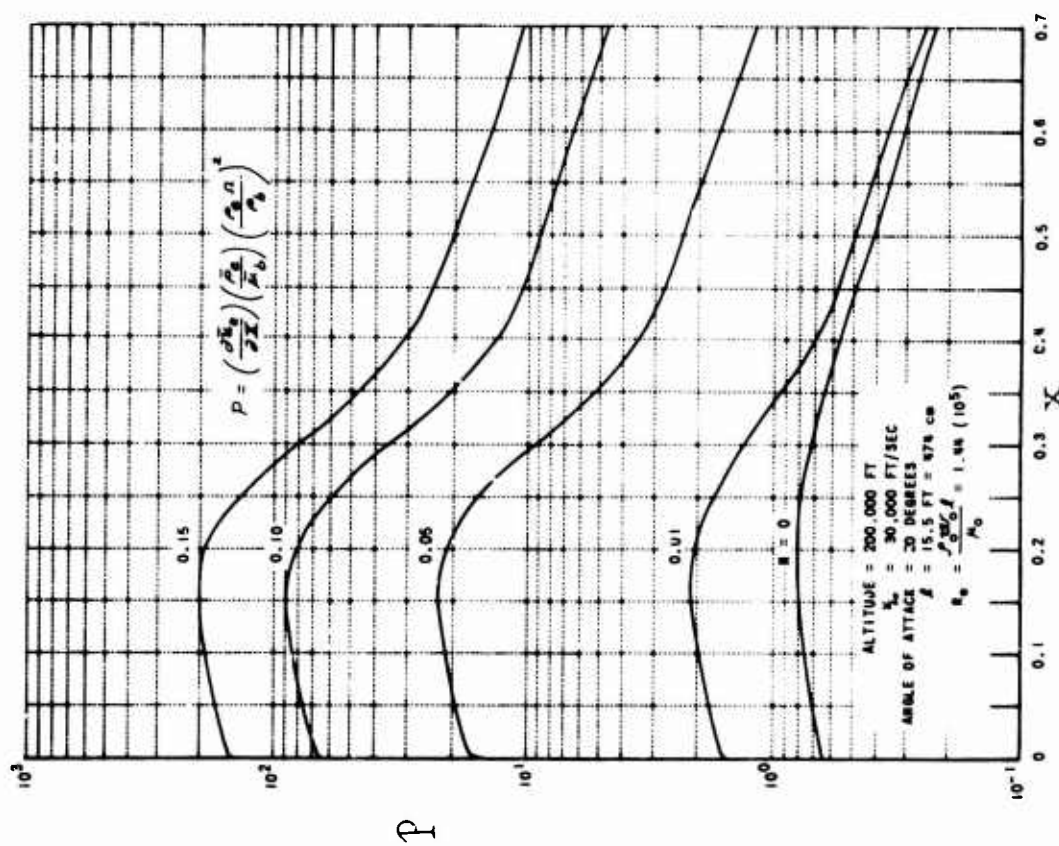


Fig. 11 Distributions of Pressure-Gradient Parameter along Streamline for Various Mass-Injection Rates

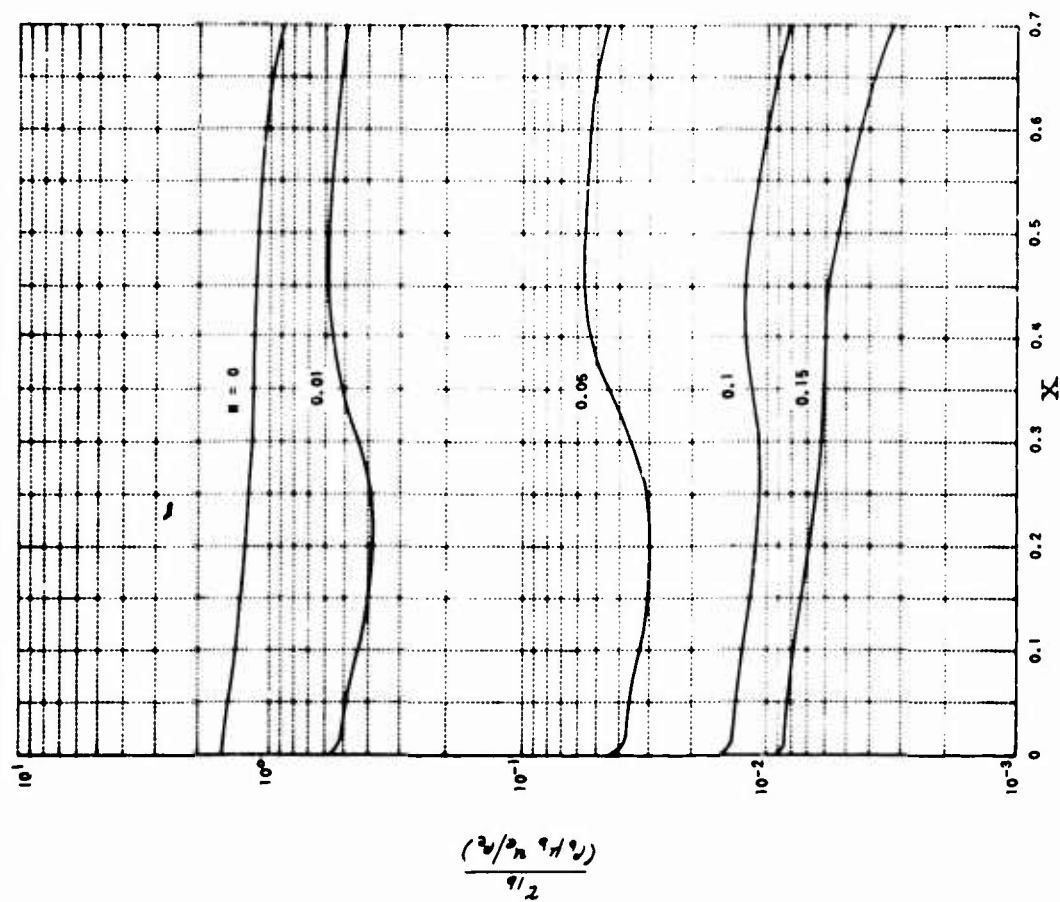


Fig. 13 Distributions of Streamwise Wall Shear along Streamline for Various Mass-Injection Rates

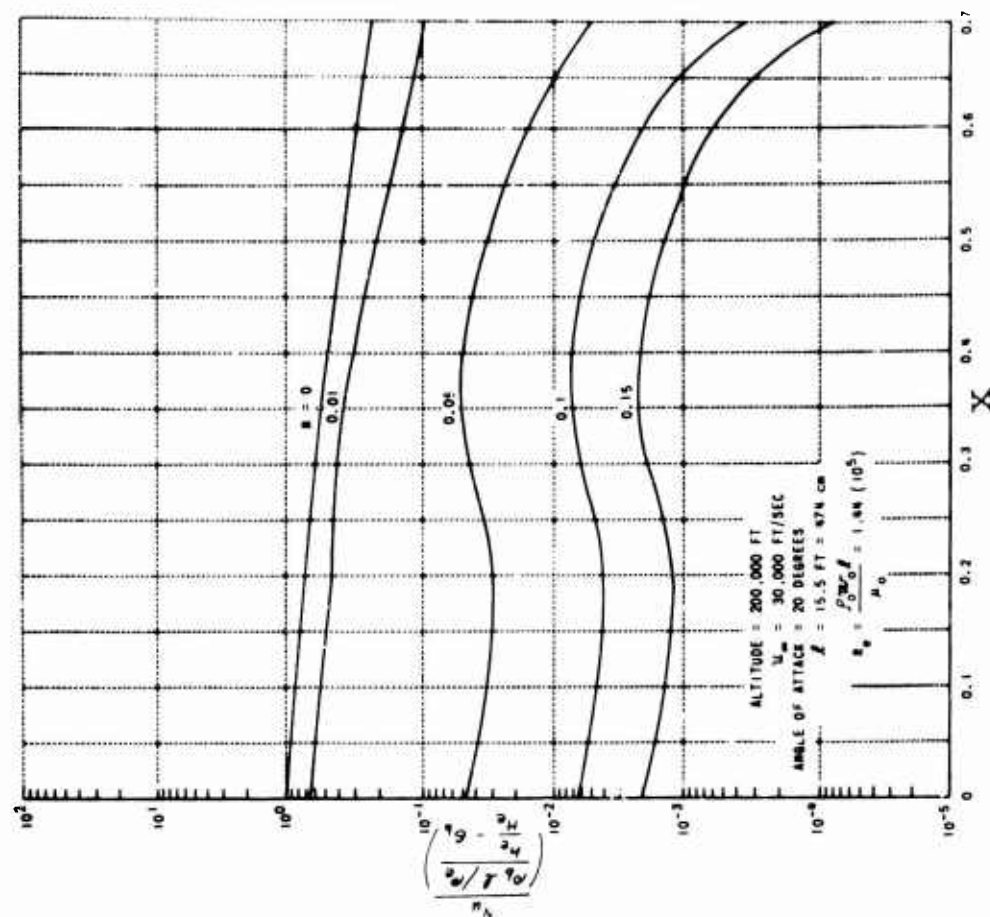


Fig. 14 Distributions of Heat-Transfer Parameter along Streamline for Various Mass-Injection Rates

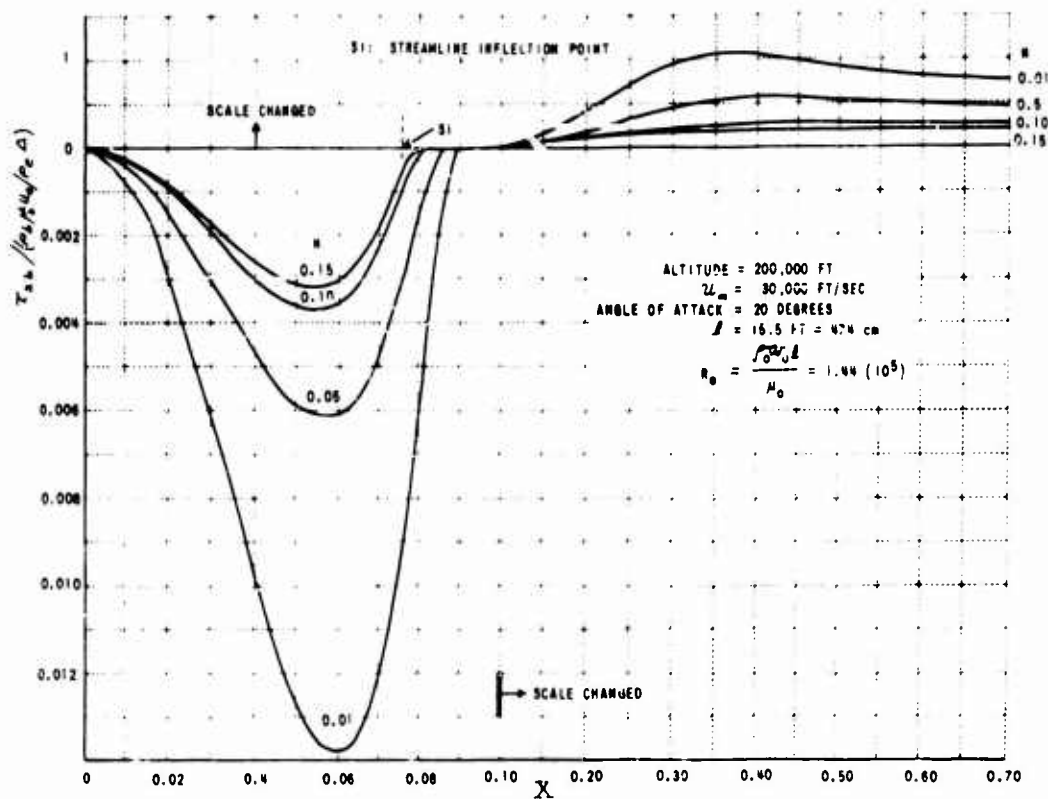


Fig. 15 Distributions of Transverse Wall Shear along Streamline for Various Mass-Injection Rates

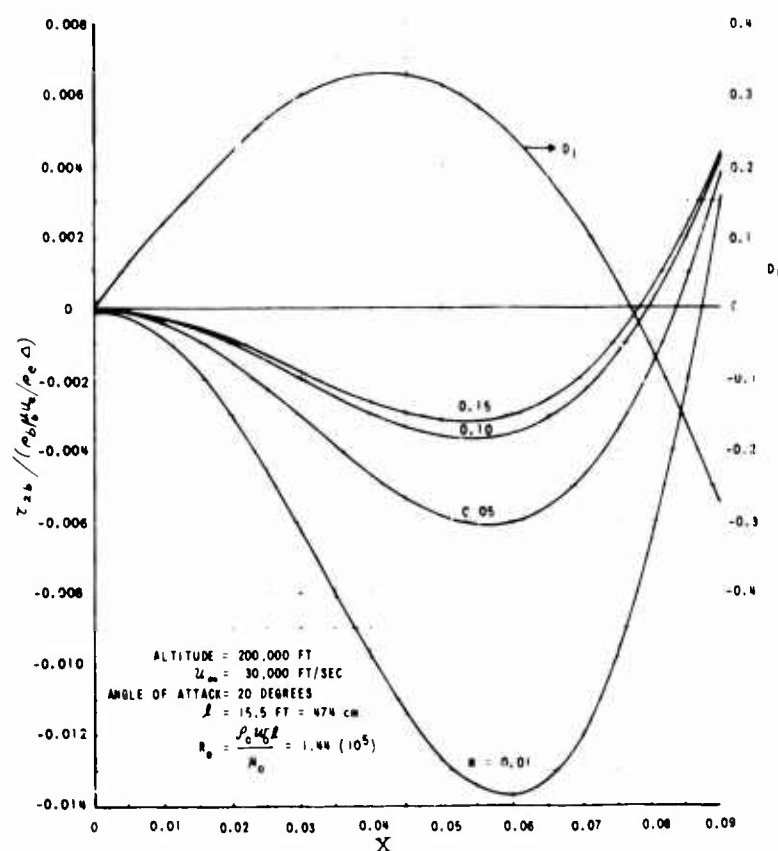


Fig. 16 Distributions of Transverse Wall Shear along Streamline for Various Mass-Injection Rates

Information regarding the availability of further copies of AGARD publications may be obtained from

The Scientific Publications Officer,
Advisory Group for Aerospace Research and Development,
7, rue Ancelle,
92 Neuilly-sur-Seine,
France.